Solid Mechanics and Its Applications

Oana Cazacu · Benoit Revil-Baudard
Nitin Chandola

Plasticity–Damage Couplings: From Single Crystal to Polycrystalline Materials

Springer

Solid Mechanics and Its Applications

Volume 253

Aims and Scope of the Series

The fundamental questions arising in mechanics are: *Why*?, *How*?, and *How much*? The aim of this series is to provide lucid accounts written by authoritative researchers giving vision and insight in answering these questions on the subject of mechanics as it relates to solids.

The scope of the series covers the entire spectrum of solid mechanics. Thus it includes the foundation of mechanics; variational formulations; computational mechanics; statics, kinematics and dynamics of rigid and elastic bodies: vibrations of solids and structures; dynamical systems and chaos; the theories of elasticity, plasticity and viscoelasticity; composite materials; rods, beams, shells and membranes; structural control and stability; soils, rocks and geomechanics; fracture; tribology; experimental mechanics; biomechanics and machine design.

The median level of presentation is to the first year graduate student. Some texts are monographs defining the current state of the field; others are accessible to final year undergraduates; but essentially the emphasis is on readability and clarity.

More information about this series at http://www.springer.com/series/6557

Oana Cazacu · Benoit Revil-Baudard
Nitin Chandola

Plasticity–Damage Couplings: From Single Crystal to Polycrystalline Materials

Springer

Oana Cazacu
Department of Mechanical and Aerospace Engineering
University of Florida/REEF
Shalimar, FL
USA

Nitin Chandola
Department of Mechanical and Aerospace Engineering
University of Florida/REEF
Shalimar, FL
USA

Benoit Revil-Baudard
Department of Mechanical and Aerospace Engineering
University of Florida/REEF
Shalimar, FL
USA

ISSN 0925-0042 ISSN 2214-7764 (electronic)
Solid Mechanics and Its Applications
ISBN 978-3-319-92921-7 ISBN 978-3-319-92922-4 (eBook)
https://doi.org/10.1007/978-3-319-92922-4

Library of Congress Control Number: 2018942930

Printed on acid-free paper

This Springer imprint is published by the registered company Springer International Publishing AG part of Springer Nature
The registered company address is: Gewerbestrasse 11, 6330 Cham, Switzerland

Preface

Advances in the theory of plasticity and damage of metallic materials are driven by the demand to improve performance and safety of structures and machine parts while reducing the environmental impact and manufacturing cost. While the last decade has seen increased efforts in the automotive, aerospace, and energy industries toward development of new lightweight and high-strength alloys, the challenges associated with predicting the mechanical behavior of these materials can be overcome only by development of new and more realistic models that are applicable to general three-dimensional loadings.

Designed as a well-balanced blend of theory and applications, the book presents a unified and rigorous framework for description of the main dissipative phenomena in metallic materials: plasticity and damage. Being based on the theory of representation of tensor functions, and theorems for scale bridging, this framework enables development of constitutive models that account for the influence of the crystallographic structure and deformation mechanisms on the macroscopic behavior. Recent constitutive models developed by the authors that are currently accessible only in journal articles widely scattered through the literature are presented in this book. The emphasis is on providing the reader with a clear understanding of the range of applicability of any given model, its capabilities, and its limitations. Furthermore, for any given model procedures for the identification of the parameters are provided along with key concepts necessary to numerically solve boundary-value problems.

While this book is based on the research of the authors in the field of plasticity and ductile damage, we made a point to give detailed explanations completed with mathematical proofs and numerous examples such as to facilitate the application of the constitutive models presented and their transition to industry. We trust that the book will be useful to engineers, scientists, and graduate students alike.

In Chap. 1 of the book are introduced the key mathematical concepts and theorems that will be used to develop constitutive models along with the constitutive assumptions that are at the foundation of the theory of plasticity. While in the literature, there is ample exposure of elastic–plastic models formulated in the stress space, the dual formulations in the strain-rate space are less known. Chapter 2

presents both approaches to modeling plasticity along with the numerical integration algorithms for solving boundary-value problems within the framework of the finite-element method.

Chapter 3 is devoted to constitutive relations for metallic single crystals. After introducing the key concepts of crystallography, an overview of the experimental evidence of plastic deformation mechanisms is presented. The yield criteria for description of the onset of plastic deformation in cubic crystals are introduced. Application of the most recent single crystal yield criterion to the prediction of the directionality of the macroscopic tensile properties of polycrystalline sheets are also provided.

Chapter 4 is devoted to modeling the plastic behavior of isotropic polycrystalline metallic materials. A review of the classic yield criteria and corresponding stress-based plastic potentials with discussion concerning the predicted mechanical response for various three-dimensional loadings is presented along with the most recent contributions devoted to the description of the behavior of incompressible materials displaying tension–compression asymmetry. On the basis of these new models, a new interpretation and explanation of the Swift phenomenon occurring in monotonic and cyclic free-end torsion are provided.

Chapter 5 is devoted to modeling the elastic–plastic behavior of anisotropic polycrystalline metals. After introducing the only two rigorous methodologies for extending isotropic formulations such as to account for anisotropy, the most versatile three-dimensional orthotropic yield criteria for materials with the same response in tension and in compression are presented. While the need for analytic yield criteria that account for both anisotropy and tension–compression asymmetry in the plastic deformation of hexagonal materials such as magnesium, zirconium, and titanium alloys has long been recognized, only recently models that describe these key features have been developed. These contributions along with applications for a variety of loadings are discussed.

Although the existence of strain-rate-based potentials which are work-conjugate of given stress potentials has been theoretically demonstrated, analytical expressions of strain-rate potentials are only known for a very few cases. In Chap. 6, closed-form expressions for strain-rate based plastic potentials are derived for both isotropic and anisotropic fully-dense polycrystalline materials. Besides their intrinsic importance in design and optimization of metal forming processes, these analytic strain-rate potentials enable the development of closed-form expressions of plastic potentials for porous metallic materials that are presented in Chaps. 7 and 8.

Specifically, key contributions toward elucidating the role of the plastic deformation on damage evolution for both isotropic (Chap. 7) and anisotropic metallic materials (Chap. 8) are introduced. The ductile damage models presented are derived using rigorous upscaling techniques and limit-analysis methods. Along with classical models for porous metals, the latest research work done on this subject is presented. Special attention is given to the contributions toward solving open problems posed in the mechanics community in the late 1960s concerning modeling the plastic behavior of porous materials, notably on the manner in which the matrix plastic behavior influences the rate of damage evolution under given loading conditions. In view

of their importance for the prediction of plasticity–damage couplings in hcp-Ti, recent models that account for both anisotropy and tension–compression asymmetry on yielding and damage evolution are discussed. Moreover, new single crystal models accounting for the combined effects of the stress path and crystal orientation on porosity evolution under creep loadings are described.

As the reader may see from the foregoing presentation, this book gathers numerous mathematical models developed to predict the plastic behavior and plasticity–damage couplings for a large range of materials from single crystals to anisotropic polycrystalline materials. However, the book is far more than a collection of constitutive models. The rationale for adopting the respective constitutive hypotheses is provided for each constitutive model, so the readers will have appreciation of the importance of using the appropriate model for each type of material and gain full understanding of the range of applicability of each model.

We are grateful to our teachers and collaborators who have influenced and contributed to our research. Research funding on plasticity provided to Oana Cazacu by NSF, US Air Force, and US Army, over the years, is gratefully acknowledged. Funding provided by the Army Research Office, grant W911NF-16-1-0159, has greatly facilitated writing of this book.

Shalimar, USA

Oana Cazacu
Benoit Revil-Baudard
Nitin Chandola

Contents

Chapter 1
Mathematical Framework

The theory of scalar- and tensor-valued functions constitutes the mathematical framework based on which modeling of the elasticity, plasticity, and damage in polycrystalline metallic materials is built. In this chapter, we provide the basic concepts and key mathematical results to be used in the rest of the book.

We begin by presenting a concise survey of the basic results of vector algebra. This is also a natural starting point for the development of *tensor* algebra.

1.1 Elements of Vector Algebra

From elementary geometry, we know that to every three-dimensional point space, E, we can associate a vector space, V. An element of E is a point in space and a free vector connects any two points. A free vector is characterized by direction, magnitude, and sense. Free vectors can be added together and multiplied by numbers.

The generalization of the properties of free vectors of elementary geometry led to the general concept of vector space.

Definition of a Vector Space

A set V is called a vector space over the field R of real numbers, and its elements are called vectors, if the following conditions are fulfilled:

(I) To any pair of vectors $\mathbf{u}, \mathbf{v} \in V$, corresponds a vector $\mathbf{u}+\mathbf{v} \in V$, called the sum of these vectors, such that:

(V.1) $\mathbf{u}+\mathbf{v}=\mathbf{v}+\mathbf{u}$ (commutativity),
(V.2) For any three vectors $\mathbf{u}, \mathbf{v}, \mathbf{w}$: $\mathbf{u}+(\mathbf{v}+\mathbf{w})=(\mathbf{u}+\mathbf{v})+\mathbf{w}$ (associativity),

O. Cazacu et al., *Plasticity–Damage Couplings: From Single Crystal to Polycrystalline Materials*, Solid Mechanics and Its Applications 253,
https://doi.org/10.1007/978-3-319-92922-4_1

(V.3) There exists an element of V, called the zero vector (or null vector), denoted by $\mathbf{0}$ such that for any vector $\mathbf{u} \in V$: $\mathbf{u} = \mathbf{u} + \mathbf{0}$.
(V.4) For any vector $\mathbf{u}$, there exists another vector, denoted –$\mathbf{u}$, such that $\mathbf{u} + (-\mathbf{u}) = \mathbf{0}$.

(II) The product of any vector $\mathbf{u} \in V$ with a real number α is also a vector. It has the following properties:

(V.5) For any $\alpha, \beta \in R, \alpha(\beta\mathbf{u}) = (\alpha\beta)\mathbf{u}$ (associativity),
(V.6) $(\alpha + \beta)\mathbf{u} = \alpha\mathbf{u} + \beta\mathbf{u}$ (distributivity relative to number addition),
(V.7) $\alpha(\mathbf{u} + \mathbf{v}) = \alpha\mathbf{u} + \alpha\mathbf{v}$ (distributivity relative to vector addition),
(V.8) $1\mathbf{u} = \mathbf{u}$.

Using the above axioms, it can be shown that the following relations hold:

$$0\mathbf{u} = \mathbf{0}, (-1)\mathbf{u} = -\mathbf{u}, \alpha\mathbf{0} = \mathbf{0}.$$

The difference between any two vectors $\mathbf{u}$ and $\mathbf{v}$ is defined as:

$$\mathbf{u} - \mathbf{v} = \mathbf{u} + (-\mathbf{v}).$$

Linear Independence of Vectors

Definition A set of n vectors $\mathbf{u}_1, \mathbf{u}_2, \ldots, \mathbf{u}_n$ is said to be linearly independent if the relation:

$$\alpha_1\mathbf{u}_1 + \alpha_2\mathbf{u}_2 + \cdots + \alpha_n\mathbf{u}_n = \mathbf{0},$$

with $\alpha_1, \ldots, \alpha_n \in R$, can take place if and only if: $\alpha_1 = \alpha_2 = \cdots = \alpha_n = 0$. Otherwise, the set of vectors is said to be linearly dependent.

Dimension of a Vector Space

Definition A vector space V is called n-dimensional, if in V there exists at least one set of n linearly independent vectors, and any set containing $n + 1$ vectors is linearly dependent.

Basis of a Vector Space

Definition In an n-dimensional vector space V, any set of n linearly independent vectors is called a basis of V.

Inner Product

Definition Let V be a vector space. An application which associates to any vectors $\mathbf{u}$ and $\mathbf{v} \in V$ a real number, denoted $\mathbf{u} \cdot \mathbf{v}$, is called an inner product if it satisfies the following properties:

(I1) $\mathbf{u} \cdot \mathbf{v} = \mathbf{v} \cdot \mathbf{u}$ (commutativity);
(I2) For any $\alpha \in R$: $(\alpha \mathbf{u}) \cdot \mathbf{v} = \alpha(\mathbf{u} \cdot \mathbf{v})$ (associativity with respect to multiplication with real numbers);
(I3) $\mathbf{u} \cdot (\mathbf{v} + \mathbf{w}) = \mathbf{u} \cdot \mathbf{v} + \mathbf{u} \cdot \mathbf{w}$ (distributivity with respect to vector addition);
(I4) $\mathbf{u} \cdot \mathbf{u} \geq 0$;
(I5) $\mathbf{u} \cdot \mathbf{u} = 0$ if and only if $\mathbf{u} = \mathbf{0}$.

The scalar product can then be used to define the *norm* (or magnitude) of any vector $\mathbf{u} \in V$. The *norm* of the vector $\mathbf{u}$ is defined by:

$$|\mathbf{u}| = \sqrt{\mathbf{u} \cdot \mathbf{u}}, \tag{1.1}$$

and a vector with unit norm is termed a *unit vector*. By definition, two vectors are said to be *orthogonal* if their inner product is zero.

Euclidean Vector Space

Definition A vector space V endowed with an inner product is called a Euclidean vector space.

Einstein Summation Convention

In this book, we adopt the Einstein summation convention which states that whenever the same letter subscript occurs twice in a term, that subscript is to be given all possible values and the results added together. For example, if $i = 1, \ldots, 3$, then, $u_i^2 = u_1^2 + u_2^2 + u_3^2$

Components of a Vector

Theorem 1.1 *Let* $\mathbf{g}_1, \mathbf{g}_2, \ldots, \mathbf{g}_n$ *be a basis for the n-dimensional vector space V. Any vector* $\mathbf{u} \in V$ *may be uniquely represented as a linear combination of the basis vectors* $\mathbf{g}_i$, $i = 1, \ldots, n$, i.e.,

$$\mathbf{u} = u_1 \mathbf{g}_1 + \cdots + u_n \mathbf{g}_n, \tag{1.2}$$

The numbers (or scalars) u_i are called the *components of* $\mathbf{u}$ relative to this basis.

Proof Since V is a n-dimensional vector space, the set of $n+1$ vectors $\{\mathbf{g}_1, \mathbf{g}_2, \ldots, \mathbf{g}_n, \mathbf{u}\}$ is linearly dependent. Hence, there exist a set of real numbers $\alpha, \alpha_1, \ldots, \alpha_n$, not all of them zero, such that

$$\alpha\mathbf{u} + \alpha_1\mathbf{g}_1 + \cdots + \alpha_n\mathbf{g}_n = \mathbf{0}, \tag{1.3}$$

Note that α ought to be nonzero. Indeed, if $\alpha = 0$ the above equation reduces to $\alpha_1\mathbf{g}_1 + \cdots + \alpha_n\mathbf{g}_n = \mathbf{0}$, and since $\mathbf{g}_1, \mathbf{g}_2, \ldots, \mathbf{g}_n$ are linearly independent, this would imply that all α_i ought to be zero. Since $\alpha \neq 0$, from Eq. (1.3) it follows that $\mathbf{u} = u_k\mathbf{g}_k$, with $u_k = -\alpha_k/\alpha$, $k = 1, \ldots, n$.

Therefore, $\mathbf{u}$ is a linear combination of the base vectors. Furthermore, the numbers u_k are uniquely determined. Indeed, $\mathbf{u}$ may also be expressed as

$$\mathbf{u} = u'_k\mathbf{g}_k, \tag{1.4}$$

by subtracting Eq. (1.2) from Eq. (1.4), we obtain

$$\left(u'_k - u_k\right)\mathbf{g}_k = \mathbf{0}.$$

Given that vectors $\mathbf{g}_k$ form a basis, it follows that necessarily $u'_k = u_k$.

Using Theorem 1.1 in conjunction with the properties (I2) and (I3), it can be easily shown that the inner product between any two vectors $\mathbf{u}$ and $\mathbf{v}$ can be expressed in component form as:

$$\mathbf{u} \cdot \mathbf{v} = g_{km}\mathrm{u}_k\mathrm{v}_m, \quad \text{with} \quad g_{km} = \mathbf{g}_k \cdot \mathbf{g}_m, k, m = 1, \ldots, n \tag{1.5}$$

Obviously, due to the commutativity of the inner product (i.e., property (I1)),

$$g_{km} = g_{mk}.$$

Given that $\{\mathbf{g}_k\}$ form a basis, it can also be easily shown that the determinant of the matrix $[g_{km}]$ is nonzero.

Orthonormal Basis

A basis $\{\mathbf{e}_1, \mathbf{e}_2, \ldots, \mathbf{e}_n\}$ of the n-dimensional vector space V is called orthonormal, if any two vectors of the basis are mutually orthogonal and of unit length, i.e.,

$$\mathbf{e}_i \cdot \mathbf{e}_j = \delta_{ij}, \tag{1.6}$$

where δ_{ij} denotes the Kronecker delta symbol,

$$\delta_{ij} = \begin{cases} 1, & \text{if } i = j \\ 0, & \text{otherwise.} \end{cases} \tag{1.7}$$

Note that in view of the orthonormality condition (1.6), the components of a vector $\mathbf{u}$ relative to the orthonormal basis $\{\mathbf{e}_1, \mathbf{e}_2, \ldots, \mathbf{e}_n\}$ are:

$$u_k = \mathbf{u} \cdot \mathbf{e}_k. \tag{1.8}$$

Let $\mathbf{u}$ and $\mathbf{v}$ be an arbitrary pair of vectors having components u_k, v_k relative to the same basis. Then, using Eqs. (1.5) and (1.6), we obtain:

$$\mathbf{u} \cdot \mathbf{v} = u_k \mathrm{v}_k. \tag{1.9}$$

Cross Product

Definition An application which associates to any vectors $\mathbf{u}$ and $\mathbf{v} \in V$ a vector denoted $\mathbf{u} \times \mathbf{v}$, is called the cross product (or vector product) of $\mathbf{u}$ and $\mathbf{v}$ if it satisfies the following properties:

(C1) $\mathbf{u} \times \mathbf{v} = -\mathbf{v} \times \mathbf{u}$ for any $\mathbf{u}, \mathbf{v} \in V$ (anti-commutativity);
(C2) $(\alpha\mathbf{v} + \beta\mathbf{w}) \times \mathbf{u} = \alpha(\mathbf{v} \times \mathbf{u}) + \beta(\mathbf{w} \times \mathbf{u})$ for any $\mathbf{u}, \mathbf{v}, \mathbf{w} \in V$ and $\alpha, \beta \in R$;
(C3) $\mathbf{u} \cdot (\mathbf{u} \times \mathbf{v}) = \mathbf{0}$ for any $\mathbf{u}, \mathbf{v} \in V$;
(C4) $(\mathbf{u} \times \mathbf{v}) \cdot (\mathbf{u} \times \mathbf{v}) = (\mathbf{u} \cdot \mathbf{u})(\mathbf{v} \cdot \mathbf{v}) - (\mathbf{u} \cdot \mathbf{v})^2$ for any $\mathbf{u}, \mathbf{v} \in V$.

Using the above properties, it can be easily shown that $\mathbf{u} \times \mathbf{v} = \mathbf{0}$ if and only if $\mathbf{u}$ and $\mathbf{v}$ are linearly dependent.

Scalar Triple Product

The scalar triple product of three vectors $\mathbf{u}, \mathbf{v}, \mathbf{w}$, denoted by $[\mathbf{u}, \mathbf{v}, \mathbf{w}]$, is defined by:

$$[\mathbf{u}, \mathbf{v}, \mathbf{w}] = \mathbf{u} \cdot (\mathbf{v} \times \mathbf{w}). \tag{1.10}$$

Properties of the Scalar Triple Product

- The scalar triple product is invariant under a circular permutation of the members of the product, i.e., $[\mathbf{u}, \mathbf{v}, \mathbf{w}] = [\mathbf{v}, \mathbf{w}, \mathbf{u}] = [\mathbf{w}, \mathbf{u}, \mathbf{v}]$.
- The sign of scalar triple product is reversed when the second and third members of the product are reversed, i.e., $[\mathbf{u}, \mathbf{v}, \mathbf{w}] = -[\mathbf{u}, \mathbf{w}, \mathbf{v}] = -[\mathbf{v}, \mathbf{u}, \mathbf{w}] = -[\mathbf{w}, \mathbf{v}, \mathbf{u}]$.
- The scalar triple product is equal to zero if and only if $\mathbf{u}, \mathbf{v}$ and $\mathbf{w}$ are linearly dependent.
- For any $\mathbf{u}, \mathbf{v}, \mathbf{t}, \mathbf{w} \in V$ and $\alpha, \beta \in R$: $[\alpha\mathbf{u} + \beta\mathbf{v}, \mathbf{t}, \mathbf{w}] = \alpha[\mathbf{u}, \mathbf{t}, \mathbf{w}] + \beta[\mathbf{v}, \mathbf{t}, \mathbf{w}]$.

In a three-dimensional vector space, there exists an orthonormal basis $(\mathbf{e}_k)_{k=1,\ldots,3}$. Based on the properties of the cross product and scalar triple product, it follows that:

$$\mathbf{e}_2 \times \mathbf{e}_3 = [\mathbf{e}_1, \mathbf{e}_2, \mathbf{e}_3]\mathbf{e}_1, \mathbf{e}_3 \times \mathbf{e}_1 = [\mathbf{e}_1, \mathbf{e}_2, \mathbf{e}_3]\mathbf{e}_2, \mathbf{e}_1 \times \mathbf{e}_2 = [\mathbf{e}_1, \mathbf{e}_2, \mathbf{e}_3]\mathbf{e}_3 \tag{1.11}$$

$$[\mathbf{e}_1, \mathbf{e}_2, \mathbf{e}_3] = \pm 1 \tag{1.12}$$

Let ε_{ijk} designate the Ricci symbol, which takes the value 1 when (i, j, k) is a cyclic permutation of 1, 2, 3, and the value (-1) when (i, j, k) is a anticyclic permutation of 1, 2, 3, and it is otherwise zero. Therefore,

$$\mathbf{e}_i \times \mathbf{e}_j = \pm \varepsilon_{ijk}\mathbf{e}_k. \tag{1.13}$$

Two bases are said to be similar if their triple products have the same sign.

A basis $\{\mathbf{e}_1, \mathbf{e}_2, \mathbf{e}_3\}$ is said to be positively oriented if $[\mathbf{e}_1, \mathbf{e}_2, \mathbf{e}_3] > 0$.

The formula for the cross product between any two vectors in terms of their components relative to the orthonormal basis $(\mathbf{e}_k)_{k=1,\ldots,3}$ is found by using the axioms (C1)–(C2) and Eq. (1.13):

$$\mathbf{u} \times \mathbf{v} = \pm \varepsilon_{ijk} u_i \mathrm{v}_j \mathbf{e}_k, \tag{1.14}$$

Also, using Eq. (1.14) one obtains the formula for the scalar triple product of any three vectors $\mathbf{u}, \mathbf{v}, \mathbf{w}$ to be:

$$[\mathbf{u}, \mathbf{v}, \mathbf{w}] = \pm \varepsilon_{ijk} u_i \mathrm{v}_j \mathrm{w}_k. \tag{1.15}$$

If the basis is positively oriented, the scalar triple product is the determinant of the matrix having on the first row the components of $\mathbf{u}$, on the second row the components of $\mathbf{v}$, and on the third row the components of $\mathbf{w}$. In elementary geometry, the scalar product of any two nonzero free vectors $\mathbf{u}$ and $\mathbf{v}$ is designated by $\mathbf{u} \cdot \mathbf{v}$ and is defined as:

$$\mathbf{u} \cdot \mathbf{v} = |\mathbf{u}||\mathbf{v}|\cos(\theta), \tag{1.16}$$

where $|\mathbf{u}|$ and $|\mathbf{v}|$ designate the magnitude (or length) of each vector and θ is the angle between the two vectors. If one of the two vectors is zero, their inner product is, by definition, zero.

By definition, the cross product $\mathbf{u} \times \mathbf{v}$ of two free vectors $\mathbf{u}$ and $\mathbf{v}$ which are linearly independent is a vector that is orthogonal to both $\mathbf{u}$ and $\mathbf{v}$, and therefore normal to the two-dimensional plane containing them. The magnitude of $\mathbf{u} \times \mathbf{v}$ is given by,

$$\mathbf{u} \times \mathbf{v} = |\mathbf{u}||\mathbf{v}| \sin\theta \ \text{ for } (0 < \theta < \pi) \tag{1.17}$$

where θ is the angle between the vectors $\mathbf{u}, \mathbf{v}$.

It can be easily shown that the free vector space is three-dimensional (any three vectors which are not coplanar form a basis) and that the scalar product defined by Eq. (1.16) satisfies the properties (I1)–(I5) and the cross product defined by Eq. (1.17) satisfies the axioms (C1)–(C4), i.e., the space of free vectors is endowed with an inner product and a vector product.

Therefore, the 3-D physical space is a Euclidean vector space. In this space, the scalar triple product is the volume of the parallelepiped defined by the respective vectors. If this volume is nonzero, then the three vectors are linearly independent. If $\mathbf{u}, \mathbf{v}, \mathbf{w}$ are linearly independent, then the triad $\{\mathbf{u}, \mathbf{v}, \mathbf{w}\}$ forms a basis.

Cartesian Coordinate Frame

A Cartesian coordinate frame for the three-dimensional Euclidean space consists of a reference point **O** called the origin together with a positively oriented orthonormal basis $\{\mathbf{e}_1, \mathbf{e}_2, \mathbf{e}_3\}$. Being positively oriented, the basis vectors satisfy:

$$\mathbf{e}_i \cdot \mathbf{e}_j = \delta_{ij}, \quad \text{and} \quad \left[\mathbf{e}_i, \mathbf{e}_j, \mathbf{e}_k\right] = \varepsilon_{ijk}.$$

So far, we have provided a concise survey of basic results of vector algebra. A vector is also referred to as a first-order tensor, while a scalar is a tensor of order zero. In the next section, we shall introduce the concept of a second-order tensor and their properties.

1.2 Elements of Tensor Algebra

1.2.1 Second-Order Tensors

Definition A second-order tensor is a linear transformation of the vector space V into itself. Specifically, a second-order tensor **T** assigns to an arbitrary vector **v** a vector denoted by **Tv** in such a way that for any vectors **u** and **v**, and any real number α, and β:

$$\mathbf{T}(\alpha\mathbf{u} + \beta\mathbf{v}) = \alpha(\mathbf{T}\mathbf{u}) + \beta(\mathbf{T}\mathbf{v}) \tag{1.18}$$

The set of second-order tensors on the three-dimensional Euclidean vector space is denoted by L. From here on, a second-order tensor will be simply called tensor.

We say that two tensors $\mathbf{T}$ and $\mathbf{U}$ are equal if,

$$\mathbf{T}\mathbf{v} = \mathbf{U}\mathbf{v}, \quad \forall \mathbf{v} \in V.$$

The null tensor, denoted by $\mathbf{O}$ assigns to any vector $\mathbf{v}$ the zero vector and the identity tensor $\mathbf{I}$ assigns to $\mathbf{v}$ the vector $\mathbf{v}$ itself:

$$\mathbf{O}\mathbf{v} = \mathbf{0}, \mathbf{I}\mathbf{v} = \mathbf{v} \quad \forall \mathbf{v} \in V.$$

The sum $\mathbf{T} + \mathbf{U}$ of tensors $\mathbf{T}$ and $\mathbf{U}$ and the product $a\mathbf{T}$ of a tensor $\mathbf{T}$ and a real number (scalar) a are defined as follows,

$$\begin{aligned}(\mathbf{T} + \mathbf{U})\mathbf{v} &= \mathbf{T}\mathbf{v} + \mathbf{U}\mathbf{v} \quad \forall \mathbf{v} \in V \\ (a\mathbf{T})\mathbf{v} &= a(\mathbf{T}\mathbf{v}), \quad \forall \mathbf{v} \in V, a \in R.\end{aligned}$$

Moreover, for any tensor $\mathbf{T}$, there exists another tensor, denoted $-\mathbf{T}$, such that:

$$(-\mathbf{T})\mathbf{v} = -\mathbf{T}\mathbf{v} \cdot \mathbf{T} + (-\mathbf{T}) = \mathbf{O}.$$

It can be easily shown from their definitions that $\mathbf{I}, \mathbf{O}, (-\mathbf{T}), \mathbf{T} + \mathbf{U}, a\mathbf{T}$ are actually linear transformations [i.e., satisfy the requirement (1.18)].

On the basis of the same definitions, it can be readily established that the *set of all tensors L*, endowed with the addition and scalar multiplications is a *vector space* (i.e., the axioms (V1)–(V8) concerning the addition and scalar multiplication and existence of a null element are satisfied, see Sect. 1.1). It will be later shown that L is nine-dimensional.

Multiplication of Tensors

The rule for multiplication (or composition) of tensors is:

$$(\mathbf{A}\mathbf{B})\mathbf{u} = \mathbf{A}(\mathbf{B}\mathbf{u}) \quad \forall \mathbf{A}, \mathbf{B} \in L \quad \text{and} \quad \forall \mathbf{u} \in V \tag{1.19}$$

We leave to the reader to establish that:

$$\begin{aligned}&\alpha(\mathbf{A}\mathbf{B}) = (\alpha\mathbf{A})\mathbf{B} = \mathbf{A}(\alpha\mathbf{B}) \quad \forall \mathbf{A}, \mathbf{B} \in L \text{ and } \alpha \in R \\ &\mathbf{A}(\mathbf{B} + \mathbf{C}) = \mathbf{A}\mathbf{B} + \mathbf{A}\mathbf{C} \\ &(\mathbf{A} + \mathbf{B})\mathbf{C} = \mathbf{A}\mathbf{C} + \mathbf{B}\mathbf{C} \\ &\mathbf{A}(\mathbf{B}\mathbf{C}) = (\mathbf{A}\mathbf{B})\mathbf{C} \\ &\mathbf{A}\mathbf{O} = \mathbf{O}\mathbf{A} = \mathbf{O}, \ \mathbf{A}\mathbf{I} = \mathbf{I}\mathbf{A} = \mathbf{A}\end{aligned} \tag{1.20}$$

In order to construct bases in the vector space of all second-order tensors, L, we now introduce the concept of tensor product of two vectors.

Tensor Product (Dyadic Product) of Two Vectors

Definition The tensor product or dyadic product of two vectors $\mathbf{u}, \mathbf{v}$ is a tensor, denoted by $\mathbf{u} \otimes \mathbf{v}$, and defined by:

$$(\mathbf{u} \otimes \mathbf{v})(\mathbf{w}) = \mathbf{u}(\mathbf{v} \cdot \mathbf{w}) \quad \forall \mathbf{w} \in V \tag{1.21}$$

The proof that $\mathbf{u} \otimes \mathbf{v}$ is actually a second-order tensor follows from the properties of the inner product (see axioms (I1)–(I5)). Furthermore, the properties

$$\begin{aligned} (\alpha_1 \mathbf{w}_1 + \alpha_2 \mathbf{w}_2) \otimes \mathbf{u} &= \alpha_1 (\mathbf{w}_1 \otimes \mathbf{u}) + \alpha_2 (\mathbf{w}_2 \otimes \mathbf{u}) \\ \mathbf{u} \otimes (\alpha_1 \mathbf{w}_1 + \alpha_2 \mathbf{w}_2) &= \alpha_1 (\mathbf{u} \otimes \mathbf{w}_1) + \alpha_2 (\mathbf{u} \otimes \mathbf{w}_2), \end{aligned} \tag{1.22}$$

can be easily deduced from (1.21) by using the properties of commutativity and distributivity with respect to addition of the inner product of two vectors [i.e., axioms (I1) and (I2)].

Let $\{\mathbf{e}_1, \mathbf{e}_2, \mathbf{e}_3\}$ be a positive-oriented orthonormal basis of the three-dimensional space. We have the following identity:

$$\mathbf{e}_\mathrm{i} \otimes \mathbf{e}_\mathrm{i} = \mathbf{I}. \tag{1.23}$$

Proof Note that for any vector $\mathbf{v}$,

$$(\mathbf{e}_\mathrm{i} \otimes \mathbf{e}_\mathrm{i})\mathbf{v} = (\mathbf{v} \cdot \mathbf{e}_\mathrm{i})\mathbf{e}_\mathrm{i} = \mathbf{v} = \mathbf{I}\mathbf{v}.$$

Theorem 1.2 *The set of tensors* $\{\mathbf{e}_k \otimes \mathbf{e}_m\}$ *with* $k, m = 1, \ldots, 3$ *are a basis of* L, *which is thus a nine-dimensional vector space. Moreover, any tensor* $\mathbf{T}$ *admits the representation*

$$\mathbf{T} = T_{km} \mathbf{e}_k \otimes \mathbf{e}_m \quad \text{with} \quad T_{km} = \mathbf{e}_k \cdot \mathbf{T}\mathbf{e}_m, k, m = 1, \ldots, 3. \tag{1.24}$$

Proof Assuming that there exist the real numbers λ_{km}, with $k, m = 1, \ldots, 3$ such that,

$$\lambda_{km} \mathbf{e}_k \otimes \mathbf{e}_m = \mathbf{0},$$

we get,

$$\mathbf{0} = \mathbf{0}\mathbf{e}_l = (\lambda_{km} \mathbf{e}_k \otimes \mathbf{e}_m)\mathbf{e}_l = (\lambda_{km} \mathbf{e}_k)(\mathbf{e}_m \cdot \mathbf{e}_l) = \lambda_{km} \mathbf{e}_k \delta_{ml} = \lambda_{kl} \mathbf{e}_k. \tag{1.25}$$

Since $\{\mathbf{e}_k\}$ is a basis, it follows that $\lambda_{kl} = 0$, for any $k, l = 1, \ldots, 3$. Consequently, $\{\mathbf{e}_k \otimes \mathbf{e}_m\}$, $k, m = 1, \ldots, 3$ are a linearly independent set of tensors in the space L.

Let us consider now an arbitrary tensor $\mathbf{T}$ and denote by T_{km} the components relative to the orthonormal basis $\{\mathbf{e}_k\}$ of the vector $\mathbf{T}\mathbf{e}_m$, so that,

$$\mathbf{T}\mathbf{e}_m = T_{km}\mathbf{e}_k \quad \text{and} \quad T_{km}=\mathbf{e}_k \cdot \mathbf{T}\mathbf{e}_m.$$

Using the orthonormality of the basis $\{\mathbf{e}_k\}$, the properties of the tensor product and the above relation, it follows that for an arbitrary vector $\mathbf{v}$ of components v_s relative to this basis, we have:

$$\begin{aligned}(\mathbf{T} - T_{km}\mathbf{e}_k \otimes \mathbf{e}_m)\mathbf{v} &= (\mathbf{T} - T_{km}\mathbf{e}_k \otimes \mathbf{e}_m)(\mathrm{v}_s\mathbf{e}_s) = \mathrm{v}_s\mathbf{T}\mathbf{e}_s - \mathrm{v}_s T_{km}\mathbf{e}_k(\mathbf{e}_m \cdot \mathbf{e}_s) \\ &= \mathrm{v}_s(T_{ks}\mathbf{e}_k - T_{km}\mathbf{e}_k\delta_{ms}) = \mathrm{v}_s(T_{ks}\mathbf{e}_k - T_{ks}\mathbf{e}_k) = \mathbf{0}\end{aligned} \tag{1.26}$$

Hence, $\mathbf{T}$ admits the representation given by Eq. (1.24).

The nine real numbers T_{km}, uniquely defined by Eq. (1.24), are called the Cartesian components of the tensor $\mathbf{T}$ relative to the basis $\{\mathbf{e}_1, \mathbf{e}_2, \mathbf{e}_3\}$. If $\mathbf{v} = \mathbf{T}\mathbf{u}$, we also have by Eq. (1.24)

$$\mathbf{v} = (T_{km}\mathbf{e}_k \otimes \mathbf{e}_m)\mathbf{u} = T_{km}u_m\mathbf{e}_k,$$

and hence,

$$\mathrm{v}_k = T_{km}u_m. \tag{1.27}$$

Based on the representation given by Eq. (1.24), it follows that:

$$(\mathbf{AB})_{km} = A_{kp}B_{pm}.$$

Transpose of a Tensor

Definition Associated with any tensor $\mathbf{T}$, there is a unique tensor denoted $\mathbf{T}^T$, called the transpose of $\mathbf{T}$, defined as:

$$\left(\mathbf{T}^T\mathbf{u}\right) \cdot \mathbf{v} = \mathbf{u} \cdot \mathbf{T}\mathbf{v} \text{ for any } \mathbf{u}, \mathbf{v} \in V. \tag{1.28}$$

The above rule defines in a unique way $\mathbf{T}^T$. At the same time, using the above definition, the linearity of $\mathbf{T}$, and the properties of the scalar product in V, it can be shown that $\mathbf{T}^T$ is a linear mapping, hence, a second-order tensor. Denoting by T_{km} and T^T_{km}, the components of $\mathbf{T}$ and $\mathbf{T}^T$ in the basis $\{\mathbf{e}_k \otimes \mathbf{e}_m\}$ k, m = 1, …, 3, according to the definition of the components of a tensor given by Eq. (1.24),

$$T^T_{km} = \mathbf{e}_k \cdot \mathbf{T}^T\mathbf{e}_m = \mathbf{e}_m \cdot \mathbf{T}\mathbf{e}_k = T_{mk},$$

Hence, $\mathbf{T}^{\mathrm{T}} = T_{mk}\mathbf{e}_k \otimes \mathbf{e}_m$.

In other words, the matrix of the Cartesian components of the transpose tensor $\mathbf{T}^T$ is the transpose of the matrix of the components of the tensor $\mathbf{T}$. Also, it follows from the definition of the transpose of a tensor that,

$$\left(\mathbf{T}^{\mathrm{T}}\right)^{\mathrm{T}}=\mathbf{T},\ (\mathbf{TU})^{\mathrm{T}}=\ \mathbf{U}^{\mathrm{T}}\mathbf{T}^{\mathrm{T}}\ \text{ for any } \mathbf{T},\mathbf{U}\in \mathrm{L}$$

and,

$$(\mathbf{u}\otimes\mathbf{v})^{\mathrm{T}}=\mathbf{v}\otimes\mathbf{u}\ \text{ for any } \mathbf{u},\mathbf{v}\in V.$$

Definition A tensor $\mathbf{T}$ is called symmetric if,

$$\mathbf{T}^{T}=\mathbf{T}$$

and skew or antisymmetric if,

$$\mathbf{T}^{T}=-\mathbf{T}$$

If the tensor $\mathbf{T}$ is symmetric, the matrix of its components is also symmetric; if the tensor $\mathbf{T}$ is antisymmetric, the matrix of its components is also antisymmetric. Consequently, in the three-dimensional vector space, a symmetric tensor has six independent components, and an antisymmetric tensor has three independent components.

Moreover, if $\mathbf{\Omega}$ is an antisymmetric tensor, all its diagonal components are zero, and there exists a unique vector $\boldsymbol{\omega}$ such that,

$$\mathbf{\Omega}\,\mathbf{u}=\boldsymbol{\omega}\times\mathbf{u}\ \text{ for any } \mathbf{u}\in V. \tag{1.29}$$

If $\mathbf{T}$ is an arbitrary tensor, the symmetric part, $\mathbf{T}^{S}$, of $\mathbf{T}$ and the skew-symmetric part, $\mathbf{T}^{A}$, of $\mathbf{T}$ are defined as:

$$\mathbf{T}^{S}=\frac{1}{2}\left(\mathbf{T}+\mathbf{T}^{\mathrm{T}}\right),\mathbf{T}^{\mathrm{A}}=\frac{1}{2}\left(\mathbf{T}-\mathbf{T}^{\mathrm{T}}\right),$$

such that,

$$\mathbf{T}=\mathbf{T}^{\mathrm{S}}+\mathbf{T}^{\mathrm{A}} \tag{1.30}$$

The above identity demonstrates that an arbitrary tensor $\mathbf{T}$ can be uniquely expressed as the sum of a symmetric tensor and an antisymmetric tensor. Moreover, on the basis of (1.29)–(1.30) it follows that the set of symmetric tensors, denoted L_S, forms a six-dimensional subspace of L while the set of all skew-symmetric tensors, denoted L_A, forms a three-dimensional subspace of L.

Trace of a Tensor

Definition The trace of the tensor $\mathbf{T}$, denoted $tr\,(\mathbf{T})$, is the real number given by,

$$tr(\mathbf{T}) = T_{kk}, \quad k = 1, \ldots, 3. \tag{1.31}$$

where T_{km} are the components of $\mathbf{T}$ in the basis $\{\mathbf{e}_k\}$.

It can be easily seen that the trace is a linear function from L to R, and that,

$$\begin{aligned} &tr\,(\mathbf{u} \otimes \mathbf{v}) = \mathbf{u} \cdot \mathbf{v} \ \text{ for any } \mathbf{u}, \mathbf{v} \in V, \\ &tr\big(\mathbf{T}^{\mathrm{T}}\big) = tr(\mathbf{T}), \quad tr(\mathbf{AB}) = tr(\mathbf{BA}) \ \text{ for any tensors } \mathbf{A}, \mathbf{B}, \mathbf{T} \in L. \end{aligned} \tag{1.32}$$

Inner Product (Contracted Product) of Two Tensors

Definition The *inner product* (*contracted product*) of any two tensors $\mathbf{T}$ and $\mathbf{U}$, denoted by $\mathbf{T} : \mathbf{U}$ is the real number:

$$\mathbf{T} : \mathbf{U} = tr\big(\mathbf{T}\mathbf{U}^{T}\big) \tag{1.33}$$

It is easily seen that this operation defined on the Cartesian product $L \times L$ and having values in R, satisfies the axioms (I1)–(I5) of a scalar product over the vector space of second-order tensors. Moreover, if T_{km} and U_{km} are the components of $\mathbf{T}$ and $\mathbf{U}$ relative to the basis $\{\mathbf{e}_k\}$, then,

$$\mathbf{T}{:}\mathbf{U} = T_{km}U_{km}. \tag{1.34}$$

This scalar product can be used to define the *norm* (also called the magnitude) of any tensor $\mathbf{T}$, as the real number,

$$\|T\| = (\mathbf{T} : \mathbf{T})^{1/2} = T_{km}T_{km}. \tag{1.35}$$

From the definition of the scalar product of second-order tensors, it follows that for any vectors $\mathbf{u}, \mathbf{v}, \mathbf{a}, \mathbf{b} \in V$,

$$(\mathbf{a} \otimes \mathbf{b}) : (\mathbf{u} \otimes \mathbf{v}) = (\mathbf{a} \cdot \mathbf{u})(\mathbf{b} \cdot \mathbf{v}) \tag{1.36}$$

In particular, if $\{\mathbf{e}_k\}$ with k = 1, …, 3 is an orthonormal basis in V,

$$\begin{aligned} &\big(\mathbf{e}_i \otimes \mathbf{e}_j\big) \cdot (\mathbf{e}_k \otimes \mathbf{e}_m) = (\mathbf{e}_i \cdot \mathbf{e}_k)\big(\mathbf{e}_j \cdot \mathbf{e}_m\big) = \\ &\delta_{ik}\delta_{jm} = \begin{cases} 1, & \text{if } i = k, j = m \\ 0, & \text{otherwise} \end{cases} \end{aligned} \tag{1.37}$$

Hence, $\{\mathbf{e}_k \otimes \mathbf{e}_m\}$ with $k, m = 1, \ldots, 3$ is an orthonormal basis in the space L of second-order tensors.

In many computations, it is useful to present the components T_{km} of a tensor $\mathbf{T}$ relative to a given Cartesian basis $\{\mathbf{e}_k\}$ $k = 1, \ldots, 3$ as the 3×3 matrix:

$$\mathbf{T} = [T_{km}] = \begin{bmatrix} T_{11} & T_{12} & T_{13} \\ T_{21} & T_{22} & T_{23} \\ T_{31} & T_{32} & T_{33} \end{bmatrix}.$$

Determinant of a Tensor

Definition The *determinant* of a tensor $\mathbf{T}$, denoted by $\det \mathbf{T}$ is defined by:

$$\det \mathbf{T} = \det[T_{km}] = \varepsilon_{pqr} T_{1p} T_{2q} T_{3r}, \tag{1.38}$$

where $[T_{km}]$ denotes the matrix of the Cartesian components of $\mathbf{T}$ in the basis $\{\mathbf{e}_k\}$ and $p, q, r = 1, \ldots, 3$. From this definition, it follows that for any tensors $\mathbf{T}, \mathbf{U}$ and real number α:

$$\det(\alpha \mathbf{T}) = \alpha^3 \det(\mathbf{T}), \det \mathbf{T}^T = \det \mathbf{T}, \det(\mathbf{TU}) = (\det \mathbf{T})(\det \mathbf{U}) \tag{1.39}$$

If $\det \mathbf{T} = 0$, the tensor $\mathbf{T}$ is said to be singular.

Inverse of a Second-Order Tensor

If $\det \mathbf{T} \neq 0$, the tensor $\mathbf{T}$ is said to be invertible (or non-singular) since there exists a unique tensor, called the inverse of $\mathbf{T}$, and denoted by $\mathbf{T}^{-1}$ such that

$$\mathbf{T}\mathbf{T}^{-1} = \mathbf{T}^{-1}\mathbf{T} = \mathbf{I}. \tag{1.40}$$

From Eqs. (1.39) to (1.40), it follows that

$$\det \mathbf{T}^{-1} = (\det \mathbf{T})^{-1}, (\mathbf{TU})^{-1} = \mathbf{U}^{-1}\mathbf{T}^{-1}, \left(\mathbf{T}^T\right)^{-1} = \left(\mathbf{T}^{-1}\right)^T \tag{1.41}$$

Orthogonal Tensors

A special class of tensors has as a defining property the invariance of the scalar product of any two vectors.

Definition A tensor $\mathbf{Q}$ is orthogonal if,

$$\mathbf{Qu} \cdot \mathbf{Qv} = \mathbf{u} \cdot \mathbf{v} \text{ for any } \mathbf{u}, \mathbf{v} \in V. \tag{1.42}$$

Taking $\mathbf{u} = \mathbf{v}$ in the above equation, it follows that

$$|\mathbf{Qu}| = |\mathbf{u}|,$$

so an orthogonal tensor applied to any vector $\mathbf{u}$ preserves its length. Furthermore, from Eq. (1.42) we obtain

$$\frac{\mathbf{Qu}\cdot\mathbf{Qv}}{|\mathbf{Qu}||\mathbf{Qv}|} = \frac{\mathbf{u}\cdot\mathbf{v}}{|\mathbf{u}||\mathbf{v}|},$$

so the angle between two vectors $\mathbf{u}$ and $\mathbf{v}$ is preserved whenever $\mathbf{u}$ and $\mathbf{v}$ are transformed by an orthogonal tensor $\mathbf{Q}$. Since by definition of the transpose of a tensor [see Eq. (1.28)],

$$\mathbf{Qu}\cdot\mathbf{Qv} = \mathbf{u}\cdot\left\{\mathbf{Q}^T(\mathbf{Qv})\right\} = \mathbf{u}\cdot\left\{\left(\mathbf{Q}^T\mathbf{Q}\right)\mathbf{v}\right\},$$

making use of Eq. (1.42) we obtain that a necessary and sufficient condition for $\mathbf{Q}$ to be orthogonal is

$$\mathbf{Q}^T\mathbf{Q} = \mathbf{I}. \tag{1.43}$$

From Eq. (1.43), it follows $\det\left(\mathbf{Q}^T\mathbf{Q}\right) = (\det\mathbf{Q})^2$, hence,

$$\det\mathbf{Q} = \pm 1,\ \ \mathbf{Q}^T = \mathbf{Q}^{-1}. \tag{1.44}$$

$\mathbf{Q}$ is said to be a proper orthogonal tensor if $\det\mathbf{Q} = 1$ and an improper orthogonal tensor if $\det\mathbf{Q} = -1$.

Note also that from Eq. (1.42), it follows that if $\{\mathbf{e}_k\}$ is an orthonormal basis, the set $\{\mathbf{Qe}_k\}$ also forms an orthonormal basis.

Change of Coordinate System: Transformation Matrix and Transformation Rules of Vector and Second-Order Tensor Components

Let us assume now that $\{\mathbf{e}_1, \mathbf{e}_2, \mathbf{e}_3\}$ and $\left\{\mathbf{e}_1^*, \mathbf{e}_2^*, \mathbf{e}_3^*\right\}$ are three-dimensional positive-oriented orthonormal bases of the three-dimensional space. Relative to these bases, an arbitrary vector $\mathbf{u}$ has the components u_i and respectively u_i^*, i = 1, …, 3. Then,

$$u_j = q_{ji}u_i^* \quad \text{with} \quad q_{ji} = \mathbf{e}_\mathrm{j}\cdot\mathbf{e}_\mathrm{i}^*, i,j = 1,\ldots,3 \tag{1.45}$$

or, in matrix form:

$$\boldsymbol{u}_{(e_i)} = \mathbf{Q}\boldsymbol{u}_{(e_i^*)}$$

where $\mathbf{Q} = \left[q_{ij}\right]$ is the transformation matrix from the basis $\left\{\mathbf{e}_1^*, \mathbf{e}_2^*, \mathbf{e}_3^*\right\}$ to the basis $\{\mathbf{e}_1, \mathbf{e}_2, \mathbf{e}_3\}$, and $\boldsymbol{u}_{(e_i)} = (u_1, u_2, u_3)$, $\boldsymbol{u}_{(e_i^*)} = \left(u_1^*, u_2^*, u_3^*\right)$ are the components of $\mathbf{u}$ in the respective basis.

Proof First, let's express each of the vectors of the basis $\{\mathbf{e}_1^*, \mathbf{e}_2^*, \mathbf{e}_3^*\}$ relative to the basis $\{\mathbf{e}_1, \mathbf{e}_2, \mathbf{e}_3\}$. For i-fixed,

$$\mathbf{e}_i^* = (\mathbf{e}_i^* \cdot \mathbf{e}_j)\mathbf{e}_j = q_{ji}\mathbf{e}_j = q_{1i}\mathbf{e}_1 + q_{2i}\mathbf{e}_2 + q_{3i}\mathbf{e}_3 \tag{1.46}$$

i.e., the column "i" of the matrix $\mathbf{Q}$ contains the components of $\mathbf{e}_i^*$ relative to the basis $\{\mathbf{e}_1, \mathbf{e}_2, \mathbf{e}_3\}$. Therefore, relative to the basis given by $\{\mathbf{e}_1^*, \mathbf{e}_2^*, \mathbf{e}_3^*\}$, the vector $\mathbf{u}$ can be expressed as:

$$\mathbf{u} = u_i^*\mathbf{e}_i^* = u_i^* q_{ji}\mathbf{e}_j \tag{1.47}$$

In view of Theorem 1.1, the representation of a vector as a linear combination of the vectors of a given basis is unique. Thus from Eq. (1.47), it follows that for j-fixed, the component u_j of the vector $\mathbf{u}$ is:

$$u_j = q_{ji}u_i^* \quad \text{or} \quad \boldsymbol{u}_{(e_i)} = \mathbf{Q}\boldsymbol{u}_{(e_i^*)}.$$

As already mentioned, the transformation matrix $\mathbf{Q}$ is orthogonal, and accordingly, $\mathbf{Q}^{-1} = \mathbf{Q}^T$ [Eq. (1.44)], thus,

$$\boldsymbol{u}_{(\mathbf{e}_i^*)} = \mathbf{Q}^T\boldsymbol{u}_{(\mathbf{e}_i)}.$$

In a similar manner, it can be shown that the transformation rule for tensor components is:

$$T_{km} = q_{kr}q_{ms}T_{rs}^* \quad \text{and} \quad T_{rs}^* = q_{kr}q_{ms}T_{km}, k, r, m, s = 1, \ldots, 3,$$

or

$$\mathbf{T} = \mathbf{Q}\mathbf{T}^*\mathbf{Q}^T \quad \text{and} \quad \mathbf{T}^* = \mathbf{Q}^T\mathbf{T}\mathbf{Q} \tag{1.48}$$

Orthogonal tensors and their properties are of great importance for the description of the mechanical response of polycrystalline materials. For instance, intrinsic crystal symmetries are characterized by various orthogonal tensors or transformations (see Chap. 3).

Remark It is important to note that the trace and determinant of a tensor are invariants, i.e., have the same value irrespective of the Cartesian coordinate system in which the tensor is described. Indeed, using the transformation rule given by Eq. (1.48), it follows that:

$$tr(\mathbf{T}) = T_{kk} = q_{kr}q_{ks}T_{rs}^* = \delta_{rs}T_{rs}^* = tr(\mathbf{T}^*),$$

$$\det(\mathbf{T}^*) = \det(\mathbf{Q}^T)\det(\mathbf{T}\mathbf{Q}) = \det(\mathbf{Q}^{-1})\det(\mathbf{T})\det(\mathbf{Q}) = \det(\mathbf{T}) \tag{1.49}$$

Invariants of a second-order tensor and Spectral Theorem

In the mechanics of deformable bodies, an important role is played by the eigenvalues and eigenvectors of various second-order tensors, such as Cauchy's stress tensor. Thus, we briefly present the definitions of eigenvalues, eigenvectors, and invariants highlighting some important properties of symmetric tensors.

Eigenvalues and Eigenvectors of Second-Order Tensors

Definition A scalar λ is said to be an *eigenvalue* of a tensor $\mathbf{T}$ if there exists a nonzero vector $\mathbf{u}$, such that

$$\mathbf{T}\mathbf{u} = \lambda\mathbf{u}; \tag{1.50}$$

where, $\mathbf{u}$ is called *eigenvector* of $\mathbf{T}$ associated to the eigenvalue λ. Reciprocally, a nonzero vector $\mathbf{u}$ is said to be an eigenvector of $\mathbf{T}$ if there exists a real number λ such that Eq. (1.50) holds. Note that in this case λ is an eigenvalue of $\mathbf{T}$ associated to $\mathbf{u}$.

The set of all vectors $\mathbf{u}$ satisfying the Eq. (1.50) forms a subspace of V, which is called the *characteristic space* of $\mathbf{T}$ corresponding to the eigenvalue λ. A unit eigenvector of $\mathbf{T}$ is called a *principal direction* of the tensor $\mathbf{T}$. Equation (1.50) implies that λ is an *eigenvalue* of $\mathbf{T}$ if and only if it is a real root of the algebraic equation,

$$\det(\mathbf{T} - \lambda\mathbf{I}) = 0 \tag{1.51}$$

The above equation is called the *characteristic equation of* $\mathbf{T}$.

Let $\{\mathbf{e}_k\}$, $k = 1, \ldots, 3$ be an orthonormal basis. By expanding the determinant in Eq. (1.51), the characteristic equation can be written as a third-order algebraic equation for λ:

$$\lambda^3 - I_T\lambda^2 - II_T\lambda - III_T = 0, \tag{1.52}$$

where

$$I_T = T_{11} + T_{22} + T_{33} = tr\mathbf{T}, \tag{1.53}$$

$$II_T = -\begin{vmatrix} T_{22} & T_{23} \\ T_{32} & T_{33} \end{vmatrix} - \begin{vmatrix} T_{11} & T_{13} \\ T_{31} & T_{33} \end{vmatrix} - \begin{vmatrix} T_{11} & T_{12} \\ T_{21} & T_{22} \end{vmatrix} = \frac{1}{2}\left[tr\left(\mathbf{T}^2\right) - (tr\mathbf{T})^2\right] \tag{1.54}$$

$$III_T = \det[T_{km}] = \det\mathbf{T}. \tag{1.55}$$

The scalars I_T, II_T, III_T are referred to as *principal invariants* of $\mathbf{T}$, with I_T being called the *first invariant*, II_T the *second invariant*, and III_T *third-invariant* of the tensor $\mathbf{T}$, respectively.

It is important to recall that since the trace and determinant of any tensor do not depend on the basis $\{\mathbf{e}_k\}$ [see Eq. (1.49)] I_T, II_T, III_T have the same values irrespective of the basis $\{\mathbf{e}_k\}$ used to write the characteristic equation, i.e., they are *invariants relative to a change of basis in V*.

Let $\lambda_1, \lambda_2, \lambda_3$ be the roots of the third-order characteristic Eq. (1.52). Classical linear algebra results in conjunction with Eqs. (1.53)–(1.55) lead to

$$\begin{aligned} I_T &= tr\mathbf{T} = \lambda_1 + \lambda_2 + \lambda_3 \\ II_T &= \frac{1}{2}\left[tr\left(T^2\right) - (trT)^2\right] = -(\lambda_1\lambda_2 + \lambda_2\lambda_3 + \lambda_3\lambda_1), \\ III_T &= \det\mathbf{T} = \lambda_1\lambda_2\lambda_3. \end{aligned} \tag{1.56}$$

The next result, whose proof we omit, is a central theorem of linear algebra and one of great importance in modeling the behavior of materials.

Cayley–Hamilton Theorem

A symmetric second-order tensor $\mathbf{T}$ satisfies its own characteristic equation, i.e.,

$$\mathbf{T}^3 - I_T\mathbf{T}^2 - II_T\mathbf{T} - III_T\mathbf{I} = 0. \tag{1.57}$$

It can also be shown (see, e.g., Halmos [3]) that:

Spectral Theorem

A *symmetric second-order tensor* $\mathbf{T}$ has three real eigenvalues (not necessarily distinct) and an orthonormal basis $\{\mathbf{n}_1, \mathbf{n}_2, \mathbf{n}_3\}$ such that:

$$\mathbf{T} = \lambda_1\boldsymbol{n}_1 \otimes \boldsymbol{n}_1 + \lambda_2\boldsymbol{n}_2 \otimes \boldsymbol{n}_2 + \lambda_3\boldsymbol{n}_3 \otimes \boldsymbol{n}_3. \tag{1.58}$$

- If λ_1, λ_2 and λ_3 are distinct, the characteristic spaces of $\mathbf{T}$ are one-dimensional vector subspaces of V, generated by the principal directions $\mathbf{n}_1, \mathbf{n}_2$ and $\mathbf{n}_3$, respectively.
- If two principal values are equal, $\lambda_1 \neq \lambda_2 = \lambda_3$, $\mathbf{T}$ has only two distinct characteristic spaces, namely the line generated by $\mathbf{n}_1$ and the plane perpendicular to $\mathbf{n}_1$ and the representation (1.58) reduces to:

$$\mathbf{T} = \lambda_1\boldsymbol{n}_1 \otimes \boldsymbol{n}_1 + \lambda_2(\mathbf{I} - \boldsymbol{n}_1 \otimes \boldsymbol{n}_1). \tag{1.59}$$

- If $\lambda_1 = \lambda_2 = \lambda_3$, then $\mathbf{T}$ has a single characteristic space, and:

$$\mathbf{T} = \lambda_1 \mathbf{I}. \tag{1.60}$$

The relations (1.58)–(1.60) give the spectral decomposition of the tensor $\mathbf{T}$.

Proof To prove that the eigenvalues of a symmetric tensor $\mathbf{T}$ are all real, we will show that if λ is a root of the characteristic Eq. (1.52), then $\lambda = \bar{\lambda}$. Indeed, if $\lambda = a + ib$, $\left(i = \sqrt{-1}\right)$, there exist $\mathbf{u} = \mathbf{v} + i\mathbf{w}$ nonzero such that $\mathbf{Tu} = \lambda\mathbf{u}$. Writing this latter equation in component form relative to the basis $\{\mathbf{e}_k\}$ and separating the real and imaginary parts, we have:

$$T_{km}v_m - av_k + bw_k = 0, \quad \text{and} \quad T_{km}w_m - aw_k - bv_k = 0, \quad \text{with} \quad k, m = 1\ldots3 \tag{1.61}$$

Since $T_{km} = T_{mk}$, by multiplying the first Eq. (1.61) by w_k and the second one by $(-v_k)$ and then subtracting one from another, we obtain:

$$b(v_k v_k + w_k w_k) = b\left(|\mathbf{v}|^2 + |\mathbf{w}|^2\right) = 0.$$

Since $\mathbf{u}$ is nonzero, from the above equation it follows that $b = 0$, and thus $\lambda \in R$. On the other hand, the characteristic equation is of order 3, and it has *three* roots (not necessarily distinct).

Assuming that the eigenvalues $\lambda_1, \lambda_2, \lambda_3$ are distinct, and denoting by $\mathbf{n}_1, \mathbf{n}_2, \mathbf{n}_3$ the corresponding principal directions of the respective eigenvalues, we have:

$$\mathbf{T}\boldsymbol{n}_1 = \lambda_1\boldsymbol{n}_1, \mathbf{T}\boldsymbol{n}_2 = \lambda_2\boldsymbol{n}_2, \mathbf{T}\boldsymbol{n}_3 = \lambda_3\boldsymbol{n}_3. \tag{1.62}$$

It can be easily shown that the proper vectors of a symmetric tensor $\mathbf{T}$ corresponding to two distinct eigenvalues are reciprocally orthogonal, hence $\mathbf{n}_1, \mathbf{n}_2$ and $\mathbf{n}_3$ form an orthonormal basis. Next, using successively Eqs. (1.23) and the definition of the dyadic product, we can express:

$$\mathbf{T} = \mathbf{TI} = \mathbf{T}(\boldsymbol{n}_i \otimes \boldsymbol{n}_i) = (\mathbf{T}\boldsymbol{n}_i) \otimes \boldsymbol{n}_i = \sum_{i=1}^{3} \lambda_i(\boldsymbol{n}_i \otimes \boldsymbol{n}_i).$$

The proof for the other two cases (i.e., repeated roots) can be obtained in a similar manner.

Equation (1.58) is referred to as the *spectral decomposition of a symmetric second-order tensor*. The spectral theorem is of great importance for the theory of elasticity and plasticity.

Positive-Definite Tensor, Polar Decomposition Theorem

Definition A tensor $\mathbf{T}$ is said to be *positive semi-definite* if for any vector $\mathbf{u}$:

$$\mathbf{u} \cdot \mathbf{Tu} \geq 0.$$

If the stronger requirement,

$$\mathbf{u} \cdot \mathbf{Tu} > 0 \quad \forall \mathbf{u} \neq 0 \tag{1.63}$$

is fulfilled, $\mathbf{T}$ is said to be *positive-definite*. Using the above definition, it follows that the *eigenvalues of a symmetric positive-definite tensor are strictly positive*. Hence,

$$\det \mathbf{T} > 0,$$

and, $\mathbf{QTQ}^T$ is symmetric and positive-definite for any proper orthogonal tensor $\mathbf{Q}$. This implies that any symmetric positive-definite tensor $\mathbf{T}$ admits an inverse. Moreover, from the spectral theorem [Eq. (1.58)], it follows that the inverse of $\mathbf{T}$ has the following spectral representation:

$$\mathbf{T}^{-1} = \sum_{i=1}^{3} \lambda_i^{-1} (\boldsymbol{n}_i \otimes \boldsymbol{n}_i),$$

where λ_i are the eigenvalues of $\mathbf{T}$ and $\{\mathbf{n}_1, \mathbf{n}_2, \mathbf{n}_3\}$ are the associated eigenvectors (with corresponding representations deduced from Eqs. (1.59) and (1.60), respectively, if the eigenvalues λ_i are not distinct).

Another important result in the mechanics of materials, obtained using the spectral theorem, concerns the existence of the square root of a positive-definite tensor. It can be shown that given a symmetric positive semi-definite tensor $\mathbf{T}$, there exists a unique symmetric and positive semi-definite tensor $\mathbf{U}$, called the square root of $\mathbf{T}$, and denoted $\sqrt{\mathbf{T}}$, such that

$$\mathbf{U}^2 = \mathbf{T}. \tag{1.64}$$

Indeed, if $\mathbf{T} = \lambda_1 \boldsymbol{n}_1 \otimes \boldsymbol{n}_1 + \lambda_2 \boldsymbol{n}_2 \otimes \boldsymbol{n}_2 + \lambda_3 \boldsymbol{n}_3 \otimes \boldsymbol{n}_3$, with $\lambda_1 \geq 0, \lambda_2 \geq 0, \lambda_3 \geq 0$ then the tensor, defined by $\sqrt{\mathbf{T}} = \sum_{i=1}^{3} \sqrt{\lambda_i} (\boldsymbol{n}_i \otimes \boldsymbol{n}_i)$ is symmetric, positive-definite, and satisfies the requirement (1.64).

Polar Decomposition Theorem

Any invertible tensor $\mathbf{A}$ with $\det \mathbf{A} > 0$ has two unique multiplicative decompositions,

$$\mathbf{A} = \mathbf{RU} \text{ and } \mathbf{A} = \mathbf{VR},$$

with **U** and **V** *symmetric and positive-definite*, and **R** orthogonal.

Deviator of a Symmetric Tensor

Definition The deviator of a nonzero symmetric tensor **T**, denoted $\mathbf{T}'$, is defined as:

$$\mathbf{T}' = \mathbf{T} - \frac{tr\mathbf{T}}{3}\mathbf{I}. \tag{1.65}$$

To simplify writing let us denote, $(tr\mathbf{T})/3 = p$.

Note that $\mathbf{T}'$ is symmetric and traceless ($tr\mathbf{T}' = 0$) and, its second and third-invariants can be expressed in terms of the invariants of **T** as:

$$\begin{aligned} I_{\mathbf{T}'} &= 0 \\ II_{\mathbf{T}'} &= \frac{1}{2}\left[tr\left(\mathbf{T}'^2\right)\right] = II_T + 3p^2, \\ III_{\mathbf{T}'} &= \det(\mathbf{T}') = III_T + p(II_T) + 2p^3. \end{aligned} \tag{1.66}$$

Lemma 1.1 *Let* **T** *be a symmetric second-order tensor, and* λ_i, $i = 1, \ldots, 3$, *its principal values. Let* $\Gamma_n = \lambda_1^n + \lambda_2^n + \lambda_3^n$, *where n is a positive integer. Then, the following recurrence relation holds*:

$$\Gamma_{n+1} = (3p)\Gamma_n + II_T\Gamma_{n-1} + III_T\Gamma_{n-2} \quad \text{for } n \geq 2 \tag{1.67}$$

Proof Let us note that by definition, $\Gamma_0 = 3$, and from Eq. (1.56) we have:

$$\begin{aligned} \Gamma_1 &= I_T = 3p, \\ \Gamma_2 &= (\lambda_1 + \lambda_2 + \lambda_3)^2 - 2(\lambda_1\lambda_2 + \lambda_1\lambda_3 + \lambda_2\lambda_3) = (3p)^2 + 2II_T \\ \Gamma_3 &= \lambda_1^3 + \lambda_2^3 + \lambda_3^3 = (3p)\Gamma_2 + II_T\Gamma_1 + 3III_T = 27p^3 + 9pII_T + 3III_T \end{aligned}$$

On the other hand,

$$\begin{aligned} \Gamma_{n+1} = &\left(\lambda_1^n + \lambda_2^n + \lambda_3^n\right)(\lambda_1 + \lambda_2 + \lambda_3) - \lambda_1^n(\lambda_2 + \lambda_3) - \lambda_2^n(\lambda_1 + \lambda_3) \\ &- \lambda_3^n(\lambda_1 + \lambda_2) \end{aligned}$$

Therefore,

$$\begin{aligned} \Gamma_{n+1} = &(3p)\Gamma_n - (\lambda_1\lambda_2 + \lambda_2\lambda_3 + \lambda_3\lambda_1)\left(\lambda_1^{n-1} + \lambda_2^{n-1} + \lambda_3^{n-1}\right) \\ &+ \left(\lambda_1\lambda_3\lambda_2^{n-1} + \lambda_2\lambda_3\lambda_1^{n-1} + \lambda_1\lambda_2\lambda_3^{n-1}\right) \end{aligned}$$

or,

$$\Gamma_{n+1} = (3p)\Gamma_n - (\lambda_1\lambda_2 + \lambda_2\lambda_3 + \lambda_3\lambda_1)(\Gamma_{n-1}) + \lambda_1\lambda_2\lambda_3\left(\lambda_1^{n-2} + \lambda_2^{n-2} + \lambda_3^{n-2}\right)$$

Further substitution of Eq. (1.56) leads to the recurrence relation Eq. (1.67). Another useful result of importance in defining yield criteria for isotropic materials with the same behavior in tension–compression is given below.

Lemma 1.2 *For any integer* $n \geq 1$, *the following recurrence relation holds*:

$$\Gamma_{2n+4} = \Gamma_{2n+2}\left(\lambda_1^2 + \lambda_2^2 + \lambda_3^2\right) - \Gamma_{2n}\left(\lambda_1^2\lambda_2^2 + \lambda_1^2\lambda_3^2 + \lambda_2^2\lambda_3^2\right) + \Gamma_{2n-2}\left(\lambda_1^2\lambda_2^2\lambda_3^2\right) \tag{1.68}$$

Proof

$$\Gamma_{2n+4} = \left(\lambda_1^{2n+4} + \lambda_2^{2n+4} + \lambda_3^{2n+4}\right) = \left(\lambda_1^{2n+2} + \lambda_2^{2n+2} + \lambda_3^{2n+2}\right)\left(\lambda_1^2 + \lambda_2^2 + \lambda_3^2\right) - \lambda_1^{2n+2}\left(\lambda_2^2 + \lambda_3^2\right) - \lambda_2^{2n+2}\left(\lambda_1^2 + \lambda_3^2\right) - \lambda_3^{2n+2}\left(\lambda_1^2 + \lambda_2^2\right)$$

or,

$$\Gamma_{2n+4} = \Gamma_{2n+2}\left(\lambda_1^2 + \lambda_2^2 + \lambda_3^2\right) - \Gamma_{2n}\left(\lambda_1^2\lambda_2^2 + \lambda_1^2\lambda_3^2 + \lambda_2^2\lambda_3^2\right) + \lambda_1^2\lambda_2^2\lambda_3^{2n} + \lambda_1^2\lambda_3^2\lambda_2^{2n} + \lambda_2^2\lambda_3^2\lambda_1^{2n}$$

Further collecting the last three terms in the above expression, we obtain,

$$\Gamma_{2n+4} = \Gamma_{2n+2}\left(\lambda_1^2 + \lambda_2^2 + \lambda_3^2\right) - \Gamma_{2n}\left(\lambda_1^2\lambda_2^2 + \lambda_1^2\lambda_3^2 + \lambda_2^2\lambda_3^2\right) + \lambda_1^2\lambda_2^2\lambda_3^2\Gamma_{2n-2}$$

1.2.2 Higher-Order Tensors

Tensor of Order n

Definition A *tensor of order n* (or *n*th-*order tensor*) is a linear mapping that assigns to each vector **u** a tensor of order (*n*–1), for $n \geq 3$. This definition, in conjunction with that of a second-order tensor given in the previous subsection, allows the iterative introduction of tensors of an arbitrary order. We denote by L_n the set of all tensors of order *n*, $n \geq 3$. The sum $\mathbf{A} + \mathbf{B}$ of any two *n*th-order tensors **A** and **B**, and the product $\alpha\mathbf{A} = \mathbf{A}\alpha$ of a *n*th-order tensor and a real number α are defined by the equations:

$$(\mathbf{A}+\mathbf{B})\mathbf{v}=\mathbf{A}\mathbf{v}+\mathbf{B}\mathbf{v},(\alpha\mathbf{A})\mathbf{v}=\alpha(\mathbf{A}\mathbf{v}). \tag{1.69}$$

As in the case of second-order tensors, it is easy to see that L_n endowed with the above operations and similar definitions for the zero tensor and opposite tensor $(-\mathbf{A})$, respectively, form a vector space.

Definition The tensor product or dyadic product of n vectors $\mathbf{u}_i$, with $i = 1, \ldots, n$, is a tensor of nth-order, denoted by $\mathbf{u}_1 \otimes \mathbf{u}_2 \ldots \otimes \mathbf{u}_n$ and is defined by:

$$(\mathbf{u}_1 \otimes \mathbf{u}_2 \ldots \otimes \mathbf{u}_n)(\mathbf{w}) = \mathbf{u}_1 \otimes \mathbf{u}_2 \ldots \otimes \mathbf{u}_{n-1}(\mathbf{u}_n \cdot \mathbf{w}) \quad \forall \mathbf{w} \in V. \tag{1.70}$$

Note that for $n = 2$ the above definition reduces to the definition of a dyadic product of any two vectors given by Eq. (1.21). In particular, the tensor product of three vectors $\mathbf{u}_1, \mathbf{u}_2, \mathbf{u}_3 \in V$ is a third-order tensor $\mathbf{u}_1 \otimes \mathbf{u}_2 \otimes \mathbf{u}_3$, which assigns to any vector $\mathbf{a}$ the second-order tensor $(\mathbf{u}_1 \otimes \mathbf{u}_2)(\mathbf{u}_3 \cdot \mathbf{a})$, so:

$$(\mathbf{u}_1 \otimes \mathbf{u}_2 \otimes \mathbf{u}_3)\mathbf{a} = (\mathbf{u}_1 \otimes \mathbf{u}_2)(\mathbf{u}_3 \cdot \mathbf{a}) \quad \forall \mathbf{a} \in V \tag{1.71}$$

In the mechanics of deformable bodies, the role of the third-order tensors is relatively reduced. However, in order to introduce the gradient of a second-order tensor field, and to obtain in this way the divergence of a second-order tensor field, we must use third-order tensor fields.

In general, the products $\mathbf{e}_{k_1} \otimes \mathbf{e}_{k_2} \ldots \otimes \mathbf{e}_{k_n}, k_1, \ldots, k_n = 1, \ldots, 3$ form a basis of L_n. Hence, L_n the vector space of nth-order tensors is 3^n dimensional, and every tensor $\mathbf{A}$ can be uniquely written in the form:

$$\mathbf{A} = A_{k_1 \ldots k_n} \mathbf{e}_{k_1} \otimes \mathbf{e}_{k_2} \ldots \otimes \mathbf{e}_{k_n}, \tag{1.72}$$

where the scalars $A_{k_1 \ldots k_n}$ are the Cartesian components of $\mathbf{A}$ in the considered basis. Furthermore, if $\mathbf{T} = \mathbf{A}\mathbf{v}$ and $\mathbf{T} = T_{k_1 \ldots k_{n-1}} \mathbf{e}_{k_1} \otimes \mathbf{e}_{k_2} \ldots \otimes \mathbf{e}_{k_n}$ by applying the definition (1.70), we obtain the expression of the components of the $(n - 1)$th-order tensor $\mathbf{T}$ in terms of the components of $\mathbf{A}$ and of the vector $\mathbf{v}$ as:

$$T_{k_1 \ldots k_{n-1}} = A_{k_1 \ldots k_n} \mathrm{v}_{k_n}.$$

Fourth-Order Tensors

The dimension of the vector space of fourth-order tensors, L_4, is $3^4 = 81$, and any fourth-order tensor $\mathbf{\Phi}$ can be expressed in a unique way as a linear combination of fourth-order dyads $\mathbf{e}_k \otimes \mathbf{e}_l \otimes \mathbf{e}_m \otimes \mathbf{e}_n$, k, l, m, $n = 1, \ldots, 3$; i.e.,

$$\mathbf{\Phi} = \Phi_{klmn} \mathbf{e}_k \otimes \mathbf{e}_l \otimes \mathbf{e}_m \otimes \mathbf{e}_n, \tag{1.73}$$

the numbers Φ_{klmn}, k, l, m, $n = 1, \ldots, 3$ being the components of $\mathbf{\Phi}$ in the considered basis; if $\mathbf{A} = \mathbf{\Phi}\,\mathbf{v}$ the components of the third-order tensor $\mathbf{A}$ are:

$$A_{klm} = \Phi_{klmn} \mathrm{v}_n. \tag{1.74}$$

Transformation Rules for the Components of Fourth-Order Tensors

If $\left\{\mathbf{e}_1^*, \mathbf{e}_2^*, \mathbf{e}_3^*\right\}$ are three-dimensional positive-oriented orthonormal bases of the three-dimensional space V, then the components of the fourth-order tensor in the basis $\left\{\mathbf{e}_1^*, \mathbf{e}_2^*, \mathbf{e}_3^*\right\}$ are:

$$\Phi_{rstu} = q_{kr} q_{ls} q_{mt} q_{nu} \Phi_{klmn}, \tag{1.75}$$

where $\mathbf{Q} = \left[q_{ij}\right]$ is the transformation matrix from the new basis $\left\{\mathbf{e}_1^*, \mathbf{e}_2^*, \mathbf{e}_3^*\right\}$ to the old basis $\left\{\mathbf{e}_1, \mathbf{e}_2, \mathbf{e}_3\right\}$ and r, s, t, $u = 1, \ldots, 3$.

Relative to any orthonormal basis, the fourth-order identity tensor $\mathbf{I}_4$ has the components:

$$\mathbf{I}_4 = \delta_{km}\delta_{ln} \mathbf{e}_k \otimes \mathbf{e}_l \otimes \mathbf{e}_m \otimes \mathbf{e}_n. \tag{1.76}$$

Contracted Products Between Tensors

In the previous section, we defined the inner product (contracted product) of any two second-order tensors [see Eq. (1.33)]. In the following, we introduce contracted products between various nth-order tensors, which will be later used to define anisotropic yield criteria in terms of transformed tensors (see Chap. 5).

Definition The *left dot product* and *right dot product* (contracted product) of a *vector* $\mathbf{v}$ and a *second-order tensor* $\mathbf{T}$ is the vector defined as:

$$\begin{aligned} \mathbf{v} \cdot \mathbf{T} &= \mathbf{T}^T \mathbf{v} \\ \mathbf{T} \cdot \mathbf{v} &= \mathbf{T}\mathbf{v} \end{aligned} \tag{1.77}$$

Relative to an orthonormal basis $\left\{\mathbf{e}_1, \mathbf{e}_2, \mathbf{e}_3\right\}$,

$$\mathbf{v} \cdot \mathbf{T} = v_k T_{kl} \mathbf{e}_l, \quad \mathbf{T} \cdot \mathbf{v} = T_{kl} v_l \mathbf{e}_k \tag{1.78}$$

with k, $l = 1, \ldots, 3$.

Definition The *left dot product* and *right dot product* (contracted product) of a *vector* $\mathbf{v}$ and a *third-order tensor* $\mathbf{A}$ is the second-order tensor defined as:

$$\begin{aligned} \mathbf{v} \cdot \mathbf{A} &= \mathbf{A}^T \mathbf{v} = \mathrm{v}_k A_{klm} \mathbf{e}_l \otimes \mathbf{e}_m, \\ \mathbf{A} \cdot \mathbf{v} &= \mathbf{A}^T \mathbf{v} = A_{klm} \mathrm{v}_m \mathbf{e}_k \otimes \mathbf{e}_l. \end{aligned} \tag{1.79}$$

with k, l, m, $n = 1, \ldots, 3$.

Definition The *contracted product* of a *fourth-order tensor* $\mathbf{\Phi}$ and *a second-order tensor* $\mathbf{T}$ is a second-order tensor defined as:

$$\mathbf{\Phi T} = \Phi_{klmn} T_{mn} \mathbf{e}_k \otimes \mathbf{e}_l. \tag{1.80}$$

Using the transformation rules of the components of vectors, second-order, third-order, and fourth-order tensors [see Eqs. (1.45), (1.48), (1.74)–(1.75)], it can be shown that these contracted products are independent of the basis used.

Remark Note that if $\mathbf{U} = \mathbf{\Phi T}$ then the inner product of $\mathbf{U}$ with any second-order tensor $\mathbf{B} = B_{kl} \mathbf{e}_k \otimes \mathbf{e}_l$ is given by:

$$\mathbf{B} \cdot \mathbf{U} = \Phi_{klmn} B_{kl} T_{mn} \tag{1.81}$$

and in particular the norm of $\mathbf{U}$ is:

$$\|U\|^2 = \mathbf{U} \cdot \mathbf{U} = \mathbf{U} \cdot \mathbf{\Phi T} = \Phi_{klmn} U_{kl} T_{mn} \tag{1.82}$$

Remark On the basis of the definition and properties of the contracted product between a fourth-order tensor and a second-order tensor, it can be concluded that *a fourth-order tensor can be considered as being a linear mapping of the vector space L of second-order tensors onto itself*. Therefore, we can introduce the product or composition of two fourth-order tensors using the usual rule of composition of functions.

Product (Composition) of Fourth-Order Tensors

Definition The product (or composition) of any fourth-order tensors $\mathbf{\Phi}$ and $\mathbf{\Psi}$ is the fourth-order tensor defined as:

$$(\mathbf{\Phi}\,\mathbf{\Psi})(\mathbf{T}) = \mathbf{\Phi}(\mathbf{\Psi T}) \text{ for any } \mathbf{T} \in L. \tag{1.83}$$

Let $\{\mathbf{e}_1, \mathbf{e}_2, \mathbf{e}_3\}$ be an orthonormal basis, the product $\mathbf{L} = \mathbf{\Phi}\,\mathbf{\Psi}$ has the components:

$$L_{klmn} = \Phi_{klrs} \Psi_{rsmn}, \quad \text{with } k, l, m, n = 1, \ldots, 3.$$

It can be easily shown that fourth-order identity tensor $\mathbf{I}_4$ [see Eq. (1.76)] has the following properties:

$\mathbf{I}_4 \mathbf{T} = \mathbf{T}$, for any second-order tensor $\mathbf{T}$ and for any fourth-order tensor $\mathbf{\Phi}$,

$$\mathbf{I}_4 \mathbf{\Phi} = \mathbf{\Phi} \mathbf{I}_4 = \mathbf{\Phi}.$$

Given the above properties of $\mathbf{I}_4$ and of the product of fourth-order tensors, the inverse and transpose of a fourth-order tensor are defined in the same manner as the inverse and transpose of second-order tensors [see definitions and Eq. (1.40)].

Transpose of a Fourth-Order Tensor

Definition Associated with any fourth-order tensor $\mathbf{\Phi}$, there is a fourth-order tensor called the transpose of $\mathbf{\Phi}$, denoted by $\mathbf{\Phi}^T$ such that:

$$\mathbf{A} : \left(\mathbf{\Phi}^T \mathbf{B}\right) = \mathbf{B} : \mathbf{\Phi}\,\mathbf{A}, \quad \forall \mathbf{A}, \mathbf{B} \in L \tag{1.84}$$

It can be easily shown that the above requirement uniquely defines the transpose $\mathbf{\Phi}^T$ and that it is indeed a fourth-order tensor, its components relative to an orthonormal basis being:

$$\Phi^T_{klmn} = \Phi_{mnkl} \tag{1.85}$$

Symmetric Fourth-Order Tensors

Definition A fourth-order tensor $\mathbf{\Phi}$ is symmetric if,

$$\mathbf{\Phi}^T = \mathbf{\Phi}. \tag{1.86}$$

Therefore, it follows that if $\mathbf{\Phi}$ is symmetric its components satisfy the requirements:

$$\Phi_{klmn} = \Phi_{mnkl}, \quad \text{with} \quad k, l, m, n = 1, 2, 3. \tag{1.87}$$

We shall denote by L_4^S the set of all symmetric fourth-order tensors. From Eq. (1.87), it follows that a symmetric fourth-order tensor has only 45 independent components (dimension of L_4^S = 45). When introducing anisotropy using the linear transformation approach (see Chap. 5), an important role is played by those symmetric fourth-order tensors which also satisfy the additional symmetry property:

$$\mathbf{\Phi}\mathbf{T}^T = \mathbf{\Phi}\mathbf{T}, \quad \forall \mathbf{T} \in L. \tag{1.88}$$

Denoting by Φ_{klmn} the components of the symmetric fourth-order tensor $\mathbf{\Phi}$, it follows that the requirements (1.87) and (1.88) imply that:

$$\Phi_{klmn} = \Phi_{lkmn} = \Phi_{klnm} = \Phi_{mnkl}, \quad \text{with} \quad k, l, m, n = 1 \ldots 3, \tag{1.89}$$

so the tensor $\mathbf{\Phi}$ *has only 21 independent components*. Note that the above symmetry requirements imply

$$(\mathbf{\Phi}\mathbf{T})^T = \mathbf{\Phi}\mathbf{T}, \quad \forall \mathbf{T} \in \mathrm{L}$$

so,

$$\mathbf{\Phi T} = \mathbf{\Phi T}^S,$$

where $\mathbf{T}^S$ denotes the symmetric part of the second-order tensor $\mathbf{T}$ [see Eq. (1.30)]. An immediate consequence is that:

$$\mathbf{\Phi\, \Omega} = \mathbf{0}, \quad \text{for any skew tensor } \mathbf{\Omega}. \tag{1.90}$$

This means that a symmetric fourth-order tensor $\mathbf{\Phi}$, having the additional symmetry properties of Eq. (1.89) is not a one-to-one mapping of L, the space of second-order tensors. However, a symmetric tensor $\mathbf{\Phi}$ satisfying the symmetry conditions of Eq. (1.89) may admit an inverse in the space of symmetric fourth-order tensors.

Let us first note that the tensor $\hat{\mathbf{I}}$ defined as:

$$\hat{I}_{klmn} = \frac{1}{2}(\delta_{km}\delta_{\ln} + \delta_{kn}\delta_{lm}), \tag{1.91}$$

is indeed a fourth-order symmetric tensor and satisfies the additional symmetry requirements of Eq. (1.89). Moreover, it has the following property:

$$\hat{\mathbf{I}}\mathbf{\Phi} = \mathbf{\Phi}\hat{\mathbf{I}} = \mathbf{\Phi}, \quad \text{for any symmetric tensor } \mathbf{\Phi}. \tag{1.92}$$

In other words, $\hat{\mathbf{I}}$ *is the unit tensor in the space of symmetric fourth-order tensors*. Similarly with the definitions of positive-definiteness of second-order tensors [see Eq. (1.63)], we say that a fourth-order tensor $\mathbf{\Phi} \in L_4$ is positive-definite if:

$$\mathbf{T} : \Phi\mathbf{T} \geq \mathbf{0}, \quad \text{for any symmetric tensor } \mathbf{T} \tag{1.93}$$

and,

$$\mathbf{T}\colon \mathbf{\Phi T} = \mathbf{0} \quad \text{if and only if } \mathbf{T} = \mathbf{0}.$$

It can be easily seen that if a symmetric fourth-order tensor $\mathbf{\Phi}$ is positive-definite, there exists a fourth-order symmetric tensor Ψ such that:

$$\mathbf{\Phi\Psi} = \mathbf{\Psi\Phi} = \hat{\mathbf{I}}. \tag{1.94}$$

This result is of great importance for the theory of elasticity, since it ensures that the inverse of the stiffness tensor exists and it is positive definite. In the mathematical theory of plasticity use is also made of the deviator of $\hat{\mathbf{I}}$. This fourth-order symmetric deviatoric tensor is generally denoted by $\mathbf{K}$, and its components with respect to any Cartesian coordinate system are given by:

$$K_{ijkl} = 1/2\left(\delta_{ik}\delta_{jl} + \delta_{il}\delta_{jk}\right) - 1/3\left(\delta_{ij}\delta_{kl}\right) \tag{1.95}$$

1.3 Elements of Vector and Tensor Calculus

In this section, we provide a brief review of differentiation of functions of a scalar variable t (e.g., time). Differentiation of a scalar function of a tensor and ensuing identities are essential in calculating the plastic strain-rate tensor once the expression of the plastic potential is known.

In this section, components of vectors and tensors are relative to a *fixed* orthonormal basis $\{\mathbf{e}_k\}$, k = 1, …, 3. The position vector of a point M in space will be denoted by $\mathbf{x} = x_k \mathbf{e}_k$, with x_1, x_2, x_3 being the Cartesian coordinates of M in the Cartesian coordinate system $(O, \mathbf{e}_1, \mathbf{e}_2, \mathbf{e}_3)$.

Derivative of a Point Function of a Scalar

Definition The derivative of a point function $\mathbf{x}(t)$ of a scalar variable t, denoted $\dot{\mathbf{x}}(t)$, is a vector function defined as:

$$\dot{\mathbf{x}}(t) = \lim_{h \to 0} \frac{\mathbf{x}(t+h) - \mathbf{x}(t)}{h} \tag{1.96}$$

Given a scalar f, vector $\mathbf{v}$, or second-order tensor function $\mathbf{T}$ of the scalar variable t, we write:

$$\begin{aligned} \dot{f}(t) &= \frac{\mathrm{d}f(t)}{\mathrm{d}t} = \lim_{h \to 0} \frac{f(t+h) - f(t)}{h}, \\ \dot{\mathbf{v}}(t) &= \dot{\mathrm{v}}_i(t) \mathbf{e}_i, \\ \dot{\mathbf{T}}(t) &= \dot{T}_{ij}(t) \mathbf{e}_i \otimes \mathbf{e}_j, \quad i,j = 1, \ldots, 3. \end{aligned}$$

Using the above definition, it can be shown that for any nonzero tensor function $\mathbf{T}(t)$,

$$\frac{\mathrm{d}}{\mathrm{d}t} \|\mathbf{T}(t)\| = \frac{\mathbf{T}(t) : \dot{\mathbf{T}}(t)}{\|\mathbf{T}(t)\|}. \tag{1.97}$$

Boundaries of the regions in the three-dimensional Euclidean space where these functions are defined are assumed to have continuity and differentiability properties sufficient to ensure that the boundary-value problems are well-posed. Thus, the domain of definition is the bounded open set D, the boundary of D, denoted ∂D, being a closed regular surface (i.e., unit normal fields over the bounding surface are well-defined).

Definition A function that assigns to each point of a region D a scalar, vector, or tensor function is called *scalar, vector, or tensor field on D*, respectively.

A vector or tensor field is said to be of class C^n on D if its components with respect to a fixed coordinate system are continuous on D together with their partial derivatives up to the nth-order.

Additionally, it is important to note that these regularity properties are independent of the chosen basis.

Gradient of a Scalar, Vector, or Tensor Field

Consider a scalar field $\phi : D \to R$ of class C^1. The gradient of ϕ, denoted $grad\varphi$, is the vector field:

$$grad\varphi(\mathbf{x}) = \frac{\partial \varphi}{\partial x_i}\mathbf{e}_i, \quad i = 1, \ldots, 3. \tag{1.98}$$

To differentiate a function $f(\mathbf{x}(t))$, where $\mathbf{x}(t)$ is a point function with real values, the chain rule in conjunction with the above definition is used:

$$\frac{\mathrm{d}}{\mathrm{d}t}(f(\mathbf{x}(t))) = grad\, f(\mathbf{x}) \cdot \dot{\mathbf{x}}(t) = \frac{\partial f}{\partial x_i}\dot{x}_i.$$

Gradient, Curl, Divergence of a Vector Field

Definition Let $\mathbf{u}(\mathbf{x})$ be a vector field of class C^1 in D. The *gradient of* $\mathbf{u}(\mathbf{x})$ *is the second-order tensor field,*

$$\mathrm{grad}\, \mathbf{u}(\mathbf{x}) = \frac{\partial u_i}{\partial x_j}\mathbf{e}_i \otimes \mathbf{e}_j,$$

the *curl* of $\mathbf{u}(\mathbf{x})$ is a vector field defined as:

$$\mathrm{curl}\ \mathbf{u}(\mathbf{x}) = \varepsilon_{mrs}\frac{\partial \mathbf{u}_r(\mathbf{x})}{\partial x_s}\mathbf{e}_m, \tag{1.99}$$

and the *divergence* of $\mathbf{u}(\mathbf{x})$ is the scalar:

$$\mathrm{div}\ \mathbf{u}(\mathbf{x}) = tr(grad\, \mathbf{u}(\mathbf{x})) = u_{kk}(\mathbf{x}). \tag{1.100}$$

We define the Laplace operator Δ for scalar and vector fields as:

$$\Delta\varphi(\mathbf{x}) = \mathrm{div}(\mathrm{grad}\varphi(\mathbf{x})), \tag{1.101}$$

and,

$$\Delta\mathbf{u}(\mathbf{x}) = \mathrm{div}(\mathrm{grad}\ \mathbf{u}(\mathbf{x})). \tag{1.102}$$

The operators *grad*, *curl*, *div*, Δ are linear mappings and therefore they are independent of the coordinate system (for proof, see, e.g., Malvern [5]).

Gradient, Curl, Divergence of a Tensor Field

Definition Let $\mathbf{T} : D \to L$ be a second-order tensor field of class C^1 on D. The gradient of $\mathbf{T}$ is the third-order tensor field defined as follows:

$$\mathrm{grad}\,\mathbf{T}(\mathbf{x}) = \frac{\partial T_{lm}(\mathbf{x})}{\partial x_k}\mathbf{e}_k \otimes \mathbf{e}_l \otimes \mathbf{e}_m, \tag{1.103}$$

the curl of $\mathbf{T}$ $(\mathbf{x})$ is the second-order tensor field,

$$\mathrm{curl}\,\mathbf{T}(\mathbf{x}) = \varepsilon_{ijk}\frac{\partial T_{lj}(\mathbf{x})}{\partial x_k}\mathbf{e}_l \otimes \mathbf{e}_i, \tag{1.104}$$

the divergence of $\mathbf{T}$ $(\mathbf{x})$ is the vector field:

$$\mathrm{div}\,\mathbf{T}(\mathbf{x}) = \frac{\partial T_{ij}(\mathbf{x})}{\partial x_j}\mathbf{e}_i,$$

while the Laplacian of $\mathbf{T}$ $(\mathbf{x})$ is the tensor field:

$$\Delta\mathbf{T}(\mathbf{x}) = \frac{\partial^2 T_{ij}}{\partial x_k \partial x_k}\mathbf{e}_i \otimes \mathbf{e}_j. \tag{1.105}$$

Differentiation of a Scalar Function of a Tensor

Definition For a scalar function $\Phi(\mathbf{A})$ of a second-order tensor variable $\mathbf{A}$, the derivative $\partial\Phi(\mathbf{A})/\partial\mathbf{A}$ is the tensor function defined such that:

$$\frac{\partial\Phi(\mathbf{A})}{\partial\mathbf{A}} : \mathbf{B} = \lim_{s\to 0}\frac{\Phi(\mathbf{A}+s\mathbf{B}) - \Phi(\mathbf{A})}{s} \quad \forall\mathbf{B} \in L. \tag{1.106}$$

It follows that:

$$\left[\frac{\partial \Phi(\mathbf{A})}{\partial \mathbf{A}}\right]_{ij} = \frac{\partial \Phi(\mathbf{A})}{\partial A_{ij}}. \tag{1.107}$$

Note that if $\mathbf{A}$ is a symmetric second-order tensor, $\dfrac{\partial \Phi(\mathbf{A})}{\partial \mathbf{A}}$ is a symmetric second-order tensor. The following result is central to the theory of plasticity.

1.4 Elements of the Theory of Tensor Representation

1.4.1 Symmetry Transformations and Groups

We will use the following notations:

L	the set of second-order tensors on V;
L^+	the set of all second-order tensors $\mathbf{A}$ with $\det(\mathbf{A}) > 0$;
Sym	the set of all symmetric second-order tensors;
$PSym^+$	the set of all symmetric and positive-definite second-order tensors;
Orth	the set of all orthogonal tensors on V;
$Orth^+$	the set of all rotations (proper orthogonal group).

Definition Let $\Delta \subset L$ and G a group of Orth. We say that a scalar function $\Phi: \Delta \rightarrow R$ is invariant relative to the group G, if for any $\mathbf{T} \in \Delta$ and for any $\mathbf{Q} \in G$, we have:

$$\Phi(\mathbf{T}) = \Phi\left(\mathbf{Q}\mathbf{T}\mathbf{Q}^T\right). \tag{1.108}$$

Similarly, a vector function $h: V \rightarrow R$ is invariant relative to the group G, if for any $\mathbf{v} \in V$ and for any $\mathbf{Q} \in G$, we have:

$$h(\mathbf{Q}\mathbf{v}) = \mathbf{Q}h(\mathbf{v}) \tag{1.109}$$

A tensor function $S : \Delta \rightarrow R$ is invariant relative to the group G, if for any $\mathbf{T} \in \Delta$ and for any $\mathbf{Q} \in G$, we have:

$$S\left(\mathbf{Q}\mathbf{T}\mathbf{Q}^T\right) = \mathbf{Q}S(\mathbf{T})\mathbf{Q}^T \tag{1.110}$$

Definition An isotropic function is a function invariant relative to the full orthogonal group.

In Sect. 1.2, we have shown that:

(a) The determinant, *det*, and the trace function, *tr*, are isotropic functions;
(b) The principal invariants

$$I_T = tr\mathbf{T}; II_T = \frac{1}{2}\left[(tr\mathbf{T})^2 - tr(\mathbf{T}^2)\right]; III_T = \det(\mathbf{T}) \tag{1.111}$$

of a symmetric tensor $\mathbf{T}$ are isotropic functions.

Representation Theorems for Isotropic Scalar Functions

Let us denote by $\mathbf{I}(\Delta) = \{\mathbf{I}_T | \mathbf{T} \in \Delta\}$ the set of all possible lists of invariants for symmetric tensors. Next, we present several representation theorems for scalar functions which are due to Cauchy and Wang [6].

Representation Theorem for Isotropic Scalar Function of a Symmetric Tensor

A scalar function $\Phi : \Delta \to R$, where $\Delta \subset Sym$, is isotropic if and only if there exists a function $\hat{\Phi} : \mathbf{I}(\Delta) \to R$ such that,

$$\Phi(\mathbf{T}) = \hat{\Phi}(\mathbf{I}_T) \text{ for any } \mathbf{T} \in \Delta \tag{1.112}$$

Proof That Eq. (1.112) defines an isotropic function is a direct consequence of Theorem 1.1. To prove the converse statement, let us assume that Φ is isotropic. It is sufficient to prove that if any two symmetric tensors $\mathbf{T}_1$ and $\mathbf{T}_2$ have the same spectrum, i.e., the same invariants [see Eq. (1.111)] then $\Phi(\mathbf{T}_1) = \Phi(\mathbf{T}_2)$. Indeed, if $\mathbf{I}_{\mathbf{T}_1} = \mathbf{I}_{\mathbf{T}_2}$ then $\mathbf{T}_1$ and $\mathbf{T}_2$ have the same eigenvalues λ_i, $i = 1, \ldots, 3$. By the spectral theorem, there exist orthonormal bases $\{\mathbf{e}_i\}$ and $\{\mathbf{f}_i\}$ such that $\mathbf{T}_1 = \sum_i \lambda_i \mathbf{e}_i \otimes \mathbf{e}_i$ and $\mathbf{T}_2 = \sum_i \lambda_i \mathbf{f}_i \otimes \mathbf{f}_i$. Let $\mathbf{Q}$ be the orthogonal transformation from one basis to the other, i.e., $\mathbf{Q}(\mathbf{f}_i) = \mathbf{e}_i$. Then,

$$\mathbf{Q}\mathbf{T}_2\mathbf{Q}^T = \sum_i \lambda_i \mathbf{Q}(\mathbf{f}_i \otimes \mathbf{f}_i)\mathbf{Q}^T = \sum_i \lambda_i (\mathbf{Q}\mathbf{f}_i) \otimes (\mathbf{Q}\mathbf{f}_i) = \sum_i \lambda_i \mathbf{e}_i \otimes \mathbf{e}_i = \mathbf{T}_1 \tag{1.113}$$

But since Φ is isotropic, $\Phi(\mathbf{T}_2) = \Phi\left(\mathbf{Q}\mathbf{T}_2\mathbf{Q}^T\right)$; thus by Eq. (1.113) we obtain that $\Phi(\mathbf{T}_1) = \Phi(\mathbf{T}_2)$. So, if Φ is an isotropic scalar function, it depends on $\mathbf{T}$ only through its invariants. Representation theorems for isotropic scalar-valued functions of an arbitrary number of symmetric tensors, skew-symmetric tensors, and vectors have been derived by Wang [6].

Representation Theorem for Isotropic Scalar Function

A scalar function $\Phi(\mathbf{T}_1, \mathbf{T}_2, \ldots, \mathbf{T}_a, \mathbf{W}_1, \mathbf{W}_2, \ldots, \mathbf{W}_b, \mathbf{v}_1, \mathbf{v}_2, \ldots, \mathbf{v}_k)$, where $\mathbf{T}_\mathrm{i}, \mathbf{W}_\mathrm{j}, \mathbf{v}_\mathrm{k}$ are respectively an arbitrary number of symmetric tensors,

skew-symmetric tensors, and vectors, is isotropic if and only if there exists a scalar function $\hat{\Phi}\left(I_{\mathbf{T}_1,\mathbf{T}_2,\ldots,\mathbf{T}_a,\mathbf{W}_1,\mathbf{W}_2,\ldots,\mathbf{W}_b,\mathbf{v}_1,\mathbf{v}_2,\ldots,\mathbf{v}_k}\right)$ such that

$$\begin{aligned}&\Phi(\mathbf{T}_1,\mathbf{T}_2,\ldots,\mathbf{T}_a,\mathbf{W}_1,\mathbf{W}_2,\ldots,\mathbf{W}_b,\mathbf{v}_1,\mathbf{v}_2,\ldots,\mathbf{v}_k)\\&=\hat{\Phi}\left(I_{\mathbf{T}_1,\mathbf{T}_2,\ldots,\mathbf{T}_a,\mathbf{W}_1,\mathbf{W}_2,\ldots,\mathbf{W}_b,\mathbf{v}_1,\mathbf{v}_2,\ldots,\mathbf{v}_k}\right)\end{aligned}\tag{1.114}$$

where, $I_{\mathbf{T}_1,\mathbf{T}_2,\ldots,\mathbf{T}_a,\mathbf{W}_1,\mathbf{W}_2,\ldots,\mathbf{W}_b,\mathbf{v}_1,\mathbf{v}_2,\ldots,\mathbf{v}_k}$ is an irreducible set of invariants for the arguments of the function Φ .

By definition, a set of invariants is called "functional basis" for the list of arguments if any arbitrary scalar function of these arguments can be expressed in terms of these basic invariants. A functional basis is called irreducible if none of its elements can be expressed as a function of the others. The complete list of invariants for the set of arguments $\mathbf{T}_1,\mathbf{T}_2,\ldots,\mathbf{T}_a,\mathbf{W}_1,\mathbf{W}_2,\ldots,\mathbf{W}_b,\mathbf{v}_1,\mathbf{v}_2,\ldots,\mathbf{v}_k$ is obtained considering all the (unordered) combinations of one, two, three, and four variables given in Table 1.1.

For example, the representation for an isotropic scalar function of two symmetric second-order tensors, $\mathbf{T}_1,\mathbf{T}_2$ involves ten invariants, i.e.,

Table 1.1 Irreducible isotropic functional bases

Arguments	Set of invariants
$\mathbf{T}$	$\mathrm{tr}(\mathbf{T})$, $\mathrm{tr}(\mathbf{T}^2)$, $\mathrm{tr}(\mathbf{T}^3)$
$\mathbf{W}$	$\mathrm{tr}(\mathbf{W}^2)$
$\mathbf{v}$	$\mathbf{v}\cdot\mathbf{v}$
$\mathbf{T}_1,\mathbf{T}_2$	$\mathrm{tr}(\mathbf{T}_1\mathbf{T}_2),\mathrm{tr}(\mathbf{T}_1^2\mathbf{T}_2),\mathrm{tr}(\mathbf{T}_1\mathbf{T}_2^2),\mathrm{tr}(\mathbf{T}_1^2\mathbf{T}_2^2)$
$\mathbf{T}$, $\mathbf{W}$	$tr(\mathbf{T}\mathbf{W}^2),tr(\mathbf{T}^2\mathbf{W}^2),tr(\mathbf{T}^2\mathbf{W}^2\mathbf{T}\mathbf{W})$
$\mathbf{T}$, $\mathbf{v}$	$\mathbf{v}\cdot\mathbf{T}\mathbf{v},\mathbf{v}\cdot\mathbf{T}^2\mathbf{v}$
$\mathbf{W}_1,\mathbf{W}_2$	$\mathrm{tr}(\mathbf{W}_1\mathbf{W}_2)$
$\mathbf{W}$, $\mathbf{v}$	$\mathbf{v}\cdot\mathbf{W}^2\mathbf{v}$
$\mathbf{v}_1,\mathbf{v}_2$	$\mathbf{v}_1\cdot\mathbf{v}_2$
$\mathbf{T}_1,\mathbf{T}_2,\mathbf{T}_3$	$\mathrm{tr}(\mathbf{T}_1\mathbf{T}_2\mathbf{T}_3)$
$\mathbf{T}_1,\mathbf{T}_2,\mathbf{W}$	$\mathrm{tr}(\mathbf{T}_1\mathbf{T}_2\mathbf{W}),\mathrm{tr}(\mathbf{T}_1^2\mathbf{T}_2\mathbf{W}),\mathrm{tr}(\mathbf{T}_1\mathbf{T}_2^2\mathbf{W}),\mathrm{tr}(\mathbf{T}_1\mathbf{W}^2\mathbf{T}_2\mathbf{W})$
$\mathbf{T}$, $\mathbf{W}_1,\mathbf{W}_2$	$\mathrm{tr}(\mathbf{T}\mathbf{W}_1\mathbf{W}_2),\mathrm{tr}(\mathbf{T}\mathbf{W}_1^2\mathbf{W}_2),\mathrm{tr}(\mathbf{T}\mathbf{W}_1\mathbf{W}_2^2)$
$\mathbf{W}_1,\mathbf{W}_2,\mathbf{W}_3$	$tr(\mathbf{W}_1\mathbf{W}_2\mathbf{W}_3)$
$\mathbf{T}_1,\mathbf{T}_2,\mathbf{v}$	$\mathbf{T}_1\mathbf{v}\cdot\mathbf{T}_2\mathbf{v}$
$\mathbf{T}$, $\mathbf{v}_1,\mathbf{v}_2$	$\mathbf{v}_1\cdot\mathbf{T}\mathbf{v}_2,\mathbf{v}_1\cdot\mathbf{T}^2\mathbf{v}_2$
$\mathbf{W}_1,\mathbf{W}_2$, $\mathbf{v}$	$\mathbf{W}_1\mathbf{v}\cdot\mathbf{W}_2\mathbf{v},\mathbf{W}_1^2\mathbf{v}\cdot\mathbf{W}_2\mathbf{v},\mathbf{W}_1\mathbf{v}\cdot\mathbf{W}_2^2\mathbf{v}$
$\mathbf{W}$, $\mathbf{v}_1,\mathbf{v}_2$	$\mathbf{v}_1\cdot\mathbf{W}\mathbf{v}_2,\mathbf{v}_1\cdot\mathbf{W}^2\mathbf{v}_2$
$\mathbf{T}$, $\mathbf{W}$, $\mathbf{v}$	$\mathbf{T}\mathbf{v}\cdot\mathbf{W}\mathbf{v},\mathbf{T}^2\mathbf{v}\cdot\mathbf{W}\mathbf{v},\mathbf{T}\mathbf{W}\mathbf{v}\cdot\mathbf{W}^2\mathbf{v}$
$\mathbf{T}_1,\mathbf{T}_2\mathbf{v}_1,\mathbf{v}_2$	$\mathbf{T}_1\mathbf{v}_1\cdot\mathbf{T}_2\mathbf{v}_2-\mathbf{T}_1\mathbf{v}_2\cdot\mathbf{T}_2\mathbf{v}_1$
$\mathbf{T}$, $\mathbf{W}$, $\mathbf{v}_1,\mathbf{v}_2$	$\mathbf{T}\mathbf{v}_1\cdot\mathbf{W}\mathbf{v}_2-\mathbf{T}\mathbf{v}_2\cdot\mathbf{W}\mathbf{v}_1$
$\mathbf{W}_1,\mathbf{W}_2,\mathbf{v}_1,\mathbf{v}_2$	$\mathbf{W}_1\mathbf{v}_1\cdot\mathbf{W}_2\mathbf{v}_2-\mathbf{W}_1\mathbf{v}_2\cdot\mathbf{W}_2\mathbf{v}_1$

$$I_{\mathbf{T}_1,\mathbf{T}_2} = \{tr(\mathbf{T}_1), tr(\mathbf{T}_1^2), tr(\mathbf{T}_1^3), tr(\mathbf{T}_2), tr(\mathbf{T}_2^2), tr(\mathbf{T}_2^3), \mathrm{tr}(\mathbf{T}_1\mathbf{T}_2),$$
$$\mathrm{tr}(\mathbf{T}_1^2\mathbf{T}_2), \mathrm{tr}(\mathbf{T}_1\mathbf{T}_2^2), \mathrm{tr}(\mathbf{T}_1^2\mathbf{T}_2^2)\}.$$

To establish representation theorems for isotropic tensor functions, we need to first prove the following lemma given by Wang [6].

Lemma 1.3 *Let* $\mathbf{I}$ *be the second-order unit tensor,* $\mathbf{T}$ *be a symmetric tensor,* $\lambda_1, \lambda_2, \lambda_3$ *its eigenvalues with* $\mathbf{e}_1, \mathbf{e}_2, \mathbf{e}_3$ *corresponding eigenvectors.*

(a) If all the eigenvalues λ_i are distinct, then $\{\mathbf{I}, \mathbf{T}, \mathbf{T}^2\}$ are linearly independent;
(b) If $\mathbf{T}$ has exactly two distinct eigenvalues, then $\{\mathbf{I}, \mathbf{T}\}$ are linearly independent.

Proof

(a) To prove that the set $\{\mathbf{I}, \mathbf{T}, \mathbf{T}^2\}$ is linearly independent, we must show that,

$$a\mathbf{T}^2 + b\mathbf{T} + c\mathbf{I} = \mathbf{0}, \tag{1.115}$$

only if $a = b = c = 0$. Since $\mathbf{T}(\mathbf{e}_i) = \lambda_i\mathbf{e}_i$ and $\mathbf{T}^2(\mathbf{e}_i) = (\lambda_i)^2\mathbf{e}_i$, from Eq. (1.115) it follows that,

$$\left(a\lambda_i^2 + b\lambda_i + c\right)\mathbf{e}_i = 0, \text{so that } a\lambda_i^2 + b\lambda_i + c = 0 \text{ for any } i = 1, 2, 3. \tag{1.116}$$

The determinant of the homogeneous algebraic system (1.116) in the unknowns a, b, and c is:

$$\Delta = \begin{vmatrix} \lambda_1^2 & \lambda_1 & 1 \\ \lambda_2^2 & \lambda_2 & 1 \\ \lambda_3^2 & \lambda_3 & 1 \end{vmatrix} \tag{1.117}$$

Since the eigenvalues λ_i are distinct, $\Delta \neq 0$; thus the unique solution of (1.116) is: $a = b = c = 0$. Thus, $\{\mathbf{I}, \mathbf{T}, \mathbf{T}^2\}$ are linearly independent.

(b) To establish the linear independence of $\{\mathbf{I}, \mathbf{T}\}$ we must show that,

$$a\mathbf{I} + b\mathbf{T} = \mathbf{0}, \tag{1.118}$$

only if $a = b = 0$. Since $\mathrm{T} = \lambda_1\mathbf{e} \otimes \mathbf{e} + \lambda_2(\mathbf{I} - \mathbf{e} \otimes \mathbf{e})$, from Eq. (1.118) it follows that,

$$\begin{cases} a + b\lambda_1 = 0 \\ a + b\lambda_2 = 0 \end{cases}. \tag{1.119}$$

The eigenvalues λ_1 and λ_2 being distinct, Eq. (1.118) holds only if $a = b = 0$. Thus, $\mathbf{I}$ and $\mathbf{T}$ are linearly independent.

1.4.2 Representation Theorems for Orthotropic Scalar Functions

Certain anisotropic materials such as transversely isotropic materials as well as some crystalline solids (for detailed discussion of crystal classes and respective symmetry groups, see Chap. 3) can be characterized by preferred directions and planes, i.e., by certain vectors $\mathbf{m}_1$,$\mathbf{m}_2, \ldots, \mathbf{m}_\mathrm{p}$ and some tensors $\mathbf{M}_1, \mathbf{M}_2, \ldots, \mathbf{M}_\mathrm{q}$. The symmetry group G of such materials preserves these characteristics and is of the form:

$$G = \left\{ \mathbf{Q} \in \mathrm{O} | \mathbf{Q}\,\mathbf{m}_1 = \mathbf{m}_1, \ldots, \mathbf{Q}\,\mathbf{m}_\mathrm{p} = \mathbf{m}_\mathrm{p}, \mathbf{Q}\,\mathbf{M}_1\mathbf{Q}^T = \mathbf{M}_1, \ldots, \mathbf{Q}\,\mathbf{M}_\mathrm{q}\mathbf{Q}^T = \mathbf{M}_\mathrm{q} \right\} \tag{1.120}$$

Theorem 1.3 *A function f is invariant relative to the symmetry group G if and only if it can be represented by an isotropic function* $\hat{f}$:

$$\begin{aligned} &f(\mathbf{v}_1, \mathbf{v}_2, \ldots, \mathbf{v}_a, \mathbf{A}_1, \mathbf{A}_2, \ldots, \mathbf{A}_b) \\ &= \hat{f}(\mathbf{v}_1, \mathbf{v}_2, \ldots, \mathbf{v}_a, \mathbf{A}_1, \mathbf{A}_2, \ldots, \mathbf{A}_b, \mathbf{m}_1, \ldots, \mathbf{m}_p, \mathbf{M}_1, \ldots, \mathbf{M}_q) \end{aligned} \tag{1.121}$$

Proof While in the theorem, the function f can be either scalar-valued, vector-valued, or tensor-valued, we will present the proof only for scalar-valued functions. The proof for vector-valued and tensor-valued functions is similar and for both proofs, we refer the reader to the paper of I-Shih [4].

Assume that f admits the representation given by Eq. (1.121). We need to show that f is invariant relative to G, i.e.,

$$f(\mathbf{Q}\mathbf{v}_1, \ldots, \mathbf{Q}\mathbf{v}_a, \mathbf{Q}\mathbf{A}_1\mathbf{Q}^\mathbf{T}, \ldots, \mathbf{Q}\mathbf{A}_b\mathbf{Q}^\mathbf{T}) = f(\mathbf{v}_1, \mathbf{v}_2, \ldots, \mathbf{v}_a, \mathbf{A}_1, \ldots, \mathbf{A}_b) \quad \forall \mathbf{Q} \in \mathrm{G}.$$

Since,

$$\begin{aligned} &f(\mathbf{Q}\mathbf{v}_1, \ldots, \mathbf{Q}\mathbf{v}_a, \mathbf{Q}\mathbf{A}_1\mathbf{Q}^\mathbf{T}, \ldots, \mathbf{Q}\mathbf{A}_b\mathbf{Q}^\mathbf{T}) \\ &= \hat{f}(\mathbf{Q}\mathbf{v}_1, \ldots \mathbf{Q}\mathbf{v}_a, \mathbf{Q}\mathbf{A}_1\mathbf{Q}^\mathbf{T}, \ldots, \mathbf{Q}\mathbf{A}_b\mathbf{Q}^\mathbf{T}, \mathbf{m}_1, \ldots, \mathbf{m}_p, \mathbf{M}_1, \ldots, \mathbf{M}_q) \\ &= \hat{f}(\mathbf{Q}\mathbf{v}_1, \ldots, \mathbf{Q}\mathbf{v}_a, \mathbf{Q}\mathbf{A}_1\mathbf{Q}^\mathbf{T}, \ldots, \mathbf{Q}\mathbf{A}_b\mathbf{Q}^\mathbf{T}, \mathbf{Q}\mathbf{Q}^\mathbf{T}\mathbf{m}_1 \ldots \mathbf{Q}\mathbf{Q}^\mathbf{T}\mathbf{m}_p, \mathbf{Q}\mathbf{Q}^\mathbf{T}\mathbf{M}_1\mathbf{Q}\mathbf{Q}^\mathbf{T}, \ldots \mathbf{Q}\mathbf{Q}^\mathbf{T}\mathbf{M}_q\mathbf{Q}\mathbf{Q}^\mathbf{T}) \end{aligned}$$

and $\hat{f}$ is isotropic, it follows that:

$$\begin{aligned} &f(\mathbf{Q}\mathbf{v}_1, \ldots, \mathbf{Q}\mathbf{v}_a, \mathbf{Q}\mathbf{A}_1\mathbf{Q}^\mathbf{T}, \ldots, \mathbf{Q}\mathbf{A}_b\mathbf{Q}^\mathbf{T}) \\ &= \hat{f}(\mathbf{v}_1, \ldots \mathbf{v}_a, \mathbf{A}_1, \ldots \mathbf{A}_b, \mathbf{Q}^\mathbf{T}\mathbf{m}_1, \ldots, \mathbf{Q}^\mathbf{T}\mathbf{m}_p, \mathbf{Q}^\mathbf{T}\mathbf{M}_1\mathbf{Q}, \ldots, \mathbf{Q}^\mathbf{T}\mathbf{M}_q\mathbf{Q}) \end{aligned}$$

Given that $\mathbf{Q} \in G$, so we have: $\mathbf{Q}\mathbf{m}_1 = \mathbf{m}_1$, …, $\mathbf{Q}\mathbf{m}_p = \mathbf{m}_p$ and $\mathbf{Q}\mathbf{M}_1\mathbf{Q}^\mathbf{T} = \mathbf{M}_1$, …, $\mathbf{Q}\mathbf{M}_q\mathbf{Q}^\mathbf{T} = \mathbf{M}_q$.

Therefore,

$$\hat{f}(\mathbf{v}_1, \ldots \mathbf{v}_a, \mathbf{A}_1, \ldots, \mathbf{A}_b, \mathbf{Q}^{\mathbf{T}}\mathbf{m}_1, \ldots, \mathbf{Q}^{\mathbf{T}}\mathbf{m}_p, \mathbf{Q}^{\mathbf{T}}\mathbf{M}_1\mathbf{Q}, \ldots, \mathbf{Q}^{\mathbf{T}}\mathbf{M}_q\mathbf{Q})$$
$$= \hat{f}(\mathbf{v}_1, \ldots, \mathbf{v}_a, \mathbf{A}_1, \ldots, \mathbf{A}_b, \mathbf{m}_1, \ldots, \mathbf{m}_p, \mathbf{M}_1, \ldots, \mathbf{M}_q) = f(\mathbf{v}_1, \ldots, \mathbf{v}_a, \mathbf{A}_1, \ldots, \mathbf{A}_b).$$

Transverse isotropy is characterized by a preferred direction $\mathbf{n}$. Its symmetry group is:

$$G_T = \{\mathrm{Q} \in \mathrm{O} | \mathrm{Q}\mathbf{n} = \mathbf{n}\}. \tag{1.122}$$

(See also Chap. 5). By the above theorem, we have the following result:

A transversely isotropic function $f(\mathbf{v}_1, \mathbf{v}_2, \ldots, \mathbf{v}_a, \mathbf{A}_1, \mathbf{A}_2, \ldots, \mathbf{A}_b)$ *can be represented as*:

$$f(\mathbf{v}_1, \mathbf{v}_2, \ldots, \mathbf{v}_a, \mathbf{A}_1, \mathbf{A}_2, \ldots, \mathbf{A}_b) = \hat{f}(\mathbf{v}_1, \mathbf{v}_2, \ldots, \mathbf{v}_a, \mathbf{A}_1, \mathbf{A}_2, \ldots \mathbf{A}_b, n)$$

where $\hat{f}$ is an isotropic function.

Orthotropy is characterized by reflections on three mutually orthogonal planes. Another important result is given by:

Theorem 1.4 *Any orthotropic function* $f(\mathbf{v}_1, \mathbf{v}_2, \ldots, \mathbf{v}_a, \mathbf{A}_1, \mathbf{A}_2, \ldots, \mathbf{A}_b)$ *can be represented as*:

$$f(\mathbf{v}_1, \mathbf{v}_2, \ldots, \mathbf{v}_a, \mathbf{A}_1, \mathbf{A}_2, \ldots, \mathbf{A}_b) = \hat{f}(\mathbf{v}_1, \mathbf{v}_2, \ldots, \mathbf{v}_a, \mathbf{A}_1, \mathbf{A}_2, \ldots, \mathbf{A}_b, \mathbf{N}_1, \mathbf{N}_2) \tag{1.123}$$

where $\hat{f}$ is an isotropic function, $\mathbf{N}_1 = \mathbf{n}_1 \otimes \mathbf{n}_1$ and $\mathbf{N}_2 = \mathbf{n}_2 \otimes \mathbf{n}_2$ (see I-Shih [4]).

The above results were used by Cazacu and Barlat [1, 2] to derive yield criteria for orthotropic and transversely isotropic metallic materials (see Chap. 5).

References

1. Cazacu O, Barlat F (2001) Generalization of Drucker's yield criterion to orthotropy. Math Mech Solids 6:613–630. https://doi.org/10.1177/108128650100600603
2. Cazacu O, Barlat F (2003) Application of the theory of representation to describe yielding of anisotropic aluminum alloys. Int J Eng Sci 41:1367–1385
3. Halmos PR (1958) Finite-dimensional vector spaces. Springer, New York
4. I-Shih L (1982) On representations of anisotropic invariants. Int J Eng Sci 20:1099–1109. https://doi.org/10.1016/0020-7225(82)90092-1
5. Malvern LE (1969) Introduction to the mechanics of a continuous medium. Prentice-Hall
6. Wang C-C (1970) A new representation theorem for isotropic functions: an answer to professor GF Smith's criticism of my papers on representations for isotropic functions. Arch Ration Mech Anal 36:166–197

Chapter 2
Constitutive Equations for Elastic–Plastic Materials

In this chapter, we present a brief historical outline followed by the governing equations for a plastically deformable metallic material and the time integration algorithms developed in order to solve boundary-value problems in the context of the finite-element method. Detailed discussions of numerical aspects are beyond the scope of this review, the primary objective here is to present the key constitutive hypotheses and their relevance with respect to experimental observations.

The earliest evidence of metal working dates back to about 4500 B.C. During that time period the ability of metals to undergo permanent change in shape, i.e., plastic deformation was primarily exploited for the production of hand tools and weapons. While metal shaping processes (e.g., forging, rolling, extrusion) and alloying techniques have constantly evolved since that time, the first theoretical developments and mathematical relations relating stresses and strains in a metallic material undergoing permanent deformation were proposed toward the end of the eighteenth century. On the basis of experimental observations on torsion of iron wires and bending of iron blades, respectively, Coulomb [13] concluded that permanent changes in shape occur when the applied load becomes equal to or greater than a certain critical value. For example, during torsion of iron wires, Coulomb [13] reported that when the angle of rotation exceeds 180°, the angle of recovery becomes smaller than the angle of twisting. Moreover, using an analogy with frictional phenomena, he attributed the occurrence of permanent deformation to breaking of adhesion between particles and subsequent glide inside the metal. Almost eighty years later, at a time when the theory of elasticity flourished due to the fundamental advances in mathematics made by Poisson (1781–1840), Cauchy (1789–1857), and Lame (1795–1870), Tresca [48] conducted experiments on extrusion of metals through dies of different shapes and concluded that for the materials studied the extrusion force depends only on the shear stress. Although in these tests the stress distribution is non-uniform, Tresca arrived at the conclusion that the material studied "flows under a constant maximum shear stress" (see also Hill [26], who suggests that in formulating the yield criterion Tresca may have been guided by a failure criterion proposed in 1773 by Coulomb).

O. Cazacu et al., *Plasticity–Damage Couplings: From Single Crystal to Polycrystalline Materials*, Solid Mechanics and Its Applications 253,
https://doi.org/10.1007/978-3-319-92922-4_2

The first theory relating stresses and strains in a metallic material that undergoes plastic deformation was proposed by Saint-Venant [42] for plane-strain conditions. Neglecting elastic strains, Saint-Venant [42] assumed that: (a) plastic deformation is not accompanied by any change of volume; (b) in the domain where plastic deformation occurs, the maximum shear stress at each point is equal to a certain constant value (this last assumption is known as the Tresca yield criterion), and (c) the increment of the total strain and the applied stress have the same principal directions. Levy [31] generalized the Saint-Venant [42]'s theory to arbitrary three-dimensional loadings and pointed out the intrinsic difference between the stress–strain relations for an elastic material (proportionality between stresses and strains) and those of a plastically deformable material, namely proportionality between the strain increments and deviatoric stresses. However, the 3-D generalization proposed by Levy [31] based on Tresca's yield criterion is not correct, as it was made clear in 1913 when von Mises [51] independently arrived at the same relations on the basis of his yield criterion. The von Mises [51] model states that for an isotropic metallic material, plastic flow occurs when the second-invariant of the stress deviator, J_2, attains a critical value. Later on, von Mises introduced the concept of a plastic potential in the stress space, i.e., a scalar function of stress (e.g., J_2) such that the plastic strain increments are calculated upon differentiation of this potential with respect to stresses, when the yield condition is satisfied. He further proposed that the plastic potential should be taken the same as the yield function.

Hencky [24] demonstrated that J_2 is a measure of the elastic energy of distortion (i.e., the elastic energy less the energy required to produce volume changes) while Nadai [32] showed that J_2 is proportional to the shear stress acting on a plane whose normal makes equal angles with the eigenvectors of the stress (i.e., the octahedral plane, see also Chap. 4).

Nevertheless, as Prager and Hodge [38] pointed out: "Mises' yield criterion condition derives its importance in the mathematical theory of plasticity not from the fact that the invariant J_2 appearing therein can be interpreted physically in this or that manner, but from the fact that it has the simplest mathematical form compatible with the general postulates which any field condition must fulfill".

The experimental verification of the fact that the plastic behavior of metallic materials is not accompanied by volume changes was provided by Bridgman [7] (see also experimental results of Polanyi and collaborators (see [35]) on single crystals subjected to uniaxial tensile tests on which hydrostatic pressure was superposed). However, later on Bridgman [8] showed that if the hydrostatic stress is several orders of magnitude greater than the tensile yield stress, permanent volume changes may be expected.

An important step in the development of the discipline is the generalization of the von Mises [51] relations between the total strain increments and the stress deviators proposed by Prandtl [39] for the plane-strain case, and by Reuss [41] for general loadings. These authors assumed that the total strain increment is the sum of an elastic strain increment and a plastic strain increment, the plastic strain increment being proportional to the stress deviator. It was also pointed out that in contrast to

elastic behavior, the ratio between plastic strain increments and stresses is not a constant.

A completely different type of plasticity theories, called deformation theories, originated with Hencky [24] (see also Ilyushin [30]). The key constitutive hypothesis of theses theories is that the stress is directly related to the plastic strain. The deformation theories have been widely used, particularly in the Russian literature (see Cristescu [14]). However, it was clearly demonstrated that all deformation theories violate the basic requirement that the plastic strain should be dependent on the loading path by which it was produced. For example, Hill [26], Hodge and White [28] and Goodier and Hodge [22] demonstrated rigorously the inadequacy of all such theories for most non-proportional loadings. These authors also clearly showed that while deformation theories may seem appealing due to their mathematical simplicity, the fact that in such theories, load-path effects are neglected means that the plastic behavior is modeled as nonlinear elastic behavior. Therefore, plasticity theories of the Hencky-type will not be discussed in this book.

W. Prager and collaborators (see, e.g., Handelman et al. [23], Hodge and Prager [27], Prager [36], and Prager and Hodge [38]) introduced the fundamental assumptions concerning the form of the stress–strain relationships governing plastic deformation of metallic materials. First, it was assumed that during loading the relation between the increment of plastic strain $\Delta\boldsymbol{\varepsilon}^p$ and the stress increment $\Delta\boldsymbol{\sigma}$ should be linear, i.e.,

$$\Delta\boldsymbol{\varepsilon}^p = \mathbf{C}^{ep}\Delta\boldsymbol{\sigma}, \tag{2.1}$$

where $\mathbf{C}^{ep}$ is a function of the mechanical state of the material, but not of the stress increment. The assumptions of continuity, which is associated with the concept of neutral loading (limiting case of either loading or unloading), consistency, which ensures that loading leads from one plastic state to the other, and uniqueness of the solution to boundary-value problems, complete the specification of the evolution of the plastic strain, i.e., Eq. (2.1). Moreover, the condition or postulate of irreversibility was introduced. It states that unloading can only be elastic.

D.C. Drucker introduced postulates (see [16–20]) that have been playing a vital role in ensuring that the elastic/plastic problem is well-posed for work-hardening materials. Based on these postulates, it can be shown that a sufficient condition for the uniqueness of solution to a stated boundary-value problem for work-hardening materials is that the plastic strain-rate tensor is along the outward normal direction of the yield surface. Specifically, Drucker's postulates ensure the convexity of the yield surface and the normality of the plastic strain-rate to an evolving yield surface (for an in-depth discussion on Drucker postulates, the reader is referred to the monograph [21]). As already mentioned, the historical outline presented here gives just a brief overview of the main developments, for a thorough description of the history of plasticity, the reader is referred to the recent review paper of Osakada [34].

Before proceeding to the formal introduction of the concepts of yield function/surface, flow rule, and hardening, we will illustrate the main features of the plastic response of metallic materials that are modeled with these concepts. For this purpose, we discuss the stress–strain response of a metallic material in uniaxial tension.

Consider a specimen subject to uniaxial tension. For metallic materials, the stress–strain response is nonlinear beyond a certain level of the applied load. However, for sufficiently small values of the load the test specimen will resume its initial shape upon unloading (i.e., removal of the applied load). The elastic regime of behavior is defined by the range of stress–strain for which upon complete unloading the material recovers its initial state. The plastic regime of the behavior is defined by the states of stress and strains beyond the elastic range. The transition from elastic to plastic response can be abrupt (e.g., mild steels) or gradual (e.g., titanium materials; see, e.g., Chap. 5). The stress level corresponding to this transition is called yield stress.

The results of a uniaxial tension test are represented as a measure of stress against some measure of the total strain. Let l_0 denote the initial length of the specimen and l its current length. The amount of deformation is customarily calculated as:

$$e = (l - l_0)/l_0, \tag{2.2}$$

where e is called *engineering strain*, or as:

$$\varepsilon = \ln\left(\frac{l}{l_0}\right), \tag{2.3}$$

where ε is called *logarithmic or natural strain*.

Therefore, in uniaxial tension the relation between these two measures of deformation is:

$$\varepsilon = \ln(1 + e). \tag{2.4}$$

As concern stresses, the commonly used measures are the *engineering stress* or nominal stress calculated as the ratio between the applied axial force F and the area of the initial cross-section, A_0, i.e.,

$$S = \frac{F}{A_0}, \tag{2.5}$$

and the *true stress* σ defined as the ratio of the axial force F to the current area of cross-section, A, i.e.,

$$\sigma = \frac{F}{A}. \tag{2.6}$$

Plastic incompressibility results in $l_0 A_0 = lA$, so that the true stress is expressed in terms of the engineering stress–strain as:

$$\sigma = S(1 + e). \tag{2.7}$$

As an example, Fig. 2.1 shows for an AA2024-T4, the two ways of representing the test results. When the change in length is small, ε and e are approximately identical, but ε becomes less than e with increasing load. Likewise, for small-applied loads σ and S are practically identical, but σ diverges more rapidly from S for larger applied loads [see Eq. (2.7)]. The ultimate tensile strength (UTS) is defined as the maximum nominal stress S at the relative maximum point on the nominal stress–strain curve (point U in Fig. 2.1), so it is the stress corresponding to the maximum axial load that the specimen can withstand [see Eq. (2.5)]. Note that the true stress–strain curve continues to increase beyond the maximum load point, but this is an unstable region of the tensile test, since further deformation can continue with decreasing load; the strain localizes as manifested by the local necking of the specimen. Therefore, to estimate the true stress beyond this point necessitates taking local measurements. However, any measurements beyond this point are not very useful since the stress state cannot be approximated as uniaxial.

Remark It is important to note that in uniaxial compression of a specimen of initial height h_0 and current height h, using the same definitions, the engineering strain is $e = (h_0 - h)/h_0$ while the natural strain is $\varepsilon = \ln(h_0/h)$. So for this loading $\varepsilon = -\ln(1 - e)$. Therefore, comparison between the mechanical response in uniaxial tension and uniaxial compression cannot be based on engineering stress versus engineering strain curves since when $e = 1$, the length of the tensile specimen has only been doubled while the compression specimen height has approached zero (see also the discussion in Hill [26]).

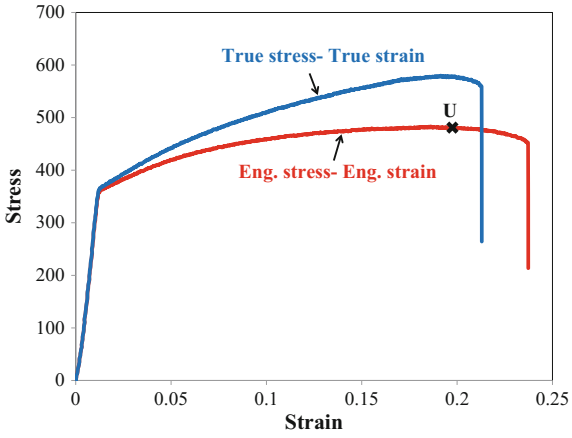

Fig. 2.1 Uniaxial tension of an AA2024-T4: comparison between the true stress-true strain curve and the engineering stress-engineering strain curve

In summary, to compare the response of a material for different loadings, only experimental true stress-true strain curves should be considered. Unless otherwise stated, throughout this book only true stress-true strain curves are presented.

The main characteristics of the mechanical response of a plastically deformable material are evident from the hypothetical stress–strain curve shown in Fig. 2.2. When a gradually increasing load F is applied, the specimen experiences changes in length and cross-sectional area. The specimen first deforms elastically, i.e., the strain is proportional to the applied stress and the specimen regains its original dimensions upon unloading. The stress level at which the strain is no longer proportional to the applied stress is called the proportional limit. The elastic range generally extends beyond this limit, and the stress, at which an appreciable amount of permanent deformation is observed, is known as the yield stress point. As already mentioned, in the case when the transition from elastic to plastic behavior is gradual, the location of the yield point on the stress–strain curve is a matter of convention. To compare the mechanical response of different materials, the yield is defined by an offset method as illustrated in Fig. 2.2: A line AA′ is drawn parallel to the initial elastic slope E offset to the right from the origin by a distance $\varepsilon_0 = 0.2\%$; where this line intersects the stress–strain curve determines the yield stress, denoted σ_Y or Y.

Concerning the post-yield behavior, in most metals, the applied force must be continually increased to produce further deformation, a phenomenon called work-hardening. Such behavior is illustrated in Fig. 2.2. Note that beyond the yield point A, the stress–strain curve rises (i.e., $d\sigma/d\varepsilon > 0$). If after yielding has occurred, the load is reduced from its current value (e.g., at point B in Fig. 2.2), the change in length of the specimen is at first elastic, the unloading stress–strain curve following approximately a straight line parallel to the original elastic slope E as illustrated by the unloading lines BC and DM in Fig. 2.2. For unloading from the point D, the elastic strain recovered is: $\varepsilon^e = \sigma_D/E$, represented by the length MN on the strain axis, while the plastic strain or permanent strain, ε^p, is represented by the length MO, and it is given by: $\varepsilon^p = \varepsilon - \sigma_D/E$. If the unloading process is stopped anywhere along DM and the load is increased again, ideally the stress–strain path is elastic until point D, where yield occurs again followed by plastic deformation

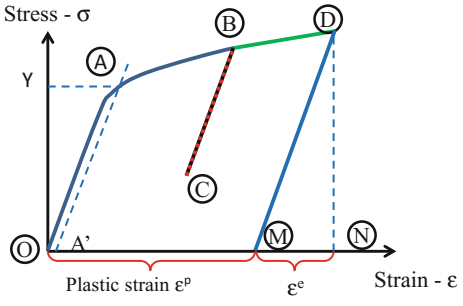

Fig. 2.2 Schematic of the tensile true stress–strain curve

along the same curve which would have been followed if the monotonically increasing load would have never been interrupted. In uniaxial tests on real materials, the loading curve may deviate slightly from a straight line. In addition, the unloading path DM is not perfectly straight either, so the unloading-reloading curves form a so-called hysteresis loop.

The discussion of the mechanical response under uniaxial tension has allowed to put into evidence the following key features of the mechanical response of plastically deformable materials:

(i) If the loading does not reach a certain threshold (yield point), the mechanical behavior is purely elastic, i.e., the specimen will return to its initial shape upon unloading.
(ii) After yielding, if the material is unloaded it will follow an elastic path and as such only part of the strain that it had undergone is recovered, while other part of the strain will remain as permanent or plastic strain.
(iii) Post-yield, there is energy dissipation.
(iv) *Plastic deformation is stress path-dependent or history-dependent.* In other words, in the plastic range there is no unique relation between the stresses and strains; to know the strains associated to a given stress state, one needs to know the loading path that the material has undergone to reach the given stress state.

In summary, the main characteristic difference between elastic behavior and plastic behavior is that plastic deformation depends on the loading path. Therefore, a simple uniaxial tension test is not sufficient to fully characterize the mechanical behavior. To quantify the influence of the sense of loading on the mechanical response, uniaxial compression tests are performed. Generally, to characterize the response under shear, torsion tests on thin-walled cylinders are carried out. Experimental data can also be obtained with combined loadings tests such as tension-torsion or compression-torsion, but this type of data is rarely available (see also Chap. 4).

Therefore, one of the greatest challenges that a researcher in the field of the mathematical theory of plasticity faces is that of formulating a general theory, i.e., general mathematical relations between stresses and strains in a plastically deformable material that are applicable to any loading, although information is available mainly from 1-D tests. Another task of the researchers in this field is to recommend and design experiments or numerical tests to verify the theories developed and further demonstrate their validity through applications to industrial processes. In the following, the basic constitutive assumptions and the general framework of stress-based and strain-rate based theories of plasticity are presented. Description of temperature effects and rate-effects on the plastic behavior is outside the scope of this book. The constitutive equations presented in this book are rate-insensitive, therefore invariant with respect to timescale (the rate-form and incremental form are equivalent to each other).

2.1 Stress-Based Formulation of Elastic–Plastic Models

A general theory of plasticity should capture the main features of the mechanical response observed in a uniaxial tension test. Therefore, it should describe the conditions for the onset of plastic deformation, or initial yielding, the equations for the evolution of the plastic strain and the manner in which the accumulated plastic strains influence subsequent yielding after unloading and subsequent reloading. For the purpose of describing the mechanical state at a point in a material subject to general three-dimensional loadings, the state of stress is represented by a point in the six-dimensional stress space $\sigma_{ij},\ i,j = 1,\ldots,3$.

Before presenting the governing equations that describe the deformation response of work-hardening materials, we will first consider ideal plastic behavior, i.e., the case when yielding depends only on the state of stress. That such an assumption and ensuing theory of plasticity, called ideal plasticity, is a reasonable representation of the behavior of certain engineering materials will be discussed later. For now, let us note that the assumption of ideal plastic behavior or perfectly plastic behavior has led to the formulation of the general framework and the formal definition of the key "ingredients" that should constitute a general theory of plasticity.

2.1.1 Ideal Plasticity

The basic assumption is that there exists a continuous scalar *yield function* $f(\boldsymbol{\sigma})$ which has the following properties:

(I1) For stress states such that:

$$f(\boldsymbol{\sigma}) < 0 \quad \text{or} \quad \text{when} \quad f(\boldsymbol{\sigma}) = 0 \quad \text{and} \quad \frac{\partial f(\boldsymbol{\sigma})}{\partial \boldsymbol{\sigma}} : \dot{\boldsymbol{\sigma}} < 0 \tag{2.8}$$

the *material behavior is elastic* (see also Fig. 2.3).

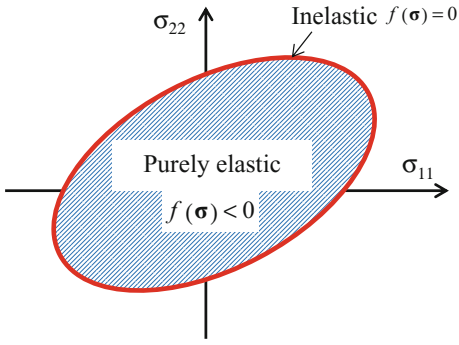

Fig. 2.3 Projection in a 2-D plane of a 6-D yield surface in the stress space

(I2) The plastic strain-rate tensor, $\mathbf{d}^p$, can be nonzero only in the region where $f(\boldsymbol{\sigma}) = 0$.
(I3) No physical meaning is associated with stress states with $f(\boldsymbol{\sigma}) > 0$.

As already mentioned, D.C. Drucker introduced postulates [16–20], collectively known as the Drucker's uniqueness and stability postulates, that have been vital in ensuring that initial- and boundary-value problems are well-posed, and that plastic structural problems admit unique solutions and exhibit stable equilibrium configurations. According to Drucker's hypotheses, neglecting work-hardening means that:

$$\mathrm{d}\boldsymbol{\sigma} : \mathbf{d}^p = 0 \tag{2.9}$$

when plastic deformation occurs. Since the yield function is assumed to be a function of stresses only, any changes in stresses during plastic deformation must satisfy the relation:

$$\mathrm{d}f = \frac{\partial f(\boldsymbol{\sigma})}{\partial \boldsymbol{\sigma}} : \mathrm{d}\boldsymbol{\sigma} = 0, \tag{2.10}$$

also called the condition of consistency for ideal plasticity.

From the above relations, it follows that:

$$\mathbf{d}^p = \dot{\lambda} \frac{\partial f(\boldsymbol{\sigma})}{\partial \boldsymbol{\sigma}}, \tag{2.11}$$

the sign of $\dot{\lambda}$ being restricted by the condition that plastic deformation always involves dissipation, i.e.,

$$\boldsymbol{\sigma} : \mathbf{d}^p > 0. \tag{2.12}$$

Remark

(i) Equation (2.11) gives the *plastic flow rule in ideal plasticity*.
(ii) In Eq. (2.11), $\dot{\lambda}$ is not a material constant and may vary during the deformation. If $f(\boldsymbol{\sigma})$ has the dimension of stress, say 1 Pa, then $\dot{\lambda}$ has the dimension of s^{-1}.

The equation $f(\boldsymbol{\sigma}) = 0$ defines a closed surface in the six-dimensional stress space with $\sigma_{ij},\ i,j = 1,\ldots,3$ as coordinates. The interior of this surface defines the elastic domain of behavior (see also Fig. 2.3 for the 2-D projection of a generic yield surface). The outward normal vector to this surface is $\dfrac{\partial f}{\partial \boldsymbol{\sigma}}$. Hence, as pointed out by Prager, the plastic strain-rate tensor is directed along the normal to the yield surface. The geometric interpretation of Eq. (2.8) is that during unloading the stress increment is pointing inward from the yield surface. On the other hand, during further loading or neutral loading:

$$f(\boldsymbol{\sigma}) = 0 \quad \text{and} \quad \frac{\partial f(\boldsymbol{\sigma})}{\partial \boldsymbol{\sigma}} : \dot{\boldsymbol{\sigma}} = 0,$$

i.e., the stress-rate $\dot{\boldsymbol{\sigma}}$ is on the tangential plane at a stress point on the yield surface.

Note also that for uniaxial tensile loading, the condition for the onset of plastic deformation is: $\sigma = Y$; the concept of a yield surface thus extends the definition of the yield point to general stress states.

Generally, the yield surface is expressed in the form:

$$f(\boldsymbol{\sigma}) = \varphi(\boldsymbol{\sigma}) - Y = 0, \tag{2.13}$$

where Y is a positive material constant.

The function $\varphi(\boldsymbol{\sigma})$ is also called the yield criterion. A detailed discussion of yield criteria for isotropic and anisotropic metallic materials will be given in Chaps. 4 and 5, respectively.

2.1.2 Elastic–Plastic Work-Hardening Materials

As discussed in the introduction, the results of uniaxial tension tests indicate that for certain metallic materials the yield limit is not a constant, but depends on the loading path. Therefore, the yield surface cannot be defined by a function that depends solely on the stress tensor. Since the shape of the yield surface may evolve during the deformation process, the yield function may depend on other variables, for example, the plastic strain itself. Such variables are collectively termed "internal variables."

As already mentioned, the constitutive assumptions and ensuing restrictions on the form of the yield function and flow rule of work-hardening materials are due to W. Prager and D.C. Drucker, and their collaborators. On the basis of Drucker's definition of work-hardening and its postulates, it can be proven that:

(P1) the yield surface and all subsequent yield surfaces must be convex (see Fig. 2.4);
(P2) the plastic strain increment vector must be normal to the yield surface at a regular point, and it must lie between the adjacent normals to the yield surface at a corner of the surface;
(P3) the plastic strain-rate must be a linear function of the stress-rate [see Eq. (2.1)].

Therefore, for a work-hardening material the yield function $f(\boldsymbol{\sigma}, \xi_k)$, with ξ_k designating the set of internal variables, is also playing the role of plastic potential [see also (P2)], i.e.,

$$\mathbf{d}^p = \dot{\lambda} \frac{\partial f(\boldsymbol{\sigma}, \xi_k)}{\partial \boldsymbol{\sigma}} \tag{2.14}$$

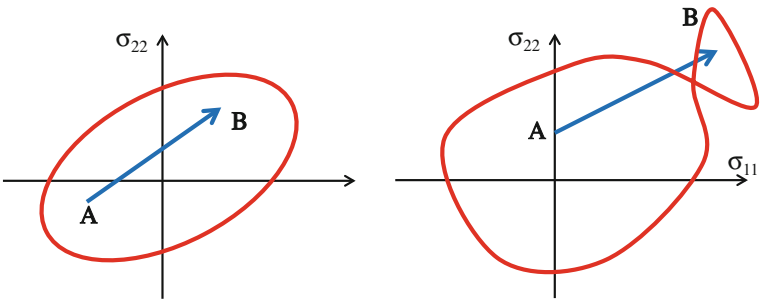

Fig. 2.4 Illustration of convexity

where $\dot{\lambda}$ is a scalar positive factor, which can be a function of strain, or strain history.

Note that the flow rule is of the same form as for ideal plastic materials. Moreover, only states such as $f(\boldsymbol{\sigma}, \xi_k) \leq 0$ are admissible (see also hypothesis P3 and the definition of the domain of elastic–plastic deformation for an ideal plastic material).

The evolution laws for the internal variables ξ_k defining hardening are considered to be of the general form:

$$\dot{\xi}_k = \dot{\lambda} h(\boldsymbol{\sigma}, \xi_k) \tag{2.15}$$

The plastic multiplier is determined by enforcing that as plastic deformation proceeds,

$$\dot{f} = \frac{\partial f(\boldsymbol{\sigma}, \xi_k)}{\partial \sigma_{ij}} \dot{\sigma}_{ij} + \frac{\partial f(\boldsymbol{\sigma}, \xi_k)}{\partial \xi_k} \dot{\xi}_k = 0 \tag{2.16}$$

Equation (2.16) expresses the consistency condition for work-hardening materials.

As seen on the stress–strain diagram obtained for a uniaxial tensile test, the total strain $\boldsymbol{\varepsilon}$ can be decomposed into an elastic part $\boldsymbol{\varepsilon}^{\mathbf{e}}$ and a plastic part $\boldsymbol{\varepsilon}^{\mathbf{p}}$ (see Fig. 2.2). For small strains, the strain-rate tensor $\mathbf{d}$ can be decomposed into an elastic part, $\mathbf{d}^e$, and a plastic part, $\mathbf{d}^p$ such that,

$$\mathbf{d} = \mathbf{d}^e + \mathbf{d}^p. \tag{2.17}$$

Generally, linear elastic and isotropic behavior governed by Hooke's law is considered, so that

$$\dot{\boldsymbol{\sigma}} = \mathbf{C}^e : (\mathbf{d} - \mathbf{d}^p), \tag{2.18}$$

with $\mathbf{C}^e$ is the constant elastic fourth-order tensor,

$$\mathbf{C}^e = 2G\,\mathbf{I}_4^s + K\,\mathbf{I}\otimes\mathbf{I}$$

where K and G are the bulk and shear modulus, respectively; or

$$\mathbf{C}^e_{ijkl} = \left(\frac{Ev}{(1+v)(1-2v)}\right)\delta_{ij}\delta_{kl} + \left(\frac{E}{2(1+v)}\right)\delta_{ik}\delta_{jl}, \tag{2.19}$$

where E and v are the Young's modulus and Poisson coefficient, respectively.

Also,

$$\boldsymbol{\varepsilon}^e = \int_t \mathbf{d}^e\,\mathrm{dt} \quad \text{and} \quad \boldsymbol{\varepsilon}^p = \int_t \mathbf{d}^p\,\mathrm{dt}. \tag{2.20}$$

As mentioned, metallic materials deform plastically without change of volume, i.e.,

$$tr(\mathbf{d}^p) = 0 \tag{2.21}$$

Further substitution in Eq. (2.14) leads to the restriction that the yield function depends on stress only through its deviator, $\mathbf{s} = \boldsymbol{\sigma} - \sigma_m\mathbf{I}$ (see proof in Chap. 4).

The manner in which the yield surface shape changes as the plastic deformation proceeds is described by specifying the nature and type of the hardening variables (i.e., scalar or tensorial) and evolution laws for these variables, known as hardening laws.

The first hardening model was introduced by Odqvist [33], who assumed that as the deformation proceeds the loading surfaces are self-similar and affine with regard to the origin. This model is called isotropic hardening because it implies a uniform expansion of the initial yield surface.

The constitutive assumptions for an elastic/plastic material with isotropic hardening are the following:

(H1) Hardening is described by a scalar variable, denoted as ξ
(H2) The yield function is represented as:

$$f(\boldsymbol{\sigma},\xi) = \varphi(\boldsymbol{\sigma}) - Y(\xi) = \bar{\sigma}(\boldsymbol{s}) - Y(\xi) \le 0, \tag{2.22}$$

where $Y(\xi)$ is a monotonically increasing function.
(H3) $f(\mathbf{0},\xi) < 0$.

The function $\bar{\sigma}$ is called effective stress or equivalent stress, and it is taken to be homogeneous of degree one in stresses (see Chap. 4). The specific form of $\bar{\sigma}(\boldsymbol{s})$ dictates the shape of the yield surface; since the hardening variable is a scalar, only the size of the surface changes with accumulated plastic deformation, and as deformation proceeds, the yield surface expands in a self-similar manner. As concerns the choice or definition of the scalar variable, in the early 1920s, it was recognized that in order to capture the main features of the plastic response, a measure of the hardening of a material must be either some scalar measure of the

plastic strains experienced by the material or some measure of the dissipation associated with plastic deformation. Most importantly, efforts have been undertaken to derive hardening laws that are general, i.e., applicable to any loadings. Comparison of the stress–strain curves in uniaxial tension, uniaxial compression, and torsion has led to the idea that a "universal measure" of hardening can be considered, for example, W^I, the total plastic work per unit volume expended over the actual strain path from some initial state of the material, i.e.,

$$W^I(t) = W^I(t_0) + \int_{t_0}^{t} \boldsymbol{\sigma} : \mathbf{d}^p \tag{2.23}$$

For example, Taylor and Quinney [46] considered as a universal measure of stress, the von Mises effective stress, defined as: $\bar{\sigma} = \sqrt{3J_2}$ (for more details see Chap. 4). To model work-hardening of a given material, Taylor and Quinney [46] first established the relationship between $\bar{\sigma}$ and W^I based on uniaxial tension data, and then checked the applicability of the respective relation to the description of hardening during torsional loadings (for more details, see Hill [26]). Later on, hardening laws expressed as relationships between $\bar{\sigma}$ and $\bar{\varepsilon}^p$ were proposed with

$$\dot{\bar{\varepsilon}}^p = \sqrt{\frac{2}{3}\mathbf{d}^p : \mathbf{d}^p}.$$

Remark It is to be noted that for uniaxial tension, $\bar{\sigma}$ reduces to the applied axial stress while $\bar{\varepsilon}^p$ given by the above equation reduces to the natural plastic strain, so that the relation between $\bar{\sigma}$ and $\bar{\varepsilon}^p$ can be easily determined from the true stress–strain diagram.

The most widely used isotropic hardening laws are the Swift [45] law

$$Y(\bar{\varepsilon}^p) = K_0(\varepsilon_0 + \bar{\varepsilon}^p)^n \tag{2.24}$$

where K_0, ε_0 and n are material parameters, and the Voce [50] exponential law, given by,

$$Y = Y_0 + R_{\text{sat}}(1 - \exp(-n\bar{\varepsilon}^p)) \tag{2.25}$$

where Y_0, R_{sat} and n are parameters.

It is worth noting that if the yield function [see Eq. (2.22)] is homogeneous of degree one in stresses, in the case of plastic loading use of the flow rule [see Eq. (2.14)] leads to:

$$\dot{\lambda} = \dot{\bar{\varepsilon}}^p \text{ and } \dot{W}^I = \bar{\sigma}\,\dot{\bar{\varepsilon}}^p \tag{2.26}$$

Isotropic hardening is widely used for description of the plastic behavior under monotonic loadings or loadings that do not involve stress path changes.

Kinematic Hardening

Bauschinger [5] found that if a specimen is stretched beyond its initial yield limit in tension, its elastic limit in compression is reduced, or reciprocally if the specimen is first compressed beyond its yield limit, the yield limit in tension is reduced. In order to account in a quantitative manner for the Bauschinger effect, Prager [37] introduced the concept of kinematic hardening. Prager [37]'s kinematic hardening model implies that the yield surface undergoes a translation in the stress space without change in size and shape.

Suppose that the initial yield surface is $f(\boldsymbol{\sigma}) = 0$. According to Prager's assumption, the subsequent yield surfaces should be of the form:

$$f(\boldsymbol{\sigma} - \mathbf{X}) = 0,$$

where $\mathbf{X}$ is a second-order symmetric tensor, called the back-stress. Formulation of a kinematic hardening model amounts to specifying the evolution of the hardening variable $\mathbf{X}$. Prager assumed a linear kinematic hardening law,

$$\mathbf{X} = \mathrm{c}\dot{\lambda}\mathbf{d}^p,$$

where c is a constant. Armstrong and Frederick [1] introduced a nonlinear term in Prager's evolution law. Further developments were proposed by Chaboche et al. [9]. Combined isotropic and kinematic hardening laws as well as more involved hardening laws accounting for stress-path changes under combined loadings have also been proposed (e.g., Teodosiu and Hu [47]).

As mentioned, in this book the emphasis is placed on the description of plastic behavior under monotonic loadings, so that only isotropic hardening models will be considered in conjunction with yield criteria for isotropic and anisotropic materials (see Chaps. 4 and 5). It is worth summarizing the set of equations for rate-independent elastic–plastic models that will be considered:

$$\begin{cases} \mathbf{d} = \mathbf{d}^e + \mathbf{d}^p \\ \dot{\boldsymbol{\sigma}} = \mathbf{C}^e : \mathbf{d}^e \\ f(\boldsymbol{\sigma}, \bar{\varepsilon}^p) = \varphi(\boldsymbol{\sigma}) - Y(\bar{\varepsilon}^p) \leq 0 \\ \mathbf{d}^p = \dot{\lambda}\dfrac{\partial \varphi}{\partial \boldsymbol{\sigma}} \\ \dot{\bar{\varepsilon}}^p = \dot{\lambda} \end{cases} \tag{2.27}$$

In the next section, we present a general implicit time integration algorithm developed in order to solve boundary-value problems for elastic–plastic materials described by the set of constitutive equations given by Eq. (2.27). This algorithm was developed in the framework of corotational algorithms established by Hughes [29]. Specifically, the constitutive equations are written in an appropriate orthogonal rotating frame. This allows the description of large deformations and transformations, in a form identical to their simpler small strains counterpart while verifying the objectivity principle (objectivity of the time derivatives). For a detailed discussion, the reader is referred to the recent review paper by Balan [3].

The algorithm presented can serve for the implementation of general elastic–plastic constitutive models in a finite-element (F.E.) code, or can be used as a stand-alone code outside a F.E. code.

2.1.3 Time Integration Algorithm for Stress-Based Elastic–Plastic Constitutive Models

The algorithm discussed in this section is generic such that it can be applied to any of the yield criteria that are presented in this book. While the algorithm allows the F.E. implementation of elastic–plastic constitutive models, the F.E. framework is not described, the reader being referred to the seminal books of Zienkiewicz et al. [54] and of Belytschko et al. [6]. The time integration scheme is based on the method proposed by Simo and Taylor [44]. Concerning the yield function, one needs to calculate its first and second derivatives such that quadratic rate of convergence is achieved. For a more exhaustive list of integration algorithms and further discussion, the reader is referred to the books of Simo and Hughes [43] and of de Souza Neto et al. [15].

As discussed, due to the fact that for an elastic–plastic material the response depends on the loading path, the constitutive equations are in incremental form. The F.E. implementation requires a time integration algorithm of these rate equations over the time interval $\Delta t = t_{n+1} - t_n$ when a total strain increment $\Delta\varepsilon$ is imposed. The backward Euler time integration scheme is the most widely applied scheme in implicit F.E. solvers. It consists in using the time derivatives at the end of the increment, i.e., incremental variation of a variable, say $\Delta\alpha$, is defined as,

$$\Delta\alpha = \dot{\alpha}_{n+1}\Delta t, \tag{2.28}$$

where, $\dot{\alpha}_{n+1}$ is the value of the rate of change of the variable α at the end of the time increment. In addition to a very good accuracy, the backward Euler method was shown to be unconditionally stable with respect to the size of the strain increment (see Simo and Taylor [44]).

The application of this scheme, to the set of constitutive equations of an elastic–plastic model, written in incremental form [see Eq. (2.27)] leads to the following set of equations that needs to be solved:

$$\begin{cases} \boldsymbol{\sigma}_{n+1} = \boldsymbol{\sigma}_n + \mathbf{C}^e : \Delta\boldsymbol{\varepsilon}^e \\ \Delta\boldsymbol{\varepsilon} = \Delta\boldsymbol{\varepsilon}^p + \Delta\boldsymbol{\varepsilon}^e \\ \varphi(\boldsymbol{\sigma}_{n+1}) - Y\left(\bar{\varepsilon}^p_n + \Delta\bar{\varepsilon}^p\right) \leq 0 \\ \Delta\boldsymbol{\varepsilon}^p = \Delta\lambda \dfrac{\partial\varphi(\boldsymbol{\sigma}_{n+1})}{\partial\boldsymbol{\sigma}_{n+1}} \\ \boldsymbol{\sigma}_{n+1} : \Delta\boldsymbol{\varepsilon}^p = \varphi(\boldsymbol{\sigma}_{n+1})\Delta\bar{\varepsilon}^p \end{cases} \tag{2.29}$$

where $\boldsymbol{\sigma}_{n+1}$ and the equivalent plastic strain $\bar{\varepsilon}^p_{n+1} = \bar{\varepsilon}^p_n + \Delta\bar{\varepsilon}^p$ are unknowns, while $\boldsymbol{\sigma}_n$ and $\bar{\varepsilon}^p_n$ are known at the beginning of the increment.

The main difficulty consists in updating the stresses, which requires checking whether the incremental deformation is elastic or elastic–plastic, i.e., whether plastic loading conditions were fulfilled. Given that the plastic multiplier is nonzero only for plastic loadings, the conditions to be verified are the so-called Kuhn–Tucker conditions:

$$\Delta\lambda\left[\varphi(\boldsymbol{\sigma}_{n+1}) - Y\left(\bar{\varepsilon}_n^p + \Delta\bar{\varepsilon}^p\right)\right] = 0.$$

The method to update the state of the material is the so-called elastic predictor/plastic corrector method. First, it is assumed that the incremental deformation $\Delta\boldsymbol{\varepsilon}$ is purely elastic, and a trial stress tensor $\boldsymbol{\sigma}_{n+1}^{\text{trial}}$ is calculated as,

$$\boldsymbol{\sigma}_{n+1}^{\text{trial}} = \boldsymbol{\sigma}_n + \mathbf{C}^e : \Delta\boldsymbol{\varepsilon} \tag{2.30}$$

If $\varphi(\boldsymbol{\sigma}_{n+1}) - Y\left(\bar{\varepsilon}_n^p\right) < 0$, the incremental deformation is indeed elastic and therefore the updated stress is: $\boldsymbol{\sigma}_{n+1} = \boldsymbol{\sigma}_{n+1}^{\text{trial}}$. Otherwise, the material deforms plastically during the increment. In this case, one needs to solve the following nonlinear system of two equations with unknowns $\Delta\lambda$ and $\boldsymbol{\sigma}_{n+1}$

$$\begin{cases} \varphi(\boldsymbol{\sigma}_{n+1}) - Y\left(\bar{\varepsilon}_n^p + \Delta\lambda\right) = 0 \\ \left[\mathbf{C}^e\right]^{-1} : \left(\boldsymbol{\sigma}_{n+1}^{\text{trial}} - \boldsymbol{\sigma}_{n+1}\right) - \Delta\lambda \dfrac{\partial\varphi(\boldsymbol{\sigma}_{n+1})}{\partial\boldsymbol{\sigma}_{n+1}} = 0 \end{cases} \tag{2.31}$$

Note that use was made of the fact that $\varphi(\boldsymbol{\sigma})$ is a first-order homogenous function in stresses, which implies $\Delta\lambda = \Delta\bar{\varepsilon}^p$, so that $\bar{\varepsilon}_{n+1}^p = \bar{\varepsilon}_n^p + \Delta\lambda$ [see also Eq. (2.26)]. This latter system of equations is solved using a Newton–Raphson method. Let m denote the iteration counter for the Newton–Raphson algorithm. If $\boldsymbol{\sigma}_{n+1}^0 = \boldsymbol{\sigma}_{n+1}^{\text{trial}}$ and $\Delta\lambda_{n+1}^0 = 0$ (i.e., $m = 0$ corresponds to the elastic trial state), the plastic multiplier and the stress increment are updated as follows:

$$\begin{aligned} \Delta\lambda^{m+1} &= \Delta\lambda^m + \delta\lambda^{m+1} \\ \boldsymbol{\sigma}_{n+1}^{m+1} &= \boldsymbol{\sigma}_{n+1}^m + \delta\boldsymbol{\sigma}_{n+1}^{m+1}, \end{aligned} \tag{2.32}$$

where δ denotes the variation of the respective variable between iterations m and $m+1$. The incremental variation of the plastic multiplier $\delta\lambda^{m+1}$ is given by:

$$\delta\lambda^{m+1} = \frac{\varphi\left(\sigma_{n+1}^m\right) - Y\left(\bar{\varepsilon}_n^p + \Delta\lambda^m\right) + \left(\dfrac{\partial\varphi\left(\sigma_{n+1}^m\right)}{\partial\sigma_{n+1}^m}\right) : [\mathbf{P}] : \left(\left[\mathbf{C}^e\right]^{-1} : \left(\sigma_{n+1}^{\text{trial}} - \sigma_{n+1}^m\right) - \Delta\lambda^m \left(\dfrac{\partial\varphi\left(\sigma_{n+1}^m\right)}{\partial\sigma_{n+1}^m}\right)\right)}{\left(\dfrac{\partial\varphi\left(\sigma_{n+1}^m\right)}{\partial\sigma_{n+1}^m}\right) : [\mathbf{P}] : \left(\dfrac{\partial\varphi\left(\sigma_{n+1}^m\right)}{\partial\sigma_{n+1}^m}\right) + \left(\dfrac{\partial Y\left(\bar{\varepsilon}_n^p + \Delta\lambda^m\right)}{\partial\Delta\lambda^m}\right)} \tag{2.33}$$

where $\mathbf{P}$ denotes the fourth-order tensor expressed as:

$$\mathbf{P} = \left(\mathbf{I}_4 + \Delta\lambda_{n+1}^{m} \, \mathbf{C}^e \frac{\partial^2 \varphi\left(\boldsymbol{\sigma}_{n+1}^{m}\right)}{\partial \left(\boldsymbol{\sigma}_{n+1}^{m}\right)^2} \right)^{-1} \mathbf{C}^e. \tag{2.34}$$

and $\mathbf{I}_4$ is the fourth-order identity tensor. The variation of the stress increment $\delta\boldsymbol{\sigma}_{n+1}^{m+1}$ is,

$$\delta\boldsymbol{\sigma}_{n+1}^{m+1} = [\boldsymbol{P}] : \left([\mathbf{C}^e]^{-1} : \left(\boldsymbol{\sigma}_{n+1}^{trial} - \boldsymbol{\sigma}_{n+1}^{m} \right) - \Delta\lambda_{n+1}^{m+1} \left(\frac{\partial \varphi\left(\boldsymbol{\sigma}_{n+1}^{m}\right)}{\partial \boldsymbol{\sigma}_{n+1}^{m}} \right) \right) \tag{2.35}$$

The incremental variation of the plastic multiplier and the stress tensor are obtained through a Taylor expansion of Eq. (2.31) about the current state. The stresses and the plastic strains are then updated until a specified tolerance is met. Once convergence is reached, i.e., $\left| \Phi(\boldsymbol{\sigma}_{n+1}) - Y\left(\bar{\varepsilon}_n^p + \Delta\lambda\right) \right| \leq \text{tol}$, the updated stresses and strains are accepted as the current state.

To implement an elastic–plastic constitutive model in an implicit finite-element code, a consistent tangent modulus $\mathbf{C}^{ep}$ that relates the current stress increment $\Delta\boldsymbol{\sigma} = \boldsymbol{\sigma}_{n+1} - \boldsymbol{\sigma}_n$ to the current total strain increment $\Delta\boldsymbol{\varepsilon}$ should be determined. For the time integration scheme adopted here, the consistent tangent modulus is given by,

$$\Delta\boldsymbol{\sigma} = \mathbf{C}^{ep} : \Delta\boldsymbol{\varepsilon} \tag{2.36}$$

For a purely elastic deformation during the increment, the consistent tangent modulus is $\mathbf{C}^{ep} = \mathbf{C}^e$, while if elastic–plastic deformation occurs the consistent tangent modulus is

$$\mathbf{C}^{ep} = \mathbf{P} - \frac{\left(\frac{\partial \varphi(\boldsymbol{\sigma}_{n+1})}{\partial \boldsymbol{\sigma}_{n+1}} \right) : \mathbf{P} \otimes \mathbf{P} : \left(\frac{\partial \varphi(\boldsymbol{\sigma}_{n+1})}{\partial \boldsymbol{\sigma}_{n+1}} \right)}{\left(\frac{\partial \varphi(\boldsymbol{\sigma}_{n+1})}{\partial \boldsymbol{\sigma}_{n+1}} \right) : \mathbf{P} : \left(\frac{\partial \varphi(\boldsymbol{\sigma}_{n+1})}{\partial \boldsymbol{\sigma}_{n+1}} \right) + \left(\frac{\partial Y\left(\bar{\varepsilon}_n^p + \Delta\lambda\right)}{\partial \Delta\lambda} \right)} \tag{2.37}$$

2.2 Strain-Rate-Based Formulation for Elastic–Plastic Models

2.2.1 Mathematical Framework

To model an elastic–plastic material, it is essential to accurately describe the plastic dissipation, i.e., the part of the mechanical work which is irreversible. Ziegler [53] and Hill [25] have shown that a plastic strain-rate potential $\psi(\mathbf{d}^p)$ can be associated to any convex stress potential represented by a homogeneous function of degree one in stresses, $\varphi(\boldsymbol{\sigma})$. Indeed,

$$\dot{W}^I = \dot{\lambda}\boldsymbol{\sigma} : \frac{\partial \varphi(\boldsymbol{\sigma})}{\partial \boldsymbol{\sigma}} = \dot{\lambda}\varphi(\boldsymbol{\sigma}) \tag{2.38}$$

so that

$$\dot{W}^I = \varphi(\boldsymbol{\sigma})\psi(\mathbf{d}^p) \tag{2.39}$$

with

$$\psi(\mathbf{d}^p) = \dot{\lambda}. \tag{2.40}$$

Equation (2.39) shows that $\psi(\mathbf{d}^p)$ and $\varphi(\boldsymbol{\sigma})$ are work-conjugated. Hence, the strain-rate potential can be used instead of the stress potential $\varphi(\boldsymbol{\sigma})$ to describe the plastic response of materials. If a strain-rate based potential is used, during plastic deformation the stress tensor is calculated as:

$$\boldsymbol{\sigma} = \bar{\sigma}\frac{\partial \psi(\mathbf{d}^p)}{\partial \mathbf{d}^p} \tag{2.41}$$

It is worth noting that for certain plastically deformable materials that display the same response in tension–compression, Eq. (2.41) writes,

$$\mathbf{s} = \bar{\sigma}\frac{\partial \psi(\mathbf{d}^p)}{\partial \mathbf{d}^p} \tag{2.42}$$

where $\mathbf{s}$ is the Cauchy stress deviator (see Chap. 6 for examples). Thus, the elastic–plastic behavior of a metallic material can also be described using a strain-rate based formulation instead of the classical formulation in the stress space presented in Sect. 2.1. It is worth noting that the plastic stress potential coincides with the yield function and thus defines the boundary between the elastic and plastic domains. The strain-rate potential [Eq. (2.40)] does not provide any information about this boundary. Therefore, the plastic loading/unloading condition cannot be determined in terms of $\psi(\mathbf{d}^p)$.

However, a strain-rate based formulation could be advantageous for design optimization problems [10–12]]. From an experimental point of view, use of a strain-rate formulation can also be advantageous, given that what we measure in experiments are strains and strain-rates. A lot of progress has been achieved in the development of digital image correlation techniques that allow the measurements of local strain fields. Note that the use of strain-rate based formulations would allow the determination of the stress field from the strain-rate fields using Eq. (2.42) and thus lead to information on the local stresses. If isotropic hardening is considered, with the equivalent plastic strain as a hardening variable, the set of constitutive equations of a strain-rate based formulation of an elastic–plastic model consists of:

$$\begin{cases} \mathbf{d} = \mathbf{d}^e + \mathbf{d}^p \\ \dot{\boldsymbol{\sigma}} = \mathbf{C}^e : \mathbf{d}^e \\ \psi\left(\mathbf{d}^P\right) = \dot{\bar{\varepsilon}}^p \\ \boldsymbol{\sigma} = Y(\bar{\varepsilon}^p)\dfrac{\partial \psi(\mathbf{d}^p)}{\partial \mathbf{d}^p} \end{cases} \tag{2.43}$$

2.2.2 Time Integration Algorithm for Strain-Rate-Based Elastic–Plastic Models

In order to solve boundary-value problems, implementation of the constitutive model into a F.E. framework needs to be conducted. The set of constitutive equations given by Eq. (2.43) should be discretized. Using the backward Euler scheme, i.e., stating that the plastic strain-rate tensor $\mathbf{d}^p$ is constant over the time increment Δt, and taking into account that the strain-rate potential is a first-order homogeneous function of the strain-rate tensor, one can write:

$$\mathbf{s}_{n+1} = \mathrm{Y}\left(\bar{\varepsilon}_n^p + \psi(\boldsymbol{\Delta\varepsilon}^p)\right)\frac{\partial \psi(\boldsymbol{\Delta\varepsilon}^p)}{\partial \boldsymbol{\Delta\varepsilon}^p} \tag{2.44}$$

where $\mathbf{s}_{n+1}$, $\Delta\bar{\varepsilon}^p$ and $\boldsymbol{\Delta\varepsilon}^p$ is the stress deviator at t_{n+1}, the increment in equivalent plastic strain and the increment of the plastic strain tensor that have to be determined at the end of the time increment, respectively, while $\bar{\varepsilon}_n^p$ is the equivalent plastic strain at t_n. It follows that the set of equations to be solved are:

$$\begin{cases} \mathbf{s}_{n+1} = \mathbf{s}_n + \mathbf{C}^e : \left(\boldsymbol{\Delta\varepsilon}^e - \dfrac{1}{3}\mathrm{tr}(\boldsymbol{\Delta\varepsilon})\mathbf{I}\right) \\ \mathrm{p}_{n+1} = \mathrm{p}_n + \dfrac{1}{3}\mathrm{tr}(\boldsymbol{\Delta\varepsilon})\mathbf{C}^e : \mathbf{I} \\ \psi(\boldsymbol{\Delta\varepsilon}^p) = \Delta\bar{\varepsilon}^p \\ \mathbf{s}_{n+1} = \mathrm{Y}\left(\bar{\varepsilon}_n^p + \psi(\boldsymbol{\Delta\varepsilon}^p)\right)\dfrac{\partial \psi(\boldsymbol{\Delta\varepsilon}^p)}{\partial \boldsymbol{\Delta\varepsilon}^p} \\ \boldsymbol{\Delta\varepsilon} = \boldsymbol{\Delta\varepsilon}^e + \boldsymbol{\Delta\varepsilon}^p \end{cases} \tag{2.45}$$

In the strain-rate space, the definition of the boundary surface between the elastic domain and the inelastic one is not explicit. Unlike the stress-based formulation where loading–unloading conditions are defined in terms of the plastic potential $\varphi(\boldsymbol{\sigma})$, in the case of strain-rate based formulations, knowledge of $\psi(\mathbf{d}^p)$ is not sufficient to determine whether an incremental deformation $\boldsymbol{\Delta\varepsilon}$ will produce plastic strains. Alternative solutions need to be considered, as proposed by Van Houtte et al. [49]. Here, let's define the function,

$$\mathrm{k}(\mathbf{N}) = \psi(\mathbf{N}) - \frac{\boldsymbol{\sigma}_{n+1}^{\mathrm{trial}}}{\mathrm{Y}(\bar{\varepsilon}_n^{\mathrm{p}})} : \mathbf{N} \tag{2.46}$$

where $\mathbf{N} = \Delta\boldsymbol{\varepsilon}^{\mathrm{p}}/\|\Delta\boldsymbol{\varepsilon}^{\mathrm{p}}\|$ is the normalized plastic strain increment and $\boldsymbol{\sigma}_{\mathrm{n}+1}^{\mathrm{trial}} = \boldsymbol{\sigma}_{\mathrm{n}} + \mathbf{C}^{e} : \Delta\boldsymbol{\varepsilon}$ the trial stress. Loading/unloading conditions can be defined based on the principle of maximum work as,

$$\underset{\mathbf{N}}{\mathrm{Min}}\, k(\mathbf{N}) \begin{cases} <0 & \text{if} \quad \boldsymbol{\sigma}_{n+1}^{\mathrm{trial}} & \text{is outside the yield surface,} \\ =0 & \text{if} \quad \boldsymbol{\sigma}_{n+1}^{\mathrm{trial}} & \text{is on the yield surface,} \\ >0 & \text{if} \quad \boldsymbol{\sigma}_{n+1}^{\mathrm{trial}} & \text{is inside the yield surface.} \end{cases} \tag{2.47}$$

[see also Bacroix and Gilormini [2]]. Plastic incompressibility requires that $tr(\boldsymbol{\varepsilon}^{p}) = 0$, so the tensor $\mathbf{N}$ has five independent components. Since $\|\mathbf{N}\| = 1$, the components of $\mathbf{N}$ can be written as:

$$\begin{array}{lcl} N_1 = (N_{11} - N_{22})/\sqrt{2} & = & \sin\theta_1 \sin\theta_2 \sin\theta_3 \sin\theta_4 \\ N_2 = \sqrt{3}(N_{11} + N_{22})/\sqrt{2} & = & \cos\theta_1 \sin\theta_2 \sin\theta_3 \sin\theta_4 \\ N_3 = \sqrt{2}N_{12} & = & \cos\theta_2 \cos\theta_3 \sin\theta_4 \\ N_4 = \sqrt{2}N_{23} & = & \cos\theta_3 \sin\theta_4 \\ N_5 = \sqrt{2}N_{31} & = & \cos\theta_4 \end{array} \tag{2.48}$$

with $0 \leq \theta_1 \leq 2\pi$ and $0 \leq \theta_{\mathrm{i}} \leq \pi$ for i = 2,3 and 4. Therefore, the minimization of $k(\mathbf{N})$ with respect to $\boldsymbol{\theta} = (\theta_1, \theta_2, \theta_3, \theta_4)$ requires the solution of the equation $\partial \mathrm{k}/\partial\boldsymbol{\theta} = 0$. Minimizing the function $k(\mathbf{N})$ can be avoided for specific cases. For example, during plastic loading, when the initial stress $\boldsymbol{\sigma}_{\mathrm{n}}$ is already on the yield surface, the condition $\left(\boldsymbol{\sigma}_{\mathrm{n}+1}^{\mathrm{trial}} - \boldsymbol{\sigma}_{\mathrm{n}}\right) : \mathbf{N}_{\mathrm{n}} \geq 0$, guarantees that the trial stress is outside the yield surface [29], where $\mathbf{N}_{\mathrm{n}}$ is the normalized plastic strain for the previous increment, which can be stored at each increment for future use. However, when the minimization of $k(\mathbf{N})$ is required, it can be stopped as soon as a tensor $\mathbf{N}$ gives $k(\mathbf{N}) < 0$. Indeed, in this case, the minimum of $k(\mathbf{N})$ is guaranteed to be negative; therefore, the increment is elastic–plastic. In practice, several simple initializations for $\mathbf{N}$ already fulfill this condition in most cases (see Rabahallah et al. [40], Balan and Cazacu [4]). In the case of $\min\limits_{\mathbf{N}} k(\mathbf{N}) > 0$, the incremental deformation is purely elastic, therefore we update the stress as $\boldsymbol{\sigma}_{\mathrm{n}+1} = \boldsymbol{\sigma}_{\mathrm{n}+1}^{\mathrm{trial}}$. Otherwise, the incremental deformation for the given time increment is elastic–plastic and the system of Eq. (2.45) should be solved. Solving this system reduces to finding the unknown plastic increment such that $\rho(\Delta\boldsymbol{\varepsilon}^{p}) = 0$,

where

$$\rho(\Delta\boldsymbol{\varepsilon}^{p}) = Y\left(\bar{\varepsilon}_{n}^{p} + \psi(\Delta\boldsymbol{\varepsilon}^{p})\right)\frac{\partial\psi(\Delta\boldsymbol{\varepsilon}^{p})}{\partial\Delta\boldsymbol{\varepsilon}^{p}} - \mathbf{C}^{e} : \left(\Delta\boldsymbol{\varepsilon} - \frac{1}{3}tr(\Delta\boldsymbol{\varepsilon})\mathbf{I} - \Delta\boldsymbol{\varepsilon}^{p}\right) - \mathbf{s}_{\mathbf{n}} \tag{2.49}$$

Generally, the equation $\boldsymbol{\rho}(\Delta\boldsymbol{\varepsilon}^{p}) = \mathbf{0}$ is solved using a Newton–Raphson procedure. An initial value $\Delta\boldsymbol{\varepsilon}_{0}^{p}$ for the plastic strain increment is calculated and then corrected at each iteration "m" with the correction term given as,

$$\delta \Delta \boldsymbol{\varepsilon}^{p}_{m+1} = -\left[\frac{\partial \boldsymbol{\rho}\left(\Delta \boldsymbol{\varepsilon}^{p}_{m}\right)}{\partial \Delta \boldsymbol{\varepsilon}^{p}_{m}}\right]^{-1} : \boldsymbol{\rho}\left(\Delta \boldsymbol{\varepsilon}^{p}_{m}\right) \tag{2.50}$$

This correction is carried out until a given numerical tolerance is met (usually a tolerance value of 10^{-8} is used). In Eq. (2.50), the derivative of the residual function ρ are

$$\begin{aligned}\frac{\partial \boldsymbol{\rho}\left(\Delta \boldsymbol{\varepsilon}^{p}_{j}\right)}{\partial \Delta \boldsymbol{\varepsilon}^{p}_{j}} = &\left(\frac{\partial Y\left(\bar{\varepsilon}^{p}_{n} + \psi\left(\Delta \boldsymbol{\varepsilon}^{p}_{j}, \chi_i\right)\right)}{\partial \psi\left(\Delta \boldsymbol{\varepsilon}^{p}_{j}, \chi_i\right)} \frac{\partial \psi\left(\Delta \boldsymbol{\varepsilon}^{p}_{j}, \chi_i\right)}{\partial\left(\Delta \boldsymbol{\varepsilon}^{p}_{j}\right)}\right) \otimes \frac{\partial \psi\left(\Delta \boldsymbol{\varepsilon}^{p}_{j}, \chi_i\right)}{\partial\left(\Delta \boldsymbol{\varepsilon}^{p}_{j}\right)} \\ &+ Y\left(\bar{\varepsilon}^{p}_{n} + \psi\left(\Delta \boldsymbol{\varepsilon}^{p}_{j}, \chi_i\right)\right) \frac{\partial^2 \psi\left(\Delta \boldsymbol{\varepsilon}^{p}_{j}, \chi_i\right)}{\partial\left(\Delta \boldsymbol{\varepsilon}^{p}_{j}\right)^2} + \mathbf{C}^{\mathrm{e}} : \mathbf{K}\end{aligned} \tag{2.51}$$

with $\mathbf{K}$ the fourth-order symmetric deviatoric unit tensor. In the Newton–Raphson procedure, the initial estimate $\Delta \boldsymbol{\varepsilon}^{p}_{(0)}$ is taken proportional to the unit length tensor normal to the von Mises yield surface passing through the elastic trial stress (see Rabahallah et al. [40], Yoon et al. [52]). Thus, solving Eq. (2.49) requires the calculation of $\psi(\Delta \boldsymbol{\varepsilon}^{p})$ as well as its first and second-order derivatives.

The implementation of a strain-rate based elastic–plastic formulation into an implicit finite-element code also requires the calculation of a consistent tangent modulus $\mathbf{C}^{ep}$ that relates the current stress increment $\Delta \boldsymbol{\sigma} = \boldsymbol{\sigma}_{n+1} - \boldsymbol{\sigma}_{n}$ to the current total strain increment $\Delta \boldsymbol{\varepsilon}$. While for a purely elastic incremental deformation, $\mathbf{C}^{ep} = \mathbf{C}^{e}$, for an elastic–plastic increment further calculations are necessary to determine $\mathbf{C}^{ep}$.

To obtain the expression of $\mathbf{C}^{ep}$, one can write

$$\Delta \boldsymbol{\sigma} = \mathbf{C}^{e} : \left(\Delta \boldsymbol{\varepsilon} - \Delta \boldsymbol{\varepsilon}^{p}\right) \tag{2.52}$$

Then differentiation of the dual form of the flow rule [i.e., Equation (2.44)] leads to:

$$\Delta \mathbf{s} = \left(\frac{\partial Y\left(\bar{\varepsilon}^{p}_{n} + \psi\left(\Delta \boldsymbol{\varepsilon}^{p}, \chi_i\right)\right)}{\partial\left(\Delta \boldsymbol{\varepsilon}^{p}\right)} \otimes \frac{\partial \psi\left(\Delta \boldsymbol{\varepsilon}^{p}, \chi_i\right)}{\partial\left(\Delta \boldsymbol{\varepsilon}^{p}\right)} + Y\left(\bar{\varepsilon}^{p}_{n} + \psi\left(\Delta \boldsymbol{\varepsilon}^{p}, \chi_i\right)\right) \frac{\partial^2 \psi\left(\Delta \boldsymbol{\varepsilon}^{p}, \chi_i\right)}{\partial\left(\Delta \boldsymbol{\varepsilon}^{p}\right)^2}\right) : \Delta \boldsymbol{\varepsilon}^{p} \tag{2.53}$$

Denoting,

$$\mathbf{C}^{p} = \left(\frac{\partial Y\left(\bar{\varepsilon}^{p}_{n} + \psi\left(\Delta \boldsymbol{\varepsilon}^{p}, \chi_i\right)\right)}{\partial\left(\Delta \boldsymbol{\varepsilon}^{p}\right)} \otimes \frac{\partial \psi\left(\Delta \boldsymbol{\varepsilon}^{p}, \chi_i\right)}{\partial\left(\Delta \boldsymbol{\varepsilon}^{p}\right)} + Y\left(\bar{\varepsilon}^{p}_{n} + \psi\left(\Delta \boldsymbol{\varepsilon}^{p}, \chi_i\right)\right) \frac{\partial^2 \psi\left(\Delta \boldsymbol{\varepsilon}^{p}, \chi_i\right)}{\partial\left(\Delta \boldsymbol{\varepsilon}^{p}\right)^2}\right) \tag{2.54}$$

From Eq. (2.53), it follows that,

$$\Delta\boldsymbol{\varepsilon}^p = (\mathbf{C}^p)^{-1}\colon \Delta\mathbf{s} = (\mathbf{C}^p)^{-1}\colon \mathbf{K} : \Delta\boldsymbol{\sigma} \tag{2.55}$$

Substituting Eq. (2.55) into Eq. (2.52) and after some algebraic manipulations, we get:

$$\mathbf{C}^{ep} = \left[(\mathbf{C}^e)^{-1} + (\mathbf{C}^p)^{-1}\colon \mathbf{K}\right]^{-1} \tag{2.56}$$

Note that calculation of the consistent elastoplastic modulus using Eq. (2.56) involves two matrix inversions. The consistent tangent modulus can be rewritten in a way such as to avoid doing matrix inversion. Indeed, differentiation of Eq. (2.49) leads to:

$$\frac{\partial\boldsymbol{\rho}(\Delta\boldsymbol{\varepsilon}^p)}{\partial\Delta\boldsymbol{\varepsilon}^p} : \Delta\boldsymbol{\varepsilon}^p - \mathbf{C}^e : \left(\Delta\boldsymbol{\varepsilon} - \frac{1}{3}tr(\Delta\boldsymbol{\varepsilon})\mathbf{I}\right) = 0 \tag{2.57}$$

It follows that,

$$\Delta\boldsymbol{\varepsilon}^p = \left[\frac{\partial\boldsymbol{\rho}(\Delta\boldsymbol{\varepsilon}^p)}{\partial\Delta\boldsymbol{\varepsilon}^p}\right]^{-1} : \mathbf{C}^e : \mathbf{K} : \Delta\boldsymbol{\varepsilon} \tag{2.58}$$

Substituting Eq. (2.58) into Eq. (2.52) leads to,

$$\mathbf{C}^{ep} = \mathbf{C}^e - \mathbf{C}^e : \left[\frac{\partial\boldsymbol{\rho}(\Delta\boldsymbol{\varepsilon}^p)}{\partial\Delta\boldsymbol{\varepsilon}^p}\right]^{-1} : \mathbf{C}^e : \mathbf{K} \tag{2.59}$$

This time integration algorithm for implementing a strain-rate based formulation of an elastic–plastic model into the F.E. framework has been used for orthotropic materials by Rabahallah et al. [40], Yoon et al. [52]. Isotropic and orthotropic strain-rate potentials for metallic materials are presented and discussed in Chap. 6.

References

1. Armstrong PJ, Frederick CO (1966) A mathematical representation of the multiaxial Bauschinger effect. CEBG Rep RDBN 731
2. Bacroix B, Gilormini P (1995) Finite-element simulations of earing in polycrystalline materials using a texture-adjusted strain-rate potential. Model Simul Mater Sci Eng 3:1
3. Balan T (2015) On the numerical implementation of elasto-plastic constitutive equations for metal forming. Romanian J Tech Sci-Appl Mech 60:89–104
4. Balan T, Cazacu O (2013) Elastic–plastic ductile damage model based on strain-rate plastic potential. Mech Res Commun 54:21–26

5. Bauschinger J (1887) Variations in the elastic limit of iron and steel. J Iron Steel Inst 12: 442–444
6. Belytschko T, Liu WK, Moran B, Elkhodary K (2013) Nonlinear finite elements for continua and structures. John Wiley & Sons
7. Bridgman PW (1923) The compressibility of thirty metals as a function of pressure and temperature. In: Proceedings of the American academy of arts and sciences. JSTOR, pp 165–242
8. Bridgman PW (1952) Studies in large plastic flow and fracture. McGraw-Hill, New York
9. Chaboche J-L (2008) A review of some plasticity and viscoplasticity constitutive theories. Int J Plast 24:1642–1693
10. Chung K, Richmond O (1992) Ideal forming—I. Homogeneous deformation with minimum plastic work. Int J Mech Sci 34:575–591
11. Chung K, Richmond O (1992) Ideal forming—II. Sheet forming with optimum deformation. Int J Mech Sci 34:617–633
12. Chung K, Yoon J-W, Richmond O (2000) Ideal sheet forming with frictional constraints. Int J Plast 16:595–610
13. Coulomb CA (1784) Recherches théoriques et expérimentales sur la force de torsion: & sur l'élasticité des fils de métal: application de cette théorie à l'emploi des métaux dans les arts & dans différentes expériences de physique: construction de différentes balances de torsion, pour mesurer les plus petits degrés de force: observations sur les loix de l'élasticité & de la coherence. Memoires Acad R Sci
14. Cristescu N (1967) Dynamic plasticity. North Holland
15. de Souza Neto EA, Peric D, Owen DRJ (2011) Computational methods for plasticity: theory and applications. John Wiley & Sons
16. Drucker DC (1956) On uniqueness in the theory of plasticity. Q Appl Math 14:35–42
17. Drucker DC (1957) A definition of stable inelastic material. Brown Univ Providence RI
18. Drucker DC (1960) Extension of the stability postulate with emphasis on temperature changes. In: Plasticity. Elsevier, pp 170–184
19. Drucker DC (1949) Relation of experiments to mathematical theories of plasticity. ASME J Appl Mech 16:349–357
20. Drucker DC (1950) A more fundamental approach to plastic stress–strain relations. Proc 1st US Nat Congr Appl Mech ASME NY 487–491
21. Fung Y, Tong P, Chen X (2017) Classical and computational solid mechanics. World Scientific Publishing Company
22. Goodier JN, Hodge PG (1958) Elasticity and plasticity. John Wiley & Sons
23. Handelman GH, Lin C, Prager W (1947) On the mechanical behaviour of metals in the strain-hardening range. Q Appl Math 4:397–407
24. Hencky H (1924) Zur Theorie plastischer Deformationen und der hierdurch im Material hervorgerufenen Nachspannungen. ZAMM-J Appl Math Mech Für Angew Math Mech 4:323–334
25. Hill R (1987) Constitutive dual potentials in classical plasticity. J Mech Phys Solids 35:23–33
26. Hill R (1950) The mathematical theory of plasticity. Oxford university press
27. Hodge P, Prager W (1948) A variational principle for plastic materials with strain-hardening. J Math Phys 27:1–10
28. Hodge PG, White GN (1950) A quantitative comparison of flow and deformation theories of plasticity. J Appl Mech-Trans ASME 17:180–184
29. Hughes TJ (1984) Numerical implementation of constitutive models: rate-independent deviatoric plasticity. In: Theoretical foundation for large-scale computations for nonlinear material behavior. Springer, pp 29–63
30. Ilyushin A (1945) Relation between the theory of saint venent-levy-mises and the theory of small elastic-plastic deformations. Applied Mathematics Group, Brown University
31. Levy M (1871) Mémoire sur les équations générales des mouvements intérieurs des corps solides ductiles au delà des limites où l'élasticité pourrait les ramener à leur premier état. J Mathématiques Pures Appliquées 16:369–372

32. Nadai A (1937) Plastic behavior of metals in the strain-hardening range. Part I. J Appl Phys 8:205–213
33. Odqvist F (1933) Die verfestigung von flu\s seisenähnlichen körpern. ein beitrag zur plastizitätstheorie. ZAMM-J Appl Math Mech Für Angew Math Mech 13:360–363
34. Osakada K (2010) History of plasticity and metal forming analysis. J Mater Process Technol 210:1436–1454
35. Polanyi M, Schmid E (1923) Ist die Gleitreibung vom Druck normal zu den Gleitflächen abhängig? Z Für Phys 16:336–339
36. Prager W (1949) Recent developments in the mathematical theory of plasticity. J Appl Phys 20:235–241
37. Prager W (1956) A new method of analyzing stresses and strains in work-hardening plastic solids. J Appl Mech 23:493–496
38. Prager W, Hodge PG (1951) Theory of perfectly plastic solids
39. Prandtl L (1924) Spannungsverteilung in plastischen Körpern. In: Proceedings of the 1st international congress on applied mechanics. pp 43–54
40. Rabahallah M, Balan T, Bouvier S, Teodosiu C (2009) Time integration scheme for elastoplastic models based on anisotropic strain-rate potentials. Int J Numer Methods Eng 80:381–402
41. von Reuss A (1930) Berücksichtigung der elastischen Formänderung in der Plastizitätstheorie. ZAMM-J Appl Math Mech Für Angew Math Mech 10:266–274
42. de Saint-Venant B (1870) Mémoire sur l'établissement des equations différentielles des mouvements intérieurs opérés dans les corps solides ductiles. CR Acad Sci Paris 70:473–484
43. Simo JC, Hughes TJ (2006) Computational inelasticity. Springer Science & Business Media
44. Simo JC, Taylor RL (1985) Consistent tangent operators for rate-independent elastoplasticity. Comput Methods Appl Mech Eng 48:101–118
45. Swift H (1952) Plastic instability under plane stress. J Mech Phys Solids 1:1–18
46. Taylor GI, Quinney H (1932) The plastic distortion of metals. Philos Trans R Soc Lond Ser Contain Pap Math Phys Character 230:323–362
47. Teodosiu C, Hu Z (1998) Microstructure in the continuum modelling of plastic anisotropy. In: Nineteenth Riso international symposium on materials science. pp 149–168
48. Tresca H (1868) Memoire sur l'ecoulement des corps solides, par M. H. Tresca. Imprimerie Imperiale, Paris
49. Van Houtte P, Van Bael A, Winters J (1995) The incorporation of texture-based yield loci into elasto-plastic finite element programs. Texture Stress Microstruct 24:255–272
50. Voce E (1948) The relationship between stress and strain for homogeneous deformation. J Inst Met 74:537–562
51. von Mises R (1913) Mechanik der festen Körper im plastisch deformablen Zustand. Nachrichten Von Ges Wiss Zu Gött Math-Phys Kl 582–592
52. Yoon J-H, Cazacu O, Yoon JW (2011) Strain-rate potential based elastic/plastic anisotropic model for metals displaying tension–compression asymmetry. Comput Methods Appl Mech Eng 200:1993–2004
53. Ziegler H (1977) An introduction to thermodynamics. North-Holland Publishing Company
54. Zienkiewicz OC, Taylor RL, Zienkiewicz OC, Taylor RL (1977) The finite element method. McGraw-hill, London

Chapter 3
Plastic Deformation of Single Crystals

3.1 Elements of Crystallography

A crystalline material is one in which the atoms are situated in a pattern that repeats itself periodically in three dimensions. The actual arrangement of atoms that defines the crystal structure is described with respect to a three-dimensional lattice formed by three straight lines (see Fig. 3.1). In describing the crystal structure, we must distinguish between the pattern of repetition (lattice type) and what is repeated (i.e., the unit cell). The first direct experimental proof of the lattice structure was made possible by von Laue, who in 1912 diffracted X-ray from copper sulfate crystals. Following the first determination of the internal structure for ionic crystals made by H. Bragg and W. L. Bragg in 1913 and their discovery that the reflection of X-rays differs from ordinary optical reflection, significant progress has been made in the following decade, leading to detailed documentation of the crystal structures together with numerical values of the lattice dimensions of various metals and ionic crystals (for a detailed account of the early history and the distribution of the various structures among the elements of the periodic table, the reader is referred to the English translation of the monograph by Schmid and Boas [95] due to F. A. Hughes & Co. Limited, London, 1950).

It is also worth noting that long before the discovery of X-rays, the structural symmetries have been studied and classified by examining the shapes of the crystals formed naturally in the process of crystallization of various materials. Most importantly, all the possible symmetries were described mathematically. In fact, the classification of the symmetries and the arrangement of crystals in thirty-two classes and crystal systems that is in use today dates back to Hessel [46] and Bravais [15] (see also [70]).

Specifically, it was recognized that for a crystal there exist, in the undeformed state, preferred directions of deformation. Associated with each crystal class is a group of symmetry transformations, G. When subjected to one of these transformations, the crystal is carried into a configuration which is indistinguishable from

O. Cazacu et al., *Plasticity–Damage Couplings: From Single Crystal to Polycrystalline Materials*, Solid Mechanics and Its Applications 253,
https://doi.org/10.1007/978-3-319-92922-4_3

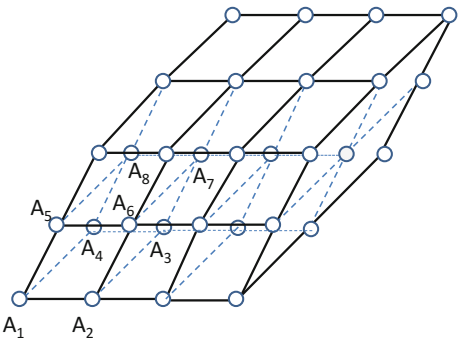

Fig. 3.1 General lattice space

its initial one. Obviously, the identity is a symmetry transformation. If the symmetry group of a crystal consists of the identity **I** alone, the corresponding material has no symmetry, and it is called triclinic. If the symmetry group contains besides the identity **I** only the inversion ($-\mathbf{I}$), the symmetry of the corresponding material is described as central. It was later proved rigorously that any other symmetry group G can be represented as a direct product of the minimal symmetry group $\{-\mathbf{I}, \mathbf{I}\}$ and another group G^+, which consists only of proper orthogonal transformations (i.e., transformations for which the determinant is equal to unity; see also Chap. 1). Therefore, the symmetry group of a crystal is completely characterized by G^+, and it is sufficient to determine the *generators of* G^+, which are defined as the set of transformations of G^+ with the property that any transformation of G^+ can be represented as a product of generators, and possibly of their inverses (see also [104]). Moreover, it can be proven that even if an infinite number of subgroups of the proper orthogonal group Orth^+ exist, only twelve of them exhaust the kind of symmetries occurring in the materials known to man. Eleven of these subgroups correspond to exactly the thirty-two crystal classes identified in the late nineteenth century, while the last type of anisotropy, called transverse isotropy (say with respect to a unit direction **e**), is characterized by the symmetry group consisting of the identity **I** and all the rotations $R(\mathbf{e}, \theta)$ of angle θ with $0 < \theta < 2\pi$ about an axis along **e** (see Chap. 1 for more discussion on basic concepts and definition of Orth^+; for yield criteria and plastic potentials for fully-dense and porous transversely isotropic metallic materials, see Chaps. 5 and 8, respectively). Further arrangements of the crystal classes into six crystal systems was undertaken on the basis of the symmetry axes and/or planes that a crystal may possess.

Symmetry axis

Definition 3.1 A crystal possesses an m-gonal symmetry axis of unit vector **n**, if G^+ contains the right-handed rotation $R_{\mathbf{n}}^{2\pi/m}$.

Note that an axis of symmetry of order m converts the lattice points into m equivalent positions, and so covers the plane at right angles to the axis with an unbroken series of points which form regular polygons of order m. As shown in

Fig. 3.1, all points on a plane must also appear as the corners of a net of parallelograms. The only angles of rotation which fulfill both conditions are 2π (or 0), π, $2\pi/3$, $\pi/2$, and $\pi/3$, corresponding to $m = 1$, 2 (diagonal), 3 (trigonal), 4 (tetragonal), or 6 (hexagonal) or sixfold axes of symmetry, respectively.

Reflection

Definition 3.2 Reflection with respect to a plane of unit normal $\mathbf{n}$ is specified by:

$$\boldsymbol{Q}^{\boldsymbol{n}} = \mathbf{I} - 2\boldsymbol{n} \otimes \boldsymbol{n} \tag{3.1}$$

Note that $\boldsymbol{Q}^{\mathbf{e}} = -R(\mathbf{e}, \pi)$. For example, if $Oxyz$ is a Cartesian coordinate system and $\mathbf{e} = \boldsymbol{e}_z$, the matrix of the reflection $\boldsymbol{Q}^{\boldsymbol{e}_z}$ has the following form:

$$\mathbf{Q}^{\mathbf{e}_z} = \begin{bmatrix} 1 & 0 & 0 \\ 0 & 1 & 0 \\ 0 & 0 & -1 \end{bmatrix}.$$

It can be easily seen that $Q^{\boldsymbol{e}_z}\boldsymbol{e}_x = \boldsymbol{e}_x$ and $Q^{\boldsymbol{e}_z}\boldsymbol{e}_y = \boldsymbol{e}_y$, and that if $Q^{\boldsymbol{e}_z}$ belongs to the symmetry group, then the plane $\mathbf{z} = 0$ is a plane of symmetry. In general, a crystal possesses a plane of symmetry of unit normal $\mathbf{n}$, if G contains the reflection $\boldsymbol{Q}^{\boldsymbol{n}}$. It can also be demonstrated that the existence of a digonal axis at right angles to a m-gonal axis implies the existence of m such axes. The existence of a plane of symmetry passing through an m-gonal axis implies the existence of m such planes. Based on these elements of symmetry, crystals are further grouped in the following systems: triclinic, monoclinic, tetragonal, rhombic, cubic, and hexagonal.

Although the geometrical nature of each of the thirty-two types of crystal classes is absolute, and their arrangements in the six systems is generally accepted, there is a great diversity in the terminology used by different authors and communities (e.g., spectroscopy, crystallography, or engineering sciences community). Table 3.1 shows the names of the classes of crystals and their grouping in systems, the symbols of the corresponding symmetry groups of transformations used by Schoenflies [95], and the set of generators of the respective groups. For the generators of various crystal classes, in this book, we follow Green and Adkins [41] and Teodosiu [104], who in turn used the terminology of Smith and Rivlin [96]. Thus, we denote by $R^{\phi}_{\mathbf{n}}$ the proper rotation (i.e., $\det R^{\phi}_{\mathbf{n}} = 1$) through an angle ϕ about an axis in the direction of the unit vector $\mathbf{n}$; $(\boldsymbol{e}_x, \boldsymbol{e}_y, \boldsymbol{e}_z)$ denote a right-handed orthonormal basis and $\boldsymbol{f} = (\boldsymbol{e}_x + \boldsymbol{e}_y + \boldsymbol{e}_z)/\sqrt{3}$.

Unit cell

The unit cell is the smallest unit of volume that contains all the structural and symmetry information (e.g., the parallelepiped $A_1A_2A_3A_4A_5A_6A_7A_8$ in Fig. 3.1; see also [54]), the crystal being constructed by stacking identical unit cells face to face in perfect alignment in three dimensions. In this book, the discussion will be restricted to cubic and hexagonal structures. The unit cell for a cubic crystal is shown in Fig. 3.2a with reference to the three principal axes $\mathbf{x}, \mathbf{y}, \mathbf{z}$ (a crystal is said

Table 3.1 Generators for the symmetry groups of various crystal classes (after [28])

Crystal system	Class symbol [Schoenflies]	Proper orthogonal generators of the symmetry group
Triclinic	C_1	$\mathbf{I}$
Monoclinic	$S,\ C_2,\ C_{2h}$	$R^{\pi}_{\mathbf{e}_z}$
Rhombic or prismatic	$C_{2v},\ D_2,\ D_{2h}$	$R^{\pi}_{\boldsymbol{e}_x}, R^{\pi}_{\boldsymbol{e}_y}$
Tetragonal	$C_{4h},\ S_4,\ C_4$	$R^{\pi/2}_{\boldsymbol{e}_z}$
	$C_{4v}, D_{26}, D_4, D_{4h}$	$R^{\pi/2}_{\boldsymbol{e}_z},\ R^{\pi}_{\boldsymbol{e}_x}$
Cubic { tetratoidal, diploidal }	T, T_h	$R^{\pi}_{\boldsymbol{e}_x}, R^{\pi}_{\boldsymbol{e}_y}, R^{2\pi/3}_{f}$
{ hextetrahedral, gyroidal, hexoctahedral }	T_d, O, O_h	$R^{\pi/2}_{\boldsymbol{e}_x}, R^{\pi/2}_{\boldsymbol{e}_y}$
Hexagonal	C_3, C_{3i}	$R^{2\pi/3}_{\boldsymbol{e}_z}$
	C_{3v}, D_3, D_{3d}	$R^{\pi}_{\boldsymbol{e}_x},\ R^{2\pi/3}_{\boldsymbol{e}_z}$
	C_6, C_{3h}, C_{6h}	$R^{\pi/3}_{\boldsymbol{e}_z}$
	$C_{6v}, D_6, D_{3h}, D_{6h}$	$R^{\pi}_{\boldsymbol{e}_x}, R^{\pi/3}_{\boldsymbol{e}_z}$

to have a principal axis if every axis of symmetry other than the principal axis is at right angles with that axis and each plane of symmetry either passes through the principal axis or is at right angles to that axis). For example, in the body-centered cubic (bcc) structure, the atoms are situated at the corners of the cubic unit cell and at its center (Fig. 3.2a), where a indicates the cell dimension. In the face-centered cubic (fcc) structure, the atoms are situated at the corners of the cubic unit cell and at the centers of all cube faces (Fig. 3.2b).

The hexagonal close-packed (hcp) unit cell with lattice parameters a, a, c is shown in Fig. 3.2c. There are two atoms per lattice site. The atomic planes perpendicular to the c-axis are close-packed. If the atoms are considered as rigid spheres, the c/a ratio is $\sqrt{8}/\sqrt{3} = 1.633$. In practice, this ratio varies from 1.57 to 1.89. For hcp Ti, the c/a ratio is 1.587, while for pure Zn this ratio is 1.86.

Representation of the orientation of crystallographic planes and directions

The symmetry groups of the crystals belonging to the cubic and hexagonal systems have been defined in Table 3.1, while the most suitable coordinate systems associated to theses symmetries were described in Fig. 3.2. In the following, we succinctly present and illustrate the methods by which lattice planes and directions are indexed. For a more detailed discussion, the reader is referred to the relevant crystallographic literature. Let us first note that in a cubic crystal, any plane, say $A_2B_2C_2$ in Fig. 3.3, can be defined by the intercepts OA_2, OB_2, OC_2 that it makes with the three principal axes $\mathbf{x}, \mathbf{y}, \mathbf{z}$. Thus, it is sufficient to indicate the ratios of these intercepts to describe its orientation. Haüy discovered the law of rational

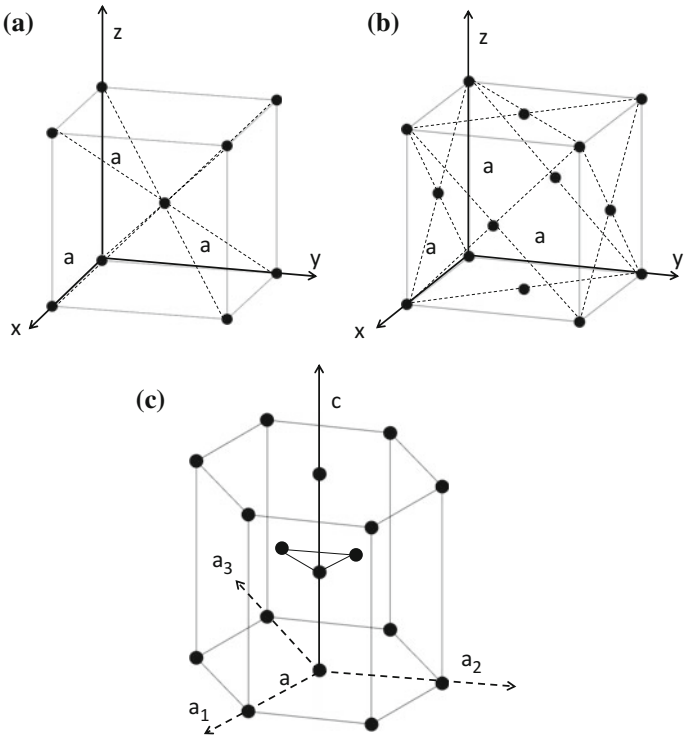

Fig. 3.2 Unit cells showing positions of principal axes and atoms and cell dimensions: **a** body-centered cubic, **b** face-centered cubic, and **c** hexagonal close-packed

indices which states that if three non-coplanar edges of a crystal are taken to define the directions of three axes of a coordinate system, then the ratios of the axial intercepts of two crystal faces are always found to be rational fractions (see [45]). Therefore, if for a plane $A_1B_1C_1$ the ratios of the axial intercepts are $a_1 : b_1 : c_1$ while for another plane $A_2B_2C_2$ of the same crystal the ratios of the axial intercepts are $a_2 : b_2 : c_2$, then there exist m_i, n_i, p_i (i = 1, 2) integers such that:

$$m_1a_1 : n_1b_1 : p_1c_1 = m_2a_2 : n_2b_2 : p_2c_2, \tag{3.2}$$

It follows that if the plane $A_1B_1C_1$ is chosen to be the unit plane (i.e., $a_1 = b_1 = c_1 = 1$), the numbers m_1/m_2, n_1/n_2 and p_1/p_2 express the multiple of the unit distance at which the three axes are intersected by the plane $A_2B_2C_2$. Therefore, the plane $A_2B_2C_2$ can be defined by the three indices $h = m_2/m_1$, $k = n_2/n_1$, and $l = p_2/p_1$ reduced to prime whole numbers. Theses indices are called Miller indices and are calculated as follows: First, the axial intercepts are normalized by the corresponding cell dimensions, the reciprocals of these numbers are taken, and these numbers are then reduced to the smallest integers. For example, if $OA_2 = 3a$, $OB_2 = 2a$ and $OC_2 = 3a$, the Miller indices (hkl) of the plane $A_2B_2C_2$

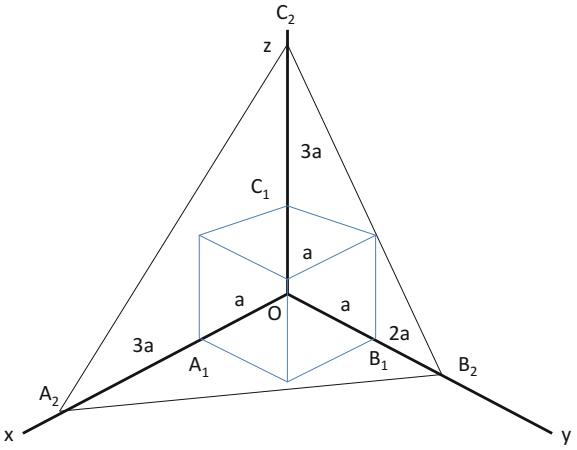

Fig. 3.3 Cubic unit-cell and the method of describing the orientation of crystallographic planes

or of other planes parallel to it are obtained by reducing to the smallest integers $\left(\frac{a}{3a}, \frac{a}{2a}, \frac{a}{3a}\right)$, and these planes are designated (232).

The minus sign above an index [e.g., $(\bar{1}01)$] indicates that a plane intersects the axis on the negative side of the origin. A plane with a zero index is parallel to the corresponding axis (i.e., intercepts the axis at ∞). Consequently, planes of coordinates, which contain two axes parallel to the principal axes, are designated by two zero indices (see also Fig. 3.4).

Directions are also described by three indices. The procedure is as follows: Take the line parallel to the given direction that passes through the origin *O* of the

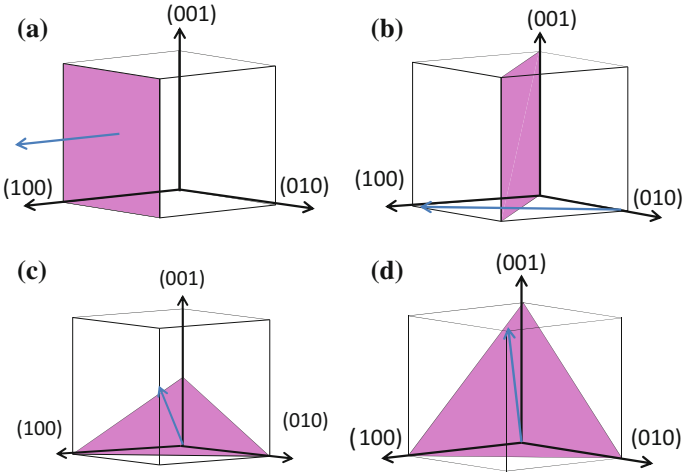

Fig. 3.4 Cubic cells illustrating the method of describing the orientation of planes and cube faces (pink) and normal directions (blue): **a** (100); **b** (110); **c** (112); **d** (111)

coordinate system, resolve this line along the three principal axes, and then reduce to the three smallest integers the ratios of the lengths of these projections to the corresponding cell dimensions. The indices for directions are distinguished from the indices for planes by being placed in square brackets, i.e., $[uvw]$. A zero index indicates that the direction is parallel to one of the coordinate planes. Thus, the coordinate axes (or principal axes of symmetry) are designated by indices [100], [010], and [001], respectively.

It is important to note that for cubic crystals, the Miller indices of a plane (hkl) are related to the indices of the direction normal to that plane $[uvw]$ by $u = h$, $v = k$ and $w = l$. This is also shown in Fig. 3.4, which illustrates the indexing method for describing planes and directions, and the indices of some important planes of cubic crystals. The cube faces being parallel to the coordinates planes have indices (100), (010), and (001), respectively. Of the four octahedral planes contained in the cubic unit cell, the one shown in Fig. 3.4d has the indices (111), while the others have indices $(11\bar{1})$,$(1\bar{1}1)$ and $(\bar{1}11)$, respectively. The plane (112) represented in Fig. 3.4c makes equal intercepts on the [100] and [010] axes and half of that intercept on the [001] axis. Of the directions represented in Fig. 3.4, [100] designates one of the three edges of the cube (see Fig. 3.4a), [110] is one of the six face diagonals (see Fig. 3.4b), [112] direction is one of twelve directions which connects a corner of the cube with a face center on the opposite side (see Fig. 3.4c), and [111] is one of the four cube diagonals (see Fig. 3.4d).

In the following and throughout this book, brackets [ ] and ( ) imply specific directions and planes, respectively, while $\langle\ \rangle$ and { } refer, respectively, to directions and planes of the same type (or family). For example, the cube diagonals, namely $[11\bar{1}]$, $[\bar{1}11]$, $[\bar{1}1\bar{1}]$, and $[\bar{1}\bar{1}1]$, belong to a group of directions of the same type (i.e., closed-packed directions, see also Figs. 3.2a, b, and 3.4d) and are described collectively as $\langle 111\rangle$, while the planes normal to these directions are designated as $\{111\}$.

Indexing of planes and directions in hexagonal crystals can also be based on the Miller–Bravais method. To describe the orientation of a plane, first, the reciprocal intercepts of the plane on the four symmetry axes $\boldsymbol{a}_1, \boldsymbol{a}_2, \boldsymbol{a}_3$, and $\boldsymbol{c}$ used in the hexagonal system (see Fig. 3.2) are found and then reduced to the smallest integers (see also [50]). Given that the three axes $\boldsymbol{a}_1, \boldsymbol{a}_2, \boldsymbol{a}_3$ are equivalent and lie in the same plane, called the basal plane, the indices associated to these symmetry axes are not independent. If a plane is specified by $(hkil)$, the first three indices which refer to the $\boldsymbol{a}_1, \boldsymbol{a}_2, \boldsymbol{a}_3$ axes are such that $i = -(h + k)$ (i.e., the third index is always the negative of the sum of the first two). Equivalent planes are obtained by interchanging the position and sign of the first three indexes.

For the hexagonal unit cell, several planes of interest have been given specific names. The (0001) plane (of normal [0001]) is the basal plane, as shown in Fig. 3.5a. The planes parallel to the **c**-axis and of normal $\langle 10\bar{1}0\rangle$ are called prismatic planes of type I. As an example, in Fig. 3.5b are plotted the prismatic planes of type I defined

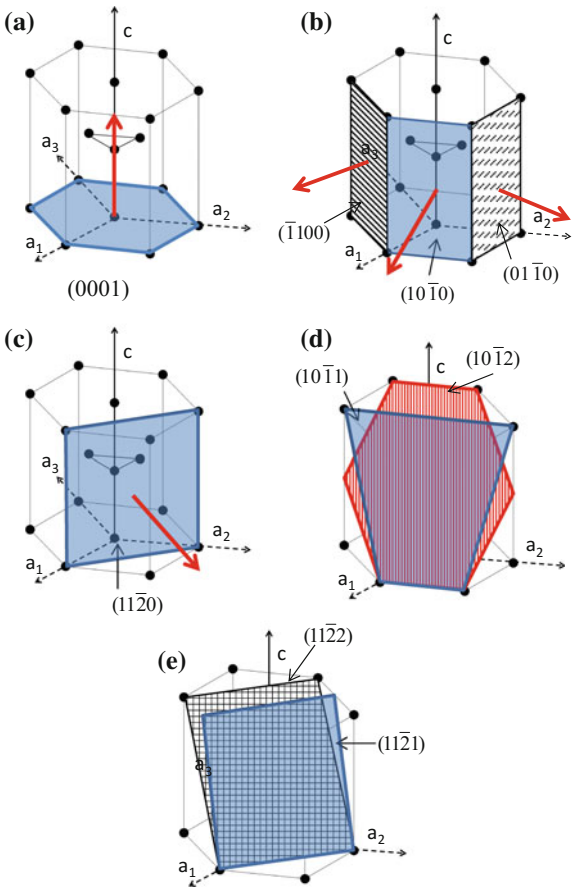

Fig. 3.5 Hexagonal cells illustrating the Miller–Bravais indices and the designation of specific planes and directions. **a** Basal plane (0001); **b** prismatic plane of type I: $(10\bar{1}0)$, $(\bar{1}100)$ and $(01\bar{1}0)$; **c** prismatic plane of type II: $(11\bar{2}0)$; **d** pyramidal plane of type I: $(10\bar{1}1)$ and $(10\bar{1}2)$; **e** pyramidal plane of type II: $(11\bar{2}1)$ and $(11\bar{2}2)$

by the indices $(10\bar{1}0), (01\bar{1}0), (\bar{1}100)$ and their normals. The planes parallel to the **c**-axis and of normal $\langle 11\bar{2}0\rangle$ are called prismatic planes of type II, the plane $(11\bar{2}0)$ being represented in Fig. 3.5c, the planes which pass through the edges of the basal hexagon and that are not parallel to the **c**-axis are called pyramidal planes of type I and are indexed by $(10\bar{1}l)$ [see Fig. 3.5d that shows the plane $(10\bar{1}1)$ and the plane $(10\bar{1}2)$]. The family of planes $(11\bar{2}l)$ is called pyramidal planes of type II, the planes $(11\bar{2}1)$ and $(11\bar{2}2)$ being plotted in Fig. 3.5e. Among the important directions, the **c**-axis (hexagonal axis) is designated by the direction $[0001]$, while the axes $\boldsymbol{a}_1, \boldsymbol{a}_2, \boldsymbol{a}_3$ defining the basal plane are denoted by the indices $[2\bar{1}\bar{1}0], [\bar{1}2\bar{1}0]$ and $[\bar{1}\bar{1}20]$, respectively.

3.2 Plastic Deformation Mechanisms in Crystals: Experimental Evidence

3.2.1 Crystallographic Slip

While it has long been known that crystals can undergo permanent or plastic deformation, experimental evidence of the mechanisms responsible, namely glide and mechanical twinning, was first provided by Reusch [84]. For detailed reviews of the early studies and methods of investigation, we refer to the classical monographs of Elam [33] and Schmid and Boas [94]. Here, we just mention the remarkable studies of Ewing and Rosenhain [36] who by microscopic examination of the surfaces of deformed crystals have put into evidence the existence of lines that they called slip bands and concluded that "*when the metal is strained beyond its elastic limit, yielding takes place by finite amounts of slip at a limited number of places.*" Moreover, these authors hypothesized that there must exist planes inside the crystal along which slip occurs and that the slip bands would then be made up of the lines of intersection of the face of the specimen with these crystal planes (see, e.g., the optical micrograph of deformed lead specimens reported in [36]). However, only after the discovery of X-ray diffraction and the possibility of the analysis of crystals by X-rays, proof of the structure of crystals and verification of the assumptions concerning the planes of slip could be made (e.g., [99, 100]).

The work of Carpenter and Elam [22] has enabled the production of crystals of Al sufficiently large such that specimens in the form of bars of square cross-section and dimensions of $1 \times 1 \times 20$ cm could be cut. This enabled a systematic analysis of strains that develop under uniaxial tension. These test results were published in 1925 by Taylor and Elam (although the results were presented at a Bakerian lecture delivered by G.I. Taylor in 1923). Detailed measurements of various strains (axial strain, angles between cross marks and longitudinal marks on each face of the specimen, the thickness of the specimen between pairs of opposite faces) at different stages of the tests corresponding to 5%, 10%, 15%, 20%, 30%, 40%, and 60% extension were reported. Taylor and Elam [99] assumed that homogenous deformation occurs by slip on certain crystallographic planes and in certain crystallographic directions, as X-ray analyses showed that the symmetry of the crystal was not changed by the test. Therefore, it is geometrically necessary that there exists a set of parallel planes that should remain undeformed (i.e., the length of any lines contained in these planes must not change during the deformation). These planes are called slip planes. Therefore, it is possible to experimentally identify a slip plane from the change in the geometry of the faces of the specimen, a method called "the unstretched cone method" (for more details, see [33]). Based on this thorough analysis, these authors provided a quantitative description of the slip phenomenon and the interpretation of the kinematics of the plastic deformation in terms of the crystal structure. After identifying the slip planes and the slip directions and observing that slip occurs preferentially, it was concluded that "*when a single crystal bar of Al is stretched the whole distortion during a large part of stretching is*

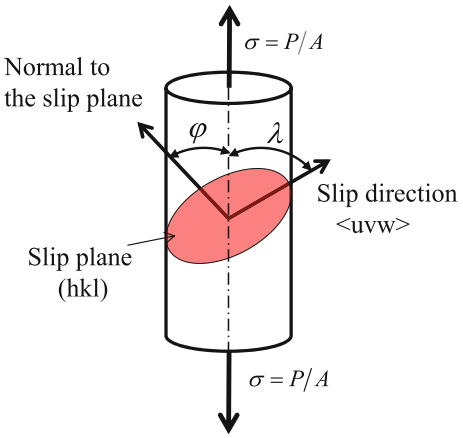

Fig. 3.6 Schematic of a single crystal sample subjected to an applied tensile force

due to a simple shear parallel to the octahedral (111) plane and in the direction of one of the three dyad $\langle 110 \rangle$ *axes lying in that plane. Of the twelve crystallographic similar possible modes of shearing, the one for which the component of shear stress in the direction of shear was greatest was the one along which slip actually occurred*" (see also Fig. 3.6). In the last stages of the tests (extension of 62% and 78%), it was put into evidence that slip occurs simultaneously on two octahedral planes, which are at nearly equal angles to the axis of the specimen. Moreover, the measurements indicated that the central portion of each specimen was uniformly strained, especially in the early stages of the test.

Based on measurements of slip bands on the surface of the specimen, Mark et al. [72] established that in hcp Zn crystals subjected to uniaxial tension slip or glide (the synonymous terminology preferred by Schmid and collaborators) occurs more readily in the basal plane and that the slip direction is the digonal axis $\langle \bar{2}110 \rangle$ (see also Fig. 3.5; for photographs showing slip bands of deformed Zn and Cd crystals, see [94]). It is worth noting that at this stage of discovery of the plastic deformation mechanisms at the single crystal scale, hcp materials, like Zn or Cd, were considered because the phenomena are easier to understand. This is due to the fact that these materials primarily slip on the (0001) basal plane, and slip bands and cleavage plane are clearly marked. For other materials where slip takes place on more than one plane (e.g., Al), the method of Mark et al. [72] is inapplicable (see [33]).

In 1924, on the basis of experimental studies of the relationship between the yield stress and the angle between the slip plane and the direction of the tensile axis in hexagonal crystals, Schmid established that irrespective of the orientation of the tensile axis, "*a critical value of the resolved shear stress is required for the initiation of glide.*" This is Schmid's law of the critical shear stress. Specifically, for a cylindrical crystal under uniaxial tensile load P, if λ and φ are the angles between the tensile axis and the slip direction, and slip plane normal, respectively (see Fig. 3.6), then the resolved shear stress is:

$$\tau = \frac{P}{A}\cos\varphi\cos\lambda, \tag{3.3}$$

where A is the current area of the cross-section. Therefore, according to Schmid's law, (P/A) varies inversely with the orientation factor, $\cos\varphi\cos\lambda$, also known as Schmid factor. As pointed out by Schmid and Boas [94], the verification of the law is much simpler in the case of crystals of the hexagonal system than in the case of cubic crystals. For example, owing to the fact that Zn has hexagonal symmetry and as such there is only one most probable slip plane, the examination of a large range of the Schmid factor was possible. Comparisons between the theoretical relationship between the yield stress (P/A) and the orientation of the slip system given by Eq. (3.3) and data on hcp Cd, Zn, Mg can be found in Schmid and Boas [94]. The agreement with the experimental observations was found satisfactory. Moreover, Schmid reported that the "*normal stress operating on the respective glide plane is of no importance*" thus confirming the conclusion reached earlier by Polanyi and Schmid [80] on the basis of results of tensile tests under hydrostatic pressure.

As already mentioned, Taylor and Elam [99, 103] studies on pure Al single crystals contributed to the conclusion that the Schmid law is applicable to pure single crystals with fcc structure. As concerns fcc crystals containing alloying elements, the experimental data also agree well with the Schmid law, deviations occurring only when the tensile axis orientation is such that the simultaneous operation of several slip systems is favored (see Elam [33]; for α-brass containing 72% Cu, see Masima and Sachs [73]; for a Cu-Al single crystal, see Karnop and Sachs [58], etc.).

In summary, based on the experimental evidence, it can be concluded that plastic deformation in fcc single crystals occurs through slip on the {111} octahedral planes along the close-packed directions ⟨110⟩.

As concerns bcc single crystals, Taylor and Elam (see [100]) experimental study of the plastic behavior of α-iron single crystal (bcc structure) under tension revealed a completely different kinematics of slip than that observed in the fcc single crystals. To this day, we rely on Taylor and Elam explanation of how slip in α-iron single crystal can occur parallel to a crystal axis, but on a plane which is related to the direction of applied stress rather than to the orientation of the crystal axes. While slip in fcc crystals may be represented by a model consisting of a pack of cards sliding over one another, Taylor and Elam hypothesized that the model for representing slip in bcc-iron crystals might be that of a bundle of rods sheared in the direction of their length; these rods ought to be hexagonal in section in order to respect the threefold symmetry about their axes. This led to the model coined "⟨*111*⟩ *pencil glide*" where the slip surface is considered to be a prismatic cylinder made of strips of slip planes bounded by the common slip direction ⟨111⟩.

To verify the validity of this explanation, Taylor (see [101]) conducted similar tests on a β-brass single crystal. The results show that the plane of slip varies depending on the relative orientation of the crystal axes with respect to the direction of the principal stress. However, there were noticed differences in the plastic behavior

of β-brass single crystal with respect to that of the α-iron single crystal. While Taylor and Elam (see [100]) determined that the planes $\{110\}$ and $\{112\}$ are slip planes for the α-iron single crystal, for the β-brass single crystal, Taylor concluded that $\{110\}$ are slip planes, and that there must be other slip planes that he could not clearly identify; however none of them are the $\{112\}$ planes. Most importantly, Taylor has reported that in β-brass, "*resistance to slipping in one direction on a given plane of slip is not the same as the resistance offered to slipping in the opposite direction.*" Therefore, for a bcc single crystal the resistance to shear depends not only on the component collinear with the slip direction of the projected stress on the slip plane, but also on the component orthogonal to the slip direction (component of shear transverse to the slip direction). This means that the plastic behavior of bcc single crystal cannot be described by the Schmid law (see Eq. 3.3).

For bcc crystal structure, this controversy dating from the 1920s concerning what happens inside a crystal when subject to uniaxial tension–compression is still ongoing; the quantitative description of the physics of plastic deformation remains a subject of intense research (e.g., see [18]). Although at present it is generally accepted that the dominant slip directions are the $\langle 111 \rangle$ directions and that slip may occur on the high-density planes $\{110\}$, $\{112\}$, and $\{123\}$ depending on temperature (see, e.g., [51]), it is not definitively elucidated how the slip activity switches between these systems. For example, for single crystal bcc Mo, Luft, and Ritschel [71] reported slip only on the $\{112\}$ and $\{110\}$ planes along the $\langle 111 \rangle$ directions, while Yoo and collaborators (e.g., see [110]) showed that up to a plastic strain of about 10% the dominant slip system is $\{123\}\langle 111 \rangle$, and that the $\{110\}\langle 111 \rangle$ and $\{211\}\langle 111 \rangle$ systems become operational only beyond this plastic strain level. Moreover, the applicability of Schmid law for the description of yielding in bcc crystals is severely questioned from an experimental standpoint (for evidence of the breakdown of Schmid law for several bcc materials, see, e.g., [52, 60, 61]). Specifically, it was shown that contrary to Schmid law and as reported early by Taylor (e.g., see [101]) for β-brass, plastic flow exhibits tension–compression asymmetry and that slip may occur on planes on which the shear stress is not the largest. The tension–compression asymmetry in flow stresses of bcc Mo single crystals (mm size) has been reported in several studies (e.g., [49]). Moreover, in experimental studies of the tensile and compressive behavior of $\langle 001 \rangle$ oriented Mo micropillars of nanometer dimensions (smallest size $\sim$200 nm diameter), it was reported that the flow stresses in compression are approximately 67% greater than in uniaxial tension (e.g., [60]). Atomistic simulations studies have also provided confirmation of these characteristics of the plastic flow of bcc metals. For example, the results of Gröger and collaborators (e.g., [42]) show deviations from Schmid law for Mo and W, which were explained by the influence of normal stresses (i.e., stress components who are not along the slip plane) on the onset of plastic flow. However, these authors considered that slip occurs only on $\{110\}$ planes.

For hcp crystals, based on experiments on Zn, Mg, and Cd (see [72, 92, 94]), it was concluded that the basal plane is a slip plane with the three axes $\langle 11\bar{2}0 \rangle$ as slip directions (see Fig. 3.5a). Further studies on hcp Mg single crystals conducted, either

at higher temperatures [93] or at loadings along specific orientations such as to suppress basal slip [83], allowed to determine that the prismatic $\{10\bar{1}0\}\langle 11\bar{2}0\rangle$ (see Fig. 3.5b) and pyramidal $\{10\bar{1}1\}\langle 11\bar{2}0\rangle$ (see Fig. 3.5c) slip systems could also be operational in hcp crystals. Furthermore, experimental work on Zn [87] led to the conclusion that the direction $\langle 11\bar{2}3\rangle$ (or $\langle \mathbf{c+a}\rangle$) can also be a slip direction when slip takes place on the pyramidal plane $\{11\bar{2}2\}$ (see Fig. 3.5e). The independent modes of slip in hcp single crystals are summarized in Table 3.2. Note that hcp metals show a large variation in terms of the slip systems that can be operational, the slip activity of any given system depending on the type of loading and its relative orientation to the crystal axes. Nowadays, it is commonly accepted that the two most common primary slip systems are: basal slip for metals with a high c/a ratio and prismatic slip for the ones with a low c/a ratio. As an example, Cd ($c/a = 1.886$), Zn ($c/a = 1.856$), Mg ($c/a = 1.624$) crystals deform primarily by slip on the basal slip plane, while Ti ($c/a = 1.599$) and Zr ($c/a = 1.593$) crystals deform more readily on the prismatic plane. It has been experimentally established that for Ti (see [2]) and Zr (see [81]), the resolved shear stress on the $\{10\bar{1}0\}$ prismatic plane was lower than the one on the $\{0001\}$ basal plane. However, for Be ($c/a = 1.568$), the lowest critical resolved shear stress is obtained on the basal plane. Therefore, the primary slip systems of hcp metals cannot be inferred solely based on the c/a ratio.

Of particular interest is the activation of slip along the $\langle 11\bar{2}3\rangle$ (or $\langle \mathbf{c+a}\rangle$) direction through glide on the $\{11\bar{2}2\}$ pyramidal II plane. This is because only slip along the $\langle \mathbf{c+a}\rangle$ directions can provide five independent deformation modes for an hcp crystal and thus satisfy Taylor requirement (see [102]). Indeed, Taylor stated that for a polycrystalline material to accommodate general deformation without producing cracks, at least five independent slip systems should be available. Furthermore, the pyramidal $\langle \mathbf{c+a}\rangle$ slip is the only slip mechanism that could produce deformation of the **c**-axis. This particular slip system can be activated in a material that has the basal slip system as primary slip system (e.g., Cd, Zn, Mg); however, it is also known that $\{11\bar{2}2\}$ is a twinning plane for Ti and Zr (see discussion on twinning later in this section). For more details on the slip systems in hcp materials, the reader is referred to Rosenbaum [88].

Table 3.2 Slip planes and directions for the common crystal structures

Structure	Slip direction	Slip plane	
Fcc	$\langle 110\rangle$	$\{111\}$	Fig. 3.4d
Bcc	$\langle 111\rangle$	$\{110\}$	Fig. 3.4b
	$\langle 111\rangle$	$\{112\}$	Fig. 3.4c
	$\langle 111\rangle$	$\{123\}$	
Hcp			
Basal	$\langle 11\bar{2}0\rangle$	$\{0001\}$	Fig. 3.5a
Prismatic	$\langle 11\bar{2}0\rangle$	$\{10\bar{1}0\}$	Fig. 3.5b
Pyramidal I	$\langle 11\bar{2}0\rangle$	$\{1\bar{1}01\}$	Fig. 3.5d
Pyramidal II	$\langle 11\bar{2}3\rangle$	$\{11\bar{2}2\}$	Fig. 3.5e

As stated previously, Schmid law has been developed based on observations on Zn single crystal, which deforms primarily by slip on the basal plane followed by slip on the prismatic plane. Later studies have confirmed that in general the Schmid law (Eq. 3.3) is applicable for hcp metals that deform primarily on the basal plane and secondary on the prismatic plane [38], but it does not describe well the plastic deformation in materials for which the primary slip system is prismatic (e.g., Ti) (see [90]).

The slip systems for each lattice structure are summarized in Table 3.2. It is worth noting that only in the case of the fcc lattice, there exists a unique slip system that is potentially active for all the materials. For the bcc and hcp lattices, the slip systems that may be operational vary among materials; whether a system is active depends on the orientation of the applied loading with respect to the crystal axes.

3.2.2 *Deformation Twinning*

The other deformation mechanisms by which single crystals can be plastically deformed is called mechanical twinning or deformation twinning. First observations of deformation twins were made in 1859 by Pfaff (see [79]) who investigated how the mechanical pressure influences the birefringence of crystals of quartz and calcite. This author attributed the change in the optical properties of the crystal to a change of the lattice orientation. Based on these data and his own observations, Dove [32] realized that twinning can also be induced by mechanical deformation.

Formalization and description of deformation twinning were made possible by the findings of Kelvin and Tait [59] who proved the existence of a type of deformation, that they called simple shear, which allows two planes to remain undeformed. Moreover, these authors described precisely what is meant by simple shear deformation: "*the plane of shear is a plane perpendicular to the undistorted planes, and parallel to the line of their relative motion. It has: (1) the property that one set of parallel planes remain each unaltered in itself; (2) that another set of parallel planes remains each other unaltered in itself*" and that "*the plane of no distortion in simple shear are clearly the circular sections of the strain ellipse.*"

Being aware of the work of Kelvin and Tait [59], Liebisch [68] made the link between simple shear and the experimental observations of mechanical twinning. This link was further investigated by Mügge [77] who concluded that twinning deformation is a simple shear deformation and further described and classified the deformation twins by means of two planes, the K_1 plane and the associated shearing direction $\boldsymbol{\eta}_1$ and the K_2 plane and its characteristic direction $\boldsymbol{\eta}_2$ (see Fig. 3.7). This description of deformation twinning is still used today. For more details about the history of the discovery of mechanical twinning, the reader is referred to Hardouin Duparc [43, 44].

From the description of Mügge [77], it follows that during twinning deformation, the shear plane K_1 does not change its shape or its position (first undeformed plane). On the other hand, all the other planes are tilted such that the second

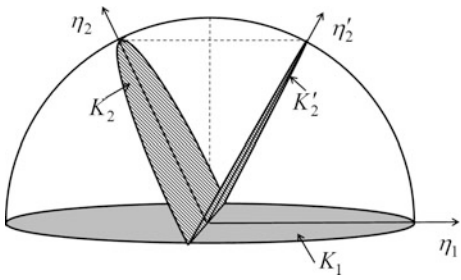

Fig. 3.7 Geometrical description of mechanical twinning

twinning plane K_2 remains undeformed, but it is tilted to K_2' (see Fig. 3.7). Also, the amount by which a point at a unit distance of the twinning plane is sheared is termed the shear strain s, the amount of shear strain being fully determined by the crystallographic properties of the two undeformed planes K_1 and K_2.

It is important to compare the two deformation mechanisms for plastic deformation, namely slip and twinning. While neither induces volume change, slip and twinning are totally different. Figure 3.8 illustrates the lattice movement during slip and twinning, respectively. Concerning the slip mechanism, each atom cannot move less than an interatomic distance in the direction of slip (identity translation), while for deformation twinning, the magnitude of displacement of each atom is no more than a small fraction of the lattice spacing.

Another important difference between deformation twinning and crystallographic slip is that twinning is polarized; i.e., reversal of the η_1 direction will not produce a twin. It follows that for a given single crystal some twin mode should operate only in tension, whereas other twin mode should operate only in compression, depending on the relative orientation between the crystal orientation and the loading orientation.

As seen previously, a twinning mode is completely defined by crystallography. It induces a change of the lattice orientation of the twin part with respect to the rest of the single crystal. As a consequence, for a long time, twinning has been mainly studied by mineralogists, while metallurgists focused mainly on the description of

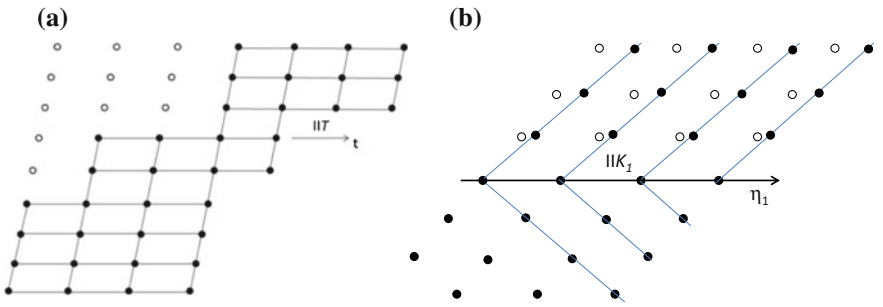

Fig. 3.8 Illustration of the movement of lattice point during **a** slip along the direction t, **b** deformation twinning in the plane K_1 along the direction η_1

slip mechanisms. Furthermore, most studies have been performed on fcc metals, which have been long believed incapable of twinning. While the first suggestion that twinning can be a deformation mechanism in fcc metals was made in the beginning of the twentieth century [74, 91], the occurrence of twinning in fcc cubic metals was first characterized by Blewitt et al. [14] in copper at low temperature (4.2 K). These authors also observed that twinning in copper can also be active at a higher temperature (77.3 K), but only when the crystal is loaded in tension along an orientation close to the $[111]$ direction. Blewitt et al. [14] found that the primary twinning plane is $(11\bar{1})$ and the associated shearing direction is the $[112]$ direction, while the conjugate twinning plane is $(1\bar{1}1)$ with shearing along the $[121]$ direction. Based on crystallographic and geometric considerations, Bevis and Crocker [12] have determined the possible twin modes for cubic single crystals and their associated shear strain s. Assuming that the primary twinning mode is the mode associated with the smallest possible homogenous shear, it was shown that the primary twin mode should be $\{111\}\langle 11\bar{2}\rangle$ for a fcc single crystal, as observed by Blewitt et al. [14], and $\{112\}\langle 1\bar{1}\bar{1}\rangle$ for a bcc single crystal. It is worth noting that for bcc metals, a large diversity of twin systems apart from the well-known $\{112\}\langle 1\bar{1}\bar{1}\rangle$ mode have been observed. For an in-depth discussion on twinning in fcc metals, the reader is referred to Venables [107], while for an overview of the experimental evidence on twinning in bcc metals, see Richman [86] and Reed-Hill et al. [82] monograph.

While in fcc and bcc metals, twinning occurs as a secondary deformation mechanism due to the large number of slip planes available in the respective lattice structure, this is not generally the case with hcp metals where the number of potential slip systems is not so numerous (see Table 3.2). Specifically, in hcp metals, deformation twinning is often competitive with slip. It follows that understanding which twin modes operate and the conditions to be met for the onset of twinning are of great importance for hcp metals.

Mathewson and Phillips [75] reported that deformation twinning occurs in Be, Mg, Zn, and Cd in the $\{10\bar{1}2\}$ planes. Nowadays, it is well established that twinning on the plane $\{10\bar{1}2\}\langle 10\bar{1}\bar{1}\rangle$ is the most common mode for hcp crystals and that almost all hcp materials twin on this plane.

As seen previously in the case of slip, the possible slip systems vary from material to material. This is also the case for twinning. The most commonly observed twins systems in hcp metals are summarized in Table 3.3. Following Yoo [109], in Fig. 3.9 is plotted the variation of the twinning shear with respect to the ratio c/a for the four twinning systems listed in Table 3.3. It can be seen that the

Table 3.3 Twins systems in hcp structure

Twin systems	K_1	η_1	K_2	η_1
1	$\{10\bar{1}2\}$	$\langle 10\bar{1}\bar{1}\rangle$	$\{10\bar{1}\bar{2}\}$	$\langle 10\bar{1}1\rangle$
2	$\{10\bar{1}1\}$	$\langle 10\bar{1}\bar{2}\rangle$	$\{10\bar{1}\bar{3}\}$	$\langle 30\bar{3}2\rangle$
3	$\{11\bar{2}2\}$	$\langle 11\bar{2}\bar{3}\rangle$	$\{11\bar{2}\bar{4}\}$	$\langle 22\bar{4}\bar{3}\rangle$
4	$\{11\bar{2}1\}$	$\langle\bar{1}\bar{1}26\rangle$	$\{0002\}$	$\langle 1120\rangle$

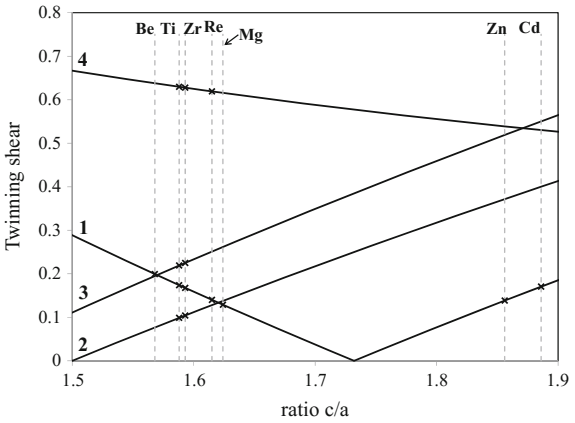

Fig. 3.9 Variation of the twinning shear versus the *c/a* ratio for the four twinning systems listed in Table 3.3; symbols indicate the twin systems potentially active for a given hcp material

twinning system $\{10\bar{1}2\}\langle 10\bar{1}\bar{1}\rangle$ is active for all the listed metals. However, depending on the slope of the twinning shear curve, the twin is either called "compression" twin for a positive slope or "tension" twin for a negative slope. In other words, a "compression" twin will allow a compression deformation along the **c**-axis, while a "tension" twin will produce a tensile deformation along the **c**-axis. As an example, for hcp metal such Be, Ti, Zr, Re, and Mg, the twin system $\{10\bar{1}2\}\langle 10\bar{1}\bar{1}\rangle$ is a "tension" twin, while for Zn and Cd, $\{10\bar{1}2\}\langle 10\bar{1}\bar{1}\rangle$ is a "compression" twin. As pointed out by Yoo [109], the most ductile hcp metals (e.g., Ti, Zr) twin profusely by both tension–compression twin modes, while the hcp metals with low ductility (e.g., Mg, Zn, Cd) twin only by the most common type, the $\{10\bar{1}2\}\langle 10\bar{1}\bar{1}\rangle$ system.

3.3 Yield Criteria for Single Crystals

In order to accurately model the plastic behavior of single crystals, it is essential to account for their intrinsic symmetries and develop models applicable to general three-dimensional loadings. For fcc single crystals, the primary deformation mechanism for plastic deformation is crystallographic slip on the $\{111\}$ crystallographic planes along the $[100]$ crystallographic directions. As shown earlier, according to the Schmid law, slip initiates when the resolved shear stress on any given slip system reaches the critical resolved shear stress for that particular system. For uniaxial tensile loading, the expression of the critical resolved shear stress was given in Eq. (3.3).

In the following, we first present the expression of Schmid law in terms of the Cauchy stress for general loadings. Next, the so-called generalized Schmid criterion proposed by Arminjon [3] (see also [30]) is introduced. This criterion is a differentiable and convex approximation of the Schmid law with a nth order homogenous

function of stresses. The effect of the loading orientation on yielding in uniaxial tension predicted by this criterion is discussed in detail, with emphasis on assessing its predictive capabilities for various single crystals. Lastly, a very recent yield criterion for fcc single crystals applicable to any loading that was recently developed by Cazacu et al. [26] is presented. We conclude with comparisons between the predictions of the generalized Schmid criterion and this new yield criterion.

3.3.1 Generalized Schmid Yield Criterion

As shown in the previous section, according to Schmid's law, a critical value of the resolved shear stress is required for the initiation of slip. For uniaxial loadings, the expression for the resolved shear stress τ^s acting along the slip direction of unit vector $\boldsymbol{b}^s$ in a plane of unit normal $\boldsymbol{n}^s$ is given by Eq. (3.3) (see also Fig. 3.6), and the slip system (s) defined by $\boldsymbol{b}^s$ and $\boldsymbol{n}^s$ is active (operational) if and only if $\tau^s = \tau_c^s$, with τ_c^s being the critical resolved shear stress for the respective slip system (s). For multiaxial loadings, the resolved shear stress for the slip system (s) is:

$$\tau^s = |\mathbf{M}^s : \boldsymbol{\sigma}| = |\mathbf{M}^s : \mathbf{s}|, \tag{3.4}$$

where $\boldsymbol{M}^s$ denotes the Schmid tensor of the slip system (s), defined as:

$$\mathbf{M}^s = (\mathbf{b}^s \otimes \mathbf{n}^s + \mathbf{n}^s \otimes \mathbf{b}^s)/2, \tag{3.5}$$

In Eq. (3.4), $\mathbf{s}$ denotes the deviator of the applied Cauchy stress tensor $\boldsymbol{\sigma}$ (i.e. $\mathbf{s} = \boldsymbol{\sigma} - \frac{1}{3}\mathrm{tr}(\boldsymbol{\sigma})\mathbf{I}$) while ":" stands for the scalar product between two second-order tensors, and "$\otimes$" for the dyadic product between any two vectors (see also Chap. 1 for the definitions of these products and the trace operator "tr" relative to any given Cartesian coordinate system).

If the critical resolved shear stress is considered to be the same for all potential slip systems (i.e., $\tau_c^s = \tau_c$ for any system (s)), then for multiaxial loadings the Schmid law states that of all potentially active slip systems, slip begins on the slip system (s) for which

$$\tau^s = |\mathbf{M}^s : \boldsymbol{\sigma}| = |\mathbf{M}^s : \mathbf{s}| = \tau_c, \tag{3.6}$$

The generalized Schmid criterion is a differentiable and convex approximation of the Schmid law (see Eq. 3.6) with an nth order homogenous function of stresses (see [3]). The generalized Schmid yield criterion is expressed as:

$$\left(\sum_s \left| \frac{\mathbf{s} : \mathbf{M}^s}{\tau_c} \right|^n \right)^{1/n} = 1, \tag{3.7}$$

the exponent n being an integer such that $1 < n < \infty$, and τ_c being the critical resolved shear stress, which is considered to be the same for all potentially active slip systems.

As already mentioned, at room temperature for fcc single crystals, there are twelve slip systems corresponding to the $\{111\}$ planes and the $\langle 110 \rangle$ directions (see Table 3.2). Note that the yield function given by Eq. (3.7) is arbitrarily close to the inner envelope of the Schmid hyperplanes, $|\mathbf{s} : \mathbf{M}^s| = \tau_c$. In the $Oxyz$ coordinate system with axes along the $\langle 100 \rangle$ directions of the crystal, the generalized Schmid criterion is expressed as:

$$\begin{aligned}
&\left|\sigma_{yy} - \sigma_{zz} + \sigma_{xy} - \sigma_{xz}\right|^n + \left|\sigma_{zz} - \sigma_{xx} - \sigma_{xy} + \sigma_{yz}\right|^n + \left|\sigma_{xx} - \sigma_{yy} + \sigma_{xz} - \sigma_{yz}\right|^n \\
&\quad + \left|\sigma_{yy} - \sigma_{zz} + \sigma_{xy} + \sigma_{xz}\right|^n + \left|\sigma_{zz} - \sigma_{xx} - \sigma_{xy} - \sigma_{yz}\right|^n + \left|\sigma_{xx} - \sigma_{yy} - \sigma_{xz} + \sigma_{yz}\right|^n \\
&\quad + \left|\sigma_{yy} - \sigma_{zz} - \sigma_{xy} + \sigma_{xz}\right|^n + \left|\sigma_{zz} - \sigma_{xx} + \sigma_{xy} + \sigma_{yz}\right|^n + \left|\sigma_{xx} - \sigma_{yy} - \sigma_{xz} - \sigma_{yz}\right|^n \\
&\quad + \left|\sigma_{yy} - \sigma_{zz} - \sigma_{xy} - \sigma_{xz}\right|^n + \left|\sigma_{zz} - \sigma_{xx} + \sigma_{xy} - \sigma_{yz}\right|^n + \left|\sigma_{xx} - \sigma_{yy} + \sigma_{xz} + \sigma_{yz}\right|^n \\
&= 4\tau_c^n.
\end{aligned} \tag{3.8}$$

According to this yield criterion, the yield stresses in uniaxial tension along the [110], [111], [112], and [210] directions, respectively, are given by:

$$\begin{aligned}
\frac{Y_{110}}{Y_{100}} &= 2^{1/n}; \\
\frac{Y_{111}}{Y_{100}} &= \frac{3}{2}\left(\frac{4}{3}\right)^{1/n}; \\
\frac{Y_{112}}{Y_{100}} &= \frac{4^{1/n}}{\left(1 + 2(2/3)^n + (1/3)^n\right)^{1/n}}; \\
\frac{Y_{210}}{Y_{100}} &= \frac{4^{1/n}}{\left[3\left(\frac{3}{5}\right)^n + \left(\frac{6}{5}\right)^n + \left(\frac{1}{5}\right)^n + \left(\frac{2}{5}\right)^n\right]^{1/n}}
\end{aligned} \tag{3.9}$$

It is worth noting that according to the generalized Schmid criterion, the ratios between the uniaxial tensile yield stresses along different orientations are completely determined by the value of the coefficient n. Furthermore, for any integer $n > 1$:

$$1 \le \frac{Y_{110}}{Y_{100}} \le \sqrt{2} \text{ and } Y_{110} < Y_{111}. \tag{3.10}$$

Therefore, irrespective of the value of the exponent n, the generalized Schmid criterion (Eq. 3.7) predicts that the yield stress in the [111] direction should be larger than the yield stress in the [110] direction, which in turn should be greater than the yield stress along the [100] direction:

$$Y_{111} > Y_{110} \geq Y_{100}. \tag{3.11}$$

Moreover, for very large values of the exponent n in Eq. (3.7), i.e., $n \to \infty$, the yield stresses in the [110] and [112] directions should be the same and equal to the yield stress in the [100] directions, while the ratio between the yield stresses in the [111] direction should be exactly (3/2) larger than in the [100] direction, i.e.,

$$Y_{111} = \frac{3}{2} Y_{100}. \tag{3.12}$$

3.3.2 *Cazacu et al. [26] Yield Criterion*

The regularized form of the Schmid law involves a single parameter, n. As discussed in the previous section, irrespective of the value of this parameter, this yield criterion (see Eq. 3.7) predicts that the yield stress in uniaxial tension along the direction [100] is lower than or equal to the one along the [110] direction and that the highest yield stress is always along the direction [111]. Therefore, this yield criterion cannot capture the plastic deformation of a Cu single crystal, which exhibits the lowest yield stress in uniaxial tension along [110] (see [98]). Another example where the limitations of the generalized Schmid yield criterion are highlighted is that of Ni-based superalloys. For example, Lall et al. [64] showed that for Ni_3 (Al, Nb) single crystals at room temperature, the yield stress in uniaxial tension along the direction [110] is greater than the yield stress in uniaxial tension along the direction [111], which in turn is greater than the yield stress in uniaxial tension along the direction [100]. Additionally, while for large values of the parameter n, the generalized Schmid yield criterion (Eq. 3.8) is able to capture the yielding response of certain materials such as Al; it is represented by a function only of class C^0, the corresponding yield surface having singularities.

The main idea put forward in Cazacu and Barlat [23] and Cazacu et al. [26] is that in order to describe accurately the effect of the crystal structure on plastic deformation for general loading conditions, the analytical function, say $\Phi(\boldsymbol{\sigma})$, that describes the onset of yielding should be form-invariant with respect to any proper orthogonal transformation $\mathbf{Q}$ belonging to the symmetry group G^+ (see also Sect. 3.1 for the definition of G^+), i.e.,

$$\Phi\left(\mathbf{Q}\boldsymbol{\sigma}\mathbf{Q}^{\mathrm{T}}\right) = \Phi(\boldsymbol{\sigma}). \tag{3.13}$$

To obtain the general form of the yield function $\Phi(\boldsymbol{\sigma})$ that contains the minimum number of coefficients such as to automatically satisfy these symmetry requirements, these authors developed generalizations of the classic isotropic stress invariants such as to account for cubic symmetries. In the following, we will present

the derivation of the expressions of these generalized cubic invariants and the single crystal yield criterion of Cazacu et al. [26] that is expressed in terms of these invariants.

The main idea that enabled the derivation of the generalized cubic stress invariants is that the cubic systems constitute a subset of the rhombic system (see Table 3.1). Relative to the *Oxyz* coordinate system associated with the symmetry axes of the rhombic system, the set of irreducible invariants of the stress tensor is:

$$\sigma_{xx}, \sigma_{yy}, \sigma_{zz}, \sigma_{xy}^2, \sigma_{yz}^2, \sigma_{xz}^2, \sigma_{xy}\sigma_{xz}\sigma_{yz}. \tag{3.14}$$

Thus, any rhombic (or) orthotropic polynomial $P(\boldsymbol{\sigma})$ must be of the form:

$$P = P\left(\sigma_{xx}, \sigma_{yy}, \sigma_{zz}, \sigma_{xy}^2, \sigma_{yz}^2, \sigma_{xz}^2, \sigma_{xy}\sigma_{xz}\sigma_{yz}\right) \tag{3.15}$$

Let $J_2 = \mathrm{tr}\mathbf{s}^2/2$, and $J_3 = \mathrm{tr}\mathbf{s}^3/3$ denote the second and third-invariant of $\boldsymbol{s}$, respectively. Using Smith and Rivlin's representation theorem, Cazacu and Barlat [24] derived orthotropic generalizations of the isotropic invariants J_2, and J_3, respectively. These generalized invariants, denoted J_2^o and J_3^o, were required to be: homogeneous polynomials of degree two and three in $\boldsymbol{\sigma}$, respectively, pressure-insensitive (i.e., $P(\boldsymbol{\sigma}+p\mathbf{I}) = P(\boldsymbol{\sigma})$ for any $\boldsymbol{\sigma}$ and scalar p), and orthotropic. Therefore, relative to the Cartesian coordinate system *Oxyz* associated with the axes of symmetry, the orthotropic generalization of J_2 must be of the form:

$$J_2^o = \frac{a_1}{6}\left(\sigma_{xx}-\sigma_{yy}\right)^2 + \frac{a_2}{6}\left(\sigma_{yy}-\sigma_{zz}\right)^2 + \frac{a_3}{6}\left(\sigma_{xx}-\sigma_{zz}\right)^2 + a_4\sigma_{xy}^2 + a_5\sigma_{xz}^2 + a_6\sigma_{yz}^2 \tag{3.16}$$

while the orthotropic generalization of J_3 must be of the form:

$$\begin{aligned} J_3^o = {} & \frac{1}{27}(b_1+b_2)\sigma_{xx}^3 + \frac{1}{27}(b_3+b_4)\sigma_{yy}^3 + \frac{1}{27}\left[2(b_1+b_4)-b_2-b_3\right]\sigma_{zz}^3 \\ & - \frac{1}{9}\left(b_1\sigma_{yy}+b_2\sigma_{zz}\right)\sigma_{xx}^2 - \frac{1}{9}(b_3\sigma_{zz}+b_4\sigma_{xx})\sigma_{yy}^2 \\ & - \frac{1}{9}\left[(b_1-b_2+b_4)\sigma_{xx}+(b_1-b_3+b_4)\sigma_{yy}\right]\sigma_{zz}^2 \\ & + \frac{2}{9}(b_1+b_4)\sigma_{xx}\sigma_{zz}\sigma_{yy} - \frac{\sigma_{xz}^2}{3}\left[2b_9\sigma_{yy}-b_8\sigma_{zz}-(2b_9-b_8)\sigma_{xx}\right] \\ & - \frac{\sigma_{xy}^2}{3}\left[2b_{10}\sigma_{zz}-b_5\sigma_{yy}-(2b_{10}-b_5)\sigma_{xx}\right] - \frac{\sigma_{yz}^2}{3}\left[(b_6+b_7)\sigma_{xx}-b_6\sigma_{yy}-b_7\sigma_{zz}\right] \\ & + 2b_{11}\sigma_{xy}\sigma_{xz}\sigma_{yz} \end{aligned} \tag{3.17}$$

In the above expressions, a_i, $i = 1\ldots6$ and b_k, $k = 1\ldots11$ are constants. If each of these constants $a_i = 1$, J_2^o reduces to J_2; and if each of the constants $b_k = 1$, J_3^o reduces to J_3. Any function $\Phi\left(J_2^o, J_3^o\right)$ is pressure-insensitive and automatically satisfies the form-invariance requirements with respect to any transformation belonging to the symmetry group of any class of the rhombic system (see Table 3.1). For the mathematical proofs and details of the derivations of the above expressions for the orthotropic generalizations of the classic isotropic invariants, the reader is referred to Chap. 5.

Generalized invariants for cubic symmetries

For the crystals belonging to the five cubic crystal classes, the axes of symmetry parallel to the $\langle 100\rangle$ directions have threefold symmetry (see Table 3.1 for the proper orthogonal generators characterizing the respective group of symmetry of each of the five cubic crystal classes; in this table $\mathbf{f} = \left(1/\sqrt{3}\right)\left(\mathbf{e}_x + \mathbf{e}_y + \mathbf{e}_z\right) = [111]$). Note that for each of the tetratoidal and diploidal classes, $R^{\pi}_{\mathbf{e}_x}$ and $R^{\pi}_{\mathbf{e}_y}$ are generators. It follows that for a polynomial $P(\boldsymbol{\sigma})$ to fulfill the symmetries associated with these crystal classes, it should be of the form given by Eq. (3.15) and in addition be invariant to circular permutations, i.e.,

$$\begin{aligned} &P\left(\sigma_{xx}, \sigma_{yy}, \sigma_{zz}, \sigma_{xy}^2, \sigma_{yz}^2, \sigma_{xz}^2, \sigma_{xy}\sigma_{xz}\sigma_{yz}\right) \\ &= P\left(\sigma_{yy}, \sigma_{zz}, \sigma_{xx}, \sigma_{yz}^2, \sigma_{xz}^2, \sigma_{xy}^2, \sigma_{xy}\sigma_{yz}\sigma_{zx}\right) \\ &= P\left(\sigma_{zz}, \sigma_{xx}, \sigma_{yy}, \sigma_{xz}^2, \sigma_{xy}^2, \sigma_{yz}^2, \sigma_{xy}\sigma_{yz}\sigma_{zx}\right) \end{aligned} \tag{3.18}$$

Proposition 3.1 *For all crystal classes of the cubic system, the generalized second-invariant of the stress deviator should involve only two independent parameters, and its expression with respect to the Cartesian system associated with the crystal axes should be of the form:*

$$J_2^c = \frac{m_1}{6}\left[\left(\sigma_{xx} - \sigma_{yy}\right)^2 + \left(\sigma_{xx} - \sigma_{zz}\right)^2 + \left(\sigma_{zz} - \sigma_{yy}\right)^2\right] + m_2\left(\sigma_{xy}^2 + \sigma_{xz}^2 + \sigma_{yz}^2\right) \tag{3.19}$$

where m_1 and m_2 are material constants.

Proof The extension of the isotropic second-invariant of the stress deviator J_2 to cubic symmetries should be a polynomial of second-order, homogeneous in stresses, pressure-insensitive, and should satisfy the symmetries associated to the respective crystal classes. It follows that for the tetratoidal and diploidal classes of the cubic system, the generalized J_2 should be of the form given by Eq. (3.16), and in addition satisfy the constraints given by Eq. (3.18), which lead to:

$$a_1 = a_2 = a_3 \text{ and } a_4 = a_5 = a_6. \tag{3.20}$$

It means that J_2^c, the generalized second-invariant of the stress deviator depends on only two independent constants, say m_1 and m_2, and in the reference frame associated with the $\langle 100 \rangle$ axes, it has the expression given by Eq. (3.19). The proof that for the remaining three classes of the cubic system, the generalized second-invariant of the stress deviator should also be of the form given by Eq. (3.19) is straightforward. Indeed, for the hextetrahedral, gyroidal, and hexoctahedral classes, the generators of the symmetry group are the rotations by $\pi/2$ with respect to each of the crystal axes (see Table 3.1) and J_2^c given by Eq. (3.19) is invariant under these transformations.

Note also that for $m_1 = m_2 = 1$, i.e., isotropic conditions, the generalized second-invariant J_2^c given by Eq. (3.19) reduces to J_2.

Proposition 3.2 *For the tetratoidal and diploidal crystal classes of the cubic system, the generalized third-invariant of the stress deviator should involve five independent parameters, and its expression with respect to the Cartesian system associated with the crystal axes should be of the form:*

$$\begin{aligned} J_3^C = {} & \frac{2}{27} n_1 \left(\sigma_{xx}^3 + \sigma_{yy}^3 + \sigma_{zz}^3 \right) + \frac{4}{9} n_1 \sigma_{xx} \sigma_{yy} \sigma_{zz} \\ & + \frac{1}{9} (3n_2 - 4n_1) \left(\sigma_{xx} \sigma_{zz}^2 + \sigma_{yy} \sigma_{xx}^2 + \sigma_{zz} \sigma_{yy}^2 \right) \\ & + 2n_4 \sigma_{xy} \sigma_{xz} \sigma_{yz} \\ & + \frac{1}{9} (2n_1 - 3n_2) \left(\sigma_{xx} \sigma_{yy}^2 + \sigma_{yy} \sigma_{zz}^2 + \sigma_{zz} \sigma_{xx}^2 \right) \\ & + \frac{\sigma_{xy}^2}{3} \left[-2n_3 \sigma_{zz} + (4n_3 - 3n_5) \sigma_{xx} + (3n_5 - 2n_3) \sigma_{yy} \right] \\ & + \frac{\sigma_{xz}^2}{3} \left[-2n_3 \sigma_{yy} + (4n_3 - 3n_5) \sigma_{zz} + (3n_5 - 2n_3) \sigma_{xx} \right] \\ & + \frac{\sigma_{yz}^2}{3} \left[-2n_3 \sigma_{xx} + (4n_3 - 3n_5) \sigma_{yy} + (3n_5 - 2n_3) \sigma_{zz} \right], \end{aligned} \tag{3.21}$$

while for the hextetrahedral, gyroidal, and hexoctahedral classes, the generalized third-invariant of the stress deviator should involve three independent parameters, its expression being:

$$\begin{aligned} J_3^c = {} & \frac{n_1}{27} (2\sigma_{xx} - \sigma_{yy} - \sigma_{zz}) (2\sigma_{yy} - \sigma_{zz} - \sigma_{xx}) (2\sigma_{zz} - \sigma_{xx} - \sigma_{yy}) + 2n_4 \sigma_{xy} \sigma_{xz} \sigma_{yz} \\ & - \frac{n_3}{3} \left[\sigma_{yz}^2 (2\sigma_{xx} - \sigma_{yy} - \sigma_{zz}) + \sigma_{xz}^2 (2\sigma_{yy} - \sigma_{zz} - \sigma_{xx}) + \sigma_{xy}^2 (2\sigma_{zz} - \sigma_{xx} - \sigma_{yy}) \right]. \end{aligned} \tag{3.22}$$

Proof The generalization of the third-invariant of the stress deviator should be a polynomial of third-order, homogeneous in stresses, pressure-insensitive, and should satisfy the symmetries associated to the respective crystal classes. It follows that for the tetratoidal and diploidal crystal classes of the cubic system, the generalization of the third-invariant of the stress deviator that satisfies the symmetries associated to these crystal classes should be of the form given by Eq. (3.17), and subject to the additional constraints given by Eq. (3.18), which result in:

$$\begin{aligned} &b_1 = b_3,\ b_2 = b_4,\ b_5 = b_7, \\ &b_6 = b_8,\ b_9 = b_{10} = \frac{b_7 + b_6}{2}. \end{aligned} \tag{3.23}$$

Therefore, the generalized third-invariant of the stress deviator J_3^C should involve only five independent parameters, b_1, b_2, b_5, b_6, b_{11}. Alternatively, the following five coefficients n_k, k = 1…5, which are linearly independent combinations of b_1, b_2, b_5, b_6, b_{11} can be considered,

$$\begin{aligned} &n_1 = (b_1 + b_2)/2,\ n_2 = (b_1 + 2b_2)/3,\ n_3 = (b_5 + b_6)/2 \\ &n_4 = b_{11},\ n_5 = (2b_5 + b_6)/3, \end{aligned} \tag{3.24}$$

resulting in the expression of J_3^C given by Eq. (3.21). It should be noted that if each of the coefficients n_k is set to unity (i.e., isotropy is imposed), J_3^C reduces to J_3.

Next, form-invariance of a polynomial with respect to each of the hextetrahedral, gyroidal, and hexoctahedral classes imposes that the generalized third-invariant of the stress deviator should be of the form given by Eq. (3.17), and fulfill the additional restrictions:

$$\begin{aligned} J_3^C\left(\sigma_{xx}, \sigma_{yy}, \sigma_{zz}, \sigma_{xy}^2, \sigma_{yz}^2, \sigma_{xz}^2, \sigma_{xy}\sigma_{xz}\sigma_{yz}\right) &= J_3^C\left(\sigma_{xx}, \sigma_{zz}, \sigma_{yy}, \sigma_{xz}^2, \sigma_{yz}^2, \sigma_{xy}^2, \sigma_{xy}\sigma_{xz}\sigma_{yz}\right) \\ &= J_3^C\left(\sigma_{yy}, \sigma_{xx}, \sigma_{zz}, \sigma_{xy}^2, \sigma_{xz}^2, \sigma_{yz}^2, \sigma_{xy}\sigma_{xz}\sigma_{yz}\right) \\ &= J_3^C\left(\sigma_{zz}, \sigma_{yy}, \sigma_{xx}, \sigma_{yz}^2, \sigma_{xy}^2, \sigma_{xz}^2, \sigma_{xy}\sigma_{xz}\sigma_{yz}\right) \\ &= J_3^C\left(\sigma_{yy}, \sigma_{zz}, \sigma_{xx}, \sigma_{yz}^2, \sigma_{xz}^2, \sigma_{xy}^2, \sigma_{xy}\sigma_{xz}\sigma_{yz}\right) \\ &= J_3^C\left(\sigma_{zz}, \sigma_{xx}, \sigma_{yy}, \sigma_{xz}^2, \sigma_{xy}^2, \sigma_{yz}^2, \sigma_{xy}\sigma_{xz}\sigma_{yz}\right) \end{aligned} \tag{3.25}$$

which result in:

$$n_1 = n_2 \text{ and } n_3 = n_5. \tag{3.26}$$

Thus, for these classes of the cubic systems, the expression of the generalized third-invariant of the stress deviator, denoted hereafter J_3^c, involves only three independent coefficients n_1, n_3, and n_4, and its expression is given by Eq. (3.22). It should

be noted that if each of these coefficients is set to unity (i.e., isotropy is imposed), J_3^c reduces to J_3. Using these generalized cubic invariants, one can construct yield criteria that are pressure-insensitive and satisfy the invariance requirements associated with the symmetries of the crystal classes of the cubic system.

It is worth noting that most of the face-centered cubic metals (e.g., copper; Al) belong to the hextetrahedral, gyroidal, and hexoctahedral cubic classes (e.g., see Dana and Ford [29] textbook on mineralogy). Any function $\Phi\left(J_2^c, J_3^c\right)$ with J_2^c and J_3^c given by Eqs. (3.19) and (3.22), respectively, is independent of the hydrostatic pressure and automatically respects the intrinsic symmetries of any crystal belonging to these classes. Moreover, for fcc crystals, it is generally assumed that the mechanical response in tension–compression is the same; therefore, the yield function should be an even function of stresses.

The following yield criterion was proposed in Cazacu et al. [26]:

$$\left(J_2^c\right)^3 - c\left(J_3^c\right)^2 = k^6, \tag{3.27}$$

with c being a material constant that controls the relative importance of the generalized invariants on yielding of the single crystal and k being the yield limit in simple shear in any of the crystallographic planes $\{100\}$. Using Eqs. (3.19), (3.22) and (3.26), respectively, it can be easily seen that in the coordinate system $Oxyz$ associated with the $\langle 100\rangle$ crystal axes, the yield criterion given by Eq. (3.27) is expressed as:

$$\begin{aligned}&\left\{\frac{m_1}{6}\left[\left(\sigma_{xx}-\sigma_{yy}\right)^2+\left(\sigma_{xx}-\sigma_{zz}\right)^2+\left(\sigma_{zz}-\sigma_{yy}\right)^2\right]+m_2\left(\sigma_{xy}^2+\sigma_{xz}^2+\sigma_{yz}^2\right)\right\}^3\\&-\frac{c}{27}\left\{\begin{array}{l}n_1\left(2\sigma_{xx}-\sigma_{yy}-\sigma_{zz}\right)\left(2\sigma_{yy}-\sigma_{zz}-\sigma_{xx}\right)\left(2\sigma_{zz}-\sigma_{xx}-\sigma_{yy}\right)+2n_4\sigma_{xy}\sigma_{xz}\sigma_{yz}\\-9n_3\left[\sigma_{yz}^2\left(2\sigma_{xx}-\sigma_{yy}-\sigma_{zz}\right)+\sigma_{xz}^2\left(2\sigma_{yy}-\sigma_{zz}-\sigma_{xx}\right)+\sigma_{xy}^2\left(2\sigma_{zz}-\sigma_{xx}-\sigma_{yy}\right)\right]\end{array}\right\}^2=k^6.\end{aligned} \tag{3.28}$$

Alternatively, using Eq. (3.28), one can obtain the expression of the yield criterion in terms of the components of the stress deviator $\boldsymbol{s}$ as:

$$\begin{aligned}&\left[\frac{m_1}{2}\left(s_{xx}^2+s_{yy}^2+s_{zz}^2\right)+m_2\left(s_{xy}^2+s_{xz}^2+s_{yz}^2\right)\right]^3\\&-c\left[n_1 s_{xx}s_{yy}s_{zz}-n_3\left(s_{zz}s_{xy}^2+s_{xx}s_{yz}^2+s_{yy}s_{xz}^2\right)+2n_4 s_{xy}s_{xz}s_{yz}\right]^2=k^6.\end{aligned} \tag{3.29}$$

In summary, Cazacu et al. [26] yield criterion for cubic single crystals involves five anisotropy coefficients, m_1, m_2, n_1, n_3, n_4, and the constant c. All these parameters can be determined from uniaxial tension tests along several crystallographic directions. In the following subsection, an identification procedure based on such data is presented. Moreover, the capabilities of this criterion to account for the effect of the loading orientation on yielding in several crystallographic planes of interest are also examined.

3.3.2.1 Effect of Loading Orientation on Yielding

The most widely used method to visualize and represent the deformation of fcc crystals is by projections on a sphere (see [33, 94]). The most convenient of these is the stereographic projection, which is the projection from a point on the surface of the sphere on the plane through the center parallel to the tangent plane at the point of projection, the northern hemisphere being viewed from the South pole. The stereographic projection of a cubic crystal is shown in Fig. 3.10; the square, circle, and triangular symbols represent the points at which the fourfold, threefold, and twofold symmetry axes of the crystal intersect the surface of the unit sphere. Also as an example, the stereographic projection of an arbitrary direction $\mathbf{d} = \mathbf{OP}$, whose orientation with respect to the crystal axes is given by (θ, φ), on the equatorial plane is shown in Fig. 3.10.

Due to the symmetries of the fcc single crystal, to quantify the influence of the loading orientation on yielding under uniaxial tension, it is sufficient to perform and analyze tests along directions contained in the basic stereographic triangle with corners along [001], [101], and [111] (see also Fig. 3.10). Note also that for a direction $\mathbf{d}$ to be in this stereographic triangle, its latitude angle φ and its longitude angle θ should be in the following range: $0 \leq \varphi \leq \pi/4$ and $0 \leq \theta \leq \arctan(1/\cos\varphi)$, respectively, (see Fig. 3.11).

Let us denote by Y_d the yield limit in uniaxial tension along any given direction $\mathbf{d}$. In the $Oxyz$ system with axes along the $\langle 100 \rangle$ directions of the crystal (e.g., see Fig. 3.11):

$$\mathbf{d} = \sin\theta\cos\varphi\mathbf{e_x} + \sin\theta\sin\varphi\mathbf{e_y} + \cos\theta\mathbf{e_z} \tag{3.30}$$

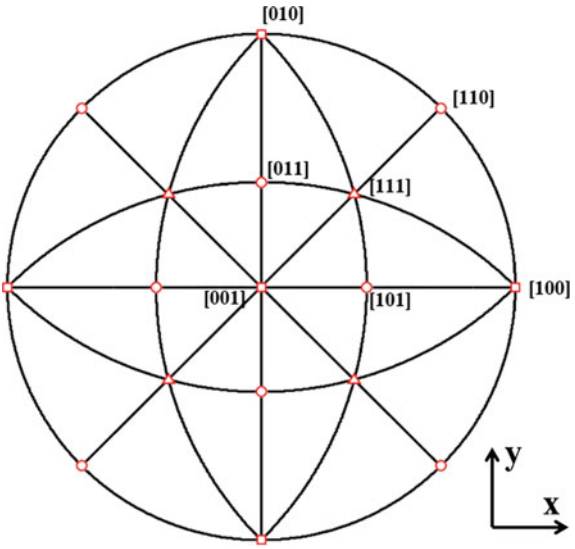

Fig. 3.10 Stereographic projection of a cubic crystal also showing the basic stereographic triangle of corners [001], [101], and [111]. The square, circle, and triangular symbols represent the points at which the fourfold, threefold, and twofold symmetry axes of the crystal intersect the surface of the unit sphere

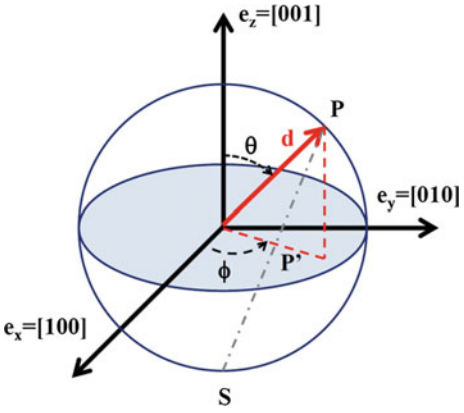

Fig. 3.11 Stereographic projection of a direction **d** of latitude $0 \leq \theta \leq \pi$ and longitude $0 \leq \varphi \leq 2\pi$; S denotes the South pole ($\theta = \pi$), the northern hemisphere being viewed from S; $(\mathbf{e_x}, \mathbf{e_y}, \mathbf{e_z})$ are the unit vectors of the crystal axes [100], [010], and [111], respectively

Under uniaxial tension along the direction **d**, the applied stress tensor is $\boldsymbol{\sigma} = Y_d(\mathbf{d} \otimes \mathbf{d})$, and it is expressed in the *Oxyz* coordinate system as:

$$\boldsymbol{\sigma} = Y_d \begin{bmatrix} \sin^2\theta\cos^2\varphi & \sin^2\theta\cos\varphi\sin\varphi & \cos\theta\sin\theta\cos\varphi \\ & \sin^2\theta\sin^2\varphi & \cos\theta\sin\theta\sin\varphi \\ & & \cos^2\theta \end{bmatrix}_{(\mathbf{e_x},\mathbf{e_y},\mathbf{e_z})} \tag{3.31}$$

Substituting Eq. (3.31) into the expression of Cazacu et al. [26] yield criterion given by Eq. (3.28), we obtain that Y_d, the yield stress in uniaxial tension along any direction **d**, is:

$$Y_d = k\left\{\begin{array}{l} \left[\frac{m_1}{3} + (m_2 - m_1)\sin^2\theta\left(\cos^2\theta + \sin^2\theta\sin^2\varphi\cos^2\varphi\right)\right]^3 \\ -c\left[\frac{2n_1}{27} + \frac{n_3 - n_1}{3}\sin^2\theta\left(\cos^2\theta + \sin^2\theta\sin^2\varphi\cos^2\varphi\right) + \right. \\ \left.(n_1 - 3n_3 + 2n_4)\sin^4\theta\cos^2\theta\sin^2\varphi\cos^2\varphi\right] \end{array}\right\}^{-1/6} \tag{3.32}$$

In particular, Y_{100} the yield stress in uniaxial tension along [100], which corresponds to $\varphi = 0,$ and $\theta = \pi/2$ (see also Fig. 3.10), is:

$$\frac{Y_{100}}{k} = \frac{3}{\left(27m_1^3 - 4cn_1^2\right)^{1/6}} \tag{3.33}$$

It can be easily verified that the yield criterion respects the symmetries of the cubic single crystal. Using Eq. (3.32) to calculate the yield limit under uniaxial tension along the [010], [001], $[\bar{1}00]$, $[0\bar{1}0]$, and $[00\bar{1}]$ directions, respectively, it can be seen that these limits coincide with the expression of the normalized Y_{100} given by Eq. (3.33). Moreover, according to the criterion (i.e., Eq. (3.32) with $\varphi = \pi/4, \theta = \pi/2$), Y_{110}, the yield stress along the [110] direction, is given by:

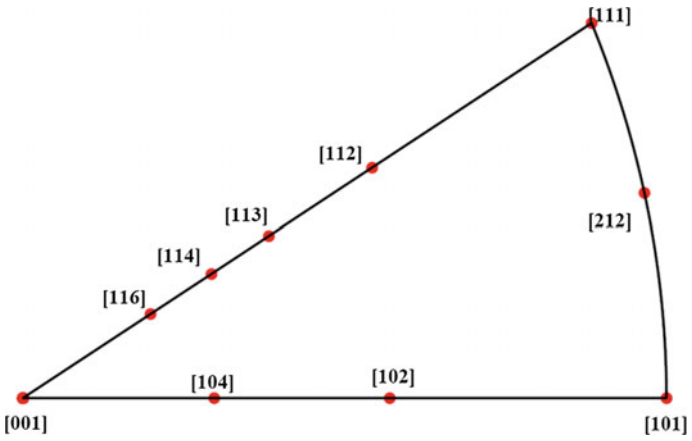

Fig. 3.12 Specific directions of a FCC single crystal along which tensile data are generally reported

$$\frac{Y_{110}}{k} = \frac{2}{\left[\left(\frac{m_1}{3} + m_2\right)^3 - \frac{4c}{9}\left(-\frac{1}{9}n_1 + n_3\right)^2\right]^{1/6}} \tag{3.34}$$

The fact that the yield criterion predicts the same value of the yield limit in uniaxial tension along any of the $\langle 110 \rangle$ orientations (see Eq. 3.32) is a direct consequence of the criterion being form-invariant to the crystal symmetries. In the same manner, one can determine the theoretical yield limit under uniaxial tension along any other orientations in the basic stereographic triangle, (see also Fig. 3.12 which shows some specific directions in this stereographic triangle). Moreover, it means that all the parameters involved in the Cazacu et al. [26] criterion have physical meaning and can be determined from simple uniaxial tension tests. The identification procedure is outlined in the following.

3.3.2.2 Procedure for Identification of the Yield Criterion

If we impose that the Cazacu et al. [26] single crystal yield surface (see Eq. 3.27) passes through the yield point in uniaxial tension along $\langle 100 \rangle$, the yield criterion is expressed as:

$$\frac{27^2}{27m_1^3 - 4cn_1^2}\left[(J_2^c)^3 - c(J_3^c)^2\right] = Y_{100}^6, \tag{3.35}$$

or,

$$\frac{27^2}{27m_1^3-4cn_1^2}\left\{\begin{array}{l}\left[m_1\left(s_{xx}^2+s_{yy}^2+s_{zz}^2\right)/2+m_2\left(s_{xy}^2+s_{xz}^2+s_{yz}^2\right)\right]^3\\ -c\left[n_1 s_{xx}s_{yy}s_{zz}-n_3\left(s_{zz}s_{xy}^2+s_{xx}s_{yz}^2+s_{yy}s_{xz}^2\right)+2n_4 s_{xy}s_{xz}s_{yz}\right]^2\end{array}\right\}$$
$$=Y_{100}^6, \tag{3.36}$$

with J_2^c and J_3^c given by Eqs. (3.19) and (3.22), respectively.

Given that the criterion is represented by a homogeneous function in stresses, the yield limit is the same if the coefficients m_1, m_2, n_1, n_3, n_4 are replaced by $\alpha m_1, \alpha m_2, \alpha n_1, \alpha n_3, \alpha n_4$, with α being an arbitrary positive constant. Therefore, without loss of generality one of the parameters, for example m_1, can be set equal to unity. Note also that the coefficient cn_1^2 has a clear physical significance being directly expressible in terms of the ratio between the yield limits in uniaxial tension along $\langle 100\rangle$, i.e., Y_{100} and the yield limit in simple shear, i.e., k (see Eq. 3.33). The remaining coefficients m_2, n_3, n_4, and c can be determined from the tensile yield stresses along four different loading orientations. Indeed, from Eq. (3.32), it follows that:

$$\begin{aligned}\frac{Y_{110}}{Y_{100}}&=\frac{2\left(27m_1^3-4cn_1^2\right)^{1/6}}{3\left[\left(\frac{m_1}{3}+m_2\right)^3-\frac{4c}{9}\left(-\frac{n_1}{9}+n_3\right)^2\right]^{1/6}}\\ \frac{Y_{111}}{Y_{100}}&=\left(\frac{27m_1^3-4cn_1^2}{27m_2^3-4cn_4^2}\right)^{1/6}\\ \frac{Y_{112}}{Y_{100}}&=\frac{\left(27m_1^3-4cn_1^2\right)^{1/6}}{3\left[\left(\frac{m_1}{12}+\frac{m_2}{4}\right)^3-\frac{c}{108^2}\left(n_1+4n_4+3n_3\right)^2\right]^{1/6}}\\ \frac{Y_{210}}{Y_{100}}&=\frac{\left(27m_1^3-4cn_1^2\right)^{1/6}}{3\left[\left(\frac{13}{75}m_1+\frac{4}{25}m_2\right)^3-c\left(\frac{14}{675}n_1+\frac{4}{75}n_3\right)^2\right]^{1/6}}\end{aligned} \tag{3.37}$$

Alternatively, if tensile data in other four different loading orientations are available, those data could be used to determine the coefficients m_2, n_3, n_4 and c.

3.3.3 *Application to the Description of Yielding in Cu and Al Single Crystals*

3.3.3.1 Cu Single Crystal

Experimental data reported in the literature show that for certain fcc single crystals such as Cu the initial yield limit along the [100] orientation is greater than the yield limit along the [110] orientation; moreover, the hardening rate is also greater along the [100] orientation (see [98]). From the experimental uniaxial tension stress–strain curves at −195 °C reported, one cannot infer the exact ratios between the tensile yield stresses along various crystal directions just their ordering, namely that: $Y_{111} > Y_{100} > Y_{112} > Y_{210} > Y_{110}$, with the yield limits along the [110] and [120] orientations being close. Assuming that $Y_{111}/Y_{100} = 1.5, Y_{110}/Y_{100} = 0.7$, $Y_{211}/Y_{100} = 0.8$, $Y_{210}/Y_{100} = 0.75$, and using the procedure for identification of the material parameters outlined in Sect. 3.3.2.2, the numerical values of the parameters of Cazacu et al. [26] criterion are: $m_2 = 1.92$, $n_1 = 2.16$, $n_3 = 0.37$, $n_4 = 0.98$, $c = 0.48$. In Fig. 3.13, the isocontours of the normalized yield stresses in uniaxial tension according to the yield criterion of Eq. 3.36 are represented in the stereographic triangle. Note that this criterion is able to describe the data of Takeuchi [98] and it predicts that the yield stress for the orientation [101] is smaller than that for the orientation [001].

It is also of interest to compare the anisotropy in uniaxial yield stresses in the crystallographic planes of normal $\langle 100 \rangle$ and $\langle 1\bar{1}0 \rangle$, respectively, predicted by the criterion and data of Takeuchi [98].

Let Y_θ be the yield stress in uniaxial tension along an axis at orientation θ to the crystallographic axis [001] (i.e., axis of equation $\mathbf{d}_1 = \sin\theta \mathbf{e_x} + \cos\theta \mathbf{e_z}$ in the plane $\varphi = 0$) (see also Fig. 3.11). According to the criterion:

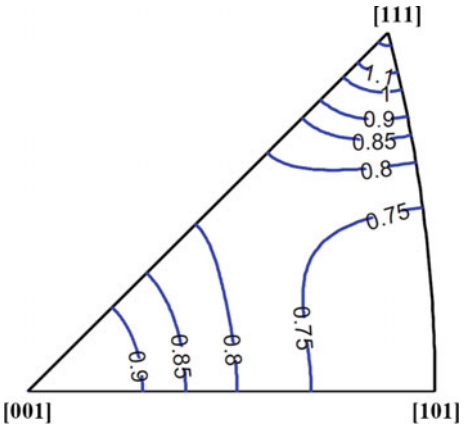

Fig. 3.13 Anisotropy in yield stress ratio in uniaxial tension for a Cu single crystal according to Cazacu et al. [26] criterion

$$\frac{Y_\theta}{Y_{100}} = \frac{\left(27 - 4cn_1^2\right)^{1/6}}{3\left[\left(\frac{1}{3} + (m_2 - 1)\sin^2\theta\cos^2\theta\right)^3 - c\left(\frac{2n_1}{27} + \frac{(n_3 - n_1)}{3}\sin^2\theta\cos^2\theta\right)^2\right]^{1/6}} \tag{3.38}$$

Note that the material symmetry is correctly described. Indeed, Eq. (3.38) is invariant by the transformation $\theta \to (\pi/2 - \theta)$, so the yield stress remains identical under rotations of $\pi/2$ about the **z**-axis (see Fig. 3.11 for the definition of the Cartesian system *Oxyz* associated with the $\langle 100\rangle$ crystal axes). Moreover, for $c > 0$, in the variation of the yield limit Y_θ with the loading axis θ, there should be only one peak at $\pi/4$. For the Cu single crystal, c = 0.48 and the theoretical predictions using Eq. 3.38 are in good agreement with data (see Fig. 3.14a).

On the other hand, if $Y_{\langle 110\rangle}(\theta)$ denotes the yield stress in uniaxial tension along an arbitrary axis $\mathbf{t} = \sin\theta/\sqrt{2}\mathbf{e_x} + \sin\theta/\sqrt{2}\mathbf{e_y} + \cos\theta\mathbf{e_z}$ in the plane of normal $\langle 1\bar{1}0\rangle$ (see also Fig. 3.11) according to the criterion (Eq. 3.32 with $\varphi = \pi/4$),

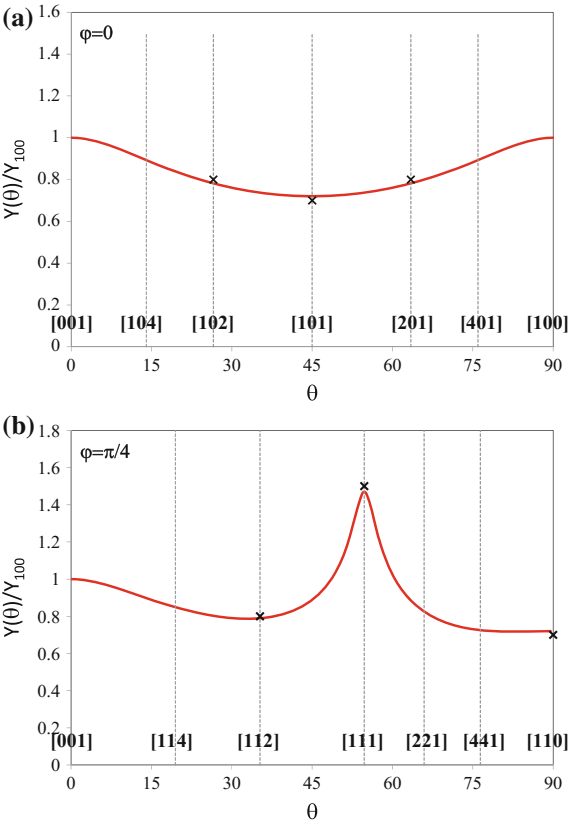

Fig. 3.14 Comparison between the anisotropy in yield stress ratio in uniaxial tension for a Cu single crystal predicted by Cazacu et al. [26] criterion and data of Takeuchi [98]: **a** in the plane of normal $\langle 100\rangle$; **b** in the plane of normal $\langle 1\bar{1}0\rangle$ (for the definition of the angle φ, see Fig. 3.11)

$$\frac{Y_{\langle 110\rangle}(\theta)}{Y_{100}} = \frac{\left(27 - 4cn_1^2\right)^{1/6}}{\left\{\left[\frac{1}{3} + \frac{1}{4}(m_2 - m_1)\sin^2\theta\left(3\cos^2\theta + 1\right)\right]^3 - c\left[\begin{array}{l}\frac{2n_1}{27} + \frac{n_3 - n_1}{12}\sin^2\alpha\left(3\cos^2\theta + 1\right) \\ + \frac{(n_1 - 3n_3 + 2n_4)}{4}\sin^4\theta\cos^2\theta\end{array}\right]^2\right\}^{1/6}} \tag{3.39}$$

For the Cu single crystal, comparison between the theoretical predictions according to Eq. (3.39) and data is shown in Fig. 3.14b. Note that the Cazacu et al. [26] yield criterion is flexible enough to capture the difference in yield stresses along the [100], [101], and [111] orientations. On the other hand, irrespective of the value of the exponent n, the generalized Schmid criterion [see Eqs. (3.7) and (3.10)] cannot capture the observed behavior. This is also clearly seen in Fig. 3.15a, b which show quantitative comparisons between data and the variation of the yield stress in tension with the loading orientation in the crystallographic planes of

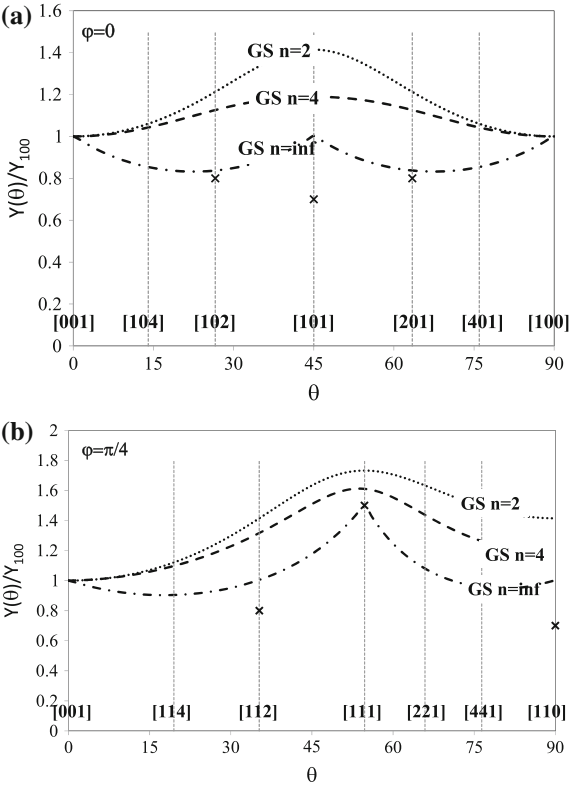

Fig. 3.15 Comparison between the anisotropy in yield stress ratio in uniaxial tension for a Cu single crystal as predicted by the generalized Schmid criterion corresponding to $n = 2$, $n = 4$, and $n = 300$ (inf), respectively, and data ([99]): **a** in the plane of normal $\langle 100\rangle$; **b** in the plane of normal $\langle 1\bar{1}0\rangle$ (for the definition of the angle φ, see Fig. 3.11)

normal $\langle 100 \rangle$ and $\langle 1\bar{1}0 \rangle$, respectively, predicted by the generalized Schmid criterion corresponding to $n = 2$, $n = 4$, and $n = 300$, respectively.

In Fig. 3.16, the isocontours of the normalized yield stresses in uniaxial tension according to the generalized Schmid yield criterion (see Eq. 3.7) for the same values of the parameter n are represented in the basic stereographic triangle. Comparison between Figs. 3.12 and 3.15 also highlights that in contrast to the generalized Schmid criterion, the recent criterion of Cazacu et al. [26] can capture the behavior of single crystals for which $Y_{110} < Y_{100}$.

As already mentioned, if we consider the $(1\bar{1}1)[011]$ slip system to be active in the stereographic triangle with corners along [001], [101], and [111], the anisotropy in uniaxial yield stresses predicted by the Schmid law [see Eqs. (3.4)–(3.6)] is the same for any cubic crystal. This is also clearly seen by substituting the expression of the applied stress tensor $\boldsymbol{\sigma}$ given by Eq. (3.31) in Eqs. (3.4)–(3.6), which gives:

$$Y_d/\tau_c = \frac{\sqrt{6}}{\left| -\sin^2\theta \sin^2\varphi + \cos^2\theta + \sin^2\theta \sin\varphi \cos\varphi + \cos\theta \sin\theta \cos\varphi \right|} \tag{3.40}$$

Thus, the predicted uniaxial tensile yield stress normalized by the value of the critical resolved shear stress τ_c does not depend on any material parameter. Irrespective of the single crystal, the isocontours of Y_d/τ_c in the basic stereographic triangle are the same.

To enable direct comparison between the isocontours for Cu single crystal according to Cazacu et al. [26] and the generalized Schmid criterion (see Figs. 3.13 and 3.16, respectively), in Fig. 3.17 are shown the predictions based on the Schmid law. As mentioned, the Schmid law is not valid for cubic single crystals for which $Y_{110} < Y_{100}$.

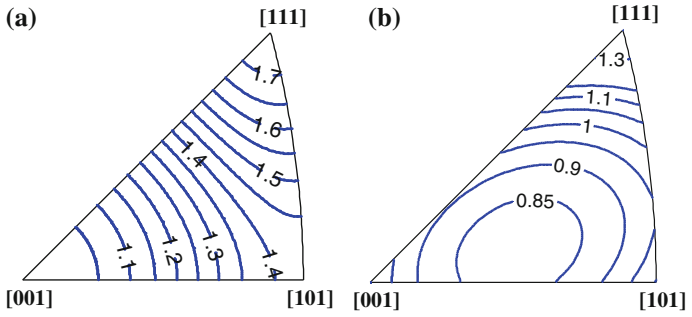

Fig. 3.16 Isocontours in the basic stereographic triangle of the normalized yield stress in uniaxial tension predicted by the generalized Schmid criterion for different values of the exponent n: **a** $n = 2$; **b** $n = 300$ (After Cazacu et al. [26])

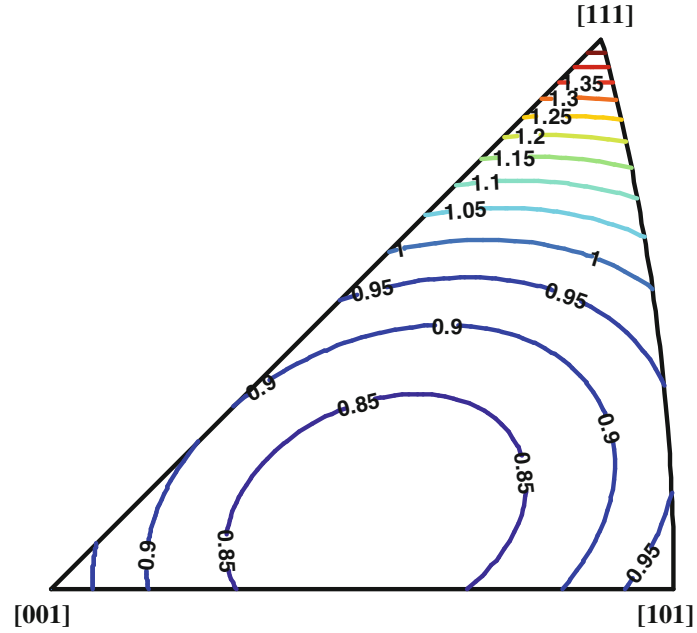

Fig. 3.17 Isocontours of the yield stress ratio Y_d/Y_{100} according to Schmid law

3.3.3.2 Al 5% Cu Single Crystal

Karnop and Sachs [58] reported room-temperature uniaxial yield stress data for a single crystal of Al containing a small fraction of alloying elements (95% Al, 5% Cu). Figure 3.18a shows in the basic stereographic triangle these experimental values normalized by $Y_{100} = 235.4$ MPa. Note that for this material, the maximum uniaxial tensile yield stress is along the [111] direction and that no experimental data were reported for orientations close to [110]. The parameters of the Cazacu et al. [26] yield criterion determined using the available experimental data in conjunction with Eq. (3.32) are: $m_2 = 1.39$, $n_1 = 2.42$, $n_3 = 0.37$, $n_4 = 6.8$, $c = 0.35$, whereas $m_1 = 1$ (see identification procedure outlined in previous section). The predicted yield stresses are shown in Fig. 3.18b. For comparison, Fig. 3.18c shows the predicted yield stresses according to the generalized Schmid criterion (Eq. 3.8) corresponding to a large value of the exponent n ($n = 300$).

Note that the agreement between the yield criterion and data is satisfactory. The evolution of the yield stress in uniaxial tension $Y(\theta)/Y_{100}$ with the angle θ in the plane of normal $\langle 100\rangle$ and $\langle 1\bar{1}0\rangle$, respectively, (Fig. 3.18a, b) reveal the main differences between the Cazacu et al. [26] yield criterion (solid line) and the generalized Schmid criterion with n very large. Note that the latter criterion is not differentiable for some orientations, e.g., [101] and [111] directions, while the Cazacu et al. [26] predicts a smooth variation of the yield stress with the loading orientation.

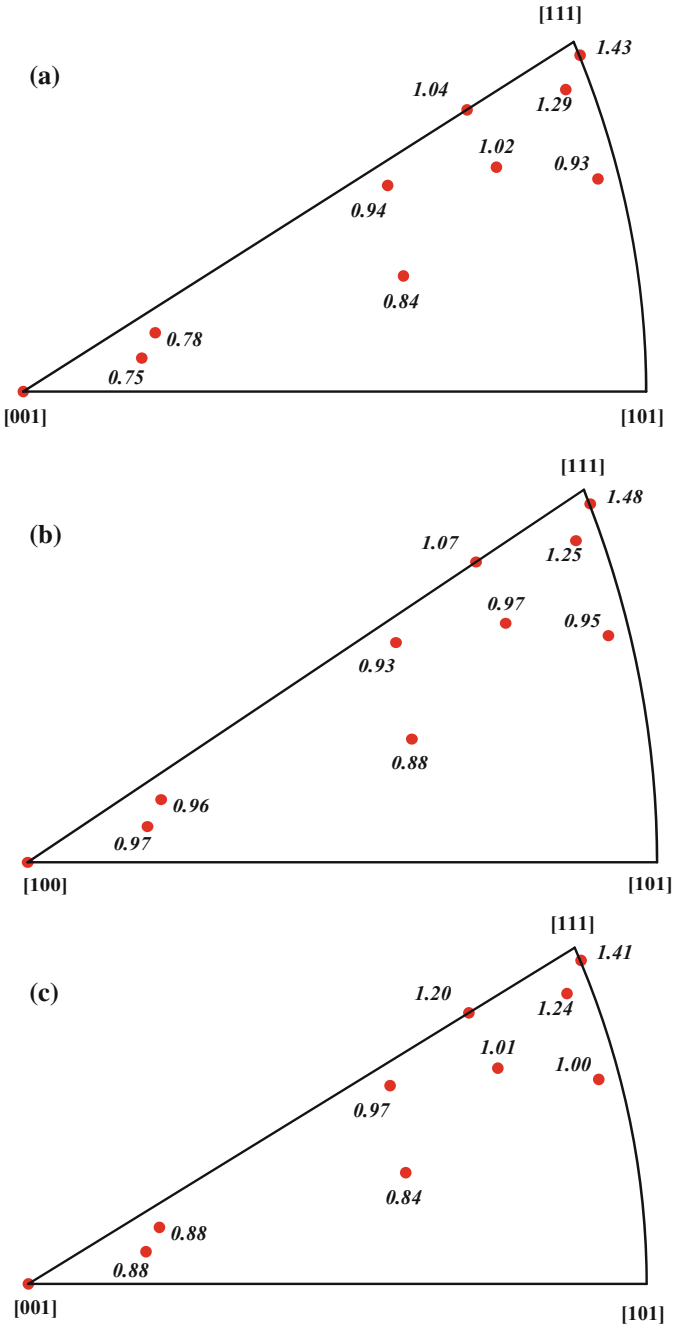

Fig. 3.18 Yield stresses for a Al 5% Cu single crystal in uniaxial tension: **a** experimental data [58], **b** predictions according to Cazacu et al. [26] yield criterion; **c** theoretical predictions using the generalized Schmid criterion with $n = 300$. Yield stresses normalized by the yield stress along [100]

It is important to note that although for this Al 5% Cu single crystal the predictions of the Cazacu et al. [26] yield criterion and the generalized Schmid criterion are similar in uniaxial tension (e.g., see results of Figs. 3.18 and 3.19), for more complex loadings the mechanical response predicted by this criterion and the generalized Schmid criterion is completely different.

For example, for biaxial loadings in the crystallographic plane of normal [100] (i.e., only σ_{xx}, σ_{yy} and σ_{xy} are different from zero), the projections in the (σ_{xx}, σ_{yy}) plane of the yield surfaces according to the new criterion and the generalized Schmid criterion are very different irrespective of the level of shear, σ_{xy}/Y_{100} (see Fig. 3.20a, b for the projections of the yield surfaces corresponding to $\sigma_{xy}/Y_{100} = 0, 0.11, 0.23, 0.34$, respectively).

Also, in Fig. 3.21 are shown the projections in the plane (σ_{xz}, σ_{xy}) corresponding to different fixed values of the normal stress σ_{xx} according to both yield criteria. Note that irrespective of the type of loading, the yield surface according to the new yield criterion is smooth, whereas the yield surfaces according to the generalized Schmid criterion have singularities. Moreover, according to the generalized Schmid criterion, small changes in either the level of shear (see Fig. 3.20b) or the level of normal stress (see Fig. 3.21b) result in drastic changes in the shape of the isocontours.

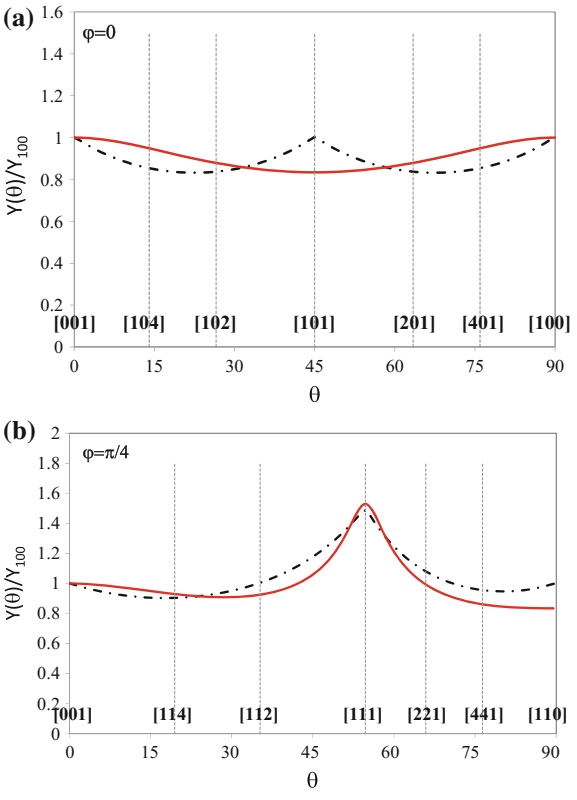

Fig. 3.19 Comparison between the anisotropy in yield stress under uniaxial tension for a Al 5% Cu single crystal predicted by Cazacu et al. [26] (solid line) criterion and the generalized Schmid criterion (dashed line), respectively: **a** in the plane (100); **b** in the plane of normal $\langle 1\bar{1}0 \rangle$ (for the definition of the angle φ, see Fig. 3.11)

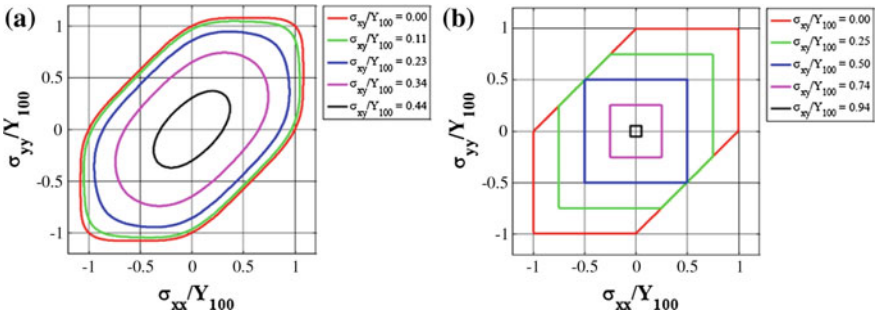

Fig. 3.20 Projection in the (σ_{xx}, σ_{yy}) plane of the yield surface of the single crystal Al alloy obtained with: **a** the Cazacu et al. [26] criterion, and **b** the generalized Schmid criterion with $n = 300$. The constant normalized shear stress contours correspond to $\sigma_{xy}/Y_{100} = 0, 0.11, 0.23, 0.34$, respectively. Stresses are normalized by Y_{100}, the uniaxial yield limit along [100]. Note that irrespective of the loading the yield surface according to the criterion is smooth

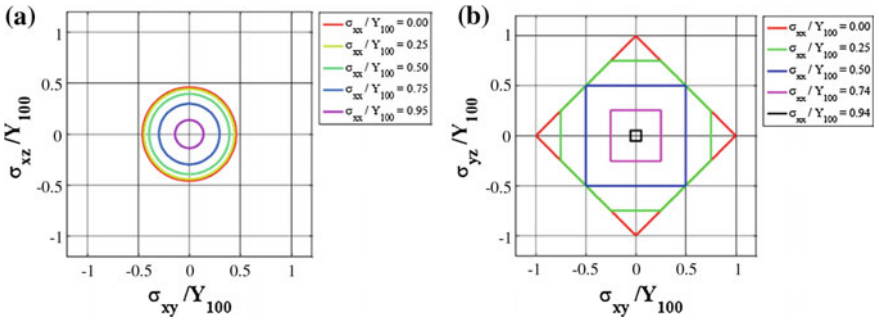

Fig. 3.21 Projection in the (σ_{xz}, σ_{xy}) plane of the yield surface of the single crystal Al alloy obtained with: **a** the Cazacu et al. [26] yield criterion, and **b** the generalized Schmid criterion with $n = 300$. The constant normalized shear stress contours correspond to $\sigma_{xx}/Y_{100} = 0, 0.25, 0.50, 0.95$, respectively. Stresses are normalized by Y_{100}, the uniaxial yield limit along [100]. Note that irrespective of the loading the yield surface according to the proposed criterion is smooth

3.3.4 *Application of Cazacu et al. [26] Single Crystal Criterion to Deep Drawing*

Cup drawing is one of the forming processes where the influence of anisotropy of the metal sheet is most evident. If the material were isotropic, the height of the cup would be uniform. In contrast, anisotropic material behavior has pronounced effects on the strain distribution in the sheet metal during deep drawing resulting in a non-uniform cup height with maxima and minima, commonly known as "ears," along the rim. Modeling and simulation of the formation of ears in deep drawing of

polycrystalline metal sheets have been a subject of intense research since the late 1970s (e.g., [40]). At present, F.E. simulations based on advanced orthotropic yield criteria for polycrystalline metals (see Chap. 5 for the presentation of these criteria) describe with great accuracy earing formation during deep drawing of strongly textured Al and steel alloys (e.g., see [9, 111, 112]).

In contrast, simulation of earing development during forming of single crystal sheets has received little attention. To the best of our knowledge, only F.E. simulations of the cup height for single crystal sheets in the $\{100\}\langle 001\rangle$ orientation have been reported (see [1, 10]).

In the following, we present a numerical F.E. study on the influence of the single crystal orientation on the earing profile of single crystal Al sheets using Cazacu et al. [26] single crystal yield criterion (see Eq. 3.27). The experimental information available in the open literature on forming single crystals is scarce. Nevertheless, the results of cup drawing tests conducted by Tucker [106] for single crystal pure Al sheets indicate that the number of ears that develop depends on the orientation of the single crystal; for some single crystal sheets, formation of six or eight ears is reported. Most importantly, these ears are not equally spaced or of equal height. It should be noted that Tucker study does not include any experimental characterization of the uniaxial tensile properties of the pure Al single crystals sheets used for conducting the cup drawing tests. Therefore, the data necessary for the identification of the material parameters involved in the yield criterion are lacking. Nevertheless, the experimental earing profiles are invaluable and serve as verification for the trends predicted by constitutive models.

The F.E. analyses presented hereafter were performed with ABAQUS/Standard F.E. code using a user material subroutine (UMAT) developed for the elastic/plastic model with yielding described by the Cazacu et al. [26] single crystal yield criterion and associated flow rule. An implicit time integration algorithm was used. For more details about this time integration algorithm used in the F.E. implementation, the reader is referred to Chap. 2.

In all the F.E. simulations of cup drawing tests, the same values for the parameters involved in the single crystal yield criterion are used, namely $m_1 = 1$, $m_2 = 1.39$, $n_1 = 2.42$, $n_3 = 0.37$, $n_4 = 6.8$, $c = 0.35$ (see Eq. 3.27). These numerical values correspond to an Al single crystal (with 5% Cu) for which uniaxial yield stress data were reported by Karnop and Sachs [58] (for these data and details on the identification procedure used for the determination of the material parameters, see Sect. 3.3.3.2). The single crystal behavior is assumed isotropic in the elastic regime, with $E = 69$ GPa and $\nu = 0.3$, and an isotropic hardening governed by a Swift-type law is considered [$K_0 = 478$ MPa, $\varepsilon_0 = 0.0004$ and $n = 0.17$ in Eq. (2.24)].

The schematic view of the cup drawing process is shown in Fig. 3.22a, and the tool dimensions used in the simulations are given in Table 3.4. Due to geometrical and material symmetries (i.e., the cubic symmetry of the single crystal), only a quarter of the cup needs to be modeled. The blank is discretized with C3D8H elements in ABAQUS (eight-node brick elements with constant pressure). Figure 3.22b shows the F.E. mesh used in all the simulations; it is composed of a

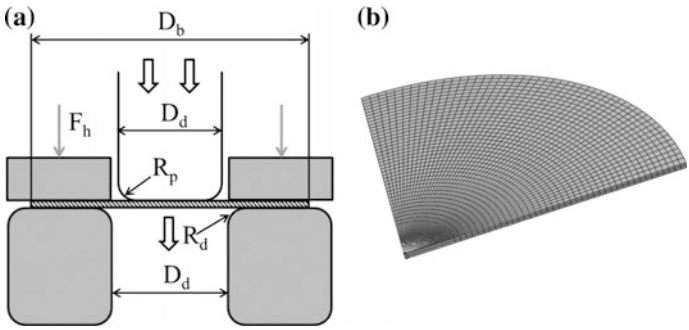

Fig. 3.22 **a** Details of deep drawing experiment geometry; **b** finite elements mesh for the blank

Table 3.4 Dimensions of deep drawing experiment geometry (see also Fig. 3.22)

Punch diameter	D_p = 41.27 mm
Punch radius	R_p = 4.57 mm
Die diameter	D_d = 44.07 mm
Die radius	R_d = 5.08 mm
Drawing ratio	LDR = 1.91

total of 4200 elements. The blank sheet is circular in shape with a diameter of 79 mm and an initial thickness of 0.813 mm. The blank holder force used has a value of F_h = 1000 N.

Simulations are presented for three single crystal sheets of different $\{hkl\}\langle uvw\rangle$ orientations. For any given sheet, $\{hkl\}$ designates the Miller indices of the rolling plane, and $\langle uvw\rangle$ denotes the rolling direction. The crystal orientations analyzed are: $\{100\}\langle 001\rangle$, $\{111\}\langle 1\bar{1}0\rangle$, and $[122]\langle 1\bar{1}0\rangle$, respectively.

Before proceeding with the discussion of the results, let us recall that for polycrystalline sheets it has been established that the height profile of a drawn cup can be correlated to the directionality in *r*-values and yield stresses in the plane of the blank (e.g., see mechanical tests and cup drawing tests on AA 2008-T4 polycrystalline sheets reported by [66]).

For the case of single crystal sheets, such correlations will also be discussed. For this purpose, for each single crystal sheet analyzed, the theoretical variation in uniaxial yield stress and Lankford coefficients with respect to the orientation α between the tensile loading direction and the rolling direction are also presented. While complete proofs are given later (see Sect. 3.4.1), it is important to note here that all these theoretical predictions of the anisotropy in uniaxial tensile properties of single crystal sheets were calculated with simple analytical formulas.

Cup drawing simulations of a $\{100\}\langle 001\rangle$ *single crystal sheet*

For this $\{100\}\langle 001\rangle$ single crystal sheet, the rolling (RD), transverse (TD), and normal direction (ND) of the sheet coincide with the $\langle 100\rangle$ axes of the crystal. Let $\sigma(\alpha)$ denote the yield stress of the single crystal under uniaxial tension in a direction

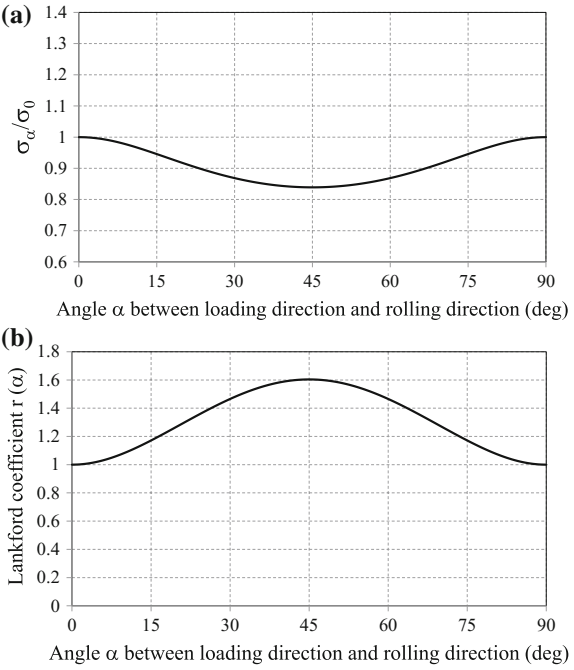

Fig. 3.23 **a** Predicted variation of the yield stress ratios $\sigma(\alpha)/\sigma(0)$ and **b** Lankford coefficients $r(\alpha)$ with respect to the angle between the loading axis and [100] (RD) in the plane of the $\{100\}\langle 001\rangle$ Al 5% Cu single crystal sheet obtained with Cazacu et al. [26] yield criterion

at angle α with respect to RD and $r(\alpha)$ the corresponding Lankford coefficient, which is defined as the ratio between the in-plane transverse strain-rate and the through-thickness strain-rate. Figure 3.23a shows the predicted evolution of yield stress ratio $\sigma(\alpha)/\sigma_0$ and Lankford coefficients $r(\alpha)$ with the loading orientation α (for the analytical expressions see Eqs. (3.43) and (3.45), respectively). It is worth noting that for this Al-5% Cu single crystal, both the $\sigma(\alpha)$ versus α and the $r(\alpha)$ versus α curves admit an extremum at 45° to RD and that the predicted response is symmetric with respect to the 45° orientation to the rolling direction. Furthermore, $r(0°) = r(90°) = 1$, while for all other orientations $r(\alpha) > 1$ (Fig. 3.23b).

Figure 3.24a shows the deformed shape of a completely drawn cup of the $\{100\}\langle 001\rangle$ crystal sheet and the isocontours of the equivalent plastic strain associated with the yield criterion. The simulated evolution of the cup height with the angle from RD is shown in Fig. 3.24b.

Note that for this $\{100\}\langle 001\rangle$ initial orientation of the single crystal sheet, the fully drawn cup displays fours ears with the maximum height located at 45° from RD, in agreement with the experimental observations of Tucker [106]. Figure 3.25 presents the thickness evolution along the cup as a function of the initial radial coordinate.

Since Cazacu et al. [26] yield criterion accounts for the single crystal cubic symmetry, it correctly predicts that the thickness strain distribution along RD and TD should be the same. A reduction in thickness is predicted for an initial radial coordinate of about 20 mm (corresponding to the punch radius) while thickening

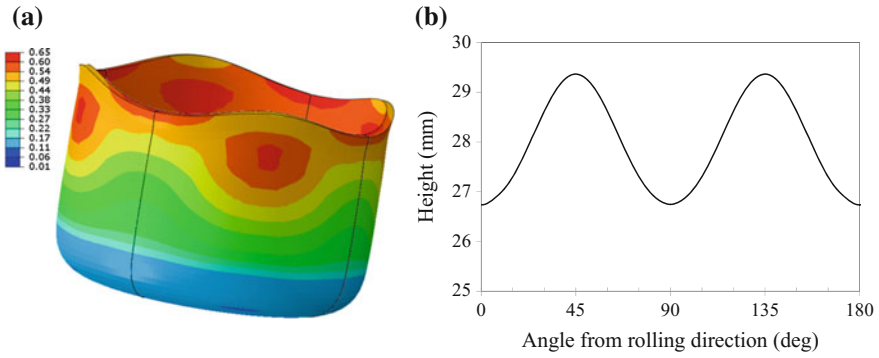

Fig. 3.24 **a** Deformed shape of a fully drawn cup of a $\{100\}\langle 001\rangle$ Al 5% Cu single crystal sheet showing the isocontours of the equivalent plastic strain associated with the Cazacu et al. [26] single crystal yield criterion; **b** predicted cup height versus the angle from the [100] direction (RD)

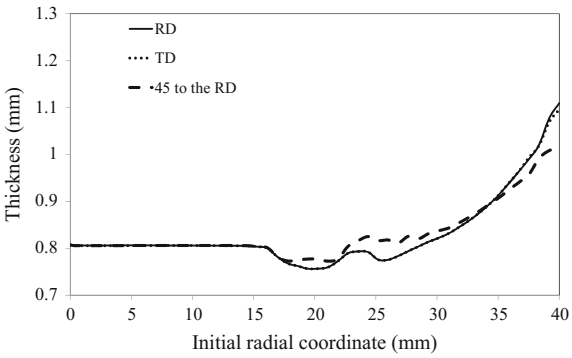

Fig. 3.25 Predicted evolution of the thickness (mm) along the RD, TD and 45° to the RD direction, respectively, as a function of the initial radial coordinate (mm) for the Al 5% Cu single crystal sheet in the $\{100\}\langle 001\rangle$ orientation. F.E. results based on the Cazacu et al. [26] criterion

occurs from about 30 mm onward. Note that for this fully drawn cup, the maximum thickness strain is along the rolling and transverse directions, while the minimum thickness strain corresponds to the 45° orientation to the rolling direction. Those results are consistent with the cup height predictions (see Fig. 3.24b); the larger the cup height is in a given direction, the more thinning occurs in that direction.

Cup drawing simulations of a $\{111\}\langle 1\bar{1}0\rangle$ *single crystal sheet*

Next, the results of the F.E. analyses carried out for a $\{111\}\langle 1\bar{1}0\rangle$ crystal orientation are discussed. In this case, the RD of the sheet is along $[1\bar{1}0]$, TD is along $[11\bar{2}]$, while the ND coincides with the $[111]$ direction. The evolution of the yield stress and Lankford coefficients in the plane of the sheet according to the Cazacu et al. [26] yield criterion is shown in Fig. 3.26. It should be noted that for this crystal orientation, the normalized yield stress ratio $\sigma(\alpha)/\sigma_0$ and Lankford coefficients, $r(\alpha)$, variation with the loading direction α display four maxima and minima. Note the striking difference in terms of the in-plane anisotropy of this sheet as

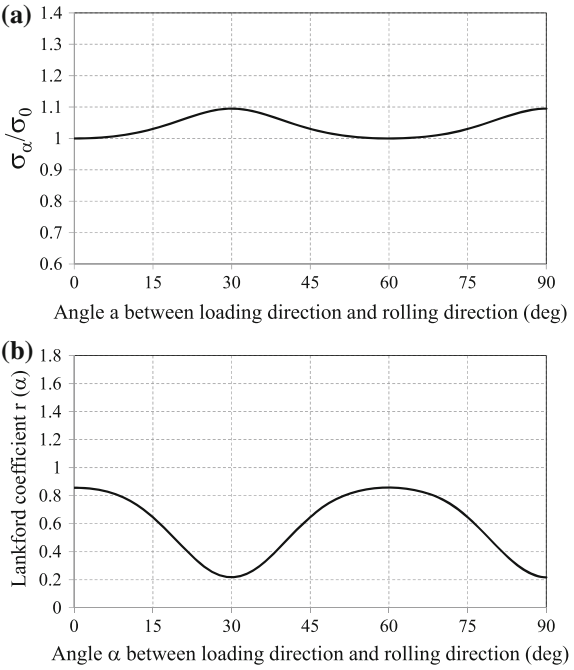

Fig. 3.26 **a** Predicted variation of the yield stress ratios $\sigma(\alpha)/\sigma(0)$ and **b** Lankford coefficients $r(\alpha)$ with respect to the angle between the loading axis and the $[1\bar{1}0]$ direction (RD) in the plane of the (111) of the $\{111\}\langle 1\bar{1}0\rangle$ Al 5% Cu single crystal sheet obtained with the Cazacu et al. [26] yield criterion

compared to that of the $\{100\}\langle 001\rangle$ single crystal sheet (see Fig. 3.23 showing two extrema at $\alpha = 0°$ and $\alpha = 45°$ for the $\{100\}\langle 001\rangle$ sheet).

Specifically, for the $\{111\}\langle 1\bar{1}0\rangle$ sheet, the in-plane $\sigma(\alpha)$ versus α curve admits two maxima, one at $\alpha = 30°$ and the other one at $\alpha = 90°$ (TD), while the minima are located at $\alpha = 0°$ (RD) and at $\alpha = 60°$. The reverse holds true for the evolution of the Lankford coefficients; i.e., minima are at $\alpha = 30°$ and $\alpha = 90°$, respectively, and maxima are at $\alpha = 0°$ and $\alpha = 60°$, respectively. It is also worth noting that for the $\{111\}\langle 1\bar{1}0\rangle$ sheet, irrespective of the in-plane tensile loading direction α: $r(\alpha) < 1$.

For the $\{111\}\langle 1\bar{1}0\rangle$ single crystal sheet, the fully drawn cup displays six ears located at 30° from RD and TD, respectively, (see Fig. 3.27). Note that the cup height at 90° is a little larger than that at 30° from RD (i.e., the ears along TD are more pronounced). It is also worth noting that the location of the ears correlates with the minima for the Lankford coefficients (see Fig. 3.27b). The evolution of the cup thickness along the three directions of interest (i.e., RD, TD and 45° to RD) is shown in Fig. 3.28. As a general observation, let us note that due to the strong in-plane anisotropy, there is a clear difference in the thickness strains along these directions, with most thickening occurring along $[1\bar{1}0]$ (RD). These results correlate with the predicted cup height profile and r-values variation (see Figs. 3.26 and 3.27).

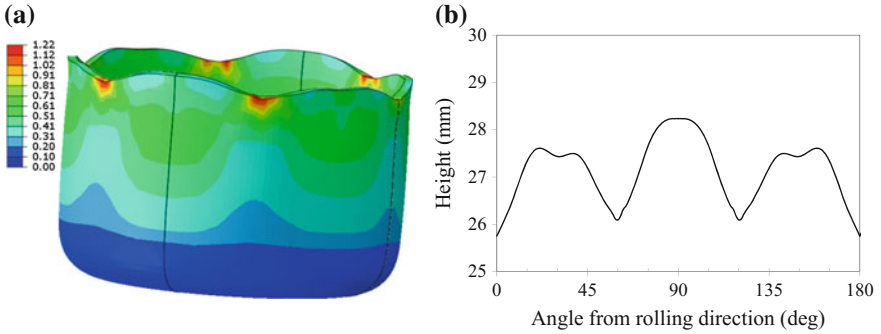

Fig. 3.27 **a** Deformed shape of a fully drawn cup of $\{111\}\langle 1\bar{1}0\rangle$ Al 5% Cu single crystal sheet showing the isocontours of the equivalent plastic strain associated with the Cazacu et al. [26] single crystal yield criterion. **b** Predicted cup height versus the angle from the rolling direction $[1\bar{1}0]$

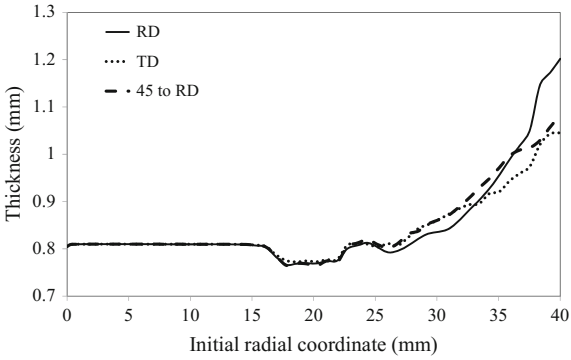

Fig. 3.28 Evolution of the thickness (mm) for the RD, TD and 45° to the RD direction, respectively, as a function of the initial radial coordinate for a full drawn cup from the $\{111\}\langle 1\bar{1}0\rangle$ crystal sheet: F.E. results based on Cazacu et al. [26] yield criterion

So far, it has been shown that the Cazacu et al. [26] yield criterion predicts either four or six ears depending on the orientation of the single crystal sheet. In the following are presented simulation results for a $\{122\}\langle 1\bar{1}0\rangle$ single crystal sheet.

Cup drawing simulations of a $\{122\}\langle 1\bar{1}0\rangle$ *single crystal sheet*

For this crystal orientation, the RD of the sheet coincides with $[0\bar{1}1]$, TD with $[4\bar{1}\bar{1}]$, and ND with $[122]$. The evolution of the normalized yield stresses and Lankford coefficients in the (122) plane according to Cazacu et al. [26] yield criterion is shown in Fig. 3.29. Note that according to this single crystal criterion the variation of the tensile yield stresses $\sigma(\alpha)/\sigma_0$ and Lankford coefficients, $r(\alpha)$, with the loading direction α displays four extrema located at RD, 30°, 50°, and ND, respectively. Note also the strong anisotropy in $r(\alpha)$, the value of the Lankford coefficient varying from $r = 0.18$ at $\alpha = 30°$ to $r = 1.22$ at $\alpha = 50°$.

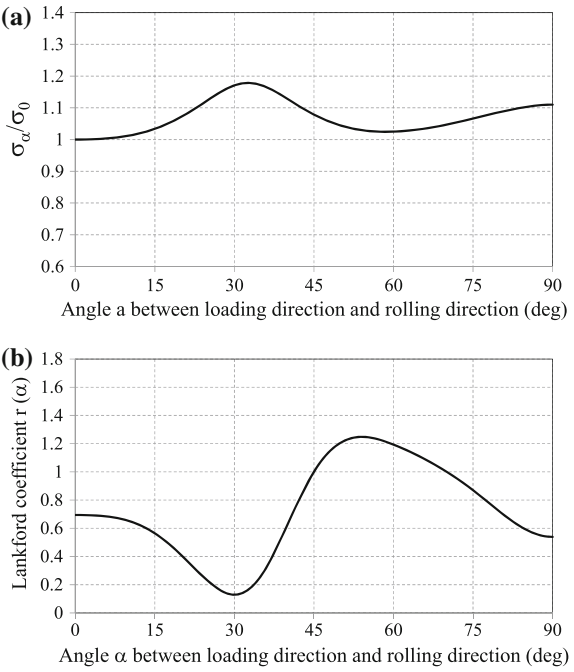

Fig. 3.29 **a** Predicted variation of the normalized yield stress $\sigma(\alpha)/\sigma(0)$ and **b** Lankford coefficients $r(\alpha)$ with loading direction α in the (122) plane of the Al 5% Cu $\{122\}\langle 1\bar{1}0\rangle$ single crystal sheet according to the Cazacu et al. [26] yield criterion

For this $\{122\}\langle 1\bar{1}0\rangle$ single crystal sheet, the fully drawn cup displays eight ears, four large ears located at 30° and 150° from $[1\bar{1}0]$ (i.e. RD), and four small ears located at 80° and 100° from RD, as shown in Fig. 3.30. The same number of ears has been observed experimentally. The evolution of the cup thickness along the three directions of interest (i.e., RD, TD and 45° to RD) is shown in Fig. 3.31. Note the pronounced influence of the crystal anisotropy on the thickness distribution, which correlates to the Lankford coefficients variation in the plane (122) of the sheet.

In summary, it has been shown that using Cazacu et al. [26] yield criterion for cubic single crystals, it is possible to account for the influence of the crystal orientation on the number and location of ears that develop during deep drawing.

As an example, for an Al 5% Cu single crystal sheet, using the same set of parameters, it was predicted that four ears develop for the $\{100\}\langle 001\rangle$ single crystal sheet, six ears for the $\{111\}\langle 1\bar{1}0\rangle$ sheet and eight ears for the $\{122\}\langle 1\bar{1}0\rangle$ sheet, as observed in the cup drawing tests on single crystal sheets of Al conducted by Tucker [106]. Furthermore, it was predicted that the ears are not necessarily equally spaced or of equal height.

It is important to note the significant influence of the choice of the yield criterion on the prediction of the cup height profile. Only if the combined anisotropy and third-invariant effects on the yielding behavior of the single crystal are taken into account, it is possible to predict the occurrence of more than four ears with different heights and locations along the cup edge. Specifically, the use of a quadratic yield

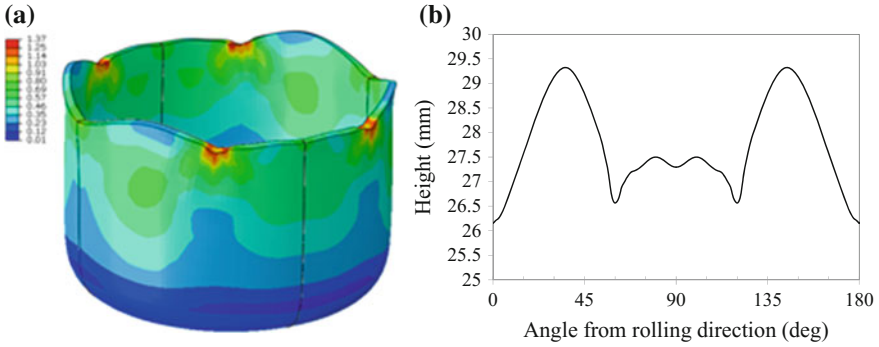

Fig. 3.30 **a** Deformed configuration of a fully drawn cup from a Al 5% Cu single crystal $\{122\}\langle 1\bar{1}0\rangle$ sheet showing the isocontours of the equivalent plastic strain associated with the Cazacu et al. [26] single crystal yield criterion. **b** Predicted cup height as a function of the angle with the rolling direction $[1\bar{1}0]$

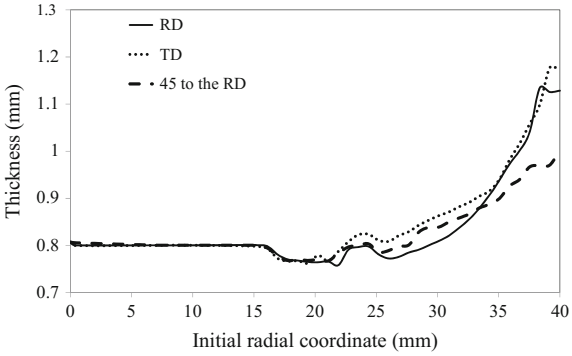

Fig. 3.31 Evolution of the thickness (mm) for the $[0\bar{1}1]$ (RD), $[4\bar{1}\bar{1}]$ (TD) and 45° to the RD direction, respectively, as a function of the initial radial coordinate of the full drawn cup from the $\{122\}\langle 1\bar{1}0\rangle$ crystal sheet: F.E. results based on Cazacu et al. [26] yield criterion

criterion ($c = 0$ in the Cazacu et al. [26] yield criterion) would lead to predictions of four ears irrespective of the single crystal orientation. Moreover, those ears would be located either at 45° from RD or at TD.

3.4 Modeling of Plastic Anisotropy of Polycrystalline Textured Sheets Based on Cazacu et al. [26] Single Crystal Criterion

Controlling the mechanical behavior is essential when developing new materials. Substituting mechanical tests by simulation studies to evaluate the mechanical performance of alloys is highly desirable as it enables a significant reduction of resource allocation in the alloy design process. However, in order to get reliable

results, the models need to accurately predict the mechanical behavior. Description of the plastic deformation of materials which display strong texture components is particularly challenging. Generally, in industrial applications, macroscopic analytic yield criteria are used (e.g., [6]). Examples of such yield criteria for textured polycrystalline materials that are defined for three-dimensional loadings and capture with accuracy the anisotropy in mechanical response of the metal in bulk are presented in Chap. 5.

Modeling the plastic anisotropy of polycrystalline textured sheets based on the single crystal description of plastic deformation is mainly done assuming that the plastic deformation of the constituent grains is described by Schmid law (see Eq. 3.4) or regularized forms of the Schmid law such as the generalized Schmid law (see Eq. 3.7) or a viscoplastic power-law [4, 5].

For a comprehensive presentation of the theory and recent advances, the reader is referred to the monographs of Hosford [50], Kocks et al. [62], and review papers of Tomé and Lebensohn [105], Wenk and Van Houtte [108]. Here, we mention only the main assumptions and very early contributions that laid the foundation of crystal plasticity theory.

Assuming homogeneous stress in the polycrystal and Schmid law at grain level, Sachs [89] calculated the uniaxial yield stress of an isotropic fcc polycrystal (polycrystal of randomly oriented single crystals). Later on, Taylor [102] predicted the stress–strain relation of an fcc polycrystal on the basis of the following assumptions:

i. Rigid-plastic behavior of the constituent crystals is governed by Schmid law,
ii. The critical shear stress τ_c is the same for all twelve slip systems (see Eq. 3.6).
iii. Any given constituent crystal undergoes hardening according to the following law:

$$\tau_c = h\left(\sum_{s=1}^{12} |\gamma^s|\right),$$

where γ^s is the shear due to slip in the system (s). The specific mathematical form of the function h in the above equation should be determined based on measurements.

iv. Each constituent crystal undergoes the same strain (homogeneous strain assumption).

This model was extended to multiaxial loadings by Bishop and Hill [13]. Lin [69] proposed an extension of the Taylor model such as to account for elastic deformations. An additive decomposition of the total strain of the crystal into an elastic and plastic part was considered (for the small-strain formulation of an elastic/plastic model for fcc single crystals and calculation of the stress–strain response of a polycrystal on the basis of this model, see Payne [78]). A general kinematics of the finite-deformation of elastic-plastic single crystals deforming by slip according to Schmid law which includes lattice rotations was developed by Rice [85].

Budiansky and Mangasarian [16] used the solution given by Eshelby [35] for the elasticity problem of an ellipsoidal inclusion embedded in an unbounded matrix loaded uniformly at infinity to obtain the stress–strain in a spherical crystal embedded in an elastic matrix. Kroner [63] modified the Eshelby solution to include the effect of plastic strain in the surrounding matrix and, thus, to account for plastic grain interactions. The self-consistent approach and model of interaction between single crystals undergoing slip was proposed by Budiansky and Wu [17]. In this model, the stress–strain in a single crystal surrounded by its plastically deformed neighbors are obtained by considering the deformation of a spherical single crystal embedded in an infinite matrix. The matrix is subject to a stress at infinity which is equal to the stress of the polycrystal, and the plastic strain in the matrix is considered uniform and equal to the polycrystal plastic strain. The stress and plastic strain in the spherical grain are related through a modified form of the Eshelby [35] solution. For detailed investigations of the capabilities of this model for isotropic fcc and bcc polycrystalline materials subject to various loading scenarios as well as discussion and comparison with the Lin [69] model, the reader is referred to Hutchinson [55, 56].

Hill [47] demonstrated that the self-consistent method developed for polycrystal elasticity can be extended such as to account for nonlinear behavior by performing incremental linearization. As an alternative method, Berveiller and Zaoui [11] proposed a secant method, while Molinari et al. [76] and Lebensohn and Tomé [65] developed a tangent approach. The latter applied this nonlinear extension of the self-consistent method to polycrystals with hcp structure. An evaluation of various nonlinear extensions of the self-consistent approach can be found in Gilormini [39]. The basic assumption of the classical self-consistent approach that each grain in a polycrystal is surrounded by the homogeneous equivalent medium means that heterogeneous intragranular deformation cannot be described. To overcome this limitation, Canova [20] developed an N-site self-consistent model, which considers that the deformation of a grain cannot be deduced using a homogeneous effective surrounding only, and at least one neighboring grain must also be taken into account. This implies that the Eshelby [35] solution cannot be used directly so complex numerical schemes need to be considered. The complexity and number of unknowns further increase when passing from only one neighbor (as in [21]) to the case when each grain is subdivided into smaller homogeneously deformed units (as originally described in Canova et al. [19]). The theory was applied to dual-phase materials with sharp contrast between the phases (see also [62]).

While increasingly complex homogenization schemes have been proposed (e.g., see [105]), use of such models for solving large-scale boundary value problems is still limited, mainly due to the prohibitive computational cost (e.g., see [37]).

Recently, Cazacu et al. [25] and Chandola et al. [26] modeled the polycrystalline mechanical response using the Cazacu et al. [26] criterion for the description of yielding of the constituent crystals. We begin by presenting the predicted polycrystalline yielding response for ideal texture components reported by Cazacu et al. [25] (see Sect. 3.4.1). For the case of strongly textured sheets containing a spread about the ideal texture components, the polycrystalline response obtained

numerically on the basis of the same single crystal criterion is presented in Sect. 3.4.2. It is shown that for textures obtained with rotationally symmetric misorientations of scatter width of up to 35° from the ideal orientation, the numerical predictions have the same trend as those obtained analytically for ideal textures, but the anisotropy is less pronounced. Furthermore, irrespective of the number of grains in the sample, Lankford coefficients have finite values for all loading orientations. Illustrative examples for sheets with textures containing a combination of few ideal texture components are also presented. The numerical simulation results are also compared to analytical estimates obtained using the closed form formulas for the ideal components in conjunction with simple laws of mixtures. Section 3.4.2.3 presents applications of this polycrystalline model to the prediction of the directionality of macroscopic tensile properties of steel and Al sheets.

3.4.1 *Analytical Expressions for the Yield Stress and Lankford Coefficients of Ideal Texture Components*

Generally, in polycrystalline sheets, grains are not randomly oriented, but are distributed along preferred orientations that result from rotations during processing. For a given fabrication process, the textures that develop contain either one or a relatively small number of ideal components (e.g., see [31, 48, 62]). It is therefore of great interest to estimate the effect of each individual texture component on the plastic anisotropy at minimum computational cost. Cazacu et al. [25] have shown that using the single crystal yield criterion given by Eq. (3.27) in conjunction with associated flow rule, it is possible to obtain analytical expressions for the variation of the uniaxial flow properties of polycrystalline sheets with ideal textures. Indeed, in the coordinate system $Oxyz$ associated with the $\langle 100 \rangle$ crystal axes, the effective stress, $\bar{\sigma}$, associated with the Cazacu et al. [26] single crystal yield criterion given by Eq. (3.27) is:

$$\bar{\sigma} = \frac{3}{\left(27 - 4cn_1^2\right)^{1/6}} \left\{ \begin{array}{l} \left[\left(s_{xx}^2 + s_{yy}^2 + s_{zz}^2\right)/2 + m_2\left(s_{xy}^2 + s_{xz}^2 + s_{yz}^2\right)\right]^3 \\ - c\left[n_1 s_{xx} s_{yy} s_{zz} - n_3\left(s_{zz} s_{xy}^2 + s_{xx} s_{yz}^2 + s_{yy} s_{xz}^2\right) + 2n_4 s_{xy} s_{xz} s_{yz}\right]^2 \end{array} \right\}^{1/6} \tag{3.41}$$

Assuming associated flow rule, the plastic strain-rate tensor of each grain, $\mathbf{d}^p$, can be easily calculated as:

$$\mathbf{d}^p = \dot{\lambda}\frac{\partial \bar{\sigma}}{\partial \boldsymbol{\sigma}}, \tag{3.42}$$

where $\dot{\lambda}$ is the plastic multiplier. Assuming that the polycrystalline sheet of interest displays a single ideal texture whose Miller indices are $\{hkl\}\ \langle uvw\rangle$ (i.e., all the grains in the sheet material are oriented such that their $\{hkl\}$ planes are nearly parallel to the rolling plane and their $\langle uvw\rangle$ directions are parallel to the rolling direction), let $\sigma(\alpha)$ denote the yield stress of the polycrystalline sheet under uniaxial stress in a direction at angle α with respect to the rolling direction and $r(\alpha)$ the corresponding Lankford coefficient, which is defined as the ratio between the in-plane transverse strain-rate and the through-thickness strain-rate. The Cartesian coordinate system associated with the loading frame is denoted $(\mathbf{e}_1, \mathbf{e}_2, \mathbf{e}_3)$. Analytical expressions for the evolution of $\sigma(\alpha)$ and $r(\alpha)$ with the orientation α are deduced for the following ideal texture components: $\{100\}\langle 001\rangle$ (cube), $\{110\}\langle 001\rangle$ (Goss), $\{112\}\langle 11\bar{1}\rangle$ (copper), $\{\bar{2}1\bar{1}\}\langle 011\rangle$ and $\{100\}\langle 011\rangle$ (rotated cube). It is worth noting that irrespective of the texture component considered, the expressions of $\sigma(\alpha)$ and $r(\alpha)$ should depend only on the parameters m_2, n_1, n_3, n_4, c that characterize the plastic behavior of the constituent crystals. Illustration of the predicted evolution of $\sigma(\alpha)$ and $r(\alpha)$ for each texture component will be done with the following numerical values of the parameters: $m_2 = 0.38$, $n_1 = 0.98$, $n_3 = 0.04$, $n_4 = 0.08$, c = 2.3 of the yield criterion.

3.4.1.1 Cube Texture

The first ideal texture component that is discussed is the $\{100\}\langle 001\rangle$ (cube). For this texture, the rolling (RD), transverse (TD), and normal direction (ND) of the sheet coincide with the $\langle 100\rangle$ axes of each of the constituent crystals (see Fig. 3.32a). Under uniaxial tension in the (RD, TD) plane, the only nonzero stress components are the in-plane stresses: $\sigma_{xx} = \sigma(\alpha)\cos^2\alpha$, $\sigma_{yy} = \sigma(\alpha)\sin^2\alpha$ and $\sigma_{xy} = \sigma(\alpha)\sin\alpha\cos\alpha$, with $\sigma(\alpha)$ being the yield stress in a direction α with respect to the rolling direction in the plane of the sheet. Further substitution in Eq. (3.41) leads to the following evolution of the yield stress ratio $\sigma(\alpha)/\sigma(0)$:

$$\frac{\sigma(\alpha)}{\sigma(0)} = \frac{\left(27 - 4cn_1^2\right)^{1/6}}{\left\{27\left[1 + 3(m_2 - 1)\sin^2\alpha\cos^2\alpha\right]^3 - c\left[2n_1 + 9(n_3 - n_1)\sin^2\alpha\cos^2\alpha\right]^2\right\}^{1/6}} \tag{3.43}$$

Note that the symmetry of the cube-textured sheet is correctly described. Indeed, Eq. (3.43) is invariant by the transformation $\alpha \rightarrow (90^\circ - \alpha)$, so the yield stress remains identical under rotations of $\pi/2$ about the normal to the sheet. In particular, $\sigma(0) = \sigma(90)$; i.e., the yield stress in uniaxial tension along TD should be the same as the yield stress in uniaxial tension along the reference direction, RD. Moreover, it

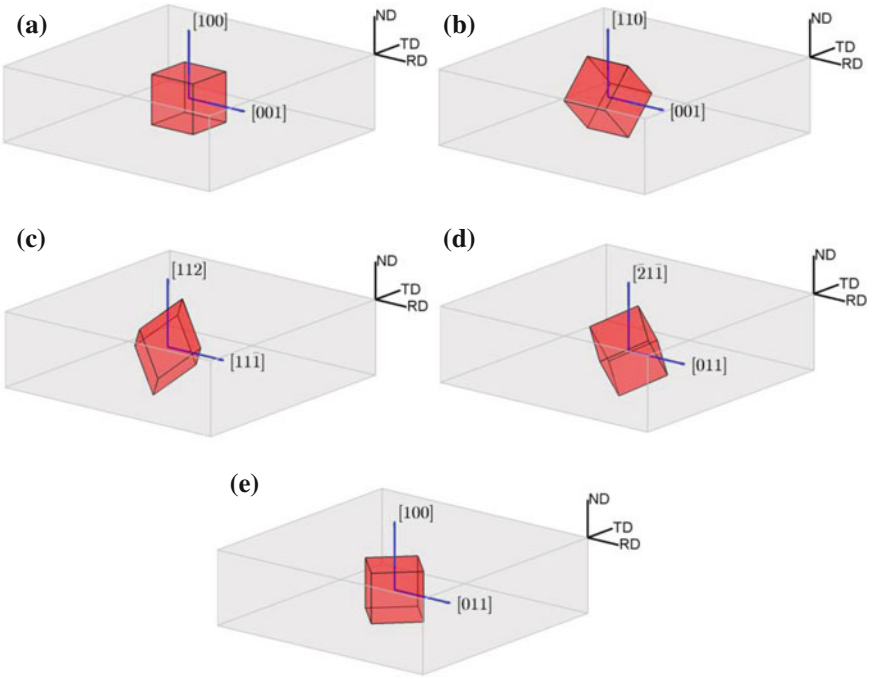

Fig. 3.32 System of coordinate axes for ideal texture components: **a** $\{100\}\langle 001\rangle$ (cube), **b** $\{110\}\langle 001\rangle$ (Goss), **c** $\{112\}\langle 11\bar{1}\rangle$ (copper), **d** $\{\bar{2}1\bar{1}\}\langle 011\rangle$ (brass), and **e** $\{100\}\langle 011\rangle$ (rotated cube)

can be easily shown that there are at most five extrema for $\sigma(\alpha)$. Irrespective of the values of the parameters m_2, n_1, n_3, n_4, c that describe the single crystal behavior, three of these extrema are located at 0°, 45°, and 90° with respect to RD, and:

$$\frac{\sigma(45^\circ)}{\sigma(0)} = \frac{\left(27 - 4cn_1^2\right)^{1/6}}{2\left[27(3m_2+1)^3 - 4c(9n_3 - n_1)^2\right]^{1/6}}. \tag{3.44}$$

It is worth noting that if $c = 0$, then 0°, 45°, and 90° are the only extrema. Furthermore, if $m_2 = 1$ and $n_1 > 9n_3 > 0$, irrespective of the value of c there should be additional extrema at $\alpha_1 = \arcsin\left(\sqrt{8n_1/9(n_1 - n_3)}\right)/2$ and $\alpha_2 = 90^\circ - \alpha_1$. Under equibiaxial tension, yielding occurs at the same yield stress as along RD and TD, i.e., $\sigma_b = \sigma(90^\circ) = \sigma(0^\circ)$.

For a cube-textured sheet, use of the flow rule given by Eq. (3.42) leads to the following expression for the variation of the strain-rate ratios $r(\alpha)$ with the loading orientation, α,

$$r(\alpha) = -\frac{\sin^2\alpha\dfrac{\partial\bar{\sigma}}{\partial\sigma_{xx}} - \sin 2\alpha\dfrac{\partial\bar{\sigma}}{\partial\sigma_{xy}} + \cos^2\alpha\dfrac{\partial\bar{\sigma}}{\partial\sigma_{yy}}}{\dfrac{\partial\bar{\sigma}}{\partial\sigma_{xx}} + \dfrac{\partial\bar{\sigma}}{\partial\sigma_{yy}}}, \tag{3.45}$$

with $\bar{\sigma}$ being the effective stress given by Eq. (3.41). The partial derivatives of $\bar{\sigma}$ are expressed in terms of those of the generalized cubic invariants J_2^c and J_3^c given by Eqs. (3.19) and (3.22), respectively. It can be easily seen that

$$\frac{\partial J_2^c}{\partial\sigma} = m_2\boldsymbol{s},$$

while the partial derivatives of the generalized third-invariant J_3^c are expressed as:

$$\begin{aligned}
\frac{\partial J_3^c}{\partial\sigma_{xx}} &= n_1\left(2s_{xx}^2 - s_{yy}^2 - s_{zz}^2\right)/3 + n_3\left(s_{xy}^2 + s_{xz}^2 - 2s_{yz}^2\right)/3\\
\frac{\partial J_3^c}{\partial\sigma_{yy}} &= n_1\left(2s_{yy}^2 - s_{xx}^2 - s_{zz}^2\right)/3 + n_3\left(s_{xy}^2 + s_{yz}^2 - 2s_{xz}^2\right)/3\\
\frac{\partial J_3^c}{\partial\sigma_{zz}} &= n_1\left(2s_{zz}^2 - s_{xx}^2 - s_{yy}^2\right)/3 + n_3\left(s_{xz}^2 + s_{yz}^2 - 2s_{yx}^2\right)/3\\
\frac{\partial J_3^c}{\partial\sigma_{xy}} &= -n_3 s_{zz}s_{xy} + n_4 s_{xz}s_{yz}\\
\frac{\partial J_3^c}{\partial\sigma_{yz}} &= -n_3 s_{xx}s_{yz} + n_4 s_{xy}s_{xz}\\
\frac{\partial J_3^c}{\partial\sigma_{xz}} &= -n_3 s_{yy}s_{xz} + n_4 s_{xy}s_{yz}
\end{aligned} \tag{3.46}$$

First, let us note that for $c > 0$, irrespective of the values of the parameters m_2 and n_1, the variation of the Lankford coefficient $r(\alpha)$ with the orientation α is continuous, and $r(\alpha) = r(90^\circ - \alpha)$. Moreover, in the evolution of the Lankford coefficients with orientation, there are extrema at 0°, 45°, and 90°. In particular, the Lankford coefficients along RD and TD should be identical and equal to unity,

$$r(0^\circ) = r(90^\circ) = 1, \tag{3.47}$$

and

$$r(45^\circ) = \frac{27(3m_2+1)^2(3m_2-1) + 4c(n_1 - 9n_3)(n_1 + 3n_3)}{54(3m_2+1)^2 - 8c(n_1 - 9n_3)(n_1 - 3n_3)} \tag{3.48}$$

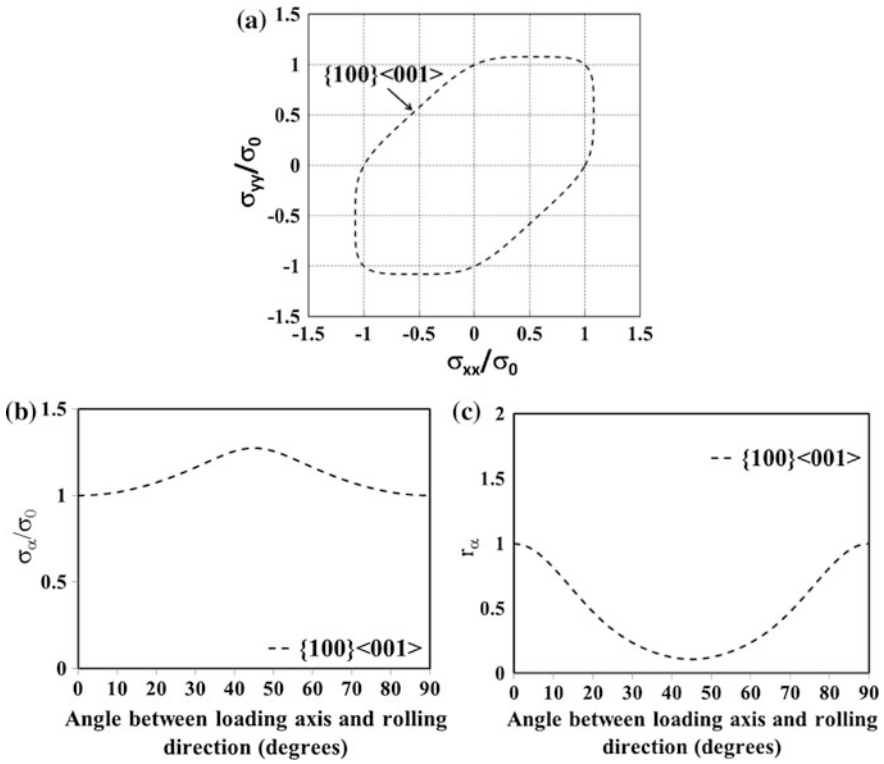

Fig. 3.33 **a** Plane-stress yield surface; **b** predicted yield stress ratios $\sigma(\alpha)/\sigma(0)$; and **c** Lankford coefficients $r(\alpha)$ versus loading direction α in the plane of the cube-textured sheet. Single crystal material parameters: $m_2 = 0.38$, $n_1 = 0.98$, $n_3 = 0.04$, $n_4 = 0.08$, $c = 2.3$

As an example, in Fig. 3.33 is shown the plane-stress yield locus ($\sigma_{xy} = 0$) of the cube-textured sheet and the predicted evolution of yield stress ratio $\sigma(\alpha)/\sigma(0)$ and $r(\alpha)$ with the loading direction α corresponding to $m_2 = 0.38$, $n_1 = 0.98$, $n_3 = 0.04$, $n_4 = 0.08$, $c = 2.3$.

3.4.1.2 Goss Texture $\{110\}\langle 001\rangle$

For a Goss-textured $\{110\}\langle 001\rangle$ polycrystalline sheet (see Fig. 3.32b), uniaxial tension along the direction $\mathbf{x_1}$ at orientation α to RD corresponds to:

$$\boldsymbol{\sigma} = \sigma(\alpha)(\mathbf{x_1} \otimes \mathbf{x_1}), \text{with } \mathbf{x_1} = \frac{\sin\alpha}{\sqrt{2}}\left(\mathbf{e}_x - \mathbf{e}_y\right) + \cos\alpha \mathbf{e}_z \tag{3.49}$$

Thus, in the crystallographic axes $(\boldsymbol{x}, \boldsymbol{y}, \boldsymbol{z})$, the components of the applied stress tensor are:

$$\sigma_{xx} = \sigma_{yy} = -\sigma_{xy} = \frac{\sigma_\alpha \sin^2 \alpha}{2}, \sigma_{zz} = \sigma_\alpha \cos^2 \alpha, \sigma_{xz} = -\sigma_{yz} = \frac{\sigma_\alpha \sin 2\alpha}{2\sqrt{2}}. \quad (3.50)$$

Next, substituting Eq. (3.50) into Eq. (3.41), we obtain that the yield stress ratio $\sigma(\alpha)/\sigma(0)$ variation with the loading direction α in the plane (RD, TD) of the sheet is:

$$\frac{\sigma(\alpha)}{\sigma(0)} = \frac{2\left(27 - 4cn_1^2\right)^{1/6}}{\left\{\begin{array}{l}\left[12 + 9(m_2 - 1)(1 + 3\cos^2\alpha)\sin^2\alpha\right]^3 \\ -c\left[16n_1 + 54(n_1 - 3n_3 + 2n_4)\sin^4\alpha\cos^2\alpha + 18(n_3 - n_1)\sin^2\alpha(1 + 3\cos^2\alpha)\right]^2\end{array}\right\}^{1/6}} \quad (3.51)$$

It can be easily shown that extrema for $\sigma(\alpha)$ are along RD ($\alpha = 0°$) and TD ($\alpha = 90°$). If $4n_1(n_1 - n_3)c + 27(m_2 - 1) < 0$ and $4(n_1 - 9n_3)(n_1 - 7n_3 + 6n_4)c + 27(m_2 - 1)(3m_2 + 1)^2 > 0$, the minimum is along RD and the maximum along TD, and vice versa. For this Goss-textured sheet, the variation of the Lankford coefficients with the loading orientation α is given by:

$$r(\alpha) = \frac{(3\cos^2\alpha - 2)\left(\frac{\partial\bar{\sigma}}{\partial\sigma_{xx}} + \frac{\partial\bar{\sigma}}{\partial\sigma_{yy}}\right) - 2\cos^2\alpha\frac{\partial\bar{\sigma}}{\partial\sigma_{xy}} - \sqrt{2}\sin(2\alpha)\frac{\partial\bar{\sigma}}{\partial\sigma_{xz}}}{\frac{\partial\bar{\sigma}}{\partial\sigma_{xx}} + \frac{\partial\bar{\sigma}}{\partial\sigma_{yy}} + 2\frac{\partial\bar{\sigma}}{\partial\sigma_{xy}}} \quad (3.52)$$

with $\bar{\sigma}$ being the effective stress of Eq. (3.41) and the derivatives being calculated using Eq. (3.46) with $\mathbf{s}$ being the deviator of the applied stress, $\boldsymbol{\sigma}$, which in the $Oxyz$ system has the nonzero components given by Eq. (3.50). Note that since for this texture, RD is along the [001] direction of the constituent grains, it follows that irrespective of the values of the material parameters m_2, n_1, n_3, n_4, c, we have: $r(0°) = 1$. Making use of Eq. (3.52), it follows that the expressions of the Lankford coefficients along 45° and TD (90°) directions are given by:

$$r(45°) = \frac{27(15m_2 + 1)^2(9m_2 - 1) + 4c(n_1 - 27n_3 - 18n_4)}{54(15m_2 + 1)^2(3m_2 + 1) - 8c(n_1 + 9n_3 + 18n_4)(n_1 + 45n_3 + 54n_4)};$$
$$r(90°) = \frac{54(3m_2 + 1)^2 - 8c(n_1 - 9n_3)(n_1 - 3n_3)}{27(3m_2 - 1)(3m_2 + 1)^2 + 4c(n_1 - 9n_3)(n_1 + 3n_3)} \quad (3.53)$$

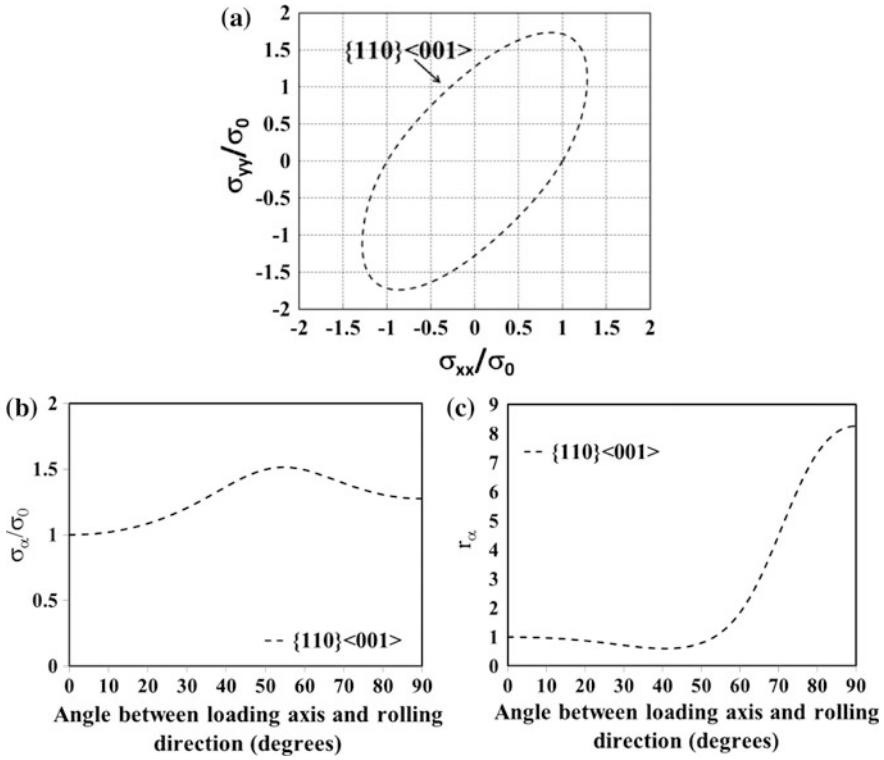

Fig. 3.34 **a** Plane-stress yield surface; **b** predicted yield stress ratios $\sigma(\alpha)/\sigma(0)$; and **c** Lankford coefficients $r(\alpha)$ versus loading direction α in the plane of a Goss-textured sheet. Single crystal material parameters: $m_2 = 0.38$, $n_1 = 0.98$, $n_3 = 0.04$, $n_4 = 0.08$, $c = 2.3$

Note that for $c = 0$, $r(90°) > 1$ if and only if $1/3 < m_2 < 1$. For $c \neq 0$, a very high value of the Lankford coefficient in the transverse direction can be obtained. As an example, for a material with $m_2 = 0.38$, $n_1 = 0.98$, $n_3 = 0.04$, $n_4 = 0.08$, $c = 2.3$, the predicted value of $r(90°) = 10.69$.

To enable analysis of the effect of the crystal orientation on the uniaxial plastic properties of this ideal Goss-textured sheet, in Fig. 3.34 are shown the theoretical plane-stress yield surface (RD-TD plane; shear stress zero), the predicted yield stress ratios, and Lankford coefficients variation with the orientation α.

3.4.1.3 Brass Texture $\{\bar{2}1\bar{1}\}\langle 011\rangle$

For an ideally textured $\{\bar{2}1\bar{1}\}\langle 011\rangle$ sheet (see Fig. 3.32d), uniaxial tension along an axis at orientation α to the rolling direction corresponds to:

$$\boldsymbol{\sigma} = \sigma(\alpha)(\mathbf{y_1} \otimes \mathbf{y_1}),\ \text{with}\ \mathbf{y_1} = \frac{\sin\alpha}{\sqrt{3}}\mathbf{e}_x + \left(\frac{\cos\alpha}{\sqrt{2}} + \frac{\sin\alpha}{\sqrt{3}}\right)\mathbf{e}_y + \left(\frac{\cos\alpha}{\sqrt{2}} - \frac{\sin\alpha}{\sqrt{3}}\right)\mathbf{e}_z \tag{3.54}$$

The applied stress tensor given by Eq. (3.54) is expressed in the crystallographic frame ($\boldsymbol{x}$, $\boldsymbol{y}$, $\boldsymbol{z}$), as:

$$\begin{aligned}
\sigma_{xx} &= \frac{\sigma_\alpha \sin^2\alpha}{3}, \sigma_{yy} = \sigma_\alpha\left(\sqrt{3}\cos\alpha + \sqrt{2}\sin\alpha\right)^2/6,\\
\sigma_{zz} &= \sigma_\alpha\left(\sqrt{3}\cos\alpha - \sqrt{2}\sin\alpha\right)^2/6,\\
\sigma_{xy} &= \sigma_\alpha \sin\alpha\left(\sqrt{3}\cos\alpha + \sqrt{2}\sin\alpha\right)/3\sqrt{2},\\
\sigma_{xz} &= \sigma_\alpha \sin\alpha\left(\sqrt{3}\cos\alpha - \sqrt{2}\sin\alpha\right)/3\sqrt{2},\\
\sigma_{yz} &= \sigma_\alpha \frac{3\cos^2\alpha - 2\sin^2\alpha}{6}.
\end{aligned} \tag{3.55}$$

The variation of the yield stress ratio $\sigma(\alpha)/\sigma(0)$ with the loading direction α in the plane of the sheet is deduced by substituting the respective stress components given by Eq. (3.55) in Eq. (3.41). When this is done the following relation is obtained:

$$\frac{\sigma(\alpha)}{\sigma(0)} = \frac{\left[(9m_2+3)^3 - 256cn_1^2\right]^{1/6}}{\left\{\begin{array}{l}\left[12 + 3(m_2-1)\left(3\cos^4\alpha + 4\sin^4\alpha\right)\right]^3 - \\ c\left[16n_1 + 2(n_1 - 3n_3 + 2n_4)(5\cos^2\alpha - 2)\sin^2\alpha + 6(n_3 - n_1)\left(3\cos^4\alpha + 4\sin^4\alpha\right)\right]^2\end{array}\right\}^{1/6}} \tag{3.56}$$

Irrespective of the values of the parameters m_2, n_1, n_3, n_4, c, there is an extremum in the yield stress variation with orientation at $\alpha = 0°$ (RD). The predicted ratio between the yield stresses along TD and RD is:

$$\frac{\sigma(90°)}{\sigma(0°)} = \frac{\left[\left(\frac{1+3m_2}{12}\right)^3 - c\left(\frac{9n_3 - n_1}{108}\right)^2\right]^{1/6}}{\left(27m_2^3 - 4cn_4^2\right)^{1/6}}$$

On the other hand,

$$\frac{\sigma(45^\circ)}{\sigma(0^\circ)} = \frac{\left[\left(\frac{1+3m_2}{12}\right)^3 - c\left(\frac{9n_3 - n_1}{108}\right)^2\right]^{1/6}}{\left[\left(\frac{9+7m_2}{48}\right)^3 - c\left(\frac{23n_1 + 39n_3 + 2n_4}{864}\right)^2\right]^{1/6}}.$$

Moreover, for the $\{\bar{2}1\bar{1}\}\langle 011\rangle$ textured sheet, the variation of the Lankford coefficients with orientation is given by:

$$r(\alpha) = \frac{1}{3\left(\frac{\partial\bar{\sigma}}{\partial\sigma_{xx}}\right) + 2\left(\frac{\partial\bar{\sigma}}{\partial\sigma_{xz}} - \frac{\partial\bar{\sigma}}{\partial\sigma_{xy}} - \frac{\partial\bar{\sigma}}{\partial\sigma_{yz}}\right)} \times \begin{bmatrix} (1 - 5\cos 2\alpha)\frac{\partial\bar{\sigma}}{\partial\sigma_{yz}} - \left(3\sin^2\alpha + \sqrt{6}\sin 2\alpha\right)\frac{\partial\bar{\sigma}}{\partial\sigma_{xx}} \\ +4\cos^2\alpha\left(\frac{\partial\bar{\sigma}}{\partial\sigma_{xy}} - \frac{\partial\bar{\sigma}}{\partial\sigma_{xz}}\right) - 2\sqrt{6}\sin 2\alpha\frac{\partial\bar{\sigma}}{\partial\sigma_{yy}} \\ -\sqrt{6}\sin 2\alpha\left(\frac{\partial\bar{\sigma}}{\partial\sigma_{xy}} + \frac{\partial\bar{\sigma}}{\partial\sigma_{xz}}\right) \end{bmatrix}, \tag{3.57}$$

where $\bar{\sigma}$ is the effective stress given by Eq. (3.41). The expression of $r(\alpha)$ depends only on the loading orientation α and the single crystal parameters m_2, n_1, n_3, n_4, c, and it is found by substituting in the expression of the derivatives of $\bar{\sigma}$ [see Eq. (3.46)] the stresses given by Eq. (3.55). In particular, the Lankford coefficient along RD is:

$$r(0^\circ) = \frac{54m_2\left(3m_2+1\right)^2 + 16cn_3(n_1 - 9n_3)}{27\left(m_2+1\right)\left(3m_2+1\right)^2 - 4c(n_1 - 9n_3)(n_1 - 5n_3)} \tag{3.58}$$

and along TD is:

$$r(90^\circ) = \frac{243m_2^3 - 4c(3n_4 - 2n_3)(2n_3 + 3n_4)}{243m_2^3 - 4c(3n_4 + 6n_3)(2n_3 + 3n_4)}. \tag{3.59}$$

Note that if the parameter $c = 0$, irrespective of the value of the parameter m_2, $r(90^\circ) = 1$. It means that with a quadratic yield criterion for the constituent crystals, the Lankford coefficient corresponding to TD for a $\{\bar{2}1\bar{1}\}\langle 011\rangle$ textured polycrystalline sheet should be necessarily equal to unity. If $c \neq 0$ and $n_3 \neq 0$, the predicted Lankford coefficient along TD is not unity, as should be the case since the mechanical response in the [100] and $[\bar{2}1\bar{1}]$ crystallographic directions is not the same. The plane-stress yield surface (RD-TD plane projection) and the predicted yield stress ratios and Lankford coefficients variation with the orientation α according to Eqs. (3.56) and (3.57), respectively, and corresponding to $m_2 = 0.38$, $n_1 = 0.98$, $n_3 = 0.04$, $n_4 = 0.08$, $c = 2.3$ are shown in Fig. 3.35.

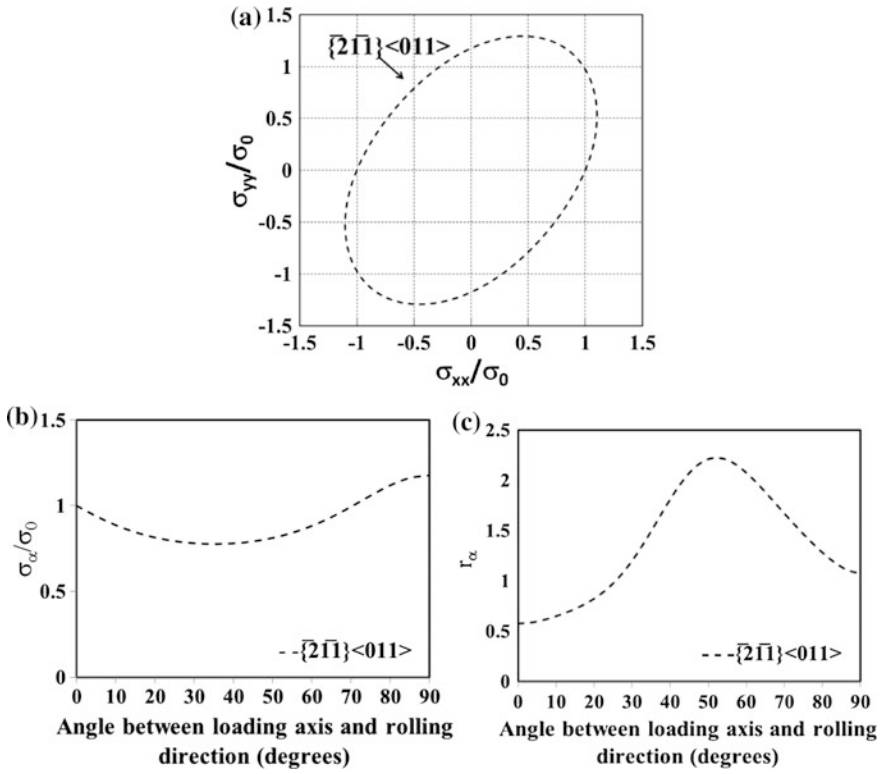

Fig. 3.35 **a** Plane-stress yield surface; **b** predicted yield stress ratios $\sigma(\alpha)/\sigma(0)$; and **c** Lankford coefficients $r(\alpha)$ versus loading direction α in the plane of the $\{\bar{2}1\bar{1}\}\langle 011\rangle$ textured sheet. Single crystal material parameters: $m_2 = 0.38$, $n_1 = 0.98$, $n_3 = 0.04$, $n_4 = 0.08$, $c = 2.3$

3.4.1.4 Copper Texture $\{112\}\langle 11\bar{1}\rangle$

For a copper $\{112\}\langle 11\bar{1}\rangle$ textured sheet (see Fig. 3.32c) under uniaxial tension along a direction at an orientation α to RD in the plane of the sheet, the stress tensor in the loading frame is:

$$\begin{aligned} &\boldsymbol{\sigma} = \sigma(\alpha)(\mathbf{z_1} \otimes \mathbf{z_1}), \\ &\text{with } \mathbf{z_1} = \left(\frac{\cos\alpha}{\sqrt{3}} - \frac{\sin\alpha}{\sqrt{2}}\right)\mathbf{e}_x + \left(\frac{\cos\alpha}{\sqrt{3}} + \frac{\sin\alpha}{\sqrt{2}}\right)\mathbf{e}_y - \frac{\cos\alpha}{\sqrt{3}}\mathbf{e}_z \end{aligned} \tag{3.60}$$

To obtain the variation of the yield stress ratio $\sigma(\alpha)/\sigma(0)$ with the loading direction α in the plane of the sheet, first, the stress tensor given by Eq. (3.60) is referred to the crystallographic frame, and then the respective components are substituted in Eq. (3.41). The following relation is obtained:

$$\frac{\sigma(\alpha)}{\sigma(0)} = \frac{2\left(27 - 4cn_1^2\right)^{1/6}}{\left\{\begin{array}{l}\left[12 + 3(m_2 - 1)\left(4\cos^4\alpha + 3\sin^4\alpha\right)\right]^3 \\ -c\left[16n_1 + 2(n_1 - 3n_3 + 2n_4)\sin^2\alpha\left(5\sin^2\alpha - 2\right) + 6(n_3 - n_1)\left(4\cos^4\alpha + 3\sin^4\alpha\right)\right]^2\end{array}\right\}^{1/6}} \tag{3.61}$$

As concerns the variation of the Lankford coefficients $r(\alpha)$ with orientation, the relation is given by:

$$r(\alpha) = \frac{1}{3\left(\frac{\partial\bar{\sigma}}{\partial\sigma_{zz}}\right) + 2\left(\frac{\partial\bar{\sigma}}{\partial\sigma_{xy}} + 2\frac{\partial\bar{\sigma}}{\partial\sigma_{xz}} + 2\frac{\partial\bar{\sigma}}{\partial\sigma_{yz}}\right)} \times \begin{bmatrix} -3\cos^2\alpha\dfrac{\partial\bar{\sigma}}{\partial\sigma_{zz}} + \sqrt{6}\sin 2\alpha\left(\dfrac{\partial\bar{\sigma}}{\partial\sigma_{xx}} - \dfrac{\partial\bar{\sigma}}{\partial\sigma_{yy}}\right) \\ -4\sin^2\alpha\left(\dfrac{\partial\bar{\sigma}}{\partial\sigma_{yz}} + \dfrac{\partial\bar{\sigma}}{\partial\sigma_{xz}}\right) + \sqrt{6}\sin 2\alpha\left(\dfrac{\partial\bar{\sigma}}{\partial\sigma_{yz}} - \dfrac{\partial\bar{\sigma}}{\partial\sigma_{xz}}\right) \\ -2(5\cos^2\alpha - 2)\dfrac{\partial\bar{\sigma}}{\partial\sigma_{xy}} \end{bmatrix} \tag{3.62}$$

In the above equation, the derivatives of $\bar{\sigma}$ are calculated using the expressions given by Eq. (3.46) and substituting for the appropriate stresses. In particular, the Lankford coefficients along RD, 45°, and TD are:

$$\begin{aligned} r(0^\circ) &= \frac{243m_2^3 - 4c(4n_3 + 3n_4)(2n_3 + 3n_4)}{243m_2^3 - 12cn_4(3n_4 + 2n_3)} \\ r(45^\circ) &= \frac{243(m_2 + 7)(7m_2 + 9)^2 - 4c(27n_1 + 47n_3 + 18n_4)(69n_1 + 121n_3 + 6n_4)}{486(3m_2 + 1)(7m_2 + 9)^2 - 8c(69n_1 + 121n_3 + 6n_4)(21n_1 + 37n_3 - 6n_4)} \\ r(90^\circ) &= \frac{54m_2(3m_2 + 1)^2}{27(3m_2 + 1)^2(m_2 + 1) - 4c(n_1 - 9n_3)^2} \end{aligned} \tag{3.63}$$

The plane-stress yield surface for the copper-textured sheet (projection in the RD-TD plane; shear stress = 0) and the predicted yield stress ratios and Lankford coefficients variation with the orientation α according to Eqs. (3.61) and (3.63), and corresponding to $m_2 = 0.38$, $n_1 = 0.98$, $n_3 = 0.04$, $n_4 = 0.08$, $c = 2.3$ are shown in Fig. 3.36.

3.4.1.5 Rotated Cube Texture $\{100\}\langle 011\rangle$

The ideal texture component $\{100\}\langle 011\rangle$ is the cube texture rotated by 45° around the normal to the sheet plane (see Fig. 3.32e). Therefore, the variation of the yield

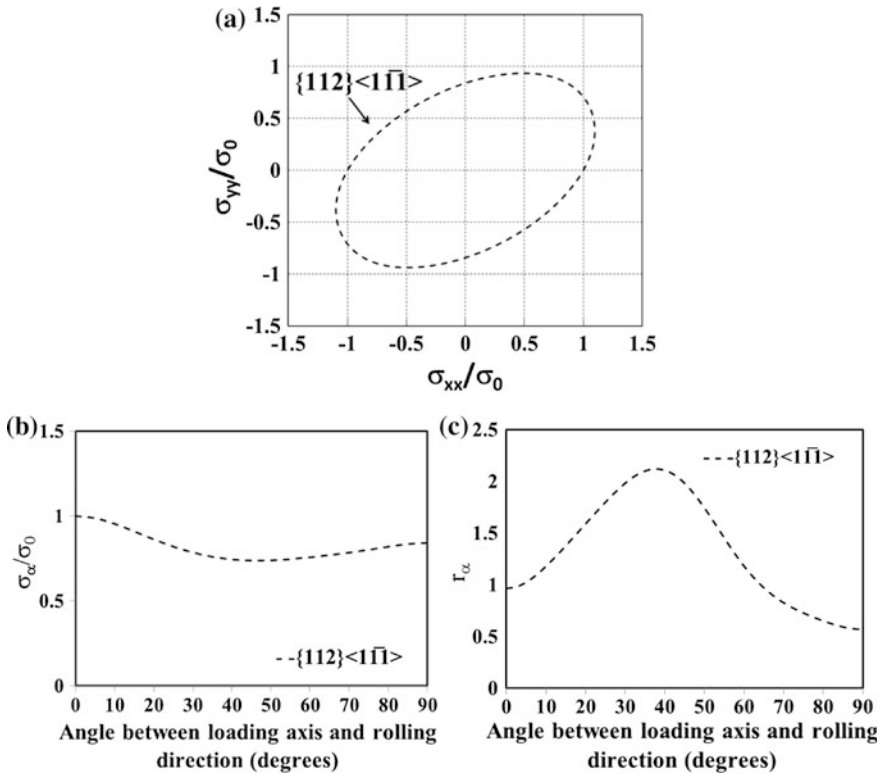

Fig. 3.36 **a** Plane-stress yield surface; **b** predicted yield stress ratios $\sigma(\alpha)/\sigma(0)$; and **c** Lankford coefficients $r(\alpha)$ versus loading direction α in the plane of the copper-textured sheet. Single crystal coefficients $m_2 = 0.38$, $n_1 = 0.98$, $n_3 = 0.04$, $n_4 = 0.08$, $c = 2.3$

stress and the Lankford coefficient with the orientation θ in the sheet plane ($\theta = 0°$ being the yield stress in the RD direction) is obtained by setting $\alpha = \theta - 45°$ in Eqs. (3.43) and (3.45), respectively. It follows that for the $\{100\}\langle 011\rangle$ textured sheet,

$$\frac{\sigma(\theta)}{\sigma(45)} = \frac{2\left(27 - 4cn_1^2\right)^{1/6}}{\left\{27[4 + 3(m_2 - 1)\cos^2 2\theta]^3 - 4c[8n_1 + 9(n_3 - n_1)\cos^2 2\theta]^2\right\}^{1/6}} \quad (3.64)$$

with

$$\sigma(0^\circ) = \sigma_{\text{cube}}(45^\circ) = \frac{\left(27 - 4cn_1^2\right)^{1/6} Y_{[100]}}{2\left[27(3m_2+1)^3 - 4c(9n_3 - n_1)^2\right]^{1/6}}$$

$$r(0^\circ) = r_{\text{cube}}(45^\circ) = \frac{27(3m_2+1)^2(3m_2-1) + 4c(n_1 - 9n_3)(n_1 + 3n_3)}{54(3m_2+1)^2 - 8c(n_1 - 9n_3)(n_1 - 3n_3)}$$

$$r(45^\circ) = 1.$$

Obviously, the same mechanical response is predicted along the RD and TD orientations, respectively. The plane-stress yield surface for the rotated cube-textured sheet and the predicted yield stress ratios and Lankford coefficients variation with the orientation α corresponding to $m_2 = 0.38$, $n_1 = 0.98$, $n_3 = 0.04$, $n_4 = 0.08$, $c = 2.3$ are shown in Fig. 3.37.

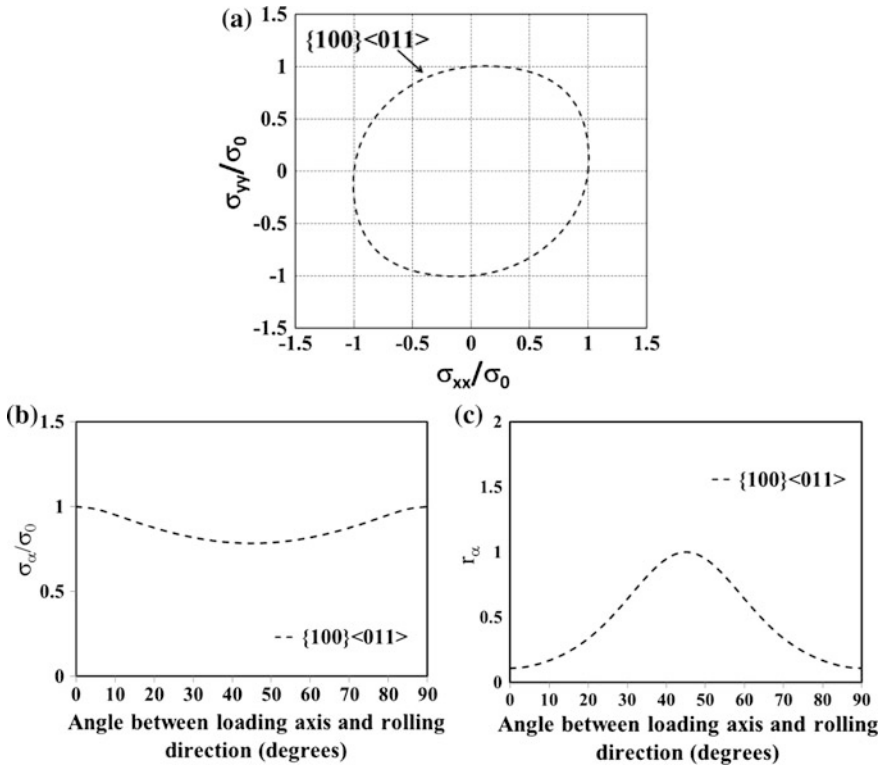

Fig. 3.37 **a** Plane-stress yield surface; **b** predicted yield stress ratios $\sigma(\alpha)/\sigma(0)$; and **c** Lankford coefficients $r(\alpha)$ versus loading direction α in the plane of the rotated cube-textured sheet. Single crystal coefficients $m_2 = 0.38$, $n_1 = 0.98$, $n_3 = 0.04$, $n_4 = 0.08$, $c = 2.3$

It is worth noting that the predicted trends in yield stresses and Lankford coefficient evolution with loading orientation for all the ideal textures shown are in good qualitative agreement with those expected for the given texture components. Moreover, finite values for the yield stresses and Lankford coefficients are predicted irrespective of the in-plane orientation considered. Most importantly, an estimate of the trends to be expected in terms of anisotropy of the plastic properties of the polycrystalline sheet can be obtained without using any numerical code.

Although the textures most commonly observed experimentally contain a spread of orientations around the ideal texture components, the estimates obtained with the analytical formulas should be useful for assessing very rapidly how the initial texture will influence the anisotropy in the macroscopic plastic flow properties. Another added advantage is that once the single crystal behavior is known, no additional calibration or macroscopic mechanical tests are needed in order to obtain an estimate of the *r*-values and yield stress anisotropy. It is also to be noted that these analytical formulas provide insights into the height profiles to be expected for full drawn cups of single crystal sheets (see also the F.E. results and discussion presented in Sect. 3.3.4).

3.4.2 *Prediction of Plastic Anisotropy of Textured Polycrystalline Sheets with Several Texture Components*

As already mentioned, experimentally, a spread is generally observed around the various ideal texture components. Furthermore, several texture components may be present. Thus, in order to describe the polycrystalline response, Chandola et al. [27] used the single crystal model of Cazacu et al. [26] and the assumption of uniform stress in each grain. Thus, the effective stress $\bar{\sigma}_{\text{poly}}$ of the polycrystalline material as a function of the applied stress tensor $\boldsymbol{\sigma}$, expressed in the loading frame, is:

$$\bar{\sigma}_{\text{poly}}(\boldsymbol{\sigma}) = \frac{1}{N}\sum_{i=1}^{N} \bar{\sigma}^{i}_{\text{grain}}\left(\mathbf{R}_i^T \boldsymbol{\sigma} \mathbf{R}_i\right), \tag{3.65}$$

with N being the number of grains considered in the polycrystalline material, $\bar{\sigma}^{i}_{\text{grain}}$ is the effective stress associated with the single crystal criterion computed for any given grain i using Eq. (3.41), and $\mathbf{R}_i$ is the transformation matrix for passage from the crystal axes of the grain i to the loading frame axes. The plastic strain-rate deviator $\mathbf{d}^p$ of the polycrystalline material, expressed in the loading frame, is:

$$\mathbf{d}^p = \frac{\dot{\lambda}}{N}\sum_{i=1}^{n} \mathbf{R}_i \frac{\partial \bar{\sigma}^{i}_{\text{grain}}\left(\mathbf{R}_i^T \boldsymbol{\sigma} \mathbf{R}_i\right)}{\partial\left(\mathbf{R}_i^T \boldsymbol{\sigma} \mathbf{R}_i\right)} \mathbf{R}_i^T \tag{3.66}$$

The predictive capabilities of the polycrystal model given by Eqs. (3.65) and (3.66) were used to predict the anisotropy of the plastic flow properties in uniaxial tension of textured steel sheets (see [27]).

In the following, this polycrystalline model will be used to investigate the influence of the effect of the spread about ideal texture components.

3.4.2.1 Effect of the Spread About Ideal Textures on the Uniaxial Plastic Properties

The polycrystalline model given by Eqs. (3.65) and (3.66) is used to predict the plastic properties of strongly textured sheets containing a spread about the ideal texture components. These predictions are also compared to the model predictions for ideal texture components obtained with the analytical formulas given in Sect. 3.4.1. For this purpose, following Lequeu et al. [67], a rotationally symmetric Gaussian distribution of misorientations ω_0 about a given ideal orientation is considered. The rotation angle ω for the spread is specified as:

$$p(\omega) = p(0)\exp\left(-\frac{1}{2}\omega^2/\omega_0^2\right), \tag{3.67}$$

Cube-textured sheets

For polycrystalline sheets with textures of scatter widths of $\omega_0 = 25°$ and $\omega_0 = 35°$ from the ideal $\{100\}\langle 001\rangle$ cube texture (see Fig. 3.38 for the (111) pole figures of the textures considered), simulation results obtained using the polycrystal model Eqs. (3.65) and (3.66) for samples of 400 crystals are presented in Fig. 3.39. On this figure are also superposed the predictions for the ideal cube texture ($\omega_0 = 0°$)

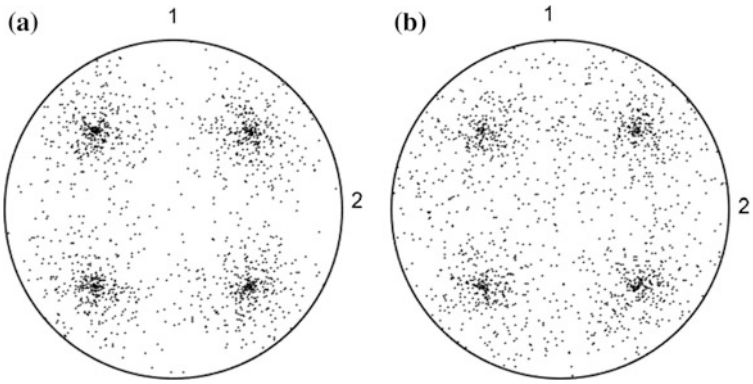

Fig. 3.38 (111) pole figures for $\{100\}\langle 001\rangle$ texture corresponding to a series of Gaussian distributions of increasing scatter width: **a** $\omega_0 = 25°$ and **b** $\omega_0 = 35°$

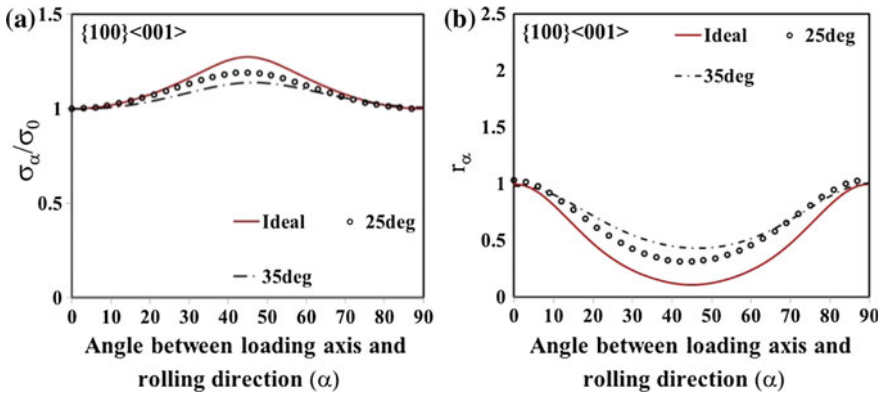

Fig. 3.39 Numerical simulations, using Chandola et al. [27] model, of the anisotropy in **a** yield stress ratio $\sigma(\alpha)$ and **b** strain-ratio $r(\alpha)$ in the plane of the $\{100\}\langle 001\rangle$ textured polycrystalline sheet. The textures for different scatter width ω_0 are shown in Fig. 3.38. The results for ideal texture were obtained with the analytical formulas [Eqs. (3.43)–(3.45)], respectively

obtained with the analytical formulas [Eqs. (3.43)–(3.45)] for the same values of the parameters describing the constituent grain behavior, $m_2 = 0.38$, $n_1 = 0.98$, $n_3 = 0.04$, $n_4 = 0.08$, $c = 2.3$. Note that irrespective of the scatter width ω_0 about the ideal texture both the predicted macroscopic yield stresses and r-values vary smoothly with the loading orientation (see Fig. 3.39). Additionally, irrespective of the scatter width, for the given values of the parameters characterizing the grains behavior, minima in yield stresses are along the 0° and 90° orientations and there is only one minimum which corresponds to uniaxial loading at 45° in-plane direction. Also, note that for the rotationally symmetric Gaussian distribution of misorientations with $\omega_0 = 25°$ and $\omega_0 = 35°$, the directional dependence of the macroscopic plastic properties in the plane of the sheet is similar to that predicted analytically for an ideal texture ($\omega_0 = 0°$), but the anisotropy is less pronounced. As already mentioned, for an ideal ($\omega_0 = 0°$) $\{100\}\langle 001\rangle$ texture, the yield stress variation with the loading orientation according to the Taylor-Bishop-Hill model displays two cusps, while the Lankford coefficients are not defined for the 0° and 90° tensile loadings (e.g., see [67]); i.e., $r(0°)$ and $r(90°)$ have infinite values. Additionally, with TBH model, only when the texture is characterized by a larger spread, the predicted variation in both the macroscopic yield stresses and Lankford coefficients is smooth.

Goss texture

The effect of the spread ω_0 with respect to the ideal Goss texture on the directional dependence of the same macroscopic properties (yield stresses, plastic strain ratios) simulated with the polycrystalline model is shown in Fig. 3.41. Note that for the ideal Goss texture ($\omega_0 = 0°$) the results were obtained using the analytical formulas [see Eqs. (3.51) and (3.52)]. For the texture obtained from rotationally symmetric Gaussian distribution of misorientation with ω_0 up to 35° (see Fig. 3.40 for the

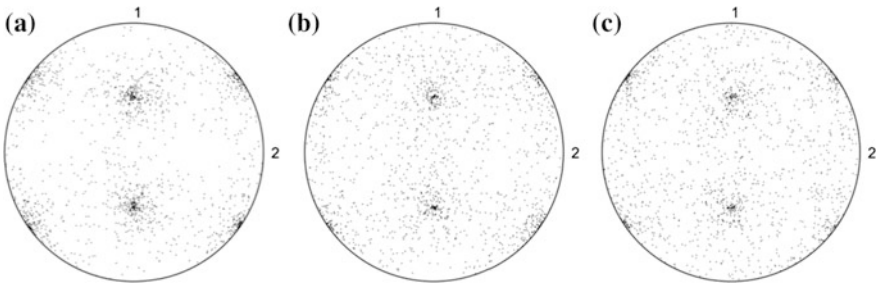

Fig. 3.40 (111) pole figures for $\{110\}\langle 001\rangle$ texture considered in the simulations corresponding to a series of Gaussian distributions of increasing scatter width: **a** $\omega_0 = 25°$, **b** $\omega_0 = 35°$, **c** $\omega_0 = 45°$

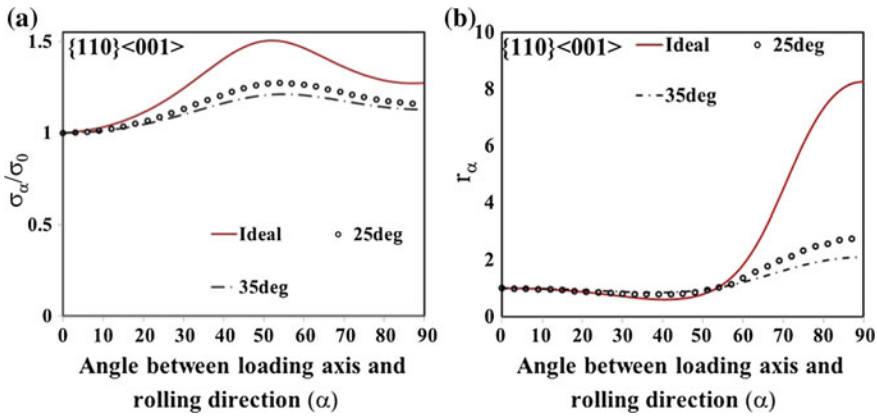

Fig. 3.41 Numerical simulation results using the polycrystal model [Eqs. (3.65) and (3.66)]: **a** yield stress ratio $\sigma(\alpha)$ and **b** strain-ratio $r(\alpha)$ variation with the orientation α in the plane of the $\{110\}\langle 001\rangle$ textured polycrystalline sheets of various scatter width. The results for ideal texture were obtained with the analytical formulas [Eqs. (3.51) and (3.52)], respectively

respective (111) pole figures), the anisotropy in $\sigma(\alpha)/\sigma(0)$ versus α and $r(\alpha)$ versus α variations is much less pronounced than the respective curves for the ideal Goss texture. For example, for $\omega_0 = 35°$, the value of $r(90°)$ is about five times smaller than that for ($\omega_0 = 0$). Nevertheless, the nature of the $r(\alpha)$ variation is similar irrespective of the spread, with a point of inflection at around 55° from the reference direction (see Fig. 3.41).

It is also worth noting that the use of this polycrystalline model leads to finite values for the Lankford coefficients irrespective of the in-plane loading direction. This is not the case if the TBH model is applied. It is well documented (e.g., see [8]) that in order to obtain a smooth variation in r-values with the TBH model, in the polycrystalline sample a large percentage of the grains should be taken with random orientations. For example, by considering as much as 50% of the total volume

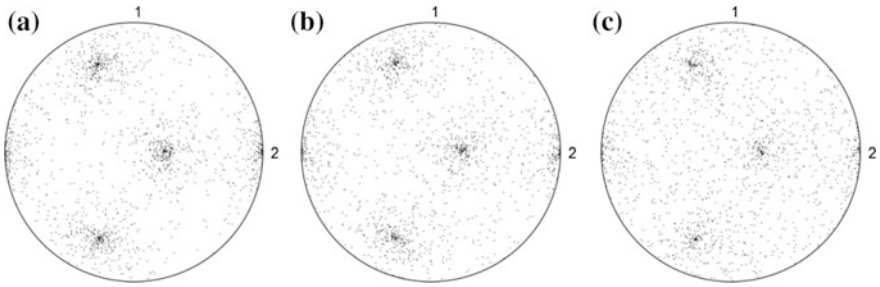

Fig. 3.42 (111) pole figures for $\{\bar{2}1\bar{1}\}\langle 011\rangle$ texture corresponding to a series of Gaussian distributions of increasing scatter width: **a** $\omega_0 = 25°$, **b** $\omega_0 = 35°$ and **c** $\omega_0 = 45°$

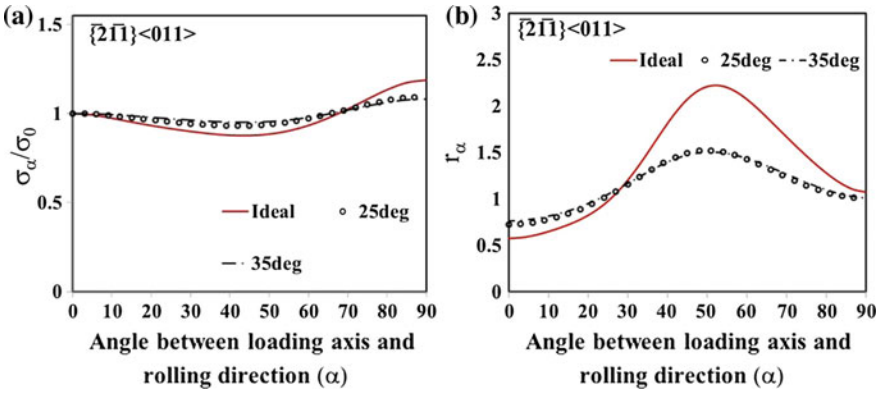

Fig. 3.43 Numerical simulations using the polycrystalline model [Eqs. (3.65) and (3.66)]: **a** anisotropy in yield stress ratio $\sigma(\alpha)$ and **b** anisotropy of strain-ratios $r(\alpha)$ in the plane of the $\{\bar{2}1\bar{1}\}\langle 011\rangle$ textured polycrystalline sheets of different scatter width ω_0 in comparison with the predictions for ideal texture $\omega_0 = 0$ based on the analytical formulas [Eqs. (3.55) and (3.57)]

fraction of grains having isotropic orientations and 50% having almost ideal texture (i.e., ω_0 very small $\sim 5°$), Barlat and Richmond [8] obtained a smooth variation of the r-values with loading direction. However, the predicted $r(\alpha)$ versus α curve has a vertical asymptote at $\alpha \approx 70°$. As concerns the predictions of the Cazacu et al. [26] in terms of yield stress anisotropy, the absolute maximum in yield stresses is at a loading orientation of about 55°. Note that this holds true for both the ideal Goss texture and for rotationally symmetric texture with scatter widths of $\omega_0 = 25°$ and $\omega_0 = 35°$ about the ideal Goss orientation.

$\{\bar{2}1\bar{1}\}\langle 011\rangle$ *Texture*

For strongly $\{\bar{2}1\bar{1}\}\langle 011\rangle$ (brass) textured polycrystalline sheets for the given set of numerical values of the single crystal parameters, the predicted variation obtained with the polycrystalline model is shown in Fig. 3.43. For textures with spreads

$\omega_0 = 25°$ and $\omega_0 = 35°$ (see Fig. 3.42 for the (111) pole figures), the trends in the directional dependence of the macroscopic plastic properties are similar to the ideal orientation case obtained with the analytical formulas [see Eqs. (3.55) and (3.57), respectively]. Irrespective of the spread, the maximum value for the Lankford coefficients is obtained in uniaxial tension at an orientation $\alpha \sim 50°$ from the reference direction while the maximum uniaxial yield stress is at $\alpha = 90°$.

Copper texture

In Fig. 3.45 are shown the predicted macroscopic mechanical properties in uniaxial tension for the material with ideal texture calculated using the analytical formulas [Eqs. (3.61) and (3.62)] and the polycrystalline simulation results obtained with the polycrystalline model [Eqs. (3.65) and (3.66)] for the textures corresponding to Gaussian distributions of scatter width of $\omega_0 = 25°$ and 35° with respect to the ideal $\{112\}\langle 11\bar{1}\rangle$ copper texture (see Fig. 3.44 for the (111) pole figures of these textures). First, let us note that for $\omega_0 = 25°$ and $\omega_0 = 35°$, a very moderate anisotropy in yield stresses is predicted, the variation of the yield stresses with the loading orientation being almost the same, with a minimum at $\alpha \sim 45°$ loading orientation, and a maximum at $\alpha = 0°$. As concerns the predicted anisotropy in Lankford coefficients (see Fig. 3.45b) irrespective of ω_0 the trends are the same, the anisotropy becoming less pronounced as the width spread ω_0 increases.

In summary, irrespective of the texture component considered, the analytical formulas provide a very good estimate of the trend in anisotropy in macroscopic plastic properties. Next, using the Cazacu et al. [26] yield criterion for the description of the plastic behavior of the constituent grains, it is investigated the predicted mechanical response of strongly textured polycrystalline materials containing various combinations of ideal texture components.

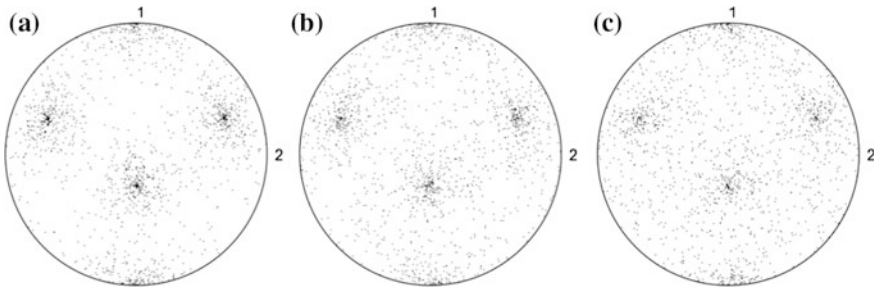

Fig. 3.44 (111) pole figures for $\{112\}\langle 11\bar{1}\rangle$ texture corresponding to a series of Gaussian distributions of increasing scatter width: **a** $\omega_0 = 25°$, **b** $\omega_0 = 35°$ and **c** $\omega_0 = 45°$

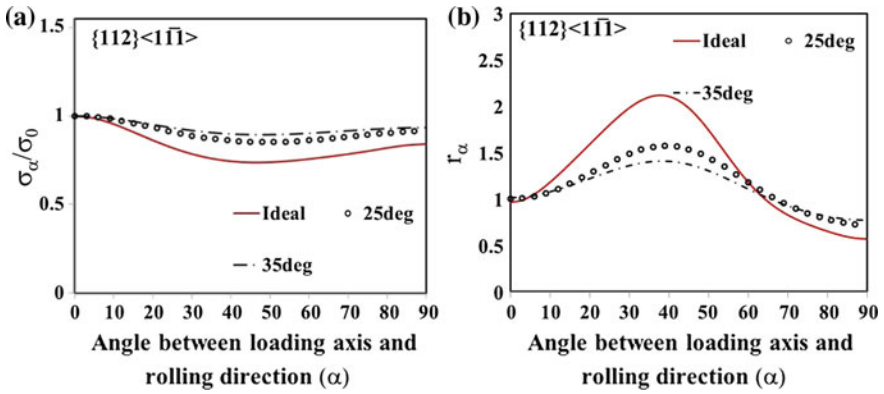

Fig. 3.45 Numerical simulations, using the polycrystal model [Eqs. (3.65) and (3.66)] of the anisotropy in: **a** yield stress ratio $\sigma(\alpha)$; **b** strain-ratio $r(\alpha)$ in the plane of the $\{112\}\langle 11\bar{1}\rangle$ textured polycrystalline sheet. The textures for different scatter width ω_0 are shown in Fig. 3.44. The results for ideal texture were obtained with the analytical formulas Eqs. (3.61) and (3.62), respectively

3.4.2.2 Predictions of Anisotropy of Yield Stresses and Lankford Coefficients for Textured Sheets

Let us first consider a polycrystalline sheet with components spread around the $\{100\}\langle 001\rangle$ (80% volume fraction) and $\{110\}\langle 001\rangle$ (20% volume fraction) ideal orientation, respectively. The texture of the polycrystalline sheet is shown in Fig. 3.46. The results of numerical simulations using the polycrystalline model [Eqs. (3.65) and (3.66)] are compared with the macroscopic yield stress and plastic

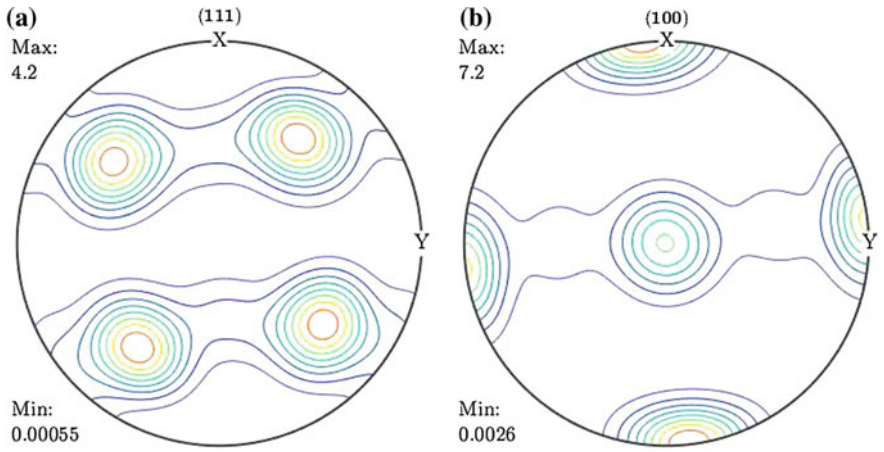

Fig. 3.46 Pole figures for a sheet with mixture of $\{100\}\langle 001\rangle$ component (80%) and $\{110\}\langle 001\rangle$ component (20%). **a** (111). **b** (100)

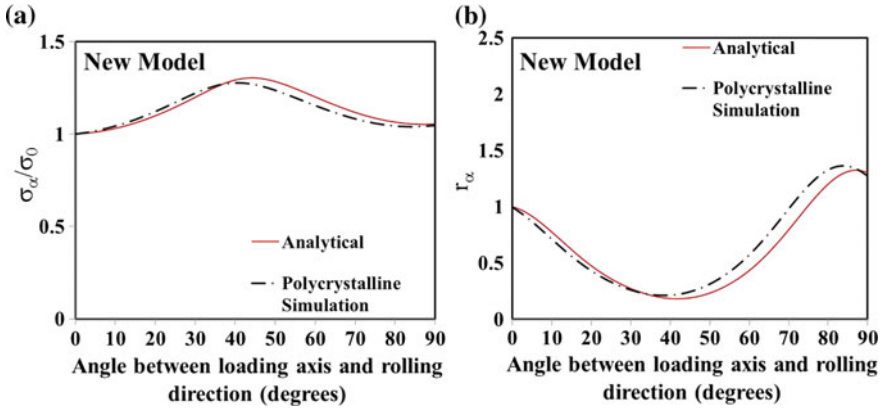

Fig. 3.47 Numerical simulations of anisotropy in **a** yield stress ratio and **b** strain-ratio in the plane of the polycrystalline sheet predicted by the polycrystal model [Eqs. (3.65) and (3.66)] for a strongly textured polycrystal with components spread around the $\{100\}\langle 001\rangle$ (80%) and $\{110\}\langle 001\rangle$ (20%) orientation. The texture is shown in Fig. 3.46

strain ratios obtained by using the analytical formulas for $\{100\}\langle 001\rangle$ [Eqs. (3.43)–(3.45)] and $\{110\}\langle 001\rangle$ ideal textures [Eqs. (3.51) and (3.52)] in conjunction with simple laws of mixtures (Fig. 3.47).

Note that the analytical estimates are very close to the numerical polycrystalline simulations results obtained using the same criterion (i.e., [26]) for the description of the plastic behavior of the constituent grains. The shapes of both the $\sigma(\alpha)/\sigma(0)$ and $r(\alpha)$ curves are similar to those corresponding to the cube texture (compare Fig. 3.47 with Fig. 3.33). However, the presence of the Goss component (20% volume fraction) results in $r(90^\circ)$ larger than $r(0^\circ)$, and the minimum r-value is slightly larger than in the case of the ideal cube texture. Specifically, for the given values of the coefficients characterizing the behavior of the constituents grains, $r(90^\circ) = 1.27 > r(0^\circ) = 1$ and the minimum r-value corresponds to $\alpha = 39^\circ$. Note also that $r(39^\circ) = 0.21$, whereas the minimum r-value for an ideal cube texture is $r(45^\circ) = 0.1$ (see Fig. 3.33b); the minimum value is almost double that of an ideal cube texture.

For a polycrystalline sheet with texture containing copper and Goss components in the same proportion (see pole figures in Fig. 3.48), the results of the polycrystalline numerical simulations and analytical estimates obtained using the formulas for each ideal texture component in conjunction with laws of mixtures are shown in Fig. 3.49. Note that the analytical predictions are very close to the numerical predictions.

It is interesting to note that the predicted $\sigma(\alpha)/\sigma(0)$ curve is almost flat indicating little variation in yield stresses for loading orientation α between 0° and 20°, the anisotropy becoming slightly more pronounced for loading directions between 20° and 70°, with a peak in yield stress around 50°, and very little difference between yield stresses for loadings between 70° and 90°. While the shape of the

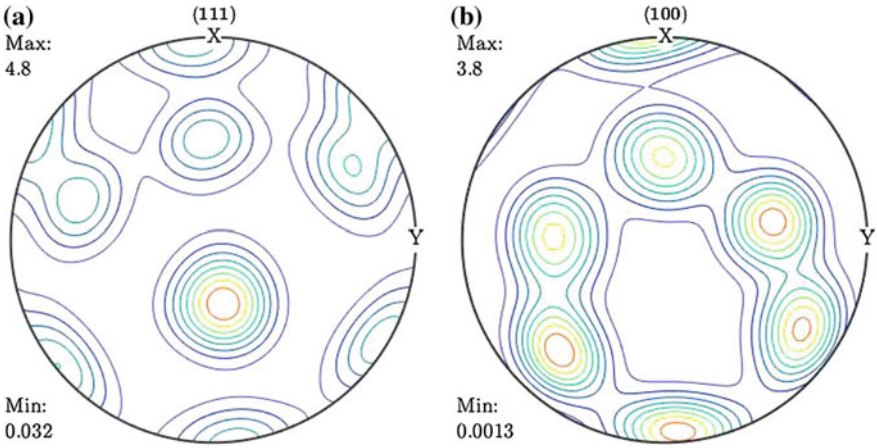

Fig. 3.48 Pole figures for a sheet with mixture of $\{112\}\langle 11\bar{1}\rangle$ component (50%) and $\{110\}\langle 001\rangle$ component (50%). **a** (111). **b** (100)

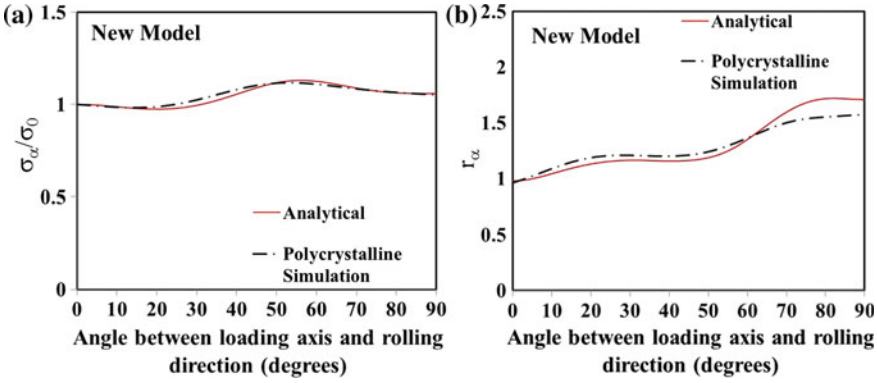

Fig. 3.49 Numerical simulations of anisotropy in **a** yield stress ratio and **b** strain-ratio in the plane of the polycrystalline sheet predicted by the polycrystal model [Eqs. (3.65) and (3.66)] for a strongly textured polycrystal with components spread around the $\{112\}\langle 11\bar{1}\rangle$ (50%) and $\{110\}\langle 001\rangle$ (50%) orientation. The texture is shown in Fig. 3.48

$\sigma(\alpha)/\sigma(0)$ curve is concave down thus closer to that of the ideal Goss component (see also Fig. 3.34a), the anisotropy is much less pronounced and similar to that of the ideal copper component (compare with Fig. 3.36). It is interesting to note that $r(0^\circ) = 1$ as it is the case for an ideal Goss component, and in the $r(\alpha)$ versus α curve, there is an inflexion point between 40° and 50°, also observed in the *r*-value variation for the ideal Goss component (see Fig. 3.34b). However, the *r*-value predicted for tensile loading at $\alpha = 90^\circ$ is much lower. The presence of the copper

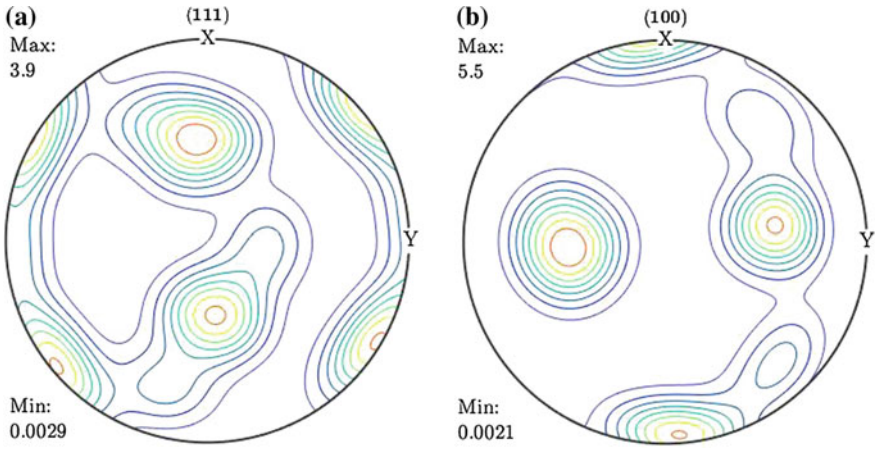

Fig. 3.50 Pole figures for a sheet with mixture of $\{\bar{2}1\bar{1}\}\langle 011\rangle$ component (30%) and $\{110\}\langle 001\rangle$ component (70%). **a** (111). **b** (100)

component in the texture lowers the $r(90^\circ)$ value from about $r(90^\circ) \sim 8$, in the case of an ideal Goss component (see Fig. 3.34b) to $r(90^\circ) = 1.57$.

Next, we consider a polycrystalline sheet with texture shown in Fig. 3.50. While the dominant texture component (70% volume fraction) has a spread about $\{110\}\langle 001\rangle$ Goss texture, this texture also contains a component with a spread about $\{\bar{2}1\bar{1}\}\langle 011\rangle$ (30% volume fraction). Figure 3.51 presents the predicted evolution of the macroscopic yield stresses and plastic strain ratios for this material

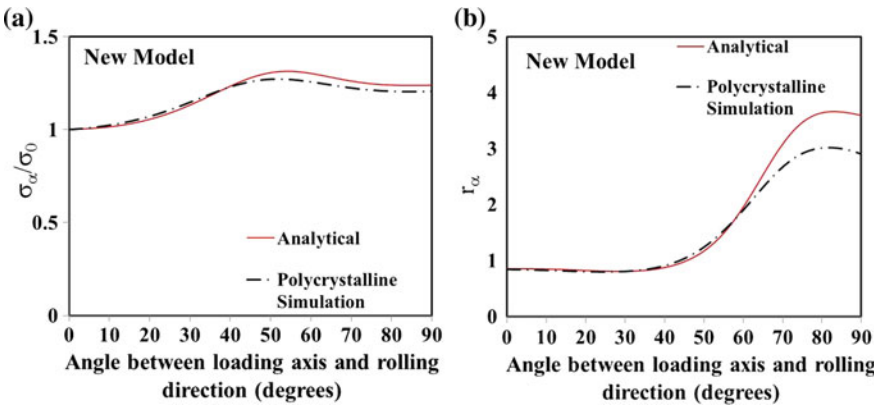

Fig. 3.51 Numerical simulations of anisotropy in **a** yield stress ratio and **b** strain-ratio in the plane of the polycrystalline sheet predicted by the polycrystal model [Eqs. (3.65) and (3.66)] for a strongly textured polycrystal with components spread around the $\{\bar{2}1\bar{1}\}\langle 011\rangle$ (30%) and $\{110\}\langle 001\rangle$ (70%) orientation. The texture is shown in Fig. 3.50

obtained on the basis of the same yield criterion for the constituent grains, i.e., the analytical estimate (based on the analytical formulas for each ideal component present in the texture) and the results of polycrystalline simulations.

The analytical $\sigma(\alpha)/\sigma(0)$ versus α variation is very close to the numerical one. The analytical $r(\alpha)$ versus α and the polycrystalline simulation results are similar with $r(0^\circ) = 1$, very little variation in r-values for loading orientations α between 0° and 40°, an inflection point at $\alpha \sim 45^\circ$ and a sharp upward trend as in the case of the ideal Goss component. Let us also recall that the point of inflection is at $\alpha = 39^\circ$ for an ideal Goss texture.

It is to be noted that although analytically a higher r-value is predicted in the transverse direction ($\alpha = 90^\circ$) than the numerically predicted value, the analytical estimate captures the influence of the $\{\bar{2}1\bar{1}\}\langle 011\rangle$ component. Namely, it predicts that the $\{\bar{2}1\bar{1}\}\langle 011\rangle$ component contributes to a significant decrease in anisotropy of the material. For example, the predicted r-value in the transverse direction is significantly lower than that predicted for the ideal Goss component (compare Fig. 3.51b with Fig. 3.34b).

3.4.2.3 Applications to Polycrystalline Al and Steel Sheets

Chandola et al. [27] reported applications to the description of plastic anisotropy of steel sheets of the polycrystalline model given by Eqs. (3.65) and (3.66), each crystal being modeled using the Cazacu et al. [26] yield criterion. Therefore, the only parameters involved in the polycrystalline model are those characterizing the plastic behavior of the constituent crystals, i.e., m_2, n_1, n_3, n_4 and c (see Eq. 3.41).

The first example presented concerns a cold rolled-annealed low-carbon steel sheet. The model parameters were identified using as input the room-temperature yield stress data on single crystal Fe–3.25% Si for different crystallographic directions in the plane of normal $\langle 100\rangle$, reported by Hull [53] in conjunction with Eq. (3.41). These numerical values are: $m_2 = 0.41$, $n_1 = 1.13$, $n_3 = 0.03$, $n_4 = 0.11$, $c = 1.85$. The texture and plastic strain-rate ratios obtained from tension tests on samples taken in the longitudinal (RD), diagonal (45°), and transverse direction (TD) of the sheet were reported in Elias et al. [34]. The texture measurements indicate that the sheet displays two dominant texture components: $\{111\}\langle 11\bar{2}\rangle$ and $\{100\}\langle 011\rangle$. A set of 400 grains was considered in the simulations. The distribution of orientations was weighted according to the intensity of the poles observed experimentally. Specifically, the contributions of pole areas of random intensity were neglected, and it was assumed that half of the crystals have $\{111\}\langle 11\bar{2}\rangle$ orientation and half have $\{100\}\langle 011\rangle$ orientation. Comparison between the model predictions and the r-values determined from the respective tension tests is shown in Fig. 3.52. The simulated results show a smooth variation with the in-plane orientation, with a peak at 45° to the rolling direction.

The polycrystalline model was also applied to the description of the plastic anisotropy of the in-plane tensile properties of a steel sheet for which the

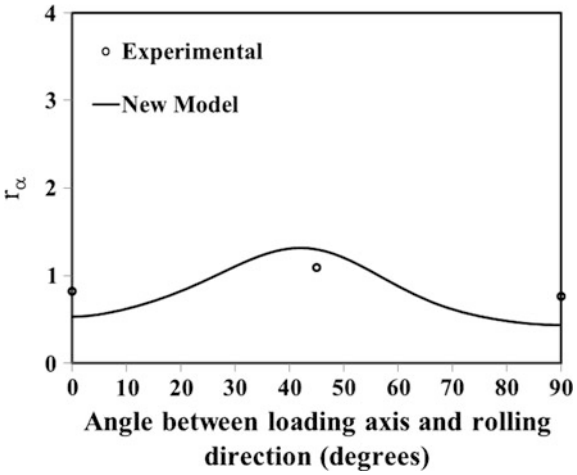

Fig. 3.52 Comparison between experimental and predicted variation of Lankford coefficients $r(\alpha)$ with the angle α between the tensile loading axis and the rolling direction using the polycrystalline model [Eqs. (3.65) and (3.66)]

experimental r-values and yield stresses in several in-plane orientations were obtained by Ito et al. [57]. As concerns the texture, no pole figure data were available, only the information given by Lequeu et al. [67] which states that the $\{100\}\langle 011\rangle$ Goss component is dominant (>70% volume fraction) and that the $\{\bar{2}1\bar{1}\}\langle 011\rangle$ component is also present (volume fraction > 20%). Thus, for this material, in the simulation it was considered the following distribution of grain orientations: 70% Goss and 30% brass ($\{\bar{2}1\bar{1}\}\langle 011\rangle$). The predicted yield stress anisotropy, shown in Fig. 3.53a, indicates a gradual rise in yield stresses as the test direction α deviates from the rolling direction, with a peak between 50° and 60°, followed by a gradual decrease, with a local minimum corresponding to the transverse direction. Note the excellent agreement between experimental (symbols) and predicted yield stresses (solid line). As concerns the simulated anisotropy in r-values, it is predicted that the Lankford coefficient in the rolling direction $r(0^\circ)$ is slightly less than unity (recall $r(0^\circ) = 1$ for ideal Goss texture), and that there is very little difference in r-values for loading orientations α between 0° and 35°. The predicted $r(\alpha)$ versus α curve has an inflection point at $\alpha \sim 35^\circ$, followed by a sharp increase (see Fig. 3.53b). Note the close agreement between the measured and predicted experimental results. In Fig. 3.34 are plotted the directional dependence of the plastic properties for an ideal Goss texture obtained with the analytical expressions and the same set of values of the single crystal parameters m_2, n_1, n_3, n_4, and c. Note that for the material with 70% volume fraction of the grains having Goss texture, the general trends in macroscopic plastic anisotropy are similar to those of an ideally textured Goss material, but the degree of anisotropy in r-values is significantly reduced (compare Fig. 3.53 with Fig. 3.34 for an ideal Goss texture).

Next, the same polycrystalline model is applied to Al sheets. The first example concerns a 10 pct. rolled-annealed Al sheet (data after Svensson [97]) for which it was reported that 60% of the total volume fraction of grains have random orientations, while 40% have $\{100\}\langle 001\rangle$ orientation. Simulation results of the variation

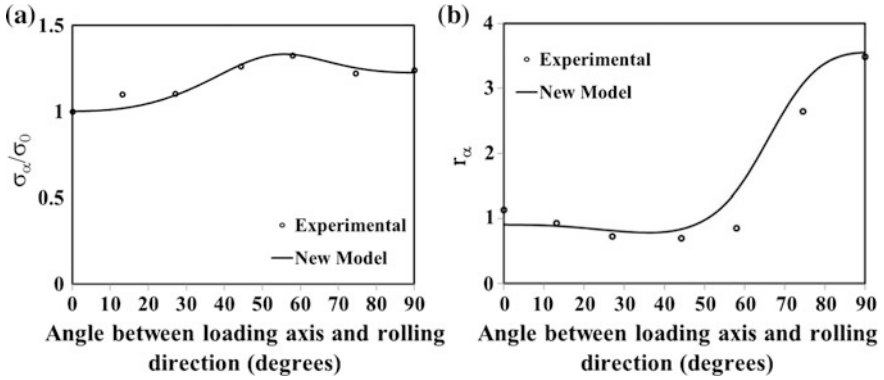

Fig. 3.53 **a** Simulated in-plane anisotropy of the yield stress ratio; **b** Lankford coefficients with the orientation α between the loading axis and the rolling direction of a steel sheet in comparison with mechanical test data of Ito et al. [57]

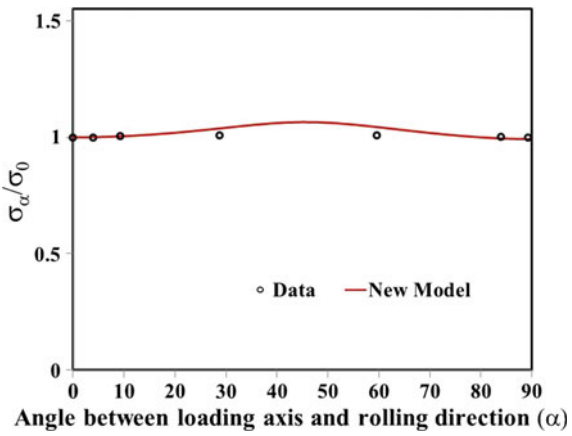

Fig. 3.54 Comparison between the experimental yield stress ratio in the plane of a annealed polycrystalline Al sheet and the numerical simulations using the polycrystal model. Data after Svensson [98]

in yield stresses with the orientation of the tensile loading direction are shown in Fig. 3.54. The numerical values for the single crystal coefficients used are: $m_2 = 0.38$, $n_1 = 0.98$, $n_3 = 0.04$, $n_4 = 0.08$, $c = 2.3$. The polycrystalline model predicts a smooth variation with the in-plane orientation, with a peak at 45° to the rolling direction (characteristic of the ideal cube texture, compared with Fig. 3.33a). However, the presence of the random texture component contributes to a significant decrease in anisotropy. The simulations results agree well with the available data.

Another example concerns a AA 2024-T3 sheet (data after Barlat et al. [7]). Figure 3.55 shows the (111) pole figure with 1000 discretized crystallite orientations while in Fig. 3.56 is presented a comparison between the experimental and predicted variation of the Lankford coefficients with the tensile loading orientation obtained using the polycrystalline model given by Eqs. (3.65) and (3.66) with the

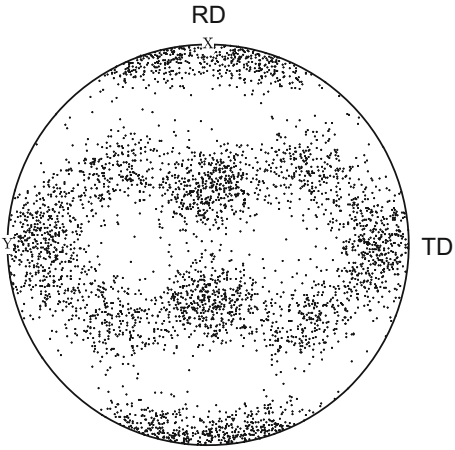

Fig. 3.55 (111) pole figure of a cold rolled AA 2024-T3 (after data reported in Barlat et al. [7])

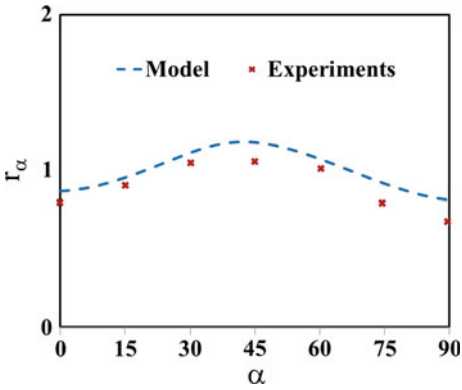

Fig. 3.56 Comparison of experimental and predicted variation of r-values with α according to **a** polycrystalline model [Eqs. (3.65) and (3.66)], **b** experiments [7]

same values for the m_2, n_1, n_3, n_4, c as in the previous example (i.e., $m_2 = 0.38$, $n_1 = 0.98$, $n_3 = 0.04$, $n_4 = 0.08$, $c = 2.3$). Note that the predictions using the polycrystalline model are in good quantitative agreement with the experimental r-values.

In summary, it can be concluded that using the single crystal model of Cazacu et al. [26] for the description of the individual constituent grains, the effect of texture on r-values and consequently formability is reasonably described. The added advantage is that for ideal texture components, analytical formulas for the variation of the macroscopic yield stress and Lankford coefficients with the in-plane loading direction exist. For the case of strongly textured materials with a distribution of grain orientations with various spreads about the ideal texture components, irrespective of the number of grains in the sample, Lankford coefficients have finite values for all loading orientations even for ideal texture components; i.e., there is no need to add random texture components to gauge the plastic properties of the polycrystal. Moreover, for textured materials with rotationally symmetric grain orientations spread around one ideal texture component $\omega_0 \leq 35°$, the

simulation results obtained with samples of 400 grains show that the anisotropy in plastic properties is much less pronounced but still similar in nature to those obtained analytically for ideal orientations. Irrespective of the texture component considered, the analytical formulas provide a good estimate of the in-plane anisotropy and its trends at a very low calculation cost.

When more than one ideal texture component exists in the material, polycrystalline simulations based on the new description of the plastic behavior of the constituent grains capture the influence of individual texture components on the overall plastic anisotropy of the polycrystal. Additionally, it was shown that the use of the analytical formulas for each ideal component in conjunction with laws of mixtures provides an adequate estimate of the in-plane anisotropy. The analytical estimates show the same trends as the simulation results in terms of both yield stress ratio and *r*-value variation. Therefore, the trends in plastic anisotropy of the macroscopic properties and most importantly how the predominant texture components affect the deformation can be adequately estimated analytically using the approach presented. Finally, the good agreement between the experimental and theoretical predictions of the anisotropy in *r*-values obtained with the polycrystalline model for AA 2024-T3 demonstrates the predictive capabilities of the model.

References

1. Anand L, Balasubramanian S (1996) Polycrystal plasticity: application to earing in cup drawing. CIRP Ann Manuf Technol 45:263–268
2. Anderson E, Jillson D, Dunbar S (1953) Deformation mechanisms in alpha titanium. Trans AIME 197:1191
3. Arminjon M (1991) A regular form of the Schmid law. Application to the ambiguity problem. Texture Stress Microstruct 14:1121–1128
4. Asaro RJ (1983) Micromechanics of crystals and polycrystals. Adv Appl Mech 23:1–115
5. Asaro RJ, Needleman A (1985) Overview no. 42. Texture development and strain hardening in rate dependent polycrystals. Acta Metall 33:923–953
6. Banabic D, Barlat F, Cazacu O, Kuwabara T (2007) Anisotropy and formability, Advances in material forming-ESAFORM 10 years on. Springer, Berlin
7. Barlat F, Lege DJ, Brem JC (1991) A six-component yield function for anisotropic materials. Int J Plast 7:693–712
8. Barlat F, Richmond O (1987) Prediction of tricomponent plane stress yield surfaces and associated flow and failure behavior of strongly textured f.c.c. polycrystalline sheets. Mater Sci Eng 95:15–29
9. Barros PD, Neto DM, Alves JL, Oliveira MC, Menezes LF (2015) DD3IMP, 3D fully implicit finite element solver: implementation of CB2001 yield criterion. Rom J Tech Sci Appl Mech 60:105–136
10. Becker R, Smelser R, Panchanadeeswaran S (1993) Simulations of earing in aluminum single crystals and polycrystals. Model Simul Mater Sci Eng 1:203
11. Berveiller M, Zaoui A (1978) An extension of the self-consistent scheme to plastically-flowing polycrystals. J Mech Phys Solids 26:325–344
12. Bevis M, Crocker A (1969) Twinning modes in lattices. Proc R Soc Lond A 313(1515): 509–529

13. Bishop J, Hill R (1951) CXXVIII. A theoretical derivation of the plastic properties of a polycrystalline face-centred metal. Lond Edinb Dublin Philos Mag J Sci 42:1298–1307
14. Blewitt T, Coltman R, Redman J (1957) Low-temperature deformation of copper single crystals. J Appl Phys 28:651–660
15. Bravais A (1849) Mémoire sur les polyèdres de forme symétrique. J Mathématiques Pures Appliquées 141–180
16. Budiansky B, Mangasarian OL (1960) Plastic stress concentration at a circular hole in an infinite sheet subjected to equal biaxial tension. J Appl Mech 27:59–64
17. Budiansky B, Wu TT (1962) Theoretical prediction of plastic strains of polycrystals. In: Proceedings of the US National Congress of Applied Mechanics, ASME. pp 1175–1185
18. Cai W, Bulatov VV, Chang J, Li J, Yip S (2004) Dislocation core effects on mobility. Dislocations Solids 12:1–80
19. Canova G, Wenk H, Molinari A (1992) Deformation modelling of multi-phase polycrystals: case of a quartz-mica aggregate. Acta Metall Mater 40:1519–1530
20. Canova GR (1994) Self-consistent methods: application to the prediction of the deformation texture of polyphase materials. Mater Sci Eng A 175:37–42
21. Canova GR, Lebensohn RA (1996) Micro–macro modelling computer simulation in materials science. In: Computer simulation in materials science : nano/meso/macroscopic space & time scales. Proceedings of the NATO Advanced Study Institute, Ile D'oleron, France, 6–16 June 1995, pp 449–481
22. Carpenter H, Elam C (1921) Stages in the recrystallization of aluminium sheet on heating—with a note on the birth of crystals in strained metals and alloys. J Inst Met 25:259–280
23. Cazacu O, Barlat F (2003) Application of the theory of representation to describe yielding of anisotropic aluminum alloys. Int J Eng Sci 41:1367–1385
24. Cazacu O, Barlat F (2001) Generalization of Drucker's yield criterion to orthotropy. Math Mech Solids 6:613–630. https://doi.org/10.1177/108128650100600603
25. Cazacu O, Chandola N, Revil-Baudard B (2017) Analytical expressions for the yield stress and Lankford coefficients of polycrystalline sheets based on a new single crystal model. Int J Mater Form. https://doi.org/10.1007/s12289-017-1366-3
26. Cazacu O, Revil-Baudard B, Chandola N (2017) A yield criterion for cubic single crystals. Int J Solids Struct. Apr 5, (in-press, corrected proof), https://doi.org/10.1016/j.ijsolstr.2017.04.006
27. Chandola N, Cazacu O, Revil-Baudard B (2017) New polycrystalline modeling as applied to textured steel sheets. Mech Res Commun 84:98–101
28. Coleman BD, Noll W (1963) The thermodynamics of elastic materials with heat conduction and viscosity. Arch Ration Mech Anal 13:167–178
29. Dana E, Ford W (1952) Dana's textbook of mineralogy. Wiley, New York
30. Darrieulat M, Piot D (1996) A method of generating analytical yield surfaces of crystalline materials. Int J Plast 12:575–610
31. Dillamore I, Roberts W (1964) Rolling textures in fcc and bcc metals. Acta Metall 12:281–293
32. Dove H (1860) Über stereoskopie. Ann Phys 186:494–498
33. Elam CF (1935) Distortion of metal crystals. Clarendon Press, UK
34. Elias J, Smith J, Heyer R (1962) Plastic anisotropy of cold rolled-annealed low-carbon steel related to crystallographic orientation. Trans Metall Soc AIME 224(4):678
35. Eshelby JD (1957) The determination of the elastic field of an ellipsoidal inclusion, and related problems. Proc R Soc Lond A Math Phys Eng Sci 241(1226):376–396
36. Ewing JA, Rosenhain W (1900) Bakerian lecture. The crystalline structure of metals. Proc R Soc Lond 65:172–177
37. Eyckens P, Mulder H, Gawad J, Vegter H, Roose D, van den Boogaard T, Van Bael A, Van Houtte P (2015) The prediction of differential hardening behaviour of steels by multi-scale crystal plasticity modelling. Int J Plast 73:119–141
38. Gilman JJ (1956) Plastic anisotropy of zinc monocrystals. JOM 8:1326–1336

39. Gilormini P (1996) A critical evaluation for various nonlinear extensions of the self-consistent model. In: IUTAM symposium on micromechanics of plasticity and damage of multiphase materials. Springer, Berlin, pp 67–74
40. Gotoh M, Ishise F (1978) A finite element analysis of rigid-plastic deformation of the flange in a deep-drawing process based on a fourth-degree yield function. Int J Mech Sci 20: 423–435
41. Green A, Adkins J (1970) Large elastic deformation. Oxford University Press, Oxford
42. Gröger R, Racherla V, Bassani J, Vitek V (2008) Multiscale modeling of plastic deformation of molybdenum and tungsten: II. Yield criterion for single crystals based on atomistic studies of glide of ½ <111> screw dislocations. Acta Mater 56:5412–5425
43. Hardouin Duparc OBM (2011) A review of some elements in the history of grain boundaries, centered on Georges Friedel, the coincident 'site' lattice and the twin index. J Mater Sci 46:4116–4134
44. Hardouin Duparc OBM (2017) A review of some elements for the history of mechanical twinning centred on its German origins until Otto Mügge's K 1 and K 2 invariant plane notation. J Mater Sci 52:4182–4196. https://doi.org/10.1007/s10853-016-0513-4
45. Haüy R-J (1784) Essai d'une theorie sur la structure des crystaux, appliquee a plusieurs genres de substances crystallisees; par M. l'abbe Hauy. chez Gogue & Nee de La Rochelle, libraires, quai des Augustins, pres le pont Saint-Michel
46. Hessel JFC (1830) Krystall. Gehler's Physikalisches Wörterbuch 5:1023
47. Hill R (1965) A self-consistent mechanics of composite materials. J Mech Phys Solids 13:213–222
48. Hirsch J (2005) Texture and anisotropy in industrial applications of aluminium alloys. Arch Metall Mater 50:21–34
49. Hollang L, Brunner D, Seeger A (2001) Work hardening and flow stress of ultrapure molybdenum single crystals. Mater Sci Eng A 319:233–236
50. Hosford WF (1993) The mechanics of crystals and textured polycrystals. Oxford University Press, USA
51. Hosford WF, Caddell RM (2011) Metal forming: mechanics and metallurgy. Cambridge University Press, Cambridge
52. Hsiung LL (2010) On the mechanism of anomalous slip in bcc metals. Mater Sci Eng A 528:329–337
53. Hull D (1963) Orientation and temperature dependence of plastic deformation processes in 3· 25% silicon iron. Proc R Soc Lond A 274(1356):5–20
54. Hull D, Bacon DJ (2011) Introduction to dislocations. Elsevier, New York
55. Hutchinson J (1964) Plastic deformation of bcc polycrystals. J Mech Phys Solids 12:25–33
56. Hutchinson J (1964) Plastic stress-strain relations of FCC polycrystalline metals hardening according to Taylor's rule. J Mech Phys Solids 12:11–24
57. Ito Y, Hashiguchi K, Ohashi N (1971) Effect of plastic anisotropy on the bore expanding behaviour of colled-rolled steel sheets. In: Proc Int Conf Sci Technol Iron Steel, Tokyo, pp 958–962
58. Karnop R, Sachs G (1928) Festigkeitseigenschaften von Kristallen einer veredelbaren Aluminiumlegierung. Z Für Phys 49:480–497
59. Kelvin WTB, Tait PG (1867) Treatise on natural philosophy. Clarendon Press, UK
60. Kim J-Y, Jang D, Greer JR (2010) Tensile and compressive behavior of tungsten, molybdenum, tantalum and niobium at the nanoscale. Acta Mater 58:2355–2363
61. Kim J-Y, Jang D, Greer JR (2012) Crystallographic orientation and size dependence of tension–compression asymmetry in molybdenum nano-pillars. Int J Plast 28:46–52
62. Kocks UF, Tomé CN, Wenk H-R (2000) Texture and anisotropy: preferred orientations in polycrystals and their effect on materials properties. Cambridge University Press, Cambridge
63. Kroner E (1961) On the plastic deformation of polycrystals. Acta Metall 9:155–161
64. Lall C, Chin S, Pope D (1979) The orientation and temperature dependence of the yield stress of Ni 3 (Al, Nb) single crystals. Metall Trans A 10:1323–1332

65. Lebensohn R, Tomé C (1993) A self-consistent anisotropic approach for the simulation of plastic deformation and texture development of polycrystals: application to zirconium alloys. Acta Metall Mater 41:2611–2624
66. Lege DJ, Barlat F, Brem JC (1989) Characterization and modeling of the mechanical behavior and formability of a 2008-T4 sheet sample. Int J Mech Sci 31:549–563
67. Lequeu P, Gilormini P, Montheillet F, Bacroix B, Jonas J (1987) Yield surfaces for textured polycrystals—I. Crystallographic approach. Acta Metall 35:439–451
68. Liebisch T (1889) Ueber eine besondere Art von homogenen Deformationen: Neues Jahrb., Beil. Nachrichten Von Königl Ges Wiss Georg-Augusts-Univ Zu Gött 6:105–120
69. Lin T (1957) Analysis of elastic and plastic strains of a face-centred cubic crystal. J Mech Phys Solids 5:143–149
70. Love AEH (1920) A treatise on the mathematical theory of elasticity. Cambridge University Press, Cambridge, UK
71. Luft A, Ritschel C (1982) Deformation and slip behaviour of cold-worked molybdenum single crystals at elevated temperature I. The effect of crystals orientation. Phys Status Solidi A 72:225–237
72. Mark H, Polanyi M, Schmid E (1923) Vorgänge bei der Dehnung von Zinkkristallen. Z Für Phys 12:78–110
73. Masima M, Sachs G (1928) Mechanische Eigenschaften von Messingkristallen. Z Für Phys 50:161–186
74. Mathewson C, Phillips A (1916) Recrystallization of cold-worked alpha brass on annealing. Trans AIME 54:608
75. Mathewson CH, Phillips AJ (1928) Twinning in Beryllium, Magnesium, Zinc, and Cadmium. American Institute of Mining [and] Metallurgical Engineers, New York
76. Molinari A, Canova G, Ahzi S (1987) A self consistent approach of the large deformation polycrystal viscoplasticity. Acta Metall 35:2983–2994
77. Mügge O (1889) Ueber homogene Deformationen (einfache Schiebungen) an den triklinen Doppelsalzen BaCdCl4. 4aq. Neues Jahrb Für Mineral Geol Palaeontol Beil 6:274–304
78. Payne H (1959) The slip theory of plasticity for crystalline aggregates. J Mech Phys Solids 7:126–134
79. Pfaff F (1859) Untersuchungen über die Ausdehnung der Krystalle durch die Wärme. Ann Phys 183:148–154
80. Polanyi M, Schmid E (1923) Ist die Gleitreibung vom Druck normal zu den Gleitflächen abhängig? Z Für Phys 16:336–339
81. Rapperport E, Hartley C (1960) Deformation modes of zirconium at 77 K, 300 K, 575 K, and 1075 K. Nuclear Metals, Inc., Concord, Mass
82. Reed-Hill RE, Hirth JP, Rogers HC (1963) Deformation twinning. Gordon and Breach Science Publishers, Philadelphia
83. Reed-Hill RE, Robertson WD (1957) Deformation of magnesium single crystals by nonbasal slip. JOM 9:496–502
84. Reusch E (1867) Ueber eine besondere Gattung von Durchgängen im Steinsalz und Kalkspath. Ann Phys 208:441–451. https://doi.org/10.1002/andp.18672081106
85. Rice JR (1971) Inelastic constitutive relations for solids: an internal-variable theory and its application to metal plasticity. J Mech Phys Solids 19:433–455
86. Richman RH (1963) The diversity of twinning in body-centered cubic structure. In: Reed-Hill RE, Hirth JP, Rogers HC (eds) Deformation twinning. Gordon and Breach, New York, pp 237–271
87. Rosenbaum H (1961) Non-basal slip and twin accommodation in zinc crystals. Acta Metall 9:742–748
88. Rosenbaum H (1963) Nonbasal slip in hcp metals and its relation to mechanical twinning. In: Reed-Hill RE, Hirth JP, Rogers HC (eds) Deformation twinning. Gordon and Breach, New York, pp 43–76
89. Sachs G (1928) On the derivation of a condition of flowing. Z Ver Deut Ing 72:734–736

90. Sakai T, Fine M (1974) Failure of Schmid's law in Ti Al alloys for prismatic slip. Scr Metall 8:541–544
91. Samans CH (1934) An x-ray study of orientation changes in cold-rolled single crystals of alpha brass. AIME Trans 111:119–134
92. Schiebold E, Siebel G (1931) Studien an Magnesium und Magnesiumlegierungen. Z Für Phys 69:458–482
93. Schmid E (1931) Mg (above 225C) determination of the t from lattice rotation in extension; Basal glide with 2 glid directions. Z Elektrochem Angew Phys Chem 37:447–459
94. Schmid E, Boas W (1951) Plasticity of crystals (trans: F.A. Hughes & Co. Limited). Chapman & Hall Ltd, London
95. Schoenflies A (1923) Theorie der Kristallstruktur. Borntraeger, Stuttgart
96. Smith GF, Rivlin RS (1958) The strain-energy function for anisotropic elastic materials. Trans Am Math Soc 88:175–193
97. Svensson N (1966) Some observations on the anisotropy of yield strength in cold rolled and annealed metals. Inst Met J 94:284–291
98. Takeuchi T (1975) Work hardening of copper single crystals with multiple glide orientations. Trans Jpn Inst Met 16:629–640
99. Taylor G, Elam C (1925) The plastic extension and fracture of aluminum single. Roy Soc Proc A 108(745):28–51
100. Taylor G, Elam C (1926) The distortion of iron crystals. Proc R Soc Lond Ser Contain Pap Math Phys Character 112:337–361
101. Taylor GI (1928) The deformation of crystals of β-brass. Proc R Soc Lond Math Phys Eng Sci 118:1–24. https://doi.org/10.1098/rspa.1928.0032
102. Taylor GI (1938) Analysis of plastic strain in a cubic crystal. In: Stephen Timoshenko 60th anniversary, pp 218–224
103. Taylor GI, Elam CF (1923) Bakerian lecture: the distortion of an aluminium crystal during a tensile test. Proc R Soc Lond Math Phys Eng Sci 102:643–667. https://doi.org/10.1098/rspa.1923.0023
104. Teodosiu C (1982) Elastic models of crystal defects. Springer, Berlin
105. Tomé CN, Lebensohn RA (2004) Self consistent homogenization methods for texture and anisotropy. Contin Scale Simul Eng Mater Fundam Microstruct Process Appl 473–499
106. Tucker G (1961) Texture and earing in deep drawing of aluminium. Acta Metall 9:275–286
107. Venables JA (1963) Deformation twinning in face-centred cubic metals. In: Reed-Hill RE, Hirth JP, Rogers HC (eds) Deformation twinning. Gordon and Breach, New York, pp 77–120
108. Wenk H-R, Van Houtte P (2004) Texture and anisotropy. Rep Prog Phys 67:1367
109. Yoo M (1981) Slip, twinning, and fracture in hexagonal close-packed metals. Metall Trans A 12:409–418
110. Yoo MK, Choi J, Hiraoka Y (1995) Deformation characteristics at 300 K of single-crystalline molybdenum sheet prepared by secondary recrystallization. Scr Metall Mater 33(9)
111. Yoon J, Barlat F, Chung K, Pourboghrat F, Yang D (2000) Earing predictions based on asymmetric nonquadratic yield function. Int J Plast 16:1075–1104
112. Yoon J-H, Cazacu O, Yoon JW, Dick RE (2010) Earing predictions for strongly textured aluminum sheets. Int J Mech Sci 52:1563–1578

Chapter 4
Yield Criteria for Isotropic Polycrystals

4.1 General Mathematical Requirements

4.1.1 General Form of Isotropic Yield Criteria

Characterization of the plastic response requires the specification of the onset of plastic deformation or yielding, and a flow rule by which the subsequent plastic deformations can be calculated for given loadings and displacements. In this chapter, we present yield criteria for isotropic fully dense metallic materials.

A yield criterion is represented by a scalar-valued function of the Cauchy stress $\boldsymbol{\sigma}$, say $F(\boldsymbol{\sigma})$ (see also Chap. 2). Let's denote by $\sigma_1, \sigma_2, \sigma_3$ the principal values of $\boldsymbol{\sigma}$.

Proposition 4.1 *The most general form of the yield function of an isotropic material is*:

$$F(\boldsymbol{\sigma}) = f(\sigma_1, \sigma_2, \sigma_3) \tag{4.1}$$

such that

$$f(\sigma_1, \sigma_2, \sigma_3) = f(\sigma_2, \sigma_3, \sigma_1) = f(\sigma_3, \sigma_1, \sigma_2). \tag{4.2}$$

Proof According to Wang [45] representation theorem (see also Chap. 1) for isotropic scalar functions of a single symmetric tensor argument, $F(\boldsymbol{\sigma})$ must depend on the stress $\boldsymbol{\sigma}$ only through its invariants, namely:

$$tr(\boldsymbol{\sigma}) = \sigma_1 + \sigma_2 + \sigma_3, \quad tr\left(\boldsymbol{\sigma}^2\right) = \sigma_1^2 + \sigma_2^2 + \sigma_3^2, \quad tr\left(\boldsymbol{\sigma}^3\right) = \sigma_1^3 + \sigma_2^3 + \sigma_3^3 \tag{4.3}$$

Using the Cayley–Hamilton theorem (see Chap. 1), it is possible to express the principal-stress values $\sigma_1, \sigma_2, \sigma_3$ in terms of the invariants given by Eq. (4.3) and obtain the representation of the yield function given by Eq. (4.1). Moreover, since each stress invariant is a symmetric function of $\sigma_1, \sigma_2, \sigma_3$ [see Eq. (4.3)], it follows

O. Cazacu et al., *Plasticity–Damage Couplings: From Single Crystal to Polycrystalline Materials*, Solid Mechanics and Its Applications 253,
https://doi.org/10.1007/978-3-319-92922-4_4

that the yield function $f(\sigma_1, \sigma_2, \sigma_3)$ should also be a symmetric function of the principal stresses.

Remark Note that the requirement in Eq. (4.2) that f is a symmetric function of $\sigma_1, \sigma_2, \sigma_3$ is a direct consequence of the fact that for an isotropic material f cannot depend on the orientation of the principal axes of stress with respect to the material (the material cannot distinguish which principal stress is labeled 1, which is labeled 2, and 3, respectively).

Let σ_{m} denote the mean normal stress, i.e.,

$$\sigma_{\mathrm{m}} = \frac{1}{3}\mathrm{tr}(\boldsymbol{\sigma}) = \frac{1}{3}(\sigma_1 + \sigma_2 + \sigma_3). \tag{4.4}$$

As already mentioned, the stress tensor $\boldsymbol{\sigma}$ can be written as the sum of a spherical tensor and the stress deviator $\mathbf{s}$, i.e.,

$$\boldsymbol{\sigma} = \mathbf{s} + \sigma_{\mathrm{m}}\mathbf{I} \tag{4.5}$$

with $\mathbf{I}$ the second-order identity tensor. Note that the stress deviator $\mathbf{s}$ and the stress tensor $\boldsymbol{\sigma}$ have the same principal directions, $\mathbf{e}_i$, i = 1, …, 3, and the principal values, s_1, s_2, s_3 of $\mathbf{s}$ are expressed in terms of the principal-stress values as:

$$\begin{aligned} s_1 &= (2\sigma_1 - \sigma_2 - \sigma_3)/3 \\ s_2 &= (2\sigma_2 - \sigma_1 - \sigma_3)/3\,. \\ s_3 &= (2\sigma_3 - \sigma_1 - \sigma_2)/3 \end{aligned}$$

In terms of s_1, s_2 and s_3, J_2, and J_3, the second and third-invariant of the stress deviator $\boldsymbol{s}$, respectively, are expressed as:

$$\begin{aligned} J_2 &= \mathrm{tr}\boldsymbol{s}^2/2 = \frac{1}{2}\left(s_1^2 + s_2^2 + s_3^2\right) = \frac{1}{6}\left[(s_1 - s_2)^2 + (s_1 - s_3)^2 + (s_2 - s_3)^2\right], \\ J_3 &= \mathrm{tr}\boldsymbol{s}^3/3 = \frac{1}{3}\left(s_1^3 + s_2^3 + s_3^3\right) = s_1 s_2 s_3. \end{aligned} \tag{4.6}$$

Therefore, the yield function of an isotropic material can be represented as:

$$F(\boldsymbol{\sigma}) = g(\sigma_{\mathrm{m}}, J_2, J_3). \tag{4.7}$$

Indeed, using the definition (4.5) of $\boldsymbol{s}$, it follows that:

$$\begin{aligned} tr\left(\boldsymbol{\sigma}^2\right) &= 2J_2 + 3\sigma_{\mathrm{m}}^2 \\ tr\left(\boldsymbol{\sigma}^3\right) &= 3J_3 + 6J_2\sigma_{\mathrm{m}} + 3\sigma_{\mathrm{m}}^3 \end{aligned}$$

Thus, the yield function of an isotropic material should be represented by an arbitrary function of σ_{m}, J_2, and J_3.

If the mechanism of plastic deformation at the single crystal level is a shear mechanism, plastic deformation of a randomly oriented polycrystal should be insensitive to the mean stress, σ_m (see Chap. 2). Hence, using the representation given by Eq. (4.7) it follows that

Proposition 4.2 *The most general form of the yield condition of a pressure-insensitive isotropic material is*:

$$F(\boldsymbol{\sigma}) = g(J_2, J_3). \tag{4.8}$$

4.1.2 Representation of the Yield Surface of Isotropic Materials in the Octahedral Plane

Since for an isotropic material, the yield function is represented by a function of the principal stresses (see Proposition 4.1), the yield condition equation $f(\sigma_1, \sigma_2, \sigma_3) = 0$ can be represented and visualized graphically in the three-dimensional principal stress space. Most importantly, the yield stresses corresponding to any type of loadings can be recorded on this surface. It is to be noted that for an anisotropic material such a three-dimensional representation is only possible for loadings that do not involve shear stresses.

Consider an isotropic material subjected to an arbitrary state of stress. Let $(\mathbf{e}_1, \mathbf{e}_2, \mathbf{e}_3)$ denote the Cartesian frame associated with the principal directions of the stress tensor, $\boldsymbol{\sigma}$. Since yielding depends only on the principal values, the stress state at yielding is fully determined by the vector $\sigma_1\mathbf{e}_1 + \sigma_2\mathbf{e}_2 + \sigma_3\mathbf{e}_3$. In this three-dimensional space, the hydrostatic axis is represented by the line: $\sigma_1 = \sigma_2 = \sigma_3$ of unit vector $\boldsymbol{n} = (\mathbf{e}_1 + \mathbf{e}_2 + \mathbf{e}_3)/\sqrt{3}$. The plane which passes through the origin and is perpendicular to the hydrostatic line is called the deviatoric or octahedral π plane.

Proposition 4.3 *Consider an arbitrary stress state represented by a point* $P(\sigma_1, \sigma_2, \sigma_3)$. *The projection of the vector* **OP** *onto the hydrostatic line is proportional to the mean stress,* $\sigma_m = (\sigma_1 + \sigma_2 + \sigma_3)/3$, *while its projection on the octahedral plane is* $\mathrm{Q}(\mathrm{s}_1, \mathrm{s}_2, \mathrm{s}_3)$.

Proof The projection of the stress vector **OP** onto the hydrostatic line (see also Fig. 4.1a) is:

$$\mathbf{QP} = (\mathbf{OP} \cdot \boldsymbol{n})\boldsymbol{n} = (\sigma_1 + \sigma_2 + \sigma_3)/\sqrt{3}\boldsymbol{n} = \sqrt{3}\sigma_m\boldsymbol{n}.$$

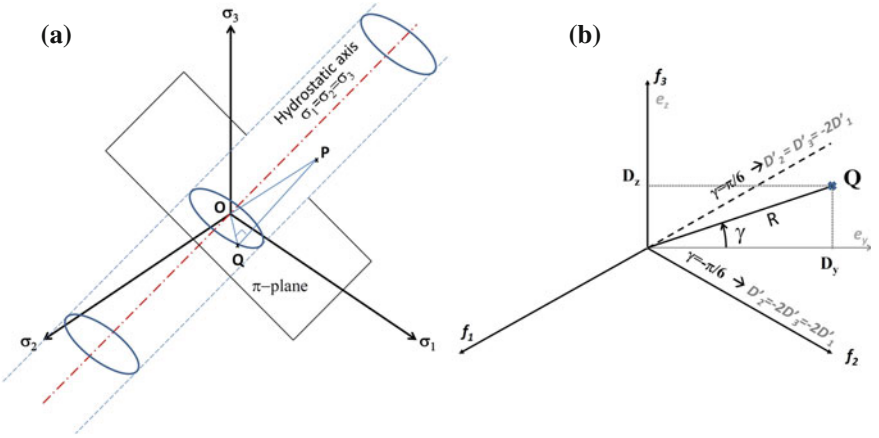

Fig. 4.1 **a** Projection of a stress vector **OP** on the deviatoric π-plane; **b** definition of the polar coordinates (R,γ) in the π-plane

while

$$\mathbf{OQ} = \mathbf{OP} - \mathbf{QP} = (\sigma_1\mathbf{e}_1 + \sigma_2\mathbf{e}_2 + \sigma_3\mathbf{e}_3) - \sqrt{3}\sigma_{\mathrm{m}}\boldsymbol{n} = s_1\mathbf{e}_1 + s_2\mathbf{e}_2 + s_3\mathbf{e}_3$$

Proposition 4.4 *The yield surface of any pressure-insensitive material is a prism or right cylinder with generators perpendicular to the octahedral plane.*

Proof According to Proposition 4.3, the stress deviator **s** is the same for all points on any line normal to the octahedral plane. The assumption that the yield condition is pressure-insensitive, requires that if $(\sigma_1, \sigma_2, \sigma_3)$ is on the yield surface, then so is $(\sigma_1 + p, \sigma_2 + p, \sigma_3 + p)$ for any value of p. In other words, if the yield criterion is satisfied by $(\sigma_1, \sigma_2, \sigma_3)$, it will be satisfied along any line parallel with the hydrostatic line. Hence, the yield surface of any pressure-insensitive material is a prism or right cylinder with generators perpendicular to the octahedral plane.

In summary, in order to specify the shape of the yield surface of any pressure-insensitive material, it is sufficient to determine its intersection with the octahedral plane. For this purpose, it is convenient to introduce the Oxyz Cartesian frame of unit vectors $(\mathbf{e}_x, \mathbf{e}_y, \mathbf{e}_z)$, which are related to the stress eigenvectors $(\mathbf{e}_1, \mathbf{e}_2, \mathbf{e}_3)$ by the following relations:

$$\mathbf{e}_x = \boldsymbol{n} = \frac{1}{\sqrt{3}}(\mathbf{e}_1 + \mathbf{e}_2 + \mathbf{e}_3), \quad \mathbf{e}_y = -\frac{1}{\sqrt{2}}(\mathbf{e}_1 - \mathbf{e}_2), \quad \mathbf{e}_z = \frac{1}{\sqrt{6}}(2\mathbf{e}_3 - \mathbf{e}_1 - \mathbf{e}_2). \tag{4.9}$$

Since $\mathbf{e}_x$ is along the hydrostatic line, $\mathbf{e}_y$ and $\mathbf{e}_z$ belong to the octahedral plane. Let $\mathbf{f}_i$ be the projections of the stress eigenvectors $\mathbf{e}_i$, $i = 1, \ldots, 3$ on the octahedral plane. Obviously, $\mathbf{f}_3 = \mathbf{e}_z$ [see Eq. (4.9) and Fig. 4.1b]. Since $\mathbf{e}_i$, $i = 1, \ldots, 3$ are

mutually orthogonal; for any $i \neq j$, the angle between $\mathbf{f}_i$ and $\mathbf{f}_j$ is $2\pi/3$, and $\mathbf{e}_y$ is the bisector of the angle formed by $(-\mathbf{f}_1, \mathbf{f}_2)$.

Thus, $\mathbf{f}_1 = \frac{1}{\sqrt{6}}(2\mathbf{e}_1 - \mathbf{e}_2 - \mathbf{e}_3)$, $\mathbf{f}_2 = \frac{1}{\sqrt{6}}(-\mathbf{e}_1 + 2\mathbf{e}_2 - \mathbf{e}_3)$. Moreover, for any stress state characterized by $(\sigma_1, \sigma_2, \sigma_3)$ where the principal values are not necessarily ordered, we have

$$\begin{cases} \sigma_x = \boldsymbol{\sigma} \cdot \mathbf{e}_x = \sqrt{3}\,\sigma_{\mathrm{m}} \\ \sigma_y = \boldsymbol{\sigma} \cdot \mathbf{e}_y = (\sigma_2 - \sigma_1)/\sqrt{2} \\ \sigma_z = \boldsymbol{\sigma} \cdot \mathbf{e}_z = (2\sigma_3 - \sigma_1 - \sigma_2)/\sqrt{6} \end{cases} \tag{4.10}$$

Therefore, the intersection of the yield surface $f = f(\sigma_1, \sigma_2, \sigma_3) = 0$ with the octahedral plane $\sigma_{\mathrm{m}} = 0$ is obtained simply by substituting in the expression of the yield function the principal stresses by their expressions in terms of $\sigma_x, \sigma_y, \sigma_z$ and imposing $\sigma_x = \sqrt{3}\sigma_{\mathrm{m}} = 0$. Alternatively, any point $\mathrm{Q}(\mathrm{s}_1, \mathrm{s}_2, \mathrm{s}_3)$ belonging to the intersection of the yield surface with the octahedral plane is characterized by two polar-type coordinates, (R, γ) (see also Fig. 4.1b):

$$\mathrm{R} = |\mathbf{OQ}| = \sqrt{s_1^2 + s_2^2 + s_3^2} = \sqrt{2J_2} \tag{4.11}$$

while γ denotes the angle between $\mathbf{e}_y$ and $\mathbf{OQ}$, so

$$\tan(\gamma) = \frac{\sigma_{\mathrm{z}}}{\sigma_{\mathrm{y}}} = \sqrt{3}\frac{s_3}{s_2 - s_1}. \tag{4.12}$$

Further using $s_1 + s_2 + s_3 = 0$ in conjunction with Eqs. (4.11) and (4.12), we obtain that the unordered eigenvalues of the stress deviator have the following expressions in terms of $\mathrm{R}(\gamma)$ and γ:

$$\begin{cases} s_1 = \dfrac{2\mathrm{R}(\gamma)}{\sqrt{6}}\sin\left(\gamma - \dfrac{2\pi}{3}\right) \\ s_2 = \dfrac{2\mathrm{R}(\gamma)}{\sqrt{6}}\sin\left(\gamma + \dfrac{2\pi}{3}\right) \\ s_3 = \dfrac{2\mathrm{R}(\gamma)}{\sqrt{6}}\sin\gamma \end{cases} \tag{4.13}$$

Using Eq. (4.13), it follows that $s_1 s_2 s_3 = -\frac{8R^3}{6\sqrt{6}}\sin(\gamma)\sin\left(\gamma - \frac{\pi}{3}\right)\sin\left(\gamma - \frac{2\pi}{3}\right)$, or

$$\sin(3\,\gamma) = \frac{-J_3}{2}\left(\frac{3}{J_2}\right)^{\frac{3}{2}}. \tag{4.14}$$

Note that Eqs. (4.11) and (4.14) also provide a physical interpretation of the invariants J_2 and J_3 of the stress deviator. The second-invariant is the norm of the stress deviator while J_3 gives the "position" of the stress deviator in the octahedral plane. Furthermore, the intersection of the yield surface $f = f(\sigma_1, \sigma_2, \sigma_3) = 0$ with the octahedral plane is given by the curve: R = R(γ). Isotropy requires that $f(\sigma_1, \sigma_2, \sigma_3)$ must be symmetric in $\sigma_1, \sigma_2, \sigma_3$, i.e., Equation (4.2) holds. Thus, the section of the yield surface in the octahedral plane must be symmetric with respect to each of the projected axes $\mathbf{e}_i$. In other words, it means that the yield locus has three axes of symmetry $\mathbf{f}_1$, $\mathbf{f}_2$, $\mathbf{f}_3$ (see Fig. 4.1b). Therefore, it is sufficient to determine the shape of the cross-section, i.e., R = R(γ), in the sector $-\pi/6 \leq \gamma \leq \pi/6$ alone, the shape in all the other sectors being obtained by symmetry arguments. Using Eq. (4.12), we obtain that for $-\pi/6 \leq \gamma \leq \pi/6$, we have $s_2 \geq s_3 \geq s_1$, and in this domain, the maximum principal stress is always positive while the minimum principal stress is always negative. The states on the line of unit vector $\mathbf{f}_2$ (i.e., $\gamma = -\pi/6$) correspond to loadings such that $s_3 = s_1 < 0$ (in particular, uniaxial tension); shear loadings with $s_3 = 0$ correspond to $\gamma = 0$ (line of unit vector $\mathbf{e}_y$) while axisymmetric loadings $s_2 = s_3 > 0$ (in particular, uniaxial compression) correspond to $\gamma = \pi/6$ (line of unit vector $(-\mathbf{f}_1)$). In the subsector $-\pi/6 \leq \gamma < 0$: $s_2 > 0 > s_3 \geq s_1$, so the third-invariant $J_3 > 0$; for $\gamma = 0$: $J_3 = 0$; in the subsector $0 < \gamma \leq \pi/6$: $s_2 \geq s_3 > 0 > s_1$, so the third-invariant $J_3 < 0$. In particular, uniaxial tension corresponds to $\gamma = -\pi/6$.

A measure of the effect of the intermediate principal stress on yielding is Lode stress parameter, μ, defined as the ratio of the difference between the intermediate principal stress and the average of the largest and smallest principal stresses to half the difference between the largest and smallest principal stresses (see [33]). Using Eq. (4.13), it follows that for $-\pi/6 \leq \gamma \leq \pi/6$, Lode's parameter is expressed as

$$\mu = \frac{2\sigma_3 - \sigma_1 - \sigma_2}{\sigma_2 - \sigma_1} = \frac{3s_3}{s_2 - s_1} = \sqrt{3}\tan(\gamma). \tag{4.15}$$

Note that $\mu = -1$ ($\gamma = -\pi/6$) corresponds to axisymmetric loadings at $J_3 > 0$ (in particular, uniaxial tension); $\mu = 0$ ($\gamma = 0$) corresponds to pure shear, while $\mu = 1$ ($\gamma = \pi/6$) corresponds to axisymmetric loadings at $J_3 < 0$ (in particular, uniaxial compression). If the assumption that the onset of yielding does not depend on the sense of loading is made, i.e., $f(\boldsymbol{\sigma}) = f(-\boldsymbol{\sigma})$, then the yield surface is symmetric with respect to the origin, hence the yield locus has sixfold symmetry, meaning that it is sufficient to determine its cross-section only in the $-\pi/6 \leq \gamma < 0$ sub-sector. Insensitivity to the sense of loading means equal yield stresses in tension–compression. In most elastic-plastic models for isotropic materials, the specific expressions of $f = f(\sigma_1, \sigma_2, \sigma_3)$ have this requirement built-in. A review of classic yield criteria for isotropic metallic materials is presented in the following.

4.2 Yield Criteria for Isotropic Metallic Materials Displaying the Same Response in Tension–Compression

4.2.1 Classical Yield Criteria

The two most widely used isotropic yield criteria are the Tresca maximum shear criterion and von Mises yield criterion. According to Tresca's criterion, the intermediate principal stress has no effect on yielding while the von Mises yield criterion gives equal weight to all principal stresses.

4.2.1.1 von Mises [44] Yield Criterion

The von Mises yield criterion is of the form:

$$J_2 - k^2 = 0, \tag{4.16}$$

where k is a material parameter, which is assumed constant in the case of ideal plastic behavior (see also Chap. 2). For general three-dimensional loadings, with respect to any Cartesian coordinate system, this criterion writes:

$$\frac{1}{6}\left[\left(\sigma_{xx}-\sigma_{yy}\right)^2+\left(\sigma_{xx}-\sigma_{zz}\right)^2+\left(\sigma_{yy}-\sigma_{zz}\right)^2\right]+\sigma_{xy}^2+\sigma_{xz}^2+\sigma_{yz}^2=k^2. \tag{4.17}$$

In terms of principal stresses, the criterion is expressed as:

$$\frac{1}{6}\left[\left(\sigma_1-\sigma_2\right)^2+\left(\sigma_1-\sigma_3\right)^2+\left(\sigma_2-\sigma_3\right)^2\right]=k^2. \tag{4.18}$$

The only parameter involved in the von Mises criterion can be specified by performing a unique test. For uniaxial tension, yielding occurs when $\sigma_1 = \sigma_T$, $\sigma_2 = 0$, and $\sigma_3 = 0$, so according to the criterion:

$$k = \frac{\sigma_T}{\sqrt{3}}, \tag{4.19}$$

where σ_T is the yield stress in uniaxial tension. Under uniaxial compression (i.e., $\sigma_1 = -\sigma_C$, $\sigma_2 = 0$, and $\sigma_3 = 0$), it is predicted that $k = \sigma_C/\sqrt{3}$. So according to the criterion, $\sigma_C = \sigma_T$, where σ_C is the yield stress in uniaxial compression.

Moreover, the von Mises criterion predicts that the ratio between the yield stress in pure shear, τ_Y, and the yield stress in uniaxial tension, σ_T is fixed:

$$\sigma_T = \sqrt{3}\tau_Y. \tag{4.20}$$

Substituting Eq. (4.19) into Eq. (4.18) we obtain:

$$(\sigma_1 - \sigma_2)^2 + (\sigma_1 - \sigma_3)^2 + (\sigma_2 - \sigma_3)^2 = 2\sigma_T^2. \tag{4.21}$$

The distance between any stress state (s_1, s_2, s_3) belonging to the intersection of the von Mises yield surface with the octahedral plane, and the origin is:

$$R = \sqrt{s_1^2 + s_2^2 + s_3^2} = \sigma_T\sqrt{\frac{2}{3}}.$$

Therefore, in the space of principal stresses the von Mises yield surface (4.21) is a right cylinder of circular cross-section and radius $\sigma_T\sqrt{\frac{2}{3}}$ (see also Fig. 4.2).

For plane-stress loadings, one of the principal stresses is zero. The $\sigma_3 = 0$ section of the von Mises yield locus is the ellipse defined by:

$$\sigma_1^2 + \sigma_2^2 - \sigma_1\sigma_2 = \sigma_T^2 \tag{4.22}$$

Isotropy dictates that the major axis of this ellipse is inclined at 45° to the σ_1 axis (see Fig. 4.3). Note also that according to the von Mises yield criterion the yield stress under equibiaxial loading ($\sigma_1 = \sigma_2$, $\sigma_3 = 0$) is the same as the yield stress in uniaxial tension.

Generally, the assumption of an associated flow rule is made (see Chap. 2). Thus, the plastic potential associated with the von Mises yield function is:

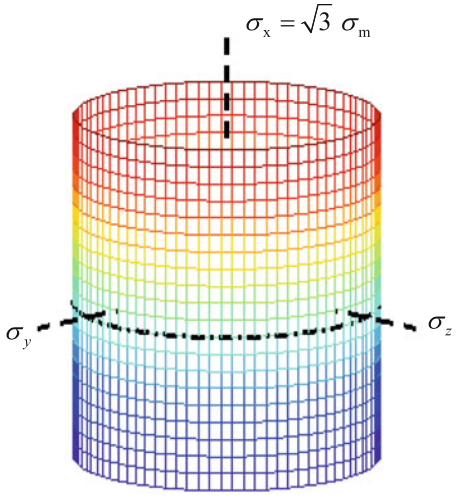

Fig. 4.2 von Mises [44] yield surface in the three-dimensional principal-stress space, with $\sigma_x, \sigma_y, \sigma_z$ given by Eq. (4.10)

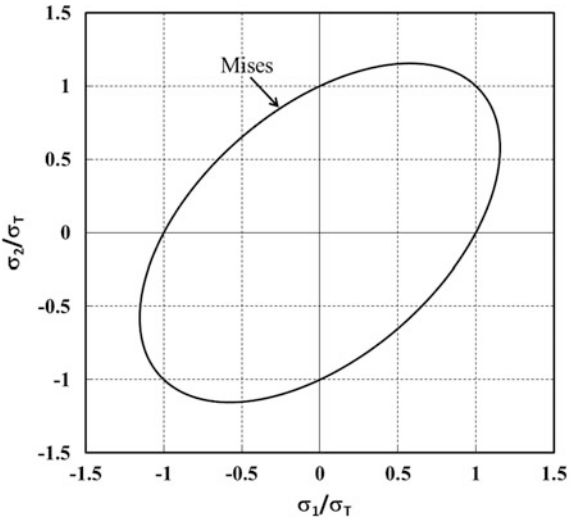

Fig. 4.3 Representation in the (σ_1, σ_2) plane of the yield locus according to the von Mises [44] yield criterion. Stresses are normalized by σ_T, the yield stress in uniaxial tension

$$\varphi_{\text{Mises}}(\boldsymbol{\sigma}) = \sqrt{3J_2} \tag{4.23}$$

Accordingly, the plastic strain-rate tensor, $\mathbf{d}^p$, is expressed as:

$$\mathbf{d}^p = \dot{\lambda}\frac{\partial \varphi_{Mises}}{\partial \boldsymbol{\sigma}} = \left(\frac{3}{2\sigma_T}\right)\dot{\lambda}\mathbf{s} \tag{4.24}$$

where $\dot{\lambda} \geq 0$ stands for the plastic multiplier. It means that for a von Mises material, the plastic strain rate is always proportional to the stress deviator. In the coordinate system associated with the principal directions of stress,

$$d_i^p = \left(\frac{3}{2\sigma_T}\right)\dot{\lambda}s_i, \quad i = 1, \ldots, 3. \tag{4.25}$$

It follows that for a material governed by the von Mises criterion and associated flow rule, equibiaxial loadings produce equibiaxial stretching. Moreover, under plane-stress loadings $(\sigma_3 = 0)$, plane-strain deformation occurs $(d_2^p = 0)$, only if $\sigma_2/\sigma_1 = 1/2$.

4.2.1.2 Tresca [42] Yield Criterion

According to Tresca [42] yield criterion, plastic deformation will occur when the maximum shear stress reaches a critical value k'. If $\sigma_1, \sigma_2, \sigma_3$ are principal stresses, not necessarily ordered, then the maximum shear stress condition is:

$$\max\left(\frac{|\sigma_1-\sigma_2|}{2},\frac{|\sigma_2-\sigma_3|}{2},\frac{|\sigma_1-\sigma_3|}{2}\right)=k'. \tag{4.26}$$

Note that this yield function is independent of hydrostatic pressure, it is symmetric in the principal stresses $\sigma_1,\sigma_2,\sigma_3$ and predicts that yielding is the same in tension–compression. The material parameter k' can be determined from simple tests. For uniaxial tension, it is predicted $k'=\sigma_{\mathrm{T}}/2$. Therefore, for the von Mises and Tresca criteria to agree in uniaxial tension–compression, Tresca yield criterion should be taken of the form:

$$\varphi(\boldsymbol{\sigma})=\max(|\sigma_1-\sigma_2|,|\sigma_2-\sigma_3|,|\sigma_1-\sigma_3|)=\sigma_T. \tag{4.27}$$

Accordingly, the yield stress in pure shear should be exactly half of the yield stress in uniaxial tension, i.e.,

$$\sigma_{\mathrm{T}}=2\tau_{\mathrm{Y}}, \tag{4.28}$$

while the yield stress under equibiaxial tension and uniaxial tension should be equal.

To obtain the intersection of the Tresca yield surface with the octahedral plane, it is sufficient to determine the curve R = R(γ) only in the sector $0\le\gamma\le\pi/6$ [see Eq. (4.13)]. Since in this sector $s_2\ge s_3>s_1$ by Eq. (4.26), we have: $s_2-s_1=\sigma_T$. Using Eq. (4.10), it follows that $\sigma_{\mathrm{y}}=\sqrt{2}\sigma_{\mathrm{T}}$, which is the equation of a line parallel to $\mathbf{f}_3$ (see Fig. 4.2) situated at a distance equal to $\sqrt{2}\sigma_{\mathrm{T}}$ from the origin.

Given that the intersection curve with the octahedral plane has sixfold symmetry, it follows that it is a regular hexagon of side equal to $\sigma_{\mathrm{T}}\sqrt{2/3}$. Therefore, this hexagon is inscribed in the von Mises circle (see Fig. 4.4). In summary, in the three-dimensional space of principal stresses, the Tresca yield surface $\varphi(\boldsymbol{\sigma})=0$ [see Eq. (4.27)] is a hexagonal prism inscribed in the von Mises cylinder.

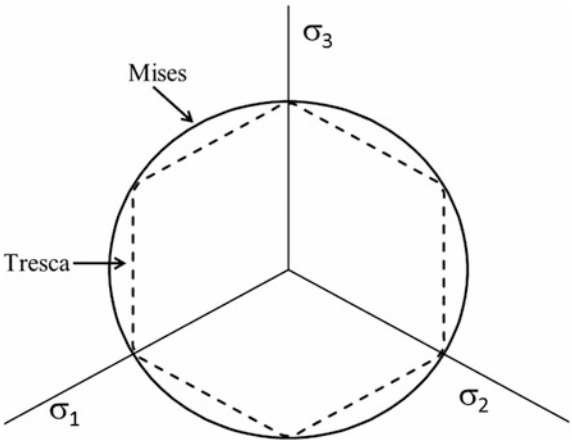

Fig. 4.4 Octahedral plane projections of the yield locus according to Tresca [42] and von Mises [44] yield criterion. Principal stresses are normalized by the uniaxial yield in tension, σ_{T}

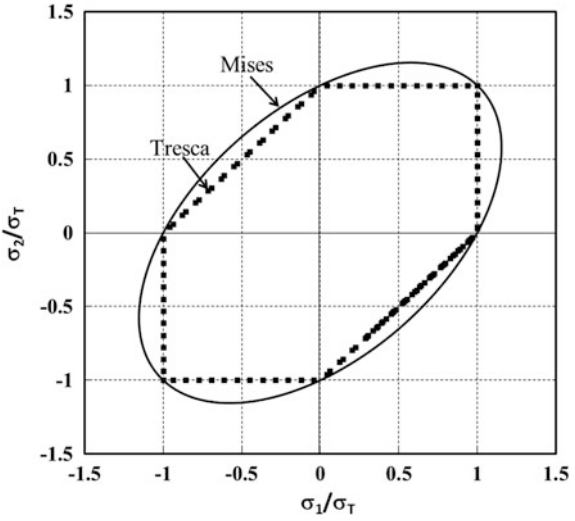

Fig. 4.5 Representation in the (σ_1, σ_2) plane of the yield locus according to Tresca [42] and von Mises [44] yield criterion. Principal stresses are normalized by the yield stress in uniaxial tension, σ_T

For plane-stress loadings (e.g., $\sigma_3 = 0$), either σ_1 or σ_2 may be the major principal stress, depending on which quadrant the point (σ_1, σ_2) occupies. Thus, the section of the Tresca yield locus is an irregular hexagon (see Fig. 4.5) of equations:

$$|\sigma_1| = \sigma_T, \tag{4.29}$$

$$|\sigma_2| = \sigma_T, \tag{4.30}$$

$$|\sigma_1 - \sigma_2| = \sigma_T. \tag{4.31}$$

Its intersections with the axes $\sigma_1 = 0$ $(\sigma_2 > 0)$, and $\sigma_2 = 0$ $(\sigma_1 < 0)$ are the points corresponding to uniaxial stress in tension σ_T and compression $(-\sigma_T)$, respectively. The intersection with the line $\sigma_1 = -\sigma_2$ corresponds to pure shear. Note that the von Mises ellipse is exterior to the Tresca yield locus, so for general biaxial loadings Tresca criterion is more conservative than von Mises criterion; the two criteria coincide for uniaxial tension, uniaxial compression, and equibiaxial loadings (see Fig. 4.5).

Plastic Potential Associated with the Tresca Criterion

Although Tresca's yield surface [see Eq. (4.27)] is not smooth, plastic flow is considered to be associated and the normality rule is used wherever the normal to Tresca's yield surface is unambiguously defined (i.e., everywhere except at vertices). To define the plastic strain-rate at a vertex, Koiter [29] first explicitly wrote the yield condition given by Eq. (4.27) for any possible ordering of the principal stresses $\sigma_1, \sigma_2, \sigma_3$, i.e., represented the yield surface by the six smooth planes each defined by an equation: $\varphi_k = 0$ (k = 1, …, 6). The elastic region is the intersection of the regions defined by $\varphi_k < 0$, the stress state is on the yield surface if at least one

of the φ_k vanishes there; and a singular point (vertex) corresponds to the case when two of the φ_k vanish. The plastic flow rule is defined as:

$$\mathbf{d}^p = \sum_{k=1}^{6} \dot{\lambda}_k \mathbf{N}^k, \tag{4.32}$$

where $\mathbf{N}^k$ is the normal to the corresponding plane, $\varphi_k = 0$ for the multifaceted Tresca yield surface and the $\dot{\lambda}_k$ (k = 1, …, 6) are nonnegative scalars. Loading–unloading conditions are defined as: $\varphi_k \geq 0$, $\dot{\lambda}_k \geq 0$, and $\varphi_k \dot{\lambda}_k = 0$, with no summation on the repeated index. Due to the isotropy and the symmetry with respect to the origin of the Tresca yield surface, it is sufficient to describe the flow rule given by Eq. (4.32) only for one sextant of the principal-stress states, say for $\sigma_1 \geq \sigma_2 \geq \sigma_3$ (see also Fig. 4.4). In this case, there are three possibilities, corresponding to the three zones in the principal-stress space into which the stress may be located:

(1) If $\sigma_1 > \sigma_2 > \sigma_3$, $\varphi_1(\sigma_1, \sigma_2, \sigma_3) = |\sigma_1 - \sigma_3| - \sigma_T = 0$, and φ_1 is differentiable, so:

$$\mathbf{d}^p = \dot{\lambda}\mathbf{N}^{\mathrm{I}},\ \mathbf{N}^{\mathrm{I}} = \mathbf{e}_1 \otimes \mathbf{e}_1 - \mathbf{e}_3 \otimes \mathbf{e}_3 \tag{4.33}$$

or in component form: $d_1^p = \dot{\lambda},\ d_2^p = 0,\ d_3^p = -\dot{\lambda}$.

(2) Right corner: The direction of the rate of plastic strain is a linear combination with nonnegative coefficients of the normals to the two intersecting planes at this point, i.e.,

$$\mathbf{d}^p = \dot{\lambda}_1 \mathbf{N}^{\mathrm{I}} + \dot{\lambda}_2 \mathbf{N}^{\mathrm{II}} \tag{4.34}$$

where $\mathbf{N}^{\mathrm{I}} = \dfrac{\partial \varphi_1}{\partial \boldsymbol{\sigma}}$ defined by Eq. (4.33) is the normal to the main plane $|\sigma_1 - \sigma_3| = \sigma_{\mathrm{T}}$ while $\mathbf{N}^{\mathrm{II}} = \mathbf{e}_1 \otimes \mathbf{e}_1 - \mathbf{e}_2 \otimes \mathbf{e}_2 = \dfrac{\partial \varphi_2}{\partial \boldsymbol{\sigma}}$, with $\varphi_2(\sigma_1, \sigma_2, \sigma_3) = |\sigma_1 - \sigma_2| - \sigma_{\mathrm{T}} = 0$. In other words, $\mathbf{N}^{\mathrm{II}}$ is the normal to the plane of the yield surface: $|\sigma_1 - \sigma_2| = \sigma_{\mathrm{T}}$, which is on the right of the main plane.

(3) Left corner: The direction of the rate of plastic strain is a linear combination with nonnegative coefficients of the normals to the two intersecting planes at this point

$$\mathbf{d}^p = \dot{\lambda}_1 \mathbf{N}^{\mathrm{I}} + \dot{\lambda}_3 \mathbf{N}^{\mathrm{III}}, \tag{4.35}$$

where $\mathbf{N}^{\mathrm{III}} = \mathbf{e}_2 \otimes \mathbf{e}_2 - \mathbf{e}_3 \otimes \mathbf{e}_3 = \dfrac{\partial \varphi_3}{\partial \boldsymbol{\sigma}}$ is the normal to the plane of the yield surface with $\varphi_3(\sigma_1, \sigma_2, \sigma_3) = |\sigma_2 - \sigma_3| - \sigma_{\mathrm{T}} = 0$, which is on the left of the main plane.

4.2.2 Drucker [15] Yield Criterion

A yield criterion that involves both invariants of the Cauchy stress deviator was proposed by Drucker [15] in the form:

$$f \equiv J_2^3 - cJ_3^2 = \tau_Y^6, \tag{4.36}$$

where τ_Y is the yield stress in pure shear and c is a material constant. For $c = 0$, the von Mises yield criterion is recovered.

For uniaxial tension ($\sigma_1 = \sigma_T$, $\sigma_2 = 0$, and $\sigma_3 = 0$), the Drucker [15] yield criterion becomes

$$\sigma_T^6(27 - 4c) = 729\,\tau_Y^6, \tag{4.37}$$

or

$$c = \frac{27}{4}\left[1 - \left(\frac{\tau_Y\sqrt{3}}{\sigma_T}\right)^6\right].$$

Therefore, the ratio between the yield stress in uniaxial tension and the yield stress in pure shear depends on the value of the parameter c. For $c > 0$: $\sigma_T > \sqrt{3}\,\tau_Y$; while for $c < 0$, $\sigma_T < \sqrt{3}\,\tau_Y$.

Proposition 4.5 (Convexity of the Drucker yield function)

For the Drucker [15] *yield surface* (4.36) *to be convex,* $c \in \left[-\frac{27}{8}, 2.25\right]$.

Proof A function f is convex if its Hessian matrix $\mathbf{H}$ of components

$$H_{ij} = \frac{\partial^2 f}{\partial\sigma_i \partial\sigma_j} \tag{4.38}$$

is positive semi-definite (i.e., its principal values are not negative). Since $\frac{\partial J_2}{\partial\sigma_i} = s_i$, $\frac{\partial J_3}{\partial\sigma_i} = t_i = s_i^2 - \frac{2}{3}J_2$, $i = 1, \ldots, 3$, we obtain:

$$
\begin{aligned}
H_{11} &= 6J_2 \cdot s_1^2 + 2J_2^2 - 2ct_1^2 - \frac{4c}{3} J_3 \cdot s_1 \\
H_{12} &= 6J_2 \cdot s_1 s_2 - J_2^2 - 2ct_1 t_2 - \frac{4c}{3} J_3 \cdot s_3 \\
H_{13} &= 6J_2 \cdot s_1 s_3 - J_2^2 - 2ct_1 t_3 - \frac{4c}{3} J_3 \cdot s_2 \\
H_{22} &= 6J_2 \cdot s_2^2 + 2J_2^2 - 2ct_2^2 - \frac{4c}{3} J_3 \cdot s_2 \\
H_{23} &= 6J_2 \cdot s_2 s_3 - J_2^2 - 2ct_2 t_3 - \frac{4c}{3} J_3 \cdot s_1 \\
H_{33} &= 6J_2 \cdot s_3^2 + 2J_2^2 - 2ct_3^2 - \frac{4c}{3} J_3 \cdot s_3
\end{aligned}
\tag{4.39}
$$

From Eq. (4.39), it follows that

$$
\begin{aligned}
H_{11} + H_{12} + H_{13} &= 0 \\
H_{12} + H_{22} + H_{23} &= 0 \\
H_{13} + H_{23} + H_{33} &= 0
\end{aligned}
$$

Thus, $III_H = \det(\mathbf{H}) = 0$ and the principal values of $\mathbf{H}$ are: λ_1, λ_2, and $\lambda_3 = 0$. Thus, the yield function is convex if: $I_H \geq 0$ and $II_H \leq 0$ (see Chap. 1 for the definition of the invariants I_H, II_H, III_H of a second-order tensor). Furthermore, using Eq. (4.39), we obtain:

$$
I_H = \lambda_1 + \lambda_2 = 2J_2^2 \left(9 - \frac{2c}{3}\right), \tag{4.40}
$$

$$
II_H = -\lambda_1 \lambda_2 = \left(\frac{40}{3} J_3^2\right) c^2 - Ec - 45J_2^3, \tag{4.41}
$$

with $E = 72J_3^2 - 4J_2^3 - 4(s_2 - s_3)^2 (s_3 - s_1)^2 (s_1 - s_2)^2$.

To study the sign of II_H, it is convenient to express the principal values of the stress deviator $\mathbf{s}$ in terms of its invariants [see Eqs. (4.13) and (4.14)]. Straightforward calculations show that

$$
(s_2 - s_3)^2 (s_3 - s_1)^2 (s_1 - s_2)^2 = 4J_2^3 \sin^2(3\alpha_1)
$$

And

$$
E = -\frac{80}{3} J_2^3 \sin\left(3\alpha_1 + \frac{\pi}{6}\right) \sin\left(3\alpha_1 - \frac{\pi}{6}\right),
$$

where α_1 is the angle satisfying $0 \leq 3\alpha_1 \leq \pi$ whose cosine is given by:

$$\cos 3\alpha_1 = \frac{J_3}{2}\left(\frac{3}{J_2}\right)^{3/2}. \tag{4.42}$$

Next, it is worth noting that for:

(i) $J_3 = 0$: $II_H = -\left(\frac{20}{3}c + 45\right)J_2^3$ so $II_H \leq 0$ for $c \geq -27/4$.

(ii) $J_3 \neq 0$: II_H is a second-order polynomial in c having a positive root c_p and a negative root c_n.

$$c_\mathrm{p} = \frac{27}{80} \cdot \frac{1}{\cos^2(3\alpha_1)}\left(3P + \sqrt{9P^2 + 200\cos^2(3\alpha_1)}\right) \tag{4.43}$$

$$c_\mathrm{n} = \frac{27}{80} \cdot \frac{1}{\cos^2(3\alpha_1)}\left(3P - \sqrt{9P^2 + 200\cos^2(3\alpha_1)}\right) \tag{4.44}$$

with $P = \frac{20}{3}\left(\cos^2(3\alpha_1) - \frac{3}{4}\right)$. Therefore, $II_H \leq 0$ for $c \in \left(c_\mathrm{n}, c_\mathrm{p}\right)$.

Using Eqs. (4.43) and (4.44), it follows that:

- The minimum value of c_p (as a function of α_1) is 9/4.
- The maximum value of c_n is −27/8.

Hence, if $c \in [-27/8, 2.25]$, $II_H \leq 0$ for any applied stress $\boldsymbol{\sigma}$. Also, from Eq. (4.40), it follows that $I_H \geq 0$ for $c \leq \frac{27}{2}$. Therefore, it follows that for $c \in [-27/8, 2.25]$, the yield function is convex.

Biaxial Loadings

For plane-stress loadings (i.e., one of the principal stresses of the applied Cauchy stress $\boldsymbol{\sigma}$ is zero), say $\sigma_3 = 0$, the Drucker [15] yield criterion writes:

$$\left[\frac{1}{3}\left(\sigma_1^2 - \sigma_1\sigma_2 + \sigma_2^2\right)\right]^3 - \frac{c}{(27)^2}\left[2\sigma_1^3 + 2\sigma_2^3 - 3(\sigma_1 + \sigma_2)\sigma_1\sigma_2\right]^2 = \tau_\mathrm{Y}^6. \tag{4.45}$$

As an example, Fig. 4.6 shows the $\sigma_3 = 0$ section of the Drucker [15] yield surfaces corresponding to $c = -27/8$ and $c = 2.25$, in comparison with the von Mises ellipse ($c = 0$). The stresses are normalized by σ_T, the yield stress in uniaxial tension. Note that for $c > 0$, the yield locus is interior to the von Mises ellipse, while for $c < 0$, it is exterior to it.

Representation of the Drucker [15] *yield surface in the space of principal stresses*

For the Drucker [15] criterion and the von Mises criterion to agree in uniaxial tension (and uniaxial compression), we express the Drucker [15] yield criterion as:

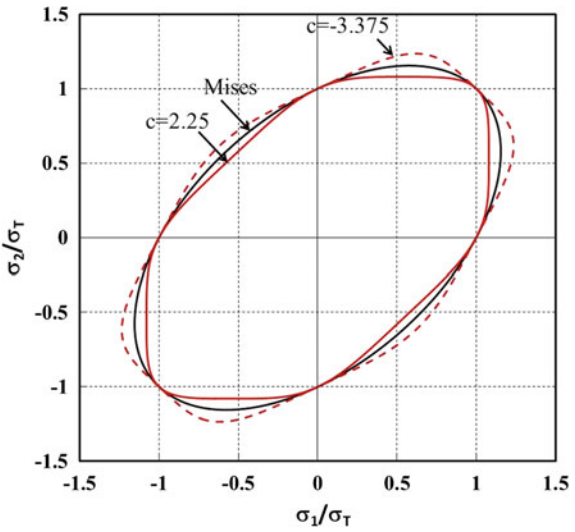

Fig. 4.6 Representation in the plane (σ_1, σ_2) of the yield locus according to the Drucker [15] isotropic yield criterion for: $c = +2.25$ and $c = -27/8$, in comparison with the von Mises yield criterion, which corresponds to $c = 0$. Principal stresses are normalized by σ_T, the yield stress in uniaxial tension

$$\frac{\sqrt{3}}{(1-4c/27)^{1/6}}(J_2^3 - cJ_3^2)^{1/6} = \sigma_T.$$

To obtain the intersection of the yield surface with the octahedral plane, we substitute Eq. (4.13) in the above equation. Thus, in the sextant $0 \leq \gamma \leq \pi/6$:

$$R(\gamma) = \frac{\sigma_T\sqrt{6}(27-4c)^{1/6}}{3\left(27 - 4c\,\sin^2(3\gamma)\right)^{1/6}} \tag{4.46}$$

Figure 4.7a shows the representation of the Drucker [15] yield surface for $c = 2.25$ (interrupted line) in comparison with the Tresca yield locus (solid line), while Fig. 4.7b shows the comparison with von Mises yield locus (which corresponds to $c = 0$). Note that for $c = 2.25$, the Drucker [15] yield locus is close to Tresca's yield locus.

As already mentioned in Sect. 4.1.2, a measure of the effect of the intermediate principal stress was introduced by Lode [33]. If $\sigma_1 \geq \sigma_2 \geq \sigma_3$, Lode's stress parameter [see Eq. (4.15)] writes:

$$\mu = \frac{2\sigma_2 - \sigma_1 - \sigma_3}{\sigma_1 - \sigma_3} = \frac{3s_2}{s_1 - s_3}$$

Note that according to the von Mises criterion [see Eq. (4.18)], at yielding the difference between the major and minor principal stresses has a parabolic dependence on μ, i.e.,

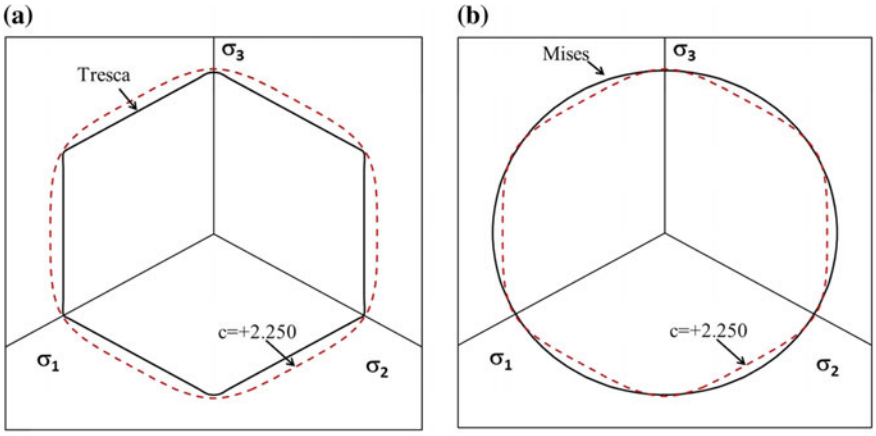

Fig. 4.7 Cross-section in the octahedral plane of the Drucker [15] yield surface [Eq. (4.46)] corresponding to $c = 2.25$ in comparison with: **a** Tresca's cross-section, and **b** von Mises cross-section [which corresponds to $c = 0$ in Eq. (4.46)]. Principal stresses are normalized by the uniaxial yield in tension, σ_T

$$\frac{\sigma_1 - \sigma_3}{\sigma_T} = \frac{2}{(3+\mu^2)^{1/2}} \tag{4.47}$$

Obviously, according to Tresca's criterion [see Eq. (4.27)], there is no influence of the intermediate principal stress on yielding, and therefore on μ, and for $\sigma_1 \geq \sigma_2 \geq \sigma_3$ the criterion writes:

$$\frac{\sigma_1 - \sigma_3}{\sigma_T} = 1. \tag{4.48}$$

Using the expression (4.15) of μ and Eq. (4.36), it follows that according to the Drucker [15] criterion, at yielding the difference of the major and minor principal stresses should have the following variation with μ:

$$\frac{\sigma_1 - \sigma_3}{\sigma_T} = \left(\frac{64\,(27 - 4c)}{27(\mu^2+3)^3 - 4c\mu^2(\mu^2-9)^2} \right)^{1/6}. \tag{4.49}$$

A judicious choice of the parameter c in the Drucker [15] yield criterion allows a very good relative weighting of all principal stresses. As an example, Fig. 4.8 shows the results of the tests on thin-walled tubes of iron under combined axial tension and internal pressure covering the range of μ from -1 to 1 performed by Lode [33]. On the same figure is plotted the variation of $(\sigma_1 - \sigma_3)/\sigma_T$ versus μ given by the Tresca, von Mises, and Drucker yield criterion with $c = 1.09$, respectively. Given that all three criteria were identified such as to agree for uniaxial tension–compression, respectively, (i.e., for $\mu = -1$ and $\mu = 1$), the maximum

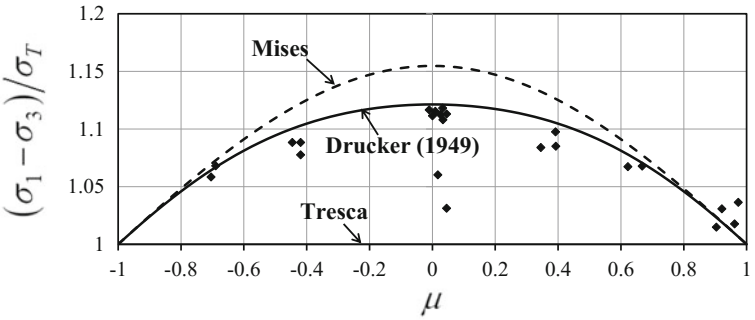

Fig. 4.8 Effect of the Lode parameter μ (or intermediate principal stress) on yielding of thin-walled steel tube according to the Tresca, von Mises, and Drucker [15] yield criterion for $c = 1.09$, and data of Lode [33] (symbols) on iron. Principal stresses $\sigma_1 \geq \sigma_2 \geq \sigma_3$ are normalized by the uniaxial yield in tension, σ_T

difference between the predictions of these criteria obviously occurs for pure shear loading when $\mu = 0$: the difference between the Tresca and von Mises criteria is $2/\sqrt{3}$, while the difference between the Tresca and Drucker criteria is $\frac{2}{\sqrt{3}}\left(1 - \frac{4c}{27}\right)^{1/6}$. The test results correlate best with Drucker [15] criterion, von Mises criterion gives a better agreement than Tresca's, although systematic deviations are observed for other loadings.

Plastic potential associated with Drucker [15] *yield condition*
The plastic potential associated with Drucker [15] criterion is of the form:

$$\varphi_{\text{Drucker}}(\boldsymbol{\sigma}) = \frac{\sqrt{3}}{(1 - 4c/27)^{1/6}}(J_2^3 - cJ_3^2)^{1/6} \tag{4.50}$$

Accordingly, the plastic strain tensor is:

$$\mathbf{d}^{\text{p}} = \dot{\lambda}\frac{\partial \varphi_{\text{Drucker}}}{\partial \boldsymbol{\sigma}} \tag{4.51}$$

where $\dot{\lambda} \geq 0$ stands for the plastic multiplier. A suitable choice of the parameter c allows increased accuracy not only in the prediction of yield data but also for post-yield deformation.

Drucker [15] has introduced a measure of the effect of the third-invariant on plastic strain, defined as the ratio between the intermediate principal value of the plastic strain-rate to the difference between the major and minor principal values, respectively. If $d_1^{\text{p}} \geq d_2^{\text{p}} \geq d_3^{\text{p}}$ are the ordered principal plastic strain-rates, this parameter, denoted as v, is:

$$v = \frac{3d_2^{\mathrm{p}}}{d_1^{\mathrm{p}} - d_3^{\mathrm{p}}} \tag{4.52}$$

In the case of the von Mises yield criterion ($c = 0$) and associated flow rule, v coincides with the Lode stress parameter μ. Indeed, using Eq. (4.24), it follows that

$$v = \frac{3d_2^{\mathrm{p}}}{d_1^{\mathrm{p}} - d_3^{\mathrm{p}}} = \frac{3s_2}{s_1 - s_3} = \mu,$$

On the other hand, since the Drucker [15] yield criterion with $c \neq 0$ involves both invariants of the stress deviator [see Eq. (4.51)],

$$v = \mu \frac{27(\mu^2+3)^2 - 4c(\mu^2-9)(\mu^2-3)}{27(\mu^2+3)^2 - 8c(\mu^2-9)\mu^2}.$$

Consideration of $c \neq 0$, i.e., third-invariant effects, enables a better correlation of the experimental μ versus v curve obtained in experiments on thin-walled tubes (see also Drucker [15]).

4.2.3 Hershey–Hosford Yield Criterion

As mentioned in Chap. 3, self-consistent calculations of the limit yield surface of macroscopically isotropic polycrystalline aggregates composed of randomly oriented, plastically deforming fcc single crystals were performed by Hershey [19], Budiansky and Wu [7], Kröner [30], and Hutchinson [26] among others. For polycrystalline aggregates comprised of randomly oriented bcc single crystals, self-consistent calculations were reported by Hutchinson [27]. An isotropic yield criterion that describes well the numerical yield points of Hutchinson [27] and Bishop and Hill [5] was introduced by Hershey [19], and further used by Hosford [22]. Its expression is given by:

$$\varphi(\sigma_1, \sigma_2, \sigma_3) = \left[\frac{|\sigma_1 - \sigma_2|^a + |\sigma_2 - \sigma_3|^a + |\sigma_3 - \sigma_1|^a}{2}\right]^{1/a} = \sigma_{\mathrm{T}}, \tag{4.53}$$

where the exponent a is such that $1 \leq a < \infty$. Note that this yield function is independent of hydrostatic pressure, and it is symmetric in the principal stresses $\sigma_1, \sigma_2, \sigma_3$. If a is an even integer, it predicts that yielding is the same in tension–compression. If $a = 1$ or $a = 2$, the Tresca and von Mises yield criterion are, respectively, recovered.

The ratio between the yield stress in uniaxial tension and in pure shear is controlled by the parameter a, i.e.,

$$\sigma_T = \tau_Y\left(1+2^{a-1}\right)^{1/a}, \tag{4.54}$$

while the yield stress under equibiaxial tension and uniaxial tension should be equal irrespective of a. If $1 \leq a \leq 2$ or $4 \leq a < \infty$, the plane-stress yield locus according to this criterion is given as,

$$|\sigma_1 - \sigma_2|^a + |\sigma_2|^a + |\sigma_1|^a = 2(\sigma_T)^a, \tag{4.55}$$

and it is located between the Tresca hexagon and the von Mises ellipse. As an example, Fig. 4.9 shows a comparison between the Hershey [20]–Hosford [22] plane-stress yield locus for a = 8 and the von Mises yield locus, respectively.

The cross-section of the Hershey [20]–Hosford [22] yield surface corresponding to $a = 8$ in the octahedral plane is shown in Fig. 4.10. Note the strong departure from the von Mises circle, indicating a very strong effect of the third-invariant J_3 on yielding for this value of the parameter a. Comparison between the yield points of an isotropic fcc polycrystal with plastic deformation of the constituents crystals governed by Bishop and Hill [5] model and the yield surface according to Hershey–Hosford criterion for $a = 6$ shows an excellent agreement (see Fig. 4.11).

Plastic potential associated with Hershey [20]–Hosford [22] *yield condition*

The flow potential associated with Hershey [20]–Hosford [22] yield condition is generally taken to have the same form as the yield function, i.e.,

$$\varphi(\sigma_1, \sigma_2, \sigma_3) = \left[\frac{|\sigma_1 - \sigma_2|^a + |\sigma_2 - \sigma_3|^a + |\sigma_3 - \sigma_1|^a}{2}\right]^{1/a}.$$

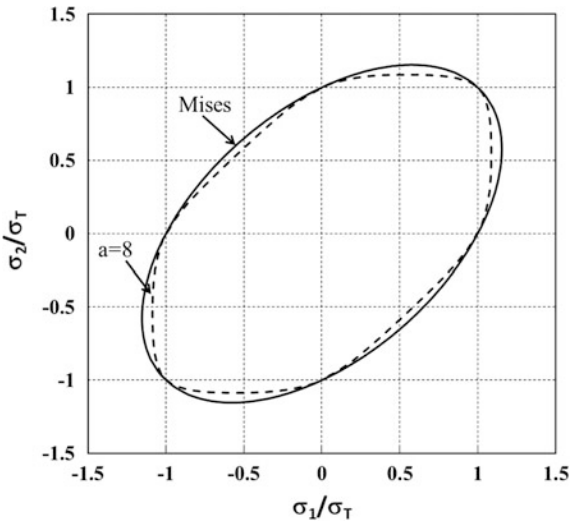

Fig. 4.9 Representation in the (σ_1, σ_2) plane of the yield locus according to Hershey [20]–Hosford [22] criterion corresponding to $a = 8$, in comparison with the von Mises yield criterion, which corresponds to $a = 2$ in Eq. (4.53). Principal stresses σ_1, σ_2 are normalized by the uniaxial yield in tension, σ_T

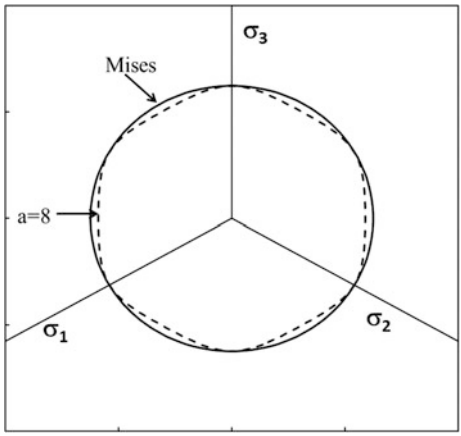

Fig. 4.10 Octahedral plane projections of the Hershey [20]–Hosford [22] yield surface corresponding to $a = 8$, and the von Mises yield surface [which corresponds to $a = 2$ in Eq. (4.53)]. Principal stresses σ_1, σ_2 , σ_3 are normalized by the uniaxial yield in tension, σ_T

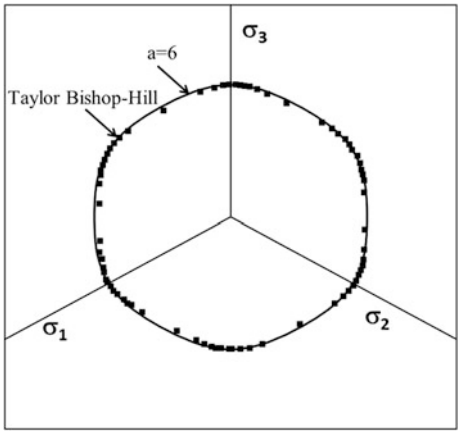

Fig. 4.11 Projection in the octahedral plane of the Hershey [20]–Hosford [22] yield surface corresponding to $a = 6$, and the numerical yield points for isotropic fcc polycrystal according to Bishop and Hill [5]. Principal stresses σ_1, σ_2 , σ_3 are normalized by the uniaxial yield in tension, σ_T

Since this function is expressed in terms of differences between principal values, it has the following property:

$$\varphi(\sigma_1, \sigma_2, \sigma_3) = \varphi(s_1, s_2, s_3), \tag{4.56}$$

so for any stress state, $\dfrac{\partial \varphi}{\partial \boldsymbol{\sigma}} = \dfrac{\partial \varphi}{\partial \mathbf{s}}$.

4.3 Yield Criteria for Isotropic Metallic Materials Showing Asymmetry Between the Response in Tension–Compression

4.3.1 Cazacu and Barlat [8] Yield Criterion

The stress–strain response in uniaxial tension–compression of isotropic maraging streel and HY-80 steel were reported by Spitzig et al. [38]. The test results indicated that these materials display strength differential effects, the ratio between the uniaxial yield stress in tension–compression, σ_T/σ_C, averaging 0.98 and 0.93, respectively. Most recently, test results on high-strength steel ES-1 indicate σ_T/σ_C of the order of 0.93 (see Bartlett [1]). Vitek et al. [43] demonstrated that a significant tension–compression asymmetry effect is obtained at the polycrystal level, if non-planar spreading of individual dislocations takes place. Also, crystallographic twinning is a directional shear deformation mechanism, and if it occurs yielding will depend on the sign of the applied stress [23]. Early simulation results by Chin et al. [12], who analyzed deformation by mixed slip and twining in fcc crystals, predicted a yield stress in uniaxial tension 25% lower than that in uniaxial compression. Hosford and Allen [24] performed the same type of calculations for other biaxial loadings. Based on their simulation results, these authors concluded that yield loci with a strong asymmetry between tension–compression should be expected in any isotropic pressure-insensitive material that deforms by twinning or directional slip. If the internal shear mechanism of plastic deformation is sensitive to the sign of the stress, then the macroscopic yield function ought to be represented by an odd function of the principal values of the Cauchy stress deviator $\mathbf{s}$. To account for strength differential effects in isotropic materials that are insensitive to hydrostatic pressure, Cazacu and Barlat [8] proposed the following isotropic criterion:

$$g \equiv (J_2)^{\frac{3}{2}} - cJ_3 = \tau_Y^3, \tag{4.57}$$

where τ_Y is the yield stress in pure shear and c is a material parameter. The physical significance of the constant c may be revealed from uniaxial tests. Indeed, according to this yield criterion:

$$\sigma_T = \tau_Y \left(\frac{27}{3\sqrt{3} - 2c} \right)^{\frac{1}{3}}. \tag{4.58}$$

Yielding in uniaxial compression occurs when $\sigma_1 = -\sigma_C$, $\sigma_2 = \sigma_3 = 0$. Substituting these values in Eq. (4.57) one obtains,

$$\sigma_C = \tau_Y \left(\frac{27}{3\sqrt{3} + 2c} \right)^{\frac{1}{3}}, \tag{4.59}$$

Hence,

$$c = \frac{3\sqrt{3}\left(\sigma_T^3 - \sigma_C^3\right)}{2\left(\sigma_T^3 + \sigma_C^3\right)}. \tag{4.60}$$

Therefore, the material parameter c depends solely on the ratio between the yield stress in tension–compression (σ_T/σ_C) for the given material. Furthermore, for a material for which the yield stress in tension is larger than in compression, i.e., $(\sigma_T/\sigma_C > 1)$ the parameter c should be positive $(c > 0)$. On the other hand, for a material which has the yield in compression larger than yield in tension, i.e., $\sigma_T < \sigma_C$, it follows that $c < 0$. It is worth noting that if a material has the same yield stresses in tension–compression, $c = 0$, and the criterion reduces to the von Mises yield criterion.

Proposition 4.6 (Convexity of the isotropic Cazacu and Barlat [8] yield function) *For the yield function g given by* Eq. (4.57) *to be convex, the parameter c is limited to the following numerical range*:

$$c \in \left(-\frac{3\sqrt{3}}{2}, \frac{3\sqrt{3}}{4}\right).$$

Proof Isotropy dictates threefold symmetry of the yield surface, so it is sufficient to prove its convexity for stress states corresponding to: $\sigma_1 \geq \sigma_2 \geq \sigma_3$. Let **M** be the Hessian matrix, i.e.

$$M_{ij} = \frac{\partial^2 g}{\partial \sigma_i \partial \sigma_j},$$

where $i, j = 1, \ldots, 3$ and σ_i are the principal stresses. It can be easily seen that the determinant of **M** is zero and the principal values are ξ_1, ξ_2 and $\xi_3 = 0$.

Furthermore,

$$\begin{aligned} I_M &= \frac{9}{2}\sqrt{J_2}, \\ II_M &= -\xi_1\xi_2 = \frac{4}{9}(s_1 - s_3)(s_2 - s_3)c^2 - \frac{s_3}{2\sqrt{J_2}}(s_1 - s_3)(s_2 - s_3)c \\ &\quad - \frac{9}{16J_2}\left[8J_2^2 + s_3^2(s_1 - s_2)^2\right] \end{aligned} \tag{4.61}$$

The function g is convex if and only if $I_M \geq 0$ and $II_M \leq 0$. From Eq. (4.61), it follows that $I_M \geq 0$. To study the sign of II_M, it is convenient to express the principal values of the stress deviator in terms of J_2 and J_3. As already mentioned, if $s_1 \geq s_2 \geq s_3$, these principal values can be given alternatively by:

$$s_k = 2\cos(\alpha_k)\sqrt{\frac{J_2}{3}}, \tag{4.62}$$

with α_1, the solution in the interval $0 \le \alpha_1 \le \pi/3$ of Eq. (4.42) while $\alpha_2 = \alpha_1 - 2\pi/3$. Further substitution into Eq. (4.61) leads to:

$$\begin{aligned} II_M &= -\frac{243}{16}s_2^2, \text{ if } s_2 = s_3 \\ II_M &= -A\,c^2 - Bc - D, \text{if } s_1 \ge s_2 > s_3, \\ \text{with } A &= -\frac{16}{9}J_2\sin(\alpha_1)\sin\left(\alpha_1 + \frac{\pi}{3}\right) \\ B &= \frac{4}{\sqrt{3}}J_2\sin(\alpha_1)\sin\left(\alpha_1 + \frac{\pi}{3}\right)\cos\left(\alpha_1 + \frac{2\pi}{3}\right), \text{and} \\ D &= \frac{9}{2}J_2 + 3J_2\sin^2\left(\alpha_1 - \frac{\pi}{3}\right)\cos^2\left(\alpha_1 + \frac{2\pi}{3}\right) \end{aligned}$$

Note that for any $0 < \alpha_1 < \pi/3$: $A < 0$ and $D > 0$. Thus, $II_M < 0$ for $c \in [c_1(\alpha_1),\ c_2(\alpha_1)\ ]$, where $c_1(\alpha_1)$ is the negative root and $c_2(\alpha_1)$ is the positive root of $II_M = 0$. These roots are:

$$c_1(\alpha_1) = \frac{\frac{1}{\sqrt{3}}\sin(\alpha_1)\sin\left(\alpha_1 + \frac{\pi}{3}\right)\cos\left(\alpha_1 + \frac{2\pi}{3}\right) - \sqrt{\Delta}}{\frac{8}{9}\sin(\alpha_1)\sin\left(\alpha_1 + \frac{\pi}{3}\right)}, \tag{4.63}$$

$$c_2(\alpha_1) = \frac{\frac{1}{\sqrt{3}}\sin(\alpha_1)\sin\left(\alpha_1 + \frac{\pi}{3}\right)\cos\left(\alpha_1 + \frac{2\pi}{3}\right) + \sqrt{\Delta}}{\frac{8}{9}\sin(\alpha_1)\sin\left(\alpha_1 + \frac{\pi}{3}\right)}, \tag{4.64}$$

where $\Delta = \sin(\alpha_1)\sin\left(\alpha_1 + \frac{\pi}{3}\right)\left\{2 + \cos^2\left(\alpha_1 + \frac{2\pi}{3}\right)\left(\frac{1}{4} + \sin^2\left(\alpha_1 - \frac{\pi}{3}\right)\right)\right\}$ is greater or equal to zero for any $0 \le \alpha_1 \le \pi/3$. Using Eqs. (4.63) and (4.64), we obtain that

$$\min(c_1(\alpha_1)) = c_1\left(\frac{\pi}{3}\right) = \frac{3\sqrt{3}}{4}; \quad \max(c_2(\alpha_1)) = c_2\left(\frac{\pi}{3}\right) = \frac{-3\sqrt{3}}{2}.$$

Therefore, if $c \in \left(-\frac{3\sqrt{3}}{2}, \frac{3\sqrt{3}}{4}\right)$ then $II_M < 0$ for any stress state $\sigma_1 \ge \sigma_2 \ge \sigma_3$.

Yielding Predictions for Biaxial Loadings

For plane-stress loadings ($\sigma_3 = 0$) according to the criterion [Eq. (4.57)] yielding occurs when:

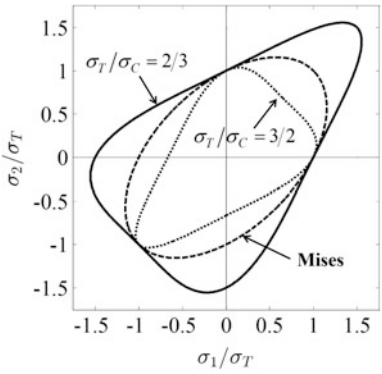

Fig. 4.12 Plane-stress yield loci according to the Cazacu and Barlat [8] criterion for different values of the ratio σ_T/σ_C between the yield stress in tension–compression, in comparison with the von Mises yield locus. The principal stresses are normalized by the yield stress in uniaxial tension, σ_T

$$\left[\frac{1}{3}\left(\sigma_1^2 - \sigma_1\sigma_2 + \sigma_2^2\right)\right]^{3/2} - \frac{c}{27}\left[2\sigma_1^3 + 2\sigma_2^3 - 3\,(\sigma_1 + \sigma_2)\sigma_1\sigma_2\right] = \tau_Y^3. \tag{4.65}$$

For any $c \neq 0$, Eq. (4.65) represents a "triangle" with rounded corners. For $c > 0$, the equibiaxial yield stress is larger than the yield stress in simple tension (triangle points toward the tension–tension quadrant). The reverse holds true for $c < 0$ (see also Fig. 4.12). Note that according to the criterion, the yield stress under equibiaxial tension, σ_b is given by:

$$\sigma_b = \tau_Y\left(\frac{27}{3\sqrt{3} + 2c}\right)^{\frac{1}{3}} = \frac{3\sqrt{3} - 2c}{3\sqrt{3} + 2c}\sigma_T \tag{4.66}$$

Equation (4.66) indicates that the yield stress under equibiaxial tension is the absolute value of the yield stress in simple compression [see Eq. (4.59)]. This is a direct consequence of the yield function being independent of the hydrostatic pressure. Indeed, if the stress point $(\sigma_b, \sigma_b, 0)$ is on the yield surface then the point $(0, 0, -\sigma_b)$ is also on the yield surface. Isotropy then dictates that $\sigma_b = \sigma_C$. As an example, in Fig. 4.12 are shown the plane-stress yield loci corresponding to $\sigma_T/\sigma_C = 2/3$ $(c = -1.41)$, 1 $(c = 0$, i.e., von Mises), and 3/2 $(c = 1.41)$, respectively. The principal stresses are normalized by σ_T. Irrespective of the value of the parameter c, the criterion predicts the same yield stress in pure shear [see Eq. (4.57)].

As already mentioned, the effect of the third-invariant J_3 on yielding is readily observed in combined tension and torsion tests (e.g., Taylor and Quinney [40]). If a normal stress is set equal to σ, a shear stress is set equal to τ, and all other stress components are set equal to zero, using Eq. (4.57), we obtain the Cazacu and Barlat [8] yield locus cross-section in the (σ, τ) plane as

$$\left[\frac{1}{3}\left(\sigma^2 + 3\tau^2\right)\right]^{3/2} - \frac{c}{27}\left[2\sigma^3 + 9\tau^2\sigma\right] = \tau_Y^3 \tag{4.67}$$

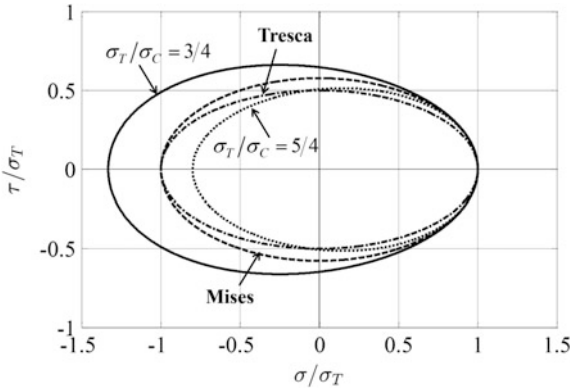

Fig. 4.13 Section of the yield loci in the (σ, τ) plane (tension–torsion; compression-torsion) predicted by the Tresca and Cazacu and Barlat [8] isotropic yield criterion (Eq. (4.57) for $\sigma_T/\sigma_C = 3/4, 1$ (von Mises) and 5/4, respectively. The stresses are normalized by the yield stress in uniaxial tension, σ_T

Note also that the cross-section of the Tresca yield criterion in the (σ, τ) plane is

$$\sqrt{\sigma^2 + 4\tau^2} = \sigma_T, \tag{4.68}$$

and that of von Mises' surface is given by Eq. (4.67) with $c = 0$. The representation in the tension–torsion plane $(\sigma/\sigma_T, \tau/\sigma_T)$ of the Tresca yield locus, and the Cazacu and Barlat [8] yield locus corresponding to $\sigma_T/\sigma_C = 3/4, 1$ (von Mises), and 5/4 is shown in Fig. 4.13.

Comparison with the theoretically derived yield loci for isotropic polycrystalline aggregates

To illustrate the predictive capabilities of the isotropic criterion proposed by Cazacu and Barlat [8], we compare the yield loci obtained using this criterion with the theoretical yield loci for randomly oriented isotropic aggregates computed using different descriptions of the single crystal plastic deformation and various upscaling methods. As already mentioned, Hosford and Allen [24] computed the limit yield surface of isotropic fcc aggregates deforming by slip and crystallographic twinning. Each twin system (s) was considered to be characterized by a vector $\mathbf{n}^s$, the normal to the twinning plane, and a vector $\mathbf{b}^s$, the twinning shear direction. As discussed in Chap. 3 for fcc crystals, crystallographic twinning may occur along the {111} crystallographic planes in the $\langle 11\bar{2} \rangle$ crystallographic directions. Twining is unidirectional, i.e., if it occurs in the (111) plane along the $\langle \bar{2}11 \rangle$ direction, reversing the applied shear stress cannot cause twinning in the $\langle 2\bar{1}\bar{1} \rangle$ direction. Of the twelve potentially active twin systems, the ones that are operative were found by minimizing the plastic work. The calculated yield points of the isotropic aggregate comprised of fcc crystals, deforming solely by twining are shown in Fig. 4.14 (open circles). The yield locus according to the Cazacu and Barlat [8] criterion (dashed curve) is superposed on the same figure. The only parameter involved in the criterion is c, which is expressible in terms of the σ_T/σ_C ratio [see Eq. (4.60)]. Hosford and Allen [24] reported a calculated value of this ratio as 0.78 which corresponds to a value of $c = -0.92$. The yield stresses (open circles) reported in Hosford and Allen [24] are also superimposed on

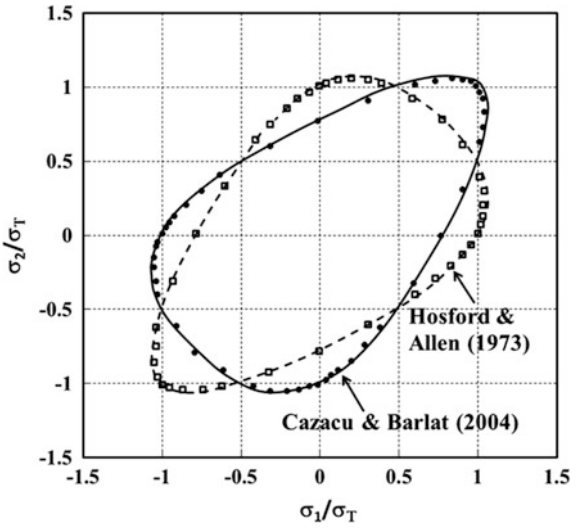

Fig. 4.14 Comparison between plane-stress yield surfaces according to the isotropic Cazacu and Barlat [8] criterion and the polycrystalline model of Hosford and Allen [24] for isotropic bcc polycrystals ($\sigma_T/\sigma_C = 1.28$) and isotropic fcc polycrystals ($\sigma_T/\sigma_C = 0.78$), respectively

the same figure. Note that the yield locus generated with the Cazacu and Barlat [8] criterion coincides with the yield locus obtained by polycrystalline calculations.

Also, Fig. 4.14 shows a comparison between the yield locus predicted by the Cazacu and Barlat [8] criterion (solid line) and the Hosford and Allen [24] predictions (full symbols) for an isotropic aggregate comprised of bcc crystals deforming solely by $\{112\}\langle\overline{1}\overline{1}1\rangle$ twinning. For the isotropic bcc polycrystal, the ratio σ_T/σ_C obtained by Hosford and Allen [24] is $\sigma_T/\sigma_C = 1.28$; hence, the value of the parameter c for bcc polycrystals is: $c = 0.92$. Comparison between the yield surface according to the Cazacu and Barlat [8] criterion [Eq. (4.60)] and the numerical yield points shows an excellent agreement for all stress states. This is remarkable given that only two data points (i.e., the values of σ_T, and σ_C) were used for identification of the Cazacu and Barlat [8] criterion.

On the basis of atomistic calculations, Vitek et al. [43] showed that in single crystal molybdenum, the critical resolved shear stress depends on the orientation of the maximum resolved shear stress plane and proposed the following criterion for the onset of slip:

$$\tau_{\text{Schmid}} + \beta\,\tau_{(0\overline{1}1)} = \tau_0 \tag{4.69}$$

Here, τ_{Schmid} is the Schmid resolved shear stress (see also Chap. 3), $\tau_{(0\overline{1}1)}$ is a non-glide stress (shear stress parallel to the Burgers vectors in the (011) plane), τ_0 is a constant threshold value, which is considered to be the same for each slip system and β is a constant. Furthermore, the same authors calculated the yield surface for an isotropic aggregate comprised of bcc crystals for which the plastic deformation is governed by Eq. (4.69) with $\beta = 0.6$. Of the twelve $\{110\}\langle\overline{1}\overline{1}1\rangle$ slip systems, the ones considered active correspond to the ones which minimize the plastic work [5].

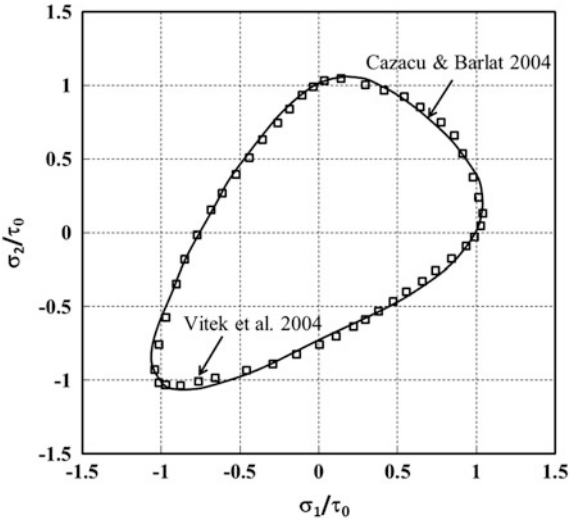

Fig. 4.15 Comparison between the yield surface for an isotropic bcc molybdenum polycrystal obtained with the Bishop and Hill [5] model in conjunction with the single crystal yield criterion (4.69) with $\beta = 0.6$ (after Vitek et al. [43]) and the theoretical yield surface according to the isotropic Cazacu and Barlat [8] criterion with $c = 1.109$ (solid line)

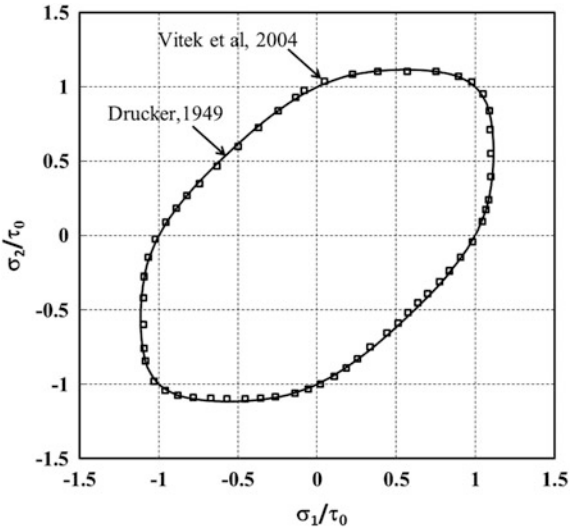

Fig. 4.16 Comparison between the yield surface for an isotropic bcc molybdenum polycrystal (symbols) obtained with the Bishop and Hill [5] model in conjunction with Schmid criterion at single crystal level (i.e., criterion given by Eq. (4.69) with $\beta = 0$) and the theoretical yield surface according to Drucker [15] criterion with $c = 0.288$

The calculated biaxial yield surface for the isotropic bcc polycrystal is represented in Fig. 4.15 by symbols. A strong tension–compression asymmetry was observed: $\sigma_T/\sigma_C = 1.22$ to which corresponds a value of $c = 1.109$ in the Cazacu and Barlat [8] isotropic criterion [see Eq. (4.60)]. Note the excellent agreement between the predictions according to the criterion and the polycrystalline simulation results. The same authors have also reported simulations using the method of Bishop and Hill [5] in conjunction with the classic Schmid law [i.e., setting $\beta = 0$ in Eq. (4.69)]. The resulting yield surface of the randomly oriented bcc polycrystal is represented in Fig. 4.16. As expected, no strength differential effects are observed

for the polycrystal. It is interesting to note that the polycrystalline results are very well approximated by the Drucker [15] isotropic yield criterion given by Eq. (4.36) (represented in Fig. 4.16 by a solid line) for $c = 0.288$. In Fig. 4.16, stresses are normalized by the uniaxial yield in tension, σ_T.

4.3.2 Cazacu et al. [9] Isotropic Yield Criterion

Cazacu et al. [9] proposed the following isotropic yield criterion:

$$F(s_1, s_2, s_3) = (|s_1| - ks_1)^a + (|s_2| - ks_2)^a + (|s_3| - ks_3)^a, \tag{4.70}$$

where s_i, i = 1, …, 3 are the principal values of the stress deviator. In Eq. (4.70), the exponent a is considered to be a positive integer, k is a material constant. Note that this yield function is symmetric in the principal values of the stress deviator s_1, s_2, s_3, therefore it is isotropic and pressure-insensitive. It is important to note that for $k \neq 0$, $F(s_1, s_2, s_3) \neq F(\sigma_1, \sigma_2, \sigma_3)$. This is unlike all the classic yield functions such as von Mises, Tresca, and Hershey–Hosford, which have the same expression whether these criteria are written in terms of $\sigma_1, \sigma_2, \sigma_3$ or s_1, s_2, s_3. Furthermore, since F is an odd function in s_1, s_2, s_3, yielding depends on the sense of loading, and $F(-s_1, -s_2, -s_3) = -F(s_1, s_2, s_3)$. As a consequence, the projection of the yield surface in the octahedral plane has threefold symmetry. The physical significance of the material parameter k may be revealed from simple uniaxial tests. Indeed, according to Eq. (4.70), the ratio of tensile to compressive uniaxial yield stress is given by:

$$\frac{\sigma_T}{\sigma_C} = \left\{ \frac{\left(\frac{2}{3}\cdot(1+k)\right)^a + 2\cdot\left(\frac{1}{3}\cdot(1-k)\right)^a}{\left(\frac{2}{3}\cdot(1-k)\right)^a + 2\cdot\left(\frac{1}{3}\cdot(1+k)\right)^a} \right\}^{\frac{1}{a}} \tag{4.71}$$

Hence,

$$k = \frac{1 - h\left(\frac{\sigma_T}{\sigma_C}\right)}{1 + h\left(\frac{\sigma_T}{\sigma_C}\right)}, \tag{4.72}$$

with

$$h(x) = \left[\frac{2^a - 2x^a}{(2x)^a - 2}\right]^{\frac{1}{a}} \tag{4.73}$$

It follows that for a fixed value of the coefficient a, the parameter k is expressible solely in terms of the ratio σ_T/σ_C [see Eqs. (4.72) and (4.73)]. Note that for any value of $a \geq 1$, where a is an integer, if $k = 0$, there is no difference between the response in tension–compression. In particular, for $k = 0$ and $a = 2$, the criterion given by Eq. (4.70) reduces to the von Mises yield criterion. Also, from Eq. (4.72), it follows that for a given value of the exponent a, for the parameter k to be real, the ratio between the uniaxial yield stresses in tension–compression is bounded,

$$2^{\frac{1-a}{a}} \leq \frac{\sigma_T}{\sigma_C} \leq 2^{\frac{a-1}{a}} \tag{4.74}$$

Specifically,

- for $2^{\frac{1-a}{a}} \leq \sigma_T/\sigma_C \leq 1 \Rightarrow -1 \leq k \leq 0$,
- for $1 \leq \sigma_T/\sigma_C \leq 2^{\frac{a-1}{a}} \Rightarrow 0 \leq k \leq 1$

Given that the yield function given by Eq. (4.70) is pressure-insensitive, the yield stress under equibiaxial tension is the absolute value of the yield stress in simple compression:

$$\sigma_b = \sigma_T \left\{ \frac{2^a(1-k)^a + 2(1+k)^a}{2^a(1+k)^a + 2(1-k)^a} \right\}^{\frac{1}{a}} = \sigma_C. \tag{4.75}$$

For thin-sheet materials, for which it is difficult to conduct compression tests to determine σ_C, the parameter k should be identified from measurements done in equibiaxial tensile tests in conjunction with Eq. (4.75).

Since the yield criterion (4.70) depends on the sign of each of the principal values of the stress deviator s_1, s_2, and s_3, for any biaxial loadings ($\sigma_3 = 0$), yielding depends on the location of the stress state with respect to the lines $s_1 = 0$, $s_2 = 0$, and $s_3 = 0$, respectively. Note that in the biaxial plane $\sigma_3 = 0$, stress states such that $s_1 = 0$ are on the line of equation $\sigma_2 = 2\sigma_1$, stress states for which $s_2 = 0$ are on the line of equation $\sigma_2 = \sigma_1/2$ while states for which $s_3 = 0$ are on the line of equation $\sigma_2 = -\sigma_1$ (see Fig. 4.17a). For direct comparison with the von Mises yield criterion predictions, in the following we deduce and represent the projection of the yield surface (4.70) corresponding to $a = 2$.

In the domain $Z_1 = \{(\sigma_1, \sigma_2) | -\sigma_1 \leq \sigma_2 \leq \sigma_1/2, \sigma_1 \geq 0\}$ delimited by the lines of equations $s_3 = 0$ and $s_2 = 0$, and σ_1 positive (see Fig. 4.17a), we have: and $s_3 \leq 0$. Therefore, the yield condition (4.70) writes:

$$\sigma_1^2 + \frac{3k^2 + 4k + 3}{3k^2 - 2k + 3}\sigma_2^2 - \sigma_1\sigma_2 = \sigma_T^2 \tag{4.76}$$

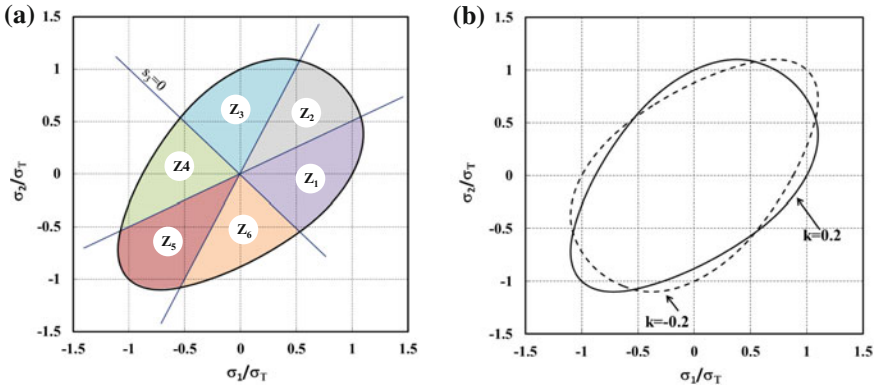

Fig. 4.17 **a** Representation of the different domains of the yield locus in the biaxial plane ($\sigma_3 = 0$) for a material characterized by $\sigma_T/\sigma_b = 1.13$ (k = 0.2). **b** Comparison between the plane-stress yield loci according to the quadratic form of the Cazacu et al. [9] criterion [see Eq. (4.70)] for materials characterized by k = 0.2 ($\sigma_T/\sigma_b = 1.13$) and k = −0.2 ($\sigma_T/\sigma_b = 0.88$)

Similarly, we obtain:

- In the domain $Z_2 = \{(\sigma_1, \sigma_2) | 0 \leq \sigma_1/2 \leq \sigma_2 \leq 2\sigma_1\}$

$$\frac{3k^2 - 4k + 3}{3k^2 - 2k + 3}\left(\sigma_1^2 + \sigma_2^2\right) - \frac{3k^2 - 10k + 3}{3k^2 - 2k + 3}\sigma_1\sigma_2 = \sigma_T^2, \tag{4.77}$$

- In the domain $Z_3 = \{(\sigma_1, \sigma_2) | 2\sigma_1 \leq \sigma_2 \leq -\sigma_1, \sigma_2 \geq 0\}$

$$\frac{3k^2 + 4k + 3}{3k^2 - 2k + 3}\sigma_1^2 + \sigma_2^2 - \sigma_1\sigma_2 = \sigma_T^2, \tag{4.78}$$

- In the domain $Z_4 = \{(\sigma_1, \sigma_2) | -\sigma_1 \leq \sigma_2 \leq \sigma_1/2, \sigma_1 \leq 0\}$

$$\sigma_1^2 + \frac{3k^2 - 4k + 3}{3k^2 - 2k + 3}\sigma_2^2 - \sigma_1\sigma_2 = \sigma_T^2, \tag{4.79}$$

- In the domain $Z_5 = \{(\sigma_1, \sigma_2) | \sigma_1/2 \leq \sigma_2 \leq 2\sigma_1 \leq 0\}$

$$\frac{3k^2 + 4k + 3}{3k^2 - 2k + 3}\left(\sigma_1^2 + \sigma_2^2\right) - \frac{3k^2 + 10k + 3}{3k^2 - 2k + 3}\sigma_1\sigma_2 = \sigma_T^2, \tag{4.80}$$

- In the domain $Z_6 = \{(\sigma_1, \sigma_2) | 2\sigma_1 \leq \sigma_2 \leq -\sigma_1, \sigma_2 \leq 0\}$

$$\frac{3k^2 - 4k + 3}{3k^2 - 2k + 3}\sigma_1^2 + \sigma_2^2 - \sigma_1\sigma_2 = \sigma_T^2, \tag{4.81}$$

It is worth noting that if $k = 0$ each of the above equations [Eqs. (4.76)–(4.81)] reduces to Eq. (4.22), i.e., the von Mises ellipse in the (σ_1, σ_2) plane. However, for

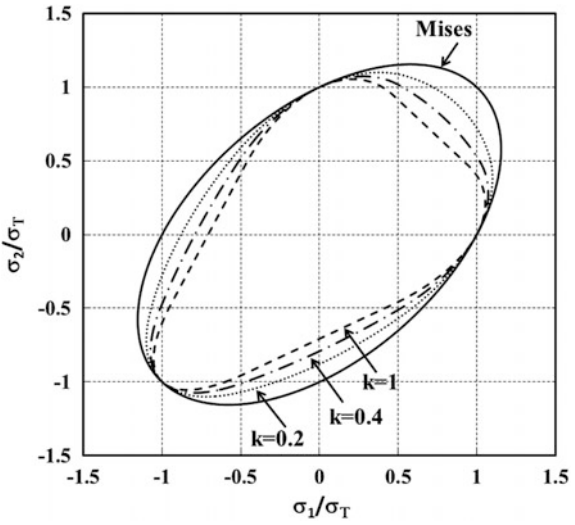

Fig. 4.18 Plane-stress yield loci according to the quadratic form of the Cazacu et al. [9] criterion [see Eq. (4.70)] for different values of the ratio σ_T/σ_b between the yield stress in simple tension and equibiaxial tension ($\sigma_T/\sigma_b = \sqrt{2}$, 1.26, 1.13 corresponding to k = 0.2, k = 0.4, k = 1) in comparison with the von Mises yield locus ($\sigma_T/\sigma_b = 1$ and k = 0). Principal stresses are normalized by the uniaxial yield stress in tension, σ_T

$k \neq 0$, the yield function accounts for the asymmetry of the mechanical behavior between tension–compression, so unlike the projection of the von Mises yield criterion in the biaxial plane [Eq. (4.22)], the yield curve defined by the Eqs. (4.76)–(4.81) admits only one reflection plane defined by the line $\sigma_2 = \sigma_1$ and is no longer invariant by the transformation $(\sigma_1, \sigma_2) \rightarrow (-\sigma_1, -\sigma_2)$ [e.g., compare the Eq. (4.78) with (4.80)]. In other words, the only symmetry of the yield curve is dictated by isotropy (invariance to permutations between σ_1 and σ_2).

It is also worth noting that $h(1/x) = 1/h(x)$; therefore,

$$k\left(\frac{\sigma_T}{\sigma_b}\right) = -k\left(\frac{\sigma_b}{\sigma_T}\right). \tag{4.82}$$

[see Eqs. (4.72) and (4.73)]. As a consequence, the biaxial yield surface corresponding to a given value of k is the mirror image with respect to the origin of the yield surface corresponding to $(-k)$. Although this property holds true irrespective of the value of the exponent a, to facilitate comparison with the predictions of the von Mises criterion, in Fig. 4.17b, we show the plane-stress yield loci according to the isotropic Cazacu et al. [9] criterion with $a = 2$ for materials characterized by $\sigma_T/\sigma_b = 1.13$ (k = 0.2) and $\sigma_T/\sigma_b = 0.88$ (k = −0.2), respectively. It is clearly seen that a change in the sign of k results in a mirror image of the yield surface Eq. (4.70) with respect to the origin [see also Eqs. (4.76)–(4.81)].

As an example, in Fig. 4.18 are shown the representation of the plane-stress yield loci ($\sigma_3 = 0$) according to the quadratic form of Cazacu et al. [9] yield criterion [i.e., a = 2 in Eq. (4.70)] for materials characterized by $\sigma_T/\sigma_b = \sqrt{2}$, 1.26, 1.13, and 1, respectively. Note that the higher is the ratio between the yield stress in tension–compression, the greater is the departure from the von Mises ellipse; for the

highest admissible σ_T/σ_b ratio, which corresponds to $k = 1$, the biaxial projection of the yield surface given by Eq. (4.70) is a triangle with rounded corners.

Proposition 4.7 (Convexity of Cazacu et al. [9] criterion)

For any integer $a \geq 1$ *and for* $-1 \leq k \leq 1$, *the* Cazacu et al. [9] *yield function given by* Eq. (4.70) *is convex.*

Proof The yield function $F(s_1, s_2, s_3)$ given by Eq. (4.70) being isotropic, it is sufficient to prove its convexity for stress states corresponding to: $s_1 \geq s_2 \geq s_3$. However, due to the fact that $F(s_1, s_2, s_3)$ is an odd function, its expressions are different depending on the sign of the principal stresses. Hence, in the calculation of the Hessian matrix, $U_{ij} = \dfrac{\partial^2 F}{\partial\sigma_i \partial\sigma_j}$, $i, j = 1, \ldots, 3$, the following loading scenarios need to be considered separately: (i) $s_1 > 0,\ s_2 \leq 0,\ s_3 < 0$, and (ii) $s_1 > 0,\ s_2 > 0,\ s_3 < 0$. It follows that:

(i) For $s_1 > 0,\ s_2 \leq 0,\ s_3 < 0$:

$$
\begin{aligned}
U_{11} &= \frac{a(a-1)}{9}\left\{4(1-k)^a s_1^{a-2} + (1+k)^a(-1)^a(s_2^{a-2} + s_3^{a-2})\right\}\\
U_{22} &= \frac{a(a-1)}{9}\left\{(1-k)^a s_1^{a-2} + (1+k)^a(-1)^a(4s_2^{a-2} + s_3^{a-2})\right\}\\
U_{33} &= \frac{a(a-1)}{9}\left\{(1-k)^a s_1^{a-2} + (1+k)^a(-1)^a(s_2^{a-2} + 4s_3^{a-2})\right\}\\
U_{12} &= \frac{a(a-1)}{9}\left\{-2(1-k)^a s_1^{a-2} - (1+k)^a(-1)^a(2s_2^{a-2} - s_3^{a-2})\right\}\\
U_{13} &= \frac{a(a-1)}{9}\left\{-2(1-k)^a s_1^{a-2} - (1+k)^a(-1)^a(-s_2^{a-2} + 2s_3^{a-2})\right\}\\
U_{23} &= \frac{a(a-1)}{9}\left\{(1-k)^a s_1^{a-2} + (1+k)^a(-1)^a(-2s_2^{a-2} - 2s_3^{a-2})\right\}
\end{aligned}
\tag{4.83}
$$

Using Eq. (4.83), we obtain that $\sum_{j=1}^{3} U_{ij} = 0$ for any $i = 1, \ldots, 3$. Thus, the determinant of $\mathbf{U}$ is zero and its principal values are $\beta_1,\ \beta_2$, and $\beta_3 = 0$. Furthermore,

$$
\begin{aligned}
I_U &= \beta_1 + \beta_2 = \frac{6\,a(a-1)}{9}\left\{(1-k)^a s_1^{a-2} + (1+k)^a(-1)^a(s_2^{a-2} + s_3^{a-2})\right\}\\
II_U &= -\beta_1\beta_2 = -\frac{a^2(a-1)^2}{9}\Big[(1-k)^{2a}\left(s_1^2\right)^{a-2} + (1+k)^{2a}\left(s_2^2\right)^{a-2} + \left(1-k^2\right)^a\\
&\qquad (s_1)^{a-2}(-s_2)^{a-2} + 3\left(1-k^2\right)^a(s_1)^{a-2}(-s_3)^{a-2} + 3(1+k)^{2a}(-s_2)^{a-2}(-s_3)^{a-2}\Big].
\end{aligned}
$$

Since $s_1 > 0,\ s_2 < 0,\ s_3 < 0$, it follows that for $k \in (-1, 1)$ and any integer $a \geq 1$ both $I_U = \beta_1 + \beta_2 \geq 0$ and $II_U = -\beta_1\beta_2 \leq 0$, i.e., the Hessian is always positive semi-definite.

For the case (ii) $s_1 > 0,\ s_2 > 0,\ s_3 < 0$, we have:

$$\begin{aligned}
U_{11} &= \frac{a(a-1)}{9}\left\{(1-k)^a(4s_1^{a-2}+s_2^{a-2})+(1+k)^a(-1)^a s_3^{a-2}\right\}\\
U_{22} &= \frac{a(a-1)}{9}\left\{(1-k)^a(s_1^{a-2}+4s_2^{a-2})+(1+k)^a(-1)^a s_3^{a-2}\right\}\\
U_{33} &= \frac{a(a-1)}{9}\left\{(1-k)^a(s_1^{a-2}+s_2^{a-2})+4(1+k)^a(-1)^a s_3^{a-2}\right\}\\
U_{12} &= \frac{a(a-1)}{9}\left\{-2(1-k)^a(s_1^{a-2}+s_2^{a-2})+(1+k)^a(-1)^a s_3^{a-2}\right\}\\
U_{13} &= \frac{a(a-1)}{9}\left\{(1-k)^a(-2s_1^{a-2}+s_2^{a-2})-2(1+k)^a(-1)^a s_3^{a-2}\right\}\\
U_{23} &= \frac{a(a-1)}{9}\left\{(1-k)^a(s_1^{a-2}-2s_2^{a-2})-2(1+k)^a(-1)^a s_3^{a-2}\right\}
\end{aligned} \tag{4.84}$$

so the determinant of $\mathbf{U}$ is zero and

$$\begin{aligned}
I_U &= \frac{6a(a-1)}{9}\left\{(1-k)^a(s_1^{a-2}+s_2^{a-2})+(1+k)^a(-1)^a s_3^{a-2}\right\}\\
II_U &= -\beta_1\beta_2 = -\frac{a^2(a-1)^2}{9}\times\\
&\quad\Big[\left(1-k^2\right)^a\left(s_2^2\right)^{a-2}+(1-k)^{2a}\left(s_2^2\right)^{a-2}+(1-k)^{2a}(s_1)^{a-2}(s_2)^{a-2}\\
&\quad+3(1+k)^{2a}(s_2)^{a-2}(-s_3)^{a-2}+3(1+k)^{2a}(s_1)^{a-2}(-s_3)^{a-2}\Big]
\end{aligned}$$

Since $s_1 > 0,\ s_2 > 0,\ s_3 < 0$, it follows that for $k \in (-1,1)$ and any integer $a \geq 1$:

$$I_U \geq 0 \text{ and } II_U \leq 0.$$

Thus, for any $k \in [-1,1]$ and any integer $a \geq 1$, the yield function given by Eq. (4.70) is convex.

Representation of the Cazacu et al. [9] *yield surface in the octahedral plane*
For the Cazacu et al. [9] criterion and the von Mises criterion to agree in uniaxial tension, we express the Cazacu et al. [9] yield condition as:

$$\mathrm{B}\left[(|s_1|-ks_1)^a+(|s_2|-ks_2)^a+(|s_3|-ks_3)^a\right]^{\frac{1}{a}} = \sigma_{\mathrm{T}}, \tag{4.85}$$

with

$$B = \left[\frac{3^a}{2^a(1-k)^a+2(1+k)^a}\right]^{\frac{1}{a}}. \tag{4.86}$$

Note that, for $a = 2$ and $k = 0$, B takes the value of $\sqrt{3/2}$ and the criterion reduces to the von Mises yield criterion. To obtain the intersection of the yield surface with the octahedral plane, we substitute Eq. (4.13) in Eq. (4.85). As already mentioned, for $k \neq 0$, the projection of the yield surface has threefold symmetry, so to determine its shape, we need to determine $R(\gamma)$ only in the sector $-\pi/6 \leq \gamma \leq \pi/6$. For example, the projection of the yield surface corresponding to $a = 2$ is given by:

$$R(\gamma) = \begin{cases} \sqrt{\left(\frac{2\sigma_T}{3}\right) \frac{3(1+k^2) - 2k}{3(1+k^2) + 8k \sin\gamma \cos(\gamma - \pi/6)}}, & -\pi/6 \leq \gamma < 0 \\ \sqrt{\left(\frac{2\sigma_T}{3}\right) \frac{3(1+k^2) - 2k}{3(1+k^2) + 8k \sin\gamma \cos(\gamma + \pi/6)}}, & 0 \leq \gamma < \pi/6 \end{cases} \tag{4.87}$$

Figure 4.19 shows the cross-section in the octahedral plane of the yield surface (4.70) with $a = 2$ [i.e., Eq. (4.87)] for materials characterized by $\sigma_T/\sigma_C > 1$ (i.e., $k > 0$) and $\sigma_T/\sigma_C = 1$ (i.e. $k = 0$, von Mises) and Tresca's yield surface for comparison. As the value of k increases, the ratio σ_T/σ_C increases, and the Cazacu et al. [9] yield loci depart drastically from the von Mises circle.

The expression of the isotropic yield criterion given by Eq. (4.70) was inspired by the shape of the yield loci for isotropic fcc and bcc polycrystals deforming by slip and twinning reported by Hosford and Allen [24]. As mentioned earlier, these authors calculated the respective yield loci using an extension of the Bishop and Hill [5] model and Taylor's assumption that the plastic strain in each constituent grain equals the imposed macroscopic strain. In view of comparison with the yield criterion given by Eq. (4.70), in Cazacu et al. [9], the crystal plasticity yield loci for isotropic fcc, bcc, and hcp polycrystals were also calculated using the one-site viscoplastic self-consistent polycrystal (VPSC) model of Lebensohn and Tomé (see Lebensohn and Tomé [31]; Lebensohn et al. [32]) which assumes a less rigid interaction between each grain and its surroundings (i.e., each grain is treated as an

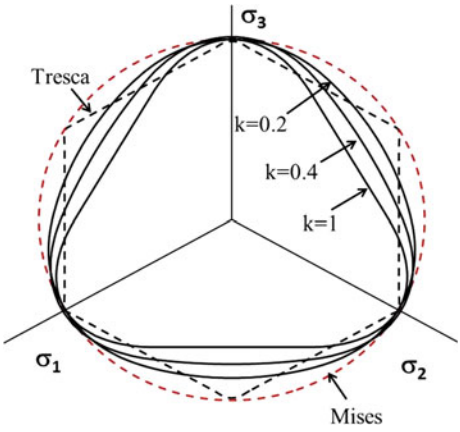

Fig. 4.19 Projection of the quadratic Cazacu et al. [9] yield surface (Eq. (4.70) with $a = 2$) in the octahedral plane for materials characterized by $k > 0$ in comparison with the von Mises cross-section (Eq. (4.70) with $k = 0$ and $a = 2$) and Tresca's cross-section. Principal stresses are normalized by the uniaxial yield stress in tension, σ_T

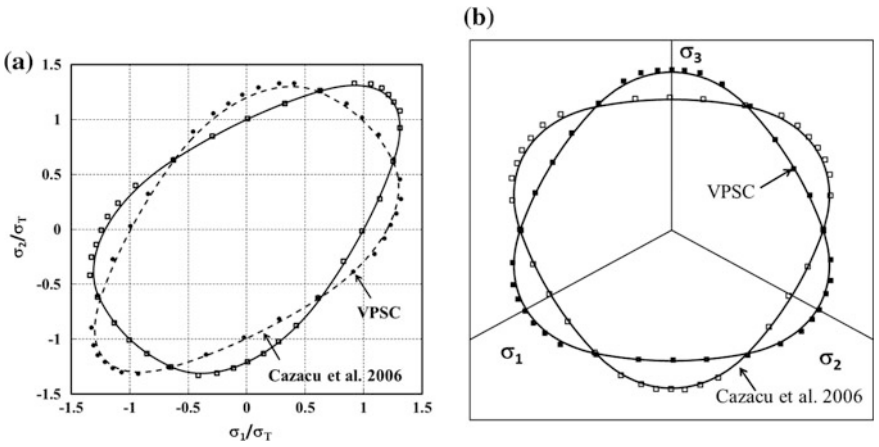

Fig. 4.20 Comparison between the VPSC yield locus for isotropic fcc (open symbols) and bcc (closed symbols) polycrystals deforming by slip and twinning and the predictions of the quadratic Cazacu et al. [9] criterion (with $k = -0.3098$ and $k = 0.3098$, respectively): **a** in the biaxial plane $(\sigma_3 = 0)$; **b** in the octahedral plane. Principal stresses are normalized by the uniaxial yield stress in tension, σ_T

anisotropic, viscoplastic, ellipsoidal inclusion embedded in a uniform matrix which has the average constitutive behavior of the polycrystal). First, let us compare the yield loci obtained using Cazacu et al. [9] criterion Eq. (4.70) with the yield loci for isotropic fcc polycrystals deforming by slip and $\{111\}\langle 11\bar{2}\rangle$ twinning calculated using the VPSC model. The yield condition (4.70) involves two parameters: the exponent a and the parameter k, which for a fixed value of the parameter a is expressible solely in terms of the σ_T/σ_C ratio [see Eq. (4.72)]. The VPSC model predicts a ratio of 0.83 between the yield stress in tension–compression; Hosford and Allen [24] reported a value of 0.78 for the same ratio. Assuming $a = 2$, we obtain $k = -0.3098$. Figure 4.20a, b show the yield stresses (open symbols) obtained using the VPSC model and the projection of the yield locus predicted by the criterion for $k = -0.3098$ (solid line) in the biaxial plane $(\sigma_3 = 0)$ and in the octahedral plane, respectively. It is clearly seen that the isotropic criterion (4.70) describes very well the polycrystalline results (see Fig. 4.20).

On the same figure are shown the comparison between the yield loci obtained with the VPSC model for isotropic bcc polycrystals deforming by slip and $\{112\}\langle\bar{1}\bar{1}1\rangle$ twinning (solid symbols) and the yield loci according to the isotropic criterion given by Eq. (4.70) with $a = 2$ and $k = 0.3098$ (which correspond to a ratio between the yield stress in tension–compression which is the reciprocal of the value for the fcc polycrystals). Figure 4.21a, b show a comparison between the yield loci obtained using the criterion with $a = 3$ and $k = -0.0645$ and the yield loci for isotropic hcp polycrystals deforming solely by tensile twinning $\{10\bar{1}2\}\langle 10\bar{1}1\rangle$ and compressive twinning $\{11\bar{2}2\}\langle 11\bar{2}\bar{3}\rangle$ calculated using the VPSC model. Again, the strength differential effect is well captured (for more details see [9]).

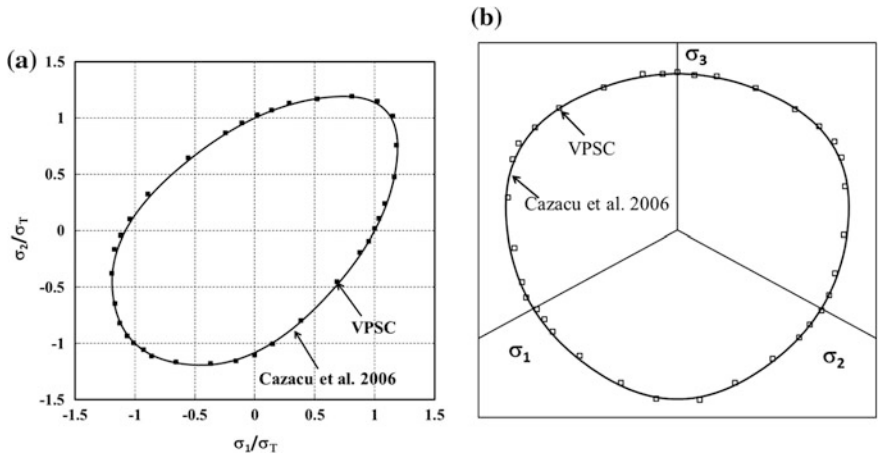

Fig. 4.21 Comparison between the VPSC yield locus for randomly oriented hcp polycrystals deforming solely by twinning (open symbols) and the predictions of Cazacu et al. [9] criterion [$a = 3$ and $k = -0.0645$ in Eq. (4.70)]: **a** in the biaxial plane; **b** in the octahedral plane

Plastic potential associated with the isotropic form of the Cazacu et al. [9] *yield condition*

Assuming associated flow rule, the plastic potential associated with the isotropic form of Cazacu et al. [9] criterion given by Eq. (4.70) is of the form:

$$\varphi(\boldsymbol{\sigma}) = \bar{\sigma}(\boldsymbol{\sigma}) = B[(|s_1| - ks_1)^a + (|s_2| - ks_2)^a + (|s_3| - ks_3)^a]^{\frac{1}{a}} \tag{4.88}$$

where B is given by Eq. (4.86).

4.4 Application of the Cazacu et al. [9] Yield Criterion to the Description of Plastic Deformation Under Torsion

4.4.1 Monotonic Torsion: Analytical Results

Swift [39] reported that specimens made of various isotropic materials with cubic crystal structure (e.g., stainless steel, aluminum, copper) and different geometries (solid rods or tubes) elongate in the direction of the axis about which the respective specimen is being twisted. At the time, Swift [39] attributed the occurrence of these plastic axial effects to strain hardening. This explanation was later invalidated by the experiments of Billington (e.g., Billington [2–4]). Hill [21] hypothesized that for initially isotropic materials the cause of this phenomenon is grains reorientation along preferred directions leading to texture development. This remained the

prevalent view until very recently. In most models, whether phenomenological (e.g., [6, 13, 14]) or crystal plasticity-based (e.g., [16, 34, 41]) plastic anisotropy is considered a precondition for observing/predicting plastic axial deformation occurring in monotonic torsion.

As concerns the occurrence of plastic axial deformation during combined tension–torsion loading, one of the earliest experimental studies were conducted by Taylor and Quinney [40]. This phenomenon has received considerable attention in the early 1960s and renewed interest in the 1990s (e.g., experimental studies reported in [18]).

Recently, in Cazacu et al. [10] and Revil-Baudard et al. [37], analytical results and numerical simulations of the torsional response of isotropic materials conducted with an elastic/plastic model with yielding described by the isotropic and quadratic form ($a = 2$) of Cazacu et al. [9] criterion [see Eq. (4.70)] and isotropic hardening were reported, and new interpretations and explanations of this phenomenon were provided. The set of constitutive equations are summarized below. The usual decomposition of the total rate of deformation $\mathbf{d}$ into an elastic part and a plastic part, $\mathbf{d}^p$ was considered. The elastic response was described as:

$$\dot{\boldsymbol{\sigma}} = \mathbf{C}^{\mathrm{e}} : (\mathbf{d} - \mathbf{d}^p), \tag{4.89}$$

where $\dot{\boldsymbol{\sigma}}$ is the Green-Naghdi rate of the Cauchy stress tensor $\boldsymbol{\sigma}$ (e.g., see [17, 35]), $\mathbf{C}^{\mathrm{e}}$ is the fourth-order stiffness tensor. The reasons for using the Green-Naghdi rate were twofold. First, it has been proved to have superior performance in simple shear (see Hughes [25]). Secondly, the Green-Naghdi rate is the objective rate used in the commercial F.E. code ABAQUS where the elastic/plastic model with yielding described by the isotropic form of the Cazacu et al. [9] yield criterion given by Eq. (4.70) was implemented. Nevertheless, the choice of objective stress rate is not significant for isotropic hardening (see Hughes [25]), which is the case treated in Cazacu et al. [10] and Revil-Baudard et al. [37]. Linear isotropic elasticity was assumed, i.e.,

$$C^{\mathrm{e}}_{ijkl} = 2G\,\delta_{ik}\delta_{jl} - \left(K - \frac{2}{3}G\right)\delta_{ij}\delta_{kl} \tag{4.90}$$

with $i, j, k, l = 1, \ldots, 3$, δ_{ij} being the Kronecker unit delta tensor while G and K are the shear and bulk moduli, respectively. As mentioned, the plastic potential is given by Eq. (4.88), so

$$\mathbf{d}^p = \dot{\lambda}\frac{\partial \bar{\sigma}}{\partial \boldsymbol{\sigma}} \tag{4.91}$$

where $\dot{\lambda}$ is the plastic multiplier. Isotropic hardening dictates that

$$\bar{\sigma}(\boldsymbol{\sigma}, \bar{\varepsilon}^p) = Y(\bar{\varepsilon}^p) \tag{4.92}$$

where the equivalent plastic strain $\bar{\varepsilon}^p$ is the work-equivalent measure of the effective stress $\bar{\sigma}$ associated with the criterion, i.e.,

$$\bar{\varepsilon}^p = \frac{\boldsymbol{\sigma} : \mathbf{d}^p}{\bar{\sigma}} \tag{4.93}$$

A power-law-type hardening law was considered, i.e.,

$$Y(\bar{\varepsilon}^p) = \alpha(\varepsilon_0 + \bar{\varepsilon}^p)^m \tag{4.94}$$

where α, ε_0, and m are material parameters. In order to gain understanding of the phenomenon, these authors first studied the case of combined axial-torsion loadings, for which analytical results can be obtained.

Analytical Results

Consider a rod, loaded axially by a force F and sheared due to a given twist applied at its end. For simplicity, the cross-section is assumed to be circular with initial radius denoted R_0. In a cylindrical coordinate system (r, θ, z), the Cauchy stress tensor is given by:

$$\boldsymbol{\sigma} = \begin{bmatrix} 0 & 0 & 0 \\ 0 & 0 & \tau(r) \\ 0 & \tau(r) & \sigma \end{bmatrix}_{r,\theta,z} \tag{4.95}$$

The principal values of the stress deviator, not necessarily ordered, are:

$$s_1 = \frac{\sigma}{6} - \frac{1}{2}\sqrt{\sigma^2 + 4\tau^2}, \quad s_2 = -\frac{\sigma}{3}, \quad s_3 = \frac{\sigma}{6} + \frac{1}{2}\sqrt{\sigma^2 + 4\tau^2} \tag{4.96}$$

while the transformation matrix from the cylindrical coordinate system to the Cartesian system associated with the principal-stress directions is:

$$\mathbf{Q} = \begin{bmatrix} 0 & 1 & 0 \\ \alpha/\sqrt{\alpha^2+1} & 0 & \beta/\sqrt{\beta^2+1} \\ 1/\sqrt{\alpha^2+1} & 0 & 1/\sqrt{\beta^2+1} \end{bmatrix} \tag{4.97}$$

where, $\alpha = \dfrac{2\tau}{\sigma - \sqrt{\sigma^2 + 4\tau^2}}$ and $\beta = \dfrac{2\tau}{\sigma + \sqrt{\sigma^2 + 4\tau^2}}$.

The material being isotropic, the principal directions of the stress $\boldsymbol{\sigma}$ are also principal directions of the plastic strain-rate tensor, $\mathbf{d}^p$. Let us denote by d_1, d_2, d_3 the principal values of $\mathbf{d}^p$. Using the associated flow rule [Eq. (4.91)] in conjunction with the quadratic form of the yield criterion [i.e., the parameter $a = 2$ in Eq. (4.88)], it follows that the eigenvalues d_i, $i = 1, \ldots, 3$, are:

$$d_i = \dot{\lambda}\frac{9}{2(3k^2 - 2k + 3)\sigma_T}\left[s_i\left(1+k^2\right) - 2k|s_i| + \frac{2k}{3}\left(|s_1| + |s_2| + |s_3|\right)\right] \quad (4.98)$$

Making use of Eq. (4.91), $\mathbf{d}^{\mathrm{p}}$ is expressed in the cylindrical coordinate system as:

$$\mathbf{d}^{\mathrm{p}} = \begin{bmatrix} d_2 & 0 & 0 \\ 0 & \left(\frac{\alpha^2}{\alpha^2+1}d_1 + \frac{\beta^2}{\beta^2+1}d_3\right) & \left(\frac{\alpha}{\alpha^2+1}d_1 + \frac{\beta}{\beta^2+1}d_3\right) \\ 0 & \left(\frac{\alpha}{\alpha^2+1}d_1 + \frac{\beta}{\beta^2+1}d_3\right) & \frac{d_1}{\alpha^2+1} + \frac{d_3}{\beta^2+1} \end{bmatrix}_{(r,\theta,z)} \quad (4.99)$$

Thus, in order to calculate the axial plastic strain along the rod axis, d^{p}_{zz}, one needs to estimate the eigenvalues d_1 and d_3. For tension–torsion loading, $\sigma > 0$, so: $s_1 > 0$, $s_2 < 0$ and $s_3 < 0$. Further substituting Eq. (4.96) into Eqs. (4.98)–(4.99), one obtains the expressions of the eigenvalues of $\mathbf{d}^{\mathrm{p}}$ in terms of the applied combined torque-axial loading (σ, τ) as:

$$d_1 = \frac{9\dot{\lambda}}{2(3k^2 - 2k + 3)\sigma_T}\left[\left(3k^2 + 10k + 3\right)\frac{\sigma}{18} - \left(3k^2 + 2k + 3\right)\frac{\sqrt{\sigma^2 + 4\tau^2}}{6}\right] \quad (4.100)$$

$$d_2 = \frac{9\dot{\lambda}}{2(3k^2 - 2k + 3)\sigma_T}\left[-\left(3k^2 + 4k + 3\right)\frac{\sigma}{9} + \frac{2k}{3}\sqrt{\sigma^2 + 4\tau^2}\right] \quad (4.101)$$

$$d_3 = \frac{3\dot{\lambda}}{4\sigma_T}\left(\frac{\sigma}{3} + \sqrt{\sigma^2 + 4\tau^2}\right). \quad (4.102)$$

It follows that the axial plastic strain, d^{p}_{zz}, is:

$$d^{\mathrm{p}}_{zz} = \frac{9\dot{\lambda}}{2(3k^2 - 2k + 3)\sigma_T}\left\{\sigma\left[\frac{3k^2 + 10k + 3}{18(\alpha^2 + 1)} + \frac{3k^2 - 2k + 3}{18\left(\beta^2 + 1\right)}\right] + \sqrt{\sigma^2 + 4\tau^2}\left[-\frac{3k^2 + 2k + 3}{6(\alpha^2 + 1)} + \frac{3k^2 - 2k + 3}{6\left(\beta^2 + 1\right)}\right]\right\}, \quad (4.103)$$

with α and β depending only on the ratio between the applied axial and shear stresses, σ/τ [see Eq. (4.97)]. In the following, we present predictions of the plastic deformation under pure shear and free-end torsion according to the model.

4.4.2 F.E. Simulations of Monotonic Free-End Torsion

The analytical calculations presented in the previous subsection have shown that if $k \neq 0$, axial plastic deformation occurs, i.e., $d^p_{zz} \neq 0$. Let's first note that under pure shear (i.e., axial stress $\sigma = 0$), we have $\alpha = -1$ and $\beta = 1$ [see Eq. (4.97)], so Eq. (4.103) becomes:

$$d^{\mathrm{p}}_{zz} = \frac{d_1 + d_3}{2} = -\frac{d_2}{2} = -\dot{\lambda}\frac{6k}{(3k^2 - 2k + 3)}\frac{\tau}{\sigma_{\mathrm{T}}} \tag{4.104}$$

Thus, if $k \neq 0$, axial plastic deformation under pure shear occurs. Furthermore,

$$\mathrm{sgn}\left(d^{\mathrm{p}}_{zz}\right) = -\mathrm{sgn}(k), \mathrm{sgn}\left(d^{\mathrm{p}}_{rr}\right) = -\mathrm{sgn}\left(d^{\mathrm{p}}_{zz}\right) \tag{4.105}$$

This means that according to the model, under pure shear:

(i) For materials characterized by $\sigma_{\mathrm{T}} < \sigma_{\mathrm{C}}$ ($k < 0$) lengthening of the specimen occurs $\left(d^{\mathrm{p}}_{zz} > 0\right)$, while the radial strain is negative (contraction);
(ii) For materials characterized by $\sigma_{\mathrm{T}} > \sigma_{\mathrm{C}}$ ($k > 0$) shortening of the specimen takes place, i.e., $\left(d^{\mathrm{p}}_{zz} < 0\right)$ while the radial strain is positive (expansion).
(iii) For $\sigma_{\mathrm{T}} = \sigma_{\mathrm{C}}$, $k = 0$, so: $d^{\mathrm{p}}_{zz} = 0$ [see Eq. (4.104)] and the isotropic form of the Cazacu et al. [9] criterion with $a = 2$ coincides with the von Mises criterion [see also Eq. (4.70)]. The same conclusions hold even for a rigid-plastic material with isotropic hardening, since the plastic axial strains result from $k \neq 0$.

Next, F.E. simulations are presented for boundary conditions close to those achieved experimentally in free-end torsion. Such calculations are useful to verify the predictions of the model, namely the correlation between the sign of the parameter k and the occurrence of either lengthening or shortening in the axial direction with respect to the direction in which the specimen is twisted. The simulations are carried out using the ABAQUS user subroutine UMAT that was developed for the implementation of the isotropic elastic-plastic model with yielding described by the isotropic form of the Cazacu et al. [9] yield criterion and isotropic hardening [see Eqs. (4.88) and (4.94)]. A fully implicit integration algorithm (see Sect. 4.2.1 of Chap. 2) was used for integration of the governing equations.

A simple test geometry consisting of a circular tube of 1.93-mm inner radius and 2.07-mm outer radius was considered. A wall thickness of 0.14 mm and specimen height, L_0, of 1 mm were assumed. The F.E. mesh consisted of 10 layers of 43 hexahedral elements with reduced integration (ABAQUS C3D8R) as shown in Fig. 4.22. Only one element was considered in the thickness of the tube such allow comparison with polycrystalline simulations where only simple shear can be imposed (see Eq. (4.108) later on). The rationale for carrying out the crystal plasticity simulations was to verify the trends predicted by the model. The lower nodes $(z = 0)$ were pinned, i.e., no displacement was allowed, while the upper

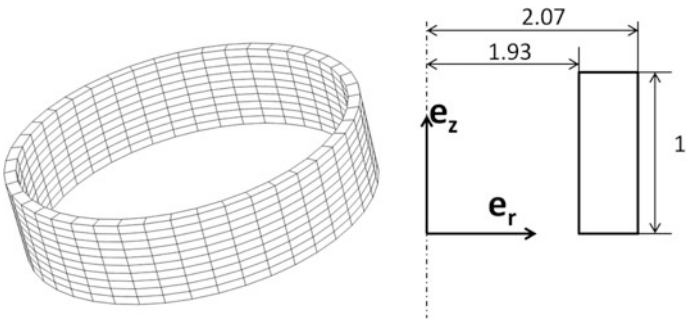

Fig. 4.22 Sample geometry and dimensions (mm) and finite-element mesh for free-end torsion (after Cazacu et al. [10])

nodes ($z = L_0$) were tied to a rigid tool. Torsion was imposed by the rotation of this tool around the tube axis. The use of a rigid tool ensured that all the upper nodes experience the same boundary conditions. Note that free displacement along the tube axis was allowed, but all the other displacements (i.e., in-plane displacements) and rotations were constrained. In the F.E. calculations, only the parameter k [see Eq. (4.72)] was varied in order to investigate its effect on the torsional response. All the other input parameters were kept the same, namely the elastic properties ($E/\sigma_T = 300$, $\nu = 0.3$), the homogeneity parameter a (a = 2) which is involved in the expression of the yield criterion, and the isotropic hardening coefficients [$\alpha/\sigma_T = 1.8$; $\varepsilon_0 = 0.0027$; $m = 0.1$ in Eq. (4.94)].

The usual definitions (see Toth et al. [41]; Duchêne et al. [16]) of the axial and shear strains were used, namely:

$$\varepsilon_{axial} = \ln\left(1 + \frac{u}{L_0}\right) \text{ and } \gamma = \frac{\Phi r}{L_0}, \tag{4.106}$$

where r is the current radius, L_0 is the initial length, u is the axial displacement, and Φ is the twist angle.

In all the F.E. simulations, equal-sized time increments $\Delta t = 10^{-3}$ s were considered. Between five and six iterations per increment were necessary for convergence in the return mapping algorithm, the tolerance in satisfying the yield criterion was set to 10^{-7} (0.1 Pa). First, simulations were carried out assuming a constant value of the parameter k such as to allow verification of the general trends predicted by the analytical results [see Eq. (4.104)]. As an example, in Fig. 4.23 is shown the axial strain as a function of the torsional shear strain according to the model for isotropic materials characterized by $k = -0.9$, $k = 0$, and $k = 0.9$, respectively. For the material with $k = 0$, which is a von Mises material, no length changes take place. For k different from zero, a clear correlation between the sign of k and the occurrence of either lengthening or shortening is observed. Indeed, for $k = -0.9$, lengthening of the specimen takes place, while for a positive value of k ($k = 0.9$), shortening occurs.

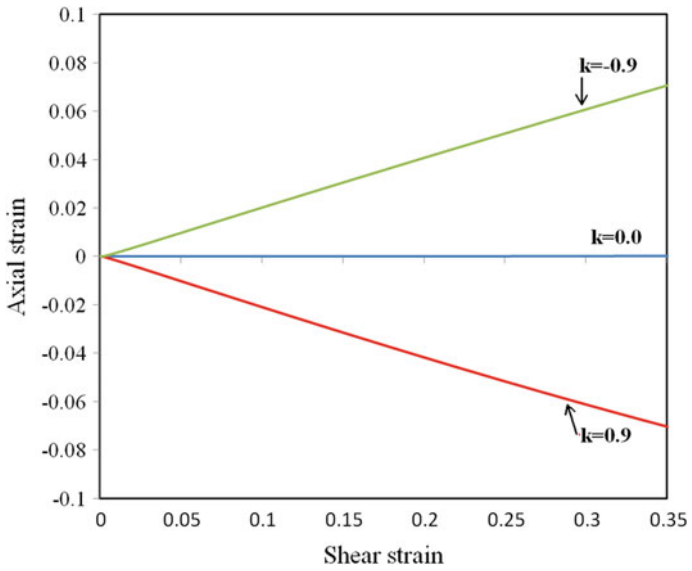

Fig. 4.23 F.E. axial strain versus shear strain γ for materials characterized by different values of k according to an elastic/plastic model based on yielding according to the quadratic form of the Cazacu et al. [9] criterion (Eq. (4.70) with $a = 2$) for $k = -0.9$ and $k = 0.9$, respectively, in comparison with the response of a von Mises material ($k = 0$) (after Cazacu et al. [10])

In both the analytical and F.E. simulations presented so far, the internal variable k was considered constant. However, in some engineering materials due to microstructural changes that occur during loading, the parameter k may not be constant. As an example, the torsional response is also examined for the case when the parameter k varies with the equivalent plastic strain according to the following law:

$$k(\bar{\varepsilon}^p) = \frac{b}{1 - \exp(\bar{\varepsilon}^p - \bar{\varepsilon}_1)/\bar{\varepsilon}_2} \tag{4.107}$$

with $b = 0.466$, $\bar{\varepsilon}_1 = 0.0767$ and $\bar{\varepsilon}_2 = 0.0067$ (see Fig. 4.24a). Such an evolution law corresponds to a material that initially has the compressive yield stress lower than its tensile yield stress ($k = 0.46$).

As the material deforms further, k tends toward zero (same yield in tension–compression). Such an evolution may describe materials for which twinning saturates at a certain level of accumulated plastic strain (see for example, data on pure Mg of Kelley and Hosford [28]). It is very interesting to note that according to Eq. (4.107) k is positive, the F.E. simulations show that continuous shortening of the specimen occurs. Yet, since k tends toward zero, the axial effects saturate, hence the horizontal asymptote of the axial strain versus shear strain curve (see Fig. 4.24b). In summary, the analytical solution of the simplified boundary-value

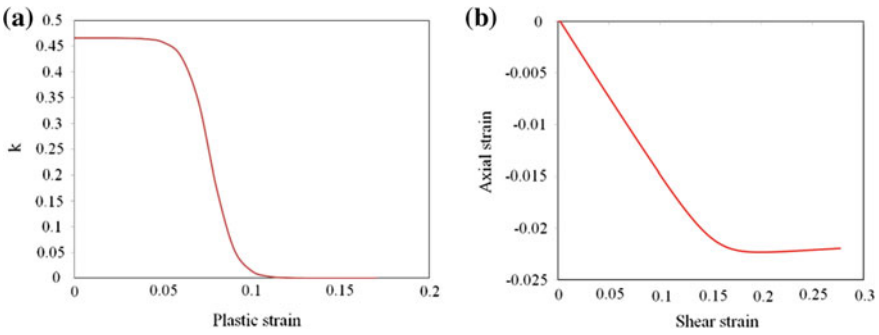

Fig. 4.24 **a** Evolution of the internal variable k with the plastic strain; **b** axial strain versus shear strain γ for a material with evolving microstructure according to Eq. (4.107) (after Cazacu et al. [10])

problem as well as the F.E. results show that Swift effects during monotonic torsional loading of isotropic materials are related to the sign of the scalar internal variable k. A nonzero value of k corresponds to a slight tension–compression asymmetry of the yield surface (see for example Fig. 4.19 for the representation of such yield surfaces in the octahedral plane).

Comparison with the predictions of plastic deformation of an isotropic hexagonal polycrystal obtained with a self-consistent crystal plasticity model

As already mentioned in Cazacu et al. [10], the VPSC polycrystal model and VPSC code (version 6) was also used to simulate the simple shear response of an isotropic hcp polycrystal consisting of 1000 randomly oriented grains. It was assumed that crystallographic slip occurs on prismatic $\{1\bar{1}00\}\ \langle 11\bar{2}0\rangle$ and pyramidal $\langle \mathbf{c+a}\rangle$ slip systems (see also Chap. 3 for the illustration of these crystallographic planes and systems).

With VPSC, torsion conditions cannot be imposed. A similar boundary-value problem, corresponding to simple shear needs to be considered. Thus, the velocity gradient imposed in the local Cartesian coordinate reference system was:

$$\boldsymbol{L} = \begin{bmatrix} 0 & 0 & 0 \\ 0 & 0 & \dot{\gamma} \\ 0 & 0 & 0 \end{bmatrix}_{(x,y,z)} \tag{4.108}$$

where **z** corresponds to the tube axis. The calculations were terminated when the shear strain reached the value of $\gamma = 1$.

For this material, the parameters involved in the elastic/plastic model [see Eq. (4.91) and the hardening law given by Eq. (4.94)] were determined based on virtual experiments using VPSC. Specifically, using the stress–strain curve in uniaxial tension calculated with the VPSC model, Eq. (4.94) was approximated, the numerical values obtained being: $\alpha = 531.8$ MPa, $\varepsilon_0 = 0.1$ and $m = 0.456$. For an equivalent plastic strain of 0.5, the VPSC model predicts a tensile flow stress, σ_T, of

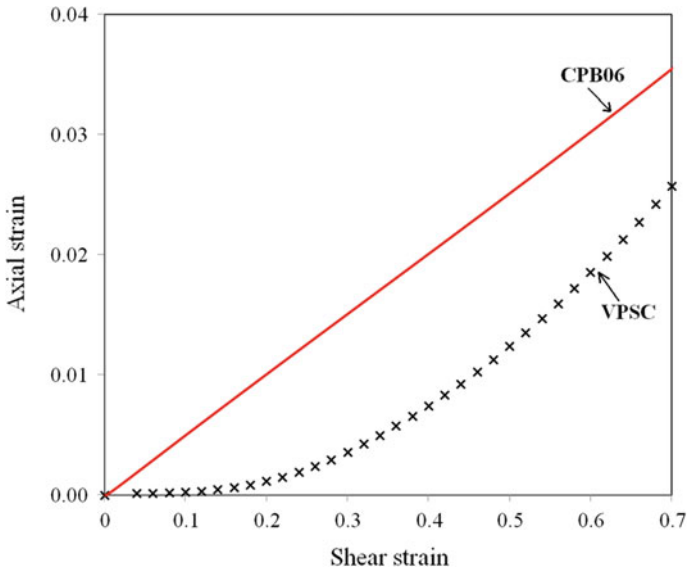

Fig. 4.25 Axial strain versus shear strain for an untextured hcp polycrystal: comparison between the predictions obtained using the self-consistent viscoplastic crystal plasticity model VPSC (symbols) and F.E simulation using the quadratic isotropic Cazacu et al. [9] criterion (Eq. (4.70) with $k = -0.128$) (after Cazacu et al. [10])

415.8 MPa while the compressive flow stress is $\sigma_C = 452.2$ MPa. Thus, for this material the tensile flow stress is slightly smaller than the compressive flow stress, the tension–compression asymmetry ratio being 1.09. For $a = 2$, we obtain $k = -0.128$ [see Eq. (4.72)]. Next, F.E. simulations were carried out. The geometry and F.E. mesh for the specimen is that shown in Fig. 4.22. With only one element in the wall thickness, the velocity gradient is close to that imposed in the VPSC simulation. Since the boundary conditions are similar, simulations results can be compared (see Fig. 4.25). Note that both simulations show continuous lengthening of the specimens and the same overall trends.

It is worth noting that even a very slight tension–compression asymmetry ratio $(\sigma_T/\sigma_C = 0.92)$ may contribute to the occurrence of Swift effects. Although the example considered is for a model material (hcp metals are generally strongly textured), the simulation results presented are still useful because they reveal that the tension–compression asymmetry in the plastic flow induces axial effects even in an untextured material. Furthermore, these results demonstrate that in order to capture the particularities of the large strain torsional response of hexagonal materials, it is critical to account for both the anisotropy and the tension–compression asymmetry of the plastic flow.

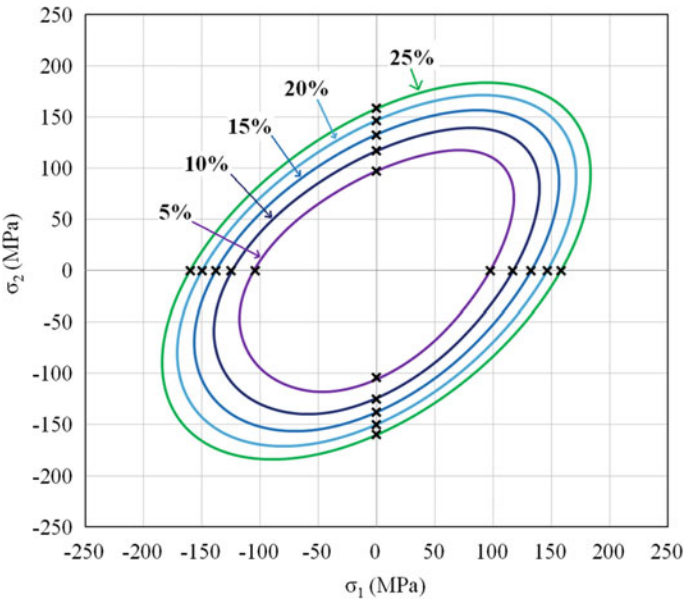

Fig. 4.26 Comparison between the theoretical yield surfaces according to the quadratic Cazacu et al. [9] isotropic criterion and data (symbols) for a commercially pure Al alloy. Data from Billington [3] (after Cazacu et al. [10])

4.4.3 Application to Commercially Pure Al

The simulations presented in the previous section concern idealized materials. The specimen geometry and F.E. element mesh were chosen such as to ensure that similar boundary conditions are imposed in the analytical, VPSC, and F.E. simulations. In this section, F.E. simulations using Cazacu et al. [9] yield criterion [Eq. (4.91) and the hardening law given by Eq. (4.94)] are performed and compared to the experimental free-end torsion response of a commercially pure Al (99.26%) reported by Billington [2–4]. For this material, both uniaxial tension–compression stress–strain curves were reported. Using the data, the parameter k was determined for several levels of accumulated plastic strain. The corresponding biaxial yield surfaces according to the Cazacu et al. [9] yield criterion (Eq. (4.91) with $a = 2$) along with the experimental data (symbols) are shown in Fig. 4.26.

Next, the evolution of the material parameter k with plastic strain in the interval $\bar{\varepsilon}^p = 0.05$ to $\bar{\varepsilon}^p = 0.3$ was approximated by the following equation:

$$k(\bar{\varepsilon}^p) = (a_1\bar{\varepsilon}^p + b_1)(1 - \exp(-c_1\bar{\varepsilon}^p)) + d_1\exp(-c_1\bar{\varepsilon}^p), \tag{4.109}$$

with $a_1 = -23.51$, $b_1 = 18.50$, $c_1 = 0.0458$, and $d_1 = -0.161$, while for strains larger than $\bar{\varepsilon}^p = 0.3$, k was considered constant. This was done to eliminate any inaccuracies that may arise when extrapolating uniaxial data. The parameters

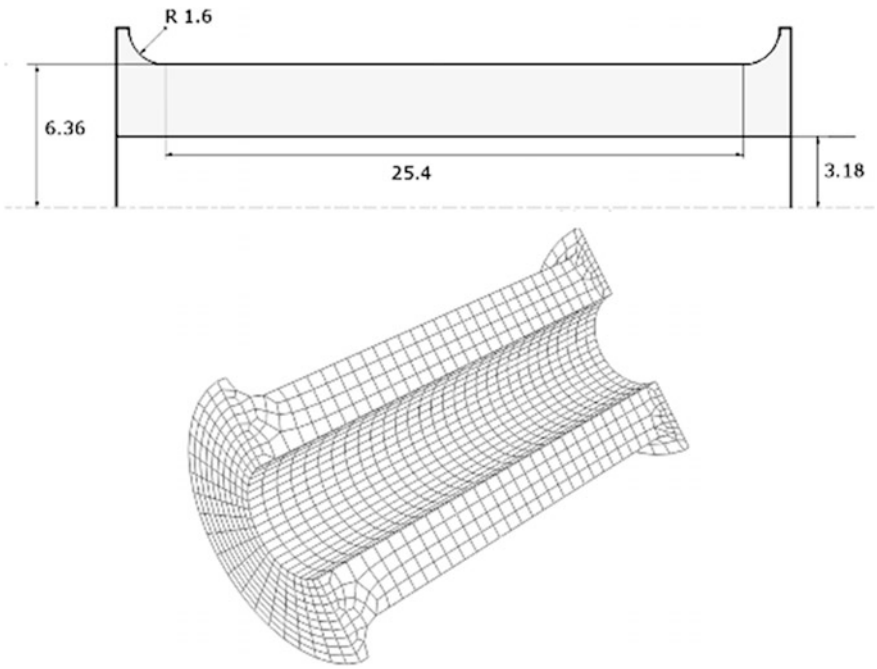

Fig. 4.27 Torsion specimen geometry and dimensions (mm) and F.E. mesh used for the free-end torsion test on an Al alloy

involved in the isotropic hardening law were estimated based on the uniaxial tensile stress–strain curve, the numerical value being $\alpha = 264.44$ MPa, $\varepsilon_0 = 0.039$ and $m = 0.413$ [see Eq. (4.94)] while the Young modulus and the Poisson coefficient were assumed to be $E = 70$ GPa and $\upsilon = 0.3$, respectively. The geometry of the specimen used in the free-end torsional experiments reported by Billington was originally proposed by Nicholas [36]. The sample dimensions (in mm) are shown in Fig. 4.27 (the length of the minimal section zone is 25.4 mm, the inner radius and the outer radius are, respectively, 3.18 and 6.36 mm; and the wall of the tubular specimen is 3.18 mm thick). The initial F.E. mesh used in the calculations consisted of 6040 hexahedral elements with reduced integration (ABAQUS C3D8R). The initial minimal section was meshed with 26 layers of elements and four elements were used along the wall thickness (see also Fig. 4.27).

Figure 4.28 shows a comparison between the experimental results reported by Billington [3] and the numerical predictions using the model. Beyond $\bar{\varepsilon}^p = 0.3$, the internal variable k was considered constant; hence, the model predicts saturation. However, the experimental trends are very well captured and the agreement between theoretical and experimental results for a shear strain below 0.3 is excellent.

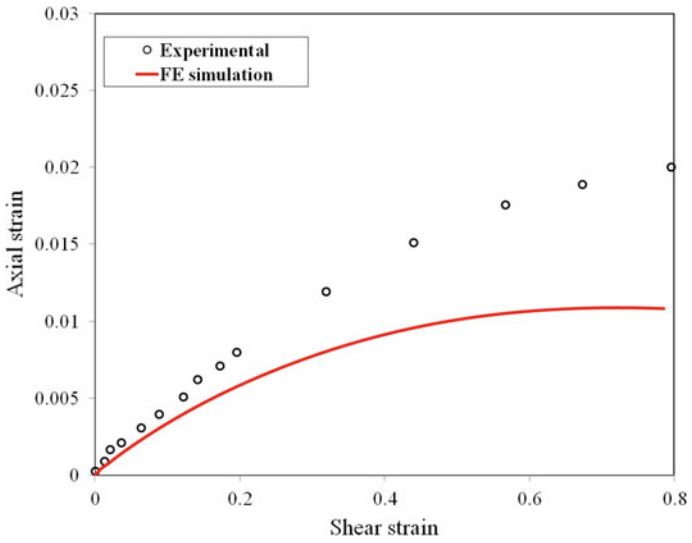

Fig. 4.28 Variation of the axial strain with the shear strain during free-end torsion of a commercially pure Al: comparison between experimental data and the numerical predictions obtained with the quadratic isotropic Cazacu et al. [9] criterion [Eq. (4.88) with k evolving according to Eq. (4.109)] (after Cazacu et al. [10])

4.5 Cyclic Torsional Loading

In the previous section, it was shown that an isotropic elastic/plastic model involving the isotropic Cazacu et al. [9] yield function in conjunction with isotropic hardening predicts the occurrence of axial effects during monotonic free-end torsion. Lengthening or shortening of the specimen was correlated with the sign of the parameter k. The analytic results presented in Sect. 4.4.1 indicate that for monotonic shearing under constant tensile loading (axial stress $\sigma > 0$ and σ constant), irrespective of the material (i.e. any value of the parameter k), the sign of the axial strain, d^{p}_{zz}, that develops, depends on the ratio between the applied shear and axial stress [see Eq. (4.103)]. It is important to note that even in a von Mises material, axial effects $(d^{\mathrm{p}}_{zz} \neq 0)$ may occur. For combined shear-compression loading with axial stress $\sigma < 0$ and σ constant, in a similar manner, it can be shown that

$$d^{\mathrm{p}}_{zz} = \frac{9\dot{\lambda}}{2(3k^2-2k+3)\sigma_T}\left\{\sigma\left[\frac{3k^2-10k+3}{18(\alpha^2+1)}+\frac{3k^2+2k+3}{18(\beta^2+1)}\right]\right.$$
$$\left.+\sqrt{\sigma^2+4\tau^2}\left[-\frac{3k^2-2k+3}{6(\alpha^2+1)}+\frac{3k^2+2k+3}{6(\beta^2+1)}\right]\right\}. \tag{4.110}$$

In conclusion, the analytical calculations show that there exists a specific value of the axial load, for which axial plastic strains do not develop.

As concerns the accumulation of axial plastic strains from cycle to cycle under combined axial-torsional loadings, Cazacu et al. [11] provided a new explanation of this phenomenon. Note that for cyclic torsion under constant axial stress, an isotropic material with a slight difference between uniaxial yield in compression and tension may accumulate axial strains from cycle to cycle. This can be clearly seen from the shape of the yield locus in the biaxial loading plane (axial stress-shear stress plane). As an example, in Fig. 4.29 is shown the projection onto the $(\sigma_{11}, \sigma_{12})$ plane of the yield surface corresponding to $k = -0.4$ $(\sigma_T/\sigma_C = 0.79)$ and $a = 2$. Note that in pure shear $(\sigma_{11} = 0)$, the normal to the yield surface (i.e., the plastic strain-rate vector) has an axial component. This explains qualitatively the reason for cumulative Swift effects. Since for cycling loading analytical calculations become intractable, numerical simulations were conducted by Cazacu et al. [11]. The results of this study are presented in the following.

Prediction of plastic deformation under cyclic loadings at constant strain amplitude
A simple specimen geometry consisting of a circular tube of 6.35-mm inner radius and 7.62-mm outer radius was considered. A wall thickness of 1.27 mm and initial specimen length, L_0, of 10 mm were assumed. The F.E. mesh consisted of 15 layers of 264 hexahedral elements with reduced integration (ABAQUS C3D8R). Cyclic torsion was imposed by the rotation of this tool around the tube. Note that free displacement along the tube axis was allowed but all the other displacements (i.e., in-plane displacements) and rotations were constrained. In the F.E. calculations, only the parameter k was varied in order to investigate its effect on the predicted

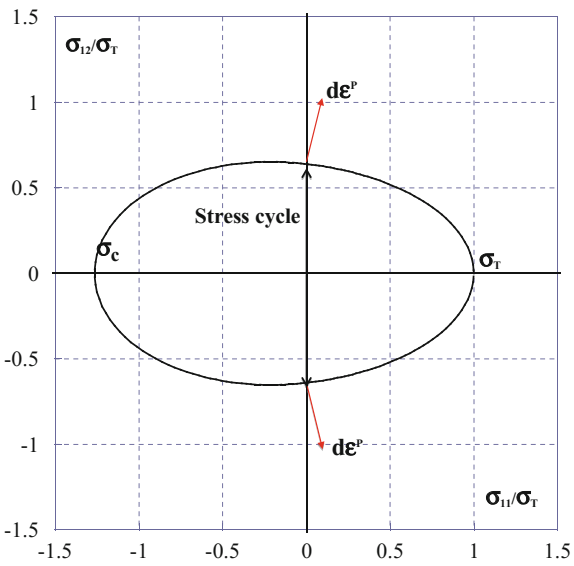

Fig. 4.29 Representation in the shear-normal stress plane of the yield locus according to the isotropic Cazacu et al. [9] yield criterion (Eq. (4.70) with $a = 2$ and $k = -0.4$ for which $\sigma_T/\sigma_C = 0.79$). Note that in pure shear $(\sigma_{11} = 0)$, the normal to the yield surface has a tangential component i.e. axial plastic strain develop

response. Specifically, three materials were considered: a material with $k = 0$ (von Mises material, same uniaxial yield in tension–compression), one with $k = 0.4$ (uniaxial yield in tension larger than in compression), and another one characterized by $k = -0.4$ (uniaxial yield in tension smaller than in compression). All the other properties were kept the same, namely the elastic properties ($E/\sigma_T = 300$, $v = 0.3$), the homogeneity parameter a ($a = 2$) which is involved in the expression of the yield criterion, and the isotropic hardening coefficients [$\alpha/\sigma_T = 1.8$; $\varepsilon_0 = 0.0027$; $m = 0.1$ in Eq. (4.94)].

Cyclic torsion tests (*axial stress* $\sigma = 0$)
We begin by presenting the results for cyclic torsion at constant strain amplitude. Figure 4.30 shows the predicted axial strain as a function of the number of cycles.

Note that for the material characterized by $k = 0$, which is a von Mises material, no axial effects occur. For k different from zero, accumulation of axial plastic strain during loading is observed. It is very interesting to note that depending on the ratio between the uniaxial yield stresses in tension–compression, the specimen either keeps lengthening ($k = -0.4$, which corresponds to $\sigma_T/\sigma_C = 0.79$) or shortening ($k = 0.4$, which corresponds to $\sigma_T/\sigma_C = 1.26$) with increasing number of cycles. However, irrespective of the sign of the parameter k, the rate at which axial strains accumulate is continuously decreasing, the incremental axial strain tends to zero within the first few cycles (see Fig. 4.31).

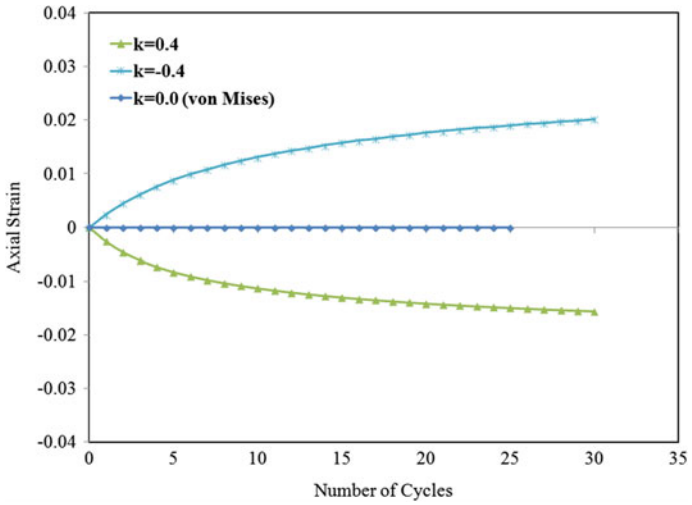

Fig. 4.30 Axial strain versus number of cycles for cyclic torsion under strain control at constant strain amplitude (torsional rotation between constant Φ_{max} and $-\Phi_{max}$ is applied) according to the Cazacu et al. [9] criterion and power-law isotropic hardening for materials characterized by $k = -0.4$ ($\sigma_T/\sigma_C = 0.79$), $k = 0.4$ ($\sigma_T/\sigma_C = 1.26$) and $k = 0$ (von Mises material, $\sigma_T = \sigma_C$) (after Cazacu et al. [11])

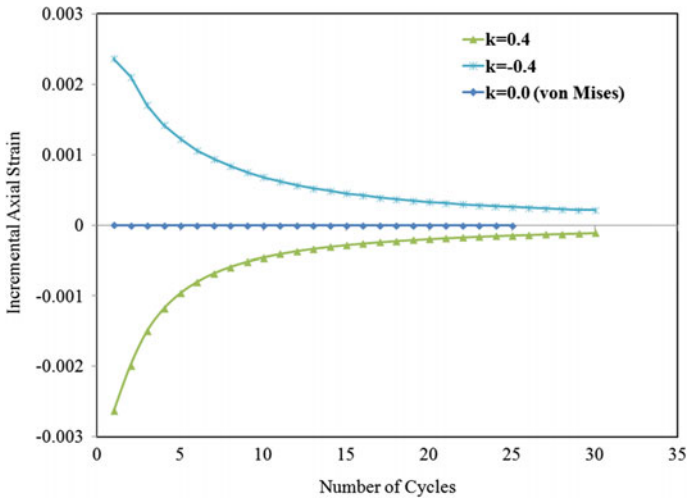

Fig. 4.31 Rate of axial plastic strain versus the number of cycles in cyclic torsion under strain control at constant strain amplitude (torsional rotation between constant $\Phi_{\max}$ and $-\Phi_{\max}$ is applied) predicted by the isotropic Cazacu et al. [9] criterion in conjunction with power-law isotropic hardening for materials characterized by $k = -0.4$ $(\sigma_T/\sigma_C = 0.79)$, $k = 0.4$ $(\sigma_T/\sigma_C = 1.26)$, and $k = 0$ (von Mises material, $\sigma_T = \sigma_C$) (after Cazacu et al. [11])

Prediction of plastic deformation under cyclic loadings at constant axial stress
The loading imposed is depicted in Fig. 4.32. First, an axial load F is applied and the axial strain is monitored. Next, the axial load is maintained constant and cyclic torsional loading under strain control (constant total strain amplitude) is applied. To achieve constant total shear strain amplitude, the torsional rotation sinusoidally varies between $\Phi_{\max}$ and $-\Phi_{\max}$ (see Eq. (4.106) for the definition of the twist angle). The maximum applied load, $F_{\max}$, was chosen such that the imposed axial stress was less than the yield limit of any given material. The main objective was to investigate the accumulation of axial plastic strain in the second phase of the test, specifically to analyze the influence of the value of the applied constant axial stress, $F_{\max}$, on the rate at which the axial strains accumulate.

Cyclic Swift effects in a von Mises material $(\sigma_T = \sigma_C;\ k = 0)$
We begin by presenting simulation results for a von Mises material ($k = 0$). The maximum levels of the axial load applied in the first phase of the numerical tests were chosen such that the material does not reach yielding under uniaxial loading. The initial yield for the material is 1 MPa while the numerical values for the parameters involved in the hardening law given by Eq. (4.94) are kept the same as in the simulations at $\sigma = 0$. Figures 4.33 and 4.34 show results of simulations of cyclic torsion under constant axial stress $\sigma = 0$ (no axial load), $\sigma = 0.5$ MPa (tensile load), and $\sigma = -0.5$ MPa (compressive load), respectively. Note the occurrence of accumulated plastic elongation under constant tensile axial stress and plastic axial contraction under constant compressive load. Indeed, according to

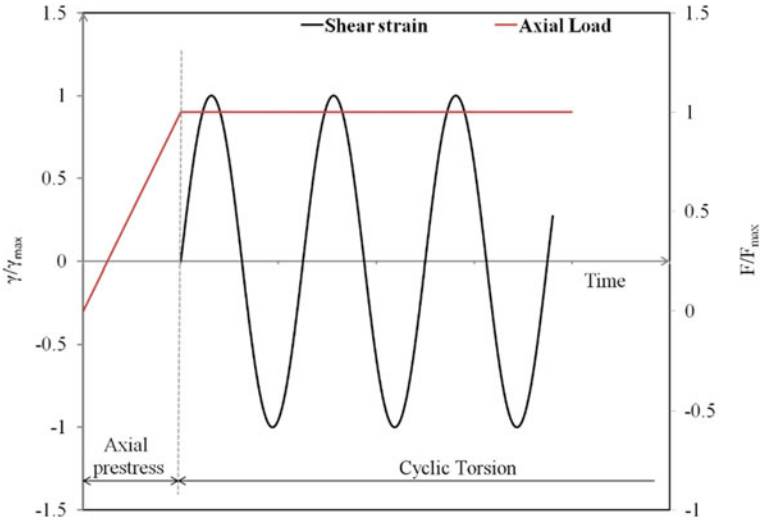

Fig. 4.32 Loading path imposed in the test: first, an axial load F is applied, next the load is kept constant $(F = F_{max})$ and strain control cyclic torsion between constant γ_{max} and $-\gamma_{max}$ is applied

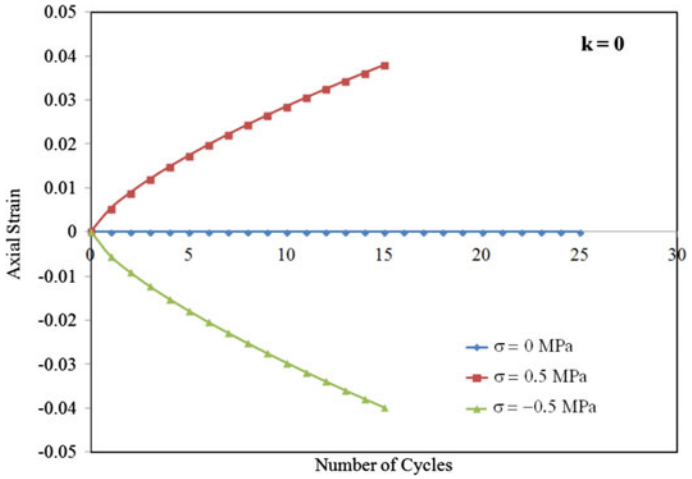

Fig. 4.33 Axial strain versus number of cycles under strain control cyclic torsion between constant γ_{max} and $-\gamma_{max}$ at constant axial stress, $\sigma = 0$, 0.5 MPa, and −0.5 MPa, respectively, for a von Mises material ($\sigma_T = \sigma_C$, so $k = 0$) and isotropic power-law hardening. Note that under constant tensile axial stress, plastic elongation occurs while under constant compressive axial stress plastic contraction takes place (after Cazacu et al. [11])

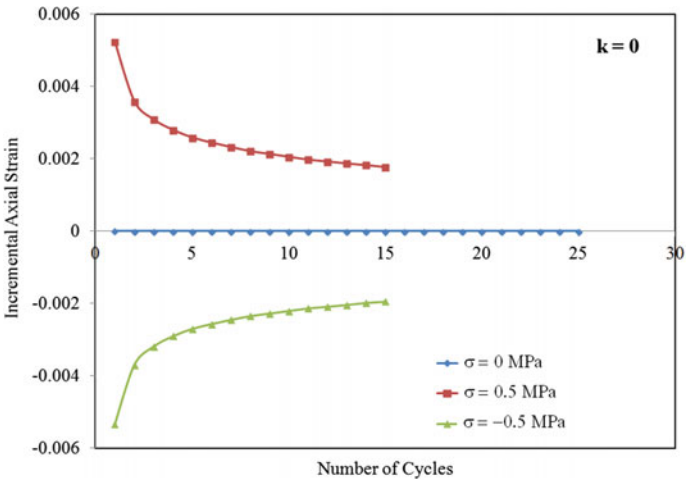

Fig. 4.34 Rate of axial plastic strain under strain control cyclic torsion between constant γ_{max} and $-\gamma_{max}$ at constant axial stress, $\sigma = 0$, 0.5 MPa, and −0.5 MPa, respectively, for a von Mises material ($\sigma_T = \sigma_C$, so $k = 0$) and isotropic power-law hardening. Note that the rate of axial plastic strain is the same if the axial stress σ has the same absolute value (after Cazacu et al. [11])

Eq. (4.103) under constant tensile axial stress $\sigma > 0$, axial plastic strain develops, i.e., $d^p_{zz} > 0$, while for cyclic torsion under constant compressive axial stress, i.e., $\sigma < 0$, we obtain $d^p_{zz} < 0$. Thus, the sign of the constant axial stress determines the sign of the axial strain that develops. However, the absolute value of the axial strain is the same, if the axial stress has the same absolute value (see Fig. 4.33 and Eq. (4.103), respectively).

Moreover, the rate of axial plastic strain is the same if the axial stress σ has the same absolute value (see Fig. 4.34).

Cyclic Torsion in materials with tension-compression asymmetry ($k \neq 0$)

Next, we present F.E. simulation results for a material with uniaxial yield in tension less than its uniaxial yield in compression ($\sigma_T/\sigma_C = 0.79$) corresponding to $k = -0.4$ in Eq. (4.88). Results for cyclic torsion without axial preload $\sigma = 0$, cyclic torsion under constant compressive axial stress ($\sigma = -0.2$ MPa, and $\sigma = -0.8$ MPa), and constant tensile axial stress ($\sigma = 0.2$ MPa and $\sigma = 0.8$ MPa), respectively, are presented in Figs. 4.35 and 4.36. It is very interesting to note that if the constant axial stress is positive, i.e., $\sigma > 0$ (tension), then plastic lengthening occurs, and the axial strain keeps accumulating with each cycle. The material is strongly deformed as compared to the case of cyclic torsion under zero axial load ($\sigma = 0$).

Indeed, the axial strain after 30 cycles reaches 2.1, 3.5, and 8.7% at $\sigma = 0$, 0.2, and 0.8 MPa, respectively. Comparison of the respective axial strain-rates is shown in Fig. 4.36. However, if the constant applied axial stress is compressive, i.e., $\sigma < 0$, accumulation of axial strain may be eliminated, or the axial strain may change sign. For example, for $\sigma = -0.2$ MPa, the axial strain after 30 cycles is only

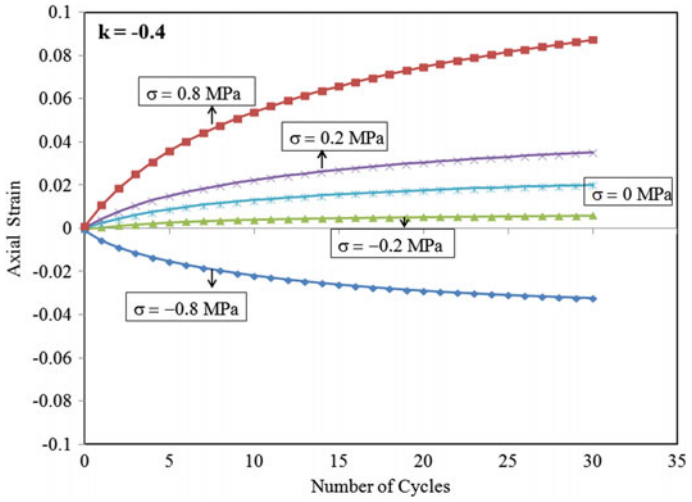

Fig. 4.35 Axial strain versus number of cycles under strain control cyclic torsion between constant γ_{max} and $-\gamma_{max}$ at constant axial stress, $\sigma = -0.8$, -0.2, 0 (no axial load), 0.2 and 0.8 MPa, respectively, according to the Cazacu et al. [9] criterion and power-law isotropic hardening for a material with uniaxial yield in tension less than in compression [$\sigma_T/\sigma_C = 0.79$, $k = -0.4$ in Eq. (4.88)]. Note the very strong influence of the sign of the constant axial stress on the sign of the axial strains (after Cazacu et al. [11])

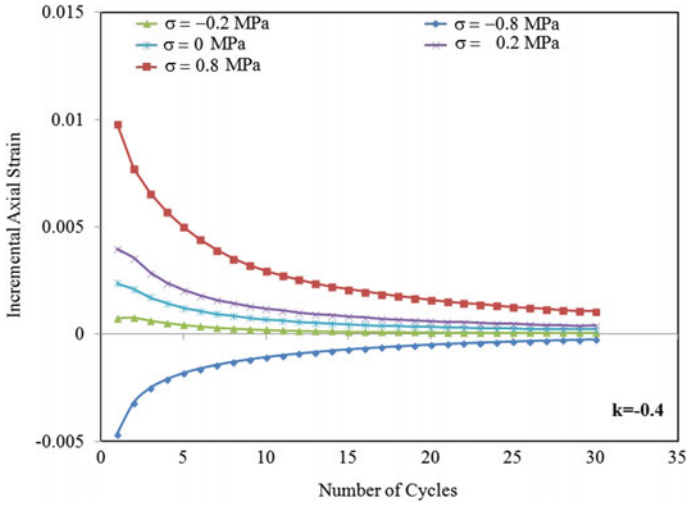

Fig. 4.36 Rate of axial plastic strain under strain control cyclic torsion between constant γ_{max} and $-\gamma_{max}$ at constant axial stress $\sigma = -0.8$, -0.2, 0 (no axial load), 0.2 and 0.8 MPa according to Cazacu et al. [9] criterion and power-law isotropic hardening for a material with uniaxial yield stress in tension greater than in compression ($\sigma_T/\sigma_C = 0.79$, $k = -0.4$) (after Cazacu et al. [11])

0.5%, thus much reduced as compared to cyclic torsion under zero load, while in the case when $\sigma = -0.8$ MPa, the axial strain is of opposite sign and the total axial strain accumulated in 30 cycles is −3.2%. These trends are also evident by examining the analytical results (see Eq. (4.103), respectively) for $k = -0.4$ and the fixed values of σ shown in Fig. 4.36.

On the other hand, for the material with uniaxial yield stress in tension larger than in compression, i.e., $k = 0.4$ $(\sigma_T/\sigma_C = 1.26)$, if $\sigma < 0$ (compression) the rate at which axial strains accumulate is faster than in the case when $\sigma = 0$ (no axial load). Furthermore, the specimen is shortening (see Fig. 4.36). The axial strain after 30 cycles attains, respectively, −1.6, −2.9, and −6.5% for $\sigma = 0$, −0.2, and −0.8 MPa, respectively. However, if the constant axial stress σ is positive (tension), axial effects may be quasi-eliminated or the axial strain may change signs. For example for $\sigma = 0.8$ MPa, the axial strain after 30 cycles is of 4.7% (see Figs. 4.37 and 4.38).

Note the strong influence of the sign and value of the imposed constant axial stress σ: the rate is faster under constant compressive axial stress ($\sigma < 0$) than when no axial load is imposed ($\sigma = 0$) while under constant tensile stress $\sigma > 0$, the rate at which axial strains accumulate is much slower; the sign of axial plastic strains can be reversed or axial effects can be quasi-eliminated.

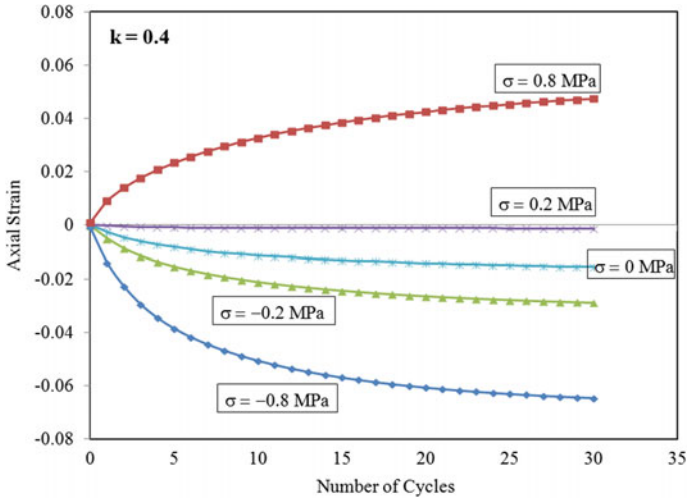

Fig. 4.37 Axial strain versus number of cycles under strain control cyclic torsion between constant γ_{max} and $-\gamma_{max}$ at constant axial stress, $\sigma = -0.8$, −0.2, 0 (no axial load), 0.2 and 0.8 MPa, respectively, according to Cazacu et al. [9] criterion and power-law isotropic hardening for a material with uniaxial yield stress in tension smaller than in compression $(\sigma_T/\sigma_C = 1.26 \geq k = 0.4)$ (after Cazacu et al. [11])

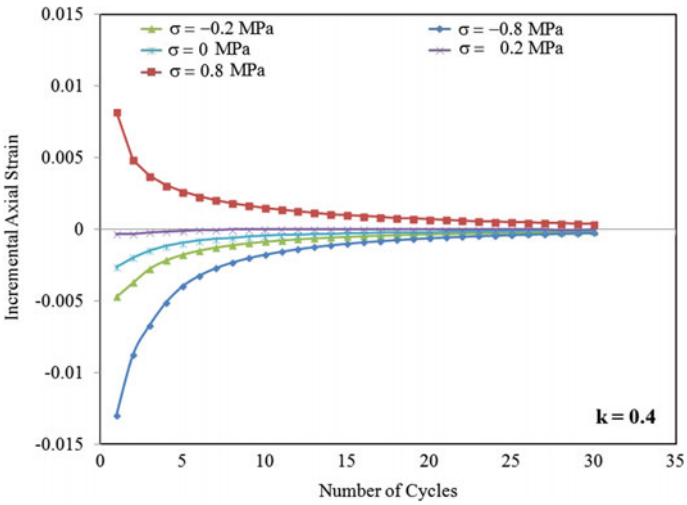

Fig. 4.38 Rate of axial plastic strain under strain control cyclic torsion between constant γ_{max} and $-\gamma_{max}$ at constant axial stress $\sigma = -0.8$, -0.2, 0 (no axial load), 0.2, and 0.8 MPa, respectively, according to Cazacu et al. [9] criterion and power-law isotropic hardening for a material with uniaxial yield stress in tension less than in compression ($\sigma_T/\sigma_C = 1.26$, i.e., $k = 0.4$) (after Cazacu et al. [11])

Prediction of plastic deformation under high number of cyclic shear loadings at constant strain amplitude

The F.E. results presented show that a slight difference between the uniaxial yield stresses in simple tension–compression leads to cyclic Swift effects in isotropic metals subjected to low-cycle loading under strain control. Next, it is examined the response for a large number of cycles (1000 cycles) under strain control simple shear cycling. The constant shear strain amplitude applied is $\Gamma = 2\,\varepsilon_{12} = 4 \times 10^{-3}$. Simulations were conducted for materials which have only a very slight tension–compression asymmetry, namely $\sigma_T/\sigma_C = 0.94$, which corresponds to $k = -0.1$ and $\sigma_T/\sigma_C = 1.07$, which corresponds to $k = 0.1$. It is supposed that in uniaxial tension the two materials have the yield stress, (σ_T) and hardening behavior, described by an isotropic Voce-type hardening law, i.e.,

$$Y(\bar{\varepsilon}^p) = M - N\exp(-\bar{\varepsilon}^p/\tilde{\varepsilon}_0) \tag{4.111}$$

with $M = 500$ MPa, $N = 400$ MPa, while the normalization constant $\tilde{\varepsilon}_0$ is set to 0.1.

Since the two materials studied have identical tensile behavior, any differences in response are due solely to the differences in the ratio σ_T/σ_C (see Fig. 4.39).

The evolution of the shear stress and axial strain as a function of the number of cycles is shown in Fig. 4.40.

Because hardening is isotropic, the stress saturates within a few cycles. However, the axial plastic strain continues to accumulate even after 1000 cycles.

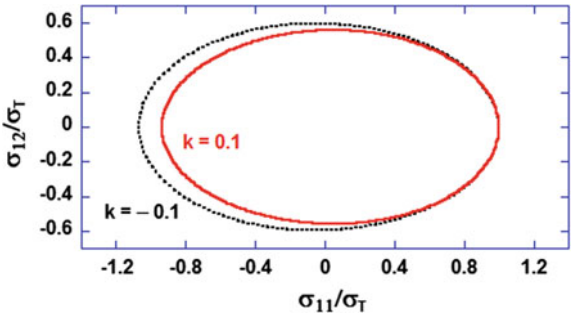

Fig. 4.39 Representation in the shear-normal stress plane of the Cazacu et al. [9] yield locus for materials with the same yield stress in tension but different yield stresses in compression, characterized by $k = -0.1$ ($\sigma_T/\sigma_C = 0.94$) and $k = 0.1$ ($\sigma_T/\sigma_C = 1.07$), respectively (after Cazacu et al. [11])

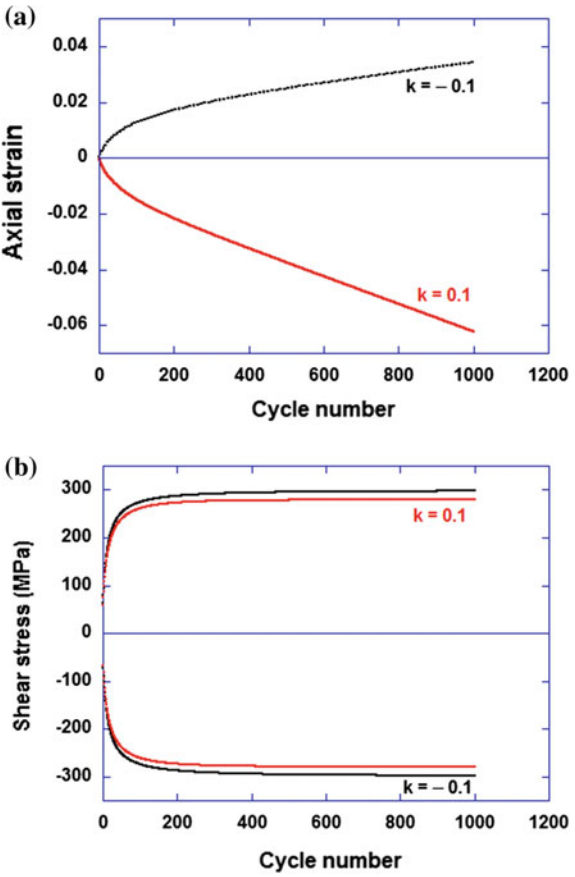

Fig. 4.40 **a** Evolution of the shear stress versus number of cycles and **b** evolution of the axial plastic strain for strain control cyclic shearing at constant strain amplitude $\Gamma = 4 \times 10^{-3}$ according to Cazacu et al. [9] criterion and Voce-type isotropic hardening for materials characterized by $k = -0.1$ ($\sigma_T/\sigma_C = 0.94$) and $k = 0.1$ ($\sigma_T/\sigma_C = 1.07$), respectively (after Cazacu et al. [11])

The ratio between the uniaxial yield stresses in tension–compression of the material dictates whether permanent shortening or lengthening of the specimen occurs. In summary, the key issue investigated by Cazacu et al. [10, 11] is whether sources other than texture-induced anisotropy may cause Swift effects under monotonic and

cyclic loadings. Specifically, the effect of tension–compression asymmetry in uniaxial yielding (i.e., $\sigma_T/\sigma_C \neq 1$) on the mechanical response in monotonic combined tension–torsion as well as strain-controlled cyclic torsion, and strain-controlled cyclic torsion under constant axial stress was investigated. For monotonic loadings, new analytical solutions show that a slight difference between the uniaxial yield in tension (σ_T), and the uniaxial yield in compression (σ_C) results in Swift effects under monotonic biaxial loadings. F.E. simulations for strain-controlled cyclic loadings, show that accumulation of axial plastic strain (cyclic Swift effects) can occur. The sign and rate at which axial effects accumulate depends strongly on the ratio (σ_T/σ_C). Specifically, under strain-controlled cyclic torsion with no axial load:

- If the material has uniaxial yield in tension greater than in compression ($\sigma_T > \sigma_C$), the axial strain is positive (specimen is lengthening).
- If the material has an uniaxial yield in tension smaller than in compression ($\sigma_T < \sigma_C$), the axial strain is negative (specimen is shortening).
- Irrespective of the ratio between the uniaxial yield in tension and the uniaxial yield in compression, the rate at which the axial strain accumulates is continuously decreasing, axial effects tend to saturate within a few cycles.

For strain-controlled cyclic torsion under constant axial stress (tension or compression):

- Axial effects occur even in a material for which the plastic behavior is described by the von Mises yield function ($k = 0$) and isotropic hardening. Specifically, it is predicted that during cyclic torsion under constant tensile load there is lengthening of the specimen while cyclic torsion under constant compressive loads leads to shortening of the specimen.
- For materials with the uniaxial yield in tension larger than the uniaxial yield in compression ($\sigma_T > \sigma_C$), if the applied constant axial stress is negative (compression), axial effects are reinforced. However, if the applied constant axial stress is positive (tension) the sign of axial strain is negative and the rate at which it accumulates is much slower than under cyclic torsion without axial load.
- For materials with uniaxial yield in tension smaller than the uniaxial yield in compression ($\sigma_T < \sigma_C$), if the applied constant axial stress is negative (compression) axial effects are reduced, the rate at which they accumulate being much slower than in cyclic torsion without any axial load. However, if the applied constant axial stress is positive (tension), the axial strain is negative and accumulates faster.

In summary, the results presented show that for any given material it is possible to control both the sign of the axial strain and the rate at which it accumulates by applying an appropriate constant axial load. It is worth noting that even if this applied prestress is less than the yielding threshold σ_T (or σ_C), its influence on how axial plastic strains accumulate with increasing number of cycles is very strong.

Most importantly, it is possible to estimate the value of the constant load and the amplitude of the cycles that need to be applied such as to suppress cumulative Swift effects. Finally, the predicted response for a large number of cycles also indicates the role played by the tension–compression asymmetry of the material.

References

1. Bartlett E (2018) Experimental characterization and modeling of high strength martensitic steels based on a new distortional hardening model. University of Florida
2. Billington EW (1977) Non-linear mechanical response of various metals. II permanent length changes in twisted tubes. J Phys Appl Phys 10:533–552
3. Billington EW (1977) Non-linear mechanical response of various metals: I permanent length changes in twisted tubes. J Phys Appl Phys 10:519–531
4. Billington EW (1977) Non-linear mechanical response of various metals: III permanent length changes in twisted tubes. J Phys Appl Phys 10:553–569
5. Bishop J, Hill R (1951) XLVI. A theory of the plastic distortion of a polycrystalline aggregate under combined stresses. Lond Edinb Dublin Philos Mag J Sci 42:414–427
6. Böhlke T, Bertram A, Krempl E (2003) Modeling of deformation induced anisotropy in free-end torsion. Int J Plast 19:1867–1884
7. Budiansky B, Wu TT (1961) Theoretical prediction of plastic strains of polycrystals. DTIC Document
8. Cazacu O, Barlat F (2004) A criterion for description of anisotropy and yield differential effects in pressure-insensitive metals. Int J Plast 20:2027–2045
9. Cazacu O, Plunkett B, Barlat F (2006) Orthotropic yield criterion for hexagonal closed packed metals. Int J Plast 22:1171–1194
10. Cazacu O, Revil-Baudard B, Barlat F (2013) New interpretation of monotonic Swift effects: role of tension–compression asymmetry. Mech Mater 57:42–52
11. Cazacu O, Revil-Baudard B, Barlat F (2014) New interpretation of cyclic Swift effects. Eur J Mech A/Solids 44:82–90
12. Chin GY, Mammel WL, Dolan MT (1969) Taylor analysis for 111 (112) twinning and 111 (110) slip under conditions of axisymmetric flow. Trans Metall Soc AIME 245:383–388
13. Colak OU (2004) Modeling of the monotonic and cyclic swift effects using anisotropic finite viscoplasticity theory based on overstress (AFVBO): part I—constitutive model. Int J Solids Struct 41:5301–5311
14. Colak OU (2004) Modeling of monotonic and cyclic Swift effect using anisotropic finite viscoplasticity theory based on overstress (AFVBO): part II—numerical experiments. Int J Solids Struct 41:5313–5325
15. Drucker DC (1949) Relation of experiments to mathematical theories of plasticity. ASME J Appl Mech 16:349–357
16. Duchêne L, El Houdaigui F, Habraken AM (2007) Length changes and texture prediction during free end torsion test of copper bars with FEM and remeshing techniques. Int J Plast 23:1417–1438
17. Green AE, Naghdi PM (1965) A general theory of an elastic-plastic continuum. Arch Ration Mech Anal 18:251–281
18. Hassan T, Kyriakides S (1992) Ratcheting in cyclic plasticity, part I: uniaxial behavior. Int J Plast 8:91–116
19. Hershey AV (1954) The plasticity of an isotropic aggregate of anisotropic face-centered cubic crystals. ASME J Appl Mech 21:241–249
20. Hershey AV (1954) The elasticity of an isotropic aggregate of anisotropic cubic crystals. ASME J Appl Mech 21:236–240

21. Hill R (1950) The mathematical theory of plasticity. Oxford University Press, Oxford, USA
22. Hosford WF (1972) A generalized isotropic yield criterion. J Appl Mech 39:607–609
23. Hosford WF (1993) The mechanics of crystals and textured polycrystals. Oxford University Press, Oxford, USA
24. Hosford WF, Allen T (1973) Twinning and directional slip as a cause for a strength differential effect. Metall Mater Trans B 4:1424–1425
25. Hughes TJ (1984) Numerical implementation of constitutive models: rate-independent deviatoric plasticity. In: Theoretical foundation for large-scale computations for nonlinear material behavior. Springer, Dordrecht, pp 29–63
26. Hutchinson J (1964) Plastic stress-strain relations of FCC polycrystalline metals hardening according to Taylor's rule. J Mech Phys Solids 12:11–24
27. Hutchinson J (1964) Plastic deformation of bcc polycrystals. J Mech Phys Solids 12:25–33
28. Kelley E, Hosford WF (1968) The deformation characteristics of textured magnesium. Trans Met Soc AIME 242
29. Koiter WT (1953) Stress-strain relations, uniqueness and variational theorems for elastic-plastic materials with a singular yield surface. Q Appl Math 11:350–354
30. Kröner E (1961) Zur plastischen verformung des vielkristalls. Acta Metall 9:155–161
31. Lebensohn R, Tomé C (1993) A self-consistent anisotropic approach for the simulation of plastic deformation and texture development of polycrystals: application to zirconium alloys. Acta Metall Mater 41:2611–2624
32. Lebensohn R, Turner P, Signorelli J, Canova G, Tomé C (1998) Calculation of intergranular stresses based on a large-strain viscoplastic self-consistent polycrystal model. Model Simul Mater Sci Eng 6:447
33. Lode W (1926) Versuche über den Einflu\s s der mittleren Hauptspannung auf das Flie\s sen der Metalle Eisen, Kupfer und Nickel. Z Für Phys 36:913–939
34. Montheillet F, Cohen M, Jonas J (1984) Axial stresses and texture development during the torsion testing of Al, Cu and α-Fe. Acta Metall 32:2077–2089
35. Nemat-Nasser S (1982) On finite deformation elasto-plasticity. Int J Solids Struct 18:857–872
36. Nicholas T (1980) Dynamic tensile testing of structural materials using a split Hopkinson bar apparatus. DTIC Document
37. Revil-Baudard B, Chandola N, Cazacu O, Barlat F (2014) Correlation between Swift effects and tension–compression asymmetry in various polycrystalline materials. J Mech Phys Solids 70:104–115
38. Spitzig WA, Sober RJ, Richmond O (1976) The effect of hydrostatic pressure on the deformation behavior of maraging and HY-80 steels and its implications for plasticity theory. Metall Trans A 7:1703–1710
39. Swift H (1947) Length changes in metals under torsional overstrain. Engineering 163:1958
40. Taylor GI, Quinney H (1932) The plastic distortion of metals. Philos Trans R Soc Lond Ser Contain Pap Math Phys Character 230:323–362
41. Toth L, Jonas J, Gilormini P, Bacroix B (1990) Length changes during free end torsion: a rate sensitive analysis. Int J Plast 6:83–108
42. Tresca H (1868) Memoire sur l'ecoulement des corps solides, par M. H. Tresca. Imprimerie Imperiale, Paris
43. Vitek V, Mrovec M, Bassani J (2004) Influence of non-glide stresses on plastic flow: from atomistic to continuum modeling. Mater Sci Eng, A 365:31–37
44. von Mises R (1913) Mechanik der festen Körper im plastisch deformablen Zustand. Nachrichten Von Ges Wiss Zu Gött Math-Phys Kl 1913:582–592
45. Wang C-C (1970) A new representation theorem for isotropic functions: an answer to Professor GF Smith's criticism of my papers on representations for isotropic functions. Arch Ration Mech Anal 36:166–197

Chapter 5
Yield Criteria for Anisotropic Polycrystals

5.1 General Methods for Extending to Anisotropy Yield Criteria for Isotropic Materials

Yield functions aimed at describing the characteristics of the plastic behavior of metallic materials are of great importance in the design and analysis of forming processes specifically intended for these materials. There are two rigorous methodologies for description of yielding anisotropy. These methodologies can be used to extend any given isotropic yield function such as to account for the specific material symmetries.

Linear Transformations methodology

One methodology is based on the use of one or several linear transformations applied to the stress tensor or its deviator (e.g., [4, 7, 8, 18]). Specifically, in the expression of the respective isotropic criterion $f(\boldsymbol{s})$, the stress deviator $\mathbf{s}$ is replaced with a transformed stress tensor $\tilde{\mathbf{S}}$, defined as:

$$\tilde{\mathbf{S}} = \mathbf{C}\mathbf{s} = \mathbf{C}\mathbf{K}\boldsymbol{\sigma} = \mathbf{L}\boldsymbol{\sigma} \tag{5.1}$$

Thus, the anisotropy is introduced by means of the anisotropic fourth-order tensor $\mathbf{C}$, while $\mathbf{K}$ denotes the fourth-order symmetric deviatoric unit tensor that transforms the Cauchy stress tensor $\boldsymbol{\sigma}$ to its deviator $\mathbf{s}$. Specifically, with respect to any Cartesian coordinate system:

$$\mathrm{K}_{ijkl} = \left(\delta_{ik}\delta_{jl} + \delta_{il}\delta_{jk}\right)/2 - \left(\delta_{ij}\delta_{kl}\right)/3 \tag{5.2}$$

where δ_{ij} denotes the Kronecker delta and $i, j, k, l = 1, 2, 3$. (see also Chap. 1)

O. Cazacu et al., *Plasticity–Damage Couplings: From Single Crystal to Polycrystalline Materials*, Solid Mechanics and Its Applications 253,
https://doi.org/10.1007/978-3-319-92922-4_5

Generalized Invariants' Methodology

As shown in Chap. 4 (see Proposition 4.2), any isotropic yield function ought to depend on stress only through the principal invariants J_2 and J_3 of the stress deviator. The methodology developed by Cazacu and Barlat [11, 12] to extend any isotropic criterion such as to account for anisotropy is based on the concept of generalized invariants. Specifically, these authors developed generalizations of the principal invariants J_2 and J_3 that satisfy the following requirements:

(i) The anisotropic generalization of J_2 should be a second-order homogeneous polynomial in stresses that is invariant to any transformation belonging to the symmetry group of the material; it is insensitive to hydrostatic pressure, and for isotropic conditions reduces to J_2,
(ii) The anisotropic generalization of J_3 should be a third-order homogeneous polynomial that is form-invariant under any transformation belonging to the symmetry group of the material; it is insensitive to hydrostatic pressure, and reduces to J_3 for isotropic conditions.

Based on these generalized invariants, it is possible to extend any isotropic yield criterion simply by replacing in its expression J_2 and J_3 by their respective anisotropic generalizations.

Although this approach is general, in the sense that the same methodology can be used to extend any isotropic yield function to include any type of material symmetry, in the following, we present the expressions of the generalized invariants corresponding to two types of symmetry that are prevalent for textured metallic materials, namely orthotropy and transverse isotropy.

5.1.1 Generalized Orthotropic Invariants

Let us first consider the case of orthotropic symmetry and define $(\mathbf{x}, \mathbf{y}, \mathbf{z})$ the reference frame associated with this symmetry. For example, for a rolled sheet, $\mathbf{x}$, $\mathbf{y}$, and $\mathbf{z}$ denote the rolling, transverse, and normal directions, respectively. The material anisotropy is fully described by the following structural tensors (see also Chap. 1):

$$\mathbf{N}_1 = \mathbf{x} \otimes \mathbf{x} = \begin{pmatrix} 1 & 0 & 0 \\ 0 & 0 & 0 \\ 0 & 0 & 0 \end{pmatrix}; \quad \mathbf{N}_2 = \mathbf{y} \otimes \mathbf{y} = \begin{pmatrix} 0 & 0 & 0 \\ 0 & 1 & 0 \\ 0 & 0 & 0 \end{pmatrix}; \quad \mathbf{N}_3 = \mathbf{z} \otimes \mathbf{z} = \begin{pmatrix} 0 & 0 & 0 \\ 0 & 0 & 0 \\ 0 & 0 & 1 \end{pmatrix} \tag{5.3}$$

According to the theorem of representation for orthotropic scalar functions of a second-order symmetric tensor (see Theorem 1.4), it follows that for a polynomial $P(\boldsymbol{\sigma})$ to be invariant with respect to the orthotropic group, it must be expressible as a polynomial in the following arguments:

$$tr(\mathbf{N}_1\boldsymbol{\sigma}), tr(\mathbf{N}_2\boldsymbol{\sigma}), tr(\mathbf{N}_3\boldsymbol{\sigma}), tr(\mathbf{N}_1\boldsymbol{\sigma}^2), tr(\mathbf{N}_2\boldsymbol{\sigma}^2), tr(\mathbf{N}_3\boldsymbol{\sigma}^2), tr(\boldsymbol{\sigma}^3) \tag{5.4}$$

Therefore, relative to the $(\mathbf{x}, \mathbf{y}, \mathbf{z})$ Cartesian frame associated with the axes of orthotropy, any orthotropic polynomial $P(\boldsymbol{\sigma})$ has the following arguments:

$$P = P\Big(\sigma_{xx},\ \sigma_{yy},\ \sigma_{zz},\ \sigma_{xy}^2,\ \sigma_{yz}^2,\ \sigma_{xz}^2,\ \sigma_{xy}\sigma_{xz}\sigma_{yz}\Big) \tag{5.5}$$

Using the above result and the requirements (i)–(ii), Cazacu and Barlat [11] derived orthotropic generalizations of the invariants J_2, and J_3, respectively.

Proposition 5.1 (J_2 orthotropic)
For an orthotropic material, the generalized second-invariant of the stress deviator should involve exactly six independent parameters, and its expression with respect to the Cartesian system associated with the orthotropic axes should be of the form:

$$\begin{aligned} J_2^0 = {} & \frac{a_1}{6}\left(\sigma_{xx}-\sigma_{yy}\right)^2 + \frac{a_2}{6}\left(\sigma_{yy}-\sigma_{zz}\right)^2 + \frac{a_3}{6}\left(\sigma_{xx}-\sigma_{zz}\right)^2 \\ & + a_4\sigma_{xy}^2 + a_5\sigma_{xz}^2 + a_6\sigma_{yz}^2 \end{aligned} \tag{5.6}$$

where a_k (k = 1, ..., 6) are constants.

Proof The general form of a second-order homogeneous polynomial in σ_{xx}, σ_{yy}, σ_{zz}, σ_{xy}^2, σ_{yz}^2, σ_{xz}^2, and $\sigma_{xy}\cdot\sigma_{xz}\cdot\sigma_{yz}$, is:

$$\begin{aligned} P_2 = {} & \alpha_1\sigma_{xx}^2 + \alpha_2\sigma_{yy}^2 + \alpha_3\sigma_{zz}^2 + \alpha_4\sigma_{xx}\sigma_{yy} \\ & + \alpha_5\sigma_{xx}\sigma_{zz} + \alpha_6\sigma_{zz}\sigma_{yy} + \alpha_7\sigma_{xy}^2 + \alpha_8\sigma_{xz}^2 + \alpha_9\sigma_{yz}^2, \end{aligned} \tag{5.7}$$

where α_i, $i = 1, \ldots, 9$ are constants. Imposing P_2 to be insensitive to pressure, i.e., $P_2(\boldsymbol{\sigma}+p\mathbf{I}) = P_2(\boldsymbol{\sigma})$ for any scalar p and any stress state $\boldsymbol{\sigma}$ results in the following relations between the constants α_i:

$$\alpha_1 = -(\alpha_4+\alpha_5)/2, \alpha_2 = -(\alpha_4+\alpha_6)/2 \quad \text{and} \quad \alpha_3 = -(\alpha_5+\alpha_6)/2.$$

For convenience, we denote $a_1 = -3\,\alpha_4$, $a_2 = -3\,\alpha_5$, $a_3 = -3\,\alpha_6$, $a_4 = \alpha_7$, $a_5 = \alpha_8$, $a_6 = \alpha_9$. Thus, relative to the Cartesian coordinate system with axes along the directions of orthotropy, the orthotropic generalization of J_2 is given by Eq. (5.6).

Proposition 5.2 (J_3 orthotropic)
For an orthotropic material, the generalized third-invariant of the stress deviator should involve exactly eleven independent parameters, and its expression with respect to the Cartesian system associated with the orthotropic axes should be of the form:

$$\begin{aligned} J_3^0 = {} & \frac{1}{27}(b_1+b_2)\sigma_{xx}^3 + \frac{1}{27}(b_3+b_4)\sigma_{yy}^3 + \frac{1}{27}[2(b_1+b_4)-b_2-b_3]\sigma_{zz}^3 \\ & - \frac{1}{9}\left(b_1\sigma_{yy}+b_2\sigma_{zz}\right)\sigma_{xx}^2 - \frac{1}{9}(b_3\,\sigma_{zz}+b_4\sigma_{xx})\sigma_{yy}^2 \\ & - \frac{1}{9}\left[(b_1-b_2+b_4)\,\sigma_{xx}+(b_1-b_3+b_4)\sigma_{yy}\right]\sigma_{zz}^2 \\ & + \frac{2}{9}(b_1+b_4)\,\sigma_{xx}\sigma_{zz}\sigma_{yy} - \frac{\sigma_{xz}^2}{3}\left[2b_9\sigma_{yy}-b_8\sigma_{zz}-(2b_9-b_8)\sigma_{xx}\right] \\ & - \frac{\sigma_{xy}^2}{3}\left[2b_{10}\sigma_{zz}-b_5\sigma_{yy}-(2b_{10}-b_5)\,\sigma_{xx}\right] - \frac{\sigma_{yz}^2}{3}\left[(b_6+b_7)\sigma_{xx}-b_6\sigma_{yy}-b_7\sigma_{zz}\right] \\ & + 2b_{11}\sigma_{xy}\sigma_{xz}\sigma_{yz} \end{aligned} \tag{5.8}$$

where b_k, k = 1, ..., 11 are constants.

Proof The general form of a third-order homogeneous polynomial in the stated quantities σ_{xx}, σ_{yy}, σ_{zz}, σ_{xy}^2, σ_{yz}^2, σ_{xz}^2, and $\sigma_{xy}\cdot\sigma_{xz}\cdot\sigma_{yz}$ is:

$$\begin{aligned} P_3 = {} & \alpha_1\,\sigma_{xx}^3 + \alpha_2\,\sigma_{yy}^3 + \alpha_3\sigma_{zz}^3 + \sigma_{xx}^2\left(\alpha_4\,\sigma_{yy} + \alpha_5\,\sigma_{zz}\right) + \sigma_{yy}^2\left(\alpha_6\,\sigma_{zz} + \alpha_7\,\sigma_{xx}\right) \\ & + \sigma_{zz}^2\left(\alpha_8\,\sigma_{xx} + \alpha_9\,\sigma_{yy}\right) + \alpha_{10}\,\sigma_{xx}\,\sigma_{zz}\sigma_{yy} + \sigma_{xx}\left(\alpha_{11}\,\sigma_{xy}^2 + \alpha_{12}\,\sigma_{yz}^2 + \alpha_{13}\,\sigma_{xz}^2\right) \\ & + \sigma_{yy}\left(\alpha_{14}\,\sigma_{xy}^2 + \alpha_{15}\,\sigma_{yz}^2 + \alpha_{16}\,\sigma_{xz}^2\right) + \sigma_{zz}\left(\alpha_{17}\,\sigma_{xy}^2 + \alpha_{18}\,\sigma_{yz}^2 + \alpha_{19}\,\sigma_{xz}^2\right) \\ & + \alpha_{20}\sigma_{xy}\,\sigma_{yz}\,\sigma_{xz}, \end{aligned} \tag{5.9}$$

where α_i, $i = 1, \ldots, 20$ are constants.

Imposing the requirement of insensitivity to hydrostatic pressure, i.e., $P_3(\boldsymbol{\sigma}+p\mathbf{I}) = P_3(\boldsymbol{\sigma})$ for any scalar p and stress $\boldsymbol{\sigma}$ results in the following relations:

$$\begin{aligned} & \alpha_1 = -(\alpha_4+\alpha_5)/3, \quad \alpha_2 = -(\alpha_6+\alpha_7)/3, \\ & \alpha_3 = [(\alpha_5+\alpha_6)-2(\alpha_4+\alpha_7)]/3, \quad \alpha_8 = \alpha_4-\alpha_5+\alpha_7, \\ & \alpha_9 = \alpha_4+\alpha_7-\alpha_6, \quad \alpha_{10} = -2(\alpha_4+\alpha_7), \quad \alpha_{11} = -(\alpha_{14}+\alpha_{17}), \\ & \alpha_{12} = -(\alpha_{15}+\alpha_{18}) \quad \text{and} \quad \alpha_{13} = -(\alpha_{16}+\alpha_{19}). \end{aligned}$$

For convenience, we denote $b_1 = -9\alpha_4$, $b_2 = -9\alpha_5$, $b_3 = -9\alpha_6$, $b_4 = -9\alpha_7$, $b_5 = 3\alpha_{14}$, $b_6 = 3\alpha_{15}$, $b_7 = 3\alpha_{18}$, $b_8 = 3\alpha_{19}$, $b_9 = -3\alpha_{16}/2$, $b_{10} = -3\alpha_{17}/2$, and $b_{11} = \alpha_{20}/2$.

Further substituting in Eq. (5.9) leads to the form (5.8) of J_3^0 .

Note that if each of the constants $a_i = 1$, J_2^0 reduces to J_2; and if each of the constants $b_k = 1$, J_3^0 reduces to J_3 (see Eqs. (5.6) and (5.8), respectively).

Note that any function $\Phi\left(J_2^0, J_3^0\right)$ is pressure-insensitive and automatically satisfies the form-invariance requirements with respect to any transformation belonging to the orthotropic group. Yield criteria in terms of J_2^0, J_3^0 were proposed by Hill [22], Cazacu [10] and Cazacu and Barlat [11–13] to model textured fcc and hcp polycrystalline materials, respectively.

5.1.2 Generalized Transversely Isotropic Invariants

Consider a material exhibiting transverse isotropy and take as coordinate system, associated with this symmetry,$(\mathbf{x}, \mathbf{y}, \mathbf{z})$, $\mathbf{z}$ being the axis of rotational symmetry, and let us define $\mathbf{N}_3 = \mathbf{z} \otimes \mathbf{z}$.

According to the Smith and Rivlin [44] theorem of representation of scalar transversely isotropic polynomials of a second-order symmetric tensor (or alternatively Theorem 1.3), it follows that for a polynomial in $\boldsymbol{\sigma}$ to be invariant with respect to rotations about the $\mathbf{z}$ axis, it must be expressible as a polynomial in:

$$tr(\boldsymbol{\sigma}), tr(\mathbf{N}_3\boldsymbol{\sigma}), tr\left(\boldsymbol{\sigma}^2\right), tr(\mathbf{N}_3\boldsymbol{\sigma}^2), tr\left(\boldsymbol{\sigma}^3\right)$$

Imposing the requirement of insensitivity to hydrostatic pressure, i.e., $P_T(\boldsymbol{\sigma} + p\mathbf{I}) = P_T(\boldsymbol{\sigma})$ for any $\boldsymbol{\sigma}$ and scalar p, Cazacu and Barlat [12] obtained the following results:

Proposition 5.3 (Generalized Transversely Isotropic Invariants)
For a transversely isotropic material, the generalized second-invariant of the stress deviator should involve only three independent parameters, and its expression with respect to the Cartesian system associated with the axes of material symmetry (with $\mathbf{z}$ *being the axis of rotational symmetry) should be of the form:*

$$\begin{aligned} J_2^T = & \frac{h_1}{6}\left(\sigma_{xx} - \sigma_{yy}\right)^2 + \frac{h_2}{6}\left[\left(\sigma_{yy} - \sigma_{zz}\right)^2 + \left(\sigma_{xx} - \sigma_{zz}\right)^2\right] \\ & + \frac{h_2 + 2h_1}{3}\sigma_{xy}^2 + h_3\left(\sigma_{xz}^2 + \sigma_{yz}^2\right), \end{aligned} \tag{5.10}$$

with h_k *being constants (k = 1, ..., 3);* J_3^T*, the generalization to transverse isotropy of the third-invariant of the stress deviator,* J_3 *should involve four constants and ought to be of the form:*

$$
\begin{aligned}
J_3^T = {} & \frac{(3d_2 - d_1)}{27}\left(\sigma_{xx}^3 + \sigma_{yy}^3\right) + \frac{2}{27}(4d_1 - 3d_2)\sigma_{zz}^3 - \frac{1}{9}d_1\left(\sigma_{xx}\sigma_{yy}^2 + \sigma_{yy}\sigma_{xx}^2\right) \\
& - \frac{1}{9}(3\,d_2 - 2d_1)\,\sigma_{zz}\left(\sigma_{yy}^2 + \sigma_{xx}^2\right) + \frac{1}{9}(3d_2 - 4d_1)\,\sigma_{zz}^2(\sigma_{xx} + \sigma_{yy}) \\
& - d_2\frac{\sigma_{xy}^2}{3}\left(2\sigma_{zz} - \sigma_{xx} - \sigma_{yy}\right) + \frac{\sigma_{xz}^2}{3}\left(d_3\sigma_{xx} - (d_3 + d_4)\sigma_{yy} + d_4\,\sigma_{zz}\right) \\
& + \frac{\sigma_{yz}^2}{3}\left(-(d_3 + d_4)\sigma_{xx} + d_3\sigma_{yy} + d_4\,\sigma_{zz}\right) + \frac{4}{9}d_1\sigma_{xx}\sigma_{yy}\sigma_{zz} \\
& + \frac{2}{3}(2d_3 + d_4)\sigma_{xy}\sigma_{xz}\sigma_{yz},
\end{aligned}
\tag{5.11}
$$

where d_i (i = 1, ..., 4) are constants. If the coefficients $h_k = 1$, (k = 1, ..., 3), J_2^T reduces to J_2, while if $d_i = 1$, (i = 1, ..., 4), J_3^T reduces to J_3.

Any function $\Phi\left(J_2^T, J_3^T\right)$ is pressure-insensitive and automatically satisfies the form-invariance requirements with respect to any transformation belonging to the transverse isotropy group (see Table 3.1). For example, a transversely isotropic criterion in terms of J_2^T, J_3^T was developed by Cazacu and Barlat [12] and applied to the description of the anisotropy in yield stresses of Al alloy extruded bars.

5.2 Orthotropic Generalization of von Mises Isotropic Criterion Due to Hill [22]

The most widely used orthotropic yield criterion for describing the directionality in plastic properties (yield stresses, strains) of sheets and plates is due to Hill [22]. In the coordinate system $(\mathbf{x}, \mathbf{y}, \mathbf{z})$ associated with the axes of orthotropy, this yield criterion is expressed as:

$$
F\left(\sigma_{yy} - \sigma_{zz}\right)^2 + G(\sigma_{zz} - \sigma_{xx})^2 + H\left(\sigma_{xx} - \sigma_{yy}\right)^2 + 2L\sigma_{yz}^2 + 2M\sigma_{xz}^2 + 2N\sigma_{xy}^2 = \bar{\sigma}^2
\tag{5.12}
$$

where F, G, H, L, M, and N are material constants, and $\bar{\sigma}$ is the equivalent stress associated with this criterion.

Proposition 5.4 Hill [22] *orthotropic yield criterion is the extension to orthotropy of the isotropic von Mises yield criterion obtained using the generalized invariants approach. Specifically, it can be expressed in the form:*

$$
3J_2^0 = \bar{\sigma}^2,
$$

where J_2^0 is the generalized second-invariant of the stress deviator given by Eq. (5.6) *and $\bar{\sigma}$ is the equivalent stress associated with the criterion (i.e., it coincides with the uniaxial tensile yield stress in the $\boldsymbol{x}$-direction).*

Proof Let us recall that the expression of the von Mises yield criterion is:

$$3J_2 = \sigma_T^2, \tag{5.13}$$

the associated plastic stress potential being

$$\varphi_{\text{Mises}}(\boldsymbol{\sigma}) = \sqrt{3J_2} \tag{5.14}$$

with σ_T the yield stress in uniaxial tension in any direction (see also Sect. 4.2.1). Using the generalized invariants' methodology, the orthotropic generalization of the von Mises criterion is obtained by replacing in the expression (5.13), J_2 by J_2^0 given by Eq. (5.6), i.e.,

$$3J_2^0 = \bar{\sigma}^2,$$

$\bar{\sigma}$ being the equivalent stress associated with the orthotropic criterion. Next, by denoting:

$$\begin{aligned} F = a_2/2; \quad G = a_3/2; \quad H = a_1/2; \\ L = 3a_6/2; \quad M = 3a_5/2; \quad N = 3a_4/2 \end{aligned} \tag{5.15}$$

the above expression reduces to the classical expression of Hill [22] given by Eq. (5.12).

It is important to note that Hill [22] orthotropic yield function can be also written in the form:

$$\bar{\sigma}^2 = \boldsymbol{\sigma} : \mathbf{M}\boldsymbol{\sigma}, \tag{5.16}$$

where $\mathbf{M}$ is an orthotropic fourth-order tensor satisfying both major and minor symmetries, i.e., $M_{ijkl} = M_{klij} = M_{jikl}$ for $i, j, k, l = 1, \ldots, 3$.

Indeed if in Voigt notation the stress tensor is represented by the six-dimensional vector $\boldsymbol{\sigma} = \left(\sigma_{xx}, \sigma_{yy}, \sigma_{zz}, \sigma_{yz}, \sigma_{xz}, \sigma_{xy}\right)$ and the fourth-order orthotropic tensor $\mathbf{M}$ is represented in the coordinate system $(\mathbf{x}, \mathbf{y}, \mathbf{z})$ associated with the axes of orthotropy by the 6×6 matrix is given as:

$$\mathbf{M} = \begin{bmatrix} H+G & -H & -G & 0 & 0 & 0 \\ -H & F+H & -F & 0 & 0 & 0 \\ -G & -F & F+G & 0 & 0 & 0 \\ 0 & 0 & 0 & L & 0 & 0 \\ 0 & 0 & 0 & 0 & M & 0 \\ 0 & 0 & 0 & 0 & 0 & N \end{bmatrix}, \tag{5.17}$$

then subsitution of Eq. (5.17) into Eq. (5.16) leads to the classical form of Hill [22] criterion (Eq. 5.12). Note that the sum of the components on the first row of $\mathbf{M}$ is equal to the sum of the components on the second row which is equal to the sum of the components on the third row, i.e.,

$$M_{iikl} = 0. \tag{5.18}$$

Thus according to Eq. (5.18), $\mathbf{M}$ is deviatoric, and consequently, Hill [22] criterion is pressure-insensitive. Note that for isotropy, the coefficients satisfy: $F = G = H = L/3 = M/3 = N/3$. It can be easily shown that the generalization to orthotropy of the von Mises yield criterion using the linear transformation methodology [see Eq. (5.1)] also leads to the classical expression of Hill [22] criterion given by Eq. (5.12).

Proposition 5.5 Hill [22] *orthotropic yield function can also be expressed in the form:*

$$\bar{\sigma} = \left\{ \frac{3}{2} tr\tilde{\mathbf{S}}^2 \right\}^{\frac{1}{2}}, \tag{5.19}$$

where $\tilde{\mathbf{S}} = \mathbf{Cs}$, with $\mathbf{C}$ being an orthotropic symmetric fourth-order tensor. For the proof of the above mathematical result, the reader is referred to Appendix 2 of Cazacu and Barlat [11].

Generally, the assumption of an associated flow rule is made. Thus, the plastic potential associated with Hill [22] yield criterion is:

$$\varphi_{\text{Hill}}(\boldsymbol{\sigma}) = \sqrt{\boldsymbol{\sigma} : \mathbf{M}\boldsymbol{\sigma}} = \sqrt{3J_2^0}, \tag{5.20}$$

with $\mathbf{M}$ given by Eq. (5.17) and J_2^0 given by Eq. (5.6) (see also relations (5.15) defining coefficients F, G, H, L, M, N in terms of a_i). Accordingly, the plastic strain-rate tensor, $\mathbf{d}^p$, is expressed as:

$$\mathbf{d}^p = \dot{\lambda} \frac{\partial \varphi_{\text{Hill}}}{\partial \boldsymbol{\sigma}} = \frac{\dot{\lambda}}{\bar{\sigma}} \mathbf{M}\boldsymbol{s}. \tag{5.21}$$

where $\dot{\lambda} \geq 0$ stands for the plastic multiplier. It means that for a material governed by Hill [22] criterion, the plastic strain-rate is always proportional to the stress deviator. In the coordinate system $(\mathbf{x}, \mathbf{y}, \mathbf{z})$ associated with the axes of orthotropy, the following linear relations hold between the plastic strain increments and the stresses:

$$
\begin{aligned}
d^p_{xx} &= \frac{\dot{\lambda}}{2\bar{\sigma}}\left[(H+G)\sigma_{xx} - H\sigma_{yy} - G\sigma_{zz}\right] = \frac{\dot{\lambda}}{\bar{\sigma}}\left[H\left(\sigma_{xx}-\sigma_{yy}\right) - G(\sigma_{zz}-\sigma_{xx})\right] \\
d^p_{yy} &= \frac{\dot{\lambda}}{2\bar{\sigma}}\left[(F+H)\sigma_{yy} - H\sigma_{xx} - F\sigma_{zz}\right] = \frac{\dot{\lambda}}{\bar{\sigma}}\left[F\left(\sigma_{yy}-\sigma_{zz}\right) - H\left(\sigma_{xx}-\sigma_{yy}\right)\right] \\
d^p_{zz} &= \frac{\dot{\lambda}}{2\bar{\sigma}}\left[(F+G)\sigma_{zz} - G\sigma_{xx} - F\sigma_{yy}\right] = \frac{\dot{\lambda}}{\bar{\sigma}}\left[G(\sigma_{zz}-\sigma_{xx}) - F\left(\sigma_{yy}-\sigma_{zz}\right)\right] \\
d^p_{yz} &= d^p_{zy} = \frac{\dot{\lambda}}{\bar{\sigma}} L\sigma_{yz} \\
d^p_{xz} &= d^p_{zx} = \frac{\dot{\lambda}}{\bar{\sigma}} M\sigma_{xz} \\
d^p_{xy} &= d^p_{yx} = \frac{\dot{\lambda}}{\bar{\sigma}} N\sigma_{xy}
\end{aligned}
\tag{5.22}
$$

For isotropy, Eq. (5.22) reduces to Eq. (4.25) for the plastic strain-rate of a von Mises material.

5.2.1 Yield Stress Anisotropy Predicted by the Hill [22] Criterion

For an orthotropic material, in order to characterize the effect of the loading orientation on yielding in uniaxial tension, it is sufficient to perform tests along directions contained in the planes $(\mathbf{x},\mathbf{y})$, $(\mathbf{x},\mathbf{z})$, and $(\mathbf{y},\mathbf{z})$, respectively. For a rolled plate, let $\mathbf{x}$ be the rolling direction (RD), $\mathbf{y}$ the transverse direction (TD) in the plane of the plate, and $\mathbf{z}$ the normal direction (ND), i.e., the direction along the thickness of the plate. Let us denote by σ_θ the yield limit in uniaxial tension along a direction $\mathbf{d}$ at an angle θ to the $\mathbf{x}$-axis (see Fig. 5.1) in the plane $(\mathbf{x},\mathbf{y})$. In the Oxyz coordinate system associated with the RD, TD, ND axes, $\mathbf{d} = \cos\theta\mathbf{e_x} + \sin\theta\mathbf{e_y}$, so the applied stress tensor is $\boldsymbol{\sigma} = \sigma_\theta(\mathbf{d}\otimes\mathbf{d})$, which has the nonzero components:

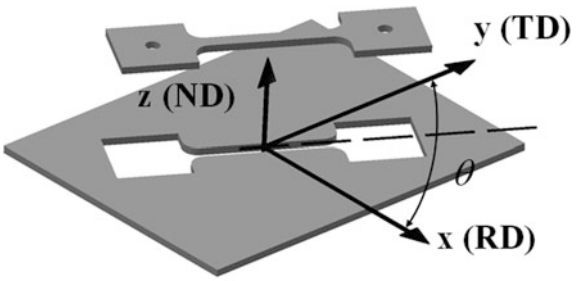

Fig. 5.1 Orientation of a tensile specimen along a direction at an angle θ to the RD

$$\begin{aligned}\sigma_{xx} &= \sigma_\theta \cos^2\theta \\ \sigma_{yy} &= \sigma_\theta \sin^2\theta \\ \sigma_{xy} &= \sigma_{yx} = \sigma_\theta \sin\theta\ \cos\theta\end{aligned} \tag{5.23}$$

Next, substitution of (5.23) in the expression of the Hill [22] yield function given by Eq. (5.12) leads to the following result:

Anisotropy in uniaxial yield stresses in the (RD–TD plane):

According to Hill [22] yield criterion, in the (RD, TD) plane the dependence of the normalized uniaxial yield stress $\sigma_\theta/\bar{\sigma}$ on the loading angle θ to the rolling direction (RD) is:

$$\frac{\sigma_\theta}{\bar{\sigma}} = \frac{1}{\sqrt{F\sin^4\theta + G\cos^4\theta + H\left(\cos^2\theta - \sin^2\theta\right)^2 + 2N\sin^2\theta\cos^2\theta}} \tag{5.24}$$

It is clearly seen that the evolution of σ_θ with the in-plane loading orientation admits at most three extrema. Irrespective of the values of the coefficients F, G, H, and N, the maxima and minima of the yield stress occur along RD and TD (i.e., at 0° and 90°, respectively). If N is intermediate to $F + 2H$ and $G + 2H$, those are the only extrema. Otherwise, there exists an additional minimum or maximum in the direction

$$\theta_1 = \arctan\left(\sqrt{(N - G - 2H)/N - F - 2H}\right).$$

The values of F, G, H, and N can be deduced from the observed dependence of the yield stress on orientation in the (RD, TD) plane. Indeed, according to Eq. (5.24):

– for uniaxial tension in the RD (***x*** direction or $\theta = 0°$),

$$(G+H)\sigma_0^2 = \bar{\sigma}^2 \tag{5.25}$$

– for uniaxial tension in the TD (***y*** direction or $\theta = 90°$),

$$(F+H)\sigma_{90}^2 = \bar{\sigma}^2 \tag{5.26}$$

– for uniaxial tension at $\theta = 45°$ from the RD (**x**),

$$(F+G+2N)\sigma_{45}^2 = 4\bar{\sigma}^2 \tag{5.27}$$

– for uniaxial tension at $\theta = 30^\circ$ from the RD (**x**),

$$(F + 9G + 4H + 6N)\sigma_{30}^2 = 16\bar{\sigma}^2 \tag{5.28}$$

Note that for equibiaxial tension, the stress components are: $\sigma_{xx} = \sigma_{yy} = \sigma_b^T$, $\sigma_{xy} = 0$ and the yield criterion predicts that:

$$(F + G)\left(\sigma_b^T\right)^2 = \bar{\sigma}^2 \tag{5.29}$$

Generally, the system of four Eqs. (5.25)–(5.27) and (5.29) is solved for F, G, H, and N

$$\begin{aligned} 2F &= (\bar{\sigma}/\sigma_{90})^2 + \left(\bar{\sigma}/\sigma_b^T\right)^2 - (\bar{\sigma}/\sigma_0)^2 \\ 2G &= \left(\bar{\sigma}/\sigma_b^T\right)^2 + (\bar{\sigma}/\sigma_0)^2 - (\bar{\sigma}/\sigma_{90})^2 \\ 2H &= (\bar{\sigma}/\sigma_0)^2 + (\bar{\sigma}/\sigma_{90})^2 - \left(\bar{\sigma}/\sigma_b^T\right)^2 \\ 2N &= 4(\bar{\sigma}/\sigma_{45})^2 - \left(\bar{\sigma}/\sigma_b^T\right)^2 \end{aligned} \tag{5.30}$$

As an example, in Fig. 5.2a is shown the predicted yield stress variation in the plane (RD, TD) according to Hill [22] corresponding to F = 0.603, G = 0.397, H = 0.603, and N = 2.537 in comparison with the measured yield stresses for a 2090-T3 Al Li alloy (data from [4]). The projection of the yield surface according to the Hill [22] criterion in the $(\sigma_{xx}, \sigma_{yy})$ plane corresponding to fixed levels of the shear stress $\sigma_{xy}/\sigma_0 = 0$, 0.25, 0.3, and 0.4 is shown in Fig. 5.2b. The stresses are normalized by the uniaxial tensile yield stress in the rolling direction, σ_0. The numerical values of the coefficients F, G, H, and N were calculated based on the experimental yield stresses along the 0°, 45°, 90° orientations and the tensile equibiaxial yield stress σ_b^T (see Table 5.1) in conjunction with the system of equations (5.30).

Anisotropy of yield stresses in the (RD–ND) plane

According to Hill [22] yield criterion, in the (RD, ND) plane the dependence of the normalized uniaxial yield stress $\sigma_\alpha/\bar{\sigma}$ on the loading angle α to the rolling direction is:

$$\frac{\sigma_\alpha}{\bar{\sigma}} = \frac{1}{\sqrt{F\sin^4\alpha + H\cos^4\alpha + G\left(\cos^2\alpha - \sin^2\alpha\right)^2 + 2M\sin^2\alpha\cos^2\alpha}} \tag{5.31}$$

Irrespective of the values of the coefficients F, G, H, and M, maxima and minima of the uniaxial yield stress occur along the orthotropic axes RD and ND ($\alpha = 0^\circ$, or

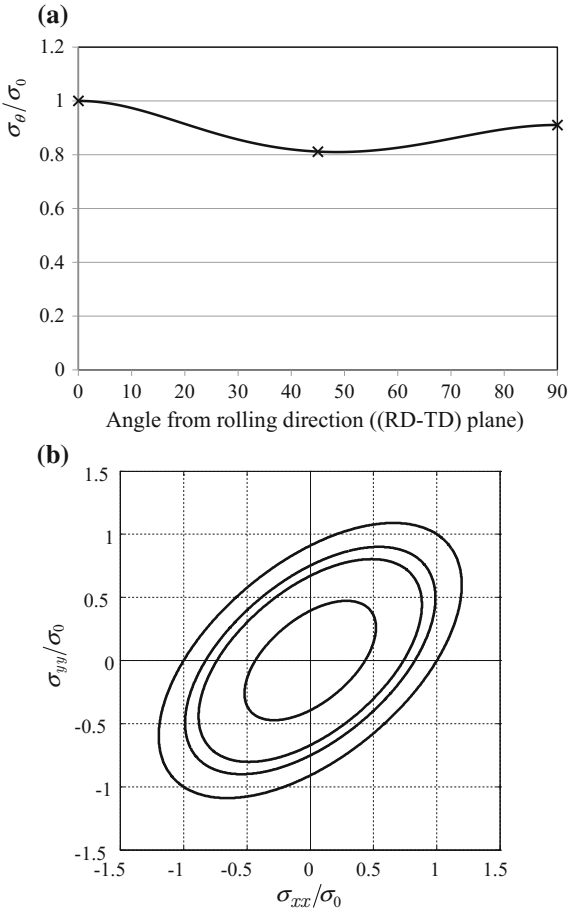

Fig. 5.2 **a** Normalized uniaxial yield stress for AA2090-T3 alloy sheet versus the tensile direction according to Hill [22] yield criterion (symbols represent experimental data). **b** Projection of the yield surfaces in the plane $(\sigma_{xx}, \sigma_{yy})$ corresponding to fixed levels of the shear stress $\sigma_{xy}/\sigma_0 = 0$, 0.25, 0.3, and 0.4 according to Hill [22] yield criterion

Table 5.1 Mechanical properties for a AA2090-T3 sheet and Hill [22] coefficients calculated using the experimental normalized yield stresses

Property	Normalized yield stress	*r*-value	F	G	H	N
Uniaxial tension 0°	1.000	0.212	0.603	0.397	0.603	2.537
Uniaxial tension 45°	0.811	1.577				
Uniaxial tension 90°	0.910	0.692				
Equibiaxial tension	1.01					

$\alpha = 90°$) and depending on the relation of M to the quantities $F + 2G$ and $H + 2G$, an extremum may occur in the direction $\alpha_1 = \arctan\left(\sqrt{(M - H - 2G)/(M - F - 2G)}\right)$.

It is worth noting that Eq. (5.31) for $\alpha = 90°$ reduces to Eq. (5.29) for σ_b^T, i.e., Hill [22] yield criterion predicts that the yield stress in uniaxial tension in the ND direction ($\alpha = 90°$) is equal the yield stress in equibiaxial tension σ_b^T in the (RD–TD) plane.

Also, substitution in the Eq. (5.12) of the criterion and comparison with the expression given by Eq. (5.26) for σ_{90} shows that according to Hill [22] yield criterion, the yield stress in equibiaxial tension in the plane (RD–ND) is equal to the yield stress in uniaxial tension along TD, i.e., σ_{90}. Furthermore, making use of Eq. (5.31) it follows that the coefficient M can be determined based on the formula:

$$2M = 4\left(\bar{\sigma}\Big/\sigma_{45}^{\mathrm{RD-ND}}\right)^2 - (\bar{\sigma}/\sigma_{90})^2, \tag{5.32}$$

where $\sigma_{45}^{\mathrm{RD-ND}}$ denotes the uniaxial tensile yield stress in a direction at 45° to RD in the (RD, ND) plane.

As an example, in Fig. 5.3a is shown for the same 2090-T3 Al alloy the predicted yield stress variation in the (RD, ND) plane according to Hill [22] while in Fig. 5.3b is presented the projection of the yield surface according to Hill [22] criterion in the $(\sigma_{xx}, \sigma_{zz})$ plane for different fixed levels $\sigma_{xz}/\sigma_0 = 0$, 0.25, 0.3, and 0.4 for the same numerical values of the coefficients F, G, H given in Table 5.1, and a value of M = 3/2, which corresponds to the value when the Hill [22] criterion is reduced to isotropy (see Eq. 5.15).

Anisotropy of yield stresses in the (TD–ND) plane

According to Hill [22] yield criterion, in the (TD, ND) plane the dependence of the normalized uniaxial yield stress $\sigma_\beta/\bar{\sigma}$ on the loading angle with respect to transverse direction, β, is:

$$\frac{\sigma_\beta}{\bar{\sigma}} = \frac{1}{\sqrt{G\sin^4\beta + H\cos^4\beta + F\left(\cos^2\beta - \sin^2\beta\right)^2 + 2L\sin^2\beta\cos^2\beta}} \tag{5.33}$$

Irrespective of the values of the coefficients F, G, H, and L, maxima and minima of the uniaxial yield stress occur along the orthotropic axes TD and ND ($\beta = 0°$ or $\beta = 90°$) and depending of the relation of L to the quantities $G + 2F$ and $H + 2F$, an extremum may occur in the direction $\beta_1 = \arctan\left(\sqrt{(L - H - 2F)/(L - G - 2F)}\right)$.

It can be easily shown that according to the [22] yield criterion the yield stress in uniaxial tension in the RD direction, σ_0, is equal to the yield stress in equibiaxial tension in the (TD–ND) plane. Therefore, if $\sigma_{45}^{\mathrm{TD-ND}}$ denotes the uniaxial tensile

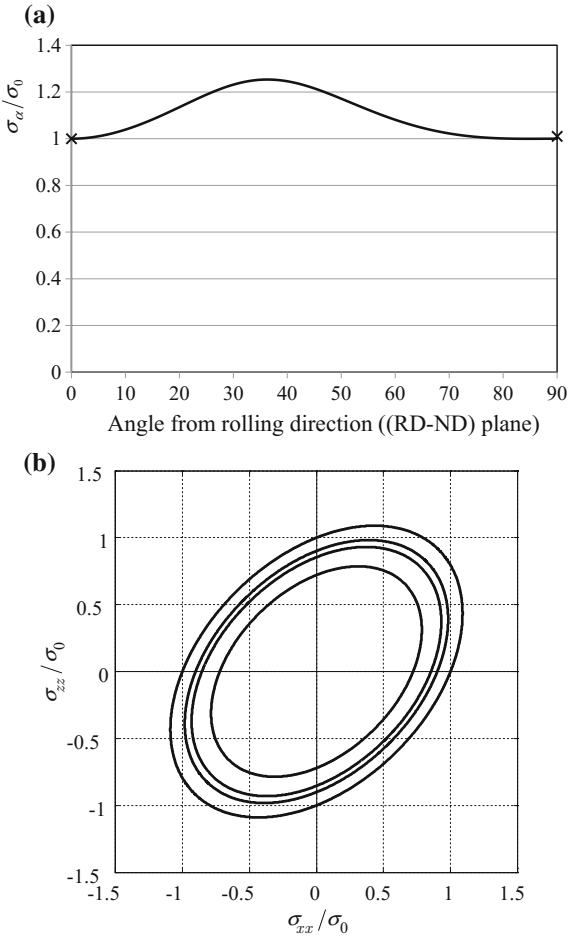

Fig. 5.3 **a** Normalized uniaxial yield stress versus tensile direction according to Hill [22] yield criterion for AA2090-T3 alloy sheet (symbols represent experimental data). **b** Projection of the yield surfaces for AA2090-T3 alloy sheet in the plane $(\sigma_{xx}, \sigma_{zz})$ corresponding to fixed levels of the shear stress $\sigma_{xz}/\sigma_0 = 0$, 0.25, 0.3, and 0.4 according to Hill [22] yield criterion

yield stress in a direction at 45° to TD in the (TD, ND) plane, then from Eqs. (5.33) and (5.26) it follows that the coefficient L can be determined based on the formula:

$$2L = 4\left(\bar{\sigma}\Big/\sigma_{45}^{\mathrm{TD-ND}}\right)^2 - (\bar{\sigma}/\sigma_0)^2. \tag{5.34}$$

As an example, in Fig. 5.4a is shown for the same 2090-T3 Al alloy the predicted yield stress variation in the (TD, ND) plane according to Hill [22] while in Fig. 5.4b is presented the projection of the yield surface in the $(\sigma_{yy}, \sigma_{zz})$ plane for different fixed levels of $\sigma_{yz}/\sigma_0 = 0$, 0.25, 0.3, and 0.4, for the same numerical values of the coefficients F, G, H given in Table 5.1, and a value of L = 3/2, which corresponds to the isotropic value (see Eq. 5.15).

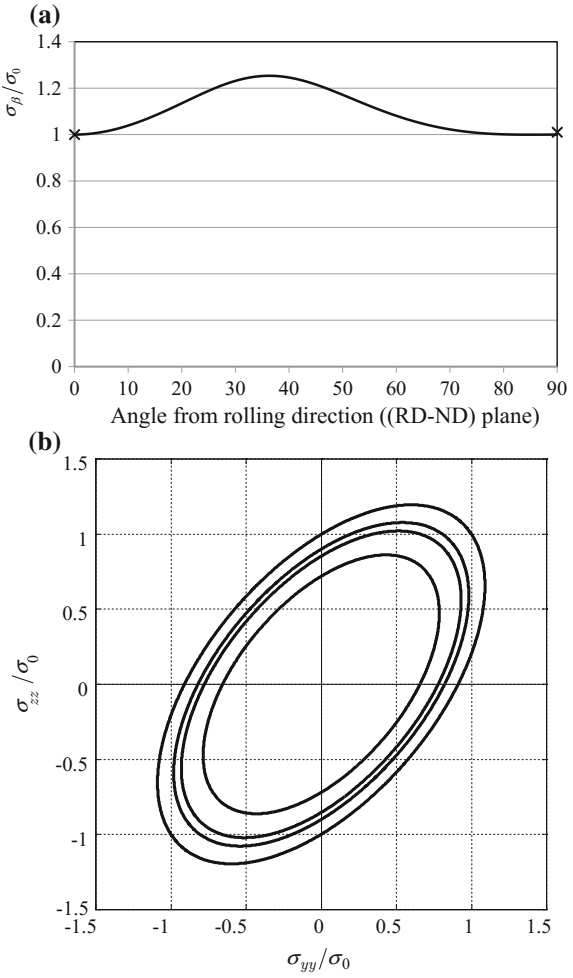

Fig. 5.4 **a** Normalized uniaxial yield stress versus tensile direction according to Hill [22] yield criterion for AA2090-T3 alloy sheet (symbols represent experimental data). **b** Projection of the yield surfaces in the plane $(\sigma_{yy}, \sigma_{zz})$ corresponding to fixed levels of the shear stress $\sigma_{yz}/\sigma_0 = 0$, 0.25, 0.3, and 0.4 according to Hill [22] yield criterion

It is also worth noting that if τ_{RD-TD}, τ_{ND-RD}, and τ_{TD-ND} are the yield stresses in pure shear in the planes, (RD–TD), (RD–ND), and (TD, ND), respectively, then according to Hill [22] criterion:

$$2N = \bar{\sigma}^2/\tau_{RD-TD}^2, 2M = \bar{\sigma}^2/\tau_{RD-ND}^2, 2L = \bar{\sigma}^2/\tau_{TD-ND}^2 \tag{5.35}$$

The relations (5.35) show that the coefficients L, M, N should always be positive. Furthermore, given that the same coefficients are also expressible in terms of the equibiaxial tensile yield stresses and the uniaxial yield stresses along 45° direction in the same plane [see Eqs. (5.30), (5.32), and (5.34), respectively], it can be concluded that Hill [22] criterion imposes the following restrictions on the yield stresses:

$$\sigma_0 > \frac{\sigma_{45}^{\mathrm{TD-ND}}}{2}, \quad \sigma_{90} > \frac{\sigma_{45}^{\mathrm{RD-ND}}}{2}, \quad \sigma_{\mathrm{ND}} > \frac{\sigma_{45}}{2}. \tag{5.36}$$

In other words, the yield stress along an orthotropic axis should be larger than half of the yield stress along a diagonal direction in the plane normal to the respective orthotropic axis.

Hill [22] criterion imposes that the yield stresses in pure shear in any given orthotropic plane are completely determined by the yield stress values in uniaxial tension along specific directions, i.e.,

$$\begin{aligned}
\tau_{\mathrm{RD-TD}}^2 &= \left[\frac{4}{\left(\sigma_{45}^{\mathrm{RD-TD}}\right)^2} - \frac{1}{\sigma_{\mathrm{ND}}^2}\right]^{-1} \\
\tau_{\mathrm{TD-ND}}^2 &= \left[\frac{4}{\left(\sigma_{45}^{\mathrm{TD-ND}}\right)^2} - \frac{1}{\sigma_0^2}\right]^{-1} \\
\tau_{\mathrm{RD-ND}}^2 &= \left[\frac{4}{\left(\sigma_{45}^{\mathrm{RD-ND}}\right)^2} - \frac{1}{\sigma_{90}^2}\right]^{-1}
\end{aligned} \tag{5.37}$$

Note that for isotropic conditions, each of the three relations given in Eq. (5.37) reduces to:

$$\sigma_T^2 = 3\tau_Y^2,$$

which expresses that the von Mises yield criterion predicts a fixed ratio between the yield stresses in uniaxial tension and pure shear (see also Sect. 4.2.1).

Remark Another important aspect concerns the predicted yield stresses under equibiaxial tension. It was shown that according to Hill [22] criterion, the yield stresses under equibiaxial tension in the (RD–TD), (RD–ND), and (TD, ND) planes are completely determined by the uniaxial yield stress values along the orthotropic axes. However, this statement holds true for any orthotropic criterion represented by a yield function which is even in stresses. Specifically, if $\sigma_b^{\mathrm{RD-TD}}$, $\sigma_b^{\mathrm{RD-ND}}$ and $\sigma_b^{\mathrm{TD-ND}}$ denote the yield stresses in under equibiaxial tension in the planes, (RD–TD), (RD–ND), and (TD, ND) respectively, then:

$$\sigma_b^{\mathrm{RD-TD}} = \sigma_{\mathrm{ND}}, \quad \sigma_b^{\mathrm{RD-ND}} = \sigma_{90}, \quad \sigma_b^{\mathrm{TD-ND}} = \sigma_0. \tag{5.38}$$

5.2.2 Variation of the Lankford Coefficients with the Tensile Loading Direction According to Hill [22] Criterion

As already mentioned, the ratio between the in-plane transverse strain and through-thickness plastic strain increments, that a material undergoes when subjected to uniaxial tension in a direction at angle θ in the RD–TD plane has been linked to the formability of thin sheets (see also Chap. 3). Assuming associated flow rule, this ratio, denoted by r_θ, is given by:

$$r_\theta = -\frac{\sin^2\theta\, d^p_{xx} - \sin(2\theta)\, d^p_{xy} + \cos^2\theta\, d^p_{yy}}{d^p_{xx} + d^p_{yy}} \tag{5.39}$$

Substituting Eq. (5.22) into Eq. (5.39), we obtain (see [22]):

$$r_\theta = \frac{(2N - G - F)\sin^2\theta\cos^2\theta + H\cos^2(2\theta)}{F\sin^2\theta + G\cos^2\theta}. \tag{5.40}$$

Note that irrespective of the values of the coefficients F, G, H, and N, the maxima and minima in the variation of the Lankford coefficients occur along RD and TD (i.e., at 0° and 90°, respectively). Depending on the relative ordering of these coefficients, there could be an additional minimum or maximum for $0° < \theta < 90°$ (see also [22]). The trends in the Lankford coefficients' variation with loading orientation, in particular the number of minima and maxima, are indicative of the drawing performance of a given material. On the basis of Eq. (5.40) for a material with yielding according to Hill [22], a maximum of four ears can be expected when drawing a cylindrical cup (see [18]).

In particular, Eq. (5.40) leads to:

$$r_0 = \frac{H}{G}, \quad r_{90} = \frac{H}{F}, \quad r_{45} = \frac{2N - G - F}{2(G + F)}. \tag{5.41}$$

5.2.3 Comments on the Identification Procedure

Using Eq. (5.39) one can obtain the following expressions for the coefficients F, G, H, N of Hill [22] criterion in terms of the r-values:

$$
\begin{aligned}
F &= \frac{r_0}{r_{90}(1+r_0)}\left(\frac{\bar{\sigma}}{\sigma_0}\right)^2 \\
G &= \frac{1}{1+r_0}\left(\frac{\bar{\sigma}}{\sigma_0}\right)^2 \\
H &= \frac{r_0}{1+r_0}\left(\frac{\bar{\sigma}}{\sigma_0}\right)^2 \\
N &= \frac{(r_0+r_{90})(2r_{45}+1)}{2r_{90}(1+r_0)}\left(\frac{\bar{\sigma}}{\sigma_0}\right)^2
\end{aligned}
\tag{5.42}
$$

As already mentioned, the in-plane coefficients F, G, H, N can be determined using as input the experimental yield stresses in the 0°, 45°, 90° directions and σ_b^T in conjunction with Eq. (5.30).

For the same Al–Li alloy 2090-T3 for which the experimental yield stresses and r-values are given in Table 5.1, in Fig. 5.5a, b is shown the r-value variation with the orientation in the plane (RD–TD) obtained using formula (5.40) for two sets of values of the coefficients F, G, H, and N. The first set of values are: $F = 0.603$, $G = 0.397$, $H = 0.603$, $N = 2.537$, which were obtained previously using as input the experimental yield stresses, and Eq. (5.30) (see Table 5.1). The second set of values are $F = 0.252$, $G = 0.825$, $H = 0.175$, $N = 2.238$ obtained using as input the experimental r-values and the uniaxial tensile yield stress along RD, in conjunction with Eq. (5.42). For this latter set of values, in Fig. 5.5c it is also presented the predicted yield stress anisotropy in (RD, TD) calculated using Eq. (5.24). Examination of Fig. 5.5a and b shows that the stress-based and r-value-based anisotropic coefficients do not lead to the same variation in r-values. It is clearly seen that if the stress-based coefficients are used, the predicted yield stress anisotropy is in good agreement with the measured yield stress anisotropy (see Fig. 5.2a) while the experimental r-values are underpredicted (see Fig. 5.5a). If the r-values based coefficients are used, the yield stress anisotropy is not well described (see Fig. 5.5c) while the predicted r-value variation is in good agreement with the experimental data.

The fact that Hill [22] yield criterion cannot capture both the yield stress and r-values' anisotropy with the same accuracy is a direct consequence of the fact that the yield function is quadratic in stresses. As demonstrated, for a function quadratic in stresses to be orthotropic and pressure-insensitive, there should be exactly six independent anisotropy coefficients. As a consequence, Hill [22] yield criterion imposes very specific couplings between the yield stresses and r-values in the (RD–TD) plane. Indeed, from Eqs. (5.25), (5.26), and (5.41), it follows that:

$$
\frac{\sigma_0}{\sigma_{90}} = \sqrt{\frac{r_0(1+r_{90})}{r_{90}(1+r_0)}}. \tag{5.43}
$$

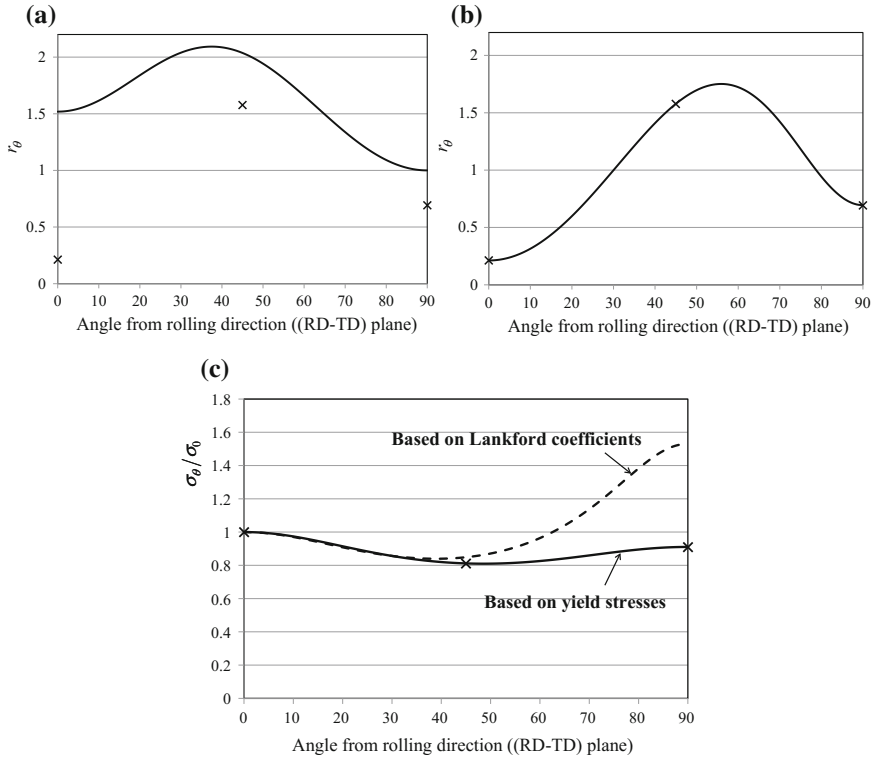

Fig. 5.5 Evolution of the Lankford coefficients versus tensile direction for AA2090-T3 alloy sheet according to Hill [22] yield criterion identified based on: **a** uniaxial yield stresses (Eq. 5.30) or **b** Lankford coefficients (Eq. 5.42). **c** Normalized uniaxial yield stress versus tensile direction according to Hill [22] yield criterion calibrated based on uniaxial yield stresses or Lankford coefficients (symbols represent experimental data)

Therefore, Hill [22] criterion cannot account for the experimentally observed behavior of certain Al alloys and brass (see for example, [35, 45] for which $\sigma_0 = \sigma_{90}$, but $r_0 \neq r_{90}$, and $r_0 = r_{90}$, but $\sigma_0 \neq \sigma_{90}$, respectively).

As demonstrated, Hill [22] criterion predicts that the yield stresses in pure shear in any given orthotropic plane are completely determined by the yield stress values in uniaxial tension along specific directions (see Eq. 5.37). To describe simultaneously the anisotropy in yielding and Lankford coefficients with improved accuracy, more anisotropy coefficients need to be included in the expression of the yield function. As discussed, orthotropic symmetries' requirements impose clear restrictions concerning the number of independent anisotropy coefficients that should appear in the expression of any yield criterion. Therefore, non-quadratic formulations need to be considered. For an overview of plane-stress (2-D) non-quadratic orthotropic yield criteria, the reader is referred to [8] and the excellent overview presented in the

monograph of [6]. In this chapter, we will only present non-quadratic orthotropic yield criteria that are defined for any three-dimensional loadings.

5.3 Non-quadratic Three-Dimensional Yield Criteria for Materials with the Same Response in Tension–Compression

As demonstrated in Sect. 5.1, in order to respect the restrictions imposed by the orthotropic symmetries a non-quadratic orthotropic yield criterion should be expressed as a function of J_2^0 and J_3^0, the orthotropic generalizations of the second and third-invariant of the stress deviator given by Eqs. (5.6) and (5.8), respectively. Therefore, to be well-defined, a 3-D orthotropic yield criterion should involve at most 17 independent anisotropy coefficients. Likewise, to ensure that the coefficients of anisotropy involved in the yield criterion are independent, when using the linear transformation methodology to account for plastic anisotropy, at most two linear transformations should be considered. We begin by presenting the orthotropic yield criteria defined explicitly in terms of J_2^0 and J_3^0 proposed by Cazacu and Barlat [11] and Cazacu [10]. We will proceed with the presentation and discussion of the orthotropic extensions of the Hershey [21]–Hosford [25] isotropic yield criterion (see Chap. 4) developed by Barlat and collaborators at Alcoa Corporation that involve one or two linear transformations. Furthermore, it will be demonstrated that explicit expressions for these criteria in terms of the stress components can be obtained.

5.3.1 Cazacu and Barlat [11] Orthotropic Criterion

Cazacu and Barlat [11] proposed an orthotropic yield criterion in terms of J_2^0 and J_3^0, which extends the isotropic yield criterion of Drucker [16] (see also, Sect. 4.2.2). The expression of this criterion is:

$$f^0(\boldsymbol{\sigma}) = \left(J_2^0\right)^3 - c\left(J_3^0\right)^2, \tag{5.44}$$

with J_2^0 and J_3^0 being given by Eqs. (5.6) and (5.8), respectively, and c being a material parameter, which ensures a proper weighting of the influence of these anisotropic invariants on yielding. Given that this criterion is represented by a homogeneous function in stresses, the yield stress is the same if the coefficients $a_k, k = 1, \ldots, 6$ and b_j,

$j = 1, \ldots, 11$ are replaced by $\alpha a_1, \alpha a_2, \alpha a_3, \alpha a_4, \alpha a_5, \alpha a_6, \alpha b_1, \alpha b_2, \ldots, \alpha b_{11}$ where α is an arbitrary positive constant. Therefore, without loss of generality one of these parameters, for example, b_6 can be set equal to unity, and for full 3-D stress conditions, the criterion involves 17 coefficients. The effective stress, $\bar{\sigma}$, associated to this criterion is:

$$\bar{\sigma} = A\left[\left(J_2^0\right)^3 - c\left(J_3^0\right)^2\right]^{1/6}, \tag{5.45}$$

with A being a constant defined such that for uniaxial tension in one of the orthotropic axes [e.g., for a rolled plate or sheet, the rolling direction (RD)] the effective stress reduces to the yield stress, i.e.,

$$A = \frac{3\sqrt{2}}{\left[27(a_1 + a_3)^3 - 8c(b_1 + b_2)^2\right]^{1/6}} \tag{5.46}$$

Assuming associated flow rule, the plastic strain-rate tensor, $\mathbf{d}^p$, can be easily calculated as:

$$\mathbf{d}^p = \dot{\lambda}\frac{\partial \bar{\sigma}}{\partial \boldsymbol{\sigma}}, \tag{5.47}$$

where $\dot{\lambda}$ is the plastic multiplier, and $\bar{\sigma}$ is given by Eq. (5.45). Therefore,

$$\frac{\partial \bar{\sigma}}{\partial \sigma_{ij}} = (A/6)\left\{3\left(J_2^0\right)^2\frac{\partial J_2^0}{\partial \sigma_{ij}} - 2c\left(J_3^0\right)\frac{\partial J_3^0}{\partial \sigma_{ij}}\right\}\left\{\left(J_2^0\right)^3 - c\left(J_3^0\right)^2\right\}^{-5/6}. \tag{5.48}$$

with $i, j = 1, \ldots, 3$. Therefore, we have:

$$\begin{aligned}
\frac{\partial J_2^0}{\partial \sigma_{xx}} &= (a_1 + a_3)s_{xx}/3 - a_1 s_{yy}/3 - a_3 s_{zz}/3 \\
\frac{\partial J_2^0}{\partial \sigma_{yy}} &= -a_1 s_{xx}/3 + (a_1 + a_2)s_{yy}/3 - a_2 s_{zz}/3 \\
\frac{\partial J_2^0}{\partial \sigma_{zz}} &= -a_3 s_{xx}/3 - a_2 s_{yy}/3 + (a_3 + a_2)s_{zz}/3 \\
\frac{\partial J_2^0}{\partial \sigma_{yz}} &= a_6 s_{yz}, \quad \frac{\partial J_2^0}{\partial \sigma_{xz}} = a_5 s_{xz}, \quad \frac{\partial J_2^0}{\partial \sigma_{xy}} = a_4 s_{xy}
\end{aligned} \tag{5.49}$$

The partial derivatives of the orthotropic third-invariant J_3^0 are expressed as:

$$\begin{aligned}
\frac{\partial J_3^0}{\partial \sigma_{xx}} &= \frac{b_1}{9}\left(\sigma_{xx}-\sigma_{yy}\right)^2+\frac{b_2}{9}\left(\sigma_{xx}-\sigma_{zz}\right)^2-\frac{b_1+b_4}{9}\left(\sigma_{yy}-\sigma_{zz}\right)^2 \\
&\quad -\frac{1}{3}\left[(b_6+b_7)\sigma_{yz}^2-(2b_9-b_8)\sigma_{xz}^2-(2b_{10}-b_5)\sigma_{xy}^2\right] \\
\frac{\partial J_3^0}{\partial \sigma_{yy}} &= \frac{b_4}{9}\left(\sigma_{xx}-\sigma_{yy}\right)^2-\frac{b_1+b_4}{9}\left(\sigma_{xx}-\sigma_{zz}\right)^2+\frac{b_3}{9}\left(\sigma_{yy}-\sigma_{zz}\right)^2 \\
&\quad -\frac{1}{3}\left[2b_9\sigma_{xz}^2-b_5\sigma_{xy}^2-b_6\sigma_{yz}^2\right] \\
\frac{\partial J_3^0}{\partial \sigma_{zz}} &= -\frac{\partial J_3^0}{\partial \sigma_{xx}}-\frac{\partial J_3^0}{\partial \sigma_{yy}} \\
\frac{\partial J_3^0}{\partial \sigma_{yz}} &= -\frac{\sigma_{yz}}{3}\left[(b_6+b_7)\sigma_{xx}-b_6\sigma_{yy}-b_7\sigma_{zz}\right]+b_{11}\sigma_{xy}\sigma_{xz} \\
\frac{\partial J_3^0}{\partial \sigma_{xz}} &= -\frac{\sigma_{xz}}{3}\left[2b_9\sigma_{yy}-b_8\sigma_{zz}-(2b_9-b_8)\sigma_{xx}\right]+b_{11}\sigma_{xy}\sigma_{yz} \\
\frac{\partial J_3^0}{\partial \sigma_{xy}} &= -\frac{\sigma_{xy}^2}{3}\left[2b_{10}\sigma_{zz}-b_5\sigma_{yy}-(2b_{10}-b_5)\,\sigma_{xx}\right]+b_{11}\sigma_{xz}\sigma_{yz}
\end{aligned} \tag{5.50}$$

Note that for isotropy, i.e., each of the constants $a_i = 1$ and if each of the constants $b_k = 1$, we have:

$$\frac{\partial J_2^0}{\partial \sigma_{ij}}=\frac{\partial J_2}{\partial \sigma_{ij}}=s_{ij},\quad \frac{\partial J_3^0}{\partial \sigma_{ij}}=\frac{\partial J_3}{\partial \sigma_{ij}}=\left(\boldsymbol{s}^2\right)_{ij}-\frac{2}{3}J_2\delta_{ij},\quad i,j=1,\ldots,3,$$

and the Eq. (5.50) reduces to the relationships given in Sect. 4.2.2 between the plastic strain increments and the deviatoric stresses for a material with yielding governed by the isotropic Drucker [16] yield criterion.

In the plane of the rolled plate or sheet (RD, TD), the Cazacu and Barlat [11] orthotropic yield criterion predicts the following dependence of the normalized uniaxial yield stress $\sigma_\theta/\bar{\sigma}$ on the angle θ between the direction of loading and the rolling direction (see also Fig. 5.1):

$$A\left(\frac{\sigma_\theta}{\sigma_0}\right)=\left\{\begin{array}{l}\left[\frac{1}{6}(a_1+a_3)\cos^4\theta+(a_4-a_1/3)\cos^2\theta\sin^2\theta+\frac{1}{6}(a_1+a_2)\sin^4\theta\right]^3 \\ -c\left[\begin{array}{l}\frac{1}{27}(b_1+b_2)\cos^6\theta+\frac{1}{27}(b_3+b_4)\sin^6\theta \\ -\frac{1}{9}\left[(b_1+3b_5-6b_{10})\cos^2\theta+(b_4-3b_5)\sin^2\theta\right]\sin^2\theta\cos^2\theta\end{array}\right]^2\end{array}\right\}^{-1/6} \tag{5.51}$$

with the constant A being given by Eq. (5.46).

In particular,

$$\frac{\sigma_{30}}{\sigma_0}=\frac{4\sqrt{3}}{A}\left[\frac{(4a_1+a_2+9a_3+18\,a_4)^3}{8}-\frac{c}{27}(27b_2+b_3-8b_4+54(3b_{10}-b_5))^2\right]^{-1/6} \tag{5.52}$$

$$\frac{\sigma_{45}}{\sigma_0}=\frac{2\sqrt{3}}{A}\left[\frac{(a_2+a_3+6a_4)^3}{8}-\frac{c}{27}(-2b_1+b_2+b_3-2b_4+18b_{10})^2\right]^{-1/6} \tag{5.53}$$

$$\frac{\sigma_{90}}{\sigma_0}=\frac{1}{A}\left[\left(\frac{a_1+a_2}{6}\right)^3-c\left(\frac{b_3+b_4}{27}\right)^2\right]^{-1/6}. \tag{5.54}$$

Yielding under equal-biaxial tension in the plane (RD–TD) occurs when $\sigma_{xx}=\sigma_{yy}=\sigma_b^T$ where:

$$\frac{\sigma_b^T}{\sigma_0}=\frac{1}{A}\left[\left(\frac{a_2+a_3}{6}\right)^3-c\left(\frac{2b_1-b_2-b_3+2b_4}{27}\right)^2\right]^{-1/6} \tag{5.55}$$

Yielding under pure shear in the (RD, TD) plane is equal to

$$\tau_{\mathrm{RD-TD}}=\frac{\sigma_0}{A\sqrt{a_4}}. \tag{5.56}$$

The Lankford coefficients r_θ are calculated based on the formula:

$$r_\theta=-\frac{\sin^2\theta\,\dfrac{\partial\bar{\sigma}}{\partial\sigma_{xx}}-\sin(2\theta)\,\dfrac{\partial\bar{\sigma}}{\partial\sigma_{xy}}+\cos^2\theta\,\dfrac{\partial\bar{\sigma}}{\partial\sigma_{yy}}}{\dfrac{\partial\bar{\sigma}}{\partial\sigma_{xx}}+\dfrac{\partial\bar{\sigma}}{\partial\sigma_{yy}}}, \tag{5.57}$$

with the specific expressions for $\dfrac{\partial\bar{\sigma}}{\partial\sigma_{ij}}$ given by Eq. (5.48).

Therefore,

$$\begin{aligned}
&(r_0a_3-a_1)(a_1+a_3)^2-\frac{8c}{27}(b_1+b_2)(b_2r_0-b_1)=0\\
&(r_{90}a_2-a_1)(a_1+a_2)^2-\frac{8c}{27}(b_3+b_4)(b_3r_{90}-b_4)=0\\
&[\beta(2r_{45}+1)-6a_4]\frac{(\beta+6a_4)^2}{8}-\frac{c}{27}(\alpha+18b_6)[2r_{45}(\alpha+6b_{10})-\alpha+6b_{10}]=0
\end{aligned} \tag{5.58}$$

with $\alpha=-2b_1+b_2+b_3-2b_4$, $\beta=a_2+a_3$.

In summary, for description of plastic properties in the (RD–TD) plane the criterion involves ten anisotropy coefficients: a_1, a_2, a_3, a_4, b_1, b_2, b_3, b_4, b_5, b_{10} and the parameter c. Generally, uniaxial tension and bulging test data are available. Therefore, the most commonly used procedure for parameters identification is based on the following system of equations:

- Five equations of the type (5.51) to be satisfied by the yield stresses corresponding to different orientations θ,
- One equation to be satisfied by σ_b^T measured in a bulge test,
- Five equations of the type (5.57) and (5.58) to be satisfied by the strain ratios r_θ corresponding to several different orientations θ.

5.3.1.1 Predicted Anisotropy in Yield Stresses and Lankford Coefficients

The significance of any yield criterion ultimately lies in its ability to describe the behavior of real materials. In this section, the plastic anisotropy of thin rolled steel and Al alloys exhibiting orthotropic symmetry is predicted by the Cazacu and Barlat [11] yield criterion.

As an example, in Fig. 5.6a, b are shown the predicted variation of the yield stresses and r-values in the (RD, TD) plane according to the Cazacu and Barlat [11] and Hill [22] criterion, respectively, in comparison with measured yield stresses for a DC06 steel sheet (data from [20, 34]). The coefficients involved in the criterion were determined from the experimental yield stresses and r-values for $\theta = 0°, 30°, 45°, 60°$, $90°$ and the equibiaxial tensile yield stress σ_b^T (see Table 5.2), and their numerical values are: $a_1 = 1.303$, $a_2 = 0.968$, $a_3 = 0.9822$, $a_4 = 1.0471$, $b_1 = 1.531$, $b_2 = 2.247$, $b_3 = 2.399$, $b_4 = 0.6070$, $b_5 = 1.6540$, $b_{10} = 1.248$, and $c = 1.30$ (for more details on the identification procedure, see [2]). The numerical values of Hill [22] criterion coefficients for this material, calculated using the experimental r-values at $\theta = 0°, 45°, 90°$ are: $F = 0.263$, $G = 0.284$, $H = 0.716$, and $N = 1.28$.

Note that the Cazacu and Barlat [11] criterion can describe with accuracy both the anisotropy in yielding and r-values of this steel sheet. The projection in the $(\sigma_{xx}, \sigma_{yy})$ plane of the yield surface corresponding to $\sigma_{xy} = 0$, according to the Cazacu and Barlat [11], and Hill [22] yield criterion, respectively, is shown in Fig. 5.6c. Also, in Fig. 5.7 is shown a comparison of the yield surface according to Cazacu and Barlat [11] with the corresponding isotropic yield surface to which this orthotropic yield surface reduces when the anisotropy coefficients are set to unity (i.e., for $a_1 = a_2 = a_3 = a_4 = b_1 = b_2 = b_3 = b_4 = b_5 = b_{10} = 1$ and $c = 1.30$).

For the 2090-T3 Al alloy (data given in Table 5.1), the anisotropy coefficients are: $a_1 = 1.358$, $a_2 = 1.848$, $a_3 = 1.075$, $a_4 = 1.709$; $b_1 = 5.357$, $b_2 = -0.623$, $b_3 = -4.386$, $b_4 = -3.654$, $b_5 = -6.046$, and $b_{10} = -0.882$, while $c = 0.857$. The theoretical yield surfaces corresponding to the normalized shear stresses σ_{xy}/σ_o of

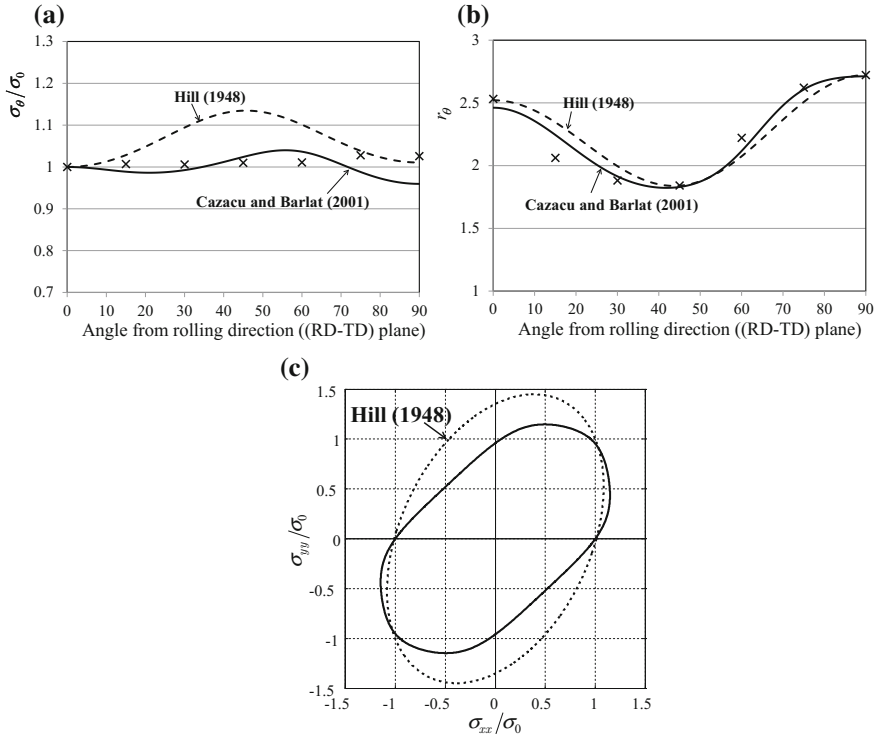

Fig. 5.6 DC06 alloy sheet: **a** Normalized uniaxial yield stress versus tensile direction according to Cazacu and Barlat [11] and Hill [22] (dashed line) yield criterion. **b** Evolution of the Lankford coefficient versus tensile direction according to Cazacu and Barlat [11] and Hill [22] (dashed line) yield criterion (symbols represent experimental data). **c** Projection of the yield surfaces in the plane $(\sigma_{xx}, \sigma_{yy})$ according to the two criteria

Table 5.2 Experimental data for a DC06 steel sheet (after [20, 34])

Property	Normalized yield stress	r value
Uniaxial tension 0°	1.000	2.53
Uniaxial tension 15°	1.007	2.06
Uniaxial tension 30°	1.006	1.88
Uniaxial tension 45°	1.010	1.84
Uniaxial tension 60°	1.011	2.22
Uniaxial tension 75°	1.028	2.62
Uniaxial tension 90°	1.026	2.72
Equibiaxial tension	1.208	

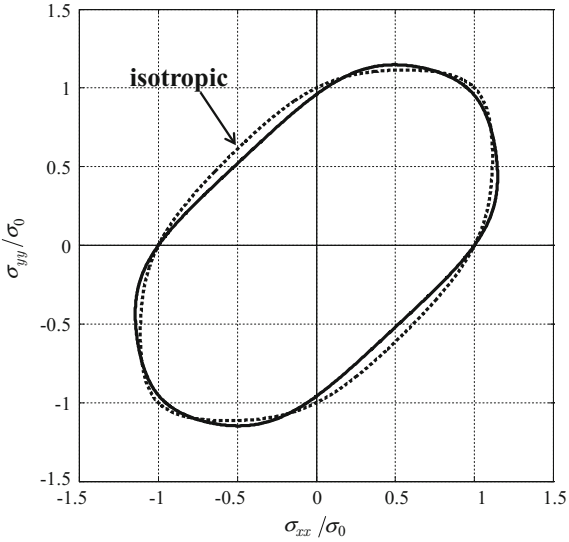

Fig. 5.7 Projection of the yield surfaces for DC06 alloy sheet in the plane $(\sigma_{xx}, \sigma_{yy})$ according to the Cazacu and Barlat [11] yield criterion: Comparison of the orthotropic yield surface with the corresponding isotropic yield surface (c = 1.30)

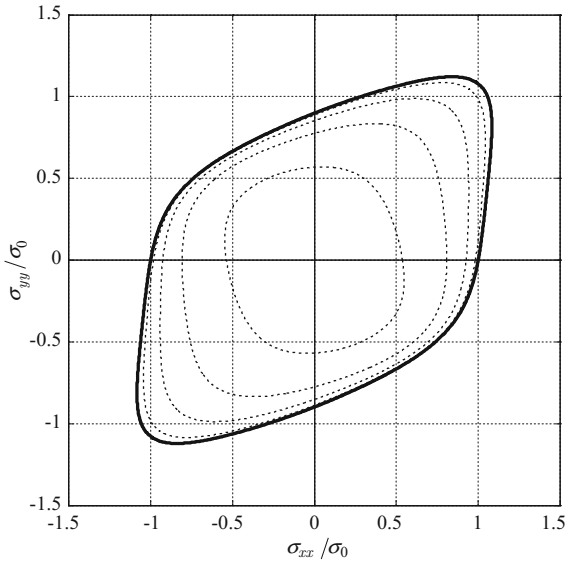

Fig. 5.8 Projection of the yield surfaces for AA2090-T3 alloy sheet in the plane $(\sigma_{xx}, \sigma_{yy})$ corresponding to fixed levels of the shear stress $\sigma_{yz}/\sigma_0 = 0$, 0.1, 0.2, 0.3, and 0.4 according to Cazacu and Barlat [11] yield criterion

0, 0.1, 0.2, 0.3, and 0.4 are depicted in Fig. 5.8. The stresses are normalized with the experimental tensile yield stress in the rolling direction. The experimental variation of the normalized uniaxial yield stress and r-ratio with the orientation and the predictions of Hill [22] yield criterion and Cazacu and Barlat [11] yield criterion is shown in Fig. 5.9a, b. It can be seen that the agreement between the prediction with Cazacu and Barlat [11] yield criterion and the experimental results is very

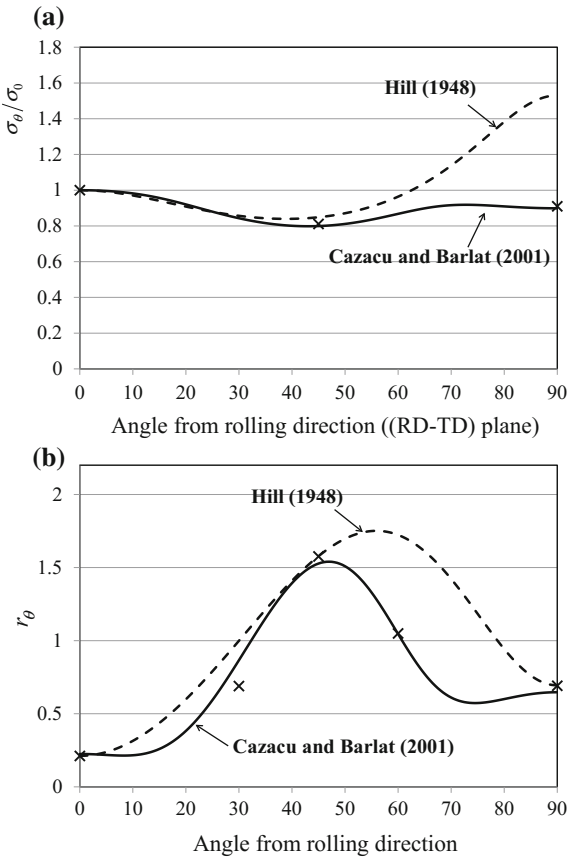

Fig. 5.9 AA2090-T3 alloy sheet: **a** Normalized uniaxial yield stress versus tensile direction according to the Cazacu and Barlat [11] and Hill [22] (dashed line) yield criterion. **b** Evolution of the Lankford coefficient versus tensile direction according the two yield criteria (symbols represent experimental data)

good. Furthermore, this yield criterion predicts the variation in height (earings) observed for a fully drawn cylindrical cup of this AA2090-T3 sheet (see [9]).

It is worth pointing out that the shape of the Cazacu and Barlat [11] yield surface strongly depends on the experimental data used for the identification. The parameters are determined through the minimization of an objective function, which is defined according to the experimental data available. It is advised that the target application for the material should carefully considered when assigning weights to various input data in the objective function.

5.3.1.2 Extension of Drucker [16] Isotropic Yield Criterion to Transversely Isotropic Materials

Cazacu and Barlat [12] proposed the following extension to transverse isotropy of the isotropic Drucker [16] yield criterion:

$$f^T = \left(J_2^T\right)^3 - c\left(J_3^T\right)^2, \tag{5.59}$$

where J_2^T and J_3^T are the generalized transversely isotropic invariants of the stress deviator [see Eqs. (5.10) and (5.11)]. For 3-D stress conditions, this criterion involves seven anisotropy coefficients. As an example, this criterion was applied to a laboratory-processed 2026-T3511 Al alloy. This material was extruded at elevated temperature up to a true strain of about 3.0, but did not recrystallize after annealing due to the presence of very fine Zr particles that pin the grain boundaries. As a result, the material exhibited a strong deformation texture consisting of a mixture of $\langle 111\rangle$ and $\langle 100\rangle$ fibers, i.e., grains with $\langle 111\rangle$ and $\langle 100\rangle$ crystal axes aligned with the extrusion axis, respectively. Duplicate uniaxial tension tests were conducted in different directions from the extrusion direction to the radial direction in 15° intervals to measure the yield stress anisotropy. The data indicated that the material is transversely isotropic with respect to the extrusion direction.

If σ_β is the tensile yield stress along an axis at angle β to the extrusion direction **z**, then according to the yield criterion given by Eq. (5.59) it follows that:

$$\left(\sigma_\beta/\sigma_0\right) = k\left\{\begin{array}{l}\left[\dfrac{h_2}{3}\cos^4\beta + (h_3 - h_2/3)\cos^2\beta\sin^2\beta + \dfrac{1}{6}(h_1 + h_2)\sin^4\beta\right]^3 \\ -c\left[\dfrac{2}{27}(4d_1 - 3d_2)\cos^6\beta + \dfrac{1}{27}(3d_2 - d_1)\sin^6\beta \right. \\ \left. + \dfrac{1}{9}\left[\begin{array}{l}(-4d_1 + 3d_2 + 3d_4)\cos^2\beta \\ + (2d_1 - 3d_2 + 3d_3)\sin^2\beta\end{array}\right]\sin^2\beta\cos^2\beta\right]^2\end{array}\right\}^{-1/6}$$

where $k = (1/3)\left[27h_2^3 - c(9d_4 + 3d_2 - 4d_1)^2\right]^{1/6}$.

Setting $c = 2.25$, the anisotropy coefficients h_i and d_j with $i = 1, \ldots, 3$ and $j = 1, \ldots, 4$ can be estimated using the available uniaxial tensile data in conjunction with the above equation. The numerical values of these coefficients are: $h_1 = 1.871$, $h_2 = 1.4$, $h_3 = 2.05$, whereas $d_1 = 0.3$, $d_2 = -0.424$, $d_3 = 5.92$, and $d_4 = -2.28$. The variation of the tensile yield stress with orientation as described by the proposed criterion in comparison with the data and polycrystal predictions using the Taylor-Bishop-Hill (TBH) model (see Chap. 3 for more details on this model) is shown in Fig. 5.10. Note the very good agreement between the predictions of the yield criterion given by Eq. (5.59) and data. The TBH model results lead to good trends compared to experiments, but they underestimate the amplitude of anisotropy.

5.3.2 *Cazacu [10] Orthotropic Yield Criterion*

To describe plastic anisotropy of rolled sheets, Cazacu [10] proposed the following yield criterion:

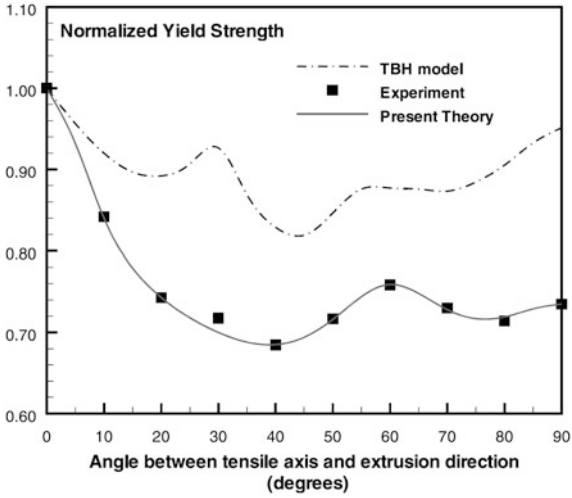

Fig. 5.10 Normalized uniaxial yield stress versus tensile direction according to the Cazacu and Barlat [12] yield criterion and TBH model (dashed line) for an extruded 2026-T3511 Al alloy (transverse isotropic material)

$$F\left(J_2^0, J_3^0\right) = \left(J_2^0\right)^4 - \alpha\left(J_2^0\right)\left(J_3^0\right)^2, \tag{5.60}$$

where J_2^0, J_3^0 are the orthotropic invariants of the stress deviator given by Eqs. (5.6) and (5.8), respectively. The effective stress, $\bar{\sigma}$, associated to this criterion is:

$$\bar{\sigma} = B\left[\left(J_2^0\right)^4 - \alpha\left(J_2^0\right)\left(J_3^0\right)^2\right]^{1/8}, \tag{5.61}$$

with B being a constant defined such that for uniaxial tension in one of the orthotropic axes [e.g., for a rolled plate or sheet, in the **x** axis or the rolling direction (RD)], the effective stress $\bar{\sigma}$ reduces to the yield stress. Therefore, B is defined as:

$$B = \frac{3\sqrt{2}}{\left\{\left[27(a_1 + a_3)^3 - 8\alpha\,(b_1 + b_2)^2\right](3a_1 + 3a_3)\right\}^{1/8}}. \tag{5.62}$$

Note that according to this criterion, the yielding response is the same if the anisotropy coefficients b_k ($k = 1, \ldots, 11$) involved in the expression of J_3^0 and the anisotropy coefficients a_i ($i = 1 \ldots 6$) involved in the expression of J_2^0 are replaced by βa_i, βb_k, with β being an arbitrary positive constant. Therefore, without loss of generality one of the parameters, for example b_6, can be set equal to unity, and for full 3-D stress conditions, the criterion involves 17 coefficients. Assuming associated flow rule, the plastic strain-rate tensor can be easily calculated as:

$$\mathbf{d}^p = \dot{\lambda}\frac{\partial \bar{\sigma}}{\partial \boldsymbol{\sigma}}, \tag{5.63}$$

where $\bar{\sigma}$ is given by Eq. (5.61). Therefore,

$$\frac{\partial \bar{\sigma}}{\partial \sigma_{ij}} = \left(\frac{B}{8}\right)\left\{\left[4\left(J_2^0\right)^3 - \alpha\left(J_3^0\right)^2\right]\frac{\partial J_2^0}{\partial \sigma_{ij}} - 2\alpha\left(J_3^0\right)\left(J_2^0\right)\frac{\partial J_3^0}{\partial \sigma_{ij}}\right\} \times \left[\left(J_2^0\right)^4 - \alpha\left(J_2^0\right)\left(J_3^0\right)^2\right]^{-7/8}, \tag{5.64}$$

with $i, j = 1, \ldots, 3$. Relative to the coordinate system $(\mathbf{x}, \mathbf{y}, \mathbf{z})$ associated with the orthotropic axes, the expressions of the partial derivatives of the orthotropic invariants J_2^0 and J_3^0 are given by Eqs. (5.49) and (5.50), respectively.

5.3.2.1 Anisotropy in Lankford Coefficients and Uniaxial Yield Stresses in the Plane (RD, TD)

In the plane $(\mathbf{x}, \mathbf{y})$ [i.e., the plane of the rolled plate or sheet (RD, TD)], the orthotropic yield criterion given by Eq. (5.60) predicts the following dependence of the normalized uniaxial yield stress $\sigma_\theta/\bar{\sigma}$ on the angle θ between the direction of loading and the $\boldsymbol{x}$ direction (or RD):

$$B(\sigma_\theta/\sigma_0) = \left\{\begin{array}{l}\left[(a_1/6 + a_3/6)\cos^4\theta + (a_4 - a_1/3)\cos^2\theta\sin^2\theta + (a_1/6 + a_2/6)\sin^4\theta\right]^4 \\ -\alpha\left[\begin{array}{l}\cos^6\theta(b_1 + b_2)/27 + \sin^6\theta(b_3 + b_4)/27 \\ -\sin^2\theta\cos^4\theta(b_1 + 3b_5 - 6b_{10})/9 \\ -\sin^4\theta\cos^2\theta(b_4 - 3b_5)/9\end{array}\right]^2 \times \left[\begin{array}{l}(a_1/6 + a_3/6)\cos^4\theta \\ +(a_4 - a_1/3)\cos^2\theta\sin^2\theta \\ +(a_1/6 + a_2/6)\sin^4\theta\end{array}\right]\end{array}\right\}^{-1/8} \tag{5.65}$$

with the constant B being given by Eq. (5.62). In particular,

$$\frac{\sigma_{30}}{\sigma_0} = \frac{4\sqrt{3}}{B}\left[\begin{array}{l}(4a_1 + a_2 + 9a_3 + 18\,a_4)^4/16 \\ -\alpha(27\,b_2 + b_3 - 8b_4 + 54(3b_{10} - b_5))^2(4a_1 + a_2 + 9a_3 + 18a_4)/54\end{array}\right]^{-1/8} \tag{5.66}$$

$$\frac{\sigma_{45}}{\sigma_0} = \frac{1}{B}\left[\left(\frac{a_2 + a_3 + 6a_4}{24}\right)^4 - \alpha\left(\frac{-2b_1 + b_2 + b_3 - 2b_4 + 18b_{10}}{216}\right)^2\left(\frac{a_2 + a_3 + 6a_4}{24}\right)\right]^{-1/8} \tag{5.67}$$

$$\frac{\sigma_{90}}{\sigma_0} = \frac{1}{B}\left[\left(\frac{a_1 + a_2}{6}\right)^4 - \alpha(a_1 + a_2)\left(\frac{b_3 + b_4}{27}\right)^2 \Big/ \; 6\right]^{-1/8} \tag{5.68}$$

Yielding under equibiaxial tension in the plane $(\mathbf{x},\mathbf{y})$ occurs when $\sigma_{xx}=\sigma_{yy}=\sigma_b^T$ with

$$\frac{\sigma_b^T}{\sigma_0}=\frac{1}{B}\left[\left(\frac{a_2+a_3}{6}\right)^4-\alpha\left(\frac{2b_1-b_2-b_3+2b_4}{27}\right)^2(a_2+a_3)\Big/6\right]^{-1/8} \tag{5.69}$$

Yielding under pure shear in the (RD, TD) plane is equal to:

$$\tau_{\mathrm{RD-TD}}=\frac{\sigma_0}{B\sqrt{a_4}}. \tag{5.70}$$

The Lankford coefficients r_θ are calculated based on Eq. (5.57), with the specific expressions for $\dfrac{\partial\bar{\sigma}}{\partial\sigma_{ij}}$ being given by Eq. (5.64).

In summary, for description of plastic properties in the plane $(\mathbf{x},\mathbf{y})$ or (RD–TD) the criterion involves ten anisotropy coefficients $a_1,a_2,a_3,a_4,b_1,b_2,b_3,b_4,b_5,b_{10}$ and the parameter α. Using Eqs. (5.65) and (5.69), these parameters can be determined by minimizing an error function of the form:

$$E(a_1,a_2,a_3,a_4,b_1,b_2,b_3,b_4,b_5,b_{10},\alpha)=$$
$$\sum_i^n \eta_i\left(1-\frac{(\sigma_\theta)_i^{\mathrm{th}}}{(\sigma_\theta)_i^{\mathrm{data}}}\right)^2+\sum_j^m \gamma_j\left(1-\frac{(r_\theta)_j^{\mathrm{th}}}{(r_\theta)_j^{\mathrm{data}}}\right)^2+\delta\left(1-\frac{\left(\sigma_b^T\right)_i^{\mathrm{th}}}{\left(\sigma_b^T\right)_i^{\mathrm{data}}}\right)^2 \tag{5.71}$$

In the above equation, "n" and "m" represent the number of experimental yield stresses and r-values, respectively, corresponding to different orientations θ that are available, the superscript indicates whether the respective value is experimental or it is calculated using the expressions (5.65), (5.69), (5.57), while η_i, γ_j, and δ are weight factors. As an example, in Fig. 5.11a, b are shown the predicted variation of the yield stresses and r-values in the plane of the plate or sheet [i.e., $(\mathbf{x},\mathbf{y})$ or (RD, TD)] according to the Cazacu [10] and Hill [22] criterion, respectively, in comparison with the measured yield stresses for an AA 6022-T4 sheet (data after [5]). The stresses are normalized by the uniaxial tensile yield stress in the rolling direction. The numerical values of the coefficients involved in the criterion that were determined from the experimental yield stresses and r-values for $\theta=0°$, 30°, 45°, 60°, 90°, and the tensile equibiaxial yield stress σ_b^T are: $a_1=0.709$, $a_2=1.36$; $a_3=1.18$, $a_4=0.96$, $b_1=0.2$, $b_2=-1.334$, $b_3=-1.53$,$b_4=0.94$, $b_5=1.18$, $b_{10}=0.988$, and $\alpha=1.5$. The numerical values of Hill [22] coefficients for this material calculated based on the experimental r-values at $\theta=0°$, 45°, 90° are: $F=0.706$, $G=0.587$, $H=0.413$, and $N=1.27$.

Note that only the Cazacu [10] criterion describes with accuracy both the anisotropy in yielding and r-values for this Al sheet. The projection in the $(\sigma_{xx},\sigma_{yy})$ plane of the yield surface corresponding to $\sigma_{xy}=0$, according to Cazacu [10] criterion and Hill [22] criterion, respectively, is shown in Fig. 5.12. Note that in contrast to

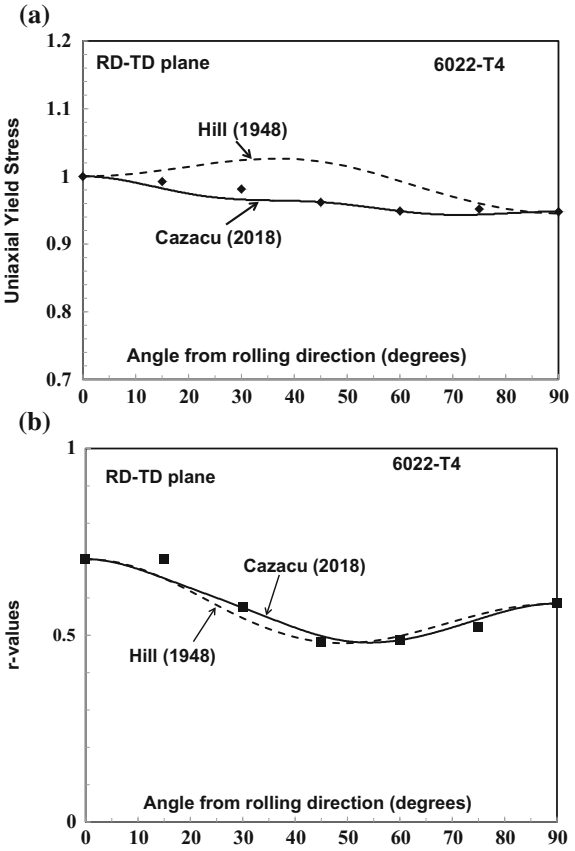

Fig. 5.11 Predicted anisotropy according to Cazacu [10] orthotropic criterion (interrupted line) and Hill [22] criterion for an AA 6022-T4 sheet. **a** Uniaxial yield stress variation. **b** Lankford coefficients. Data (symbols) from [5]. Stresses are normalized by the uniaxial yield stress in tension in the rolling direction

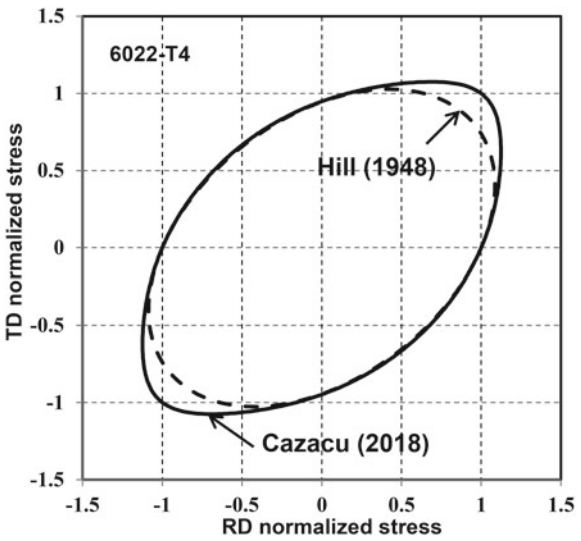

Fig. 5.12 Projection of the yield surface in the plane $(\sigma_{xx}, \sigma_{yy})$ (with $\sigma_{xy} = 0$) for AA 6022-T4 sheet as predicted by the orthotropic Cazacu [10] yield criterion and Hill [22] criterion

the Hill [22] criterion, the Cazacu [10] criterion captures with accuracy both the anisotropy in yield stresses and *r*-values. Moreover, Hill [22] criterion underpredicts the experimental equibiaxial yield stress.

5.3.2.2 Anisotropy in Yield Stresses in the Other Symmetry Planes

It is also of interest to understand the effects of anisotropy in plastic properties for out-of-plane loadings. Moreover, examination of the predicted anisotropy in yield stresses in the $(\mathbf{x}, \mathbf{z})$ and $(\mathbf{y}, \mathbf{z})$ symmetry planes provides insights on the shape of the yield locus and the relationships between the yield stresses in uniaxial tension and pure shear imposed by a given 3-D yield criterion. Using Eq. (5.61), it follows that in the $(\mathbf{x}, \mathbf{z})$ plane the dependence of the normalized uniaxial yield stress σ_φ/σ_0 on the loading angle φ to the $\boldsymbol{x}$ direction [or rolling direction (RD)] is:

$$B\frac{\sigma_\varphi}{\sigma_0} = \left\{ \begin{array}{l} \left[\left(\frac{a_1}{6}+\frac{a_3}{6}\right)\cos^4\varphi + \left(a_5-\frac{a_3}{3}\right)\cos^2\varphi\,\sin^2\varphi + \left(\frac{a_2}{6}+\frac{a_3}{6}\right)\sin^4\varphi\right]^4 \\ -\alpha\left[\begin{array}{l} \frac{1}{27}(b_1+b_2)\cos^6\varphi + \frac{1}{27}(2b_1-b_2-b_3+2b_4)\sin^6\varphi \\ -\frac{1}{9}\left[\begin{array}{c}(b_2+3b_8-6b_9)\cos^2\varphi \\ +(b_1-b_2+b_4-3b_8)\sin^2\varphi\end{array}\right]\sin^2\varphi\cos^2\varphi \end{array}\right]^2 \\ \times\left[\left(\frac{a_1}{6}+\frac{a_3}{6}\right)\cos^4\varphi + \left(a_5-\frac{a_3}{3}\right)\cos^2\varphi\,\sin^2\varphi + \left(\frac{a_2}{6}+\frac{a_3}{6}\right)\sin^4\varphi\right] \end{array} \right\}^{-1/8} \tag{5.72}$$

where the constant B is given by Eq. (5.62), and σ_0 is the uniaxial tensile yield stress in the $\boldsymbol{x}$ direction ($\varphi = 0$). In particular, the yield stress in uniaxial tension along a direction at 45° to RD in the (RD–ND) plane is:

$$\frac{\sigma_{45}^{\mathrm{RD-ND}}}{\sigma_0} = \frac{1}{B}\left[\left(\frac{a_1+a_2+6a_5}{24}\right)^4 - \alpha\left(\frac{18b_9-b_3-b_4}{216}\right)^2\left(\frac{a_1+a_2+6a_5}{24}\right)\right]^{-1/8} \tag{5.73}$$

The yield stress under pure shear in the (RD, ND) plane is:

$$\tau_{\mathrm{RD-ND}} = \frac{\sigma_0}{B\sqrt{a_5}}. \tag{5.74}$$

The above relations provide the procedure to be used for identification of the coefficient b_9. Indeed, once the coefficients a_1, a_2, b_3, b_4 are determined based on the yield stresses in the (RD–TD) plane [see Eqs. (5.66)–(5.69)] and a_5 is obtained using the yield stress in pure shear [in conjunction with Eq. (5.74)], the coefficient b_9 can be obtained using relation (5.73). For example, for the same AA 6022-T4 material if we assume $\tau_{\mathrm{RD-ND}}/\sigma_0 = 0.55$ and $\sigma_{45}^{\mathrm{RD-ND}}/\sigma_0 = 0.96$, we obtain $b_9 = 0.597$. It is also worth noting that if $\alpha = 0$ (which is the value of the parameter

α for which the proposed criterion reduces to [22]), the yield stress in pure shear parallel to the plane (RD, ND), τ_{RD-ND}, is completely determined by the uniaxial yield stresses σ_0 and σ_{90} along RD and TD, respectively, and the yield stress in a direction 45° to RD in the (RD, ND) plane, i.e.,

$$\tau_{RD-ND}^2 = \left[\frac{4}{\left(\sigma_{45}^{RD-ND}\right)^2} - \frac{1}{\sigma_{90}^2}\right]^{-1}, \tag{5.75}$$

or alternatively, the predicted yield stress in a direction at 45° to RD in the (RD, ND) plane is completely determined by τ_{RD-ND} and σ_{90}.

For the same AA 6022-T4 material assuming $\tau_{RD-ND}/\sigma_0 = 0.55$, it follows that the Hill [22] anisotropy coefficient $M = 1.67$. As an example, in Fig. 5.13a is shown the predicted variation of the yield stresses in the (RD, ND) plane according to the Cazacu [10] orthotropic criterion (Eq. 5.72) and Hill [22]. Figure 5.13b shows the projection of the respective yield surfaces in the $(\sigma_{xx}, \sigma_{zz})$ plane (with $\sigma_{xz} = 0$). Stresses are normalized by the tensile uniaxial yield stress along RD. Note that Hill [22] criterion underpredicts the uniaxial tensile yield stress along ND. This is consistent with the results presented in Fig. 5.12, i.e., with the fact that Hill [22] criterion underpredicts the experimental equibiaxial yield stress in the (RD–TD) plane. Indeed, given that the [22] criterion predicts the same yielding response in tension–compression and it is pressure-insensitive, the tensile yield stress along ND should be equal to the equibiaxial yield stress in the (RD, TD) plane. In general, if data for identification of the coefficients of anisotropy b_8 and b_9 are not available, the recommendation is either to set the value of these parameters to unity (i.e., isotropic values) or to set the $b_8 = b_9 = b_{10}$.

Using Eq. (5.61), it follows that in the $(\mathbf{y}, \mathbf{z})$ plane, the proposed yield criterion predicts the following variation of the normalized yield stress σ_β/σ_0 with the loading angle β to the transverse direction, TD (or $\mathbf{y}$):

$$B\left(\frac{\sigma_\beta}{\sigma_0}\right) = \left\{\begin{array}{l}\left[\frac{1}{6}(a_1+a_2)\cos^4\beta + (a_6 - a_2/3)\cos^2\beta\,\sin^2\beta + \frac{1}{6}(a_3+a_2)\sin^4\beta\right]^4 \\ -\frac{\alpha}{27^2}\left[\begin{array}{l}\cos^6\beta(b_3+b_4) + \sin^6\beta(2b_1 - b_2 - b_3 + 2b_4) \\ -3\sin^2\beta\cos^4\beta(b_3 - 3b_6) - 3\sin^4\beta\,\cos^2\beta(b_1 - b_3 - b_4 - 3b_7)\end{array}\right]^2 \\ \times\left[\frac{1}{6}(a_1+a_2)\cos^4\beta + (a_6 - a_2/3)\cos^2\beta\,\sin^2\beta + \frac{1}{6}(a_3+a_2)\sin^4\beta\right]\end{array}\right\}^{-1/8} \tag{5.76}$$

It follows that according to the proposed yield criterion, the normalized uniaxial yield stress in uniaxial tension along ND is:

$$\frac{\sigma_{ND}}{\sigma_0} = \frac{1}{B}\left[\left(\frac{a_2+a_3}{6}\right)^4 - \alpha\left(\frac{2b_1 - b_2 - b_3 + 2b_4}{27}\right)^2\left(\frac{a_2+a_3}{6}\right)\right]^{-1/8} \tag{5.77}$$

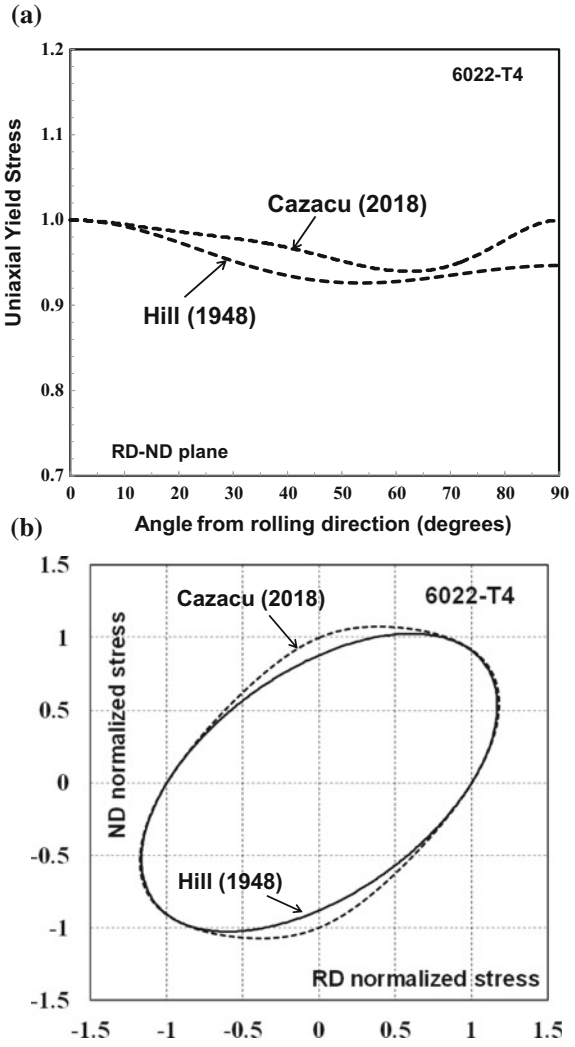

Fig. 5.13 **a** Predicted variation of the yield stresses for AA 6022-T4 in the (RD, ND) plane according to the orthotropic Cazacu [10] yield criterion and Hill [22] criterion. **b** Projection of the yield surface in the plane $(\sigma_{xx}, \sigma_{zz})$ (with $\sigma_{xz} = 0$) as predicted by these criteria. Stresses are normalized by the uniaxial tensile yield stress along RD

Let $\tilde{b}_7 = (b_6 + b_7)/2$. Therefore, the yield stress in uniaxial tension along a direction at 45° to TD in the (TD–ND) plane is:

$$\frac{\sigma_{45}^{\mathrm{TD-ND}}}{\sigma_0} = \frac{1}{B}\left[\left(\frac{a_1 + a_3 + 6a_6}{24}\right)^4 - \alpha\left(\frac{18\tilde{b}_7 - b_1 - b_2}{216}\right)^2\left(\frac{a_1 + a_3 + 6a_6}{24}\right)\right]^{-1/8} \tag{5.78}$$

According to the criterion [see Eq. (5.61)], the yield stress under pure shear in the (TD, ND) plane is:

$$\tau_{\mathrm{TD-ND}} = \frac{\sigma_0}{B\sqrt{a_6}}. \tag{5.79}$$

Note that the above relations provide the procedure to be used for identification of the coefficient $\tilde{b}_7$. Indeed, once the coefficients a_1, a_3, b_1, b_2 are determined based on the yield stresses in the (RD–TD) plane [see Eq. (5.66)–(5.69)] and a_6 is obtained using the yield stress in pure shear [in conjunction with Eq. (5.79)], the coefficient $\tilde{b}_7$ can be calculated using the relation (5.78). For example, for the same AA 6022-T4 material if we assume $\tau_{\mathrm{TD-ND}}/\sigma_0 = 0.54$ and $\sigma_{45}^{\mathrm{TD-ND}}/\sigma_0 = 0.95$, we obtain $\tilde{b}_7 = 0.179$. It is also worth noting that only if $\alpha = 0$ (i.e., the value of the parameter α for which the criterion reduces to Hill [22] criterion), the yield stress in pure shear in the plane (TD, ND), $\tau_{\mathrm{TD-ND}}$, is completely determined by the uniaxial yield stresses along RD, TD, and the yield stress in a direction at 45º to TD in the (TD, ND) plane,

$$\tau_{\mathrm{TD-ND}}^2 = \left[\frac{4}{\left(\sigma_{45}^{\mathrm{TD-ND}}\right)^2} - \frac{1}{\sigma_0^2}\right]^{-1}, \tag{5.80}$$

or alternatively, the predicted yield stress in a direction at 45° to TD in the (TD, ND) plane is completely determined by $\tau_{\mathrm{TD-ND}}$ and σ_0.

For the same AA 6022-T4 material assuming $\tau_{\mathrm{RD-ND}}/\sigma_0 = 0.54$, it follows that the Hill [22] anisotropy coefficient $L = 1.713$. As an example, in Fig. 5.14a is shown the predicted variation of the yield stresses in the (TD, ND) plane according to the Cazacu [10] criterion and Hill [22], respectively. Figure 5.14b shows the projection of the yield surfaces in the $(\sigma_{yy}, \sigma_{zz})$ plane (with $\sigma_{yz} = 0$) according to these criteria, respectively. Stresses are normalized by, σ_0, the tensile uniaxial yield stress along RD. The results presented are consistent with the results presented in Figs. 5.12 and 5.13.

It is also worth noting that for a yield criterion constructed such as to have the same mechanical response in tension–compression, the yield stresses under equibiaxial tension in the (RD, TD), (RD, ND), and (TD, ND) planes are completely determined by the uniaxial yield stress values along the orthotropic axes. Therefore, if $\sigma_b^{\mathrm{RD-TD}}$, $\sigma_b^{\mathrm{RD-ND}}$, and $\sigma_b^{\mathrm{TD-ND}}$ denote the yield stresses under equibiaxial tension in the planes, (RD–TD), (RD–ND), and (TD–ND), respectively, then according to Cazacu [10] criterion:

$$\frac{\sigma_b^{\mathrm{RD-TD}}}{\sigma_0} = \frac{1}{B}\left[\left(\frac{a_2+a_3}{6}\right)^4 - \alpha\left(\frac{2b_1-b_2-b_3+2b_4}{27}\right)^2\left(\frac{a_2+a_3}{6}\right)\right]^{-1/8} \tag{5.81}$$

$$\frac{\sigma_b^{\mathrm{RD-ND}}}{\sigma_0} = \frac{1}{B}\left[\left(\frac{a_1+a_2}{6}\right)^4 - \alpha\left(\frac{b_3+b_4}{27}\right)^2\left(\frac{a_1+a_2}{6}\right)\right]^{-1/8} \tag{5.82}$$

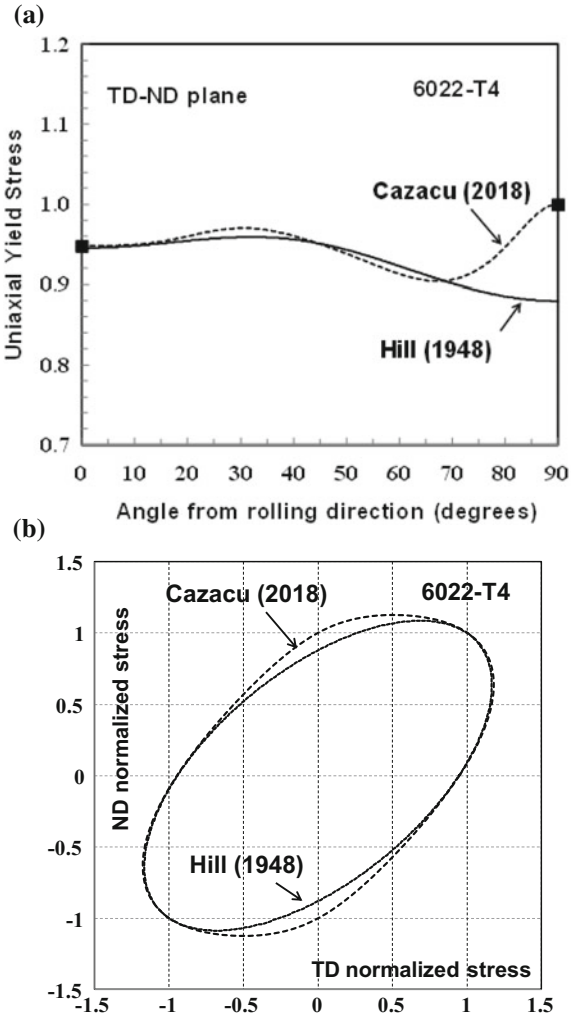

Fig. 5.14 **a** Predicted variation of the yield stresses for AA 6022-T4 in the (TD, ND) plane according to the orthotropic Cazacu [10] yield criterion and Hilll [22]. **b** Projection of the yield surface in the plane $(\sigma_{yy}, \sigma_{zz})$ (with $\sigma_{yz} = 0$) as predicted by these criteria. Stresses are normalized by the tensile uniaxial yield stress along RD

$$\frac{\sigma_b^{\mathrm{TD-ND}}}{\sigma_0} = 1 \tag{5.83}$$

Standard uniaxial tension and biaxial tensile tests carried out on cruciform specimens for a nominal 1.2 mm thick AA 3103-O sheet were presented in [6]. The parameters of the Cazacu [10] orthotropic yield function [see Eq. (5.61)] determined from the experimental yield stresses and r-values for $\theta = 0°$, $30°$, $45°$, $75°$, $90°$ and the tensile equibiaxial yield stress σ_b^T using the cost function given by Eq. (5.71) are: $a_1 = 1.133$, $a_2 = 1.5$; $a_3 = 2.1$, $a_4 = 1.3$, $b_1 = 0.107$, $b_2 = 3.52$, $b_3 = -0.4$, $b_4 = -2.32$, $b_5 = -1.96$, $b_{10} = -1.18$, and $\alpha = 1.2$.

The projection in the $(\sigma_{xx}, \sigma_{yy})$ plane of the yield surface according to Cazacu [10] criterion in comparison with data is shown in Fig. 5.15a for $\sigma_{xy} = 0$. Also, in Fig. 5.15b are presented the isocontours of the yield surface corresponding to σ_{xy}/σ_0 = 0, 0.3, 0.5, and 0.6. Comparisons between the theoretical predictions of the *r*-values and uniaxial yield stress anisotropy in the plane of the sheet and the mechanical data are shown in Fig. 5.16a, b. A good agreement between the experimental and simulation results is observed.

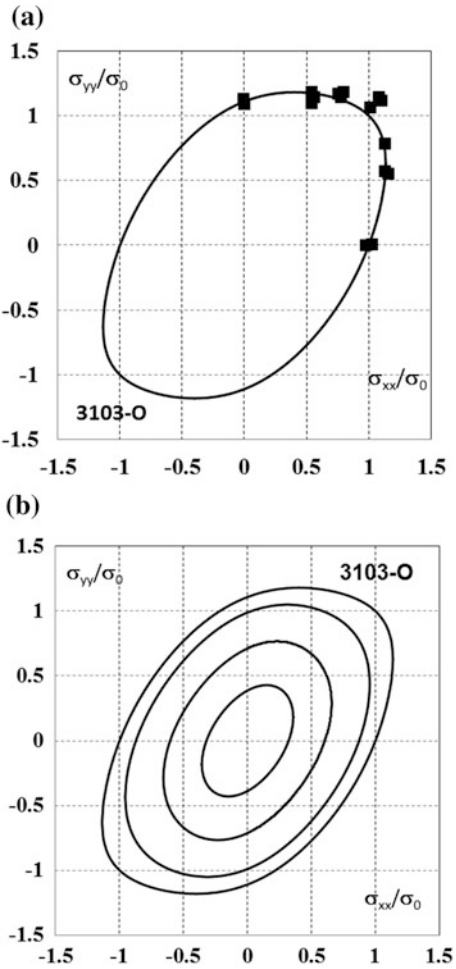

Fig. 5.15 **a** Yield surface in the $(\sigma_{xx}, \sigma_{yy})$ plane (with $\sigma_{xy} = 0$) of AA 3103-O as predicted by the Cazacu [10] yield criterion in comparison with data (symbols). **b** Predicted isocontours of the yield surface corresponding to $\sigma_{xy}/\sigma_0 = 0$, 0.3, 0.5, and 0.6. Stresses are normalized by the tensile uniaxial yield stress along RD

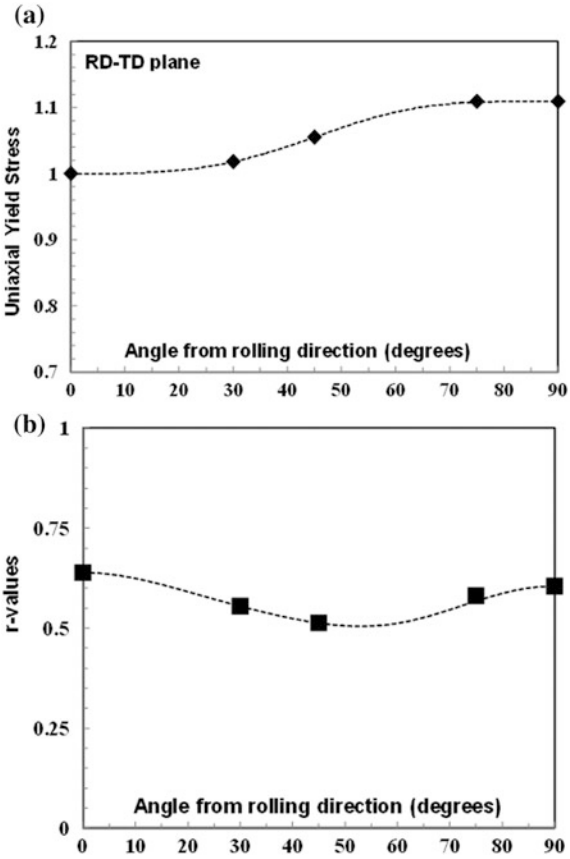

Fig. 5.16 Predicted anisotropy according to Cazacu [10] orthotropic criterion of AA 3103-O. **a** Uniaxial yield stresses. **b** Lankford coefficients. Data (symbols) from [6]. Stresses are normalized by the uniaxial yield stress in tension in the rolling direction

5.3.3 *Explicit Expression of the Barlat et al. [4] Orthotropic Yield Criterion in Terms of Stresses*

The 3-D extension to orthotropy of Hershey [21]-Hosford [25] isotropic criterion

$$\phi_1(s_1, s_2, s_3) = |s_1 - s_2|^m + |s_2 - s_3|^m + |s_3 - s_1|^m = 2\sigma_T^m, \tag{5.84}$$

where m is an even integer (see also Chap. 4; Sect. 2.3) was developed for the first time by Barlat et al. [4]. The Barlat et al. [4] orthotropic yield function, denoted Yld91, can be expressed as:

$$\phi = \phi(\tilde{\mathbf{S}}) = \left|\tilde{S}_1 - \tilde{S}_2\right|^m + \left|\tilde{S}_2 - \tilde{S}_3\right|^m + \left|\tilde{S}_3 - \tilde{S}_1\right|^m = 2\bar{\sigma}^m, \tag{5.85}$$

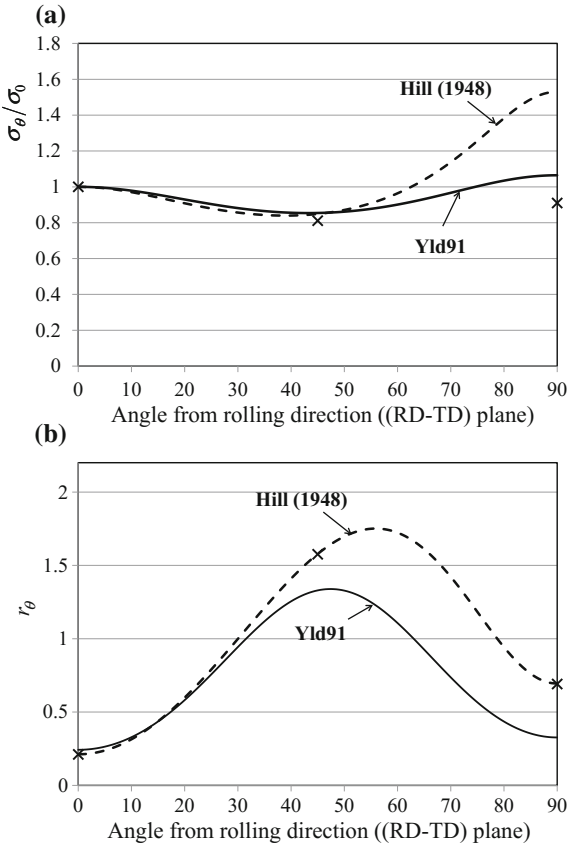

Fig. 5.17 Predicted anisotropy according to the Yld91 [4] and Hill [22] yield criteria for an AA2090-T3 sheet. **a** Uniaxial yield stresses. **b** Lankford coefficients. Stresses are normalized by the uniaxial yield stress in tension along the rolling direction

where $\tilde{S}_k$ are the principal values of the transformed stress tensor $\tilde{\mathbf{S}} = \mathbf{C}\mathbf{s}$ [see also Eq. (5.1)] with the fourth-order order tensor $\mathbf{C}$ being orthotropic, symmetric, and deviatoric.

If $(\mathbf{x}, \mathbf{y}, \mathbf{z})$ denote the coordinate system associated with the orthotropic axes, and if in Voigt notations the stress tensor is represented by the 6-dimensional vector $\boldsymbol{\sigma} = \left(\sigma_{xx}, \sigma_{yy}, \sigma_{zz}, \sigma_{yz}, \sigma_{xz}, \sigma_{xy}\right)$, the fourth-order orthotropic tensor $\mathbf{C}$ is represented by the 6×6 matrix:

$$\mathbf{C} = \frac{1}{3}\begin{bmatrix} b+\bar{c} & -\bar{c} & -b & 0 & 0 & 0 \\ -\bar{c} & \bar{c}+a & -a & 0 & 0 & 0 \\ -b & -a & a+b & 0 & 0 & 0 \\ 0 & 0 & 0 & 3f & 0 & 0 \\ 0 & 0 & 0 & 0 & 3g & 0 \\ 0 & 0 & 0 & 0 & 0 & 3h \end{bmatrix}, \tag{5.86}$$

where a, b, $\bar{c}$, f, g, h are independent parameters (see also [8]). When all these coefficients are equal to unity, $\tilde{\mathbf{S}}$ reduces to the stress deviator $\mathbf{s}$, and $\phi = \phi_1$, i.e., the isotropic Hershey [21]-Hosford [25] criterion is recovered. To apply this yield criterion for general 3-D loadings, the principal values of the transformed tensors $\tilde{\mathbf{S}} = \mathbf{Cs}$ need to be calculated, i.e., one needs to solve a third-order algebraic characteristic equation. It is important to note that if the fourth-order orthotropic tensor $\mathbf{C}$ is given by Eq. (5.86), $\tilde{\mathbf{S}}$ is deviatoric, i.e., $\tilde{S}_1 + \tilde{S}_2 + \tilde{S}_3 = 0$, and the principal values of $\tilde{\mathbf{S}}$ can be expressed as:

$$\tilde{S}_k = 2\cos(\theta_k)\sqrt{\frac{\tilde{J}_2}{3}}, \quad \mathrm{k} = 1, \ldots, 3, \tag{5.87}$$

with $\tilde{J}_2 = tr\left(\tilde{\mathbf{S}}^2\right)/2$ and $\tilde{J}_3 = tr\left(\tilde{\mathbf{S}}^3\right)/3$ being the second-invariant and third-invariant of $\tilde{\mathbf{S}}$, and θ_1 the solution in the interval $0 \leq \theta \leq \pi/3$ of the equation:

$$\cos 3\theta = \frac{\tilde{J}_3}{2}\left(\frac{3}{\tilde{J}_2}\right)^{3/2}, \tag{5.88}$$

$$\theta_2 = \theta_1 + \frac{2\pi}{3} \text{ and } \theta_3 = \theta_1 - \frac{2\pi}{3} \quad \text{for } \tilde{S}_1 \geq \tilde{S}_2 \geq \tilde{S}_3.$$

In the expression of Yld91, the recommended value for the exponent is $m = 6$ for textured bcc materials, and $m = 8$ for textured fcc materials (see [4]). Since no explicit expressions of Yld91 criterion in terms of the components of the stress deviator are available, identification of the anisotropy parameters a, b, $\bar{c}$, f, g, h and its F.E. implementation is rather complex. This contributes to the limited use of Yld91 as compared to Hill [22] criterion and Yld89, the 2-D orthotropic extensions of the same isotropic criterion (see [3, 6]) for which analytical expressions for the principal values of $\tilde{\mathbf{S}}$ in terms of stresses exist.

It can be shown that the Yld91 yield criterion for bcc and fcc materials, denoted hereafter $\mathrm{Yld91_{FCC}}$ and $\mathrm{Yld91_{BCC}}$, are expressible in terms of $\tilde{J}_2 = tr\left(\tilde{\mathbf{S}}^2\right)/2$ and $\tilde{J}_3 = tr\left(\tilde{\mathbf{S}}^3\right)/3$, the second and third-invariant of the transformed tensor $\tilde{\mathbf{S}}$, as:

$$\mathrm{Yld91_{FCC}} = \left(\tilde{S}_1 - \tilde{S}_2\right)^8 + \left(\tilde{S}_2 - \tilde{S}_3\right)^8 + \left(\tilde{S}_1 - \tilde{S}_3\right)^8 = 258\tilde{J}_2^4 - 648\tilde{J}_2\tilde{J}_3^2 \tag{5.89}$$

with the associated equivalent stress being: $\bar{\sigma} = 1.836\left(\tilde{J}_2^4 - 2.511\,\tilde{J}_2\tilde{J}_3^2\right)^{1/8}$ while,

$$\mathrm{Yld91_{BCC}} = \left(\tilde{S}_1 - \tilde{S}_2\right)^6 + \left(\tilde{S}_2 - \tilde{S}_3\right)^6 + \left(\tilde{S}_1 - \tilde{S}_3\right)^6 = 66\tilde{J}_2^3 - 81\tilde{J}_3^2, \tag{5.90}$$

with the associated equivalent stress being: $\bar{\sigma} = 1.746\left(\tilde{J}_2^3 - 1.227\tilde{J}_3^2\right)^{1/6}$.

Obviously, the quadratic form ($m = 2$) of Yld91 depends only on $\tilde{J}_2$ and it expressed as:

$$\text{Yld91}_{m=2} = \left(\tilde{S}_1 - \tilde{S}_2\right)^2 + \left(\tilde{S}_2 - \tilde{S}_3\right)^2 + \left(\tilde{S}_1 - \tilde{S}_3\right)^2 = 2\tilde{J}_2^2 \tag{5.91}$$

Note that the invariants $\tilde{J}_2$ and $\tilde{J}_3$ of the transformed tensor $\tilde{\mathbf{S}}$ can be easily expressed in terms of the components of the stress deviator $\mathbf{s}$ using the definition of $\tilde{\mathbf{S}}$ in conjunction with Eq. (5.86). Thus,

$$\begin{aligned}\tilde{J}_2 = {} & f^2 s_{yz}^2 + g^2 s_{xz}^2 + h^2 s_{xy}^2 + \left[(b+\bar{c})s_{xx} - \bar{c}s_{yy} - bs_{zz}\right]^2/18 \\ & + \left[-\bar{c}s_{xx} + (\bar{c}+a)s_{yy} - as_{zz}\right]^2/18 + \left[-bs_{xx} - as_{yy} + (a+b)s_{zz}\right]^2/18\end{aligned} \tag{5.92}$$

$$\begin{aligned}\tilde{J}_3 = {} & 2(fgh)s_{xy}s_{xz}s_{yz} + \frac{1}{27}\left[\left[(b+\bar{c})s_{xx} - \bar{c}s_{yy} - bs_{zz}\right] \cdot \left[-\bar{c}s_{xx} + (\bar{c}+a)s_{yy} - as_{zz}\right]\right. \\ & \left. \cdot\left[-bs_{xx} - as_{yy} + (a+b)s_{zz}\right]\right] \\ & - \frac{f^2 s_{yz}^2}{3}\left[(b+\bar{c})s_{xx} - \bar{c}s_{yy} - bs_{zz}\right] - \frac{g^2 s_{xz}^2}{3}\left[-\bar{c}s_{xx} + (\bar{c}+a)s_{yy} - as_{zz}\right] \\ & - \frac{h^2 s_{xy}^2}{3}\left[-bs_{xx} - as_{yy} + (a+b)s_{zz}\right]\end{aligned} \tag{5.93}$$

Most importantly, the closed-form expressions of $\text{Yld91}_{\text{FCC}}$ and of $\text{Yld91}_{\text{BCC}}$ in terms of the invariants $\tilde{J}_2$ and $\tilde{J}_3$ allow us to recognize that Yld91 yield criterion is a particular case of other orthotropic yield criteria.

Proposition 5.6 *The Yld91 yield criterion for bcc materials [$m = 6$ in* Eq. (5.85)*]* is a *particular case of the orthotropic yield criterion of Cazacu and Barlat* [11] *corresponding to $c = 81/66$; the Yld91 yield criterion for fcc materials [$m = 8$ in* Eq. (5.85)*] is a particular case of the orthotropic yield criterion of* Cazacu [10] *corresponding to $\alpha = 648/258$, and involving only six independent anisotropy coefficients a, b, $\bar{c}$, f, g, h.*

Proof Indeed, comparing the expression of $\tilde{J}_2$ [see Eq. (5.92)] with Eq. (5.6) for the orthotropic second-invariant J_2^0, it is evident that $\tilde{J}_2$ is a particular case of J_2^0 which involves only 6 anisotropy coefficients, the expressions of the coefficient a_i, $i = 1, \ldots, 6$ in terms of a, b, $\bar{c}$, f, g, h being:

$$\begin{aligned}& a_1 = \frac{\bar{c}(2\bar{c}+a+b) - ab}{3};\quad a_2 = \frac{a(2a+b+\bar{c}) - b\bar{c}}{3};\quad a_3 = \frac{b(2b+a+\bar{c}) - a\bar{c}}{3}; \\ & a_4 = h^2;\quad a_5 = g^2;\quad a_6 = f^2\end{aligned} \tag{5.94}$$

As demonstrated in Cazacu and Barlat [11], $\tilde{J}_3$ is a particular form of J_3^0 [see also Eq. (5.8) and Eq. (5.93)] which involves only six independent coefficients. The expressions of the parameters b_k, $k = 1, \ldots, 11$ in terms of a, b, $\bar{c}$, f, g, h are:

$$\begin{aligned} &b_1 = a\left(b^2 - \bar{c}^2\right)/3 + b\bar{c}(2\bar{c} + b)/3; b_2 = b\bar{c}(b + \bar{c}) - b_1; \\ &b_3 = b\left(\bar{c}^2 - a^2\right)/3 + a\bar{c}(2a + \bar{c})/3; b_4 = a\bar{c}(a + \bar{c}) - b_3; \\ &b_5 = ah^2;\ b_6 = \bar{c}f^2;\ b_7 = bf^2;\ b_8 = ag^2;\ b_9 = g^2(a + b)/2; \\ &b_{10} = h^2(a + b)/2;\ b_{11} = fgh \end{aligned} \tag{5.95}$$

Comparison between the expression of $\text{Yld91}_{\text{BCC}}$ in terms $\tilde{J}_2$ and $\tilde{J}_3$ [see Eq. (5.90)] and the expression of Cazacu and Barlat [11] criterion [see Eq. (5.44)] shows that $\text{Yld91}_{\text{BCC}}$ is a particular form of the latter corresponding to $c = 81/66$, and with parameters a_i, $i = 1, \ldots, 6$ and b_k, $k = 1, \ldots, 11$ expressible in terms of the six independent coefficients a, b, $\bar{c}$, f, g, h [see Eqs. (5.94) and (5.95)].

Similarly, comparison between the expression of $\text{Yld91}_{\text{FCC}}$ in terms $\tilde{J}_2$ and $\tilde{J}_3$ [see Eq. (5.89)] and the expression of the Cazacu [10] criterion [see Eq. (5.60)] shows that $\text{Yld91}_{\text{FCC}}$ is a particular form of the latter corresponding to $\alpha = 648/258$, and involves only six independent anisotropy coefficients a, b, $\bar{c}$, f, g, h.

For $m = 2$, Yld91 reduces to the Hill [22] orthotropic criterion [see also Eq. (5.91)], and the relations between the coefficients F, G, H, L, M and N of Hill [22] and the anisotropy coefficients a, b, $\bar{c}$,f, g, h can be easily deduced either by direct comparison between Eqs. (5.12) and (5.92), or by making use of Proposition 5.4 and Eq. (5.94):

$$\begin{aligned} &F = \frac{a(2a + b + \bar{c}) - b\bar{c}}{18}; G = \frac{b(2b + a + \bar{c}) - a\bar{c}}{18}; H = \frac{\bar{c}(2\bar{c} + a + b) - ab}{18}; \\ &L = f^2/2; M = g^2/2; N = h^2/2 \end{aligned}$$

As an example, in Fig. 5.18a, b are shown the predicted variation of the yield stresses and r-values in the (RD, TD) plane according to Yld91 criterion and Hill [22] (identified on the basis of experimental r-values, $F = 0.252$, $G = 0.825$, $H = 0.175$, $N = 2.238$) in comparison with the experimental measurements for the same AA2090-T3 sheet (data given in Table 5.1). The value of the exponent m was set equal to eight. The numerical values of the anisotropy coefficients a, b, $\bar{c}$, f, g, h involved in the Yld91 criterion were determined from the experimental yield stresses and r-values for $\theta = 0°$, $30°$, $45°$, $60°$, $90°$, and the tensile equibiaxial yield stress σ_b^T by minimizing a cost function of the form given by Eq. (5.71). These values are: $a = 1.11$, $b = 1.224$, $\bar{c} = 0.835$, $f = g = h = 1.238$.

Note that Yld91 predictions are in better agreement with data than Hill [22]. Although the yielding anisotropy is modeled with the same number of independent coefficients as in Hill [22], the improved predictive capabilities of Yld91 are due to the presence of $\tilde{J}_3$ in its expression and the imposed relative weight between $\tilde{J}_2$ and $\tilde{J}_3$ in the formulation [see Eq. (5.89)]. Furthermore, this imposed relative weight ensures the convexity of the yield locus. The respective projection of the yield surfaces in the (RD, TD) plane is depicted in Fig. 5.17.

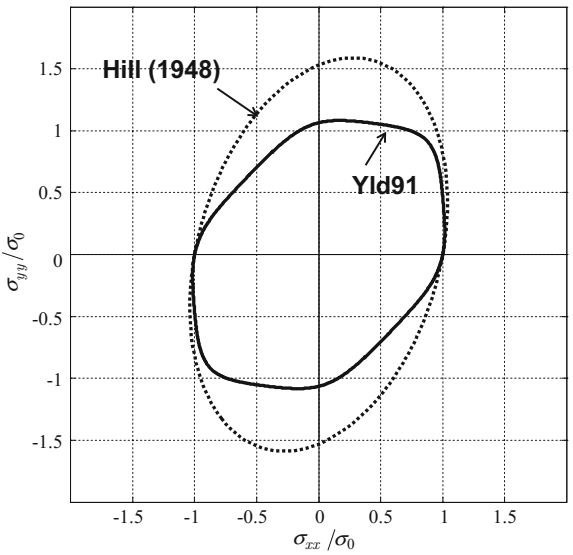

Fig. 5.18 Yield surface in the plane $(\sigma_{xx}, \sigma_{yy})$ of Al AA2090-T3 as predicted by the Yld91 and Hill [22] yield criterion

5.3.4 *Explicit Expression of the Karafillis and Boyce [28] Orthotropic Yield Criterion in Terms of Stresses*

Using the linear transformation approach, Karafillis and Boyce [28] developed an extension to orthotropy of the following generic isotropic yield function:

$$F_{\mathrm{KB}}(s_1, s_2, s_3) = (1-\chi)\phi_1(s_1, s_2, s_3) + (\chi)\frac{3^m}{2^{m-1}+1}\phi_2(s_1, s_2, s_3), \tag{5.96}$$

where m is an even integer and $0 \leq \chi \leq 1$, $\phi_1(s_1, s_2, s_3)$ is the Hershey [21]-Hosford [25] yield function [see also Eq. (5.84)] and

$$\phi_2(s_1, s_2, s_3) = |s_1|^m + |s_2|^m + |s_3|^m. \tag{5.97}$$

Thus, the orthotropic form of the Karafillis and Boyce [28] yield function is:

$$F^0_{\mathrm{KB}}(\tilde{\mathbf{S}}) = (1-\chi)\phi_1(\tilde{S}_1, \tilde{S}_2, \tilde{S}_3) + (\chi)\frac{3^m}{2^{m-1}+1}\phi_2(\tilde{S}_1, \tilde{S}_2, \tilde{S}_3) = 2\bar{\sigma}^m.$$

Note that this yield function contains an additional coefficient, χ, compared to Yld91 [see Eq. (5.85)]. For an isotropic fcc material, Karafillis and Boyce [28] recommend ($m = 30$ and $\chi = 0.835$) or ($m = 12$ and $\chi = 0.3$). For isotropic bcc materials, it was recommended that ($m = 30$ and $\chi = 0.948$) or ($m = 6$ and $\chi = 0.17$).

It can be easily demonstrated that for $m = 6$, both $\phi_1(s_1, s_2, s_3)$ and $\phi_2(s_1, s_2, s_3)$ reduce to the Drucker [16] yield function with $c = 1.227$ and $c = -3/2$, respectively.

Noting that the isotropic form of Karafillis and Boyce [28] yield function $F_{\mathrm{KB}}(s_1, s_2, s_3)$ is obtained by interpolation between $\phi_1(s_1, s_2, s_3)$ and $\phi_2(s_1, s_2, s_3)$ [see Eq. (5.96)], it follows that for $m = 6$, this yield criterion is in fact Drucker [16] yield function corresponding to:

$$c = c_{\mathrm{KB}} = \frac{1792\chi - 3}{1456\chi + 2}. \tag{5.98}$$

Remark Note that for the value recommended in Karafillis and Boyce [28], namely $\chi = 0.17$, using Eq. (5.98) we obtain $c_{\mathrm{KB}} = 1.209$. This explains why Hershey [21]-Hosford [25] $\phi_1(s_1, s_2, s_3)$ for $m = 6$ and Karafillis and Boyce [28] yield surfaces for isotropic bcc materials are very close. Most importantly, this result shows that for orthotropic bcc materials, the yield surfaces Yld91 and the Karafillis and Boyce [28] surface are practically the same.

It can also be shown that if $m = 12$, the isotropic yield functions $\phi_1(s_1, s_2, s_3)$ and $\phi_2(s_1, s_2, s_3)$ can be expressed as polynomials in terms of the invariants J_2 and J_3, i.e,

$$\phi_{2,m=12}(s_1, s_2, s_3) = s_1^{12} + s_2^{12} + s_3^{12} = 2J_2^6 + 24J_2^3J_3^2 + 3J_3^4, \tag{5.99}$$

$$\begin{aligned}\phi_{1,m=12}(s_1, s_2, s_3) &= (s_1 - s_2)^{12} + (s_2 - s_3)^{12} + (s_1 - s_3)^{12} \\ &= 4098J_2^6 - 18144J_2^3J_3^2 + 2187J_3^4\end{aligned} \tag{5.100}$$

Therefore, we obtain the following general result:

Proposition 5.7 *For bcc and fcc orthotropic materials, the equivalent stress associated with the* Karafillis and Boyce [28] *criterion is expressed in terms of the second and third-invariant of the transformed tensor* $\tilde{\mathbf{S}}$*, as:*

– *bcc orthotropic materials:*

$$\bar{\sigma} = 2.235\left(\tilde{J}_2^3 - 1.209\tilde{J}_3^2\right)^{1/6} \tag{5.101}$$

– *fcc orthotropic materials:*

$$\bar{\sigma} = 1.84\left(\tilde{J}_2^6 - 3.5822\tilde{J}_2^3\tilde{J}_3^2 + 0.5834\tilde{J}_3^4\right)^{1/12}, \tag{5.102}$$

with the explicit expressions of $\tilde{J}_2$ *and* $\tilde{J}_3$ *in terms of the applied stress components being given by* Eqs. (5.92) and (5.93)*, respectively.*

5.3.5 Explicit Expression of Yld 2004-18p Orthotropic Yield Criterion in Terms of Stresses

The orthotropic yield function, denoted Yld 2004-18p, developed by Barlat et al. [7] involves two linear transformations. This yield function is expressed as:

$$\begin{aligned} f(\mathbf{X},\mathbf{Y}) = f(x_i,y_i) =& (x_1-y_1)^m + (x_2-y_1)^m + (x_3-y_1)^m \\ &+ (x_1-y_2)^m + (x_2-y_2)^m + (x_3-y_2)^m \\ &+ (x_1-y_3)^m + (x_2-y_3)^m + (x_3-y_3)^m = 4\bar{\sigma}^m, \end{aligned} \tag{5.103}$$

where x_k and y_k, $k = 1, \ldots, 3$, are the principal values of the transformed stress tensors $\mathbf{X}$ and $\mathbf{Y}$ that are defined as:

$$\begin{aligned} \mathbf{X} &= \mathbf{C}'\mathbf{s} \\ \mathbf{Y} &= \mathbf{C}''\mathbf{s}, \end{aligned} \tag{5.104}$$

with the fourth-order tensors $\mathbf{C}'$ and $\mathbf{C}''$ being orthotropic. It is recommended to take $m = 6$ for bcc materials and $m = 8$ for fcc materials.

In the coordinate system $(\mathbf{x},\mathbf{y},\mathbf{z})$ associated with the orthotropic axes, the fourth-order tensors $\mathbf{C}'$ and $\mathbf{C}''$ are expressed in matrix form using Voigt notations as:

$$\mathbf{C}' = \begin{bmatrix} 0 & -c'_{12} & -c'_{13} & 0 & 0 & 0 \\ -c'_{21} & 0 & -c'_{23} & 0 & 0 & 0 \\ -c'_{31} & -c'_{32} & 0 & 0 & 0 & 0 \\ 0 & 0 & 0 & c'_{44} & 0 & 0 \\ 0 & 0 & 0 & 0 & c'_{55} & 0 \\ 0 & 0 & 0 & 0 & 0 & c'_{66} \end{bmatrix}$$

and

$$\mathbf{C}'' = \begin{bmatrix} 0 & -c''_{12} & -c''_{13} & 0 & 0 & 0 \\ -c''_{21} & 0 & -c''_{23} & 0 & 0 & 0 \\ -c''_{31} & -c''_{32} & 0 & 0 & 0 & 0 \\ 0 & 0 & 0 & c''_{44} & 0 & 0 \\ 0 & 0 & 0 & 0 & c''_{55} & 0 \\ 0 & 0 & 0 & 0 & 0 & c''_{66} \end{bmatrix} \tag{5.105}$$

with c'_{ij}, c''_{ij} being material parameters (see [7]). It is important to note that the tensors $\mathbf{C}'$ and $\mathbf{C}''$ are neither symmetric nor deviatoric. Therefore, the transformed stress tensors $\mathbf{X}$ and $\mathbf{Y}$ involved in the expression of Yld 2004-18p are not deviatoric.

Let us denote as p_x, I_{2x}, I_{3x} the first, second, and, third-invariants associated with the tensor $\mathbf{X}$, i.e.,

$$\begin{aligned} p_x &= (tr\mathbf{X})/3 = \left(X_{xx} + X_{yy} + X_{zz}\right)/3 \\ I_{2x} &= \left[tr\left(\mathbf{X}^2\right) - (tr\mathbf{X})^2\right]/2 \\ I_{3x} &= \det(\mathbf{X}) \end{aligned} \tag{5.106}$$

and the associated invariants of the tensor $\mathbf{Y}$ by p_y, I_{2y}, I_{3y}. In Barlat et al. [7], the principal values x_k and y_k, $k = 1, \ldots, 3$ of the tensors $\mathbf{X}$ and $\mathbf{Y}$ are obtained by solving the respective characteristic equations, i.e., the third-order algebraic equations:

$$\lambda^3 - 3p_x\lambda^2 - I_{2x}\lambda - I_{3x} = 0 \quad \text{and} \quad \lambda^3 - 3p_y\lambda^2 - I_{2y}\lambda - I_{3y} = 0 \tag{5.107}$$

No explicit expressions of Yld 2004-18p in terms of the components of the stress deviator $\boldsymbol{s}$ and the anisotropy coefficients c'_{ij}, c''_{ij} were given. In the following, we will first provide the explicit expressions of the invariants of the transformed tensors $\mathbf{X}$ and $\mathbf{Y}$ in terms of the stress components.

As already mentioned, in general, the transformed tensors $\mathbf{X}$ and $\mathbf{Y}$ are not deviatoric, i.e., $p_x \neq 0$ and $p_y \neq 0$ [see Eq. (5.106)]. The invariants of $\mathbf{X}'$, the deviator of $\mathbf{X}$, will be denoted J_{2x} and J_{3x}. Thus,

$$J_{2x} = I_{2x} + 3p_x^2, \quad J_{3x} = I_{3x} + p_x I_{2x} + 2p_x^3, \tag{5.108}$$

with similar relationships for the invariants J_{2y} and J_{3y} of $\mathbf{Y}'$, the deviator of $\mathbf{Y}$. Using Eq. (5.104) it follows that the expressions of the invariants p_x, J_{2x}, J_{3x} in terms of the components of the stress deviator $\boldsymbol{s}$ and the anisotropy coefficients c'_{ij} are:

$$p_x = -\left[s_{xx}\left(c'_{21} + c'_{31}\right) + s_{yy}\left(c'_{12} + c'_{32}\right) + s_{zz}\left(c'_{13} + c'_{23}\right)\right]/3 \tag{5.109}$$

$$\begin{aligned} J_{2x} = {} & \left(d_{13}s_{zz} + d_{12}s_{yy}\right)^2/2 + \left(d_{23}s_{zz} + d_{21}s_{xx}\right)^2/2 + \left(d_{31}s_{xx} + d_{32}s_{yy}\right)^2/2 \\ & + d_{44}^2 s_{yz}^2 + d_{55}^2 s_{xz}^2 + d_{66}^2 s_{xy}^2 \end{aligned} \tag{5.110}$$

$$\begin{aligned} J_{3x} = {} & -\left(s_{yy}d_{12} + s_{zz}d_{13}\right)\left(s_{xx}d_{21} + s_{zz}d_{23}\right)\left(s_{xx}d_{31} + s_{yy}d_{32}\right) \\ & + d_{44}^2 s_{yz}^2\left(s_{yy}d_{12} + s_{zz}d_{13}\right) + d_{55}^2 s_{xz}^2\left(s_{xx}d_{21} + s_{zz}d_{23}\right) + d_{66}^2 s_{xy}^2\left(s_{xx}d_{31} + s_{yy}d_{32}\right) \\ & + 2d_{44}d_{55}d_{66}s_{xy}s_{xz}s_{yz} \end{aligned} \tag{5.111}$$

with the coefficients d_{ij} being expressed in terms of c'_{ij} as:

$$\begin{aligned} d_{12} &= \left(2c'_{12}+c'_{21}+c'_{31}-c'_{32}\right)/3, \quad d_{13} = \left(2c'_{13}+c'_{21}+c'_{31}-c'_{23}\right)/3,\ d_{44} = c'_{44} \\ d_{21} &= \left(c'_{12}+2c'_{21}-c'_{31}+c'_{32}\right)/3, \quad d_{23} = \left(c'_{12}-c'_{13}+2c'_{23}+c'_{32}\right)/3,\ d_{55} = c'_{55} \\ d_{31} &= \left(c'_{13}-c'_{21}+2c'_{31}+c'_{23}\right)/3, \quad d_{32} = \left(c'_{13}-c'_{12}+c'_{23}+2c'_{32}\right)/3,\ d_{66} = c'_{66} \end{aligned} \tag{5.112}$$

The expressions for p_y, I_{2y}, I_{3y} are obtained from Eqs. (5.109)–(5.112) by replacing c'_{ij} with c''_{ij}. Further substitution in Eq. (5.103) leads to the following result.

Theorem 5.1 *The yield function Yld 2004-18p for bcc materials is a polynomial of order 6 in stresses, and it is expressed in terms of the invariants of the transformed tensors* $\mathbf{X}$ *and* $\mathbf{Y}$ *as:*

$$\begin{aligned} \text{Yld-18p}_{\text{BCC}} &= 9\left(p_x-p_y\right)^6+90\left(p_x-p_y\right)^4\left(J_{2x}+J_{2y}\right) \\ &\quad +90\left(p_x-p_y\right)^2\left(J_{2x}^2+J_{2y}^2+4J_{2x}J_{2y}\right)+180\left(p_x-p_y\right)^3\left(J_{3x}-J_{3y}\right) \\ &\quad +90\left(p_x-p_y\right)\left(4J_{3x}J_{2y}-4J_{2x}J_{3y}+J_{2x}J_{3x}-J_{2y}J_{3y}\right) \\ &\quad +\left(9J_{3x}^2+6J_{2x}^3\right)+\left(9J_{3y}^2+6J_{2y}^3\right)+60(J_{2x}J_{2y}^2+J_{2y}J_{2x}^2-3J_{3y}J_{3x}) \\ &= 4\bar{\sigma}^6. \end{aligned} \tag{5.113}$$

Proposition 5.8 *The expression of Yld-18p$_{BCC}$given by* Eq. (5.113) *allows us to recognize that the 18 material parameters are not independent.*

Proof Indeed, the yielding response according to the criterion is the same if the coefficients c'_{ij}, c''_{ij} are replaced by $\beta c'_{ij}$, $\beta c''_{ij}$ with β being an arbitrary positive constant [see also Eqs. (5.110) and (5.111)]. Therefore, without loss of generality one of these parameters, for example, c'_{12} can be set equal to unity.

Proposition 5.9: *If the orthotropic extension of the* Hershey [21]-Hosford [25] *yield function* [see Eq. (5.84)] *is done by means of only one linear transformation and the fourth-order tensor associated with this linear transformation is deviatoric, Yld-18p$_{BCC}$reduces to Yld91$_{BCC}$:*

Proof Indeed, if $\mathbf{C}' = \mathbf{C}''$ is deviatoric then $\mathbf{X} = \mathbf{Y}$ and $p_x = p_y = 0$, so Eq. (5.113) becomes:

$$\text{Yld-18p}_{\text{BCC}} = 2\left(66J_{2x}^3-81J_{3x}^2\right) = 4\bar{\sigma}^6,$$

i.e., $\phi_1(x_1,x_2,x_3) = 2\bar{\sigma}^6$ for $m = 6$ [see also expression of Yld91$_{\text{BCC}}$ given by Eq. (5.90)]. Let us also note that the condition $p_x = 0$ imposes three additional constraints for the coefficients of $\mathbf{C}'$, so this tensor has only six independent

coefficients, with the expressions of the coefficients c'_{ij} and c'_{kk} in terms of the anisotropy coefficients $a, b, \bar{c}, f, g, h$ appearing in the original formulation of Yld91 [see Eq. (5.86)] being:

$$\begin{aligned} &c'_{12} = 2\bar{c} + b, \quad c'_{13} = 2b + \bar{c}, \quad c'_{21} = 2\bar{c} + a, \quad c'_{23} = 2a + \bar{c}, \\ &c'_{21} = 2\bar{c} + a, \quad c'_{23} = 2a + \bar{c}, \quad c'_{31} = 2b + a, \quad c'_{32} = 2a + b, \\ &c'_{44} = f, \qquad c'_{55} = g \qquad\qquad c'_{44} = h. \end{aligned} \tag{5.114}$$

Using Eq. (5.114), it can be easily seen that the expressions of J_{2x}, J_{3x} reduce to $\tilde{J}_2$ and $\tilde{J}_3$, respectively, i.e., the expression of $\text{Yld91}_{\text{BCC}}$ given by Eq. (5.90) is recovered.

This result also has important consequences in terms of the identification of $\text{Yld-18p}_{\text{BCC}}$. To speed up the convergence of the optimization procedure used for determination of the anisotropy coefficients, the initial guess values should be taken such that $c'_{ij} = c''_{ij}$, and the respective numerical values should be calculated using Eq. (5.114) and the values of the anisotropy coefficients $a, b, \bar{c}, f, g, h$ of Yld 91 for the given material.

Theorem 5.2 *Yld 2004-18p for fcc materials is a polynomial of order 8 in stresses, and its expression in terms of the invariants of the transformed tensors* $\mathbf{X}$ *and* $\mathbf{Y}$ *is:*

$$\begin{aligned} \text{Yld-18p}_{\text{FCC}} &= 9\left(p_x - p_y\right)^8 + 168\left(p_x - p_y\right)^6\left(J_{2x} + J_{2y}\right) \\ &\quad + 504\left(p_x - p_y\right)^5\left(J_{3x} - J_{3y}\right) + 420\left(p_x - p_y\right)^4\left(J_{2x}^2 + J_{2y}^2 + 4J_{2x}J_{2y}\right) \\ &\quad + 840\left(p_x - p_y\right)^3\left(4J_{3x}J_{2y} - 4J_{2x}J_{3y} + J_{2x}J_{3x} - J_{2y}J_{3y}\right) \\ &\quad + \left(p_x - p_y\right)^2\left[1680\left(J_{2x}J_{2y}^2 + J_{2y}J_{2x}^2\right) - 5040J_{3y}J_{3x}\right. \\ &\quad \left. + 252\left(J_{3x}^2 + J_{3y}^2\right) + 168\left(J_{2y}^3 + J_{2x}^3\right)\right] \\ &\quad + 168\left(p_x - p_y\right)\left[J_{2x}^2J_{3x} - J_{2y}^2J_{3y} + 10J_{2x}J_{2y}\left(J_{3x} - J_{3y}\right)\right. \\ &\quad \left. + 10\left(J_{3x}J_{2y}^2 - J_{3y}J_{2x}^2\right)\right] \\ &\quad + 6\left(J_{2x}^4 + 4J_{2x}J_{3x}^2\right) + 6\left(J_{2y}^4 + 4J_{2y}J_{3y}^2\right) \\ &\quad + 56\left[3\left(J_{2y}J_{3x}^2 + J_{2x}J_{3y}^2\right) + 2\left(J_{2x}^3J_{2y} + J_{2y}^3J_{2x}\right)\right. \\ &\qquad \left. + 5J_{2y}^2J_{2x}^2 - 15J_{3y}J_{3x}\left(J_{2y} + J_{2x}\right)\right] \\ &= 4\bar{\sigma}^8 \end{aligned} \tag{5.115}$$

Proposition 5.10 *If* $\mathbf{C}' = \mathbf{C}''$*, i.e., the Yld18p*$_{FCC}$ *involves only one linear transformation, and* $\mathbf{C}'$ *is also deviatoric, Yld18p*$_{FCC}$ *reduces to Yld91*$_{FCC}$.

Proof Indeed, if $\mathbf{C}' = \mathbf{C}''$ and this fourth-order tensor is also deviatoric, then $\mathbf{X} = \mathbf{Y}$, $p_x = p_y = 0$ and Eq. (5.115) becomes:

$$\text{Yld-18p}_{\text{FCC}} = 2(258J_{2x}^4 - 648J_{2x}J_{3x}^2) = 4\bar{\sigma}^8,$$

i.e., $\phi_1(x_1, x_2, x_3) = 2\bar{\sigma}^8$ for $m = 8$ [see also the expression of Yld91$_{\text{FCC}}$ given by Eq. (5.89)].

Another advantage of formulating Yld18p$_{\text{FCC}}$ and Yld18p$_{\text{BCC}}$ in terms of the stress components is the fact that it becomes evident that these formulations do not involve 18 independent anisotropy parameters.

5.3.6 Explicit Expression of Yld 2004-13p Orthotropic Yield Criterion in Terms of Stresses

The orthotropic yield function denoted Yld 2004-13p, developed by Barlat et al. [7], is of the form:

$$\begin{aligned} g(\mathbf{X}, \mathbf{Y}) = g(x_i, y_i) = (x_1 - x_2)^m + (x_2 - x_3)^m + (x_1 - x_3)^m \\ - \left(x_1^m + x_2^m + x_3^m\right) + \left(y_1^m + y_2^m + y_3^m\right) = 2\bar{\sigma}^m, \end{aligned} \tag{5.116}$$

where the exponent $m = 6$ for bcc materials, and $m = 8$ for fcc materials, respectively; x_i and y_i for i = 1, …, 3 are the principal values of the transformed stress tensors $\mathbf{X}$ and $\mathbf{Y}$ defined by Eq. (5.104) with the fourth-order order tensors $\mathbf{C}'$ and $\mathbf{C}''$ given by Eq. (5.105) and subjected to the additional constraints:

$$c'_{12} = c'_{31} = c'_{32} = 1 \quad \text{and} \quad c''_{31} = c''_{32} = 1 \tag{5.117}$$

Let us first note that when all the anisotropy coefficients are set to unity, i.e., $c'_{ij} = c''_{ij} = 1$ (isotropy), Yld 2004-13p reduces to:

$$g_{\text{isotropic}} = \phi_1(s_1, s_2, s_3),$$

which is Hershey [21]-Hosford [25] isotropic yield function [see Eq. (5.84)].

Theorem 5.3 *For bcc materials, Yld 2004-13p is a polynomial of order 6 in stresses, and it is expressed in terms of the invariants of the transformed tensors* $\mathbf{X}$ *and* $\mathbf{Y}$ *as:*

$$\begin{aligned}\text{Yld-13p}_{\text{BCC}} &= 64J_{2x}^3 - 84J_{3x}^2 + 2J_{2y}^3 + 3J_{3y}^2 \\ &+ 3\left(p_y^6 - p_x^6\right) + 30\left(p_y^4 J_{2y} - p_x^4 J_{2x}\right) + 60\left(p_y^3 J_{3y} - p_x^3 J_{3x}\right) \\ &+ 30\left(p_y^2 J_{2y}^2 - p_x^2 J_{2x}^2\right) + 30\left(p_y J_{2y} J_{3y} - p_x J_{2x} J_{3x}\right)\end{aligned} \tag{5.118}$$

The proof follows along the same arguments as Theorem 5.1.

Remark In contrast to Yld 2004-18p$_{\text{BCC}}$, the orthotropic yield function Yld 2004-13p does not contain any mixed terms involving the invariants of both transformed tensors **X** and **Y**

In particular, when the formulation accounts for only one linear transformation, i.e., $\mathbf{C}' = \mathbf{C}''$ and this tensor is deviatoric, Yld-13p$_{\text{BCC}}$ reduces to Yld91$_{\text{BCC}}$ [see Eq. (5.90)].

Theorem 5.4 *For fcc materials, Yld 2004-13p is a polynomial of order 8 in terms of stresses, and it is expressed in terms of the invariants of the transformed tensors* **X** *and* **Y** *as:*

$$\begin{aligned}\text{Yld-13p}_{\text{FCC}} &= 256J_{2x}^4 - 656J_{2x}J_{3x}^2 + 2J_{2y}^4 + 8J_{2y}J_{3y}^2 \\ &+ 3\left(p_y^8 - p_x^8\right) + 56\left(p_y^6 J_{2y} - p_x^6 J_{2x}\right) + 168\left(p_y^5 J_{3y} - p_x^5 J_{3x}\right) \\ &+ 140\left(p_y^4 J_{2y}^2 - p_x^4 J_{2x}^2\right) + 280\left(p_y^3 J_{2y} J_{3y} - p_x^3 J_{2x} J_{3x}\right) \\ &+ 28\left[p_y^2\left(2J_{2y}^3 + 3J_{3y}^2\right) - p_x^2\left(2J_{2x}^3 + 3J_{3x}^2\right)\right] \\ &+ 56\left(p_y J_{2y}^2 J_{3y} - p_x J_{2x}^2 J_{3x}\right)\end{aligned} \tag{5.119}$$

5.4 Yield Criteria for Textured Polycrystals with Tension–Compression Asymmetry

Basal or near-basal textures are common for cold-rolled hcp materials (see for example, [1, 17, 25, 32] etc.). Due to this strong basal pole alignment in the thickness direction, as seen in Chap. 3, a twinning system can be easily activated by compression perpendicular to this direction, but the same twinning system is not active in tension within the plane of the sheet (e.g., the $\{10\bar{1}2\}\langle 10\bar{1}\bar{1}\rangle$ twinning mode which is activated during the compression of the *c*-axis for Ti, Zr, and Mg, see Sect. 3.2.2 for more details). Because of the directionality of twinning, a very pronounced strength differential (SD) effect is observed. Furthermore, the strong crystallographic texture, exhibited by these hcp materials, leads to a pronounced anisotropy. Hence, the yield loci of rolled hcp metals are highly asymmetrical in shape. Although very versatile anisotropic criteria exist in the literature (e.g., the anisotropic criteria presented in Sects. 5.2 and 5.3), they were all intended to model

metals with cubic crystal structure and as such were represented by even functions of stresses. Therefore, none of these anisotropic yield criteria can capture tension–compression asymmetry in yielding. In a first attempt to account for SD effects, Hosford [24] modified the Hill [22] criterion by adding terms linear in stresses:

$$\begin{aligned} A\sigma_{xx} + B\sigma_{yy} + (-B - A)\sigma_{zz} + F\left(\sigma_{yy} - \sigma_{zz}\right)^2 \\ + G(\sigma_{zz} - \sigma_{xx})^2 + H\left(\sigma_{xx} - \sigma_{yy}\right)^2 = 1 \end{aligned} \tag{5.120}$$

where A, B, F, G, H are constants. This criterion predicts elliptical yield loci with the center given by the values of the two new added constants. This formulation could describe correctly the behavior of hcp metals having elliptical yield loci of low eccentricity. However, the Hosford [24] yield criterion is not homogenous in stresses, which leads to the inapplicability of the flow rule (derivatives w.r.t. stresses do not have the dimension of strain-rates). In order to describe the highly asymmetric yield loci of hcp alloys, other formulations should be considered. Obviously, anisotropic formulations that describe asymmetry in yielding due to hydrostatic effects (e.g., criteria for soils and rocks) cannot be applicable to hcp metals, which are essentially pressure-insensitive. Nevertheless, in most studies on hcp metals, the tension–compression asymmetry is neglected, and Hill [22] criterion is used (see for example [46]). Very recently, macroscopic yield criteria that could accurately describe both anisotropy and SD effects in such pressure-insensitive metals have been developed by Cazacu and Barlat [13], Cazacu et al. [14] and these yield functions are presented in the following section.

5.4.1 Orthotropic Yield Criterion of Cazacu and Barlat [13]

As discussed in Sect. 4.3, to account for SD effects in isotropic metals, Cazacu and Barlat [13] developed a yield criterion which is an odd function. Its expression is:

$$f(\boldsymbol{s}) \equiv (J_2)^{\frac{3}{2}} - c\,J_3 = \tau_Y^3, \tag{5.121}$$

where J_2, J_3 are the invariants of the stress deviator and τ_Y is the yield stress in pure shear; c being a material parameter (for a detailed presentation and discussion of this isotropic criterion, the reader is referred to Chap. 4). To describe both the anisotropy and tension–compression asymmetry of hcp metals, these authors also proposed an orthotropic extension of this criterion using the generalized invariants approach (see Sect. 5.1). The expression of this orthotropic and asymmetric yield criterion is:

$$\phi = \left(J_2^0\right)^{3/2} - c\left(J_3^0\right), \tag{5.122}$$

with the expressions of the orthotropic invariants J_2^0 and J_3^0 being given by Eqs. (5.6) and (5.8), respectively. Since the criterion is a homogeneous function in stresses

thus, for 3-D loadings it involves 17 independent coefficients. In the case of a sheet, where the only nonzero stress components are the in-plane stresses $(\sigma_{xx}, \sigma_{yy}, \sigma_{xy})$, the orthotropic criterion given by Eq. (5.122) involves 10 material parameters (9 anisotropy coefficients and the value of the constant c), and it is written as:

$$f_2^0 \equiv \left[\frac{1}{6}(a_1+a_3)\sigma_{xx}^2 - \frac{a_1}{3}\sigma_{xx}\sigma_{yy} + \frac{1}{6}(a_1+a_2)\sigma_{yy}^2 + a_4\sigma_{xy}^2\right]^{3/2} - c\left\{\begin{array}{c}\frac{1}{27}(b_1+b_2)\sigma_{xx}^3 + \frac{1}{27}(b_3+b_4)\sigma_{yy}^3 - \frac{1}{9}\left(b_1\sigma_{xx}+b_4\sigma_{yy}\right)\sigma_{xx}\sigma_{yy} \\ -\frac{1}{3}\sigma_{xy}^2\left[(b_5-2b_{10})\sigma_{xx} - b_5\sigma_{yy}\right]\end{array}\right\} = \tau_Y^3. \tag{5.123}$$

If σ_θ^T and σ_θ^C denote the absolute values of the yield stress in uniaxial tension–compression, respectively, along an axis at orientation θ to the rolling direction $\mathbf{x}$, it follows that

$$\sigma_\theta^T = \tau_Y\left\{\begin{array}{l}\left[\frac{1}{6}(a_1+a_3)\cos^4\theta + (a_4-a_1/3)\cos^2\theta\,\sin^2\theta + \frac{1}{6}(a_1+a_2)\sin^4\theta\right]^{3/2} \\ -c\left[\begin{array}{l}\frac{1}{27}(b_1+b_2)\cos^6\theta + \frac{1}{27}(b_3+b_4)\sin^6\theta \\ -\frac{1}{9}\left[(b_1+3b_5-6b_{10})\cos^2\theta + (b_4-3b_5)\sin^2\theta\right]\sin^2\theta\cos^2\theta\end{array}\right]\end{array}\right\}^{-1/3} \tag{5.124}$$

and

$$\sigma_\theta^C = \tau_Y\left\{\begin{array}{l}\left[\frac{1}{6}(a_1+a_3)\cos^4\theta + (a_4-a_1/3)\cos^2\theta\,\sin^2\theta + \frac{1}{6}(a_1+a_2)\sin^4\theta\right]^{3/2} \\ +c\left[\begin{array}{l}\frac{1}{27}(b_1+b_2)\cos^6\theta + \frac{1}{27}(b_3+b_4)\sin^6\theta \\ -\frac{1}{9}\left[(b_1+3b_5-6b_{10})\cos^2\theta + (b_4-3b_5)\sin^2\theta\right]\sin^2\theta\cos^2\theta\end{array}\right]\end{array}\right\}^{-1/3} \tag{5.125}$$

In particular, if σ_0^T and σ_0^C denote the absolute values of the yield stress in tension–compression along the rolling direction, it follows that

$$\begin{aligned}\sigma_0^T &= \tau_Y\left\{\left[\frac{1}{6}(a_1+a_3)\right]^{3/2} - \frac{c}{27}(b_1+b_2)\right\}^{-1/3} \\ \sigma_0^C &= \tau_Y\left\{\left[\frac{1}{6}(a_1+a_3)\right]^{3/2} + \frac{c}{27}(b_1+b_2)\right\}^{-1/3},\end{aligned} \tag{5.126}$$

Similarly, defining σ_{90}^T and σ_{90}^C the absolute values of the yield stress in tension–compression along the transverse direction, according to the orthotropic Cazacu and Barlat [13] criterion we have:

$$\begin{aligned}\sigma_{90}^T &= \tau_Y\left\{\left[\frac{1}{6}(a_1+a_2)\right]^{3/2} - \frac{c}{27}(b_3+b_4)\right\}^{-1/3}\\ \sigma_{90}^C &= \tau_Y\left\{\left[\frac{1}{6}(a_1+a_2)\right]^{3/2} + \frac{c}{27}(b_3+b_4)\right\}^{-1/3},\end{aligned} \tag{5.127}$$

Yielding under equibiaxial tension occurs when $\sigma_{xx} = \sigma_{yy} = \sigma_b^T$ and all the other stress components are zero, the expression of σ_b^T being:

$$\sigma_b^T = \tau_Y\left[\left(\frac{a_2 + a_3}{6}\right)^{3/2} - c\left(\frac{-2\,b_1 + b_2 + b_3 - 2b_4}{27}\right)\right]^{-\frac{1}{3}} \tag{5.128}$$

while yielding under equibiaxial compression occurs when $\sigma_{xx} = \sigma_{yy} = -\sigma_b^C$

$$\sigma_b^C = \tau_Y\left[\left(\frac{a_2 + a_3}{6}\right)^{3/2} + c\left(\frac{-2\,b_1 + b_2 + b_3 - 2b_4}{27}\right)\right]^{-\frac{1}{3}} \tag{5.129}$$

Note that plastic incompressibility results in: $\sigma_b^T = \sigma_{\mathrm{ND}}^C$ and $\sigma_b^C = \sigma_{\mathrm{ND}}^T$, where σ_{ND}^T and σ_{ND}^C denote the absolute values of the yield stress in tension–compression along the normal direction, or **z** axis, respectively.

Further, let r_θ^T and r_θ^C denote the *r*-value [see Eq. (5.39)] under uniaxial tension or uniaxial compression loading in a direction at angle θ to the **x**-axis or rolling direction. The *r*-values can be calculated by making use of the associated flow rule in conjunction with Eq. (5.122) (for the expression of the partial derivatives of J_2^0 and J_3^0, see Eqs. (5.49) and (5.50)). In particular,

$$\left(r_0^T a_3 - a_1\right)\left(\frac{a_1+a_3}{6}\right)^{1/2} - \frac{2\,c}{9}\left(b_2\, r_0^T - b_1\right) = 0 \tag{5.130}$$

$$\left(r_0^C a_3 - a_1\right)\left(\frac{a_1+a_3}{6}\right)^{1/2} + \frac{2c}{9}\left(b_2\, r_0^C - b_1\right) = 0 \tag{5.131}$$

$$\left(r_{90}^T a_2 - a_1\right)\left(\frac{a_1 + a_2}{6}\right)^{1/2} - \frac{2c}{9}\left(-b_4 + b_3\, r_{90}^T\right) = 0 \tag{5.132}$$

$$\left(r_{90}^C a_2 - a_1\right)\left(\frac{a_1 + a_2}{6}\right)^{1/2} - \frac{2c}{9}\left(b_4 - b_3\, r_{90}^C\right) = 0 \tag{5.133}$$

$$\left[-\beta\left(2\,r_{45}^{C}+1\right)\;+\;6a_4\right]3\sqrt{\beta+6a_4}\;-\;\frac{4}{\sqrt{6}}c\,\alpha\,\left(1+2\,r_{45}^{C}\right)\;=\;0 \qquad (5.134)$$

$$\left[\beta\left(-2\,r_{45}^{T}+1\right)\;-\;6a_4\right]3\sqrt{\beta+6a_4}\;-\;\frac{4}{\sqrt{6}}c\,\alpha\left(1-2\,r_{45}^{T}\right)\;=\;0 \qquad (5.135)$$

with $\alpha\;=\;-2b_1\;+\;b_2\;+b_3\;-2\,b_4+6\,b_{10}$, $\beta\;=\;a_2\;+\;a_3$.

In the following, applications of the Cazacu and Barlat [13] orthotropic criterion [see Eq. (5.122)] to the description of the anisotropy and asymmetry of the experimental yield loci of textured pure Mg and binary Mg–Th and Mg–Li alloys are presented. The data on these materials were reported in [29].

Pure Mg

For pure Mg plane-strain compression, results were reported in six orientations that correspond to the six combinations of the rolling direction (RD or $\boldsymbol{x}$-direction), transverse direction (TD or $\boldsymbol{y}$-direction), and thickness direction (ND or $\boldsymbol{z}$-direction). Three duplicate specimens were tested in each of these six orientations. Uniaxial compression tests were performed in the RD, TD, and ND directions, respectively, while uniaxial tension tests were carried out in the RD and TD directions. Based on the data, the experimental yield loci corresponding to several constant levels (1%, 5%, and 10%) of the equivalent plastic strain were constructed (see Fig. 5.19 where the experimental points are represented by symbols).

The 1% yield locus for the textured pure Mg has a highly asymmetrical shape. Note the much greater strength in tension than in compression and the higher tensile strength in the transverse direction than in the rolling direction. This is due to the

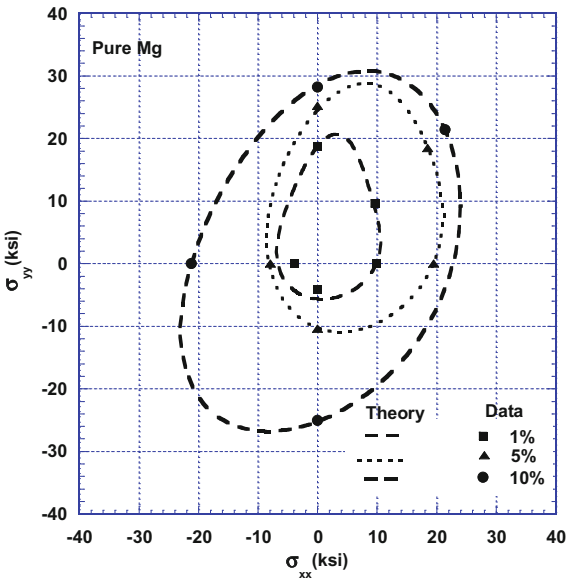

Fig. 5.19 Comparison between the plane stress yield loci for a Mg sheet predicted by the Cazacu and Barlat [13] orthotropic criterion and experiments (data after [29])

texture that presents strong basal pole alignment in the thickness direction, $\{10\bar{1}2\}\langle 10\bar{1}\bar{1}\rangle$ twinning is easily activated by compression perpendicular to this direction, but is not active in tension within the plane. This results in much lower compressive strengths as compared to the tensile strengths. The greater spread of the texture about the transverse direction allows more widespread operation of basal slip for loading in the rolling direction; hence, the tensile strength is significantly lower in the rolling direction than in the transverse direction (see [29]). The yield locus at 5% strain shows asymmetry similar to that of the locus at 1% strain. Since $\{10\bar{1}2\}\langle 10\bar{1}\bar{1}\rangle$ twinning is still operational, the yield strength in compression is much lower than in tension. At 10% strain, the third quadrant strengths are comparable to the first quadrant strengths, owing to the exhaustion of $\{10\bar{1}2\}\langle 10\bar{1}\bar{1}\rangle$ twinning at about 6% strain. Figure 5.19 shows the theoretical yield loci in the plane $(\sigma_{xx}, \sigma_{yy})$ together with the experimental data reported in [29]. The parameters involved in the 2-D form of the Cazacu and Barlat [13] yield loci were determined using Eqs. (5.125)–(5.129) and the data. The values of the anisotropy coefficients obtained at 1%, 5%, and 10% strain are given in Table 5.3. Note that the proposed theory reproduces very well the observed asymmetry in yielding.

Mg–0.49% Th alloy

Because of the relatively symmetric texture and the solution-hardening effect of thorium, the experimental yield loci for Mg–Th alloy plates reported by Kelley and Hosford [29] are much more elliptical than those for pure Mg. The compressive yield strengths are 60–65% of the tensile yield strengths, while for pure Mg the compressive yield strengths are only 20–40% of tensile values. The yield strengths for the transverse and rolling directions are essentially identical. The parameters involved in the 2-D form of the Cazacu and Barlat [13] criterion [see Eq. (5.123)] corresponding to different strain levels were calculated using Eqs. (5.125)–(5.129) and the available data (see Table 5.4). Good agreement is obtained between the theoretical surfaces and available data for Mg–Th (see Fig. 5.20).

Table 5.3 Parameters involved in the Cazacu and Barlat [13] criterion for textured Mg

Strain (%)	a_1	a_2	a_3	b_1	b_2	b_3	b_4	c
1	−0.014	0.611	0.718	−0.338	1.428	1.164	−0.065	0.74
5	−0.018	0.67	0.906	−0.319	2.156	1.434	−0.219	0.712
10	0.586	0.85	1.513	0.132	0.112	0.548	−0.071	1.4

Table 5.4 Parameters involved in the Cazacu and Barlat [13] criterion for Mg–0.5% Th alloy

Strain (%)	a_1	a_2	a_3	b_1	b_2	b_3	b_4	c
1	0.178	1.213	1.325	−0.145	1.453	1.449	−0.362	1.436
5	0.391	1.739	1.784	−0.107	2.685	2.662	−0.537	1.466
10	4.527	5.828	5.841	−1.93	6.27	3.955	−0.917	1.594

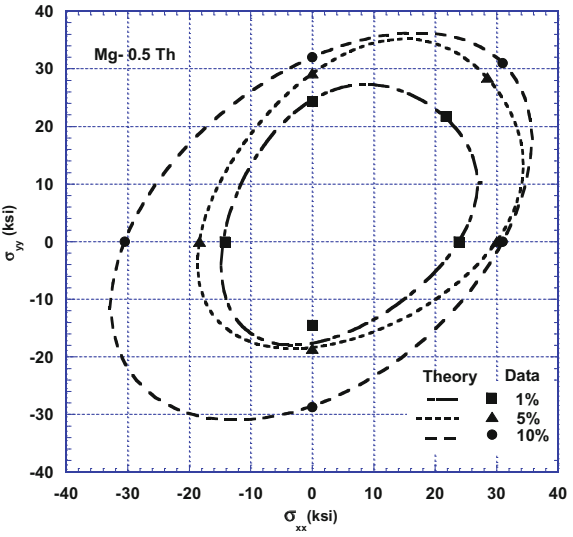

Fig. 5.20 Comparison between the plane stress yield loci for a Mg–0.5% Th sheet predicted by the Cazacu and Barlat [13] orthotropic criterion and experiments (data after [29])

Mg–4% Li alloy

The experimental yield loci for Mg–Li alloy plates reported by Kelley and Hosford [29] are similar in shape to those for the Mg–Th alloy but with much reduced yield stresses due to the occurrence of prism slip and to the weaker crystallographic texture. The effect of $\{10\bar{1}2\}\langle 10\bar{1}\bar{1}\rangle$ twinning is evident in the low compressive strengths at 1% and 5% strains. The values of the anisotropy coefficients corresponding to 1, 5, and 10% were calculated using the procedure outlined in the previous section and are given in Table 5.5. Figure 5.21 shows the theoretical yield loci together with the experimental data of [29]. Again, the agreement between the Cazacu and Barlat [13] yield criterion and experiments is very good.

5.4.2 *Orthotropic Yield Criterion of Nixon et al. [36]*

5.4.2.1 Yielding Formulation

The 3-D orthotropic and asymmetric yield criterion of Cazacu and Barlat [13] [see Eq. (5.122)] is written in terms of orthotropic invariants. Therefore, it involves 17

Table 5.5 Parameters involved in the Cazacu and Barlat [13] criterion for Mg–4% Li alloy

Strain (%)	a_1	a_2	a_3	b_1	b_2	b_3	b_4	c
1	0.896	3.371	3.509	−1.591	5.414	3.957	0.259	2.01
5	1.254	2.07	2.109	0.128	0.875	0.995	−0.354	5.262
10	3.032	3.735	3.922	−0.829	0.895	0.741	−0.327	5.85

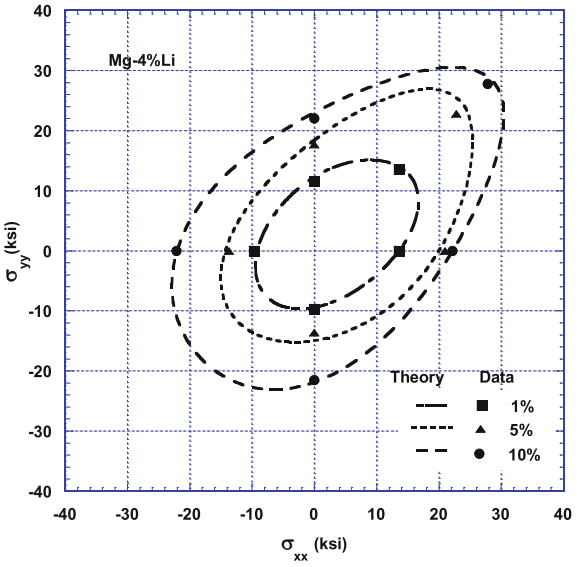

Fig. 5.21 Comparison between the plane stress yield loci for a Mg–4% Li sheet predicted by the Cazacu and Barlat [13] orthotropic criterion and experiments (data after [29])

independent parameters and as such can account for yielding behavior for complex loadings involving tension-shear couplings and compression-shear couplings. However, if fewer experimental data are available, the orthotropic extension of the same isotropic criterion using one linear transformation applied to the Cauchy stress tensor may be used. This methodology was used by Nixon et al. [36], the expression of this orthotropic and asymmetric yield criterion being:

$$G(\tilde{\mathbf{S}}) = (\tilde{J}_2)^{3/2} - c(\tilde{J}_3), \tag{5.136}$$

where $\tilde{J}_2 = tr\left(\tilde{\mathbf{S}}^2\right)/2$ and $\tilde{J}_3 = tr\left(\tilde{\mathbf{S}}^3\right)/3$ are the second and third-invariant of the transformed tensor $\tilde{\mathbf{S}} = \mathbf{L}\boldsymbol{\sigma} = \mathbf{L}\mathbf{s}$, with $\mathbf{L}$ a fourth-order tensor, orthotropic and symmetric. If in the Cartesian coordinate system $(\mathbf{x}, \mathbf{y}, \mathbf{z})$ associated with the orthotropic axes, the stress tensor is represented in Voigt notations by the six-dimensional vector $\boldsymbol{\sigma} = (\sigma_{xx}, \sigma_{yy}, \sigma_{zz}, \sigma_{yz}, \sigma_{xz}, \sigma_{xy})$, and the fourth-order orthotropic tensor $\mathbf{L}$ is represented by the 6×6 matrix:

$$\mathbf{L} = \frac{1}{3}\begin{bmatrix} a_2+a_3 & -a_3 & -a_2 & 0 & 0 & 0 \\ -a_3 & a_3+a_1 & -a_1 & 0 & 0 & 0 \\ -a_2 & -a_1 & a_1+a_2 & 0 & 0 & 0 \\ 0 & 0 & 0 & 3a_4 & 0 & 0 \\ 0 & 0 & 0 & 0 & 3a_5 & 0 \\ 0 & 0 & 0 & 0 & 0 & 3a_6 \end{bmatrix}, \tag{5.137}$$

with a_i (i = 1, …, 6) being anisotropy parameters, the expressions of the invariants $\tilde{J}_2$ and $\tilde{J}_3$ of the transformed tensor $\tilde{\mathbf{S}}$ in terms of the components of the stress deviator $\mathbf{s}$ are given by equations similar with Eqs. (5.92) and (5.93). Therefore, the equivalent stress $\bar{\sigma}$ associated to the Nixon et al. [36] yield criterion (5.136) is:

$$\bar{\sigma} = \mathrm{A}_1 \left(\tilde{J}_2^{3/2} - c\tilde{J}_3 \right)^{1/3}, \tag{5.138}$$

where A_1 is a constant defined such $\bar{\sigma}$ reduces to the tensile yield stress along RD, i.e.,

$$A_1 = \frac{3}{\left[\left(a_2^2 + a_3^2 + a_2 a_3 \right)^{3/2} - c(a_2 + a_3) a_2 a_3 \right]^{1/3}} \tag{5.139}$$

The effective stress $\bar{\sigma}$ is homogeneous of degree one in its arguments. Thus, if we replace a_i by ωa_i, with ω being any positive number, the expression for the effective stress remains unchanged. Hence, we can scale the anisotropy coefficients by a_1, or equivalently, set $a_1 = 1$. The anisotropy coefficients, a_j with j = 2, …, 4, and the parameter c associated with the tension–compression asymmetry of the material can be determined using the experimentally determined uniaxial tensile and compressive flow stresses along the axes of orthotropy of the material.

If σ_θ^T and σ_θ^C are the absolute values of the yield stress in uniaxial tension–compression, respectively, along an axis at orientation θ to the rolling direction $\mathbf{x}$, according to Nixon et al. [36] criterion, we have:

$$\sigma_0^C / \sigma_0^T = \frac{1}{A_1} \left[\left(a_2^2 + a_3^2 + a_2 a_3 \right)^{3/2} + c(a_2 + a_3) a_2 a_3 \right]^{-1/3} \tag{5.140}$$

Similarly, this criterion predicts that the tensile and compressive yield stress along the transverse direction $\mathbf{y}$ are:

$$\sigma_{90}^T / \sigma_0^T = \frac{1}{A_1} \left[\left(a_1^2 + a_3^2 + a_1 a_3 \right)^{3/2} - c(a_1 + a_3) a_1 a_3 \right]^{-1/3} \tag{5.141}$$

and

$$\sigma_{90}^C / \sigma_0^T = \frac{1}{A_1} \left[\left(a_1^2 + a_3^2 + a_1 a_3 \right)^{3/2} + c(a_1 + a_3) a_1 a_3 \right]^{-1/3} \tag{5.142}$$

Moreover, the tensile and compressive yield stresses along the normal direction $\mathbf{z}$ are:

$$\sigma_z^T/\sigma_0^T = \frac{1}{A_1}\left[\left(a_1^2 + a_2^2 + a_1a_2\right)^{3/2} - c(a_1 + a_2)a_1a_2\right]^{-1/3} \tag{5.143}$$

$$\sigma_z^C/\sigma_z^T = \frac{1}{A_1}\left[\left(a_1^2 + a_2^2 + a_1a_2\right)^{3/2} + c(a_1 + a_2)a_1a_2\right]^{-1/3} \tag{5.144}$$

Plastic incompressibility implies that yielding under equibiaxial tension occurs when $\sigma_{xx} = \sigma_{yy} = \sigma_b^T$ and all the other stress components are zero, the expression of σ_b^T being:

$$\sigma_b^T = \sigma_z^C$$

while yielding under equibiaxial compression occurs when $\sigma_{xx} = \sigma_{yy} = -\sigma_b^C = -\sigma_z^T$ and all other stress components are zero.

Further, let r_θ^T and r_θ^C be the r-value [see Eq. (5.39)] under uniaxial tension stress or uniaxial compression in a direction at angle θ to the **x**-axis. According to the Nixon et al. [36] orthotropic yield criterion,

$$3\left[r_0^T(3\alpha_1 + \alpha_2 - \alpha_3) - (\alpha_3 - \alpha_2 - \alpha_1)\right]\sqrt{\alpha_1} - 2c\left[(3\beta_1 - \beta_3)r_0^T - \beta_3\right] = 0 \tag{5.145}$$

$$3\left[r_0^C(3\alpha_1 + \alpha_2 - \alpha_3) - (\alpha_3 - \alpha_2 - \alpha_1)\right]\sqrt{\alpha_1} + 2c\left[(3\beta_1 - \beta_3)r_0^T - \beta_3\right] = 0 \tag{5.146}$$

$$3\left[r_{90}^T(3\alpha_2 + \alpha_1 - \alpha_3) - (\alpha_3 - \alpha_2 - \alpha_1)\right]\sqrt{\alpha_2} - 2c\left[(3\beta_2 - \beta_4)r_{90}^T - \beta_3\right] = 0 \tag{5.147}$$

$$3\left[r_{90}^C(3\alpha_2 + \alpha_1 - \alpha_3) - (\alpha_3 - \alpha_2 - \alpha_1)\right]\sqrt{\alpha_2} + 2c\left[(3\beta_2 - \beta_4)r_{90}^C - \beta_3\right] = 0 \tag{5.148}$$

In the above equations, α_i, i = 1, …, 3, and β_j, j = 1, …, 4 are constants which have the following expressions in terms of the anisotropy coefficients a_i, i = 1, …, 3:

$$\begin{aligned}
&\alpha_1 = \left(a_2^2 + a_3^2 + a_2a_3\right)/9;\ \alpha_2 = \left(a_1^2 + a_3^2 + a_1a_3\right)/9;\ \alpha_3 = \left(a_1^2 + a_2^2 + a_2a_1\right)/9;\\
&\beta_1 = (a_2a_3)(a_2 + a_3)/27;\ \beta_2 = (a_1a_3)(a_1 + a_3)/27;\\
&\beta_3 = \beta_1 + \left(a_2a_3^2 + a_2^2a_1 - a_3^2a_1\right)/27;\ \beta_4 = \beta_2 + \left(a_1a_3^2 + a_2^2a_1 - a_3^2a_2\right)/27
\end{aligned} \tag{5.149}$$

In summary, using Eqs. (5.140)–(5.149) with a_1 = 1, the coefficients a_j, j = 2, …, 4 and the tension–compression parameter c can be determined by minimizing the cost function

$$E(a_2, a_3, a_4, c) = \sum_j w_j \left(\sigma_\theta^T / \sigma_\theta^{\exp} - 1\right)^2 + \sum_k z_k \left(\sigma_\theta^C / \sigma_\theta^{\exp} - 1\right)^2 + \sum_{jj} t_{jj} \left(r_\theta^T / r_\theta^{\exp} - 1\right)^2 + \sum_{kk} m_{kk} \left(r_\theta^C / r_\theta^{\exp} - 1\right)^2, \tag{5.150}$$

where the range of j, k, jj, kk is given by the number of experimental tensile yield stresses, experimental compressive yield stresses, tensile Lankford coefficients, and the compressive ellipticity ratio available, while w_j, z_k, t_{jj}, and m_{kk} are weights given to the respective experimental values. The remaining anisotropy coefficients a_4 and a_5, which are associated with out-of-plane properties may be determined using data such as the yield stress in simple shear in the $(\mathbf{y}, \mathbf{z})$ and $(\mathbf{x}, \mathbf{z})$ planes, respectively.

5.4.2.2 Applications: Tension, Compression, and Bending of hcp-Ti

Pure Ti has a hcp structure with a c/a ratio of 1.587, i.e., lower than the ideal c/a ratio of 1.633 (see also Chap. 3). There are three principal types of Ti alloys: α or near α phase alloys, α–β phase alloys and β phase alloys. Ti alloys in the low- and medium-temperature regime mainly consist of the hcp α-phase. These hcp materials are known to display plastic anisotropy and a strong tension–compression asymmetry (see, for example, [43]). Numerous studies (e.g., [30, 33]) have shown that classic yield criteria, such as Hill [22] are unable to capture this asymmetry.

Nixon et al. [36, 37] have reported the results of a comprehensive experimental study on the quasi-static mechanical response of a high-purity α-Ti. This material was supplied in the form of a 15.87 mm thick cross-rolled disk of 254 mm diameter. Optical microscopy showed that the as-received material has equiaxed grains with an average grain size of about 20 μm. The basal plane (0001) pole figures measured by X-ray diffraction show that the plate exhibits orthotropic texture. The basal plane aligns maximally in the normal-transverse plane at 30°–40° from the plate normal direction (ND) towards the transverse direction (TD). This result was also confirmed by neutron diffraction measurements of the initial texture carried out in the neutron time-of-flight (TOF) diffractometer High-Pressure-Preferred Orientation at Los Alamos Neutron Science Center (for more details on the initial texture, see [36]).

Quasi-static characterization tests consisted of uniaxial tension–compression tests that were conducted at room temperature and at a nominal strain-rate of 0.001/s. To characterize the anisotropy of the material, standard tensile specimens were machined such that the tensile direction was either parallel to the rolling direction (RD) or the transverse direction, while a specialized miniature test specimen was used for the through-thickness (TT or ND) tensile tests. The uniaxial tensile test results (see Fig. 5.22) show that the material displays orthotropic behavior, the material being weakest in the rolling direction and strongest in the through-thickness direction.

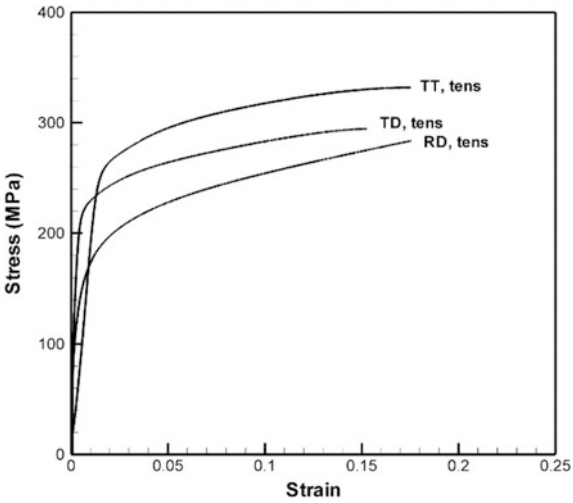

Fig. 5.22 Uniaxial tensile test results along the rolling (RD), transverse (TD), and through-thickness direction (TT) of the high-purity α-Ti. Experimental data from [36]

To examine the effect of the loading orientation on the mechanical response, cylindrical compression specimens were machined such that the axes of the cylinders were either along RD, TD, or TT directions. The test results showed that the tension–compression asymmetry of this material is highly directional; the most pronounced asymmetry being observed for specimens cut along RD (see Fig. 5.23). It is worth analyzing in more detail, the compressive and tensile true stress–strain response along the rolling direction shown in Fig. 5.24. Although, initially there is no significant difference in yielding behavior (at 0.02% strain offset, the yield stress in tension or compression is about 175 MPa), a very pronounced tension–compression asymmetry is observed after about 10% strain. Note the especially sharp difference in hardening rate. While in tension, the material hardens gradually until plastic localization (necking) occurs at about 30% strain, in compression strain-hardening is strongly non-linear, with a very pronounced increase in hardening rate observed at about 10% strain. This change in hardening may be indicative of deformation twinning. This hypothesis was verified by the analysis of the textures of the deformed specimens (see [36]).

Nixon et al. [36] applied the orthotropic and asymmetric yield criterion given by Eq. (5.136) to model the observed anisotropy and asymmetry in yielding of this α-Ti. Since r-values were not measured, the experimental data used in the cost function given by Eq. (5.150) consisted of the measured tensile and compressive flow data in the RD, TD, and TT directions, respectively. Equal weights were given to the experimental data (i.e., $w_j = z_k = 1$, $t_{jj} = m_{kk} = 0$). The coefficient a_1 was set equal to unity while the numerical values of the coefficients a_2, a_3 and a_6 corresponding to fixed levels of the equivalent plastic strain, $\bar{\varepsilon}^p$ are given in Table 5.6. Note that $\bar{\varepsilon}^p$ was calculated using the work-equivalence principle in conjunction with Eq. (5.138) for the equivalent stress $\bar{\sigma}$ associated to the yield criterion (5.136). No data were available for the determination of the coefficients a_4 and a_5.

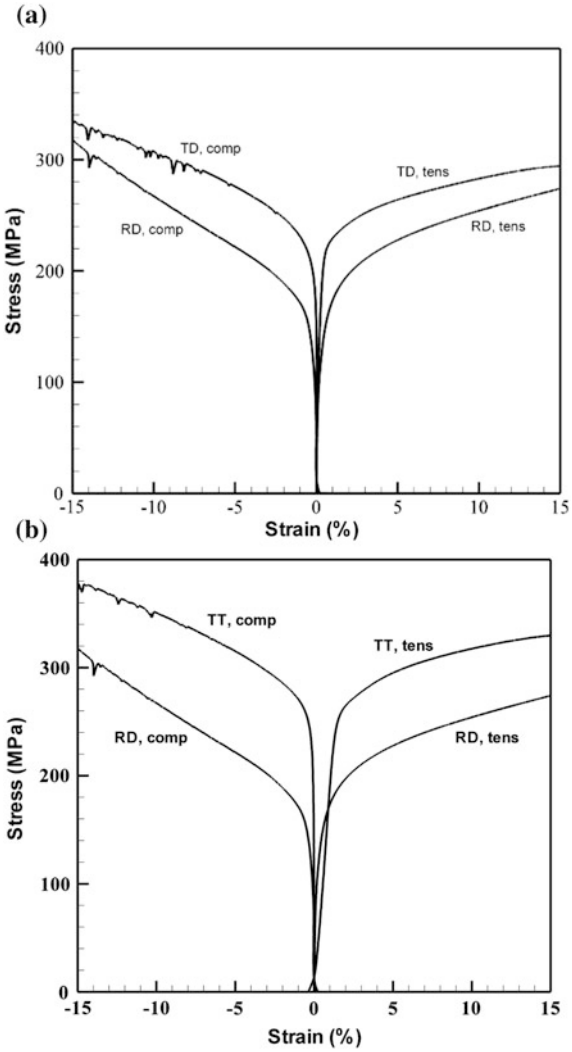

Fig. 5.23 Comparison between the stress–strain response in tension–compression and experimental data for **a** rolling (RD) and transverse (TD) directions, respectively. **b** Rolling (RD) and normal (TT) directions, respectively of the high-purity α-Ti. Experimental data from [36]

Therefore, in the simulations of the mechanical response these values were set equal to the isotropic values (i.e., unity).

The corresponding theoretical yield loci along with the experimental values (represented by symbols) are shown in Fig. 5.25. The orthotropic yield criterion given by Eq. (5.136) captures with accuracy both the asymmetry and anisotropy in yielding exhibited by this high-purity α-Ti material. Note that for $\bar{\varepsilon}^p$ below 10% strain, the predicted yield loci have an elliptical type shape, which is typical for slip-dominated plastic deformation. Beyond this strain level, the criterion predicts that the yield loci have a triangular shape and that the tension–compression asymmetry is very pronounced. It is worth noting that this change in shape occurs at

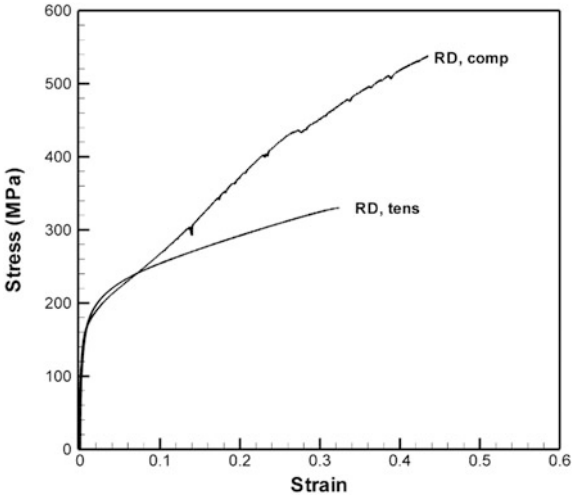

Fig. 5.24 Comparison between the uniaxial compression and tension response in the rolling direction of the high-purity α-Ti. Experimental data from [36]

Table 5.6 Nixon et al. [36] yield function coefficients for high-purity α-Ti corresponding to the onset of yielding ($\bar{\varepsilon}^p = 0$) and at fixed values of the equivalent plastic strain

$\bar{\varepsilon}^p$ (%)	a_2	a_3	a_6	c
0	0.92	1.99	1.33	−0.217
2.5	0.92	1.73	1.4	−0.220
5	0.834	1.648	1.366	−0.229
7.5	0.86	1.62	1.41	−0.260
10	0.89	1.606	1.45	−0.2754
20	0.944	1.425	1.426	−0.5908

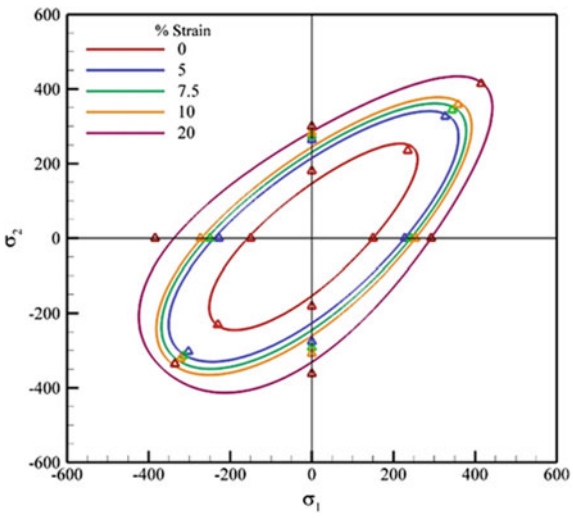

Fig. 5.25 Projection in the biaxial plane (RD, TD) of Nixon et al. [36] yield criterion for a high-purity α-Ti and experimental data (symbols) corresponding to fixed values of the equivalent plastic strain $\bar{\varepsilon}^p$. Stresses are in MPa

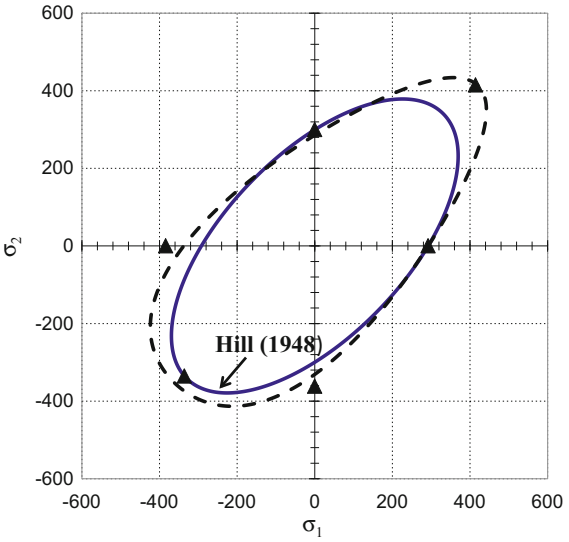

Fig. 5.26 Theoretical yield loci according to Hill [22] criterion and the Nixon et al. [36] criterion in comparison with experimental flow stresses (symbols) on high-purity α-Ti for an equivalent plastic strain of $\bar{\varepsilon}^p = 0.2$. Stresses are in MPa

the strain level associated with twin activation in the RD direction. For comparison purposes, the Hill [22] criterion was also applied to the same material. The coefficients F, G, and H were calculated using the analytic expressions of these coefficients in terms of the flow stresses along the axes of symmetry of the material [see Eq. (5.30)] corresponding to an equivalent plastic strain of 20%, the numerical values being: $F = 0.2251$, $G = 0.2639$, and $H = 0.7361$. In Fig. 5.26 are shown the theoretical yield loci according to the Hill [22] criterion along with the yield locus according to the orthotropic and asymmetric yield criterion given by Eq. (5.136) for $\bar{\varepsilon}^p = 0.2$. As expected, Hill [22] yield criterion cannot capture the observed yielding behavior while the proposed model describes very well the pronounced strength differential effects displayed by the material.

For hcp materials and in particular this α-Ti material even for monotonic loadings, the tension–compression asymmetry and the texture evolve with accumulated plastic deformation (see Figs. 5.23 and 5.24 and the texture measurements reported in [36]). However, specifying the expression of the yield function in the form:

$$F(\boldsymbol{\sigma}, \bar{\varepsilon}^p) = \bar{\sigma}(\boldsymbol{\sigma}, \bar{\varepsilon}^p) - Y(\bar{\varepsilon}^p) \tag{5.151}$$

where $\bar{\sigma}$ is given by Eq. (5.138) and $Y(\bar{\varepsilon}^p)$ is the effective stress–effective plastic strain relationship in a given direction (e.g., the tensile rolling direction). Even if the components of the fourth-order tensor $\mathbf{L}$ given by Eq. (5.137) and of the coefficient c, for a given level of strain can be determined based on the available experimental data, establishing analytical expressions for the evolution of all these parameters in terms of $\bar{\varepsilon}^p$ is very challenging. Therefore, Nixon et al. [36] used the methodology proposed in Plunkett et al. [38] for the description of the evolution of the anisotropy and tension–compression asymmetry. Specifically, using the experimental yield

stress data, the coefficients involved in the yield criterion corresponding to initial yielding and a set of values of the equivalent plastic strain, say $\bar{\varepsilon}_1^p < \bar{\varepsilon}_2^p < \cdots < \bar{\varepsilon}_m^p$ were identified and then the effective stress $\tilde{\sigma}^j = \bar{\sigma}\{\boldsymbol{\sigma}, a_i(\bar{\varepsilon}_j^p), c(\bar{\varepsilon}_j^p)\}$ according to the criterion [see Eq. (5.138)] as well as $Y^j = Y(\bar{\varepsilon}_j^p)$ corresponding to the each of the individual strain level $\bar{\varepsilon}_j^p$, j = 1, …, m were calculated. To obtain the yield surface corresponding to any given level of accumulated strain, an interpolation procedure was used. Specifically, for a given arbitrary level of $\bar{\varepsilon}^p$, the anisotropic yield function was taken of the form:

$$F(\boldsymbol{\sigma}, \bar{\varepsilon}^p) = \Gamma(\sigma, \bar{\varepsilon}^p) - \Pi(\bar{\varepsilon}^p), \tag{5.152}$$

with

$$\Gamma = \xi(\bar{\varepsilon}^p)\tilde{\sigma}^j + (1 - \xi(\bar{\varepsilon}^p))\tilde{\sigma}^{j+1} \tag{5.153}$$

and

$$\Pi = \xi(\bar{\varepsilon}^p) \cdot Y^j + (1 - \xi(\bar{\varepsilon}^p)) \cdot Y^{j+1} \tag{5.154}$$

for any $\bar{\varepsilon}_j^p \leq \bar{\varepsilon}^p \leq \bar{\varepsilon}_{j+1}^p$, j = 1, …, m − 1. For a linear interpolation scheme, the weighting parameter $\xi(\bar{\varepsilon}_p)$ appearing in Eqs. (5.153) and (5.154) is defined as:

$$\xi(\bar{\varepsilon}^p) = \frac{\bar{\varepsilon}_{j+1}^p - \bar{\varepsilon}^p}{\bar{\varepsilon}_{j+1}^p - \bar{\varepsilon}_j^p} \tag{5.155}$$

such that $\xi(\bar{\varepsilon}_j^p) = 1$ and $\xi(\bar{\varepsilon}_{j+1}^p) = 0$.

For a detailed discussion of the F.E. implementation of an elastic-plastic model, the reader is referred to Chap. 2. In the following, are presented the F.E. simulations for uniaxial loadings using the orthotropic and asymmetric Nixon et al. [36] yield criterion in conjunction with Eqs. (5.152)–(5.155) and associated flow rule carried out with the explicit F.E. code EPIC [27]. The F.E. simulations shown in Figs. 5.27, 5.28 and 5.29 involve a single element with eight nodes and a single integration point. The cell was stretched uniaxially and the stress versus strain results obtained were compared to the appropriate experimental data. For each simulation, four nodes on one face of the element were restrained and the four nodes on the opposite face were given a constant velocity in either the tensile or compressive direction. Note that the model accurately reproduces the data for each loading condition (see Fig. 5.29).

Moreover, the asymmetric and orthotropic yield criterion given by Eq. (5.138) in conjunction with the interpolation procedure described by Eqs. (5.152)–(5.155) was benchmarked against beam bending test results reported in [37]. The reason for choosing the bending test is that it provides validation for the theoretical description of the tension–compression asymmetry in yielding. The bending tests were carried out on rectangular bars of square cross-section. Four beams were cut from the plate: two with

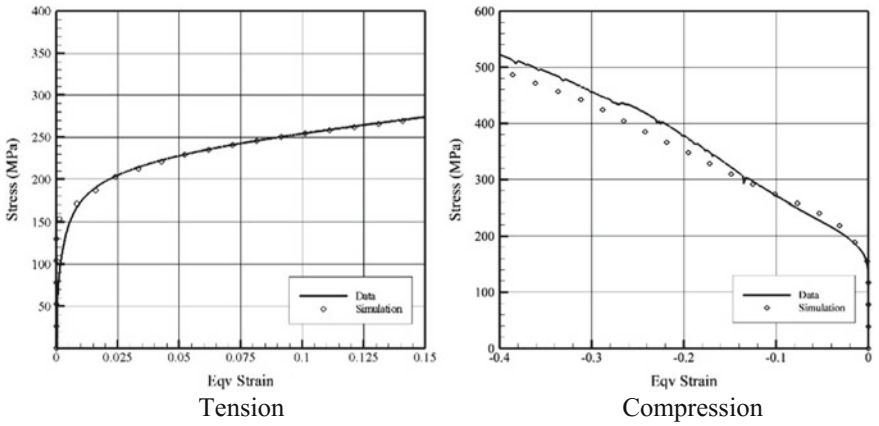

Fig. 5.27 Comparison between finite element simulation results using the Nixon et al. [36] model (Eq. 5.138) and experimental data corresponding to uniaxial loading in the rolling direction (RD) of a high-purity α-Ti. Symbols are simulation results

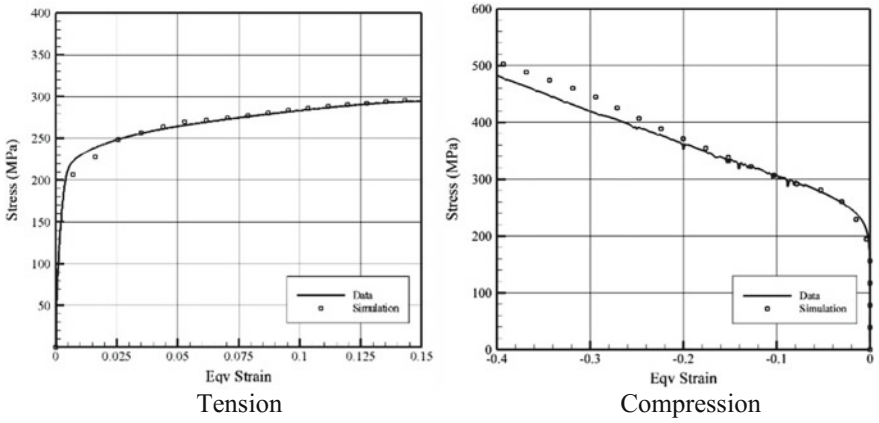

Fig. 5.28 Comparison between finite element simulation results using the Nixon et al. [36] model (Eq. 5.138) and experimental data corresponding to uniaxial loading in the transverse direction (TD) of a high-purity α-Ti. Symbols are simulation results

the long axis along the rolling direction (RD) and two with the long axis along the transverse direction (TD). These four test configurations are shown in Fig. 5.30a.

Along one side of each beam tested, a speckle pattern was sprayed and digital image correlation (DIC) was used to determine the strain field after deformation (see Fig. 5.30b). The grid and subsequent strain field did not cover the entire speckle field (see [37]). The deformed specimens were cut at the midpoint along the axis to examine the final deformed cross-sections. Measurements at this cross-section were taken for comparison to the F.E. simulations. The simulated final

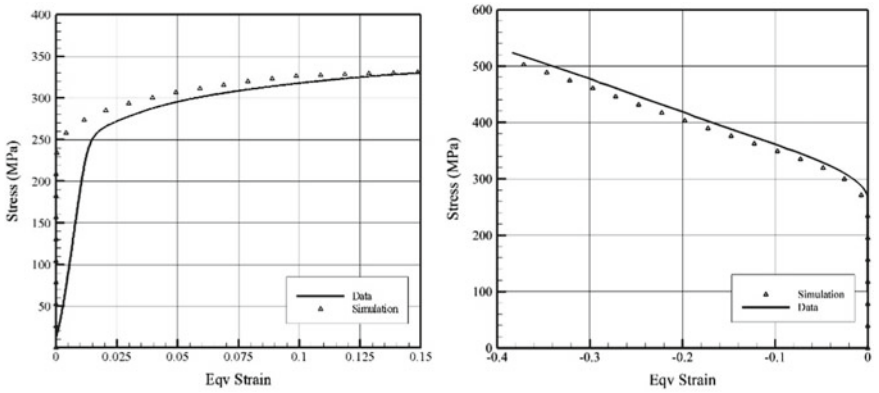

Fig. 5.29 Comparison between finite element simulation results using the Nixon et al. [36] model and experimental data corresponding to uniaxial loading in the through-thickness direction (TT) of a high-purity α-Ti. Symbols are simulation results

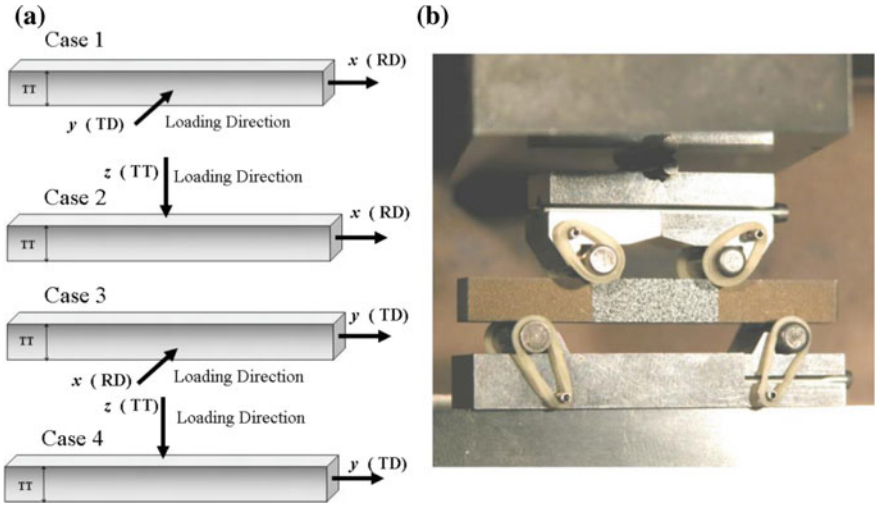

Fig. 5.30 Four point beam bending test **a** specimen configurations: in Cases 1 and 2 the long axis of the specimen is aligned with the rolling direction of the α-Ti-plate (*x*-axis = RD); for Cases 3 and 4, the long axes of the respective specimens are aligned with the transverse direction of the plate (*y*-axis = TD); TT designates the through-thickness direction of the plate. **b** Four point beam bending test jig with test specimen

cross-sections for the four configurations shown in Fig. 5.31 confirm that the model captures the major features of the mechanical behavior of the high-purity Ti tested. Indeed, it accurately predicts that when the TT direction is perpendicular to the loading direction i.e., Case 1 and Case 3 in Fig. 5.30, the cross-sections of the

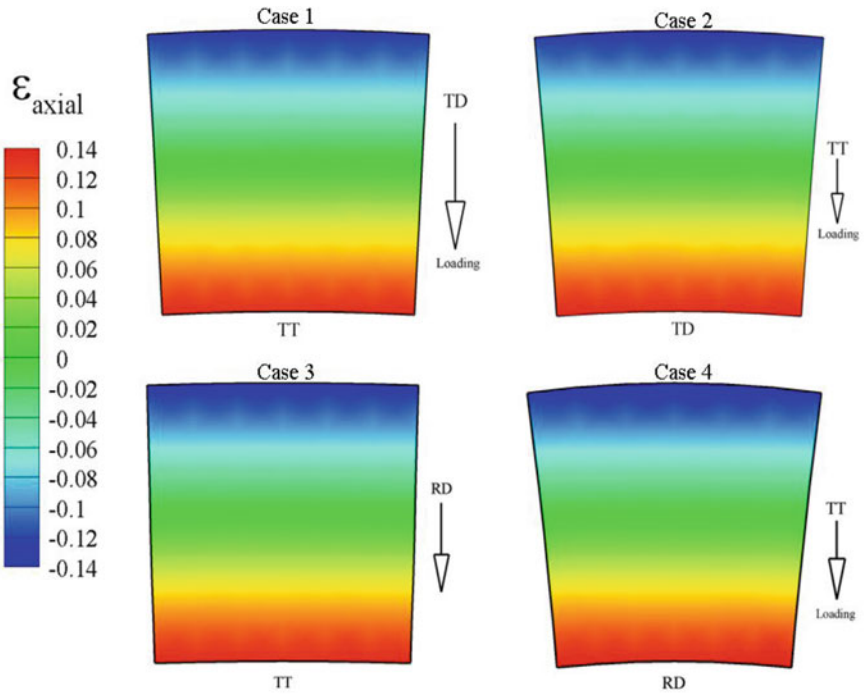

Fig. 5.31 F.E. simulated cross-section of the bent bars using the Nixon et al. [36] model for the four loading configurations shown in Fig. 5.30 (after Nixon et al. [37])

deformed beams are nearly square. This is because the hardest to deform direction is the TT direction (or **z**-axis).

On the other hand, for the bending tests where the loading direction is along the TT direction (Case 2 and Case 4 in Fig. 5.30a), it is predicted that the deformed cross-sections are wedge-shaped. This is because the material deforms much more in the TD direction and RD direction than along the TT direction (Case 2). In Case 4, there is more lateral strain than in Case 2, which is consistent with the material being harder in the TD than the RD as revealed by the results of the uniaxial loading tests (see Fig. 5.23). A comparison between the photographed cross-sections and F.E. simulations is shown in Fig. 5.32. Excellent agreement is observed.

In what follows, comparisons between F.E. axial strains obtained with the Nixon et al. [36] model and the experimental axial strains obtained by DIC are discussed. The axial strain is defined as the strain along the long axis of the given beam specimen. Thus, for Case 1 loading the axial strain is along the x-axis (RD) of the plate (see also Fig. 5.30a). For this loading case, the comparison of the respective strain contours is shown in Fig. 5.33a. Figure 5.33b presents a comparison between the experimental and theoretical predictions of the variation of the axial strain along the height of this beam (**y**-axis which corresponds to the TD direction of the plate from which the beam specimen was cut) at the mid-section of the beam. Note again

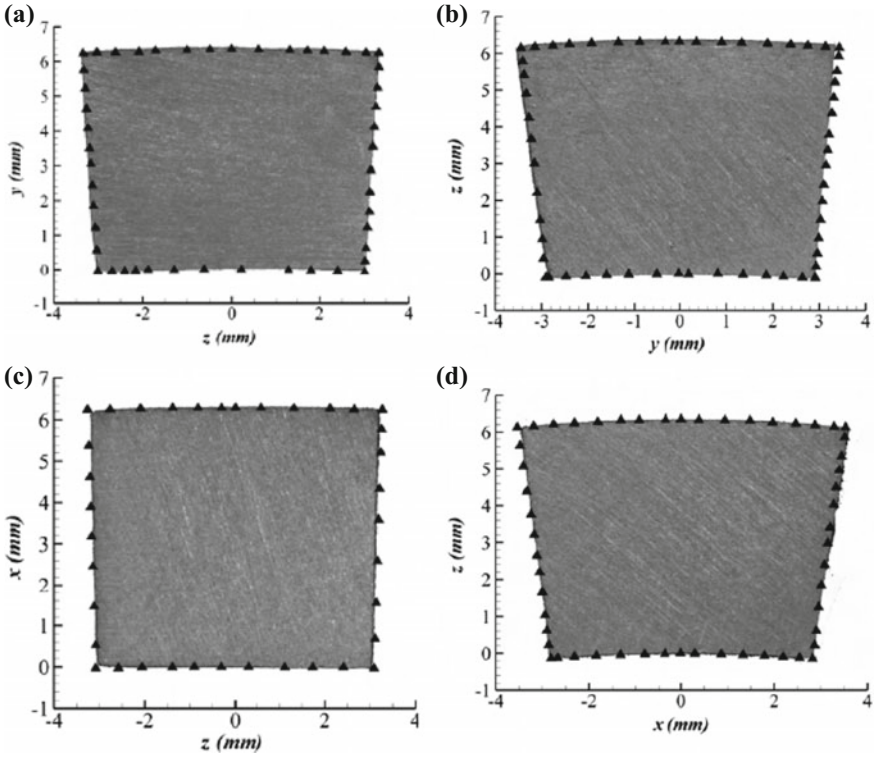

Fig. 5.32 Comparison of the photographed cross-sections of the bent bars and F.E. simulation using Nixon et al. [36] model (symbols) for the four loading configurations shown in Fig. 5.30: **a** Case 1. **b** Case 2. **c** Case 3 and **d** Case 4; x-axis designates the rolling direction (RD); y-axis denotes the transverse direction (TD), and z-axis the through-thickness (TT) direction of the high-purity α-Ti plate from which the specimens were cut (after Nixon et al. [37])

that the data from the experiment does not cover the entire area, due to the DIC technique used. A very good agreement between the experimental and simulation results is observed. In particular, the model captures very well the upward shift of the neutral axis of the beam (i.e., the point at which the longitudinal strain vanishes is above the beam midpoint in the vertical direction). The reason for this shift is that the material is softer in tension than in compression. Let us recall that in the model (Eq. 5.138), the anisotropy coefficients a_2, a_3, a_6 and the strength differential parameter c were considered functions of the accumulated plastic strain (see Table 5.6). The accuracy of the F.E. results also shows that for this material, the model captures accurately the evolution of the tension–compression asymmetry of this material. Figure 5.34a shows the comparison of the respective strain contours for Case 2 (see Fig. 5.30a) while a plot of the axial strain versus the height of the beam is shown in Fig. 5.34b. Again, there is very good agreement between experimental data and simulated results. Figure 5.35a shows the comparison

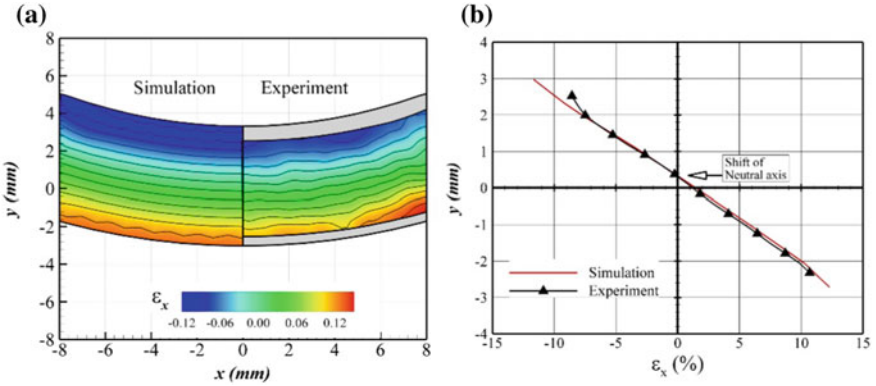

Fig. 5.33 Case 1 loading: **a** Comparison of the F.E. axial strain contours (ε_x) obtained with Nixon et al. [36] model against experimental data. **b** Axial strain ε_x versus height at the centerline (x = rolling direction, y = transverse direction) of the high-purity α-Ti plate (after Nixon et al. [37])

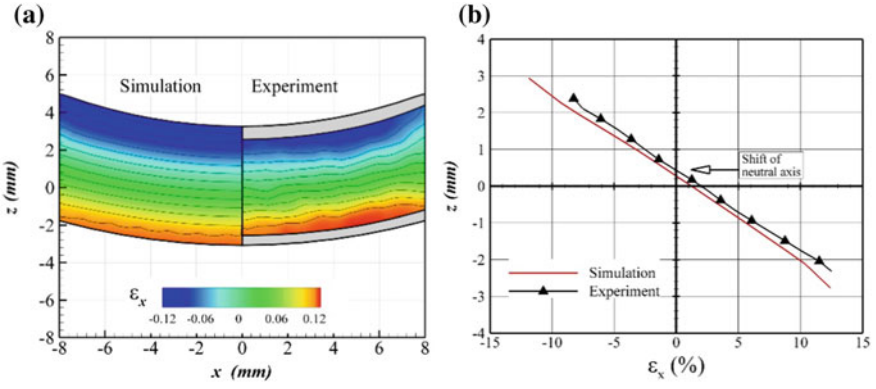

Fig. 5.34 Case 2 loading: **a** Comparison of the F.E. axial strain contours (ε_x) obtained with Nixon et al. [36] model against experimental data. **b** Axial strain ε_x versus height at the centerline (x = rolling direction, z = through-thickness direction) of the high-purity α-Ti plate (after Nixon et al. [37])

between experimental and simulated strain contours for Case 3. Note the good agreement between the experimental and simulation results; in particular, the model (see Fig. 5.35b) describes very well the upward shift of the neutral axis. Finally, Fig. 5.36a shows the comparison of the simulated and experimental axial strain contours in Case 4, while Fig. 5.36b shows that for this loading scenario, once again, the model correctly predicts the shift of the neutral axis. In summary, the model correctly predicts that for the bent α-Ti beams, the larger is the σ_T/σ_C ratio along the beam longitudinal direction, the larger is the upward shift of the neutral axis becomes.

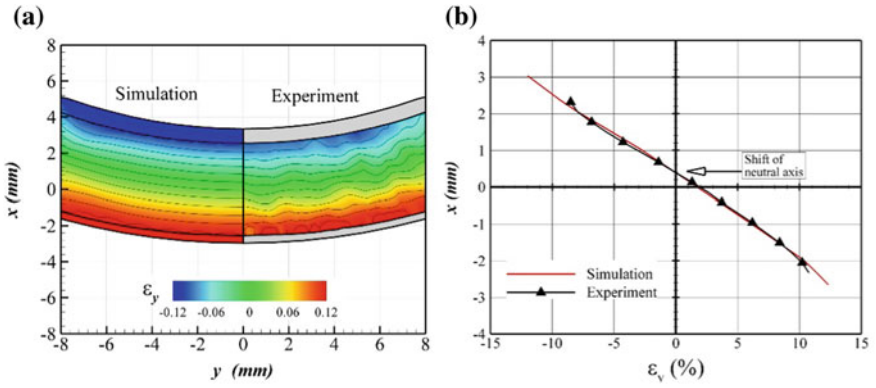

Fig. 5.35 Case 3 loading: **a** Comparison of the F.E. axial strain contours (ε_y) obtained with Nixon et al. [36] model against experimental data. **b** Axial strain ε_y versus height at the centerline (x = rolling direction, y = transverse direction) of the high-purity α-Ti plate (after Nixon et al. [37])

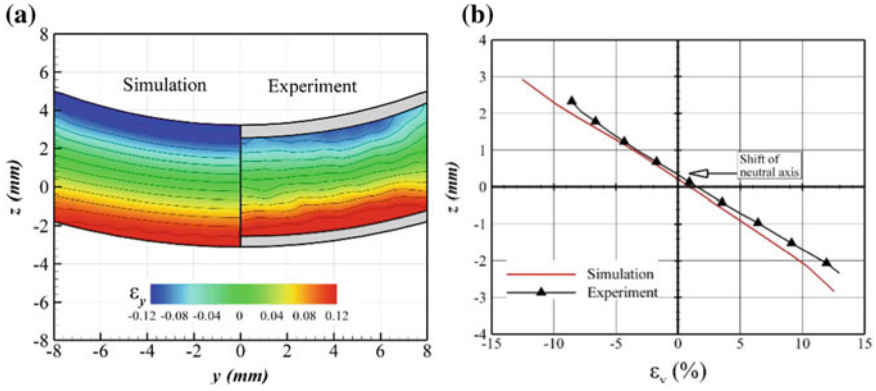

Fig. 5.36 Case 4 loading: **a** Comparison of the F.E. axial strain contours (ε_y) obtained with Nixon et al. [36] model against experimental data. **b** Axial strain ε_y versus height at the centerline (y = transverse direction, z = through-thickness direction) of the high-purity α-Ti plate (after Nixon et al. [37])

5.4.3 Orthotropic and Asymmetric Yield Criterion of Cazacu et al. [14]

5.4.3.1 Yielding Description

To model the observed anisotropy and tension–compression asymmetry of textured polycrystalline metallic materials, Cazacu et al. [14] used the linear transformation approach (see Sect. 5.1) to extend to orthotropy the isotropic and asymmetric yield criterion

$$F(s_1, s_2, s_3) = (|s_1| - ks_1)^a + (|s_2| - ks_2)^a + (|s_3| - ks_3)^a \tag{5.156}$$

(see Chap. 4 for the detailed presentation of this isotropic criterion) where a and k are material parameters and s_i, $i = 1, \ldots, 3$ are the principal values of the stress deviator $\mathbf{s}$. Specifically, a single linear transformation $\mathbf{L}$ was applied to the stress deviator $\mathbf{s}$, i.e., in the above expression s_1, s_2, s_3 were substituted by $\widehat{\sigma}_1$, $\widehat{\sigma}_2$, $\widehat{\sigma}_3$, the principal values of the transformed tensor,

$$\widehat{\sigma} = \mathbf{L}\mathbf{s}. \tag{5.157}$$

Thus, the Cazacu et al. [14] orthotropic yield condition is of the form:

$$g(\widehat{\sigma}_1, \widehat{\sigma}_2, \widehat{\sigma}_3) = \left(|\widehat{\sigma}_1| - k\widehat{\sigma}_1\right)^a + \left(|\widehat{\sigma}_2| - k\widehat{\sigma}_2\right)^a + \left(|\widehat{\sigma}_3| - k\widehat{\sigma}_3\right)^a. \tag{5.158}$$

It is important to note that the only restriction imposed on the fourth-order symmetric tensor $\mathbf{L}$ is to be invariant with respect to any transformation belonging to the orthotropic group (see Chap. 3). Thus, the tensor $\mathbf{L}$ is represented in the $(\mathbf{x}, \mathbf{y}, \mathbf{z})$ coordinate associated to the orthotropic axes and in Voigt notation by the following 6×6 matrix:

$$\mathbf{L} = \begin{bmatrix} L_{11} & L_{12} & L_{13} & 0 & 0 & 0 \\ L_{12} & L_{22} & L_{23} & 0 & 0 & 0 \\ L_{13} & L_{23} & L_{33} & 0 & 0 & 0 \\ 0 & 0 & 0 & L_{44} & 0 & 0 \\ 0 & 0 & 0 & 0 & L_{55} & 0 \\ 0 & 0 & 0 & 0 & 0 & L_{66} \end{bmatrix} \tag{5.159}$$

Due to the homogeneity in stresses of the yield function given by Eq. (5.158), we can scale the anisotropy coefficients by L_{11}, or equivalently, set $L_{11} = 1$. Therefore, for 3-D stress conditions the Cazacu et al. [14] orthotropic yield criterion involves eight anisotropy coefficients, the homogeneity parameter a, and a parameter k associated with strength differential effects in plastic flow. For untextured (i.e., isotropic materials) $\mathbf{L} = \mathbf{I_4}$, where $\mathbf{I_4}$ is the fourth-order symmetric identity tensor (for the definition of $\mathbf{I_4}$, see Chap. 1).

It is very important to note that in general for orthotropic symmetry, the tensor $\mathbf{L}$ is not deviatoric, and therefore, the transformed tensor $\widehat{\sigma}$ is not traceless. Nevertheless because of the specific expression of $g(\widehat{\sigma}_1, \widehat{\sigma}_2, \widehat{\sigma}_3)$, the orthotropic Cazacu et al. [14] yield criterion is insensitive to hydrostatic pressure and as such the incompressibility condition is satisfied (for the mathematical proof, the reader is referred to [14]). Given that for $-1 \leq k \leq 1$ and any $a \geq 1$, the isotropic form of the criterion is convex (for the mathematical proof, see Chap. 4), the orthotropic yield function $g(\widehat{\sigma}_1, \widehat{\sigma}_2, \widehat{\sigma}_3)$ is also convex in the variables $\widehat{\sigma}_1$, $\widehat{\sigma}_2$, $\widehat{\sigma}_3$.

It was shown that for most textured polycrystalline materials (e.g., Mg, Ti, Zr, Al alloys), the quadratic form of the Cazacu et al. [14] orthotropic yield criterion [i.e., the coefficient $a = 2$ in Eq. (5.158)] and only one linear transformation $\mathbf{L}$, describes with accuracy the yielding behavior (see for example, [14, 38, 41]). For this reason, in the following we present the key properties and the procedure for identification of the parameters for the quadratic form of this criterion. The effective stress associated with the quadratic form of the Cazacu et al. [14] orthotropic yield criterion is:

$$\tilde{\sigma}_e = \tilde{m}\sqrt{\sum_{i=1}^{3}\left(\left|\widetilde{\sigma}_i\right| - k\widetilde{\sigma}_i\right)^2}, \tag{5.160}$$

where $\tilde{m}$ is a constant defined such that the equivalent stress, $\tilde{\sigma}_e$, reduces to the tensile flow stress along the $\mathbf{x}$ (or RD) direction. Thus, $\tilde{m}$ is expressed in terms of the anisotropy coefficients L_{ij} with $i, j = 1, \ldots, 3$ and the material parameter k as follows:

$$\tilde{m} = 1/\sqrt{(|\Phi_1| - k\Phi_1)^2 + (|\Phi_2| - k\Phi_2)^2 + (|\Phi_3| - k\Phi_3)^2} \tag{5.161}$$

where

$$\begin{aligned} &\Phi_1 = (2L_{11} - L_{12} - L_{13})/3; \quad \Phi_2 = (2L_{12} - L_{22} - L_{23})/3; \\ &\Phi_3 = (2L_{13} - L_{23} - L_{33})/3 \end{aligned} \tag{5.162}$$

Let σ_x^T denote the uniaxial tensile yield stress along the $\mathbf{x}$-axis (RD direction). The strength differential parameter k and the anisotropy coefficients L_{ij}, with $i, j = 1, \ldots, 3$ and L_{44} can be determined from the experimental normalized tensile flow stress values $\tilde{\sigma}_\theta^T = \sigma_\theta^T/\sigma_x^T$ and the absolute values of the compressive flow stresses $\tilde{\sigma}_\theta^C = \sigma_\theta^C/\sigma_x^T$ and Lankford coefficients r_θ, where θ represents the angle between the uniaxial loading direction and the rolling direction (see also [14]). Indeed, let us first note that for in-plane loadings (i.e., the only nonzero stress components σ_{xx}, σ_{yy}, σ_{xy}), the only nonzero components of the transformed stress tensor $\widetilde{\sigma}$ [see Eq. (5.157)] are:

$$\begin{aligned} &\widetilde{\sigma}_{xx} = \Phi_1\sigma_{xx} + \Psi_1\sigma_{yy}; \quad \widetilde{\sigma}_{yy} = \Phi_2\sigma_{xx} + \Psi_2\sigma_{yy}; \quad \widetilde{\sigma}_{zz} = \Phi_3\sigma_{xx} + \Psi_3\sigma_{yy}; \\ &\text{and } \widetilde{\sigma}_{xy} = L_{66}\sigma_{xy}, \end{aligned} \tag{5.163}$$

with

$$\begin{aligned} &\Psi_1 = (-L_{11} + 2L_{12} - L_{13})/3; \quad \Psi_2 = (-L_{12} + 2L_{22} - L_{23})/3; \\ &\Psi_3 = (-L_{13} + 2L_{23} - L_{33})/3, \end{aligned} \tag{5.164}$$

Hence, the principal values of the transformed tensor $\widehat{\sigma}$ are given by:

$$\widehat{\sigma}_{1,2}=\left(\widehat{\sigma}_{xx}+\widehat{\sigma}_{yy}\pm\sqrt{\left(\widehat{\sigma}_{xx}-\widehat{\sigma}_{yy}\right)^2+4\widehat{\sigma}_{xy}^2}\right)/2 \quad \text{and} \quad \widehat{\sigma}_3=\widehat{\sigma}_{zz} \tag{5.165}$$

Using Eqs. (5.163)–(5.165), it follows that according to the quadratic form of the Cazacu et al. [14] criterion (Eq. 5.160),

$$\sigma_\theta^T=\sigma_x^T\sqrt{\frac{(|\Phi_1|-k\Phi_1)^2+(|\Phi_2|-k\Phi_2)^2+(|\Phi_3|-k\Phi_3)^2}{(|A_1(\theta)|-k|A_1(\theta)|)^2+(|A_2(\theta)|-k|A_2(\theta)|)^2+(|A_3(\theta)|-k|A_3(\theta)|)^2}} \tag{5.166}$$

where

$$\begin{aligned}A_{1,2}(\theta)&=\cos^2\theta(\Phi_1+\Phi_2)/2\ +\ \sin^2\theta(\Psi_1+\Psi_2)/2\pm\sqrt{\Delta}\\ A_3(\theta)&=\Phi_3\cos^2\theta+\Psi_3\sin^2\theta,\end{aligned}$$

with

$$\Delta=\sqrt{\left(\cos^2\theta(\Phi_1-\Phi_2)/2+\ \sin^2\theta(\Psi_1-\Psi_2)/2\right)^2+L_{66}^2\sin^2\theta\cos^2\theta}. \tag{5.167}$$

For uniaxial compressive loadings in the plane of the plate,

$$\sigma_\theta^C=\sigma_x^T\sqrt{\frac{(|\Phi_1|-k\Phi_1)^2+(|\Phi_2|-k\Phi_2)^2+(|\Phi_3|-k\Phi_3)^2}{(|A_1(\theta)|+k|A_1(\theta)|)^2+(|A_2(\theta)|+k|A_2(\theta)|)^2+(|A_3(\theta)|+k|A_3(\theta)|)^2}} \tag{5.168}$$

Note that for uniaxial loadings in the normal direction (**z**-axis) of the plate, the respective yield stresses in uniaxial compression and tension are:

$$\begin{aligned}\sigma_z^C&=\sigma_x^T\sqrt{\frac{(|\Phi_1|-k\Phi_1)^2+(|\Phi_2|-k\Phi_2)^2+(|\Phi_3|-k\Phi_3)^2}{(|\Omega_1|+k|\Omega_1|)^2+(|\Omega_2|+k|\Omega_2|)^2+(|\Omega_3|+k|\Omega_3|)^2}},\\ \sigma_z^T&=\sigma_x^T\sqrt{\frac{(|\Phi_1|-k\Phi_1)^2+(|\Phi_2|-k\Phi_2)^2+(|\Phi_3|-k\Phi_3)^2}{(|\Omega_1|-k|\Omega_1|)^2+(|\Omega_2|-k|\Omega_2|)^2+(|\Omega_3|-k|\Omega_3|)^2}}\end{aligned} \tag{5.169}$$

where

$$\begin{aligned}&\Omega_1=(L_{11}+L_{12}-2L_{13})/3;\quad \Omega_2=(L_{12}+L_{22}-2L_{23})/3;\\ &\Omega_3=(L_{13}+L_{23}-2L_{33})/3,\end{aligned} \tag{5.170}$$

Moreover, plastic incompressibility results in: $\sigma_b^T = \sigma_z^C$ and $\sigma_b^C = \sigma_z^T$, where σ_b^T and σ_b^C denote the absolute values of the yield stress in equibiaxial tension–compression, respectively.

The plastic strain ratio, r_θ, under uniaxial loading in a direction at angle θ with the rolling direction in the plane $(\mathbf{x}, \mathbf{y})$ is:

$$r_\theta = -\frac{\sin^2\theta \dfrac{\partial \tilde{\sigma}_e}{\partial \sigma_{xx}} - \sin(2\theta)\dfrac{\partial \tilde{\sigma}_e}{\partial \sigma_{xy}} + \cos^2\theta \dfrac{\partial \tilde{\sigma}_e}{\partial \sigma_{yy}}}{\dfrac{\partial \tilde{\sigma}_e}{\partial \sigma_{xx}} + \dfrac{\partial \tilde{\sigma}_e}{\partial \sigma_{yy}}}, \tag{5.171}$$

with $\tilde{\sigma}_e$ is given by Eq. (5.160).

In particular, it follows that:

$$\begin{aligned}
r_0^T &= -\frac{(1-k)^2\Phi_1\Psi_1 + (1+k)^2(\Phi_2\Psi_2 + \Phi_3\Psi_3)}{(1-k)^2\Phi_1(\Psi_1+\Phi_1) + (1+k)^2(\Phi_2\Psi_2 + \Phi_3\Psi_3 + \Phi_2^2 + \Phi_3^2)} \\
r_{90}^T &= -\frac{(1-k)^2\Psi_2\Phi_2 + (1+k)^2(\Psi_1\Phi_1 + \Psi_3\Phi_3)}{(1-k)^2\Psi_2(\Phi_2+\Psi_2) + (1+k)^2(\Psi_1\Phi_1 + \Psi_3\Phi_3 + \Psi_1^2 + \Psi_3^2)} \\
r_0^C &= -\frac{(1+k)^2\Phi_1\Psi_1 + (1-k)^2(\Phi_2\Psi_2 + \Phi_3\Psi_3)}{(1+k)^2\Phi_1(\Psi_1+\Phi_1) + (1-k)^2(\Phi_2\Psi_2 + \Phi_3\Psi_3 + \Phi_2^2 + \Phi_3^2)} \\
r_{90}^C &= -\frac{(1+k)^2\Psi_2\Phi_2 + (1-k)^2(\Psi_1\Phi_1 + \Psi_3\Phi_3)}{(1+k)^2\Psi_2(\Phi_2+\Psi_2) + (1-k)^2(\Psi_1\Phi_1 + \Psi_3\Phi_3 + \Psi_1^2 + \Psi_3^2)}
\end{aligned} \tag{5.172}$$

with Φ_1 to Φ_3 given by Eq. (5.162), Ψ_1 to Ψ_3 given by Eq. (5.164), and the superscripts T and C designating tensile and compressive states, respectively.

In conclusion, using the above equations, the strength differential parameter k and the anisotropy coefficients L_{ij}, with $i, j = 1, \ldots, 3$ and L_{66} can be determined by minimizing an error function of the form

$$\begin{aligned}
E(L_{12}, L_{13}, L_{22}, L_{23}, L_{33}, L_{66}, k) = &\sum_i^n \eta_i \left(1 - \frac{\left(\sigma_\theta^T\right)_i^{\text{th}}}{\left(\sigma_\theta^T\right)_i^{\text{data}}}\right)^2 \\
&+ \sum_j^m \gamma_j \left(1 - \frac{\mathrm{r}_j^{\text{th}}}{\mathrm{r}_j^{\text{data}}}\right)^2 + \sum_l^p \alpha_l \left(1 - \frac{\left(\sigma_\theta^C\right)_l^{\text{th}}}{\left(\sigma_\theta^C\right)_l^{\text{data}}}\right)^2
\end{aligned} \tag{5.173}$$

In the above equation, the variable "n" (respectively, m and p) represents the number of experimental directional tensile flow stresses (respectively, r-ratios and directional compressive flow stresses) available, the superscript indicates whether the respective value is experimental or calculated using the above expressions while the constants η_i, γ_j, and α_l are weight factors. The remaining anisotropy coefficients

L_{44} and L_{55} which are associated with out-of-plane properties may be determined using data such as the yield stress in simple shear in the $(\mathbf{y}, \mathbf{z})$ and $(\mathbf{x}, \mathbf{z})$ planes, respectively (see [14]).

It is worth noting that the use of the Cazacu et al. [14] yield criterion has contributed to an improved understanding of the plastic behavior of hcp alloys. In particular, the capabilities of the Cazacu et al. [14] model to capture the anisotropy and tension–compression asymmetry of hcp materials have been clearly demonstrated. For example, excellent quantitative agreement between the finite-element axial strain and bending tests results has been obtained for Zr specimens by Plunkett et al. [38], the shift of the neutral axis (i.e., during bending test, the neutral axis is no longer at mid-height), and the final shape of the cross-section being accurately predicted. Furthermore, Revil-Baudard [40] has shown that an accurate prediction of strain localization prior to failure in a commercially pure Ti (T40) can only be achieved using a yield criterion that accounts for both the tension–compression asymmetry and the anisotropic behavior of this material. By comparing the F.E. predictions using the Cazacu et al. [14] and Hill [22] yield criteria to the DIC measurements of hydroforming tests, Revil-Baudard [40] concluded that the strain localization zone and the sudden drop of the thickness of the respective specimens are directly correlated to the tension compression asymmetry of the commercially pure Ti alloy. The predictive capabilities of the Cazacu et al. [14] yield criterion have also been assessed for Taylor impact tests on Zr ([39]) and Ti ([42]), and excellent quantitative agreement was obtained between the model predictions and the measured minor and major profiles of the impacted specimens.

In the next section, we present only few applications of this criterion [see Eq. (5.160)]. Specifically, it will be used to describe the anisotropy and tension–compression asymmetry of high-purity Ti and Mg AZ31 for uniaxial loadings. Furthermore, on the basis of an elastic-plastic model based on this yield criterion, it is shown that there is a correlation between Swift effects and the stress–strain behavior in uniaxial tension–compression of hcp metals. Moreover, following [41] it is shown that it is possible to explain and predict the strikingly different Swift effects in Ti- and Mg-based alloys.

5.4.3.2 Applications: Tension, Compression, and Torsion of hcp-Ti and Mg AZ31

Orthotropic high-purity α-Ti

First, it is presented the application of the quadratic form of the orthotropic yield criterion of Cazacu et al. [14] criterion to the description of the mechanical response of a high-purity α-Ti material for which quasi-static mechanical test data have been reported in [37] and were summarized in Sect. 5.4.2. To capture the experimentally observed difference in strain hardening rates between tension–compression loadings, all the material parameters involved in the expression of the Cazacu et al. [14]

Table 5.7 Cazacu et al. [14] yield function coefficients for high-purity α-Ti corresponding to the onset of yielding ($\bar{\varepsilon}^p = 0$) and several fixed values of the equivalent plastic strain $\bar{\varepsilon}^p$

$\bar{\varepsilon}^p$	L_{22}	L_{33}	L_{12}	L_{13}	L_{23}	L_{44}	L_{55}	L_{66}	k
0	0.850	0.836	0.281	0.388	0.439	0.476	0.527	0.639	−0.024
0.025	0.981	1.013	0.847	0.885	0.904	0.128	0.120	0.154	−0.070
0.05	0.971	1.009	0.750	0.801	0.824	0.218	0.206	0.259	−0.061
0.075	0.917	0.985	0.374	0.478	0.516	0.555	0.528	0.657	−0.084
0.2	0.975	0.898	−0.018	0.034	0.052	1.050	0.986	1.285	−0.392
0.3	1.032	0.954	−0.024	0.001	0.010	1.161	1.063	1.436	−0.650

Data after [37]. For any strain level $L_{11} = 1$ and $a = 2$

yield function, namely the anisotropy coefficients as well as the parameter k were considered to evolve with the equivalent plastic strain, $\bar{\varepsilon}^p$. The equivalent plastic $\bar{\varepsilon}^p$ strain associated with the criterion was calculated using the expression of $\tilde{\sigma}_e$ given by Eq. (5.160) and the work-equivalence principle (see also [23]). The procedure used for the identification of the parameters is that detailed in the preceding section. The numerical values of the parameter k and that of the anisotropy coefficients L_{ij} corresponding to initial yielding and four other individual levels of equivalent plastic strains (up to 0.3 strain) determined in this manner are listed in Table 5.7 while the values corresponding to any given intermediate level of plastic strain $\bar{\varepsilon}^p_j \leq \bar{\varepsilon}^p \leq \bar{\varepsilon}^p_{j+1}$ were obtained by linear interpolation, i.e.,

$$\begin{aligned} L_{ij}(\bar{\varepsilon}^p) &= \alpha(\bar{\varepsilon}^p) L_{ij}\left(\bar{\varepsilon}^p_j\right) + (1 - \alpha(\bar{\varepsilon}^p)) L_{ij}\left(\bar{\varepsilon}^p_{j+1}\right) \\ k(\bar{\varepsilon}^p) &= \alpha(\bar{\varepsilon}^p) k\left(\bar{\varepsilon}^p_j\right) + (1 - \alpha(\bar{\varepsilon}^p)) k\left(\bar{\varepsilon}^p_{j+1}\right) \end{aligned} \tag{5.174}$$

The interpolation parameter α involved in Eq. (5.174) is defined as:

$$\alpha = \frac{\bar{\varepsilon}^p - \bar{\varepsilon}^p_j}{\bar{\varepsilon}^p_{j+1} - \bar{\varepsilon}^p_j}.$$

In Fig. 5.37 are represented in the plane $(\sigma_{xx}, \sigma_{yy})$ the theoretical yield surfaces for the orthotropic α-Ti material according to the Cazacu et al. [14] yield criterion (Eq. 5.160) for several individual strain levels $\bar{\varepsilon}^p_j, j = 1, \ldots, 6$. It is worth noting that although at initial yielding and for strains under 10%, the tension–compression asymmetry is small (compare the tension–tension–compression–compression quadrants) and the surfaces have an elliptical shape, at 20% strain and beyond, the surfaces have a triangular shape, and the difference in response between tension–compression is pronounced (see also Fig. 5.38).

The Young modulus and Poisson coefficient for this high-purity α-Ti material are: E = 110 GPa and $\nu = 0.3$, respectively. Also, for this material, a Voce-type effective stress-effective plastic strain law of the form:

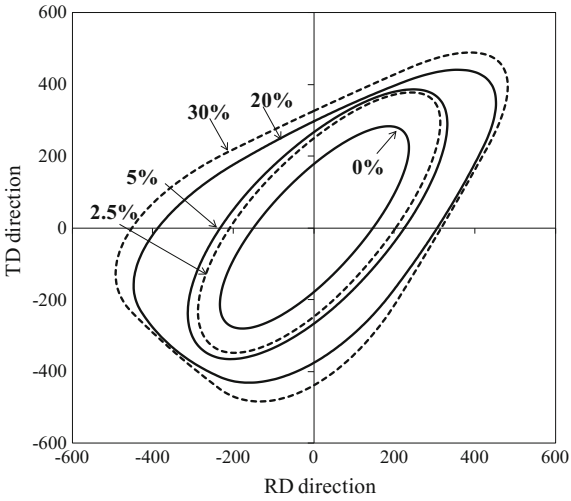

Fig. 5.37 Theoretical yield surfaces according to the Cazacu et al. [14] criterion for a high-purity α-Ti for different levels of accumulated plastic strain. Note the evolution of the shape of the yield locus from an elliptical toward a triangular shape

$$Y(\bar{\varepsilon}^p) = A_0 - A_1 \exp(-A_2 \bar{\varepsilon}^p), \tag{5.175}$$

where A_0, A_1, A_2 are constants approximates well the data in uniaxial tension along RD. The numerical values of the constants are: A_0 = 341 MPa, A_1 = 170 MPa and A_2 = 7.03.

Next, the stress–strain response in uniaxial tension along RD, TD, and ND directions was simulated and compared to the experimental stress–strain curves (see Fig. 5.38). All the simulations were carried out using the commercial F.E. code ABAQUS and a user material routine (UMAT) that was developed for this orthotropic elastic-plastic model. A fully implicit integration algorithm was used for solving the governing equations (for more details, see Chap. 2). It is worth noting that the quadratic form of Cazacu et al. [14] yield criterion in conjunction with the isotropic hardening law given by Eq. (5.175) identified from the RD data is able to capture precisely the key features of the plastic behavior of high-purity α-Ti (see Fig. 5.38); specifically, the strength differential between tension–compression is correctly predicted for all the three orthotropic directions.

Although no data were available concerning the response in torsion of the material, it is worth analyzing the material response according to the model and thus to provide insights on the behavior of the material. For more details about this initial and boundary problem, the reader should refer to Sect. 4.4.2. Here, we only recall the usual definitions of the axial and shear strains (see also Chap. 4) used, i.e.,

$$\varepsilon = \ln\left(1 + \frac{u}{L_0}\right) \quad \text{and} \quad \gamma = \frac{\Phi r}{L_0} \tag{5.176}$$

where r is the current radius, L_0 is the initial length, u is the axial displacement, and Φ is the twist angle. Simulation of the torsional response of the high-purity α-Ti is

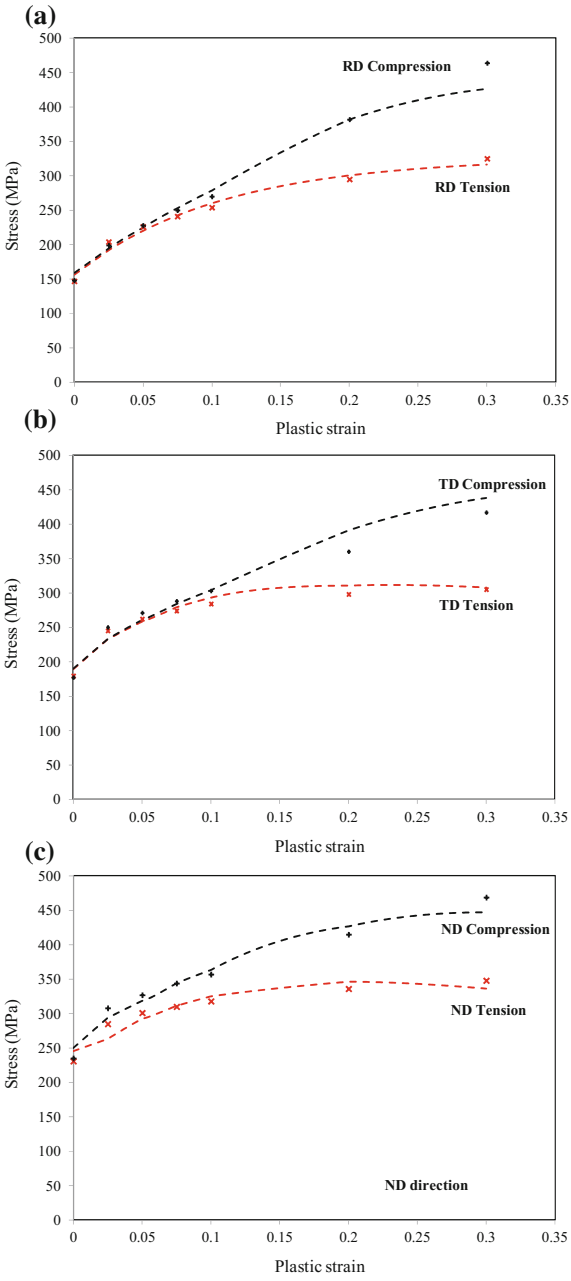

Fig. 5.38 stress–strain response in uniaxial tension–compression for a high-purity α-Ti in **a**. RD, **b**. TD, and **c**. ND directions. The symbols represent the experimental data and the solid lines the prediction of the orthotropic Cazacu et al. [14] yield criterion and isotropic hardening law

presented in Fig. 5.39. Note that irrespective of the direction about which the specimen is twisted, axial elongation is predicted. The nature of the axial strains (Swift effects) that develop correlates with the tension–compression asymmetry ratio in each direction. Indeed, for both RD and ND, the material is harder in

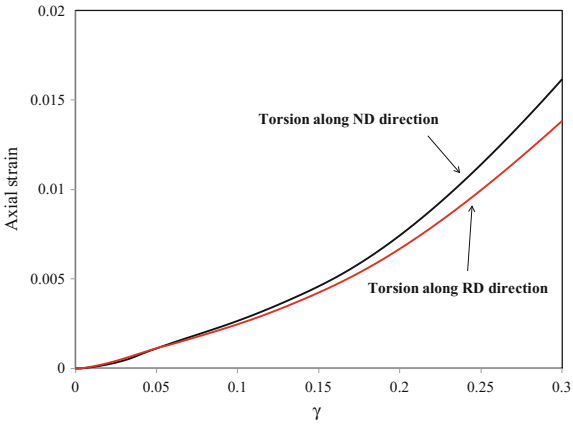

Fig. 5.39 Variation of the axial strain with shear strain during free-end torsion along RD and ND direction of a high-purity α-Ti obtained with the Cazacu et al. [14] yield criterion (after Revil-Baudard et al. [41])

compression than in tension, so elongation of the specimen occurs. The Swift effects are more pronounced in the ND direction, which correlates with this direction being that of most pronounced tension–compression asymmetry. It is worth noting that the F.E. prediction for the plastic behavior of Ti under free-end torsion, i.e., lengthening of the specimen, has been recently confirmed experimentally for a different high-purity Ti (see [48]).

Orthotropic AZ31-Mg alloy

Data concerning the monotonic quasi-static tension–compression responses of a Mg alloy AZ31 have been recently reported by Khan et al. [31]. Results of the tests on specimens cut along the RD, TD directions, and at 45° (DD) from RD have shown that the plastic response of this material is highly directional. The compression stress–strain curves exhibit a concave-up shape and steadily increasing hardening rate while the tensile curves have the standard concave-down appearance. Concerning the through-thickness direction (ND), only results in uniaxial compression were reported in [31]. Based on the experimental data provided in tension–compression, the parameters involved in the quadratic form of the orthotropic yield criterion of Cazacu et al. [14] criterion were identified using the procedure summarized in the preceding section. To describe the evolving anisotropy and tension–compression asymmetry observed experimentally, all the material parameters involved in the expression of the yield function were considered to evolve with accumulated plastic deformation. Specifically, using the experimental flow stress data, the parameter k and the anisotropy coefficients L_{ij} corresponding to initial yielding and several individual levels of equivalent plastic strains were determined. The numerical values of these parameters are listed in Table 5.8. Next, to obtain the values of these parameters corresponding to any given level of accumulated plastic strain $\bar{\varepsilon}_j^p \leq \bar{\varepsilon}^p \leq \bar{\varepsilon}_{j+1}^p$, linear interpolations were used [see Eq. (5.174)].

Table 5.8 Cazacu et al. [14] yield function coefficients for Mg AZ31 alloy corresponding to the onset of yielding ($\bar{\varepsilon}^p = 0$) and several fixed values of the equivalent plastic strain $\bar{\varepsilon}^p$

$\bar{\varepsilon}^p$	L_{22}	L_{33}	L_{12}	L_{13}	L_{23}	L_{44}	L_{55}	L_{66}	k
0.03	1.090	3.342	−0.168	0.098	0.243	7.30	7.74	0.730	−0.625
0.05	1.090	3.342	−0.168	0.098	0.243	7.30	7.74	0.730	−0.625
0.06	1.072	2.905	−0.595	−0.279	−0.096	10.39	11.02	1.039	−0.520
0.08	1.099	1.439	−0.817	−0.516	−0.350	11.28	11.95	1.128	−0.215
0.10	1.082	0.885	−0.762	−0.657	−0.509	10.12	11.21	1.058	−0.169

Data after [31]. For any strain level $L_{11} = 1$ and $a = 2$

The Young modulus and Poisson coefficient for this material are: $E = 45$ GPa and $v = 0.3$, respectively. The isotropic hardening law was identified from the uniaxial tension stress–strain response along the RD direction, the numerical values of the parameters involved in Eq. (5.175) being: $A_0 = 315.4$ MPa, $A_1 = 140.6$ MPa, $A_2 = 16.3$.

For Mg AZ31, the yield surfaces associated with the yield criterion corresponding to different levels of plastic strain are plotted in Fig. 5.40. Note that the criterion predicts that the shape of the surface evolves from a triangular shape to an elliptical shape. This evolution of the shape of the yield surfaces with accumulated plastic deformation is completely different than that for Ti materials (compare with Fig. 5.37). Nevertheless, with the same criterion it is possible to account for these strikingly different yielding evolutions in hcp Ti and hcp Mg-based materials.

The stress–strain response in uniaxial tension along RD, TD, and ND directions was simulated and compared to the experimental stress–strain curves available (see Fig. 5.41). It is worth noting that the yield criterion in conjunction with isotropic hardening captures precisely the unusual features of the plastic behavior of Mg AZ31 alloy, notably the S-shape of the experimental stress–strain curve in uniaxial

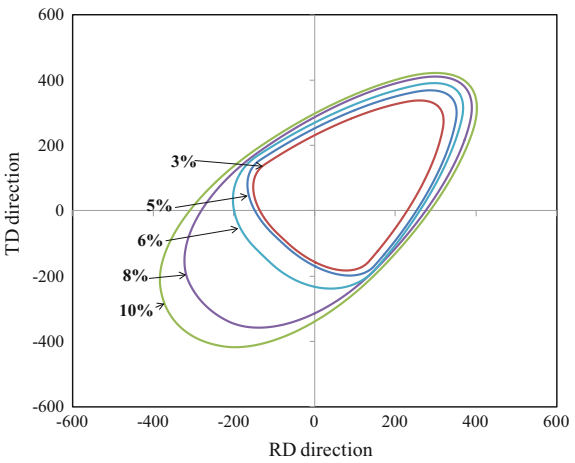

Fig. 5.40 Theoretical yield surfaces according to the Cazacu et al. [14] criterion for a Mg–AZ31 alloy for different level of accumulated plastic strain. Note the evolution of the shape of the yield locus from a triangular shape to an elliptical shape

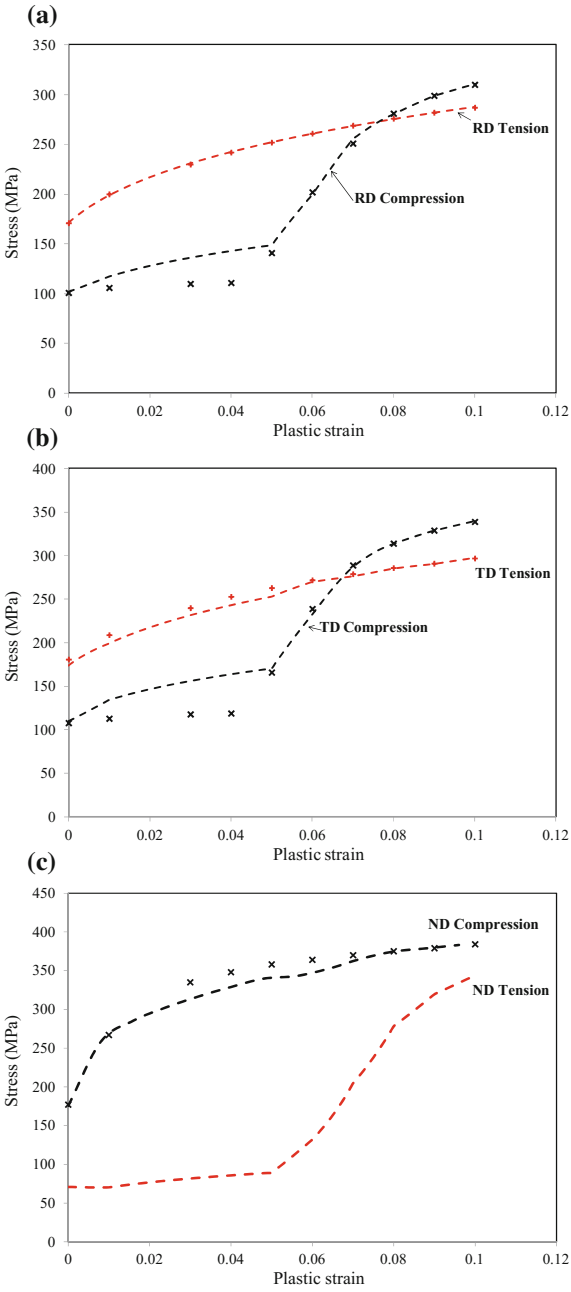

Fig. 5.41 stress–strain response in uniaxial tension–compression for a Mg AZ31 alloy in **a**. RD, **b**. TD, and **c**. ND directions. The symbols represent the experimental data from [31] and the dashed lines the prediction of the Cazacu et al. [14] yield criterion and isotropic hardening law (after Revil-Baudard et al. [41])

compression along RD and TD directions. Moreover, it predicts that in uniaxial tension along ND, the material should also display a sigmoidal shaped stress–strain curve. While in [31] are not provided any experimental data for tensile loading along ND, these predictions of the Cazacu et al. [14] criterion reported in [41] have been later confirmed by Guo et al. [19], namely these authors reported that for a Mg AZ31 material under ND uniaxial tension loading, the stress–strain curve has a *S*-shape.

For an isotropic material, the tension–compression asymmetry is the same for any direction. As demonstrated in [15], the sign of the axial strains that develop during free-end torsion depends on whether the ratio σ^T/σ^C is greater than or less than 1 (see also the discussion presented in Chap. 4). For an anisotropic material, the tension–compression asymmetry is dependent on the direction of loading.

In Revil-Baudard et al. [41], it was hypothesized that the nature of the axial strains that develop in free-end torsion (i.e., whether elongation or contraction of the specimen occurs) should also depend on the direction about which the material is twisted. This correlation appears to be true for Mg AZ31.

Indeed, comparisons between F.E. simulations and experiments performed by Guo et al. [19] for Mg AZ31 under free-end torsion (see Fig. 5.42) show that if the twist axis is along the RD direction shortening occurs, but if torsional loading is applied along the ND direction, lengthening is observed. The model predictions are in excellent agreement with the experimental observations. In particular, irrespective of orientation the calculated initial slope which is a physical parameter that depends little on texture evolution, is almost in perfect agreement with the experimental one. An even more remarkable result is that the model correctly reproduces

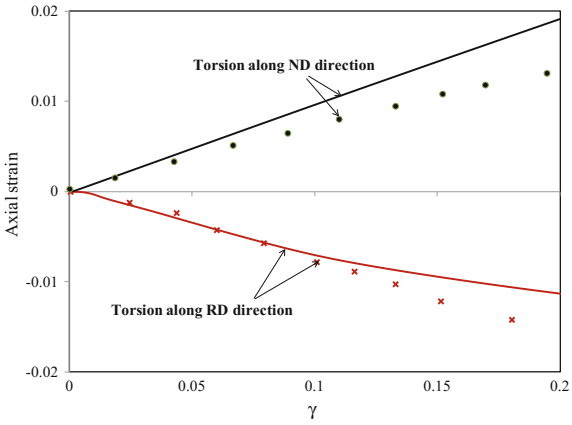

Fig. 5.42 Variation of the axial strain with the shear strain during free-end torsion along RD and ND directions for a Mg–AZ31 alloy: Comparison between experimental data by Guo et al. [19] and the numerical predictions obtained with the Cazacu et al. [14] yield criterion. Note that depending on the direction of torsion, the axial strain is either positive (torsion along ND direction) or negative (torsion along RD direction) (after Revil-Baudard et al. [41])

the fact that the sign of the axial strain depends on the direction of twist (RD, or ND). Moreover, the sign of the axial strain can be correlated to the tension–compression asymmetry for the respective direction. In the RD direction, the strength is higher in uniaxial tension than in compression, so shortening of the specimen occurs during free-end torsion along this direction. On the other hand, in the ND direction, the material has higher strength in compression than in tension, which results in lengthening of the specimen during torsion. Thus, the sign of the axial strain that develops (elongation or contraction) under free-end torsion depends on the ratio between uniaxial tension–compression in the given direction.

To further explain why a negative axial strain develops during free-end torsion for the RD specimen, it is worth examining the projection of the Cazacu et al. [14] yield criterion in the tension-shear planes. Due to the tension–compression asymmetry of the material along RD, the normal to the $(\sigma_{xx}, \sigma_{xy})$ and $(\sigma_{xx}, \sigma_{xz})$ surfaces for states corresponding to pure shear loading (i.e., $\sigma_{xx} = 0$) is pointed such that the axial strain is negative. Therefore, according to the Cazacu et al. [14] yield criterion for torsion of a specimen with the long axis along RD shortening of the specimen occurs. On the other hand, because in the ND direction the yield stress in tension is smaller than in compression, the predicted shape of the yield surface in $(\sigma_{zz}, \sigma_{xz})$ and $(\sigma_{zz}, \sigma_{yz})$ (see Fig. 5.44) is such that for pure shear (i.e., $\sigma_{zz} = 0$), the normal is pointed such that positive axial strain develops.

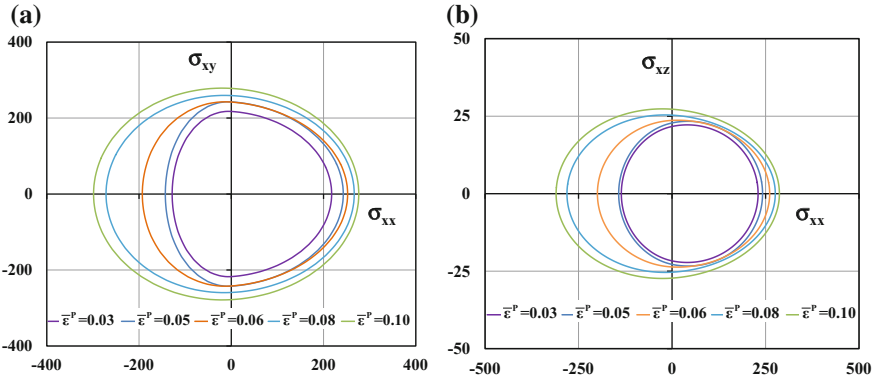

Fig. 5.43 Projection of the yield surfaces according to the Cazacu et al. [14] criterion for a Mg–AZ31 alloy for different levels of accumulated plastic strain: **a** $(\sigma_{xx}, \sigma_{xy})$ plane; **b** $(\sigma_{xx}, \sigma_{xz})$ plane

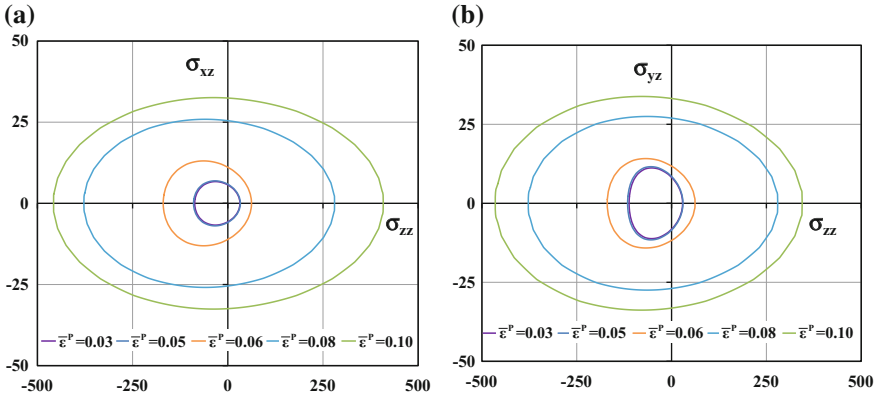

Fig. 5.44 Projection of the yield surfaces according to the Cazacu et al. [14] criterion for a Mg–AZ31 alloy for different levels of accumulated plastic strain: **a** $(\sigma_{zz}, \sigma_{xz})$ plane; **b** $(\sigma_{zz}, \sigma_{yz})$ plane

References

1. Agnew S, Yoo M, Tome C (2001) Application of texture simulation to understanding mechanical behavior of Mg and solid solution alloys containing Li or Y. Acta Mater 49:4277–4289
2. Alves JL (2003) Simulação numérica do processo de estampagem de chapas metálicas. Ph.D. thesis, University of Minho
3. Barlat F, Lian K (1989) Plastic behavior and stretchability of sheet metals. Part I: a yield function for orthotropic sheets under plane stress conditions. Int J Plast 5:51–66
4. Barlat F, Lege DJ, Brem JC (1991) A six-component yield function for anisotropic materials. Int J Plast 7:693–712
5. Barlat F, Becker RC, Hayashida Y, Maeda Y, Yanagawa M, Chung K, Brem JC, Lege DJ, Matsui K, Murtha SJ, Hattori S (1997) Yielding description for solution strengthened aluminum alloys. Int J Plast 13:385–401
6. Banabic D, Barlat F, Cazacu O, Kuwabara T (2010) Advances in anisotropy and formability. Int J Mater Form 3:165–189
7. Barlat F, Aretz H, Yoon J, Karabin M, Brem J, Dick R (2005) Linear transfomation-based anisotropic yield functions. Int J Plast 21:1009–1039
8. Barlat F, Yoon JW, Cazacu O (2007) On linear transformations of stress tensors for the description of plastic anisotropy. Int J Plast 23:876–896
9. Barros P, Alves J, Oliveira M, Menezes L (2017) Study on the effect of tension–compression asymmetry on the cylindrical cup forming of an AA2090-T3 alloy. Int J Solids Struct
10. Cazacu O (2018) New yield criteria for isotropic and textured metallic materials. Int J Solids Struct. https://doi.org/10.1016/j.ijsolstr.2018.01.036
11. Cazacu O, Barlat F (2001) Generalization of Drucker's yield criterion to orthotropy. Math Mech Solids 6:613–630. https://doi.org/10.1177/108128650100600603
12. Cazacu O, Barlat F (2003) Application of the theory of representation to describe yielding of anisotropic aluminum alloys. Int J Eng Sci 41:1367–1385
13. Cazacu O, Barlat F (2004) A criterion for description of anisotropy and yield differential effects in pressure-insensitive metals. Int J Plast 20:2027–2045
14. Cazacu O, Plunkett B, Barlat F (2006) Orthotropic yield criterion for hexagonal closed packed metals. Int J Plast 22:1171–1194

15. Cazacu O, Revil-Baudard B, Barlat F (2013) New interpretation of monotonic Swift effects: role of tension–compression asymmetry. Mech Mater 57:42–52
16. Drucker DC (1949) Relation of experiments to mathematical theories of plasticity. ASME J Appl Mech 16:349–357
17. Fundenberger J, Philippe M, Wagner F, Esling C (1997) Modelling and prediction of mechanical properties for materials with hexagonal symmetry (zinc, titanium and zirconium alloys). Acta Mater 45:4041–4055
18. Glazoff MV, Barlat F, Weiland H (2004) Continuum physics of phase and defect microstructures: bridging the gap between physical metallurgy and plasticity of aluminum alloys. Int J Plast 20:363–402
19. Guo XQ, Wu W, Wu PD, Qiao H, An K, Liaw PK (2013) On the Swift effect and twinning in a rolled magnesium alloy under free-end torsion. Scr Mater 69:319–322. https://doi.org/10.1016/j.scriptamat.2013.05.010
20. Haddadi H, Bouvier S, Banu M, Maier C, Teodosiu C (2006) Towards an accurate description of the anisotropic behaviour of sheet metals under large plastic deformations: modelling, numerical analysis and identification. Int J Plast 22:2226–2271. https://doi.org/10.1016/j.ijplas.2006.03.010
21. Hershey AV (1954) The plasticity of an isotropic aggregate of anisotropic face-centered cubic crystals. ASME J Appl Mech 21:241–249
22. Hill R (1948) A theory of the yielding and plastic flow of anisotropic metals. In: Proceedings of the Royal Society of London A: mathematical, physical and engineering sciences. The Royal Society, pp 281–297
23. Hill R (1987) Constitutive dual potentials in classical plasticity. J Mech Phys Solids 35:23–33
24. Hosford W (1966) Texture strengthening. Met Eng Quart 6:13–19
25. Hosford WF (1979) On yield loci of anisotropic cubic metals. In: Proceedings of the seventh North American metalworking research conference, pp 191–196
26. I-Shih L (1982) On representations of anisotropic invariants. Int J Eng Sci 20:1099–1109. https://doi.org/10.1016/0020-7225(82)90092-1
27. Johnson GR, Beissel SR, Stryk RA, Gerlach CA, Holmquist TJ (2003) User instructions for the 2003 version of the EPIC code
28. Karafillis A, Boyce M (1993) A general anisotropic yield criterion using bounds and a transformation weighting tensor. J Mech Phys Solids 41:1859–1886
29. Kelley E, Hosford WF (1968) The deformation characteristics of textured magnesium. Trans Met Soc AIME 242
30. Khan AS, Suh YS, Kazmi R (2004) Quasi-static and dynamic loading responses and constitutive modeling of titanium alloys. Int J Plast 20:2233–2248
31. Khan AS, Pandey A, Gnäupel-Herold T, Mishra RK (2011) Mechanical response and texture evolution of AZ31 alloy at large strains for different strain rates and temperatures. Int J Plast 27:688–706. https://doi.org/10.1016/j.ijplas.2010.08.009
32. Klimanek P, Pötzsch A (2002) Microstructure evolution under compressive plastic deformation of magnesium at different temperatures and strain rates. Mater Sci Eng A 324:145–150
33. Kuwabara T (2001) Cup drawing of pure titanium sheet-finite element analysis and experimental validation. Proc NUMIFORM 2001 Simul Mater Process, 781–787
34. Mattiasson K, Sigvant M (2008) An evaluation of some recent yield criteria for industrial simulations of sheet forming processes. Int J Mech Sci 50:774–787. https://doi.org/10.1016/j.ijmecsci.2007.11.002
35. Muller W (1996) Characterization of sheet metal under multi-axial load. Springer, Berlin
36. Nixon ME, Cazacu O, Lebensohn RA (2010) Anisotropic response of high-purity α-titanium: experimental characterization and constitutive modeling. Int J Plast 26:516–532
37. Nixon ME, Lebensohn RA, Cazacu O, Liu C (2010) Experimental and finite-element analysis of the anisotropic response of high-purity α-titanium in bending. Acta Mater 58:5759–5767

38. Plunkett B, Lebensohn RA, Cazacu O, Barlat F (2006) Anisotropic yield function of hexagonal materials taking into account texture development and anisotropic hardening. Acta Mater 54:4159–4169. https://doi.org/10.1016/j.actamat.2006.05.009
39. Plunkett B, Cazacu O, Lebensohn R, Barlat F (2007) Elastic-viscoplastic anisotropic modeling of textured metals and validation using the Taylor cylinder impact test. Int J Plast 23:1001–1021
40. Revil-Baudard B (2010) Simulation du comportement mécanique des alliages de titane pour les procédés de mise en forme à froid. Ph.D. thesis, École Nationale Supérieure des Mines de Paris
41. Revil-Baudard B, Chandola N, Cazacu O, Barlat F (2014) Correlation between Swift effects and tension–compression asymmetry in various polycrystalline materials. J Mech Phys Solids 70:104–115
42. Revil-Baudard B, Cazacu O, Flater P, Kleiser G (2015) Plastic deformation of high-purity α-titanium: model development and validation using the Taylor cylinder impact test. Mech Mater 80(Part B):264–275
43. Salem AA, Kalidindi SR, Doherty RD (2003) Strain hardening of titanium: role of deformation twinning. Acta Mater 51:4225–4237
44. Smith GF, Rivlin RS (1958) The strain-energy function for anisotropic elastic materials. Trans Am Math Soc 88:175–193
45. Stout M, Hecker S (1983) Role of geometry in plastic instability and fracture of tubes and sheet. Mech Mater 2:23–31
46. Takuda H, Yoshii T, Hatta N (1999) Finite-element analysis of the formability of a magnesium-based alloy AZ31 sheet. J Mater Process Technol 89:135–140
47. Wang CC (1970) A new representation theorem for isotropic functions: an answer to Professor GF Smith's criticism of my papers on representations for isotropic functions. Arch Ration Mech Anal 36:166–197
48. Zhai J, Luo T, Gao X, Graham SM, Baral M, Korkolis YP, Knudsen E (2016) Modeling the ductile damage process in commercially pure titanium. Int J Solids Struct 91:26–45

Chapter 6
Strain-Rate-Based Plastic Potentials for Polycrystalline Materials

Although the existence of a potential in the strain-rate space which is the work-conjugate of the stress potential $\varphi(\boldsymbol{\sigma})$ of a plastically deformable solid has been theoretically demonstrated (see [23]), analytical expressions for strain-rate potentials are only known for a very few cases. However, without knowledge of the closed-form expressions for the strain-rate potential associated with a given $\varphi(\boldsymbol{\sigma})$, it is impossible to derive the plastic potential of a porous solid with matrix behavior described by $\varphi(\boldsymbol{\sigma})$. While in this chapter, we focus on deriving analytic expressions of strain-rate potentials for fully dense materials, in Chap. 7, all these potentials will be used to model the response of porous materials. Moreover, we demonstrate that due to the duality between the stress-based potential and the strain-rate-based potential, the tensors that account for plastic anisotropy in the respective spaces should be inverse of each other.

6.1 Isotropic Strain-Rate Plastic Potentials

We begin with the discussion of isotropic strain-rate potentials. First, let us note that isotropy dictates that the most general form of a strain-rate potential is:

$$\psi(\mathbf{d}^{\mathrm{p}}) = g(d_1, d_2, d_3) \tag{6.1}$$

such that

$$g(d_1, d_2, d_3) = g(d_2, d_3, d_1) = g(d_3, d_1, d_2). \tag{6.2}$$

In the above equations, (d_1, d_2, d_3) are the principal values of the plastic strain-rate tensor $\mathbf{d}^{\mathrm{p}}$. Given that for a fully dense isotropic metallic material, plastic deformation is not accompanied by changes in volume, i.e., $tr(\mathbf{d}^{\mathrm{p}}) = 0$ or

O. Cazacu et al., *Plasticity–Damage Couplings: From Single Crystal to Polycrystalline Materials*, Solid Mechanics and Its Applications 253,
https://doi.org/10.1007/978-3-319-92922-4_6

$d_1 + d_2 + d_3 = 0$, the use of the Wang [22] representation theorems (see also Chap. 1) leads to the following alternative general form of the strain-rate potential (SRP):

$$\psi(\mathbf{d}^{\mathrm{p}}) = g(j_2, j_3), \tag{6.3}$$

where j_2 and j_3 denote the second and third-invariant of the plastic strain-rate tensor $\mathbf{d}^{\mathrm{p}}$, respectively. In terms of the principal values d_1, d_2, d_3:

$$\begin{aligned} j_2 &= tr\left(\mathbf{d}^{\mathrm{p}}\right)^2/2 = \frac{1}{2}\left(d_1^2 + d_2^2 + d_3^2\right) \\ &= \frac{1}{2}\left[\left(\frac{2d_1 - d_2 - d_3}{3}\right)^2 + \left(\frac{2d_2 - d_1 - d_3}{3}\right)^2 + \left(\frac{2d_3 - d_2 - d_1}{3}\right)^2\right], \\ j_3 &= tr\left(\mathbf{d}^{\mathrm{p}}\right)^3/3 = \frac{1}{3}\left(d_1^3 + d_2^3 + d_3^3\right) = d_1 d_2 d_3. \end{aligned}$$

Let $\mathbf{e}_i$, i = 1, …, 3, be the eigenvectors of the plastic strain-rate tensor $\mathbf{d}^{\mathrm{p}}$. Any isosurface $\psi(\mathbf{d}^{\mathrm{p}})$ = constant can be visualized graphically in the three-dimensional space of the principal strain-rates (d_1, d_2, d_3). Given that isotropy implies that $\mathbf{e}_i$ are also the eigenvectors of the stress deviator $\mathbf{s}$, using the same arguments as in the proof of Proposition 4.4 in Chap. 4, it follows that the SRP of an isotropic material is either a prism or a right cylinder with generators normal to the octahedral plane (i.e., the plane passing through the origin and of normal $\mathbf{e}_x = \frac{1}{\sqrt{3}}(\mathbf{e}_1 + \mathbf{e}_2 + \mathbf{e}_3)$). Moreover, if the unit vectors $\left(\mathbf{e}_x, \mathbf{e}_y, \mathbf{e}_z\right)$ are defined in terms of the eigenvectors $(\mathbf{e}_1, \mathbf{e}_2, \mathbf{e}_3)$ as:

$$\mathbf{e}_x = \frac{1}{\sqrt{3}}(\mathbf{e}_1 + \mathbf{e}_2 + \mathbf{e}_3),\ \mathbf{e}_y = -\frac{1}{\sqrt{2}}(\mathbf{e}_1 - \mathbf{e}_2),\ \mathbf{e}_z = \frac{1}{\sqrt{6}}(2\mathbf{e}_3 - \mathbf{e}_1 - \mathbf{e}_2), \tag{6.4}$$

then any point $\mathbf{P}(d_1, d_2, d_3)$ belonging to the intersection of the SRP with the octahedral plane is characterized by two polar-type coordinates, (R, γ), such that:

$$R = |\mathbf{OP}| = \sqrt{d_1^2 + d_2^2 + d_3^2} = \sqrt{2j_2}, \tag{6.5}$$

and γ which denotes the angle between $\mathbf{e}_y$ and $\mathbf{OP}$ is given as:

$$\tan(\gamma) = \sqrt{3}\frac{d_3}{d_2 - d_1}. \tag{6.6}$$

The intersection of any isosurface $\psi(\mathbf{d}^{\mathrm{p}})$ = constant with the octahedral plane is thus defined by the curve:

$$R = R(\gamma). \tag{6.7}$$

To simplify the writing, in the following, we denote the plastic strain-rate tensor simply by $\mathbf{d}$.

6.1.1 Strain-Rate Potentials for Isotropic Metallic Materials with the Same Response in Tension–Compression

6.1.1.1 Exact Duals of the von Mises and Tresca Stress Potentials

Strain-rate potential associated with the von Mises stress potential

As shown in Chap. 4, the stress potential associated with the von Mises yield criterion can be represented by the following function, homogeneous of degree one with respect to positive multipliers,

$$\varphi_{\text{Mises}}(\boldsymbol{\sigma}) = \sqrt{(3/2)\mathbf{s}:\mathbf{s}} = \sigma_{\text{T}}, \tag{6.8}$$

where $\mathbf{s}$ is the deviator of the Cauchy stress tensor $\boldsymbol{\sigma}$ and σ_{T} denotes the yield stress in uniaxial tension. Hence, according to the flow rule:

$$\mathbf{d} = \frac{\partial \varphi_{\text{Mises}}}{\partial \sigma} = \dot{\lambda}\frac{3\mathbf{s}}{2\sigma_{\text{T}}}, \tag{6.9}$$

where $\dot{\lambda} \geq 0$ stands for the plastic multiplier. Substitution of Eq. (6.9) into Eq. (6.8) leads to

$$\mathbf{d}:\mathbf{d} = 9\left(\dot{\lambda}\right)^2 \frac{\mathbf{s}:\mathbf{s}}{4\sigma_{\text{T}}^2} = \frac{3}{2}\left(\dot{\lambda}\right)^2$$

Therefore, the strain-rate potential associated with the von Mises stress potential [see Eq. (6.8)] is:

$$\psi_{\text{Mises}}(\mathbf{d}) = \sqrt{(2/3)\mathbf{d}:\mathbf{d}} = \sqrt{(2/3)\left(d_1^2 + d_2^2 + d_3^2\right)} = \dot{\bar{\varepsilon}}, \tag{6.10}$$

where $\dot{\bar{\varepsilon}}$ is the axial strain-rate in uniaxial tension.

Remark Note that in virtue of the duality between the stress-based and strain-rate-based formulations, the only parameter involved in the von Mises strain-rate potential given by Eq. (6.10) can be specified by performing a unique test, e.g., uniaxial tension. Obviously, according to the von Mises SRP, the plastic response is the same in tension–compression [see Eq. (6.10)]. Since the von

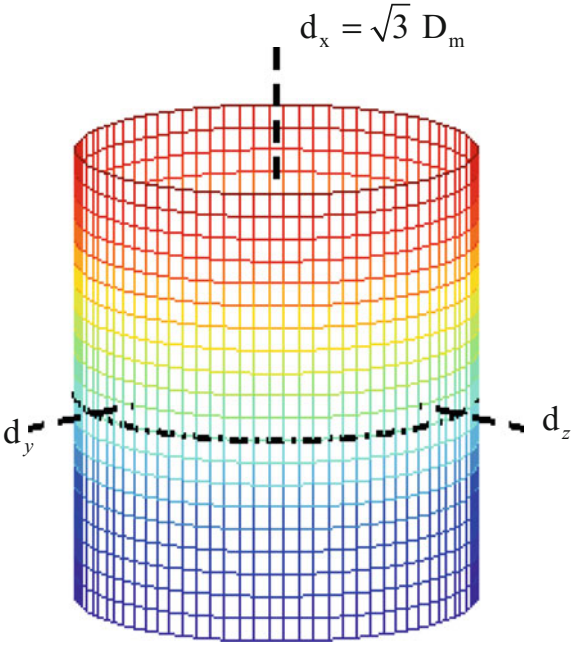

Fig. 6.1 The von Mises strain-rate potential in the three-dimensional space of the principal values of the strain-rate tensor $\mathbf{d}$; $(\mathbf{e}_x, \mathbf{e}_y, \mathbf{e}_z)$ given by Eq. (6.4)

Mises SRP depends only on j_2, its projection in the octahedral plane is the circle given by $R(\gamma) = \sqrt{d_1^2 + d_2^2 + d_3^2} = \text{constant}(= \sqrt{3/2}\dot{\bar{\varepsilon}})$. Moreover, in the space of the principal strain-rates, the von Mises SRP is a right cylinder, as shown in Fig. 6.1.

Strain-rate potential associated with the Tresca stress potential

The stress potential associated with the Tresca yield criterion is expressed as (see Sect. 4.2.1):

$$\varphi_{Tresca}(\boldsymbol{\sigma}) = \max(|\sigma_1 - \sigma_2|, |\sigma_2 - \sigma_3|, |\sigma_1 - \sigma_3|),$$

with σ_1, σ_2, and σ_3 being the principal values of the Cauchy stress $\boldsymbol{\sigma}$. If the principal stresses are all distinct, and ordered such that $\sigma_1 > \sigma_2 > \sigma_3$, then:

$$d_1 = \dot{\lambda},\ d_2 = 0,\ d_3 = -\dot{\lambda} \tag{6.11}$$

On the other hand, if $\sigma_1 = \sigma_2 > \sigma_3$,

$$d_1 = \frac{1}{2}\dot{\lambda}(1+\beta),\ d_2 = \frac{1}{2}\dot{\lambda}(1-\beta),\ d_3 = -\dot{\lambda}, \tag{6.12}$$

where β is any real number between -1 and 1. The expression of $\dot{\lambda}$ for all other loadings can be obtained by symmetry arguments. Thus, for any stress state,

$$\dot{\lambda} = \frac{1}{2}\left(|d_1| + |d_2| + |d_3|\right),$$

and the Tresca strain-rate potential is expressed as:

$$\psi_{\text{Tresca}}(\mathbf{d}) = \left(|d_1| + |d_2| + |d_3|\right)/2. \tag{6.13}$$

Given the isotropy and tension–compression symmetry of the Tresca SRP given by Eq. (6.13), to obtain its intersection with the octahedral plane, it is sufficient to find the expression of the curve $R = R(\gamma)$ [see Eqs. (6.5)–(6.7)] only in the $-\pi/6 \leq \gamma \leq \pi/6$ sector, the expression in any other sector being obtained by symmetry arguments. Since in this sector, the principal values of the strain-rate tensor are:

$$\begin{cases} d_1 = \dfrac{2R(\gamma)}{\sqrt{6}} \sin\left(\gamma - \dfrac{2\pi}{3}\right) \\ d_2 = \dfrac{2R(\gamma)}{\sqrt{6}} \sin\left(\gamma + \dfrac{2\pi}{3}\right), \\ d_3 = \dfrac{2R(\gamma)}{\sqrt{6}} \sin\,\gamma \end{cases} \tag{6.14}$$

(for more details, the reader is referred to Sect. 4.1.1), it follows that the expression of the curve $R = R(\gamma)$ for the Tresca SRP is:

$$\begin{aligned} R(\gamma) &= \frac{\dot{\bar{\varepsilon}}\sqrt{6}}{2}\left(\frac{1}{\sqrt{3}\cos(\gamma) - \sin(\gamma)}\right) \quad \text{if} \quad -\pi/6 \leq \gamma \leq 0 \\ R(\gamma) &= \frac{\dot{\bar{\varepsilon}}\sqrt{6}}{2}\left(\frac{1}{\sqrt{3}\cos(\gamma) + \sin(\gamma)}\right) \quad \text{if } 0 \leq \gamma \leq \pi/6, \end{aligned} \tag{6.15}$$

which represents a regular hexagon (see also Fig. 6.2). Let us recall that the von Mises yield surface is an upper bound for Tresca's, so in the octahedral plane the von Mises circle circumscribes the Tresca hexagon (see also Chap. 4, Fig. 4.4). Since each SRP is the exact conjugate of the respective stress potential, it follows that the Tresca SRP is an upper bound of the von Mises SRP. Therefore, in the space of the principal strain-rates, the projection of the Tresca strain-rate potential circumscribes the von Mises SRP projection (see also Fig. 6.2).

In Fig. 6.3 are represented the Tresca SRP and the von Mises SRP in the biaxial plane (d_1, d_2). These projections are obtained using Eqs. (6.10) and (6.13), respectively, and imposing: $d_3 = -(d_1 + d_2)$. It is important to note that in this space, the Tresca SRP is a hexagon that circumscribes the von Mises SRP, which is an ellipse.

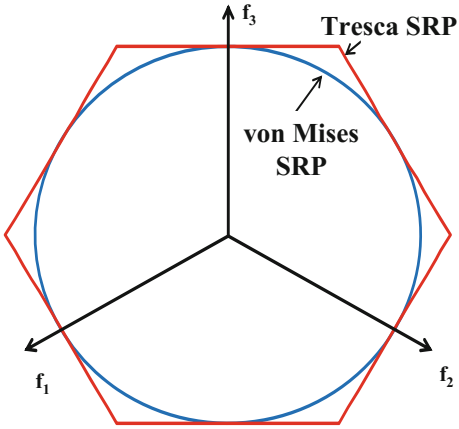

Fig. 6.2 Cross-section of the von Mises strain-rate potential [Eq. (6.10)] and the Tresca SRP [Eq. (6.13)] in the octahedral plane. $\mathbf{f}_i$ are the projections of the eigenvectors of the plastic strain-rate tensor

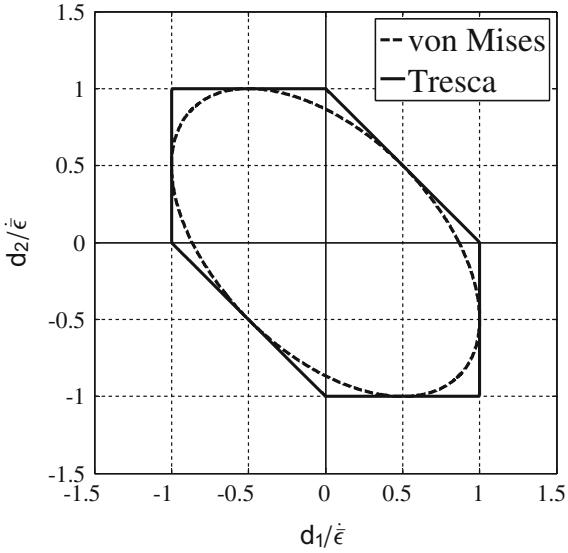

Fig. 6.3 Representation in the biaxial plane (d_1, d_2) of the strain-rate potentials associated with the von Mises and the Tresca stress potentials, respectively

6.1.1.2 Hershey–Hosford Pseudo-Strain-Rate Potential

As previously mentioned, for non-quadratic stress potentials, their work-conjugate potentials in the strain-rate space cannot be determined explicitly. In particular, the expression of the strain-rate potential associated with the Hershey [12] and Hosford [13] stress potential (see also Chap. 4) given by

$$\varphi_{\text{Hershey–Hosford}}(\sigma_1,\sigma_2,\sigma_3)=\left[\frac{|\sigma_1-\sigma_2|^a+|\sigma_2-\sigma_3|^a+|\sigma_3-\sigma_1|^a}{2}\right]^{1/a}=\bar{\sigma} \tag{6.16}$$

is not known.

Barlat et al. [2] proposed a strain-rate potential of the form,

$$\psi_{HH}(\mathbf{d})=\left|\frac{2d_1-d_2-d_3}{3}\right|^b+\left|\frac{2d_2-d_3-d_1}{3}\right|^b+\left|\frac{2d_3-d_1-d_2}{3}\right|^b=2\dot{\bar{\varepsilon}}^b, \tag{6.17}$$

where b is a material constant and $\dot{\bar{\varepsilon}}$ denotes the axial strain-rate in uniaxial tension. Making use of the plastic incompressibility condition, Eq. (6.17) becomes

$$\psi_{HH}(\mathbf{d})=|d_1|^b+|d_2|^b+|d_3|^b=2\dot{\bar{\varepsilon}}^b. \tag{6.18}$$

It is worth noting that for $b=1$, the isotropic Barlat et al. [2] SRP reduces to the Tresca SRP [see Eq. (6.13)], while for $b=2$, the von Mises SRP [Eq. (6.10)] is recovered. Indeed,

$$\psi_{HH}(\mathbf{d})\Big|_{b=2}=\sqrt{3/4}\,\psi_{\text{Mises}}(\mathbf{d}). \tag{6.19}$$

Also, for $1<b<2$, the Barlat et al. [2] SRP is in between the Tresca SRP and the von Mises SRP (see Fig. 6.4).

Remark Barlat et al. [2] have shown that for $b=4/3$ and $b=3/2$, the strain-rate potential given by Eq. (6.17) approximates well the numerical strain-rate potentials for isotropic fcc and bcc polycrystals, respectively, that were obtained using the Taylor-Bishop-Hill (TBH) polycrystal model (see Chap. 3 for more details on this model). Moreover, Barlat et al. [2] have verified numerically that the particular

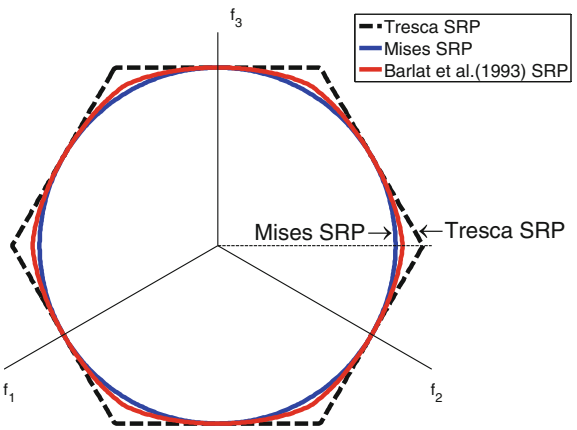

Fig. 6.4 Cross-section in the octahedral plane of the isotropic form of Barlat et al. [2] strain-rate potential [Eq. (6.18)] corresponding to $b=1.5$ in comparison with: **a** the Tresca SRP, and **b** the von Mises SRP

expression of $\psi_{HH}(\mathbf{d})$ corresponding to $b = 4/3$ and $b = 3/2$, respectively, is the work-conjugate of $\varphi_{\text{Hershey}-\text{Hosford}}(\sigma_1, \sigma_2, \sigma_3)$ corresponding to $a = 6$ and $a = 8$, respectively.

In Fig. 6.5 is shown the representation in the biaxial plane $d_3 = -(d_1 + d_2)$ of the Barlat et al. [2] isotropic SRP corresponding to $b = 3/2$ and $b = 4/3$, respectively, along with the von Mises SRP and the Tresca SRP. Note that the Barlat et al. [2] isotropic SRP lies between the von Mises SRP and the Tresca SRP, the Tresca SRP surface being an upper bound to the Barlat et al. [2] isotropic SRP.

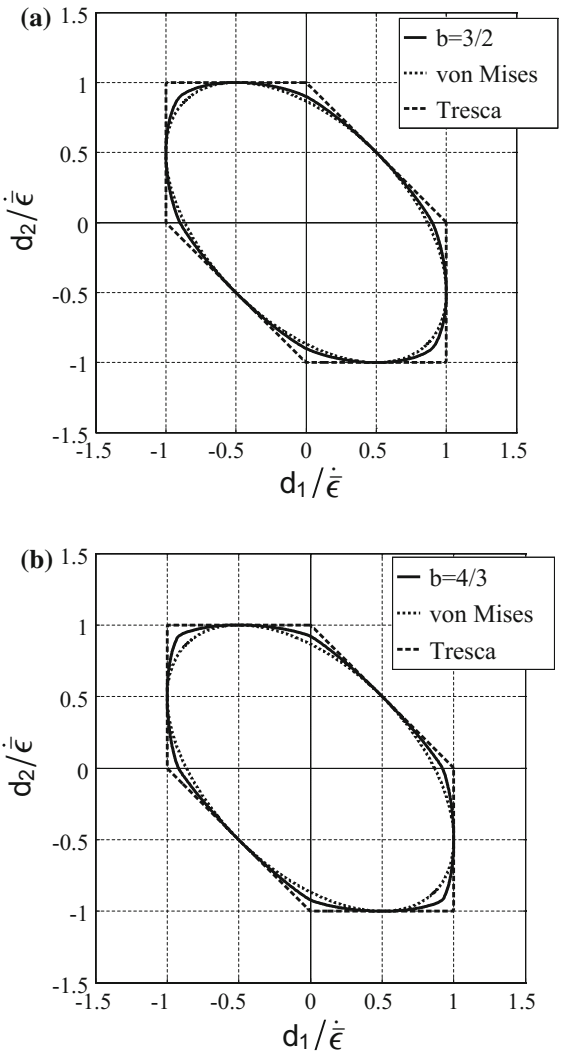

Fig. 6.5 Representation in the biaxial plane (d_1, d_2) of Barlat et al. [2] isotropic strain-rate potential corresponding to: **a** $b = 3/2$ and **b** $b = 4/3$ along with the von Mises SRP and the Tresca SRP

6.1.1.3 Strain-Rate Potential of Cazacu and Revil-Baudard [7]

Cazacu and Revil-Baudard [7] have proposed an isotropic strain-rate potential that involves both invariants j_2 and j_3 of the plastic strain-rate tensor. The expression of this strain-rate potential is:

$$\psi(\mathbf{d}) = \frac{\sqrt{j_2}}{B}\left(1 + \beta\frac{j_3^2}{j_2^3}\right), \tag{6.20}$$

where β is a parameter and

$$B = \frac{1 + 4\beta/27}{\sqrt{4/3}}. \tag{6.21}$$

The constant B appearing in the expression of this SRP is defined such that for uniaxial tension, $\psi(\mathbf{d})$ is equal to the axial strain-rate. It is worth noting that for $\beta = 0$, this strain-rate potential reduces to the von Mises SRP [see Eq. (6.10)]. Indeed, for $\beta = 0$:

$$\psi(\mathbf{d}) = \sqrt{4j_2/3} = \sqrt{(2/3)\mathbf{d}:\mathbf{d}} \tag{6.22}$$

If $\beta \neq 0$, the Cazacu and Revil-Baudard [7] SRP accounts for the combined effects of j_2 and j_3 on the plastic behavior.

Proposition 6.1 ***Convexity of the*** **Cazacu and Revil-Baudard [7]** ***strain-rate potential***

For $\psi(\mathbf{d})$ to be convex, the range of variation of β is:

$$\frac{-9}{24} \leq \beta \leq \frac{27}{68}. \tag{6.23}$$

Proof In terms of the principal values d_i (i = 1, …, 3) of the plastic strain-rate tensor $\mathbf{d}$, the strain-rate potential is expressed as:

$$\psi(d_1, d_2, d_3) = \left(1 + \beta\frac{8d_1^2d_2^2d_3^2}{\left(d_1^2 + d_2^2 + d_3^2\right)^3}\right)\sqrt{\frac{\left(d_1^2 + d_2^2 + d_3^2\right)}{2}} \tag{6.24}$$

Since $\psi(d_1, d_2, d_3)$ given by the above equation is an isotropic and even function (the same response in tension–compression), any isosurface $\psi(\mathbf{d}) = A$, with A being a constant, has sixfold symmetry. Therefore, it is sufficient to prove its convexity in one sector, say the one corresponding to $d_2 \geq d_3 > d_1$. In this sector, the expressions of the principal values of the strain-rate tensor in terms of the polar coordinates R and γ are given by Eq. (6.14). Note that shear loadings correspond to $\gamma = 0$ (for which $d_3 = 0$), while axisymmetric loadings correspond to $\gamma = \pi/6$ $(d_2 = d_3 = -d_1/2)$, and $\gamma = -\pi/6$ $(d_1 = d_3 = -d_2/2)$, respectively.

Substituting Eq. (6.14) into Eq. (6.24), we obtain that the cross-section of the isosurface $\psi(\mathbf{d}) =$ constant in the octahedral plane is represented in polar coordinates as:

$$\begin{cases} x(\gamma) = R(\gamma)\cos\gamma \\ y(\gamma) = R(\gamma)\sin\gamma \end{cases}$$

with

$$R(\gamma) = \frac{A\sqrt{2}}{1 + (4\beta/27)\sin^2(3\gamma)} \tag{6.25}$$

The curvature of the surface can be expressed as:

$$\kappa(\gamma) = \frac{2(R'(\gamma))^2 - R(\gamma)R''(\gamma) + R^2(\gamma)}{\left((R'(\gamma))^2 + R^2(\gamma)\right)^{3/2}} \tag{6.26}$$

Note that the denominator of the above relation (6.26) is always positive,

$$\kappa(\gamma) \geq 0 \Leftrightarrow 2(R'(\gamma))^2 - R(\gamma)R''(\gamma) + R^2(\gamma) \geq 0$$

Substituting relation (6.25) into (6.26), lengthy but straightforward calculations lead to:

$$\kappa(\gamma) \geq 0 \Leftrightarrow \frac{-9}{24} \leq \beta \leq \frac{27}{68}$$

In particular,

- for shear loadings $(\gamma = 0)$: $\kappa(\gamma) \geq 0$ if and only if $(1 + 24\beta/9) \geq 0$
- for axisymmetric loadings: $\kappa(\gamma) \geq 0$ if and only if $\left(1 - \frac{72\beta}{27 + 4\beta}\right) \geq 0$.

It is thus proven that for $\beta = 27/68$, the curvature of the cross-section is zero for axisymmetric states; if $\beta = -9/24$, the curvature is zero for shear loading. Therefore, convexity is ensured for $-9/24 \leq \beta \leq 27/68$.

As an example, in Fig. 6.6 is shown the representation in the octahedral plane of the strain-rate potential given by Eq. (6.20) for $\beta = -0.35$, -0.15, and $\beta = 0.38$, respectively. Note that for $\beta = 0.38$, the cross-section is a hexagon with rounded corners exterior to the von Mises SRP (which corresponds to $\beta = 0$). On the other hand, for $\beta = -0.35$, the Cazacu and Revil-Baudard [7] strain-rate potential is interior to the von Mises SRP.

It is also worth comparing the Cazacu and Revil-Baudard [7] strain-rate potential with the Tresca SRP [Eq. (6.13)] and the von Mises SRP [Eq. (6.10)]. Let us first compare the cross-sections of these potentials in the octahedral plane (see Fig. 6.7). It is to be noted that irrespective of the value of the parameter β, the Tresca SRP is

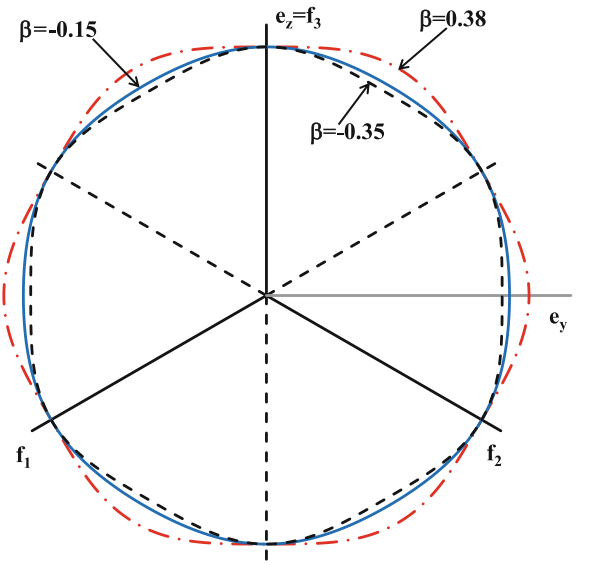

Fig. 6.6 Representation in the octahedral plane of the Cazacu and Revil-Baudard [7] strain-rate potential [Eq. (6.20)] corresponding to: $\beta = -0.35$, $\beta = -0.15$, and $\beta = 0.38$, respectively

an upper bound (exterior to the other surfaces). For $\beta > 0$, the Cazacu and Revil-Baudard [7] strain-rate potential lies between the von Mises SRP ($\beta = 0$) and the Tresca SRP (see also Fig. 6.7a). On the other hand for $\beta < 0$, the von Mises SRP is exterior to the Cazacu and Revil-Baudard [7] strain-rate potential, and the smaller the value of β, the stronger is the deviation of the projection of this SRP from the von Mises circle (e.g., compare the cross-section corresponding to $\beta = -0.15$ shown in Fig. 6.7b with that corresponding to $\beta = -0.35$ given in Fig. 6.7c).

Comparisons between the projections of the same potentials in the biaxial plane (d_1, d_2) (with $d_3 = -(d_1 + d_2)$) are shown in Fig. 6.8. The upper-bound character of the Tresca SRP is clearly seen. However, depending on the value of β, the Cazacu and Revil-Baudard [7] SRP can be either interior or exterior to the von Mises SRP. It is also important to note that the Cazacu and Revil-Baudard [7] SRP is the only potential that is expressed by an even function in strain-rate for which the von Mises SRP is not a lower bound.

6.1.2 Strain-Rate Potentials for Isotropic Metallic Materials with Asymmetry Between Tension–Compression

6.1.2.1 Exact Dual of the Isotropic Cazacu et al. [5] Stress Potential

The strain-rate potentials presented so far are applicable only to isotropic materials with the same response in tension–compression. As discussed in Chaps. 4 and 5, certain metallic materials are pressure-insensitive and exhibit tension–compression

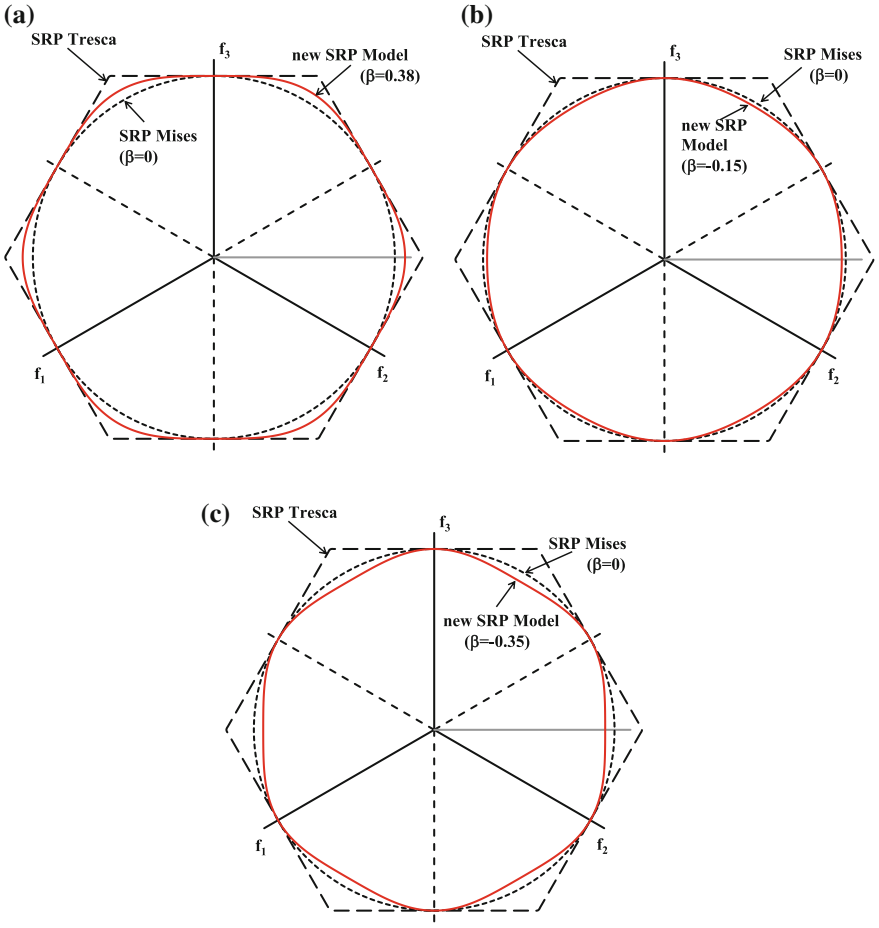

Fig. 6.7 Comparisons of the von Mises strain-rate potential (dotted line), the Tresca strain-rate potential (dashed line), and the Cazacu and Revil-Baudard [7] strain-rate potential corresponding to several values of the parameter β: **a** $\beta = 0.38$, **b** $\beta = -0.15$, and **c** $\beta = -0.35$

asymmetry in the plastic response even for monotonic loading. This strength differential effect is due to the activation of specific single crystal deformation mechanisms such as twinning or slip with pronounced non-Schmid effects (see also Chap. 3).

Recently, Cazacu et al. [8] have derived a strain-rate potential that can capture both anisotropy and tension–compression asymmetry. Furthermore, this strain-rate potential is the exact dual of the quadratic form of the stress potential of Cazacu et al. [5] (see Chap. 5). The derivation of the isotropic form of Cazacu et al. [6] SRP is presented in the following, while the derivation of the orthotropic form of this SRP is presented in Sect. 6.2.2.

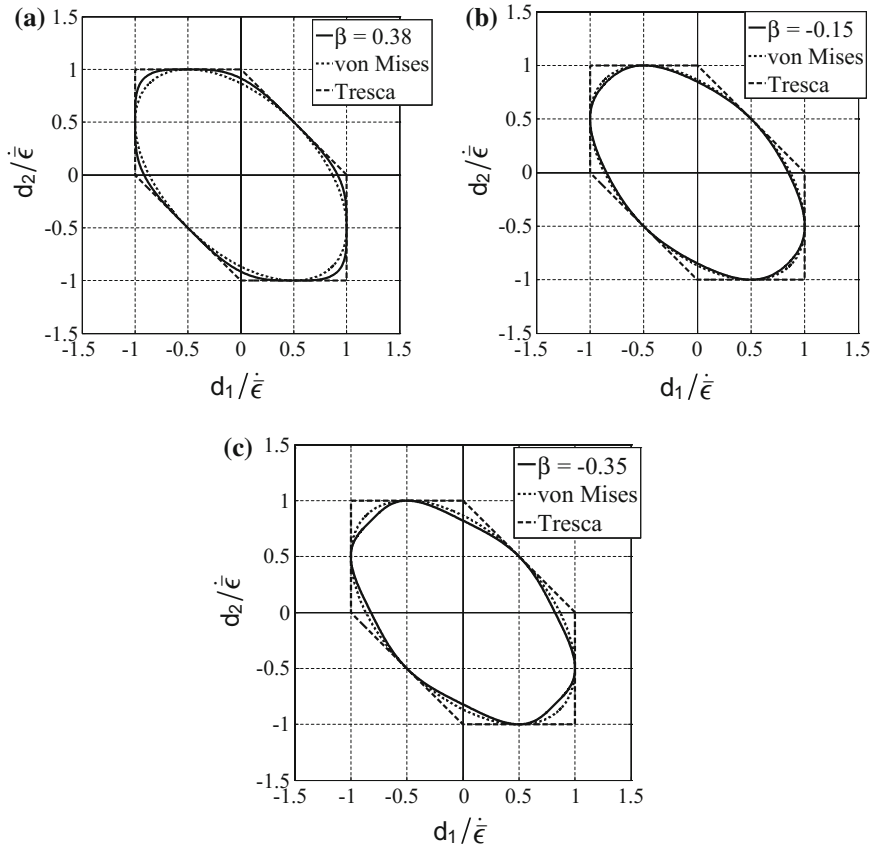

Fig. 6.8 Representation in the biaxial plane (d_1, d_2) of the Cazacu and Revil-Baudard [7] strain-rate potential for several values of the parameter β: **a** $\beta = 0.38$, **b** $\beta = -0.15$, and **c** $\beta = -0.35$ along with the von Mises SRP and the Tresca SRP

Let us note that in the case when the degree of homogeneity $a = 2$, the isotropic form of the Cazacu et al. [5] stress potential (see also Sect. 4.3.2) can be rewritten as:

$$g(\mathbf{s}, m, \sigma_T) = m\sqrt{f(\mathbf{s})} - \sigma_T = 0 \tag{6.27}$$

where

$$f(\mathbf{s}) = \sum_{i=1}^{3} (|s_i| - k s_i)^2, \text{and}$$
$$m = \sqrt{\frac{9}{2(3k^2 - 2k + 3)}}. \tag{6.28}$$

Moreover, the material constant k has the following simple expression in terms of the ratio between the uniaxial yield in tension, σ_T, and the uniaxial yield in compression, σ_C

$$k = \frac{1 - h\left(\frac{\sigma_T}{\sigma_C}\right)}{1 + h\left(\frac{\sigma_T}{\sigma_C}\right)} \quad \text{with} \quad h(x) = \sqrt{\frac{2 - x^2}{2x^2 - 1}} \tag{6.29}$$

As mentioned previously, if there is no difference between the response in tension–compression (i.e., $\sigma_T = \sigma_C$), then $k = 0$ and the quadratic isotropic form of the Cazacu et al. [5] criterion reduces to the von Mises yield criterion.

Because for $k \neq 0$ the isotropic Cazacu et al. [5] criterion is represented by an odd function in stresses [see Eq. (6.27)], the projection of the yield surface in the octahedral plane has only threefold symmetry. Consequently, its projection is fully determined once its shape is known on any of the domains Z_1, Z_2, or Z_3 shown in Fig. 6.9. Specifically, the domain Z_3 is delimited by the straight line T_1 $(s_1 = 0)$ and the straight line T_2 $(s_2 = 0)$, i.e.,

$$Z_3 = Z_3^+ \cup Z_3^- \tag{6.30}$$

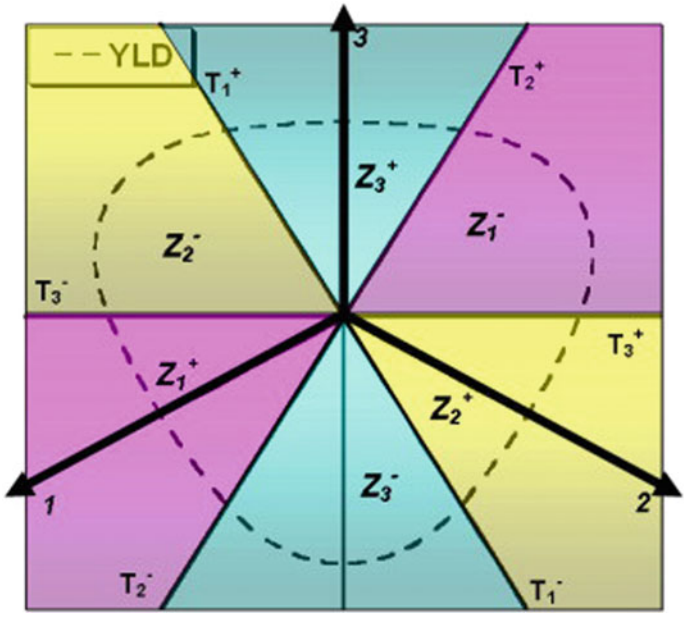

Fig. 6.9 Representation of the domains Z_1, Z_2, Z_3 of the isotropic Cazacu et al. [5] yield surface ($k = -0.4$) in the octahedral plane (after Cazacu et al. [6])

where $Z_3^+ = \{(s_1, s_2, s_3) | s_3 \geq 0,\ s_2 \leq 0, s_1 \leq 0\}$ and $Z_3^- = \{(s_1, s_2, s_3) | s_3 \leq 0,\ s_1 \geq 0, s_2 \geq 0\}$, with similar definition for the domains Z_1 and Z_2, respectively (for the detailed discussion and analytical expressions of this criterion in each of these domains, see Sect. 4.3.2).

Using Eq. (6.27), the eigenvalues d_i (i = 1, …, 3) of the plastic strain-rate tensor **d** are expressed as:

$$d_i = \dot{\lambda} \frac{m^2}{\sigma_T} \left[s_i (1 + k^2) - 2k|s_i| + \frac{2k}{3} (|s_1| + |s_2| + |s_3|) \right]. \tag{6.31}$$

It is important to note that since the stress potential involves all principal values of the stress deviator **s**, its associated SRP should also depend on all the principal values of **d** and should also display tension–compression asymmetry. Consequently, the projection of this SRP in the octahedral plane has threefold symmetry. Thus, it is sufficient to determine its expression on only one of the domains D_i, i = 1, …, 3 (see Fig. 6.10), D_i being the image of Z_i onto the strain-rate space by the flow rule, i.e., $(s_1, s_2, s_3) \in Z_i \Leftrightarrow (d_1, d_2, d_3) \in D_i$, where d_i, i = 1, …, 3, are given by Eq. (6.31).

As an example, in the following, we will derive the expression of the SRP in the domain D_3; the expressions on the others domains can be obtained by symmetry. The first step consists in describing the domain D_3.

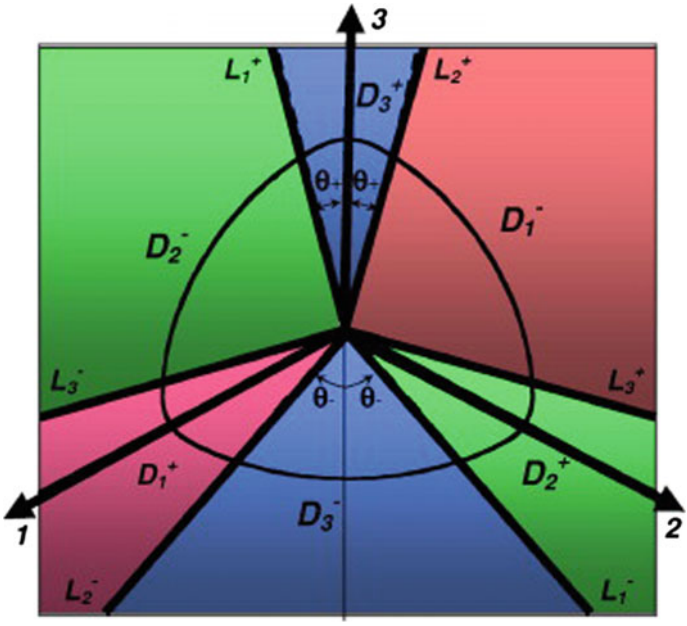

Fig. 6.10 Representation of the domains D_1, D_2, D_3 of the strain-rate potential (SRP) isosurface associated with the isotropic Cazacu et al. [5] stress potential ($k = -0.4$) in the octahedral plane (after Cazacu et al. [6])

Expression of the domain D_3

Recall that $\mathbf{f}_i$, $i = 1\ldots3$, denote the projections in the octahedral plane of the strain-rate eigenvectors $\mathbf{e}_i$ and that Z_3^+ is delimited by the half-lines T_1^+ and T_2^+, which are at $\pi/6$ and $-\pi/6$ with respect to the axis $\mathbf{f}_3$; similarly, Z_3^- is delimited by the half-lines T_1^- and T_2^- [see Fig. 6.9 and Eq. (6.30)].

Since $(s_1, s_2, s_3) \in T_1^+ \Leftrightarrow s_1 = 0,\ s_3 \geq 0,\ s_2 = -s_3 \leq 0$, using Eq. (6.31), it follows that:

$$\begin{cases} d_1 = \dfrac{4k}{3k^2 - 2k + 3} d_3 \\ d_2 = -\dfrac{3k^2 + 2k + 3}{3k^2 - 2k + 3} d_3 \end{cases} \tag{6.32}$$

Note that Eq. (6.32) is the equation of a straight line that passes through the origin; it will be denoted L_1^+ (see Fig. 6.10). Similarly, it can be shown that T_2^+ is mapped on the half-line of equation:

$$\begin{cases} d_1 = -\dfrac{3k^2 + 2k + 3}{3k^2 - 2k + 3} d_3 \\ d_2 = \dfrac{4k}{3k^2 - 2k + 3} d_3 \end{cases} \tag{6.33}$$

that will be denoted L_2^+. In conclusion, the image of Z_3^+ is the domain D_3^+ delimited by the half-line L_1^+ and L_2^+. Comparison between Eqs. (6.32) and (6.33) shows that L_1^+ and L_2^+ are symmetric with respect to the axis $\mathbf{f}_3$ (see Fig. 6.10). Let θ^+ be the angle between L_1^+ and $\mathbf{f}_3$.

This angle can be determined using Eq. (6.32) as:

$$\cos\theta^+ = \frac{\sqrt{\frac{3}{2}} d_3}{\sqrt{d_1^2 + d_2^2 + d_3^2}} = \frac{1}{2} \frac{3k^2 - 2k + 3}{\sqrt{3k^4 + 10k^2 + 3}} \frac{d_3}{|d_3|}. \tag{6.34}$$

Since for any point on T_1^+: $s_3 \geq 0$ using Eq. (6.32), we obtain that $\mathrm{sgn}(d_3) = \mathrm{sgn}(s_3) = 1$. Thus,

$$\cos\theta^+ = \frac{1}{2} \frac{3k^2 - 2k + 3}{\sqrt{3k^4 + 10k^2 + 3}}$$

and

$$\tan\left(\theta^+\right) = \frac{\sqrt{3}}{3k^2 - 2k + 3} (k + 1)^2. \tag{6.35}$$

Note that from Eq. (6.35), it follows that: $\theta^+ \leq \pi/3$. By geometric considerations, it can be shown that the subdomain Z_3^+ of the isotropic Cazacu et al. [5] yield surface maps onto the domain D_3^+ of the associated SRP, given by:

$$D_3^+ = \left\{ (d_1, d_2, d_3) | \frac{d_3}{\sqrt{d_1^2 + d_2^2 + d_3^2}} \geq \frac{3k^2 - 2k + 3}{\sqrt{6(k^2+3)(3k^2+1)}} \right\} \tag{6.36}$$

Indeed, $\mathbf{d} = (d_1, d_2, d_3) \in D_3^+$ if and only if: $\theta \leq \theta^+$, where θ denotes the angle between the projection of $\mathbf{d}$ on the π-plane and $\mathbf{f}_3$. Since $0 \leq \theta \leq \pi/3$, then $\cos\theta > \cos\theta^+$, and consequently,

$$\frac{d_3}{\sqrt{d_1^2 + d_2^2 + d_3^2}} \geq \frac{3k^2 - 2k + 3}{\sqrt{6(k^2+3)(3k^2+1)}}$$

Similarly, it can be shown that the subdomain Z_3^- maps onto the domain D_3^- delimited by the half-lines L_1^- and L_2^- (see Fig. 6.10). The angle between L_2^- and $(-\mathbf{f}_3)$ is given by:

$$\tan(\theta^-) = \frac{\sqrt{3}}{3k^2 - 2k + 3}(k-1)^2 \tag{6.37}$$

while the domain D_3^- is:

$$D_3^- = \left\{ (d_1, d_2, d_3) | \frac{d_3}{\sqrt{d_1^2 + d_2^2 + d_3^2}} \leq \frac{-(3k^2 + 2k + 3)}{\sqrt{6(k^2+3)(3k^2+1)}} \right\} \tag{6.38}$$

and $(s_1, s_2, s_3) \in Z_3^-$ if and only if $(d_1, d_2, d_3) \in D_3^-$. In conclusion, the domain $D_3 = D_3^+ \cup D_3^-$ is described by Eqs. (6.36) and (6.38), respectively (see also Fig. 6.10). Furthermore, using Eqs. (6.35) and (6.37), it can be easily shown that:

$$\theta^- + \theta^+ = \frac{\pi}{3}, \tag{6.39}$$

which is a consequence of the material's isotropy.

Remark

- Only for $k = 0$ (i.e., von Mises material), $\theta^- = \theta^+ = \pi/6$, and the domain D_3^- is the symmetric with respect to the origin of the subdomain D_3^+. In other words, only for a material obeying the von Mises yield criterion: $s_i = 0$ *if and only if* $d_i = 0$.
- If a material displays tension–compression asymmetry (i.e., $k \neq 0$), then $\theta^- \neq \theta^+$ and the domains D_3^+ and D_3^- are no longer symmetric about the origin (see also Fig. 6.10).

Expression of the Cazacu et al. [6] *strain-rate potential in the subdomain* D_3

Let us first determine the expression of $\dot{\lambda}$ in the subdomain D_3^+ of the SRP. Since $(d_1, d_2, d_3) \in D_3^+$ if and only if $(s_1, s_2, s_3) \in Z_3^+$ (i.e., $s_3 \geq 0, s_1 \leq 0, s_2 \leq 0$), from the flow rule [Eq. (6.31)], it follows that in the domain D_3^+

$$\begin{aligned} s_1 &= \left[\frac{\sigma_T}{m^2\dot{\lambda}}d_1 - \frac{4k}{3}s_3\right]\frac{1}{(1+k)^2} \\ s_2 &= \left[\frac{\sigma_T}{m^2\dot{\lambda}}d_2 - \frac{4k}{3}s_3\right]\frac{1}{(1+k)^2} \\ s_3 &= \frac{\sigma_T}{m^2\dot{\lambda}}\left(\frac{3}{3k^2-2k+3}\right)d_3 \end{aligned} \tag{6.40}$$

and the yield condition is satisfied, i.e.,

$$m^2\left[s_1^2(1+k)^2 + s_2^2(1+k)^2 + s_3^2(1-k)^2\right] = \sigma_T^2. \tag{6.41}$$

Substitution of the expressions (6.40) for s_i into Eq. (6.41) leads to:

$$\dot{\lambda} = \psi(\mathbf{d}) = \sqrt{\frac{2}{9}\frac{(3k^2-2k+3)}{(1+k)^2}\left[\left(d_1^2+d_2^2\right) + \frac{(3k^2+10k+3)}{(3k^2-2k+3)}d_3^2\right]} \tag{6.42}$$

for any $(d_1, d_2, d_3) \in D_3^+$. Similar arguments are used to deduce the expression of the strain-rate potential in the domain D_3^-.

In summary, the expression of the exact dual of the isotropic Cazacu et al. [5] quadratic stress potential [Eq. (6.27)] is the strain-rate potential $\psi(\mathbf{d})$ given by:

$$\psi(\mathbf{d}) = \begin{cases} \dfrac{1}{m(1-k)}\cdot\sqrt{d_1^2+d_2^2+\left[\dfrac{3k^2-10k+3}{3k^2+2k+3}\right]d_3^2}, & \text{if } (d_1,d_2,d_3)\in D_3^-, \\ \dfrac{1}{m(1+k)}\cdot\sqrt{d_1^2+d_2^2+\left[\dfrac{3k^2+10k+3}{3k^2-2k+3}\right]d_3^2}, & \text{if } (d_1,d_2,d_3)\in D_3^+, \end{cases} \tag{6.43}$$

with the domains D_3^+ and D_3^- described by Eqs. (6.36) and (6.38), respectively. The expressions of the other branches of $\psi(\mathbf{d})$, corresponding to the domains D_j^+ and D_j^- (j = 1, 2), are obtained from Eq. (6.43) by symmetry (see also Fig. 6.10 for the geometric representation of these domains in the octahedral plane).

Remark Note that if there is no difference between the plastic response in tension–compression, i.e., $k = 0$, then the Cazacu et al. [8] strain-rate potential reduces to: $\psi(\mathbf{d}) = \sqrt{\frac{2}{3}\left(d_1^2+d_2^2+d_3^2\right)}$ [i.e., the von Mises SRP given by Eq. (6.10)]. As an example, in Fig. 6.11 is shown the representation in the octahedral plane of the

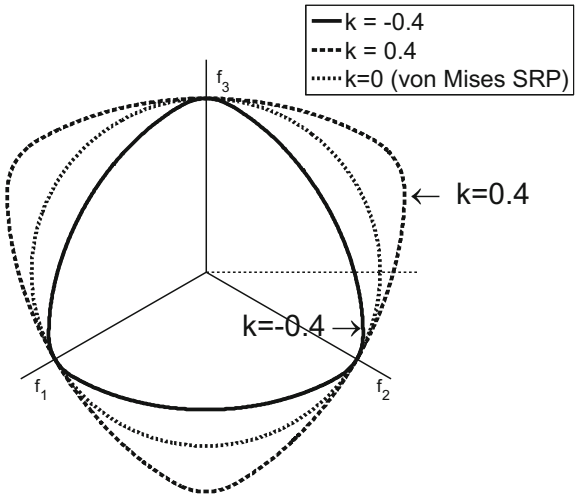

Fig. 6.11 Representation in the octahedral plane of the Cazacu et al. [6] isotropic strain-rate potential [Eq. (6.43)] corresponding to $k = -0.4$, $k = 0.4$; and $k = 0$ (the von Mises SRP), respectively

strain-rate potential given by Eq. (6.43) corresponding to $k = -0.4$ $(\sigma_T/\sigma_C = 0.79)$ and $k = 0.4$ $(\sigma_T/\sigma_C = 1.26)$ along with the von Mises SRP ($k = 0$ or $\sigma_T/\sigma_C = 1$), respectively. Note a clear difference in shape between this SRP and the von Mises SRP (circle). This strong difference is a result of the tension–compression asymmetry of the plastic flow.

It is worth representing side-by-side the plastic potentials in the two dual spaces, i.e., the strain-rate space and the stress space. Figure 6.12a shows the Cazacu et al. [6] strain-rate potential for $k = 0.3$, $k = -0.3$, and $k = 0$, respectively, while Fig. 6.12b shows the representation of the associated stress potential in the dual space, i.e., the stress space. It is worth noting that while the Cazacu et al. [6] SRP corresponding to $k = 0.3$ is the outer surface in the strain-rate space, on account of plastic energy equivalence, it becomes the inner surface in the stress space.

Figures 6.13 and 6.14 show the representation in the biaxial plane (d_1, d_2) with $d_3 = -d_1 - d_2$ of the Cazacu et al. [6] isotropic SRP corresponding to $k = 0.4$ (σ_T/σ_C = 1.26), $k = -0.4$ (σ_T/σ_C = 0.79) along with the von Mises SRP ($k = 0$ or σ_T/σ_C = 1), respectively. It is clearly seen that a change in the sign of the parameter k results in a mirror image of the strain-rate potential.

6.1.2.2 Application to Fixed-End Torsion

In Chap. 4, it was presented the application of the isotropic and quadratic form of the Cazacu et al. [5] stress potential in conjunction with an isotropic hardening law to the description of shear and monotonic combined axial-torsional loadings. In particular, for the case of free-end torsion of a rod, the analytical calculations have shown that for an isotropic material with yielding displaying tension–compression asymmetry $(k \neq 0)$ axial plastic deformation should occur.

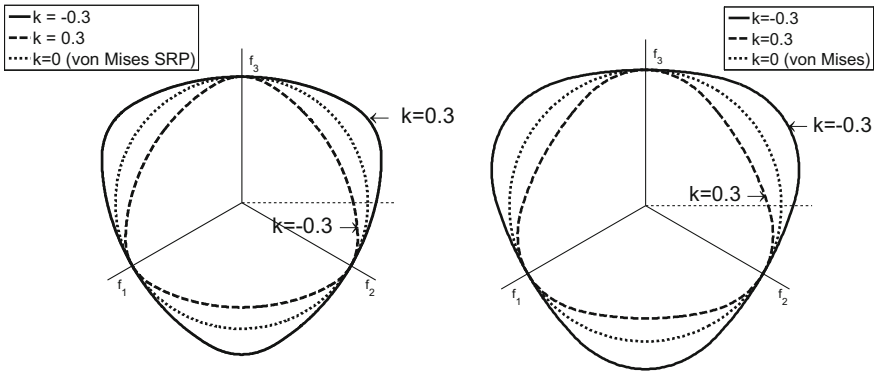

(a) Strain-rate space (b) Stress space

Fig. 6.12 Representation in the octahedral plane of the exact work-conjugate dual: **a** the Cazacu et al. [6] isotropic strain-rate potential [Eq. (6.43)], **b** the Cazacu et al. [5] stress potential corresponding to $k = 0.3$, $k = -0.3$, and $k = 0$, respectively

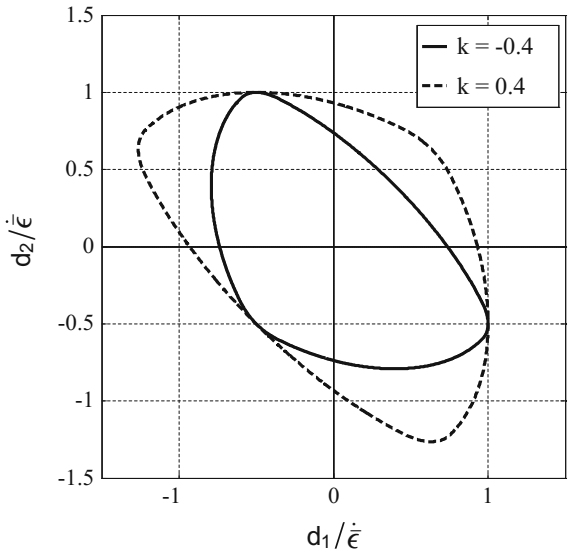

Fig. 6.13 Representation in the biaxial plane of the Cazacu et al. [6] isotropic strain-rate potential corresponding to $k = 0.4$ and $k = -0.4$, respectively

For fixed-end torsion loadings, the strain-rate-based formulation of the elastic-plastic response (see Chap. 2 for the general form of the governing equations) is more suitable to analytical calculations.

Consider a rod, sheared due to a given twist applied at its end. Fixed-end boundary conditions are imposed, i.e., the axial length of the rod cannot change. For simplicity, the cross-section is assumed to be circular. In the cylindrical

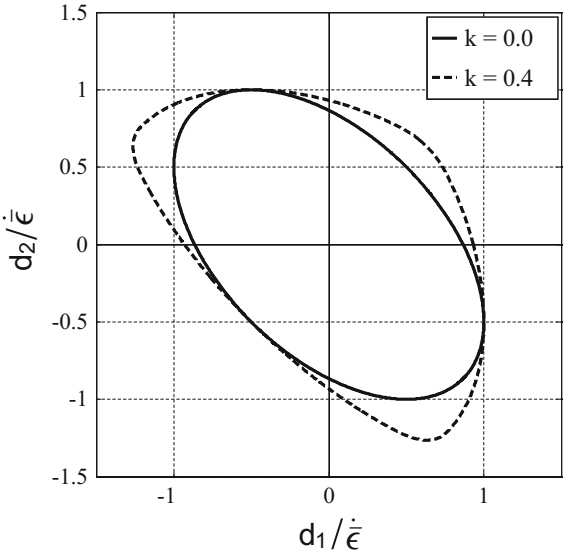

Fig. 6.14 Representation in the biaxial plane of the Cazacu et al. [6] isotropic strain-rate potential corresponding to $k = 0.4$ in comparison with the von Mises SRP ($k = 0$)

coordinate system $(\mathbf{e}_r, \mathbf{e}_\theta, \mathbf{e}_z)$, the plastic strain-rate tensor is of the form $\mathbf{d} = \gamma(\mathbf{e}_z \otimes \mathbf{e}_\theta + \mathbf{e}_\theta \otimes \mathbf{e}_z)$ and its principal values are:

$$d_1 = -\dot{\gamma};\ d_2 = 0;\ d_3 = \dot{\gamma}. \tag{6.44}$$

The plastic behavior is described by the isotropic form of the Cazacu et al. [6] SRP given by Eq. (6.43), and the stress is given by the gradient of this potential. Given that the material is isotropic, the principal directions of the stress $\boldsymbol{\sigma}$ are also principal directions of the plastic strain-rate tensor, $\mathbf{d}$, and the eigenvalues σ_i, i = 1, …, 3, have the following expressions:

- For $\dfrac{-1}{\sqrt{2}} \leq \dfrac{-(3k^2+2k+3)}{\sqrt{6(k^2+3)(3k^2+1)}}$,

$$\begin{cases} \dfrac{\sigma_1}{\sigma_T} = \dfrac{-\dot{\gamma}(3k^2-10k+3)}{m(1-k)\sqrt{2(3k^2-4k+3)(3k^2+2k+3)}}, \\ \dfrac{\sigma_2}{\sigma_T} = 0 \\ \dfrac{\sigma_3}{\sigma_T} = \dfrac{\dot{\gamma}\sqrt{3k^2+2k+3}}{m(1-k)\sqrt{2(3k^2-4k+3)}} \end{cases} \tag{6.45}$$

- For $\dfrac{1}{\sqrt{2}} \geq \dfrac{3k^2-2k+3}{\sqrt{6(k^2+3)(3k^2+1)}}$,

$$\begin{cases} \dfrac{\sigma_1}{\sigma_T} = \dfrac{-\dot{\gamma}}{m(1+k)}\sqrt{\dfrac{3k^2-2k+3}{2(3k^2+4k+3)}}, \\ \dfrac{\sigma_2}{\sigma_T} = 0 \\ \dfrac{\sigma_3}{\sigma_T} = \dfrac{\dot{\gamma}(3k^2+10k+3)}{m(1+k)\sqrt{2(3k^2+4k+3)(3k^2-2k+3)}} \end{cases} \tag{6.46}$$

Making use of Eqs. (6.45) and (6.46), the Cauchy stress tensor can be expressed in the cylindrical coordinate system as:

$$\boldsymbol{\sigma} = \begin{bmatrix} 0 & 0 & 0 \\ 0 & 0 & \tau \\ 0 & \tau & \sigma \end{bmatrix}_{(r,\theta,z)} \tag{6.47}$$

where the axial stress is given by:

$$\sigma = \begin{cases} \dfrac{12k(\dot{\gamma})}{m(1-k)\sqrt{2(3k^2+2k+3)(3k^2-4k+3)}} & \text{if } \dfrac{-1}{\sqrt{2}} \leq \dfrac{-(3k^2+2k+3)}{\sqrt{6(k^2+3)(3k^2+1)}} \\ \dfrac{12k(\dot{\gamma})}{m(1+k)\sqrt{2(3k^2-2k+3)(3k^2+4k+3)}} & \text{if } \dfrac{1}{\sqrt{2}} \geq \dfrac{3k^2-2k+3}{\sqrt{6(k^2+3)(3k^2+1)}} \end{cases} \tag{6.48}$$

and the ratio between the axial and shear stresses is:

$$\frac{\sigma}{\tau} = \begin{cases} \dfrac{12k}{\sqrt{(3k^2+2k+3)(3k^2-10k+3)}} & \text{if } \dfrac{-1}{\sqrt{2}} \leq \dfrac{-(3k^2+2k+3)}{\sqrt{6(k^2+3)(3k^2+1)}} \\ \dfrac{12k}{\sqrt{(3k^2-2k+3)(3k^2+10k+3)}} & \text{if } \dfrac{1}{\sqrt{2}} \geq \dfrac{3k^2-2k+3}{\sqrt{6(k^2+3)(3k^2+1)}} \end{cases} \tag{6.49}$$

Therefore, if $k \neq 0$, axial stress σ develops under fixed-end torsion, and $\text{sgn}(\sigma) = \text{sgn}(k)$. This means that according to the model, under fixed-end torsion:

(i) For materials characterized by $\sigma_T < \sigma_C$ for which $k < 0$ [see Eq. (6.29)], the axial stress that develops is negative (compression).
(ii) For materials characterized by $\sigma_T > \sigma_C$ for which $k > 0$ [see Eq. (6.29)], the axial stress that develops is positive (tension).
(iii) Only if $\sigma_T = \sigma_C$ $(k = 0)$, no axial stress develops during the test.

This predicted evolution of the ratio σ/τ as a function of the parameter k is also illustrated in Fig. 6.15.

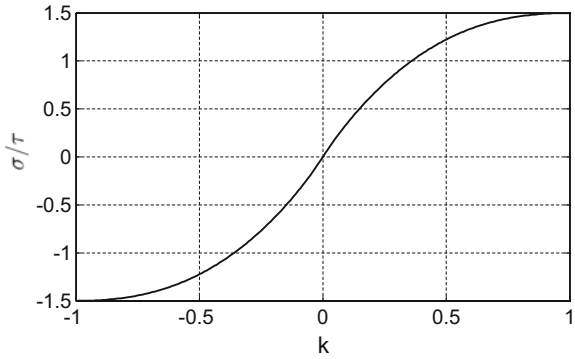

Fig. 6.15 Evolution of the ratio between the axial stress and the shear stress in a fixed-end torsion test as a function of the tension–compression parameter k predicted by the isotropic Cazacu et al. [6] SRP

In summary, the analytical solutions based on the isotropic and quadratic form of the Cazacu et al. [5] stress potential and its SRP, respectively, lead to the conclusion that even a slight difference between the uniaxial yield in tension, σ_T, and the uniaxial yield in compression, σ_C, results in Swift effects, i.e., development of axial strains under free-end torsion (see Chap. 4) and uniaxial stresses under fixed-end torsion, respectively. The sign of the axial strain, or stress depends on the ratio σ_T/σ_C. Specifically, if $\sigma_T/\sigma_C > 1$, the axial strain that develops under free-end torsion is negative (shortening of the specimen occurs) and the uniaxial stress that develops under fixed-end torsion is tensile. On the other hand, if $\sigma_T/\sigma_C < 1$, the axial strain is positive (lengthening of the specimen) and the uniaxial stress is negative (compression), respectively.

6.2 Orthotropic Strain-Rate Plastic Potentials

6.2.1 Strain-Rate Potentials for Orthotropic Materials with the Same Response in Tension–Compression

In this section are presented the most widely used strain-rate potentials for anisotropic metallic materials that have the same mechanical response in tension–compression. It is demonstrated that the quadratic orthotropic Hill [15] strain-rate potential is the exact dual of the orthotropic stress potential of Hill [14]. The complete proof is given in Sect. 6.2.1.1. Moreover, using arguments similar to the ones that were used for demonstrating Proposition 5.4 in Chap. 5, it is shown that the extension to orthotropy of the von Mises SRP [see Eq. (6.10)] obtained using the generalized invariants approach is in fact the Hill [15] orthotropic strain-rate potential. Next, non-quadratic orthotropic strain-rate potentials that involve one or several linear transformations applied to the plastic strain-rate tensor **d** are discussed. While none of these strain-rate potentials are exact work-conjugate of the respective non-quadratic stress potentials, it is shown that these strain-rate formulations describe the plastic anisotropy of textured polycrystalline metals with a degree of accuracy comparable to that obtained using the stress potentials.

6.2.1.1 Exact Dual of the Hill [14] Stress Potential

Using the work-equivalence principle (see Sect. 2.2), Hill [15] derived the expression of a three-dimensional orthotropic strain-rate potential that is the exact dual of the orthotropic stress potential that this author had proposed in Hill [14] (see Sect. 5.2).

In the coordinate system $(\mathbf{x}, \mathbf{y}, \mathbf{z})$ associated with the axes of orthotropic symmetry, this strain-rate potential is expressed as:

$$\psi(\mathbf{d}) = \sqrt{\frac{F}{\Delta} d_{xx}^2 + \frac{G}{\Delta} d_{yy}^2 + \frac{H}{\Delta} d_{zz}^2 + \frac{2}{L} d_{yz}^2 + \frac{2}{M} d_{xz}^2 + \frac{2}{N} d_{xy}^2}, \tag{6.50}$$

where F, G, H, L, M, and N are anisotropy coefficients and $\Delta = FH + FG + GH$. In the following, we present the proof provided in Hill [15].

Proposition 6.2 Hill [15] *orthotropic strain-rate potential (SRP) can be expressed as:*

$$\psi(\mathbf{d}) = \sqrt{\mathbf{d} : \mathbf{U}\mathbf{d}}, \tag{6.51}$$

where $\mathbf{U}$ *is an orthotropic constant fourth-order tensor satisfying both major and minor symmetries, i.e.,* $U_{ijkl} = U_{klij} = U_{jikl}$ *for i, j, k, l = 1, 2, 3 and* $U_{iikl} = 0$ *(sum over i). Moreover, this SRP is the exact dual of* Hill [14] *orthotropic stress potential.*

Proof As shown in Sect. 5.2, the Hill [14] orthotropic stress potential can be written as:

$$\varphi_{\text{Hill}}(\boldsymbol{\sigma}) = \sqrt{\boldsymbol{\sigma} : \mathbf{M}\,\boldsymbol{\sigma}}, \tag{6.52}$$

where $\mathbf{M}$ is a fourth-order orthotropic constant tensor satisfying both major and minor symmetries, i.e., $M_{ijkl} = M_{klij} = M_{jikl}$ for $i, j, k, l = 1, 2, 3$, and the additional constraints:

$$M_{iikl} = 0 \tag{6.53}$$

Therefore, according to the flow rule and making use of Eq. (6.53),

$$\mathbf{d} = \dot{\lambda} \frac{\partial \varphi_{\text{Hill}}}{\partial \boldsymbol{\sigma}} = \frac{\dot{\lambda}}{\tau} (\mathbf{M}\mathbf{s}) \tag{6.54}$$

with $\varphi_{\text{Hill}}(\boldsymbol{\sigma}) = \tau$ defining the yield surface and τ a positive scalar with the dimension of stress.

Let $\mathbf{K}$ be the fourth-order symmetric deviatoric unit tensor (see Chap. 1 for the expressions of its components with respect to any Cartesian coordinate system), and $\mathbf{U}$ a fourth-order symmetric tensor such that: $\mathbf{UM} = \mathbf{MU} = \mathbf{K}$. Making use of Eq. (6.54), we obtain:

$$\mathbf{Ud} = \dot{\lambda}\frac{\boldsymbol{s}}{\tau}. \tag{6.55}$$

Therefore, $\boldsymbol{s} = \frac{\tau}{\dot{\lambda}}(\mathbf{Ud})$, and the work-rate per unit current volume is given by:

$$\dot{\mathrm{W}}^{\mathrm{I}} = \boldsymbol{\sigma} : \mathbf{d} = \frac{\tau}{\dot{\lambda}}(\mathbf{Ud}) : \mathbf{d} = \dot{\lambda}\tau. \tag{6.56}$$

It follows that $\dot{\lambda}$ can be expressed as:

$$\dot{\lambda} = \sqrt{\mathbf{d} : \mathbf{Ud}}.$$

In conclusion, it was demonstrated that the strain-rate potential $\psi(\mathbf{d}) = \sqrt{\mathbf{d} : \mathbf{Ud}}$ is the exact work-conjugate of the Hill [14] stress potential $\varphi_{\mathrm{Hill}}(\boldsymbol{\sigma})$ given by Eq. (6.52). Furthermore, the expression given by Eq. (6.51) of this SRP allows us to recognize that $\psi(\mathbf{d})$ is the orthotropic generalization of the second-invariant of the strain-rate tensor $\mathbf{d}$ (see also the proof of Proposition 5.4 of Chap. 5).

To determine the components of $\mathbf{U}$ in the coordinate system $(\boldsymbol{x}, \boldsymbol{y}, \boldsymbol{z})$ associated with the axes of orthotropy, let us first recall that with respect to these axes and in Voigt notations, the fourth-order orthotropic and symmetric tensor $\mathbf{M}$ is represented by the 6×6 symmetric matrix (see also Sect. 5.2):

$$\mathbf{M} = \begin{bmatrix} H+G & -H & -G & 0 & 0 & 0 \\ -H & F+H & -F & 0 & 0 & 0 \\ -G & -F & F+G & 0 & 0 & 0 \\ 0 & 0 & 0 & L & 0 & 0 \\ 0 & 0 & 0 & 0 & M & 0 \\ 0 & 0 & 0 & 0 & 0 & N \end{bmatrix} \tag{6.57}$$

Since $\mathbf{UM} = \mathbf{MU} = \mathbf{K}$, with respect to the same coordinate system, the fourth-order tensor $\mathbf{U}$ is represented by the following matrix:

$$\mathbf{U} = \begin{bmatrix} \frac{4F+G+H}{9\Delta} & \frac{H-2F-2G}{9\Delta} & \frac{G-2F-2H}{9\Delta} & 0 & 0 & 0 \\ \frac{H-2F-2G}{9\Delta} & \frac{4G+F+H}{9\Delta} & \frac{F-2G-2H}{9\Delta} & 0 & 0 & 0 \\ \frac{G-2F-2H}{9\Delta} & \frac{F-2G-2H}{9\Delta} & \frac{4H+G+F}{9\Delta} & 0 & 0 & 0 \\ 0 & 0 & 0 & \frac{1}{L} & 0 & 0 \\ 0 & 0 & 0 & 0 & \frac{1}{M} & 0 \\ 0 & 0 & 0 & 0 & 0 & \frac{1}{N} \end{bmatrix} \tag{6.58}$$

where $\Delta = FH + FG + GH$. Note that $\mathbf{U}$ is orthotropic and satisfies $U_{iikl} = 0$ (sum over i).

By substituting $\mathbf{U}$ given by Eq. (6.58) into Eq. (6.51), and taking into account that the plastic strain-rate tensor $\mathbf{d}$ is traceless, we obtain the expression of the strain-rate potential given by Eq. (6.50).

Proposition 6.3 The Hill [15] *orthotropic strain-rate potential is the extension to orthotropy of the von Mises strain-rate potential given by* Eq. (6.10).

Proof The Hill [15] orthotropic strain-rate potential can be expressed as

$$\psi(\mathbf{d}) = \sqrt{(4/3)j_2^0},$$

where j_2^0 is the orthotropic second-invariant of $\mathbf{d}$, i.e.,

$$\begin{aligned} j_2^0 = {} & \frac{a_1}{6}\left(d_{xx} - d_{yy}\right)^2 + \frac{a_2}{6}\left(d_{yy} - d_{zz}\right)^2 + \frac{a_3}{6}\left(d_{xx} - d_{zz}\right)^2 \\ & + a_4 d_{xy}^2 + a_5 d_{xz}^2 + a_6 d_{yz}^2. \end{aligned} \tag{6.59}$$

In the above equation, a_j, $j = 1, \ldots, 6$, are constants. Their expressions in terms of the anisotropy coefficients F, G, H, L, M, and N can be easily obtained from Eq. (6.50) using Eq. (6.59) and the plastic incompressibility condition $(d_{xx} + d_{yy} + d_{zz} = 0)$.

Note also that for isotropic materials, the tensor $\mathbf{M}$ should be proportional to the fourth-order symmetric and deviatoric tensor $\mathbf{K}$, i.e., $F = G = H = L/3 = M/3 = N/3$ [see Eq. (6.57)]. Therefore, for isotropic materials, the Hill [14] stress potential reduces to the von Mises stress potential, and consequently, the Hill [15] SRP reduces to the von Mises SRP.

In closing, let us note that if the plastic behavior is described using the Hill [14] stress potential, the plastic strain-rates (or plastic strain increments) are proportional to the gradient of $\varphi_{\text{Hill}}(\boldsymbol{\sigma})$ [see Eq. (7.22)]. Alternatively, if the plastic behavior is modeled with the strain-rate potential given by Eq. (6.50), the stresses are calculated by taking the gradient of this SRP. Specifically, using the Hill [15] strain-rate potential, we obtain that in the coordinate system associated with the axes of orthotropy, the components of the stress deviator are:

$$\begin{aligned} s_{xx} &= \tau\frac{\partial\psi}{\partial d_{xx}} = \frac{2\tau}{9\Delta\psi}\left[2Fd_{xx} - Gd_{yy} - Hd_{yy}\right] \\ s_{yy} &= \tau\frac{\partial\psi}{\partial d_{yy}} = \frac{2\tau}{9\Delta\psi}\left[2Gd_{yy} - Fd_{xx} - Hd_{zz}\right] \\ s_{zz} &= \tau\frac{\partial\psi}{\partial d_{zz}} = \frac{2\tau}{9\Delta\psi}\left[2Hd_{zz} - Fd_{xx} - Gd_{yy}\right] \\ s_{yz} &= \tau\frac{\partial\psi}{\partial d_{yz}} = \frac{2\tau}{3\Delta\psi}\frac{d_{yz}}{L}, \\ s_{xz} &= \tau\frac{\partial\psi}{\partial d_{xz}} = \frac{2\tau}{3\Delta\psi}\frac{d_{xz}}{M}, \\ s_{xy} &= \tau\frac{\partial\psi}{\partial d_{xy}} = \frac{2\tau}{3\Delta\psi}\frac{d_{xy}}{N}. \end{aligned} \tag{6.60}$$

It is also important to note that if the plastic behavior is described with Hill's SRP given by Eq. (6.50), we obtain Eq. (5.40), which is the expression for the

Lankford coefficients deduced using Hill [14] stress-based potential. This is a direct consequence of the fact that the Hill [15] SRP is the exact dual of the Hill [14] stress potential. The complete proof is given in the following.

Uniaxial tension: variation of the Lankford coefficient with tensile direction obtained using Hill [15] *orthotropic SRP*

Let us denote as $(1,2,3)$ the loading frame. In this frame, for uniaxial tension along the direction 1 at an angle ξ from the rolling direction $\boldsymbol{x}$, the plastic strain-rate tensor is:

$$\boldsymbol{d} = d_{11}\begin{pmatrix} 1 & d_{12}/d_{11} & 0 \\ d_{12}/d_{11} & -r(\xi)/(1+r(\xi)) & 0 \\ 0 & 0 & -1/(1+r(\xi)) \end{pmatrix} \tag{6.61}$$

where $r(\xi)$ denotes the Lankford coefficient. Therefore, in the reference frame $(\mathbf{x},\mathbf{y},\mathbf{z})$ associated with the axes of orthotropy, the only nonzero plastic strain-rate components are:

$$\begin{aligned} d_{xx}/d_{11} &= \cos^2\xi - \frac{r(\xi)}{1+r(\xi)}\sin^2\xi - (d_{12}/d_{11})\sin 2\xi \\ d_{yy}/d_{11} &= \sin^2\xi - \frac{r(\xi)}{1+r(\xi)}\cos^2\xi + (d_{12}/d_{11})\sin 2\xi \\ d_{xy}/d_{11} &= \frac{1+2r(\xi)}{1+r(\xi)}\sin\xi\,\cos\xi + (d_{12}/d_{11})\cos 2\xi \end{aligned} \tag{6.62}$$

and $d_{zz} = -\left(d_{xx}+d_{yy}\right)$, while the only nonzero stress components are:

$$\begin{aligned} \sigma_{xx} &= \sigma(\xi)\cos^2\xi \\ \sigma_{yy} &= \sigma(\xi)\sin^2\xi \\ \sigma_{xy} &= \sigma(\xi)\sin\xi\,\cos\xi \end{aligned} \tag{6.63}$$

Since $\sigma_{zz} = 0$, it follows that the mean stress $\sigma_{\mathrm{m}} = (tr\boldsymbol{\sigma})/3$ is equal to $(-s_{zz})$ or:

$$\sigma_{\mathrm{m}} = -s_{zz} = -\tau\frac{\partial\psi}{\partial d_{zz}} = \frac{\sigma(\xi)}{3} \tag{6.64}$$

and consequently,

$$\begin{aligned}\sigma_{xx} &= \tau\left(\frac{\partial\psi}{\partial d_{xx}} - \frac{\partial\psi}{\partial d_{zz}}\right) = \sigma(\xi)\cos^2\xi \\ \sigma_{yy} &= \tau\left(\frac{\partial\psi}{\partial d_{yy}} - \frac{\partial\psi}{\partial d_{zz}}\right) = \sigma(\xi)\sin^2\xi \\ \sigma_{xy} &= s_{xy} = \tau\frac{\partial\psi}{\partial d_{xy}} = \sigma(\xi)\sin\xi\cos\xi\end{aligned} \tag{6.65}$$

Therefore, for $\xi \neq 0^\circ$ and $\xi \neq 90^\circ$ (i.e., uniaxial tension along a direction other than the rolling or transverse directions)

$$\sigma_{yy}\cos^2\xi - \sigma_{xx}\sin^2\xi = 0, \tag{6.66}$$

which upon substitution in Eq. (6.60) leads to:

$$\left(Gd_{yy} - Hd_{zz}\right)\cos^2\xi = \left(Fd_{xx} - Hd_{zz}\right)\sin^2\xi \tag{6.67}$$

Next, substituting in the above equation the expressions of d_{xx}, d_{yy}, d_{zz} given by Eq. (6.62), we obtain the expression of d_{12} in terms of the anisotropy coefficients and $r(\xi)$, i.e.,

$$\frac{d_{12}}{d_{11}} = \frac{F\sin^2\xi(\cos^2\xi + r(\xi)\cos(2\xi)) + G\cos^2\xi\left(-\sin^2\xi + r(\xi)\cos(2\xi)\right) - H\cos(2\xi)}{(1+r(\xi))\left(F\sin^2\xi + G\cos^2\xi\right)\sin(2\xi)} \tag{6.68}$$

Substituting Eq. (6.68) in Eq. (6.62), leads to:

$$\begin{aligned}\frac{d_{xx}}{d_{11}} &= \frac{G\cos^2\xi + H\cos 2\xi}{(1+r(\xi))\left(F\sin^2\xi + G\cos^2\xi\right)} \\ \frac{d_{yy}}{d_{11}} &= \frac{F\sin^2\xi - H\cos 2\xi}{(1+r(\xi))\left(F\sin^2\xi + G\cos^2\xi\right)} \\ \frac{d_{xy}}{d_{11}} &= \frac{r(\xi)}{\sin 2\xi(r(\xi)+1)} + \frac{(F+G)\sin^2\xi\cos^2\xi - H\cos^2 2\xi}{(1+r_\xi)\left(F\sin^2\xi + G\cos^2\xi\right)\sin 2\xi}\end{aligned} \tag{6.69}$$

To obtain the expression of the Lankford coefficient $r(\xi)$ as a function of the angle ξ, we need to minimize the plastic work-rate per unit of the current volume $\dot{W}^I = \tau\psi(\mathbf{d})$ with respect to $r(\xi)$. This amounts to minimizing $\{\mathbf{d}{:}\mathbf{U}\mathbf{d}\}^{\frac{1}{2}}$ with respect to $r(\xi)$. For this purpose, Eq. (6.69) are substituted in the expression of the SRP given by Eq. (6.50), and then the differential with respect to $r(\xi)$ is set to zero, leading to the following equation:

$$\frac{r(\xi)}{\sin 2\xi} + V(\xi) = NX(\xi) \tag{6.70}$$

where

$$V(\xi) = \frac{(F+G)\sin^2\xi\cos^2\xi - H\cos^2 2\xi}{\sin 2\xi\left(F\sin^2\xi + G\cos^2\xi\right)}$$

$$X(\xi) = \frac{F(G\cos^2\xi + H\cos 2\xi)^2 + G\left(F\sin^2\xi - H\cos 2\xi\right)^2}{2\Delta(-V(\xi) + 1/\sin 2\xi)\left(F\sin^2\xi + G\cos^2\xi\right)^2} + \frac{H}{2\Delta(-V(\xi) + 1/\sin 2\xi)}$$

and $\Delta = FH + FG + GH$.

After further simplifications, we obtain:

$$r(\xi) = \frac{(2N - G - F)\sin^2\xi\cos^2\xi + H\cos^2(2\xi)}{F\sin^2\xi + G\cos^2\xi}, \tag{6.71}$$

which is exactly the same expression of the Lankford coefficient obtained based on the Hill [14] stress potential [see Chap. 5, Eq. (5.40)].

As an example, for the AA2090-T3 for which uniaxial tensile data and the anisotropy in the plastic behavior were discussed in Chap. 5, Fig. 6.16 shows the projections in various biaxial planes of the SRP isosurfaces according to Hill [9] with coefficients $F = 0.252$, $G = 0.825$, $H = 0.175$, $N = 2.238$ obtained using as input the experimental r-values. Also, for the same AA2090-T3, in Fig. 6.17 are represented the strain-rate isosurfaces, plotted for several fixed levels of the shear strain-rate $d_{xy}/\bar{\dot{\varepsilon}} = 0, 0.5, 0.75, 1,$ and 1.05, respectively. As expected, according to the Hill [15] quadratic SRP, all the cross-sections are elliptical.

6.2.1.2 Orthotropic Strain-Rate Potential of Barlat et al. [2]: SRP93

Barlat et al. [2] have extended to orthotropy the isotropic strain-rate potential given by Eq. (6.18) by making use of the linear transformation approach (see also the discussion in Chap. 5 about this rigorous methodology for introducing anisotropy in any given isotropic formulation). The expression of the orthotropic Barlat et al. [5] strain-rate potential, denoted SRP93, is

$$\psi_{BC}(\mathbf{d}) = \left(\frac{1}{2}\left(\left|\tilde{E}_1\right|^b + \left|\tilde{E}_2\right|^b + \left|\tilde{E}_3\right|^b\right)\right)^{1/b} \tag{6.72}$$

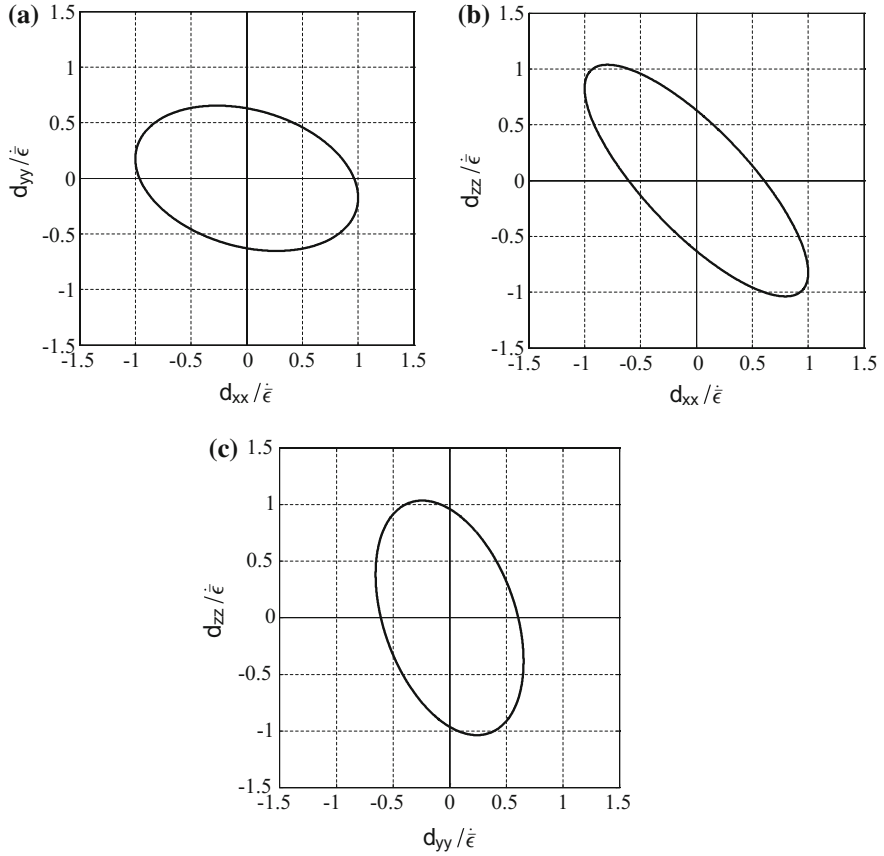

Fig. 6.16 Representation in the biaxial planes of the Hill [15] strain-rate potential for an AA2090-T3 for loadings such that $d_{xy} = d_{xz} = d_{yz} = 0$: **a** cross-section in the plane (d_{xx}, d_{yy}), **b** cross-section in the plane (d_{xx}, d_{zz}), **c** cross-section in the plane (d_{yy}, d_{zz})

with $b = 4/3$ for fcc polycrystals and $b = 3/2$ for bcc polycrystals. In Eq. (6.72), $\tilde{E}_1$, $\tilde{E}_2$, and $\tilde{E}_3$ denote the principal values (not necessarily ordered) of the transformed strain-rate tensor $\tilde{\mathbf{E}}$ defined as:

$$\tilde{\mathbf{E}} = \mathbf{L}\mathbf{d},$$

where $\mathbf{L}$ is an orthotropic fourth-order symmetric and deviatoric tensor. If in Voigt notations, the plastic strain-rate tensor is represented by the six-dimensional vector $\mathbf{d} = \left(d_{xx}, d_{yy}, d_{zz}, d_{yz}, d_{xz}, d_{xy}\right)$ in the coordinate system associated with the orthotropy axes, the fourth-order orthotropic tensor $\mathbf{L}$ is represented by the 6×6 matrix:

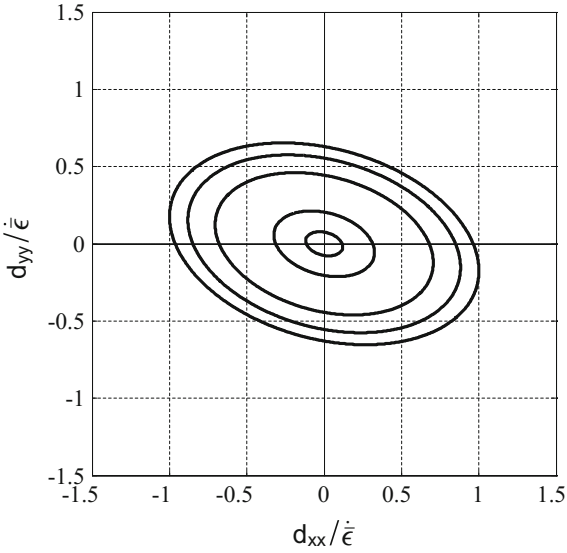

Fig. 6.17 Projection of the yield surfaces for AA2090-T3 sheet in the plane (d_{xx}, d_{yy}) corresponding to fixed levels of the shear strain $d_{xy}/\dot{\bar{\varepsilon}} = 0, 0.5, 0.75, 1,$ and 1.05 according to Hill [15]. The outer curve corresponds to $d_{xy} = 0$

$$\mathbf{L} = \frac{1}{3}\begin{bmatrix} c_3 + c_2 & -c_3 & -c_2 & 0 & 0 & 0 \\ -c_3 & c_1 + c_3 & -c_1 & 0 & 0 & 0 \\ -c_2 & -c_1 & c_1 + c_2 & 0 & 0 & 0 \\ 0 & 0 & 0 & 3c_4 & 0 & 0 \\ 0 & 0 & 0 & 0 & 3c_5 & 0 \\ 0 & 0 & 0 & 0 & 0 & 3c_6 \end{bmatrix} \tag{6.73}$$

where c_i, i = 1, …, 6, are independent anisotropy coefficients.

It can be easily seen that for $b = 2$, the SRP93 reduces to the Hill [15] strain-rate potential given by Eq. (6.51).

It is also worth noting that the SRP93 has been applied to numerous anisotropic metallic sheets, the general consensus being that it is as performant as the Yld 91 orthotropic stress potential of Barlat et al. [1] (for an in-depth presentation and discussion of the Barlat et al. [1] yield function and stress potential, the reader is referred to Sect. 5.3.3). Although in Barlat et al. [2] it was shown numerically that for certain materials the SRP93 given by Eq. (6.72) and the Yld 91 stress potential are work-conjugate, a formal proof has not yet been given. Most importantly, no general relationships have been established between the fourth-order anisotropy tensors involved in the expression of Yld 91 and that of SRP93, respectively. For this reason, even if the anisotropy coefficients involved in Yld 91 stress potential are known for a given material, when the plastic behavior is described using SRP93, an additional identification of the anisotropy coefficients, i.e., components of $\mathbf{L}$ given by Eq. (6.72), is generally done. The procedure for the identification of the coefficients c_i, i = 1, …, 6, uses as input the experimental yield stresses and the Lankford coefficients for several loading orientations in the plane of the sheet (at

Table 6.1 Experimental data for a DP600 steel alloy reported in Kim et al. [17]

Property	Normalized yield stress	r value
Uniaxial tension 0°	1.000	0.86
Uniaxial tension 15°	0.977	0.87
Uniaxial tension 30°	1.000	1.01
Uniaxial tension 45°	1.031	1.15
Uniaxial tension 60°	0.987	1.20
Uniaxial tension 75°	0.987	1.10
Uniaxial tension 90°	0.997	1.04
Equibiaxial tension	0.961	

least the data for RD, 45°, and TD orientations). For example, for the same AA2090-T3, Rabahallah et al. [20] reported the following numerical values of the coefficients involved in the SRP: $c_1 = 0.9056$, $c_2 = 0.9138$, $c_3 = 1.0606$, $c_4 = c_5 = 1.0$, $c_6 = 0.8245$ and $b = 4/3$ while for a DP 600 steel alloy (mechanical data given in Table 6.1) $c_1 = 0.8072$, $c_2 = 0.9663$, $c_3 = 1.0129$, $c_4 = c_5 = 1.0$, $c_6 = 0.9958$ and $b = 4/3$. For AA2090-T3, the corresponding SRP cross-sections in several biaxial planes are shown in Fig. 6.18. The strain-rates are normalized by the equivalent strain-rate in uniaxial tension along the rolling (**x**)-direction.

For the same materials, the coefficients F, G, H, N associated with the Hill [14] potential and the Hill [15] SRP were $F = 0.252$, $G = 0.825$, $H = 0.175$, $N = 2.238$ for AA2090-T3, and $F = 0.493$, $G = 0.511$, $H = 0.489$, $N = 1.307$ for DP600, respectively. Figure 6.19 shows a comparison of the isocontours in the biaxial plane (d_{xx}, d_{yy}) of the strain-rate isosurface according to Hill [15] and Barlat et al. [2], respectively, for these materials. Note that for either material, the Hill [15] surface is circumscribed by the Barlat et al. [2] one. While the Hill [15] cross-section is of elliptical shape, the cross-section according to the Barlat et al. [2] strain-rate potential is a hexagon with rounded corners. Note that the models predict different values of the Lankford coefficient along RD (**x**-direction) and the TD (**y**-direction), respectively. Moreover, there is a strong difference in the predicted response for equibiaxial states (i.e., for states such that $d_{xx} = d_{yy}$).

6.2.1.3 Orthotropic Strain-Rate Potential of Barlat and Chung [4]: SRP2004-18p

The orthotropic strain-rate potential SRP 93 was used in the framework of the ideal forming theory (see Chung and Richmond [9–11]) to determine the initial blank shape necessary to obtain a full drawn cup with uniform height. For the orthotropic AA2090-T3 material (see Table 5.1 for the material's plastic properties), the predictions based on the SRP93 were reported in [3]. These predictions were partially successful, the departure from the data was attributed to the inability of SRP93 to capture the anisotropy of the Lankford coefficients for this material. In an effort to

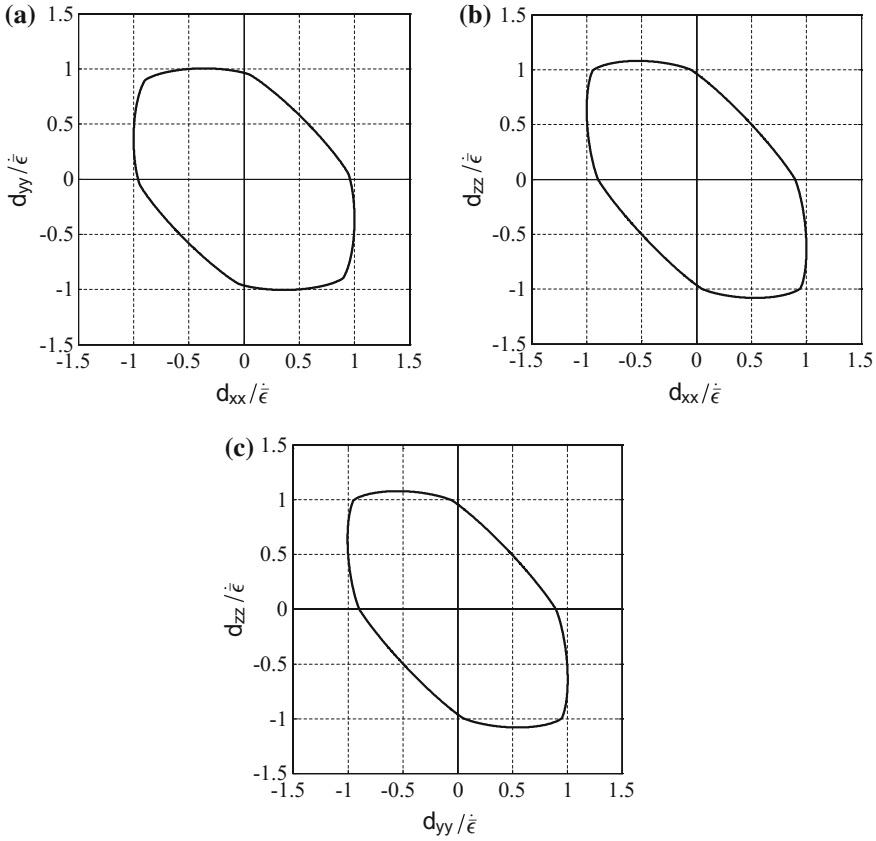

Fig. 6.18 Representation of the cross-sections in the biaxial planes with $d_{xy} = d_{xz} = d_{yz} = 0$ of the strain-rate surface for an AA2090-T3 according to Barlat et al. [2]: **a** cross-section in the plane (d_{xx}, d_{yy}), **b** cross-section in the plane (d_{xx}, d_{zz}), **c** cross-section in the plane (d_{yy}, d_{zz})

keep the characteristics of the SRP93 while improving the description of the plastic anisotropy, Barlat and Chung [4] proposed a 3-D anisotropic strain-rate potential, denoted SRP2004-18p, which involves two linear transformations.

The expression of the SRP2004-18p is:

$$\begin{aligned}\psi = \psi\left(\tilde{E}'_i, \tilde{E}''_j\right) = &\left|\tilde{E}'_1\right|^b + \left|\tilde{E}'_2\right|^b + \left|\tilde{E}'_3\right|^b \\ &+ \left|\tilde{E}''_2 + \tilde{E}''_3\right|^b + \left|\tilde{E}''_3 + \tilde{E}''_1\right|^b + \left|\tilde{E}''_1 + \tilde{E}''_2\right|^b\end{aligned} \tag{6.74}$$

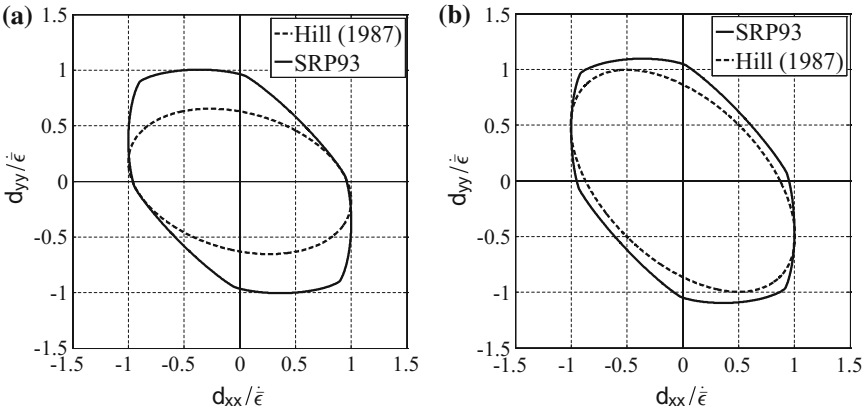

Fig. 6.19 Comparison between the cross-sections in the plane (d_{xx}, d_{yy}) of the strain-rate surface according to the Hill [15] strain-rate potential and the Barlat et al. [2] strain-rate potential, respectively, for: **a** AA2090-T3, **b** DP600 steel alloy. Parameters for each model reported in Rabahallah [19]

where $\tilde{E}'_i$ and $\tilde{E}''_i$ are the principal values of the tensors $\tilde{\dot{\boldsymbol{\varepsilon}}}'$ and $\tilde{\dot{\boldsymbol{\varepsilon}}}''$ defined as:

$$\begin{aligned} \tilde{\dot{\boldsymbol{\varepsilon}}}' &= \mathbf{B}'\mathbf{d} \\ \tilde{\dot{\boldsymbol{\varepsilon}}}'' &= \mathbf{B}''\mathbf{d} \end{aligned} \tag{6.75}$$

In the coordinate system associated with the axes of orthotropy, using Voigt notations, the fourth-order orthotropic tensors $\mathbf{B}'$ and $\mathbf{B}''$ are represented by the following 6×6 matrices:

$$\mathbf{B}' = \begin{bmatrix} 0 & -b'_{12} & -b'_{13} & 0 & 0 & 0 \\ -b'_{21} & 0 & -b'_{23} & 0 & 0 & 0 \\ -b'_{31} & -b'_{32} & 0 & 0 & 0 & 0 \\ 0 & 0 & 0 & b'_{44} & 0 & 0 \\ 0 & 0 & 0 & 0 & b'_{55} & 0 \\ 0 & 0 & 0 & 0 & 0 & b'_{66} \end{bmatrix} \tag{6.76}$$

$$\mathbf{B}'' = \begin{bmatrix} 0 & -b''_{12} & -b''_{13} & 0 & 0 & 0 \\ -b''_{21} & 0 & -b''_{23} & 0 & 0 & 0 \\ -b''_{31} & -b''_{32} & 0 & 0 & 0 & 0 \\ 0 & 0 & 0 & b''_{44} & 0 & 0 \\ 0 & 0 & 0 & 0 & b''_{55} & 0 \\ 0 & 0 & 0 & 0 & 0 & b''_{66} \end{bmatrix} \tag{6.77}$$

In Barlat and Chung [4], it is stated that for orthotropy, the SRP2004-18p strain-rate potential involves 18 independent anisotropy coefficients, and that the

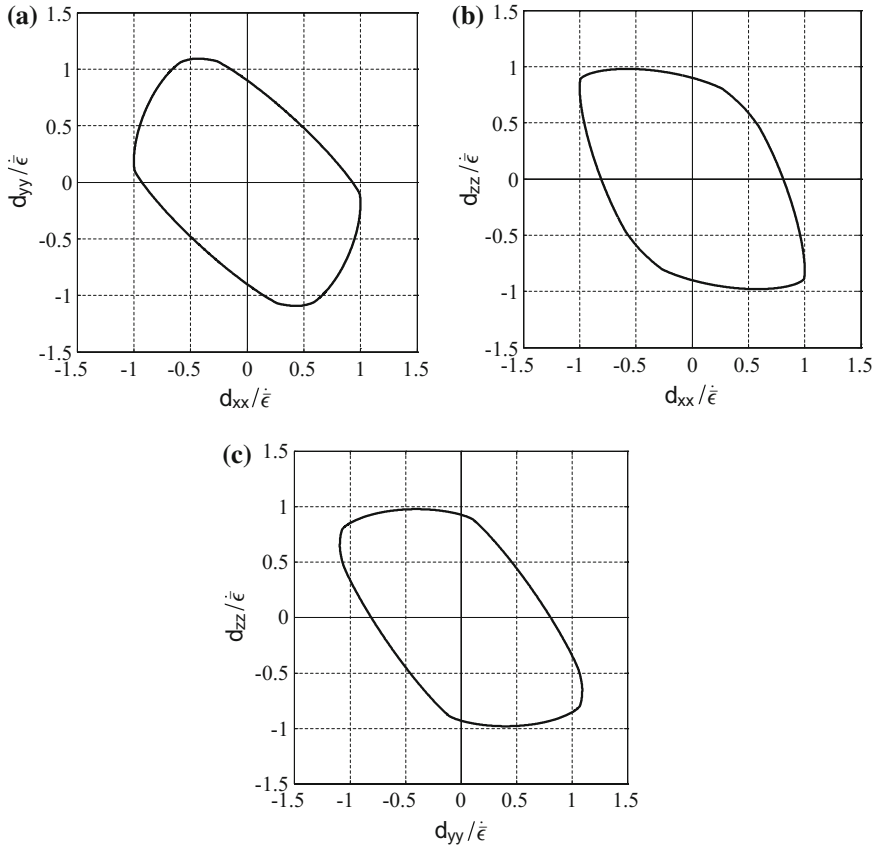

Fig. 6.20 Representation in several biaxial planes $\left(d_{xy} = d_{xz} = d_{yz} = 0\right)$ of the cross-sections of the orthotropic SRP2004-18p (Barlat and Chung [4]) for an AA2090-T3: **a** cross-section in the plane $\left(d_{xx}, d_{yy}\right)$, **b** cross-section in the plane $\left(d_{xx}, d_{zz}\right)$, **c** cross-section in the plane $\left(d_{yy}, d_{zz}\right)$

parameter b should be set to $b = 4/3$ for fcc materials and $b = 3/2$ for bcc materials, respectively.

As an example, in the following are presented the isosurfaces according to the SRP2004-18p strain-rate potential for AA2090-T3 and DP600 sheets (see Figs. 6.20 and 6.21). The numerical values for the anisotropic coefficients of the strain-rate potential for each material that are given in Table 6.2 were reported in Rabahallah [19] and Kim et al. [17], respectively. The parameter b was set to the recommended values for each crystal structure.

Comparison between the isosurfaces according to the SRP93 and the SRP2004-18p presented in Fig. 6.21 for the AA2090-T3 shows that both criteria predict similar curvatures and normals in the biaxial tension quadrant, i.e., $d_{xx} > 0$ and $d_{yy} > 0$. On the other hand, for the DP600 steel alloy, there is a large difference

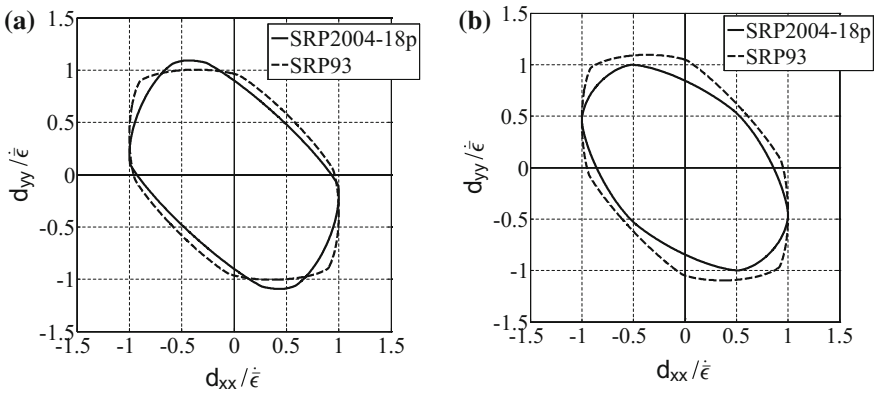

Fig. 6.21 Comparison between the cross-sections of the strain-rate isosurfaces according to the orthotropic SRP 93 [2] and SRP2004-18p [4], respectively, for textured sample sheets: **a** AA2090-T3, **b** DP600 steel alloy

Table 6.2 Anisotropy coefficients of the SRP2004-18p strain-rate potential [4] for AA2090-T3 (after Rabahallah [19]) and DP600 steel alloy (after Kim et al. [17])

	b'_{12}	b'_{13}	b'_{21}	b'_{23}	b'_{31}	b'_{32}	b'_{44}	b'_{55}	b'_{66}
2090-T3	0.39	0.68	0.91	1.01	1.13	0.63	1.00	0.56	1.07
DP600	1.67	0.85	0.62	1.12	0.53	1.10	1.04	1.04	1.43
	b''_{12}	b''_{13}	b''_{21}	b''_{23}	b''_{31}	b''_{32}	b''_{44}	b''_{55}	b''_{66}
2090-T3	1.37	0.77	1.45	0.68	0.94	1.11	1.00	0.56	0.51
DP600	0.89	1.29	0.23	0.34	1.06	0.82	1.04	1.04	0.45

between the shapes of the cross-sections of SRP93 and that of the SRP2004-18p, respectively. The behavior predicted for equibiaxial loadings is completely different. Nevertheless, both isosurfaces are symmetric with respect to the origin, i.e., are invariant by the transformation $(d_{xx}, d_{yy}) \rightarrow (-d_{xx}, -d_{yy})$.

In closing, we note that Barlat and Chung [4] stated that the orthotropic SRP2004-18p involves 18 anisotropy coefficients. For general orthotropy, only 17 of these coefficients are independent (see also discussion in Sect. 5.1 on form-invariance and the possibility of expressing the pseudo-dual stress potentials in terms of generalized invariants). Therefore, an optimal identification of the Barlat and Chung [4] strain-rate potential requires at least 17 independent experimental data to populate the strain-rate space.

6.2.2 Exact Dual of the Orthotropic Cazacu et al. [5] Stress Potential

The orthotropic strain-rate potentials presented in Sect. 6.2.1 are applicable only to the description of the plastic behavior of fully dense textured materials with cubic crystal structure (bcc or fcc) for which the mechanical response is the same in tension–compression. A strain-rate potential that accounts for both orthotropy and the tension–compression asymmetry of polycrystalline materials was developed by Cazacu et al. [6]. This strain-rate potential is the exact dual of the quadratic form of the anisotropic stress potential of Cazacu et al. [5] [see Sect. 5.4.3 and Eq. (5.160)]. The complete proof is presented in the following along with examples that show the ability of this strain-rate potential to describe the complex behavior of hcp metals.

As discussed in Sect. 5.4.3, the quadratic form of the Cazacu et al. [5] orthotropic stress potential is:

$$g\left(\widehat{\sigma}_1,\widehat{\sigma}_2,\widehat{\sigma}_3\right)=\tilde{\sigma}_e-\sigma_0^T=\tilde{m}\sqrt{\sum_{i=1}^{3}\left(\left|\widehat{\sigma}_i\right|-k\widehat{\sigma}_i\right)^2}-\sigma_0^T=0 \tag{6.78}$$

where σ_0^T is the yield stress in tension in the rolling direction, k is a parameter describing the tension–compression asymmetry, $\widehat{\sigma}_1,\widehat{\sigma}_2,\widehat{\sigma}_3$ are the principal values of the transformed tensor $\widehat{\boldsymbol{\sigma}}=\mathbf{L}\mathbf{s}$, where $\mathbf{L}$ is a fourth-order orthotropic and symmetric tensor. In Eq. (6.78), $\tilde{m}$ is a constant defined such that for uniaxial tensile loading, the effective stress $\tilde{\sigma}_e$ reduces to σ_0^T (see Eq. (5.161) for the expression of $\tilde{m}$ in terms of the orthotropy coefficients and the parameter k). Relative to the orthotropy axes, this fourth-order tensor $\mathbf{L}$ operating on the stress deviator $\mathbf{s}$ is represented in Voigt notations by:

$$\mathbf{L}=\begin{bmatrix} L_{11} & L_{12} & L_{13} & 0 & 0 & 0\\ L_{12} & L_{22} & L_{23} & 0 & 0 & 0\\ L_{13} & L_{23} & L_{33} & 0 & 0 & 0\\ 0 & 0 & 0 & L_{44} & 0 & 0\\ 0 & 0 & 0 & 0 & L_{55} & 0\\ 0 & 0 & 0 & 0 & 0 & L_{66} \end{bmatrix} \tag{6.79}$$

[see also Chap. 5, Eq. (5.159)]. To deduce the work-conjugate of the orthotropic stress potential given by Eq. (6.78), Cazacu et al. [8] further assumed that the fourth-order tensor $\mathbf{L}$ is also deviatoric, i.e.,

$$L_{11}+L_{12}+L_{13}=L_{12}+L_{22}+L_{23}=L_{13}+L_{23}+L_{33}=A \tag{6.80}$$

where A is a constant. The additional constraints ensure that $\widehat{\boldsymbol{\sigma}}=\mathbf{L}\mathbf{s}=\mathbf{L}\boldsymbol{\sigma}$.

Next, to calculate the plastic multiplier $\dot{\lambda}$, the expression of g given by Eq. (6.78) is substituted in the flow rule, to obtain:

$$d_{ij} = \dot{\lambda} \frac{\partial g}{\partial \widehat{\sigma}_{kl}} L_{klij} \tag{6.81}$$

when

$$g\left(\widehat{\sigma}_1, \widehat{\sigma}_2, \widehat{\sigma}_3\right) = 0. \tag{6.82}$$

It is worth noting that the symmetric tensor $\mathbf{L}$, given by Eq. (6.79), and satisfying the additional constraints given by Eq. (6.80) is not invertible. However, there exists a 4th order symmetric tensor $\mathbf{H}$ such that

$$\mathbf{HL} = \mathbf{K}, \tag{6.83}$$

where $\mathbf{K}$ is the fourth-order symmetric deviatoric unit tensor (see also Chap. 1). Using (6.81) and (6.83), we obtain that

$$H_{pqij} d_{ij} = \dot{\lambda} \frac{\partial g}{\partial \widehat{\sigma}_{kl}} H_{pqij} L_{ijkl} = \dot{\lambda} K_{pqkl} \frac{\partial g}{\partial \widehat{\sigma}_{kl}}. \tag{6.84}$$

Let us denote the deviator of $\left(\dfrac{\partial g}{\partial \widehat{\boldsymbol{\sigma}}}\right)$ as $\left(\dfrac{\partial g}{\partial \widehat{\boldsymbol{\sigma}}}\right)'$. Hence, in the orthotropic case we have:

$$\mathbf{H} : \mathbf{d} = \dot{\lambda} \left(\frac{\partial g}{\partial \widehat{\boldsymbol{\sigma}}}\right)' \text{ with } g\left(\widehat{\sigma}_1, \widehat{\sigma}_2, \widehat{\sigma}_3\right) = 0. \tag{6.85}$$

Remark Note that in the isotropic case [see Sect. 6.2.1, Eq. (6.31)],

$$\mathbf{d} = \dot{\lambda} \left(\frac{\partial g}{\partial \mathrm{s}}\right)' \text{ when } g(\boldsymbol{s}, m, \sigma_{\mathrm{T}}) = 0. \tag{6.86}$$

Comparison between Eqs. (6.85) and (6.86) shows that the expression of the plastic multiplier for orthotropic materials is obtained simply by replacing in the expression of the isotropic strain-rate potential [Eq. (6.43)] the plastic strain-rate tensor $\mathbf{d}$ by $\mathbf{Hd}$ and the constant m by the constant $\tilde{m}$. Thus, the expression of the Cazacu et al. [8] orthotropic strain-rate potential is:

$$\psi(\mathbf{d}) = \begin{cases} \dfrac{1}{\tilde{m}(1-k)} \cdot \sqrt{B_1^2 + B_2^2 + \left[\dfrac{3k^2 - 10k + 3}{3k^2 + 2k + 3}\right] B_3^2}, & \text{if } (B_1, B_2, B_3) \in D_3^-, \\ \dfrac{1}{\tilde{m}(1+k)} \cdot \sqrt{B_1^2 + B_2^2 + \left[\dfrac{3k^2 + 10k + 3}{3k^2 - 2k + 3}\right] B_3^2}, & \text{if } (B_1, B_2, B_3) \in D_3^+. \end{cases} \tag{6.87}$$

In Eq. (6.87), (B_1, B_2, B_3) are the principal values of the transformed strain-rate tensor $\mathbf{B}$ defined as:

$$\mathbf{B} = \mathbf{H}\mathbf{d}, \tag{6.88}$$

while the domains D_3^+ and D_3^- are described by Eqs. (6.36) and (6.38), respectively. The expressions of the branches of the orthotropic strain-rate potential corresponding to the subspaces D_1^+, D_1^-, D_2^+, and D_2^- are obtained from Eq. (6.88) by symmetry. Thus, for any 3-D loading, the Cazacu et al. [6] orthotropic strain-rate potential writes

$$\psi(\mathbf{d}) = \begin{cases} \dfrac{1}{\tilde{m}(1+k)} \sqrt{\left(B_1^2 + B_2^2 + a_1 B_3^2\right)} & \text{if} \quad \dfrac{B_3|B_3|}{B_1^2 + B_2^2 + B_3^2} \geq X_1 \\ \dfrac{1}{\tilde{m}(1-k)} \sqrt{\left(B_1^2 + B_2^2 + a_2 B_3^2\right)} & \text{if} \quad \dfrac{B_3|B_3|}{B_1^2 + B_2^2 + B_3^2} \leq X_2 \\ \dfrac{1}{\tilde{m}(1+k)} \sqrt{\left(B_1^2 + B_3^2 + a_1 B_2^2\right)} & \text{if} \quad \dfrac{B_2|B_2|}{B_1^2 + B_2^2 + B_3^2} \geq X_1 \\ \dfrac{1}{\tilde{m}(1-k)} \sqrt{\left(B_1^2 + B_3^2 + a_2 B_2^2\right)} & \text{if} \quad \dfrac{B_2|B_2|}{B_1^2 + B_2^2 + B_3^2} \leq X_2 \\ \dfrac{1}{\tilde{m}(1+k)} \sqrt{\left(a_1 B_1^2 + B_2^2 + B_3^2\right)} & \text{if} \quad \dfrac{B_1|B_1|}{B_1^2 + B_2^2 + B_3^2} \geq X_1 \\ \dfrac{1}{\tilde{m}(1-k)} \sqrt{\left(a_2 B_1^2 + B_2^2 + B_3^2\right)} & \text{if} \quad \dfrac{B_1|B_1|}{B_1^2 + B_2^2 + B_3^2} \leq X_2 \end{cases} \tag{6.89}$$

where the following notations have been introduced

$$\begin{aligned} X_1 &= \frac{(3k^2 - 2k + 3)^2}{6(k^2+3)(3k^2+1)}, \quad X_2 = -\frac{(3k^2 + 2k + 3)^2}{6(k^2+3)(3k^2+1)} \\ a_1 &= \frac{3k^2 + 10k + 3}{3k^2 - 2k + 3}, \quad a_2 = \frac{3k^2 - 10k + 3}{3k^2 + 2k + 3} \end{aligned} \tag{6.90}$$

Remark Note that for isotropic materials, for which $\mathbf{L} = \mathbf{K}$ the Cazacu et al. [6] orthotropic strain-rate potential given by Eq. (6.87) reduces to the isotropic Cazacu et al. [6] strain-rate potential given by Eq. (6.43). If a material does not display tension–compression asymmetry (yield in tension is equal to the yield in compression), the parameter k associated with strength differential effects is automatically zero and the Cazacu et al. [6] orthotropic strain-rate potential given by Eq. (6.87) reduces to the Hill [15] orthotropic strain-rate potential given by Eq. (6.50).

Components of the fourth-order orthotropic tensor **H**

Using Voigt notations, the fourth-order orthotropic tensor **L** involved in the expression of the Cazacu et al. [5] stress potential is represented in the reference system associated with orthotropy by the 6×6 matrix given by Eq. (6.79). Therefore, using the definition of **H** given by Eq. (6.83), relative to the same coordinate system, **H** is represented by the matrix of components:

$$\begin{aligned}
H_{11} &= -(H_{12}+H_{13}) \\
H_{12} &= H_{21} = \frac{1}{3}\cdot\frac{2(L_{32}-L_{12})+(L_{31}-L_{11})}{(L_{21}-L_{11})(L_{32}-L_{12})-(L_{22}-L_{12})(L_{31}-L_{11})} \\
H_{13} &= H_{31} = \frac{1}{3}\cdot\frac{(L_{11}-L_{21})+2(-L_{22}+L_{12})}{(L_{21}-L_{11})(L_{32}-L_{12})-(L_{22}-L_{12})(L_{31}-L_{11})} \\
H_{22} &= -(H_{21}+H_{23}) \\
H_{23} &= H_{32} = \frac{1}{3}\cdot\frac{2(L_{11}-L_{21})+(-L_{22}+L_{12})}{(L_{11}-L_{21})(L_{32}-L_{22})-(-L_{22}+L_{12})(L_{31}-L_{21})} \\
H_{33} &= -(H_{31}+H_{23}) \\
H_{44} &= \frac{1}{L_{44}}; H_{55} = \frac{1}{L_{55}}; H_{66} = \frac{1}{L_{66}}
\end{aligned} \tag{6.91}$$

First derivatives of the Cazacu et al. [6] *orthotropic strain-rate potential for plane-stress loadings*

The Cazacu et al. [6] orthotropic strain-rate potential was developed for full 3-D loading conditions. In view of applications to sheet forming, in the following, we present the explicit expressions of the first derivatives of this SRP for plane-stress conditions. Let us first note that under plane-stress conditions ($\sigma_{zz} = \sigma_{zy} = \sigma_{zx} = 0$), the only nonzero components of the transformed tensor $\mathbf{B} = \mathbf{Hd}$ are B_{xx}, B_{yy}, B_{zz}, and B_{xy}. Therefore, the principal values B_1, B_2, B_3 of the transformed tensor **B** are:

$$B_{1,2} = \frac{B_{xx}+B_{yy}}{2} \pm \sqrt{\left(\frac{B_{xx}-B_{yy}}{2}\right)^2 + B_{xy}^2}; \quad B_3 = B_{zz}. \tag{6.92}$$

The first derivatives of the orthotropic Cazacu et al. [6] strain-rate potential (6.89) are given as:

$$\frac{\partial \psi}{\partial d_{ij}} = \frac{\partial \psi}{\partial B_\alpha}\cdot\frac{\partial B_\alpha}{\partial d_{ij}} \tag{6.93}$$

where

$$\frac{\partial\psi}{\partial B_1}=\begin{cases}\dfrac{1}{\tilde{m}(1+k)}\dfrac{B_1}{\sqrt{\left(B_1^2+B_2^2+a_1B_3^2\right)}} & \text{if} \quad \dfrac{B_3|B_3|}{B_1^2+B_2^2+B_3^2}\geq X_1\\ \dfrac{1}{\tilde{m}(1-k)}\dfrac{B_1}{\sqrt{\left(B_1^2+B_2^2+a_2B_3^2\right)}} & \text{if} \quad \dfrac{B_3|B_3|}{B_1^2+B_2^2+B_3^2}\leq X_2\\ \dfrac{1}{\tilde{m}(1+k)}\dfrac{B_1}{\sqrt{\left(B_1^2+B_3^2+a_1B_2^2\right)}} & \text{if} \quad \dfrac{B_2|B_2|}{B_1^2+B_2^2+B_3^2}\geq X_1\\ \dfrac{1}{\tilde{m}(1-k)}\dfrac{B_1}{\sqrt{\left(B_1^2+B_3^2+a_2B_2^2\right)}} & \text{if} \quad \dfrac{B_2|B_2|}{B_1^2+B_2^2+B_3^2}\leq X_2\\ \dfrac{1}{\tilde{m}(1+k)}\dfrac{a_1B_1}{\sqrt{\left(a_1B_1^2+B_2^2+B_3^2\right)}} & \text{if} \quad \dfrac{B_1|B_1|}{B_1^2+B_2^2+B_3^2}\geq X_1\\ \dfrac{1}{\tilde{m}(1-k)}\dfrac{a_2B_1}{\sqrt{\left(a_2B_1^2+B_2^2+B_3^2\right)}} & \text{if} \quad \dfrac{B_1|B_1|}{B_1^2+B_2^2+B_3^2}\leq X_2\end{cases} \tag{6.94}$$

$$\frac{\partial\psi}{\partial B_2}=\begin{cases}\dfrac{1}{\tilde{m}(1+k)}\dfrac{B_2}{\sqrt{B_1^2+B_2^2+a_1B_3^2}} & \text{if} \quad \dfrac{B_3|B_3|}{B_1^2+B_2^2+B_3^2}\geq X_1\\ \dfrac{1}{\tilde{m}(1-k)}\dfrac{B_2}{\sqrt{B_1^2+B_2^2+a_2B_3^2}} & \text{if} \quad \dfrac{B_3|B_3|}{B_1^2+B_2^2+B_3^2}\leq X_2\\ \dfrac{1}{\tilde{m}(1+k)}\dfrac{a_1B_2}{\sqrt{B_1^2+a_1B_2^2+B_3^2}} & \text{if} \quad \dfrac{B_2|B_2|}{B_1^2+B_2^2+B_3^2}\geq X_1\\ \dfrac{1}{\tilde{m}(1-k)}\dfrac{a_2B_2}{\sqrt{B_1^2+a_2B_2^2+B_3^2}} & \text{if} \quad \dfrac{B_2|B_2|}{B_1^2+B_2^2+B_3^2}\leq X_2\\ \dfrac{1}{\tilde{m}(1+k)}\dfrac{B_2}{\sqrt{a_1B_1^2+B_2^2+B_3^2}} & \text{if} \quad \dfrac{B_1|B_1|}{B_1^2+B_2^2+B_3^2}\geq X_1\\ \dfrac{1}{\tilde{m}(1-k)}\dfrac{B_2}{\sqrt{a_2B_1^2+B_2^2+B_3^2}} & \text{if} \quad \dfrac{B_1|B_1|}{B_1^2+B_2^2+B_3^2}\leq X_2\end{cases} \tag{6.95}$$

$$\frac{\partial\psi}{\partial B_3}=\begin{cases}\dfrac{1}{\tilde{m}(1+k)}\dfrac{a_1B_3}{\sqrt{B_1^2+B_2^2+a_1B_3^2}} & \text{if} \quad \dfrac{B_3|B_3|}{B_1^2+B_2^2+B_3^2}\geq X_1\\ \dfrac{1}{\tilde{m}(1-k)}\dfrac{a_2B_3}{\sqrt{B_1^2+B_2^2+a_2B_3^2}} & \text{if} \quad \dfrac{B_3|B_3|}{B_1^2+B_2^2+B_3^2}\leq X_2\\ \dfrac{1}{\tilde{m}(1+k)}\dfrac{B_3}{\sqrt{B_1^2+a_1B_2^2+B_3^2}} & \text{if} \quad \dfrac{B_2|B_2|}{B_1^2+B_2^2+B_3^2}\geq X_1\\ \dfrac{1}{\tilde{m}(1-k)}\dfrac{B_3}{\sqrt{B_1^2+a_2B_2^2+B_3^2}} & \text{if} \quad \dfrac{B_2|B_2|}{B_1^2+B_2^2+B_3^2}\leq X_2\\ \dfrac{1}{\tilde{m}(1+k)}\dfrac{B_3}{\sqrt{a_1B_1^2+B_2^2+B_3^2}} & \text{if} \quad \dfrac{B_1|B_1|}{B_1^2+B_2^2+B_3^2}\geq X_1\\ \dfrac{1}{\tilde{m}(1-k)}\dfrac{B_3}{\sqrt{a_2B_1^2+B_2^2+B_3^2}} & \text{if} \quad \dfrac{B_1|B_1|}{B_1^2+B_2^2+B_3^2}\leq X_2\end{cases} \tag{6.96}$$

while the derivatives:

$$\frac{\partial B_k}{\partial B_{mm}};\ k=1,\ \ldots,\ 3 \text{ and } (m,n) \text{ either } (x,x),\ (y,y),\ \text{or } (x,y)$$

are given by:

$$\frac{\partial B_1}{\partial B_{xx}}=\frac{1}{2}+\frac{B_{xx}-B_{yy}}{2\sqrt{\left(B_{xx}-B_{yy}\right)^2+4B_{xy}^2}},\frac{\partial B_2}{\partial B_{xx}}=\frac{1}{2}-\frac{1}{2}\frac{B_{xx}-B_{yy}}{\sqrt{\left(B_{xx}-B_{yy}\right)^2+4B_{xy}^2}}$$

$$\frac{\partial B_1}{\partial B_{yy}}=\frac{1}{2}+\frac{B_{yy}-B_{xx}}{2\sqrt{\left(B_{xx}-B_{yy}\right)^2+4B_{xy}^2}}\quad;\quad\frac{\partial B_2}{\partial B_{yy}}=\frac{1}{2}+\frac{1}{2}\frac{B_{xx}-B_{yy}}{\sqrt{\left(B_{xx}-B_{yy}\right)^2+4B_{xy}^2}}$$

$$\frac{\partial B_1}{\partial B_{zz}}=0\quad;\quad\frac{\partial B_2}{\partial B_{zz}}=0$$

$$\frac{\partial B_1}{\partial B_{xy}}=\frac{B_{xy}}{\sqrt{\left(B_{xx}-B_{yy}\right)^2+4B_{xy}^2}}\quad;\quad\frac{\partial B_2}{\partial B_{xy}}=-\frac{B_{xy}}{\sqrt{\left(B_{xx}-B_{yy}\right)^2+4B_{xy}^2}}$$

$$\frac{\partial B_3}{\partial B_{xx}}=0,\frac{\partial B_3}{\partial B_{yy}}=0,\frac{\partial B_3}{\partial B_{xy}}=0,\frac{\partial B_3}{\partial B_{zz}}=1 \tag{6.97}$$

and the derivatives of B_{ij} with respect to d_{xx}, d_{yy}, d_{zz}, d_{xy} are:

$$\frac{\partial B_{ij}}{\partial d_{kl}}=H_{ijkl} \tag{6.98}$$

Remark Note that the derivatives in Eq. (6.97) have singular values when the denominator vanishes, i.e., for $B_{xx}=B_{yy}$ and $B_{xy}=0$. In this case, the following equations should be used to calculate the first derivatives:

$$\frac{\partial\psi}{\partial B_{xx}}=\frac{\partial\psi}{\partial B_1};\frac{\partial\psi}{\partial B_{yy}}=\frac{\partial\psi}{\partial B_2};\frac{\partial\psi}{\partial B_{xy}}=0;\frac{\partial\psi}{\partial B_{zz}}=\frac{\partial\psi}{\partial B_3} \tag{6.99}$$

in conjunction with Eqs. (6.94)–(6.96).

Identification procedure for the material parameters of the Cazacu et al. [6] *orthotropic strain-rate potential*

As demonstrated, the orthotropic strain-rate potential of Cazacu et al. [6] given by Eq. (6.89) is the exact dual of the orthotropic and quadratic stress potential proposed by Cazacu et al. [5] given by Eq. (6.78). Thus, for full 3-D conditions, the seven anisotropy coefficients involved in the expression of the SRP [see Eq. (6.89)] can be obtained simply by using Eq. (6.83) that relates the tensor $\mathbf{H}$ to the tensor $\mathbf{L}$ involved in the expression of the stress potential [see also the expressions of the coefficients H_{ij} in terms of L_{ij} given by Eq. (6.91)]. The strength differential coefficient k in Eq. (6.89) of the strain-rate potential is the same coefficient that appears in the

Eq. (6.78) of the stress potential. These seven anisotropy coefficients (either the components of **H** or **L**) as well as k can be determined from at least eight experimental measurements through the minimization of an error function. The experimental data may consist of flow stresses and r-values in tension–compression corresponding to different orientations in the plane of the metallic sheet, biaxial flow stress in tension–compression, as well as out-of-plane yield stresses and r-values:

$$\text{Error} = \sum_{n} \text{weight}\left(1 - \frac{\sigma^n_{\text{th}}}{\sigma^n_{\text{data}}}\right)^2 + \sum_{\text{m}} \text{weight}\left(1 - \frac{r^m_{\text{th}}}{r^m_{\text{data}}}\right)^2 \tag{6.100}$$

Regardless of the potential used, the description of the plastic response of a given material is identical. Thus, in the above Eq. (6.100), the subscript "data" may refer to data points obtained from direct measurements (uniaxial loading tests), while "theoretical" refers to predicted values obtained with either potential. Specifically, if one chooses to determine from data the coefficients L_{ij}, then the subscript "theoretical" in the error function refers to theoretical values obtained using Eqs. (5.166)–(5.172) (see Chap. 5). Subsequently, Eq. (6.91) are used to calculate the coefficients H_{ij}. This is the procedure that will be used to generate the isosurfaces according to the orthotropic strain-rate potential of Cazacu et al. [6] for a Mg AZ31 and a high-purity Ti (identification of the parameter k and anisotropy coefficients L_{ij} presented in Sect. 5.4.3.1).

Application of the Cazacu et al. [6] *orthotropic strain-rate potential to hexagonal-closed packed metallic materials*

As discussed in Sect. 5.4.3, for a strongly anisotropic Mg AZ31 alloy Revil-Baudard et al. [21] (see also Chandola et al. [8]) have identified the parameters involved in the quadratic form of the Cazacu et al. [7] orthotropic stress potential using the experimental data reported by Khan et al. [16]. The values of these parameters were given in Table 5.8. Using Eq. (6.91), the components H_{ij} of the fourth-order tensor **H** can be easily determined (see Table 6.3).

For the Mg AZ31 alloy, Fig. 6.22 shows the isocontours of the Cazacu et al. [5] stress potential (see Fig. 6.22a) in the biaxial plane $(\sigma_{xx}, \sigma_{yy})$ for several levels of the equivalent plastic strain along with the isocontours of its dual, i.e., the Cazacu et al. [6] strain-rate potential, in the biaxial plane (d_{xx}, d_{yy}) (see Fig. 6.22b). It is worth noting that in both the stress space and the strain-rate space, the shape of the

Table 6.3 Anisotropy coefficients involved in the Cazacu et al. [6] orthotropic strain-rate potential for a Mg AZ31 alloy

Plastic strain	H_{11}	H_{12}	H_{13}	H_{23}	H_{66}	k
0.05	0.473	−0.340	−0.134	−0.1575	1.3699	−0.625
0.06	0.366	−0.236	−0.130	−0.156	0.9625	−0.520
0.08	0.359	−0.165	−0.194	−0.219	0.887	−0.215
0.1	0.378	−0.163	−0.215	−0.242	0.945	−0.169

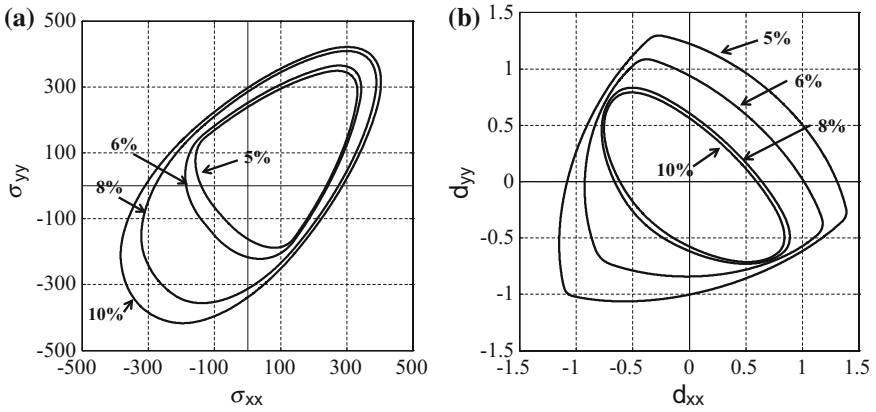

Fig. 6.22 Representation in the biaxial plane of: **a** the Cazacu et al. [5] stress potential and **b** the Cazacu et al. [6] dual strain-rate potential for an Mg AZ31 alloy, respectively

surface evolves from a triangular shape at low levels of equivalent plastic strain toward an elliptical shape for larger values of the equivalent plastic strain. Furthermore, an outer isocontour in the stress space becomes an inner isocontour in the strain-rate space. This is due to the fact that all the isocontours correspond to the same plastic dissipation.

It is also worth comparing the prediction of the Cazacu et al. [6] strain-rate potential with the prediction of the Hill [15] strain-rate potential for this material (see Fig. 6.23 for the respective isocontours corresponding to an equivalent plastic strain of 5%). Let us recall that these two strain-rate potentials are the only potentials which are the exact duals of their respective stress potentials. As already discussed, according to the Hill [15] quadratic SRP, the mechanical response is the same in tension–compression, so the isocontours can only be elliptical and invariant to the transformation $(d_{xx}, d_{yy}) \rightarrow (-d_{xx}, -d_{yy})$. On the other hand, the Cazacu

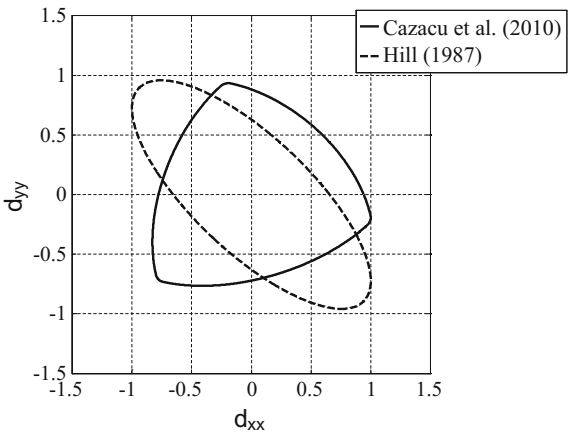

Fig. 6.23 Strain-rate isocontours according to the Cazacu et al. [6] strain-rate potential and the Hill [15] strain-rate potential, respectively, for an Mg AZ31 alloy at an equivalent plastic strain of 5%

Table 6.4 Anisotropy coefficients involved in the Cazacu et al. [6] orthotropic strain-rate potential for a high-purity hcp-Ti

Plastic strain	H_{11}	H_{12}	H_{13}	H_{23}	H_{66}	k
0.05	2.833	−1.1437	−1.690	−2.33	3.861	−0.06
0.08	1.142	−0.4790	−0.663	−0.8714	1.522	−0.084
0.2	0.679	−0.305	−0.374	−0.397	0.778	−0.392
0.3	0.657	−0.307	−0.350	−0.345	0.696	−0.650

et al. [6] strain-rate potential accounts simultaneously for the anisotropy and tension–compression asymmetry of the material.

It is also worth mentioning that both SRPs have been identified solely based on measurements of the yield stresses along different orientations. The predicted values of the Lankford coefficients along RD (the **x**-direction) are: $r(0^\circ) = 0.25$ for the Cazacu et al. [6] SRP and $r(0^\circ) = 2.6$ for the Hill [15] SRP. Along TD (or the **y**-direction): $r(90^\circ) = 0.26$ for the Cazacu et al. [6] SRP, while the Hill [15] SRPs predict $r(90^\circ) = 3.7$. Note also that one of the advantages of a strain-rate formulation is that the Lankford coefficients in RD and TD can be directly estimated by plotting the normals to the respective SRP isosurfaces in the biaxial plane.

Next, the orthotropic SRP of Cazacu et al. [6] is applied to high-purity hcp-Ti, with a strong initial basal texture for which the mechanical characterization data were reported in Nixon et al. [18]. These test results in uniaxial tension–compression along the RD, TD, and ND directions were discussed in detail in Chap. 5 and further used to identify the material parameters involved in the Cazacu et al. [5] stress potential, namely the coefficients L_{ij} as well as the parameter k [see Eq. (6.78)]. Therefore, the coefficients H_{ij} of the Cazacu et al. [6] SRP can be directly calculated using Eq. (6.83) (see Table 6.4), while the k parameter is the same in both stress-based and strain-rate-based formulations.

For this hcp-Ti, Fig. 6.24a shows the isocontours of the Cazacu et al. [5] stress potential in the biaxial plane $(\sigma_{xx}, \sigma_{yy})$ for several levels of the equivalent plastic strain, while Fig. 6.24b shows the isocontours of its dual, the Cazacu et al. [6] strain-rate potential in the biaxial plane (d_{xx}, d_{yy}). It is worth noting that in either stress space or strain-rate space, at the onset of plastic deformation and under 10% strain, the theoretical surfaces have an elliptical shape and the predicted tension–compression asymmetry is small, as observed experimentally. However, at 20% strain and above, the surfaces have a triangular shape, and the difference in response between tension–compression is pronounced. It is also important to note the yield surfaces and the strain-rate isosurfaces exhibit the same evolution in shape with accumulated plastic deformation, which should be the case given that the tensors **L** and **H** describing the evolving anisotropy of the material are related by Eq. (6.83).

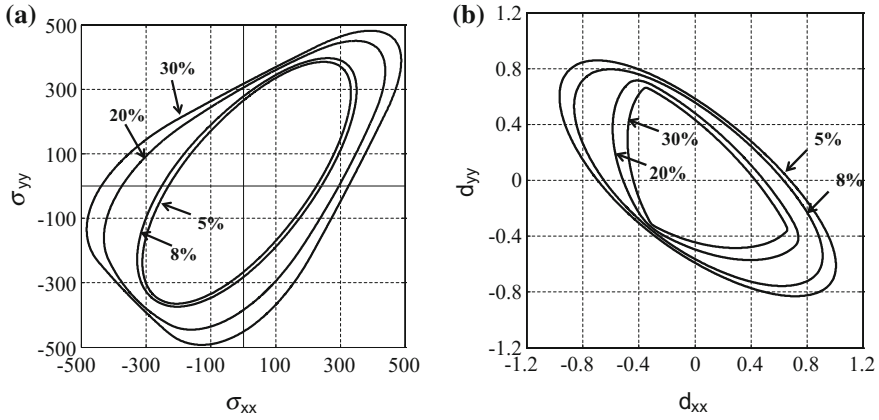

Fig. 6.24 Representation in the biaxial plane of: **a** the Cazacu et al. [5] orthotropic stress potential and **b** its work-conjugate, the Cazacu et al. [6] strain-rate potential for a hcp-Ti, respectively

References

1. Barlat F, Lege DJ, Brem JC (1991) A six-component yield function for anisotropic materials. Int J Plast 7:693–712
2. Barlat F, Chung K, Richmond O (1993) Strain rate potential for metals and its application to minimum plastic work path calculations. Int J Plast 9:51–63
3. Barlat F, Chung K, Richmond O (1994) Anisotropic plastic potentials for polycrystals and application to the design of optimum blank shapes in sheet forming. Metall Mater Trans A 25:1209–1216
4. Barlat F, Chung K (2005) Anisotropic strain rate potential for aluminum alloy plasticity. In: Banabic D (ed) Proceedings of the 8th ESAFORM conference on material forming. The Publishing House of the Romanian Academy, Bucharest, pp 415–418
5. Cazacu O, Plunkett B, Barlat F (2006) Orthotropic yield criterion for hexagonal closed packed metals. Int J Plast 22:1171–1194
6. Cazacu O, Ionescu IR, Yoon JW (2010) Orthotropic strain rate potential for the description of anisotropy in tension–compression of metals. Int J Plast 26:887–904
7. Cazacu O, Revil-Baudard B (2017) New analytic criterion for porous solids with pressure-insensitive matrix. Int J Plast 89:66–84
8. Chandola N, Lebensohn RA, Cazacu O, Revil-Baudard B, Mishra RK, Barlat F (2015) Combined effects of anisotropy and tension–compression asymmetry on the torsional response of AZ31 Mg. Int J Solids Struct 58:190–200
9. Chung K, Richmond O (1992) Ideal forming—I. Homogeneous deformation with minimum plastic work. Int J Mech Sci 34:575–591
10. Chung K, Richmond O (1992) Ideal forming—II. Sheet forming with optimum deformation. Int J Mech Sci 34:617–633
11. Chung K, Richmond O (1994) The mechanics of ideal forming. J Appl Mech 61:176–181
12. Hershey AV (1954) The plasticity of an isotropic aggregate of anisotropic face-centered cubic crystals. ASME J Appl Mech 21:241–249
13. Hosford WF (1972) A generalized isotropic yield criterion. J Appl Mech 39:607–609
14. Hill R (1948) A theory of the yielding and plastic flow of anisotropic metals. In: Proceedings of the Royal Society of London A: mathematical, physical and engineering sciences. The Royal Society, pp 281–297

15. Hill R (1987) Constitutive dual potentials in classical plasticity. J Mech Phys Solids 35:23–33
16. Khan AS, Pandey A, Gnäupel-Herold T, Mishra RK (2011) Mechanical response and texture evolution of AZ31 alloy at large strains for different strain rates and temperatures. Int J Plast 27:688–706. https://doi.org/10.1016/j.ijplas.2010.08.009
17. Kim D, Barlat F, Bouvier S, Rabahallah M, Balan T, Chung K (2007) Non-quadratic anisotropic potentials based on linear transformation of plastic strain rate. Int J Plast 23:1380–1399. https://doi.org/10.1016/j.ijplas.2007.01.006
18. Nixon ME, Cazacu O, Lebensohn RA (2010) Anisotropic response of high-purity α-titanium: experimental characterization and constitutive modeling. Int J Plast 26:516–532
19. Rabahallah M (2007) Modélisation de l'anisotropie plastique et application à la mise en forme des tôles métalliques. University of Metz
20. Rabahallah M, Balan T, Bouvier S, Bacroix B, Barlat F, Chung K, Teodosiu C (2009) Parameter identification of advanced plastic strain rate potentials and impact on plastic anisotropy prediction. Int J Plast 25:491–512. https://doi.org/10.1016/j.ijplas.2008.03.006
21. Revil-Baudard B, Chandola N, Cazacu O, Barlat F (2014) Correlation between swift effects and tension–compression asymmetry in various polycrystalline materials. J Mech Phys Solids 70:104–115
22. Wang C-C (1970) A new representation theorem for isotropic functions: an answer to Professor GF Smith's criticism of my papers on representations for isotropic functions. Arch Ration Mech Anal 36:166–197
23. Ziegler H (1977) An introduction to thermodynamics. North-Holland Publishing Company, Amsterdam

Chapter 7
Plastic Potentials for Isotropic Porous Materials: Influence of the Particularities of Plastic Deformation on Damage Evolution

It is well documented that in metals, damage and ultimately failure is the result of nucleation, growth, and coalescence of voids (e.g., McClintock [47]; Hancock and Mackenzie [31]; Hosokawa et al. [36]). Void nucleation occurs mainly by decohesion at the particle matrix interface (e.g., Kwon and Asaro [40]) and micro-cracking of second-phase particles (see, e.g., Tvergaard and Needleman [69]). Constitutive models for porous ductile materials are thus needed as the basis for ductile failure theories, or for understanding and describing consolidation processes aimed at reducing porosity [59]. One of the most widely used models are those derived by Gurson [29] for porous materials containing randomly distributed voids of either spherical or cylindrical geometry. These plastic potentials were deduced by conducting limit analysis of a hollow sphere or hollow cylinder obeying von Mises yield criterion. It was proven that the presence of voids in a von Mises matrix induces dependence on the mean stress. To better account for void evolution, various modifications of Gurson's [30] criteria have been proposed (e.g., Tvergaard and Needleman [69]; Richmond and Smelser [59]; Leblond et al. [41]). In the past couple of years, growing experimental evidence has shown the role played by all stress invariants in ductile failure of metallic materials. In particular, the combined effects of the second and third-invariants of the stress deviator (i.e., Lode parameter) have been well documented (e.g., recent data reported by Bao and Wierzbicki [8]; Barsoum and Faleskog [9]; Lou and Huh [44]). Using an extensive set of experimental data and sophisticated fitting procedures, criteria that postulate the dependence of the equivalent plastic strain at fracture on both the stress triaxiality and the Lode parameter were proposed (e.g., Bai and Wierzbicki [6]).

Since void evolution is due to the plastic deformation of the surrounding fully dense material (matrix), it is essential to understand how the particularities of the plastic deformation influence void evolution. In their seminal study, Rice and Tracey [58] formulated variational principles for void growth in rigid-plastic materials and compared growth of spherical voids in a Tresca material with that in a von Mises material for very high stress triaxialities. It was found that the rate of void growth in a Tresca material is much faster than in a von Mises material.

O. Cazacu et al., *Plasticity–Damage Couplings: From Single Crystal to Polycrystalline Materials*, Solid Mechanics and Its Applications 253,
https://doi.org/10.1007/978-3-319-92922-4_7

Nevertheless, within the last decades, most efforts have been devoted to the description of void interaction or to the effects of void geometry on the mechanical response of porous metallic materials (e.g., Leblond and Gologanu [43]). Indeed, in most of the available models for isotropic porous materials, the matrix material is described by the von Mises yield criterion.

Recently, efforts have been devoted toward describing the role played by the particularities of the plastic deformation of the matrix on yielding and void evolution. In this chapter are presented these new analytic plastic potentials. First, the general mathematical framework and the limit-analysis theorems used for the derivation of these potentials are briefly described. On the basis of these theorems, the general properties of the yield surface of an isotropic porous material for which the matrix behavior is governed by a yield function which is even in stresses are deduced. The analysis of yielding and void evolution in porous materials with Mises matrix is revisited, and the previously unrecognized combined effects of the mean stress and third-invariant of the stress deviator on yielding of a porous Mises solid put into evidence by Cazacu et al. [19] are discussed along with the criterion derived by these authors. Next, the case when the matrix is governed by the Tresca yield criterion is analyzed, and the derivation of the plastic potential for a porous Tresca material is presented, along with comparison with the predictions of the porous von Mises criterion in terms of void growth/collapse under axisymmetric loadings. However, to gain understanding of the combined effects of all invariants on the mechanical response of porous solids for general three-dimensional loadings, a strain-rate-based approach appears more appropriate. Three-dimensional strain-rate-based potentials for porous solids are presented. It is demonstrated that the presence of voids induces dependence on all invariants, the noteworthy result being that the couplings between invariants are very specific and depend strongly on the particularities of the plastic flow of the matrix. This in turn strongly influences void evolution. It is shown that the fastest rate of void growth or collapse occurs in a porous Tresca material. However, depending on the relative weight of the invariants of the stress deviator on yielding of the matrix, the rate of void evolution can be either slower or faster than in a porous von Mises material. Most importantly, it is revealed that depending on the yield criterion for the matrix, the third-invariant effects (or Lode effects) on void evolution can be either enhanced or completely eliminated.

Finally, recent contributions to the understanding of the influence of the tension–compression asymmetry of the plastic deformation of the isotropic and incompressible matrix on yielding and void evolution of porous materials are presented. It is shown that if the yield function that governs the matrix behavior is an odd function, there is a very strong effect of the third-invariant of the stress deviator for all loadings. Moreover, the yield surface of the porous material lacks any symmetry.

We begin with a brief overview of the mathematical framework for developing plastic potentials for porous metallic materials. For an in-depth presentation of both the kinematic and static limit-analysis theorems and complete proofs of the mathematical results, the reader is referred to books devoted entirely to this subject (e.g., Salençon [60, 61]). Here focus is on the general properties of the potentials,

and the challenges and roadblocks associated to the derivation of their expression in closed form. As concerns the notations used throughout this chapter and Chap. 8, the strain-rate and stress associated with the matrix (fully dense material) are denoted by $\mathbf{d}$, and $\boldsymbol{\sigma}$ while those associated with the porous material (matrix and voids) are denoted by $\mathbf{D}$, and $\boldsymbol{\Sigma}$.

The mean strain-rate of the porous material is denoted as

$$D_m = (\mathrm{tr}\mathbf{D})/3, \tag{7.1}$$

$\mathbf{D}'$ stands for the deviator of $\mathbf{D}$, i.e., $\mathbf{D}' = \mathbf{D} - D_m\mathbf{I}$, its invariants are denoted asloadings at

$$J_2^D = \mathrm{tr}\left(\mathbf{D}'^2\right)/2 \text{ and } J_3^D = \mathrm{tr}\left(\mathbf{D}'^3\right)/3, \tag{7.2}$$

and

$$D_e = \left(2/\sqrt{3}\right)\sqrt{J_2^D}, \tag{7.3}$$

denotes von Mises equivalent strain-rate associated to $\mathbf{D}$.

The mean stress of the porous material, i.e., the first invariant of $\boldsymbol{\Sigma}$ is denoted as $\Sigma_m = \mathrm{tr}(\boldsymbol{\Sigma})/3$, while the invariants of the stress deviator $\boldsymbol{\Sigma}' = \boldsymbol{\Sigma} - (\Sigma_m/3)\mathbf{I}$ and of the stress triaxiality T are denoted as:

$$\Sigma_e = \sqrt{3\left(\Sigma'_{ij}\Sigma'_{ij}\right)/2} = \sqrt{3J_2^\Sigma},\ J_3^\Sigma = \mathrm{tr}(\boldsymbol{\Sigma}')^3/3, \tag{7.4}$$

$$T = \Sigma_m/\Sigma_e. \tag{7.5}$$

7.1 Kinematic Homogenization Framework for Development of Plastic Potentials for Porous Metallic Materials

Consider a representative volume element Ω, composed of a homogeneous rigid-plastic matrix and a traction-free void. Let f be the void volume fraction. The plastic deformation of the matrix material is described by a yield function $\varphi(\boldsymbol{\sigma})$ which is convex and homogeneous of degree one, and an associated flow rule, i.e.,

$$\mathbf{d} = \dot{\lambda}\,\frac{\partial\varphi}{\partial\boldsymbol{\sigma}}. \tag{7.6}$$

In Eq. (7.6), $\mathbf{d} = (\nabla\mathbf{v} + \nabla\mathbf{v}^T)/2$ is the strain-rate tensor with $\mathbf{v}$ being the velocity field; $\dot{\lambda} \geq 0$ is the plastic multiplier. If σ_T denotes the yield limit in uniaxial

tension, in a specified direction, then the yield surface is defined as: $\varphi(\boldsymbol{\sigma}) = \sigma_T$ (see also Chap. 2). The plastic dissipation is then defined as

$$\pi(\mathbf{d}) = \sup_{\boldsymbol{\sigma} \in C} (\boldsymbol{\sigma} : \mathbf{d}). \tag{7.7}$$

In Eq. (7.7), C denotes the convex domain delimited by the yield surface, i.e.,

$$C = \{\boldsymbol{\sigma} | \varphi(\boldsymbol{\sigma}) \leq \sigma_T\}. \tag{7.8}$$

For uniform strain-rate boundary conditions on $\partial\Omega$, i.e.,

$$\mathbf{v}(\mathbf{x}) = \mathbf{D}\mathbf{x}, \text{for any } \mathbf{x} \in \partial\Omega, \text{ where } \mathbf{D} = \text{const}, \tag{7.9}$$

Hill [32]-Mandel [46] lemma applies, i.e.,

$$\langle \boldsymbol{\sigma} : \mathbf{d} \rangle_\Omega = \langle \boldsymbol{\sigma} \rangle_\Omega : \langle \mathbf{d} \rangle_\Omega = \boldsymbol{\Sigma} : \mathbf{D} \tag{7.10}$$

In the above equation, $\langle\,\rangle$ denotes the average value over the representative volume Ω, and

$$\boldsymbol{\Sigma} = \langle \boldsymbol{\sigma} \rangle_\Omega, \tag{7.11}$$

denotes the average stress. Moreover, there exists a plastic potential $\Pi = \Pi(\mathbf{D}, f)$ such that the stress at any point in the porous solid is given by:

$$\boldsymbol{\Sigma} = \frac{\partial \Pi(\mathbf{D}, f)}{\partial \mathbf{D}} \tag{7.12}$$

and

$$\Pi(\mathbf{D}, f) = \inf_{\mathbf{v}(\mathbf{x}) \text{ K.A.with } \mathbf{D}} \langle \pi(\mathbf{d}) \rangle_\Omega. \tag{7.13}$$

In Eq. (7.13) inf stands for infimum, the minimization being done over the set of incompressible velocity fields compatible with $\mathbf{D}$ [i.e., velocity fields $\mathbf{v}$ satisfying Eq. (7.9)]. For the proof of this lemma, the reader is referred to Garajeu and Suquet [28], Leblond [42].

Remark (a) To derive an analytic expression of the plastic potential of the porous solid, $\Pi(\mathbf{D}, f)$, one needs to know the closed-form expression of the local plastic dissipation,

$$\pi(\mathbf{d}) = \dot{\lambda}\sigma_T = \psi(\mathbf{d})\sigma_T, \tag{7.14}$$

where $\psi(\mathbf{d})$ is the strain-rate potential (SRP) associated to $\varphi(\boldsymbol{\sigma})$, the plastic potential of the matrix. Given that analytic expressions for SRPs which are exact

duals of yield functions are known only in a few cases (see the examples presented in Chap. 6), closed-form expressions of analytic plastic potentials for porous metallic materials have been developed only for the cases when the matrix is described by von Mises [70], Tresca [66], Hill [33], and Cazacu et al. [15] yield criteria.

Remark (b) Another key ingredient needed for the homogenization procedure is the knowledge of velocity fields which are kinematically admissible. It is very important to note that only very few velocity fields compatible with uniform strain-rate boundary conditions are known.

In the case of spherical void geometry, the only known velocity fields are those deduced by Rice and Tracey [58], Budiansky et al. [10], and Huang [37]. The Rice and Tracey [58] velocity field is presented in Sect. 7.2.2. For other examples of velocity fields, which were deduced using an Eshelby-type approach, the reader is referred to Monchiet et al. [50]. In the case of cylindrical void geometry, generally the velocity field deduced by Gurson [29] is used (see Sect. 7.4.1).

In closing, it should be mentioned that while for metallic materials the most widely used approach is that of kinematic homogenization, for modeling porous geologic materials and polymers, the use of the static homogenization approach (e.g., see Thoré et al. [64]) is more prevalent. In this latter framework, minimization of the local plastic dissipation is done over the set of statically and plastically admissible stress fields (i.e., stresses that belong to the plasticity convex C defined by Eq. (7.8), satisfy the equilibrium equations, and uniform stress boundary conditions). For more details concerning this approach and its application to porous geological materials, the reader is referred to the monographs of Salençon [60] and Dormieux et al. [24].

7.2 Constitutive Models for Porous Isotropic Metallic Materials with Incompressible Matrix Governed by an Even Yield Function

On the basis of the mathematical results presented in Sect. 7.1, Cazacu et al. [19] demonstrated that for spherical void geometry, the dependence of the yield function of the porous solid, $F(\boldsymbol{\Sigma}, f)$, on the invariants of $\boldsymbol{\Sigma}$ cannot be arbitrary. Moreover, it was put into evidence that a very specific coupling between the signs of the mean stress Σ_m and the third-invariant J_3^{Σ} exists. These general results with complete proofs are presented in the following.

7.2.1 General Properties of the Yield Surface of Porous Metallic Materials Containing Spherical Voids in an Incompressible Matrix Governed by an Even Yield Function

Theorem 7.1 *The yield surface of a porous isotropic material containing randomly distributed spherical voids and matrix governed by a yield criterion represented by an even function* $\varphi(\boldsymbol{\sigma})$ *ought to be centro-symmetric, and the yield function* $F(\boldsymbol{\Sigma},f)$ *should satisfy the following invariance requirement*:

$$F\left(\Sigma_m, \Sigma_e, J_3^{\Sigma}\right) = F\left(-\Sigma_m, \Sigma_e, -J_3^{\Sigma}\right) \tag{7.15}$$

Proof Indeed, if the matrix behavior is described by a yield function $\varphi(\boldsymbol{\sigma})$ which is an even function in stresses, then the local plastic dissipation $\pi(\mathbf{d})$ is an even function of the local strain-rate tensor $\mathbf{d}$. By Eq. (7.13) it follows that the exact macroscopic strain-rate potential of the porous aggregate, $\Pi = \Pi(\mathbf{D},f)$, is also an even function of the strain-rate tensor $\mathbf{D}$ and consequently, the yield function of the porous material, which is defined as,

$$F(\boldsymbol{\Sigma},f) = \sup_{\mathbf{D}} \left[\boldsymbol{\Sigma} : \mathbf{D} - \Pi(\mathbf{D},f)\right] \tag{7.16}$$

is also an even function.

Because the voids are spherical and randomly distributed in the matrix, the yield function of the porous solid, $F(\boldsymbol{\Sigma},f)$, ought to be isotropic. By the usual arguments based on theorems of representation of scalar isotropic functions (see Chap. 1), it follows that $F(\boldsymbol{\Sigma},f)$ should depend on the stress tensor $\boldsymbol{\Sigma}$ only through its invariants, i.e.,

$$F(\boldsymbol{\Sigma},f) = F\left(\Sigma_m, \Sigma_e, J_3^{\Sigma},f\right).$$

Since $F(\boldsymbol{\Sigma})$ is an even function, the following restriction on the form of the yield function

$$F\left(\Sigma_m, \Sigma_e, J_3^{\Sigma}\right) = F\left(-\Sigma_m, \Sigma_e, -J_3^{\Sigma}\right) \tag{7.17}$$

ought to be satisfied.

In other words, the origin is a center of symmetry for the yield surface of the porous solid. Indeed, Eq. (7.15) implies that the point on the yield surface that is characterized by a given stress triaxiality, (T and $J_3^{\Sigma} \geq 0$) is symmetric with respect to the axis $\Sigma_m = 0$ to the point corresponding to ($-T$) and $J_3^{\Sigma} \leq 0$. Only for purely hydrostatic loading ($T = \infty$ and $J_3^{\Sigma} = 0$) or purely deviatoric axisymmetric loadings ($T = 0$), there is no effect of the sign of the third-invariant on the yielding response.

Moreover, it can be shown that irrespective of the expression of the yield function of the matrix, $\varphi(\boldsymbol{\sigma})$, the hydrostatic yield limit is the same.

Theorem 7.2 *If the yield function of the matrix is an even function then the hydrostatic yield limit of the porous solid is equal to* $\pm(2/3)\sigma_T \ln f$.

Proof For spherical void geometry, a representative volume element (RVE) is a hollow sphere of inner radius a and outer radius $b = af^{-1/3}$, where f is the porosity (see Fig. 7.1). The outer boundary of the RVE is subjected to purely hydrostatic loading $\boldsymbol{\Sigma} = p\mathbf{I}$, p real. The hydrostatic limit p_Y is the solution to the following limit-analysis problem:

Find the maximum pressure p, for which there exists a stress field statically and plastically admissible, i.e.,

$$\begin{cases} \operatorname{div} \boldsymbol{\sigma} = 0 \\ \boldsymbol{\sigma}\boldsymbol{n} = 0|_{r=a} \quad \text{i.e., the void is traction-free,} \\ \boldsymbol{\sigma}\boldsymbol{n} = p\boldsymbol{e}_r|_{r=b}, \\ \varphi(\boldsymbol{\sigma}) \leq 0 \ \text{ for } \ a \leq r \leq b. \end{cases} \tag{7.18}$$

In the spherical coordinate system (r, θ, φ), the deviator of the local stress $\boldsymbol{\sigma}$ is given by

$$\mathbf{s} = \frac{1}{3}\begin{pmatrix} 2X & 0 & 0 \\ 0 & -X & 0 \\ 0 & 0 & -X \end{pmatrix} \text{ with } X = \sigma_{rr} - \sigma_{\theta\theta} \tag{7.19}$$

Therefore, the invariants of $\mathbf{s}$ are expressed as:

$$J_2 = \operatorname{tr}(\boldsymbol{s}^2)/2 = X^2/3 \text{ and } J_3 = \operatorname{tr}(\boldsymbol{s}^3)/3 = 2X^3/27. \tag{7.20}$$

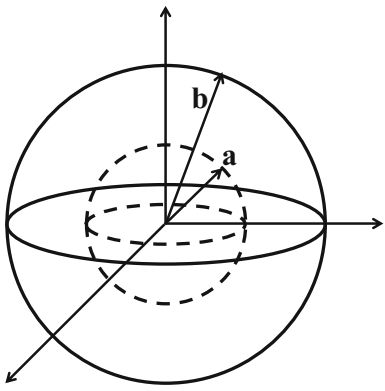

Fig. 7.1 Representative volume element (RVE) for a porous solid containing spherical voids

The equilibrium equations, div $\boldsymbol{\sigma} = 0$, reduce to:

$$\frac{\partial \sigma_{rr}}{\partial r} + 2\frac{\sigma_{rr} - \sigma_{\theta\theta}}{r} = 0, \tag{7.21}$$

with boundary conditions: $\sigma_{rr}|_{r=a} = 0$ and $\sigma_{rr}|_{r=b} = p$.

For compressive hydrostatic loadings $p \leq 0$, while for tensile loading $p \geq 0$. The matrix is incompressible, so the isotropic yield function $\varphi(\boldsymbol{\sigma})$ is represented as:

$$\varphi(\boldsymbol{\sigma}) = \varphi(J_2, J_3)$$

(see Theorem 4.1, Chap. 4). Therefore, using the relations given by Eq. (7.20), the yield criterion writes:

$$\varphi\left(X^2/3,\ 2X^3/27\right) = \sigma_T \tag{7.22}$$

Since $\varphi\left(\sigma_T^2/3,\ 2\sigma_T^3/27\right) = \sigma_T$, and $\varphi(\boldsymbol{\sigma})$ is an even function and homogeneous of degree one in stresses, it follows that the solution of Eq. (7.22) is:

$$|X| = \sigma_T. \tag{7.23}$$

If $X = \sigma_{rr} - \sigma_{\theta\theta} \geq 0$, substitution in the equilibrium Eq. (7.21) and further integration leads to:

$$\sigma_{rr} = -2\sigma_T \ln r + \text{constant}.$$

Imposing the boundary conditions, it follows that the maximum compressive pressure is: $p_Y^- = \frac{2}{3}\sigma_T \ln f$.

Similarly, for tensile hydrostatic loading, it follows that the maximum pressure is $p_Y^+ = -\frac{2}{3}\sigma_T \ln f$. Therefore, irrespective of the specific expression of the yield function $\varphi(\boldsymbol{\sigma})$ describing the plastic deformation of the matrix, if $\varphi(\boldsymbol{\sigma})$ is an even function, the absolute value of the hydrostatic yield limit of the porous material is $|(2/3)\sigma_T \ln f|$.

7.2.2 *Velocity Field Compatible with Uniform Strain-Rate Boundary Conditions*

As already mentioned, for porous materials containing spherical voids randomly distributed in the fully dense matrix, a representative volume element is a hollow sphere. If the inner radius is denoted by a and outer radius b (see Fig. 7.1), the void volume fraction (porosity) is expressed as: $f = a^3/b^3$. In the following, we present the velocity field proposed by Rice and Tracey [58]. This velocity field has been

used for the derivation of all the analytic plastic potentials for porous materials containing spherical voids that will be presented in this book.

7.2.2.1 Rice and Tracey [58] Velocity Field

Rice and Tracey [58] proposed a velocity field of the form:

$$\mathbf{v} = \mathbf{v}^v + \mathbf{v}^S, \tag{7.24}$$

where $\mathbf{v}^v$ is associated with expansion of the void, whereas $\mathbf{v}^S$ is related to shape changes. Imposing the incompressibility condition

$$\text{div } \mathbf{v} = 0,$$

and uniform strain-rate boundary conditions on the outer boundary of the RVE, i.e.,

$$\mathbf{v}|_{\mathbf{x}=b\mathbf{e}_\mathbf{r}} = \mathbf{D}\mathbf{x} \text{ with } \mathbf{D} = \text{constant},$$

where $\mathbf{x}$ is the position vector, originating from the center of the sphere, and $\mathbf{e}_\text{r}$ is the radial unit vector, it follows that:

$$\mathbf{v}^v = \left(b^3/r^2\right) D_m \mathbf{e}_r \quad \text{and} \quad \mathbf{v}^S = \mathbf{D}'\mathbf{x}. \tag{7.25}$$

In Eq. (7.25), both Cartesian and spherical coordinates have been used.

In spherical coordinates (r, θ, φ), the local rate of deformation $\mathbf{d} = \frac{1}{2}\left(\nabla\mathbf{v} + \nabla\mathbf{v}^T\right)$ corresponding to $\mathbf{v}$ given by Eq. (7.25) is as follows:

$$\mathbf{d}_{(\text{r},\theta,\varphi)} = \begin{pmatrix} d_{rr} & d_{r\theta} & 0 \\ d_{r\theta} & d_{\theta\theta} & 0 \\ 0 & 0 & d_{\varphi\varphi} \end{pmatrix}$$

where

$$\begin{cases} d_{rr} = D'_{rr} - 2D_m(b/r)^3 \\ d_{\theta\theta} = D'_{\theta\theta} + D_m(b/r)^3 \\ d_{\varphi\varphi} = D'_{\varphi\varphi} + D_m(b/r)^3 \\ d_{r\theta} = D'_{r\theta} = D_{r\theta} \end{cases}. \tag{7.26}$$

For general 3-D loadings,

$$\mathbf{D} = D_1\mathbf{e}_1 \otimes \mathbf{e}_1 + D_2\mathbf{e}_2 \otimes \mathbf{e}_2 + D_3\mathbf{e}_3 \otimes \mathbf{e}_3, \tag{7.27}$$

with $(\mathbf{e}_1, \mathbf{e}_2, \mathbf{e}_3)$ denoting the eigenvectors of $\mathbf{D}$ and D_1, D_2, D_3 its eigenvalues (unordered). In this Cartesian system, the components of the local strain-rate tensor $\mathbf{d} = (\nabla\mathbf{v} + \nabla\mathbf{v}^T)/2$ corresponding to the Rice and Tracey [58] velocity field are:

$$\begin{aligned}
d_{11} &= D'_1 + \left(b^3 D_m\right)\frac{1 - 3x_1^2/\left(x_1^2 + x_2^2 + x_3^2\right)}{\left(x_1^2 + x_2^2 + x_3^2\right)^{3/2}} \\
d_{22} &= D'_2 + \left(b^3 D_m\right)\frac{1 - 3x_2^2/\left(x_1^2 + x_2^2 + x_3^2\right)}{\left(x_1^2 + x_2^2 + x_3^2\right)^{3/2}} \\
d_{33} &= D'_3 + \left(b^3 D_m\right)\frac{1 - 3x_3^2/\left(x_1^2 + x_2^2 + x_3^2\right)}{\left(x_1^2 + x_2^2 + x_3^2\right)^{3/2}} \\
d_{12} &= -\frac{3b^3 D_m x_1 x_2}{\left(x_1^2 + x_2^2 + x_3^2\right)^{3/2}}; d_{13} = -\frac{3b^3 D_m x_1 x_3}{\left(x_1^2 + x_2^2 + x_3^2\right)^{3/2}} \\
d_{23} &= -\frac{3b^3 D_m x_2 x_3}{\left(x_1^2 + x_2^2 + x_3^2\right)^{3/2}}.
\end{aligned} \tag{7.28}$$

where $D'_i = D_i - D_m$, i = 1, …, 3 being the eigenvalues of $\mathbf{D}'$.

In particular, for two-dimensional axisymmetric loadings, say,

$$\boldsymbol{D} = D_{11}(\mathbf{e}_1 \otimes \mathbf{e}_1 + \mathbf{e}_2 \otimes \mathbf{e}_2) + D_{33}(\mathbf{e}_3 \otimes \mathbf{e}_3), \tag{7.29}$$

by using either Eq. (7.27) or Eq. (7.28), it follows that the expressions of the eigenvalues (not necessarily ordered) of the strain-rate field $\mathbf{d}$ are given for any $a \le r \le b,\ 0 \le \theta \le \pi$ are given by:

$$\begin{cases}
d_I = D'_{11} + D_m(b/r)^3 \\
d_{II} = -d_I/2 + (3/2)\sqrt{D'^2_{11} + D_m^2(b/r)^6 + 2D'_{11}D_m(b/r)^3\cos 2\theta} \\
d_{III} = -d_I/2 - (3/2)\sqrt{D'^2_{11} + D_m^2(b/r)^6 + 2D'_{11}D_m(b/r)^3\cos 2\theta}
\end{cases}. \tag{7.30}$$

Remark For hydrostatic loadings, the Rice and Tracey [58] velocity field reduces to:

$$\mathbf{v}^{\mathrm{v}} = \left(b^3/r^2\right)D_m\mathbf{e}_{\mathrm{r}}.$$

If the plastic behavior of the matrix is governed by an isotropic and pressure-insensitive yield function, this field is also the only plastically admissible field (see also [45]).

7.2.3 Porous Materials with von Mises Matrix

7.2.3.1 Gurson [30] Plastic Potentials

Gurson [29] was the first to use the kinematic homogenization approach to model porous solids. The matrix behavior was considered to be rigid-plastic and governed by the von Mises yield function, $\varphi_{\text{Mises}}(\boldsymbol{\sigma}) = \sqrt{(3/2)\boldsymbol{s}:\boldsymbol{s}}$. Let us recall that for any strain-rate field $\mathbf{d}$, the local plastic dissipation associated with $\varphi_{\text{Mises}}(\boldsymbol{\sigma})$ has the following closed-form expression:

$$\pi_{\text{Mises}}(\mathbf{d}) = \sigma_T \dot{\lambda} = \sigma_T \psi_{\text{Mises}}(\mathbf{d}), \tag{7.31}$$

with the von Mises SRP expressed as:

$$\psi_{\text{Mises}}(\mathbf{d}) = \sqrt{(2/3)\text{tr}\mathbf{d}^2},$$

(see Sect. 6.1.1).

For spherical void geometry, the RVE considered by Gurson [29] is the hollow sphere, shown in Fig. 7.1. To arrive at a closed-form expression of the plastic potential for the porous Mises material, the analysis was done for a unique velocity field, namely that of Rice and Tracey [58] and axisymmetric loadings [see Eqs. (7.25) and (7.29)]. For the corresponding strain-rate field $\mathbf{d}$, [see Eq. (7.30)], the local plastic dissipation given by Eq. (7.31) takes the form:

$$\pi_{\text{Mises}}(\mathbf{d}) = \sigma_T \sqrt{4D_m^2\left(\frac{b}{r}\right)^6 + 4D_{11}'^2 + 2D_{11}'D_m\left(\frac{b}{r}\right)^3(1+3\cos 2\theta)}, \tag{7.32}$$

and the average value of this local plastic dissipation is:

$$\begin{aligned}\Pi^+_{\text{Mises}}(\mathbf{D},f) &= \frac{1}{\text{V}}\int_\Omega \pi(\mathbf{d})\text{d}\Omega \\ &= \frac{\sigma_T}{V}\int_\Omega \sqrt{4D_m^2(b/r)^6 + 4D_{11}'^2 + 2D_{11}'D_m(b/r)^3(1+3\cos 2\theta)}\ \text{d}\Omega\end{aligned} \tag{7.33}$$

with $V = 4\pi b^3/3$ and Ω is the domain occupied by the matrix (see Fig. 7.1). As discussed in Sect. 7.1, $\Pi^+_{\text{Mises}}(\mathbf{D},f)$ is an upper bound of the exact potential [i.e., the potential obtained through minimization over the entire set of velocity fields compatible with uniform boundary conditions given by Eq. (7.13)].

It is important to note that Gurson [29, 30] did not estimate the integral given by Eq. (7.33). Instead, Gurson made the following simplifying hypothesis:

(H1) In the expression (7.32) of the local plastic dissipation $\pi_{\text{Mises}}(\mathbf{d})$, the "cross-term" $D_m D'_{11}$ can be neglected, i.e.,

$$\pi_{\text{Mises}}(\mathbf{d}) \simeq \pi^{\text{Gurson}}_{\text{Mises}}(\mathbf{d}) = \sigma_T \sqrt{4D_m^2 (b/r)^6 + 4\, D'^2_{11}}. \tag{7.34}$$

Moreover, the truncated plastic dissipation $\pi^{\text{Gurson}}_{\text{Mises}}(\mathbf{d})$ given by Eq. (7.34) involves only dependence on the radial coordinate. This means that the local plastic dissipation is the same on every spherical surface $S(r)$, with $a \leq r \leq b$. Neglecting the cross-term $D_m D'_{11}$ is thus a strong approximation of the distribution of the plastic dissipation in the matrix (i.e., plastic flow is such that the local plastic dissipation for axisymmetric states does not depend on the spherical coordinate θ). Using this simplifying hypothesis, Gurson [29] obtained the following approximate overall plastic dissipation for the porous von Mises material:

$$\begin{aligned} \Pi_{\text{Gurson}}(\mathbf{D},f) &= \frac{1}{\mathrm{V}} \int_{\Omega} \pi^{\text{Gurson}}_{\text{Mises}}(\mathbf{d}) = \sigma_T \int_{\Omega} \sqrt{4D_m^2 (b/r)^6 + 4\, D'^2_{11}}\, \mathrm{dV} \\ &= \frac{3\sigma_T}{b^3} \int_{a^3}^{b^3} r^2 \sqrt{4D_m^2 (b/r)^6 + 4\, D'^2_{11}}\, \mathrm{d}r. \end{aligned} \tag{7.35}$$

Later on, using Cauchy–Schwarz inequality, Leblond [42] has shown that $\Pi_{\text{Gurson}}(\mathbf{D},f)$ is an upper bound of the exact plastic potential. Let us denote the overall strain-rate triaxiality as:

$$u \overset{def}{=} \frac{2|D_m|}{D_e}. \tag{7.36}$$

Theorem 7.3 *The* Gurson [29] *strain-rate potential for a porous von Mises solid is given by*:

$$\Psi_{\text{Gurson}}(\mathbf{D},f) = 2|D_m| \left[\frac{\sqrt{1+u^2} - \sqrt{f^2+u^2}}{u} + \ln\left(\frac{u + \sqrt{f^2+u^2}}{u + \sqrt{1+u^2}} . \frac{1}{f} \right) \right]. \tag{7.37}$$

Proof Since the applied loading is axisymmetric [see Eq. (7.29)], the equivalent strain-rate D_e and the absolute value of the strain-rate triaxiality take the form

$$D_e = 2\left|\mathrm{D}'_{11}\right| \text{ and } u = |D_m|/D'_{11}. \tag{7.38}$$

Taking into account that the void volume fraction $f = a^3/b^3$, and making the change of variable $y = u(b/r)^3$ in the integral given by Eq. (7.35), Gurson [29] obtained the following closed-form expression of the overall plastic dissipation $\Pi_{\text{Gurson}}(\mathbf{D},f)$ and strain-rate potential $\Psi_{\text{Gurson}}(\boldsymbol{D},f)$ of a porous Mises material:

$$\Pi_{\text{Gurson}}(\mathbf{D},f) = \sigma_T \Psi_{\text{Gurson}}(\mathbf{D},f), \tag{7.39}$$

with $\Psi_{\text{Gurson}}(\mathbf{D},f)$ given by Eq. (7.37).

Let us recall that at yielding, the stresses of the porous materials are: (see Sect. 7.1)

$$\frac{\boldsymbol{\Sigma}}{\sigma_T} = \frac{\partial \Psi_{\text{Gurson}}(\mathbf{D}, f)}{\partial \mathbf{D}}.$$

Therefore, knowledge of $\Psi_{\text{Gurson}}(\mathbf{D}, f)$ leads to the expression of the yield locus in parametric form. At yielding, the mean stress and effective stress of the porous von Mises material, respectively [see Eq. (7.4)] are:

$$\begin{cases} \dfrac{\Sigma_m}{\sigma_T} = \dfrac{1}{3}\dfrac{\partial \Psi_{\text{Gurson}}(\mathbf{D}, f)}{\partial D_m} = \dfrac{2}{3}\ln\left(\dfrac{u + \sqrt{u^2 + f^2}}{u + \sqrt{u^2 + 1}} \cdot \dfrac{1}{f}\right), \\ \dfrac{\Sigma_e}{\sigma_T} = \left|\dfrac{\partial \Psi_{\text{Gurson}}(\mathbf{D}, f)}{\partial D_e}\right| = \sqrt{1 + u^2} - \sqrt{u^2 + f^2} \end{cases} \tag{7.40}$$

Theorem 7.4 Gurson [30] *yield function for a porous material with matrix governed by the von Mises yield criterion and containing spherical voids is given by*:

$$\Phi(\boldsymbol{\Sigma}, f) = \left(\frac{\Sigma_e}{\sigma_T}\right)^2 + 2f \cosh\left(\frac{3\Sigma_m}{2\sigma_T}\right) - 1 - f^2 = 0. \tag{7.41}$$

Proof Using Eq. (7.40), we obtain that:

$$\begin{aligned} \cosh\left(\frac{3}{2}\frac{\Sigma_m}{\sigma_T}\right) &= \cosh\left(\ln\left(\frac{u + \sqrt{u^2 + f^2}}{u + \sqrt{u^2 + 1}} \cdot \frac{1}{f}\right)\right) \\ &= \frac{1}{f}\left(\sqrt{(f^2 + u^2)(1 + u^2)} - u^2\right) \end{aligned} \tag{7.42}$$

and

$$\begin{aligned} \left(\frac{\Sigma_e}{\sigma_T}\right)^2 &= \left(\sqrt{1 + u^2} - \sqrt{u^2 + f^2}\right)^2 \\ &= 1 + f^2 + 2u^2 - 2\sqrt{(f^2 + u^2)(1 + u^2)} \end{aligned} \tag{7.43}$$

By eliminating the parameter u between Eqs. (7.42) and (7.43), one obtains the classical form of the Gurson [30] yield criterion given by Eq. (7.41).

Remark

(i) It is very important to note that Gurson's stress potential $\Phi(\boldsymbol{\Sigma}, f)$ given by Eq. (7.41) is the exact dual of the strain-rate potential $\Psi_{\text{Gurson}}(\mathbf{D}, f)$ given by Eq. (7.37). This is a direct consequence of the kinematic homogenization procedure used to obtain these potentials (see Sect. 7.1).

(ii) If the void volume fraction $f = 0$, the Gurson [30] stress potential $\Phi(\boldsymbol{\Sigma}, f)$ given by Eq. (7.41) reduces to the von Mises [70] stress potential (see Chap. 4 for more details about the von Mises yield criterion), while the porous SRP given by Eq. (7.37) reduces to the von Mises SRP (see Chap. 6).

(iii) Both potentials of the porous material display very strong symmetries. The strain-rate potential $\Psi_{\text{Gurson}}(\mathbf{D}, f)$ is invariant to the transformation: $(D_m, D_e) \rightarrow (-D_m, D_e)$ while the stress potential $\Phi(\boldsymbol{\Sigma}, f)$ is invariant to the transformation $(\Sigma_m, \Sigma_e) \rightarrow (-\Sigma_m, \Sigma_e)$.

Due to the property (iii), the Gurson [30] yield surface and the SRP isosurface are represented only for $\Sigma_m \geq 0$, and $D_m \geq 0$, respectively, while for compressive states the mechanical response/shape is obtained by symmetry. As an example, in Fig. 7.2a is shown the representation of the Gurson's [29] strain-rate potential given by Eq. (7.37) in the plane (D_m, D_e) for $D_m \geq 0$ for different initial porosities $f = 0.001$, $f = 0.01$, and $f = 0.1$, respectively, while in Fig. 7.2b are shown the projections in the plane (Σ_m, Σ_e) of its exact dual, i.e., the classical Gurson's stress potential [Eq. (7.41)] for the same porosities.

It should be also mentioned that F.E. analyses of the behavior of porous materials are generally done using Gurson's [30] yield function [Eq. (7.41)]. In Balan and Cazacu [7], it was shown that the strain-rate-based formulation in conjunction with Gurson [29] strain-rate potential given by Eq. (7.37) can be used instead of the stress-based formulation. Moreover, these authors analyzed the void volume fraction evolution in a tensile bar. The results indicate that an elastic–plastic model based on the strain-rate potential predicts the dilatational response with the same level of accuracy as the classic stress-based model.

Remark

(a) For hydrostatic loadings, the yield limit according to the Gurson's [30] criterion coincides with the exact solution of the limit-analysis problem (see Theorem 7.2 of Sect. 7.1).
Proof Indeed, it can be easily seen that for purely hydrostatic loadings, i.e., for $u \rightarrow \infty$ in Eq. (7.40), we obtain

$$|\Sigma_m| = -\frac{2}{3}\sigma_T \ln f \quad \text{and} \quad \Sigma_e = 0, \tag{7.44}$$

(b) For axisymmetric and purely deviatoric loadings (i.e., $\Sigma_m = 0$), Gurson [30] predicts that the yield limit is $\sigma_T(1-f)$.
Proof For such loadings, i.e., for $u \rightarrow 0$ in Eq. (7.40), we obtain:

$$\Sigma_m = 0 \quad \text{and} \quad \Sigma_e = \sigma_T(1-f). \tag{7.45}$$

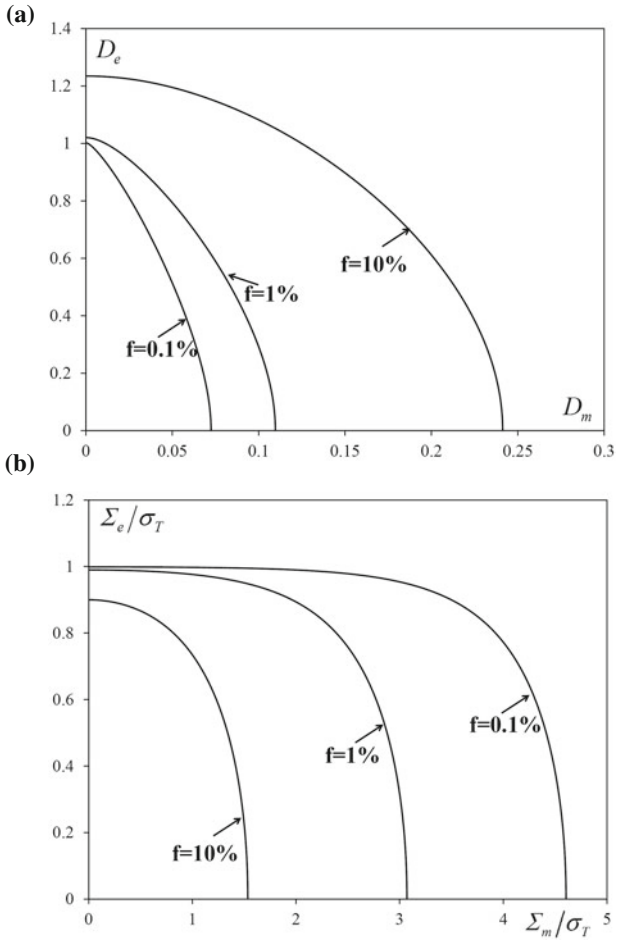

Fig. 7.2 **a** Representation of the Gurson's [29] strain-rate potential [Eq. (7.37)] in the plane (D_m, D_e) for $D_m \geq 0$; **b** isocontours in the plane (Σ_m, Σ_e) of the Gurson's [30] criterion for initial porosities $f = 0.001$, $f = 0.01$, and $f = 0.1$, respectively

7.2.3.2 Modified Versions of Gurson [30] Criterion

Unit-cell models for porous solids and method of analysis

Beginning with the pioneering studies of Needleman [51], Tvergaard [67], Koplik and Needleman [39], F.E. analyses using unit-cell models, representative of a material containing a periodic array of spherical voids, have provided insights into the micromechanics of ductile damage and fracture. With the exception of a few investigations (e.g., Tvergaard [67]; Zhang et al. [71]; Alves et al. [4]; Alves and Cazacu [1] for isotropic materials; Srivastava and Needleman [63] for anisotropic

single crystal behavior), two-dimensional axisymmetric unit-cell models are considered, the RVE being a cylinder with a single spherical void at its center. Therefore, only axisymmetric loadings can be applied.

In three-dimensional analyses, it is generally assumed that the porous solid contains a regular array of initially spherical voids, the inter-void spacing is the same in any direction. Thus, the RVE or unit cell is initially cubic with side lengths $2C_0$, and contains a single void of radius r_0 at its center. The initial porosity is:

$$f_0 = \frac{\pi}{6}\left(\frac{r_0}{C_0}\right)^3 \tag{7.46}$$

A Cartesian coordinate system is used with the origin at the center of the void (see Fig. 7.3a). Let **u** denote the incremental displacement between the current and reference configuration, and **t** the prescribed Cauchy stress vector, defined on the current configuration. Symmetry conditions are imposed on the planes $x = 0$, $y = 0$, and $z = 0$, respectively:

$$\begin{aligned} &u_1(0,y,z) = 0, \;\; t_2(0,y,z) = 0, \;\; t_3(0,y,z) = 0, \\ &u_2(x,0,z) = 0, \;\; t_1(x,0,z) = 0, \;\; t_3(x,0,z) = 0, \\ &u_3(x,y,0) = 0, \;\; t_1(x,y,0) = 0, \;\; t_2(x,y,0) = 0. \end{aligned} \tag{7.47}$$

Therefore, only one-eighth of the unit cell needs to be analyzed numerically (see Fig. 7.3b). To simulate the constraints of the surrounding material, it is enforced that the faces of the unit cell, which are initially planes parallel to the coordinate planes, remain plane and shear free. Therefore, the boundary conditions imposed on the faces of the unit cell are:

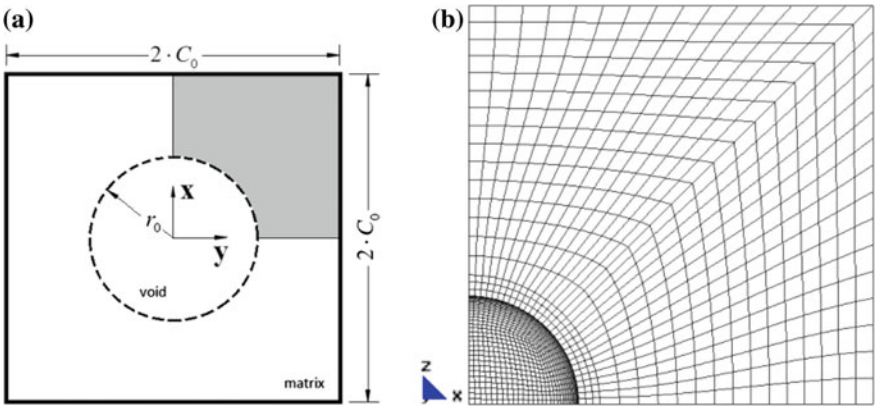

Fig. 7.3 **a** Schematic two-dimensional projection of a three-dimensional cubic cell model; 2 C_0 and r_0 denote the length of the undeformed cubic cell and the initial radius of the spherical void, respectively. **b** Finite-element mesh of one-eight of the unit cell with a spherical void at its center

$$\begin{aligned} u_1(C_0, y, z) &= U_1^*(t),\ t_2(C_0, y, z) = t_3(C_0, y, z) = 0, \\ u_2(x, C_0, z) &= U_2^*(t),\ t_1(x, C_0, z) = t_3(x, C_0, z) = 0, \\ u_3(x, y, C_0) &= U_3^*(t),\ t_1(x, y, C_0) = t_2(x, y, C_0) = 0. \end{aligned} \tag{7.48}$$

The time histories of the displacements, $U_1^*(t)$, $U_2^*(t)$, and $U_3^*(t)$ in Eq. (7.48) are determined by the analysis in such a way that the principal values of the overall Cauchy stresses Σ_1, Σ_2, Σ_3 follow a prescribed proportional loading history that is given by:

$$\frac{\Sigma_1}{\Sigma_2} = \frac{\rho_1}{\rho_2} \quad \text{and} \quad \frac{\Sigma_1}{\Sigma_3} = \frac{\rho_1}{\rho_3} \tag{7.49}$$

where ρ_1, ρ_2 and ρ_3 are prescribed constants, and Σ_1, Σ_2, Σ_3 are calculated as:

$$\begin{aligned} \Sigma_1 &= \frac{1}{C_2 C_3} \int_0^{C_2} \int_0^{C_3} t_1 \, \mathrm{d}z\mathrm{d}y, \\ \Sigma_2 &= \frac{1}{C_1 C_3} \int_0^{C_3} \int_0^{C_1} t_2 \, \mathrm{d}z\mathrm{d}x, \\ \Sigma_3 &= \frac{1}{C_1 C_2} \int_0^{C_1} \int_0^{C_2} t_3 \, \mathrm{d}x\mathrm{d}y. \end{aligned} \tag{7.50}$$

where $C_i = C_0 + U_i^*$ are the current cell dimensions. The void is considered to be traction-free. The invariants of the stress field $\boldsymbol{\Sigma}$ of the porous material (matrix and void) are then calculated using Eq. (7.4). The eigenstrains and the von Mises equivalent strain E_e are calculated as follows:

$$\begin{aligned} E_1 &= \ln\left(\frac{C_1}{C_0}\right), E_2 = \ln\left(\frac{C_2}{C_0}\right), E_3 = \ln\left(\frac{C_3}{C_0}\right), \\ E_e &= \sqrt{\frac{2}{3}\left(E_1^2 + E_2^2 + E_3^2\right)}. \end{aligned} \tag{7.51}$$

As already mentioned, such prescribed proportional loading is of interest for assessing the capabilities of models to capture the effects of the stress state (stress invariants) on the response of porous solids.

If axisymmetric loadings are considered, $\rho_1 = \rho_2$ [see Eq. (7.49)]. Generally, the simulations are done such that the stress triaxiality, T, is maintained constant. For this purpose, at the end of each time increment, the condition of constant proportionality between the true stresses is strictly verified, so it is ensured that the stress triaxiality remains constant throughout the given deformation history. For axisymmetric loadings, $J_3^\Sigma = -2(\Sigma_1 - \Sigma_3)^3/27$ thus only the effect of the sign of the third-invariant can be investigated. To assess the influence of J_3^Σ on the stress–strain

response and the evolution of porosity, for each fixed value of the triaxiality T [see definition given in Eq. (7.5)], simulations need to be conducted for the two possible ordering of the principal values, i.e.,

(a) $\rho_1 = \rho_2 \leq \rho_3$, which corresponds to $J_3^{\Sigma} \geq 0$, *and*
(b) $\rho_1 = \rho_2 \geq \rho_3$, which corresponds to $J_3^{\Sigma} \leq 0$.

It is worth noting that:

- For loadings (a), two principal values of the stress deviator $\boldsymbol{\Sigma}'$ are *compressive* (*negative*) but the maximum principal value is *tensile (positive).*
- For loadings (b), two principal values of $\boldsymbol{\Sigma}'$ are *tensile* (positive) but *the minor principal value,* which is *compressive (negative),* has the largest absolute value.

The void volume fraction f is evaluated at the end of each time increment as:

$$f = \frac{V_{\text{matrix}}}{V_{\text{cell}}} \tag{7.52}$$

In the above equation, $V_{\text{cell}} = C_1 C_2 C_3$, while the volume of the deformed matrix, V_{matrix}, is determined directly from the integration of the F.E. domain using the finite-element formulation ($V_{\text{matrix}} = \sum_{i=1}^{N_E} V_i$, where V_i is the volume of the element i and N_E is the total number of finite elements in the mesh).

When the focus of the F.E. unit-cell model investigations is on assessing an upper-bound model (e.g., such as the Gurson's [30] model), elastic/ideal plastic behavior is considered. For example, Alves et al. [4] considered that the material in the cell obeys a power-law-type hardening, i.e.,

$$Y = A(\varepsilon_0 + \bar{\varepsilon}^p)^n, \tag{7.53}$$

with hardening exponent $n = 10^{-4}$, which corresponds to almost ideal plastic behavior (see also Chap. 2). In Eq. (7.53), Y denotes the current flow stress while A, and ε_0 are material parameters, and $\bar{\varepsilon}^p$ is the equivalent plastic strain. The numerical values of the elastic parameters and matrix yield stress, Y_0, which are typically used in cell calculations, are respectively: $Y_0/E = 500$ and $\nu = 1/3$ (see also Koplik and Needleman [39]). Various F.E. softwares are used to conduct F.E. analyses with the unit-cell models described. For example, the F.E. analyses reported in Alves et al. [4] were performed with DD3IMP (Menezes and Teodosiu [49], Oliveira et al. [53]). The fact that DD3IMP is an in-house code facilitated an accurate implementation of the boundary-value problem. Specifically, the degrees of freedom of all F.E. nodes belonging to the same planar bounding surface of the cubic surface were associated in the global stiffness matrix, and the equations of all these degrees of freedom were replaced by only one unknown variable. In this way,

it was ensured that all initially planar boundary surfaces remain strictly flat during the entire loading history.

Gurson–Tvergaard–Needleman model

Numerical studies of Koplik and Needleman [39] using cylindrical unit-cell geometry with a single spherical void at its center have put into evidence that Gurson's [30] criterion given by Eq. (7.41) underestimates the rate of void growth. It is to be noted that in the F.E. unit-cell calculations reported, the applied axisymmetric loading was imposed such as to have the axial stress always greater than the lateral stress, i.e., such that $J_3^{\Sigma} \geq 0$. As already mentioned, later on numerical studies were conducted to assess the influence of the loading path on porosity evolution (e.g., Faleskog et al. [26]; Zhang et al. [71]; Kim et al. [38]). For example, in order to investigate the influence of the sign of J_3^{Σ} on void evolution, Alves et al. [4] conducted F.E. analyses on a cubic unit cell subjected to axisymmetric loadings corresponding to $J_3^{\Sigma} \geq 0$ [$\rho_1 = \rho_2 \leq \rho_3$, see Eq. (7.49)] or $J_3^{\Sigma} \leq 0$ ($\rho_1 = \rho_2 \geq \rho_3$), and fixed stress triaxiality T. As an example, in Fig. 7.4 are shown the evolution of the void volume fraction as a function of the overall equivalent strain E_e [see Eq. (7.51)] for $T = 2$. The initial F.E. mesh of one-eighth of the unit-cubic cell consisted of 12150 elements (8-node hexahedral finite elements; selective reduced integration technique, with 8 and 1 Gauss points for the deviatoric and volumetric parts of the velocity field gradient, respectively) and a total of 13,699 nodes (see also Fig. 7.3b). The initial porosity was $f_0 = 0.0013$ (same initial porosity as in the 2-D unit-cell F.E. calculations of Koplik and Needleman [39]). On the same figure is plotted the void evolution according to the Gurson [30]

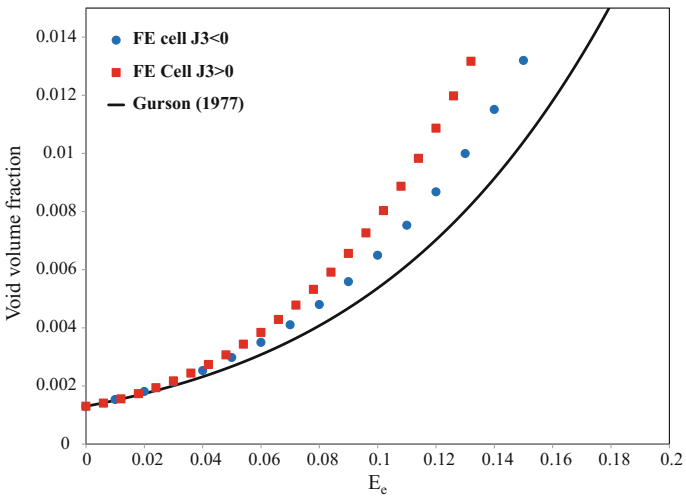

Fig. 7.4 Comparison between the void volume fraction evolution with equivalent strain E_e according to Gurson [30] model (solid line), and unit-cell calculations (symbols) for $T = 2$ for $J_3^{\Sigma} \geq 0$ and $J_3^{\Sigma} \leq 0$; initial porosity $f_0 = 0.0013$

criterion [see Eq. (7.41)]. Note that the F.E. results show that there is an effect of the sign of the third-invariant J_3^{Σ} on void evolution that Gurson [30] model cannot capture (see Fig. 7.4).

Tvergaard [67, 68] studied the onset of shear band instabilities in a voided medium. By conducting F.E. calculations for both plane-strain and axisymmetric conditions, Tvergaard found that the agreement with the numerical results can be improved by introducing additional parameters q_1 and q_2 in the expression of the Gurson [30] yield criterion. This modified form of Eq. (7.41) has been further used as a basis for description of ductile fracture by Tvergaard and Needleman [69]. The expression of this modified version of Gurson [30] yield criterion, called Gurson–Tvergaard–Needleman (GTN) criterion, is:

$$\left(\frac{\Sigma_e}{\sigma_T}\right)^2 + 2q_1 f \cosh\left(\frac{3q_2\Sigma_m}{2\sigma_T}\right) - 1 - q_1^2 f^2 = 0 \tag{7.54}$$

There is a very large body of literature on the GTN criterion and model of ductile fracture and its applications. Mention is made here only of general features of the GTN criterion. For detailed discussion see for example Gao et al. [27], who performed micromechanics calibration of the model for a range of engineering materials.

First, let us note that the GTN criterion can be obtained from the Gurson [30] yield criterion given by Eq. (7.41) by making use of the change of variables: $f \rightarrow q_1 f$ and $\Sigma_m \rightarrow q_2\Sigma_m$. Therefore, according to the GTN criterion for purely deviatoric loading, yielding occurs for

$$\Sigma_m = 0 \quad \text{and} \quad \Sigma_e = \sigma_T(1 - q_1 f). \tag{7.55}$$

For purely hydrostatic loadings, the GTN criterion predicts that yielding occurs for

$$|\Sigma_m| = -\frac{2}{3q_2}\sigma_T \ln(q_1 f) \quad \text{and} \quad \Sigma_e = 0. \tag{7.56}$$

Therefore, the exact solution for yielding of a hollow sphere under hydrostatic loadings (see Theorem 7.2 in Sect. 7.2.1) is not recovered.

Concerning the values of the parameters q_1 and q_2, Tvergaard [67] has shown that $q_1 = 1.5$ and $q_2 = 1$ provide the best approximation of the numerical results for fracture strain and porosity. On the basis of axisymmetric 2-D F.E. unit-cell model calculations, Koplik and Needleman [39] concluded that in order to obtain a good agreement with the numerical results for void growth at fixed stress triaxiality $T = 1, 2, 3$ respectively, the values of these parameters should be: $q_1 = 1.25$ and $q_2 = 1$.

In Fig. 7.5 are shown comparisons between the predicted void volume fraction evolution according to the GTN criterion with $q_1 = 1.25$ and $q_2 = 1$ and the F.E. cell calculations results obtained with a cubic cell subjected to axisymmetric loadings and fixed stress triaxiality: $T = 2$. While the GTN model [Eq. (7.54)]

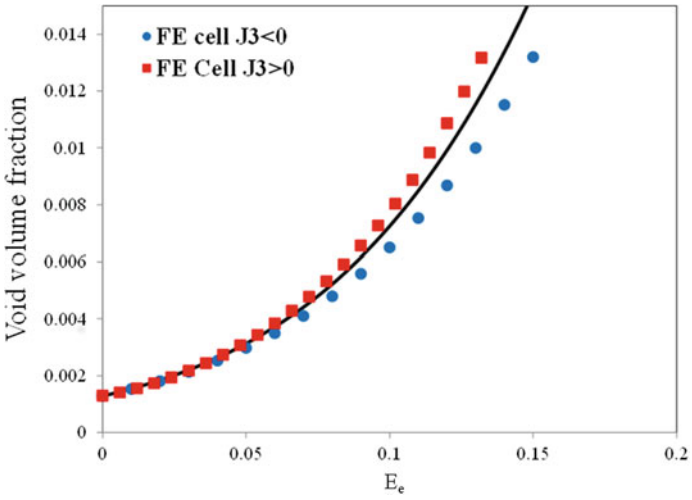

Fig. 7.5 Comparison between the void volume fraction evolution with equivalent strain E_e according to the GTN model (solid line) and cell calculations (symbols) for $T = 2$ for $J_3^{\Sigma} \geq 0$ and $J_3^{\Sigma} \leq 0$; initial porosity $f_0 = 0.0013$

predicts a faster rate of void growth than the Gurson [30] criterion (see Fig. 7.4), it does not capture third-invariant effects.

Richmond and Smelser [59] *yield criterion*

In parallel with the aforementioned F.E. numerical studies of Tvergaard [67] and Koplik and Needleman [39], Richmond and collaborators at Alcoa designed an experimental program to assess the capabilities of Gurson's [30] model to describe void growth and closure. Uniaxial tension–compression tests on specimens consolidated to various initial porosities from iron powder were conducted (data reported in Richmond and Smelser [59]; Spitzig et al. [62]). Moreover, in order to better describe the experimentally observed evolution of porosity, Richmond and Smelser [59] proposed the following modification of the Gurson's [30] yield function:

$$\left(\frac{\Sigma_e}{\bar{\sigma}}\right)^2 + 2f^m \cosh\left(\frac{3m\Sigma_m}{2\bar{\sigma}}\right) - 1 - f^{2m} = 0, \tag{7.57}$$

where $\bar{\sigma}$ denotes the effective stress of the matrix material, and m is a coefficient between 2/3 and unity describing strain-hardening. Let us first note that for $m = 1$, Eq. (7.57) reduces to Eq. (7.41), i.e., Gurson's [30] yield criterion is recovered as a special case.

For hydrostatic loadings, the Richmond and Smelser's [59] criterion predicts that:

$$\left|\frac{\Sigma_m}{\bar{\sigma}}\right| = \frac{2}{3m}\cosh^{-1}\left(\frac{1+f^{2m}}{2f^m}\right) = -\frac{2}{3}\ln(f) \quad \text{and} \quad \Sigma_e = 0,$$

while for purely deviatoric loadings ($\Sigma_m = 0$), it predicts that:

$$\frac{\Sigma_e}{\bar{\sigma}} = (1-f)^m.$$

It was shown that for strain-hardening described by a power-type law with exponent 0.31 and for $m = 2.31$, the experimental porosity evolution of iron compacts is predicted with improved accuracy (see Spitzig et al. [62]).

7.2.3.3 Combined Effects of Mean Stress and Third-Invariant on the Mechanical Response According to Cazacu et al. [19] Plastic Potential

The Gurson's [30] yield criterion (Eq. (7.41) and its modifications presented in Sect. 7.2.3) involve only the mean stress, Σ_m and the von Mises effective stress, Σ_e. However, as discussed in the previous section, F.E. unit-cell model calculations either for axisymmetric or more general 3-D tensile loading configurations (e.g., see Fig. 7.5) have shown that in a porous von Mises material, the void growth rate depends on the loading path. To better reproduce void growth, it was suggested that in the GTN model [see Eq. (7.54)], different values of the q_i parameters should be taken depending on the applied loading (e.g., see Zhang et al. [71]). Moreover, for tensile loadings the aforementioned numerical studies have also shown that the stress triaxiality T [see Eq. (7.5)] by itself is insufficient to characterize yielding of a porous Mises material.

In turn, Cazacu and Stewart [20] conducted axisymmetric 2-D F.E. unit-cell model calculations for both tensile and compressive loadings and generated numerical yield surfaces for a porous Mises material. In the plane (Σ_m, Σ_e), the reported F.E. results describe two yield curves (see Fig. 7.6). For tensile loadings, the yield curve corresponding to $J_3^\Sigma \geq 0$ is below that corresponding to $J_3^\Sigma \leq 0$, while for compressive loadings the reverse is true (see Fig. 7.6). Moreover, a point on the yield curve for $J_3^\Sigma \geq 0$ corresponding to a given stress triaxiality, T, is symmetric with respect to the hydrostatic axis to the point on the other yield curve $(J_3^\Sigma \leq 0)$ corresponding to $(-T)$. The Gurson [30] yield criterion or any of its modified versions do not capture these very specific couplings between the signs of the mean stress and the third-invariant, J_3^Σ.

In the past, this insensitivity to the sign of J_3^Σ as well as the invariance with respect to the sense of the applied load of Gurson-type models have been attributed to the pressure-insensitivity of the matrix yield criterion (see, e.g., McElwain et al. [48]).

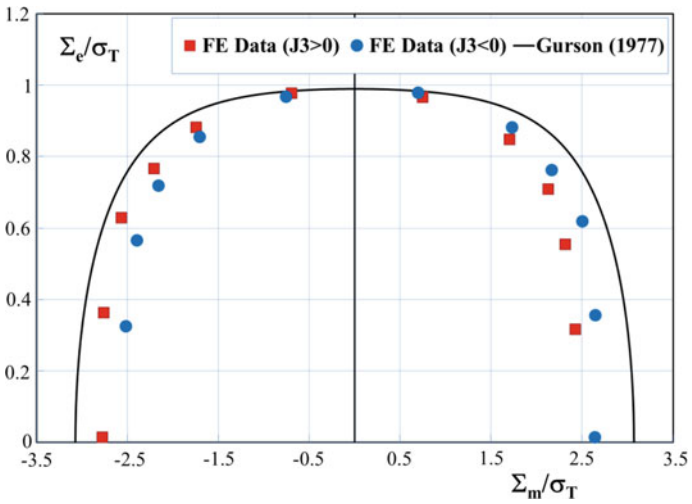

Fig. 7.6 Influence of the third-invariant on yielding of the porous von Mises material for axisymmetric loadings such that $\Sigma_{11} = \Sigma_{22} \geq \Sigma_{33}$ $(J_3^{\Sigma} \leq 0)$ and $\Sigma_{11} = \Sigma_{22} \leq \Sigma_{33}$ $(J_3^{\Sigma} \geq 0)$ for porosity $f_0 = 1\%$: comparison between F.E. unit-cell calculations (symbols) and the Gurson [30] theoretical yield surface (after Cazacu and Stewart [20])

As shown in Sect. 7.2.3, if the matrix behavior is governed by the von Mises yield criterion, the plastic dissipation is a function of both the radial coordinate r, and the polar coordinate, θ [see Eq. (7.32)]. However, in his analysis Gurson [30] approximated the matrix plastic dissipation with a function that depends only on the radial coordinate [see Eq. (7.34)]. In Cazacu et al. [19], it was shown that this approximation amounts to discarding any combined shear mean stress effects on yielding of the porous material. Moreover, the insensitivity of Gurson's [30] criterion to the third-invariant J_3^{Σ} is a direct consequence of this approximation. Furthermore, Cazacu et al. [19] solved the limit-analysis problem for axisymmetric stress states without making Gurson's simplification. The plastic dissipation $\Pi^{+}_{\text{Mises}}(\boldsymbol{D},f)$ and consequently the strain-rate potential of the porous von Mises material, $\Psi^{+}_{\text{Mises}}(\boldsymbol{D},f) = \Pi^{+}_{\text{Mises}}(\boldsymbol{D},f)/\sigma_T$ was obtained in closed form, and an explicit analytic expression of a new yield criterion for the porous von Mises material was derived, namely:

$$\begin{cases} \Sigma_m/\sigma_T = \dfrac{1}{3}\dfrac{\partial \Psi^{+}_{\text{Mises}}(\boldsymbol{D},f)}{\partial D_m} \\ \Sigma_e/\sigma_T = \left|\dfrac{\partial \Psi^{+}_{\text{Mises}}(\boldsymbol{D},f)}{\partial D_e}\right| \end{cases} \tag{7.58}$$

While the explicit expression of $\Psi^{+}_{\text{Mises}}(\boldsymbol{D},f)$ and the parametric representation of this yield surface will be given later in this section, it is important to note here that

the key features of the plastic behavior of a porous Mises solid revealed by the analysis can be deduced without calculation of the integrals representing $\Psi^{+}_{\text{Mises}}(\boldsymbol{D},f)$.

Theorem 7.5 Cazacu et al. [19] *predict that for a porous von Mises material*:

i. *Yielding depends on the sign of the third-invariant of the stress deviator,* J_3^{Σ}.
ii. *For stress triaxialities T different from* 0 *and* $\pm\infty$, *there is a combined effect of the signs of* J_3^{Σ} *and the mean stress* Σ_m, *on yielding. Moreover, a point belonging to one of the yield surfaces given by* Eq. (7.58) *(e.g.,* $J_3^{\Sigma} \geq 0$*) corresponding to a given stress triaxiality T is symmetric, with respect to the hydrostatic axis* $\Sigma_m = 0$, *to the point on the other yield surface (e.g.,* $J_3^{\Sigma} \leq 0$*) corresponding to* $(-T)$.
iii. *Irrespective of the sign of* J_3^{Σ}, *for purely deviatoric axisymmetric loadings, yielding occurs at* $\Sigma_e = \sigma_T(1-f)$; *for purely hydrostatic loadings, yielding occurs at:* $|\Sigma_m| = \frac{2}{3}\sigma_T \ \ln f$.

Proof As mentioned analysis needs to be done for both tensile and compressive states. Thus, the following axisymmetric loading scenarios need to be considered separately: (a) $D'_{11} \geq 0$ and $D_m \geq 0$; (b) $D'_{11} \geq 0$ and $D_m \leq 0$; (c) $D'_{11} \leq 0$ and $D_m \geq 0$; and (d) $D'_{11} \leq 0$ and $D_m \leq 0$. Given that the expression of the local plastic dissipation $\pi_{\text{Mises}}(\boldsymbol{d})$ is given by Eq. (7.32), its expression is the same for the loadings (a) and (d) and, respectively, for the loadings (b) and (c). Therefore, only two loading cases need to be considered separately.

Case (a): $D'_{11} \geq 0$ and $D_m \geq 0$

Since for this loading, $D'_{11} = D_e/2 \geq 0$, substitution into Eq. (7.32) leads to the following expression of the strain-rate potential of the porous Mises material:

$$\Psi^{+}_{\text{Mises}}(\mathbf{D},f) = \frac{1}{\mathrm{V}}\int_{\Omega} \sqrt{4D_m^2(b/r)^6 + D_e^2 + D_eD_m(b/r)^3(1+3\cos 2\theta)}\mathrm{d}V \quad (7.59)$$

with $V = 4\pi b^3/3$ and $\mathrm{d}V = r^2 \sin\theta \mathrm{d}\theta\mathrm{d}\varphi\mathrm{d}r$.

Therefore, $\dfrac{\partial \Psi^{+}_{\text{Mises}}(\mathbf{D},f)}{\partial D_{11}} \geq \dfrac{\partial \Psi^{+}_{\text{Mises}}(\mathbf{D},f)}{\partial D_{33}}$ and $\dfrac{\partial \Psi^{+}_{\text{Mises}}(\mathbf{D},f)}{\partial \mathrm{D}_m} \geq 0$. Hence using Eq. (7.58) it follows that the stress state at yielding is such that: $\Sigma_m \geq 0$ and $J_3^{\Sigma} = -2(\Sigma_{11} - \Sigma_{33})^3/27 \leq 0)$.

Case (c): In a similar manner, for $D'_{11} \leq 0$ and $D_m \geq 0$, we obtain:

$$\Psi^{+}_{\text{Mises}}(\mathbf{D},f) = \frac{\sigma_T}{\mathrm{V}}\int_{\Omega} \sqrt{4D_m^2(b/r)^6 + D_e^2 - D_eD_m(b/r)^3(1+3\cos 2\theta)}\mathrm{d}\Omega \quad (7.60)$$

Thus, $\frac{\partial \Psi^{+}_{\text{Mises}}(\mathbf{D},f)}{\partial D_{11}} \leq \frac{\partial \Psi^{+}_{\text{Mises}}(\mathbf{D},f)}{\partial D_{33}}$ and $\frac{\partial \Psi^{+}_{\text{Mises}}(\mathbf{D},f)}{\partial D_m} \geq 0$, so at yielding the stress state is such that ($\Sigma_m \geq 0$ and $J_3^{\Sigma} \geq 0$). Therefore, according to the criterion, given by Eq. (7.58), yielding depends on the sign of the third-invariant J_3^{Σ}. Moreover, Eqs. (7.59) and (7.60) show that for stress triaxialities $T = \Sigma_m/\Sigma_e$ different from 0 and $\pm\infty$, yielding also depends on the sign of the mean stress Σ_m, which has the same sign as D_m.

As already mentioned, Cazacu et al. [19] showed that the overall plastic dissipation can be obtained in closed form and a new strain-rate potential and yield criterion for porous von Mises materials were deduced.

Theorem 7.6 *The* Cazacu et al. [19] *strain-rate potential for a porous von Mises material is given by*:

(a) *For* $D_m \geq 0$ *and* $J_3^D \leq 0$, *and any value of* $u = \frac{2|D_m|}{D_e}$:

$$\Psi^{+}_{\text{Mises}}(\mathbf{D},f) \quad = D_e u\left[F(\sqrt{u}/f) - F(\sqrt{u})\right] \tag{7.61}$$

with:

$$\begin{aligned} F(z) = &-\frac{2}{3z^2} + \frac{1}{3\sqrt{3}}\left[\tan^{-1}\left(2z+\sqrt{3}\right) - \tan^{-1}\left(2z-\sqrt{3}\right)\right] \\ &+ \frac{1}{2}\ln\left(z^4-z^2+1\right) + \ln\left(\frac{z^2+z\sqrt{3}+1}{z^2-z\sqrt{3}+1}\right)\frac{3z^4+3z^2-1}{6\sqrt{3}z^3} \end{aligned} \tag{7.62}$$

(b) *For* $D_m \leq 0$ *and* $J_3^D \leq 0$,

$$\Psi^{+}_{\text{Mises}}(\mathbf{D},f) = \begin{cases} 2D_m\left[G(\sqrt{u/f}) - G(\sqrt{u})\right], & \text{if } u \leq f, \\ 2D_m\left[G(\sqrt{u}) + G(\sqrt{u/f}) + 2\ln(3) - \frac{2}{9}\frac{\pi}{\sqrt{3}}\right], & \text{if } f < u < 1 \\ 2D_m\left[G(\sqrt{u}) - G(\sqrt{u/f})\right], & \text{if } u \geq 1. \end{cases} \tag{7.63}$$

with $G(z)$ *being given by*:

$$\begin{aligned} G(z) = &-2/\left(3z^2\right) + \frac{3z^4-3z^2-1}{3\sqrt{3}z^3}\tan^{-1}\left(\frac{z\sqrt{3}}{1-z^2}\right) \\ &+ \frac{1}{3\sqrt{3}}\left(\tan^{-1}\left(\frac{2z+1}{\sqrt{3}}\right) - \tan^{-1}\left(\frac{2z-1}{\sqrt{3}}\right)\right) - \ln\sqrt{z^4+z^2+1}. \end{aligned} \tag{7.64}$$

Proof In the following, we will present in detail the calculations that lead to the parametric representation of the yield surface of the von Mises porous material corresponding to the case (a), i.e., $D_m \geq 0$ and $J_3^D \leq 0$. For all the other cases, the proof can be found in Cazacu et al. [19]. As already discussed, for case (a) $\Psi^+_{\text{Mises}}(\mathbf{D},f)$ is given by Eq. (7.59). Using the change of variable, y = u$(b/r)^3$ and $\alpha = \cos\theta$, respectively, in this integral we obtain:

$$\Psi^+_{\text{Mises}}(\mathbf{D},f) \;\; = D_e u \int_u^{u/f} \int_0^1 \frac{\sqrt{1+y^2+y(3\alpha^2-1)}}{y^2}\, \mathrm{d}\alpha \mathrm{d}y \tag{7.65}$$

Note that:

$$\int_0^1 \frac{\sqrt{1+y^2+y(3\alpha^2-1)}}{y^2}\, \mathrm{d}\alpha = \frac{1+y}{2y^2} + \frac{1+y^2-y}{2\sqrt{3}y^{5/2}} \ln\left(\frac{1+y+\sqrt{3y}}{\sqrt{1+y^2-y}}\right)$$

Further integration with respect to y leads to the expression given in Eq. (7.61). Since the plastic dissipation is invariant under the transformation $\left(D_m, D'_{11}\right) \rightarrow \left(-D_m, -D'_{11}\right)$, the expression of the SRP for all other loadings is deduced from Eqs. (7.61) to (7.63) by symmetry.

The parametric representation of the yield surface is further obtained by substituting the above expressions of $\Psi^+_{\text{Mises}}(\mathbf{D},f)$ into Eq. (7.58).

Theorem 7.7 *The* Cazacu et al. [19] *yield criterion for porous von Mises is given by*:

(a) *For* $J_3^\Sigma \leq 0$, $\Sigma_m \geq 0$, *and any value of* $u = \frac{2|D_m|}{D_e}$:

$$\begin{cases} \dfrac{\Sigma_m}{\sigma_T} = \dfrac{1-f}{9u} + \dfrac{1}{3}\ln\left(\dfrac{u^2-uf+f^2}{u^2-u+1}\dfrac{1}{f^2}\right) \\ \quad + \dfrac{1}{18\sqrt{3}}\ln\left(\dfrac{u+\sqrt{3uf}+f}{u-\sqrt{3uf}+f}\right)\left(\dfrac{9u^2+3uf+f^2}{u^{3/2}\sqrt{f}}\right) \\ \quad - \dfrac{1}{18\sqrt{3}}\ln\left(\dfrac{u+\sqrt{3u}+1}{u-\sqrt{3u}+1}\right)\left(\dfrac{9u^2+3u+1}{u^{3/2}}\right) \\ \quad + \dfrac{2}{18\sqrt{3}}\left(\tan^{-1}\left(2\sqrt{\dfrac{u}{f}}+\sqrt{3}\right) - \tan^{-1}\left(2\sqrt{\dfrac{u}{f}}-\sqrt{3}\right)\right) \\ \quad - \dfrac{2}{18\sqrt{3}}\left(\tan^{-1}\left(2\sqrt{u}+\sqrt{3}\right) - \tan^{-1}\left(2\sqrt{u}-\sqrt{3}\right)\right) \\ \dfrac{\Sigma_e}{\sigma_T} = \dfrac{1-f}{2} + \dfrac{1}{4\sqrt{3u}}\left[\begin{array}{l}\left(u^2-u+1\right)\ln\left(\dfrac{u+\sqrt{3u}+1}{u-\sqrt{3u}+1}\right) \\ -\dfrac{\left(u^2-uf+f^2\right)}{\sqrt{f}}\ln\left(\dfrac{u+\sqrt{3uf}+f}{u-\sqrt{3uf}+f}\right)\end{array}\right] \end{cases} \tag{7.66}$$

(b) *For* $J_3^{\Sigma} \leq 0$ *and* $\Sigma_m \leq 0$:

- If $u \leq f$:

$$\begin{cases} \dfrac{\Sigma_m}{\sigma_T} = \dfrac{f-1}{9u} + \dfrac{1}{3}\ln\left(\dfrac{u^2+uf+f^2}{(u^2+1+u)f^2}\right) \\ \qquad - \dfrac{1}{9\sqrt{3fu^3}} \begin{pmatrix} (9u^2-3uf+f^2)\tan^{-1}\left(\dfrac{\sqrt{3uf}}{f-u}\right) \\ -(9u^2-3u+1)\tan^{-1}\left(\dfrac{\sqrt{3u}}{1-u}\right) \end{pmatrix} \\ \qquad - \dfrac{2}{9\sqrt{3}} \begin{pmatrix} \tan^{-1}\left(\dfrac{2\sqrt{u}+\sqrt{f}}{\sqrt{3f}}\right) + \tan^{-1}\left(\dfrac{2\sqrt{u}-1}{\sqrt{3}}\right) \\ -\tan^{-1}\left(\dfrac{2\sqrt{u}-\sqrt{f}}{\sqrt{3f}}\right) - \tan^{-1}\left(\dfrac{2\sqrt{u}+1}{\sqrt{3}}\right) \end{pmatrix} \\ \dfrac{\Sigma_e}{\sigma_T} = \dfrac{f|u-1| - |u-f|}{2u} - \dfrac{1}{2\sqrt{3}} \begin{bmatrix} \dfrac{(u^2+uf+f^2)\tan^{-1}\left(\dfrac{\sqrt{3uf}}{|f-u|}\right)}{\sqrt{uf}} \\ - \dfrac{(1+u+u^2)\tan^{-1}\left(\dfrac{\sqrt{3u}}{|1-u|}\right)}{\sqrt{u}} \end{bmatrix} \end{cases} \tag{7.67}$$

- If $f < u < 1$:

$$\begin{cases} \dfrac{\Sigma_m}{\sigma_T} = \dfrac{2}{3}\ln(3) - \dfrac{2}{18}\dfrac{\pi}{\sqrt{3}} - \dfrac{1+f-2u}{9u} - \dfrac{1}{3}\ln\left(\dfrac{(u^2+1+u)(u^2+uf+f^2)}{f^2}\right) \\ \qquad + \dfrac{1}{9\sqrt{3u^3}} \begin{pmatrix} (9u^2-3u+1)\tan^{-1}\left(\dfrac{\sqrt{3u}}{1-u}\right) \\ -(9u^2-3uf+f^2)\tan^{-1}\left(\dfrac{\sqrt{3fu}}{f-u}\right) \end{pmatrix} \\ \qquad + \dfrac{2}{9\sqrt{3}} \begin{pmatrix} \tan^{-1}\left(\dfrac{2\sqrt{u}+\sqrt{f}}{\sqrt{3f}}\right) - \tan^{-1}\left(\dfrac{2\sqrt{u}-\sqrt{f}}{\sqrt{3f}}\right) \\ + \tan^{-1}\left(\dfrac{2\sqrt{u}+1}{\sqrt{3}}\right) - \tan^{-1}\left(\dfrac{2\sqrt{u}-1}{\sqrt{3}}\right) \end{pmatrix} \\ \dfrac{\Sigma_e}{\sigma_T} = \dfrac{1}{2}(1+f) - u + \dfrac{1}{2\sqrt{3u}} \begin{pmatrix} \dfrac{(u^2+uf+f^2)}{\sqrt{f}}\tan^{-1}\left(\dfrac{\sqrt{3uf}}{f-u}\right) \\ + (u^2+1+u)\tan^{-1}\left(\dfrac{\sqrt{3u}}{1-u}\right) \end{pmatrix} \end{cases} \tag{7.68}$$

- If $u \geq 1$:

$$\begin{cases} \dfrac{\Sigma_m}{\sigma_T} = \dfrac{1-f}{9u} - \dfrac{1}{3}\ln\left(\dfrac{u^2+uf+f^2}{(u^2+1+u)f^2}\right) \\ \qquad + \dfrac{1}{9\sqrt{3fu^3}}\left(\begin{array}{l}(9u^2-3uf+f^2)\tan^{-1}\left(\dfrac{\sqrt{3uf}}{f-u}\right) \\ -(9u^2-3u+1)\tan^{-1}\left(\dfrac{\sqrt{3u}}{1-u}\right)\end{array}\right) \\ \qquad + \dfrac{2}{9\sqrt{3}}\left(\begin{array}{l}\tan^{-1}\left(\dfrac{2\sqrt{u}+\sqrt{f}}{\sqrt{3f}}\right)+\tan^{-1}\left(\dfrac{2\sqrt{u}-1}{\sqrt{3}}\right) \\ -\tan^{-1}\left(\dfrac{2\sqrt{u}-\sqrt{f}}{\sqrt{3f}}\right)-\tan^{-1}\left(\dfrac{2\sqrt{u}+1}{\sqrt{3}}\right)\end{array}\right) \\ \dfrac{\Sigma_e}{\sigma_T} = \dfrac{f|u-1|-|u-f|}{2u} - \dfrac{1}{2\sqrt{3}}\left[\begin{array}{l}\dfrac{(u^2+uf+f^2)\tan^{-1}\left(\dfrac{\sqrt{3uf}}{|f-u|}\right)}{\sqrt{uf}} \\ -\dfrac{(1+u+u^2)\tan^{-1}\left(\dfrac{\sqrt{3u}}{|1-u|}\right)}{\sqrt{u}}\end{array}\right] \end{cases} \tag{7.69}$$

Based on the property (ii) demonstrated earlier (see Theorem 7.5*), the parametric representation of the yield locus corresponding to* $J_3^\Sigma \geq 0$ *can be easily obtained from* Eqs. (7.66) *to* (7.69)*, i.e.,*

(c) *For* $J_3^\Sigma \geq 0$ *and* $\Sigma_m \geq 0$:

$$\begin{cases} \dfrac{\Sigma_m}{\sigma_T} = -\dfrac{\Sigma_m}{\sigma_T}\Big|_{J_3^\Sigma \leq 0,\ \Sigma_m \leq 0} \\ \dfrac{\Sigma_e}{\sigma_T} = \dfrac{\Sigma_e}{\sigma_T}\Big|_{J_3^\Sigma \leq 0,\ \Sigma_m \leq 0} \end{cases}, \tag{7.70}$$

where the right-hand expressions are given by Eqs. (7.67)–(7.69).

By the same arguments,

(d) *For* $J_3^\Sigma \geq 0$ *and* $\Sigma_m \leq 0$:

$$\begin{cases} \dfrac{\Sigma_m}{\sigma_T} = -\dfrac{\Sigma_m}{\sigma_T}\Big|_{J_3^\Sigma \leq 0,\ \Sigma_m \geq 0} \\ \dfrac{\Sigma_e}{\sigma_T} = \dfrac{\Sigma_e}{\sigma_T}\Big|_{J_3^\Sigma \leq 0,\ \Sigma_m \geq 0} \end{cases} \tag{7.71}$$

where the right-hand expressions are given by Eq. (7.66).

Proof For case (a), i.e., $J_3^\Sigma \leq 0$, $\Sigma_m \geq 0$, as already discussed, $D_m \geq 0$ and $D'_{11} > 0$. Using Eqs. (7.58) *and* (7.61), we obtain that the parametric representation of the yield surface is:

$$\begin{cases} \dfrac{\Sigma_m}{\sigma_T}=\dfrac{1}{3}\dfrac{\Psi^{+}_{\text{Mises}}(\mathbf{D},f)}{\partial \mathrm{D}_m}=\dfrac{2}{3}\left[\begin{array}{l} F\left(\sqrt{u/f}\right)-F(\sqrt{u}) \\ +\dfrac{\sqrt{u}}{2}\left(\dfrac{F'\left(\sqrt{u/f}\right)}{\sqrt{f}}-F'\left(\sqrt{u}\right)\right) \end{array}\right] \\ \dfrac{\Sigma_e}{\sigma_T}=\left|\dfrac{\Psi^{+}_{\text{Mises}}(\mathbf{D},f)}{\partial D_e}\right|=\left|\dfrac{u\sqrt{u}}{2}\left(\dfrac{F'\left(\sqrt{u/f}\right)}{\sqrt{f}}-F'\left(\sqrt{u}\right)\right)\right| \end{cases} \tag{7.72}$$

In the above equation $F'(z)$ denotes the first derivative of $F(z)$ given in Eq. (7.62). Further substitution of Eq. (7.62) into Eq. (7.72) leads to Eq. (7.66).

Remark Let us also note that since $\Pi^{+}_{\text{Mises}}(\mathbf{D},f)\leq\Pi_{Gurson}(\mathbf{D},f)$, the Cazacu et al. [19] criterion (7.58) is a better estimate of the exact potential of the porous Mises material than Gurson [30] [see Eq. (7.13)]. The two yield criteria coincide only for the special cases of purely hydrostatic ($\mathbf{D}'=0$), or purely deviatoric loading ($D_m=0$). This can be easily verified by taking $u\to\infty$ (i.e., imposing purely hydrostatic loading) in Eqs. (7.66)–(7.69), respectively. Indeed, we obtain: $|\Sigma_m|=\frac{2}{3}\sigma_T\ln f$, and $\Sigma_e=0$; on the other hand for $u\to 0$ (purely deviatoric loading) from Eqs. (7.66) to 7.67), we obtain: $\Sigma_m=0$, and $\Sigma_e=\sigma_T(1-f)$, irrespective of the sign of the third-invariant of the stress deviator.

For illustration of the features of Cazacu et al. [19], in what follows we present plots of the resulting yield surface. Let us first recall that for axisymmetric loadings: $\mathbf{\Sigma}=\Sigma_{11}(\mathbf{e}_1\otimes\mathbf{e}_1+\mathbf{e}_2\otimes\mathbf{e}_2)+\Sigma_{33}(\mathbf{e}_3\otimes\mathbf{e}_3)$, so the von Mises equivalent stress reduces to: $\Sigma_e=\sqrt{\frac{3}{2}\Sigma'_{\text{ij}}\Sigma'_{\text{ij}}}=|\Sigma_{11}-\Sigma_{33}|$, the mean stress is $\Sigma_m=(2\Sigma_{11}+\Sigma_{33})/3$, and the third-invariant of the stress deviator is: $J^{\Sigma}_3=-\frac{2}{27}(\Sigma_{11}-\Sigma_{33})^3$. It follows that for axisymmetric stress states such that the axial stress is less than the lateral stress, i.e., $\Sigma_{33}\leq\Sigma_{11}=\Sigma_{22}$, we have $J^{\Sigma}_3\leq 0$, while for axisymmetric stress states for which the axial stress is larger than the lateral stress, i.e., $\Sigma_{11}=\Sigma_{22}\leq\Sigma_{33}$, we have $J^{\Sigma}_3\geq 0$. Figure 7.7 shows the representation in the plane $(\Sigma_m/\sigma_T,\Sigma_e/\sigma_T)$ of the yield surface corresponding to $J^{\Sigma}_3\leq 0$ [Eqs. (7.66)–(7.69)] for a porosity $f=0.05$. Clearly, for triaxialities T different from 0 and $\pm\infty$, the yield surface according to this criterion is no longer symmetric with respect to the axis $\Sigma_m=0$. For any given absolute value of the strain-rate triaxiality, u, there are two yield points on the surface which have a different absolute value of the stress triaxiality, T. For example, in Fig. 7.7 are shown the yield points A ($\Sigma_m/\sigma_T=1.861$, $\Sigma_e/\sigma_T=0.4$) and B ($\Sigma_m/\sigma_T=-1.861$, $\Sigma_e/\sigma_T=0.381$), which correspond to $u=0.935$. For the same porosity $f=0.05$, the yield surface corresponding to $J^{\Sigma}_3\geq 0$ is plotted in Fig. 7.8. Examination of Figs. 7.7 and 7.8 shows that a yield point on one yield surface ($J^{\Sigma}_3\geq 0$) corresponding to a given stress triaxiality T is symmetric, with respect to the hydrostatic axis, to the point on the other yield surface ($J^{\Sigma}_3\leq 0$) corresponding to $(-T)$. For example, the yield point C ($\Sigma_m/\sigma_T=-1.861,\Sigma_e/\sigma_T=0.4$) which lies on the yield surface corresponding to $J^{\Sigma}_3\geq 0$ (see Fig. 7.8) has the same absolute value of stress triaxiality as the yield point

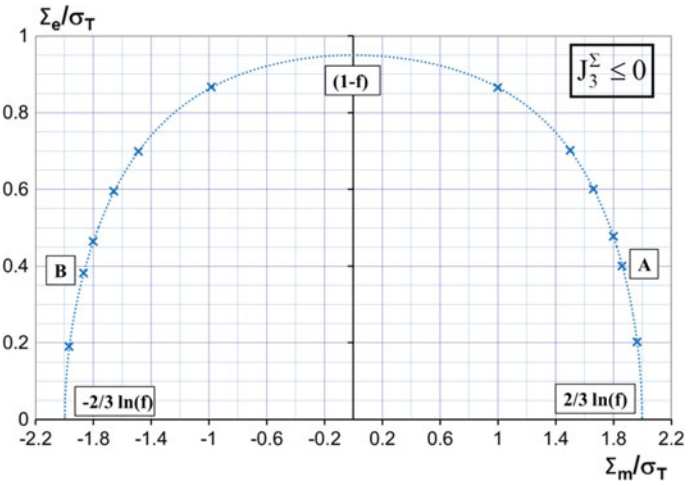

Fig. 7.7 Yield surface according to the Cazacu et al. [19] criterion, corresponding to $\Sigma_{11} = \Sigma_{22} \geq \Sigma_{33}$ ($J_3^\Sigma \leq 0$) and porosity $f = 0.05$, showing the sensitivity of yielding to the sign of the mean stress

A ($\Sigma_m/\sigma_T = 1.861, \Sigma_e/\sigma_T = 0.4$), which lies on the yield surface corresponding to $J_3^\Sigma \leq 0$ (see Fig. 7.7). In other words, the yield locus according to Cazacu et al. [19] is invariant to the transformation: $\left(\Sigma_m, \Sigma_e, J_3^\Sigma\right) \rightarrow \left(-\Sigma_m, \Sigma_e, -J_3^\Sigma\right)$, as it should be given that the matrix behavior is governed by an even yield function in stresses [see also Theorem 7.1, Sect. 7.2.1 and Eq. (7.17)].

Figure 7.9 shows the yield curves according to the Cazacu et al. [19] criterion corresponding to $J_3^\Sigma \geq 0$ and $J_3^\Sigma \leq 0$, respectively, and the Gurson [30] yield surface for a porosity $f = 5\%$. It is clearly seen that Gurson [30] criterion is an upper bound of the Cazacu et al. [19] criterion. Note also the sensitivity of the latter criterion to the sign of the mean stress Σ_m.

Most importantly, note that according to the Cazacu et al. [19] criterion, for states corresponding to $\Sigma_m \geq 0$, the response is softer for $J_3^\Sigma \geq 0$ than for $J_3^\Sigma \leq 0$ (see also Fig. 7.10, showing different zooms on the yield surfaces in the tensile quadrant). For purely deviatoric loading, the response is the same, and the effect of J_3^Σ becomes noticeable with increasing triaxiality (see Fig. 7.10a, b). The normal to the yield surfaces are clearly different, determining distinct plastic flow directions and resulting porosity evolution. For triaxialities approaching infinity, the effect of J_3^Σ starts to decrease, and the yield surfaces coincide at the purely hydrostatic point (see Fig. 7.10c).

For completion, Fig. 7.11 shows the yield surface in the plane $(\Sigma_{11} - \Sigma_{33}, \Sigma_m)$ according to the Cazacu et al. [19] criterion and Gurson [30], for several porosities, $f = 1$, 5, and 15%, respectively. Stresses are normalized by the matrix yield stress in uniaxial tension σ_T. All yield surfaces show the same trends described above. Irrespective of the porosity, the intersection of the curves corresponding to $J_3^\Sigma \geq 0$

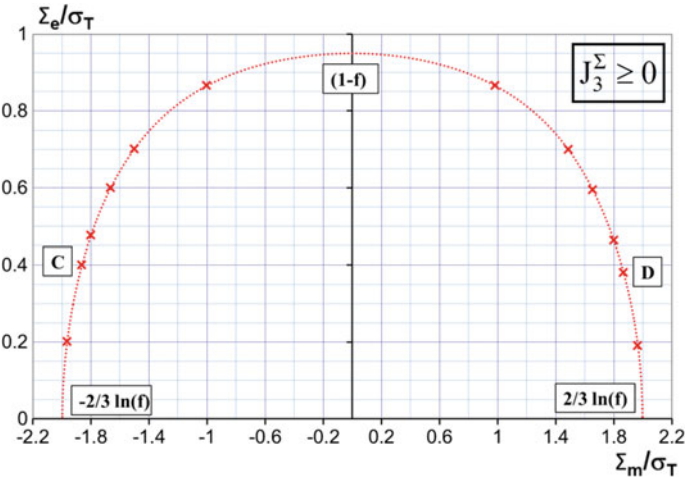

Fig. 7.8 Yield surface according to Cazacu et al. [19] criterion, corresponding to $\Sigma_{11} = \Sigma_{22} \leq \Sigma_{33}$ $(J_3^\Sigma \geq 0)$ and porosity $f = 0.05$

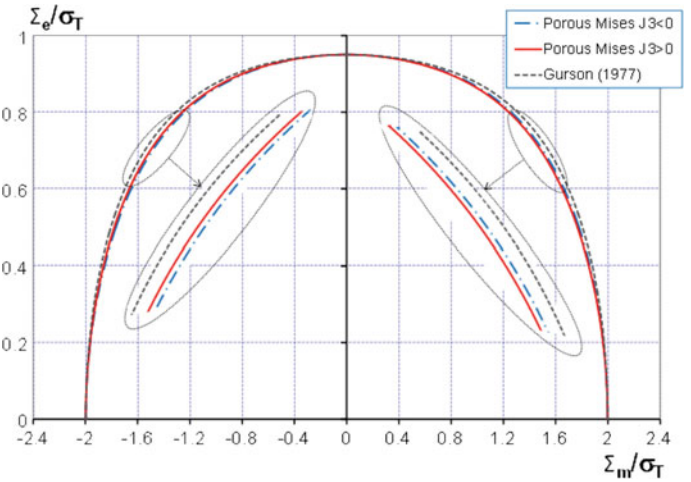

Fig. 7.9 Yield surface of the porous Von Mises material according to the Cazacu et al. [19] criterion for $\Sigma_{11} = \Sigma_{22} \leq \Sigma_{33} (J_3^\Sigma \geq 0)$ and $\Sigma_{11} = \Sigma_{22} \geq \Sigma_{33}$ $(J_3^\Sigma \leq 0)$, respectively, and in comparison with Gurson [30] yield surface. Porosity $f = 0.05$

$(\Sigma_{11} = \Sigma_{22} \leq \Sigma_{33})$ and $J_3^\Sigma \leq 0$ $(\Sigma_{11} = \Sigma_{22} \geq \Sigma_{33})$ belong to the axis $\Sigma_m = 0$ (i.e., the yield surface has no corners); and the criterion coincides with Gurson [30] only for the purely hydrostatic $(\Sigma_{11} = \Sigma_{22} = \Sigma_{33})$ or purely deviatoric loadings $(\Sigma_m = 0)$.

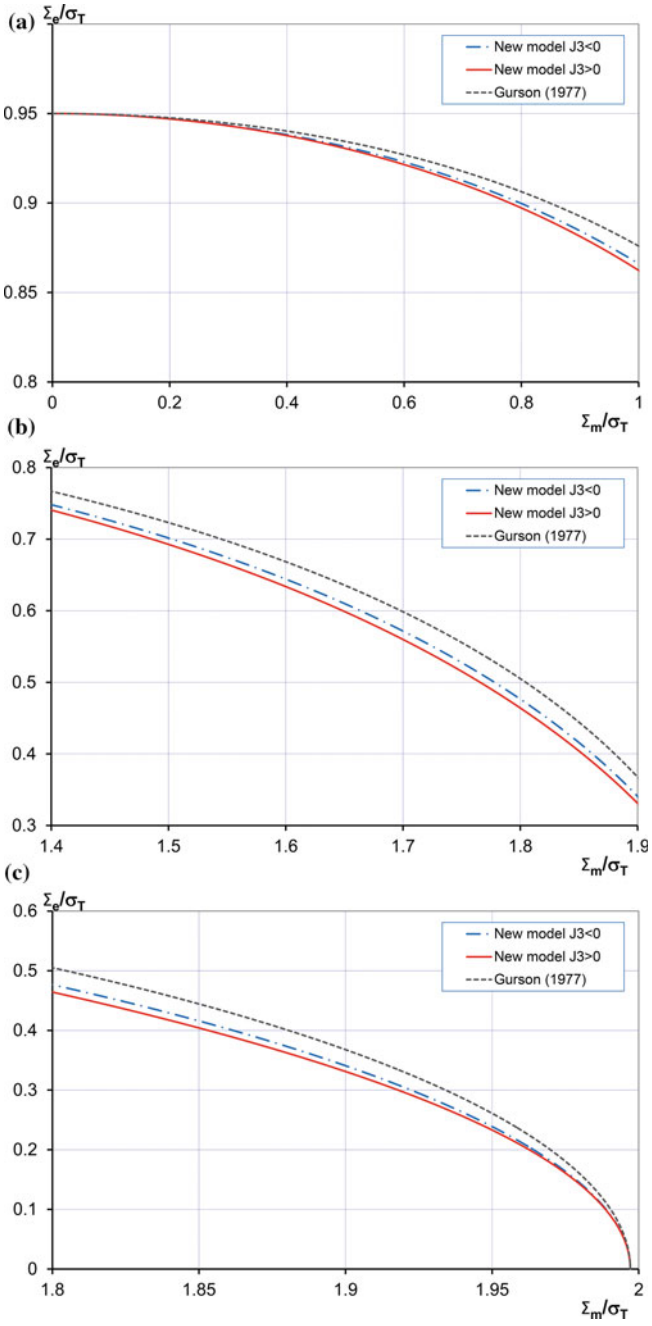

Fig. 7.10 Zoom on the tensile quadrant of the yield surfaces according to the Cazacu et al. [19] criterion, for $J_3^{\Sigma} \leq 0$ and $J_3^{\Sigma} \geq 0$, and Gurson [30] criterion, for porosity $f = 0.05$, within following ranges: **a** $(\Sigma_m \geq 0, 0.8 < \Sigma_e/\sigma_T < (1-f)$; **b** $\Sigma_m \geq 0,\ 0 < \Sigma_e/\sigma_T < 0.5$

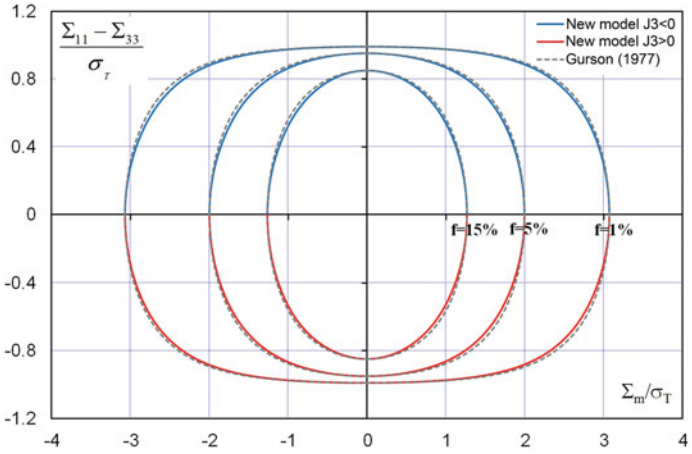

Fig. 7.11 Yield surfaces obtained with the Cazacu et al. [19] criterion, and with Gurson [30], for porosities $f = 1$, 5 and 15%. The blue lines represent the yield surfaces for $\Sigma_{11} = \Sigma_{22} \geq \Sigma_{33}$ ($J_3^{\Sigma} \leq 0$), and the red lines $\Sigma_{11} = \Sigma_{22} \leq \Sigma_{33}$ ($J_3^{\Sigma} \geq 0$). The dashed lines are Gurson's [30] yield surfaces

Effect of the centro-symmetry of the Cazacu et al. [19] *surface on void evolution*

Although the effect of the sign of J_3^{Σ} is small, it affects not only the onset of plastic flow of the porous von Mises material, but it also influences void evolution. Indeed, even small changes in the direction of the normal to the yield surface affect plastic flow of the porous material and lead to changes in the rate at which the porosity evolves (see Revil-Baudard and Cazacu [54]). As an example, Fig. 7.12 shows a comparison between the void evolution as a function of the effective macroscopic equivalent strain, E_e, according to the Gurson [30] and Cazacu et al. [19] criterion for axisymmetric loadings at fixed triaxiality, $|T| = 2$ for loadings such that $J_3^{\Sigma} \leq 0$ and $J_3^{\Sigma} \geq 0$, respectively. The initial porosity is: $f_0 = 0.5\%$. Note that irrespective of the sign of the third-invariant, the rate of void growth according to Cazacu et al. [19] criterion is faster than that predicted by Gurson [30] model. For example, for loadings such that $J_3^{\Sigma} \geq 0$ at a macroscopic equivalent plastic strain $E_e = 0.15$, the porosity according to Gurson [30] is 15% lower than that predicted by the Cazacu et al. [19] criterion. Comparison between the results presented in Fig. 7.12a shows that Cazacu et al. [19] model captures the influence of the sign of the third-invariant of the stress deviator on void growth, the rate of void growth being faster for $J_3^{\Sigma} \geq 0$ than for $J_3^{\Sigma} \leq 0$. For example, at an equivalent plastic strain $E_e = 0.15$, the void volume fraction is almost 4% higher for $J_3^{\Sigma} \geq 0$ than for $J_3^{\Sigma} \leq 0$. Obviously, Gurson [30] model cannot capture the influence of the sign of J_3^{Σ} on void growth. Figure 7.12b shows the evolution of the void volume fraction as a function of the effective equivalent strain, E_e for axisymmetric loadings and negative stress triaxiality, $T = -2$. Since the mean stress, Σ_m, is negative (compression) void collapse

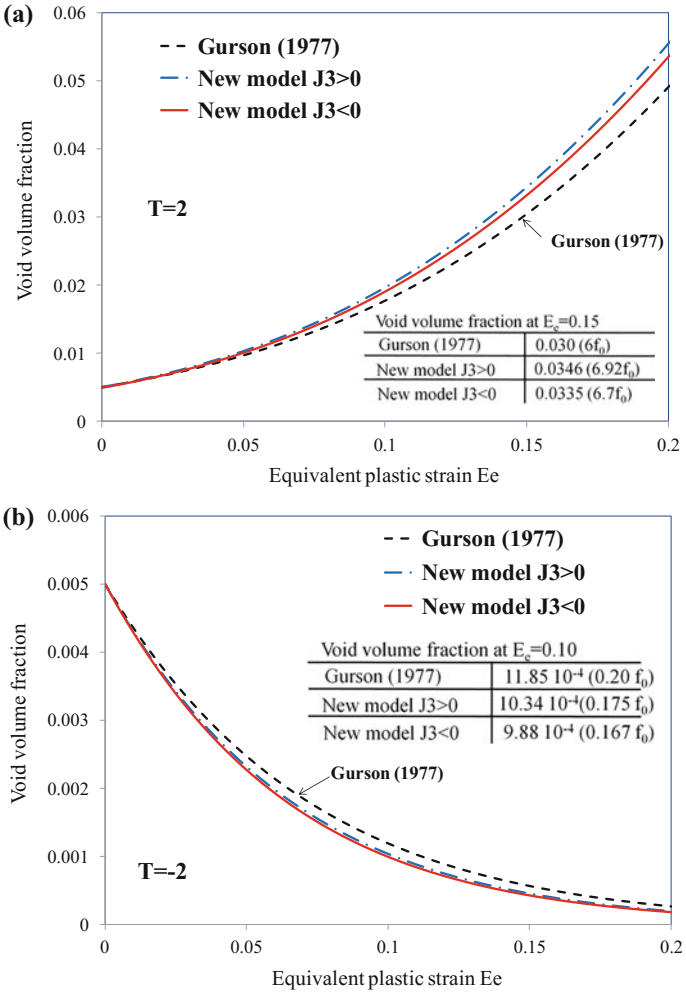

Fig. 7.12 Comparison between the evolution of the void volume fraction with equivalent strain E_e for axisymmetric stress states such as $J_3^{\Sigma} \geq 0$ and $J_3^{\Sigma} \leq 0$ and fixed stress triaxiality $T = \pm 2$ predicted by the Gurson [30] and Cazacu et al. [19] criterion; initial porosity, $f_0 = 0.5\%$: **a** void growth; **b** void collapse

occurs. However, irrespective of the sign of J_3^{Σ} the rate of void collapse according to the Cazacu et al. [19] criterion is faster than that according to the Gurson [30] criterion. For example, at $E_e = 0.1$, the void volume fraction according to Cazacu et al. [19] for $J_3^{\Sigma} \leq 0$ and Gurson [30] is: $f = 0.167 f_0$ and $f = 0.2 f_0$, respectively. Furthermore, comparison between Fig. 7.12a, b shows the effects of the centro-symmetry of Cazacu et al. [19] yield locus on void evolution. Indeed, for $T = 2$, the rate of void growth is faster for loadings at $J_3^{\Sigma} \geq 0$ than for $J_3^{\Sigma} \leq 0$ while

the rate of void collapse is faster for axisymmetric loadings at $J_3^{\Sigma} \leq 0$ than for loadings at $J_3^{\Sigma} \geq 0$.

7.2.3.4 Void Growth and Collapse According to Cazacu et al. [19] Model and F.E. Unit-Cell Model Calculations

The new features of the mechanical response of von Mises porous materials that were revealed by the Cazacu et al. [19] analysis and model, namely the centro-symmetry of the yield surface and the coupled effects of the signs of the means stress and third-invariant J_3^{Σ} on void growth and collapse were verified by comparison with the results of F.E. unit-cell model simulations. Detailed numerical analyses of the dilatational response of a porous von Mises material for axisymmetric stress histories at fixed triaxialities were conducted by Alves et al. [4] using cubic unit cells containing one void at the center (for the geometry of the cell and the methodology used to solve the boundary-value problem, see Sect. 7.2.3.2).

For loadings at fixed positive triaxialities, the initial porosity considered was: $f_0 = 0.13\%$. In the F.E. calculations corresponding to loadings at fixed negative triaxialities, the initial porosity was considered higher ($f_0 = 1.04\%$) such as to allow plastic strains to develop prior to pore closure. For any given triaxiality, T, calculations were done for loadings corresponding to $\Sigma_{11} = \Sigma_{22} \geq \Sigma_{33}$ (i.e., $J_3^{\Sigma} \leq 0$) and for loadings corresponding to $\Sigma_{11} = \Sigma_{22} \leq \Sigma_{33}$ (i.e., $J_3^{\Sigma} \geq 0$). For each loading case, the stress–strain response (Σ_e vs. E_e) as well as the evolution of the void volume fraction as a function of the von Mises effective macroscopic equivalent strain, E_e were reported. As a general observation, the F.E. results show that irrespective of the sign of J_3^{Σ}, there is a very strong effect of the stress triaxiality on void evolution (see Figs. 7.13 and 7.14). Secondly, the numerical results indicate a combined effect of the signs of the mean stress and J_3^{Σ} on void evolution. The trends predicted by the Cazacu et al. [19] model were confirmed. Indeed, for $T > 0$ the rate of void growth is faster for the case when the loading is such that $J_3^{\Sigma} \geq 0$ than in the case when the loading is such that $J_3^{\Sigma} \leq 0$ (see Fig. 7.13). However, for $T < 0$, void evolution is faster for loadings with $J_3^{\Sigma} \leq 0$ than for loading at $J_3^{\Sigma} \geq 0$ (see Fig. 7.14). The agreement between the numerical results and the Cazacu et al. [19] model is very good. For completeness, also note that irrespective of the sign of J_3^{Σ}, the Cazacu et al. [19] criterion is in better agreement with the numerical predictions than Gurson [30] criterion (see Fig. 7.15 for void growth and Fig. 7.16 for void collapse).

Figure 7.17 shows the effective stress Σ_e versus equivalent strain, E_e curves for axisymmetric loadings at positive fixed stress triaxialities. Since the Cazacu et al. [19] model captures the effects of the stress triaxiality and J_3^{Σ} on void growth (see Figs. 7.13 and 7.14), it describes correctly the influence of the loading path on the softening or hardening of the porous material. Note that for negative stress

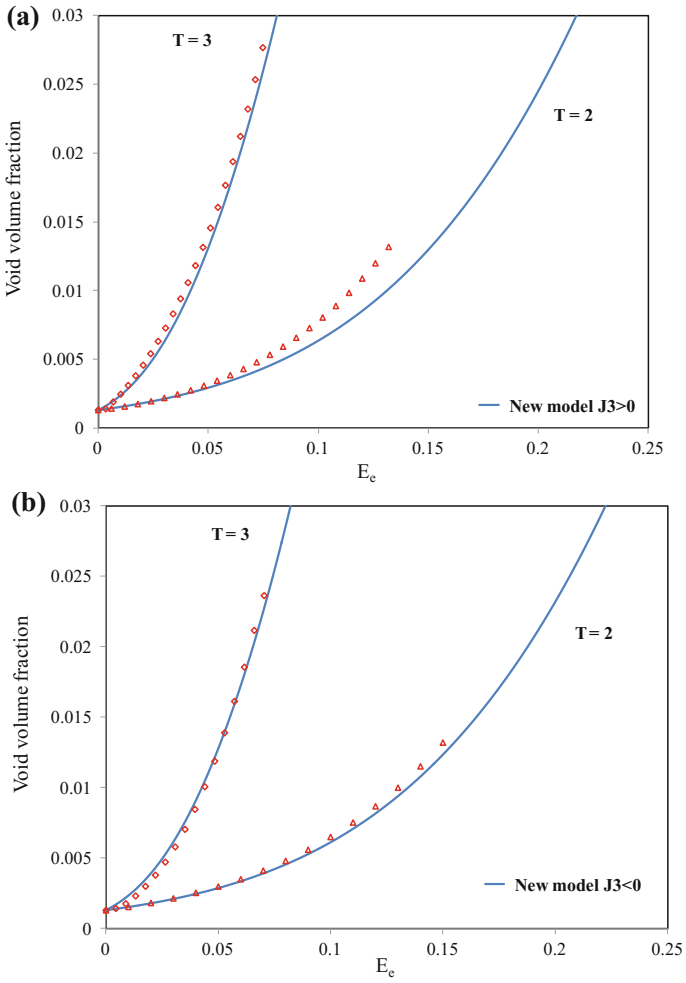

Fig. 7.13 Comparison between the void volume fraction evolution with equivalent strain E_e according to the Cazacu et al. [19] model and F.E. unit-cell model calculations (symbols) corresponding to axisymmetric stress states for stress triaxialities: $T = 2$ and $T = 3$, respectively; initial porosity, $f_0 = 0.13\%$: **a** axisymmetric loadings such that the axial stress is greater than the lateral stress ($J_3^{\Sigma} \geq 0$); **b** axisymmetric loadings such that the axial stress is less than the lateral stress ($J_3^{\Sigma} \leq 0$)

triaxialities (compressive mean stress), this model correctly captures that for $T = -3$ the rate of void collapse is faster than for $T = -2$ (see also Fig. 7.15), which in turn affects the rate of hardening. This correlates with the predicted stress–strain response shown in Fig. 7.18.

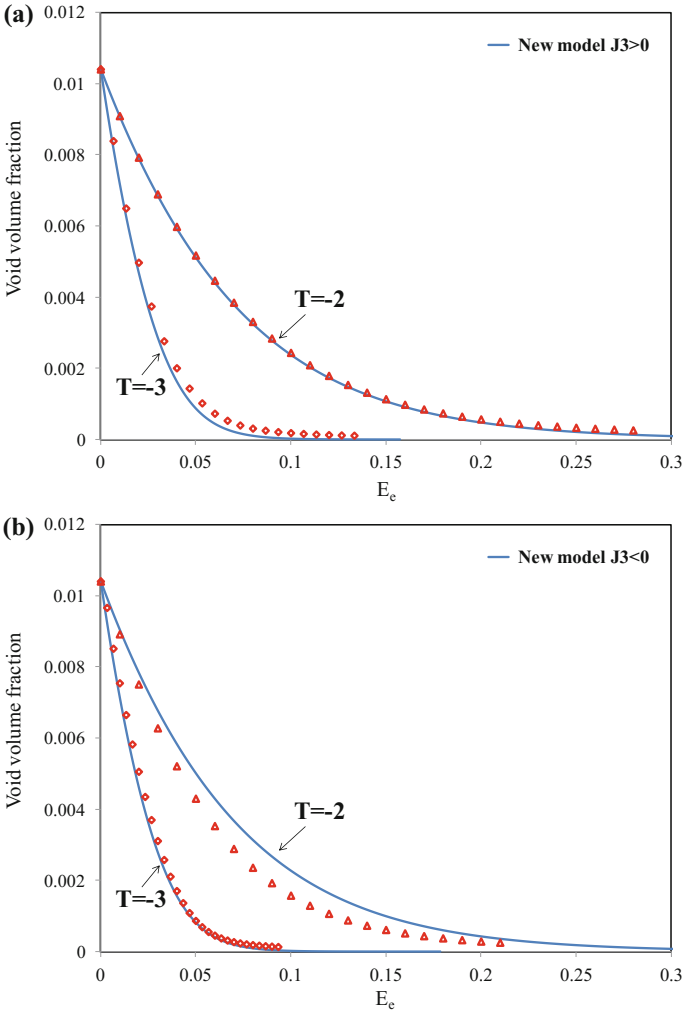

Fig. 7.14 Comparison between the void volume fraction evolution (collapse) as a function of the equivalent strain E_e according to the Cazacu et al. [19] model and F.E. unit-cell calculations (symbols) corresponding to axisymmetric loadings at fixed stress triaxialities: $T = -2$ and $T = -3$; initial porosity, $f_0 = 1.04\%$: **a** axisymmetric loadings such that the axial stress is greater than the lateral stress ($J_3^{\Sigma} \geq 0$); **b** axisymmetric loadings such that the axial stress is less than the lateral stress ($J_3^{\Sigma} \leq 0$)

7.2.3.5 Cazacu and Revil-Baudard [16] 3-D Plastic Potentials

Cazacu et al. [19] analysis and model presented in Sect. 7.2.3.3 was conducted for axisymmetric states. It was shown that the strain-rate potential and the yield criterion of the porous Mises material can be deduced without making the

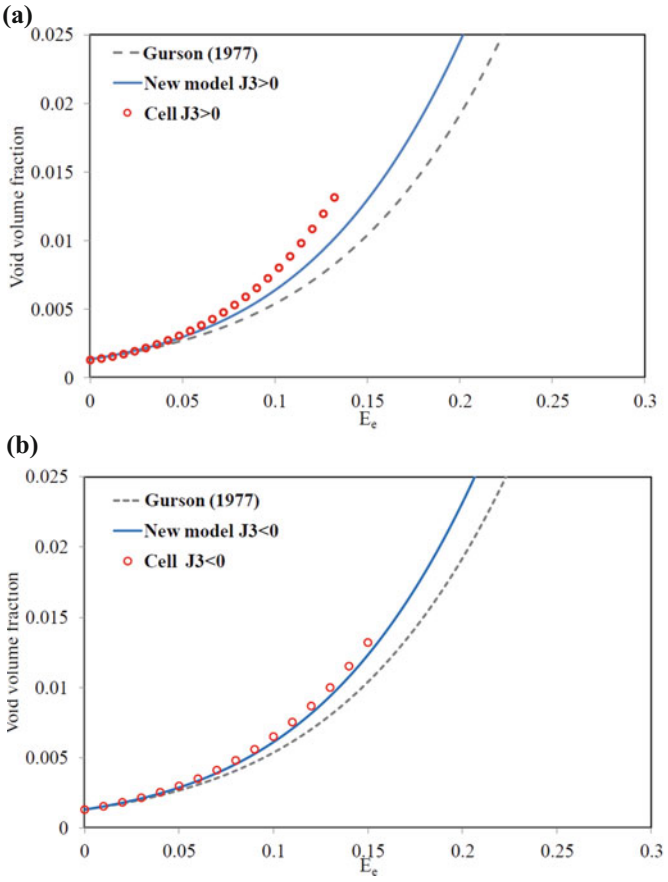

Fig. 7.15 Comparison between the void volume fraction evolution with equivalent strain E_e according to the Cazacu et al. [19] model (line), Gurson [30] model (dashed line), and F.E. unit-cell calculations (symbols) for $T = 2$; initial porosity $f_0 = 0.13\%$: **a** axisymmetric loadings such that the axial stress is greater than the lateral stress ($J_3^{\Sigma} \geq 0$); **b** axisymmetric loadings such that the axial stress is less than the lateral stress ($J_3^{\Sigma} \leq 0$)

simplifications that are generally done in the literature. While for general 3-D loadings, the integrals representing the plastic dissipation of the porous material cannot be obtained in closed form, the combined effects of all the invariants of the strain-rate **D** on the plastic response can be assessed. Cazacu and Revil-Baudard [16] conducted such an analysis, and established that the maximum influence of J_3^{Σ} on yielding of a porous Mises solid occurs for axisymmetric states.

Moreover, based on this analysis these authors proposed 3-D approximate potentials that preserve the key properties of the exact one. For axisymmetric states, the 3-D model developed reduces to the Cazacu et al. [19] criterion [see Eqs. (7.66)–(7.69)].

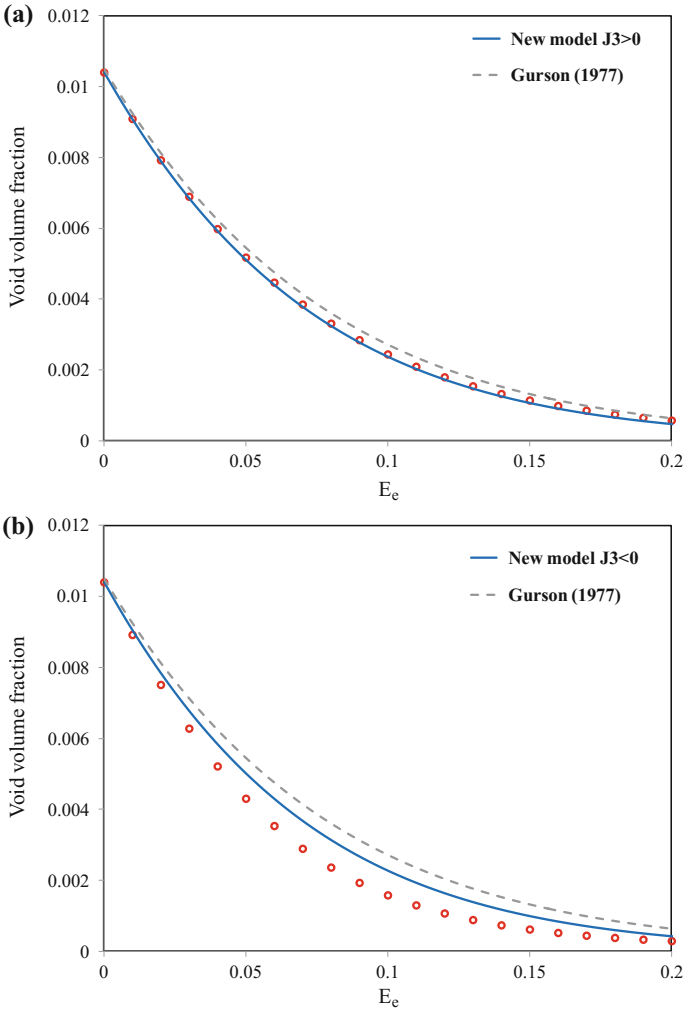

Fig. 7.16 Comparison between the void volume fraction evolution with equivalent strain E_e according to the Cazacu et al. [19] model (line), Gurson's [30] model (dashed line), and F.E. unit-cell calculations (symbols) for $T = -2$; initial porosity $f_0 = 1.04\%$: **a** axisymmetric loadings such that the axial stress is greater than the lateral stress ($J_3^{\Sigma} \geq 0$); **b** axisymmetric loadings such that the axial stress is less than the lateral stress ($J_3^{\Sigma} \leq 0$)

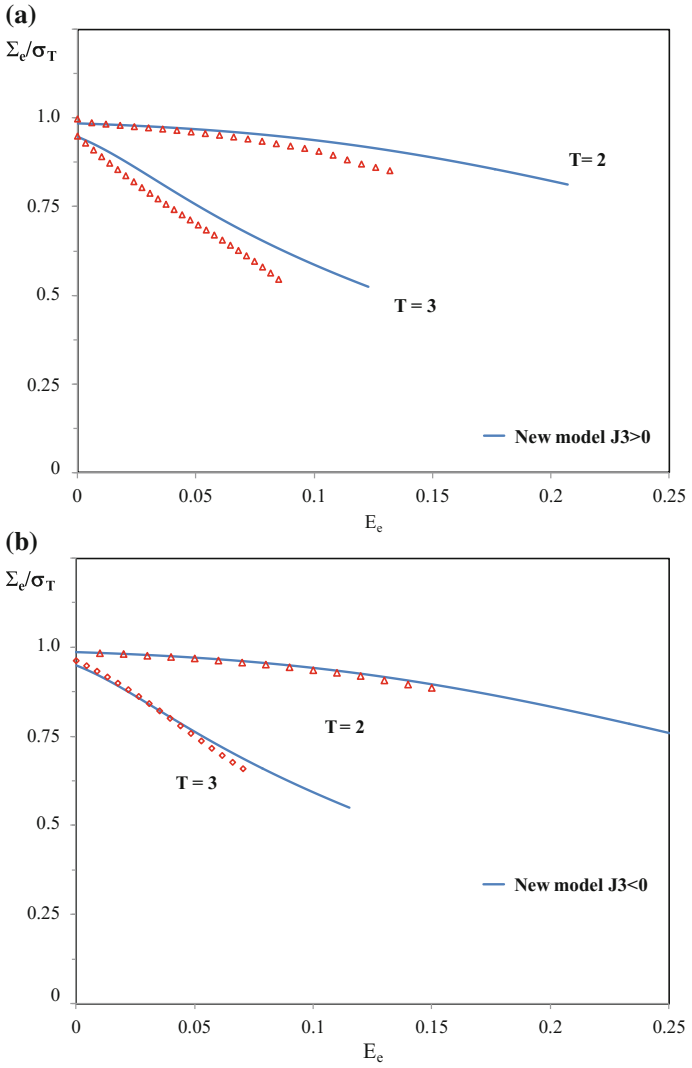

Fig. 7.17 Comparison between the effective stress Σ_e evolution with equivalent strain E_e according to the Cazacu et al. [19] model and F.E. unit-cell calculations (symbols) corresponding to axisymmetric stress states and different stress triaxialities: $T = 2$ and $T = 3$; initial porosity, $f_0 = 0.13\%$: **a** axisymmetric loadings such that the axial stress is greater than the lateral stress ($J_3^{\Sigma} \geq 0$); **b** axisymmetric loadings such that the axial stress is less than the lateral stress ($J_3^{\Sigma} \leq 0$)

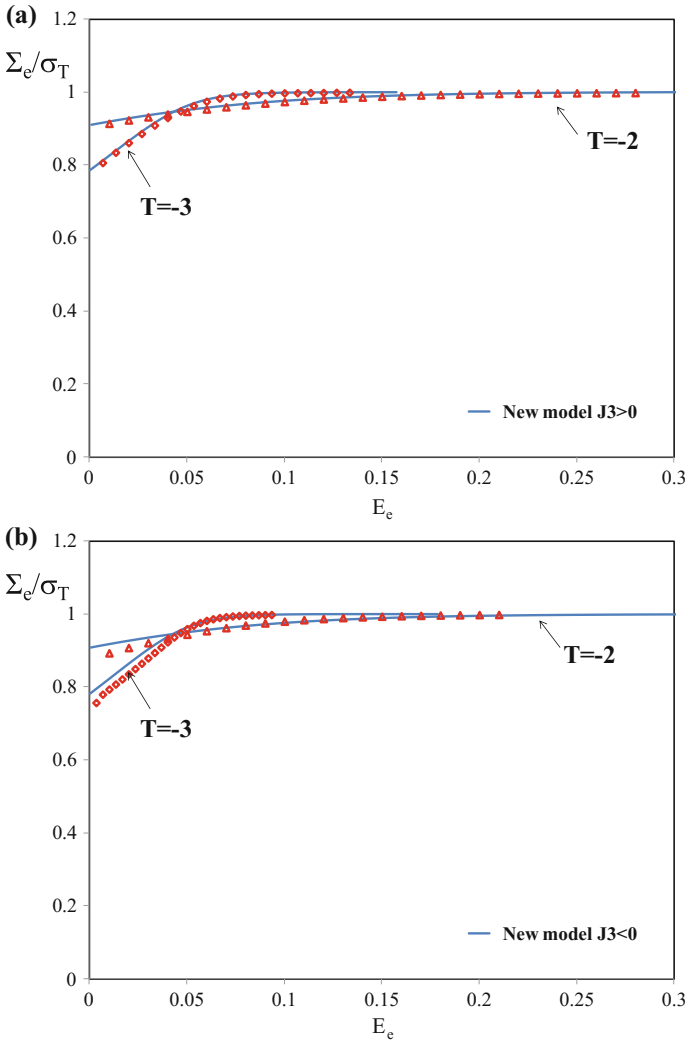

Fig. 7.18 Comparison between the effective stress Σ_e evolution with equivalent strain E_e according to the Cazacu et al. [19] model and cell calculations (symbols) corresponding to axisymmetric stress states and different stress triaxialities: $T = -2$ and $T = -3$; initial porosity, $f_0 = 0.13\%$: **a** axisymmetric loadings such that the axial stress is greater than the lateral stress ($J_3^{\Sigma} \geq 0$); **b** axisymmetric loadings such that the axial stress is less than the lateral stress ($J_3^{\Sigma} \leq 0$)

Let us first recall that for 3-D loadings, in the Cartesian basis $(\mathbf{e}_1, \mathbf{e}_2, \mathbf{e}_3)$ associated with the eigenvectors of $\mathbf{D}$ [see also Eq. (7.27)], the local strain-rate tensor $\mathbf{d} = (\nabla \mathbf{v} + \nabla \mathbf{v}^T)/2$ corresponding to Rice and Tracey [58] velocity field is given by Eq. (7.28), and consequently the plastic dissipation of the porous von Mises material is of the form:

$$\Pi^{+}_{\text{Mises}}(\mathbf{D},f) \;= \sigma_T \Psi^{+}_{\text{Mises}}(\mathbf{D},f),$$

with

$$\Psi^{+}_{\text{Mises}}(\mathbf{D},f) = \frac{1}{V}\int_{\Omega}\sqrt{(2/3)\left(D_1'^2+D_2'^2+D_3'^2\right)+4D_m^2(b/r)^6-4D_m(b/r)^3\left(D_1'x_1^2+D_2'x_2^2+D_3'x_3^2\right)}\,\mathrm{d}V \tag{7.73}$$

In Eq. 7.73, $D_i' = D_i - D_m$, i = 1, …, 3 are the eigenvalues of $\mathbf{D}'$, $\mathrm{V} = 4\pi \mathrm{b}^3/3$ and Ω is the domain occupied by the matrix and the void (see Fig. 7.1).

As demonstrated in Sect. 7.2.3.3 (see Theorem 7.6), for axisymmetric states, $\Psi^{+}_{\text{Mises}}(\mathbf{D},f)$ can be calculated analytically without making any of the approximations generally considered in the literature (e.g., the hypothesis (H1), Sect. 7.2.3.1). For all other loadings, $\Psi^{+}_{\text{Mises}}(\mathbf{D},f)$ cannot be calculated analytically and numerical integration methods need to be used. Isotropy dictates that $\Psi^{+}_{\text{Mises}}(\mathbf{D},f)$ has threefold symmetry with respect to the origin. Thus, it is sufficient to evaluate the integral given by Eq. (7.73) only for states corresponding to one sector of the octahedral plane. Any state in the sector $D_2 \geq D_3 \geq D_1$ is characterized by two polar coordinates (R, γ) with

$$R = \sqrt{D_1'^2+D_2'^2+D_3'^2} = D_e\sqrt{3/2} = \sqrt{2J_2^D} \tag{7.74}$$

and γ being the angle satisfying: $-\pi/6 \leq \gamma \leq \pi/6$ and whose sine is given by:

$$\sin 3\gamma = -\frac{3\sqrt{3}}{2}\cdot\frac{J_3^D}{\left(J_2^D\right)^{3/2}}. \tag{7.75}$$

(see also Chap. 6 for more details about the representation in the octahedral plane of an isotropic function of $\mathbf{D}$). Using Eqs. (7.74) and (7.75), the integral expressing $\Psi^{+}_{\text{Mises}}(\mathbf{D},f)$ can be put in the form:

$$\Psi^{+}_{Mises}(\mathbf{D},f) = \frac{1}{V}\int_{\Omega} 2\sigma_T\sqrt{\left(R^2/6\right)+D_m^2(b/r)^6-4\,R\,D_m(b/r)^3F(\gamma,x_i^2)/(r^2/\sqrt{6})}\mathrm{d}V \tag{7.76}$$

with $F\left(\gamma, \mathrm{x}_1^2, \mathrm{x}_2^2, \mathrm{x}_3^2\right) = \sqrt{3}\left(x_2^2 - x_1^2\right)\cos\gamma + \left(2x_3^2 - x_1^2 - x_2^2\right)\sin\gamma$.

Next, Gaussian quadrature integration is used to evaluate the integral for any 3-D loadings. For this purpose, the hollow sphere is discretized with 125,000 hexahedral

elementary volumes with one integration point at the center. For axisymmetric loadings, the numerical estimate of $\Psi^{+}_{\text{Mises}}(\mathbf{D},f)$ was compared to the exact result [i.e., Eqs. (7.66)–(7.69)], the differences being negligible (less than 10^{-7}).

As an example, in Fig. 7.19 is shown a 3-D isosurface of the von Mises porous solid [calculated using Eq. (7.76)] corresponding to a porosity $f = 1\%$. Specifically, this convex surface contains all the points (D_m, R, γ) that produce the same plastic dissipation $\Psi^{+}_{\text{Mises}}(\mathbf{D},f) = 9.21 \times 10^{-3}$ for the porous solid.

First, let us note that the presence of voids induces a strong influence of the mean strain-rate D_m on the plastic dissipation, the surface being closed on the hydrostatic axis. Indeed, for purely hydrostatic states (i.e., $\mathbf{D} = D^H_m \mathbf{I}$) according to Eq. (7.73), $\Psi^{+}_{\text{Mises}}(\mathbf{D},f) = 2\left|D^H_m\right| \ln(1/f)$. In particular, for $f = 1\%$ and dissipation of 9.21×10^{-3}, $\mathrm{D}^{\mathrm{H}}_m = \pm 1 \times 10^{-3}\ \mathrm{s}^{-1}$. Thus, the intersection of the isosurface with the planes $D_m = 1 \times 10^{-3}\ \mathrm{s}^{-1}$ and $D_m = -1 \times 10^{-3}\ \mathrm{s}^{-1}$, respectively are two points on the hydrostatic axis that are symmetric with respect to the origin (see also Fig. 7.19).

To fully assess the effects of all invariants of the strain-rate, $\mathbf{D}$, on the plastic response of the porous von Mises material, the cross-sections of the same 3-D isosurface with several deviatoric planes $D_m =$ constant are considered (see Fig. 7.20). Note that the intersection of any surface $\Psi^{+}_{\text{Mises}}(\mathbf{D},f)$ = constant with the plane $D_m = 0$, is a circle (see, e.g., Fig. 7.19). This is to be expected since states for which $D_m = 0$ correspond to purely deviatoric loadings for which the plastic dissipation of the porous material coincides with that of the matrix (von Mises behavior). The cross-sections with all the other deviatoric planes $D_m = c$, with $c \neq 0$ have threefold symmetry with respect to the origin, and deviate slightly from a circle. This indicates that the third-invariant $J^D_3 = D'_1 D'_2 D'_3$ affects the plastic response of the porous Mises material. It is also clearly seen that as D_m increases the response of the material becomes softer (the inner cross-section depicted in

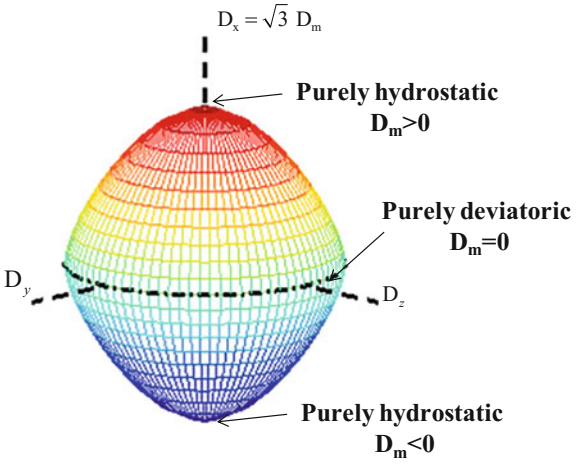

Fig. 7.19 3-D surface of a porous solid with von Mises matrix according to Eq. (7.76) for both tensile ($D_m = \mathrm{tr}(\mathbf{D}) > 0$) and compressive ($D_m < 0$) states. Note that this convex surface contains all the points (D_m, R, γ) that produce the same plastic dissipation $\Psi^{+}_{Mises}(\mathbf{D},f) = 9.21 \times 10^{-3}$ for the porous solid. Porosity: $f = 0.01$ (after Cazacu and Revil-Baudard [16])

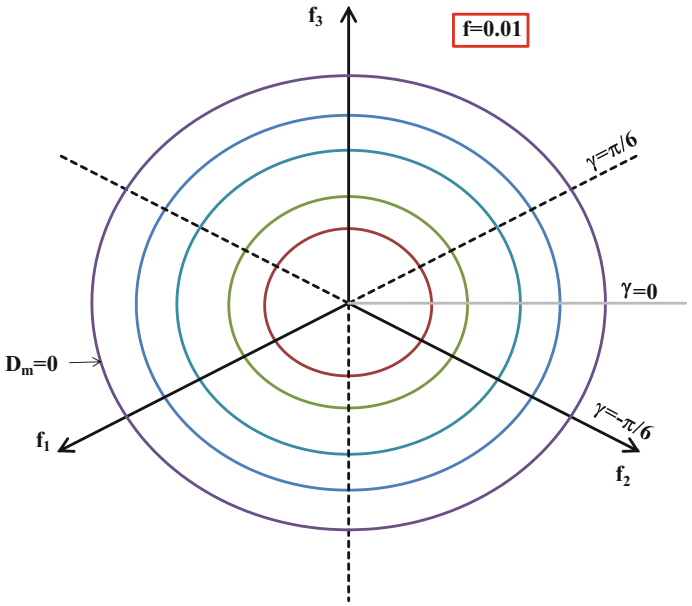

Fig. 7.20 Cross-sections of the 3-D isosurface of a porous von Mises material with several deviatoric planes D_m = constant; the outermost cross-section represents the intersection with the plane $D_m = 0$ while the innermost cross-section corresponds to $D_m = 9 \times 10^{-4}$ s^{-1}. Porosity: f = 0.01 (after Cazacu and Revil-Baudard [16])

Fig. 7.20 corresponds to $D_m = 9 \times 10^{-4}$ s^{-1}, the outer cross-section correspond to $D_m = 0$).

To assess the combined effects of the invariants J_3^D and J_2^D on the mechanical response of the porous von Mises material, the shapes of its cross-sections with the deviatoric planes $D_m = c\,(c \neq 0)$ need to be determined. Due to isotropy, it is sufficient to study how the distance between the origin and any point on the cross-section evolves with γ in the sector $-\pi/6 \leq \gamma \leq \pi/6$. In this sector, axisymmetric conditions correspond to $\gamma = -\pi/6$ $(D_1 = D_3 < D_2)$ or $\gamma = \pi/6$ $(D_2 = D_3 < D_1)$. As an example, in Fig. 7.21 is plotted $R(\gamma)$ (normalized by $R(-\pi/6)$) for the cross-section corresponding to $D_m = 6 \times 10^{-4}$ s^{-1} and $D_m = 0$, respectively. As already mentioned, the cross-section $D_m = 0$ corresponds to the matrix behavior (von Mises behavior) and as such it is a circle, $R(\gamma)$ = constant. As concerns the cross-section $D_m = 6 \times 10^{-4}$ s^{-1}, note the influence of the third-invariant J_3^D (or γ) as evidenced by the deviation of $R(\gamma)/R(-\pi/6)$ from a straight line.

Remark The noteworthy result is that the maximum difference is between the axisymmetric states, i.e., between $\mathrm{R}(-\pi/6)$ and $\mathrm{R}(\pi/6)$. This holds true irrespective of the level of D_m (see also Fig. 7.20). It follows that the maximum influence of γ (or J_3^D) on the response of the porous von Mises material, and

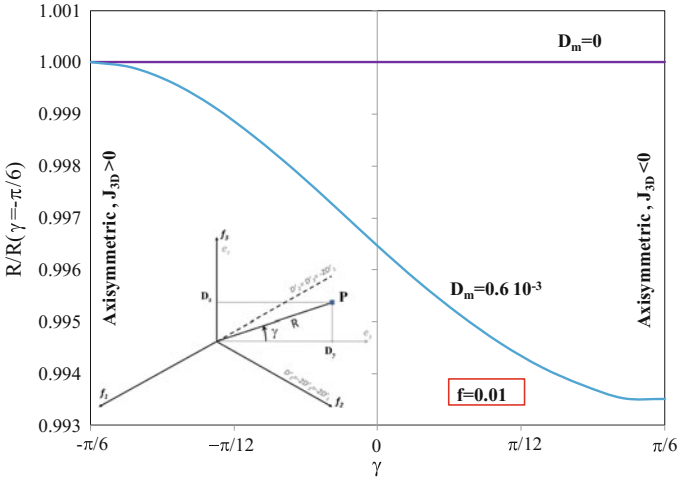

Fig. 7.21 Evolution of $R(\gamma)$ (normalized by $R(-\pi/6)$) with γ for the cross-section of the surface of the porous Mises material with the deviatoric planes $D_m = 6 \times 10^{-4}$ s^{-1} and $D_m = 0$ (von Mises behavior), respectively. Initial porosity: f = 0.01. Note that the response depends on the third-invariant as revealed by the very specific coupling between R (= $\sqrt{2J_{2D}}$) and γ (measure of J_3^D and J_2^D) (after Cazacu and Revil-Baudard [16])

consequently the maximum influence on void growth or void collapse occurs for axisymmetric loadings. It is worth noting that for the case of large positive and negative triaxialities, the same conclusions concerning the influence of the third-invariant on void evolution were obtained in their seminal study by Rice and Tracey [58].

Cazacu and Revil-Baudard [16] *strain-rate plastic potential for a porous Mises material*

A remarkable property of the exact plastic potentials (stress-based and strain-rate-based formulations) of a porous solid with von Mises matrix is their centro-symmetry [see also Theorem 7.1 and Eq. (7.17)]. This property is preserved by $\Psi^+_{\text{Mises}}(\mathbf{D},f)$. This means that for any porosity f:

$$\Psi^+_{\text{Mises}}(D_m, R, \gamma, f) = \Psi^+_{\text{Mises}}(-D_m, R, -\gamma, f),$$

i.e., the surface is symmetric with respect to the origin (see also Eq. (7.76) and Fig. 7.19). More specifically, in Fig. 7.20 it is clearly seen that for a given value of D_m in order to reach the same plastic dissipation in the porous solid, there should be a very specific dependence between the invariants of $\mathbf{D}'$, i.e., between R and γ. Indeed, the analysis of the cross-sections shows that for $D_m > 0$, $R(\gamma)$ is a monotonically decreasing function of γ (see Fig. 7.21). Due to the centro-symmetry

of $\Psi^{+}_{\text{Mises}}(\mathbf{D},f)$ for $D_m<0$, $R(\gamma)$ must be a monotonically increasing function of γ. A function that has these properties and coincides with the exact values of $R(\gamma)$ for axisymmetric states was proposed by Cazacu and Revil-Baudard [16], i.e.,

$$R(\gamma)=\frac{R_-+R_+}{2}+\frac{R_--R_+}{2}\left(\frac{\sinh(\gamma)-\gamma\cosh(\pi/6)}{-\sinh(\pi/6)+\pi\cosh(\pi/6)/6}\right), \tag{7.77}$$

where R_- and R_+ are the values of the SRP corresponding to axisymmetric loadings at $\gamma=-\pi/6$ and $\gamma=\pi/6$, respectively that are calculated using Eqs. (7.61) and (7.63), respectively.

Figure 7.22 shows the comparison between the evolution of $R(\gamma)$ (normalized by $R(\pi/6)$) according to Eq. (7.77) and the numerical values (symbols) obtained by estimating numerically the plastic dissipation given by Eq. (7.76) for the cross-sections of the isosurface $\Psi^{+}_{\text{Mises}}(\mathbf{D},f)=9.21\times10^{-3}$ corresponding to $f=0.01$. In the sector $-\pi/6\le\gamma\le\pi/6$, the shapes of the cross-sections of the analytical SRP [Eq. (7.77)] with several deviatoric planes $D_m=constant$ and the numerical points (symbols) are shown in Fig. 7.23. Note that the Cazacu and Revil-Baudard [16] SRP is a very good approximation of the SRP of the porous von Mises material for all values of $D_m>0$ considered.

Comparison between the Cazacu and Revil-Baudard [16] *strain-rate potential and Gurson strain-rate potential*

It is also interesting to compare the 3-D SRP of Cazacu and Revil-Baudard [16] with that developed by Gurson [29]. As already mentioned in Sect. 7.2.3.1,

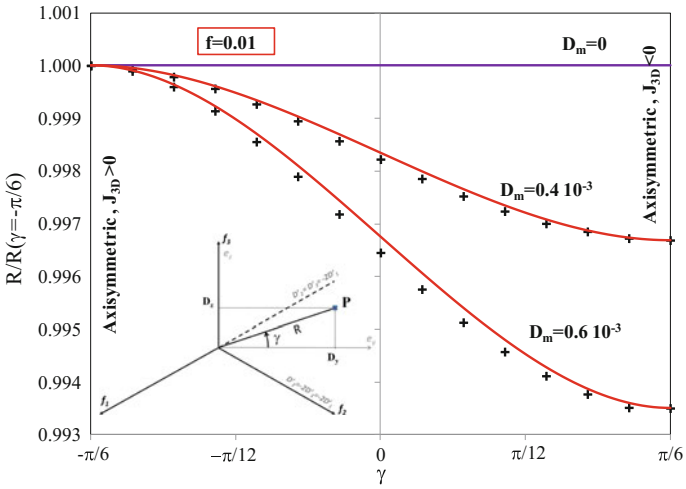

Fig. 7.22 Comparison between the evolution of $R(\gamma)$ (normalized by $R(-\pi/6)$) according to Eq. (7.77) and the numerical values (symbols) for the cross-section of the surface of the porous von Mises material with the deviatoric planes: $D_m=6\times10^{-4}$ s^{-1}, $D_m=4\times10^{-4}$ s^{-1}, and $D_m=0$, respectively. f = 0.01 (after Cazacu and Revil-Baudard [16])

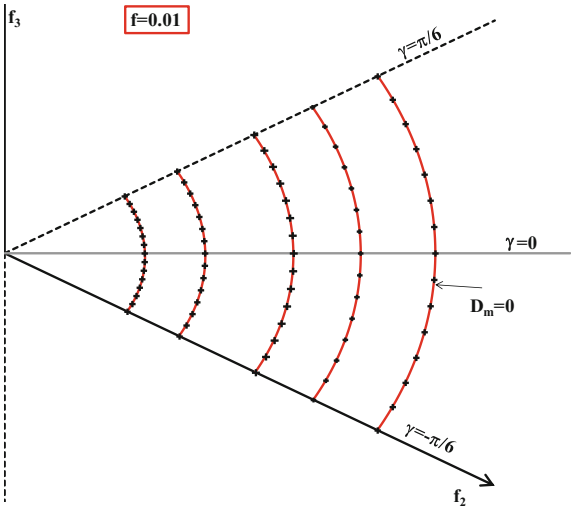

Fig. 7.23 Cross-sections of the Cazacu and Revil-Baudard [16] 3-D strain-rate potential corresponding to a fixed value of the plastic dissipation of 9.21×10^{-3} with several deviatoric planes $D_m =$ *constant*; the outer cross-section represents the intersection with the plane $D_m = 0$ while the inner cross-section corresponds to $D_m = 9 \times 10^{-4}$ s^{-1}. Numerical points are represented by symbols. Porosity $f = 0.01$

Gurson's [29] SRP for a porous Mises material, $\Psi_{Gurson}(\mathbf{D}, f)$, given by Eq. (7.37), does not involve any dependence on the third-invariant J_3^D (or γ). Therefore, irrespective of the value of D_m or the porosity level the cross-section with any deviatoric plane $D_m =$ constant is a circle, i.e., $R(\gamma) =$ constant (see also Fig. 7.24).

On the other hand, the analytical SRP of Cazacu and Revil-Baudard [16] [Eq. (7.77)] depends on all the invariants of $\mathbf{D}$. It has the following properties:

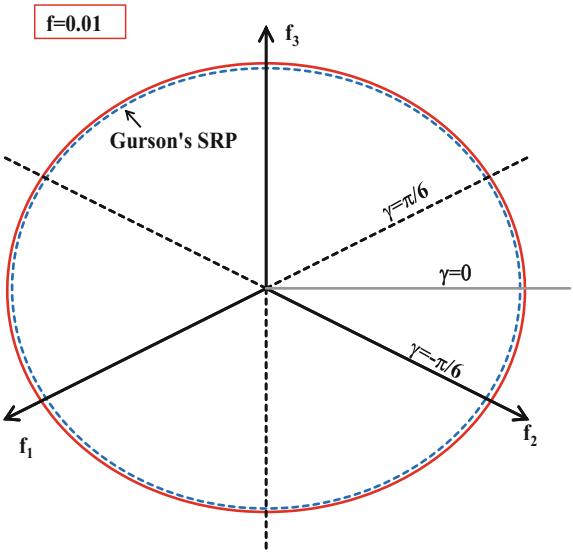

Fig. 7.24 Comparison between the cross-sections of the Cazacu and Revil-Baudard [16] strain-rate potential [solid line; Eq. (7.77)] and that of Gurson's [29] strain-rate potential [interrupted line, Eq. (7.37)] corresponding to the same level of plastic energy 9.21×10^{-3}. The cross-section corresponds to $D_m = 6 \times 10^{-4}$ s^{-1}. Note that Gurson's [29] SRP is more dissipative than the new model. Porosity: $f = 0.01$

- For axisymmetric states, it coincides with $\Psi^{+}_{\text{Mises}}(\mathbf{D},f)$ [see Eqs. (7.61)–(7.63)]
- Since $R(\gamma)$ given by Eq. (7.77) is an odd function, it satisfies automatically the centro-symmetry requirement.
- The derivative of $R(\gamma)$ with respect to γ is null for axisymmetric loadings [see Eq. (7.77)].
- The Cazacu and Revil-Baudard [16] SRP displays threefold symmetry with respect to the origin.

Thus, the Cazacu and Revil-Baudard [16] potential given by Eq. (7.77) preserves all the key features of the exact SRP of a porous von Mises material. To further illustrate the specific differences between the Cazacu and Revil-Baudard [16] SRP and Gurson's [29] SRP in Fig. 7.24 are shown the cross-sections with the deviatoric plane $D_m = 6 \times 10^{-4}\ \text{s}^{-1}$ of the respective isosurfaces corresponding to the same value of the plastic dissipation (9.21×10^{-3}) and the same void volume fraction $f = 1\%$. Since the Gurson [29] SRP was obtained by truncating the plastic dissipation associated with Rice and Tracey's [58] velocity field [see Eq. (7.34)], it is necessarily interior to the Cazacu and Revil-Baudard [16] SRP. This means that Gurson's [29] SRP is more dissipative, i.e., in order to reach the same value of the plastic dissipation, the norm of the loading, $R(\gamma)$, for the Gurson [29] SRP is lower than that for the Cazacu and Revil-Baudard [16] SRP [Eq. (7.77)]. Only for purely hydrostatic loading $(\mathbf{D}' = 0)$, and purely deviatoric states $(D_m = 0)$, the two potentials coincide.

Cazacu and Revil-Baudard [16] *3-D stress-based potential for a porous solid with von Mises matrix*

Based on the numerical calculations of the plastic dissipation for full 3-D loadings presented in the previous subsection, it can also be concluded that the stress potential and yield function of a porous Mises material has the following remarkable properties:

(i) It depends on all stress invariants,
(ii) It is centro-symmetric, i.e., invariant to the transformation: $\left(\Sigma_m, \Sigma_e, J_3^{\Sigma}\right) \rightarrow \left(-\Sigma_m, \Sigma_e, -J_3^{\Sigma}\right)$,
(iii) It is an even function in stresses,
(iv) The maximum influence of the third-invariant of the stress deviator occurs for axisymmetric states.

Cazacu and Revil-Baudard [16] also proposed a 3-D stress potential that has all the properties (i)-(iv). This stress potential being isotropic, it is sufficient to provide its expression in the sector $\Sigma_2 \geq \Sigma_3 \geq \Sigma_1$. Let us recall that if $\Sigma_2 \geq \Sigma_3 \geq \Sigma_1$, it follows that:

$$\begin{aligned}
\Sigma'_1 &= -\frac{\tilde{R}}{\sqrt{6}}\left(\sqrt{3}\cos\theta + \sin\theta\right) \\
\Sigma'_2 &= \frac{\tilde{R}}{\sqrt{6}}\left(\sqrt{3}\cos\theta - \sin\theta\right) \\
\Sigma'_3 &= \frac{2\tilde{R}}{\sqrt{6}}\sin\theta
\end{aligned} \tag{7.78}$$

with

$$\tilde{R} = \sqrt{\Sigma_1'^2 + \Sigma_2'^2 + \Sigma_3'^2} = \Sigma_e\sqrt{(2/3)} \tag{7.79}$$

and θ is the angle satisfying: $-\pi/6 \le \theta \le \pi/6$ and whose sine is given by:

$$\sin 3\theta = -\frac{3\sqrt{3}}{2}\cdot\frac{J_3^{\Sigma}}{\left(J_2^{\Sigma}\right)^{3/2}} \tag{7.80}$$

As already mentioned, the sub-sector $-\pi/6 \le \theta \le 0$ corresponds to states on the surface for which $(\Sigma'_2 \ge 0, \Sigma'_3 \le 0, \Sigma'_1 \le 0)$ so the third-invariant $J_3^{\Sigma} \ge 0$ while the sub-sector $0 \le \theta \le \pi/6$ corresponds to states for which $(\Sigma'_2 \ge 0, \Sigma'_3 \ge 0, \Sigma'_1 \le 0)$ so $J_3^{\Sigma} \le 0$. In this sector, axisymmetric states correspond to either $\theta = -\pi/6$ $(\Sigma'_1 = \Sigma'_3 < \Sigma'_2)$ or $\theta = \pi/6$ $(\Sigma'_2 = \Sigma'_3 > \Sigma'_1)$.

To describe the variation of $\tilde{R} = \Sigma_e\sqrt{(2/3)}$ with the angle θ (a measure of the combined influence of Σ_e and J_3^{Σ}), Cazacu and Revil-Baudard [16] proposed the following function:

$$\widetilde{R}(\theta) = \frac{\widetilde{R}_+ + \widetilde{R}_-}{2} + \frac{\widetilde{R}_- - \widetilde{R}_+}{2}\left(\frac{\sinh(\theta) - \theta\cosh(\pi/6)}{-\sinh(\pi/6) + \frac{\pi}{6}\cosh(\pi/6)}\right) \tag{7.81}$$

where $\tilde{R}_-$ and $\tilde{R}_+$ are the exact values corresponding to axisymmetric loadings at $\theta = -\pi/6$ and $\theta = \pi/6$, respectively [calculated using Eqs. (7.66)–(7.71)].

As an example, in Fig. 7.25 is shown the 3-D yield surface given by Eq. (7.81) corresponding to a porosity $f = 1\%$ for both tensile $(\Sigma_m > 0)$ and compressive $(\Sigma_m < 0)$ states. Specifically, this convex surface contains all the stress points corresponding to the same plastic dissipation for the porous solid. Note that the

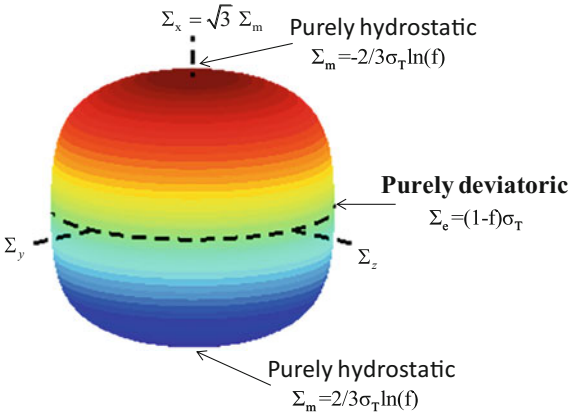

Fig. 7.25 Cazacu and Revil-Baudard [16] 3-D yield surface for a porous solid with von Mises matrix. Porosity: f = 0.01

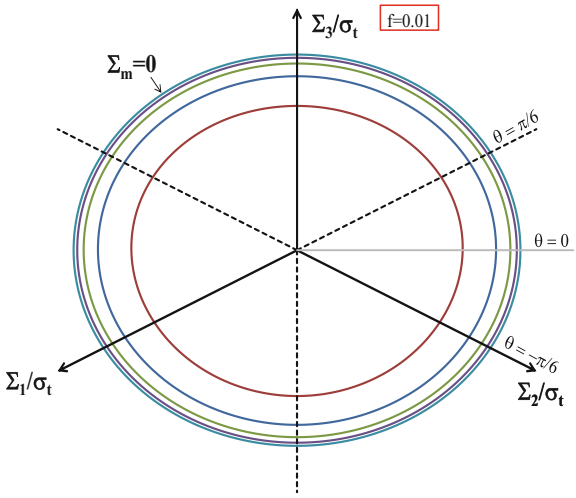

Fig. 7.26 Cross-sections of the Cazacu and Revil-Baudard [16] 3-D yield surface [Eq. (7.81)] for a porous von Mises material with several deviatoric planes Σ_m = constant; the outer cross-section represents the intersection with the plane $\Sigma_m/\sigma_T = 0$ while the inner cross-section corresponds to $\Sigma_m/\sigma_T = 2.5$. Porosity: f = 0.01

presence of voids induces a strong influence of the mean stress Σ_m on yielding, and that the yield surface is closed on the hydrostatic axis.

Figure 7.26 shows the cross-sections of the 3-D yield criterion given by Eq. (7.81) with several deviatoric planes Σ_m = constant. Note that irrespective of the value of Σ_m, the cross-sections slightly deviate from circles, the maximum influence of the third-invariant of the stress deviator occurs for axisymmetric conditions. Also, with increasing Σ_m, the influence of the third-invariant (or θ) is increasing. Since the dependence of $\tilde{R}$ with θ given by Eq. (7.81) relies on the exact solution of the limit-analysis problem for axisymmetric loadings (associated with the Rice and Tracey's [58] velocity field), and it is an odd function, it satisfies the key properties (i)–(iv) of the exact stress-based plastic potential for a porous Mises material.

Most importantly, the yield surface according to the Cazacu and Revil-Baudard [16] criterion is centro-symmetric. To illustrate this noteworthy property, in Fig. 7.27 are shown the cross-sections of the yield surface according to Eq. (7.81) for f = 0.01 with a deviatoric plane corresponding to a positive mean stress ($\Sigma_m/\sigma_T = 2$, interrupted line) and a compressive mean stress ($\Sigma_m/\sigma_T = -2$, solid line), respectively. The symmetry of the respective cross-sections with respect to the origin is clearly seen. For example, for loadings corresponding to $J_3^{\Sigma} \geq 0$ (i.e., $-\pi/6 \leq \theta \leq 0$) to produce the same plastic dissipation, $\tilde{R}(\theta)$ at yielding is lower for compressive states ($\Sigma_m < 0$—interrupted line) than for tensile states ($\Sigma_m > 0$—solid line). The reverse holds true for loadings corresponding to $J_3^{\Sigma} \leq 0$ ($0 \leq \theta \leq \pi/6$).

As an example, in Fig. 7.28 are shown the cross-sections of the Cazacu and Revil-Baudard [16] yield surface [Eq. (7.81)] and that of Gurson's [30] [Eq. (7.41)] with the deviatoric planes $\Sigma_m/\sigma_T = 1.5$ and $\Sigma_m/\sigma_T = 2$, respectively, for a void

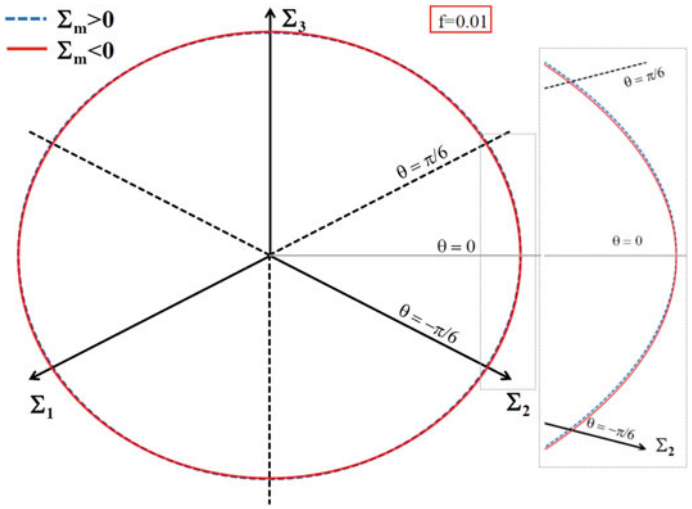

Fig. 7.27 Cross-sections of the Cazacu and Revil-Baudard [16] 3-D yield surface for the porous von Mises material with the deviatoric planes $\Sigma_m/\sigma_T = 2$ (interrupted lines) and $\Sigma_m/\sigma_T = -2$ (solid lines), respectively. Note the centro-symmetry of the cross-sections due to the invariance of the plastic response to the transformation $(\Sigma_m, \boldsymbol{\Sigma}') \rightarrow (-\Sigma_m, -\boldsymbol{\Sigma}')$. Porosity: $f = 0.01$

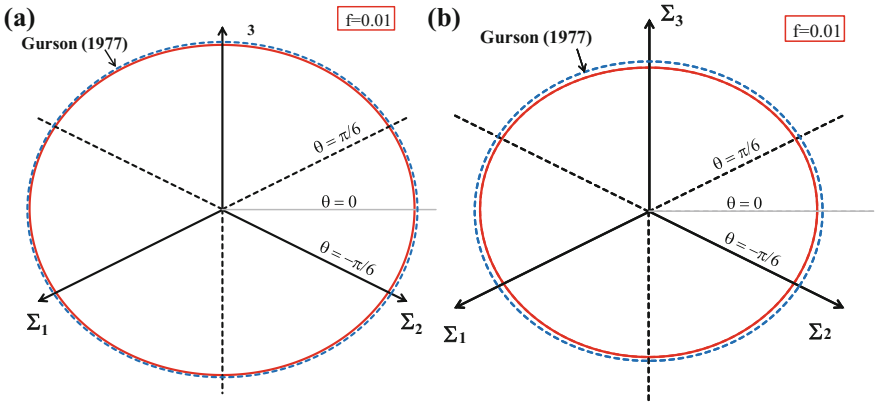

Fig. 7.28 Comparison between the cross-sections of the Cazacu and Revil-Baudard [16] 3-D yield surface [solid line; Eq. (7.81)] and that of the Gurson's [30] yield surface [interrupted line; (Eq. (7.41)] with several deviatoric planes: **a** $\Sigma_m/\sigma_T = 1.5$; **b** $\Sigma_m/\sigma_T = 2$. Note that Gurson's [30] surface is always exterior. Porosity $f = 0.01$

volume fraction $f = 1\%$. The Gurson's [30] criterion (interrupted line) is an upper bound to the new criterion, the correction brought to the Gurson's [30] criterion becoming more important with increasing Σ_m. This point is further illustrated in Fig. 7.29, which shows the differences between the two criteria as a function of the

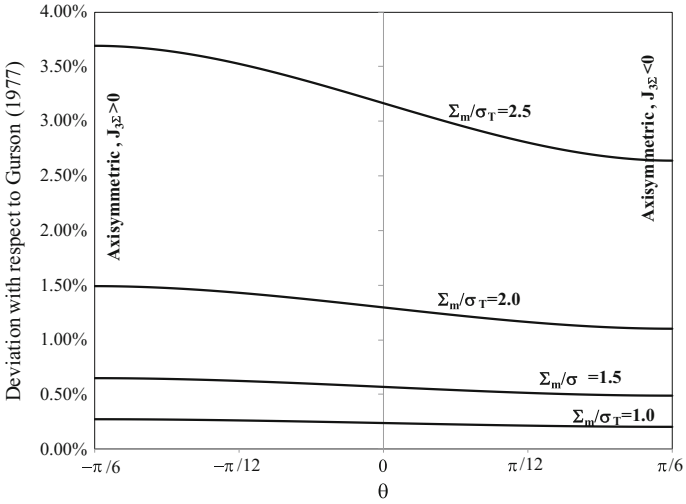

Fig. 7.29 Corrections brought by the Cazacu and Revil-Baudard [16] 3-D model to Gurson's [30] as a function of the Lode parameter μ ($\mu = \sqrt{3}\tan\theta$) for loadings at constant positive mean stress Σ_m. Irrespective of the level of Σ_m the maximum deviation corresponds to axisymmetric states corresponding to $\theta = -\pi/6$. The higher the mean stress, the greater is the correction to Gurson [30]. Porosity: f = 0.01

loading path. The differences between the two criteria are calculated for loadings at Σ_m = constant and Lode parameter μ = constant. Let us recall that $\mu = \sqrt{3}\tan\theta$, with θ given by Eq. (7.80). It is also worth noting that the most important difference between the Gurson [30] criterion and the Cazacu and Revil-Baudard [16] criterion correspond to tensile axisymmetric conditions at $\theta = -\pi/6$., i.e., $\mu = -1$.

Using the yield criterion of Cazacu and Revil-Baudard [16] given by Eq. (7.81), one can easily establish the relation between Σ_e and Σ_m at yielding for loadings corresponding to Lode parameter $\mu = \sqrt{3}\tan(\theta)$ = constant. As an example, in Fig. 7.30 are shown the projections of the yield surface in the (Σ_m, Σ_e) plane for tensile loadings $(\Sigma_m \geq 0)$ at $\mu = -0.464$ $(\theta = -\pi/12)$, $\mu = 0$, and axisymmetric loadings, i.e., at $\mu = -1$ $(\theta = -\pi/6)$ and $\mu = 1$ $(\theta = \pi/6)$, respectively.

Note that according to the yield criterion, for low triaxialities the difference between the yield curves at $\theta =$ constant is very small. However, the difference

Fig. 7.30 Zooms on the tensile quadrant of the cross-sections of the 3-D yield surface for the porous von Mises material according to Cazacu and Revil-Baudard [16] [Eq. (7.81)] in the (Σ_m, Σ_e) plane at fixed values of the Lode parameter $\mu = \sqrt{3}\tan\theta$ in the range $(-\pi/6, \pi/6)$; **a** low stress triaxialities $(1 \leq \Sigma_m/\sigma_T \leq 2, 0.9 \leq \Sigma_e/\sigma_T \leq 0.98)$; **b** intermediate triaxialities $(2.5 \leq \Sigma_m/\sigma_T \leq 2.8, 0.6 \leq \Sigma_e/\sigma_T \leq 0.742)$: **c** high stress triaxialities $(2.8 \leq \Sigma_m/\sigma_T \leq 3.07, 0 \leq \Sigma_e/\sigma_T \leq 0.6)$; axisymmetric loadings correspond to $\mu = -1$ $(\theta = -\pi/6)$ and $\mu = 1$ $(\theta = \pi/6)$ ▶

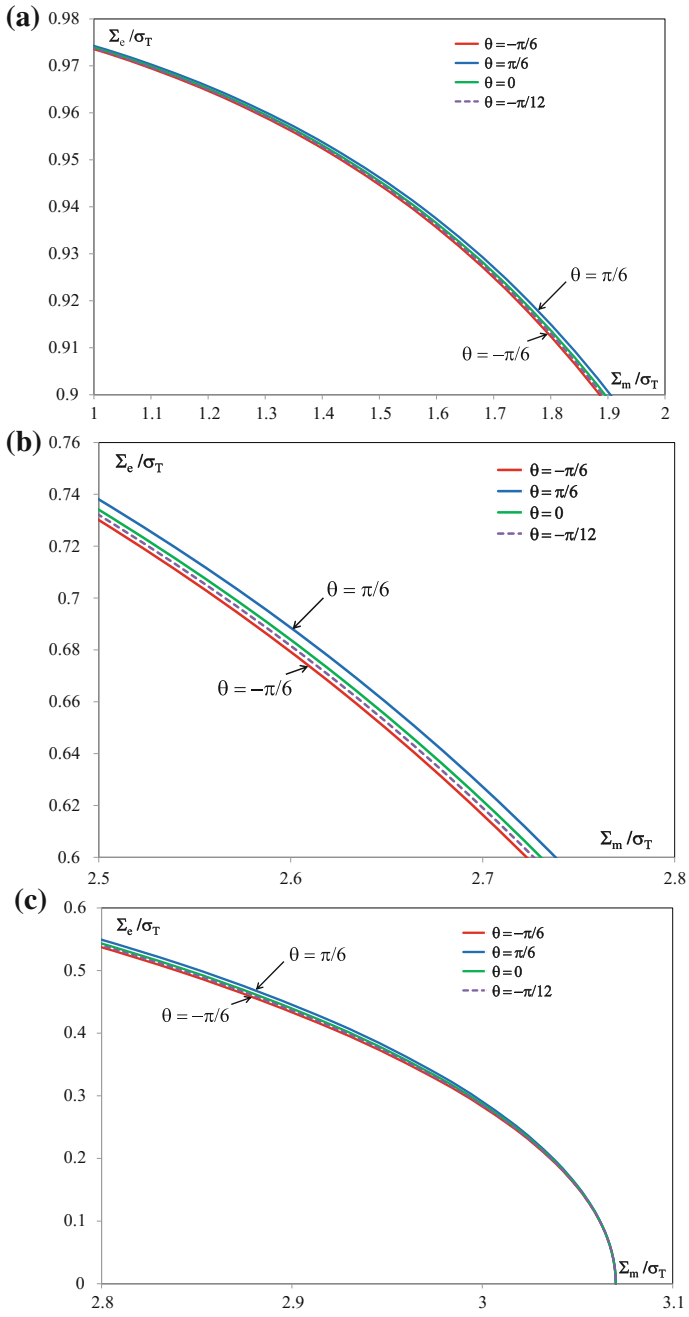
(a)
Σe /σT
θ=−π/6
θ=π/6
θ=0
θ=−π/12
θ = π/6
θ = −π/6
Σm /σT
0.98
0.97
0.96
0.95
0.94
0.93
0.92
0.91
0.9
1
1.1
1.2
1.3
1.4
1.5
1.6
1.7
1.8
1.9
2
(b)
Σe /σT
θ=−π/6
θ=π/6
θ=0
θ=−π/12
θ = π/6
θ = −π/6
Σm /σT
0.76
0.74
0.72
0.7
0.68
0.66
0.64
0.62
0.6
2.5
2.6
2.7
2.8
(c)
Σe /σT
θ=−π/6
θ=π/6
θ=0
θ=−π/12
θ = π/6
θ = −π/6
Σm /σT
0.6
0.5
0.4
0.3
0.2
0.1
0
2.8
2.9
3
3.1

becomes more important with increasing stress triaxiality (see also Fig. 7.30a, b); for stress states corresponding to stress triaxialities $T = (\Sigma_m/\Sigma_e)$ approaching infinity (i.e., purely hydrostatic states), the difference in the yielding response starts to decrease, and all the yield curves coincide at the purely hydrostatic point ($\Sigma_e = 0$) (see Fig. 7.30c). Irrespective of the level of the stress triaxiality T, the softest response is for axisymmetric loadings corresponding to $\mu = -1$ ($\theta = -\pi/6$) while the hardest response is for axisymmetric loadings at $\mu = 1$ ($\theta = \pi/6$).

Note that due to the centro-symmetry of the yield surface, for compressive loadings ($\Sigma_m \leq 0$) the hardest response is for axisymmetric loadings corresponding to $\mu = -1$ ($\theta = -\pi/6$) while the softest response is for axisymmetric loadings at $\mu = 1$ (see Fig. 7.31).

7.2.4 Porous Materials with Tresca Matrix

The recent studies on void evolution in a porous Mises material presented in the previous section have put into evidence the fact that even if the matrix response does not depend on the third-invariant of stress (or strain-rate), the presence of voids induces dependence on all invariants. In the case when the plastic deformation of the matrix is governed by the von Mises criterion, it was demonstrated that the influence of the third-invariant on the plastic flow and void evolution is most pronounced for axisymmetric states.

The fundamental question that arises concerns the effect of the third-invariant on yielding and void evolution in a porous material with matrix governed by a yield criterion that depends on both invariants of the stress deviator. Specifically, it is important to compare the rate of void growth or collapse with that of a porous von Mises material.

A partial response to this question was given by Rice and Tracey [58], who proved that for loadings at high triaxialities the rate of void growth in a porous Tresca material is much faster than in a porous von Mises material. Whether this holds true for all loadings has remained an open question. Adressing this question is also of interest in view of engineering applications, given that the plastic behavior of certain fully dense metallic materials is described with improved accuracy by Tresca yield criterion (for more details about the Tresca yield criterion and stress potential, see Chap. 4; for discussion on its exact work-conjugate in the strain-rate space, see Chap. 6).

Fig. 7.31 Zooms on the tensile quadrant of the cross-sections of the 3-D yield surface for the porous von Mises material according to Cazacu and Revil-Baudard [16] [Eq. (7.81)] in the (Σ_m, Σ_e) plane at fixed values of the Lode parameter $\mu = \sqrt{3}\tan\theta$ in the range $(-\pi/6, \pi/6)$; for: **a** low stress triaxialities ($-2 \leq \Sigma_m/\sigma_T \leq -1, 0.9 \leq \Sigma_e/\sigma_T \leq 0.98$); **b** intermediate triaxialities ($-2.8 \leq \Sigma_m/\sigma_T \leq -2.5, 0.6 \leq \Sigma_e/\sigma_T \leq 0.742$): **c** high stress triaxialities ($-3.07 \leq \Sigma_m/\sigma_T \leq -2.8, 0 \leq \Sigma_e/\sigma_T \leq 0.6$); axisymmetric loadings correspond to $\mu = -1$ ($\theta = -\pi/6$) and $\mu = 1$ ($\theta = \pi/6$) ▶

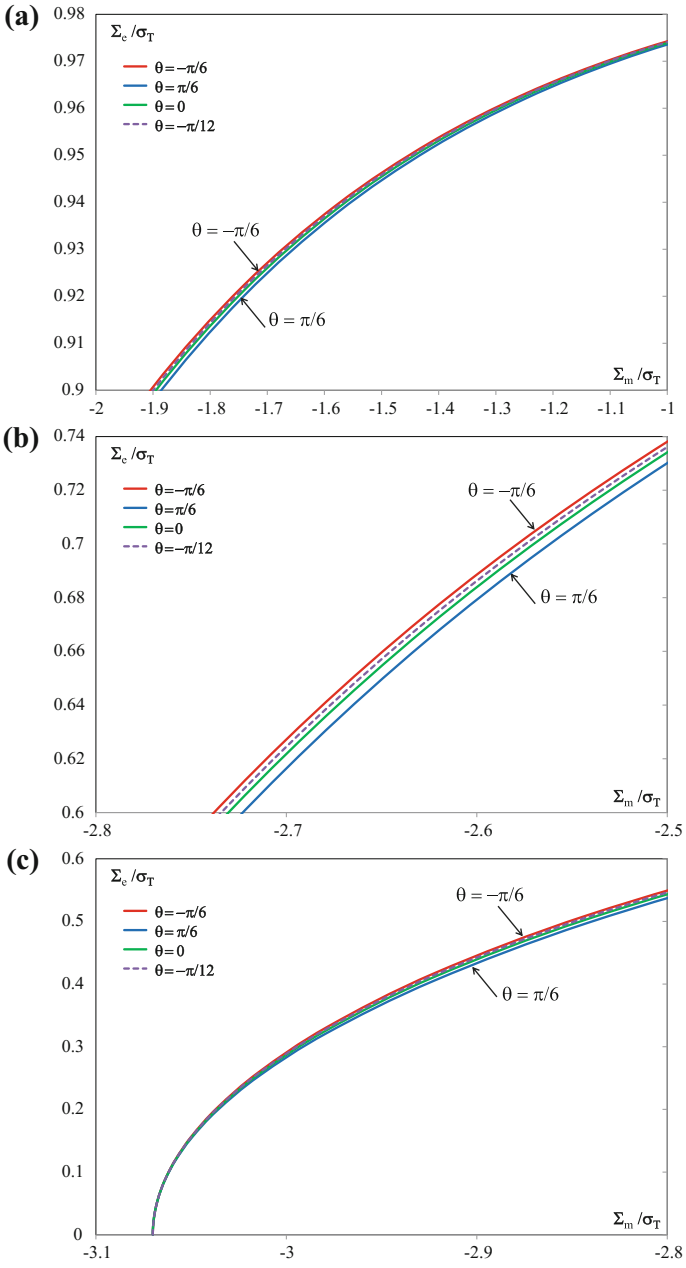
(a)
Σe /σT
θ=−π/6
θ=π/6
θ=0
θ=−π/12
θ = −π/6
θ = π/6
Σm /σT
0.98
0.97
0.96
0.95
0.94
0.93
0.92
0.91
0.9
-2
-1.9
-1.8
-1.7
-1.6
-1.5
-1.4
-1.3
-1.2
-1.1
-1
(b)
Σe /σT
θ=−π/6
θ=π/6
θ=0
θ=−π/12
θ = −π/6
θ = π/6
Σm /σT
0.74
0.72
0.7
0.68
0.66
0.64
0.62
0.6
-2.8
-2.7
-2.6
-2.5
(c)
Σe /σT
θ=−π/6
θ=π/6
θ=0
θ=−π/12
θ = −π/6
θ = π/6
Σm /σT
0.6
0.5
0.4
0.3
0.2
0.1
0
-3.1
-3
-2.9
-2.8

Recently, Cazacu et al. [18] derived an analytic plastic potential for porous solids with matrix obeying Tresca's yield criterion. It is to be noted that a major difficulty in deriving such a potential in closed form is related to the calculation of the overall plastic dissipation. This is a direct consequence of Tresca's criterion being dependent on the third-invariant of the stress deviator. Indeed, in contrast with the case when the matrix is described by the von Mises yield criterion, mathematical difficulties arise in the analysis because the expression of the local plastic dissipation depends on the sign of each of the principal values of the local strain-rate tensor.

In the following, it is shown that, despite of these fresh difficulties, for axisymmetric states the integrals representing the overall plastic dissipation can be calculated analytically. Moreover, an explicit parametric representation of the yield surface for porous solids with randomly distributed spherical voids in a Tresca matrix can be derived. The new results put into evidence in Cazacu et al. [18] concerning a very specific coupling between the mean stress and the third-invariant of the stress deviator and its effects on yielding and void evolution of porous Tresca materials are also discussed.

7.2.4.1 Cazacu et al. [18] Yield Criterion

Cazacu et al. [18] used the kinematic homogenization approach to model the mechanical response of a porous Tresca material. The matrix behavior was considered to be rigid-plastic and governed by the Tresca's yield function (see also Sect. 4.2.1),

$$\varphi_{\text{Tresca}}(\boldsymbol{\sigma}) = \max(|\sigma_1 - \sigma_2|, |\sigma_2 - \sigma_3|, |\sigma_1 - \sigma_3|),$$

with σ_1, σ_2 and σ_3 being the principal values of the Cauchy stress $\boldsymbol{\sigma}$. Let us recall that for any strain-rate field $\mathbf{d}$, the local plastic dissipation associated with $\varphi_{\text{Tresca}}(\boldsymbol{\sigma})$ has the following closed-form expression:

$$\pi_{\text{Tresca}}(\mathbf{d}) = \sigma_T \dot{\lambda} = \sigma_T \psi_{\text{Tresca}}(\mathbf{d}), \tag{7.82}$$

the exact strain-rate potential $\psi_{\text{Tresca}}(\mathbf{d})$ being given by:

$$\psi_{\text{Tresca}}(\mathbf{d}) = (|d_I| + |d_{II}| + |d_{III}|)/2,$$

where d_I,d_{II}, d_{III} denote the principal values of $\mathbf{d}$ (see Sect. 6.1.1).

For spherical void geometry, the RVE considered is the hollow sphere, shown in Fig. 7.1. The analysis was done for a unique velocity field, namely that of Rice and Tracey [58] and axisymmetric loadings [see Eqs. (7.25) and (7.29)]. For this strain-rate field $\mathbf{d}$, the principal values are given by Eq. (7.30). It is to be noted that in contrast to the case when the plastic flow of the matrix is described by the von Mises criterion, the local plastic dissipation $\pi_{\text{Tresca}}(\mathbf{d})$ depends on the sign of d_I, d_{II},

d_{III}. This is a direct consequence of Tresca's yield function depending on the relative ordering of the principal stresses, i.e., on the third-invariant of the stress deviator. Nevertheless, it is possible to solve the limit-analysis problem analytically and to obtain the plastic dissipation $\Pi^{+}_{\text{Tresca}}(\boldsymbol{D},f)$ and consequently the strain-rate potential of the porous Tresca material, $\Psi^{+}_{\text{Tresca}}(\boldsymbol{D},f) = \Pi^{+}_{\text{Tresca}}(\boldsymbol{D},f)/\sigma_T$ in closed form. Moreover, Cazacu et al. [18] derived an explicit analytic expression of the yield criterion for the porous Tresca material, namely:

$$\begin{cases} \Sigma_m/\sigma_T = \dfrac{1}{3}\dfrac{\partial \Psi^{+}_{\text{Tresca}}(\boldsymbol{D},f)}{\partial D_m} \\ \Sigma_e/\sigma_T = \left|\dfrac{\partial \Psi^{+}_{\text{Tresca}}(\boldsymbol{D},f)}{\partial D_e}\right| \end{cases} \tag{7.83}$$

Let us first note that $\Pi^{+}_{\text{Tresca}}(\boldsymbol{D},f)$ is an upper bound of the exact potential (i.e., the potential obtained through minimization over all the velocity fields compatible with uniform boundary conditions given by Eq. (7.13), see Sect. 7.1). While the explicit expression of $\Psi^{+}_{\text{Tresca}}(\boldsymbol{D},f)$ and the parametric representation of the yield surface (7.83) will be given later on, it is important to note here that there are key features of the plastic behavior of a porous Tresca material that can be deduced without calculation of the integrals representing the plastic dissipation.

Indeed, since $\varphi_{\text{Tresca}}(\boldsymbol{\sigma})$ is an even function of stresses, according to Theorem 7.1:

- The yield surface of a porous Tresca material given by Eq. (7.83) is centro-symmetric.
- Irrespective of the sign of J_3^{Σ}, for purely deviatoric loading, yielding occurs at $\Sigma_e = \sigma_T(1-f)$; for purely hydrostatic loadings, yielding occurs at: $|\Sigma_m| = \frac{2}{3}\sigma_T \ln f$.

Theorem 7.8 (Strain-rate potential of a porous Tresca material under axisymmetric loadings)

For axisymmetric states, the strain-rate potential of a porous Tresca material is given by:

(a) *For* $D_m \geq 0$ *and* $J_3^D \leq 0$ ($D'_{11} \geq 0$), *and any value of* $u = \dfrac{2|D_m|}{D_e}$:

$$\Psi^{+}_{\text{Tresca}}(\boldsymbol{D},f) = \begin{cases} \dfrac{uD_e}{8}\left(F_1\left(\dfrac{u}{f}\right) - F_1(u)\right), & \forall u \leq f \\ \dfrac{uD_e}{8}\left(F_2\left(\dfrac{u}{f}\right) - F_1(u)\right), & \forall f < u < 1 \\ \dfrac{uD_e}{8}\left(F_2\left(\dfrac{u}{f}\right) - F_2(u)\right) & \forall u \geq 1 \end{cases} \tag{7.84}$$

with $F_1(y)$ *and* $F_2(y)$ *given by*:

$$F_1(y) = 1 - 16\ln(2) - \frac{6}{y} + \frac{\left(3y^2 + 8y^{3/2} + 6y - 1\right)}{y^{3/2}} \ln\left(\frac{\sqrt{y}+1}{1-\sqrt{y}}\right) + 16\ln\left(1-\sqrt{y}\right)$$
$$F_2(y) = 1 - 16\ln(2) - \frac{6}{y} + \frac{\left(3y^2 + 8y^{3/2} + 6y - 1\right)}{y^{3/2}} \ln\left(\frac{\sqrt{y}+1}{\sqrt{y}-1}\right) + 16\ln\left(\sqrt{y}-1\right) \tag{7.85}$$

(b) *For* $D_m \geq 0$ *and* $J_3^D \geq 0$ ($D'_{11} \leq 0$),

$$\Psi^+_{\text{Tresca}}(\boldsymbol{D}, f) = \begin{cases} \dfrac{uD_e}{8}\left(G_1(u/f) - G_1(u)\right) & ,\forall u \leq f \\ \dfrac{uD_e}{8}\left(G_2(u/f) - G_1(u) - 12 - 16\ln(2)\right), & \forall f < u < 1 \\ \dfrac{uD_e}{8}\left(G_2(u/f) - G_2(u)\right) & \forall u \geq 1 \end{cases} \tag{7.86}$$

with:

$$G_1(y) = -\frac{6}{y} - \arctan\left(\frac{2\sqrt{y}}{y-1}\right)\frac{\left(3y^2 - 6y - 1\right)}{y^{3/2}} - 8\ln(y+1),$$
$$G_2(y) = \frac{6}{y} + \frac{\left(3y^2 - 6y - 1\right)}{y^{3/2}} \arcsin\left(\frac{2\sqrt{y}}{y+1}\right) + 8\ln(y+1). \tag{7.87}$$

For all other states, the expression of the strain-rate potential can be deduced taking into account the centro-symmetry properties of $\Psi^+_{\text{Tresca}}(\boldsymbol{D}, f)$.

Proof As already mentioned, to calculate the local plastic dissipation $\pi_{\text{Tresca}}(\mathbf{d})$ [see Eq. (7.82)], one needs to determine the signs of the principal values d_I, d_{II}, d_{III} given by Eq. (7.30).

Case (a): $D_m \geq 0$ and $J_3^D \leq 0$ ($D'_{11} \geq 0$)

Since $d_I = D'_{11} + D_m(b/r)^3$, for the imposed loading it follows that everywhere in the RVE $\mathrm{d_I}$ is positive, and consequently $\mathrm{d_{III}}$ is negative [see Eq. (7.30)]. Moreover, $\mathrm{d_{II}}$ can be considered to be positive everywhere in the RVE (see analysis of the sign of $\mathrm{d_{II}}$ presented in Cazacu et al. [18]). Thus, the local plastic dissipation is given by:

$$\pi_{\text{Tresca}}(d) = \sigma_T(d_I + d_{II} - d_{III})/2 = -\sigma_T d_{III}, \quad \text{for any } a \leq r \leq b \tag{7.88}$$

Further substituting Eq. (7.30) into Eq. (7.82), we obtain:

$$\Psi^{+}_{\text{Tresca}}(D,f) = \frac{1}{V}\int_{\Omega}\left(\frac{1}{2}\sqrt{D_m^2\frac{b^6}{r^6} + D_{11}'^2 + 2D_{11}'D_m\frac{b^3}{r^3}} + \frac{3}{2}\sqrt{D_m^2\frac{b^6}{r^6} + 2D_{11}'D_m\frac{b^3}{r^3}\cos(2\theta) + D_{11}'^2}\right)\mathrm{d}V.$$

Since for Case (i), the strain-rate triaxiality $u = 2D_m/D_e$, it follows that:

$$\Psi^{+}_{\text{Tresca}}(\boldsymbol{D},f) = \frac{3D_e}{16\pi b^3}\int_{\Omega}\left[1 + u\left(\frac{b}{r}\right)^3 + 3\sqrt{1 + u^2\left(\frac{b}{r}\right)^6 + 2u\left(\frac{b}{r}\right)^3\cos(2\theta)}\right]\mathrm{d}V \tag{7.89}$$

By the change of variable, $y = u(b/r)^3$, the above integral becomes:

$$\Psi^{+}_{\text{Tresca}}(\boldsymbol{D},f) = \frac{uD_e}{8}\int_{u}^{u/f}\int_{0}^{\pi}\left(1 + y + 3\sqrt{y^2 + 2y\,\cos(2\theta) + 1}\right)\frac{\mathrm{d}y}{y^2}\sin\theta\,\mathrm{d}\theta \tag{7.90}$$

Noting that:

$$\int_{0}^{\pi}\left((1+y) + 3\sqrt{y^2 + 2y\,\cos(2\theta) + 1}\right)\frac{\sin\theta}{y^2}\,\mathrm{d}\theta = 5\frac{(1+y)}{y^2} + \frac{3}{2}\frac{(y-1)^2}{4y^{5/2}}\ln\left(\frac{\sqrt{y}+1}{|\sqrt{y}-1|}\right) \tag{7.91}$$

further integration with respect to y leads to the expression of $\Psi^{+}_{\text{Tresca}}(\boldsymbol{D},f)$ given by Eq. (7.84)-(7.85), respectively.

Case (b): $D_m \geq 0$ and $J_3^D \geq 0$ ($D_{11}' \leq 0$),

For this loading analysis of the sign of the principal values of d_I , d_{II}, d_{III} leads to the following expression for the SRP:

$$\Psi^{+}_{\text{Tresca}}(\boldsymbol{D},f) = \frac{D_e}{4\text{V}}\int_{\Omega}\left(\left(u\frac{b^3}{r^3} - 1\right) + 3\sqrt{u^2\frac{b^6}{r^6} - 2u\frac{b^3}{r^3}\cos(2\theta) + 1}\right)\mathrm{d}V, \quad \text{for } u\frac{b^3}{r^3} > 1$$

$$\Psi^{+}_{\text{Tresca}}(\boldsymbol{D},f) = \frac{D_e}{4\text{V}}\int_{\Omega}\left(\left(1 - u\frac{b^3}{r^3}\right) + 3\sqrt{u^2\frac{b^6}{r^6} - 2u\frac{b^3}{r^3}\cos(2\theta) + 1}\right)\mathrm{d}V, \quad \text{otherwise} \tag{7.92}$$

With $\mathrm{V} = 4\pi \mathrm{b}^3/3$ and $\mathrm{d}V = r^2 \sin\theta \mathrm{d}\theta \mathrm{d}\varphi \mathrm{d}r$. Using the change of variable, $y = u(b/r)^3$, these integrals can be written in the form:

For $y > 1$,

$$\Psi^{+}_{\text{Tresca}}(\boldsymbol{D},f) = \frac{D_e u}{8} \int_u^{u/f} \int_0^{\pi} \left((y-1) + 3\sqrt{y^2 - 2y\cos(2\theta) + 1} \right) \frac{\mathrm{d}y}{y^2} \sin\theta \, \mathrm{d}\theta,$$

while for $y < 1$,

$$\Psi^{+}_{\text{Tresca}}(\boldsymbol{D},f) = \frac{D_e u}{8} \int_u^{u/f} \int_0^{\pi} \left((1-y) + 3\sqrt{y^2 - 2y\cos(2\theta) + 1} \right) \frac{\mathrm{d}y}{y^2} \sin\theta \, \mathrm{d}\theta \tag{7.93}$$

Next, integration with respect to θ leads to:

For $y > 1$,

$$\Psi^{+}_{\text{Tresca}}(\boldsymbol{D},f) = \frac{D_e u}{8} \int_u^{u/f} 5\frac{(y-1)}{y^2} + \frac{3}{2}\frac{(y^2+2y+1)}{y^2\sqrt{y}} \arcsin\left(\frac{2\sqrt{y}}{y+1}\right) \mathrm{d}y,$$

while for $y < 1$, (7.94)

$$\Psi^{+}_{\text{Tresca}}(\boldsymbol{D},f) = \frac{D_e u}{8} \int_u^{u/f} 5\frac{(1-y)}{y^2} - \frac{3}{2}\frac{(y^2+2y+1)}{y^2\sqrt{y}} \arctan\left(\frac{2\sqrt{y}}{y-1}\right) \mathrm{d}y.$$

Further integration with respect to y leads to the expression of $\Psi^{+}_{\text{Tresca}}(\boldsymbol{D},f)$ given by Eqs. (7.86)–(7.87), respectively.

Theorem 7.9 (Cazacu et al. [18] *yield criterion of a porous Tresca material under axisymmetric loadings*)
For any absolute value of the strain-rate triaxiality, $u = 2|D_m|/D_e$, *the parametric representation of the yield surface of the Tresca porous solid is*:

(a) *For stress states such that* $\Sigma_m \geq 0$ *and* $J_3^{\Sigma} \leq 0$:

- *For* $u \leq f$:

$$\begin{cases} \dfrac{\Sigma_m}{\sigma_T} = \dfrac{1-f}{12u} + \dfrac{1}{24}\dfrac{16u\sqrt{uf}+6uf+f^2+9u^2}{u\sqrt{uf}}\ln\left(\dfrac{\sqrt{u}+\sqrt{f}}{\sqrt{f}-\sqrt{u}}\right) \\ \qquad -\dfrac{1}{24}\dfrac{6u+16u^{3/2}+1+9u^2}{u^{3/2}}\ln\left(\dfrac{\sqrt{u}+1}{1-\sqrt{u}}\right)+\dfrac{4}{3}\ln\left(\dfrac{\sqrt{f}-\sqrt{u}}{\sqrt{f}(1-\sqrt{u})}\right) \\ \dfrac{\Sigma_e}{\sigma_T} = -\dfrac{1}{8}\left(\begin{array}{l} 5(f-1)+\frac{3}{2}\dfrac{u^2-2uf+f^2}{\sqrt{uf}}\ln\left(\dfrac{\sqrt{u}+\sqrt{f}}{\sqrt{f}-\sqrt{u}}\right) \\ -\dfrac{3}{2}\dfrac{(u^2-2u+1)}{\sqrt{u}}\ln\left(\dfrac{\sqrt{u}+1}{1-\sqrt{u}}\right) \end{array}\right) \end{cases} \tag{7.95}$$

- *For* $f < u < 1$:

$$\begin{cases} \dfrac{\Sigma_m}{\sigma_T} = \dfrac{1-f}{12u} + \dfrac{1}{24}\dfrac{16u\sqrt{uf}+6uf+f^2+9u^2}{u\sqrt{uf}}\ln\left(\dfrac{\sqrt{u}+\sqrt{f}}{\sqrt{u}-\sqrt{f}}\right) \\ \qquad -\dfrac{1}{24}\dfrac{6u+16u^{3/2}+1+9u^2}{u^{3/2}}\ln\left(\dfrac{\sqrt{u}+1}{1-\sqrt{u}}\right)+\dfrac{4}{3}\ln\left(\dfrac{\sqrt{u}-\sqrt{f}}{\sqrt{f}(1-\sqrt{u})}\right) \\ \dfrac{\Sigma_e}{\sigma_T} = -\dfrac{1}{8}\left(\begin{array}{l} 5(f-1)+\dfrac{3}{2}\dfrac{u^2-2fu+f^2}{\sqrt{uf}}\ln\left(\dfrac{\sqrt{u}+\sqrt{f}}{\sqrt{u}-\sqrt{f}}\right) \\ -\dfrac{3}{2}\dfrac{u^2-2u+1}{\sqrt{u}}\ln\left(\dfrac{1+\sqrt{u}}{1-\sqrt{u}}\right) \end{array}\right) \end{cases} \tag{7.96}$$

- *For* $u \geq 1$:

$$\begin{cases} \dfrac{\Sigma_m}{\sigma_T} = \dfrac{1-f}{12u} + \dfrac{1}{24}\dfrac{16u\sqrt{uf}+6uf+f^2+9u^2}{u\sqrt{uf}}\ln\left(\dfrac{\sqrt{u}+\sqrt{f}}{\sqrt{u}-\sqrt{f}}\right) \\ \qquad -\dfrac{1}{24}\dfrac{6u+16u^{3/2}+1+9u^2}{u^{3/2}}\ln\left(\dfrac{\sqrt{u}+1}{\sqrt{u}-1}\right)+\dfrac{4}{3}\ln\left(\dfrac{\sqrt{u}-\sqrt{f}}{\sqrt{f}(\sqrt{u}-1)}\right) \\ \dfrac{\Sigma_e}{\sigma_T} = -\dfrac{1}{8}\left(\begin{array}{l} 5(f-1)+\dfrac{3}{2}\dfrac{u^2-2fu+f^2}{\sqrt{uf}}\ln\left(\dfrac{\sqrt{u}+\sqrt{f}}{\sqrt{u}-\sqrt{f}}\right) \\ -\dfrac{3}{2}\dfrac{u^2-2u+1}{\sqrt{u}}\ln\left(\dfrac{1+\sqrt{u}}{\sqrt{u}-1}\right) \end{array}\right) \end{cases} \tag{7.97}$$

(b) *For stress states such that* $\Sigma_m \geq 0$ *and* $J_3^{\Sigma} \geq 0$:

- *For* $u \leq f$:

$$\begin{cases} \dfrac{\Sigma_m}{\sigma_T} = \dfrac{1-f}{12u} + \dfrac{1}{24}\dfrac{(9u^2-6fu+f^2)}{u\sqrt{uf}}\arctan\left(\dfrac{2\sqrt{uf}}{f-u}\right) \\ \qquad -\dfrac{1}{24}\dfrac{(9u^2-6u+1)}{u^{3/2}}\arctan\left(\dfrac{2\sqrt{u}}{1-u}\right) + \dfrac{2}{3}\ln\left(f\dfrac{u+1}{u+f}\right) \\ \dfrac{\Sigma_e}{\sigma_T} = -\dfrac{1}{8}\left(\begin{array}{l} 5(f-1) + \dfrac{3}{2}\dfrac{u^2+2uf+f^2}{\sqrt{uf}}\arctan\left(\dfrac{2\sqrt{uf}}{f-u}\right) \\ \qquad -\dfrac{3}{2}\dfrac{u^2+2u+1}{\sqrt{u}}\arctan\left(\dfrac{2\sqrt{u}}{1-u}\right) \end{array}\right) \end{cases} \tag{7.98}$$

- *For* $f < u < 1$

$$\begin{cases} \dfrac{\Sigma_m}{\sigma_T} = \dfrac{1+f}{12u} + \dfrac{1}{24}\dfrac{9u^2-6uf+f^2}{u\sqrt{uf}}\arcsin\left(\dfrac{2\sqrt{uf}}{u+f}\right) \\ \qquad -\dfrac{1}{24}\dfrac{(9u^2-6u+1)}{u^{3/2}}\arctan\left(\dfrac{2\sqrt{u}}{1-u}\right) + \dfrac{2}{3}\ln\left(\dfrac{(u+f)(u+1)}{f}\right) - 16\ln(2) - 2 \\ \dfrac{\Sigma_e}{\sigma_T} = -\dfrac{1}{8}\left(\begin{array}{l} 10u - 5(f+1) + \dfrac{3}{2}\dfrac{(u^2+2uf+f^2)}{\sqrt{uf}}\arcsin\left(\dfrac{2\sqrt{uf}}{u+f}\right) \\ -\dfrac{3}{2}\dfrac{(u^2+2u+1)}{\sqrt{u}}\arctan\left(\dfrac{2\sqrt{u}}{1-u}\right) \end{array}\right) \end{cases} \tag{7.99}$$

- *For* $u \geq 1$

$$\begin{cases} \dfrac{\Sigma_m}{\sigma_T} = \dfrac{f-1}{12u} + \dfrac{1}{24}\dfrac{9u^2-6uf+f^2}{u\sqrt{uf}}\arcsin\left(\dfrac{2\sqrt{uf}}{u+f}\right) \\ \qquad -\dfrac{1}{24}\dfrac{9u^2-6u+1}{u^{3/2}}\arcsin\left(\dfrac{2\sqrt{u}}{u+1}\right) + \dfrac{2}{3}\ln\left(\dfrac{u+f}{f(u+1)}\right) \\ \dfrac{\Sigma_e}{\sigma_T} = -\dfrac{1}{8}\left(\begin{array}{l} 5(1-f) + \dfrac{3}{2}\dfrac{(u^2+2uf+f^2)}{\sqrt{uf}}\arcsin\left(\dfrac{2\sqrt{uf}}{u+f}\right) \\ -\dfrac{3}{2}\dfrac{(u^2+2u+1)}{\sqrt{u}}\arcsin\left(\dfrac{2\sqrt{u}}{u+1}\right) \end{array}\right) \end{cases} \tag{7.100}$$

Based on the centro-symmetry property of the yield locus, demonstrated earlier, the parametric representation of the yield locus corresponding to stress states such that $\Sigma_m \leq 0$ and $J_3^{\Sigma} \geq 0$ *can be easily obtained from* Eqs. (7.95) to (7.100).
Thus,

(c) *For stress states such that* $\Sigma_m \leq 0$ *and* $J_3^{\Sigma} \geq 0$:

$$\begin{cases} \dfrac{\Sigma_m}{\sigma_T} = -\dfrac{\Sigma_m}{\sigma_T}\Big|_{J_3^{\Sigma} \leq 0,\ \Sigma_m \geq 0} \\ \dfrac{\Sigma_e}{\sigma_T} = \dfrac{\Sigma_e}{\sigma_T}\Big|_{J_3^{\Sigma} \leq 0,\ \Sigma_m \geq 0} \end{cases} \tag{7.101}$$

the right-hand expressions of Eq. (7.101) *are given by the corresponding* Eqs. (7.95)–(7.97).

(d) *For* $\Sigma_m \leq 0$ and $J_3^{\Sigma} \leq 0$:

$$\begin{cases} \dfrac{\Sigma_m}{\sigma_T} = -\dfrac{\Sigma_m}{\sigma_T}\Big|_{J_3^{\Sigma} \geq 0,\ \Sigma_m \geq 0} \\ \dfrac{\Sigma_e}{\sigma_T} = \dfrac{\Sigma_e}{\sigma_T}\Big|_{J_3^{\Sigma} \geq 0,\ \Sigma_m \geq 0} \end{cases} \tag{7.102}$$

where the right-hand side of the expression in Eq. (7.102) *is given by the corresponding* Eqs. (7.98)–(7.100).

Proof In the following, we present the calculations that lead to the parametric representation of the yield surface of the porous aggregate for Case (a). For all the other loading conditions, the analysis can be done in a similar manner.

It can be easily seen that for $D_m \geq 0$ and $D'_{11} \geq 0$, Eqs. (7.84)–(7.85) lead to:

$$(\partial \Psi^{+}_{\text{Tresca}} / \partial \mathrm{D}_{11}) > (\partial \Psi^{+}_{\text{Tresca}} / \partial \mathrm{D}_{33}) \tag{7.102}$$

and $\partial \Psi^{+}_{\text{Tresca}} / \partial \mathrm{D}_m \geq 0$,

so the stress state at yielding obtained with Eq. (7.83) is such that $\Sigma_{11} > \Sigma_{33}$ ($J_3^{\Sigma} \leq 0$) and $\Sigma_m \geq 0$. Moreover, for any absolute value of the strain-rate triaxiality, $u = 2|\mathrm{D}_m|/\mathrm{D}_e$, we obtain:

$$\begin{cases} \dfrac{\Sigma_m}{\sigma_T} = \dfrac{1}{12}\left(F_i\left(\dfrac{u}{f}\right) - F_i(u) + u\left(\dfrac{1}{f}F_i'\left(\dfrac{u}{f}\right) - F_i'(u)\right)\right) \\ \dfrac{\Sigma_e}{\sigma_T} = -\dfrac{u^2}{8}\left(\dfrac{1}{f}F_i'\left(\dfrac{u}{f}\right) - F_i'(u)\right) \end{cases} \tag{7.103}$$

In the above equation, $i = 1, 2$, and the prime symbol indicates the first derivative of the respective functions. Further substitution of the expressions of $F_1(y)$ and $F_2(y)$ given by Eq. (7.85) into Eq. (7.103) leads to Eqs. (7.95)–(7.97).

Remark It is worth noting that according to Cazacu et al. [18] criterion, the yield surface of the porous Tresca material is smooth. In particular, there are no singularities for hydrostatic states. Indeed, although in the plane $(\Sigma_m/\sigma_T, \Sigma_e/\sigma_T)$ the yield locus is represented by two curves, one corresponding to axisymmetric stress states for which $J_3^{\Sigma} \leq 0$ while the other corresponds to axisymmetric stress states for

which $J_3^{\Sigma} \geq 0$, these two curves coincide for purely hydrostatic loading. This is because the limit when $u \to \infty$ of the Eq. (7.97) is:

$$\lim_{\substack{J_3^{\Sigma}\to 0 \\ J_3^{\Sigma}\leq 0}} (\Sigma_m) = -\frac{2}{3}\sigma_T \ln f \quad \text{and} \quad \lim_{\substack{J_3^{\Sigma}\to 0 \\ J_3^{\Sigma}\leq 0}} (\Sigma_e) = 0$$

while the limit when $u \to \infty$ of Eq. (7.100) is given by:

$$\lim_{\substack{J_3^{\Sigma}\to 0 \\ J_3^{\Sigma}\geq 0}} (\Sigma_m) = -\frac{2}{3}\sigma_T \ln f \quad \text{and} \quad \lim_{\substack{J_3^{\Sigma}\to 0 \\ J_3^{\Sigma}\geq 0}} (\Sigma_e) = 0$$

This means that

$$\lim_{\substack{J_3^{\Sigma}\to 0 \\ J_3^{\Sigma}\leq 0}} (\Sigma_m) = \lim_{\substack{J_3^{\Sigma}\to 0 \\ J_3^{\Sigma}\geq 0}} (\Sigma_m) = -\frac{2}{3}\sigma_T \ln f \text{ and } \lim_{\substack{J_3^{\Sigma}\to 0 \\ J_3^{\Sigma}\leq 0}} (\Sigma_e) = \lim_{\substack{J_3^{\Sigma}\to 0 \\ J_3^{\Sigma}\geq 0}} (\Sigma_e) = 0. \quad (7.104)$$

Similarly, using Eqs. (7.101) and (7.102), it can be easily shown that according to Cazacu's et al. [18] criterion for a porous Tresca material under compressive hydrostatic loading yielding occurs at $|\Sigma_m| = \frac{2}{3}\sigma_T \ln f$. Therefore, for hydrostatic loadings the exact solution is predicted (see also Theorem 7.2 and discussion). Also, it can verified that Cazacu's et al. [18] criterion predicts the exact value of the yield stress for purely deviatoric axisymmetric loadings, namely that $\Sigma_e = \sigma_T(1-f)$. Indeed, by taking $u \to 0$ in Eq. (7.95) one obtains:

$$\lim_{\substack{u\to 0 \\ J_3^{\Sigma}\leq 0}} (\Sigma_m) = 0 \quad \text{and} \quad \lim_{\substack{u\to 0 \\ J_3^{\Sigma}\leq 0}} (\Sigma_e) = \sigma_T(1-f); \quad (7.105)$$

on the other hand by taking the limit when $u \to 0$ in Eq. (7.98), one obtains:

$$\lim_{\substack{u\to 0 \\ J_3^{\Sigma}\geq 0}} (\Sigma_m) = 0 \quad \text{and} \quad \lim_{\substack{u\to 0 \\ J_3^{\Sigma}\geq 0}} (\Sigma_e) = \sigma_T(1-f). \quad (7.106)$$

To better illustrate the very specific dependence on the signs of the mean stress, Σ_m, and the third-invariant J_3^{Σ} of the yield locus of the porous Tresca material, in Fig. 7.32 is shown the theoretical yield surface in the plane $((\Sigma_{33}-\Sigma_{11})/\sigma_T, \Sigma_m/\sigma_T)$ for several porosities $f = 0.1\%$, 1%, 2% and 5%, respectively. All the yield surfaces show the same trends described above. Irrespective of the porosity, the intersection of the curves corresponding to $\Sigma_{11} = \Sigma_{22} \leq \Sigma_{33}$ $(J_3^{\Sigma} \geq 0)$ and $\Sigma_{11} = \Sigma_{22} \geq \Sigma_{33}$ $(J_3^{\Sigma} \leq 0)$ belongs to the axis $\Sigma_m = 0$ (i.e., there are no discontinuities by passing from states characterized by $J_3^{\Sigma} \geq 0$ to states characterized by $J_3^{\Sigma} \leq 0$).

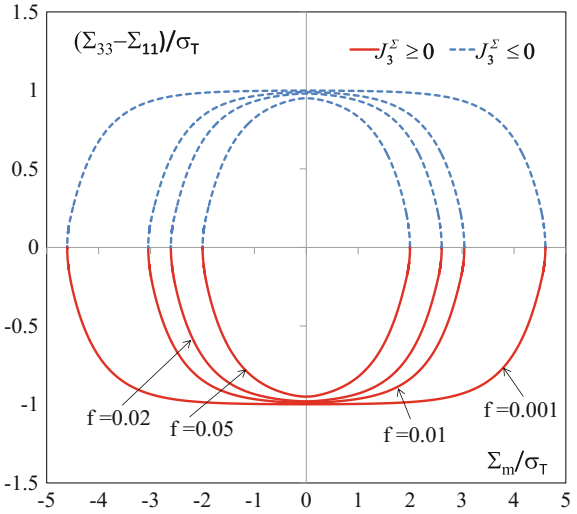

Fig. 7.32 Yield surface of a porous Tresca material according to the Cazacu et al. [18] criterion for loadings such $\Sigma_{11} = \Sigma_{22} \geq \Sigma_{33}$ ($J_3^{\Sigma} \leq 0$) and loadings such $\Sigma_{11} = \Sigma_{22} \leq \Sigma_{33}$ ($J_3^{\Sigma} \geq 0$), respectively, for porosity $f = 0.001$, $f = 0.01$, $f = 0.02$, and $f = 0.05$, respectively. Stresses are normalized by the matrix yield stress in uniaxial tension, σ_T

7.2.4.2 Implications of Adopting the Classic Simplifying Hypothesis When Modeling Porous Materials with Tresca Matrix

As discussed in Sect. 7.2.3.1, the insensitivity of Gurson's [30] criterion to J_3^{Σ}, the third-invariant of the stress deviator, [see also Eq. (7.41)] and the ensuing strong symmetry properties of Gurson [30] yield surface for a porous Mises material are direct consequences of neglecting the "cross-term" $D_m D'_{11}$ in the expression of the local plastic dissipation [see Eq. (7.34)]. It is worth analyzing the implications of adopting the same simplifying hypothesis when deriving the plastic potential of a porous material with matrix described by Tresca's yield criterion.

It can be easily shown that irrespective of the loading scenario (i.e., the respective signs of D_m and D'_{11}), if we neglect the cross-term in the expression of the local plastic dissipation associated with Tresca yield criterion, the strain-rate potential of the porous Tresca material reduces to the Gurson's [29] strain-rate potential for a von Mises material.

For example, in the case when ($D_m \geq 0$ and $D'_{11} > 0$), the expression of the strain-rate potential of the porous Tresca material is (see Theorem 7.8):

$$\Psi^{+}_{\text{Tresca}}(\mathbf{D}, f) = \frac{1}{V}\int_{\Omega}\left(\frac{1}{2}\sqrt{D_m^2\frac{b^6}{r^6} + D_{11}'^2 + 2D'_{11}D_m\frac{b^3}{r^3}} + \frac{3}{2}\sqrt{D_m^2\frac{b^6}{r^6} + 2D'_{11}D_m\frac{b^3}{r^3}\cos(2\theta) + D_{11}'^2}\right)\mathrm{d}\Omega. \tag{7.107}$$

Note that if in the above equation the cross-term $D_m D'_{11}$ is neglected, we obtain:

$$\Psi^{++}_{\text{Tresca}}(\mathbf{D},f) \simeq \frac{1}{V}\int_{\Omega} \sqrt{4D_m^2(b/r)^6 + 4\,D_{11}'^2}\, d\Omega = \Psi_{Gurson}(\mathbf{D},f). \tag{7.108}$$

It is thus clearly demonstrated that neglecting the cross-term $D_m D'_{11}$ amounts to erasing the specificities of the plastic flow of the matrix, the resulting criterion for the porous material being the same whether the plastic response of the matrix is described by Tresca criterion, which incorporates dependence on both the second and third-invariant of stress, or by von Mises criterion which describes only the influence of the second-invariant of stress. Furthermore, Cazacu et al. [18] also demonstrated that Gurson [30] yield criterion is an upper bound of the yield criterion for porous solids with Tresca matrix developed in Cazacu et al. [18].

Figure 7.33 shows different zooms of the yield surface in the tensile quadrant in comparison with the Gurson's [30] yield surface for the same porosity. Note that the Gurson's [30] criterion is an upper bound of the exact yield locus of a porous material with Tresca matrix and coincides with it only for purely hydrostatic ($\Sigma_{11} = \Sigma_{22} = \Sigma_{33}$) or purely deviatoric loadings ($\Sigma_m = 0$) (for a complete proof see Cazacu et al. [18]).

In contrast to Gurson [30] model, the Cazacu et al. [18] criterion for a porous Tresca material predicts that there is an increasing influence of J_3^{Σ} as stress triaxiality increases. It is predicted that only for stress states corresponding to stress triaxialities T approaching infinity (i.e., purely hydrostatic states), the effect of J_3^{Σ} starts to decrease, the Gurson [30] and Cazacu et al. [18] yield curves coinciding at the purely hydrostatic point ($J_3^{\Sigma} = 0$), as it should be [see Eq. (7.108)].

It is worth summarizing the key features of the Cazacu et al. [18] criterion for porous Tresca materials under axisymmetric states:

- Yielding is invariant to the transformation: $(\Sigma_m, \boldsymbol{\Sigma}') \rightarrow (\Sigma_m, -\boldsymbol{\Sigma}')$, so the dilatational response of the porous Tresca material depends on the sign of mean stress, Σ_m (tension–compression asymmetry);
- Yielding of the porous Tresca material depends on the third-invariant of the stress deviator. Furthermore for tensile hydrostatic pressure ($\Sigma_m \geq 0$) the response for axisymmetric stress states corresponding to $J_3^{\Sigma} \geq 0$ is softer than for axisymmetric stress states corresponding to $J_3^{\Sigma} \leq 0$. For purely deviatoric loadings, the response is the same, and the effect of J_3^{Σ} becomes noticeable with

Fig. 7.33 Zoom on the tensile quadrant of the yield surface for a porous von Mises material according to Gurson [30] criterion in comparison with Cazacu et al. [18] yield surface for a porous Tresca material (solid line) for the same porosity ($f = 5\%$) and axisymmetric stress states corresponding to $\Sigma_{11} = \Sigma_{22} \geq \Sigma_{33}$ ($J_3^{\Sigma} \leq 0$) and $\Sigma_{11} = \Sigma_{22} \leq \Sigma_{33}$ ($J_3^{\Sigma} \geq 0$), respectively, within following ranges: **a** low stress triaxialities ($0 \leq \Sigma_m/\sigma_T \leq 0.8$; $0.85 < \Sigma_e/\sigma_T < (1-f)$); **b** intermediate triaxialities ($0.8 < \Sigma_e/\sigma_T < 1.8$; $0.5 < \Sigma_e/\sigma_T < 0.9$): (c) high stress triaxialities ($1.8 < \Sigma_m/\sigma_T < 2.1; 0 < \Sigma_e/\sigma_T < 0.7$) ▶

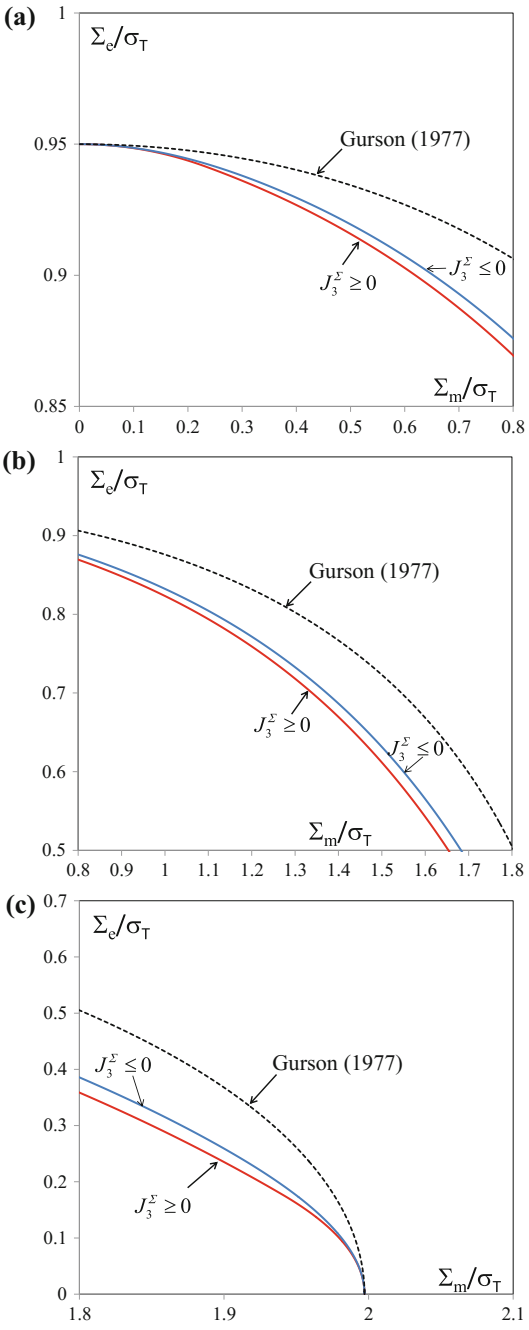
(a)
Σ_e/σ_T
Gurson (1977)
$J_3^\Sigma \le 0$
$J_3^\Sigma \ge 0$
Σ_m/σ_T
(b)
Σ_e/σ_T
Gurson (1977)
$J_3^\Sigma \ge 0$
$J_3^\Sigma \le 0$
Σ_m/σ_T
(c)
Σ_e/σ_T
$J_3^\Sigma \le 0$
Gurson (1977)
$J_3^\Sigma \ge 0$
Σ_m/σ_T

increasing triaxiality. For triaxialities approaching infinity, the effect of J_3^{Σ} starts to decrease, and both yield surfaces coincide at the purely hydrostatic point (e.g., see Fig. 7.33).

- The criterion reproduces the exact solution of a hollow sphere obeying Tresca's yield criterion and subjected to hydrostatic loading.
- The Gurson's [30] criterion is an upper bound of the Cazacu et al. [18]. The two criteria coincide only for purely deviatoric axisymmetric loading or purely hydrostatic loading. Specifically, for purely deviatoric loading, yielding occurs at $\Sigma_e = \sigma_T(1-f)$, while for purely hydrostatic loadings, yielding occurs at $\Sigma_m = \pm\frac{2}{3}\sigma_T \ln f$.

7.2.4.3 Comparison of the Cazacu et al. [18] Yield Criterion with F.E. Unit-Cell Calculations

Cazacu et al. [13] reported results of F.E. unit-cell calculations for the case when the matrix is governed by Tresca yield criterion. The main focus was on assessing the importance of the consideration of the specificities of the local plastic dissipation on yielding and void evolution of a porous Tresca material, and verify the trends predicted by Cazacu et al. [18] criterion. Given that previous F.E. unit-cell studies did not concern porous Tresca materials, another outcome of the study is the possibility to compare the F.E. unit-cell results for a von Mises material with that of a Tresca material using the same unit-cell geometry and loading history.

In the following, we present only the main results of Cazacu et al. [13] F.E. analyses of cubic unit cells containing a single initially spherical cavity. For more details concerning the boundary-value problem, and the geometry of the unit cell considered, the reader is referred to Sect. 7.2.3.2. Likewise, for details concerning the F.E. implementation of an elastic–plastic model with yielding according to Tresca criterion, the reader should refer to Chap. 4.

As an example, in Fig. 7.34a–d are presented comparisons between the theoretical yield surfaces according to the Cazacu et al. [18] criterion and the F.E. unit-cell results for several porosities ranging from $f = 0.001$ to $f = 0.04$. The numerical points correspond to prescribed axisymmetric loads such that the stress triaxiality, T, is fixed. For either loading scenarios (i.e., $J_3^{\Sigma} \leq 0$ or $J_3^{\Sigma} \geq 0$), the stress triaxialities T range from ± 0.25 to ± 25. Note that the unusual features of the dilatational response predicted by the Cazacu et al. [18] criterion [Eqs. (7.95)–(7.102)], namely the sensitivity to the sign of the applied stress for triaxialities different from 0 and $\pm\infty$, and the very specific coupling between the mean stress and the third-invariant of the stress deviator are confirmed by the numerical results. Irrespective of the porosity level, f, the numerical yield surface is no longer

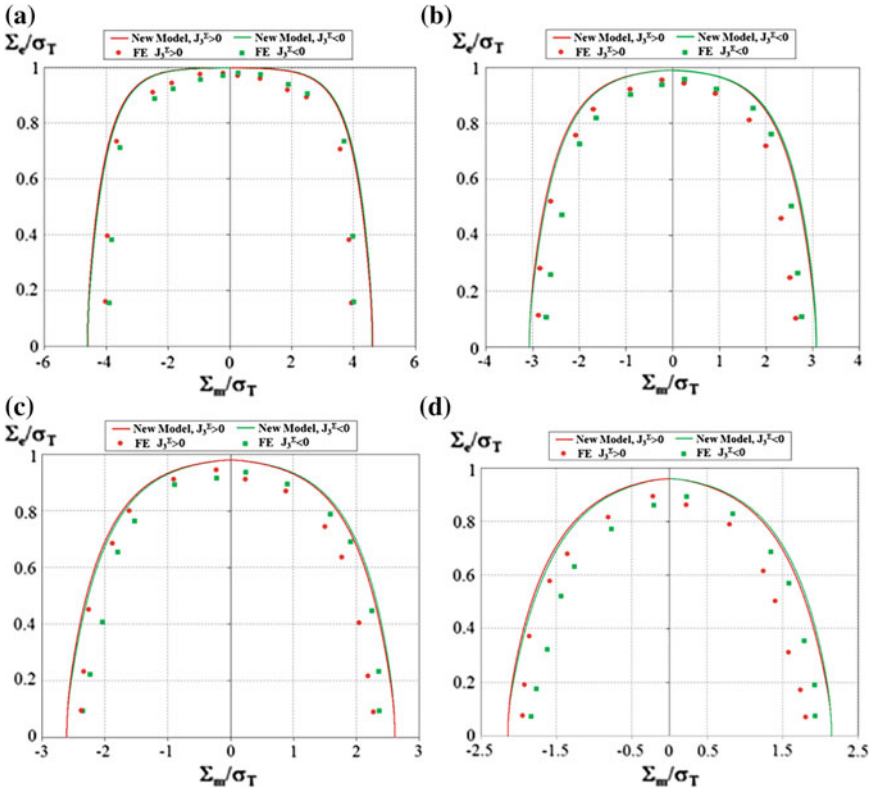

Fig. 7.34 Comparison between finite-element calculations and the analytical Cazacu et al. [18] yield criterion for an porous material with Tresca matrix and initial porosity: **a** $f = 0.001$, **b** $f = 0.01$, **c** $f = 0.02$, and **d** $f = 0.04$

symmetric with respect to the axis $\Sigma_m = 0$; a given fixed value of the stress triaxiality T corresponds to two different yield points. It is also worth noting that for both tensile and compressive loadings, the relative positions of the theoretical yield points for $J_3^\Sigma \leq 0$ and $J_3^\Sigma \geq 0$ are also confirmed by the F.E. results. Specifically, for tensile axisymmetric loadings such that the axial stress is larger than the lateral stress ($J_3^\Sigma \geq 0$), the response is softer than in the case when the applied stresses are such that the axial stress is smaller than the lateral stress ($J_3^\Sigma \leq 0$) (see Fig. 7.34). Hence, the very specific coupling between the mean stress Σ_m and the third-invariant J_3^Σ on yielding of the porous Tresca material predicted by the analytic criterion is also confirmed by the F.E. unit-cell calculations. Also, it is clearly

seen that the sensitivity to J_3^{Σ} is strongly influenced by the level of porosity in the material. For a low porosity, the third-invariant effects are less pronounced than in the case of a larger porosity (e.g., compare Fig. 7.34a, d).

Cazacu et al. [13] also reported F.E. cell calculations of the stress–strain response, and void evolution. The F.E simulations were conducted for a fixed ratio of the axial and lateral true stresses corresponding to different levels of stress triaxiality, T, for stress histories corresponding to positive and negative values of J_3^{Σ}, respectively. Figure 7.35 compares the porosity f versus the overall equivalent strain E_e [for the definition E_e see Eq. (7.51)] curves for axisymmetric loading histories at fixed stress triaxialities $T = 2$ and $T = 3$, respectively. The initial porosity was taken $f_0 = 0.0013$ such as to also enable comparison with the results for a porous von Mises material with the same initial porosity (see Sect. 7.2.3.4).

Let us first note the very strong influence of the stress triaxiality on the rate of void growth for the porous Tresca material. Secondly, irrespective of the value of the triaxiality both the analytical and F.E. cell calculations show that there is a marked influence of the third-invariant of the stress deviator on void growth. Indeed, comparison between the results presented in Fig. 7.35a, b shows that the criterion accounts for the influence of the third-invariant on void growth, the rate of void growth being faster for loadings such that $J_3^{\Sigma} \geq 0$. This is to be expected since according to the Cazacu et al. [18] model for states corresponding to tensile mean stresses, the response is softer for $J_3^{\Sigma} \geq 0$ than for $J_3^{\Sigma} \leq 0$ (see Fig. 7.33). Note also that the agreement between numerical results and model is good, in particular for axisymmetric loadings corresponding to $\Sigma_1 = \Sigma_2 \geq \Sigma_3$ ($J_3^{\Sigma} \leq 0$).

Figure 7.36 shows a comparison between the macroscopic stress–strain response (Σ_e vs. E_e) according to Cazacu et al. [18] criterion and the numerical points. Note that since the analytical model captures the effects of the stress triaxiality and J_3^{Σ} on void growth, it describes correctly the influence of the loading history on the softening of the porous solid.

Figure 7.37 shows the comparison between the predictions for void collapse according to the analytical model and the F.E. unit-cell results while Fig. 7.38 shows the predictions of the effective stress versus equivalent strain response (Σ_e vs. E_e) for the porous Tresca material. The loading histories considered correspond to axisymmetric states at fixed compressive triaxialities $T = -2$ and $T = -3$, respectively. The initial porosity was considered higher ($f_0 = 0.0104$) such as to allow plastic strains to develop prior to void closure. It is worth noting that the rate of void collapse is much faster for loadings at stress triaxiality $T = -3$ than at $T = -2$. The agreement between numerical results and the model is very good.

Analysis of the effective stress Σ_e versus E_e curves in Fig. 7.38 shows that the analytical model predicts that the rate of hardening is higher for $T = -3$ than for

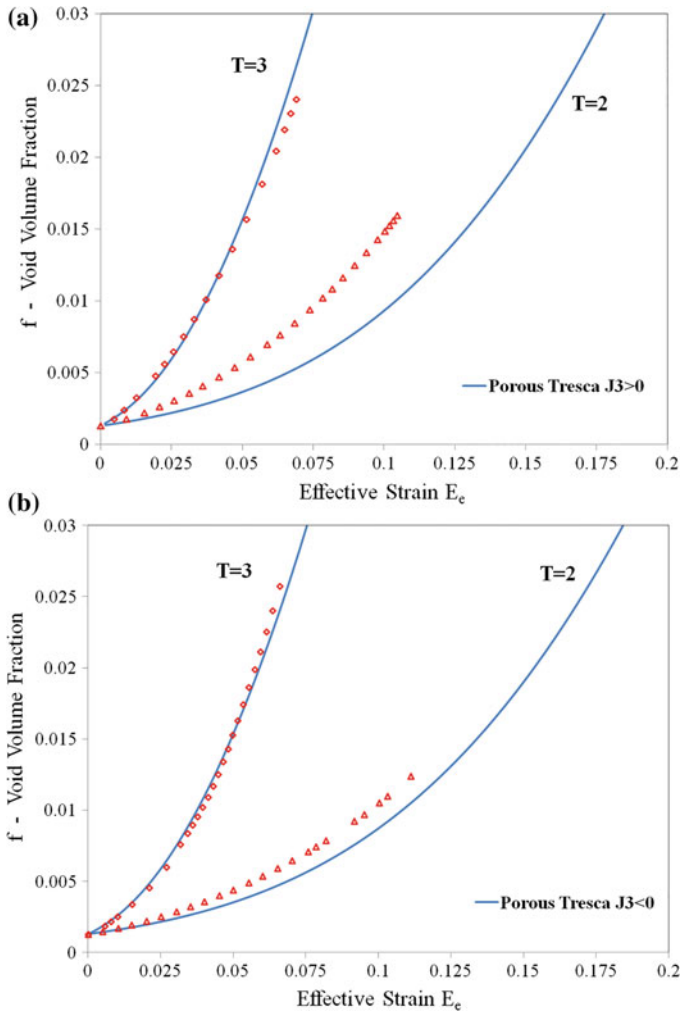

Fig. 7.35 Comparison between the void volume fraction evolution with the equivalent strain E_e according to the Cazacu et al. [18] analytical model, and F.E. unit-cell model calculations (symbols) for axisymmetric loadings at fixed stress triaxialities $T = 2$ and $T = 3$, respectively: **a** loadings such that $\Sigma_1 = \Sigma_2 \leq \Sigma_3$ ($J_3^{\Sigma} \geq 0$); **b** loadings such that $\Sigma_1 = \Sigma_2 \geq \Sigma_3$ ($J_3^{\Sigma} \leq 0$). Initial porosity f_0 = 0.0013 (after Cazacu et al. [13])

$T = -2$, but that the limiting state, which corresponds to f close to zero (void closure), is the same. This is in agreement with the F.E. unit-cell results.

Most importantly, these results correlate with the predicted void evolution shown in Fig. 7.37, i.e., for $T = -3$ the rate of void collapse is faster than for $T = -2$. Also, the specific influence of the coupling effect between Σ_m and J_3^{Σ} on

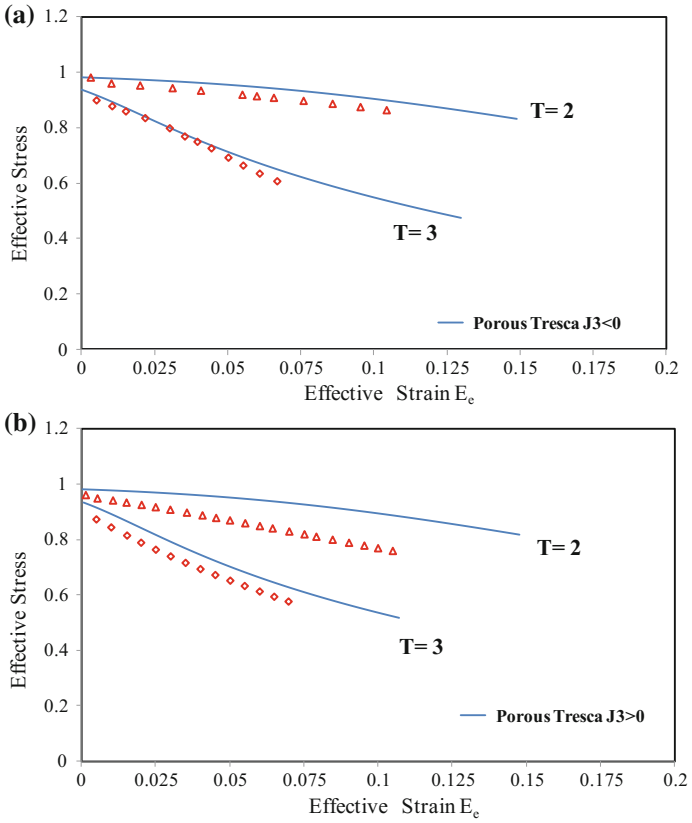

Fig. 7.36 Comparison between the effective stress $\Sigma_e = |\Sigma_1 - \Sigma_3|$ evolution with the equivalent strain E_e, according to the Cazacu et al. [18] analytical model and F.E. unit-cell model calculations (symbols) for axisymmetric loadings at fixed positive (tensile) triaxialities, $T = 2$ and $T = 3$, respectively: **a** loadings such that $\Sigma_1 = \Sigma_2 \geq \Sigma_3$ $(J_3^{\Sigma} \leq 0)$; **b** loadings such that $\Sigma_1 = \Sigma_2 \leq \Sigma_3$ $(J_3^{\Sigma} \geq 0)$. Initial porosity, f_0 = 0.0013 (after Cazacu et al. [13])

void evolution, predicted by the model, is confirmed by the F.E. unit-cell model (see Figs. 7.35 and 7.37). Indeed, for positive stress triaxialities (i.e., $\Sigma_m > 0$) the rate of void growth is faster for the case when loading is such that $\Sigma_1 = \Sigma_2 \leq \Sigma_3$ $(J_3^{\Sigma} \geq 0)$, and the overall response is softer than in the case when loading is such that $\Sigma_1 = \Sigma_2 \geq \Sigma_3$ $(J_3^{\Sigma} \leq 0)$ (see Fig. 7.35). However, for negative stress triaxialities (i.e., $\Sigma_m < 0$), the reverse holds true, i.e., void collapse is faster for axisymmetric loadings with $(J_3^{\Sigma} \leq 0)$ than for axisymmetric loadings with $(J_3^{\Sigma} \geq 0)$ (see Fig. 7.37).

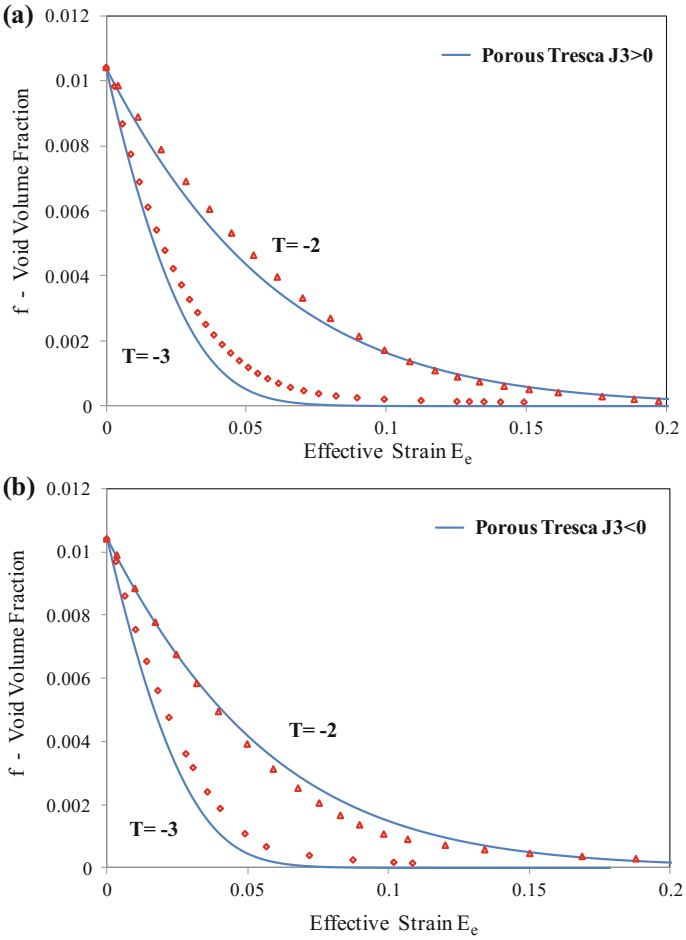

Fig. 7.37 Comparison between the void volume fraction evolution (collapse) as a function of the equivalent strain E_e according to the Cazacu et al. [18] analytical model, and F.E. unit-cell model calculations (symbols) for axisymmetric loadings at fixed negative (compressive) stress triaxialities $T = -2$ and $T = -3$, respectively, for: **a** loadings such that $\Sigma_1 = \Sigma_2 \leq \Sigma_3 (J_3^{\Sigma} \geq 0)$; (b) loadings such that $\Sigma_1 = \Sigma_2 \geq \Sigma_3$ $(J_3^{\Sigma} \leq 0)$. Initial porosity f_0 = 0.0104 (after Cazacu et al. [13])

7.2.4.4 Importance of the Local Plastic Heterogeneity on the Dilatational Response of a Porous Tresca Material

To assess the importance of accounting for the local heterogeneity of the plastic flow, in Fig. 7.39 are shown contours of constant equivalent plastic strain (i.e., local plastic dissipation $\pi_{\text{Tresca}}(\mathbf{d})$ normalized by σ_T) at various stages of the deformation process for axisymmetric loadings at fixed stress triaxiality $T = 2$ corresponding to

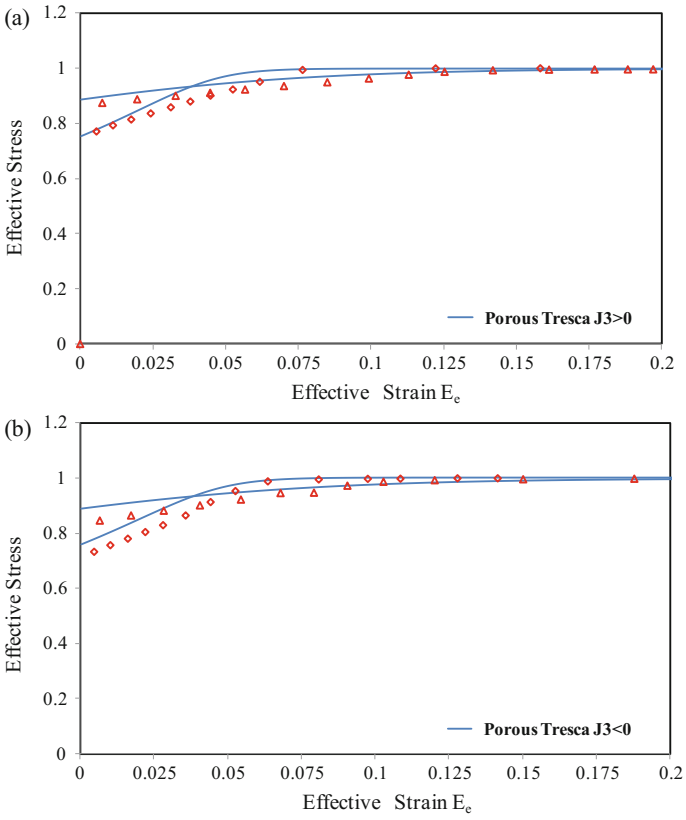

Fig. 7.38 Comparison between the effective stress $\Sigma_e = |\Sigma_1 - \Sigma_3|$ evolution with the equivalent strain E_e according to the Cazacu et al. [18] analytical model and F.E. unit-cell model calculations (symbols) for axisymmetric loadings at fixed negative (compressive) triaxialities, $T = -2$ and $T = -3$, respectively: **a** loadings such that $\Sigma_1 = \Sigma_2 \leq \Sigma_3$ ($J_3^{\Sigma} \geq 0$); **b** loadings such that $\Sigma_1 = \Sigma_2 \geq \Sigma_3$ ($J_3^{\Sigma} \leq 0$). Initial porosity, f_0 = 0.0104 (after Cazacu et al. [13])

$\Sigma_1 = \Sigma_2 \leq \Sigma_3$ $(J_3^{\Sigma} \geq 0)$ (Fig. 7.39a) and $\Sigma_1 = \Sigma_2 \geq \Sigma_3$ $(J_3^{\Sigma} \leq 0)$, respectively, (Fig. 7.39b) for an initial porosity $f_0 = 0.0013$. To allow comparison, we present the isocontours of the local plastic strain that correspond to the same level of the overall equivalent strain E_e. Note that for the two loadings, the distribution of plastic deformation in the unit cell is markedly different. For any fixed level of the overall equivalent strain E_e, the plastic zone is larger for loadings corresponding to $J_3^{\Sigma} \leq 0$ (see Fig. 7.39b) than in the case when loadings are such that $J_3^{\Sigma} \geq 0$ (Fig. 7.39a). This correlates with the rate of void growth being slower for $J_3^{\Sigma} \leq 0$ than for $J_3^{\Sigma} \geq 0$ (see Fig. 7.35). Also note, that for the axisymmetric loading such that $J_3^{\Sigma} \geq 0$ (i.e., axial stress greater than the lateral stresses throughout the

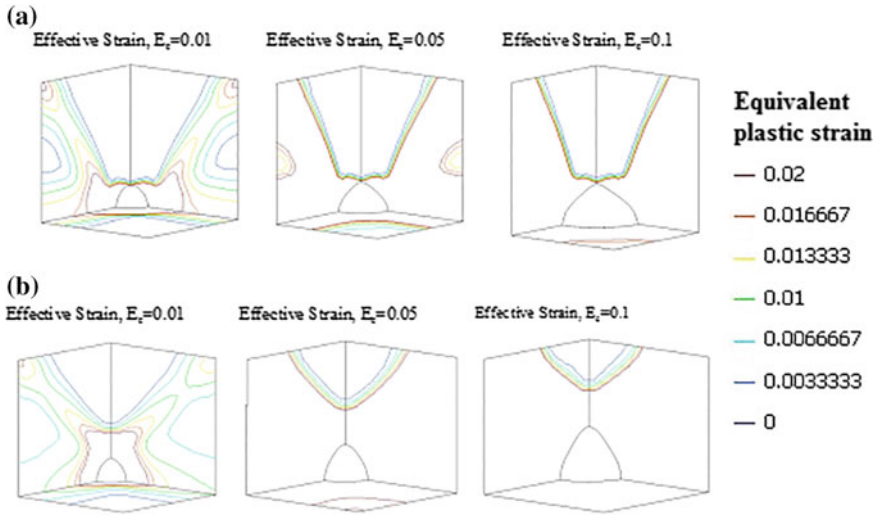

Fig. 7.39 Isocontours of the local equivalent plastic strain in the F.E. unit cell corresponding to several levels of the equivalent strain E_e of a porous Tresca material with an initial porosity $f_0 = 0.0013$ subject to axisymmetric loadings at fixed stress triaxiality, $T = 2$: **a** loadings with $\Sigma_1 = \Sigma_2 \leq \Sigma_3$ ($J_3^{\Sigma} \geq 0$); **b** loadings with $\Sigma_1 = \Sigma_2 \geq \Sigma_3$ ($J_3^{\Sigma} \leq 0$)

deformation history) the plastic zone extends less in the axial direction than in the case when $J_3^{\Sigma} \leq 0$ (i.e., axial stress less than the lateral stresses).

As discussed in Sect. 7.2.4.2, neglecting the "cross-term" $D_m D'_{11}$ in the expression of the matrix plastic dissipation leads to an approximate local plastic dissipation, which depends only on the radial coordinate [see Eq. (7.108)], so the heterogeneities in the plastic flow of the matrix are "smoothed out." However, comparison between Fig. 7.39a, b clearly illustrates that the local heterogeneities of the plastic dissipation are very important. Moreover, neglecting the heterogeneity of the plastic dissipation in the matrix, leads to a potential for the porous Tresca material identical to Gurson [30]. The fact that the Gurson's [30] model is not a good approximation for the mechanical response of a porous Tresca material is clearly seen from the results presented in Fig. 7.40. This figure shows the void evolution according to the Cazacu et al. [18] analytical model for the porous Tresca material, the F.E. unit-cell model with matrix governed by Tresca yield criterion, and the Gurson's [30] criterion predictions. The comparisons correspond to axisymmetric loadings at fixed triaxiality $T = 2$ and $\Sigma_1 = \Sigma_2 \leq \Sigma_3$ ($J_3^{\Sigma} \geq 0$) (Fig. 7.40a) and $\Sigma_1 = \Sigma_2 \geq \Sigma_3$ ($J_3^{\Sigma} \leq 0$), respectively (see Fig. 7.40b). Note that the differences in the rate of void growth between the Gurson [30] model and F.E. unit-cell results are significant. Moreover, irrespective of the sign of J_3^{Σ}, the Gurson [30] model predicts a lower porosity level in the material than the Cazacu et al. [18] criterion. Because Cazacu et al. [18] model for a porous Tresca material accounts for the coupling between Σ_m and J_3^{Σ}, void evolution depends on J_3^{Σ}. Indeed,

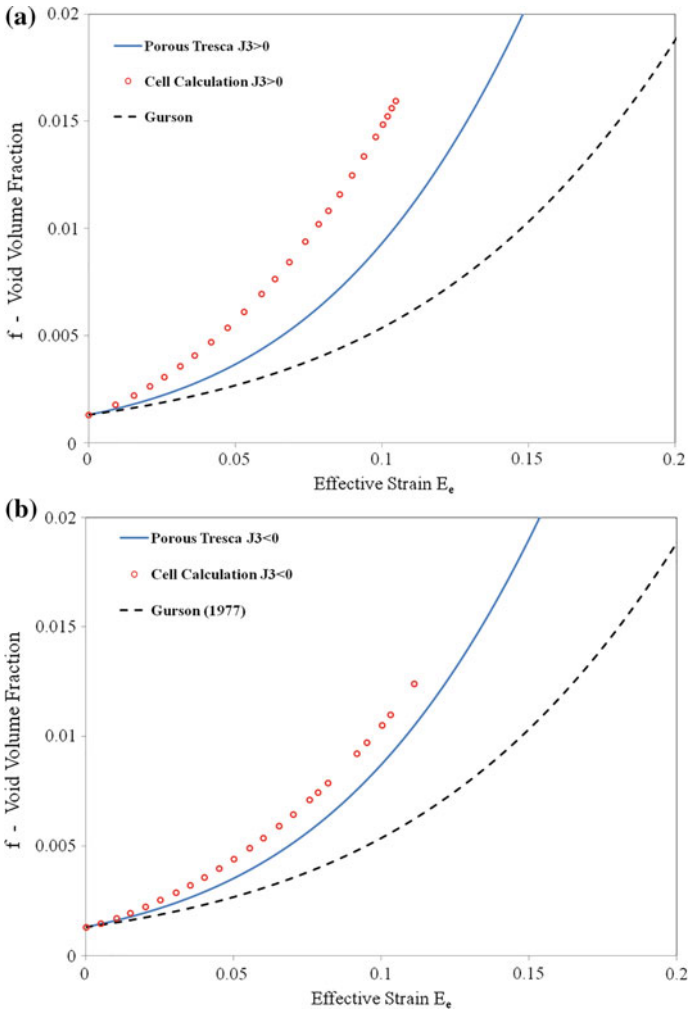

Fig. 7.40 Comparison between the void volume fraction evolution with equivalent strain E_e according to the porous Tresca model (Cazacu et al. [18]) (line), the Gurson [30] model (dashed line), and F.E. unit-cell calculations with matrix behavior governed by Tresca yield criterion (symbols) for axisymmetric loadings at fixed triaxiality $T = 2$ corresponding to: **a** loadings such that $\Sigma_1 = \Sigma_2 \leq \Sigma_3$ $(J_3^{\Sigma} \geq 0)$ and **b** loadings with $\Sigma_1 = \Sigma_2 \geq \Sigma_3$ $(J_3^{\Sigma} \leq 0)$. Initial porosity $f_0 = 0.0013$

according to the criterion the rate of void growth is faster for loadings such that $J_3^{\Sigma} \geq 0$ than for loadings corresponding to $J_3^{\Sigma} \leq 0$. Also, the rate of void collapse is much faster in a porous solid with Tresca matrix than in a porous solid governed by Gurson's [30] criterion (see Fig. 7.41). For example, for the same initial porosity

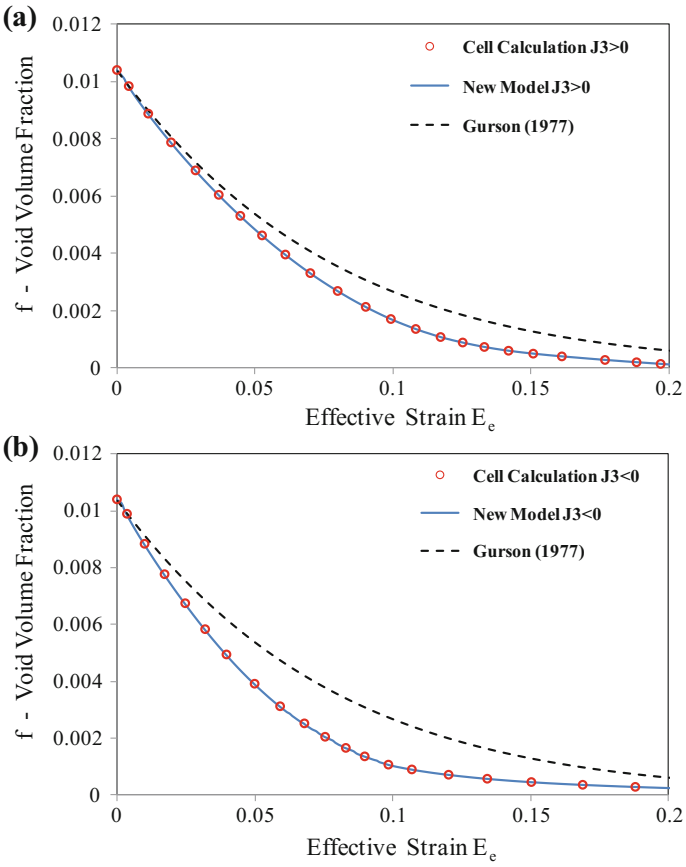

Fig. 7.41 Comparison between the void volume fraction evolution with the equivalent strain E_e according to the porous Tresca model (Cazacu et al. [18]) (line), the Gurson [30] model (dashed line), and F.E. unit-cell calculations with matrix behavior governed by Tresca yield criterion (symbols) for axisymmetric loadings at fixed triaxiality (symbols) $T = -2$ corresponding to: **a** loadings such that $\Sigma_1 = \Sigma_2 \leq \Sigma_3$ ($J_3^{\Sigma} \geq 0$) and **b** loadings with $\Sigma_1 = \Sigma_2 \geq \Sigma_3$ ($J_3^{\Sigma} \leq 0$). Initial porosity $f_0 = 0.01$

$f_0 = 1.1\%$, for axisymmetric loadings at a fixed negative triaxiality $T = -2$ (compressive mean stress) at $E_e = 0.1$, the void volume fraction according to the porous Tresca criterion are: $f = 0.16 f_0$ for loadings with $J_3^{\Sigma} \geq 0$ (Fig. 7.41a) and $f = 0.1 f_0$ for loadings with $J_3^{\Sigma} \leq 0$ (Fig. 7.41b), while according to the Gurson's [30] criterion: $f = 0.24 f_0$. Thus, Gurson's [30] criterion predicts that the porosity is almost double for the Cazacu et al. [18] porous Tresca material.

In summary, it is clearly seen that irrespective of the loading history, if the local plastic heterogeneity of the matrix is neglected, the rate of void growth or collapse

is drastically underestimated. It also reveals that one cannot adopt a Gurson-type model for description of the mechanical behavior of porous ductile materials with plastic deformation governed by a criterion other than von Mises.

7.2.4.5 3-D Strain-Rate Potential

The analysis of the mechanical response of a porous von Mises material for general 3-D loadings has revealed that although the presence of voids induces dependence on all invariants, the shape of the cross-sections of the yield surface with the octahedral plane deviates slightly from a circle, and changes very little as the absolute value of the mean strain-rate D_m increases (see Sect. 7.2.3.5). In the case when the matrix behavior is governed by Tresca yield criterion, which depends on both invariants, Cazacu et al. [18] analysis conducted for axisymmetric states has revealed that the effects of the third-invariant on the behavior of the porous material are much stronger than in case when the matrix is governed by von Mises criterion. Moreover, it was shown that for axisymmetric states the strain-rate potential and yield criterion of the porous Tresca material can be obtained analytically [e.g., see Eqs. (7.95)–(7.102)].

For general 3-D states, the integral representing the plastic dissipation of the porous Tresca material cannot be obtained in closed form, however the combined effects of all the invariants of the strain-rate $\mathbf{D}$ on the plastic response can be assessed numerically. Such an analysis was conducted by Revil-Baudard and Cazacu [55] who established that for a porous Tresca material the relationship between J_2^D and J_3^D at yielding depends on both the level of the mean strain-rate D_m and on the porosity. Specifically, there is a drastic change in the shape of the cross-section of the isosurface in the octahedral plane. As the absolute value of the mean strain-rate D_m increases, the shape of the cross-section evolves from a regular hexagon $(D_m = 0)$ to a triangle with rounded corners. However, the level of porosity is key in how fast the shape of the cross-section changes with increasing D_m. In the following are presented the main findings, for more details the reader is referred to Revil-Baudard and Cazacu [55].

As discussed in Sect. 7.2.4.1, an upper-bound estimate of the exact strain-rate potential of a porous Tresca material is:

$$\Psi^{+}_{\text{Tresca}}(\mathbf{D},f) = \frac{1}{2\text{V}}\int_{\Omega}\left(|d_I| + |d_{II}| + |d_{III}|\right)\mathrm{d}V, \tag{7.109}$$

with d_I, d_{II} and d_{III} being the principal values (unordered) of the strain-rate $\mathbf{d} = (\nabla\mathbf{v} + \nabla\mathbf{v}^T)/2$ corresponding to Rice and Tracey [58] velocity field given by Eq. (7.28). Only for axisymmetric loadings one can determine the signs of d_I, d_{II} and d_{III} and calculate the integral of Eq. (7.109) explicitly, without any approximation (see Sect. 7.2.4.1). For general 3-D states, $\Psi^{+}_{\text{Tresca}}(\mathbf{D},f)$ can only be estimated numerically. To this end, in Revil-Baudard and Cazacu [55], the hollow

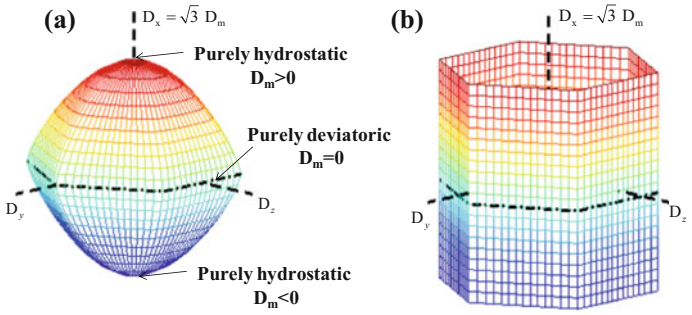

Fig. 7.42 **a** The 3-D isosurface for a porous Tresca material for both tensile ($D_m > 0$) and compressive ($D_m < 0$) states. Note that this convex surface contains all the points (D_m, R, γ) such that $\Psi^{+}_{\text{Tresca}}(\mathbf{D}, f) = 9.21 \times 10^{-3}$ with $f = 1\%$. **b** Fully dense material (Tresca SRP) (after Revil-Baudard and Cazacu [55])

sphere was discretized with 125,000 hexahedral elementary volumes with one integration point at the center. For axisymmetric loadings, the numerical estimate of $\Psi^{+}_{\text{Tresca}}(\mathbf{D}, f)$ was compared to the analytical results [Eqs. (7.84)–(7.87)], the differences being negligible (error less than 10^{-7}).

As an example, in Fig. 7.42a is shown the normalized 3-D isosurface of the porous Tresca material with $f = 1\%$ for states characterized by $(D_m \geq 0)$ and $(D_m \leq 0)$, respectively. Specifically, this convex surface contains all states (D_m, R, γ) that produce the same plastic dissipation $\Psi^{+}_{\text{Tresca}}(\mathbf{D}, f) = 9.21 \times 10^{-3}\ \text{s}^{-1}$ for the porous material [for the definitions of R and γ, see Eqs. (7.74)–(7.75)]. Let us note that the presence of voids induces a strong influence of the mean strain-rate D_m on the overall plastic dissipation (e.g., compare the isosurface for the porous Tresca material with that of the fully dense material (hexagonal prism) shown in Fig. 7.42b). The SRP for $f = 1\%$ is closed on the hydrostatic axis. As already mentioned for purely hydrostatic states, i.e., $\mathbf{D} = D^H_m \mathbf{I}$, according to Eqs. (7.73) and (7.109), $\Psi^{+}_{\text{Mises}}(\mathbf{D}, f) = \Psi^{+}_{\text{Tresca}}(\mathbf{D}, f) = 2\left|D^H_m\right| \ln(1/f)$. Thus the intersection of the isosurface with the planes $D_m = D^H_m$ and $D_m = -D^H_m$ are two points on the hydrostatic axis, which are symmetric with respect to the origin (see Fig. 7.42).

To investigate the effects of all invariants on the response of the porous Tresca material, the cross-sections of the same 3-D isosurface with the planes $D_m =$ constant are considered (see Fig. 7.43). Note that the intersection of the isosurface with the plane $D_m = 0$ is a regular hexagon. This is to be expected since states for which $D_m = 0$ correspond to purely deviatoric loadings for which the plastic dissipation of the porous solid coincides with that of the matrix (i.e., Tresca behavior).

Due to the presence of voids, the cross-sections of the isosurface with all the other deviatoric planes $D_m = c$, with $c \neq 0$ are "smoothed out." It is worth noting the very strong influence of D_m on the shape of the cross-sections, which changes

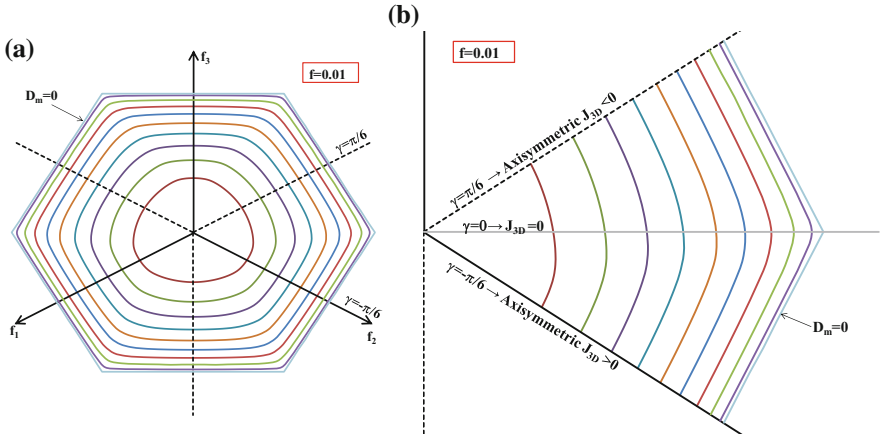

Fig. 7.43 Cross-sections of the 3-D isosurface of a porous Tresca material with several planes D_m = constant: Outer cross-section corresponds to $D_m = 0$ (matrix behavior) and the innermost cross-section corresponds to $D_m = 9 \times 10^{-4}$ s^{-1}: **a** entire cross-section displaying threefold symmetry; **b** zoom in the sector: $-\pi/6 \leq \gamma \leq \pi/6$. Initial porosity: f = 1% (after Revil-Baudard and Cazacu [55])

drastically with the level of D_m (see Fig. 7.43). Specifically, the shape of the cross-section evolves from a regular hexagon ($D_m = 0$) to a triangle with rounded corners (the innermost cross-section corresponding to $D_m = 9 \times 10^{-4}$ s^{-1}).

It is also worth noting the strong coupling between all invariants D_m, R, [or J_2^D, see Eq. (7.74)], and γ [see Eq. (7.75)] on the plastic response of the porous Tresca material. Note also that at yielding the relationship between the invariants associated with shear effects, i.e., the relationship between R and γ (or between J_2^D and J_3^D) is very specific and depends strongly on the mean strain-rate D_m as shown in the zoom of the same cross-sections in the sector: $-\pi/6 \leq \gamma \leq \pi/6$ (see Fig. 7.43b). Also in Fig. 7.44 is plotted $R(\gamma)$ (normalized by $R(\gamma = -\pi/6)$) for cross-sections corresponding to $D_m =$ constant (in the range $D_m = 0$ to $D_m = 9 \times 10^{-4}$ s^{-1}). Since Tresca's SRP depends on both J_2^D and J_3^D, even the cross-section corresponding to $D_m = 0$ (matrix behavior) is not a circle.

This is clearly seen by comparing the curve $R(\gamma)/R(-\pi/6)$ versus γ at $D_m = 0$ for the porous Tresca material (Fig. 7.44) with that corresponding to a porous von Mises material, which is a straight line (see Fig. 7.21).

Furthermore, for the porous Tresca material only for loading at $D_m = 0$, R(γ) has a maximum at $\gamma = 0$ ($J_3^D = 0$) while the minima corresponding to axisymmetric states ($\gamma = \pm\pi/6$) and $R(-\pi/6) = R(\pi/6)$.

For all other loadings at $D_m =$ constant, the maximum of $R(\gamma)$ is no longer at $\gamma = 0$, but shifts towards the axisymmetric state corresponding to $\gamma = -\pi/6$ ($D_1 = D_3 < D_2$ and $J_3^D > 0$); on the other hand, the minimum of $R(\gamma)$ is always obtained for $\gamma = \pi/6$ (axisymmetric state corresponding to $J_3^D < 0$). Another

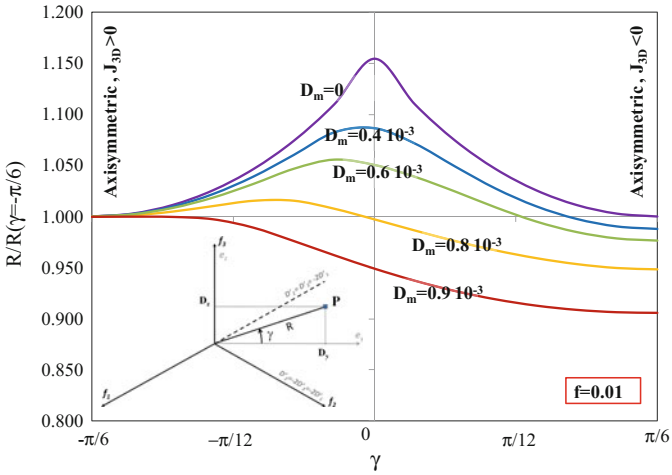

Fig. 7.44 Shape of the cross-sections revealed by the variation of $R(\gamma)$ vs. γ corresponding to D_m = constant. Note that the plane $D_m = 0$ represents the matrix behavior (i.e., Tresca). Initial porosity: $f = 0.01$ (after Revil-Baudard and Cazacu [55])

specificity of the dilatational response of a porous Tresca material is that irrespective of the cross-section D_m = constant, there are two states with the same R (or J_2^D): the axisymmetric state $\gamma = -\pi/6$ and another state say $\gamma = \gamma_1$; the value of γ_1 depending on D_m (e.g., for $D_m = 0$, $\gamma_1 = \pi/6$), the higher the level of D_m, the lower is the value of γ_1.

As already mentioned, $\Psi^+_{\text{Tresca}}(\mathbf{D},f)$ is centro-symmetric. This means that for any porosity f:

$$\Psi^+_{\text{Tresca}}(D_m,R,\gamma,f) = \Psi^+_{\text{Tresca}}(-D_m,R,-\gamma,f).$$

To illustrate this remarkable property, in Fig. 7.45 are shown the cross-sections of the same 3-D isosurface $\Psi^+_{\text{Tresca}}(\mathbf{D},f) = 9.21 \times 10^{-3}$ ($f = 1\%$) with the deviatoric planes $D_m = 7 \times 10^{-4}$ s^{-1} and $D_m = 9 \times 10^{-4}$ s^{-1}, respectively, (interrupted lines) as well as the cross-sections with the planes $D_m = -7 \times 10^{-4}$ s^{-1} and $D_m = -9 \times 10^{-4}$ s^{-1}, respectively (solid lines). The symmetry of all these cross-sections with respect to the origin is clearly seen. For example, for states corresponding to $J_3^D > 0$ ($-\pi/6 \leq \gamma < 0$) to produce the same plastic dissipation, R (or J_2^D) must be higher for tensile states ($D_m > 0$: interrupted line) than for compressive states ($D_m < 0$: solid line). The reverse holds true for loadings corresponding to $J_3^D < 0$ ($0 < \gamma \leq \pi/6$). It is worth mentioning that this remarkable property was put into evidence experimentally by Combaz et al. [23] for Al foams. Moreover, the shapes of the experimental cross-sections in the octahedral plane are triangles with rounded corners, the directions to which the apex of the triangle points depending on the sign of the applied mean stress (or D_m).

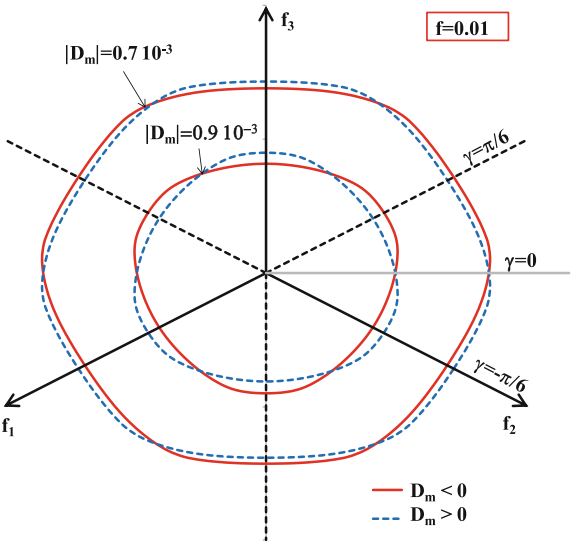

Fig. 7.45 Cross-sections of the isosurface of the porous Tresca material, $\Psi^{+}_{\text{Tresca}}(\mathbf{D},f) = 9.21 \times 10^{-3}$ ($f = 1\%$) with the deviatoric planes $D_m = 7 \times 10^{-4}\ \text{s}^{-1}$ and $D_m = 9 \times 10^{-4}\ \text{s}^{-1}$, respectively (interrupted lines) as well as the cross-sections with the planes $D_m = -7 \times 10^{-4}\ \text{s}^{-1}$ and $D_m = -9 \times 10^{-4}\ \text{s}^{-1}$, respectively (solid lines). Note the centro-symmetry of the cross-sections which is due to the invariance of the plastic response to the transformation $(D_m, \mathbf{D}') \rightarrow (-D_m, -\mathbf{D}')$

Remark While in the case of a porous von Mises material, the most pronounced difference in plastic response is between the axisymmetric states (i.e., between $R(\gamma = \pi/6)$ and $R(\gamma = -\pi/6)$, in the case of a porous Tresca material, no general conclusions can be drawn because the relationship between R and γ (i.e., the dependence between the invariants J_2^D and J_3^D) at yielding depends both on the level of D_m and porosity (e.g., compare Fig. 7.20 with Fig. 7.43).

To further illustrate the specificities of the plastic response of a porous Tresca material in Fig. 7.46a are shown the cross-sections with deviatoric planes of the

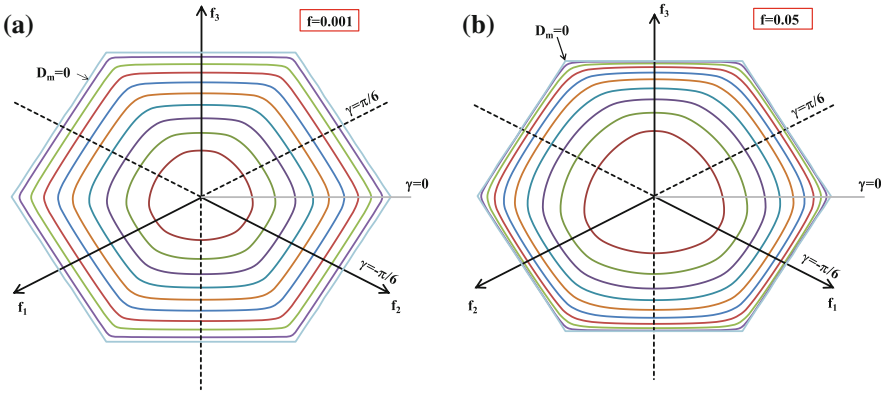

Fig. 7.46 Cross-sections of the 3-D isosurfaces of the porous Tresca material with several deviatoric planes D_m = constant for: **a** porosity $f = 0.1\%$ and **b** porosity $f = 5\%$. In each case, the outermost cross-section corresponds to $D_m = 0$ while the innermost cross-section corresponds to $D_m/D_m^H = 0.9$, where D_m^H represents the hydrostatic limit (after Revil-Baudard and Cazacu [55])

surface corresponding to $f = 0.1\%$ while in Fig. 7.46b are shown the cross-section of the surface corresponding to $f = 5\%$ and the same plastic dissipation 9.21×10^{-3} s^{-1}. Note that irrespective of the level of porosity, the same general trends are observed. Namely, due to the presence of the voids, the shape of the cross-section changes from a regular hexagon ($D_m = 0$; matrix behavior) to a triangle with rounded corners as the absolute value of D_m increases. It is very interesting to note the important role played by the level of porosity. Indeed, the porosity is key in how fast the shape of the cross-section changes along the hydrostatic axis. If the level of porosity is small (e.g., $f = 0.1\%$ see Fig. 7.46a), the cross-sections smooth out slower than in the case when the level of porosity in the matrix is higher (e.g., compare with the cross-sections corresponding to $f = 1\%$ shown in Fig. 7.43). The same conclusion can be drawn by comparing the cross-sections shown in Fig. 7.43 ($f = 1\%$) and those presented in Fig. 7.46b, which correspond to a porosity $f = 5\%$. For example, the cross-section of triangular shape corresponds to a lower value of D_m/D_m^H in the case when $f = 5\%$ than in the case when $f = 1\%$.

7.2.4.6 Comparison Between the Theoretical Response of Porous Solids with Tresca and von Mises Matrices

The influence of the yield criterion describing the plastic flow of the matrix on the mechanical response of a porous solid for both tensile and compressive states can be put into evidence through direct comparisons between the mechanical response of a porous Tresca material and porous Mises material. Specifically, Revil-Baudard and Cazacu [54] analyzed yielding and void evolution under axisymmetric loadings using the porous Tresca criterion [see Eqs. (7.95)–(7.100)], the Cazacu et al. [19] [Eqs. (7.66)–(7.71)] and the Gurson [30] [Eq. (7.41)] criteria in which the matrix is modeled by the von Mises yield criterion.

As an example, Fig. 7.47a, b show in the plane (Σ_e, Σ_m) the theoretical yield surfaces corresponding to the same porosity $f = 3\%$. Both the stress states corresponding to $\Sigma_{11} = \Sigma_{22} \geq \Sigma_{33}$ $(J_3^{\Sigma} \leq 0)$, and $\Sigma_{11} = \Sigma_{22} \leq \Sigma_{33}$ $(J_3^{\Sigma} \geq 0)$ are represented. The strong influence of the particularities of the plastic flow of the matrix on yielding of the porous materials is clearly seen. In particular, the third-invariant effects on yielding are much stronger for a porous material with matrix obeying Tresca criterion than for the porous material with matrix obeying von Mises yield criterion. Furthermore, for stress triaxialities, T, different from zero or infinity, the response of the porous Tresca material is softer than that of a porous material with von Mises matrix. Note that the Gurson [30] model is an upper bound for both criteria, the difference between the predictions of the porous Tresca model and Gurson [30] being pronounced. This very strong influence of the plastic flow of the matrix on yielding of the porous solid can be easily explained by comparing $\Psi^{+}_{\text{Tresca}}(\boldsymbol{D}, f)$ [Eqs. (7.84)–(7.87)], $\Psi^{+}_{\text{Mises}}(\boldsymbol{D}, f)$ [Eqs. (7.61)–(7.63)] and $\Psi_{Gurson}(\mathbf{D}, f)$ [Eq. (7.37)]. All criteria coincide for $T = 0$ (i.e., purely deviatoric loadings) when the yield limit is given by: $\Sigma_e = |\Sigma_{11} - \Sigma_{33}| = \sigma_T(1 - f)$ or for $T = \infty$ (i.e., purely hydrostatic loadings) when the yield limit

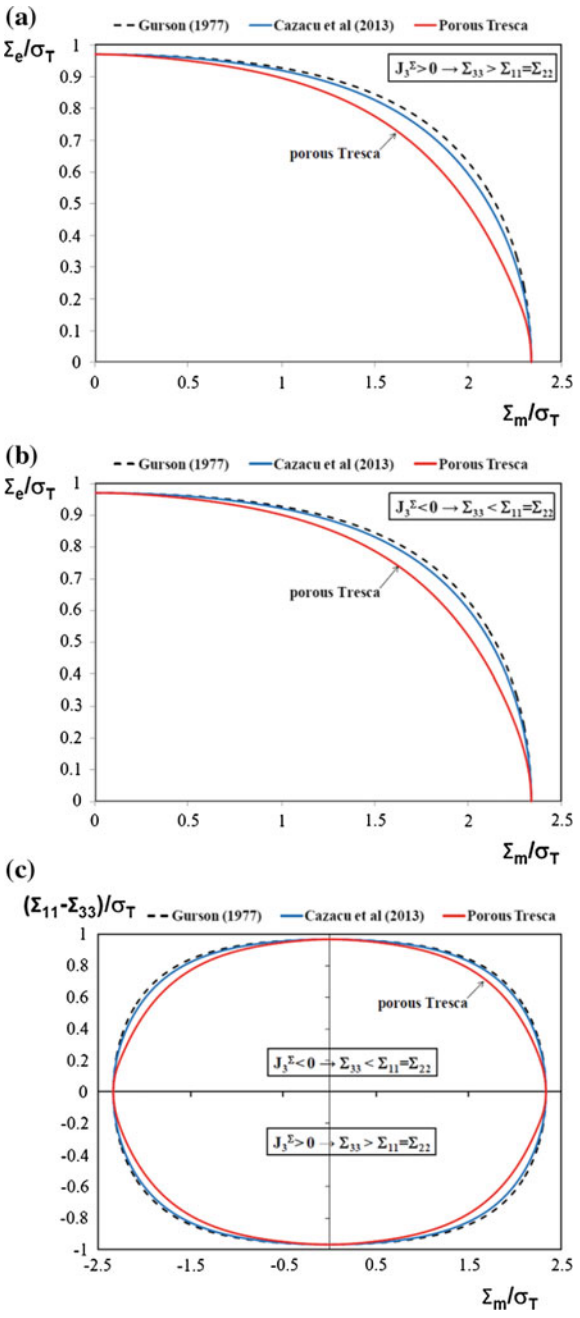
(a)
Gurson (1977)
Cazacu et al (2013)
Porous Tresca
Σ_e/σ_T
$J_3^{\Sigma}>0 \rightarrow \Sigma_{33} > \Sigma_{11}=\Sigma_{22}$
porous Tresca
Σ_m/σ_T
(b)
Gurson (1977)
Cazacu et al (2013)
Porous Tresca
Σ_e/σ_T
$J_3^{\Sigma}<0 \rightarrow \Sigma_{33} < \Sigma_{11}=\Sigma_{22}$
porous Tresca
Σ_m/σ_T
(c)
$(\Sigma_{11}-\Sigma_{33})/\sigma_T$
Gurson (1977)
Cazacu et al (2013)
Porous Tresca
porous Tresca
$J_3^{\Sigma}<0 \rightarrow \Sigma_{33} < \Sigma_{11}=\Sigma_{22}$
$J_3^{\Sigma}>0 \rightarrow \Sigma_{33} > \Sigma_{11}=\Sigma_{22}$
Σ_m/σ_T

◂**Fig. 7.47** Comparison between the yield surfaces for porous solids with von Mises matrix according to Gurson [30] and Cazacu et al. [19] criterion and the yield surface for a porous Tresca material according to Cazacu et al. [18] criterion for axisymmetric tensile loadings corresponding to: **a** $\Sigma_{11} = \Sigma_{22} \leq \Sigma_{33}$ $(J_3^{\Sigma} \geq 0)$ and **b** $\Sigma_{11} = \Sigma_{22} \geq \Sigma_{33}$ $(J_3^{\Sigma} \leq 0)$; **c** representation in the plane $((\Sigma_m)/\sigma_T, (\Sigma_{11} - \Sigma_{33})/\sigma_T)$ of all surfaces for axisymmetric loadings at both positive and negative triaxialities. Porosity $f = 3\%$

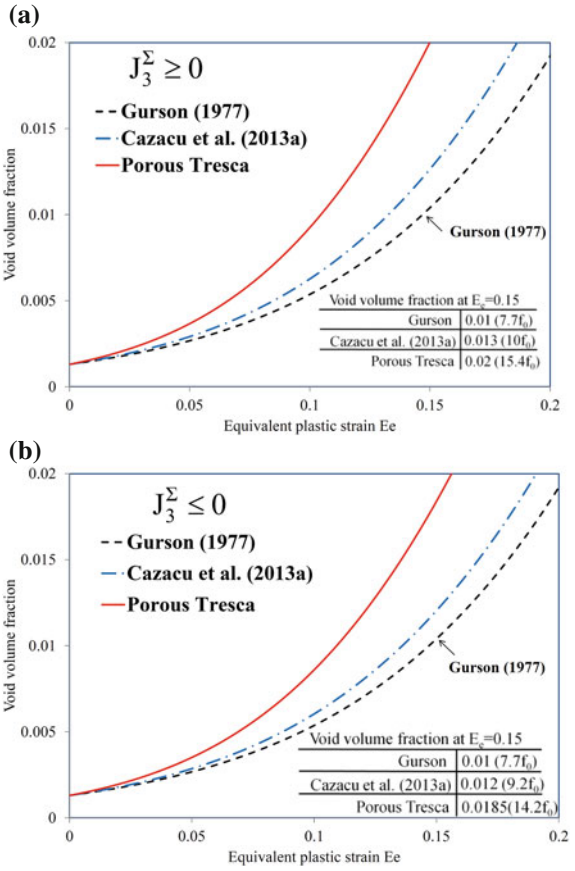

Fig. 7.48 Comparison between the evolution of the void volume fraction with the overall equivalent strain E_e for axisymmetric loadings at fixed stress triaxiality $T = 2$ predicted by Gurson [30], Cazacu et al. [19], and the criterion for porous Tresca materials of Cazacu et al. [18]; initial porosity, $f_0 = 0.13\%$: **a** $\Sigma_{11} = \Sigma_{22} \leq \Sigma_{33}$ $(J_3^{\Sigma} \geq 0)$ and **b** $\Sigma_{11} = \Sigma_{22} \geq \Sigma_{33}$ $(J_3^{\Sigma} \leq 0)$

is: $|\Sigma_m| = |2\Sigma_{11} + \Sigma_{33}| = -\frac{2}{3}\sigma_T \ln f$. Note also that the curvature of the yield surface of the porous material depends strongly on the criterion that governs the plastic behavior of the matrix. This implies a marked difference in void evolution that will be discussed further.

Figure 7.48 shows the predicted void evolution as a function of the equivalent strain, E_e for axisymmetric loadings at fixed triaxiality, $T = 2$ corresponding to $\Sigma_{11} = \Sigma_{22} \geq \Sigma_{33}$ $(J_3^{\Sigma} \leq 0)$, and $\Sigma_{11} = \Sigma_{22} \leq \Sigma_{33}$ $(J_3^{\Sigma} \geq 0)$, respectively. The initial porosity is $f = 0.13\%$. Irrespective of the sign of the third-invariant, the rate of void growth is much faster in a porous solid with Tresca matrix than in a porous solid

with von Mises matrix. Furthermore, because Gurson's [30] criterion is an upper bound for both criteria, it predicts the slowest void growth. The differences in the rate of void growth are significant. For example, for loadings at $J_3^\Sigma \geq 0$ at $E_e = 0.15$, the Gurson [30] model predicts a porosity $f = 0.01$, the Cazacu et al. [19] model predicts $f = 0.013$ while according to the porous Tresca criterion of Cazacu et al. [18], $f = 0.02$. Thus, the porosity according to the Gurson [30] criterion is half that predicted for the porous Tresca material. These results also show that neglecting the coupling between shear and mean stress in the expression of the local plastic dissipation amounts not only to erasing the particularities of the plastic flow of the matrix (see also discussion in Sects. 7.2.4.2 and 7.2.4.4, respectively) but also to a drastic underestimate of the rate of void growth. The same conclusions can be drawn by analyzing the predicted void evolution for $T = 2$ and $J_3^\Sigma \leq 0$ (Fig. 7.48b).

As already discussed, the Cazacu et al. [19] criterion for a porous Mises material and Cazacu et al. [18] model for a porous Tresca material predict that the rate of void growth is faster for axisymmetric loadings at $J_3^\Sigma \geq 0$ than for axisymmetric loading at $J_3^\Sigma \leq 0$ (compare Fig. 7.48a with Fig. 7.48b). According to both criteria at an equivalent plastic strain $E_e = 0.15$, the void volume fraction is almost 8% higher for loadings such that $J_3^\Sigma \geq 0$ than for loadings such that $J_3^\Sigma \leq 0$. As already mentioned, since the Gurson [30] criterion does not account for couplings between mean stress and shear stresses, it cannot capture the influence of the sign of J_3^Σ on void growth.

Figure 7.49 shows the evolution of the void volume fraction as a function of the overall equivalent strain, E_e for axisymmetric loadings and negative stress triaxiality, $T = -2$, the initial porosity being set to $f_0 = 5\%$. Since the mean stress, Σ_m, is negative (compression), void collapse occurs. Note that the rate of void collapse is much faster in a porous solid with Tresca matrix than in a porous solid with von Mises matrix. Furthermore, as demonstrated previously, the Gurson [30] criterion is an upper bound for both criteria and as such predicts the slowest rate of void collapse. For example, at $E_e = 0.15$, the void volume fraction according to the

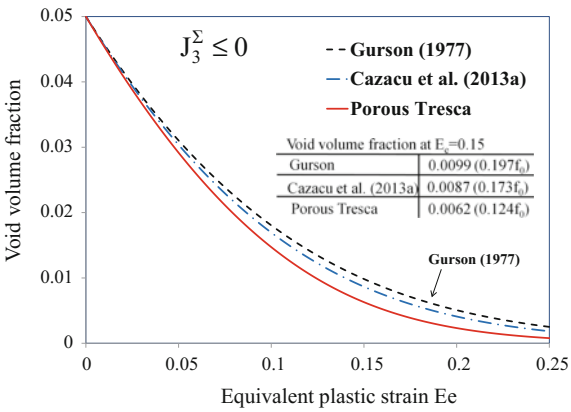

Fig. 7.49 Comparison between the evolution of the void volume fraction with the equivalent strain E_e (void collapse) under axisymmetric loadings such that $\Sigma_{11} = \Sigma_{22} \geq \Sigma_{33}$ ($J_3^\Sigma \leq 0$) and fixed stress triaxiality $T = -2$ according to Gurson [30], Cazacu et al. [19], and the porous Tresca criterion (Cazacu et al. [18]); initial porosity, $f = 5\%$

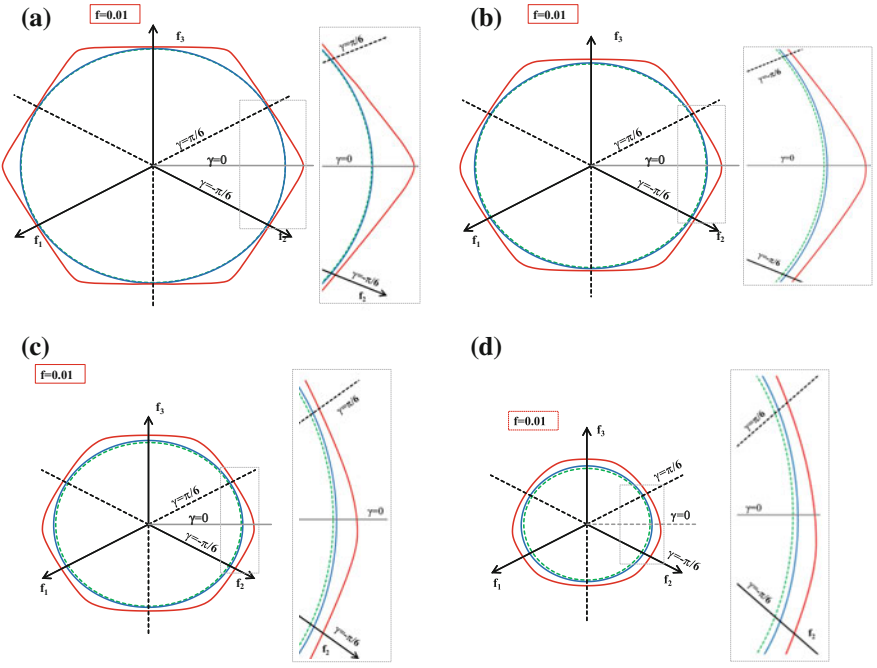

Fig. 7.50 Comparison between the shapes of the cross-sections in the octahedral plane of the 3-D isosurfaces of a porous Tresca material (Revil-Baudard and Cazacu [55]) (red solid line) and porous von Mises material according to Gurson [29] (interrupted line), and Cazacu and Revil-Baudard [16] respectively, corresponding to: **a** $D_m = 2 \times 10^{-4}\ s^{-1}$; **b** $D_m = 4 \times 10^{-4}\ s^{-1}$; **c** $D_m = 6 \times 10^{-4}\ s^{-1}$; **d** $D_m = 8 \times 10^{-4}\ s^{-1}$. Initial porosity $f = 0.01$. Note that of the three potentials, Gurson [29] is the most dissipative (interrupted line) while the porous Tresca potential is the least dissipative

porous Tresca criterion of Cazacu et al. [18], the porous von Mises criterion of Cazacu et al. [19], and the Gurson [30] criterion are: $f = 0.0062$, $f = 0.0087$, and $f = 0.0099$, respectively. It is very interesting to note that the influence of the plastic flow of the matrix is stronger on void growth than on void collapse.

For general 3-D loadings, Revil-Baudard and Cazacu [55] investigated the role played by the plastic behavior of the matrix on the mechanical response by comparing the isosurfaces of equal plastic dissipation corresponding to porous materials with matrix obeying the Tresca yield criterion and the von Mises yield criterion, respectively. For this purpose, comparisons were made between the predictions of the 3-D strain-rate potentials for a porous Mises material $\Psi_{Gurson}(\mathbf{D},f)$ [see Eq. (7.37)] developed by Gurson [29] and $\Psi^{+}_{\text{Mises}}(\mathbf{D},f)$ developed by Cazacu and Revil-Baudard [16] [see Sect. 7.2.3.5 and Eq. (7.73)], and the 3-D strain-rate potential for a porous Tresca material $\Psi^{+}_{\text{Tresca}}(\mathbf{D},f)$ given by Eq. (7.109) (see also Sect. 7.2.4.5).

Figure 7.50 shows the cross-sections in the octahedral plane of the respective isosurfaces corresponding to the same void volume fraction $f = 1\%$. Each of these

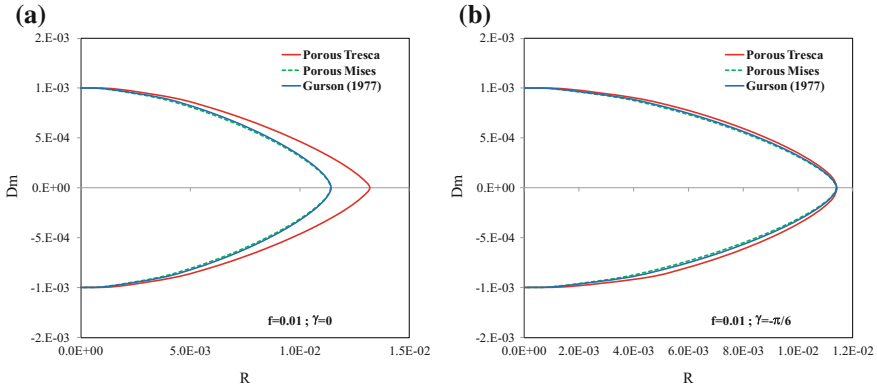

Fig. 7.51 Comparison between the shapes of the cross-sections γ = constant of the 3-D isosurfaces of a porous Tresca material (Revil-Baudard and Cazacu [55]) and porous Mises material according to Cazacu and Revil-Baudard [16], and Gurson [29], respectively: **a** $\gamma = 0$ (pure shear); **b** $\gamma = -\pi/6$ (axisymmetric loadings). Initial porosity $f = 0.01$

surfaces correspond to the same plastic dissipation (equal to 9.21×10^{-3}). Since the Gurson [29] potential was obtained by truncating the local plastic dissipation, it is necessarily interior to the exact potential, which is $\Psi^{+}_{\text{Mises}}(\mathbf{D}, f)$ [see Eq. (7.73)]. Note that irrespective of the value of the mean strain-rate D_m, the isosurface corresponding to the porous Tresca material is exterior to the isosurfaces corresponding to the porous von Mises material. This also means that the Gurson [29] SRP is the most dissipative of the three SRP's, since in order to reach the same value of the plastic dissipation, the norm of the loading, $R(\gamma)$, [see definition given in Eqs. (7.74) and (7.75)] is lower than that for a porous Mises or a porous Tresca material. On the other hand, $\Psi^{+}_{\text{Tresca}}(\mathbf{D}, f)$ is the least dissipative potential.

To summarize, the noteworthy result is the very strong influence of the plastic flow of the matrix on the response of a porous solid. If the matrix obeys the von Mises criterion, the shape of the cross-sections of the plastic surface of the porous solid changes very little as D_m increases. However, if the matrix behavior is described by the Tresca's criterion, the shape of the cross-section evolves from a regular hexagon to a triangle with rounded corners (compare Fig. 7.50a which shows the cross-sections with the plane $D_m = 2 \times 10^{-4}$ s^{-1} with Fig. 7.50c which shows the cross-section with the plane $D_m = 8 \times 10^{-4}$ s^{-1}). Although the difference between the surfaces of the porous solids with von Mises matrix and Tresca matrix becomes less important with increasing D_m, it strongly affects void evolution.

Let us recall that a state $\mathbf{D}$ on any isosurface is defined by (D_m, R, γ); pure shear corresponds to $\gamma = 0$ $(J_3^D = 0)$; while $\gamma = -\pi/6$ corresponds to axisymmetric states such that $J_3^D \geq 0$ (i.e., the two equal eigenvalues of $\mathbf{D}$ are negative) and $\gamma = \pi/6$ corresponds to axisymmetric states at $J_3^D \leq 0$ [i.e., the two equal eigenvalues of $\mathbf{D}$ are positive, see also Eqs. (7.74) and (7.75)]. The comparison of the

cross-sections of the 3-D isosurfaces of the porous Tresca and porous Mises material corresponding to $\gamma = 0$ and $\gamma = -\pi/6$ is shown in Fig. 7.51a, b, respectively. For the porous Tresca material, the relationship between D_m and R (or J_2^D) at yielding depends strongly on the level of γ (see the difference between the shapes of the respective cross-sections).

The very pronounced difference in the response under pure shear ($\gamma = 0$) between the porous Tresca material and the porous von Mises material is also clearly seen. Only for purely hydrostatic loadings ($R = 0$) and for axisymmetric purely deviatoric states (e.g., $\gamma = -\pi/6$ and $D_m = 0$), the isosurfaces coincide (see Fig. 7.51a, b, respectively). This is to be expected since the porous von Mises and porous Tresca material have the same response for purely hydrostatic loadings and for axisymmetric purely deviatoric states.

Both the porous Mises SRP and the porous Tresca SRP involve a very specific dependence on the third-invariant, J_3^D (or γ), as shown in Figs. 7.50 and 7.51. As already mentioned, for a porous Mises solid, the maximum influence of the parameter γ is that between axisymmetric states (see Sect. 7.2.3.5), while for a porous Tresca solid, the manner in which the third-invariant, J_3^D influences the dilatational response depends on both the level of the mean strain-rate and that of the void volume fraction (see Sect. 7.2.4.5). As an example, Fig. 7.52 shows the evolution of the void volume fraction as a function of the plastic dissipation of a porous Tresca solid for loadings at a fixed strain ratio $D_m/R(\gamma) = 0.06$ for $\gamma =$ constant. For this type of loading, the rate of void growth is the fastest for shear strain-loading ($\gamma = 0$) while the lowest rate of void growth is obtained for $\gamma = \pi/6$ (i.e., axisymmetric loadings at $J_3^D \leq 0$).

To further illustrate the influence of the third-invariant, J_3^D, on the dilatational response of the porous Mises and porous Tresca materials, Fig. 7.53 shows the plastic dissipation needed to reach a given void volume fraction for loadings at fixed strain-rate ratio $D_m/R(\gamma)$ and $\gamma =$ constant. If $D_m > 0$ (i.e., void growth), for a porous Mises solid, the plastic work that must be dissipated to reach a given void

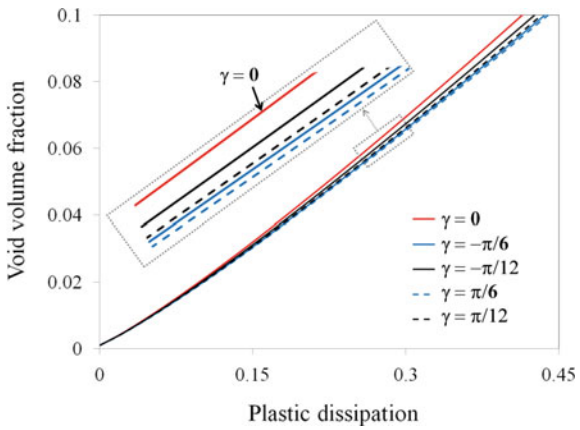

Fig. 7.52 Evolution of the void volume fraction as a function of the plastic dissipation for a porous Tresca solid subjected to loadings at fixed strain ratio $D_m/R(\gamma) = 0.06$ and γ = constant

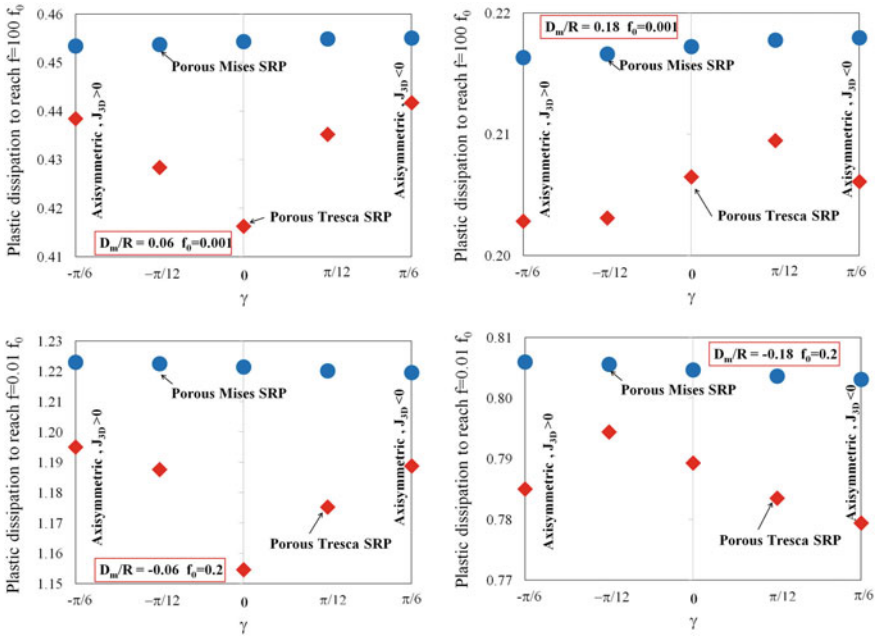

Fig. 7.53 Plastic dissipation necessary to reach a given void volume fraction f for loadings at fixed strain ratio $D_m/R(\gamma) = 0.06$ and γ = constant according to the porous von Mises SRP and the porous Tresca SRP. For loadings at $D_m > 0$, $f = 100f_0$ (with $f_0 = 0.001$); for loadings at $D_m < 0$, $f = 0.01f_0$ (with $f_0 = 0.2$)

Table 7.1 Plastic dissipation necessary to reach a given void volume fraction f for loadings at fixed strain ratio $D_m/R(\gamma)$ and γ = constant according to the porous Mises SRP

Loading	Porous Mises SRP				
	$\gamma = -\pi/6$	$\gamma = -\pi/12$	$\gamma = 0$	$\gamma = \pi/12$	$\gamma = \pi/6$
$D_m/R = 0.06$	0.4533	0.4536	0.4542	0.4548	0.4550
$D_m/R = 0.18$	0.2370	0.2373	0.2380	0.2386	0.2389
$D_m/R = -0.06$	1.2229	1.2225	1.2214	1.2201	1.2195
$D_m/R = -0.18$	0.8059	0.8056	0.8046	0.8036	0.8031

For loadings at $D_m > 0$, $f = 100f_0$ (with $f_0 = 0.001$); for loadings at $D_m < 0$, $f = 0.01f_0$ (with $f_0 = 0.2$)

volume fraction will be the smallest for axisymmetric loadings with $J_3^D \geq 0$ (i.e., $\gamma = -\pi/6$) and the largest for axisymmetric loadings with $J_3^D \leq 0$ (i.e., $\gamma = \pi/6$) (see also Table 7.1). It is to be noted that the very specific couplings between the third-invariant and the mean strain-rate (i.e., the centro-symmetry of the SRP) has strong consequences on void evolution. For $D_m < 0$, for a porous Mises solid, the plastic dissipation necessary to reach the same void volume fraction will be the

Table 7.2 Plastic dissipation necessary to reach a given void volume fraction f for loadings at fixed strain ratio $D_m/R(\gamma)$ and for different values of γ according to the porous Tresca SRP

Loading	Porous Tresca SRP				
	$\gamma = -\pi/6$	$\gamma = -\pi/12$	$\gamma = 0$	$\gamma = \pi/12$	$\gamma = \pi/6$
$Dm/R = 0.06$	0.4384	0.4284	0.4163	0.4352	0.4417
$D_m/R = 0.18$	0.2217	0.2220	0.2258	0.2292	0.2254
$D_m/R = -0.06$	1.1950	1.1875	1.1546	1.1752	1.1887
$D_m/R = -0.18$	0.7850	0.7944	0.7893	0.7835	0.7794

For loadings at $D_m > 0$, $f = 100f_0$ (with $f_0 = 0.001$); for loadings at $D_m < 0$, $f = 0.01f_0$ (with $f_0 = 0.2$)

smallest for axisymmetric loadings with $J_3^D \leq 0$ $(\gamma = \pi/6)$ and the largest for axisymmetric loadings with $J_3^D \geq 0$ $(\gamma = -\pi/6)$.

The same analysis has been conducted for a porous Tresca solid (see Table 7.2). As already mentioned, for a porous Tresca solid, the influence of the third-invariant J_3^D on the dilatational response depends on the initial void volume fraction and on D_m. As an example, for a low mean strain-rate $D_m/R(\gamma) = 0.06$, the smallest and largest plastic dissipation necessary to reach a given void volume fraction are obtained for shear loading $(\gamma = 0)$ and for axisymmetric loadings with $J_3^D \leq 0$ $(\gamma = \pi/6)$, respectively. On the other hand, for $D_m/R(\gamma) = 0.18$, the smallest and largest plastic dissipation necessary to reach the same void volume fraction are obtained for axisymmetric loadings at $J_3^D \geq 0$ $(\gamma = -\pi/6)$ and for loading at $\gamma = \pi/12$, respectively. It is to be noted that the centro-symmetry property of the porous Tresca SRP implies that if the sign of the mean strain-rate changes (i.e., $D_m/R(\gamma) = -0.18$), the maximal and minimal plastic dissipation is now obtained for $\gamma = -\pi/12$ and $\gamma = \pi/6$, respectively.

7.2.5 *Effect of the Relative Weight of the Invariants of the Matrix on Damage Evolution in Porous Materials*

The investigation of the mechanical response of porous Tresca and porous Mises materials presented in Sects. 7.2.3 and 7.2.4 has revealed the key role played by the plastic flow of the matrix. If the matrix behavior is described by Tresca's yield criterion which incorporates dependence on both invariants of the stress deviator, the combined effects of pressure and the third-invariant on yielding of the porous material are much stronger than in the case when the matrix obeys the von Mises criterion (i.e., matrix behavior independent of the third-invariant of the stress deviator). Furthermore, the rate of void growth or collapse is much faster in a porous material with a Tresca matrix than in the one with matrix behavior governed

by the von Mises yield criterion. These studies led to posing the following fundamental questions:

- Are there any materials for which the rate of void evolution is faster than in a porous Tresca material?
- What should be the relative weight of invariants in the matrix in order to have the most influence of the third-invariant (or Lode parameter) on void evolution?
- Are there any materials for which there is no effect of the third-invariant (or Lode parameter) on void evolution?

To address these questions Alves and Cazacu [2] have conducted a micro-mechanical F.E. analysis of model unit cells, considering that the matrix behavior is governed by the Drucker [25] yield criterion. Like the von Mises and Tresca yield criterion, the Drucker [25] yield criterion is pressure-insensitive and predicts the same response in tension–compression. Its expression is a smooth function of both invariants of the stress deviator and involves a unique parameter c (for a detailed discussion of Drucker [25] yield criterion see Chap. 4). F.E. unit-cell calculations were conducted for porous materials with matrix characterized by $c = -27/8$, $c = 0$ (von Mises) and $c = 2.25$. For each porous material considered, the macroscopic loadings imposed were such that the principal values of the applied stress, Σ_1, Σ_2, Σ_3 followed a prescribed proportional loading history corresponding to a constant stress triaxiality T. The mechanical response was investigated for axisymmetric loadings $(\Sigma_1 = \Sigma_2)$ where the overall axial stress Σ_3 was adjusted to ensure that a fixed value of the stress triaxiality is maintained. To investigate the influence of the third-invariant, J_3^{Σ}, of the applied stress on void growth and void collapse for any given specified value of the stress triaxiality T, loadings corresponding to either the major stress along the axial direction (i.e., $J_3^{\Sigma} \geq 0$ for the entire loading history) or to the major stress being along the lateral direction ($J_3^{\Sigma} \leq 0$ for the entire loading history) were considered. As an example, Fig. 7.54 shows a

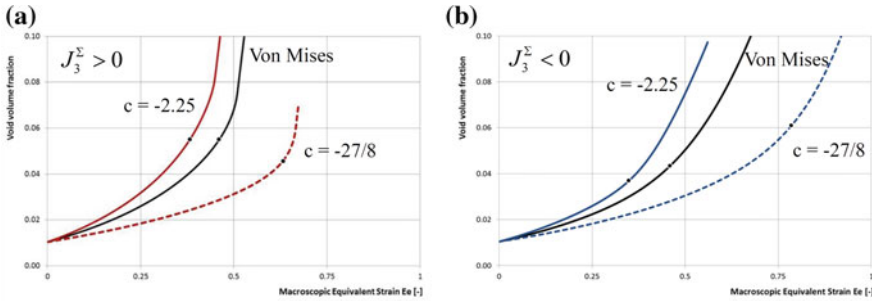

Fig. 7.54 Evolution of the void volume fraction with the overall equivalent strain E_e, obtained by F.E. unit-cell calculations for an isotropic porous material with matrix characterized by the Drucker's [25] yield criterion corresponding to $c = +2.25$ and $c = -27/8$, in comparison with that for a porous von Mises material ($c = 0$), for axisymmetric loadings corresponding to a fixed triaxiality $T = 1$ and: **a** loadings such that $\Sigma_1 = \Sigma_2 \leq \Sigma_3$ $(J_3^{\Sigma} \geq 0)$ and **b** loadings with $\Sigma_1 = \Sigma_2 \geq \Sigma_3$ $(J_3^{\Sigma} \leq 0)$. Initial porosity $f_0 = 0.01$

comparison between the evolution of the void volume fraction with the equivalent strain E_e [see definition given by Eq. (7.51)] corresponding to $T = 1$ for the porous materials. It is clearly seen that for $c = -27/8$, the rate of void growth is slower than in the case of the von Mises matrix, while for $c = 2.25$, it is faster. This study shows that the sensitivity of the plastic deformation of the matrix to the third-invariant of stress, described by the parameter c, has a very strong influence on void evolution. However, in order to draw general conclusions and provide a quantitative estimate of these effects, an analytic plastic potential needs to be developed. As discussed in Sect. 7.1, the derivation of such a potential in closed form is possible only if the analytic expression of the strain-rate potential associated to the matrix plastic behavior is known. However, a strain-rate potential associated to the Drucker [25] stress-based yield criterion cannot be determined analytically (see also discussion in Chap. 6 devoted to isotropic strain-rate potentials).

7.2.5.1 Cazacu and Revil-Baudard [17] Plastic Potential

To address the question concerning the relative weight of the matrix invariants such as to have maximum influence or erase completely the effect of J_3^{Σ} on void evolution, Cazacu and Revil-Baudard [17] adopted a two-step approach. Namely, these authors proposed a new isotropic model for fully dense materials that depends on both invariants, $\psi_{CB}(\mathbf{d})$, and then developed an analytic criterion for porous materials with matrix behavior governed by this potential $\psi_{CB}(\mathbf{d})$ (see Sect. 6.1.1.3).

Since the isotropic plastic potential for fully-dense materials of Cazacu and Revil-Baudard [17] and its properties were discussed in detail in Sect. 6.1.1.3, here we present only the main equations. This isotropic SRP is expressed as:

$$\psi_{CB}(\mathbf{d}) = \frac{\sqrt{j_2}}{B}\left(1 + \beta\frac{j_3^2}{j_2^3}\right), \tag{7.110}$$

with

$$B = \frac{1 + 4\beta/27}{\sqrt{4/3}}. \tag{7.111}$$

In Eq. (7.110), $j_2 = (\mathbf{d} : \mathbf{d})/2$ is the second-invariant of the plastic strain-rate tensor $\mathbf{d}$, $j_3 = \det(\mathbf{d})$ is the third-invariant of $\mathbf{d}$, whereas β is a parameter of the model. The constant B appearing in the expression of the criterion depends solely on β, and it is defined such that for uniaxial tension $\psi_{CB}(\mathbf{d})$ is equal to the axial strain-rate. Let us recall that for $\psi_{CB}(\mathbf{d})$ to be convex, the range of variation of β is,

$$\frac{-9}{24} \leq \beta \leq \frac{27}{68}. \tag{7.112}$$

Most importantly, depending on the sign of the parameter β, this isotropic SRP is either interior to the von Mises strain-rate potential ($\beta<0$), coincides with it ($\beta=0$), or it is exterior to it ($\beta>0$). On the other hand, irrespective of the value of β, Tresca's potential $\psi_{Tresca}(\mathbf{d})$ is an upper bound for $\psi_{CB}(\mathbf{d})$.

To arrive at a closed-form expression of the plastic potential for the porous material with matrix described by $\psi_{CB}(\mathbf{d})$ [see Eq. (7.110)], Cazacu and Revil-Baudard [17] conducted limit analysis on a hollow sphere subjected to axisymmetric loadings [see Eq. (7.29)], and made use of the Rice and Tracey [58] velocity field [see Eq. (7.25)]. For this strain-rate field $\mathbf{d}$, the principal values are given by Eq. (7.30). It was shown that it is possible to solve the limit-analysis problem analytically, and to obtain the plastic dissipation $\Pi^{+}_{CB}(\boldsymbol{D},f)$ and consequently the strain-rate potential of the porous material, $\Psi^{+}_{CB}(\boldsymbol{D},f)=\Pi^{+}_{CB}(\boldsymbol{D},f)/\sigma_T$ in closed form. Moreover, Cazacu and Revil-Baudard [17] derived an explicit analytic expression of the yield criterion for the porous material, namely:

$$\begin{cases} \Sigma_m/\sigma_T = \dfrac{1}{3}\dfrac{\partial \Psi^{+}_{CB}(\boldsymbol{D},f)}{\partial D_m} \\ \Sigma_e/\sigma_T = \left|\dfrac{\partial \Psi^{+}_{CB}(\boldsymbol{D},f)}{\partial D_e}\right| \end{cases} \tag{7.113}$$

It is worth noting that for the strain-rate $\mathbf{d}$ associated with the Rice and Tracey [58] velocity field [see Eq. (7.25)], with d_I, d_{II}, d_{III} given by Eq. (7.30), $\psi_{CB}(\mathbf{d})$ is invariant under the transformation: $\left(D_m, D'_{11}\right) \rightarrow \left(-D_m, -D'_{11}\right)$. Thus the potential of the porous material, $\Psi^{+}_{CB}(\boldsymbol{D},f)$, needs to be calculated only for loadings such that ($D_m \geq 0$, $D'_{11}>0$) and ($D_m \geq 0$, $D'_{11}<0$), respectively.

In the following, we present only the key steps of the proof and the parametric representation of the yield surface of the porous material. For more details, the reader is referred to Cazacu and Revil-Baudard [17].

Theorem 7.10 (*Strain-rate potential for porous materials with matrix depending on both invariants*)

For axisymmetric states, the strain-rate potential of the porous material is given by:

(a) *For* $D_m \geq 0$ *and* $J_3^D \leq 0$ ($D'_{11} \geq 0$), *irrespective of the value of* $u = 2|\mathrm{D}_m|/\mathrm{D}_e$:

$$\Psi^{+}_{CB}(\boldsymbol{D},f) = \frac{\sqrt{3}u\mathrm{D}_e}{4B}\left(H_1\left(\frac{u}{f}\right) - H_1(u)\right), \tag{7.114}$$

with:

$$
\begin{aligned}
H_1(y) = &-\frac{2\sqrt{3}}{3}\beta\ \tan^{-1}\left(\frac{2y-1}{\sqrt{3}}\right)\\
&+\frac{2\sqrt{3}}{9}\left(1+\frac{11}{3}\beta\right)\left(\tan^{-1}\left(\sqrt{3}+2\sqrt{y}\right)-\tan^{-1}\left(-\sqrt{3}+2\sqrt{y}\right)\right)\\
&+\left(\begin{array}{l}\dfrac{9y^{3/2}+\sqrt{3}-3y\sqrt{3}\ -3y^2\sqrt{3}}{9y^{3/2}}-\\ \beta\dfrac{6y^2\sqrt{3}+9y^{3/2}-12y\sqrt{3}\ -2\sqrt{3}}{27y^{3/2}}\end{array}\right)\ln\left(-\sqrt{3y}+y+1\right)\\
&-\frac{4}{3y}+\frac{4\beta}{27}\frac{(4y^2-4y+1)}{(y^2-y+1)y}+\frac{13}{27}\beta\ln\left(y^2-y+1\right)\\
&+\left(\begin{array}{l}\dfrac{9y^{3/2}+3y\sqrt{3}+3y^2\sqrt{3}-\sqrt{3}}{9y^{3/2}}+\\ \beta\dfrac{-12y\sqrt{3}+6y^2\sqrt{3}-9y^{3/2}-2\sqrt{3}}{27y^{3/2}}\end{array}\right)\ln\left(\sqrt{3y}+y+1\right)
\end{aligned}
\tag{7.115}
$$

(b) $D_m \geq 0$ *and* $J_3^D \geq 0$ $(D'_{11} \leq 0)$,

$$
\Psi^{+}_{CB}(\boldsymbol{D},\ \mathrm{f}) = \begin{cases}
\dfrac{\sqrt{3}uD_e}{4B}\left(A_1\left(\dfrac{u}{f}\right)-A_1(u)\right),\ \forall\, u<f\\
\dfrac{\sqrt{3}uD_e}{4B}\left(\begin{array}{l}A_2\left(\dfrac{u}{f}\right)-A_1(u)+\\ \beta\left(-\dfrac{7}{27}\pi-\dfrac{4\sqrt{3}}{27}\ln(3)+\dfrac{4\sqrt{3}}{9}\right)\\ -\sqrt{3}\ln(3)-\dfrac{4\sqrt{3}}{3}+\dfrac{\pi}{9}\end{array}\right), \quad \forall f<u<1\\
\dfrac{\sqrt{3}uD_e}{4B}\left(A_2\left(\dfrac{u}{f}\right)-A_2(u)\right), \quad \forall u>1
\end{cases}
\tag{7.116}
$$

with $A_1(u)$ and $A_2(u)$ given by:

$$A_1(y) = -\frac{2\beta}{\sqrt{3}}\tan^{-1}\left(\frac{2y+1}{\sqrt{3}}\right) - \frac{2\sqrt{3}}{27}(3+11\beta)\left(\begin{array}{c}\tan^{-1}\left(\dfrac{2\sqrt{y}-1}{\sqrt{3}}\right)\\ -\tan^{-1}\left(\dfrac{2\sqrt{y}+1}{\sqrt{3}}\right)\end{array}\right)$$
$$-\frac{2\sqrt{3}}{9y^{3/2}}\left(3y^2-3y-1+\frac{2\beta}{3}\left(3y^2+6y-1\right)\right)\tan^{-1}\left(\frac{\sqrt{3y}}{y-1}\right)$$
$$-\frac{(4\beta+27)}{27}\ln\left(y^2+y+1\right)+\left(\frac{4}{27}\frac{\beta(4y^2+4y+1)-9(y^2+y+1)}{y(y^2+y+1)}\right), \tag{7.117}$$

and

$$A_2(y) = -\frac{2}{\sqrt{3}}\beta\tan^{-1}\left(\frac{2y+1}{\sqrt{3}}\right)$$
$$+\frac{2\sqrt{3}}{27}(3+11\beta)\left(\tan^{-1}\left(\frac{2\sqrt{y}-1}{\sqrt{3}}\right)-\tan^{-1}\left(\frac{2\sqrt{y}+1}{\sqrt{3}}\right)\right)$$
$$+\frac{2\sqrt{3}}{9y^{3/2}}\left(3y^2-3y-1+\frac{2\beta}{3}\left(3y^2-1+6y\right)\right)\tan^{-1}\left(\frac{\sqrt{3y}}{y-1}\right)$$
$$+\frac{27+4\beta}{27}\ln\left(y^2+y+1\right)-\frac{4}{27}\frac{\beta(4y^2+4y+1)-9y-9-9y^2}{y(y^2+y+1)}. \tag{7.118}$$

Case (a): For $D_m \geq 0$ and $J_3^D \leq 0$ ($D'_{11} \geq 0$), substitution of d_I, d_{II}, d_{III} given by Eq. (7.30) into the expression of $\psi_{CB}(\mathbf{d})$ leads to:

$$\frac{B}{\sqrt{3}}\psi_{CB}(\mathbf{d}) = \sqrt{D_m^2(b/r)^6 + D'_{11}D_m(b/r)^3(3\cos^2\theta-1)+D'^2_{11}}$$
$$+\beta\frac{\left(D_m(b/r)^3+D'_{11}\right)^2\left(2D_m^2(b/r)^6+D_mD'_{11}(b/r)^3(9\cos^2\theta-5)+2D'^2_{11}\right)^2}{27\left(D_m^2(b/r)^6+D_mD'_{11}(b/r)^3(3\cos^2\theta-1)+D'^2_{11}\right)^{5/2}} \tag{7.119}$$

Since for the applied loading, the strain-rate triaxiality $u = 2D_m/D_e = D_m/D'_{11}$ using the change of variable $y = \mathrm{u}(b/r)^3$ and $\alpha = \cos\theta$ in the integral representing $\Psi^{+}_{CB}(\boldsymbol{D},f)$, we obtain:

$$\frac{4B}{\sqrt{3}}\Psi^{+}_{CB}(\boldsymbol{D},f)=(uD_e)\int_{u}^{u/f}\int_{-1}^{1}\left(\begin{array}{l}\sqrt{y^2+(3\alpha^2-1)y+1}\\ +\dfrac{\beta}{27}\dfrac{(y+1)^2(2y^2+(9\alpha^2-5)y+2)^2}{(y^2+(3\alpha^2-1)y+1)^{5/2}}\end{array}\right)\frac{\mathrm{d}y}{y^2}\mathrm{d}\alpha \quad (7.120)$$

Further integration with respect to y leads to the expression given in Eq. (7.114).

Furthermore, for ($D_m\geq 0$ and $D'_{11}\geq 0$) from Eq. (7.119), it follows that: $\dfrac{\partial\Psi^{+}_{CB}(\boldsymbol{D},f)}{\partial \mathrm{D}_{11}}\geq\dfrac{\partial\Psi^{+}_{CB}(\boldsymbol{D},f)}{\partial \mathrm{D}_{33}}$ and $\dfrac{\partial\Psi^{+}_{CB}(\boldsymbol{D},f)}{\partial \mathrm{D}_{m}}\geq 0$, so the stresses at yielding of the porous material are such that the third-invariant of the stress deviator $J^{\Sigma}_3=-2(\Sigma_{11}-\Sigma_{33})^3/27$ is negative, and the mean stress $\Sigma_m\geq 0$.

For all other loading scenarios, the analysis can be conducted in a similar way. Therefore, on the basis of Theorem 7.10, we obtain the following result:

Theorem 7.11 *The parametric representation of the yield surface of a porous material with matrix described by the model depending on both invariants* [Eq. (7.110)] *is*:

(a) *For* $\Sigma_m\geq 0$ *and* $J^{\Sigma}_3\leq 0$ *and any value of* $u=2|\mathrm{D}_m|/\mathrm{D}_e$:

$$\left\{\begin{array}{l}\Sigma_m/\sigma_T=\frac{2}{3}\frac{\sqrt{3}u^2}{4B}\left(H_1(u/f)-H_1(u)+u\left(\frac{1}{f}H'_1(u/f)-H'_1(u)\right)\right)\\ \Sigma_e/\sigma_T=-\frac{\sqrt{3}u^2}{4B}\left(\frac{1}{f}H'_1(u/f)-H'_1(u)\right)\end{array}\right. \quad (7.121)$$

where the prime symbol denoted the first derivative of the function $\mathrm{H}_1(y)$ *given by* Eq. (7.115).

(b) *For stress states such that* $\Sigma_m\geq 0$ *and* $J^{\Sigma}_3\geq 0$, *the yield surface of the porous material is*:

- *For* $u<f$:

$$\left\{\begin{array}{l}\Sigma_m/\sigma_T=\dfrac{2}{3}\dfrac{\sqrt{3}u^2}{4B}\left(A_1(u/f)-A_1(u)+u\left(\dfrac{1}{f}A'_1(u/f)-A'_1(u)\right)\right)\\ \Sigma_e/\sigma_T=-\dfrac{\sqrt{3}u^2}{4B}\left(\dfrac{1}{f}A'_1(u/f)-A'_1(u)\right)\end{array}\right. \quad (7.122)$$

- *For* $f<u<1$:

$$\left\{\begin{array}{l}\Sigma_m/\sigma_T=\dfrac{2}{3}\dfrac{\sqrt{3}u^2}{4B}\left(\begin{array}{l}A_2(u/f)-A_1(u)+\beta\left(-\dfrac{7}{27}\pi-\dfrac{4\sqrt{3}}{27}\ln(3)+\dfrac{4\sqrt{3}}{9}\right)\\ -\sqrt{3}\ln(3)-\dfrac{4\sqrt{3}}{3}+\dfrac{\pi}{9}+u\left(\dfrac{1}{f}A'_1(u/f)-A'_1(u)\right)\end{array}\right)\\ \Sigma_e/\sigma_T=-\dfrac{\sqrt{3}u^2}{4B}\left(\dfrac{1}{f}A'_1(u/f)-A'_2(u)\right)\end{array}\right. \quad (7.123)$$

- *For* $u > 1$:

$$\begin{cases} \Sigma_m/\sigma_T = \dfrac{2}{3}\dfrac{\sqrt{3}u^2}{4B}\left(A_2(u/f) - A_2(u) + (u/f)A_2'(u/f) - uA_2'(u)\right) \\ \Sigma_e/\sigma_T = -\dfrac{\sqrt{3}u^2}{4B}\left(\dfrac{1}{f}A_2'(u/f) - A_2'(u)\right) \end{cases} \tag{7.124}$$

where $A_1'(y)$ *and* $A_2'(y)$ *denote the first derivatives of the functions* $A_1(y)$ *and* $A_2(y)$*, respectively, which are given by* Eqs. (7.117) *and* Eq. (7.118).

(c) *For* $\Sigma_m \leq 0$ and $J_3^\Sigma \geq 0$, *the parametric representation of the yield surface of the porous material is obtained from* Eq. (7.121) *by arguments of centro-symmetry.*

(d) *Similarly, for loadings such* $\Sigma_m \leq 0$ *and* $J_3^\Sigma \leq 0$, *the parametric representation of the yield surface of the porous solid is obtained from* Eqs. (7.122) to (7.124).

Remarks It is important to note that in developing the SRP (Eqs. (7.115)–(7.118)] and the yield criterion for the porous material [Eqs. (7.121)–(7.124)], no approximations were made when calculating the local plastic dissipation. Neglecting, the cross-term $D_m D_{11}'$ involved in the expression of $\psi_{CB}(\mathbf{d})$ [e.g., see Eq. (7.119)] would have resulted in erasing the specificities of the plastic deformation of the matrix, and as such the resulting yield criterion of the porous solid would have been independent of J_3^Σ.

For $\beta = 0$, the Cazacu and Revil-Baudard [17] criterion for porous materials given by Eqs. (7.121)–(7.124) reduces to the Cazacu et al. [19] criterion for porous von Mises materials [see Eqs. (7.66)–(7.71)].

Irrespective of the value of the parameter β, it is predicted that yielding of the porous material has the following properties:

- The absolute value of the yield limit under hydrostatic tensile loadings is the same as the yield limit under purely hydrostatic compression loadings: $|\Sigma_m| = -2/3\sigma_T \ \ln f$.
- For purely deviatoric axisymmetric loadings, yielding occurs at $\Sigma_e = \sigma_T(1-f)$, irrespective of the sign of J_3^Σ.

The above properties are a direct consequence of the plastic potential of the matrix being an even function [see Eq. (7.110)].

7.2.5.2 Effect of the Matrix Sensitivity to Both Invariants on Yielding

On the basis of the analytic criterion for isotropic porous materials given by Eqs. (7.121)–(7.124), it is possible to draw general conclusions pertaining to the role played by the matrix sensitivity to both invariants of plastic deformation. In the following analysis, we will take advantage of the fact that, irrespective of the value of the parameter β, the yield surface of the porous solid is centro-symmetric. Therefore, we will represent and analyze only the quadrant of the yield surface

defined by (Σ_e, Σ_m) with $\Sigma_m \geq 0$. We recall that for axisymmetric loadings with $\Sigma_{11} = \Sigma_{22}$, the equivalent stress Σ_e reduces to $|\Sigma_{11} - \Sigma_{33}|$, the mean stress is: $\Sigma_m = (2\Sigma_{11} + \Sigma_{33})/3$, and the third-invariant of the stress deviator is: $J_3^{\Sigma} = -2(\Sigma_{11} - \Sigma_{33})^3/27$.

In Fig. 7.55 are represented for the same level of porosity ($f = 5\%$), the yield surfaces corresponding to materials with matrix characterized by $\beta = 0.38$, 0, (von Mises matrix), $\beta = -0.15$, and $\beta = -0.35$, respectively. It is very interesting to note that if the matrix is characterized by $\beta \geq 0$, i.e., its plastic potential is exterior or coincides with the von Mises SRP (see also Sect. 6.1.1.3), the response of the porous material for loadings such that $\Sigma_{11} = \Sigma_{22} \leq \Sigma_{33}$ (i.e., at $J_3^{\Sigma} \geq 0$) is softer than that for loadings such that $\Sigma_{11} = \Sigma_{22} \geq \Sigma_{33}$ (i.e., at $J_3^{\Sigma} \leq 0$), the yield curve corresponding to $J_3^{\Sigma} \geq 0$ is below that corresponding to $J_3^{\Sigma} \leq 0$. The stronger is the sensitivity of the matrix plastic deformation to the third-invariant [i.e., the larger the value of β in Eq. (7.110)], the stronger is the influence of J_3^{Σ} on yielding of the porous material.

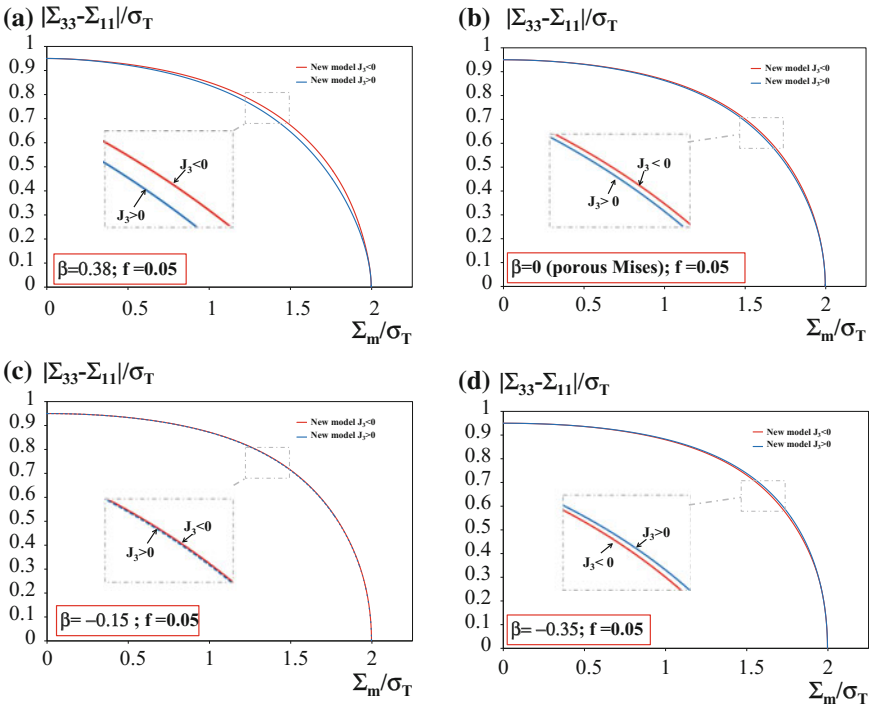

Fig. 7.55 Effect of the third-invariant J_3^{Σ} on yielding of porous materials with matrix characterized by: **a** $\beta = 0.38$; **b** $\beta = 0$ (von Mises matrix); **c** $\beta = -0.15$; **d** $\beta = -0.35$. Porosity $f = 5\%$ for all materials

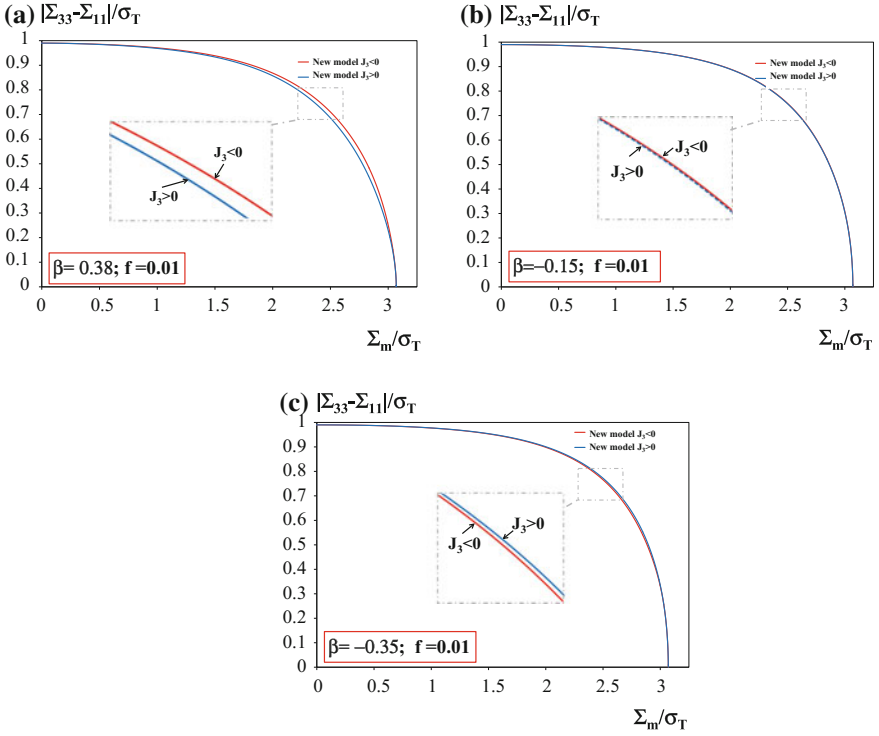

Fig. 7.56 Effect of the third-invariant J_3^{Σ} on yielding of porous materials with matrix characterized by: **a** $\beta = 0.38$; **b** $\beta = -0.15$; **c** $\beta = -0.35$. For all materials, $f = 1\%$

It is also very interesting to note that for the material with matrix characterized by $\beta = -0.15$ and porosity $f = 5\%$ there is practically no influence of J_3^{Σ} on the behavior (see Fig. 7.55c showing that the yield curve corresponding to $J_3^{\Sigma} \leq 0$ almost coincides with the one that corresponds to $J_3^{\Sigma} \geq 0$). It means that although the matrix behavior depends on both invariants, the presence of voids practically erases the influence of J_3^{Σ} on yielding of the porous material. The same conclusion, i.e., practically no influence of J_3^{Σ} on the response, applies to a material characterized by a porosity $f = 1\%$ and matrix with $\beta = -0.15$ (see Fig. 7.56b). It is to be noted that the particular value of β, say β_*, for which the porous material has no influence on the third-invariant can be determined numerically by making use of Eqs. (7.121)–(7.124). For fixed values of the porosity f, ranging from 10^{-5} to 0.15, $-0.179 < \beta_* < -0.172$.

It is also worth comparing the yield surfaces of porous materials according to Cazacu and Revil-Baudard [17] with the yield surface of a porous Tresca material obtained using the Cazacu et al. [18] criterion. For axisymmetric loadings $\Sigma_{11} = \Sigma_{22} \leq \Sigma_{33}$ (i.e., at $J_3^{\Sigma} \geq 0$) the respective surfaces for $f = 5\%$ are shown in

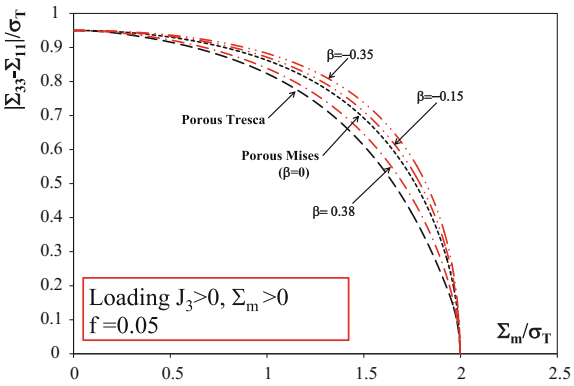

Fig. 7.57 Comparison between the yield surfaces of a porous Mises material ($\beta = 0$), a porous Tresca material according to the Cazacu et al. [18] criterion and those of porous materials with matrix characterized by $\beta = 0.38$, $\beta = -0.15$, $\beta = -0.35$, respectively, calculated with the Cazacu and Revil-Baudard [17] criterion for axisymmetric loadings such that $J_3^{\Sigma} \geq 0$ ($\Sigma_{11} = \Sigma_{22} \leq \Sigma_{33}$)

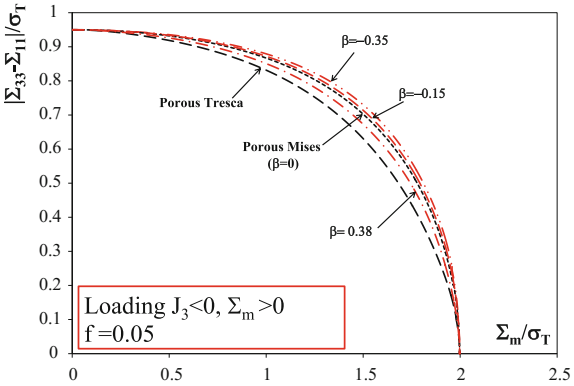

Fig. 7.58 Comparison between the yield surfaces of a porous Mises material ($\beta = 0$), a porous Tresca material according to the Cazacu et al. [18] criterion and those of porous materials with matrix characterized by $\beta = 0.38$, $\beta = -0.15$, $\beta = -0.35$, respectively, calculated with the Cazacu and Revil-Baudard [17] criterion for axisymmetric loadings such that $J_3^{\Sigma} \leq 0$ ($\Sigma_{11} = \Sigma_{22} \geq \Sigma_{33}$)

Fig. 7.57; for loadings corresponding to $\Sigma_{11} = \Sigma_{22} \geq \Sigma_{33}$ (i.e., at $J_3^{\Sigma} \leq 0$), the respective surfaces are shown in Fig. 7.58.

It is very interesting to note that irrespective of the imposed loading, if the matrix is characterized by $\beta > 0$, the yield surface of the porous material lies between the yield surface of a porous von Mises material and the yield surface of a porous Tresca material. Specifically, for $\beta > 0$ the porous Tresca yield surface is a lower bound while the porous von Mises surface is an upper bound. Moreover, the stronger the deviation of the matrix behavior from von Mises (i.e., the larger the value of β in Eq. (7.110), the closer is the yield surface is to that of a porous Tresca material.

On the other hand, the response of the porous material with von Mises matrix ($\beta = 0$) is softer than that of a porous material with matrix characterized by $\beta < 0$. The smaller the value of β, the more pronounced is the difference in response as compared to that of a porous von Mises material. As expected, the yield limit for purely deviatoric states and purely hydrostatic states is the same for all porous

materials irrespective of the criterion governing the plastic deformation of the matrix (see also Theorem 7.2).

7.2.5.3 Influence of the Matrix Sensitivity to Both Invariants on Porosity Evolution

Effect of β on void evolution

Cazacu and Revil-Baudard [17] have shown that the value of the parameter β which describes the relative weighting of the invariants on the plastic deformation of the matrix strongly affects the rate of void evolution. As an example, in Fig. 7.59 are compared the predictions of the void growth versus the overall equivalent plastic strain E_e corresponding to porous materials with a matrix characterized by $\beta = 0.38$, $\beta = -0.15$, and $\beta = -0.35$ which were subjected to axisymmetric loadings at fixed stress triaxiality $T = 1.5$ with either $\Sigma_{11} = \Sigma_{22} < \Sigma_{33}$ (i.e., at $J_3^{\Sigma} \geq 0$) or $\Sigma_{11} = \Sigma_{22} > \Sigma_{33}$ (i.e., at $J_3^{\Sigma} < 0$). For all porous materials considered the initial porosity was $f_0 = 0.5\%$.

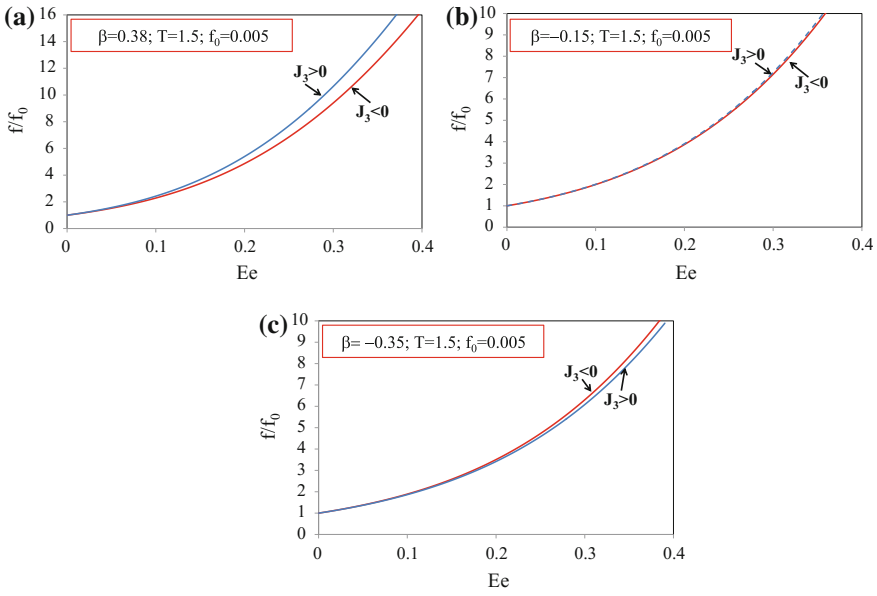

Fig. 7.59 Effect of the third-invariant J_3^{Σ} on the void volume fraction (f/f_0) evolution with the overall equivalent plastic strain for axisymmetric loadings at fixed triaxiality $T = 1.5$ predicted by the Cazacu and Revil-Baudard [17] criterion for porous materials characterized by matrix with **a** $\beta = 0.38$; **b** $\beta = -0.15$; **c** $\beta = -0.35$. For all materials, the initial porosity is: $f_0 = 0.5\%$

It is very interesting to note that for the material characterized by a matrix with a value of $\beta = -0.15$, close to β_*, the rate of void growth for loadings such that $J_3^\Sigma \geq 0$ and $J_3^\Sigma \leq 0$, respectively, are almost the same (see Fig. 7.59b). This is consistent with the fact that for the same material there is practically no effect of J_3^Σ on yielding (see Fig. 7.56b). On the other hand, if the matrix is characterized by $\beta > \beta_*$, the rate of void growth is faster for loadings such that $J_3^\Sigma \geq 0$ than for loadings at $J_3^\Sigma \leq 0$; and the larger is the value of β, the stronger is the effect of J_3^Σ on void growth. On the contrary, if the matrix is characterized by $\beta < \beta_*$, the rate of void growth is faster for $J_3^\Sigma \leq 0$ than for $J_3^\Sigma \geq 0$ (see, e.g., Fig. 7.59c which presents the void evolution for the material with matrix characterized by $\beta = -0.35$).

Since the yield criterion is centro-symmetric, the following conclusions can be drawn concerning the effect of the matrix plastic deformation on void collapse (i.e., void evolution for compressive mean stress):

- If the porous solid has the matrix characterized by $\beta > \beta_*$, the rate of void collapse is faster for loadings at $J_3^\Sigma \leq 0$ than for loadings at $J_3^\Sigma \geq 0$;
- If the porous solid has the matrix characterized by β close to β_*, there is practically no effect of J_3^Σ on void collapse;
- If the porous solid has the matrix characterized by a value of the parameter $\beta < \beta_*$ the rate of void collapse is faster for loadings at $J_3^\Sigma \geq 0$ than for loadings at $J_3^\Sigma \leq 0$.

Comparison with the void evolution of a porous Mises ($\beta = 0$) *and porous Tresca material*

It is also worth comparing the void growth rates and collapse with that of a porous Tresca material. Let us first consider a porous material with matrix characterized by $\beta = -0.15$ (close to $\beta_* = -0.175$). Note that the void growth and void closure rates in this porous material are slower than in both a porous von Mises material and a porous Tresca material, respectively (see Figs. 7.60 and 7.61). In contrast to both Tresca and von Mises porous materials, for this porous material there is practically no effect of J_3^Σ on void evolution.

On the other hand, if the matrix is characterized by $\beta > 0 > \beta_*$, the relative weight of the invariants on the matrix behavior is such that irrespective of the type of loading (i.e., sign of J_3^Σ), the rate of void growth is faster than in a porous von Mises material ($\beta = 0$) and lower than in a porous Tresca material. As an example, in Figs. 7.62 and 7.63 is presented the evolution of the void volume fraction f/f_0 with the overall effective plastic strain for a porous material with matrix characterized by $\beta = 0.38$ subjected to axisymmetric loading histories corresponding to either ($J_3^\Sigma \leq 0$) or ($J_3^\Sigma \geq 0$) and fixed positive stress triaxiality $T = 1.5$. The initial void volume fraction is $f_0 = 0.5\%$. For example, for axisymmetric loadings such that $J_3^\Sigma \leq 0$, at an equivalent plastic strain of $E_e = 0.3$, the void volume fraction is $f = 7.82 f_0$ in the porous Mises material, $9.41 f_0$ in the material with matrix characterized by $\beta = 0.38$, against $11.29 f_0$ in the porous Tresca material.

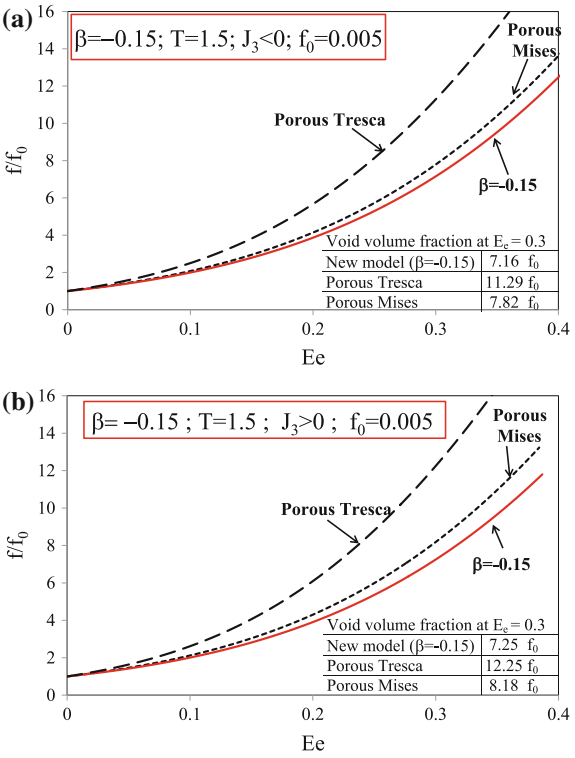

Fig. 7.60 Comparison between the evolution of the void volume fraction with the overall equivalent plastic strain E_e for axisymmetric loadings at fixed stress triaxiality $T = 1.5$ for a porous von Mises material (according to Cazacu et al. [19]), a porous Tresca material (using Cazacu et al. [18]) and for porous solids with matrix characterized by $\beta = -0.15$ according to the Cazacu and Revil-Baudard [17] criterion: **a** axisymmetric loadings such that $J_3^{\Sigma} \leq 0$ and **b** axisymmetric loadings such that $J_3^{\Sigma} \geq 0$. For the porous material with $\beta = -0.15$ there is practically no influence of J_3^{Σ} on void growth

While for all porous materials the rate of void growth is faster for axisymmetric loadings such that $J_3^{\Sigma} \geq 0$ (see Fig. 7.62b) than for axisymmetric loadings such that $J_3^{\Sigma} \leq 0$ (see Fig. 7.62a), the maximum influence of J_3^{Σ} on void evolution is displayed by the material characterized by $\beta = 0.38$. For example at $E_e = 0.3$, in this material the difference between the porosity attained in loadings with $J_3^{\Sigma} \leq 0$ and $J_3^{\Sigma} \geq 0$ is of 13% while for the porous Tresca material the difference is of 8%, and for the porous Mises material there is 5% difference. The same conclusions can be drawn from the analysis of the void evolution in a porous material with matrix characterized by $\beta = 0.2$. However, the influence of J_3^{Σ} on void growth is less pronounced. As an example, at $E_e = 0.3$, the difference between the porosity attained in loadings corresponding to $J_3^{\Sigma} \leq 0$ and $J_3^{\Sigma} \geq 0$ is 9.5%. In general, for $\beta > \beta_*$ the influence of J_3^{Σ} on void growth is less pronounced as the value of the parameter β decreases.

Since both the Cazacu and Revil-Baudard [17] criterion and the Cazacu et al. [18] criterion for a porous Tresca material display centro-symmetry, the same effects of the relative weighting of the invariants in the matrix (i.e., of β) on the rate

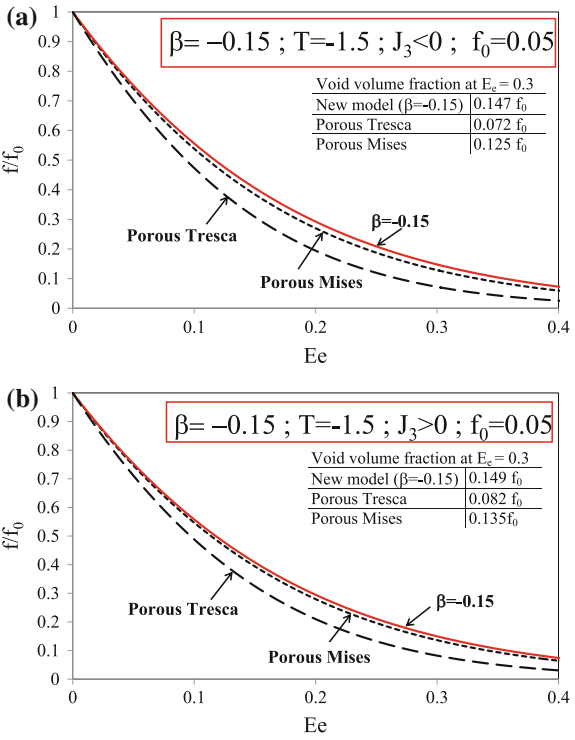

Fig. 7.61 Comparison between the evolution of the void volume fraction with the overall equivalent plastic strain E_e for compressive axisymmetric loadings at fixed stress triaxiality $T = 1.5$ for a porous von Mises material (according to Cazacu et al. [19]), a porous Tresca material (using Cazacu et al. [18]) and for a porous material with matrix characterized by $\beta = -0.15$ **a** axisymmetric loadings such that $J_3^{\Sigma} \leq 0$ and **b** axisymmetric loadings such that $J_3^{\Sigma} \geq 0$; Initial porosity $f_0 = 0.05$. For the porous material with $\beta = -0.15$, there is practically no influence of J_3^{Σ} on void collapse

of void collapse should occur. Comparisons between the predictions of void collapse as a function of the overall equivalent strain for axisymmetric loadings at fixed compressive triaxiality $T = -1.5$ corresponding to either $J_3^{\Sigma} \leq 0$ or $J_3^{\Sigma} \geq 0$ are shown in Fig. 7.63. The initial porosity was considered higher ($f_0 = 5\%$) such as to allow a larger range of plastic strain to develop prior to void closure. Irrespective of the sign of the third-invariant, the rate of void closure in the material with matrix characterized by $\beta = 0.38$ is much faster than in the porous Mises material, and only slightly slower than the rate of void closure in the porous material with Tresca matrix (see Fig. 7.63a for $J_3^{\Sigma} \leq 0$ and Fig. 7.63b for $J_3^{\Sigma} \geq 0$). While for all porous materials, the rate of void closure is faster for axisymmetric loadings such that $J_3^{\Sigma} \leq 0$ than for axisymmetric loadings such that $J_3^{\Sigma} \geq 0$, the influence of J_3^{Σ} on the rate of void collapse is more pronounced for the material with matrix characterized by $\beta = 0.38$ (18% difference between $J_3^{\Sigma} \leq 0$ and $J_3^{\Sigma} \geq 0$ at $E_e = 0.3$) than for the porous Tresca material (13% difference at $E_e = 0.3$) and the porous Mises material (8% difference at $E_e = 0.3$). The same conclusions can be drawn by analyzing the rate of void closure in a porous material with matrix characterized by $\beta = 0.2$ as compared to that in the porous von Mises and porous Tresca material, respectively. However, the influence of J_3^{Σ} on the rate of void collapse is less pronounced than in

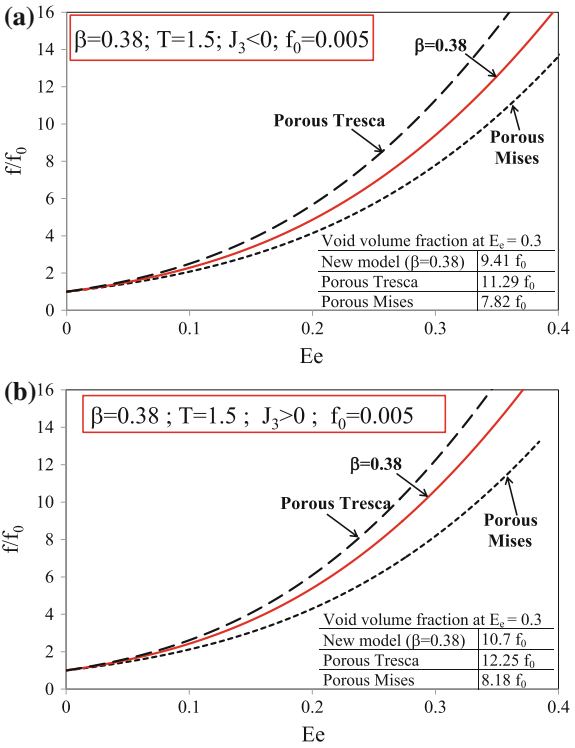

Fig. 7.62 Comparison between the evolution of the void volume fraction with equivalent plastic strain E_e for axisymmetric loadings at fixed stress triaxiality $T = 1.5$ for a porous von Mises material according to Cazacu et al. [19] criterion, a porous Tresca material according to Cazacu et al. [18] and a porous material with matrix characterized by $\beta = 0.38$ **a** axisymmetric loadings such that $J_3^{\Sigma} \leq 0$ and **b** axisymmetric loadings such that $J_3^{\Sigma} \geq 0$; Initial porosity $f_0 = 0.5\%$

the case when the matrix is characterized by $\beta = 0.38$. As an example, at $E_e = 0.3$, the difference between the porosity corresponding to loadings at $J_3^{\Sigma} \leq 0$ and $J_3^{\Sigma} \geq 0$ is of 12% for the material characterized by $\beta = 0.2$. As already mentioned, if the matrix is characterized by $\beta > \beta_*$, the influence of J_3^{Σ} on void evolution decreases as the value of the parameter β decreases.

As seen in Sect. 7.2.5.2, for stress triaxialities T different from zero or infinity the response of the porous Tresca material is softer than that of the porous von Mises material which in turn is softer than that of a porous material with matrix characterized by $\beta < 0$ (see also Figs. 7.57 and 7.58). As a consequence, in porous materials with $\beta < 0$, the rate of void growth and the rate of void closure will be slower than the rate of void evolution in a porous Mises material and a porous Tresca material, respectively. As an example, let us examine Fig. 7.64a which shows the void growth evolution with the overall equivalent strain E_e in a porous material with matrix characterized by $\beta = -0.35$ subjected to axisymmetric tensile loadings at a fixed stress triaxiality $T = 1.5$. Note that for axisymmetric loadings such that $J_3^{\Sigma} \leq 0$, at $E_e = 0.3$ in the porous material with $\beta = -0.35$, the void volume fraction is $f = 6.30 f_0$, against $f = 11.3 f_0$ in the porous Tresca material, and $f = 7.82 f_0$ in the porous Mises material ($\beta = 0$). It is also worth noting that while

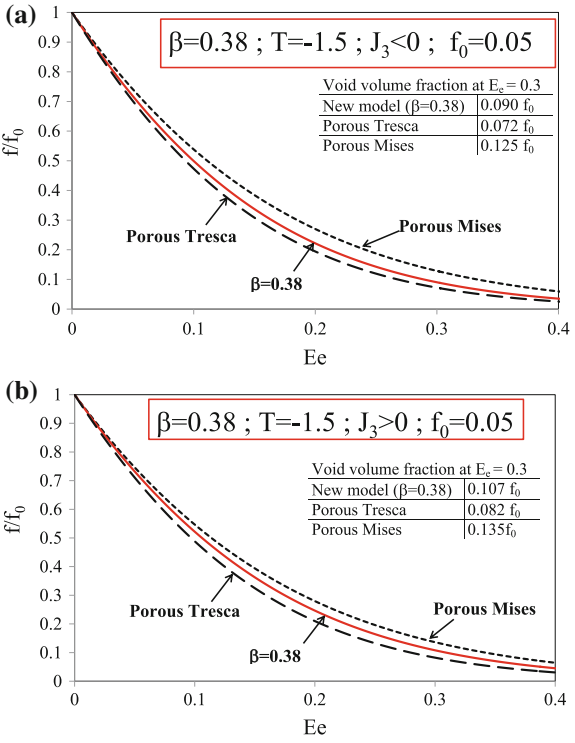

Fig. 7.63 Comparison between the evolution of the void volume fraction with equivalent plastic strain E_e for axisymmetric loadings at fixed stress triaxiality $T = -1.5$ for a porous von Mises material according to the Cazacu et al. [19] criterion, a porous Tresca material according to the Cazacu et al. [18] and a porous material with matrix characterized by $\beta = 0.38$ **a** axisymmetric loadings such that $J_3^{\Sigma} \leq 0$ and **b** axisymmetric loadings such that $J_3^{\Sigma} \geq 0$; Initial porosity $f_0 = 5\%$

for the porous Mises and porous Tresca materials, the void growth rate is faster for loadings at $J_3^{\Sigma} \geq 0$ than for loadings at $J_3^{\Sigma} \leq 0$, for the material with matrix characterized by $\beta = -0.35$, the reverse occurs, i.e., the void growth rate is slower for loadings at $J_3^{\Sigma} \geq 0$ than for loadings at $J_3^{\Sigma} \leq 0$. Due to the centro-symmetry of all criteria, it follows that the void closure rate will also be slower than in a porous von Mises material. The same conclusions, i.e., that the void closure rate will be faster for $J_3^{\Sigma} \geq 0$ than for $J_3^{\Sigma} \leq 0$ can be drawn for any porous material with matrix characterized by $\beta < \beta_*$ (see Fig. 7.65).

In summary, it was established that:

- A porous material with matrix governed by Tresca criterion has the fastest rate of void growth or collapse.
- However, depending on the specific dependence of the matrix plastic deformation to the invariants of the stress deviator, the rate of void growth or collapse in a porous material can be either faster or slower than that of a porous Mises material. Specifically,
- If the matrix is characterized by $\beta > 0$, the void growth rate is faster than in a porous Mises material; the larger is the value of β, the faster is the rate of void evolution, which approaches the one in a porous Tresca material.

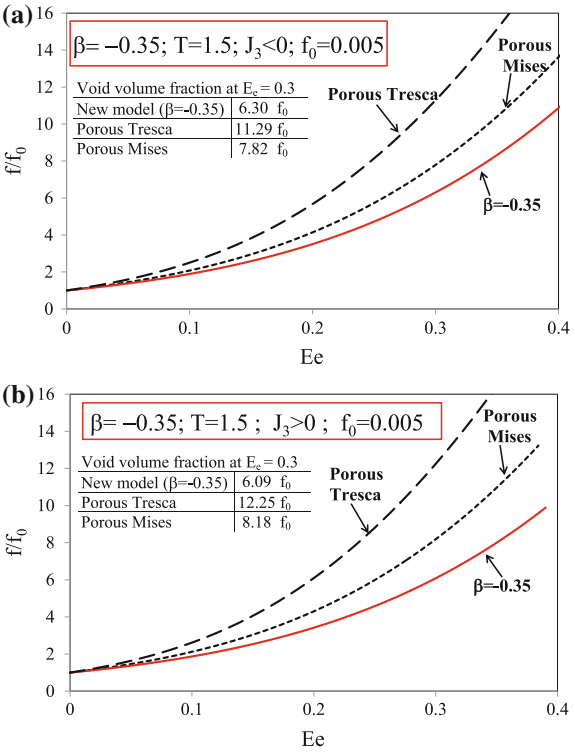

Fig. 7.64 Comparison between the evolution of the void volume fraction with equivalent plastic strain E_e for axisymmetric loadings at fixed stress triaxiality $T = 1.5$ for a porous von Mises material (according to Cazacu et al. [19]), a porous Tresca material (using Cazacu et al. [18]) and a porous material with matrix characterized by $\beta = -0.35$: **a** axisymmetric loadings such that $J_3^{\Sigma} \leq 0$ and **b** axisymmetric loadings such that $J_3^{\Sigma} \geq 0$; Initial porosity $f_0 = 0.5\%$

- If the matrix is characterized by $\beta < 0$, the rate of void growth and the rate of void closure are slower than in a porous Mises material. The smaller is the value of β, the slower is the rate of void growth as compared to a von Mises porous material.

7.3 Constitutive Model for Porous Isotropic Metallic Materials with Incompressible Matrix Governed by an Odd Yield Function

It is important to note that when modeling porous metals, it is generally assumed that the matrix material is incompressible and has the same yield in tension–compression. In fact in all the models for porous metals presented in Sect. 7.2, the plastic potential of the matrix is represented by an even function (e.g., von Mises [70], Tresca [66], Drucker [25], Cazacu and Revil-Baudard [17]). However, for certain metallic materials, a significant strength differential (SD) or tension–compression asymmetry is observed even though no volume changes accompany

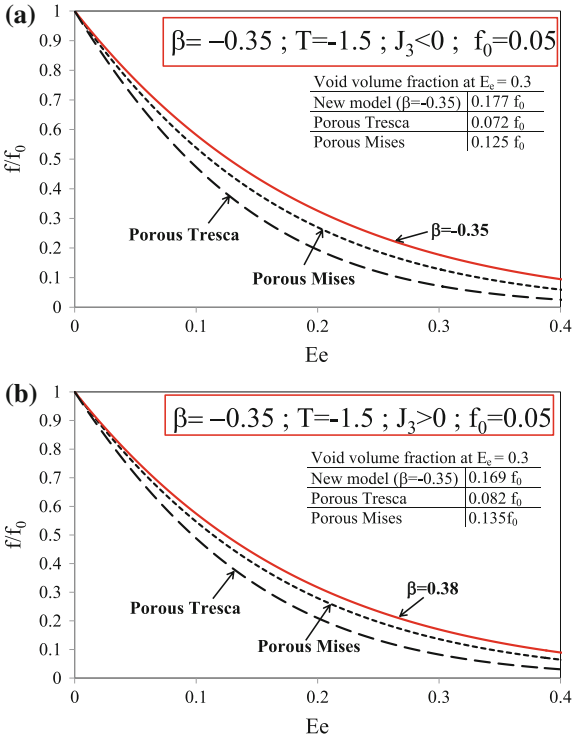

Fig. 7.65 Comparison between the evolution of the void volume fraction with equivalent plastic strain E_e under compressive axisymmetric loadings at fixed stress triaxiality $T = -1.5$ for a porous von Mises material according to Cazacu et al. [19] criterion, a porous Tresca material (according to Cazacu et al. [18]) and a porous material with matrix characterized by $\beta = 0.38, \beta = -0.35$: **a** axisymmetric loadings such that $J_3^{\Sigma} \leq 0$ and **b** axisymmetric loadings such that $J_3^{\Sigma} \geq 0$; Initial porosity $f_0 = 5\%$

yielding. For data on a variety of engineering materials and recent yield criteria that account for this asymmetry, the reader is referred to Chaps. 4–6.

The fundamental question that arises concerns the influence of the tension–compression asymmetry of the matrix on damage evolution. In this section are presented recent contributions that address this question. First, it is shown that if the matrix is incompressible and displays tension–compression asymmetry, even under hydrostatic loadings the overall mechanical response of the porous material depends on the sign of the applied pressure (tension vs. compression).

Next, the derivation of the Cazacu and Stewart [20] analytic plastic potential for porous isotropic materials with randomly distributed spherical voids in an incompressible matrix displaying tension–compression asymmetry is presented. On the basis of this criterion, the influence of the matrix asymmetry on void evolution and the location of the zone corresponding to maximum damage in round tensile specimens subject to uniaxial tension is assessed numerically. The unusual characteristics of damage evolution revealed by this model are confirmed by X-ray tomography data on engineering materials.

7.3.1 Cazacu and Stewart [20] Plastic Potential

Cazacu and Stewart [20] used the kinematic homogenization approach to model isotropic porous materials containing randomly distributed spherical voids in an incompressible matrix displaying tension–compression asymmetry. The matrix behavior was considered to be rigid-plastic and governed by the quadratic form of the isotropic stress potential of Cazacu et al. [15]:

$$\varphi(\boldsymbol{\sigma}) = m\sqrt{\sum_{i=1}^{3}\left(|s_i| - k s_i\right)^2}, \quad m = \sqrt{\frac{9}{2(3k^2 - 2k + 3)}}. \tag{7.125}$$

We recall that in Eq. (7.125), s_1, s_2 and s_3 are the principal values (not ordered) of the Cauchy stress deviator while k is a material constant expressible solely in terms of the ratio $\beta = \sigma_T/\sigma_C$ between the uniaxial yield in tension–compression, respectively, as:

$$k = \frac{1-h}{1+h}, \text{with } h = \sqrt{\frac{2-\beta^2}{2\beta^2 - 1}} \tag{7.126}$$

For more details about this stress potential and its exact dual $\psi(\mathbf{d})$, the reader is referred to the Sects. 4.3.2 and 6.1.2, respectively. Let us recall here that for any plastic strain-rate field $\mathbf{d}$, the expression of $\psi(\mathbf{d})$ is:

$$\psi(\mathbf{d}) = \begin{cases} \sqrt{\frac{2}{3}} \cdot \sqrt{\frac{d_1^2 + d_2^2 + d_3^2\left[\frac{3-2\beta^2}{\beta^2}\right]}{2-\beta^2}}, & \text{if } (d_1, d_2, d_3) \in D_3^- \\ \sqrt{\frac{2}{3}} \cdot \sqrt{\frac{d_1^2 + d_2^2 + \left[3\beta^2 - 2\right]d_3^2}{2\beta^2 - 1}}, & \text{if } (d_1, d_2, d_3) \in D_3^+ \end{cases}, \tag{7.127}$$

with d_1, d_2, d_3 denoting the eigenvalues of $\mathbf{d}$ (not necessarily ordered) and the sub-domains D_3^+ and D_3^- being defined as:

$$D_3^- = \left\{ (d_1, d_2, d_3) \middle| \frac{d_3}{\sqrt{d_1^2 + d_2^2 + d_3^2}} \le \frac{-\beta^2}{\sqrt{2\left(1 + \beta^4 - \beta^2\right)}} \right\}$$

$$D_3^+ = \left\{ (d_1, d_2, d_3) \middle| \frac{d_3}{\sqrt{d_1^2 + d_2^2 + d_3^2}} \ge \frac{1}{\sqrt{2\left(1 + \beta^4 - \beta^2\right)}} \right\},$$

The expressions of the other branches of $\psi(\mathbf{d})$, corresponding to the domains D_j^+ and D_j^- (j = 1, 2) are obtained from Eq. (7.127) by symmetry arguments (for more details and the geometric representation of these domains in the octahedral plane, see Sect. 6.1.2). Therefore, for any strain-rate field $\mathbf{d}$, the local plastic dissipation associated with the yield criterion given by Eq. (7.125) is:

$$\pi(\mathbf{d}) = \sigma_T \psi(\mathbf{d}). \tag{7.128}$$

For spherical void geometry, the RVE considered is the hollow sphere of inner radius a and outer radius b, shown in Fig. 7.1. To arrive at a closed-form expression of the plastic potential for the porous material, the analysis was done for a unique velocity field, namely that of Rice and Tracey [58] and axisymmetric loadings [see Eqs. (7.25)–(7.29)]. For this strain-rate field $\mathbf{d}$, the principal values denoted d_I, d_{II}, d_{III} are given by Eq. (7.30).

It is to be noted that due to the tension–compression asymmetry of the matrix, fresh difficulties are encountered when estimating the local plastic dissipation, $\pi(\mathbf{d})$. Indeed, for a material with matrix having $\sigma_T \neq \sigma_C$, $\pi(\mathbf{d})$ has multiple branches [see Eq. (7.127)] and its expression depends on the sign and relative ordering of the eigenvalues d_I, d_{II}, d_{III}. Nevertheless, it is possible to obtain analytically an approximate plastic potential for the porous material. This potential will be denoted $\Pi_{SD}(\boldsymbol{D},f)$. Moreover, Cazacu and Stewart [20] obtained an explicit expression of the yield criterion from the expressions of

$$\begin{cases} \Sigma_m = \dfrac{1}{3}\dfrac{\partial \Pi_{SD}(\boldsymbol{D},f)}{\partial D_m} \\ \Sigma_e = \left|\dfrac{\partial \Pi_{SD}(\boldsymbol{D},f)}{\partial D_e}\right| \end{cases} \tag{7.129}$$

General properties of the yield surface of a porous material with incompressible matrix displaying SD effects

While the explicit expression of $\Pi_{\mathrm{SD}}(\boldsymbol{D},f)$ and that of the yield criterion will be given later on, it is important to note here that for purely hydrostatic or purely deviatoric loadings, the plastic dissipation of the porous material can be obtained in closed form without making any approximations. Most importantly, the analysis of the yielding response of the porous material for these loadings leads to key findings concerning the influence of the tension–compression asymmetry of the matrix on yielding of the porous material.

It is worth recalling that if the matrix plastic behavior is governed by an even yield criterion, there is a combined effect between the mean stress Σ_m and the third-invariant J_3^{Σ} for all stress states, except for purely deviatoric or purely hydrostatic loadings. Moreover, it was shown that the yield surface of the porous material is centro-symmetric (see Theorems 7.1 and 7.2; Sect. 7.2.1). In contrast, if the matrix is incompressible and displays SD effects (i.e., $\sigma_T \neq \sigma_C$), then there is an

effect of the sign of Σ_m on yielding under purely hydrostatic loadings and of the sign of J_3^{Σ} on yielding under purely deviatoric axisymmetric loadings, respectively. Specifically, these very specific effects can be quantitatively described in terms of σ_T/σ_C, the ratio between the matrix uniaxial yield stresses in tension–compression.

Theorem 7.12 *If the matrix is governed by the isotropic form of the* Cazacu et al. [15] *yield criterion*,

- *For tensile hydrostatic loadings, the yield limit of the porous material is*:

$$p_Y^+ = -(2/3)\sigma_C \ln f \tag{7.130}$$

- *For compressive hydrostatic loadings, the yield limit of the porous material is*:

$$p_Y^- = (2/3)\sigma_T \ln f. \tag{7.131}$$

Proof Given that the matrix is governed by an isotropic yield criterion [see Eq. (7.125)] and the voids are spherical and randomly distributed in the matrix, the porous material is isotropic. Therefore, when subjected to purely hydrostatic loading, i.e., $\boldsymbol{\Sigma} = \Sigma_m \mathbf{I}$, the resulting deformation and strain-rate tensor $\mathbf{D}$ is also spherical, i.e., $\boldsymbol{D} = D_m \mathbf{I}$. Further substitution in Eq. (7.30) leads to the following expressions for the eigenvalues d_I, d_{II}, d_{III}:

- For tensile hydrostatic loadings (i.e.,$\Sigma_m > 0$):

$$\begin{cases} d_I = d_{II} = D_m (b/r)^3 > 0 \\ d_{III} = -2d_I < 0 \end{cases}$$

- For compressive hydrostatic loadings (i.e.,$\Sigma_m < 0$):

$$\begin{cases} d_I = d_{II} = D_m (b/r)^3 < 0 \\ d_{III} = -2d_I > 0 \end{cases}$$

Substituting these eigenvalues in the expression of the matrix plastic dissipation [Eqs. (7.127) and (7.128)], we obtain:

$$\pi(\mathbf{d}) = \begin{cases} (2/\beta)\sigma_T D_m (b/r)^3 & \text{if } D_m > 0, \\ 2|D_m|\sigma_T (b/r)^3 & \text{if } D_m < 0. \end{cases} \quad \text{with } \beta = \sigma_T/\sigma_C.$$

Note that for this type of loading, the local plastic dissipation is the same on every spherical surface $S(r)$ with $a \le r \le b$, therefore the integral of $\pi(\mathbf{d})$ over the hollow sphere can be done analytically, leading to the following expression of the plastic dissipation of the porous material:

$$\langle \pi(\mathbf{d}) \rangle_{\Omega} = \begin{cases} -2\sigma_C D_m \ln(f) & \text{if} \quad D_m > 0, \\ -2\sigma_T |D_m| \ln(f) & \text{if} \quad D_m < 0. \end{cases} \quad \text{with } f = (a/b)^3.$$

The stresses at yielding are obtained by differentiating the above equations with respect to $\boldsymbol{D}$ [see Eq. (7.12)].

Thus, under tensile hydrostatic loading the yield limit of the porous material is $\Sigma_m = p_Y^+ = -(2/3)\sigma_C \ln f$, while for compressive hydrostatic loading, the yield limit is $\Sigma_m = p_Y^- = (2/3)\sigma_T \ln f$ (i.e., Eqs. (7.130) and (7.131), respectively).

Remark (a) Note that if there is no asymmetry between the tensile and compressive behavior of the matrix; i.e., if $\sigma_T = \sigma_C$, then Eqs. (7.130) and (7.131) become: $|p_Y^+| = |p_Y^-| = -(2/3)\sigma_T \ln f$, i.e., we recover the yield limit under hydrostatic loadings of a porous material with matrix plastic behavior governed by an even yield criterion (e.g., von Mises, Tresca); see also Theorem 7.2, Sect. 7.2.1.

Remark (b) For the solution to the limit-analysis problem of a hollow sphere loaded hydrostatically assuming ideal plastic behavior governed by the Cazacu et al. [15] yield criterion, the reader is referred to Cazacu and Stewart [20]. Here, we mention that the solutions are p_Y^+ and p_Y^-, given by Eqs. (7.130) and (7.131), respectively. Thus, in the plane (Σ_m, Σ_e) both the exact and the approximate estimate of the yield surface based on the Rice and Tracey [58] velocity field contain the states $(p_Y^+, 0)$ and $(p_Y^-, 0)$.

Theorem 7.13 *If the matrix is governed by the isotropic form of the* Cazacu et al. [15] *yield criterion, for axisymmetric and purely deviatoric loadings (i.e.,* $\Sigma_m = 0$*), the yield limit of the porous material depends on the sign of* J_3^{Σ}:

- *For purely deviatoric axisymmetric loadings, if* $J_3^{\Sigma} \leq 0$, *yielding occurs at*:

$$\Sigma_e = \sigma_C(1 - f) \tag{7.132}$$

- *For purely deviatoric axisymmetric loadings, if* $J_3^{\Sigma} \geq 0$, *yielding occurs at*:

$$\Sigma_e = \sigma_T(1 - f). \tag{7.133}$$

Proof The porous material being isotropic under purely deviatoric axisymmetric loadings such that $\Sigma_{11} = \Sigma_{22} > 0$, $\Sigma_{33} = -2\Sigma_{11}$ ($J_3^{\Sigma} \leq 0$), the strain-rate $\mathbf{D}$ is also axisymmetric and traceless with $D'_{11} = D'_{22}$. Further substitution in Eq. (7.30) leads to: $d_I = d_{II} = D'_{11} = D_e/2 > 0$ and $d_{III} = -D_e < 0$. Moreover, it can be easily shown that for any $\beta = \sigma_T/\sigma_C$:

$$\frac{d_{III}}{\sqrt{d_I^2 + d_{II}^2 + d_{III}^2}} = -\sqrt{\frac{2}{3}} < \frac{-\beta^2}{\sqrt{2\left(\beta^4 - \beta^2 + 1\right)}}.$$

Therefore, the matrix plastic dissipation [see Eqs. (7.127) and (7.128)] is:

$$\pi(\mathbf{d}) = \sigma_C D_e,$$

while the plastic dissipation of the porous material is given by:

$$\langle \pi(\mathbf{d}) \rangle_\Omega = (\sigma_C D_e)\left(4\pi\left(b^3 - a^3\right)\right)/\left(4\pi b^3\right) = (\sigma_C D_e)(1-f). \tag{7.134}$$

The stresses at yielding are obtained by differentiating with respect to $\boldsymbol{D}$ the overall plastic dissipation given by Eq. (7.134). We obtain that yielding occurs for $\Sigma_e = \sigma_C(1-f)$. By similar arguments, it can be shown that under purely deviatoric axisymmetric loadings such that $\Sigma_{11} = \Sigma_{22} < 0$, $\Sigma_{33} = -2\Sigma_{11}$ $(J_3^\Sigma \geq 0)$, yielding occurs for $\Sigma_e = |\Sigma_{11} - \Sigma_{33}| = \sigma_T(1-f)$.

Remark Note that if there is no asymmetry between the tensile and compressive behavior of the matrix, i.e., if $\sigma_T = \sigma_C$, then Eqs. (7.132) and (7.133) coincide, and we recover the yield limit under axisymmetric purely deviatoric loading of a porous material with matrix plastic behavior governed by an even yield criterion (e.g., von Mises or Tresca): $\Sigma_e = \sigma_T(1-f)$ (see also Sect. 7.2.1).

In summary, for a porous material with matrix displaying SD effects, the yield surface does not have any symmetry. In the plane (Σ_m, Σ_e) there are two yield curves corresponding to axisymmetric states. These yield curves intersect only at $\left(p_Y^+, 0\right)$ and $\left(p_Y^-, 0\right)$, respectively (see also Fig. 7.67).

Theorem 7.14 *The* Cazacu and Stewart [20] *yield function for a porous material with matrix displaying SD effects is given by*:

$$\left(m\sqrt{\sum_{i=1}^{3}\left(\left|\frac{\Sigma'_i}{\sigma_T}\right| - k\frac{\Sigma'_i}{\sigma_T}\right)^2}\right)^2 + 2f\cosh\left(\frac{3z_s}{2}\frac{\Sigma_m}{\sigma_T}\right) - \left(1+f^2\right) = 0, \tag{7.135}$$

with Σ'_i, i = 1, …, 3 are the eigenvalues of the stress deviator, Σ_m is the mean stress, and

$$z_s = 1 + \frac{1}{2}\left[\mathrm{sgn}^2(\Sigma_m) + \mathrm{sgn}(\Sigma_m)\right]\left(\frac{\sigma_T}{\sigma_C} - 1\right). \tag{7.136}$$

Proof Since the plastic flow in the matrix is sensitive to the third-invariant of the stress deviator, the following axisymmetric loading scenarios need to be considered separately:

(i) $\Sigma_m \geq 0$ and $J_3^\Sigma \leq 0$; (ii) $\Sigma_m \geq 0$ and $J_3^\Sigma \geq 0$; (iii) $\Sigma_m \leq 0$ and $J_3^\Sigma \geq 0$; (iv) $\Sigma_m \leq 0$ and $J_3^\Sigma \leq 0$.

We will give a detailed analysis for Case (i); the other cases can be treated in a similar manner (see Cazacu and Stewart [20])

Case (i): $\Sigma_m \geq 0$ and $J_3^\Sigma \leq 0$

In this case, the RVE is subject to tensile loading such that the axial stress is less than the lateral stress; i.e., $\Sigma_{11} = \Sigma_{22} \geq \Sigma_{33} \geq 0$, so $\Sigma_m \geq 0$, $\Sigma_e = \Sigma_{11} - \Sigma_{33}$, and $J_3^\Sigma \leq 0$.

Hence, $D'_{11} > 0$ and $D_m \geq 0$ (void expansion) and the absolute value of the strain-rate triaxiality $u = 2D_m/D_e$. Since the matrix plastic dissipation $\pi(\mathbf{d})$ has multiple branches, one needs to analyze the sign and relative ordering of the eigenvalues d_I, d_{II}, d_{III} [see Eq. (7.30)]. For $D'_{11} > 0$ and $D_m \geq 0$, it follows that for any $a \leq r \leq b$, $d_I \geq 0$ hence $d_{III} \leq 0$. To determine which expression of $\pi(\mathbf{d})$ to use [see Eq. (7.127)], one further needs to calculate the sign of the following expressions

$$E_1 = \frac{d_I^2}{d_I^2 + d_{II}^2 + d_{III}^2} - \frac{1}{2\left(1 + \beta^4 - \beta^2\right)},$$

and

$$E_2 = \frac{\beta^4}{2\left(1 + \beta^4 - \beta^2\right)} - \frac{d_{III}^2}{d_I^2 + d_{II}^2 + d_{III}^2},$$

with $\beta = \sigma_T/\sigma_C$. Further substitution of Eq. (7.30) and lengthy calculations lead to: $E_1 < 0$ for any θ while $E_2 < 0$ for $\theta \in (0, \theta_1) \cup \left(\theta_2, 180^\circ\right)$, where θ_1 and θ_2 are the solutions in the interval $(0, 180^o)$ of the equation $\tan^2(\theta) = 8$. Thus, the local plastic dissipation is of the following form:

$$\pi(\mathbf{d}) = \sigma_T \sqrt{\frac{2}{3}} \cdot \sqrt{\frac{d_I^2 + d_{II}^2 + d_{III}^2 \left[\dfrac{3 - 2\beta^2}{\beta^2}\right]}{2 - \beta^2}}, \tag{7.137}$$

with d_I, d_{II}, d_{III} are given by Eq. (7.30).

To obtain an analytical expression of the plastic potential of the porous material, i.e., explicitly calculate the integral of $\pi(\mathbf{d})$ over the RVE, Cazacu and Stewart [20] made the same hypothesis as Gurson [29], i.e., they neglected the cross-term "$D_m D'_{11}$" in the expression of $\pi(\mathbf{d})$ given by Eq. (7.137). The implications of adopting this classic simplification were assessed through comparison with F.E. unit-cell calculations and experimental data (see Sects. 7.3.1.1 and 7.3.1.2). Specifically, using this simplification Eq. (7.137) becomes:

$$\pi(\mathbf{d}) \simeq \pi_{SD}(\mathbf{d}) = \sigma_C \sqrt{4D_m^2 (b/r)^6 + D_e^2}, \tag{7.138}$$

and the plastic potential of the porous material,

$$\Pi_{SD}(\boldsymbol{D}, f) = \frac{3\sigma_C}{b^3} \int_a^b r^2 \sqrt{4D_m^2 (b/r)^6 + 4\,D_{11}'^2}\, dr$$

or

$$\Pi_{\mathrm{SD}}(\boldsymbol{D},f)=\frac{2\sigma_C D_m}{b^3}\int_u^{u/f}\left(\sqrt{1+y^2}\right)\frac{dy}{y^2} \tag{7.139}$$

with $u=2D_m/D_e$ and $y=u(b/r)^3$.

Note that if there is no difference in the matrix response between tension–compression (i.e., if $\sigma_T=\sigma_C$), Eq. (7.139) reduces to Eq. (7.35), i.e., $\Pi_{\mathrm{SD}}(\boldsymbol{D},f)$ coincides with $\Pi_{Gurson}(\boldsymbol{D},f)$, the Gurson's [30] estimate of the plastic dissipation of a porous von Mises material. Calculation of the integral given by Eq. (7.139), its derivatives relative to D_m and D_e, and elimination of u between the respective expressions of Σ_m and Σ_e result in

$$\left(\frac{\Sigma_e}{\sigma_C}\right)^2+2f\,\cosh\left(\frac{3}{2}\frac{\Sigma_m}{\sigma_C}\right)-\left(1+f^2\right)=0$$

or, equivalently,

$$\left(\frac{\Sigma_e}{\sigma_T}\right)^2\left(\frac{\sigma_T}{\sigma_C}\right)^2+2f\cosh\left[\frac{3}{2}\left(\frac{\sigma_T}{\sigma_C}\right)\frac{\Sigma_m}{\sigma_T}\right]-\left(1+f^2\right)=0. \tag{7.140}$$

For any given stress state $\boldsymbol{\Sigma}$, let us denote by

$$\tilde{\Sigma}_e\overset{def}{=}m\sqrt{\sum_{i=1}^{3}\left(|\Sigma'_{\mathrm{i}}|-k\Sigma'_{\mathrm{i}}\right)^2}, \tag{7.141}$$

the equivalent stress associated with the isotropic form of the Cazacu et al. [15] yield criterion [see Eq. (7.125)]; Σ'_{i} denoting the principal values of Σ', the deviator of $\boldsymbol{\Sigma}$. Note that for axisymmetric loadings such that $\Sigma_{11}=\Sigma_{22}\geq\Sigma_{33}\geq 0$ (i.e., for $J_3^{\Sigma}\leq 0$),

$$\tilde{\Sigma}_e=\left(\frac{\sigma_T}{\sigma_C}\right)\Sigma_e. \tag{7.142}$$

Hence, Eq. (7.140) can be rewritten as

$$\left(m\sqrt{\sum_{i=1}^{3}\left(\left|\frac{\Sigma'_i}{\sigma_T}\right|-k\frac{\Sigma'_i}{\sigma_T}\right)^2}\right)^2+2f\,\cosh\left(\frac{3}{2}\frac{\Sigma_m}{\sigma_C}\right)-\left(1+f^2\right)=0 \tag{7.143}$$

Remarks

- The Cazacu and Stewart [20] criterion given by Eq. (7.135) predicts that irrespective of loading there is an effect of the sign of the mean stress Σ_m on yielding of the porous material (see also Theorem 7.12). This effect is modeled through the coefficient z_s [see Eq. (7.136)].
- Given that for $k \neq 0$, the effective stress $\tilde{\Sigma}_e = m\sqrt{\sum_{i=1}^{3}\left(|\Sigma'_i| - k\Sigma'_i\right)^2}$ depends on the relative ordering of the eigenvalues of the stress deviator Σ', the Cazacu and Stewart [20] criterion predicts that with the exception of purely hydrostatic loadings there is an effect of the third-invariant J_3^{Σ} on yielding of the porous material (see also Theorems 7.12 and 7.13).
- If $\beta = \sigma_T/\sigma_C = 1$ and consequently $k = 0$, the Cazacu and Stewart [20] criterion given by Eq. (7.135) reduces to the Gurson [30] criterion for a porous von Mises material [see Eq. (7.41)]. Indeed, for $\sigma_T/\sigma_C = 1$, the coefficient $z_s = 1$ (see Eq. (7.136) and $\tilde{\Sigma}_e = \Sigma_e$ (see Eq. (7.141).
- In the absence of voids ($f = 0$), the Cazacu and Stewart [20] criterion given by Eq. (7.135) reduces to the isotropic and quadratic form of the Cazacu et al. [15] yield criterion [see Eq. (7.125)].

As an example, in Fig. 7.66 is shown the representation in the plane (Σ_m, Σ_e) of the yield locus according to the Cazacu and Stewart [20] criterion given by Eq. (7.135) for a porous material (f = 0.01) and matrix displaying tension–compression asymmetry characterized by the ratio $\beta = 0.82$ [$k = -0.3$, see Eq. (7.126)]. Note that the yield locus is represented by two curves, one corresponding to axisymmetric stress states for which $J_3^{\Sigma} \leq 0$ while the other corresponding to axisymmetric stress states for which $J_3^{\Sigma} \geq 0$, these two curves having in common only the hydrostatic states, i.e., the points $(p_Y^+, 0)$ and $(p_Y^-, 0)$ [see Eqs. (7.130) and (7.131)].

To better put into evidence and visualize the complete lack of symmetry of the yield surface of a porous material with matrix having SD effects, in Fig. 7.67a, b are shown the projection in the $(\Sigma_{11} - \Sigma_{33}, \Sigma_m)$ plane of the Cazacu and Stewart [20] yield surface for two porous materials ($f = 0.01$), one with matrix having the yield stress in tension less than in compression [$\sigma_T/\sigma_C = 0.71$, corresponding to $k = -0.9$, see Eq. (7.126)] while the other having the yield stress in tension larger than in compression [corresponding to $\sigma_T/\sigma_C = 1.41$, k = 0.9, see Eq. (7.126)].

Irrespective of the SD ratio of the matrix, the yield locus is no longer symmetric with respect to the deviatoric axis ($\Sigma_m = 0$). Furthermore, because the Cazacu and Stewart [20] criterion depends on the sign and ordering of the eigenvalues of Σ', the yield locus is no longer symmetric with respect to the hydrostatic axis (i.e., $\Sigma_{11} = \Sigma_{22} = \Sigma_{33}$). In general, the yield surface of a porous material with incompressible matrix having the same response in tension–compression is invariant to the transformation: $(\Sigma_m, \Sigma') \rightarrow (\Sigma_m, -\Sigma')$ (see Theorem 7.1). This is no longer the

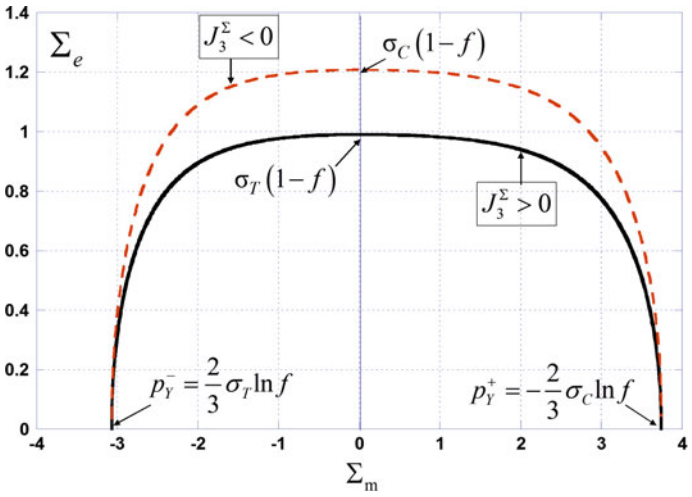

Fig. 7.66 Cazacu and Stewart [20] theoretical yield surface for a porous material with matrix displaying tension–compression asymmetry characterized by the ratio $\sigma_T/\sigma_C = 0.82$ ($k = -0.3$) and porosity $f = 0.01$. Both axisymmetric states corresponding to $J_3^\Sigma \leq 0$ ($\Sigma_{11} = \Sigma_{22} \geq \Sigma_{33}$) (interrupted line) and states corresponding to $J_3^\Sigma \geq 0 (\Sigma_{11} = \Sigma_{22} \leq \Sigma_{33})$ (solid line) are represented

case for porous materials with incompressible matrix having SD effects. This is a key difference in yielding response with respect to porous materials with matrix behavior represented by an even yield function (e.g., compare Fig. 7.67a, b with Fig. 7.32 representing in the same plane a porous Tresca material).

It is also worth mentioning that according to Cazacu and Stewart [20] criterion, the tension–compression asymmetry in the plastic deformation has a very strong influence on yielding of the porous material. In particular, the sensitivity of the mechanical response of the porous material to the third-invariant J_3^Σ is correlated to the ratio σ_T/σ_C

- For a porous material with matrix characterized by $\sigma_T < \sigma_C$ ($k < 0$), the response is softer for axisymmetric loadings at $J_3^\Sigma \geq 0$ than for axisymmetric loadings at $J_3^\Sigma \leq 0$ (see also Fig. 7.67a).
- For a porous material with matrix characterized by $\sigma_T > \sigma_C$ ($k > 0$), the response is softer for axisymmetric loadings such that $J_3^\Sigma \leq 0$ (i.e., $\Sigma_{11} = \Sigma_{22} \geq \Sigma_{33}$) than for loadings at $J_3^\Sigma \geq 0$ (i.e., $\Sigma_{11} = \Sigma_{22} \leq \Sigma_{33}$), see also Fig. 7.67b.

The effects of the tension–compression asymmetry of the matrix on void evolution will be analyzed in detail in Sect. 7.3.2.

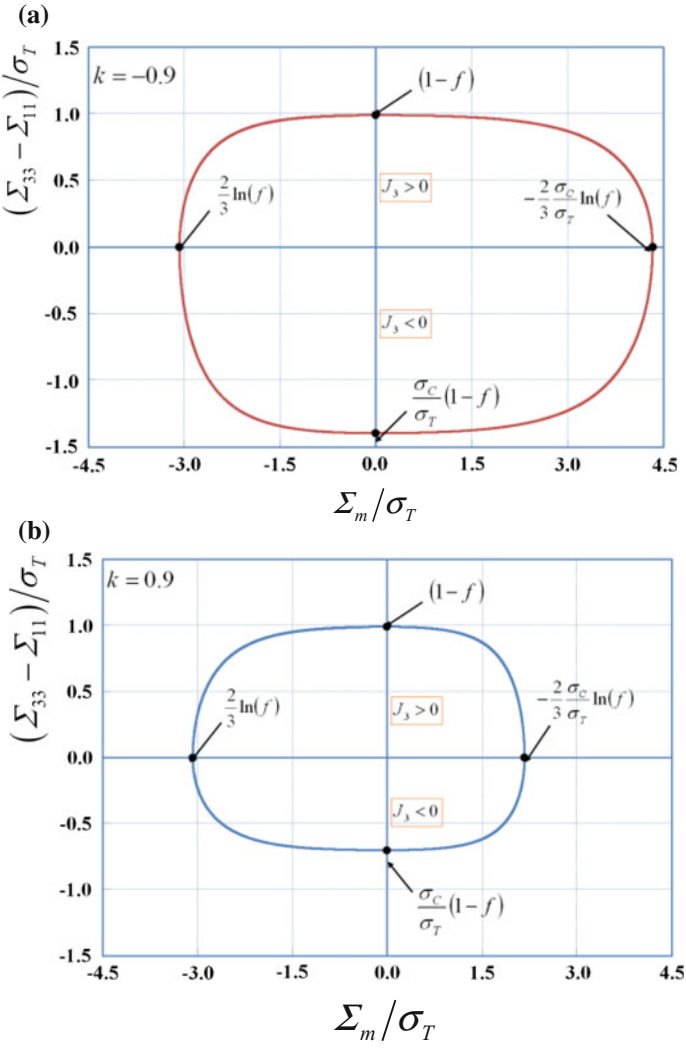

Fig. 7.67 Theoretical yield surfaces according to the Cazacu and Stewart [20] criterion for porous materials ($f = 0.01$) with incompressible matrix displaying tension–compression asymmetry **a** $k = -0.9$ ($\sigma_T/\sigma_C = 0.71$) **b** $k = 0.9$ ($\sigma_T/\sigma_C = 1.41$)

7.3.1.1 Effect of the Matrix Tension–Compression Asymmetry on Yielding

Cazacu and Stewart [20] have also reported results of F.E. unit-cell calculations where the matrix is governed by the isotropic and quadratic form of the Cazacu et al. [15] yield criterion [see Eq. (7.125)]. The main focus was on assessing the unusual features of the yielding of voided materials predicted by the model. 2-D

F.E. unit-cell model calculations for both tensile and compressive axisymmetric loadings were conducted at fixed strain triaxiality, T_E, the RVE considered being a cylinder with a single spherical void at its center. All the simulations were performed using a UMAT for the F.E. code ABAQUS. For more details concerning the boundary-value problem and the F.E. mesh, the reader is referred to Cazacu and Stewart [20], while for details concerning the F.E. implementation of an elastic–plastic model with yielding according to the Cazacu et al. [15] yield criterion, the reader should refer to Chaps. 2 and 4. The matrix elastic properties were: $E/\sigma_T = 800$ and $\nu = 0.32$. Two different porous materials (with $f = 0.01$) were considered, Material 1 with matrix characterized by $k = 0.3098$ $(\sigma_T/\sigma_C = 0.82)$ and Material 2 with matrix characterized by $k = -0.3098$ $(\sigma_T/\sigma_C = 1.22$, the reciprocal of the SD ratio of the matrix of Material 1). Such SD ratios were obtained by Hosford and Allen [35] for fcc and bcc polycrystals with random textures for which the constituent grains deform solely by twinning (for more details concerning these crystal plasticity calculations and the identification of the values of k for these materials, see also 4.3). Figures 7.68 and 7.69 show a comparison between the theoretical yield surfaces according to the Cazacu and Stewart [20] porous model and the numerical results. For the simulations corresponding to axisymmetric loadings with $J_3^\Sigma \leq 0$, the imposed strain triaxialities were as follows: for Material 1, T_E ranged from ± 0.303 to ± 3.328 while for Material 2, T_E ranged from ± 0.207 to ± 2.272. For simulations at $J_3^\Sigma \geq 0$, the numerical points correspond to strain triaxialities ranging from $T_E = \pm 0.25$ to $T_E = \pm 2.75$ for both materials. In the respective figures, the stresses are normalized by the tensile stress of the fully dense material, σ_T.

The main observation from these figures is that the strong effect of the third-invariant on yielding of the porous materials predicted by the Cazacu and Stewart [20] criterion is indeed confirmed by the F.E. unit-cell model results. For Material 1 whose matrix is softer in tension than in compression $(\sigma_T/\sigma_C = 0.82)$, the F.E. predictions corresponding to $J_3^\Sigma \leq 0$ are above those for $J_3^\Sigma \geq 0$, the maximum split corresponding to the purely deviatoric points. Meanwhile, for Material 2 whose matrix is softer in compression than in tension $(\sigma_T/\sigma_C = 1.22)$, the reverse occurs, i.e., the F.E. predictions corresponding to $J_3^\Sigma \geq 0$ are above those for $J_3^\Sigma \leq 0$, the maximum split being also for deviatoric loadings. Moreover, the maximum splits for the two materials are, within the precision of the numerical solutions, identical, as predicted by the model. Indeed, as demonstrated in Theorem 7.13 under purely deviatoric axisymmetric loadings, the ratio between the yield limits at $J_3^\Sigma \geq 0$ and $J_3^\Sigma \leq 0$ should be equal to σ_T/σ_C [see Eqs. (7.132) and (7.133)].

Note also that the F.E. unit-cell predictions show a clear effect of the sign of applied hydrostatic loading on the response of porous materials. For the Material 1 whose matrix is softer in tension than in compression $(\sigma_T/\sigma_C = 0.82)$, the F.E. predictions show that the mean stress at yielding corresponding to tensile hydrostatic loading is greater than that corresponding to compressive hydrostatic loading. On the other hand, for Material 2 with matrix having $\sigma_T > \sigma_C$, the absolute value of the mean stress corresponding to compressive hydrostatic loading is greater than

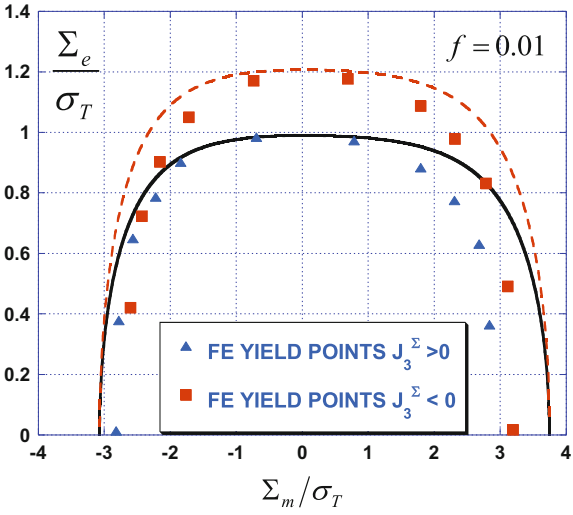

Fig. 7.68 Yield surface of a porous material with incompressible matrix characterized by $\sigma_T/\sigma_C = 0.82$ according to the Cazacu and Stewart [20] and F.E. unit-cell model yield points (symbols) for axisymmetric loadings such that $J_3^\Sigma \geq 0$ (solid line) and $J_3^\Sigma \leq 0$ (interrupted line), respectively. Initial porosity $f = 0.01$. Stresses are normalized by the matrix yield stress in uniaxial tension, σ_T

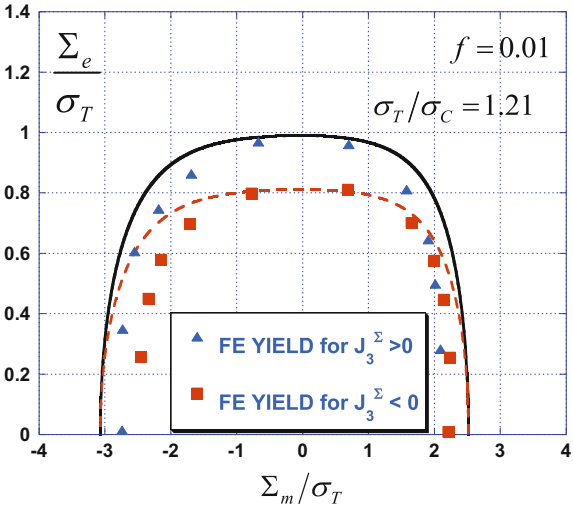

Fig. 7.69 Yield surface of a porous material with incompressible matrix characterized by $\sigma_T/\sigma_C = 1.22$ according to Cazacu and Stewart [20] criterion and F.E. unit-cell model yield points (symbols) for axisymmetric loadings such that $J_3^\Sigma \geq 0$ (solid line) and $J_3^\Sigma \leq 0$ (interrupted line), respectively. Initial porosity $f = 0.01$. Stresses are normalized by the matrix yield stress in uniaxial tension, σ_T

that corresponding to tensile hydrostatic loading. This is consistent with the model predictions. Indeed, as demonstrated in Theorem 7.12 the ratio between the hydrostatic yield limits is: $\left|p_Y^+/p_Y^-\right| = \sigma_C/\sigma_T$ [see Eqs. (7.131)–(7.133)].

As already mentioned, Cazacu and Stewart [20] also performed F.E. unit-cell calculations corresponding to a material with matrix characterized by $k = 0$ [von Mises material, see also Eq. (7.125)] (see also Sect. 7.2.3.4). The results showed that if the matrix has no SD effects: (a) for purely deviatoric axisymmetric loadings, the yield limit of the porous material point is insensitive to the sign of J_3^Σ; (b) the yielding of the porous material under purely hydrostatic loadings does not depend

on the sign of the applied load (tensile or compressive); (c) for all other loadings there is a combined effect of the signs of J_3^{Σ} and Σ_m.

Similarly to Tvergaard [67]; Tvergaard and Needleman [69], the Cazacu and Stewart [20] yield criterion can be modified to include additional parameters, q_i, as follows:

$$\left(m\sqrt{\sum_{i=1}^{3}\left(\left|\frac{\Sigma'_i}{\sigma_T}\right|-k\frac{\Sigma'_i}{\sigma_T}\right)^2}\right)^2+2q_1 f\cosh\left(\frac{3z_s}{2}q_2\frac{\Sigma_m}{\sigma_T}\right)-\left(1+q_3 f^2\right)=0 \tag{7.144}$$

with $z_s=1+\frac{1}{2}\left[\mathrm{sgn}^2(\Sigma_m)+\mathrm{sgn}(\Sigma_m)\right]\left(\frac{\sigma_T}{\sigma_C}-1\right)$.

In this manner, for $k = 0$ (von Mises matrix) the yield criterion given by Eq. (7.144) reduces to the Gurson–Tvergaard–Needleman (GTN) model [Eq. (7.54)]. In Fig. 7.70 is shown a comparison between the theoretical yield loci of this modified version of the Cazacu and Stewart [20] model [see Eq. (7.144)] corresponding to axisymmetric loading at $J_3^{\Sigma}\le 0$ and F.E. numerical results for a material with matrix characterized by $\sigma_T/\sigma_C = 0.82$ and several porosities $f = 0.01$, 0.04, and 0.14, respectively. As expected, the criterion predicts that increasing porosity results in softening of the material. Similar conclusions can be drawn for the case when $J_3^{\Sigma}\ge 0$. Application of this criterion to modeling porosity evolution in an Al alloy will be presented in Sect. 7.3.3.

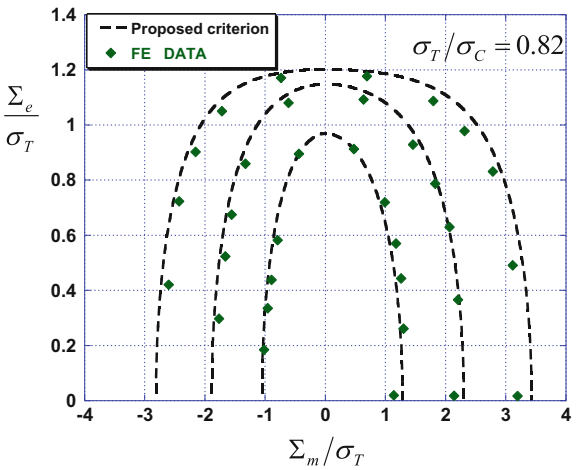

Fig. 7.70 Yield surface of a porous material with matrix characterized by an SD ratio $\sigma_T/\sigma_C = 0.82$ according to the modified version of the Cazacu and Stewart [20] criterion for axisymmetric loadings such $\Sigma_{11} = \Sigma_{22} \ge \Sigma_{33}$ ($J_3^{\Sigma}\le 0$) for several porosities: $f = 0.01$, $f = 0.04$, and $f = 0.14$, respectively. Stresses are normalized by the matrix yield stress in uniaxial tension, σ_T

7.3.1.2 Influence of the Matrix Tension–Compression Asymmetry on Void Evolution

The Cazacu and Stewart [20] analysis and model for porous materials with matrix having SD effects revealed that irrespective of loading, yielding is influenced by the third-invariant J_3^{Σ}, the strongest effect being for purely deviatoric axisymmetric loadings. Moreover, the manner in which J_3^{Σ} affects yielding depends on the ratio σ_T/σ_C. As a consequence, the influence of J_3^{Σ} on void evolution is also affected by the matrix tension–compression asymmetry. F.E. unit-cell calculations were also conducted to verify these new features predicted by the model. Only the main results of these studies are presented, for more details the reader is referred to Cazacu et al. [12]; Alves and Cazacu [1]; Alves and Cazacu [3].

The F.E. analyses of void evolution were conducted for cubic unit cells containing a single initially spherical cavity (for the geometry of the unit cell, see Sect. 7.2.3.2). For axisymmetric loadings, a fixed ratio of the axial and lateral true stresses was maintained throughout the loading history (i.e., fixed level of the stress triaxiality T). For a given value of the triaxiality, loading histories corresponding to positive and negative values of J_3^{Σ} were considered. As an example, Fig. 7.71 compares the porosity f versus the overall equivalent strain E_e [for definition E_e see Eq. (7.51)] evolution for tensile axisymmetric loading histories corresponding to $\Sigma_1 = \Sigma_2 \leq \Sigma_3$ $(J_3^{\Sigma} \geq 0)$ and a fixed positive stress triaxiality $T = 2$ for porous materials with matrix characterized by $k = -0.3$ and $k = 0.3$, respectively. The initial porosity was $f_0 = 0.0013$ such as to enable comparison with the F.E. unit-cell results for von Mises matrix behavior $(k = 0)$ presented in Sect. 7.2.3.4.

As a general observation, the strong influence of the tension–compression asymmetry of the matrix on void growth predicted by the Cazacu and Stewart [20] criterion is confirmed by the numerical results. Note that the rate of void growth is fastest in the material with $k = 0.3$ (matrix softer in compression than in tension). The effect of the stress triaxiality on void growth is also well described by the

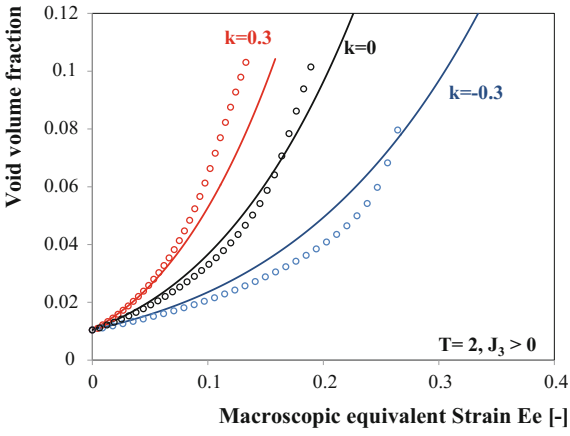

Fig. 7.71 Comparison between the evolution of the void volume fraction f with the equivalent strain E_e, obtained by F.E. unit-cell calculations and the Cazacu and Stewart [20] criterion for axisymmetric loadings at fixed stress triaxiality $T = 2$ such that $\Sigma_1 = \Sigma_2 \leq \Sigma_3$ $(J_3^{\Sigma} \geq 0)$ for materials characterized by different tension–compression asymmetry ratios corresponding to $k = -0.3$, $k = 0$, and $k = 0.3$, respectively

model. Irrespective of the tension–compression ratio, the higher is the triaxiality the faster is the rate of void growth (see Fig. 7.72 for $k = -0.3$ and $k = 0.3$, and Fig. 7.13 for $k = 0$).

For the porous materials with matrix characterized by $k = 0.3$ and $k = -0.3$, comparison between the predictions of the evolution of porosity according to the Cazacu and Stewart [20] criterion and the F.E. unit-cell calculations corresponding to axisymmetric loadings for the same triaxialities, but corresponding to $J_3^{\Sigma} \leq 0$ are presented in Fig. 7.73a, b. Note the very good agreement between the model and the numerical results.

Comparison between the results presented in Figs. 7.72 and 7.73 shows that irrespective of the value of k, there is a strong effect of J_3^{Σ} on void evolution. For the material with matrix characterized by $k = 0.3$, the rate of void growth is faster for loadings at $J_3^{\Sigma} \geq 0$ than for loadings at $J_3^{\Sigma} \leq 0$. On the other hand, for the material with matrix characterized by $k = -0.3$, the opposite holds true, i.e., the rate of void

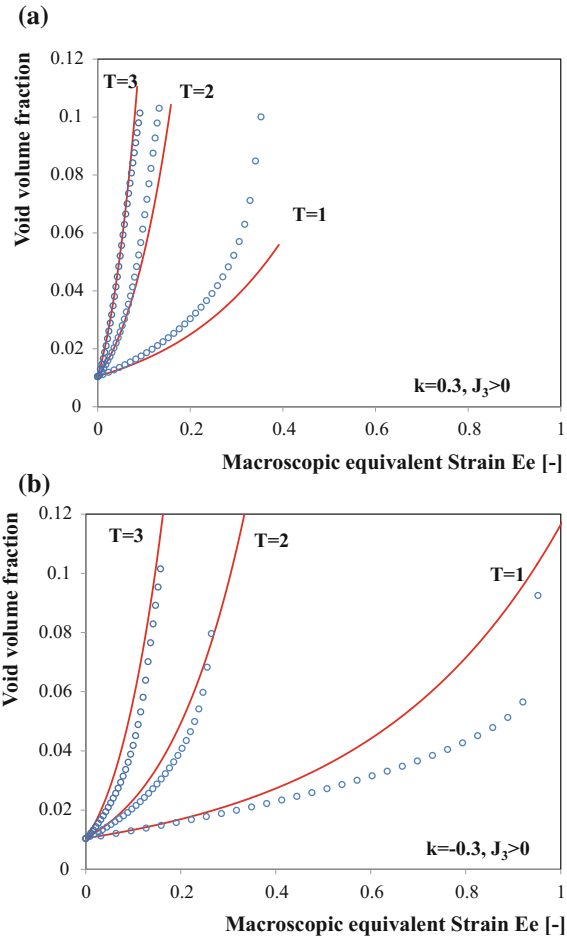

Fig. 7.72 Comparison between the evolution of the void volume fraction f with the equivalent strain E_e, obtained by F.E. unit-cell calculations and the Cazacu and Stewart [20] criterion for axisymmetric loadings at fixed stress triaxialities $T = 1$, $T = 2$, and $T = 3$, respectively, for loadings such that $\Sigma_1 = \Sigma_2 \leq \Sigma_3$ ($J_3^{\Sigma} \geq 0$) for materials characterized by different tension–compression asymmetry ratios corresponding to: **a** $k = 0.3$ and **b** $k = -0.3$, respectively

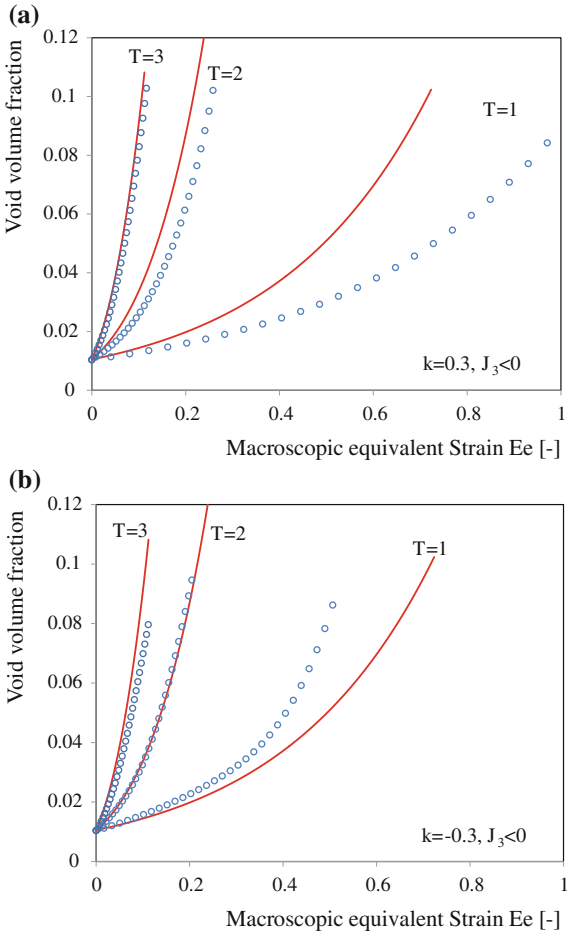

Fig. 7.73 Comparison between the evolution of the void volume fraction f with the equivalent strain E_e, obtained by F.E. unit-cell calculations and the Cazacu and Stewart [20] criterion for axisymmetric loadings at fixed stress triaxialities $T = 1$, $T = 2$, and $T = 3$, respectively, for loadings such that $\Sigma_1 = \Sigma_2 > \Sigma_3$ ($J_3^{\Sigma} \leq 0$) for materials characterized by different tension–compression asymmetry ratios corresponding to: **a** $k = 0.3$ and **b** $k = -0.3$, respectively

growth is slower for loadings at $J_3^{\Sigma} \geq 0$ than for loadings at $J_3^{\Sigma} \leq 0$. Thus, the manner in which J_3^{Σ} affects void evolution depends strongly on the matrix SD ratio described by the parameter k.

Moreover, for loadings such that $J_3^{\Sigma} \geq 0$, the fastest void growth rate occurs in the material characterized by $k = 0.3$; on the other hand, for loadings such that $J_3^{\Sigma} \leq 0$, the fastest void growth rate occurs in the material characterized by $k = -0.3$. While examples have been provided only for specific values of k, the same conclusions hold true for all k.

In summary, irrespective of the imposed loading, the Cazacu and Stewart [20] model predicts that the tension–compression asymmetry in the plastic flow of the matrix, described by the parameter k, has a very strong influence on all aspects of the mechanical response of the porous solids. Furthermore, there is a very strong effect of the loading path, in particular of J_3^{Σ} on yielding, porosity evolution, and

ultimately on the material's ductility. Specifically, for materials with matrix such that $\sigma_T/\sigma_C < 1$ ($k < 0$) for axisymmetric loadings at $J_3^{\Sigma} \leq 0$ damage growth is much faster than in the case of loadings at $J_3^{\Sigma} \geq 0$, which in turns affects the overall ductility. The reverse holds true for materials with matrix characterized by $\sigma_T/\sigma_C \geq 1$ ($k \geq 0$). All those trends predicted by the analytical criterion of Cazacu and Stewart [20] were confirmed by F.E. unit-cell calculations.

In the next section, the influence of the matrix SD ratio on damage accumulation under uniaxial tension is assessed using an elastic–plastic model based on this criterion.

7.3.2 *Effect of the Matrix Tension–Compression Asymmetry on Damage in Round Tensile Bars*

To simplify writing, in all the applications that will be discussed in Sect. 7.3.2 and 7.3.3, the Cauchy stress applied to the porous material is denoted by $\boldsymbol{\sigma}$, its deviator by $\mathbf{s}$ (and its eigenvalues by s_i) and the stress by σ_m, and the matrix effective yield stress by $\bar{\sigma}$. Thus, the modified version of the Cazacu and Stewart [20] yield criterion given by Eq. (7.144) writes:

$$\Phi = \frac{9}{2(3k^2 - 2k + 3)} \sum_{i=1}^{3} \left(\frac{|s_i| - k s_i}{\bar{\sigma}} \right)^2 + 2q_1 f \cosh\left(q_2 \frac{3 z_s \sigma_m}{2\bar{\sigma}} \right) - \left(1 + q_3 f^2 \right) \tag{7.145}$$

It is worth recalling that since Cazacu and Stewart [20] criterion was derived using rigorous upscaling methods, the dependence of the dilatational response on the mean stress, σ_m, was deduced and not postulated. Consequently, the parameter z_s involved in Eq. (7.145) has a clear physical significance, being dependent on the specificities of the plastic deformation of the matrix (through k) and on the state of stress. Its expression is:

$$z_s = \begin{cases} 1 & \text{if} \quad \sigma_m \leq 0, \\ \sqrt{\dfrac{3k^2 + 2k + 3}{3k^2 - 2k + 3}} & \text{if} \quad \sigma_m > 0. \end{cases} \tag{7.146}$$

For $k = 0$, $z_s = 1$ for any value of the mean stress, so Eq. (7.145) coincides with the GTN criterion (see Eq. (7.54) and discussion in Sect. 7.2.3.2).

Using the Cazacu and Stewart [20] criterion, Revil-Baudard and Cazacu [56] conducted a numerical study on the influence of the matrix tension–compression asymmetry on void evolution and the location of the zone corresponding to maximum damage in round tensile specimens subject to uniaxial tension.

Normality flow rule was assumed, i.e., $\mathbf{d}^p$, the plastic part of the strain-rate is given by:

$$\mathbf{d}^p = \dot{\lambda}\frac{\partial \Phi}{\partial \boldsymbol{\sigma}}, \tag{7.147}$$

Matrix hardening was considered, i.e., in Eq. (7.145) the matrix effective stress $\bar{\sigma}$ was taken to be a function of the effective plastic strain, $\bar{\varepsilon}^p$, the hardening law being of the form:

$$\bar{\sigma} = \alpha(\varepsilon_0 + \bar{\varepsilon}^p)^n \tag{7.148}$$

with the hardening exponent n being a constant and the parameters α, and ε_0 having dimensions of stress and strain, respectively. The matrix being incompressible, from mass conservation it follows that the porosity evolves according to:

$$\dot{f} = (1-f)\,\mathbf{d}^p : \mathbf{I} \tag{7.149}$$

Following the same arguments as Gurson [30], if $\bar{\sigma}$ is given by Eq. (7.148), the following work–equivalence relationship applies

$$\bar{\sigma}\dot{\bar{\varepsilon}}^p(1-f) = \boldsymbol{\sigma}:\mathbf{d}^{\mathrm{p}} \tag{7.150}$$

From Eqs. (7.147) to (7.150), the evolution law for the effective plastic strain is:

$$\dot{\bar{\varepsilon}}^{\mathrm{p}} = \dot{\lambda}\frac{\boldsymbol{\sigma}:\frac{\partial \Phi}{\partial \boldsymbol{\sigma}}}{(1-f)\bar{\sigma}}. \tag{7.151}$$

The aim of the study being the investigation of the effect of the tension–compression asymmetry of the matrix on void growth, F.E. simulations were conducted for various values of the strength differential parameter k; all the others parameters were kept the same. Specifically, in all simulations the elastic properties of the matrix were: ($E/\sigma_T = 300$, $\nu = 0.3$), the parameters involved in the law of evolution of the tensile yield stress of the matrix were taken as: $\alpha/\sigma_T = 1.8$; $\varepsilon_0 = 0.0027$; $n = 0.1$, the initial void volume fraction $f_0 = 0.04$, and $q_1 = 1.5$, $q_2 = 1$, and $q_3 = q_1^2$. Since void nucleation was not considered and all the materials have the same matrix tensile yield stresses [see Eq. (7.148)], any differences in damage evolution between porous materials are due solely to the matrix tension–compression asymmetry (SD ratio). Moreover, the numerical values that were taken for the matrix elastic properties, matrix yield stress in tension and matrix hardening in tension are the same as those given by Tvergaard and Needleman [69] and Aravas [5]. Therefore, with this choice of the numerical values for the matrix properties, the porous material with $k = 0$ (no tension–compression asymmetry in the matrix) is in fact the porous von Mises material considered by Tvergaard and Needleman [69].

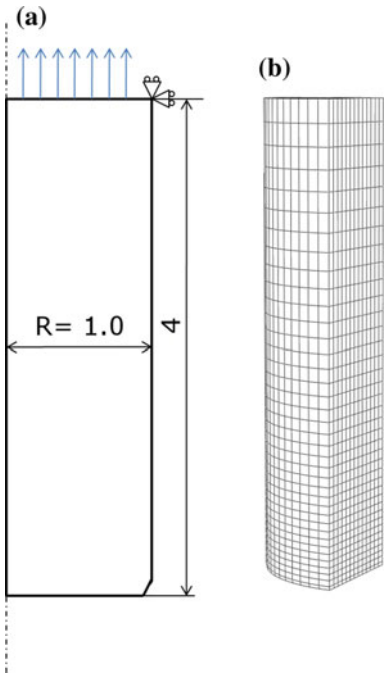

Fig. 7.74 **a** Geometry and boundary conditions for the tensile test on a notched specimen with circular cross-section; **b** F.E. mesh of one-eighth of the specimen

Results of F.E. analyses of void evolution in a long, notched specimen with circular cross-section were reported. An initial geometric imperfection was used to induce necking in the specimen (see Fig. 7.74). The specimen considered has an initial length of $2L_0$ and initial radius of R_0 with $L_0/R_0 = 4$, with R_0 set to unity. A cylindrical reference coordinate system (radial coordinate R, axial coordinate Z) was used for the analysis. The following kinematic boundary conditions were imposed: symmetry about $R = 0$ and symmetry about $Z = 0$; all the nodes along $Z = L_0$ were pulled in the Z direction while the nodes in the radial direction were free. The F.E. mesh for one-eight of the bar is shown in Fig. 7.74b. It consists of 5472 hexahedral elements with reduced integration (ABAQUS C3D8R). The simulations were carried out using a User Material Subroutine (UMAT) that was developed for the coupled elastic–plastic damage model [Eqs. (7.147)–(7.151)] and implemented in the F.E. code ABAQUS. The simulation were terminated when a critical void volume fraction f_c was reached ($f_c = 15.5\%$).

7.3.2.1 Materials with Matrix Characterized by a Constant Strength Differential Ratio

Round tensile bars made of three isotropic materials containing randomly oriented spherical voids in a matrix characterized by $\sigma_T/\sigma_C = 1.24$, and $\sigma_T/\sigma_C = 1.41$ and $\sigma_T/\sigma_C = 1$ (GTN material-no strength differential effects) were examined. For

these materials, the corresponding values of the SD parameter are: $k = 0.355$, $k = 0.9$, and $k = 0$, respectively [see Eq. (7.126)]. Figure 7.75 shows isocontours of the porosity f for the three materials. These isocontours correspond to the end of each test, i.e., corresponding to the maximum porosity $f_c = 15.5\%$. Therefore, the global strain $\varepsilon = \ln(L/L_0)$ varies from one material to another.

For all materials, the maximum void volume fraction develops at the center of the specimen. However, for the material with matrix characterized by $k = 0.9$ ($\sigma_T/\sigma_C = 1.41$), the extent of the zone of maximum damage is the smallest. Note

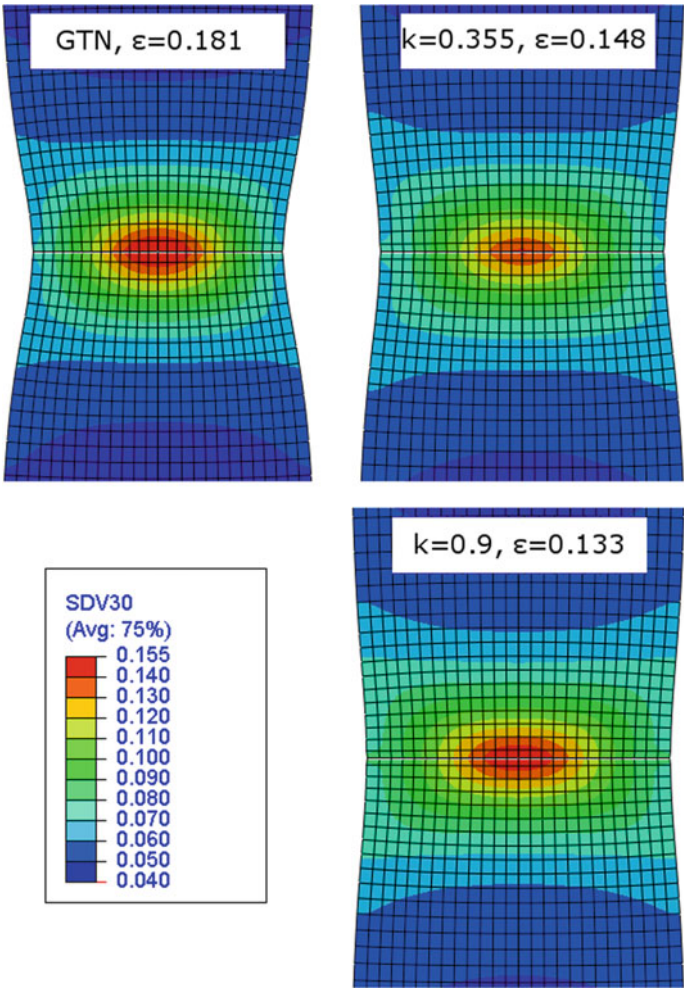

Fig. 7.75 Contours of constant void volume fraction, f, corresponding to the end of the test (i.e., for $f_{\max} = 15.5\%$) for materials with matrix having the yield in tension larger than the yield in compression $k = 0.355$ ($\sigma_T/\sigma_C = 1.24$) and $k = 0.9$ ($\sigma_T/\sigma_C = 1.41$), in comparison with a GTN material ($k = 0$)

that for the material with the highest contrast between the matrix yield stresses in tension–compression ($k = 0.9$), the damage isosurfaces become square with rounded corners whereas for lower contrast the isosurfaces are oval, and the porosity is more localized. Results of F.E. simulations were also reported for porous materials with matrix characterized by negative values of k, i.e., for materials with matrix yield in tension less than in compression ($\sigma_T < \sigma_C$). The isocontours of porosity corresponding to the end of each test, shown in Fig. 7.76, demonstrate an important influence of the tension–compression asymmetry on the void volume fraction distribution. For $k = -0.355$ ($\sigma_T/\sigma_C = 0.81$), the void volume fraction map is qualitatively similar to that for $k \geq 0$, with the maximum void volume fraction being at the center of the specimen. For $k = -0.544$ ($\sigma_T/\sigma_C = 0.75$), there is a much larger spread of the zone of maximum damage than in the case when $k = -0.355$ ($\sigma_T/\sigma_C = 0.81$); as k further decreases ($k = -0.686$ corresponding to $\sigma_T/\sigma_C = 0.72$), the zone of maximum damage extends to the entire section. *For* $k = -0.9$ ($\sigma_T/\sigma_C = 0.71$)*, the zone of maximum damage shifts from the center of the specimen toward its outer surface.* A clear correlation between the value of the tension–compression asymmetry ratio and the location of the zone of maximum damage is observed (Fig. 7.76). It is worth pointing out that $k = -0.544$ corresponds to a tension–compression asymmetry ratio σ_T/σ_C of 0.75 while $k = -0.9$ corresponds to $\sigma_T/\sigma_C = 0.71$. Thus, a difference of less than 5% in the matrix tension–compression ratio leads to a very strong difference in the location of the zone of maximum damage.

To better quantify the observed shift, in Fig. 7.77 is shown the normalized void volume fraction ($f/f_{\max}$) as a function of the distance from the center of the specimen ($R/R_{\max}$) for different materials. In each case, the void distribution corresponds to the end of the test (all simulations are terminated at $f_c = 15.5\%$; $R_{\max}$ denotes the radius of the specimen at the end of a given test). Dimensionless quantities for damage and radial distance have been used in order to allow comparison between the void volume fraction distributions corresponding to different porous materials.

The trends illustrated in Figs. 7.75 and 7.76 are confirmed. It is clearly observed that the different materials considered could be divided into two categories, namely materials for which the maximum void volume fraction develops at the center of the specimen, and materials for which the maximum void volume fraction shifts away from the center. It is very interesting to note that the void volume fraction distribution is not simply dictated by the sign of k (i.e., whether the matrix tensile yield stress in tension is larger than in compression), but also depends on the absolute value of this parameter. Indeed, the material characterized by $k = -0.355$ has a response closer to that of a material with $k > 0$ ($\sigma_T > \sigma_C$) than to a material for which $k = -0.686$. To better understand the effects of the tension–compression ratio on void evolution, in Figs. 7.78 and 7.79 are shown contours of constant void volume fraction, f, at various stages of the test (i.e., for different levels of the global axial deformation $\varepsilon = \ln(L/L_0)$) for materials with $k = -0.686$ ($\sigma_T/\sigma_C = 0.72$) and $k = -0.9$ ($\sigma_T/\sigma_C = 0.71$) respectively. Similar evolution of the porosity is

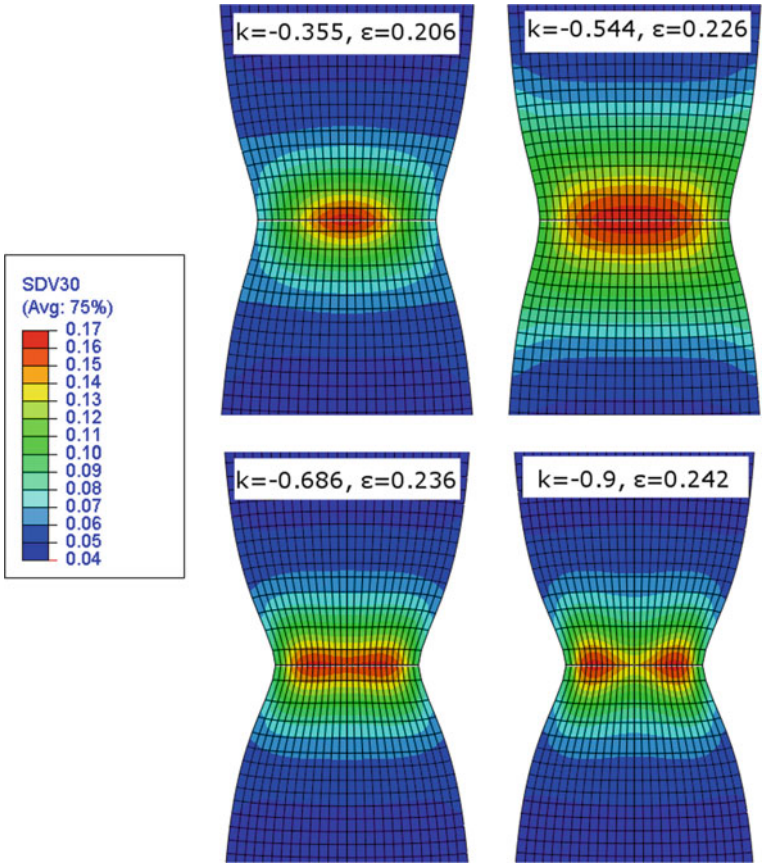

Fig. 7.76 Contours of constant void volume fraction, f, for materials with matrix having the yield in tension less than the yield in compression: $k = -0.355$ $(\sigma_T/\sigma_C = 0.81)$, $k = -0.544$ $(\sigma_T/\sigma_C = 0.75)$, $k = -0.686$ $(\sigma_T/\sigma_C = 0.72)$ and $k = -0.9$ $(\sigma_T/\sigma_C = 0.71)$, corresponding to the end of the test (i.e., for $f_{\max} = 17\%$) (after Revil-Baudard and Cazacu [56])

observed in both materials, namely the damage initiates at the center of the specimen; with increasing deformation, the damage isosurfaces become oval, then damage grows faster at mid-radius than in the center of the specimen, which leads to the final void volume fraction map shown in Fig. 7.76. However, for $k = -0.9$, the trends are much more pronounced.

Isocontours of the third-invariant of the stress deviator, J_3^{Σ}, corresponding to the end of the respective tests are shown in Fig. 7.80. It is very interesting to note that for a GTN material (i.e., $k = 0$ in Eq. (7.145) and for a material with matrix characterized by $k = 0.345$ $(\sigma_T > \sigma_C)$, J_3^{Σ} is positive everywhere in the specimen. However, for the porous materials with matrix having $\sigma_T < \sigma_C$ the sign of J_3^{Σ} is negative at the surface of the specimen. Furthermore, the higher is the contrast, the

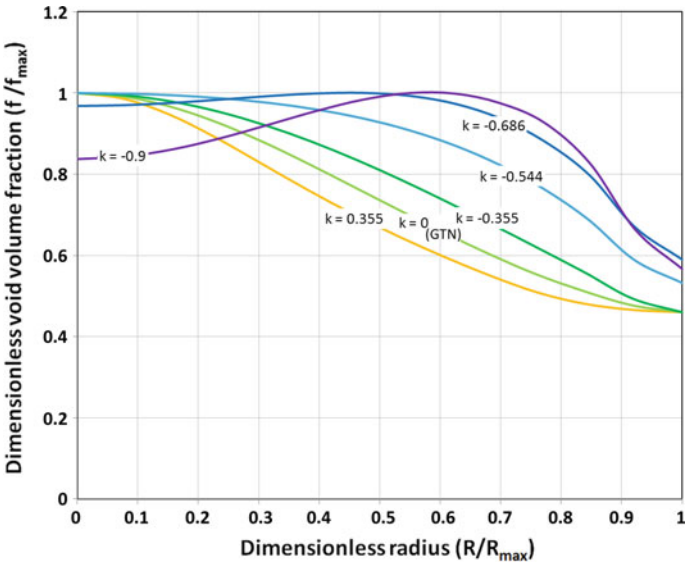

Fig. 7.77 Void volume fraction as a function of the distance from the center of the specimen at the end of the test for porous materials with matrix characterized by different tensile/compression asymmetry ratios: $k = 0.355$ ($\sigma_T/\sigma_C = 1.24$) and $k = 0.9$ ($\sigma_T/\sigma_C = 1.41$), $k = 0$ (GTN material), $k = -0.355$ ($\sigma_T/\sigma_C = 0.81$), $k = -0.544$ ($\sigma_T/\sigma_C = 0.75$), $k = -0.686$ ($\sigma_T/\sigma_C = 0.72$) and $k = -0.9$ ($\sigma_T/\sigma_C = 0.71$). Maximum void volume fraction is shifted from the center if $k < 0.544$

more extended is the zone where J_3^Σ is negative. This explains the differences in the dilatational response, since the higher the contrast, the stronger is the dependence of the yield surface on J_3^Σ, the level of plastic strain and its direction depending on the location in the specimen, i.e., whether in the center or at the surface (see also Fig. 7.67 showing the strong sensitivity of the yield surface of the porous material to the sign of J_3^Σ)

Let us also examine the local evolution of the void volume fraction corresponding to two elements. One was initially located at the center of the specimen while the other was initially at $R/R_0 = 0.582$, i.e., at about mid-radius. It is very interesting to note that for the element located at the center of the specimen, the porosity increases most rapidly in the material characterized by the largest strength differential ratio of the matrix, namely $\sigma_T/\sigma_C = 1.41$. A possible explanation is that among all the materials examined, this material has the smallest compressive yield stress. Thus, according to the Cazacu and Stewart [20] model, under tensile loading this material should yield first, which leads in turn to accelerated void growth when compared to the other materials. On the other hand, for porous materials with matrix characterized by k negative, the fact that their matrix is harder in compression than in tension appears to delay the onset of plastic flow and, thus, delay void growth (see Fig. 7.81b for comparison between the void growth rate in the center element (solid line) of material with $k = 0$ (GTN) and $k = -0.355$

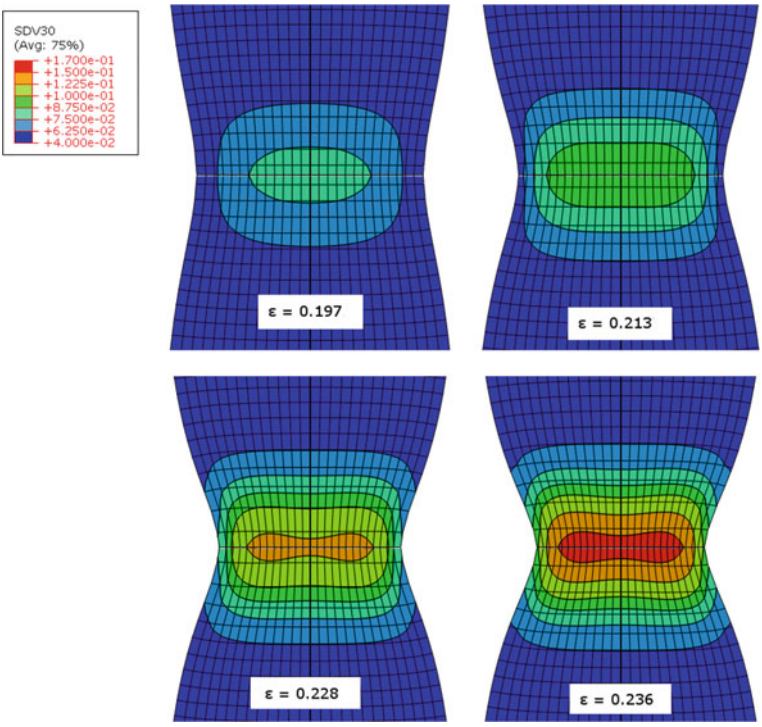

Fig. 7.78 Contours of constant void volume fraction at different stages of the test for a material with $k = -0.686$ ($\sigma_T/\sigma_C = 0.72$)

($\sigma_T/\sigma_C = 0.81$), respectively). It is also worth noting that for a GTN material and for materials with matrix characterized by k positive, the void growth rate for the two elements is similar (see Fig. 7.81a) while for the material with $k = 0.9$ the porosity evolution is almost identical. The local behavior thus correlates with the global response illustrated in Figs. 7.75 and 7.76a, which show that damage distribution is quite similar in these materials. Since damage occurs first in the center, and the void growth rate in the two elements is similar, maximum porosity develops at the center of the specimen. On the other hand, Fig. 7.81b reveals very interesting features of damage evolution for materials with $k < -0.544$. The void growth rate of the element at the center ($R = 0$, solid lines) is slower than that at mid-radius ($R/R_0 = 0.582$; interrupted lines) and there is intersection between the porosity versus local plastic strain curves associated to the two elements, which explains the shift observed previously in the location of the maximum void volume fraction (see, e.g., Fig. 7.77).

To further explain the observed behavior, for the material with matrix characterized by: $k = -0.9$, in Fig. 7.82 are plotted the radial, longitudinal, and axial stress as a function of the local plastic strain in the two elements. Note that for the element at the center of the specimen (solid line), the state of stress is axisymmetric

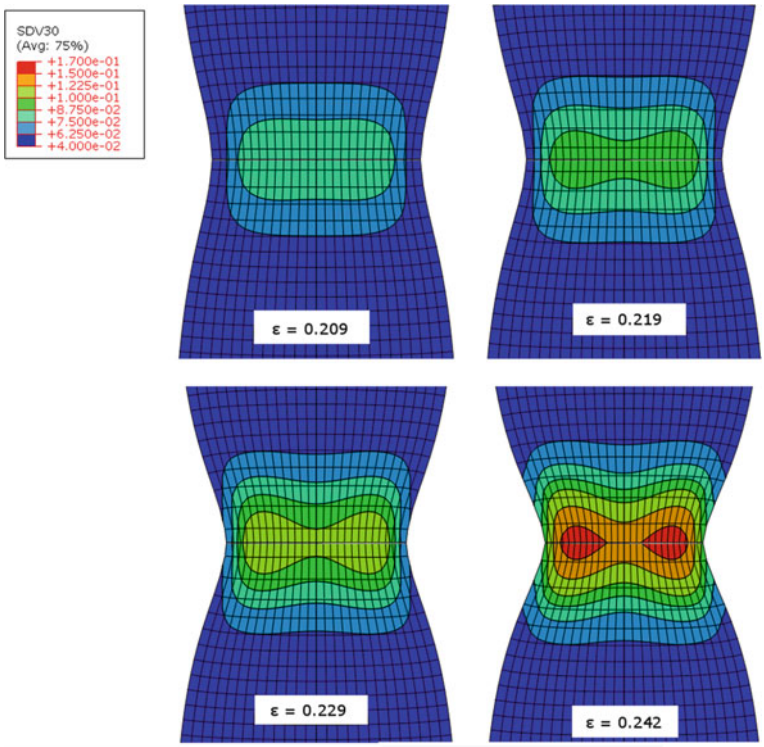

Fig. 7.79 Contours of constant void volume fraction at different levels of the global axial strain for a material with $k = -0.9$ ($\sigma_T/\sigma_C = 0.71$)

($\sigma_{\theta\theta} = \sigma_{rr}$), whereas for the element at mid-radius $\sigma_{\theta\theta} \neq \sigma_{rr}$. The curve representing the evolution of the pressure, $P = -\sigma_m$ with the local plastic strain for the element at the center ($R = 0$) has a maximum at about $\bar{\varepsilon}^p = 0.4$ and then it decreases, hence the local porosity grows faster at mid-radius than at the center (see also Fig. 7.83 and the porosity evolution law according to the Cazacu and Stewart [20] model). Thus, the shift in the location of the zone of maximum damage may be correlated to the criterion being sensitive to the third-invariant of the stress deviator, which influences the plastic flow (level of plastic deformation in the matrix and its orientation), and consequently void growth (see also Fig. 7.67).

7.3.2.2 Materials with Matrix Characterized by an Evolving Tension–Compression Strength Ratio

In all the simulations presented so far, the SD parameter k was considered to be a constant. However, in certain hcp materials the interplay between deformation twinning and slip leads to the evolution of the matrix tension–compression ratio

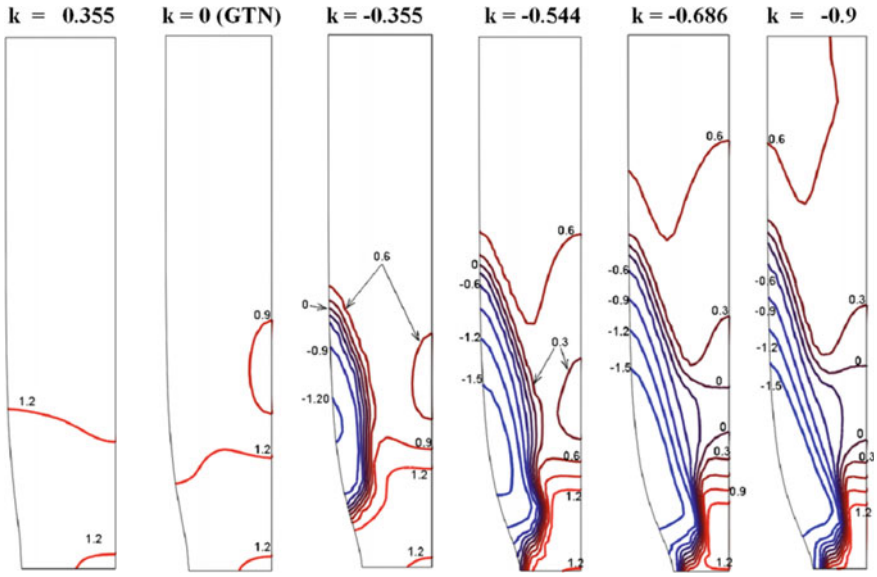

Fig. 7.80 Contours of the third-invariant of the stress deviator, J_3^{Σ} corresponding to the end of each test ($f_{max} = 17\%$) for materials characterized by matrix with different tension–compression asymmetry ratios: $k = 0.355$ $(\sigma_T/\sigma_C = 1.24)$, $k = 0$ (GTN material), $k = -0.355$ $(\sigma_T/\sigma_C = 0.81)$, $k = -0.544$ $(\sigma_T/\sigma_C = 0.75)$, $k = -0.686$ $(\sigma_T/\sigma_C = 0.72)$ and $k = -0.9$ $(\sigma_T/\sigma_C = 0.71)$

with plastic deformation. For example, in Mg alloys, at initial yielding and for equivalent plastic strains less than 10% the tensile strength is larger than the compressive strength, while above 10% the tensile strength is comparable to the compressive strength because twinning saturates (see Hosford [34];Cazacu et al. [15] and further examples in Chap. 5). In hcp-Ti, the tensile and compressive strength are comparable for strains below 10%, while the compressive strengths become larger than the tensile strength (k ranges from 0 to −0.9) as deformation twinning becomes active (see discussion and data of Nixon et al. [52] presented in Chap. 5). To get insights on the rate of void growth to be expected in such materials, Revil-Baudard and Cazacu [56] conducted F.E. analyses of the tensile test for porous materials with matrix characterized by a strength differential ratio k evolving with accumulated plastic deformation. Two evolution laws, with k ranging from zero at the onset of plastic flow to a maximum value of $k_{\max} = -0.9$ $(\sigma_T/\sigma_C = 0.71)$ were considered, namely:

$$k(\bar{\varepsilon}^p) = a + \frac{\mathrm{b}}{1 - \exp(\bar{\varepsilon} - \bar{\varepsilon}_1)/\bar{\varepsilon}_2}, \tag{7.152}$$

and

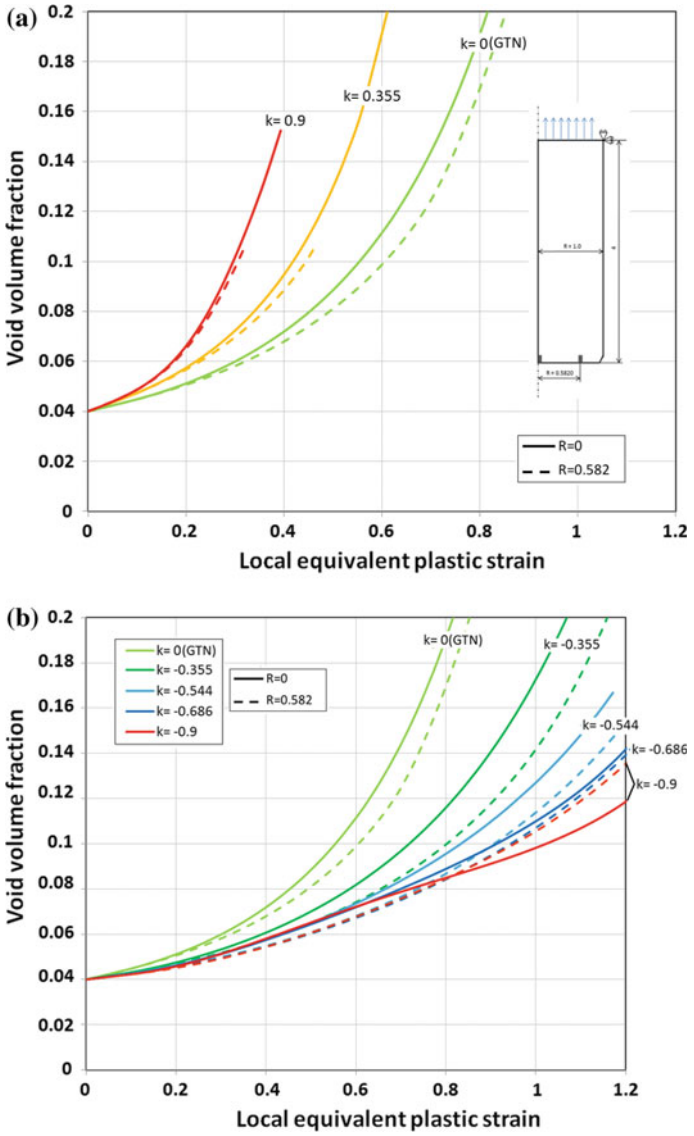

Fig. 7.81 Evolution of the void volume fraction as a function of the local plastic strain at the center of the specimen ($R = 0$) and $R/R_0 = 0.582$ (interrupted line) for different materials **a** $k = 0$ (GTN material), $k = 0.355$ ($\sigma_T/\sigma_C = 1.24$), $k = 0.9$ ($\sigma_T/\sigma_C = 1.41$) and **b** $k = 0$ (GTN material), $k = -0.355$ ($\sigma_T/\sigma_C = 0.81$), $k = -0.544$ ($\sigma_T/\sigma_C = 0.75$), $k = -0.686$ ($\sigma_T/\sigma_C = 0.72$) and $k = -0.9$ ($\sigma_T/\sigma_C = 0.71$)

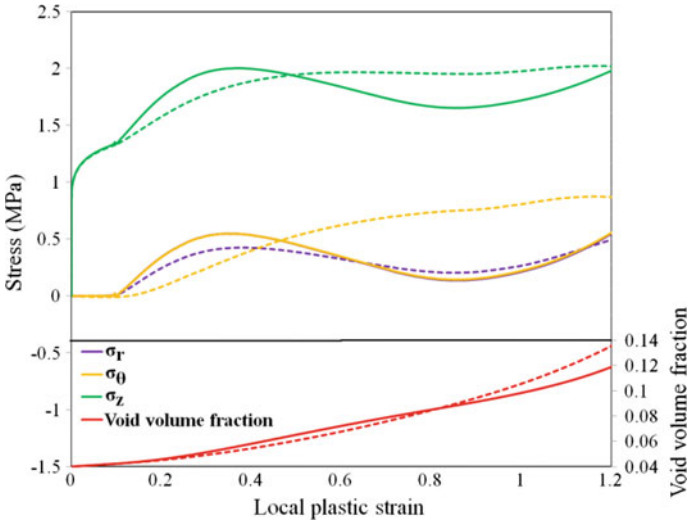

Fig. 7.82 Evolution of the components of the Cauchy stress (in a cylindrical coordinate system) and of the void volume fraction as a function of the local plastic strain at the center of the specimen ($R = 0$) and at $R/R_0 = 0.582$ (interrupted lines) for a material with matrix characterized by $k = -0.9$ ($\sigma_T/\sigma_C = 0.71$). Note that for the element at $R/R_0 = 0.582$, the state of stress is no longer axisymmetric (after Revil-Baudard and Cazacu [56])

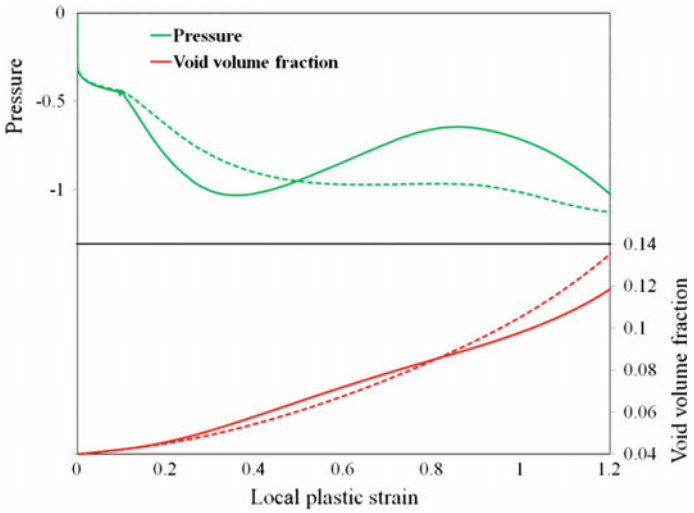

Fig. 7.83 Evolution of the pressure, $P = -\sigma_m$, and of the void volume fraction as a function of the local plastic strain at the center of the specimen ($R = 0$) and at $R/R_0 = 0.582$ for a material with matrix characterized by $k = -0.9$ ($\sigma_T/\sigma_C = 0.71$)

$$k(\bar{\varepsilon}^p) = a + \frac{b}{1 - \exp(\bar{\varepsilon} - \bar{\varepsilon}_3)/\bar{\varepsilon}_4}, \tag{7.153}$$

with $a = 0.90416$, $b = 0.009321$; $\bar{\varepsilon}_1 = 0.15$, $\bar{\varepsilon}_2 = 0.02788$, while $\bar{\varepsilon}_3 = 0.4$, $\bar{\varepsilon}_4 = 0.06788$.

Note that the only difference between these two exponential laws is the rate of change of k. Figure 7.84a shows the contour of constant void volume fraction at the end of the test for a material with matrix characterized by $k = -0.9$ while Fig. 7.84b, c present the void isocontours for a porous material with matrix characterized by an evolving k according to Eqs. (7.152) and (7.153), respectively. For all these porous materials, the calculations were terminated at a void volume fraction $f_c = 0.14$. Although, the limiting value (final value) of k for both materials with evolving microstructures (SD ratios) is the same ($k = -0.9$), there is a very striking difference in the void distribution within the respective specimens. For the material for which k evolves according to Eq. (7.152), i.e., there is a fast decrease of k from zero to the final value $k = -0.9$, the zone of maximum damage is shifted from the center of the specimen outward, i.e., the response is quite similar to that of the material with $k = -0.9$ (constant). On the other hand, if the rate at which

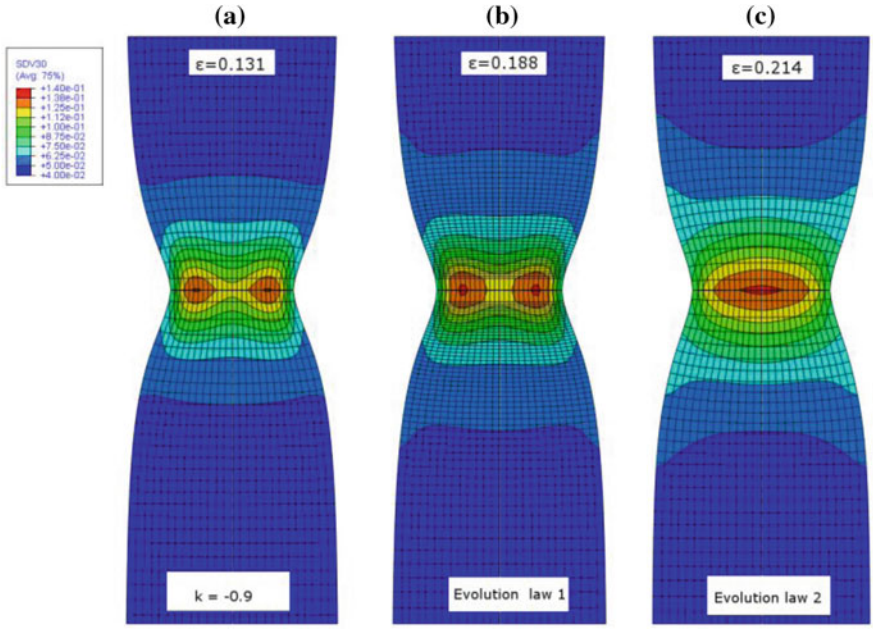

Fig. 7.84 Contours of constant void volume fraction, f, for materials with matrix having **a** constant strength ratio ($k = -0.9$); **b** evolving microstructure with k following the evolution law (7.152) and **c** evolving microstructure with k following evolution law (7.153) corresponding to the end of the test (i.e., for $f_{max} = 14\%$) (after Revil-Baudard and Cazacu [56])

k decreases from $k|_{\bar{\varepsilon}^p=0} = 0$ to $k = -0.9$ is slower [i.e., Eq. (7.152)], the void volume fraction distribution within the specimen is totally different, the zone of maximum damage develops at the center of the specimen, i.e., similar to a GTN material with $k = 0$ (constant).

Thus, it can be concluded that the evolution of the parameter k strongly influences the void volume fraction distribution. Figure 7.85 shows the local damage evolution in an element at the center of the specimen and at mid-radius $(R/R_0 = 0.582)$ for the same three materials. These results confirm the paramount influence of the rate of change of the parameter k with the accumulated plastic strain. Indeed, in a material for which k evolves according to Eq. (7.152), the void growth in both the center element $(R = 0)$ and the mid-radius element is quite similar to that obtained for a material with matrix characterized by the limiting value $k = -0.9$ (constant). Note that the void growth curves for the two elements intersect. This explains the shift in the location of the zone of maximum damage of Fig. 7.84b. It is worthwhile to note that for the material with matrix tension–compression asymmetry evolving according to Eq. (7.153), the void growth rate is similar to that corresponding to a material with no tension–compression asymmetry $(k = 0)$ up to an equivalent plastic strain of about 4%, while beyond this strain level the void growth rate becomes slower and comparable to that of a material with

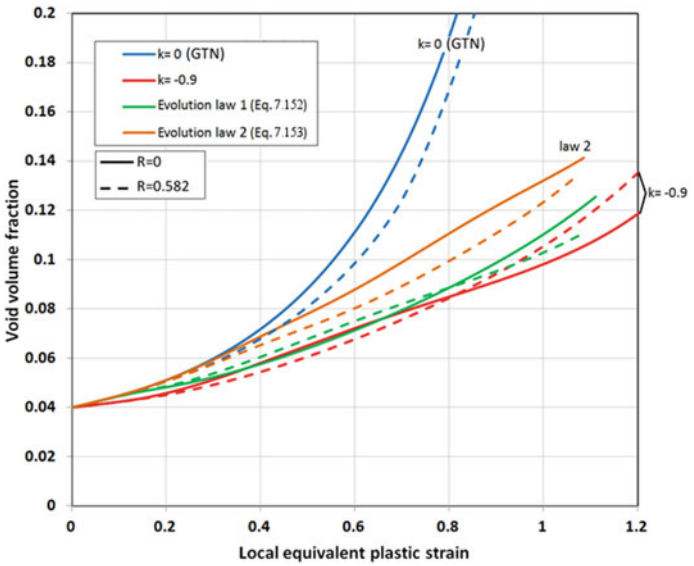

Fig. 7.85 Evolution of the void volume fraction as a function of the local equivalent plastic strain at the center of the specimen $(R = 0)$ and at $R/R_0 = 0.582$, for materials with matrix having constant strength ratio $k = -0.9$ and $k = 0$ (GTN material), respectively, in comparison with the void growth in porous materials with evolving microstructure characterized by a strength differential ratio k following the evolution law (7.152) and (7.153), respectively (after Revil-Baudard and Cazacu [56])

matrix characterized by a constant tension–compression ratio of $k = -0.9$. In conclusion, the results presented in Figs. 7.84 and 7.85 demonstrate that the final void volume fraction distribution could not be predicted based on either the initial or final value of k, the rate of change of k being of foremost importance.

In summary, on the basis of the Cazacu and Stewart [20] criterion, it was shown that in porous metallic materials with incompressible matrix softer in compression than in tension, the rate of void growth is higher than in materials with matrix governed by the von Mises criterion. On the other hand, for certain porous materials in which the matrix is softer in tension than in compression, under uniaxial tension, *damage is delayed and the void growth rate is much slower than in a GTN material. Furthermore, damage distribution is significantly different; the location of the zone of maximum porosity is shifted from the center of the specimen outwards. It should be noted that even a slight tension–compression asymmetry of the matrix (σ_T/σ_C of about 0.7) leads to damage evolution that is strikingly different than that for a material with matrix that does not display strength differential effects.* Most importantly, void growth and damage distribution are significantly affected by the rate of change of the strength differential ratio with plastic strain.

Unfortunately, complete mechanical characterization data for both tension–compression and experimental data on the void evolution of engineering materials are very scarce. Therefore, experimental validation of the trends revealed by ductile porous models is rather limited.

Partial verification of the model's predictions for an AA 6016-T4 alloy is presented in the next section.

7.3.3 Application to Al: Comparison Between Porous Models Predictions and in Situ X-Ray Tomography Data

Tensile test results on notched samples of an AA 6016-T4 and damage measurements by X-ray computed tomography for several loading orientations were reported in Thuillier et al. [65]. It was concluded that the weak texture of the material does not affect the stress–strain and damage evolution in the material. To investigate the effect of stress triaxiality on void evolution, tensile tests up to fracture were conducted on a sample with a rather smooth geometry (R = 6 mm), and also on samples with sharper notches of radius R = 2.5 mm and R = 1 mm, respectively. In the following, these specimen geometries will be referred to as $R6$, $R2p5$, and $R1$, respectively. For each specimen, the dimensions of the minimal section are 1×1 mm^2. In all tests, the axial strain was estimated from the measurements of the minimal section area. In the numerical simulations, the axial strain was calculated in the same manner, i.e., based on the displacement of the corners of the minimal cross-section. Indeed, assuming incompressibility and linear interpolation, the axial strain is related to the evolution of the minimal area S, i.e.,

$$\varepsilon = \ln(S_o/S) \tag{7.154}$$

where S_o denotes the initial area. As already mentioned, the void volume fraction was estimated using the XCMT method. The analysis of the void properties was restricted to the center of the sample, the size and the volume fraction of the porosities being determined by 3-D image analysis (see Buffiere et al. [11]). The average initial value of the void volume fraction was estimated to be: $f_0 = 0.0005$.

To describe the observed void evolution in the notched Al specimens, Thuillier et al. [65] used the GTN model. Hardening of the matrix in tension was identified from the pre-necking response of smooth specimens as

$$\bar{\sigma} = \sigma_0 + Q_\infty\left(1 - \mathrm{e}^{-b\bar{\varepsilon}^p}\right) + H\bar{\varepsilon}^p, \tag{7.155}$$

where $\bar{\varepsilon}^p$ is the effective plastic strain, $\sigma_0 = 156$ MPa, $Q_\infty = 145.6$ MPa, $b = 16$ and $H = 200$ MPa. The values considered for the q_1, q_2, and q_3 parameters are the classical ones: $q_1 = 1.5$, $q_2 = 1$, and $q_3 = q_1^2$. In the analysis, void evolution was considered to be due to both void nucleation and void growth. The contribution due to void growth was obtained from mass conservation assuming no volume change in the von Mises matrix while void nucleation was considered to follow a normal distribution with mean value ε_N and a standard deviation s_N, as proposed by Chu and Needleman [22]. The simulation results indicate that the GTN model predicts qualitatively the effect of the stress triaxiality on the void volume fraction evolution. However, a good quantitative agreement cannot be obtained for all specimens.

Revil-Baudard et al. [57] used the Cazacu and Stewart [20] model to predict the response of the same material. Given that Cazacu and Stewart [20] criterion is an extension of the GTN model, the only parameter that remains to be identified is the parameter k [see Eq. (7.145)]. For isotropic materials, its range of variation is (-1,1). The value of this parameter can be determined directly from uniaxial compression tests or shear tests, or combined tension–torsion tests (see Chap. 4). Since such data were not available for the AA 6016-T4, the parameter k was considered constant and its value was determined using the porosity data for specimen $R1$ (see also Fig. 7.86). The rate of change of the void volume fraction ($\dot{f}$) was considered to result from the growth of existing voids and the nucleation of new ones; for void nucleation, the same law of Chu and Needleman [22] was used. Thus,

$$\dot{f} = (1 - f)\,\mathbf{d}^p : \mathbf{I} + A_N\dot{\bar{\varepsilon}}^p, \tag{7.156}$$

$$\mathrm{A_N} = \frac{f_N}{s_N\sqrt{2\pi}}\exp\left[-\frac{1}{2}\left(\frac{\bar{\varepsilon}^p - \varepsilon_N}{s_N}\right)^2\right], \tag{7.157}$$

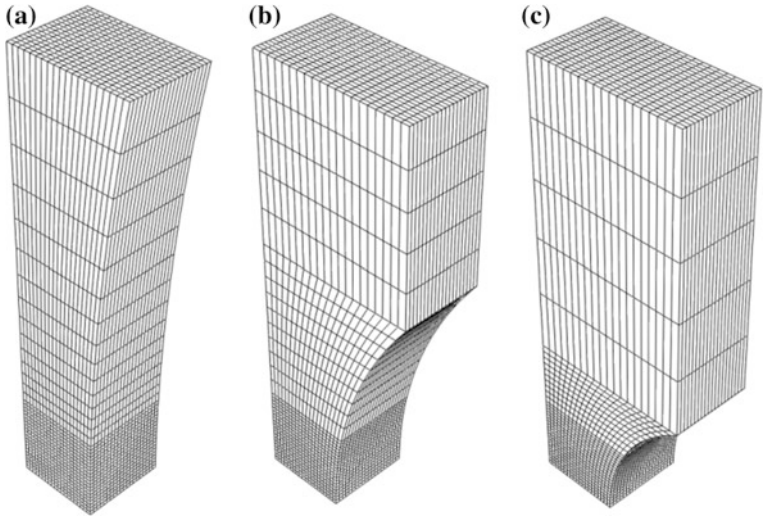

Fig. 7.86 F.E. meshes for the three AA 6016-T4 specimens used in the tests of Thuillier et al. [65]: **a** specimen *R*6, **b** specimen *R*2*p*5, **c** specimen *R*1

with $\mathbf{d}^p$ calculated using Eq. (7.147), and $\bar{\varepsilon}^p$ denoting the equivalent plastic strain of the matrix. In the F.E. calculations, the numerical values of the parameters involved in Eq. (7.157) are those reported in Thuillier et al. [65], namely $f_N = 0.0018$, $s_N = 0.4$, $\varepsilon_N = 0.9$.

Note that according to the modified Cazacu and Stewart [20] criterion [see Eq. (7.145)], the contribution due to the growth of existing voids is given by:

$$q_1 q_2 f(1-f)\sinh\left(q_2 \frac{3z_s\sigma_m}{2\bar{\sigma}}\right) \tag{7.158}$$

Thus, the rate of change of the void volume fraction ($\dot{f}$) depends on the matrix tension–compression asymmetry described by the parameter k (see Eq. (7.146) for the expression of z_s).

In the following are presented results obtained with the modified Cazacu and Stewart [20] potential (see Eqs. (7.145)–(7.148), and Eqs. (7.156) and (7.157)) in conjunction with the work-equivalence principle that allows calculation of the rate of change of the matrix equivalent strain, $\dot{\bar{\varepsilon}}^p$. The respective F.E. meshes used in the simulations are shown in Fig. 7.86 for the three AA 6016-T4 specimens. To eliminate any discussion concerning purely numerical issues that may affect the results, for all the geometries the simulations were run with the same constant time step equal to $\Delta t = 10^{-3}$s, all specimens having a similar mesh size in the reduced section zone. The mesh consisted of 14,000 hexahedral elements with reduced integration (ABAQUS C3D8R) and was refined in the reduced section zone.

As already mentioned, in order to identify the parameter k several F.E. simulations were conducted with k = constant in the range $(-1, 1)$ for the geometry $R1$. A value of $k = 0.2$ describes well the experimental evolution (see Fig. 7.87). In the same figure is also shown the porosity evolution according to GTN, which corresponds to $k = 0$ in the modified Cazacu and Stewart [20] criterion [see Eq. (7.145)]. It should be emphasized that in both calculations, all the other parameters were kept the same, i.e., the elastic properties of the matrix ($E = 70$ GPa and $\nu = 0.33$), the material parameters involved in the hardening law for the matrix, the initial void volume fraction f_0, the parameters q_1, q_2, q_3; and the parameters associated with void nucleation (f_N, s_N, ε_N). Thus, the differences between the predictions obtained with the two models are solely due to the value of the parameter k. It is interesting to note that for values of the plastic strain below 0.2 both the Cazacu and Stewart [20] model and GTN model describe well the experimental evolution; however, with increasing accumulated plastic deformation the rate of void growth predicted by the Cazacu and Stewart [20] model is faster.

Cazacu and Stewart [20] model with $k = 0.2$ was further used to predict the evolution of the void volume fraction at the center of the specimens $R2p5$ and $R6$, respectively (see Fig. 7.88). Note the excellent agreement between the numerical predictions and the X-ray porosity data. On the other hand, GTN underestimates the rate of void growth. This difference between the predictions according to the two models can be explained based on Eq. (7.158). Note that for $k > 0$, it follows that $z_s > 1$ [see Eq. (7.146)], hence void growth is accelerated as compared to the GTN model (which corresponds to $k = 0$ and $z_s = 1$). To further explain the predicted trends, in Fig. 7.89 for each specimen are shown the isocontours of the mean stress, corresponding to the same global axial strain (= 0.4) according to GTN and Cazacu and Stewart [20] model, respectively. Note that both models predict that the highest levels of mean stress occur in the specimen with the smallest notch radius

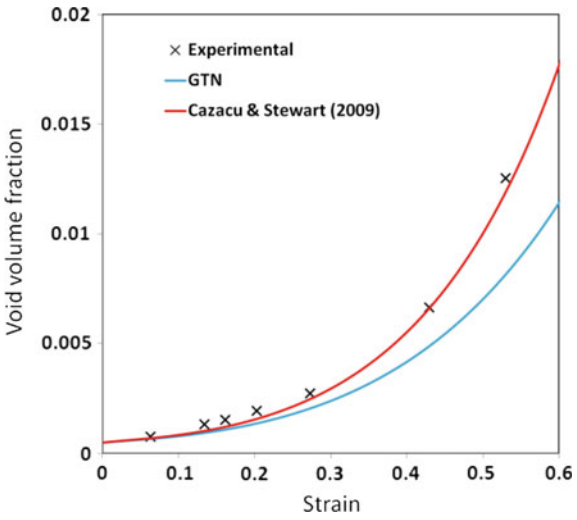

Fig. 7.87 Evolution of the void volume fraction at the center of the AA 6016-T4 specimen $R1$: comparison between the experimental X-ray data and the numerical predictions according to the GTN model ($k = 0$) and Cazacu and Stewart [20] model with $k = 0.2$, respectively (after Revil-Baudard et al. [57])

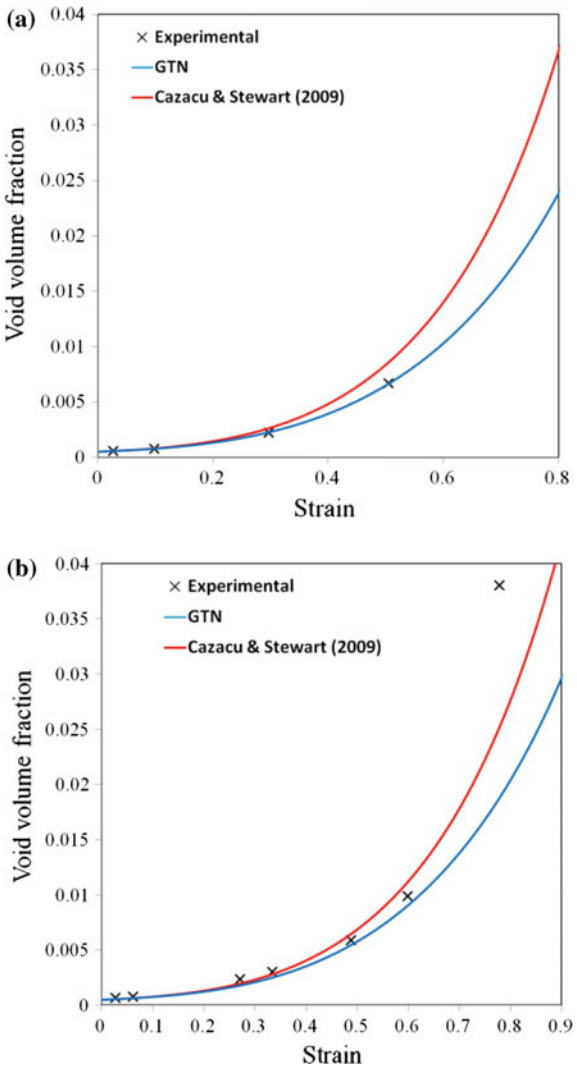

Fig. 7.88 Comparison between the experimental data obtained by X-ray tomography and the predictions of the Cazacu and Stewart [20] criterion with $k = 0.2$ for: **a** specimen $R2p5$; **b** specimen $R6$ of AA 6016-T4 (after Revil-Baudard et al. [57])

(specimen $R1$). However, irrespective of the specimen geometry, Cazacu and Stewart [20] model ($k = 0.2$) predicts higher levels of mean stress than GTN ($k = 0$), which explains the higher rate of void growth predicted by the Cazacu and Stewart [20] model as compared to the GTN model.

Fig. 7.89 Isocontours of the mean stress σ_m corresponding to a global plastic strain $\varepsilon = 0.4$ for ▶ the three AA 6016-T4 specimens of different notch acuities according to: **a** GTN model ($k = 0$) and **b** Cazacu and Stewart [20] criterion with $k = 0.2$ (after Revil-Baudard et al. [57])

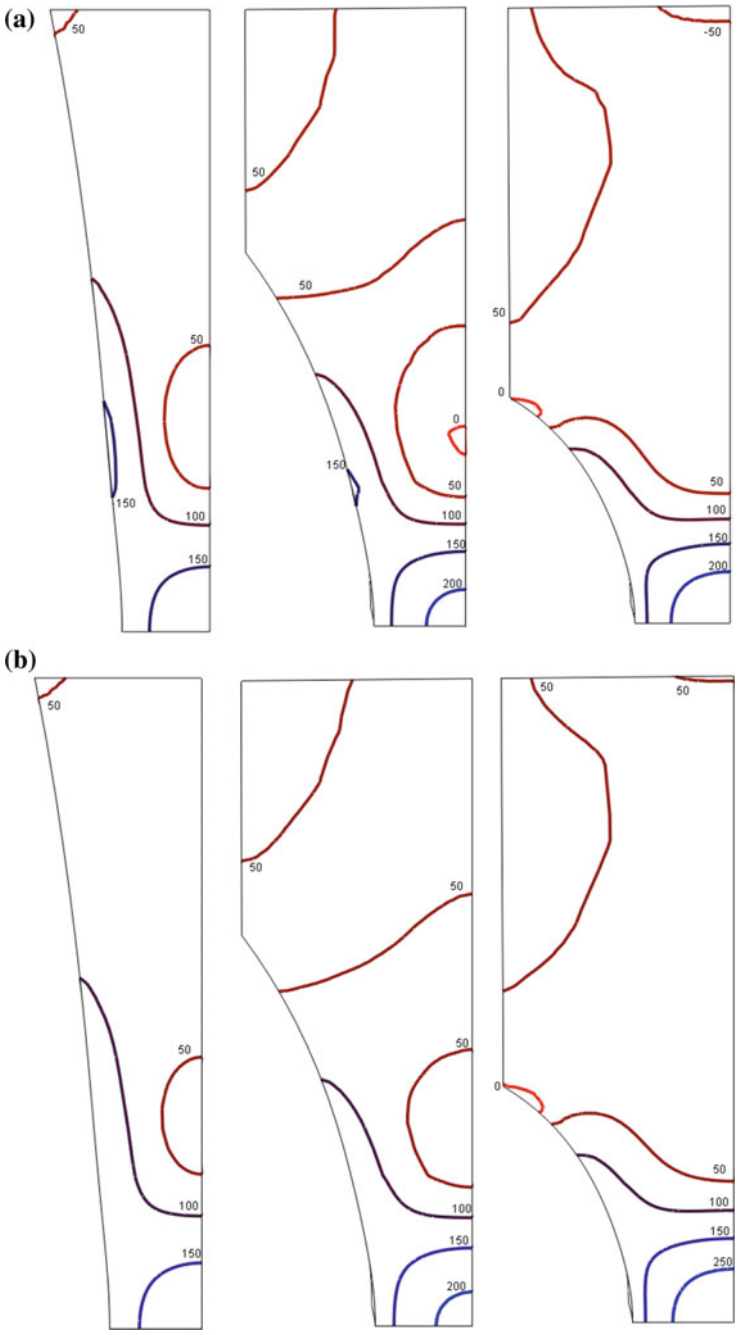
(a)
50
50
150
100
150
50
50
0
150
50
100
150
200
-50
50
0
50
100
150
200
(b)
50
50
100
150
50
50
100
150
200
50
50
0
50
100
150
250

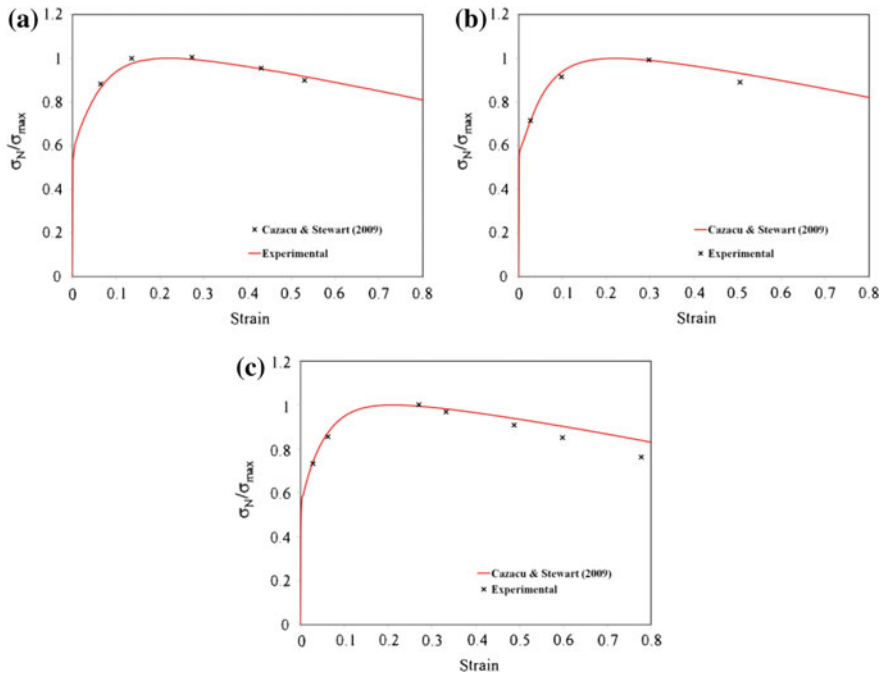

Fig. 7.90 Prediction of the nominal stress σ_N versus strain according to the Cazacu and Stewart [20] model ($k = 0.2$) in comparison with X-ray tomography data for AA 6016-T4 (symbols): **a** specimen $R1$; **b** specimen $R2p5$ and **c** specimen $R6$. σ_{max} corresponds to the maximum nominal stress reached during the respective test or numerical calculations, respectively

Concerning the strength decrease due to porosity (Fig. 7.90), as the macroscopic tensile tests and the tomography tests were performed at different aging times (see Thuillier et al. [65]), a normalized ratio defined by the nominal stress σ_N of the test, over the maximum nominal stress σ_{max} reached during the same test was calculated for all configurations (see Revil-Baudard et al. [57]). Figure 7.90 shows the experimental evolution of σ_N/σ_{max} in comparison with the F.E. results obtained using the Cazacu and Stewart [20] model. Note that the model predicts quite well the degradation of strength with increasing porosity. In particular, the shape of the experimental curve is well described for the $R1$ and $R2p5$ specimens. The model does, however, appear to slightly over predict the experimental response for the specimen $R6$, which corresponds to the lowest stress triaxiality (see also Fig. 7.89).

In summary, the results presented suggest that the porosity evolution in the AA 6016-T4 is strongly affected by the value of the parameter k, which accounts for the tension–compression asymmetry in the plastic flow of the incompressible matrix. Irrespective of the geometry of the specimen, it was shown that the Cazacu and Stewart [20] model with $k = 0.2$ predicts with accuracy the void growth evolution while the GTN model underestimates it.

Because of lack of mechanical characterization data, an isotropic porous model was used, thus neglecting the role of the initial texture of the material. A more complete data set would have allowed the experimental identification of the orthotropic extension of the Cazacu and Stewart [20] model (see Chap. 8). Nevertheless, the results reported by Revil-Baudard et al. [57] indicate that Cazacu and Stewart [20] model gives accurate predictions and does provide a basis for quantitatively relating microscale ductile damage processes to macroscopic ductility in engineering materials.

7.4 Derivation of Plastic Potentials for Porous Isotropic Metallic Materials Containing Cylindrical Voids

The constitutive models presented so far assume spherical void geometry. Long, roughly cylindrical voids may result from decohesion of cylindrical inclusions (e.g., sulfides in steels) from the matrix (e.g., see Gurson [30]). Gurson was the first to quantitatively describe the effects on yielding associated to the presence of cylindrical voids randomly distributed in the matrix (see Gurson [29]). The approach that he used is that of kinematic limit analysis (see Sect. 7.1). Assuming that the matrix is rigid-plastic and obeys the von Mises criterion, Gurson has shown that for axisymmetric loadings with one of the stress eigenvectors aligned with the axis of the cylindrical voids, it is possible to find the relation between the mean stress Σ_m and the second-invariant of the stress deviator Σ_e at yielding (Sect. 7.4.2). For any other orientation of the loading axes with respect to the void axes, the description of the induced anisotropy in yielding has remained an open question. Likewise, the influence of the characteristics of the plastic flow of the matrix on yielding of porous materials containing cylindrical voids is not well understood. Some of the challenges associated with obtaining analytical results concerning both yielding and void evolution are also discussed. Recent analytical results of Cazacu and Stewart [21] who investigated the effects of the tension–compression asymmetry of the matrix on yielding of porous materials with cylindrical voids are presented in Sect. 7.4.3. It is shown that matrix SD effects lead to unusual yielding behavior as compared to the case of a material with von Mises matrix.

We begin with the general statement of the problem and then proceed with detailed proofs for the case when the plastic behavior of the matrix is described by the von Mises [70] criterion, and the isotropic form of Cazacu et al. [15] criterion, respectively.

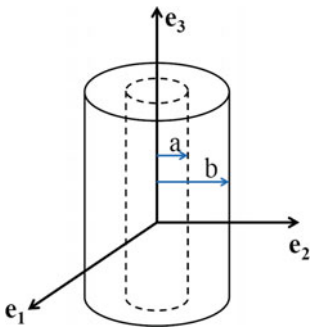

Fig. 7.91 Representative volume element for a porous material containing cylindrical voids

7.4.1 Statement of the Problem

A representative volume element (RVE) is a hollow cylinder of inner radius, a, and outer radius, $b = a/\sqrt{f}$, where f denotes the void volume fraction (or porosity) (see Fig. 7.91). Irrespective of the yield criterion describing the matrix, the imposed loading is axisymmetric, with one of the stress eigenvectors along the axis of the cylinder (see Fig. 7.91). Therefore, the outer boundary of the RVE is subjected to:

$$\boldsymbol{\Sigma} = \Sigma_{11}(\mathbf{e}_1 \otimes \mathbf{e}_1 + \mathbf{e}_2 \otimes \mathbf{e}_2) + \Sigma_{33}(\mathbf{e}_3 \otimes \mathbf{e}_3) \tag{7.159}$$

where $(\mathbf{e}_1, \mathbf{e}_2, \mathbf{e}_3)$ are the eigenvectors of $\boldsymbol{\Sigma}$ with $\mathbf{e}_3$ being along the axis of the cylinder. The boundary of the void is considered to be traction-free.

Since the applied loading is axisymmetric, the overall strain-rate $\mathbf{D}$ should also be of the form

$$\mathbf{D} = D_{11}(\mathbf{e}_1 \otimes \mathbf{e}_1 + \mathbf{e}_2 \otimes \mathbf{e}_2) + D_{33}(\mathbf{e}_3 \otimes \mathbf{e}_3) \tag{7.160}$$

Thus, its invariants are expressed as: $D_m = (2D_{11} + D_{33})/3$ and $D_e = \sqrt{\frac{2}{3}D'_{ij}D'_{ij}} = 2\left|D'_{11}\right|$ [see definitions given in Eqs. (7.1)–(7.3)].

Using axial and rotational invariance arguments and the incompressibility condition, Gurson [29] deduced the following velocity field $\mathbf{v}$ compatible with uniform strain-rate boundary conditions on the hollow cylinder:

$$\mathbf{v} = \left[\frac{3}{2}b^2 D_m\left(\frac{1}{r}\right) - \frac{D_{33}}{2}r\right]\boldsymbol{e}_r + D_{33}z\boldsymbol{e}_z \tag{7.161}$$

The eigenvalues (unordered) of the strain-rate field $\mathbf{d}$ corresponding to the velocity field $\mathbf{v}$ given by Eq. (7.161) are as follows:

$$\begin{cases} d_I = d_{rr} = -\left(\dfrac{3D_m}{2}\right)\dfrac{b^2}{r^2} - \dfrac{D_{33}}{2}, \\ d_{II} = d_{\theta\theta} = \left(\frac{3D_m}{2}\right)\dfrac{b^2}{r^2} - \dfrac{D_{33}}{2}, \\ d_{III} = d_{zz} = D_{33} \end{cases} \quad \text{for any } a \le r \le b. \tag{7.162}$$

Let $\Pi^+(\mathbf{D},f)$ be the average plastic dissipation over the domain Ω occupied by the RVE corresponding to the velocity field $\mathbf{v}$ given by Eq. (7.161); i.e.,

$$\Pi^+(\mathbf{D},f) = \langle \pi(\mathbf{d}) \rangle_\Omega = \frac{1}{\pi b^2} \int_a^b \pi(\mathbf{d}) \cdot 2\pi r \mathrm{d}r, \tag{7.163}$$

with $\pi(\mathbf{d})$ denoting the plastic dissipation of the matrix.

As seen in Sect. 7.1, $\Pi^+(\mathbf{D},f)$ is an approximate plastic potential of the porous material. Moreover, at yielding of the porous material the stresses satisfy:

$$\Sigma_{11} = \Sigma_{22} = \frac{\partial \Pi^+(\mathbf{D},f)}{\partial D_{11}} \text{ and } \Sigma_{33} = \frac{\partial \Pi^+(\mathbf{D},f)}{\partial D_{33}}, \tag{7.164}$$

Or

$$\Sigma_e = \left| \frac{\partial \Pi^+(\mathbf{D},f)}{\partial D_e} \right| \text{and } \Sigma_{\gamma\gamma} = 2\frac{\partial \Pi^+(\mathbf{D},f)}{\partial D_{11}}, \tag{7.165}$$

where $\Sigma_{\gamma\gamma} \overset{def}{=} \Sigma_{11} + \Sigma_{22}$ and $\Sigma_e = \sqrt{\frac{3}{2}\Sigma'_{ij}\Sigma'_{ij}} = |\Sigma_{11} - \Sigma_{33}|$

Equations (7.164) define the yield locus of the porous material with randomly distributed cylindrical voids.

Remark (a) $\Pi^+(\mathbf{D},f)$ is an upper-bound estimate of the exact plastic dissipation, $\Pi(\mathbf{D},f)$ of the porous material (i.e., of the void-matrix aggregate). Therefore, Eq. (7.164) defines an approximate yield locus for the porous material containing cylindrical voids.

Remark (b) A major difficulty in obtaining closed-form expressions of this yield locus is the determination of the expression of the local plastic dissipation $\pi(\mathbf{d})$ associated with the yield criterion describing the behavior of the matrix material and the calculation of the integral representing the plastic dissipation $\Pi^+(\mathbf{D},f)$ [see Eq. (7.163)].

7.4.2 Plastic Potential for a Porous Material with von Mises Matrix

Using the approach presented in Sect. 7.4.1, Gurson [29] and Gurson [30] derived an analytic plastic potential for porous materials with von Mises matrix containing cylindrical voids. In the following, it is presented the derivation of the expression of this potential, $\Phi^{\text{cyl}}_{\text{Gurson}}(\boldsymbol{\Sigma},f)$, followed by a discussion of its key properties.

Theorem 7.15 *The* Gurson [30] *yield function for a porous material with matrix governed by the von Mises criterion and containing cylindrical voids is given by*:

$$\Phi^{\text{cyl}}_{\text{Gurson}}(\boldsymbol{\Sigma},f) = \left(\frac{\Sigma_e}{\sigma_T}\right)^2 + 2f\,\cosh\left(\frac{\sqrt{3}}{2}\frac{\Sigma_{\gamma\gamma}}{\sigma_T}\right) - \left(1+f^2\right) = 0 \tag{7.166}$$

Proof Let us recall that for any strain-rate field $\mathbf{d}$, the local plastic dissipation associated with the von Mises yield function, $\varphi_{\text{Mises}}(\boldsymbol{\sigma})$, has the following closed-form expression (see Sect. 6.1.1):

$$\pi_{\text{Mises}}(\mathbf{d}) = \sigma_T\sqrt{(2/3)tr\mathbf{d}^2}$$

For cylindrical void geometry, the RVE considered by Gurson (see Gurson [29, 30]) is shown in Fig. 7.91. The analysis was done for axisymmetric tensile loadings [see Eq. (7.159)] using the velocity field given by Eq. (7.161). For the corresponding strain-rate field [see Eq. (7.162)], the local plastic dissipation takes the form:

$$\pi_{\text{Mises}}(\mathbf{d}) = \sigma_T|D_{33}|\sqrt{1+3(D_m/D_{33})^2(b/r)^4}. \tag{7.167}$$

Let us denote $t \overset{\text{def}}{=} \frac{3}{2}(|D_m|/|D_{33}|)$. Substitution of Eq. (7.167) in Eq. (7.163) leads to the following expression for the plastic dissipation of the porous von Mises material:

$$\Pi^{+}_{\text{Mises;cyl}}(\mathbf{D},f) = \frac{2\sigma_T|D_{33}|}{b^2}\int_a^b r\sqrt{1+(4t^2/3)(b/r)^4}\,\mathrm{d}r. \tag{7.168}$$

Using the change of variable $x = (2\sqrt{3})tb^2/r^2$, Eq. (7.168) becomes:

$$\Pi^{+}_{\text{Mises;cyl}}(\mathbf{D},f) = \frac{2\sigma_T|D_{33}|}{\sqrt{3}}\left[\begin{array}{l}\sqrt{t^2+3/4}-\sqrt{t^2+3f^2/4}\\ +t\,\ln\left(\dfrac{t+\sqrt{t^2+3f^2/4}}{t+\sqrt{t^2+3/4}}\cdot\dfrac{1}{f}\right)\end{array}\right] \tag{7.169}$$

Using the above expression of the plastic dissipation, the stresses at yielding are obtained by derivation [see Eq. (7.164)]:

$$\Sigma_{11} = \frac{\Sigma_{\gamma\gamma}}{2} = \frac{\partial \Pi^{+}_{\text{Mises;cyl}}(\mathbf{D},f)}{\partial D_{11}} = \frac{2\sigma_T}{\sqrt{3}} \ln\left(\frac{t+\sqrt{t^2+3f^2/4}}{t+\sqrt{t^2+3/4}} \cdot \frac{1}{f}\right)$$
$$\Sigma_{33} = \frac{\partial \Pi^{+}_{\text{Mises;cyl}}(\mathbf{D},f)}{\partial D_{33}} = \frac{2\sigma_T}{\sqrt{3}} \left[\ln\left(\frac{t+\sqrt{t^2+3f^2/4}}{t+\sqrt{t^2+3/4}} \cdot \frac{1}{f}\right) - \sqrt{t^2+3/4} + \sqrt{t^2+3f^2/4}\right] \quad (7.170)$$

Equations (7.170) define the Gurson [29] yield locus for a porous von Mises solid containing cylindrical voids in a parametric form. Eliminating the parameter t between the Eq. (7.170), one obtains the classical form [Eq. (7.166)] given in Gurson [30].

General properties of the yield surface of a porous material with von Mises matrix containing cylindrical voids

(a) For purely deviatoric axisymmetric loadings, there is no effect of the third-invariant of the stress deviator on yielding.
Proof Indeed, for purely deviatoric axisymmetric loadings according to Eq. (7.166) yielding occurs at:

$$\Sigma_e/\sigma_T = |\Sigma_{11} - \Sigma_{33}| = 1 - f. \quad (7.171)$$

Therefore, the yield surface [Eq. (7.166)] is symmetric with respect to the hydrostatic axis ($\Sigma_{11} = \Sigma_{22} = \Sigma_{33}$).

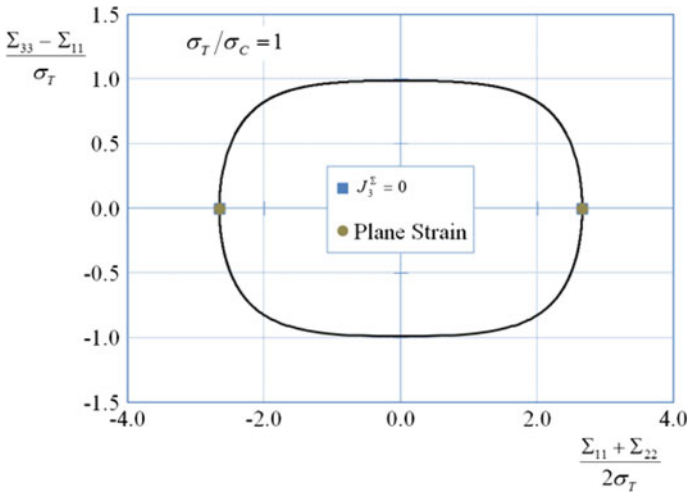

Fig. 7.92 Representation in the $((\Sigma_{33}-\Sigma_{11})/\sigma_T, (\Sigma_{11}+\Sigma_{22})/\sigma_T)$ plane of the Gurson [30] theoretical yield surface for a porous material containing randomly distributed cylindrical voids in a von Mises matrix, subjected to axisymmetric loadings with a void volume fraction (f = 0.01) (after Cazacu and Stewart [21])

(b) For generalized plane-strain conditions ($D_{33} = 0$ or $t \to \infty$), the stress state at yielding is hydrostatic.
Proof According to Eq. (7.170) for $D_{33} = 0$ and $t \to \infty$:

$$\lim_{t\to\infty} |\Sigma_{11} - \Sigma_{33}| = 0 \tag{7.172}$$

Thus, under plane strain, the stress state at yielding is hydrostatic. In other words, in the case when the matrix is described by the von Mises criterion, the yield limit under hydrostatic tension or hydrostatic compression, which corresponds to $J_3^{\Sigma} = 0$, coincides with the yield limit under plain strain conditions ($D_{33} = 0$) (see also Fig. 7.92).

(c) The yield limit under hydrostatic loadings has the absolute value:

$$|p_Y| = -\frac{\sigma_T}{\sqrt{3}} \ln f \tag{7.173}$$

Proof Indeed, from Eq. (7.166), it follows that for tensile hydrostatic loadings: $\Sigma_{11} = \Sigma_{22} = \Sigma_{33} = \dfrac{-\sigma_T}{\sqrt{3}} \ln(f)$. Since $\pi_{\text{Mises}}(\mathbf{d})$ has the same expression irrespective of the sign of D_m [see Eq. (7.167)], it follows that for compressive hydrostatic loadings, the yield limit has the same absolute value given by Eq. (7.173). Note that the expression of p_Y given by Eq. (7.173) coincides with the solution for the maximal pressure necessary to fully plastify a cylinder made of a material with ideal plastic behavior governed by the von Mises yield criterion and subjected to hydrostatic loading (see Lubliner [45]).

All these characteristics of the yielding behavior of a porous von Mises material when subjected to axisymmetric loadings such that the eigenvalue Σ_{33} is aligned along the generators of the voids are clearly seen in Fig. 7.92. In this figure the theoretical yield surface according to the Gurson [30] criterion corresponding to a void volume fraction $f = 0.01$ is represented in the plane $((\Sigma_{33} - \Sigma_{11})/\sigma_T, (\Sigma_{11} + \Sigma_{22})/\sigma_T)$.

Note also that the yield surface is invariant under the transformation $(\Sigma_{\gamma\gamma}, \Sigma_e) \to (-\Sigma_{\gamma\gamma}, \Sigma_e)$. This is a consequence of the fact that the local plastic dissipation in the von Mises matrix is invariant with respect to the transformation:$(D_m, D_{33}) \to (-D_m, D_{33})$ [see also Eq. (7.167)].

7.4.3 *Cazacu and Stewart [21] Plastic Potential for Porous Material with Matrix Displaying Tension–Compression Asymmetry*

The influence of the tension–compression asymmetry (or SD effects) of the incompressible matrix on yielding of porous materials containing cylindrical voids

was analyzed by Cazacu and Stewart [21]. For this purpose, the matrix behavior was considered to be rigid-plastic and governed by the quadratic form of the isotropic stress potential of Cazacu et al. [15] [see Chap. 4; its expression was recalled in this chapter, Eq. (7.125)]. According to this yield criterion the SD effects are described by a unique parameter k, which is expressible solely in terms of the ratio $\beta = \sigma_T/\sigma_C$ between the uniaxial yield in tension–compression [see Eq. (7.126)]. Moreover, for any strain-rate field $\mathbf{d}$, the associated plastic dissipation $\pi(\mathbf{d}) = \sigma_T\psi(\mathbf{d})$ has multiple branches [e.g., see Eq. (7.127)].

Therefore, for the same imposed loadings on the RVE [see Eq. (7.159)] and the same velocity field [see Eq. (7.161)], the analysis is very involved. Nevertheless, it is possible to obtain analytically an approximate plastic potential for the porous material. This potential will be denoted $\Pi_{SD}^{cyl}(\boldsymbol{D},f)$; moreover, the stresses at yielding for axisymmetric states having the minor or major eigenvalue along the generators of the cylindrical voids will be derived.

General properties of the yield surface of a porous material with incompressible matrix displaying SD effects containing cylindrical voids

While the explicit expression of $\Pi_{SD}^{cyl}(\boldsymbol{D},f)$ and parametric representation of the stress states at yielding of the porous material will be presented later on, for hydrostatic loadings and plane-strain deformation it is possible to obtain the solution of the limit-analysis problem directly (i.e., without calculating the integral $\Pi_{SD}^{cyl}(\boldsymbol{D},f)$).

Most importantly, the analysis of the yielding response of the porous material for these loadings leads to key findings concerning the influence of the tension–compression asymmetry of the matrix on the behavior of the porous material.

7.4.3.1 Exact Solution for the Problem of a Hollow Cylinder Loaded Hydrostatically

Theorem 7.16

- *If the matrix is harder in tension than in compression, i.e., it is characterized by* $\sigma_T/\sigma_C > 1$, *the absolute value of the hydrostatic yield limit of the porous material is*:

$$\left|p_Y^{kp}\right| = (-\sigma_T)\left(\sqrt{\frac{3\sigma_T^2-\sigma_C^2}{6\left(2\sigma_T^2-\sigma_C^2\right)}}\right)\ln(f) \tag{7.174}$$

- *If the matrix is softer in tension than in compression, i.e., it is characterized by* $\sigma_T/\sigma_C < 1$, *the absolute value of the hydrostatic yield limit of the porous material is*:

$$\left|p_Y^{kn}\right| = (-\sigma_C)\left(\sqrt{\frac{3\sigma_C^2 - \sigma_T^2}{6\left(2\sigma_C^2 - \sigma_T^2\right)}}\right)\ln(f) \tag{7.175}$$

Proof We need to calculate the limit-pressure that can sustain a hollow cylinder loaded hydrostatically under plane-strain conditions. The limit-analysis problem reads as follows:

– Find the maximal pressure for which there exists a stress field statically and plastically admissible; i.e., find $p_Y^{\mathrm{SD}} = \max(p)$ for which

$$\begin{cases} \operatorname{div}\boldsymbol{\sigma} = 0 \text{ for } a \le r \le b \\ \boldsymbol{\sigma}\mathbf{n} = 0|_{r=a} \text{ i.e., no internal pressure} \\ \boldsymbol{\sigma}\mathbf{n} = p\boldsymbol{e}_r|_{r=b}, \\ \varphi(\boldsymbol{\sigma}) \le 0, \text{ for } a \le r \le b, \end{cases} \tag{7.176}$$

with $\varphi(\boldsymbol{\sigma})$ being the quadratic form of the isotropic stress potential of Cazacu et al. [15] [see Chap. 4; its expression recalled in Eq. (7.125)]. Note that due to axial and rotational invariance, incompressibility, and plane-strain conditions, the velocity field should be radial. Therefore, in the cylindrical coordinate system $(\boldsymbol{e}_r, \boldsymbol{e}_\theta, \boldsymbol{e}_z)$, the strain-rate field is of the form:

$$d_{rr} = c/r^2,\ d_{\theta\theta} = -c/r^2,\ d_{zz} = 0,\ a \le r \le b, \tag{7.177}$$

where c is a constant. For the imposed loadings, it can be assumed that $(\boldsymbol{e}_r, \boldsymbol{e}_\theta, \boldsymbol{e}_z)$ are also eigenvectors for the stress, i.e., the stress tensor $\boldsymbol{\sigma}$ and its deviator $\mathbf{s}$ are given by

$$\boldsymbol{\sigma} = \begin{pmatrix} \sigma_{rr} & 0 & 0 \\ 0 & \sigma_{\theta\theta} & 0 \\ 0 & 0 & \sigma_{zz} \end{pmatrix} \text{ and } \mathbf{s} = \begin{pmatrix} X+Y & 0 & 0 \\ 0 & X-Y & 0 \\ 0 & 0 & -2X \end{pmatrix} \tag{7.178}$$

with $X = (\sigma_{rr} + \sigma_{\theta\theta} - 2\sigma_{zz})/6$ and $Y = (\sigma_{rr} - \sigma_{\theta\theta})/2$. Momentum balance gives $\operatorname{div}\boldsymbol{\sigma} = 0$, which reduces to one non-trivial equation:

$$\frac{\partial \sigma_{rr}}{\partial r} + \frac{1}{r}(\sigma_{rr} - \sigma_{\theta\theta}) = 0 \tag{7.179}$$

with boundary conditions $\sigma_{rr}|_{r=a} = 0$ and $\sigma_{rr}|_{r=b} = p$. For compressive loadings $p < 0$, while for tensile loading $p \ge 0$.

In the following, the solution will be given for the case when the matrix is harder in tension than in compression; i.e., $\beta = \sigma_T/\sigma_C > 1$. The solution for the case $\beta < 1$

can be obtained in a similar manner. With the notations introduced in Eq. (7.178), the matrix yield criterion [see Eq. (7.125)] writes:

$$[|X+Y|-k(X+Y)]^2+\ [|X-Y|+k(X-Y)]^2+[|2X|+k(2X)]^2=\ \frac{\sigma_T^2}{m^2} \quad (7.180)$$

On the other hand, $d_{zz}=\dfrac{\partial\varphi}{\partial\sigma_{zz}}=0$, (plane-strain condition) which writes:

$$(-2X)\left(1+k^2\right)-\frac{8k}{3}|X|+\frac{2k}{3}\ (|X-Y|+|X+Y|)=\ 0 \quad (7.181)$$

Next, we need to solve the system of Eqs. (7.180) and (7.181) for the unknowns X and Y. Note that for $\beta=\sigma_T/\sigma_C>1$, in order for this system to admit solutions, we cannot have simultaneously $X-Y>0$ and $X<0$. Let's assume that $X>0$, $Y>0$ and $X<Y$. From Eq. (7.181), it follows that $X=\left(\dfrac{2k}{3k^2+4k+3}\right)Y$. Since for $\beta>1$, k is positive [see Eq. (7.126)] this solution is acceptable. Further substitution in Eq. (7.180) leads to: $Y=\dfrac{\sigma_T\sqrt{3k^2+4k+3}}{3(k+1)}$. In terms of the matrix yield stresses σ_T and σ_C, we obtain (see Eq. (7.126) for the expression of k):

$$Y=\sigma_T\sqrt{\frac{3\sigma_T^2-\sigma_C^2}{6\left(2\sigma_T^2-\sigma_C^2\right)}}\quad \text{and}\ X=\frac{(\sigma_T/\sigma_C)\left(\sigma_T^2-\sigma_C^2\right)}{\sqrt{6\left(2\,\sigma_T^2-\sigma_C^2\right)\left(3\,\sigma_T^2-\sigma_C^2\right)}}. \quad (7.182)$$

Thus, the stress deviator components are constant [see Eq. (7.178)]. Substitution in the momentum balance Eq. (7.179) gives:

$$\frac{\mathrm{d}\sigma_{rr}}{\mathrm{d}r}+2Y/r=\ 0\Rightarrow\sigma_{rr}=\ -2Y\ln r+C_1,$$

with C_1 being a constant. Imposing the boundary conditions on the internal boundary $r=a$, it follows that:

$$C_1=2Y\ln(a)$$

Imposing the boundary conditions on the external boundary, we obtain that the external compressive pressure that needs to be applied such that the hollow cylinder is fully plastified is equal to $Y\ln(f)$; the tensile pressure that needs to be applied is equal to: $(-Y)\ln(f)$, with $f=a^2/b^2$. Further using Eq. (7.182), it follows that the absolute value of the yield limit of the porous material under hydrostatic tension is equal with the absolute value of the yield limit under hydrostatic compression, and it is given by Eq. (7.174). The proof for the case when the matrix is softer in tension than in compression can be done in a similar manner.

Remark Note that if the matrix does not display tension–compression asymmetry, i.e., if $\sigma_T = \sigma_C$, then we recover the absolute yield limit for a porous material with von Mises matrix containing cylindrical voids, i.e.,

$$\left|p_Y^{kp}\right| = \left|p_Y^{kn}\right| = |p_Y| = \frac{\sigma_T}{\sqrt{3}}\ln(f) \tag{7.183}$$

[see also Eq. (7.173)].

7.4.3.2 Cazacu and Stewart [21] Strain-Rate Plastic Potential

Due to the tension–compression asymmetry, the plastic behavior of the incompressible matrix is strongly dependent on the third-invariant of the stress deviator (see also Chap. 4). For the strain-rate field $\mathbf{d}$ corresponding to the velocity field $\mathbf{v}$ compatible with uniform strain-rate boundary conditions on the hollow cylinder with eigenvalues given by Eq. (7.162), the strain-rate potential $\psi(\mathbf{d})$ associated to the Cazacu et al. [15] stress criterion [Eq. (7.127)] and the local plastic dissipation $\pi(\mathbf{d})$ are invariant under the transformation: $(D_m, D_{33}) \rightarrow (-D_m, D_{33})$. Thus, in estimating the plastic potential of the porous material, $\Pi_{SD}^{cyl}(\boldsymbol{D}, f) = \langle \pi(\mathbf{d}) \rangle_\Omega$, only the following loadings cases need to be considered separately: Case (i): $D_m \geq 0$ and $D_{33} \leq 0$, and Case (ii): $D_m \geq 0$ and $D_{33} \geq 0$.

Case (i): $D_m \geq 0$ and $D_{33} \leq 0 \Rightarrow d_{\theta\theta} \geq 0$ and $d_{zz} \leq 0$ for any $r \in [a, b]$. Hence, in order to choose the appropriate expression for $\psi(\mathbf{d})$ [see Eq. (7.127)], we need to determine whether $(d_{rr}, d_{\theta\theta}, d_{zz})$ belong to the subdomain Δ_θ^+ or Δ_z^- (see Fig. 7.93) which are defined as follows:

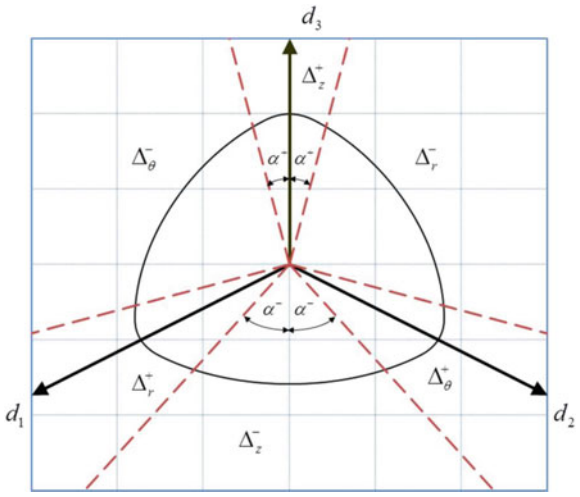

Fig. 7.93 Representation of the Cazacu et al. [14] strain-rate potential in the octahedral plane, with $k = -0.4$, of the local plastic dissipation, which presents threefold symmetry ($\alpha^+ \neq \alpha^-$) (after Cazacu and Stewart [21])

$$\begin{aligned}\Delta_\theta^+ &= \left\{(d_{rr},d_{\theta\theta},d_{zz})\middle|\frac{d_{\theta\theta}}{\|\mathbf{d}\|}\geq\frac{1}{\sqrt{2\left(1+\beta^4-\beta^2\right)}}\right\}\\ \Delta_z^- &= \left\{(d_{rr},d_{\theta\theta},d_{zz})\middle|\frac{d_{zz}}{\|\mathbf{d}\|}\leq\frac{-\beta^2}{\sqrt{2\left(1+\beta^4-\beta^2\right)}}\right\}\quad\text{with }\beta=\sigma_T/\sigma_C.\end{aligned}\tag{7.184}$$

On the other hand, for Case (ii): $D_m\geq 0$ and $D_{33}\geq 0\Rightarrow d_{rr}\leq 0$ and $d_{zz}\geq 0$ for any $r\in[a,b]$, in order to determine the appropriate branch for the local plastic dissipation $\psi(\mathbf{d})$ we need to determine whether $(d_{rr},d_{\theta\theta},d_{zz})$ belong to the subdomain Δ_z^+ or Δ_r^- (see Fig. 7.93), which are defined as:

$$\begin{aligned}\Delta_z^+ &= \left\{(d_{rr},d_{\theta\theta},d_{zz})\middle|\frac{d_{zz}}{\|\mathbf{d}\|}\geq\frac{1}{\sqrt{2\left(1+\beta^4-\beta^2\right)}}\right\}\\ \Delta_r^- &= \left\{(d_{rr},d_{\theta\theta},d_{zz})\middle|\frac{d_{rr}}{\|\mathbf{d}\|}\leq\frac{-\beta^2}{\sqrt{2\left(1+\beta^4-\beta^2\right)}}\right\}\end{aligned}\tag{7.185}$$

Irrespective of loading [cases (i) or (ii)], the location of $(d_{rr},d_{\theta\theta},d_{zz})$ depends on the ratio $t=\frac{3}{2}\frac{|D_m|}{|D_{33}|}$ between the axial and the mean value of the strain-rate tensor $\mathbf{D}$ (see also Sect. 7.4.2). In the following, we will present the parametric representation of the yield surface of the porous material. Proof will be given only for loadings corresponding to Case (i): $D_m\geq 0$ and $D_{33}\leq 0$ and $0\leq t\leq f\left(2-\beta^2\right)/2\beta^2$. For all other loadings, detailed calculations can be found in Cazacu and Stewart [21]. To simplify writing, the following notations are introduced:

$$\begin{aligned}&g=\frac{\sqrt{3\left(2-\beta^2\right)}}{2\beta};\alpha=\frac{2}{\sqrt{3}}\sqrt{\frac{3\beta^2-1}{\beta^2+1}};s=\frac{2\sqrt{3}\left(\beta^2-1\right)}{\sqrt{\left(\beta^2+1\right)\left(3\beta^2-1\right)}};\\ &\eta=\frac{2\beta^2}{2-\beta^2};g_1=\frac{\sqrt{3\left(2\beta^2-1\right)}}{2};A=\frac{2}{\sqrt{3}}\sqrt{\frac{3-\beta^2}{\beta^2+1}};\\ &s_1=\frac{2\sqrt{3}\left(1-\beta^2\right)}{\sqrt{\left(\beta^2+1\right)\left(3-\beta^2\right)}}.\end{aligned}\tag{7.186}$$

Note that all the above constants are expressible solely in terms of the ratio between the matrix tensile and compressive strengths, $\beta=\sigma_T/\sigma_C$.

Theorem 7.17 (Yield surface of a porous material with SD effects under axisymmetric loadings)

For any $t=\dfrac{3}{2}(|D_m|/|D_{33}|)$, *the strain-rate potential of a porous material with matrix displaying SD effects is given by*:

- *For* $D_m \geq 0$ *and* $D_{33} \leq 0$ *such that* $0 \leq t \leq \left(\dfrac{2-\beta^2}{2\beta^2}\right) f$:

$$\begin{cases} \dfrac{\Sigma_{\gamma\gamma}}{\sigma_T} = \dfrac{2}{\sqrt{3(2-\beta^2)}} \ln\left(\dfrac{t+\sqrt{t^2+g^2f^2}}{t+\sqrt{t^2+g^2}} \cdot \dfrac{1}{f}\right) \\ \dfrac{\Sigma_{11}-\Sigma_{33}}{\sigma_T} = \dfrac{2}{\sqrt{3(2-\beta^2)}} \left[\sqrt{t^2+g^2} - \sqrt{t^2+g^2f^2}\right] \end{cases}; \tag{7.187}$$

- *For* $D_m \geq 0$ and $D_{33} \leq 0$ *such that* $\left(\dfrac{2-\beta^2}{2\beta^2}\right) f \leq t \leq \left(\dfrac{2-\beta^2}{2\beta^2}\right)$:

$$\begin{cases} \dfrac{\Sigma_{\gamma\gamma}}{\sigma_T} = \alpha\sqrt{\dfrac{\beta^2+1}{2(2\beta^2-1)}} \ln\left(\dfrac{\alpha t + \dfrac{s}{2}f + \sqrt{\alpha^2t^2 + s\alpha tf + f^2}}{\alpha + \dfrac{s}{2}\eta + \sqrt{\alpha^2 + s\alpha\eta + \eta^2}} \cdot \dfrac{\eta}{f}\right) \\ -\dfrac{s}{2}\alpha\sqrt{\dfrac{\beta^2+1}{2(2\beta^2-1)}} \ln\left(\dfrac{\dfrac{s}{2}\alpha t + f + \sqrt{\alpha^2t^2 + s\alpha tf + f^2}}{\dfrac{s}{2}\alpha + \eta + \sqrt{\alpha^2 + s\alpha\eta + \eta^2}} \cdot \dfrac{1}{t}\right) \\ + \dfrac{2}{\sqrt{3(2-\beta^2)}} \ln\left(\dfrac{2g + \sqrt{4g^2+9}}{t + \sqrt{g^2+t^2}} \cdot \dfrac{g}{3}\right) \\ \dfrac{\Sigma_{11}-\Sigma_{33}}{\sigma_T} = \left[\dfrac{2\sqrt{u^2+g^2}}{\sqrt{3(2-\beta^2)}} - \sqrt{\dfrac{\beta^2+1}{2(2\beta^2-1)}}\sqrt{\alpha^2t^2 + s\alpha tf + f^2}\right] \end{cases} \tag{7.188}$$

- *For* $D_m \geq 0$ *and* $D_{33} \leq 0$ *such that* $t \geq \left(\dfrac{2-\beta^2}{2\beta^2}\right)$,

$$\begin{cases} \dfrac{\Sigma_{\gamma\gamma}}{\sigma_T} = \alpha\sqrt{\dfrac{\beta^2+1}{2(2\beta^2-1)}} \left[\begin{array}{l} \ln\left(\dfrac{\alpha t + \frac{s}{2}f + \sqrt{\alpha^2t^2 + s\alpha tf + f^2}}{\alpha t + \frac{s}{2} + \sqrt{\alpha^2t^2 + s\alpha t + 1}} \cdot \dfrac{1}{f}\right) \\ + \dfrac{s}{2}\ln\left(\dfrac{\frac{s}{2}\alpha t + 1 + \sqrt{\alpha^2t^2 + s\alpha t + 1}}{\frac{s}{2}\alpha t + f + \sqrt{\alpha^2t^2 + s\alpha tf + f^2}}\right) \end{array}\right] \\ \dfrac{\Sigma_{11}-\Sigma_{33}}{\sigma_T} = \sqrt{\dfrac{\beta^2+1}{2(2\beta^2-1)}}\left[\sqrt{\alpha^2t^2 + s\alpha t + 1} - \sqrt{\alpha^2t^2 + s\alpha tf + f^2}\right] \end{cases} \tag{7.189}$$

Case (ii):

- *For* $D_m \geq 0$ *and* $D_{33} \geq 0$ *such that* $0 \leq t \leq \dfrac{1}{2}\left(2\beta^2-1\right)f$,

$$\begin{cases} \dfrac{\Sigma_{\gamma\gamma}}{\sigma_T} = \dfrac{2}{\sqrt{3\left(2\beta^2-1\right)}} \ln\left(\dfrac{t+\sqrt{t^2+g_1^2 f^2}}{t+\sqrt{t^2+g_1^2}} \cdot \dfrac{1}{f}\right) \\ \dfrac{\Sigma_{33}-\Sigma_{11}}{\sigma_T} = \dfrac{2}{\sqrt{3\left(2\beta^2-1\right)}} \left[\sqrt{t^2+g_1^2} - \sqrt{t^2+g_1^2 f^2}\right]. \end{cases} \tag{7.190}$$

- *For* $D_m \geq 0$ *and* $D_{33} \geq 0$ *such that* $\dfrac{1}{2}\left(2\beta^2-1\right)f \leq t \leq \dfrac{\beta^2+1}{2\left(\beta^2-1\right)}f$,

$$\begin{cases} \dfrac{\Sigma_{\gamma\gamma}}{\sigma_T} = A\sqrt{\dfrac{\beta^2+1}{2\beta^2\left(2-\beta^2\right)}} \cdot \left\{ \begin{array}{l} \ln\left(\dfrac{A\,t+\frac{s_1}{2}f+\sqrt{A^2t^2+s_1Atf+f^2}}{A+\frac{s_1}{2}\gamma_1+\sqrt{A^2+s_1A\gamma_1+\gamma_1^2}} \cdot \dfrac{\gamma_1}{f}\right) \\ -\dfrac{s_1}{2}\ln\left(\dfrac{\frac{s}{2}At+f+\sqrt{A^2t^2+s_1Atf+f^2}}{\frac{s_1}{2}A+\gamma_1+\sqrt{A^2+s_1A\gamma_1+\gamma_1^2}} \cdot \dfrac{1}{t}\right) \end{array} \right\} \\ -\dfrac{2}{\sqrt{3\left(2\beta^2-1\right)}} \ln\left(\dfrac{t+\sqrt{t^2+g_1^2}}{g_1} \cdot \dfrac{3}{2g_1+\sqrt{4g_1^2+9}}\right) \\ \dfrac{\Sigma_{33}-\Sigma_{11}}{\sigma_T} = \dfrac{2}{\sqrt{3\left(2\beta^2-1\right)}}\sqrt{t^2+g_1^2} - \sqrt{\dfrac{\beta^2+1}{2\beta^2\left(2-\beta^2\right)}} \cdot \sqrt{A^2t^2+s_1Atf+f^2} \end{cases} \tag{7.191}$$

- *For* $D_m \geq 0$ and $D_{33} \geq 0$ *such that* $\dfrac{\beta^2+1}{2\left(\beta^2-1\right)}f \leq t \leq \dfrac{1}{2}\left(2\beta^2-1\right)$

$$\begin{cases} \dfrac{\Sigma_{\gamma\gamma}}{\sigma_T} = \alpha\sqrt{\dfrac{\beta^2+1}{2\left(2\beta^2-1\right)}} \cdot \left[\begin{array}{l} \ln\left(\dfrac{2\alpha\,t-sf+2\sqrt{\alpha^2t^2-s\alpha tf+f^2}}{\sqrt{4-s^2}\left(2+\sqrt{4-s^2}\right)} \cdot \dfrac{s}{f}\right) \\ -\dfrac{s}{2}\ln\left(\dfrac{\alpha t\sqrt{4-s^2}}{-s\alpha t+2f+2\sqrt{\alpha^2t^2-s\alpha tf+f^2}}\right) \end{array} \right] \\ +A\sqrt{\dfrac{\beta^2+1}{2\beta^2\left(2-\beta^2\right)}} \cdot \left[\begin{array}{l} \ln\left(\dfrac{-2+s_1^2/2-\sqrt{4-s_1^2}}{A\gamma_1+\gamma_1s_1/2+\sqrt{A^2+s_1A\gamma_1+\gamma_1^2}} \cdot \dfrac{\gamma_1}{s_1}\right) \\ -\dfrac{s_1}{2}\ln\left(\dfrac{A\sqrt{4-s_1^2}}{s_1A+2\gamma_1+2\sqrt{A^2+s_1A\gamma_1+\gamma_1^2}}\right) \end{array} \right] \\ -\dfrac{2}{\sqrt{3\left(2\beta^2-1\right)}} \ln\left(\dfrac{t+\sqrt{g_1^2+t^2}}{g_1} \cdot \dfrac{3}{2g_1+\sqrt{4g_1^2+9}}\right) \\ \dfrac{\Sigma_{33}-\Sigma_{11}}{\sigma_T} = \left[\dfrac{2}{\sqrt{3\left(2\beta^2-1\right)}}\sqrt{t^2+g_1^2} - \sqrt{\dfrac{\beta^2+1}{2\left(2\beta^2-1\right)}} \cdot \sqrt{\alpha^2t^2-s\alpha tf+f^2}\right] \end{cases} \tag{7.192}$$

- *For* $D_m \geq 0$ *and* $D_{33} \geq 0$ *such that* $\frac{1}{2}\left(2\beta^2-1\right) \leq t \leq \frac{\beta^2+1}{2\left(\beta^2-1\right)}$,

$$\begin{cases} \dfrac{\Sigma_{\gamma\gamma}}{\sigma_T} = \alpha\sqrt{\dfrac{\beta^2+1}{2\left(2\beta^2-1\right)}}\cdot\left[\begin{array}{l} \ln\left(\dfrac{\alpha t-\frac{s}{2}f+\sqrt{\alpha^2t^2-s\alpha tf+f^2}}{\left(2+\sqrt{4-s^2}\right)\sqrt{4-s^2}}\cdot\dfrac{2s}{f}\right) \\ -\dfrac{s}{2}\ln\left(\dfrac{\alpha t\sqrt{4-s^2}}{-s\alpha t+2f+2\sqrt{\alpha^2t^2-s\alpha tf+f^2}}\right)\end{array}\right] \\ +A\sqrt{\dfrac{\beta^2+1}{2\beta^2\left(2-\beta^2\right)}}\cdot\left[\begin{array}{l} \ln\left(\dfrac{\left(2+\sqrt{4-s_1^2}\right)\sqrt{4-s_1^2}}{2|s_1|\left(\sqrt{A^2t^2+s_1At+1}+At+s_1/2\right)}\right) \\ +\dfrac{s_1}{2}\ln\left(\dfrac{\sqrt{A^2t^2+s_1At+1}+\frac{s_1}{2}At+1}{\sqrt{4-s_1^2}}\cdot\dfrac{2}{Au}\right)\end{array}\right] \\ \dfrac{\Sigma_{11}-\Sigma_{33}}{\sigma_T} = \sqrt{\dfrac{\beta^2+1}{2}}\left(\dfrac{\sqrt{A^2t^2+s_1At+1}}{\sqrt{\beta^2\left(2-\beta^2\right)}}-\dfrac{\sqrt{\alpha^2t^2-s\alpha tf+f^2}}{\sqrt{2\beta^2-1}}\right) \end{cases} \tag{7.193}$$

- *For* $D_m \geq 0$ *and* $D_{33} \geq 0$ *such that* $t \geq \frac{\beta^2+1}{2\left(\beta^2-1\right)}$,

$$\begin{cases} \dfrac{\Sigma_{\gamma\gamma}}{\sigma_T} = \sqrt{\dfrac{2\left(3\beta^2-1\right)}{3\left(2\beta^2-1\right)}}\ln\left(\dfrac{\alpha t-\frac{s}{2}f+\sqrt{\alpha^2t^2-s\alpha tf+f^2}}{\alpha t-\frac{s}{2}+\sqrt{\alpha^2t^2-s\alpha t+1}}\cdot\dfrac{1}{f}\right) \\ +\dfrac{\sqrt{2}\left(\beta^2-1\right)}{\sqrt{\left(1+\beta^2\right)\left(2\beta^2-1\right)}}\ln\left(\dfrac{-\frac{s\alpha}{2}t+f+\sqrt{\alpha^2t^2-s\alpha tf+f^2}}{-\frac{s\alpha}{2}t+1+\sqrt{\alpha^2t^2-s\alpha t+1}}\right) \\ \dfrac{\Sigma_{11}-\Sigma_{33}}{\sigma_T} = \sqrt{\dfrac{\beta^2+1}{2(2\beta^2-1)}}\left(\sqrt{\alpha^2t^2-s\alpha t+1}-\sqrt{\alpha^2-s\alpha tf+f^2}\right) \end{cases} \tag{7.194}$$

Proof For loadings such that $D_m \geq 0$ and $D_{33} \leq 0$ and $0 \leq t \leq \left(\frac{2-\beta^2}{2\beta^2}\right)f$, the local plastic dissipation has the same expression everywhere in the hollow cylinder [see Eqs. (7.127)–(7.162)], i.e.,

$$\pi(\mathbf{d}) = \frac{1}{\beta}\sigma_T|D_{33}|\left[1+\frac{\beta^2}{\left(2-\beta^2\right)}\frac{4t^2}{3}\left(\frac{b^4}{r^4}\right)\right]^{1/2} \quad \forall a \leq r \leq b. \tag{7.195}$$

Further substitution in the integral representing the plastic dissipation of the porous material, i.e., $\Pi_{\text{SD}}^{\text{cyl}}(\boldsymbol{D},f) = \langle \pi(\mathbf{d}) \rangle_{\Omega}$ and making change of variable, $x = tb^2/gr^2$, where $g = \dfrac{\sqrt{3(2-\beta^2)}}{2\beta}$ [see also, Eq. (7.186)], leads to:

$$\Pi_{\text{SD}}^{\text{cyl}}(\boldsymbol{D},f) = \frac{2\sigma_T|D_{33}|}{\sqrt{3(2-\beta^2)}} \left[\begin{array}{l} \sqrt{g^2+t^2} - \sqrt{f^2g^2+t^2} \\ +t\ln\left(\dfrac{t+\sqrt{f^2g^2+t^2}}{t+\sqrt{g^2+t^2}} \cdot \dfrac{1}{f} \right) \end{array} \right]. \tag{7.196}$$

Using the above formula, the stresses at yielding are obtained by derivation (see Sect. 7.1) resulting in the parametric representation of the yield surface of the porous material given by Eq. (7.187).

Key features of the yielding response of a porous material according to Cazacu and Stewart [21] *criterion*

- First, let us note that if $\beta = \sigma_T/\sigma_C = 1$ (no tension–compression asymmetry of the matrix), Eqs. (7.187)–(7.194) reduce to a unique expression which is given by Eq. (7.170). In other words, Gurson [29] criterion for a porous material with von Mises matrix containing randomly distributed cylindrical voids is recovered.
- For $\beta = \sigma_T/\sigma_C \neq 1$, the yield surface of the porous material given by Eqs. (7.187)–(7.194) is not invariant to the transformation: $(\Sigma_{\gamma\gamma}, \Sigma_e) \rightarrow (\Sigma_{\gamma\gamma}, -\Sigma_e)$. Thus, according to Cazacu and Stewart [21] criterion yielding of the porous material depends on the third-invariant of the stress deviator, J_3^{Σ}:
  - The zone of the yield surface given by Eqs. (7.187)–(7.189) corresponds to stress states for which the third-invariant of the stress deviator is negative ($\Sigma_{33} < \Sigma_{11}$, so $J_3^{\Sigma} \leq 0$) while Eqs. (7.190)–(7.194) correspond to stress states for which $J_3^{\Sigma} \geq 0$.
  - The hydrostatic solution, which corresponds to $J_3^{\Sigma} = 0$, can be obtained from Eq. (7.193) by setting $\Sigma_e = |\Sigma_{11} - \Sigma_{33}| = 0$ and solving a second-order algebraic equation for t. Only one of the roots of this equation belongs to the interval $\left[\dfrac{1}{2}(2\beta^2-1), \dfrac{\beta^2+1}{2(\beta^2-1)}\right]$. This root is:

$$t(J_3^{\Sigma}=0) = \frac{2\beta^2 - 1 - \beta^2(2-\beta^2)f - (1-f)\sqrt{\beta^2(2-\beta^2)(2\beta^2-1)}}{2(\beta^2-1)^2} \tag{7.197}$$

- For purely deviatoric axisymmetric loadings, yielding occurs at either $\Sigma_e = (1-f)\sigma_C$ or at $\Sigma_e = (1-f)\sigma_T$. This sensitivity to the sign of the mean stress is

due to the tension–compression asymmetry of the plastic flow in the incompressible matrix.

- The invariance to the transformation $\left(\Sigma_{\gamma\gamma}, \Sigma_e\right) \rightarrow \left(\Sigma_{\gamma\gamma}, -\Sigma_e\right)$ is a consequence of the type of loadings imposed, namely axisymmetric stresses with either the minimum or maximum eigenstress aligned with the void generator $\mathbf{e}_3$. Indeed, this type of loadings induces invariance of the local plastic dissipation with respect to $(D_m, D_{33}) \rightarrow (-D_m, D_{33})$ and, consequently the overall plastic potential has the same property.

- For plane-strain conditions ($D_{33} = 0$ or $t \rightarrow \infty$), the stress state at yielding is not hydrostatic.
  Indeed, according to the yield criterion [see Eq. (7.194)]:

$$\begin{aligned} \lim_{t\rightarrow\infty}\left(\frac{|\Sigma_{11}-\Sigma_{33}|}{\sigma_T}\right) &= \left(\beta^2-1\right)\frac{(1-f)}{\sqrt{\frac{2}{3}\left(3\beta^2-1\right)\left(2\beta^2-1\right)}} \\ \lim_{t\rightarrow\infty}\left(\frac{\Sigma_{\gamma\gamma}}{\sigma_T}\right) &= -2\sqrt{\frac{\left(3\beta^2-1\right)}{6\left(2\beta^2-1\right)}}\,\ln(f). \end{aligned} \tag{7.198}$$

All those features of the yielding of the porous material are illustrated in Figs. 7.94 and 7.95 which show the yield surfaces of two materials having the same porosity $f = 1\%$. One of the materials has the matrix harder in tension than in

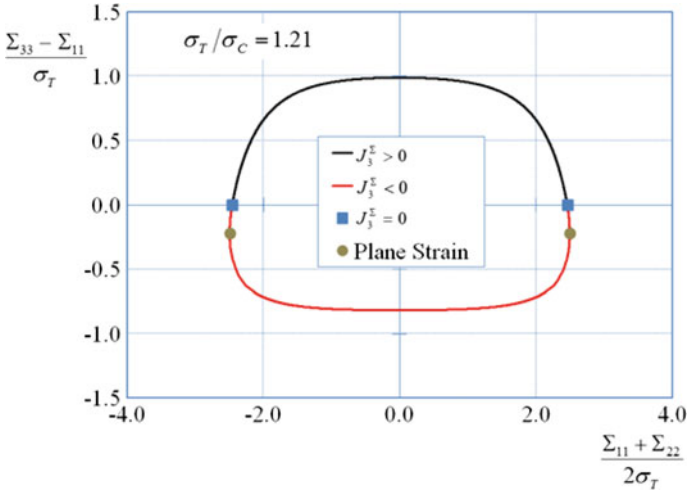

Fig. 7.94 Representation in the $((\Sigma_{33}-\Sigma_{11}/\sigma_T, (\Sigma_{11}+\Sigma_{22})/\sigma_T))$ plane of the Cazacu and Stewart [21] yield surface of a porous material containing randomly distributed cylindrical voids in a matrix having the yield in tension greater than the yield in compression ($\sigma_T/\sigma_C = 1.21$) for axisymmetric loadings; void volume fraction ($f = 0.01$)

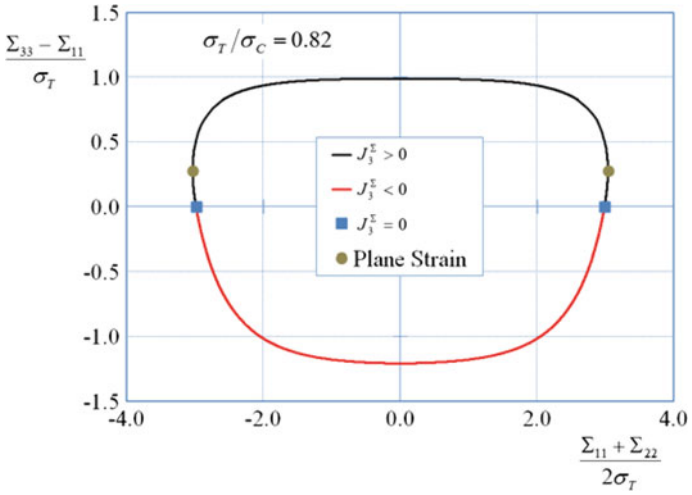

Fig. 7.95 Representation in the $((\Sigma_{33}-\Sigma_{11})/\sigma_T, (\Sigma_{11}+\Sigma_{22})/\sigma_T)$ plane of the Cazacu and Stewart [21] yield surface of a porous material containing randomly distributed cylindrical voids in a matrix having the yield in tension less than the yield in compression ($\sigma_T/\sigma_C = 0.82$) for axisymmetric loadings; void volume fraction ($f = 0.01$)

compression, being characterized by $\beta_1 = \sigma_T/\sigma_C = 1.21$ while the other has the matrix softer in tension than in compression, and it is characterized by $\beta_2 = 1/\beta_1$ (i.e., has $\sigma_C/\sigma_T = 1.21$). As a general observation, note the strong effect of the third-invariant J_3^Σ on yielding of the porous materials. Furthermore, for plane-strain conditions ($D_{33} = 0$ or $t \to \infty$), the stress state at yielding is not hydrostatic [see Eq. (7.198)].

Remark Cazacu and Stewart [21] yield surface was obtained in parametric form [see Eqs. (7.187)–(7.194)]. The elimination of the parameter t is not possible except in certain intervals. For example, the parameter t can be eliminated between the expressions (7.187) such that

$$\beta^2\left(\frac{\Sigma_e}{\sigma_T}\right)^2 + 2f\cosh\left(\frac{\sqrt{3}}{2}\sqrt{2-\beta^2}\frac{\Sigma_{\gamma\gamma}}{\sigma_T}\right) - \left(1+f^2\right) = 0$$

where, Σ_e is the von Mises effective stress and $\Sigma_{\gamma\gamma}$ $(\gamma = 1, 2)$ is the partial trace of the stress tensor, $\boldsymbol{\Sigma}$, in the plane orthogonal to the axis of voids (e.g., if the axis of voids is along the unit vector $\mathbf{e}_3$, $\Sigma_{\gamma\gamma} = \Sigma_{11} + \Sigma_{22}$). Nevertheless, the parametric form of the yield surface [see Eqs. (7.187)–(7.194)] can be easily implemented as a material subroutine in commercial F.E. codes and used to perform numerical studies of damage evolution and fracture in voided polycrystals with incompressible matrix displaying S-D effects (e.g., ultra-high strength martensitic steels).

References

1. Alves JL, Cazacu O (2015) Micromechanical study of the dilatational response of porous solids with pressure-insensitive matrix displaying tension–compression asymmetry. Eur J Mech-A Solids 51:44–54
2. Alves JL, Cazacu O (2017) Micromechanical study of the response of porous solids with pressure-insensitive matrix governed by Drucker's (1949) yield criterion
3. Alves JL, Cazacu O (2015) Correlation between strength differential effects in the plastic flow of the matrix and the rate of damage growth in porous polycrystals. Comptes Rendus Mécanique 343:107–120
4. Alves JL, Revil-Baudard B, Cazacu O (2014) Importance of the coupling between the sign of the mean stress and the third invariant on the rate of void growth and collapse in porous solids with a von Mises matrix. Model Simul Mater Sci Eng 22:025005
5. Aravas N (1987) On the numerical integration of a class of pressure-dependent plasticity models. Int J Numer Methods Eng 24:1395–1416
6. Bai Y, Wierzbicki T (2010) Application of extended Mohr-Coulomb criterion to ductile fracture. Int J Fract 161:1
7. Balan T, Cazacu O (2013) Elastic–plastic ductile damage model based on strain-rate plastic potential. Mech Res Commun 54:21–26
8. Bao Y, Wierzbicki T (2004) On fracture locus in the equivalent strain and stress triaxiality space. Int J Mech Sci 46:81–98
9. Barsoum I, Faleskog J (2007) Rupture mechanisms in combined tension and shear—Experiments. Int J Solids Struct 44:1768–1786
10. Budiansky B, Hutchinson J, Slutsky S (1982) Void growth and collapse in viscous solids. In: Mechanics of solids: the Rodney Hill 60th anniversary volume. Elsevier, pp 13–45
11. Buffiere J-Y, Maire E, Adrien J, Masse J-P, Boller E (2010) In situ experiments with X ray tomography: an attractive tool for experimental mechanics. Exp Mech 50:289–305
12. Cazacu O, Alves JL, Revil-Baudard B, Pasiliao C (2014) Unusual damage characteristics of metallic materials with matrix displaying strength differential effects. Ann Univ Buchar Math Ser 5:219–244
13. Cazacu O, Chandola N, Alves JL, Revil-Baudard B (2014) Importance of the consideration of the specificities of local plastic deformation on the response of porous solids with Tresca matrix. Eur J Mech A Solids 47:194–205
14. Cazacu O, Ionescu IR, Yoon JW (2010) Orthotropic strain rate potential for the description of anisotropy in tension–compression of metals. Int J Plast 26:887–904
15. Cazacu O, Plunkett B, Barlat F (2006) Orthotropic yield criterion for hexagonal closed packed metals. Int J Plast 22:1171–1194
16. Cazacu O, Revil-Baudard B (2015) New three-dimensional plastic potentials for porous solids with a von Mises matrix. Comptes Rendus Mécanique 343:77–94
17. Cazacu O, Revil-Baudard B (2017) New analytic criterion for porous solids with pressure-insensitive matrix. Int J Plast 89:66–84
18. Cazacu O, Revil-Baudard B, Chandola N, Kondo D (2014) New analytical criterion for porous solids with Tresca matrix under axisymmetric loadings. Int J Solids Struct 51:861–874
19. Cazacu O, Revil-Baudard B, Lebensohn RA, Garajeu M (2013) On the combined effect of pressure and third invariant on yielding of porous solids with von Mises matrix. J Appl Mech 80:064501
20. Cazacu O, Stewart JB (2009) Analytic plastic potential for porous aggregates with matrix exhibiting tension–compression asymmetry. J Mech Phys Solids 57:325–341
21. Cazacu O, Stewart JB (2013) Analytical criterion for porous solids containing cylindrical voids in an incompressible matrix exhibiting tension–compression asymmetry. Philos Mag 93:1520–1548
22. Chu CC, Needleman A (1980) Void nucleation effects in biaxially stretched sheets. J Eng Mater Technol ASME 102:249–256

23. Combaz E, Bacciarini C, Charvet R, Dufour W, Mortensen A (2011) Multiaxial yield behaviour of Al replicated foam. J Mech Phys Solids 59:1777–1793
24. Dormieux L, Kondo D, Ulm F-J (2006) Microporomechanics. Wiley
25. Drucker DC (1949) Relation of experiments to mathematical theories of plasticity. ASME J Appl Mech 16:349–357
26. Faleskog J, Gao X, Shih CF (1998) Cell model for nonlinear fracture analysis–I. Micromechanics calibration. Int J Fract 89:355–373
27. Gao X, Faleskog J, Shih CF, Dodds RH Jr (1998) Ductile tearing in part-through cracks: experiments and cell-model predictions. Eng Fract Mech 59:761–777
28. Garajeu M, Suquet P (1997) Effective properties of porous ideally plastic or viscoplastic materials containing rigid particles. J Mech Phys Solids 45:873–902
29. Gurson AL (1975) Plastic flow and fracture behavior of ductile materials incorporating void nucleation, growth and coalescence, PhD Diss, Brown University
30. Gurson AL (1977) Continuum theory of ductile rupture by void nucleation and growth: Part I —yield criteria and flow rules for porous ductile media. J Eng Mater Technol 99:2–15
31. Hancock J, Mackenzie A (1976) On the mechanisms of ductile failure in high-strength steels subjected to multi-axial stress-states. J Mech Phys Solids 24:147–160
32. Hill R (1967) The essential structure of constitutive laws for metal composites and polycrystals. J Mech Phys Solids 15:79–95
33. Hill R (1948) A theory of the yielding and plastic flow of anisotropic metals. In: Proceedings of the royal society of London A: mathematical, physical and engineering sciences. Royal Soc 281–297
34. Hosford WF (1993) The mechanics of crystals and textured polycrystals. Oxford University Press, USA
35. Hosford WF, Allen T (1973) Twinning and directional slip as a cause for a strength differential effect. Metall Mater Trans B 4:1424–1425
36. Hosokawa A, Wilkinson DS, Kang J, Maire E (2012) Effect of triaxiality on void growth and coalescence in model materials investigated by X-ray tomography. Acta Mater 60:2829–2839
37. Huang Y (1991) Accurate dilatation rates for spherical voids in triaxial stress fields. J Appl Mech 58:1084
38. Kim J, Gao X, Srivatsan TS (2004) Modeling of void growth in ductile solids: effects of stress triaxiality and initial porosity. Eng Fract Mech 71:379–400
39. Koplik J, Needleman A (1988) Void growth and coalescence in porous plastic solids. Int J Solids Struct 24:835–853
40. Kwon D, Asaro R (1990) A study of void nucleation, growth, and coalescence in spheroidized 1518 steel. Metall Trans A 21:117
41. Leblond J, Perrin G, Suquet P (1994) Exact results and approximate models for porous viscoplastic solids. Int J Plast 10:213–235
42. Leblond J-B (2003) Mécanique de la rupture fragile et ductile. Hermès science publications
43. Leblond J-B, Gologanu M (2008) External estimate of the yield surface of an arbitrary ellipsoid containing a confocal void. Comptes Rendus Mécanique 336:813–819
44. Lou Y, Huh H (2013) Extension of a shear-controlled ductile fracture model considering the stress triaxiality and the Lode parameter. Int J Solids Struct 50:447–455
45. Lubliner J (2008) Plasticity theory. Courier Corporation
46. Mandel J (1972) Plasticité classique et viscoplasticité. Academic Press
47. McClintock FA (1968) A criterion for ductile fracture by the growth of holes. J Appl Mech 35:363–371
48. McElwain DS, Roberts A, Wilkins A (2006) Yield criterion of porous materials subjected to complex stress states. Acta Mater 54:1995–2002
49. Menezes L, Teodosiu C (2000) Three-dimensional numerical simulation of the deep-drawing process using solid finite elements. J Mater Process Technol 97:100–106
50. Monchiet V, Charkaluk E, Kondo D (2011) A micromechanics-based modification of the Gurson criterion by using Eshelby-like velocity fields. Eur J Mech-ASolids 30:940–949
51. Needleman A (1972) Void growth in an elastic-plastic medium. J Appl Mech 39:964–970

52. Nixon ME, Cazacu O, Lebensohn RA (2010) Anisotropic response of high-purity α-titanium: experimental characterization and constitutive modeling. Int J Plast 26:516–532
53. Oliveira M, Alves JL, Menezes L (2008) Algorithms and strategies for treatment of large deformation frictional contact in the numerical simulation of deep drawing process. Arch Comput Methods Eng 15:113–162
54. Revil-Baudard B, Cazacu O (2014) Role of the plastic flow of the matrix on yielding and void evolution of porous solids: Comparison between the theoretical response of porous solids with Tresca and von Mises matrices. Mech Res Commun 56:69–75
55. Revil-Baudard B, Cazacu O (2014) New three-dimensional strain-rate potentials for isotropic porous metals: Role of the plastic flow of the matrix. Int J Plast 60:101–117
56. Revil-Baudard B, Cazacu O (2013) On the effect of the matrix tension–compression asymmetry on damage evolution in porous plastic solids. Eur J Mech-ASolids 37:35–44
57. Revil-Baudard B, Cazacu O, Thuillier S, Maire E (2013) Effect of stress triaxiality on porosity evolution in notched bars: quantitative agreement between a recent dilatational model and X-ray tomography data. Mech Res Commun 50:77–82
58. Rice JR, Tracey DM (1969) On the ductile enlargement of voids in triaxial stress fields. J Mech Phys Solids 17:201–217
59. Richmond O, Smelser R (1985) Alcoa technical center memorandum. Google Sch
60. Salençon J (1983) Calcul à la rupture et analyse limite. Presses De L'ecole Nationale Des Ponts Et Chaussees
61. Salençon J (2013) Yield design. Wiley
62. Spitzig W, Smelser R, Richmond O (1988) The evolution of damage and fracture in iron compacts with various initial porosities. Acta Metall 36:1201–1211
63. Srivastava A, Needleman A (2012) Porosity evolution in a creeping single crystal. Model Simul Mater Sci Eng 20:035010
64. Thoré P, Pastor F, Pastor J (2011) Hollow sphere models, conic programming and third stress invariant. Eur J Mech-ASolids 30:63–71
65. Thuillier S, Maire E, Brunet M (2012) Ductile damage in aluminium alloy thin sheets: Correlation between micro-tomography observations and mechanical modeling. Mater Sci Eng A 558:217–225
66. Tresca H (1868) Memoire sur l'ecoulement des corps solides, par M. H. Tresca. Imprimerie Imperiale, Paris
67. Tvergaard V (1981) Influence of voids on shear band instabilities under plane strain conditions. Int J Fract 17:389–407
68. Tvergaard V (1982) On localization in ductile materials containing spherical voids. Int J Fract 18:237–252
69. Tvergaard V, Needleman A (1984) Analysis of the cup-cone fracture in a round tensile bar. Acta Metall 32:157–169
70. von Mises R (1913) Mechanik der festen Körper im plastisch deformablen Zustand. Nachrichten Von Ges Wiss Zu Gött Math-Phys Kl 582–592
71. Zhang K, Bai J, Francois D (2001) Numerical analysis of the influence of the Lode parameter on void growth. Int J Solids Struct 38:5847–5856

Chapter 8
Anisotropic Plastic Potentials for Porous Metallic Materials

In all the constitutive models for porous plastic materials presented in previous chapters, it was presumed that the matrix can be regarded as isotropic. However, most engineering materials display plastic anisotropy (see Chaps. 5 and 6). In this chapter are presented key contributions toward understanding the role played by the matrix plastic anisotropy on yielding and damage evolution in single crystals and strongly textured polycrystalline materials containing randomly distributed spherical voids. The case when the matrix is governed by Hill [13] orthotropic yield criterion is first discussed (Sect. 8.1). Next, a recent analytical model that accounts for the combined effects of anisotropy and tension–compression asymmetry of the matrix on yielding and porosity evolution is presented. This model predicts a strong sensitivity to the loading path and that the triaxiality and Lode angle effects are orientation dependent. The model is applied to the description of plastic deformation and damage in hcp-Ti. The unusual damage characteristics of Ti, both in terms of the rate of void growth and location, predicted by the analytical model are confirmed by both in situ and ex situ X-ray tomography results (Sects. 8.1–8.3).

We conclude with the presentation of a new model for description of porosity evolution in single crystals subject to creep loadings. It is shown that the rate of void growth is strongly influenced by the crystal anisotropy and/or tension–compression asymmetry (Sect. 8.4).

Before proceeding with the presentation of the models, it is important to note that in the case when the matrix behavior is governed by an anisotropic yield criterion, it is extremely difficult or impossible to obtain analytically the plastic potential of the porous material. As already mentioned, in order to carry out the kinematic homogenization, one needs to know in closed form the exact strain-rate plastic potential associated to the stress-based plastic potential of the matrix (see Sect. 7.1). Only the strain-rate potentials associated with Hill [13] and Cazacu et al. [5] orthotropic potentials can be obtained analytically (see Chap. 6).

Therefore, the effects of plastic anisotropy on yielding and void evolution can be explained quantitatively only in the case when the matrix is governed by the Hill [13] or Cazacu et al. [5] orthotropic potential, respectively. The orthotropic plastic

O. Cazacu et al., *Plasticity–Damage Couplings: From Single Crystal to Polycrystalline Materials*, Solid Mechanics and Its Applications 253,
https://doi.org/10.1007/978-3-319-92922-4_8

potentials developed by Benzerga and Besson [4] and Stewart and Cazacu [32] for porous materials with matrix governed by these potentials, are presented in the following. Irrespective of the matrix behavior, the limit analysis was carried out for a hollow sphere with inner radius a and outer radius $b = af^{-1/3}$, where f is the void volume fraction (see Fig. 7.1), and for a unique velocity field $\mathbf{v}$, namely that of Rice and Tracey [27] (see also Sect. 7.2.2), which is compatible with uniform strain-rate boundary conditions on the hollow sphere, i.e.,

$$\mathbf{v}|_{\mathbf{t}=b\mathbf{e}_r} = \mathbf{D}\mathbf{t}, \tag{8.1}$$

for any position vector $\mathbf{t}$ on the outer radius. In the presentation of the models, the notations introduced in Chap. 7 will be used. Specifically, the local stresses and strain-rates are designated with $\boldsymbol{\sigma}$ and $\mathbf{d}$, while the overall fields (i.e., the averages of the local fields over the domain of the representative volume element) are designated as $\boldsymbol{\Sigma} = \langle \boldsymbol{\sigma} \rangle_\Omega$ and $\mathbf{D} = \langle \mathbf{d} \rangle_\Omega$, respectively. Likewise, the same definitions for the mean strain-rate D_m and the invariants of the deviator $\mathbf{D}'$ (see Sect. 7.1) are used. Here, we only recall that the local strain-rate tensor $\mathbf{d} = \frac{1}{2}(\nabla \mathbf{v} + \nabla^{\mathrm{T}} \mathbf{v})$ corresponding to the Rice and Tracey [27] velocity field $\mathbf{v}$ is expressed as:

$$\mathbf{d} = \mathbf{D}' + D_m (b/r)^3 \bar{\mathbf{d}} \tag{8.2}$$

with

$$\bar{\mathbf{d}} = \left(-2\mathbf{e}_r \otimes \mathbf{e}_r + \mathbf{e}_\theta \otimes \mathbf{e}_\theta + \mathbf{e}_\varphi \otimes \mathbf{e}_\varphi \right), \tag{8.3}$$

$\left(\boldsymbol{e}_r, \boldsymbol{e}_\theta, \boldsymbol{e}_\varphi \right)$ being the unit vectors associated with the spherical coordinate system and r denoting the radial coordinate (see Sect. 7.2.2).

8.1 Benzerga and Besson [4] Criterion for Orthotropic Porous Materials with Hill [13] Matrix

Benzerga and Besson [4] were the first to conduct a limit analysis for the case of an anisotropic matrix and show that it is possible to obtain an approximate relation between the stresses at yielding of a porous material with a Hill [13] matrix containing randomly distributed spherical voids. Their analysis was extended by Monchiet et al. [19] to the case of spheroidal void geometry.

In the following, we revisit the analysis conducted by Benzerga and Besson [4] and present the key challenges and the approximations that needed to be considered in order to arrive at analytic expressions of the strain-rate-based and stress-based plastic potentials of the porous material.

Theorem 8.1 *In the coordinate system* $(\mathbf{x},\mathbf{y},\mathbf{z})$ *associated with the axes of orthotropy, the* Benzerga and Besson [4] *strain-rate potential for a porous material with matrix governed by the* Hill [13] *yield criterion and containing spherical voids is given by:*

$$\Psi_{BB}(\mathbf{D},f) = 2h|D_m|\left[\frac{\sqrt{1+\gamma^2}-\sqrt{f^2+\gamma^2}}{\gamma} + \ln\left(\frac{\gamma+\sqrt{f^2+\gamma^2}}{\gamma+\sqrt{1+\gamma^2}}\frac{1}{f}\right)\right], \tag{8.4}$$

where h is a constant, expressible only in terms of the anisotropy coefficients F, G, H, L, M, and N, i.e.,

$$h = \sqrt{\frac{4}{5}\left(\frac{F+G+H}{FH+FG+GH}\right)+\frac{6}{5}\left(\frac{1}{L}+\frac{1}{M}+\frac{1}{N}\right)} \tag{8.5}$$

and γ *is an anisotropic measure of the strain-rate triaxiality defined as:*

$$\gamma \overset{\text{def}}{=} \frac{h|D_m|}{\bar{D}_e} \tag{8.6}$$

with

$$\bar{D}_e \overset{\text{def}}{=} \Psi_{\text{Hill}}(\mathbf{D}') = \sqrt{\frac{FD_{xx}'^2+GD_{yy}'^2+HD_{zz}'^2}{FH+FG+GH}+\frac{2D_{yz}'^2}{L}+\frac{2D_{xz}'^2}{M}+\frac{2D_{xy}'^2}{N}}, \tag{8.7}$$

Based on the expression of the SRP of the porous material, $\Psi_{BB}(\mathbf{D},f)$, the stresses at yielding are then obtained by differentiation with respect to $\mathbf{D}$, leading to the expression of the yield locus of the porous Hill material, in parametric form in terms of γ. Elimination of this parameter, leads to the classical form of the Benzerga and Besson [4] yield criterion, presented below.

Theorem 8.2 *In the coordinate system* $(\mathbf{x},\mathbf{y},\mathbf{z})$ *associated with the axes of orthotropy, the* Benzerga and Besson [4] *yield criterion for a porous material with matrix governed by the* Hill [13] *yield criterion and containing spherical voids is given by the following:*

$$\Phi_{BB}(\mathbf{\Sigma},f) = \left(\frac{\bar{\Sigma}_e}{\sigma_x^T}\right)^2 + 2f\,\cosh\left(\frac{3}{h}\frac{\Sigma_m}{\sigma_x^T}\right) - \left(1+f^2\right) = 0. \tag{8.8}$$

where

$$\begin{aligned}\bar{\Sigma}_e &= \left[\begin{array}{c} F\left(\Sigma_{yy}-\Sigma_{zz}\right)^2+G\left(\Sigma_{zz}-\Sigma_{xx}\right)^2+H\left(\Sigma_{xx}-\Sigma_{yy}\right)^2 \\ +2L\Sigma_{yz}^2+2M\Sigma_{xz}^2+2N\Sigma_{xy}^2\end{array}\right]^{1/2} \\ \Sigma_m &= \left(\Sigma_{xx}+\Sigma_{yy}+\Sigma_{zz}\right)/3,\end{aligned} \tag{8.9}$$

and h is a constant defined by Eq. (8.5) *and σ_x^T stands for the tensile effective stress of the fully dense material in the* **x***-direction of orthotropy of the material.*

Before proceeding with the proof of Theorem 8.1, let us first discuss the difficulties associated with estimating the plastic potential of the porous Hill [13] material even for the simplest loadings scenarios.

Remark 8.1 In contrast to the isotropic case, the solution to the problem of the hollow sphere having ideal plastic behavior governed by Hill [13] criterion and subject to hydrostatic pressure is not known.

Remark 8.2 Even for hydrostatic loadings, the overall plastic dissipation of the porous material associated with the Rice and Tracey [27] velocity field cannot be obtained in closed form. However, the following result can be deduced.

Proposition 8.1 *For hydrostatic loadings, a porous Hill material containing spherical voids yields at:*

$$\Sigma_e = 0 \text{ and } \left|\Sigma_m^H\right| = \left(\frac{\sigma_x^T}{3}\ln(f)\right)\alpha(F,G,H,L,M,N), \tag{8.10}$$

with

$$\alpha(F,G,H,L,M,N) < h, \tag{8.11}$$

and h given by Eq. (8.5).

Proof Let us first recall that for any strain-rate field $\mathbf{d}$, the local plastic dissipation associated with the Hill [13] yield function, $\varphi_{\text{Hill}}(\boldsymbol{\sigma}) = \{\boldsymbol{\sigma}:\mathbf{M}\boldsymbol{\sigma}\}^{\frac{1}{2}}$, has the following closed-form expression:

$$\pi_{\text{Hill}}(\mathbf{d}) = \sigma_x^T \psi_{\text{Hill}}(\mathbf{d}), \tag{8.12}$$

where the Hill SRP is given by:

$$\psi_{\text{Hill}}(\mathbf{d}) = \{\mathbf{d}:\mathbf{U}\mathbf{d}\}^{\frac{1}{2}},$$

In the coordinate system $(\mathbf{x},\mathbf{y},\mathbf{z})$ associated with the axes of orthotropy (see Sect. 6.2.1),

$$\psi_{\text{Hill}}(\mathbf{d}) = \sqrt{\frac{Fd_{xx}^2 + Gd_{yy}^2 + Hd_{zz}^2}{\Delta} + \frac{2d_{yz}^2}{L} + \frac{2d_{xz}^2}{M} + \frac{2d_{xy}^2}{N}}, \tag{8.13}$$

with

$$\Delta = FH + FG + GH, \tag{8.14}$$

(for the definition of the fourth-order tensors $\mathbf{M}$ and $\mathbf{U}$ and more details, the reader is referred to Chaps. 5 and 6).

For purely hydrostatic loadings ($\mathbf{D}' = \mathbf{0}$), the local strain-rate associated with the Rice and Tracey [27] velocity field is: $\mathbf{d} = D_m(b/r)^3\bar{\mathbf{d}}$, with $\bar{\mathbf{d}}$ given by Eq. (8.3). In order to evaluate the local plastic dissipation $\pi_{\text{Hill}}(\bar{\mathbf{d}})$, one needs to first express $\bar{\mathbf{d}}$ in the coordinate system $(\boldsymbol{x},\boldsymbol{y},\boldsymbol{z})$ associated with the axes of orthotropy, i.e., calculate

$$\bar{\mathbf{d}}_{(x,y,z)} = \mathbf{R}\bar{\mathbf{d}}_{(r,\theta,\varphi)}\mathbf{R}^{\mathrm{T}} \tag{8.15}$$

with

$$\mathbf{R} = \begin{bmatrix} \cos\varphi\,\sin\theta & \cos\varphi\cos\theta & -\sin\varphi \\ \sin\varphi\sin\theta & \sin\varphi\cos\theta & \cos\varphi \\ \cos\theta & -\sin\theta & 0 \end{bmatrix}, \quad \theta\in[0,\pi],\ \varphi\in[0,2\pi]. \tag{8.16}$$

Substitution of Eq. (8.3) into Eq. (8.15) leads to:

$$\bar{\mathbf{d}}_{(x,y,z)} = \begin{bmatrix} 1-3\sin^2\theta\cos^2\varphi & -3\sin^2\theta\sin\varphi\cos\varphi & -3\sin\theta\cos\theta\cos\varphi \\ -3\sin^2\theta\sin\varphi\cos\varphi & 1-3\sin^2\theta\sin^2\varphi & -3\sin\theta\cos\theta\sin\varphi \\ -3\sin\theta\cos\theta\cos\varphi & -3\sin\theta\cos\theta\sin\varphi & 1-3\cos^2\theta \end{bmatrix}. \tag{8.17}$$

Therefore for hydrostatic loadings, the overall plastic dissipation of the porous material is:

$$\begin{aligned}\Pi(\mathbf{D},f) &= \frac{\sigma_x^T}{V}\int_a^b 4\pi r^2\langle\pi_{\text{Hill}}(\mathbf{d})\rangle_{S(r)}\mathrm{d}r \\ &= \frac{-\sigma_x^T D_m\ln(f)}{4\pi} \\ &\int_0^{2\pi}\int_0^{\pi}\sqrt{\left(F\bar{d}_{xx}^2+G\bar{d}_{yy}^2+H\bar{d}_{zz}^2\right)/\Delta+2\left(\bar{d}_{yz}^2/L+\bar{d}_{xz}^2/M+\bar{d}_{xy}^2/N\right)}\sin\theta\mathrm{d}\theta\mathrm{d}\varphi,\end{aligned} \tag{8.18}$$

with $V = 4\pi b^3/3$, Ω the domain occupied by the matrix (see Fig. 7.1), and $S(r)$ being the spherical surface of radius r. In Eq. (8.18), the following notation was used:

$$\langle x\rangle_{S(r)} = \frac{1}{4\pi}\int_0^{2\pi}\int_0^{\pi} x\,\sin\theta\mathrm{d}\theta\mathrm{d}\varphi. \tag{8.19}$$

Because the components of $\bar{\mathbf{d}}_{(x,y,z)}$ depend on both $\theta \in [0,\pi]$ and $\varphi \in [0,2\pi]$, the above integral cannot be evaluated analytically, so for general orthotropic materials it is impossible to determine the specific expression of $\alpha(F,G,H,L,M,N)$.

However, since the surface integrals of the squared components of $\bar{\mathbf{d}}_{(x,y,z)}$ can be evaluated in closed form (see for example, Stewart and Cazacu [32]), namely:

$$\begin{array}{l} \langle \bar{d}^2_{xx} \rangle_{S(r)} = \langle \bar{d}^2_{yy} \rangle_{S(r)} = \langle \bar{d}^2_{zz} \rangle_{S(r)} = \frac{4}{5} \\ \langle \bar{d}^2_{yz} \rangle_{S(r)} = \langle \bar{d}^2_{xz} \rangle_{S(r)} = \langle \bar{d}^2_{xy} \rangle_{S(r)} = \frac{3}{5}, \end{array} \tag{8.20}$$

it follows that:

$$\begin{aligned} \left\langle \left(\psi_{\text{Hill}}(\bar{\mathbf{d}})\right)^2 \right\rangle_{S(r)} &= \frac{4}{5}(F+G+H)/(FH+FG+GH) \\ &+ \frac{6}{5}(1/L+1/M+1/N) = h^2 \end{aligned} \tag{8.21}$$

(see also Eq. 8.5). Further, using Cauchy–Schwarz inequality, we obtain that an approximate upper bound of the hydrostatic yield limit, $\left|\Sigma^H_m\right|$, is:

$$|p_{\text{Hill}}| = \frac{-h}{3}\sigma^T_x \ln(f). \tag{8.22}$$

It is also worth noting that for isotropic materials, i.e., the parameters $F = G = H = 1/2$ and $L = M = N = 3/2$, the Hill [13] yield criterion reduces to the von Mises yield criterion and from Eq. (8.5) it follows that: $h = 2$. Thus, the upper-bound estimate p_{Hill} coincides with the exact solution of the yield limit of a porous von Mises material under hydrostatic loadings (see Sect. 7.1).

Proposition 8.2 *For purely deviatoric loadings, i.e.,* $\mathbf{D} = \mathbf{D}' =$ *constant, the porous Hill material yields at*:

$$\Sigma_m = 0 \text{ and } \bar{\Sigma}_e = \sigma^T_x(1-f), \tag{8.23}$$

where $\bar{\Sigma}_e$ *is the effective stress associated with* Hill [13] *criterion* (see Eq. 8.9).

Proof For purely deviatoric loadings ($D_m = 0$), the local strain-rate associated with the Rice and Tracey [27] velocity field is: $\mathbf{d} = \mathbf{D}'$ = constant, so the overall plastic dissipation of the porous Hill [13] material is:

$$\Pi(\mathbf{D},f) = \langle \pi_{\text{Hill}}(\mathbf{d}) \rangle_{\Omega} = \sigma^T_x(1-f)\psi_{\text{Hill}}(\mathbf{D}').$$

Since $\psi_{\text{Hill}}(\mathbf{D}')$ is the exact work-conjugate of the Hill [13] stress potential, differentiation with respect to $\mathbf{D}$ of the above relation, leads to Eq. (8.23).

For any other loadings it is impossible to obtain the overall plastic potential $\Pi(\boldsymbol{D},f)$ associated with the Rice and Tracey [27] velocity field in closed form. To

obtain the approximate analytic criterion given by Eq. (8.8), Benzerga and Besson [4] made use of Cauchy–Schwarz inequality, i.e.,

$$\begin{aligned}\Pi(\mathbf{D},f) &= \frac{\sigma_x^T}{V}\int_a^b 4\pi r^2 \langle \psi_{\text{Hill}}(\mathbf{d})\rangle_{S(r)} \mathrm{d}r \\ &\leq \frac{\sigma_x^T}{V}\int_a^b 4\pi r^2 \left[\langle (\psi_{\text{Hill}}(\mathbf{d}))^2\rangle_{S(r)}\right]^{1/2} \mathrm{d}r\end{aligned} \tag{8.24}$$

For the Rice and Tracey [27] velocity field, $\mathbf{d} = \mathbf{D}' + D_m(b/r)^3\bar{\mathbf{d}}$ [see Eqs. (8.2) and (8.3)], therefore

$$\begin{aligned}\left\langle (\psi_{\text{Hill}}(\mathbf{d}))^2\right\rangle_{S(r)} &= \left\langle (\psi_{\text{Hill}}(\mathbf{D}'))^2\right\rangle_{S(r)} + D_m^2(b/r)^6\left\langle (\psi_{\text{Hill}}(\bar{\mathbf{d}}))^2\right\rangle_{S(r)} \\ &\quad + 2D_m(b/r)^3\langle \bar{\mathbf{d}}\rangle_{S(r)} : \mathbf{U}\mathbf{D}'.\end{aligned} \tag{8.25}$$

Noting that:

$$\langle \bar{\mathbf{d}}\rangle_{S(r)} = \langle \left[-2\mathbf{e}_r\otimes\mathbf{e}_r + \mathbf{e}_\theta\otimes\mathbf{e}_\theta + \mathbf{e}_\varphi\otimes\mathbf{e}_\varphi\right]\rangle_{S(r)} = 0, \tag{8.26}$$

and $\left\langle (\psi_{\text{Hill}}(\mathbf{D}'))^2\right\rangle_{S(r)} = \bar{D}_e^2$ [see Eq. (8.7)] and making use of Eq. (8.21), we obtain that:

$$\begin{aligned}\Psi_{BB}(\mathbf{D},f) &= \frac{1}{V}\int_a^b 4\pi r^2 \left[\langle (\psi_{\text{Hill}}(\mathbf{d}))^2\rangle_{S(r)}\right]^{1/2} \mathrm{d}r \\ &= \frac{3}{b^3}\int_a^b r^2\left(D_m^2\frac{b^6}{r^6}h^2 + \bar{D}_e^2\right)^{1/2}\mathrm{d}r \\ &= \frac{h|D_m|}{\gamma}\int_1^{1/f}\sqrt{1+\gamma^2t^2}\frac{\mathrm{d}t}{t^2}\end{aligned} \tag{8.27}$$

which after integration leads to Eq. (8.4).

Remark (a) Let us first note that if the anisotropy coefficients $F = G = H = L/3 = M/3 = N/3 = 1/2$, the potentials given by Eqs. (8.4) and (8.8) reduce to the Gurson [11] potentials for a porous von Mises material (see Sect. 7.2.3.1). Moreover, it can be easily shown (e.g., see in Chap. 6 the expressions of the SRP associated to the von Mises and Hill [13] stress potentials, respectively) that:

Remark (b) The SRP given by Eq. (8.4) can be obtained from $\Psi_{\text{Gurson}}(\mathbf{D},f)$ by making use of the change of variables:

$$D_m \rightarrow hD_m \tag{8.28}$$

$$D_e = \psi_{\text{Mises}}(\boldsymbol{D}) \rightarrow \bar{D}_e = \psi_{\text{Hill}}(\boldsymbol{D}) \tag{8.29}$$

Remark (c) The yield criterion of Benzerga and Besson [4] given by Eq. (8.8) can be obtained from that of Gurson [12] by making use of the change of variables:

$$\Sigma_m \rightarrow (2/h)\Sigma_m \tag{8.30}$$

$$\Sigma_e = \varphi_{\text{Mises}}(\boldsymbol{\Sigma}) \rightarrow \bar{\Sigma}_e = \varphi_{\text{Hill}}(\boldsymbol{\Sigma}) \tag{8.31}$$

(for the expression of the von Mises and Hill [13] criteria and their SRPs, see Chaps. 4–6).

Remark (d) Hill [13] criterion is an extension to orthotropy of the von Mises yield criterion using a linear transformation $\mathbf{M}$ on the stress tensor (see Chap. 5). If in the expression of the Gurson [12] criterion, the stress tensor is replaced by its transform $\mathbf{M\Sigma}$, the resulting criterion is:

$$\left(\frac{\bar{\Sigma}_e}{\sigma_x^T}\right)^2 + 2f\ \cosh\left(\frac{3}{2}\frac{\Sigma_m}{\sigma_x^T}\right) - \left(1+f^2\right) = 0. \tag{8.32}$$

with $\bar{\Sigma}_e$ given by Eq. (8.9). Note that Eq. (8.32) is not the Benzerga and Besson [4] criterion. Most importantly, according to Eq. (8.32), there is no effect of anisotropy on void evolution. This shows that a formulation that accounts for the effects of anisotropy on yielding and porosity evolution cannot be obtained heuristically by slightly modifying either an isotropic porous criterion (such as Gurson [12]) or the yield criterion of the matrix.

Remark (e) While the use of the Cauchy–Schwarz inequality enabled the determination of approximate potentials in closed form, at the same time it erased any dependence of the local plastic dissipation on the spherical coordinates θ and φ. Moreover, couplings between shear and mean strain-rate effects were eliminated.

This means that even for simple loadings such as axisymmetric loadings along the axes of orthotropy, the Benzerga and Besson [4] criterion cannot account for the influence of the ordering of the eigenstresses on the yielding response of the porous material. For example, for axisymmetric loadings such that: $\boldsymbol{\Sigma} = \Sigma_1\left(\mathbf{e}_y \otimes \mathbf{e}_y\right) + \Sigma_3(\mathbf{e}_x \otimes \mathbf{e}_x + \mathbf{e}_z \otimes \mathbf{e}_z)$, the criterion predicts the same yielding behavior in the case when $\Sigma_1 > \Sigma_3$ and in the case when $\Sigma_1 < \Sigma_3$, respectively, although in one case the major eigenstress is along the $\mathbf{y}$-axis while in the other case the major eigenstress is along the $\mathbf{z}$-axis of orthotropy.

Nevertheless, the Benzerga and Besson [4] criterion accounts for the main effects of the plastic anisotropy on yielding and porosity evolution. As an example, in

Fig. 8.1a–c are shown the projections of the yield surface according to the Benzerga and Besson [4] criterion (Eq. 8.8) with $f = 0.05$ for an AA2090-T3 corresponding to axisymmetric loadings such that the axial stress is oriented along either the rolling direction (RD) (unit vector $\mathbf{e}_x$); transverse direction (TD) (unit vector $\mathbf{e}_y$) or through-thickness direction (unit vector $\mathbf{e}_z$). The parameters involved in the Benzerga and Besson [4] criterion are: F, G, H, L, M, N, i.e., the Hill [13] anisotropy coefficients describing the plastic properties of the matrix. For this AA 2090-T3 material, in Chap. 5, was presented the identification of Hill [13] criterion based on the experimental uniaxial yield stresses along the RD, TD, 45° orientation from RD in the plane of the sheet, and the tensile equibiaxial yield stress σ_b^T; the numerical values of the anisotropy coefficients being: $F = 0.603$, $G = 0.397$, $H = 0.603$, $N = 2.537$. Since there were no data available for identification of the parameters L and M, their values were set equal to 3/2 (isotropic values). Using Eq. (8.5), it follows that for AA 2090-T3 the parameter $h = 1.897$. For comparison purposes, in Fig. 8.1a–c are also plotted the projections of the yield surfaces for an isotropic porous material (i.e., $F = G = H = 0.5$, $L = M = N = 3/2$) corresponding to the same porosity.

Let us first note that for the AA 2090-T3 material under purely hydrostatic loadings, the yield limit is (see Eq. 8.22):

$$\frac{|\Sigma_m|}{\sigma_x^T} = \frac{|p_{\text{Hill}}|}{\sigma_x^T} = -\frac{h}{3}\ln(f),$$

with $h = 1.897$. Thus, it is smaller than the hydrostatic yield limit of an isotropic porous material ($F = G = H = 0.5$, $L = M = N = 3/2$ and $h = 2$) with the same porosity (see Fig. 8.1).

Since the matrix is orthotropic for loadings other than pure hydrostatic loading, yielding will depend on the orientation. Note that for axisymmetric loadings such that the axial stress is along the direction $\mathbf{e}_y$ (i.e., TD), i.e., $\boldsymbol{\Sigma} = \Sigma_{\text{TD}}(\mathbf{e}_y \otimes \mathbf{e}_y) + \Sigma_{\text{RD}}(\mathbf{e}_x \otimes \mathbf{e}_x + \mathbf{e}_z \otimes \mathbf{e}_z)$ (see Fig. 8.1a), the intersection of the Benzerga and Besson [4] yield curve with the axis $\Sigma_m = 0$ (purely deviatoric loading) corresponds to:

$$\frac{\Sigma_e}{\sigma_x^T} = \frac{|\Sigma_{\text{TD}} - \Sigma_{\text{RD}}|}{\sigma_x^T} = \frac{1-f}{\sqrt{F+H}} = (1-f)\left(\sigma_y^T/\sigma_x^T\right) \tag{8.33}$$

(see also Sect. 5.2).

Since the AA 2090-T3 material is harder in the **x**-direction (RD) than in the **y**-direction (see also Table 5.1), the yield surface projection is markedly different than that of the isotropic porous material.

On the other hand, for axisymmetric loadings such that the axial stress is along the direction $\mathbf{e}_z$ (i.e., normal to the sheet plane), i.e., $\boldsymbol{\Sigma} = \Sigma_{\text{ND}}(\mathbf{e}_z \otimes \mathbf{e}_z) + \Sigma_{\text{RD}}(\mathbf{e}_x \otimes \mathbf{e}_x + \mathbf{e}_y \otimes \mathbf{e}_y)$ (see Fig. 8.1b), the predicted yield limit under purely deviatoric loadings is:

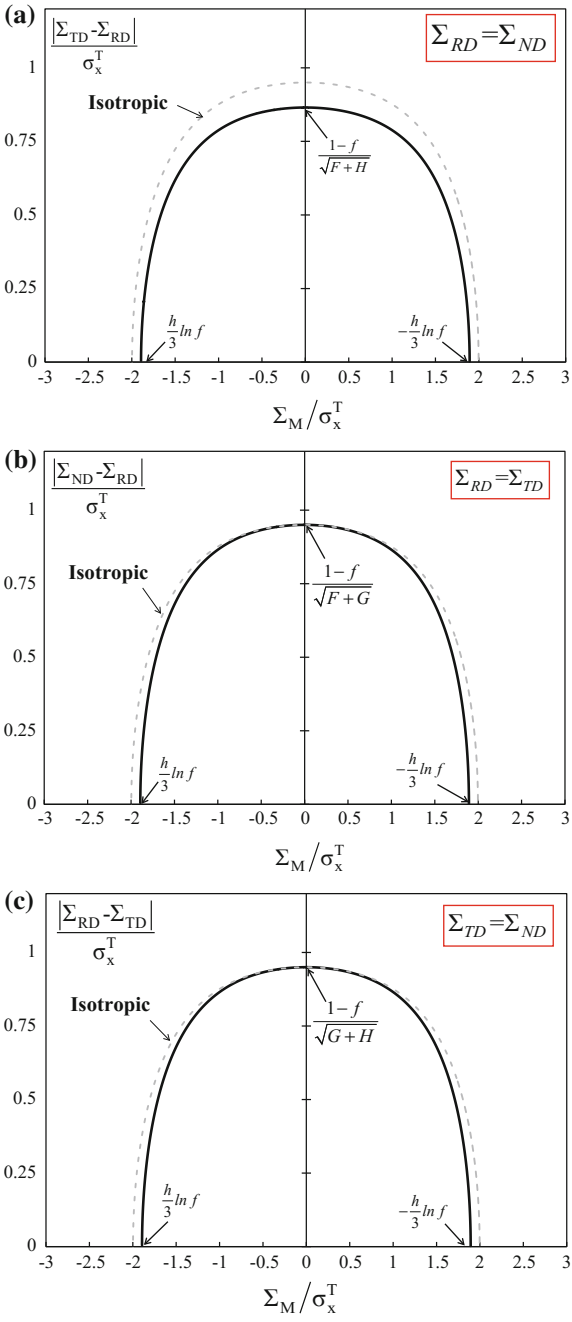

Fig. 8.1 Projection of the theoretical yield surface according to the Benzerga and Besson [4] criterion in the plane (Σ_e, Σ_m) for a porous orthotropic AA 2090-T3 subject to axisymmetric loadings such that the axial stress is aligned with: **a** the transverse direction ($\mathbf{e}_y$); **b** the normal direction ($\mathbf{e}_z$); **c** the rolling direction ($\mathbf{e}_x$); Gurson [12] (interrupted line) yield surface for an isotropic material. Porosity $f = 5\%$

$$\frac{\Sigma_e}{\sigma_x^T} = \frac{|\Sigma_{\mathrm{ND}} - \Sigma_{\mathrm{RD}}|}{\sigma_x^T} = \frac{1-f}{\sqrt{F+G}} = (1-f)\left(\sigma_b^T/\sigma_x^T\right) \tag{8.34}$$

Since for AA 2090-T3, $\left(\sigma_b^T/\sigma_x^T\right)$ = 1.01, for purely deviatoric loadings and in general for low stress triaxialities, the anisotropic yield surface is close to that corresponding to an isotropic material, the differences becoming more pronounced with increasing triaxialities (the maximum difference corresponds to $T = \infty$, i.e., hydrostatic loadings).

For axisymmetric loadings such that the axial stress is along the direction $\mathbf{e}_x$ (RD), i.e., $\boldsymbol{\Sigma} = \Sigma_{\mathrm{RD}}(\mathbf{e}_x \otimes \mathbf{e}_x) + \Sigma_{\mathrm{TD}}\left(\mathbf{e}_y \otimes \mathbf{e}_y + \mathbf{e}_z \otimes \mathbf{e}_z\right)$, the projection of the Benzerga and Besson [4] yield surface in the plane (Σ_e, Σ_m) is shown in Fig. 8.1c. Note that for purely deviatoric loadings the criterion predicts

$$\frac{\Sigma_e}{\sigma_x^T} = \frac{|\Sigma_{\mathrm{RD}} - \Sigma_{\mathrm{TD}}|}{\sigma_x^T} = \frac{1-f}{\sqrt{G+H}} \tag{8.35}$$

Since $G + H$ = 1, for purely deviatoric loading the anisotropic porous material and the isotropic porous material have the same yield limit, the difference in the yielding response increasing with increasing triaxiality.

As discussed in Chap. 5, certain textured metallic materials (e.g., Ti and Mg alloys) display plastic anisotropy and a strong tension–compression asymmetry that is evolving during deformation (due to activation of twinning). To accurately model damage in such materials, it is imperative to account for the specificities of the plastic deformation of the incompressible matrix, in particular the tension–compression asymmetry (SD effects) of the matrix behavior.

Moreover, due to the very specific couplings between all stress invariants induced by the presence of voids, a damage model cannot be postulated or obtained by heuristically modifying existing criteria. Recent contributions toward understanding the combined effects of anisotropy and tension–compression asymmetry on damage of porous polycrystals and single crystals are presented in the following.

8.2 Stewart and Cazacu [32] Yield Criterion for Orthotropic Porous Materials with Incompressible Matrix Displaying Tension–Compression Asymmetry

Stewart and Cazacu [32] used the kinematic homogenization approach to model the mechanical response of orthotropic porous materials with incompressible matrix displaying SD effects. In the following are presented the key steps in derivation of this criterion and the insights that can be gained on the basis of this criterion on damage evolution and the reasons for increased ductility or catastrophic failure under certain loadings.

The matrix behavior was considered to be rigid-plastic and governed by the quadratic form of the orthotropic stress potential of Cazacu et al. [5], i.e.,

$$\varphi(\widehat{\boldsymbol{\sigma}}, \tilde{m}, \sigma_x^T) = \tilde{\sigma}_e = \tilde{m}\sqrt{\sum_{i=1}^{3}\left(|\,\widehat{\sigma}_i\,| - k\widehat{\sigma}_i\right)^2}. \tag{8.36}$$

In Eq. (8.36), $\widehat{\sigma}_1$, $\widehat{\sigma}_2$ and $\widehat{\sigma}_3$ are the principal values (not ordered) of the transformed stress tensor

$$\widehat{\boldsymbol{\sigma}} = \mathbf{L}\mathbf{s},$$

where $\mathbf{L}$ is the orthotropic fourth-order symmetric tensor describing the anisotropy in plastic properties, $\mathbf{s}$ is the Cauchy stress deviator, k is a parameter associated to tension–compression asymmetry in yielding, and $\tilde{m}$ is a constant defined such that the equivalent stress $\tilde{\sigma}_e$ reduces to σ_x^T, the tensile yield stress along the $\mathbf{x}$ orthotropy axis. For more details about this orthotropic stress potential and its exact dual $\psi(\mathbf{d})$ the reader is referred to Chaps. 5 and 6, respectively. Let us recall here that for any strain-rate field $\mathbf{d}$:

$$\psi(\mathbf{d}) = \begin{cases} \dfrac{1}{\tilde{m}(1-k)}\sqrt{b_1^2 + b_2^2 + b_3^2\left(\dfrac{3k^2 - 10k + 3}{3k^2 + 2k + 3}\right)}, & \text{if } (b_1, b_2, b_3) \in D_3^- \\ \dfrac{1}{\tilde{m}(1+k)}\sqrt{b_1^2 + b_2^2 + b_3^2\left(\dfrac{3k^2 + 10k + 3}{3k^2 - 2k + 3}\right)}, & \text{if } (b_1, b_2, b_3) \in D_3^+ \end{cases}, \tag{8.37}$$

with b_1, b_2, b_3 the eigenvalues (not necessarily ordered) of the transformed strain-rate tensor

$$\mathbf{B} = \mathbf{H}\mathbf{d}, \tag{8.38}$$

$\mathbf{H}$ being a 4th order symmetric and orthotropic tensor that is the "inverse" of the tensor $\mathbf{L}$ describing the anisotropy of the material,

i.e.,

$$\mathbf{H}\mathbf{L} = \mathbf{K}, \tag{8.39}$$

with $\mathbf{K}$ being the 4th order deviatoric tensor (see Chap. 1).

The sub-domains D_3^+ and D_3^- are defined as:

$$\begin{aligned} D_3^- &= \left\{ (b_1,b_2,b_3) | \frac{b_3}{\sqrt{b_1^2+b_2^2+b_3^2}} \leq \frac{-(3k^2+2k+3)}{\sqrt{6(k^2+3)(3k^2+1)}} \right\} \\ D_3^+ &= \left\{ (b_1,b_2,b_3) | \frac{b_3}{\sqrt{b_1^2+b_2^2+b_3^2}} \geq \frac{3k^2-2k+3}{\sqrt{6(k^2+3)(3k^2+1)}} \right\} \end{aligned} \tag{8.40}$$

The expressions of the other branches of $\psi(\mathbf{d})$, corresponding to the domains D_j^+ and D_j^- (j = 1, 2) are obtained from Eq. (8.40) by symmetry arguments (for more details and the geometric representation of these domains in the octahedral plane, see Sect. 6.2.2).

Due to the complexity of the plastic behavior of the matrix, the analysis can be conducted only for axisymmetric loadings such that the stress eigenvectors are along the axes of orthotropy of the material. Moreover, due to the difficulties associated with the SD effects in the matrix and the fact that the choice of the branch of $\psi(\mathbf{d})$ depends on the sign of the imposed mean stress Σ_m, in order to arrive at an approximate analytic plastic potential for the porous material couplings between the mean strain-rate D_m and $\mathbf{D}'$ were neglected, and the local plastic dissipation was approximated with:

$$\pi(\mathbf{d}) \simeq \sigma_x^T \sqrt{\hat{n}(\mathbf{Hd} : \mathbf{Hd})}, \tag{8.41}$$

where

$$\tilde{n} = \begin{cases} \dfrac{1}{\tilde{m}^2}\left(\dfrac{3}{3k^2-2k+3}\right) & \text{if} \quad \Sigma_m \leq 0 \\ \dfrac{1}{\tilde{m}^2}\left(\dfrac{3}{3k^2+2k+3}\right) & \text{if} \quad \Sigma_m > 0. \end{cases} \tag{8.42}$$

Moreover, when estimating the overall plastic dissipation the loadings cases corresponding to $J_3^\Sigma \geq 0$ and $J_3^\Sigma \leq 0$ need to be considered separately. Further, using Cauchy–Schwarz inequality, lengthy calculations (for details see Stewart and Cazacu [32]) lead to an analytical estimate of the approximate overall plastic potential and the following criterion:

Theorem 8.3 *The* Stewart and Cazacu [32] *yield criterion for a porous orthotropic material with incompressible matrix displaying SD effects and containing spherical voids is given by:*

$$\Phi(\boldsymbol{\Sigma},f) = \left(\tilde{m} \sqrt{\sum_{i=1}^{3} \left(\left| \frac{\widehat{\sigma}_i}{\sigma_x^T} \right| - k \frac{\widehat{\sigma}_i}{\sigma_x^T} \right)^2} \right)^2 + 2f \cosh\left(\frac{3}{\tilde{h}} \frac{\Sigma_m}{\sigma_x^T} \right) - \left(1+f^2\right) = 0, \tag{8.43}$$

where f is the void volume fraction, $\widehat{\sigma}_1$, $\widehat{\sigma}_2$, $\widehat{\sigma}_3$ *are the principal values (not ordered) of the transformed stress tensor,* $\widehat{\boldsymbol{\sigma}} = \mathbf{L}\boldsymbol{\Sigma}'$, Σ_m *denotes the mean stress,* $\boldsymbol{\Sigma}'$ *the deviator of* $\boldsymbol{\Sigma}$ *and* σ_x^T, *the tensile yield stress along the* $\mathbf{x}$ *orthotropy axis.*

All the parameters involved in the criterion given by Eq. (8.43)*, namely* $\tilde{m}$ *and* $\tilde{h}$ *are expressible in terms of the plastic properties of the matrix described by the SD parameter* $\mathbf{k}$ *and the matrix anisotropy coefficients, i.e., the components of the tensor* $\mathbf{L}$ *in the orthotropy frame* $(\mathbf{x}, \mathbf{y}, \mathbf{z})$. *Specifically, if in Voigt notations, the fourth-order tensor* $\mathbf{L}$ *is represented by:*

$$\mathbf{L} = \begin{bmatrix} L_{11} & L_{12} & L_{13} & & & \\ L_{12} & L_{22} & L_{23} & & & \\ L_{13} & L_{23} & L_{33} & & & \\ & & & L_{44} & & \\ & & & & L_{55} & \\ & & & & & L_{66} \end{bmatrix},$$

$$\tilde{m} = \frac{1}{\sqrt{(|\Phi_1| - k\Phi_1)^2 + (|\Phi_2| - k\Phi_2)^2 + (|\Phi_3| - k\Phi_3)^2}} \tag{8.44}$$

with

$$\Phi_1 = (2L_{11} - L_{12} - L_{13})/3,\ \Phi_2 = (2L_{12} - L_{22} - L_{23})/3,$$
$$\Phi_3 = (2L_{13} - L_{23} - L_{33})/3.$$

The parameter $\tilde{h}$ *depends on the anisotropy coefficients and the sign of the mean stress,* Σ_m, *its expression being:*

$$\tilde{h} = \sqrt{\frac{\tilde{n}}{5}(4t_1 + 6t_2)} \tag{8.45}$$

with $\tilde{n}$ *given by* Eq. (8.42)

and the parameters t_1 *and* t_2 *being expressible in terms of the components of the orthotropic tensor* $\mathbf{L}$ (see Eq. 8.38):

$$\begin{aligned} t_1 &= 3\left(H_{13}H_{23} + H_{12}H_{23} + H_{12}H_{13} + 2H_{12}^2 + 2H_{13}^2 + 2H_{23}^2\right) \\ t_2 &= H_{44}^2 + H_{55}^2 + H_{66}^2. \end{aligned} \tag{8.46}$$

Remarks

- The Stewart and Cazacu [32] criterion given by Eq. (8.43) predicts that irrespective of loading there is an effect of the sign of the mean stress Σ_m on

yielding of the porous material. This effect is modeled through the coefficient $\tilde{h}$ (see Eq. 8.45).

- Given that for $k \neq 0$, the effective stress $\tilde{\sigma}_e = \tilde{m}\sqrt{\sum_{i=1}^{3}\left(\left|\frac{\widehat{\sigma}_i}{\sigma_x^T}\right| - k\frac{\widehat{\sigma}_i}{\sigma_x^T}\right)^2}$ depends on the relative ordering of the eigenvalues of the transformed $\widehat{\boldsymbol{\sigma}} = \mathbf{L}\mathbf{s}$, the Stewart and Cazacu [32] criterion depends on all the invariants of the stress deviator, $\mathbf{s}$, as well as on the mixed invariants of $\mathbf{s}$ and the symmetry tensors associated with orthotropy, namely $\mathbf{M}_1 = \mathbf{x} \otimes \mathbf{x}$, $\mathbf{M}_2 = \mathbf{y} \otimes \mathbf{y}$, $\mathbf{M}_3 = \mathbf{z} \otimes \mathbf{z}$.
- The Stewart and Cazacu [32] criterion predicts that with the exception of purely hydrostatic loadings there is an effect of the third-invariant J_3^{Σ} on yielding of the porous material; the sensitivity to J_3^{Σ} depends on the orientation of the loading axes with respect to the orthotropy axes.
- In contrast to the case when the matrix is orthotropic and has plastic behavior governed by the Hill [13] criterion (i.e., no SD effects in the matrix), the yield locus of the porous anisotropic material is no longer symmetric with respect to the axis $\Sigma_m = 0$; the Stewart and Cazacu [32] criterion predicts that the yield limit for purely tensile hydrostatic loading is different than the yield limit for purely compressive hydrostatic loadings.
- For tensile hydrostatic loadings, yielding occurs when: $\Sigma_m = \widehat{p}_Y^{+}$ with

$$\widehat{p}_Y^{+} = -\frac{\sigma_x^T}{3}\sqrt{\frac{3}{\tilde{m}^2(3k^2+2k+3)}\left(\frac{4t_1+6t_2}{5}\right)}\ln(f), \tag{8.47}$$

- For compressive hydrostatic loading, yielding occurs when $\Sigma_m = \widehat{p}_Y^{-}$ with

$$\widehat{p}_Y^{-} = \frac{\sigma_x^T}{3}\sqrt{\frac{3}{\tilde{m}^2(3k^2-2k+3)}\left(\frac{4t_1+6t_2}{5}\right)}\ln(f), \tag{8.48}$$

the expressions for $\tilde{m}$, t_1, and t_2 in terms of the anisotropy coefficients and k being given by Eqs. (8.44) and (8.46), respectively.

- Only for a porous orthotropic material with no tension–compression asymmetry in the matrix (k = 0),

$$\widehat{p}_Y^{+} = |\widehat{p}_Y^{-}| = p_{\text{Hill}}$$

(see also Eq. 8.22).

- For an isotropic matrix (i.e., $\mathbf{L} = \mathbf{I_4}$), the Stewart and Cazacu [32] criterion reduces to the Cazacu and Stewart [6] model for isotropic porous materials displaying SD effects. Indeed, for $\mathbf{L} = \mathbf{I_4}$, $\Phi_1 = 2/3$, $\Phi_2 = \Phi_3 = -1/3$ (see Eq. 8.44), so $\tilde{m} = \sqrt{\dfrac{9}{2(3k^2 - 2k + 3)}} = m$ and $\tilde{h} = 2/z_s$ (see Theorem 7.14 and the expression of the Cazacu and Stewart [6] criterion, respectively).
- In the absence of voids ($f = 0$), the Stewart and Cazacu [32] criterion given by Eq. (8.43) reduces to the matrix yield criterion, i.e., the quadratic form of the Cazacu et al. [5] orthotropic criterion given by Eq. (8.36), i.e,.

$$\tilde{\sigma}_e = \sigma_x^T.$$

Combined effects of anisotropy and tension–compression asymmetry on yielding of the porous material under axisymmetric loadings

To further illustrate the capabilities of the Stewart and Cazacu [32] criterion to model the combined effects of the tension–compression asymmetry and plastic anisotropy on the yielding response of a porous material, in the following we analyze axisymmetric loadings such that the axial stress is oriented along either the rolling direction (RD) (unit vector $\mathbf{e}_x$); transverse direction (TD) (unit vector $\mathbf{e}_y$) or through-thickness direction (unit vector $\mathbf{e}_z$). In each case, both loadings corresponding to the axial stress being the minor applied principal stress (i.e., third-invariant $J_3^{\Sigma} \leq 0$) and loadings such that axial stress is the major principal stress (i.e., third-invariant, $J_3^{\Sigma} \geq 0$) are considered.

As an example, 2-D projections of the theoretical yield surfaces corresponding to the same porosity ($f = 2\%$) and different orientations between the loading frame and the material symmetry frame are presented in Fig. 8.2a–c for a Mg AZ31 alloy at 5% equivalent plastic strain. Note that all the parameters involved in the Stewart and Cazacu [32] criterion are expressible in terms of the anisotropy coefficients L_{ij} and the parameter k, i.e., the parameters describing the plastic properties of the matrix. As discussed in Chap. 5, this hcp Mg AZ31 alloy displays a strong anisotropy and tension–compression asymmetry that evolve with accumulated plastic deformation. Its plastic behavior can be accurately described using the Cazacu et al. [5] orthotropic criterion. For more details on this material, the identification procedure and the numerical values of the parameters of the Cazacu et al. [5] orthotropic criterion at 5% equivalent plastic strain, the reader is referred to Sect. 5.4.3.

Let us first discuss the yielding response according to the Stewart and Cazacu [32] criterion for axisymmetric loadings with axial stress along the **x**-axis (RD), i.e., $\boldsymbol{\Sigma} = \Sigma_{\mathrm{RD}}(\mathbf{e}_x \otimes \mathbf{e}_x) + \Sigma_{\mathrm{TD}}\left(\mathbf{e}_y \otimes \mathbf{e}_y + \mathbf{e}_z \otimes \mathbf{e}_z\right)$ for which $\Sigma_e = |\Sigma_{\mathrm{RD}} - \Sigma_{\mathrm{TD}}|$, $J_3^{\Sigma} = 2(\Sigma_{\mathrm{RD}} - \Sigma_{\mathrm{TD}})^3/27$ (see also Fig. 8.2a).

Note that if $\Sigma_{\mathrm{RD}} \leq \Sigma_{\mathrm{TD}} = \Sigma_{\mathrm{ND}}$ ($J_3^{\Sigma} \leq 0$), i.e., the minor principal stress is along RD and $\Sigma_{\mathrm{TD}} = \Sigma_{\mathrm{ND}}$, the criterion writes:

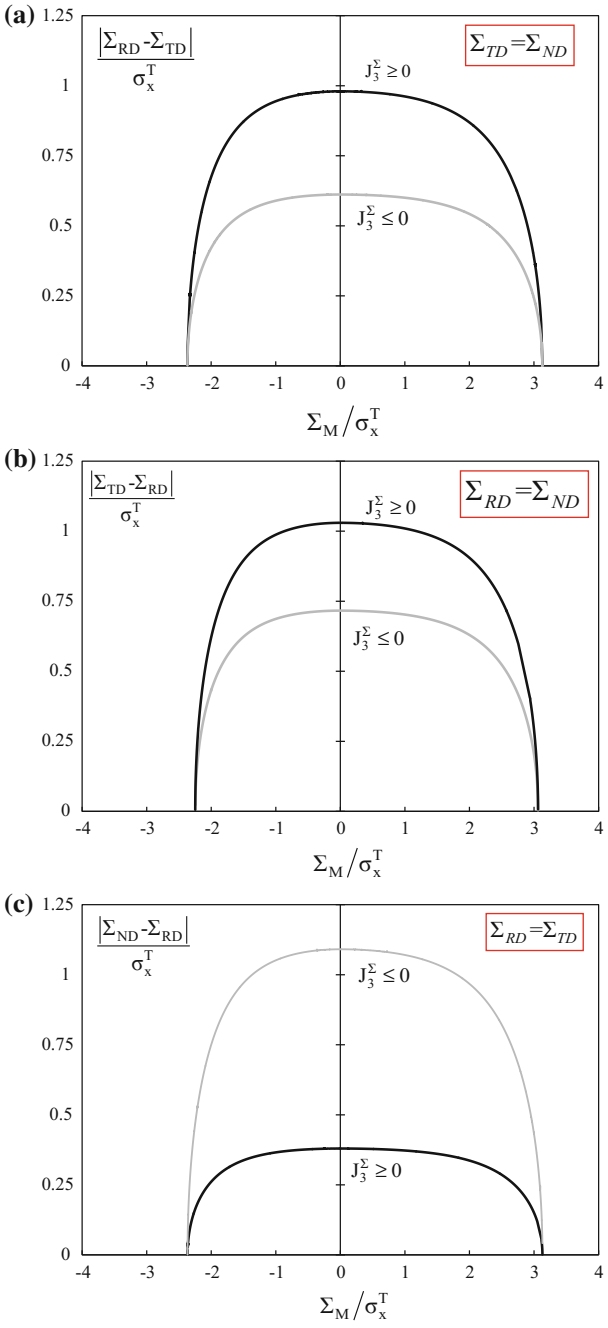

Fig. 8.2 Projection of the theoretical yield surface according to the Stewart and Cazacu [32] criterion in the plane (Σ_e, Σ_m) for a porous orthotropic Mg AZ31 alloy subject to axisymmetric loadings such that axial stress is aligned with: **a** the rolling direction ($\mathbf{e}_x$); **b** the transverse direction ($\mathbf{e}_y$); **c** the normal direction ($\mathbf{e}_z$); porosity $f = 2\%$ and anisotropy coefficients corresponding to an equivalent plastic strain of $\varepsilon^p = 0.05$

$$\Phi(\boldsymbol{\Sigma},f)=\begin{cases}\left(\dfrac{\sigma_x^T}{\sigma_x^C}\right)^2\left(\dfrac{\Sigma_{\mathrm{RD}}-\Sigma_{\mathrm{TD}}}{\sigma_x^T}\right)^2+2f\cosh\left(\dfrac{\Sigma_m}{\sigma_x^T}\sqrt{\dfrac{15\tilde{m}^2(3k^2-2k+3)}{4t_1+6t_2}}\right)-(1+f^2),\ \Sigma_m<0,\\ \left(\dfrac{\sigma_x^T}{\sigma_x^C}\right)^2\left(\dfrac{\Sigma_{\mathrm{RD}}-\Sigma_{\mathrm{TD}}}{\sigma_x^T}\right)^2+2f\cosh\left(\dfrac{\Sigma_m}{\sigma_x^T}\sqrt{\dfrac{15\tilde{m}^2(3k^2+2k+3)}{4t_1+6t_2}}\right)-(1+f^2),\ \Sigma_m\geq 0\end{cases}\tag{8.49}$$

However, if $\Sigma_{\mathrm{RD}}\geq\Sigma_{\mathrm{TD}}=\Sigma_{\mathrm{ND}}$ ($J_3^{\Sigma}\geq 0$), i.e., the minor principal stress is along TD and $\Sigma_{\mathrm{TD}}=\Sigma_{\mathrm{ND}}$, then:

$$\Phi(\boldsymbol{\Sigma},f)=\begin{cases}\left(\dfrac{\Sigma_{\mathrm{RD}}-\Sigma_{\mathrm{TD}}}{\sigma_x^T}\right)^2+2f\cosh\left(\dfrac{\Sigma_m}{\sigma_x^T}\sqrt{\dfrac{15\tilde{m}^2(3k^2-2k+3)}{4t_1+6t_2}}\right)-(1+f^2),\ \Sigma_m<0,\\ \left(\dfrac{\Sigma_{\mathrm{RD}}-\Sigma_{\mathrm{TD}}}{\sigma_x^T}\right)^2+2f\cosh\left(\dfrac{\Sigma_m}{\sigma_x^T}\sqrt{\dfrac{15\tilde{m}^2(3k^2+2k+3)}{4t_1+6t_2}}\right)-(1+f^2),\ \Sigma_m\geq 0\end{cases}\tag{8.50}$$

In the above equations, σ_x^C denotes the matrix uniaxial compressive flow stress in the **x** (RD) direction. Comparison between Eqs. (8.49) and (8.50) shows that the Stewart and Cazacu [32] criterion is sensitive to J_3^{Σ} and for the same stress triaxiality it predicts two yield values. Furthermore, the ratio between the yield values corresponding to the same triaxiality is maximum for purely deviatoric loadings. Indeed, for purely deviatoric loadings the intersections of the yield curves with the axis Σ_m = 0 correspond to:

$$\Sigma_e=|\Sigma_{\mathrm{RD}}-\Sigma_{\mathrm{TD}}|=\begin{cases}(1-f)\sigma_x^C,\ \text{if}\ \ J_3^{\Sigma}\leq 0,\\ (1-f)\sigma_x^T,\ \text{if}\ \ J_3^{\Sigma}\geq 0,\end{cases}\tag{8.51}$$

the split between the two curves for this stress state being $\dfrac{\Sigma_e|_{J_3^{\Sigma}\geq 0}}{\Sigma_e|_{J_3^{\Sigma}\leq 0}}=\dfrac{\sigma_x^T}{\sigma_x^C}$. For example, for the Mg AZ31 alloy which at 5% plastic strain has $\sigma_x^C<\sigma_x^T$, the response is softer under axisymmetric loadings corresponding to $J_3^{\Sigma}\leq 0$ compared to the response under axisymmetric loadings corresponding to $J_3^{\Sigma}\geq 0$, the maximum difference being for purely deviatoric loadings (see Fig. 8.2a).

On the other hand, for axisymmetric loadings with axial stress along the **y**-axis (TD), i.e., $\boldsymbol{\Sigma}=\Sigma_{\mathrm{TD}}(\mathbf{e}_y\otimes\mathbf{e}_y)+\Sigma_{\mathrm{RD}}(\mathbf{e}_x\otimes\mathbf{e}_x+\mathbf{e}_z\otimes\mathbf{e}_z)$ (see also Fig. 8.2b), for which $\Sigma_e=|\Sigma_{\mathrm{TD}}-\Sigma_{\mathrm{RD}}|=|\Sigma_{\mathrm{TD}}-\Sigma_{\mathrm{ND}}|$,

- if $\Sigma_{\mathrm{RD}}=\Sigma_{\mathrm{ND}}\leq\Sigma_{\mathrm{TD}}$, ($J_3^{\Sigma}\geq 0$), i.e., the minor eigenstress is along the **x**-axis (RD) and $\Sigma_{\mathrm{RD}}=\Sigma_{\mathrm{ND}}$ yielding occurs when:

$$\Phi(\boldsymbol{\Sigma},f)=\begin{cases}\left(\dfrac{\sigma_x^T}{\sigma_y^T}\right)^2\left(\dfrac{\Sigma_{\mathrm{TD}}-\Sigma_{\mathrm{RD}}}{\sigma_x^T}\right)^2+2f\cosh\left(\dfrac{\Sigma_m}{\sigma_x^T}\sqrt{\dfrac{15\tilde{m}^2(3k^2-2k+3)}{4t_1+6t_2}}\right)-(1+f^2),\ \Sigma_m<0,\\ \left(\dfrac{\sigma_x^T}{\sigma_y^T}\right)^2\left(\dfrac{\Sigma_{\mathrm{TD}}-\Sigma_{\mathrm{RD}}}{\sigma_x^T}\right)^2+2f\cosh\left(\dfrac{\Sigma_m}{\sigma_x^T}\sqrt{\dfrac{15\tilde{m}^2(3k^2+2k+3)}{4t_1+6t_2}}\right)-(1+f^2),\ \Sigma_m\geq 0,\end{cases}\tag{8.52}$$

[compare with Eq. (8.49)] while for loadings such that $\Sigma_{\mathrm{RD}}=\Sigma_{\mathrm{ND}}\geq\Sigma_{\mathrm{TD}}$, (i.e., $J_3^{\Sigma}\leq 0$), for which the minor stress is along TD (**y**-axis) and $\Sigma_{\mathrm{RD}}=\Sigma_{\mathrm{ND}}$, yielding occurs when:

$$\Phi(\boldsymbol{\Sigma},f)=\begin{cases}\left(\dfrac{\sigma_x^T}{\sigma_y^C}\right)^2\left(\dfrac{\Sigma_{\mathrm{TD}}-\Sigma_{\mathrm{ND}}}{\sigma_x^T}\right)^2+2f\cosh\left(\dfrac{\Sigma_m}{\sigma_x^T}\sqrt{\dfrac{15\tilde{m}^2(3k^2-2k+3)}{4t_1+6t_2}}\right)-(1+f^2),\ \Sigma_m<0,\\ \left(\dfrac{\sigma_x^T}{\sigma_y^C}\right)^2\left(\dfrac{\Sigma_{\mathrm{TD}}-\Sigma_{\mathrm{ND}}}{\sigma_T}\right)^2+2f\cosh\left(\dfrac{\Sigma_m}{\sigma_x^T}\sqrt{\dfrac{15\tilde{m}^2(3k^2+2k+3)}{4t_1+6t_2}}\right)-(1+f^2),\ \Sigma_m\geq 0,\end{cases}\tag{8.53}$$

In the above equations, σ_y^C denotes the matrix uniaxial compressive yield stress in the **y** (TD) direction. Comparison between Eqs. (8.52) and (8.53) shows that for axisymmetric loadings such that the axial stress is along the **y**-axis (i.e., $\Sigma_{\mathrm{ND}}=\Sigma_{\mathrm{RD}}$), the model predicts that the maximum difference between the yield curves at $J_3^{\Sigma}\geq 0$ and $J_3^{\Sigma}\leq 0$ is given by the ratio between the matrix yield stresses in tension–compression along the **y**-direction. Indeed, for purely deviatoric loadings with axial stress along TD, the intersection with the axis $\Sigma_m = 0$ is at:

$$\Sigma_e=|\Sigma_{\mathrm{TD}}-\Sigma_{\mathrm{ND}}|=\begin{cases}(1-f)\sigma_y^C,\ \text{if } J_3^{\Sigma}\leq 0,\\ (1-f)\sigma_y^T,\ \text{if } J_3^{\Sigma}\geq 0,\end{cases}\tag{8.54}$$

resulting in a ratio $\dfrac{\Sigma_e|_{J_3^{\Sigma}\geq 0}}{\Sigma_e|_{J_3^{\Sigma}\leq 0}}=\dfrac{\sigma_y^T}{\sigma_y^C}$.

Since the Mg AZ31 alloy at 5% plastic strain has $\sigma_y^T/\sigma_y^C>1$, the yield curve corresponding to $J_3^{\Sigma}\geq 0$ is above that corresponding to $J_3^{\Sigma}\leq 0$ (see Fig. 8.2b). The fact that for this material similar trends are predicted for axisymmetric loadings with the axial stress in the **x**-axis and **y**-axis (Fig. 8.2a, b, respectively) is related to the fact that the orthotropic matrix is characterized by $\sigma_x^T/\sigma_x^C>1$, and $\sigma_y^T/\sigma_y^C>1$, the split between the $J_3^{\Sigma}\geq 0$ and $J_3^{\Sigma}\leq 0$ curves is most pronounced for **x**-loading, consistent with the strength differential (SD) ratio being larger in the RD direction than in the TD direction.

Similarly, it can be shown that according to the criterion for axisymmetric loadings such as the axial stress is along the **z**-direction (ND-axis), the yielding response is different depending on whether the minimum principal stress is along

RD ($J_3^{\Sigma} \geq 0$) or along ND ($J_3^{\Sigma} \leq 0$). Specifically, if $\Sigma_{RD} = \Sigma_{TD} \leq \Sigma_{ND}$ ($J_3^{\Sigma} \geq 0$) yielding occurs when:

$$\Phi(\boldsymbol{\Sigma}, f) = \begin{cases} \left(\frac{\sigma_x^T}{\sigma_z^T}\right)^2 \left(\frac{\Sigma_{ND} - \Sigma_{RD}}{\sigma_x^T}\right)^2 + 2f \cosh\left(\frac{\Sigma_m}{\sigma_x^T} \sqrt{\frac{15\tilde{m}^2(3k^2 - 2k + 3)}{4t_1 + 6t_2}}\right) - \left(1 + f^2\right), \Sigma_m < 0, \\ \left(\frac{\sigma_x^T}{\sigma_z^T}\right)^2 \left(\frac{\Sigma_{ND} - \Sigma_{RD}}{\sigma_x^T}\right)^2 + 2f \cosh\left(\frac{\Sigma_m}{\sigma_x^T} \sqrt{\frac{15\tilde{m}^2(3k^2 + 2k + 3)}{4t_1 + 6t_2}}\right) - \left(1 + f^2\right), \Sigma_m \geq 0, \end{cases} \tag{8.55}$$

On the other hand, for loadings such that $\Sigma_{TD} = \Sigma_{RD} > \Sigma_{ND}$ ($J_3^{\Sigma} \leq 0$) yielding occurs when

$$\Phi(\boldsymbol{\Sigma}, f) = \begin{cases} \left(\frac{\sigma_x^T}{\sigma_z^C}\right)^2 \left(\frac{\Sigma_{ND} - \Sigma_{RD}}{\sigma_x^T}\right)^2 + 2f \cosh\left(\frac{\Sigma_m}{\sigma_x^T} \sqrt{\frac{15\tilde{m}^2(3k^2 - 2k + 3)}{4t_1 + 6t_2}}\right) \\ \quad - \left(1 + f^2\right), \quad \Sigma_m < 0, \\ \left(\frac{\sigma_x^T}{\sigma_z^C}\right)^2 \left(\frac{\Sigma_{ND} - \Sigma_{RD}}{\sigma_x^T}\right)^2 + 2f \cosh\left(\frac{\Sigma_m}{\sigma_x^T} \sqrt{\frac{15\tilde{m}^2(3k^2 + 2k + 3)}{4t_1 + 6t_2}}\right) \\ \quad - \left(1 + f^2\right), \quad \Sigma_m \geq 0, \end{cases} \tag{8.56}$$

and the maximum split between the yield curves at $J_3^{\Sigma} \geq 0$ and $J_3^{\Sigma} \leq 0$ corresponds to axisymmetric purely deviatoric loadings ($\Sigma_m = 0$). Specifically, for purely deviatoric loadings with axial stress along ND, the intersection with the axis $\Sigma_m = 0$ is at:

$$\Sigma_e = |\Sigma_{ND} - \Sigma_{RD}| = \begin{cases} (1 - f)\sigma_z^C, & \text{if } J_3^{\Sigma} \leq 0, \\ (1 - f)\sigma_z^T, & \text{if } J_3^{\Sigma} \geq 0, \end{cases} \tag{8.57}$$

Thus, the maximum split is given by the ratio between the matrix ND yield stresses in tension–compression:

$$\frac{\Sigma_e|_{J_3^{\Sigma} \geq 0}}{\Sigma_e|_{J_3^{\Sigma} \leq 0}} = \frac{\sigma_z^T}{\sigma_z^C} \tag{8.58}$$

In summary, according to the Stewart and Cazacu [32] criterion for axisymmetric loadings, the sensitivity of the yielding response of the porous material to the third-invariant of the stress deviator is correlated to the matrix tension–compression asymmetry ratio in the direction corresponding to the major principal stress.

Given that the Mg AZ31 alloy at 5% plastic strain has $\sigma_z^T / \sigma_z^C < 1$, the yield curve corresponding to $J_3^{\Sigma} \geq 0$ is below that corresponding to $J_3^{\Sigma} \leq 0$ (see Fig. 8.2c), i.e., the general trends are completely different for those corresponding to axisymmetric

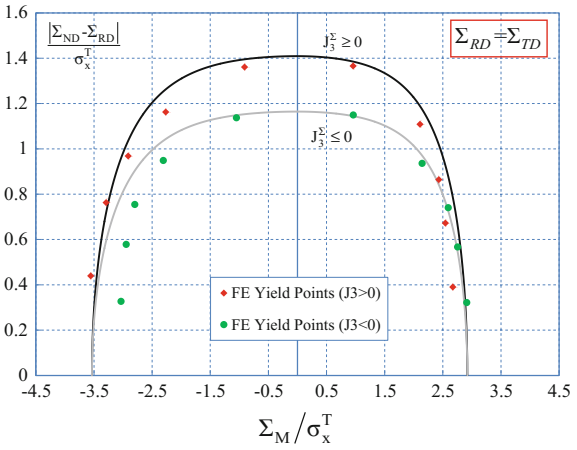

Fig. 8.3 Analytical yield curves according to the Stewart and Cazacu [32] criterion and axisymmetric F.E. unit-cell results for both $J_3^\Sigma \geq 0$ and $J_3^\Sigma \leq 0$. The anisotropic matrix material is hardest in the through-thickness direction, i.e., $\sigma_z^T > \sigma_x^T = \sigma_y^T$ and displays tension–compression asymmetry with the tensile yield strengths larger than the compressive ones ($k = 0.3098$). The void volume fraction is $f_0 = 0.01$

loadings with the axial stress along the RD axis and TD-axis (compare Fig. 8.2a–c). Comparison between the Fig. 8.2a–c shows that the model accounts for the influence of the anisotropy in plastic deformation on the response of the porous material. Indeed, the sensitivity to the third-invariant is the most pronounced for loadings with the axial stress along ND. Furthermore, irrespective of the orientation of the loading frame with respect to the axes of symmetry of the material, the yield surface projection in the plane (Σ_m, Σ_e) lacks symmetry with respect to the deviatoric axis ($\Sigma_m = 0$). In particular, the material's yield stress for purely tensile hydrostatic loadings is different than that under purely hydrostatic compressive loadings [see also Eqs. (8.47) and (8.48)].

Stewart and Cazacu [32] have also reported two-dimensional F.E. unit-cell calculations, the RVE considered being a cylinder with a single void at the center and the matrix plastic behavior governed by the Cazacu et al. [5] yield criterion (see Eq. 8.36). The F.E. analyses were conducted for transversely isotropic materials (i.e., the plane of symmetry $(\boldsymbol{e}_x, \boldsymbol{e}_y)$ is isotropic). As an example, in Fig. 8.3 are shown the F.E. results together with the theoretical yield curves [see Eqs. (8.55) and (8.56)] corresponding to a material with $L_{11} = L_{22} = 1.054$, $L_{33} = 0.85$, $L_{13} = L_{23} = 0.075$, $L_{12} = -0.129$, $L_{44} = 0.775$ and $k = 0.3098$. To examine the combined effects of anisotropy and tension–compression asymmetry, axisymmetric calculations were performed with the axial stress along the ND direction $(\boldsymbol{e}_z)$ being either the major stress $(J_3^\Sigma \geq 0)$ or to the minor stress $(J_3^\Sigma \leq 0)$. The main observation from these results is that the strong asymmetry of the yield loci and the effects of J_3^Σ predicted by the Stewart and Cazacu [32] model are indeed confirmed by the F.E. unit-cell results.

As already mentioned, experimental data on yielding of anisotropic materials with strength differential effects, e.g., polycrystals in which twinning is a predominant deformation mechanism, are lacking, so these unusual trends associated to the combined effects of the anisotropy and tension–compression asymmetry revealed by Stewart and Cazacu [32] model remain to be confirmed.

Partial verification of the trends revealed by the model, in particular the fact that under axisymmetric purely deviatoric loadings the ratios between the yield limits at $J_3^{\Sigma} \geq 0$ and $J_3^{\Sigma} \leq 0$ should be equal to the matrix tension–compression asymmetry ratio in the direction corresponding to the major principal stress were confirmed by the numerical study of Lebensohn and Cazacu [17]. These authors used the Fast Fourier Transform (FFT)-based approach of Lebensohn et al. [16] to generate gauge surfaces for porous textured polycrystals deforming by slip and twinning at single crystal level. In the case of textured fcc polycrystals, it was shown that the strong sensitivity to the sign of the third-invariant is due to the directionality of the tension–compression asymmetry. Moreover, the most pronounced split between the loadings at $J_3^{\Sigma} \geq 0$ and $J_3^{\Sigma} \leq 0$ was obtained in the direction of the highest contrast between the matrix's yield in tension–compression thus confirming the model predictions [see Eqs. (8.51), (8.54) and (8.58)]. For a textured hcp polycrystal deforming by slip and twinning, the same trends of the yielding response of the porous material were confirmed.

In summary, the Stewart and Cazacu [32] model reveals that for a plastically anisotropic porous material with matrix displaying tension–compression asymmetry, there are third-invariant effects (or Lode angle effects) on yielding and that the sensitivity to J_3^{Σ} depends drastically on the respective orientation between the loading axes and the axes of orthotropy (compare Fig. 8.2a–c). As a consequence, there should be strong effects of the loading path on void evolution.

In the following, we discuss the combined effects of anisotropy and tension–compression asymmetry on void evolution predicted by the Stewart and Cazacu [32] model. Illustration of the main trends is done for the same AZ31 Mg. As already mentioned, a complete set of experimental data including measurements of deformation and void evolution for this material is lacking, so only numerical results are presented.

Combined effects of anisotropy and tension–compression asymmetry on porosity evolution under axisymmetric loadings

By making the usual assumption of the plastic strain-rate $\mathbf{D}$ being proportional to the gradient of the potential $\Phi(\boldsymbol{\Sigma}, f)$ from mass conservation, one obtains the evolution of the void volume fraction f in the form:

$$\dot{f} = (1-f)\dot{\lambda}\left(\frac{6f}{\tilde{h}\sigma_x^T}\right)\sinh\left(\frac{3\Sigma_m}{\tilde{h}\sigma_x^T}\right). \tag{8.59}$$

where $\dot{\lambda}$ is the plastic multiplier.

To examine the effects of the loading orientation on porosity evolution that are predicted by the model, we consider three axisymmetric Mg AZ31 specimens with their long axis being along RD ($\mathbf{e}_x$), TD ($\mathbf{e}_y$) and ND ($\mathbf{e}_z$), respectively. Each specimen is subjected to the same loading. The loading imposed is axisymmetric and corresponds to a fixed ratio $\Sigma_m/\Sigma_T = 1.5$, where Σ_T is the applied tensile axial stress.

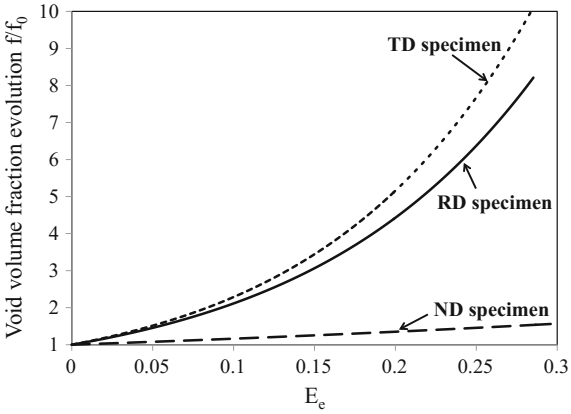

Fig. 8.4 Theoretical void volume fraction evolution as a function of the equivalent plastic strain E_e predicted by the Stewart and Cazacu [32] model for Mg AZ31 axisymmetric specimens with their long axis being along RD, TD, and ND, respectively, subjected to uniaxial tension stress Σ_T superposed to a tensile hydrostatic pressure $\Sigma_m > 0$ such that $\Sigma_m/\Sigma_T = 1.5 (J_3^{\Sigma} \geq 0)$. Initial porosity $f = 0.001$

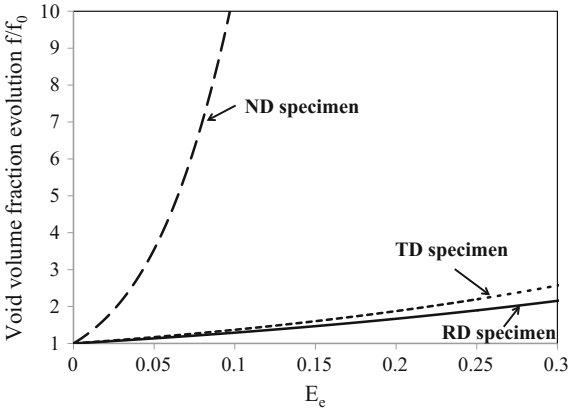

Fig. 8.5 Theoretical void volume fraction evolution as a function of the equivalent plastic strain E_e predicted by the Stewart and Cazacu [32] model for Mg AZ31 axisymmetric specimens with their long axis being along RD, TD, and ND, respectively, subjected to uniaxial compression stress Σ_T superposed to a tensile hydrostatic pressure $\Sigma_m > 0$ such that $\Sigma_m/|\Sigma_T| = 1.5 (J_3^{\Sigma} \leq 0)$. Initial porosity $f = 0.001$

Figure 8.4 shows the model predictions for the evolution of the relative void volume fraction f/f_0 with the equivalent plastic strain $E_e = \int_t \sqrt{(2/3) D'_{ij} D'_{ij}} \mathrm{d}t$ for the three specimens. The void volume fraction $f = \int_t \dot{f} \mathrm{d}t$ is calculated using Eq. (8.59). The simulations are carried out for the same values of the anisotropy coefficients and parameter k used for the predictions of the yielding behavior of the porous material. The model predictions show a very strong effect of the specimen orientation on void growth. Note that under the applied loading, the fastest void evolution is predicted for the TD specimen while the slowest void growth rate corresponds to the ND specimen (see Fig. 8.4).

On the other hand, if the axial stress is compressive (i.e., $\Sigma_T < 0$) and $\Sigma_m > 0$ while maintaining the same ratio $\Sigma_m/|\Sigma_T| = 1.5$, i.e., $J_3^{\Sigma} \leq 0$, the fastest void evolution occurs in the ND specimen while the slowest void evolution is predicted for the RD specimen (see Fig. 8.5). Therefore, for the same absolute value of the

triaxiality the effect of the specimen orientation on void evolution is completely different. This highlights the fact that for a material displaying anisotropy and tension–compression asymmetry in its plastic behavior, damage evolution is strongly dependent on the loading path. Specifically, the tension–compression asymmetry of the matrix induces sensitivity to the third-invariant of stress, J_3^{Σ}, and this sensitivity is orientation dependent. Most importantly, it is clearly seen that on the basis of data on a given loading path, no general conclusions can be drawn on the effect of texture on damage evolution for any other loading path.

In summary, irrespective of the imposed loading, the Stewart and Cazacu [32] criterion predicts that the anisotropy and tension–compression asymmetry of the incompressible matrix have a very strong influence on all aspects of the mechanical response of a porous material. In the next section, the predictions of the porosity evolution in uniaxial tension obtained with the Stewart and Cazacu [32] potential (Eq. 8.43) are compared to ex situ and in situ measurements of porosity evolution in a textured Ti material.

8.3 Coupled Plasticity-Damage in Hcp-Ti: Comparison Between Stewart and Cazacu [32] Predictions and Ex Situ and In Situ X-Ray Tomography Data

Since damage is driven by the plastic behavior, to understand and accurately model damage evolution it is essential to have complete information on the plastic behavior. In particular, for polycrystalline materials with hexagonal crystal structure (e.g., Ti, Zr, Mg) that are strongly textured and display both anisotropy and tension–compression asymmetry in plastic deformation and strength, damage evolution is orientation-dependent and strongly influenced by the loading path (see Sect. 8.2). Moreover, for hcp-Ti, the initial texture is strongly dependent not only on processing, but also on the supplier. Therefore, analysis of damage evolution in hcp-Ti cannot be done without knowledge of the initial texture, and a complete set of mechanical data, based on which the quantification of the plastic anisotropy and strength differential effects can be done.

Nevertheless, data reported in the literature on hcp materials generally include only the tensile stress–strain response and damage measurements in only one loading orientation (e.g., for Ti see Huez et al. [14]). Moreover, modeling of the room-temperature damage and failure of hcp materials is generally done using either empirical laws for the strain at failure as a function of the triaxiality, and/or the Lode parameter (e.g., Jia and Bai [15]), or void growth laws such as Rice and Tracey [27] (e.g., for commercially pure Ti, see Pushkareva et al. [22]). However, the Rice and Tracey [27] void growth law or the most widely used criteria for porous metals (e.g., the Gurson [12] criterion and its various modifications) cannot realistically describe damage in hcp materials because the core hypothesis of such

models is that the plastic behavior of the matrix is governed by the isotropic von Mises criterion, which is a criterion critically inadequate for Ti materials (see Chap. 5).

Recently, Revil-Baudard et al. [26] reported an experimental study on the plastic deformation and damage of a polycrystalline pure Ti material, as well as modeling of the observed porosity evolution using the Stewart and Cazacu [32] potential (see Eq. 8.43). As already mentioned, all the parameters involved in this model are expressible in terms of a few coefficients related to the plastic properties of the material. For this Ti material, the identification of these parameters was based on data obtained in uniaxial tension tests on flat specimens, and uniaxial compression tests on cylindrical specimens. To further study damage, these authors performed additional uniaxial tension tests on axisymmetric cylindrical specimens of circular cross-section. Both smooth and notched geometries were considered. X-ray computed micro-tomography (XCMT) measurements both ex situ and in situ were conducted. The data revealed unusual damage characteristics as compared to fcc polycrystalline materials. In the following are presented the key experimental and simulation results of this study.

8.3.1 Experimental Results in Uniaxial Compression and Uniaxial Tension of Hcp-Ti

To quantify the influence of the loading direction on the mechanical response at room-temperature, quasi-static tests in uniaxial compression were conducted on cylindrical specimens that were machined such that the axes of the cylinders were along the rolling direction (RD), and two other in-plane directions, at 45° (DD) and 90° (TD) with respect to RD, respectively. In addition, tests were conducted on specimens with the axis along the normal direction (ND) of the Ti plate. Based on these tests, it can be concluded that there is very little difference between the uniaxial compression stress–strain curves along RD, DD, and TD, yet there is a marked difference between the yield stress in the normal direction and the average in-plane yield stresses (see Fig. 8.6).

The results of the quasi-static tension tests conducted on flat dog-bone specimens of rectangular cross-section show that there is very little difference in the stress–strain response between the RD, DD, and TD orientations, respectively (see Fig. 8.7). However, the material displays a strong and evolving tension–compression asymmetry; irrespective of the in-plane loading orientation, the flow stress in uniaxial compression being higher than that in uniaxial tension (e.g., see Fig. 8.8 for the comparison between the response in uniaxial tension–compression along TD). As for most high-purity Ti materials, the difference in hardening between uniaxial tension and uniaxial compression may be attributed to occurrence of twinning (for more details on crystallographic twinning, see Chap. 3).

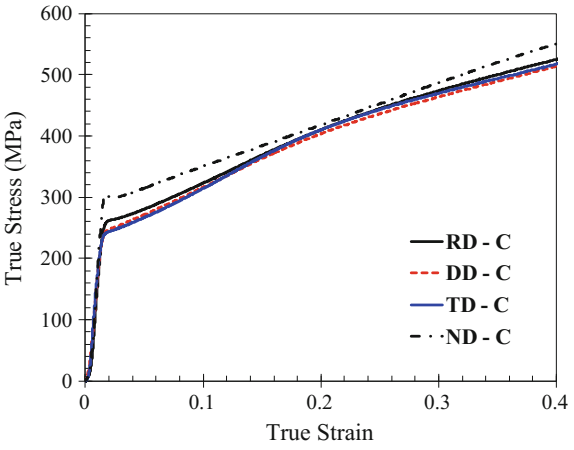

Fig. 8.6 Experimental quasi-static uniaxial compression stress–strain curves along several in-plane orientations θ, measured with respect to the rolling direction (RD) (i.e., $\theta = 0°$ (RD), 45° (DD), and 90° (TD), and in the normal direction (ND) of a hcp-Ti plate (After Revil-Baudard et al. [26])

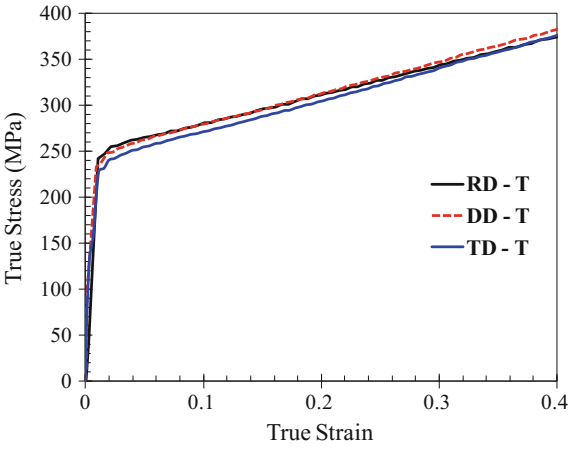

Fig. 8.7 Experimental quasi-static uniaxial tension stress–strain curves along several in-plane orientations θ, measured with respect to the rolling direction (RD) (i.e., $\theta = 0°$ (RD), 45° (DD), and 90° (TD)) of the hcp-Ti plate (After Revil-Baudard et al. [26])

Based on the stress–strain data in uniaxial compression and tension presented in Figs. 8.6 and 8.7, respectively, one may conclude that the material's in-plane anisotropy can be neglected. If this would be the case, the Lankford coefficients or r-values should be the same irrespective of the in-plane orientation θ with respect to RD (for the definition of the plastic strain ratio, $r(\theta)$ see Chap. 5). However, measurements of the Lankford coefficients for $\theta = 0°$, 45°, and 90°, respectively, show that there is a strong in-plane anisotropy in r-values. Moreover, the anisotropy in r-values evolves with the plastic strain (see Table 8.1 for the experimental r-values; for more details on the strain measurements see Revil-Baudard et al. [26]). Note also that irrespective of the plastic strain level, the largest r-value is along RD.

It can be thus concluded that the Ti material is plastically orthotropic. It is also worth noting that the r-values are very large (for comparison, see experimental

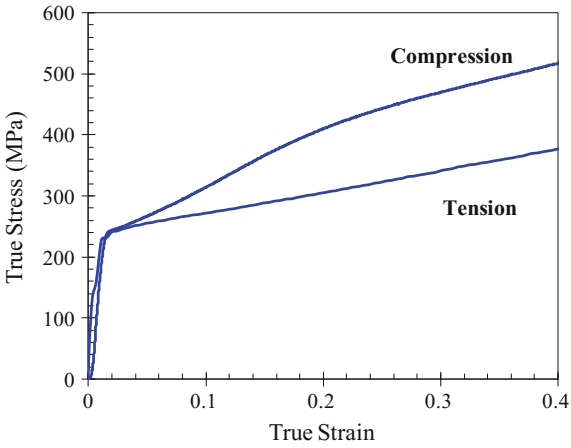

Fig. 8.8 Experimental evidence of the difference in response between uniaxial tension–compression along the transverse direction (TD) of the hcp-Ti plate. Note that the material is harder in compression than in tension (After Revil-Baudard et al. [26])

r-values for fcc Al alloys presented in Chap. 5). Generally, large *r*-values indicate that a material displays resistance to thinning (see for example, Revil-Baudard [24]); hence, from a formability standpoint, this material is very challenging. In summary, on the basis of the mechanical characterization tests in uniaxial tension–compression, it can be concluded that the high-purity Ti material displays orthotropy and tension–compression asymmetry. To describe these features of the plastic deformation of the material, and in order to account for the influence of plastic deformation on damage, Revil-Baudard et al. [26] used the Stewart and Cazacu [32] potential (see Eq. 8.43).

8.3.2 Yielding of Porous Hcp-Ti

All the parameters involved in the Stewart and Cazacu [32] potential (see Eq. 8.43), namely the anisotropy coefficients L_{ij} and the parameter k, can be identified based on the data presented in Sect. 8.3.1. As already mentioned, the evolution of the anisotropy in *r*-values with accumulated plastic deformation (see Table 8.1) and the evolving difference in hardening rates between tension–compression loadings observed from the test results (e.g., see Fig. 8.8) are indicative of texture evolution.

Table 8.1 Lankford coefficients for several in-plane orientations θ, measured with respect to the rolling direction

Orientation θ (°)	Level of equivalent plastic strain $\bar{\varepsilon}^p$							
	0	0.05	0.1	0.15	0.2	0.25	0.3	0.35
0	2.87	2.68	2.52	2.38	2.26	2.15	2.07	2.01
45	2.08	2.01	1.94	1.88	1.82	1.78	1.74	1.71
90	1.57	1.56	1.55	1.53	1.52	1.50	1.48	1.46

Table 8.2 Stewart and Cazacu [32] parameters for a high-purity orthotropic hcp-Ti corresponding to different values of the equivalent plastic strain, $\bar{\varepsilon}^p$; for any strain level L_{11} is set to unity

$\bar{\varepsilon}^p$	L_{22}	L_{33}	L_{12}	L_{13}	L_{23}	L_{44}	k
0.02	0.971	1.316	0.022	0.189	0.152	0.972	−0.304
0.05	0.989	1.243	0.089	0.193	0.173	0.909	−0.313
0.1	0.992	1.046	0.016	0.075	0.053	0.983	−0.363
0.15	0.996	0.915	−0.015	0.021	0.000	1.016	−0.419
0.2	0.998	0.849	−0.048	−0.012	−0.034	1.050	−0.472
0.25	0.998	0.815	−0.089	−0.041	−0.068	1.092	−0.518
0.3	0.998	0.797	−0.130	−0.068	−0.099	1.134	−0.554
0.35	1.000	0.772	−0.178	−0.097	−0.135	1.183	−0.635

To describe these effects, Revil-Baudard et al. [26] considered that the anisotropy coefficients and k evolve with accumulated plastic deformation. The numerical values of these parameters corresponding to eight individual levels of equivalent plastic strain $\bar{\varepsilon}^p$ (up to 0.35 strain) are listed in Table 8.2 (for the definition of the equivalent plastic strain associated with the Cazacu et al. [5] orthotropic potential, the reader is referred to Sect. 5.4.3; for more details on the identification procedure see Revil-Baudard et al. [26]).

The values of these parameters corresponding to any given level of plastic strain $\bar{\varepsilon}^p_j \leq \bar{\varepsilon}^p \leq \bar{\varepsilon}^p_{j+1}$ were obtained by linear interpolation (for more details see Revil-Baudard et al. [26]). Furthermore, it was considered that the material's hardening is isotropic and it is governed by the equivalent plastic strain according to a power law, $Y(\bar{\varepsilon}^p) = \beta(\varepsilon_0 + \bar{\varepsilon}^p)^n$ where the material parameters β and ε_0 were estimated based on the experimental uniaxial tension axial stress versus true strain curve in RD. The values of these parameters are: β = 413 MPa, ε_0 = 0.6445 and n = 1.

To illustrate the combined effects of anisotropy and tension–compression asymmetry of the plastic deformation on yielding of the material according to the Stewart and Cazacu [32] criterion, in Fig. 8.9 are shown the projections of the yield surface corresponding to an equivalent plastic strain $\bar{\varepsilon}^p = 0.25$ and a porosity $f = 0.01$ for axisymmetric loadings with axial stress oriented either along the RD (axis $\mathbf{e}_x$) (Fig. 8.9a), TD (axis $\mathbf{e}_y$) (Fig. 8.9b) or normal direction (ND) (axis $\mathbf{e}_z$) (Fig. 8.9c), respectively. In each case, loadings corresponding to the axial stress being the minor principal stress (i.e., third-invariant, $J_3 \leq 0$) and loadings such that axial stress is the major principal stress (i.e., third-invariant, $J_3 \geq 0$) were considered.

Given that irrespective of orientation this material has $\sigma_x^T/\sigma_x^C < 1$, $\sigma_y^T/\sigma_y^C < 1$ and $\sigma_z^T/\sigma_y^C < 1$, the same general trends are observed for axisymmetric loadings with the axial stress along the RD, TD, or ND-axis, respectively (compare Fig. 8.9a–c). Namely, for axisymmetric loadings at $J_3 \geq 0$, the response is softer than in the case of axisymmetric loadings at $J_3 \leq 0$. However, the influence of the anisotropy of the material is clearly observed, the sensitivity to J_3 being less pronounced for loadings with the axial stress along ND. Furthermore, the yield surface

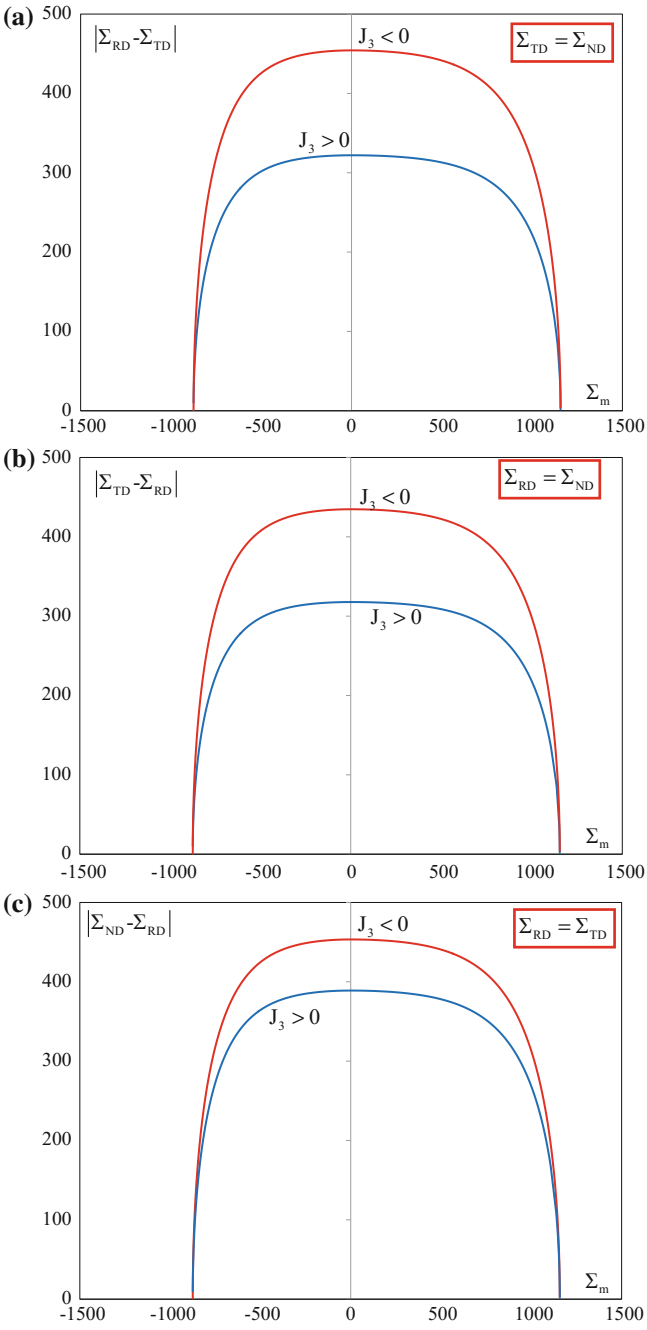

Fig. 8.9 Stewart and Cazacu [32] surfaces for the porous orthotropic hcp-Ti plate corresponding to a porosity $f = 0.01$ under axisymmetric loadings corresponding to either $J_3 \geq 0$ or $J_3 \leq 0$. **a** Loadings with axial stress along RD-axis; **b** loadings with axial stress along TD-axis, and **c** loadings with axial stress along ND-axis, respectively

lacks symmetry with respect to the deviatoric axis ($\Sigma_m = 0$). In particular, the material's yield stress for purely tensile hydrostatic loadings is different than that under purely hydrostatic compressive loadings [for further explanations see Sect. 8.2 and Eqs. (8.47)–(8.56)].

In Revil-Baudard et al. [26], the capabilities of this model to predict plastic deformation and damage in this material were assessed by comparing the predictions with data that were not used for identification of the model parameters. These data were obtained by conducting additional uniaxial tension tests on smooth specimens of circular cross-section (radius of 3.18 mm) with axis along RD, TD, and at 15°, 45°, and at 75° to the rolling direction.

F.E. simulations of the uniaxial tension response of these specimens were conducted, and the F.E. predictions were compared with the measured final cross-sections and XCMT measurements of porosity on both smooth and notched specimens. The presentation of these additional experimental tests and F.E. analyses is given in the following.

8.3.3 Comparison Between Model Predictions and Data

8.3.3.1 Comparison Between Predictions of Plastic Deformation and Data on Smooth Specimens

In the F.E. analyses, the rate of change of the void volume fraction ($\dot{f}$) was considered to result from growth of existing voids and nucleation of new ones. The contribution due to void growth was obtained from mass conservation and the condition of plastic incompressibility of the matrix. The simple idealization of nucleation controlled by plastic strain $\bar{\varepsilon}^p$ suggested by Gurson [11] based on Gurland [10] experimental data was considered. The stress controlled nucleation was considered to be governed by the mean stress, as discussed by Argon et al. [2], the specific dependencies on $\bar{\varepsilon}^p$ and the mean stress, σ_m being modelled as in Chu and Needleman [7], so that:

$$\dot{f} = (1-f)\,\mathbf{d}^p : \mathbf{I} + A_N \dot{\bar{\varepsilon}}^p + B_N \dot{\sigma}_m, \tag{8.60}$$

where

$$\begin{aligned} A_N &= \frac{f_N}{s_N\sqrt{2\pi}} \exp\left[-\frac{1}{2}\left(\frac{\bar{\varepsilon}^P - \varepsilon_N}{s_N}\right)^2\right] \\ B_N &= \begin{cases} 0 & \text{if } \dot{\sigma}_m < 0 \\ \frac{f_P}{s_P\sqrt{2\pi}} \exp\left[-\frac{1}{2}\left(\frac{\sigma_m - \sigma_P}{s_P}\right)^2\right] & \text{if } \dot{\sigma}_m > 0 \end{cases} \end{aligned} \tag{8.61}$$

i.e., both the plastic strain controlled nucleation and mean stress controlled nucleation were considered to follow a normal distribution with mean value and standard deviations (ε_N, s_N) and (σ_P, s_P), respectively.

In Eq. (8.60), the plastic strain-rate tensor $\mathbf{d}^p$ was calculated using the normality rule in conjunction with the Stewart and Cazacu [32] potential given by Eq. (8.43). The average initial value of the void volume fraction of the specimens was estimated to be: $f_0 = 0.0001$. The reported numerical values of the parameters involved in the void nucleation law (Eq. 8.61) are: $f_N = 0.001$, $s_N = 0.4$, $\varepsilon_N = 0.9$, $f_P = 0.001$, $s_P = 250$ MPa, $\sigma_P = 800$ MPa; and the elastic parameters values are: $E = 110$ GPa, $v = 0.3$.

The same numerical values for the parameters of the plastic potential, namely the anisotropy coefficients L_{ij} and the strength differential parameter k (see Table 8.2) were used in all F.E. analyses. We recall that the values of these parameters were determined from tensile tests on specimens with rectangular cross-section, and compression tests (data presented in Sect. 8.3.1).

The specimen geometry and the F.E. meshes used in the simulations are shown in Fig. 8.10. Note that for the axisymmetric specimens oriented along the axes of orthotropy of the material (i.e., either RD or TD), only one-eighth of the specimen needs to be analyzed. The mesh used consisted of 8109 hexahedral elements (see Fig. 8.10b). However, for the off-axis specimens (i.e., those specimens cut such that their respective generator is at 15°, 45°, and at 75° with respect to the rolling

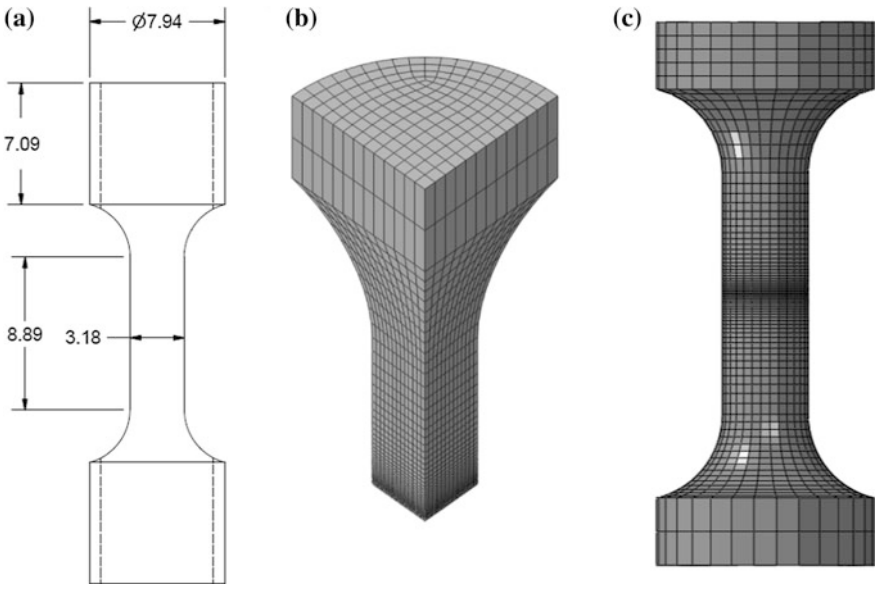

Fig. 8.10 **a** Geometries of the axisymmetric smooth tensile specimens; **b** F.E. meshes used for the specimens with axes along the directions of orthotropy: rolling direction (RD) and transverse direction (TD); **c** F.E. meshes used for the off-axis specimens. Dimensions are in mm

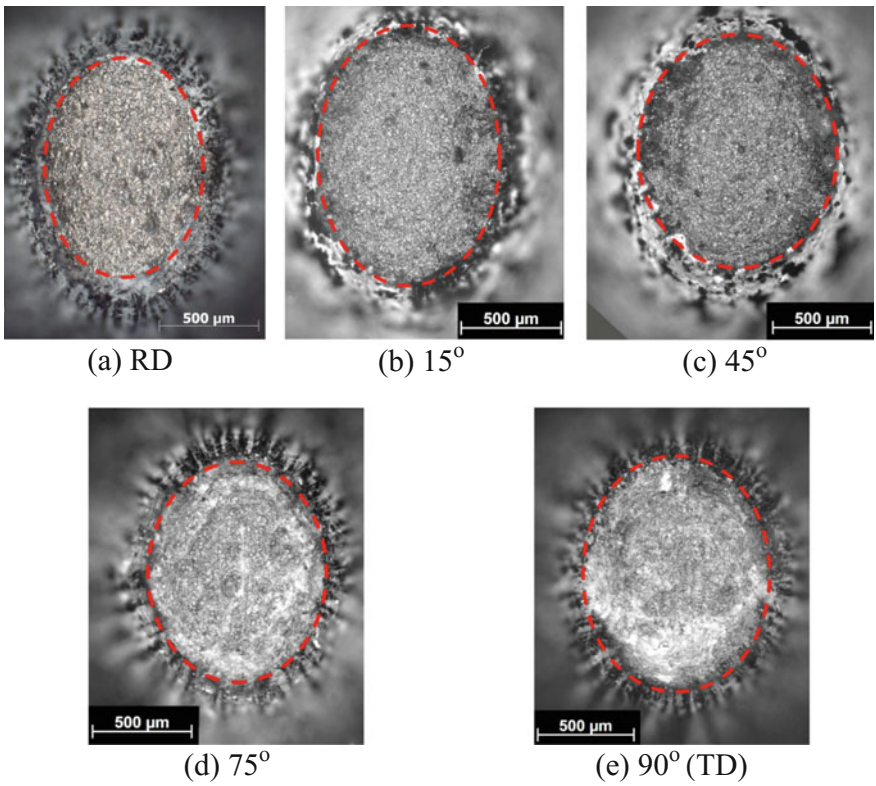

Fig. 8.11 Comparison between experimental and F.E. predictions according to the Stewart and Cazacu [32] porous model of the final cross-sections of axisymmetric tensile specimens of hcp-Ti after uniaxial tension. Specimens were cut such that the long axis is along: **a** RD; **b** 15° to RD; **c** 45° to RD; **d** 75° to RD; **e** 90° to RD, respectively. The F.E. predictions are represented as dashed lines (After Revil-Baudard et al. [26])

direction of the plate), symmetric boundary conditions cannot be applied, and the entire specimens needed to be meshed. While the F.E. mesh used in these cases consists of 16355 hexahedral elements (see Fig. 8.10c), the size of the elements in the middle of the specimen (i.e. the zone of interest) is the same as for the RD and TD axisymmetric specimens.

To assess the predictive capabilities of the model, we first present comparisons between the experimental and predicted final cross-section of each specimen. Specifically, in Fig. 8.11 are shown the photographs of the final cross-sections of the respective specimens on which are superposed the F.E. predictions obtained with the model (dashed lines). It is worth noting that for all the loading orientations, the F.E. predictions are in good agreement with the experimental data. Note that the model correctly captures the anisotropy in plastic deformation of the material; irrespective of the specimen orientation, the initial circular cross-section becomes elliptical.

Let define the ellipticity e, as

$$e = (a_1 - b_1)/b_1 \tag{8.62}$$

where a_1 and b_1 are the major and minor axes of the respective deformed cross-section. Note that the Stewart and Cazacu [32] porous model describes correctly the influence of the loading orientation on the shape of the final cross-section, the largest ellipticity being obtained for the RD specimen. Specifically, for the RD specimen, the predicted ellipticity is 28.3% against 30.4% obtained experimentally. For the specimens with axis oriented along other in-plane directions, the ellipticity predicted by the model is 25% for the 15° specimen (against 26.5% experimentally), 22% for the 45° specimen (against 21.7% experimentally), 21% for the 75° specimen (against 24% experimentally), and 19.7% for the TD specimen (against 22.7% experimentally). Thus, it can be concluded that the model predictions are in quantitative agreement with the data.

It is also worth noting that the Stewart and Cazacu [32] model captures fairly well the experimental axial load versus displacement curves for all specimens. As an example, in Fig. 8.12 are shown comparisons between the load-displacement curves obtained experimentally and theoretically for the RD specimen (Fig. 8.12a), and for the 45° specimen, respectively (Fig. 8.12b). It is worth recalling that all the F.E. simulations were conducted with the same set of values for the Stewart and Cazacu [32] parameters which were identified based on a different set of data. Thus, the results presented in Figs. 8.11 and 8.12 demonstrate that the model is truly predictive.

8.3.3.2 Comparison Between Model Prediction and XCMT Porosity Measurements for a Smooth RD Specimen

Revil-Baudard et al. [26] also reported ex situ X-ray computed micro-tomography measurements of the porosity in the smooth RD specimen. The scan was done after the specimen was subjected to uniaxial tension to an axial displacement of 5.52 mm, i.e., the deformed specimen was very close to failure. The images were taken at the necking region. Tomography acquisition was carried out with a cubic voxel size of $1.2214^3 = 1.82\,\mu m^3$ and a range of view (ROV) of 2030 pixels. The total data set consisted of 1361 images where each image was of 2030 × 2030 pixels, a total of about 5.6×10^9 voxels representing a volume of $2.48 \times 2.48 \times 1.66 = 10.2\,mm^3$.

In Fig. 8.13a are shown the reconstructed 2-D views in the (TD, TT) plane, and in the (RD, TD) plane of the specimen, respectively. For comparison purposes, in Fig. 8.13b are shown the respective views extracted from the scan of a copper specimen, which was taken at the same axial displacement. It is very important to note that for the same axial displacement, the copper material is very damaged while the Ti material shows very little damage. While a large hole/crack is seen in the middle of the copper specimen, almost no damage is observed in the hcp-Ti specimen. It means that for uniaxial tensile loading the rate of damage growth is

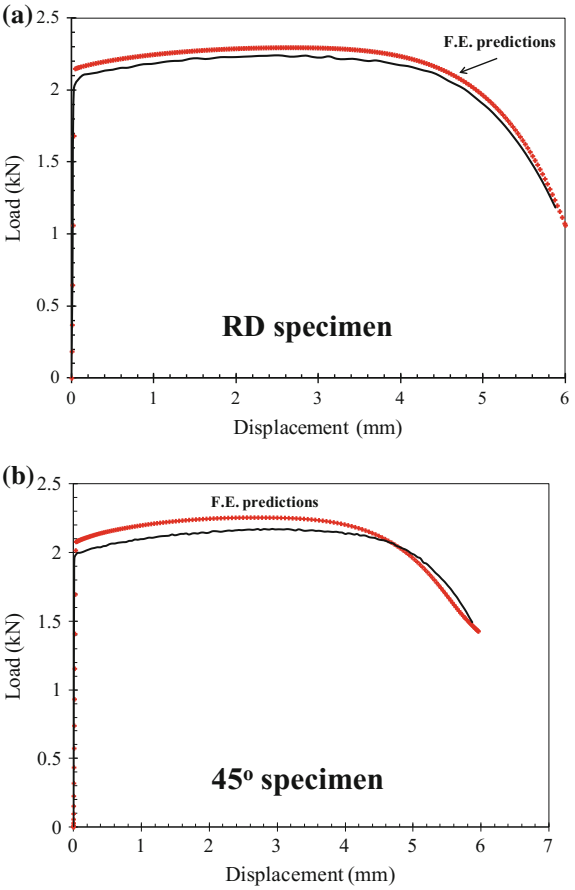

Fig. 8.12 Comparison between experimental data on hcp-Ti and F.E. predictions of the load versus axial displacement curves according to the Stewart and Cazacu [32] porous model for uniaxial tension of smooth axisymmetric specimens. **a** RD specimen, and **b** 45° specimen (After Revil-Baudard et al. [26])

slower in this Ti material than in Cu. Thus, these XCMT observations confirm the conclusions of the preliminary theoretical study of Revil-Baudard and Cazacu [25] on the influence of the tension–compression asymmetry on damage growth rate and damage distribution in a round tensile specimen which was done using the isotropic form of Stewart and Cazacu [32] model (for more details, the reader is referred to Sect. 7.3.2). Let us recall that in that theoretical study it was shown that for isotropic materials for which the flow stress in uniaxial compression is larger than the flow stress in uniaxial tension damage is delayed as compared to materials for which the matrix plastic behavior is governed by the von Mises criterion. The observed drastic difference in damage evolution between hcp-Ti, which is harder in compression than in tension (see Fig. 8.8), and the copper material, which does not display tension–compression asymmetry, validates the main conclusion of this study, namely that the rate of void growth should be much lower for Ti than for Cu (von Mises behavior). In summary, Fig. 8.13 clearly shows that there is a very strong

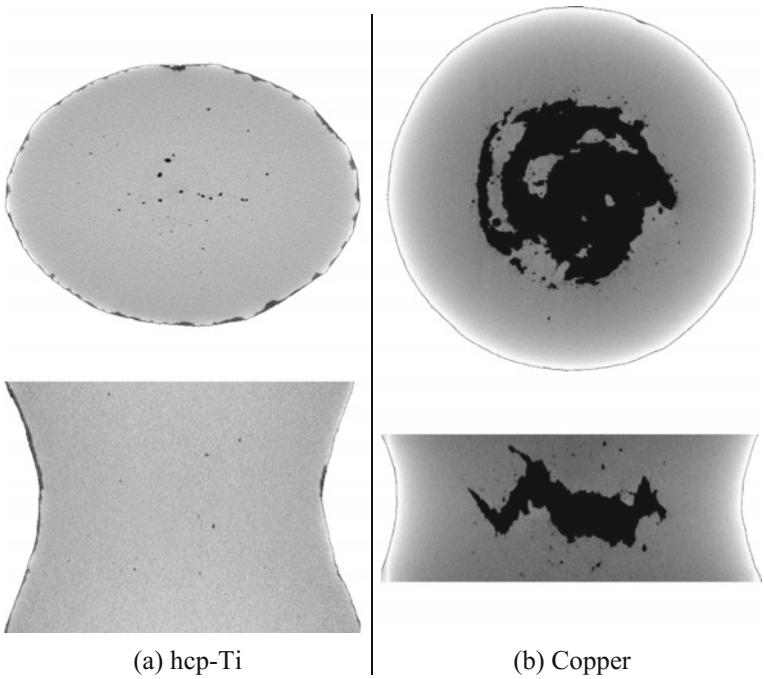

Fig. 8.13 Post-test X-ray computed micro-tomography scans of smooth axisymmetric specimens of circular cross-sections that were subjected to uniaxial tension to large plastic deformations (close to failure): **a** hcp-Ti material studied; **b** isotropic copper material (After Revil-Baudard et al. [26])

coupling between the specificities of the plastic deformation and porosity/damage evolution.

In order to assess the predictive capabilities of the Stewart and Cazacu [32] porous model in terms of damage evolution, in Revil-Baudard et al. [26], the porosity data were compared with the F.E. isocontours of the void volume fraction corresponding to the same axial displacement (see Fig. 8.14). Specifically, the F.E. predictions were superposed on the different views obtained by XCMT, namely on the experimental cross-section, the experimental (RD, TD) section, and the experimental (RD, ND) section, respectively. To extract the experimental void volume fraction, a clustering technique was applied in order to identify 3-D groups of connected voxels, and thus to identify individually each pore within the matrix. A total of 2385 pores (independent cavities) have been detected in the total volume of the specimen, which resulted in an average porosity over the specimen volume of 0.052%. It is worth noting that if only the pores of volume larger than 50 voxels are considered (i.e., number of 1857 independent cavities), the average void volume fraction in the total volume of the specimen is of 0.051%.

Irrespective of the threshold value prescribed for the pore size, the maximum average porosity corresponds to the root of the neck. The average porosity in the

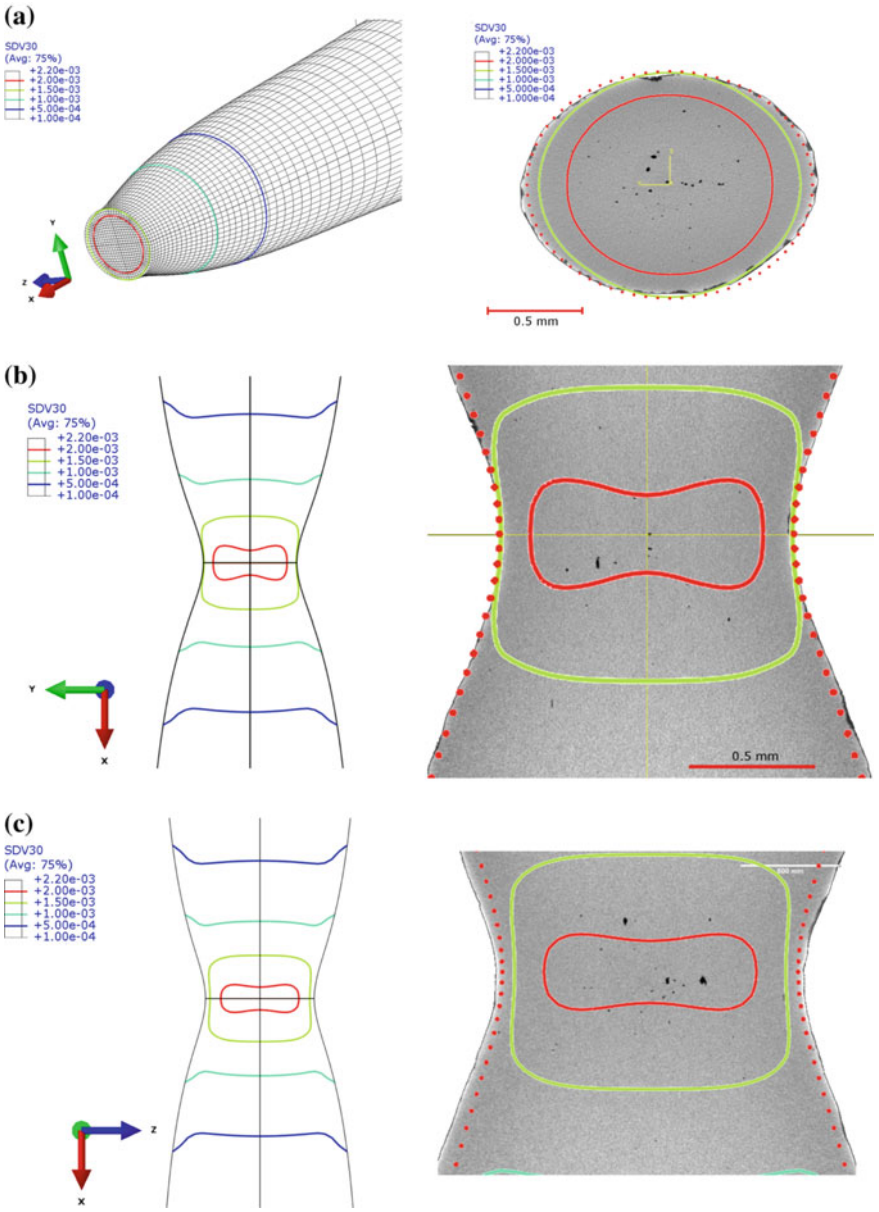

Fig. 8.14 Comparison between the F.E. cross-sections and isocontours of the void volume fraction of a smooth axisymmetric specimen of hcp-Ti subjected to uniaxial tension along **x**-direction (RD), according to the Stewart and Cazacu [32] model and XCMT data for an axial notch displacement of 5.52 mm: **a** deformed specimen cross-section; **b** (x, y) section of the deformed specimen; **c** (x, z) section of the deformed specimen. The axes x, y, z are along the rolling (RD), transverse (TD), and normal (ND) directions (After Revil-Baudard et al. [26])

minimal cross-section (root of the neck) is of 0.25%. It is worth noting that the Stewart and Cazacu [32] model also predicts that damage is diffuse, in the minimal cross-section the maximum void volume fraction predicted being of 0.22% (see Fig. 8.14a). Likewise, for the other views (Figs. 8.14b, c, respectively) most of the voids observed by XCMT are inside the region of maximum void volume fraction predicted by the model. Furthermore, in Fig. 8.14, the F.E. predictions of the geometry of the specimen for the respective axial displacement (red points) are superposed on the different experimental cut views. It is to be noted that the Stewart and Cazacu [32] model correctly predicts the cross-section geometry in each plane.

While data were obtained for an axial displacement of 5.52 mm, the same authors also reported the damage distribution predicted by the model for other axial displacements. Specifically, in Fig. 8.15 are shown the F.E. predictions of the

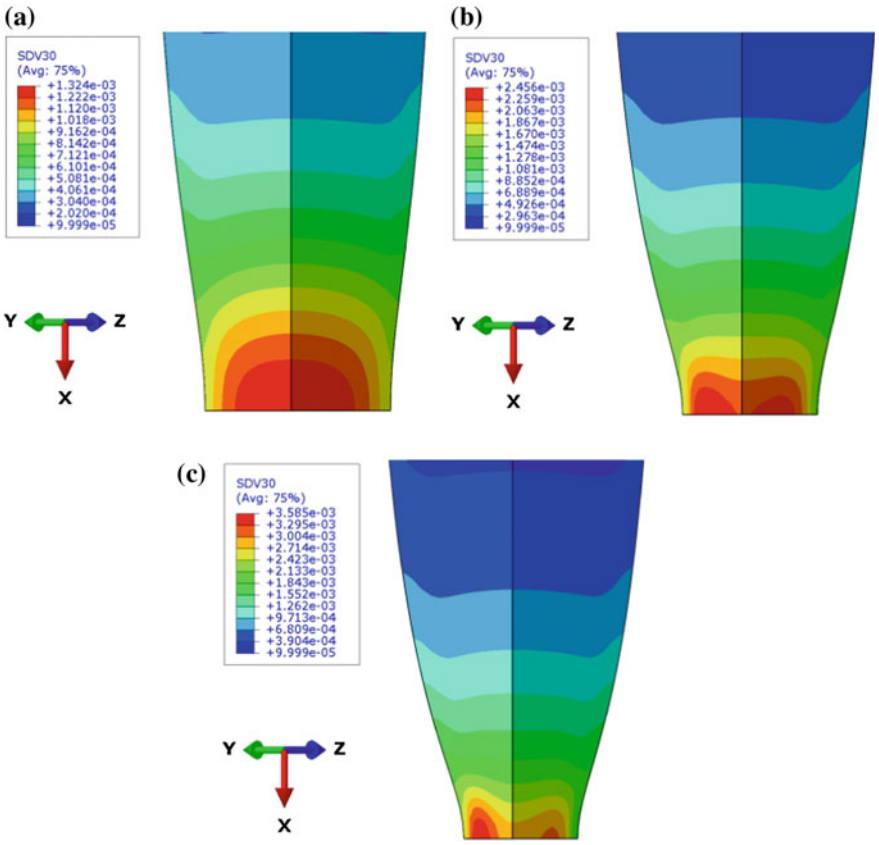

Fig. 8.15 F.E. predictions according to the Stewart and Cazacu [32] model of the isocontours for the void volume fraction of an axisymmetric smooth specimen of hcp-Ti subjected to uniaxial tension along the **x**-direction (rolling direction RD) for other axial displacements: **a** 5 mm, **b** 5.6 mm, **c** 5.85 mm. Note that for large axial displacements, the location of the zone of maximum void volume fraction shifts from the center of the specimen. The axes x, y, z are along the rolling (RD), transverse (TD), and normal (ND) directions (After Revil-Baudard et al. [26])

isocontours of the void volume fraction predicted for the same RD smooth specimen corresponding to a lower axial displacement (Fig. 8.15a) and to higher axial displacements of 5.6 mm (Fig. 8.15b), and 5.85 mm (Fig. 8.15c), respectively. Note that the model predicts that for the axisymmetric smooth specimen damage initiates at the center (see Fig. 8.15a), and shifts toward the outside surface of the specimen for large axial displacements (see Fig. 8.15b, c).

8.3.3.3 In Situ XCMT Measurements of Damage Evolution for a Notched RD Specimen of Hcp-Ti and Comparison with Model Predictions

In the previous section, it was shown that the Stewart and Cazacu [32] porous model predicts correctly the level of damage as well as plasticity-damage couplings under uniaxial tensile loading of an axisymmetric smooth specimen. The comparison between model and data were done for a fixed level of the imposed axial displacement. To assess the capabilities of the model to capture the influence of the stress state (stress triaxiality) on damage and its evolution, the same authors have conducted an uniaxial tension test up to fracture on a notched axisymmetric RD specimen. The notch radius was of 0.51 mm while the specimen cross-section radius was of 1.27 mm. The reported load-displacement curve is shown in Fig. 8.16 in comparison with the Stewart and Cazacu [32] F.E. model predictions. Given that the specimen has its axis along an orthotropy axis of the material (RD), only one-eighth of the specimen was meshed. On Fig. 8.16 are also shown for comparison the load vs. displacement curves obtained experimentally and predicted by the model for the smooth RD specimen. It is clearly seen that the model describes well that the presence of the notch induces a much softer response as compared to the smooth specimen.

To further provide insights into the porosity evolution in the material and verify the unusual damage characteristics revealed by the model, in situ XCMT tensile

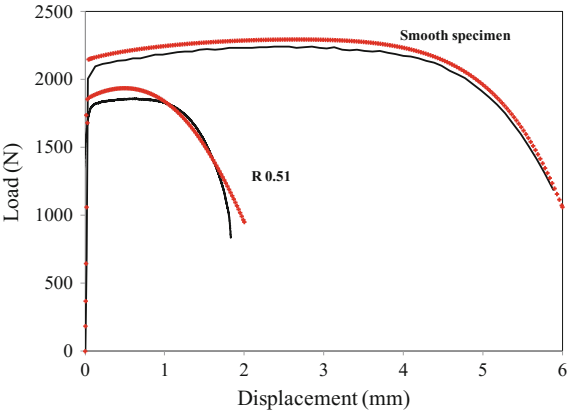

Fig. 8.16 Effect of the notch geometry on the load versus displacement response for hcp-Ti according to the Stewart and Cazacu [32] porous model and experimental data in uniaxial tension along the rolling direction (After Revil-Baudard et al. [26])

tests on RD specimens of the same notch radius were also conducted at Wright Patterson Air Force Laboratory using a Deben CT5000 5 kN in situ tomograph. Each tomography acquisition was carried out with a cubic voxel size of 3.2516^3 μm^3 and comprised 700 images of 992 $\times$ 1014 pixels each. It is to be noted that in order to be able to acquire in situ XCMT measurements for metallic specimens with this apparatus, the spatial resolution had to be larger than that used for the ex situ measurements, which were done using a Xradia X-ray microscope, VersaXRM-500. The analysis of the in situ XCMT data was done using ImageJ, which is a public domain image processing program developed at the National Institutes of Health (see Rasband [23], Abramoff et al. [1], Schneider et al. [28]).

The rationale for conducting in situ measurements was to have information on damage evolution in Ti, and to validate/invalidate the trends predicted by the model. Due to the specificity of the in situ XCMT testing capabilities, the load-displacement curve cannot be obtained directly. However, for each XCMT scan, knowing the resolution of the X-ray microscope, it was possible to deduce the displacement between the extremities of the notch. In Fig. 8.17 are shown views obtained from scans taken at notch displacement of 0.24, 0.73, 1.02 and 1.20 mm, respectively. To assess the effect of anisotropy on the mechanical response, at each individual level of displacement, the cross-sections in the (TD, ND) plane, in the (RD, TD) plane, and in the (RD, ND) plane were reported (Fig. 8.17). Model predictions of the porosity isocontours corresponding to the various cross-sections for several levels of axial displacements are presented in Figs. 8.18, 8.19 and 8.20.

A close examination of the scans shown in Fig. 8.17 for the notched specimen reveals that damage initiates at the surface of the specimen. Thus, the damage evolution predicted by the model (see Figs. 8.18 and 8.19) is confirmed experimentally.

Furthermore, it was demonstrated that the location of the zone where damage initiates strongly depends on the specimen geometry. Indeed, the model predicts that for a smooth axisymmetric specimen, damage initiates at the center of the specimen (see Fig. 8.15a), and the level of damage close to failure is very low (see also the comparison between F.E. predictions and XCMT data for an axial displacement of 5.52 mm shown in Fig. 8.14). On the other hand, for the notched specimen the model predicts that damage initiates at the outer surface of the specimen, and further grows from the outer surface to the center of the specimen (see Figs. 8.18, 8.19 and 8.20), which corroborates with the in situ XCMT data of Fig. 8.17. In other words, for the same global loading (i.e. uniaxial tension), the local stress state, which depends on the specimen geometry is different, which in turn triggers a different damage initiation site, and a markedly different damage evolution.

It is very important to note that the model predicts that for the specimen subjected to uniaxial tension along RD, damage accumulates differently along ND and TD. The predictions of the isocontours of porosity in the (TD, ND) cross-section corresponding to different levels of notch displacement are shown in Fig. 8.18.

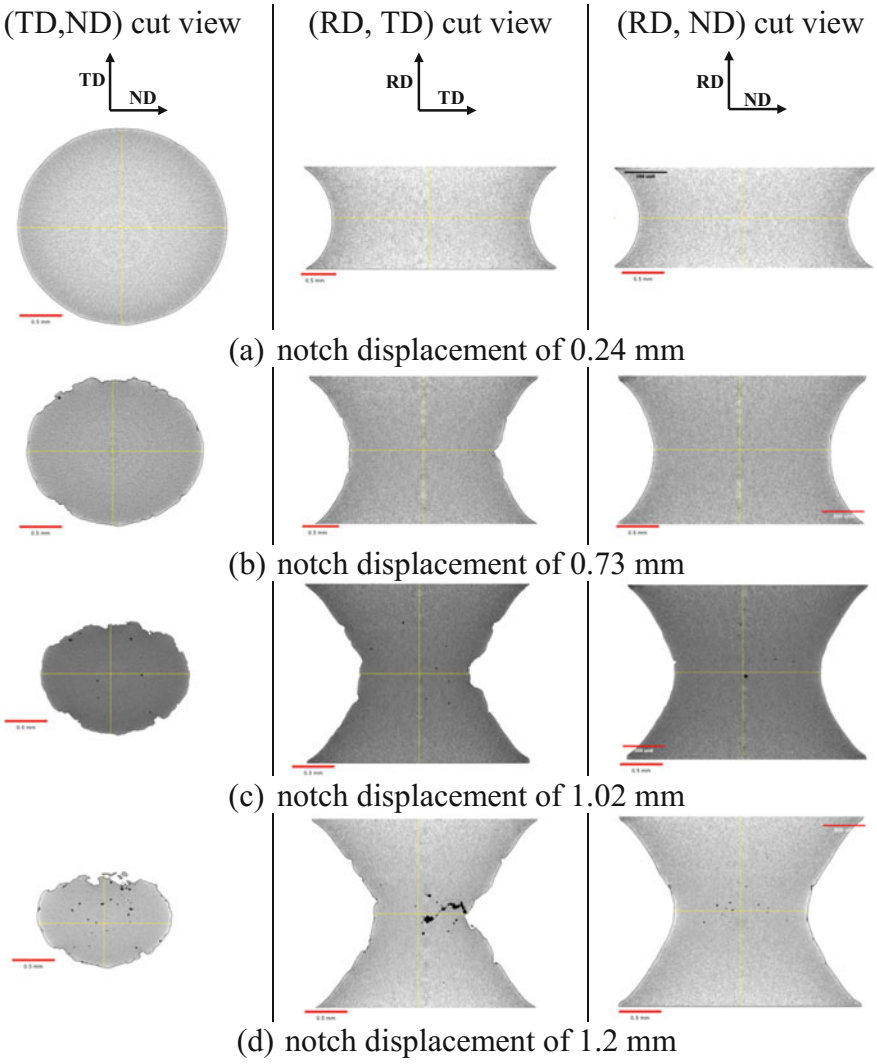

Fig. 8.17 X-ray micro-tomography in situ scans of the hcp-Ti notched specimen subject to uniaxial tension along rolling direction (RD) showing the (TD, ND) view, (RD-TD) view, and (RD, ND) view, respectively corresponding to a notch displacement of: **a** 0.24 mm, **b** 0.73 mm, **c** 1.02 mm, **d** 1.2 mm (After Revil-Baudard et al. [26])

Note that the void volume fraction is larger along TD (i.e. the small axis of the deformed elliptical cross-section) than along ND (i.e. the long axis of the elliptical cross-section).

Moreover, comparison of the XCMT (RD, TD) sections with the (RD,ND) sections (see Fig. 8.17), clearly shows that the surface of the specimen along the

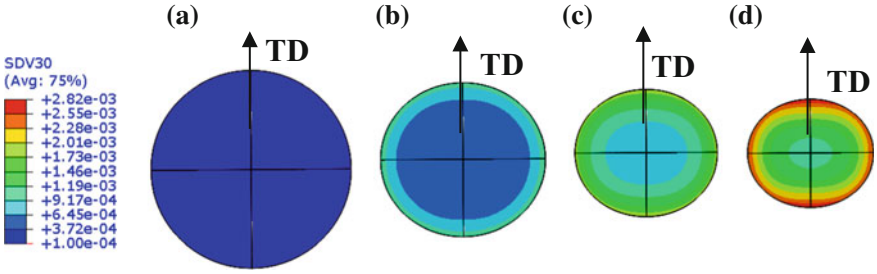

Fig. 8.18 F.E. predictions according to the Stewart and Cazacu [32] model of the void volume fraction isocontours in the (TD, ND) cross-section of an axisymmetric notched specimen of hcp-Ti subjected to uniaxial tension along RD at an axial displacement of: **a** 0.24 mm, **b** 0.73 mm, **c** 1.02 mm, **d** 1.2 mm, respectively. Initial void volume fraction $f_0 = 10^{-4}$ (After Revil-Baudard et al. [26])

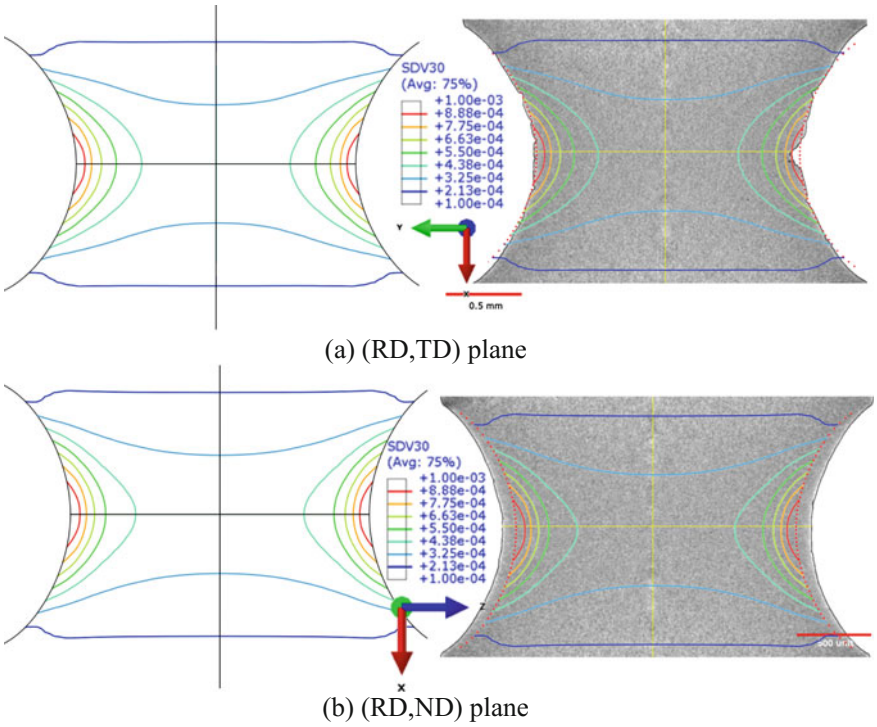

Fig. 8.19 Comparison between the F.E. cross-sections and isocontours of void volume fraction of a notched axisymmetric specimen of hcp-Ti subjected to uniaxial tension along RD, according to the Stewart and Cazacu [32] model and XCMT data corresponding to a notch axial displacement of 0.73 mm: **a** cross-section of the deformed specimen; **b** (RD-TD) section of the deformed specimen; **c** (RD-ND) section of the deformed specimen. The axes x, y, z are along the rolling (RD), transverse (TD), and normal (ND) directions (After Revil-Baudard et al. [26])

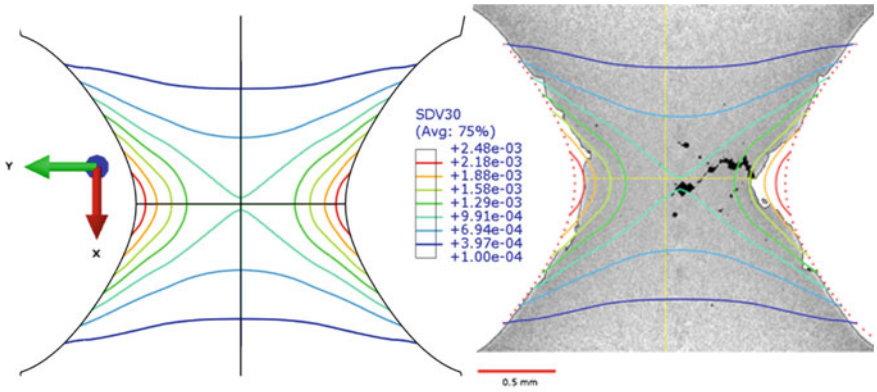

(a) (RD,TD) plane

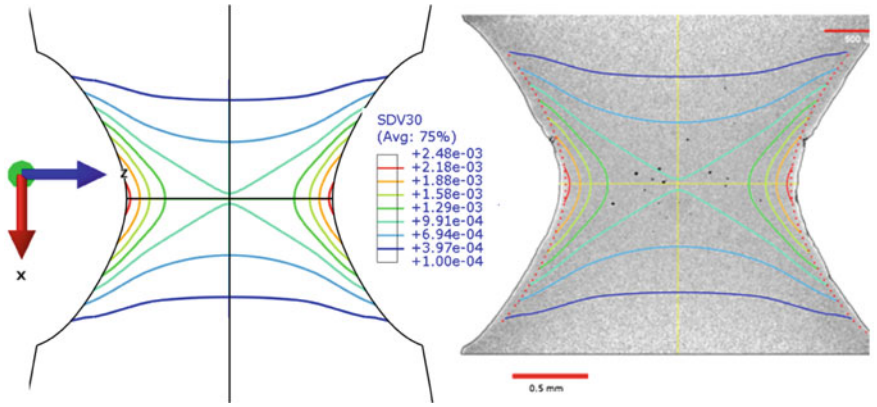

(b) (RD,ND) plane

Fig. 8.20 Comparison between the F.E. cross-sections and isocontours of void volume fraction of a notched axisymmetric specimen of hcp-Ti subjected to uniaxial tension along RD, according to the Stewart and Cazacu [32] model and XCMT data corresponding to a notch axial displacement of 1.2 mm: **a** cross-section of the deformed specimen; **b** (RD-TD) section of the deformed specimen; **c** (RD-ND) section of the deformed specimen. The axes x, y, z are along the rolling (RD), transverse (TD), and normal (ND) directions (After Revil-Baudard et al. [26])

TD-axis is more damaged than the surface along the ND axis. The prediction of the Stewart and Cazacu [32] porous model corroborates with these experimental observations. To further demonstrate that there is a good agreement between the predictions of the Stewart and Cazacu [32] model in terms of plasticity-damage couplings in Figs. 8.19 and 8.20 are also superposed on the XCMT scans the F.E. predictions of the specimen profiles (red points) corresponding to notch displacements of 0.73 and 1.2 mm, respectively. Note that the model correctly captures the change in geometry of the specimen (anisotropy in plastic deformation). Since damage is driven by the plastic deformation, and the plastic anisotropy is correctly

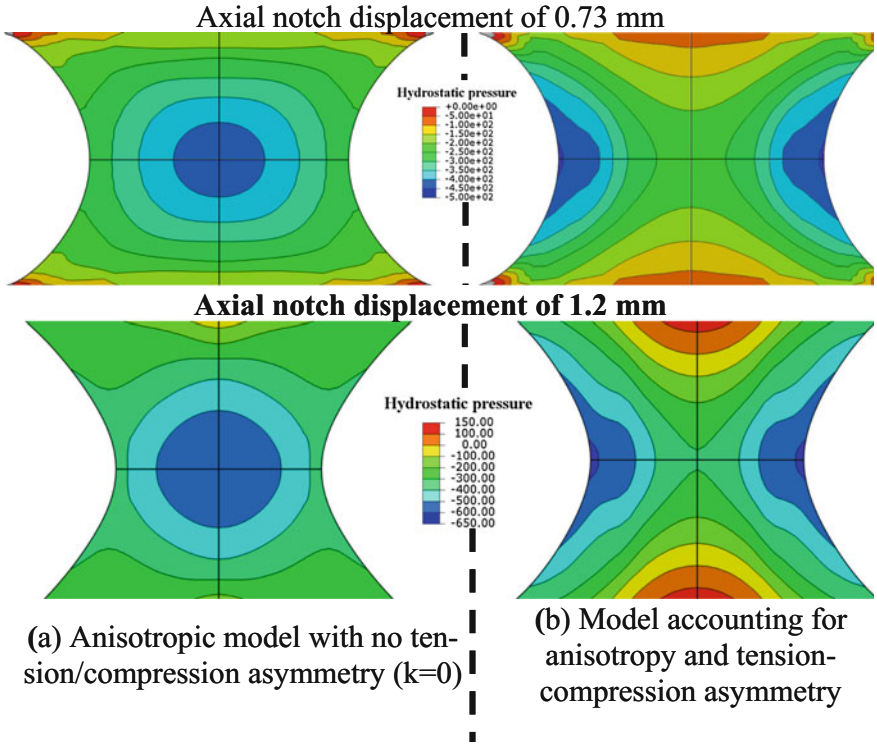

Fig. 8.21 Importance of accounting for tension–compression asymmetry in plastic behavior of hcp-Ti: comparison of the isocontours of the hydrostatic pressure ($p = -1/3\ \mathrm{tr}(\boldsymbol{\sigma})$) in the (RD-TD) section of the notched specimen for axial notch displacement of 0.73 and 1.2 mm, respectively, according to: **a** anisotropic model with no tension–compression asymmetry ($k = 0$), **b** the Stewart and Cazacu [32] model which accounts for both anisotropy and tension–compression asymmetry. Note that if the tension–compression asymmetry in plastic deformation is accounted for, the local distribution of the hydrostatic pressure is totally different (After Revil-Baudard et al. [26])

described, the model also correctly predicts the location of the zones of maximum damage in each plane.

Because the Stewart and Cazacu [32] plasticity-damage model accounts for both anisotropy and tension–compression asymmetry, it captures the main trends revealed by the XCMT scans, namely that damage initiates at the outer surface of the specimen, and further grows from the outer surface to the center of the specimen (see data shown in Fig. 8.17).

To evaluate the importance of the consideration of the tension–compression asymmetry in plastic deformation on the local fields, the authors performed additional F.E. simulations in which the tension–compression asymmetry was neglected, i.e. in the simulations the tension–compression asymmetry parameter k in Eq. (8.43) was set to zero. As an example, Fig. 8.21 compares the isocontours of the hydrostatic pressure ($p = -1/3\mathrm{tr}(\boldsymbol{\sigma})$) in the (RD-TD) section of the notched

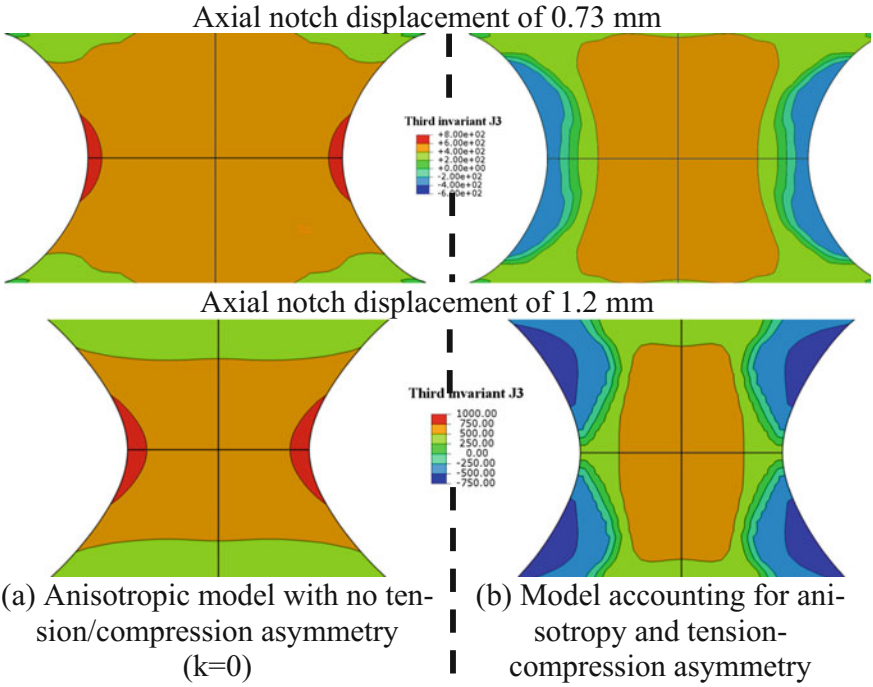

Fig. 8.22 Importance of accounting for tension–compression asymmetry of the plastic behavior of an hcp-Ti. Comparison of the isocontours of the third-invariant of the stress deviator J_3 in the (RD-TD) section of the notched specimen for an axial notch displacement of 0.73 and 1.2 mm, respectively, according to: **a** anisotropic model with no tension–compression asymmetry ($k = 0$), **b** the Stewart and Cazacu [32] model which accounts for both anisotropy and tension–compression asymmetry. Note that only if the tension–compression asymmetry in plastic deformation is neglected, the third-invariant is always positive; otherwise the local distribution is completely different (After Revil-Baudard et al. [26])

specimen at axial notch displacement of 0.73 and 1.2 mm, respectively according to the anisotropic model with no tension–compression asymmetry ($k = 0$) and the Stewart and Cazacu [32] model with parameters given in Table 8.2.

Note that the distribution of the hydrostatic pressure is totally different. If the tension–compression asymmetry is neglected, the maximum mean stress (i.e. the minimum hydrostatic pressure) occurs in the center of the specimen, while if the model accounts for tension–compression asymmetry, the maximum mean stress is located along the surface of the specimen. To pursue this analysis, in Fig. 8.22 are plotted the isocontours of the third-invariant of the stress deviator for the same axial displacements. If the tension–compression asymmetry is neglected, locally, the third-invariant of the stress deviator is always positive. However, if the model

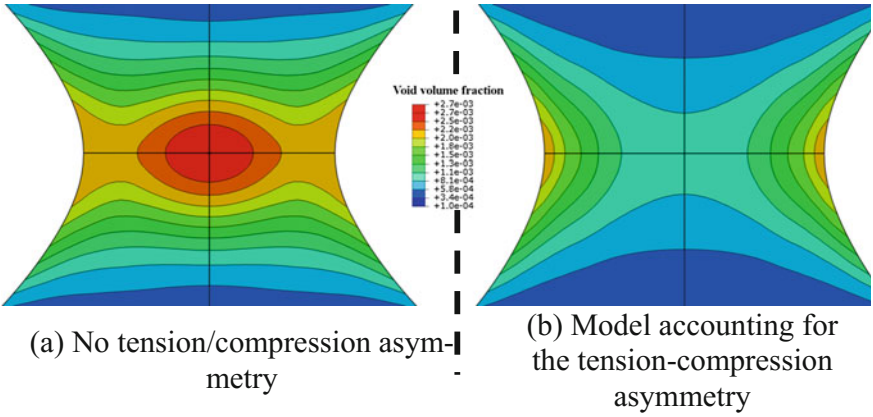

Fig. 8.23 Importance of accounting the tension–compression asymmetry of the plastic behavior of an hcp-Ti. Comparison of the isocontours of the void volume fraction in the (RD-TD) section of the notched specimen for an axial notch displacement of 1.2 mm, respectively, according to: **a** anisotropic model with no tension–compression asymmetry ($k = 0$), **b** the Stewart and Cazacu [32] model which accounts for both anisotropy and tension–compression asymmetry (After Revil-Baudard et al. [26])

accounts for both the anisotropy and tension–compression asymmetry, the third-invariant J_3 is negative close to the outside surface of the specimen and positive at the center of the specimen. Given the strong coupling between the mean stress and the third-invariant J_3 on the response of the porous material [see the Eqs. (8.49) and (8.50)] and the yield surface of the porous hcp-Ti shown in Fig. 8.9), the isocontours of the void volume fraction are completely different depending on whether the tension–compression asymmetry is accounted for in the porous model or not (see Fig. 8.23). If the tension–compression asymmetry is neglected, the maximum void volume fraction is located at the center of the specimen, while if the model accounts for the tension–compression asymmetry, the zone of maximum damage shifts toward the outside surface.

In summary, the results presented suggest that only by using a porous model that accounts for the specificities of the plastic deformation in Ti the anisotropy in plastic deformation and damage can be captured. Irrespective of the loading orientation, the final geometry of the specimens was correctly predicted. Specifically, it was shown that for a smooth axisymmetric specimen subjected to uniaxial tension, damage initiates at the center of the specimen and is diffuse; the level of damage close to failure being very low. On the other hand, for a notched specimen subject to uniaxial tension, the Stewart and Cazacu [32] porous model predicts that damage initiates at the outer surface of the specimen, and further grows from the outer surface to the center of the specimen, which corroborates with the in situ X-ray tomography data.

8.4 Effects of Anisotropy on Porosity Evolution in Single Crystals Under Multiaxial Creep

All the models discussed so far in this book and the applications presented concern rate-independent plastic behavior using plastic potentials for fully dense materials (Chaps. 4–6) or porous materials (Chap. 7; Sects. 8.1–8.3). There are circumstances however when time effects on the mechanical behavior play a significant role. An appropriate framework for modeling those effects is that of viscoplasticity theory. As already mentioned, presentation of viscoplasticity models for isotropic and anisotropic metallic materials is beyond the scope of this book. For the early history and main contributions concerning viscoplasticity models for isotropic materials, the reader is referred to the monographs of Perzyna [21] and Cristescu [8].

In the following, recent attempts toward modeling the role of anisotropy on porosity evolution during multiaxial creep in single crystals are presented. Due to its great importance in assessment of structural integrity, extensive amount of experimental work has been carried out on smooth and notched single crystals. While the data reported in the open literature is scarce and mainly concern the characterization of specimens in the $\langle 100 \rangle$ orientation (e.g., Liu et al. [18]), recent F.E. numerical studies have provided new insights into the role played by the lattice orientation on the deformation and void growth of creeping single crystals. For example, Srivastava and Needleman [29, 30] carried out detailed investigations using F.E. unit-cell models of fcc single crystals containing a single initially spherical void. The deformation of the matrix was considered to be governed by the Asaro and Needleman [3] crystal model. Simulations were carried out for different crystal orientations. The unit cell was subject to creep loadings (i.e., fixed stress) for a range of values of the imposed stress triaxialities and a range of imposed values of the Lode parameter, a measure of the third-invariant of the stress deviator J_3 (see Chap. 4 for the definition of the Lode angle). Specifically, for each value of the stress triaxiality, T, creep loadings corresponding to the third-invariant of the stress deviator, J_3, being negative, zero (shear), and positive were considered. The results of Srivastava and Needleman [30] showed a strong effect of the stress state and anisotropy on all aspects of the mechanical response of the voided single crystal. For the [100] crystal orientation, nearly no effect of J_3 was found. On the other hand, for other crystal orientations a significant effect of J_3 on the mechanical response was reported even for creep loadings at very high values of the stress triaxialities.

Very recently, an analytic model for description of the creep response of porous single crystals with fcc crystal structure was developed by Srivastava et al. [31]. To describe the anisotropy of the single crystal, these authors specialized the orthotropic Stewart and Cazacu [32] potential to cubic symmetry. To account for viscous effects, the approach introduced by Pan et al. [20] was used, namely the effective stress of the matrix was considered to obey a power-type law.

The very strong influence of the crystal's anisotropy and the loading path on the evolution of porosity is captured by the model. For the [100] crystal loading

orientation, this model predicts that void growth is not influenced by J_3. However, for the [110] orientation, irrespective of the stress triaxiality, the model predicts that there is a very strong effect of J_3, the fastest rate of void growth being for loading at $J_3 = 0$ in one of the secondary orientation while the slowest rate of void growth corresponds to loadings at $J_3 < 0$ in the other secondary orientation. For the [111] crystal orientation the fastest rate of void growth corresponds always to loadings at $J_3 > 0$ while the slowest rate corresponds to loadings at $J_3 < 0$.

While the model predicts the same trends observed in the F.E. unit-cell calculations, it has also revealed previously unrecognized features of the mechanical response, namely that for certain axisymmetric loadings at the same triaxiality and mean stress, the creep response should be the same for certain crystal orientations.

It is important to point out that in both the F.E. unit-cell model and the analytical model for creep of the porous crystal of Srivastava et al. [31], the tension–compression asymmetry of the crystal was neglected. However, for porous polycrystalline materials it was clearly demonstrated (see Chaps. 7 and 8) that only by accounting for the tension–compression asymmetry of the matrix it is possible to explain damage evolution and its distribution (e.g., see Fig. 8.23).

In the following, we present a theoretical study of the influence of the tension–compression asymmetry of the single crystal matrix on yielding and porosity evolution of voided single crystals subject to creep. To enable development of a closed-form expression for the evolution of porosity under creep loading, time effects on the irreversible deformation are modeled using an overstress-based approach in conjunction with the Stewart and Cazacu [32] porous model specialized for cubic symmetry. Creep stabilization is considered to be governed by the irreversible work per unit volume. Next, the creep response according to this model is analyzed for porous fcc single crystals for which the tension–compression asymmetry may be neglected. The influence of the loading path on yielding and porosity evolution for the case when the principal directions of the applied stress are aligned with different crystallographic directions is analyzed. We conclude with analyzing the creep response for a single crystal with incompressible matrix displaying tension–compression asymmetry. To simplify writing, in the following, we denote by $\boldsymbol{\sigma}$ the Cauchy stress applied to the porous crystal.

8.4.1 *Creep Models for Porous Single Crystals with Cubic Symmetry*

The aim is to provide insights into the combined effects of anisotropy and loading history on the evolution of porosity under multiaxial creep. Therefore, key in the formulation is the choice of the plastic potential.

8.4.1.1 Plastic Potential for a Porous Crystal with Cubic Symmetry

To describe the plastic flow of a porous single crystal, we specialize to cubic symmetry the Stewart and Cazacu [32] potential presented in Sect. 8.1.

Note that in the formulation of the Stewart and Cazacu [32] potential, the plastic anisotropy of the incompressible matrix is described by the fourth-order symmetric tensor $\mathbf{L}$. Specifically, the potential is a function of the mean stress σ_m and the principal values $\widehat{\sigma}_1$, $\widehat{\sigma}_2$, $\widehat{\sigma}_3$ of the transformed stress, $\widehat{\boldsymbol{\sigma}} = \mathbf{L}\mathbf{s}$, with $\mathbf{s} = \boldsymbol{\sigma} - \sigma_m \mathbf{I}$ denoting the deviator of the applied stress $\boldsymbol{\sigma}$ (see Eq. 8.43).

Theorem 8.4 *(Plastic potential for a porous single crystal with cubic symmetry) In the coordinate system associated with the* $\langle 100 \rangle$ *crystal axes, the potential for the porous cubic crystal is of the form:*

$$\Phi_c(\boldsymbol{\sigma}, f) = \tilde{m}^2 \left[\sum_{i=1}^{3} \left(\left| \frac{\widehat{\sigma}_i}{\sigma^T_{\langle 100 \rangle}} \right| - k \frac{\widehat{\sigma}_i}{\sigma^T_{\langle 100 \rangle}} \right)^2 \right] + 2f \cosh\left(\frac{3\sigma_m}{\tilde{h}\sigma^T_{\langle 100 \rangle}} \right) - 1 - f^2 = 0 \tag{8.63}$$

with

$$\tilde{h} = \sqrt{\frac{(3k^2 - 2k\,\mathrm{sgn}(\Phi_1) + 3)}{(3k^2 + 2k\,\mathrm{sgn}(\sigma_m) + 3)}} \sqrt{\frac{8 + 12/\beta^2}{5}} \tag{8.64}$$

$$\tilde{m}^2 = \frac{2}{\Phi_1^2 (3k^2 - 2k\,\mathrm{sgn}(\Phi_1) + 3)} \tag{8.65}$$

$$\beta = (2L_{44}/3\Phi_1),\ \Phi_1 = 2(L_{11} - L_{12})/3 \tag{8.66}$$

In Eq. (8.63) *k is a parameter associated with strength differential effects, L_{11}, L_{12} and L_{44} are the only nonzero components of the fourth-order symmetric tensor $\mathbf{L}$ describing the anisotropy in plastic properties of the single crystal, and $\sigma^T_{\langle 100 \rangle}$ is the tensile uniaxial stress in the $\langle 100 \rangle$ crystallographic directions, respectively.*

Proof Let us denote by $(\mathbf{x}, \mathbf{y}, \mathbf{z})$ the Cartesian coordinate system associated with the $\langle 100 \rangle$ crystal axes. Invariance requirements associated to the threefold symmetry of the $\langle 100 \rangle$ directions result in the fourth-order tensor $\mathbf{L}$ satisfying in the $(\mathbf{x}, \mathbf{y}, \mathbf{z})$ frame, the additional constraints:

$$L_{12} = L_{13} = L_{23};\ L_{11} = L_{22} = L_{33};\ L_{44} = L_{55} = L_{66} > 0, \tag{8.67}$$

so that in Voigt notations the transformed stress tensor $\widehat{\boldsymbol{\sigma}}$ is given by:

$$\begin{bmatrix} \widehat{\sigma}_{xx} \\ \widehat{\sigma}_{yy} \\ \widehat{\sigma}_{zz} \\ \widehat{\sigma}_{xz} \\ \widehat{\sigma}_{yz} \\ \widehat{\sigma}_{xy} \end{bmatrix} = \begin{bmatrix} L_{11} & L_{12} & L_{12} & 0 & 0 & 0 \\ L_{12} & L_{11} & L_{12} & 0 & 0 & 0 \\ L_{12} & L_{12} & L_{11} & 0 & 0 & 0 \\ 0 & 0 & 0 & L_{44} & 0 & 0 \\ 0 & 0 & 0 & 0 & L_{44} & 0 \\ 0 & 0 & 0 & 0 & 0 & L_{44} \end{bmatrix} \begin{bmatrix} s_{xx} \\ s_{yy} \\ s_{zz} \\ s_{xz} \\ s_{yz} \\ s_{xy} \end{bmatrix} \tag{8.68}$$

Note that

$$\widehat{\sigma}_{xx} + \widehat{\sigma}_{yy} + \widehat{\sigma}_{zz} = (L_{11} + 2L_{12})\left(s_{xx} + s_{yy} + s_{zz}\right) = 0;$$

i.e., for cubic symmetry, the transformed stress $\widehat{\boldsymbol{\sigma}} = \mathbf{L}\mathbf{s}$ is traceless.

Let us also recall that the parameters $\tilde{m}$ and $\tilde{h}$ involved in the Stewart and Cazacu [32] potential depend on k, a parameter associated with the tension–compression asymmetry of the matrix, and on the tensor $\mathbf{L}$. Therefore, due to the additional constraints of Eq. (8.67), it follows that these parameters become [see Eqs. (8.44)–(8.46)]:

$$\Phi = \Phi_3 = -\Phi_1/2, \text{ with } \Phi_1 = 2(L_{11} - L_{12})/3,$$

so that $\tilde{m}$ and the hydrostatic parameter $\tilde{h}$ take the form given by Eqs. (8.64)–(8.66).

Remarks

- In the absence of voids (f = 0), Eq. (8.63) reduces to the criterion for the fully dense crystal,

$$\tilde{\sigma}_e = \tilde{m}\sqrt{\sum_{i=1}^{3}\left(|\,\widehat{\sigma}_i\,| - k\widehat{\sigma}_i\right)^2} = \sigma^T_{\langle 100\rangle}. \tag{8.69}$$

- All the parameters in the plastic potential given by Eq. (8.63) have a clear physical significance, being related to the plastic properties of the fully dense crystal described by k, and the anisotropy coefficients L_{11}, L_{12}, L_{44}. In turn, these parameters can be determined from simple uniaxial tension and uniaxial compression tests along the [100], [110], and [111] directions, respectively.
- The tension–compression asymmetry of the fully dense single crystal is orientation-dependent.

For example, in any of the $\langle 100\rangle$ directions, the ratio $\sigma^T_{\langle 100\rangle}/\sigma^C_{\langle 100\rangle}$ is expressible solely in terms of the parameter k, yet the specific expression depends on the sign of Φ_1, i.e., on whether $L_{12} > L_{11}$ or $L_{12} < L_{11}$. Specifically, using Eq. (8.69), we obtain:

$$\text{if} \quad L_{12} > L_{11}\text{:}\ \frac{\sigma^T_{\langle 100\rangle}}{\sigma^C_{\langle 100\rangle}} = \sqrt{\frac{3k^2 - 2k + 3}{3k^2 + 2k + 3}}. \tag{8.70}$$

while

$$\text{if} \quad L_{12} < L_{11}\text{:}\ \frac{\sigma^T_{\langle 100\rangle}}{\sigma^C_{\langle 100\rangle}} = \sqrt{\frac{3k^2 + 2k + 3}{3k^2 - 2k + 3}}.$$

On the other hand, for the [110] direction, it is predicted that the tension–compression asymmetry ratio $\frac{\sigma^T_{\langle 110\rangle}}{\sigma^C_{\langle 110\rangle}}$ is expressible in terms of k and $\beta = (2L_{44}/3\Phi_1)$, the specific expression depending on the relative ordering of L_{12} and L_{11} and on the ratio of L_{12} to L_{44}, or alternatively on the range of β (see Eq. 8.66). Specifically, using Eq. (8.69), we obtain:

- For $\Phi_1 = 2(L_{11} - L_{12})/3 < 0$:

$$\text{if } \beta < -1/3\text{:}\ \frac{\sigma^T_{\langle 110\rangle}}{\sigma^C_{\langle 110\rangle}} = \sqrt{\frac{(3k^2 + 2k + 3) + 9\beta^2(1 - k)^2}{(3k^2 - 2k + 3) + 9\beta^2(1 + k)^2}}$$

while for

$$\text{if } -1/3 < \beta < 0 : \frac{\sigma^T_{\langle 110\rangle}}{\sigma^C_{\langle 110\rangle}} = \sqrt{\frac{(3k^2 + 4k + 3) + 9\beta^2(1 + k^2) + 12k\beta}{(3k^2 - 4k + 3) + 9\beta^2(1 + k^2) - 12k\beta}} \tag{8.71}$$

As will be shown later in Sect. 8.4.3, this orientation dependency of the tension–compression asymmetry of the single crystal has drastic implications on porosity evolution, and most importantly on the influence of the stress state on porosity evolution.

8.4.1.2 Creep Response of Porous Crystals

To model first-stage creep, the overstress-type approach (see for example Cristescu [9]) will be used. The constitutive hypotheses of the proposed model for the porous single crystal are as follows:

(H1) The creep stabilization boundary is considered to be of the form:

$$\Phi_c(\boldsymbol{\sigma}, f) = W^I, \tag{8.72}$$

where $\Phi_c(\boldsymbol{\sigma},f)$ is the yield function of the porous single crystal given by Eq. (8.63), and W^I denotes the irreversible work per unit volume.

(H2) Neglecting elasticity, the evolution of the strain, is given by:

$$\dot{\boldsymbol{\varepsilon}} = \eta\left\langle 1 - \frac{W^I}{\Phi_c(\boldsymbol{\sigma},f)}\right\rangle \frac{\partial \Phi_c(\boldsymbol{\sigma},f)}{\partial \boldsymbol{\sigma}}, \tag{8.73}$$

where η is a viscosity parameter and $\langle\ \rangle$ is the Macaulay bracket, i.e., $\langle x\rangle = (x+|x|)/2$ denotes the positive part of any number x; superposed dot on any variable denotes differentiation with respect to time. Therefore, the material undergoes irreversible deformation, i.e. $\dot{\boldsymbol{\varepsilon}} \neq 0$ only if the stress state is such that $\Phi_c(\boldsymbol{\sigma},f) > W^I$.

(H3) The evolution of the void volume fraction is obtained from conservation of mass for the matrix (fully dense crystal) so that

$$\dot{f} = \eta(1-f)\left\langle 1 - \frac{W^I}{\Phi_c(\boldsymbol{\sigma},f)}\right\rangle \frac{\partial \Phi_c(\boldsymbol{\sigma},f)}{\partial \sigma_m}. \tag{8.74}$$

Let us examine the creep response of the single crystal according to the constitutive model given by Eqs. (8.72)–(8.74). Let us assume that in the time interval (t_0, t^*), the stress is maintained constant, say, $\boldsymbol{\sigma}(t) = \boldsymbol{\sigma}^s = \text{constant}$. From the evolution law given by Eq. (8.73), we obtain:

$$\dot{W}^I = \boldsymbol{\sigma}:\dot{\boldsymbol{\varepsilon}} = \eta\left\langle 1 - \frac{W^I}{\Phi_c(\boldsymbol{\sigma},f)}\right\rangle \frac{\partial \Phi_c(\boldsymbol{\sigma},f)}{\partial \boldsymbol{\sigma}}:\boldsymbol{\sigma} \tag{8.75}$$

Assuming that the single crystal undergoes plastic deformation (i.e., the bracket in Eq. (8.75) is nonzero), by integration with respect to time of the above equation, we obtain:

$$1 - \frac{W^I(t_i)}{\Phi_c(\boldsymbol{\sigma}^s,f_{i-1})} = \left(1 - \frac{W^I(t_{i-1})}{\Phi_c(\boldsymbol{\sigma}^s,f_{i-1})}\right)\exp\left[-\eta\frac{(t_i - t_{i-1})}{\Phi_c(\boldsymbol{\sigma}^s,f_{i-1})}\left(\left.\frac{\partial \Phi_c(\boldsymbol{\sigma},f_{i-1})}{\partial \boldsymbol{\sigma}}\right|_{\boldsymbol{\sigma}=\boldsymbol{\sigma}^s}:\boldsymbol{\sigma}^s\right)\right] \tag{8.76}$$

where i is a counter for iterations, f_1 is the initial value of the porosity, i.e., $f_1 = f|_{t=t_0}$ and $W^I(t_0) = 0$. Further substitution of the right-hand side of Eq. (8.76) in the evolution law for plastic strain (Eq. 8.73) and integration leads to:

$$\boldsymbol{\varepsilon}(t_i) = \boldsymbol{\varepsilon}(t_{i-1})$$

$$+ \frac{\left(1 - \dfrac{W^I(t_{i-1})}{\Phi_c(\boldsymbol{\sigma}^s, f_{i-1})}\right) \left.\dfrac{\partial \Phi_c(\boldsymbol{\sigma}, f_{i-1})}{\partial \boldsymbol{\sigma}}\right|_{\boldsymbol{\sigma}=\boldsymbol{\sigma}^s} \left\{1 - \exp\left[-\eta \dfrac{(t_i - t_{i-1})}{\Phi_c(\boldsymbol{\sigma}^s, f_{i-1})} \cdot \left(\left.\dfrac{\partial \Phi_c(\boldsymbol{\sigma}, f_{i-1})}{\partial \boldsymbol{\sigma}}\right|_{\boldsymbol{\sigma}=\boldsymbol{\sigma}^s} : \boldsymbol{\sigma}^s\right)\right]\right\}}{\left(\left.\dfrac{\partial \Phi_c(\boldsymbol{\sigma}, f_{i-1})}{\partial \boldsymbol{\sigma}}\right|_{\boldsymbol{\sigma}=\boldsymbol{\sigma}^s} : \boldsymbol{\sigma}^s\right)} \tag{8.77}$$

Next, the porosity f is updated using Eq. (8.74). These equations will be used for simulating the creep response of porous single crystals.

To illustrate the influence of anisotropy and tension–compression asymmetry of the crystal on porosity evolution under multiaxial creep, theoretical predictions will be presented for loadings with the maximum principal stress aligned with the [100], [110] and [111] crystallographic directions, respectively. A total of five relative orientations between the loading frame and the $(\mathbf{x}, \mathbf{y}, \mathbf{z})$ frame associated with the $\langle 100 \rangle$ directions are considered (see Fig. 8.24). The crystal orientation,

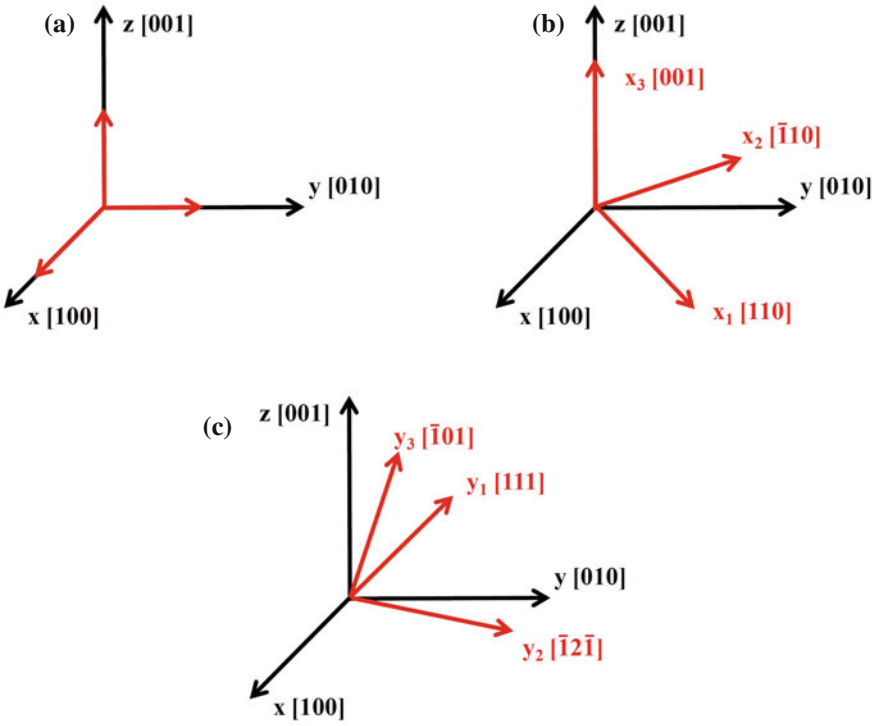

Fig. 8.24 Relative orientations of the (x, y, z) frame associated with the fcc cubic crystal axes and the frame associated with the principal stress directions for all the loading cases analyzed: **a** maximum principal stress along [100]; **b** maximum principal stress along [110] direction; **c** maximum principal stress along the [111] direction. For the case (**b**) and (**c**), two additional secondary orientations are also considered

Table 8.3 Loadings analyzed: values of the principal values of the stress tensor $\boldsymbol{\sigma}/\sigma_T$, mean stress σ_m, sign of the third-invariant, J_3 for each crystal orientation

σ_1	σ_2	σ_3	σ_m	Sign of J_3 (Lode parameter)	Orientation (see Fig. 8.24)
5.4	2.16	2.16	3.24	$J_3 > 0$ ($\mu = -1$)	
5.11	3.24	1.37	3.24	$J_3 = 0$ ($\mu = 0$)	$\langle$O1$\rangle$
5.11	1.37	3.24	3.24	$J_3 = 0$ ($\mu = 0$)	$\langle$O2$\rangle$
4.32	4.32	1.08	3.24	$J_3 < 0$ ($\mu = 1$)	$\langle$O1$\rangle$
4.32	1.08	4.32	3.24	$J_3 < 0$ ($\mu = 1$)	$\langle$O2$\rangle$

designated as "orientation 100" is such that the loading axes are aligned with the $\langle 100 \rangle$ directions. For the case when the maximum principal stress is aligned with the [110] direction, the predicted response for two possible relative orientations designated as "orientation 110$\langle$O1$\rangle$" and "orientation 110$\langle$O2$\rangle$" are investigated (see Fig. 8.24b with $\langle$O1$\rangle$ corresponding to principal stresses along $\mathbf{x}_1$, $\mathbf{x}_2$, $\mathbf{x}_3$ while $\langle$O2$\rangle$ corresponds to principal stresses along [110], [001], $[1\bar{1}0]$). The purpose of considering the secondary orientation O2 is to assess the influence of anisotropy, namely the difference in response depending whether a given value of the eigenstress corresponds to an eigenvector along [110] or $[\bar{1}10]$. Similarly, for loadings with maximum principal stress along [111], the "orientation 111$\langle$O1$\rangle$" and "orientation 111$\langle$O2$\rangle$" are discussed (see Fig. 8.24c with $\langle$O1$\rangle$ corresponding to principal stresses along $\mathbf{y}_1$, $\mathbf{y}_2$, $\mathbf{y}_3$ while $\langle$O2$\rangle$ corresponds to principal stresses along [111], $[\bar{1}01]$, $[1\bar{2}1]$).

For a given crystal orientations, creep calculations are done using the model for loadings corresponding to a fixed value of the stress triaxiality T and the same mean stress σ_m. We recall that

$$T = \frac{\sigma_m}{\sqrt{3J_2}}$$

Furthermore, to investigate the effect of the third-invariant J_3 for any given crystal orientation, calculations are done for shear loadings $J_3 = 0$ and axisymmetric loadings at $J_3 > 0$ or $J_3 < 0$, respectively. The values of the principal stresses for all the loadings considered in the illustrative examples are given in Table 8.3. Alternatively, the stress states analyzed can be defined in terms of the Lode parameter μ (see Chap. 4). Namely, for each crystal orientation, the stress paths considered correspond to the same T and σ_m; what is varied between calculations is μ, namely $\mu = 0$ (shear), $\mu = -1$ (axisymmetric loadings at $J_3 > 0$) or $\mu = 1$ (axisymmetric loadings at $J_3 < 0$), respectively.

8.4.2 Creep of Fcc Single Crystals

When modeling fcc crystals, it is generally assumed that the tension–compression asymmetry in plastic deformation is negligible (see Chap. 3). Therefore, in the expression of the plastic potential given by Eq. (8.63), the parameter k should be set to zero.

Plastic potential for a porous fcc crystal

Using the definitions in Sect. 8.4.1.1, it can be easily seen that in the crystal frame $(\mathbf{x}, \mathbf{y}, \mathbf{z})$, the plastic potential of a porous fcc crystal is of the form:

$$\varphi(\boldsymbol{\sigma}, f) = \frac{2}{3\Phi_1^2} \sum_{i=1}^{3} \left(\frac{\widehat{\sigma}_i}{\sigma^T_{\langle 100 \rangle}} \right)^2 + 2f \cosh \left(\frac{3\sqrt{5}\sigma_m}{2\sigma^T_{\langle 100 \rangle} \sqrt{2 + 3/\beta^2}} \right) - \left(1 + f^2\right) \quad (8.78)$$

with parameters β and Φ_1 as defined in Eq. (8.66); and $\sigma^T_{\langle 100 \rangle}$ the tensile uniaxial stress in the $\langle 100 \rangle$ crystallographic directions, respectively.

Remarks

- For $k = 0$, the effective stress of the fully dense crystal $\tilde{\sigma}_e$, given by Eq. (8.69), becomes:

$$\tilde{\sigma}_e = \sqrt{\frac{3}{2}\left[\left(s_{xx}^2 + s_{yy}^2 + s_{zz}^2\right) + 2\beta^2\left(s_{xy}^2 + s_{xz}^2 + s_{yz}^2\right)\right]} = \sigma^T_{\langle 100 \rangle}. \quad (8.79)$$

  (see also Srivastava et al. [31]).

- All the parameters involved in the potential for a porous fcc crystal given by Eq. (8.78) are related to the plastic properties of the matrix (i.e., the fully dense crystal) described by the coefficients L_{11}, L_{12} and L_{44} (see Eq. 8.66). Given that the effective stress of the fully dense crystal is homogeneous of degree one in stresses, without loss of generality one of these coefficients can be set equal to unity; for example, we can take $L_{11} = 1$. Moreover, the plastic response depends only on the ratio of L_{12} to L_{44}, or alternatively on β (see Eq. 8.66).
- For isotropy, $L_{12} = 0$ and $L_{44} = 1$ so that the plastic potential given by Eq. (8.78) reduces to the Gurson [12] stress potential (see Chap. 7).

In the next subsection, we present the effects of anisotropy and path-dependency on the yielding of the porous fcc crystal according to the potential given by Eq. (8.78) for loadings with the maximum principal stress aligned with the [100], [110], and [111] crystallographic directions, respectively. To simplify the writing, in all the expressions we will denote the matrix tensile yield stress in any of the $\langle 100 \rangle$ direction $\sigma^T_{\langle 100 \rangle}$ by σ_T.

8.4.2.1 Effect of the Loading Orientation and Loading Path on the Plastic Response of the Porous Fcc Crystal

Orientation 100

Let us first consider loadings such that the principal directions of stress are along the cubic axes **x**, **y**, and **z** (see Fig. 8.24a). For such loadings, the only stress components different from zero are $\sigma_{xx}, \sigma_{yy}, \sigma_{zz}$ so the potential for the porous fcc crystal given by Eq. (8.78) takes the form:

$$\varphi(\boldsymbol{\sigma},f) = \frac{3\left(s_{xx}^2 + s_{yy}^2 + s_{zz}^2\right)}{2\sigma_T^2} + 2f\cosh\left(\frac{\sqrt{5}\left(\sigma_{xx}+\sigma_{yy}+\sigma_{zz}\right)}{2\sigma_T\sqrt{2+3/\beta^2}}\right) - \left(1+f^2\right) \tag{8.80}$$

Therefore for such loadings, there is no influence of the third-invariant J_3 on yielding of the porous crystal. Those predictions are consistent with the results of F. E. unit-cell model calculations where the single crystal was considered to be governed by the TBH model, i.e., the tension–compression asymmetry in plastic deformation was also neglected (e.g., see Srivastava and Needleman [30]).

On the other hand, for the 110 and 111 crystal orientations (Fig. 8.24), the anisotropy of the matrix plays a crucial role. In the following, we will analyze the yielding response according to the model for each of these orientations separately.

Orientation 110

If the porous fcc crystal is loaded such that the principal directions of the applied stress are along the $[110]$, $[\bar{1}10]$, and $[001]$ crystallographic directions (see Fig. 8.24b), i.e.:

$$\boldsymbol{\sigma} = \sigma_1(\mathbf{x_1}\otimes\mathbf{x_1}) + \sigma_2(\mathbf{x}_2\otimes\mathbf{x}_2) + \sigma_3(\mathbf{x}_3\otimes\mathbf{x}_3) \tag{8.81}$$

with $\mathbf{x}_i$ oriented with respect to the cubic axes $(\mathbf{x},\mathbf{y},\mathbf{z})$ as:

$$\mathbf{x}_1 = \left(\frac{1}{\sqrt{2}},\frac{1}{\sqrt{2}},\ 0\right);\ \mathbf{x}_2 = \left(\frac{-1}{\sqrt{2}},\frac{1}{\sqrt{2}},\ 0\right);\ \mathbf{x}_3 = (0,\ 0,\ 1). \tag{8.82}$$

Relative to the reference frame $(\mathbf{x},\mathbf{y},\mathbf{z})$, the only nonzero components of the applied stress tensor $\boldsymbol{\sigma}$ are: $\sigma_{xx} = \sigma_{yy} = \frac{\sigma_1+\sigma_2}{2}, \sigma_{zz} = \sigma_3$, and $\sigma_{xy} = (\sigma_1 - \sigma_2)/2$, so the potential of the porous crystal $\varphi(\boldsymbol{\sigma},f)$ (see Eq. 8.78) takes the form:

$$\varphi(\boldsymbol{\sigma},f)=\frac{9}{4}\left(\frac{s_3}{\sigma_T}\right)^2+\frac{3\beta^2}{4}\left(\frac{s_1-s_2}{\sigma_T}\right)^2+2f\cosh\left(\frac{\sqrt{5}\left(\sigma_{xx}+\sigma_{yy}+\sigma_{zz}\right)}{2\sigma_T\sqrt{2+3/\beta^2}}\right)-\left(1+f^2\right) \tag{8.83}$$

In particular,

- For axisymmetric loadings at $J_3>0$, (i.e., in Eq. (8.81): $\sigma_1>\sigma_2=\sigma_3$ so: $s_1>0$, $s_1=-2s_2=-2s_3$, $J_2=3s_1^2/4$, and $J_3\geq 0$):

$$\varphi(\boldsymbol{\sigma},f)=\left(3\beta^2+1\right)\frac{3J_2}{4\sigma_T^2}+2f\cosh\left(\frac{3\sqrt{5}\sigma_m}{2\sigma_T\sqrt{2+3/\beta^2}}\right)-\left(1+f^2\right) \tag{8.84}$$

- For loadings at $J_3=0$ $\langle$O1$\rangle$ (i.e., in Eq. (8.81): $s_1=-s_3$ and $s_2=0$, so $J_2=s_1^2$), the criterion writes:

$$\varphi(\boldsymbol{\sigma},f)=\left(\beta^2+3\right)\frac{3J_2}{4\sigma_T^2}+2f\cosh\left(\frac{3\sqrt{5}\sigma_m}{2\sigma_T\sqrt{2+3/\beta^2}}\right)-\left(1+f^2\right) \tag{8.85}$$

- For loadings at $J_3=0$ $\langle$O2$\rangle$, (i.e., in Eq. (8.81): $s_1=-s_2$ and $s_3=0$, so $J_2=s_1^2$), we have:

$$\varphi(\boldsymbol{\sigma},f)=\frac{3\beta^2J_2}{\sigma_T^2}+2f\cosh\left(\frac{3\sqrt{5}\sigma_m}{2\sigma_T\sqrt{2+3/\beta^2}}\right)-\left(1+f^2\right) \tag{8.86}$$

- For axisymmetric loadings at $J_3<0$ $\langle$O1$\rangle$ (i.e., in Eq. (8.81) $s_1=s_2$ and $s_3=-2s_1$), the criterion writes:

$$\varphi(\boldsymbol{\sigma},f)=\frac{3J_2}{\sigma_T^2}+2f\cos h\left(\frac{3\sqrt{5}\sigma_m}{2\sigma_T\sqrt{2+3/\beta^2}}\right)-\left(1+f^2\right) \tag{8.87}$$

- For axisymmetric loadings at $J_3<0$ $\langle O2\rangle$ (i.e. in Eq. (8.81), $s_1=s_3$ and $s_2=-2s_1$):

$$\varphi(\boldsymbol{\sigma},f)=\left(3\beta^2+1\right)\frac{3J_2}{4\sigma_T^2}+2f\cosh\left(\frac{3\sqrt{5}\sigma_m}{2\sigma_T\sqrt{2+3/\beta^2}}\right)-\left(1+f^2\right) \tag{8.88}$$

Note that according to the criterion for loadings at the same triaxiality T and mean stress σ_m (i.e., same J_2 and σ_m):

- Only for [110] loadings at $J_3>0$ and [110]$\langle O2\rangle$ loadings at $J_3<0$ [see Eqs. (8.84) and (8.88)], the mechanical response is the same. *For all other loadings, the response in the* O1 *and* O2 *orientations is markedly different*.
- The response for [110]$\langle O1\rangle$ axisymmetric loadings at $J_3<0$ is the same as for [100] orientation [see Eqs. (8.87) and (8.80)].

Orientation 111

Let us consider that the crystal is loaded such that the principal directions of the applied stress are along the [111], [$\bar{1}2\bar{1}$], and [$\bar{1}01$] crystallographic directions (see Fig. 8.24c), i.e.,

$$\boldsymbol{\sigma}=\sigma_1(\mathbf{y_1}\otimes\mathbf{y_1})+\sigma_2(\mathbf{y}_2\otimes\mathbf{y}_2)+\sigma_3(\mathbf{y}_3\otimes\mathbf{y}_3) \tag{8.89}$$

with $\mathbf{y}_i$ oriented with respect to the cubic axes $(\mathbf{x},\mathbf{y},\mathbf{z})$ as

$$\mathbf{y}_1=\left(1/\sqrt{3},1/\sqrt{3},1/\sqrt{3}\right);\ \mathbf{y}_2=\left(-1/\sqrt{6},2/\sqrt{6},-1/\sqrt{6}\right);$$
$$\mathbf{y}_3=\left(-1/\sqrt{2},0,1/\sqrt{2}\right)$$

Relative to the crystal frame $(\mathbf{x},\mathbf{y},\mathbf{z})$, the only nonzero components of the applied stress tensor $\boldsymbol{\sigma}$ are:

$$\begin{aligned}\sigma_{xx}=\sigma_{zz}&=\frac{2\sigma_1+\sigma_2+3\sigma_3}{6},\ \sigma_{yy}=\frac{\sigma_1+2\sigma_2}{3},\\ \sigma_{xy}=\sigma_{yz}&=\frac{\sigma_1-\sigma_2}{3},\ \sigma_{xz}=\frac{2\sigma_1+\sigma_2-3\,\sigma_3}{6}.\end{aligned} \tag{8.90}$$

so that the potential $\varphi(\boldsymbol{\sigma},f)$ of the porous crystal takes the form:

$$\varphi(\boldsymbol{\sigma},f)=\left(\frac{s_3-s_2}{2\sigma_T}\right)^2+\frac{\beta^2}{4\sigma_T^2}\left(8s_1^2+3s_2^2+3s_3^2-2s_2s_3\right)+2f\cosh\left(\frac{\sqrt{5}\left(\sigma_{xx}+\sigma_{yy}+\sigma_{zz}\right)}{2\sigma_T\sqrt{2+3/\beta^2}}\right)-\left(1+f^2\right). \tag{8.91}$$

It is worth noting that according to Eq. (8.91), the plastic response should be invariant to the transformation: $(\sigma_1,\sigma_2,\sigma_3)\rightarrow(\sigma_1,\sigma_3,\sigma_2)$. Thus, the mechanical response of the porous single crystal for the $111\langle O1\rangle$ loadings is the same as for the $111\langle O2\rangle$ loadings.

- For axisymmetric loadings at $J_3>0$, (i.e., in Eq. (8.91): $\sigma_1>\sigma_2=\sigma_3$ so: $s_1>0$, $s_1=-2s_2=-2s_3$, $J_2=\frac{3}{4}s_1^2$), the criterion writes:

$$\varphi(\boldsymbol{\sigma},f)=\frac{3\beta^2J_2}{\sigma_T^2}+2f\cosh\left(\frac{3\sqrt{5}\sigma_m}{2\sigma_T\sqrt{2+3/\beta^2}}\right)-\left(1+f^2\right) \tag{8.92}$$

- For loadings at $J_3=0$, (e.g., in Eq. (8.91): $s_1=-s_3$ and $s_2=0$, so $J_2=s_1^2$), the criterion writes:

$$\varphi(\boldsymbol{\sigma},f)=\left(1+11\beta^2\right)\frac{J_2}{4\sigma_T^2}+2f\cosh\left(\frac{3\sqrt{5}\sigma_m}{2\sigma_T\sqrt{2+3/\beta^2}}\right)-\left(1+f^2\right) \tag{8.93}$$

- For axisymmetric loadings at $J_3<0$ (e.g., in Eq. (8.91), $s_1=s_2$ and $s_3=-2s_1$), the criterion writes:

$$\varphi(\boldsymbol{\sigma},f)=\left(1+3\beta^2\right)\frac{3J_2}{4\sigma_T^2}+2f\cosh\left(\frac{3\sqrt{5}\sigma_m}{2\sigma_T\sqrt{2+3/\beta^2}}\right)-\left(1+f^2\right) \tag{8.94}$$

Note that according to the criterion for loadings at the same triaxiality and mean stress σ_m (i.e., same J_2 and σ_m):

- The mechanical response for [111] axisymmetric loadings at $J_3>0$ and [110] $\langle O2\rangle$ loadings at $J_3=0$ is the same [see Eqs. (8.92) and (8.86)].
- The mechanical response for [111] axisymmetric loadings at $J_3<0$, [110] axisymmetric loadings at $J_3>0$, and $[110]\langle O2\rangle$ axisymmetric loadings at $J_3<0$ is the same [see Eqs. (8.94), (8.84), and (8.88)].

8.4.2.2 Porosity Evolution for Various Loading Paths and Crystal Orientation

In the following, we illustrate the creep model [see Eqs. (8.72)–(8.75)] predictions of porosity evolution for a fcc crystal with $L_{11} = 1$, $L_{12} = 1.60$, $L_{44} = 0.25$. For this crystal, the matrix uniaxial tensile yield stress in the [111] direction is larger than in the [100] direction (see also Eq. 8.79). The 3-D creep loadings considered are given in Table 8.3. The initial porosity is taken to be the same ($f_0 = 0.001$).

As already mentioned, for any given crystal orientation the effect of the third-invariant J_3 on porosity evolution is assessed by comparing the results for creep calculations corresponding to $J_3 = 0$ (shear) and axisymmetric loadings at $J_3 > 0$ or $J_3 < 0$, respectively Note that such comparisons are meaningful, given that for each loading path the imposed mean stress σ_m, and stress triaxiality T is the same (see Table 8.3).

For the 100 crystal orientation, in Fig. 8.25a, b are shown the evolution of the relative void volume fraction f/f_0 with the irreversible work per unit volume W^I, and the evolution of W^I with time, respectively. Since for the [100] crystal orientation, the plastic potential of the porous fcc crystal, $\varphi(\boldsymbol{\sigma}, f)$, does not depend on J_3 (see Eq. 8.80), it is predicted that the irreversible work, W^I and the porosity evolution are also independent of J_3 (see Fig. 8.25).

On the other hand, for the 110 crystal orientation the predicted mechanical response is strongly anisotropic, as evidenced by comparing the respective evolution of the irreversible work and porosity for $110\langle O1\rangle$ loadings with those for $110\langle O2\rangle$ loadings (see Fig. 8.26). Obviously, as already mentioned, the results for the $110\langle O1\rangle$ and $110\langle O2\rangle$ at $J_3 > 0$ must coincide, since the difference in these loadings corresponds to interchanging σ_2 and σ_3 and for axisymmetric loadings such that $J_3 > 0$, $\sigma_2 = \sigma_3$. Therefore, to limit the amount of text in Fig. 8.26, the results for $110\langle O1\rangle$ and $110\langle O2\rangle$ at $J_3 > 0$ are marked as $J_3 > 0$.

Note that irrespective of the imposed loadings (i.e., shear loadings or loadings at $J_3 < 0$), the rate of void growth is faster for $110\langle O2\rangle$ orientation than for the $110\langle O1\rangle$ orientation.

Note also that the effect of J_3 is very strong. The fastest rate of void growth is for loadings corresponding to $J_3 = 0$ (shear) in the O2 orientation, followed by loadings at $J_3 > 0$ and $J_3 < 0\langle O2\rangle$, and $J_3 = 0\langle O1\rangle$. The slowest rate of void growth corresponds to loadings at $J_3 < 0\langle O1\rangle$. This is consistent with Eqs. (8.84)–(8.88) which describe the effect of J_3 on yielding for the respective orientations and loadings. It is also to be noted the correlation between the energy dissipated (W^I) and void growth: the lower is the plastic energy dissipated; the faster is the void growth rate. Furthermore, it important to note that the model accounts for creep saturation, which occurs at different times and levels of plastic work depending on the type of creep loading and the orientation considered.

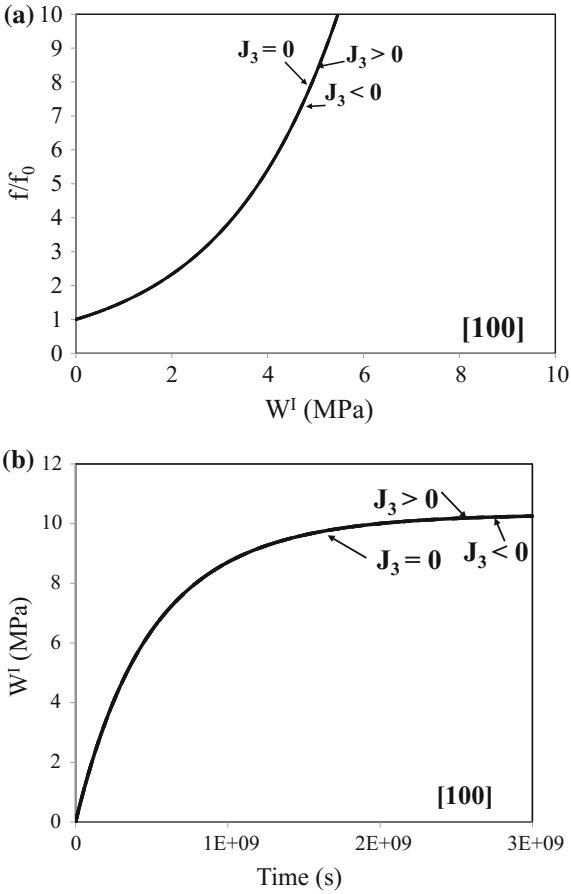

Fig. 8.25 **a** Evolution of the relative void volume fraction f/f_0 as a function of the irreversible work, W^I and **b** evolution of the irreversible work, W^I, with time for creep loadings along the crystallographic axes [100] corresponding to either $J_3 < 0$, $J_3 = 0$, or $J_3 > 0$ and the same triaxiality $T = 1$

According to Eq. (8.91), the results for $111\langle O1\rangle$ and $111\langle O2\rangle$ loadings should be the same. However, since for the 111 loadings, the potential $\varphi(\boldsymbol{\sigma},f)$ [see Eqs. (8.91)–(8.94)] depends on the third-invariant J_3, the plastic energy dissipated (see Fig. 8.27b), and consequently, the porosity evolution (see Fig. 8.27a) is sensitive to the third-invariant. The influence of J_3 is less pronounced than that predicted for the [110] loadings. The fastest rate of void growth is for loadings corresponding to $J_3 > 0$, while the slowest rate of void growth is for loadings corresponding to $J_3 < 0$.

The predictions of the model for all five relative orientations between the loading axes and crystal axes corresponding to creep loadings at the same mean stress, and same triaxiality ($T = 1$) for $\mu = -1$ ($J_3 > 0$), $\mu = 0$ ($J_3 = 0$) and $\mu = 1$ ($J_3 < 0$) are shown in Fig. 8.28.

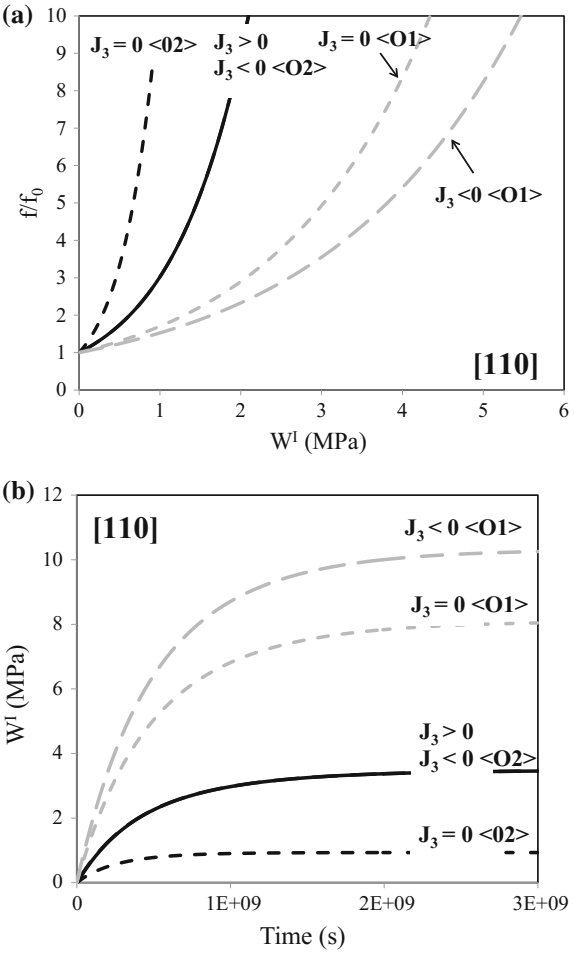

Fig. 8.26 **a** Evolution of the relative void volume fraction f/f_0 as a function of the irreversible work, W^I; **b** evolution of the irreversible work, W^I, with time for creep loadings with the major principal stress along [110] corresponding to either $J_3 < 0$, $J_3 = 0$, or $J_3 > 0$ and the same triaxiality $T = 1$

As a general observation, it is worth noting that the response is markedly different in the 100, 110, and 111 crystal orientations (compare also the expressions of the plastic potential for the five relative orientations of the loading axes and crystal axes [Eqs. (8.80)–(8.94)]). The fastest rate of void growth corresponds to loading at $J_3 = 0$ for the $110\langle O2\rangle$ orientation (and 111 $J_3 > 0$), while the slowest rate of void growth corresponds to loading at $J_3 < 0$ in the primary orientation $110\langle O1\rangle$ and 100 (all loadings). The rate of void growth for loading at $J_3 = 0$ in the 111 orientation is faster than that for shear loadings in the $110\langle O1\rangle$, but slower than for shear loadings in the $110\langle O2\rangle$ orientation.

The fact that for certain orientations and loadings, we have the same creep response was explained in Sect. 8.4.1.1.

While results have been presented only for one triaxiality value ($T = 1$), the conclusions are the same for any triaxiality [see discussion in Sect. 8.4.2.1 and

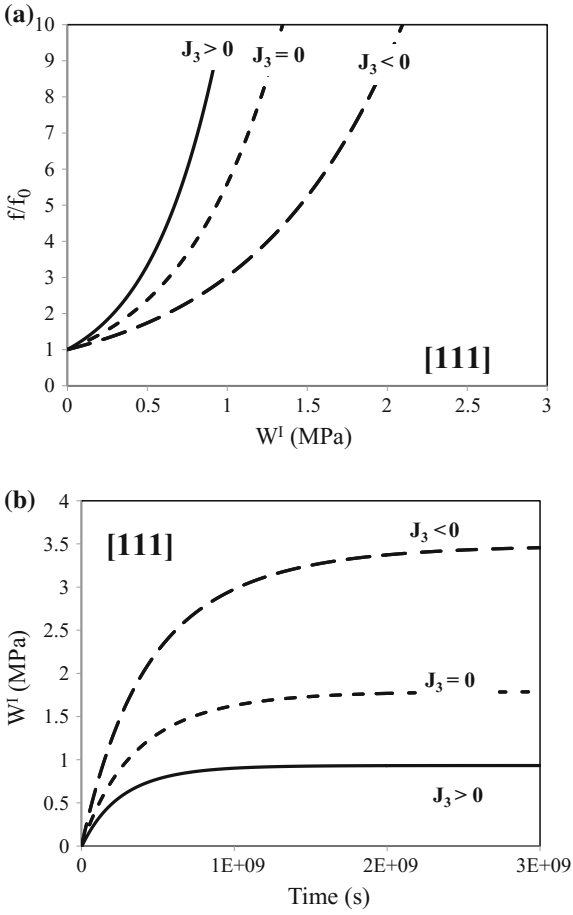

Fig. 8.27 **a** Evolution of the relative void volume fraction f/f_0 as a function of the irreversible work, W^I and **b** evolution of the irreversible work, W^I, with time for creep loadings with the major principal axis along [111] corresponding to either $J_3 < 0$, $J_3 = 0$, or $J_3 > 0$ and the same triaxiality $T = 1$

Eqs. (8.80)–(8.94)]. It means that for an fcc porous crystal, the third-invariant has a strong effect on the evolution of porosity.

8.4.3 *Creep of Single Crystals with Tension–Compression Asymmetry*

In this section, the effect of the tension–compression asymmetry of the matrix (fully dense crystal) on the creep response of the porous single crystal will be investigated. The same crystal orientations and loadings are considered (see Fig. 8.24 for the five crystal orientations and Table 8.3 for the loading conditions).

As discussed in Sect. 8.4.1.1, the tension–compression asymmetry ratio of the matrix is orientation-dependent, i.e. depends on the relative ordering of the values

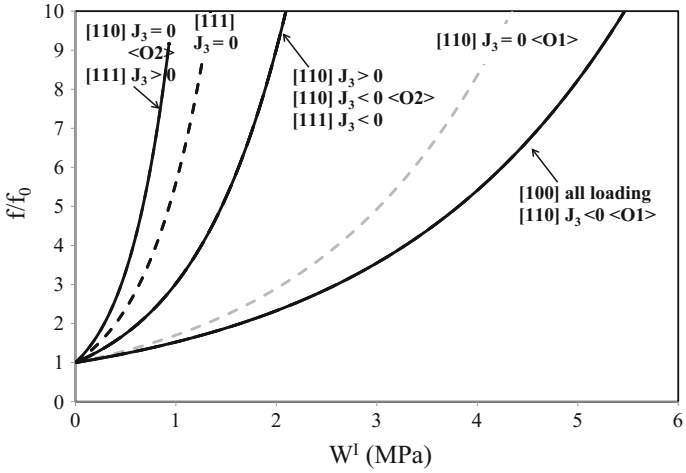

Fig. 8.28 Effect of crystal orientation on porosity evolution for creep loadings corresponding to either $J_3 < 0$, $J_3 = 0$ (shear), or $J_3 > 0$ and the same triaxiality $T = 1$. Note that due to the symmetries in plastic flow of the matrix, the response is the same for certain orientations

of the coefficients of anisotropy. Analytical results will be presented for the case $\Phi_1 < 0$ ($L_{12} > L_{11}$), while illustrative examples will be given also for crystals with anisotropy coefficients such that $L_{12} < L_{11}$. Detailed calculations and explanations of the combined effects of anisotropy and tension–compression asymmetry on the plastic response of the porous crystal will be given for the 100 and 111 orientations (Fig. 8.24a, c), the focus being on putting in evidence the importance of consideration of the matrix tension–compression asymmetry. Since we are interested in assessing stress path effects on the rate of void growth, only loadings at positive triaxialities ($\sigma_m > 0$) are considered.

8.4.3.1 Effect of Anisotropy and Loading Path on the Plastic Response of Porous Crystals with tension–compression Asymmetry

Orientation 100

Let us first consider loadings such that the principal directions of stress are along the cubic axes **x**, **y**, and **z** (see Fig. 8.24a for the definition of the 100 orientation). As mentioned, only loadings at $\sigma_m > 0$ are considered, and the following stress paths are analyzed: (a) loadings such that $s_{yy} = s_{zz} < s_{xx}$, which correspond to $J_3 > 0$; (b) $s_{xx} = -s_{yy}; s_{zz} = 0$, which correspond to $J_3 = 0$; and (c) loadings such that $s_{yy} = s_{zz} > s_{xx}$ correspond to $J_3 < 0$. From Eq. (8.63), it follows that for a single crystal with $\Phi_1 < 0$ ($L_{12} > L_{11}$) the potential is of the form:

$$\Phi_c(\boldsymbol{\sigma},f)=\begin{cases}\left(\dfrac{3k^2-2k+3}{3k^2+2k+3}\right)\dfrac{3J_2}{\sigma_T^2}+2f\cosh\left(\dfrac{3\sigma_m}{\tilde{h}\sigma_T}\right)-1-f^2, & \text{if } J_3<0,\\ \left(\dfrac{3k^2+3}{3k^2+2k+3}\right)\dfrac{3J_2}{\sigma_T^2}+2f\cosh\left(\dfrac{3\sigma_m}{\tilde{h}\sigma_T}\right)-1-f^2, & \text{if } J_3=0,\\ \dfrac{3J_2}{\sigma_T^2}+2f\cosh\left(\dfrac{3\sigma_m}{\tilde{h}\sigma_T}\right)-1-f^2, & \text{if } J_3>0.\end{cases} \tag{8.95}$$

In the above equations, $J_2=\frac{1}{2}\left(s_{xx}^2+s_{yy}^2+s_{zz}^2\right)$, $\sigma_m=\left(\sigma_{xx}+\sigma_{yy}+\sigma_{zz}\right)/3$, and $J_3=s_{xx}s_{yy}s_{zz}$.

Note that in contrast to the case when the matrix tension–compression asymmetry is neglected (see Eq. 8.80), even for loadings such that the stress eigenvectors are along the crystallographically equivalent $\langle 100\rangle$ directions, the response of the porous single crystal will depend on the stress path, in particular on the sign of J_3.

On the other hand, as discussed in Sect. 8.4.2,

$$\text{if } L_{12}>L_{11}\text{:}\frac{\sigma^T_{\langle 100\rangle}}{\sigma^C_{\langle 100\rangle}}=\sqrt{\frac{3k^2-2k+3}{3k^2+2k+3}}.$$

Therefore, if $\sigma_T=\sigma^T_{\langle 100\rangle}>\sigma^C_{\langle 100\rangle}$ then among the loading paths considered, maximum plastic dissipation will occur for axisymmetric loadings at $J_3<0$, the reverse holds true if $\sigma_T=\sigma^T_{\langle 100\rangle}<\sigma^C_{\langle 100\rangle}$ (see also the illustrative examples in the next section).

Orientation 111

Let us first consider that the crystal is loaded such that the principal directions of the applied stress are along the [111], $[\bar{1}2\bar{1}]$, and $[\bar{1}01]$ crystallographic directions, i.e., $\langle O1\rangle$ orientation [see Fig. 8.24c and Eq. (8.89)]. Relative to the crystal frame $(\mathbf{x},\mathbf{y},\mathbf{z})$, the components of the transformed stress $\widehat{\boldsymbol{\sigma}}$ (see Eq. 8.68) are:

$$\widehat{\sigma}_{xx}=\widehat{\sigma}_{zz}=\Phi_1(\sigma_3-\sigma_2)/4,\quad \widehat{\sigma}_{yy}=-2\widehat{\sigma}_{xx},$$
$$\widehat{\sigma}_{xy}=\widehat{\sigma}_{yz}=L_{44}(\sigma_1-\sigma_2)/3,\quad \widehat{\sigma}_{xz}=L_{44}(2\sigma_1+\sigma_2-3\sigma_3)/6.$$

For a single crystal with matrix such that $\Phi_1<0$ ($L_{12}>L_{11}$), for axisymmetric loadings at $J_3>0$: $\sigma_1>\sigma_2=\sigma_3$ calculation of the eigenvalues $\widehat{\sigma}_1$, $\widehat{\sigma}_2$, $\widehat{\sigma}_3$ and further substitution in the expression of the plastic potential given by Eq. (8.63), leads to

$$\Phi_c(\boldsymbol{\sigma},f)=\beta^2\left(\frac{3k^2-2k+3}{3k^2+2k+3}\right)\frac{3J_2}{\sigma_T^2}+2f\cosh\left(\frac{3\sigma_m}{\tilde{h}\sigma_T}\right)-1-f^2 \tag{8.96}$$

As discussed, for the loadings at $J_3 > 0$, the response for the $111\langle O1\rangle$ and $111\langle O2\rangle$ orientations must coincide, since for such loadings, $\sigma_2 = \sigma_3$ for both $\langle O1\rangle$ and $\langle O2\rangle$ crystal orientations.

On the other hand, for shear loadings ($J_3 = 0$), there is a marked difference in response between the $\langle O1\rangle$ and $\langle O2\rangle$ orientations.

Moreover, the difference between the response in the $\langle O1\rangle$ and $\langle O2\rangle$ orientations depends on both the matrix anisotropy, namely on the relative ordering of L_{12} and L_{11}, and on the ratio of L_{12} to L_{44} [i.e., the sign of Φ_1 and β (see Eq. (8.66))].

For example, for a single crystal with matrix characterized by $\Phi_1 < 0$ and $\beta < -1/3$

- For loadings at $J_3 = 0$ $\langle O1\rangle$ which corresponds to: $s_1 = -s_3$ and $s_2 = 0$ (see Eq. (8.89)), the plastic potential writes:

$$\Phi_c(\boldsymbol{\sigma}, f) = \frac{J_2}{8\sigma_T^2(3k^2+2k+3)}\left[\begin{array}{l} 6(1+k^2)(1+11\beta^2) \\ +2k(1+5\beta)\left(1+5\beta+\sqrt{32\beta^2+(5\beta-3)^2}\right)\end{array}\right] + 2f\cosh\left(\frac{3\sigma_m}{\tilde{h}\sigma_T}\right) - 1 - f^2 \tag{8.97}$$

- For loadings at $J_3 = 0$ $\langle O2\rangle$ which corresponds to: $s_1 = -s_2$ and $s_3 = 0$ (see Eq. (8.89)), the expression of the potential is:

$$\Phi_c(\boldsymbol{\sigma}, f) = \frac{J_2}{8\sigma_T^2(3k^2+2k+3)}\left[\begin{array}{l} 6(1+k^2)(1+11\beta^2) \\ +2k(1-\beta)\left(1-\beta-\sqrt{128\beta^2+(3+\beta)^2}\right)\end{array}\right] + 2f\cosh\left(\frac{3\sigma_m}{\tilde{h}\sigma_T}\right) - 1 - f^2 \tag{8.98}$$

Note that only for $k = 0$, the response in shear ($J_3 = 0$) for the $111\langle O1\rangle$ and $111\langle O2\rangle$ crystal orientations coincide, and both Eqs. (8.97) and (8.98) reduce to Eq. (8.93).

Also, the plastic response for axisymmetric loadings at $J_3 < 0$ is different in the $111\langle O1\rangle$ and $111\langle O2\rangle$ crystal orientations. For the $111\langle O1\rangle$ orientation the plastic potential writes:

$$\Phi_c(\boldsymbol{\sigma},f)=\frac{3J_2\left[3\left(1+3\beta^2\right)\left(1+k^2\right)+4k(1+3\beta)\right]}{4\sigma_T^2(3k^2+2k+3)}+2f\cosh\left(\frac{3\sigma_m}{\tilde{h}\sigma_T}\right)-1-f^2 \tag{8.99}$$

while for the $111\langle O2\rangle$ orientation,

$$\Phi_c(\boldsymbol{\sigma},f)=\frac{3J_2}{8\sigma_T^2(3k^2+2k+3)}\left[\begin{array}{l}6\left(1+k^2\right)\left(1+3\beta^2\right)\\ -2k(\beta+1)\left(-\beta-1+\sqrt{(3-\beta)^2+32\beta^2}\right)\end{array}\right]+2f\cosh\left(\frac{3\sigma_m}{\tilde{h}\sigma_T}\right)-1-f^2 \tag{8.100}$$

If the tension–compression asymmetry is neglected ($k = 0$), the response for axisymmetric loadings at $J_3<0$ in the $111\langle O1\rangle$ and $111\langle O2\rangle$ crystal orientations coincide, and both Eqs. (8.99) and (8.100) reduce to Eq. (8.94).

For the crystal orientation $110\langle O1\rangle$, the effect of J_3 is very pronounced, and the response in the O1 and O2 orientations is markedly different. The expressions of the porous plastic potential for the loadings considered can be also obtained in closed form, by using the transformation of coordinates given by Eq. (8.81) and conducting the analysis of the sign of the principal values of the transformed tensor $\widehat{\sigma}_1$, $\widehat{\sigma}_2$, $\widehat{\sigma}_3$.

In summary, the analysis presented shows the strong coupling effects between anisotropy and tension–compression asymmetry on yielding of the porous crystal. In the following, we present calculations of the creep response for the same loading orientations, the imposed stress states being given in Table 8.3.

Before proceeding with the presentation of illustrative examples, let us first point out that:

For creep loadings at the same triaxiality and mean stress σ_m, cubic symmetry of the cubic crystal (specially the fact that the $\langle 100\rangle$ directions are equivalent) impose that:

- the response for loadings with $\mu = 1$ (axisymmetric such that $J_3<0$) in the $110\langle O2\rangle$ and $111\langle O1\rangle$ orientations must coincide.
- the response for the $110\langle O1\rangle$ loadings with $\mu = 1$ and 100 loadings with $\mu = 1$ must coincide.

For proof, it is sufficient to represent the imposed stress tensor in the cubic axes $(\mathbf{x},\mathbf{y},\mathbf{z})$. For example, for loadings with $\mu = 1$ (axisymmetric such that $J_3<0$) in the $110\langle O2\rangle$ orientation (i.e., $\boldsymbol{\sigma}=\sigma_1(\mathbf{x_1}\otimes\mathbf{x_1})+\sigma_2(\mathbf{x}_2\otimes\mathbf{x}_2)+\sigma_3(\mathbf{x}_3\otimes\mathbf{x}_3)$ with $s_1 = s_3$ and $s_2 = -2s_1$), the stress tensor in the cubic axes $(\mathbf{x},\mathbf{y},\mathbf{z})$ is given by:

$$\boldsymbol{\sigma}_{\langle 110\rangle} = \begin{bmatrix} -s_1/2+\sigma_m & 3/2\ s_1 & 0 \\ 3/2\ s_1 & -s_1/2+\sigma_m & 0 \\ 0 & 0 & s_1+\sigma_m \end{bmatrix}_{(\mathbf{x},\mathbf{y},\mathbf{z})} \tag{8.101}$$

while for loadings with $\mu = 1$ (axisymmetric such that $J_3 < 0$) in the orientation 111, the stress tensor in the cubic axes is:

$$\boldsymbol{\sigma}_{\langle 111\rangle} = \begin{bmatrix} -s_1/2+\sigma_m & 0 & -3/2\ s_1 \\ 0 & s_1+\sigma_m & 0 \\ -3/2\ s_1 & 0 & -s_1/2+\sigma_m \end{bmatrix}_{(\mathbf{x},\mathbf{y},\mathbf{z})} \tag{8.102}$$

Due to the symmetry of the cubic single crystal (see Chap. 3 for the list of symmetry transformations under which the response is invariant), it follows that the response must coincide.

Illustrative examples of the creep predictions based on the model will be presented in the next section.

8.4.3.2 Combined Effects of Anisotropy and Tension–Compression Asymmetry on Porosity Evolution

The main focus is on assessing the importance of the consideration of the tension–compression asymmetry in the behavior of the matrix, the examples correspond to single crystals with the same anisotropy coefficients, but with $k = -0.3$ (single crystal 1) and $k = 0.3$ (single crystal 2), respectively. The numerical values of the anisotropy coefficients considered in the calculations are: $L_{11} = 1$, $L_{12} = 1.60$ and $L_{44} = 0.25$, resulting in $\Phi_1 = -0.4$ and $\beta = -0.417$. It is important to point out that although the two crystals have the same values of the anisotropy coefficients, in the absence of voids ($f = 0$) their tensile response is not the same. Furthermore, due to the fact that they are characterized by a different value of k, even in the absence of voids, the orientation-dependence of their tension–compression asymmetry ratios is different (see for example Eq. 8.70). The implications in terms of void growth are examined in the following discussion.

Single crystal 1

For this single crystal which is characterized by $k = -0.3$, $L_{11} = 1$, $L_{12} = 1.60$ and $L_{44} = 0.25$, in the absence of voids ($f = 0$), the tension–compression ratio along the direction [100] is $\sigma_{T\langle 100\rangle}/\sigma_{C\langle 100\rangle} = 1.2$ (see Eq. 8.70) while along the directions [110] and [111] it is equal to $\sigma_{T\langle 110\rangle}/\sigma_{C\langle 110\rangle} = 1.06$ and $\sigma_{T\langle 111\rangle}/\sigma_{C\langle 111\rangle} = 0.83$, respectively; the isocontours of the tension–compression ratios along any other direction $\mathbf{d}$ in the basic stereographic triangle are shown in Fig. 8.29.

In the following, we will analyze in detail the model predictions for the evolution of the relative void volume fraction f/f_0 with the plastic work W^I and the evolution

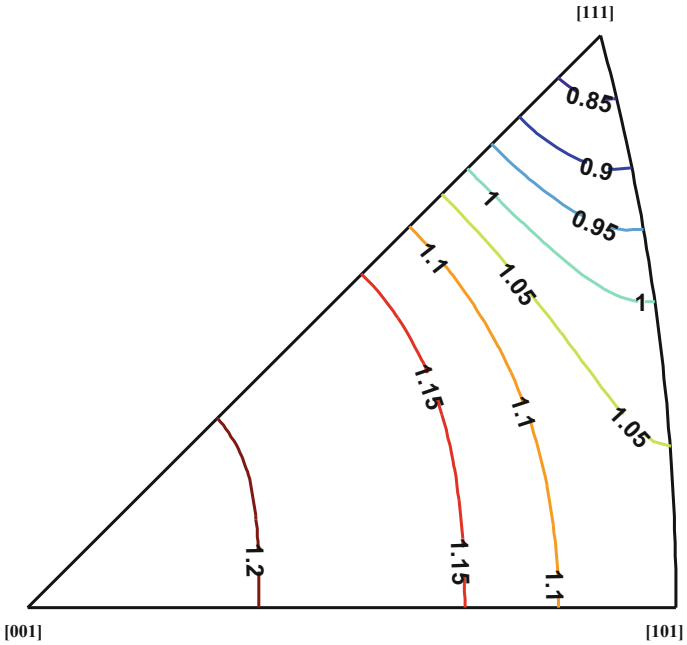

Fig. 8.29 Isocontours in the stereographic triangle of the ratios between the yield stress in uniaxial compression and tension along an arbitrary axis $\mathbf{d}$, $\sigma_{T\langle\mathbf{d}\rangle}/\sigma_{C\langle\mathbf{d}\rangle}$, according to the yield criterion (Eq. 8.78) corresponding to a fully dense ($f = 0$) single crystal with $k = -0.3$, $L_{12} = 1.60$ and $L_{44} = 0.25$

of the irreversible work, W^I with time for all five crystal orientations of the porous crystal and creep loadings corresponding to fixed triaxiality $T = 1$ (see Table 8.3).

First, the model predictions for the 100 crystal orientation subjected to creep corresponding to $\mu = 1$ (axisymmetric such that $J_3 < 0$); $\mu = -1$ (axisymmetric such that $J_3 > 0$) and $\mu = 0$ ($J_3 = 0$) are shown in Fig. 8.30.

As a general observation, consideration of the tension–compression asymmetry of the matrix leads to a sensitivity of porosity evolution to the third-invariant (compare with results in Fig. 8.25 for an fcc crystal with $k = 0$, and same values of the anisotropy coefficients).

As discussed in Sect. 8.4.3.1, for a porous single crystal with $k \neq 0$ the yielding response depends on the third-invariant J_3 (see Eq. 8.95), the maximum difference being between axisymmetric loadings. Since for the single crystal 1, $k = -0.3$, from Eq. (8.95) it follows that the softest response should be for axisymmetric loadings such that $J_3 > 0$. This is consistent with the results shown in Fig. 8.30 which indicate that the fastest rate of void growth is obtained for loading such that $J_3 > 0$, followed by shear loadings, and loadings at $J_3 < 0$. Also, the rate of void growth correlates with the plastic dissipation. Specifically, the fastest growth rate for the porosity corresponds to the loading path for which W^I is the lowest (see Fig. 8.30).

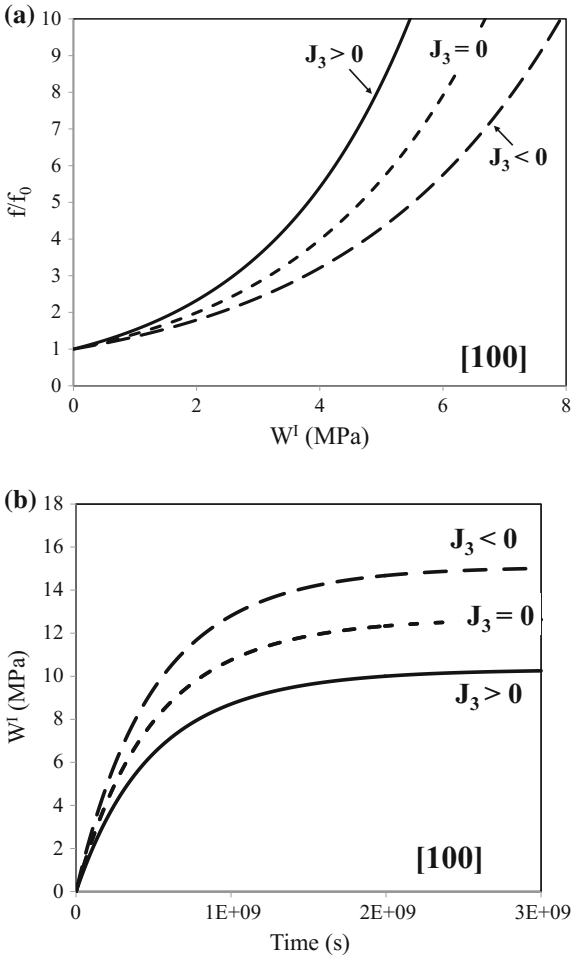

Fig. 8.30 **a** Evolution of the relative void volume fraction f/f_0 as a function of the irreversible work, W^I and **b** evolution of the irreversible work, W^I, with time for creep loadings along the crystallographic axes [100] corresponding to either $J_3 < 0$, $J_3 = 0$, or $J_3 > 0$ and the same triaxiality $T = 1$ for a single crystal characterized by $k = -0.3$, $L_{11} = 1$, $L_{12} = 1.60$ and $L_{44} = 0.25$

As discussed, the effects of the crystal anisotropy are very pronounced for loadings such that the maximum principal stress is along the [110] direction, even if the tension–compression asymmetry is neglected ($k = 0$). Only for [110] loadings at $J_3 > 0$ and [110]⟨O2⟩ loadings at $J_3 < 0$ [see Eqs. (8.84) and (8.88)], the mechanical responses coincide. *For all other loadings, the response in the* ⟨O1⟩ *and* ⟨O2⟩ *orientations is markedly different*, the rate of void growth being the fastest in the ⟨O2⟩ orientation (see Fig. 8.26).

For the single crystal 1, with $k = -0.3$ (see Fig. 8.31) there is a difference in mechanical response between loadings at $J_3 > 0$ and loadings at $J_3 < 0$ in the ⟨O2⟩ orientation. The fastest and slowest rate of void growth correspond to shear loadings in the ⟨O2⟩ orientation, and loading such that $J_3 < 0$ in the ⟨O1⟩ orientation, respectively. Moreover, the rate of void growth is faster for loadings at $J_3 > 0$ than for loadings at $J_3 < 0$ in the ⟨O2⟩ orientation.

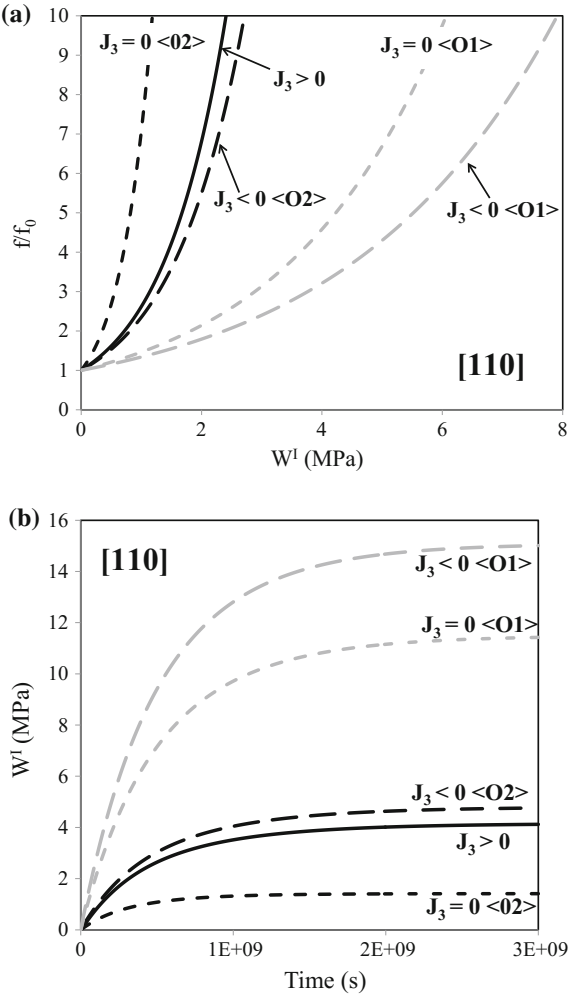

Fig. 8.31 **a** Evolution of the relative void volume fraction f/f_0 as a function of the irreversible work, W^I and **b** evolution of the irreversible work, W^I, with time for creep loadings with maximum principal value along the [110] direction corresponding to either $J_3 < 0$, $J_3 = 0$, or $J_3 > 0$ and the same triaxiality $T = 1$ for a single crystal characterized by $k = -0.3$, $L_{11} = 1$, $L_{12} = 1.60$ and $L_{44} = 0.25$

Figure 8.32 shows the evolution of the plastic work and relative porosity for the 111 crystal orientations for the various creep loadings Note that consideration of the tension–compression asymmetry leads to prediction of a difference in response between the $111\langle O1\rangle$ and $111\langle O2\rangle$ crystal orientations, for a crystal with $k = -0.3$ the void growth rate being faster for the primary crystal orientation O1 than for the orientation O2. In contrast, when the tension–compression asymmetry is neglected for all three values of the Lode parameter the response in the $111\langle O1\rangle$ and $111\langle O2\rangle$ crystal orientations coincide (see Eq. (8.91) and Fig. 8.27 for $k = 0$).

As seen from Eqs. (8.96) and (8.100) for the single crystal 1, the softest response correspond to $J_3 > 0$, followed by loadings at $J_3 = 0\langle O1\rangle$, then $J_3 = 0\langle O2\rangle$ and $J_3 < 0\langle O1\rangle$ and finally $J_3 < 0\langle O2\rangle$. This is consistent with the results of Fig. 8.32,

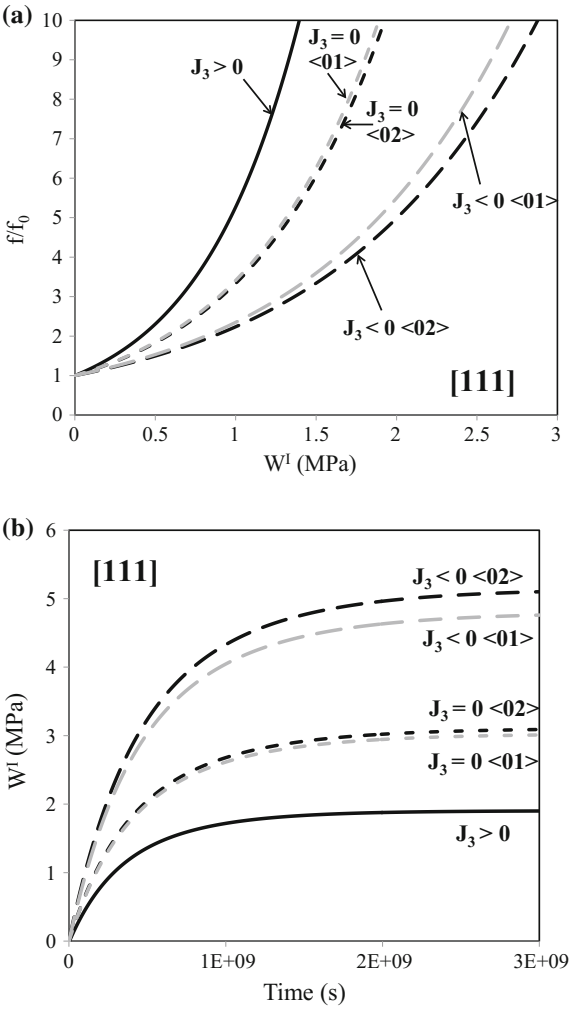

Fig. 8.32 **a** Evolution of the relative void volume fraction f/f_0 as a function of the irreversible work, W^I and **b** evolution of the irreversible work, W^I with time for creep loadings with maximum principal value along the [110] direction corresponding to either $J_3 < 0$, $J_3 = 0$, or $J_3 > 0$ and the same triaxiality $T = 1$ for a single crystal characterized by $k = -0.3$, $L_{11} = 1$, $L_{12} = 1.60$ and $L_{44} = 0.25$

the fastest growth rate of the porosity being for loadings corresponding to $J_3 > 0$, followed by loadings at $J_3 = 0\langle O1\rangle$, then $J_3 = 0\langle O2\rangle$ and $J_3 < 0\langle O1\rangle$, while the slowest rate of void growth is for loadings corresponding to $J_3 < 0\langle O2\rangle$.

Figure 8.33 compares the evolution of the porosity with W^I between all five crystallographic orientations (i.e., 100, 110, and 111) for all the loadings at the same triaxiality $T = 1$ considered (see Table 8.3). As in the case when the tension–compression asymmetry of the matrix was neglected (see results for the fcc single crystal with $k = 0$ in Fig. 8.28), the strong anisotropy of the crystal results in the mechanical response being markedly different in the 100, 110, and 111 crystal orientations. However, for the fcc single crystal ($k = 0$) for certain orientations and

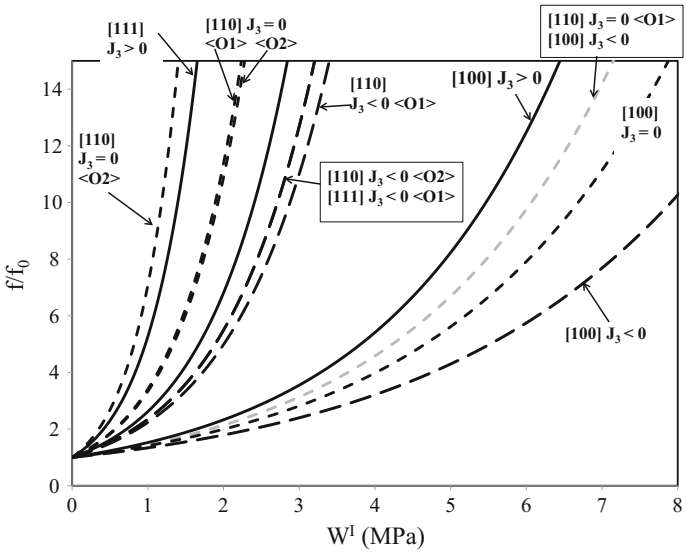

Fig. 8.33 Effect of crystal orientation on porosity evolution for creep loadings corresponding to either $J_3 < 0$, $J_3 = 0$ (shear), or $J_3 > 0$ and the same triaxiality $T = 1$ for a single crystal characterized by $k = -0.3$, $L_{11} = 1$, $L_{12} = 1.60$ and $L_{44} = 0.25$

loadings the creep response coincide (see discussion in Sect. 8.4.2.1 and compare the results of Fig. 8.33 to the results of Fig. 8.28 for $k = 0$).

On the other hand, for a single crystal displaying tension–compression asymmetry the only loadings for which the mechanical response coincide are the ones imposed by the intrinsic symmetries of the crystal lattice (see discussion in Sect. 8.4.3.1).

For all other loadings, the rate of void growth is totally dependent on the loading orientation and the relative ordering of the eigenstresses (see Fig. 8.33). Moreover, consideration of the tension–compression asymmetry in the plastic behavior of the single crystal results in a larger difference in the creep response between various conditions (compare results in Figs. 8.28 and 8.33, respectively).

Single crystal 2

The fact that the sensitivity of the mechanical response to the third-invariant depends on the combined effects of anisotropy and tension–compression asymmetry is clearly seen by comparing the void evolution in single crystal 1 with the void evolution in the single crystal 2. As mentioned in the absence of voids, the single crystal 2 has a completely different behavior in compression than single crystal 1 (see the isocontours of the ratio between the uniaxial compressive and tensile yield stresses represented in the basic stereographic triangle in Fig. 8.34).

For this single crystal which is characterized by $k = 0.3$, $L_{11} = 1$, $L_{12} = 1.60$ and $L_{44} = 0.25$, in the absence of voids ($f = 0$), the tension–compression ratio

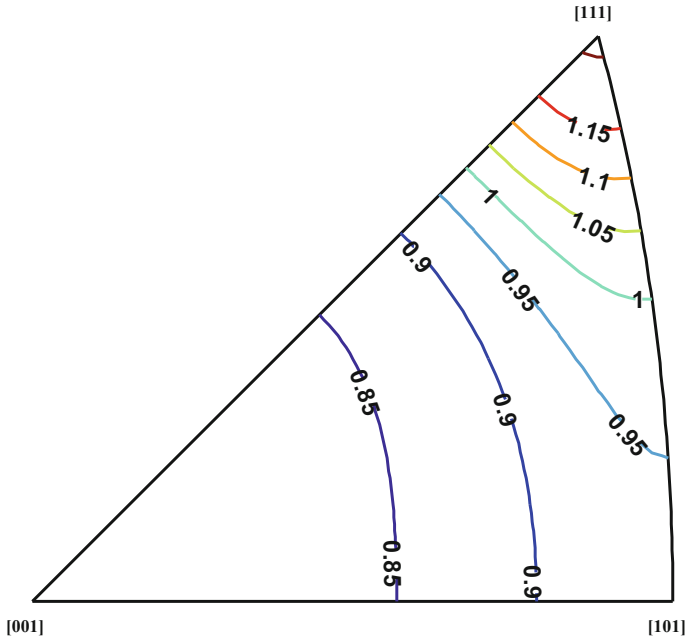

Fig. 8.34 Isocontours in the stereographic triangle of the ratios between the yield stress in uniaxial compression and tension along an arbitrary axis **d**, $\sigma_{T\langle \mathbf{d}\rangle}/\sigma_{C\langle \mathbf{d}\rangle}$ for a fully dense crystal with $k = 0.3$, $L_{12} = 1.60$, $L_{44} = 0.25$

along the direction [100] is $\sigma_{T\langle 100\rangle}/\sigma_{C\langle 100\rangle} = 0.83$ (see Eq. 8.70) while along the directions [110] and [111] it is equal to $\sigma_{T\langle 110\rangle}/\sigma_{C\langle 110\rangle} = 0.94$ and $\sigma_{T\langle 111\rangle}/\sigma_{C\langle 111\rangle} = 1.2$, respectively.

As discussed in Sect. 8.4.3.1, for a porous single crystal with $k \neq 0$ the yielding response for loadings along the cubic axes $\langle 100\rangle$ depends on the third-invariant J_3, the maximum difference being between axisymmetric loadings. Moreover, the rate of void growth is dictated by the ratio between the matrix (fully dense crystal) tensile and compressive yield stresses in the $\langle 100\rangle$ directions. Since for the single crystal 2, $\sigma_{T\langle 100\rangle}/\sigma_{\langle 100\rangle} < 1$, from Eq. (8.95) it follows that the mechanical response should be exactly the opposite to that of single crystal 1 for which $\sigma_{T\langle 100\rangle}/\sigma_{C\langle 100\rangle} > 1$. This is consistent with the results shown in Fig. 8.35 which indicate that for single crystal 2 the fastest rate of void growth is obtained for axisymmetric loadings such that $J_3 < 0$, followed by shear loadings, and axisymmetric loadings at $J_3 > 0$. Also, as seen from Eq. (8.95) the void growth rate in shear should be always intermediate.

For the single crystal 1, for loadings such that the principal stress value is along the [110] crystallographic direction, the creep response is strongly anisotropic and the rate of void growth is faster for the $110\langle O2\rangle$ than for $110\langle O1\rangle$, irrespective of the loadings, and the fastest rate of void growth is for loadings corresponding to

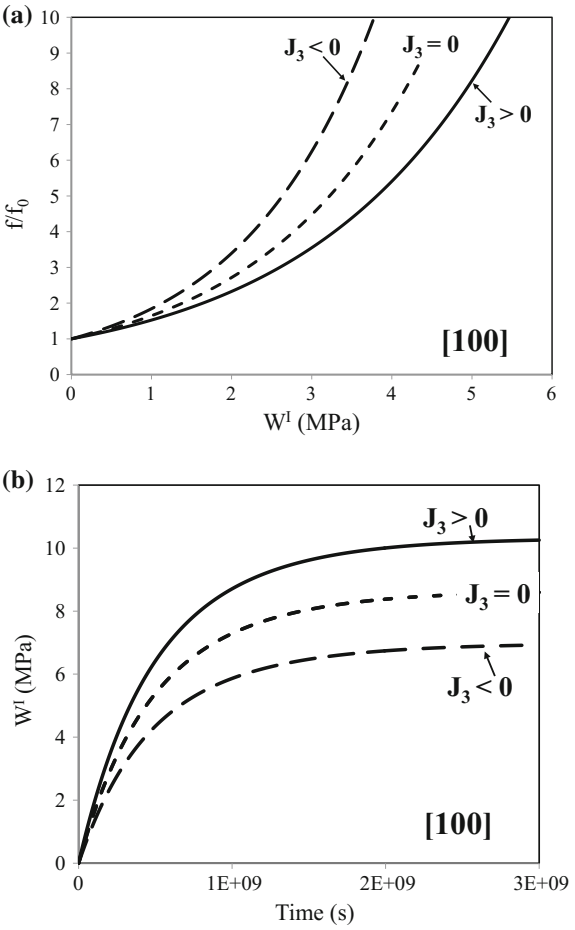

Fig. 8.35 **a** Evolution of the relative void volume fraction f/f_0 as a function of the irreversible work, W^I and **b** evolution of the irreversible work, W^I, with time for creep loadings along the crystallographic axes [100] corresponding to either $J_3 < 0$, $J_3 = 0$, or $J_3 > 0$ and the same triaxiality $T = 1$ for a single crystal characterized by $k = 0.3$, $L_{11} = 1$, $L_{12} = 1.60$ and $L_{44} = 0.25$

$J_3 = 0$ (shear) in the secondary orientation $\langle O2 \rangle$, while the slowest rate of void growth corresponds to loadings at $J_3 < 0 \langle O1 \rangle$ (see Fig. 8.31). The results for the single crystal 2 for the same crystal orientation and loadings are shown in Fig. 8.36.

The difference in response between axisymmetric loadings at $J_3 > 0$ and axisymmetric loadings at $J_3 < 0 \langle O2 \rangle$ can be correlated with the matrix tension–compression ratio in the [110] crystallographic direction. For the single crystal 2 $\sigma_{T\langle 110 \rangle} / \sigma_{C\langle 110 \rangle} < 1$ while for the single crystal 1 this ratio is greater than unity. By comparing the response of the single crystal 1(see Fig. 8.31) with that of the single crystal 2 (see Fig. 8.36) for the same loadings, it can be seen that in single crystal 2 the void growth rate for $J_3 > 0$ is slower than the one for $J_3 < 0 \langle O2 \rangle$ loadings while the reverse holds true for the single crystal 1 (see Fig. 8.36).

Concerning the creep response for the 111 crystal orientation (see Fig. 8.37), as previously seen, the fastest void growth is obtained for loadings at $J_3 > 0$, and

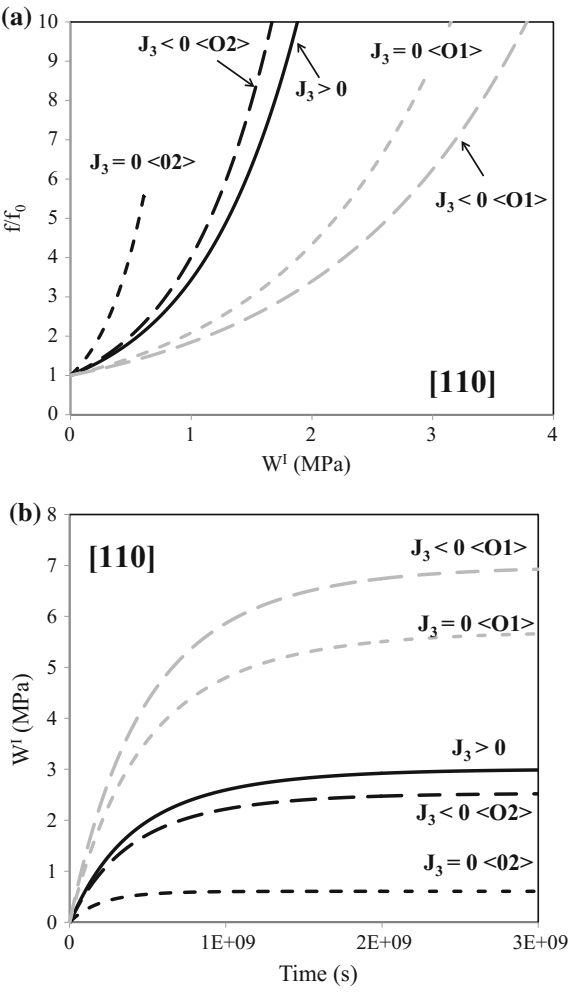

Fig. 8.36 **a** Evolution of the relative void volume fraction f/f_0 as a function of the irreversible work, W^I and **b** evolution of the irreversible work, W^I, with time for creep loadings with maximum principal value along [110] corresponding to either $J_3 < 0$, $J_3 = 0$, or $J_3 > 0$ and the same triaxiality $T = 1$ for a single crystal characterized by $k = 0.3$, $L_{11} = 1$, $L_{12} = 1.60$ and $L_{44} = 0.25$

consideration of the tension–compression asymmetry of the single crystal matrix results in different mechanical response for the $\langle O1 \rangle$ and $\langle O2 \rangle$ orientations. Comparison between the void evolution in single crystal 1 and single crystal 2 (see Figs. 8.32 and 8.37, respectively) shows that depending on whether the matrix has $\sigma_{T\langle 111\rangle}/\sigma_{C\langle 111\rangle} > 1$ (single crystal 2) or $\sigma_{T\langle 111\rangle}/\sigma_{C\langle 111\rangle} < 1$ (single crystal 1), the void evolution rate is faster for the secondary orientation $\langle O2 \rangle$ than for the primary orientation $\langle O1 \rangle$, or vice versa.

For the single crystal 2, the predictions of the model for all five crystallographic orientations and for all creep loadings considered are plotted in Fig. 8.38. Let us recall that in order to assess the importance of the consideration of the matrix tension–compression asymmetry we have done calculations for two single crystals, both crystals having $L_{11} = 1$, $L_{12} = 1.60$ and $L_{44} = 0.25$.

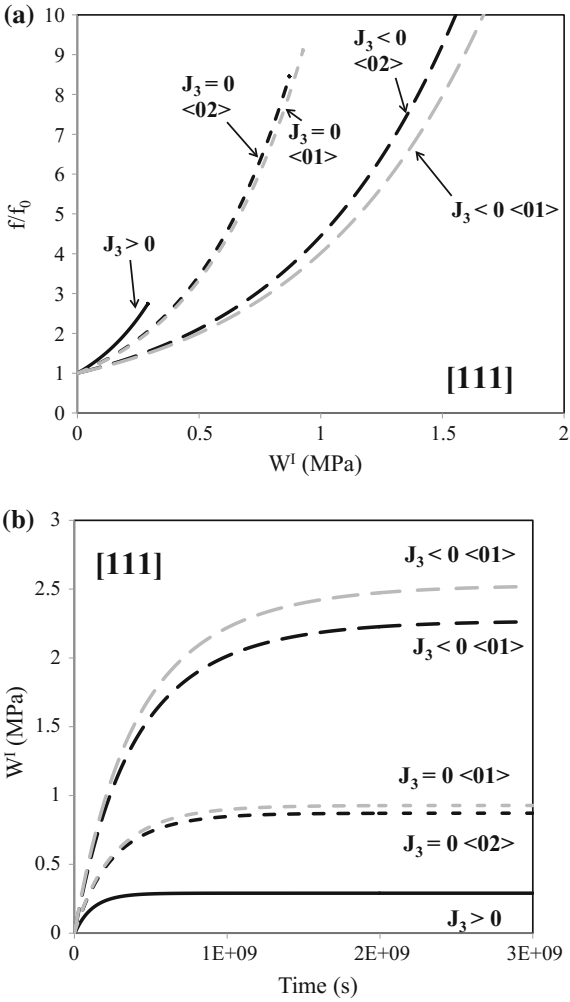

Fig. 8.37 **a** Evolution of the relative void volume fraction f/f_0 as a function of the irreversible work, W^I and **b** evolution of the irreversible work, W^I, with time for creep loadings with maximum principal value along the axis [111] corresponding to either $J_3 < 0$, $J_3 = 0$, or $J_3 > 0$ and the same triaxiality $T = 1$ for a single crystal characterized by $k = 0.3$, $L_{11} = 1$, $L_{12} = 1.60$ and $L_{44} = 0.25$

Comparison between the results for single crystal 1 (Fig. 8.33) and single crystal 2 (Fig. 8.38) shows the very strong influence of the plastic properties of the matrix (fully dense crystal) on the porosity evolution, namely the effect of the contrast between the tension–compression asymmetry ratios along crystal directions. To predict for which loading the rate of void growth is the fastest, knowledge of only the anisotropy in tensile properties of the matrix is not sufficient.

Note that for the crystal characterized by $k = 0.3$, the fastest growth rate for the porosity is obtained for axisymmetric loadings with maximum principal stress along the 111 crystallographic direction (denoted $[111]J_3 > 0$) and the slowest growth rate for axisymmetric loadings with maximum principal stress along the [100] cubic axis (denoted $[100]J_3 > 0$) (see Fig. 8.38). On the other hand, for a single crystal

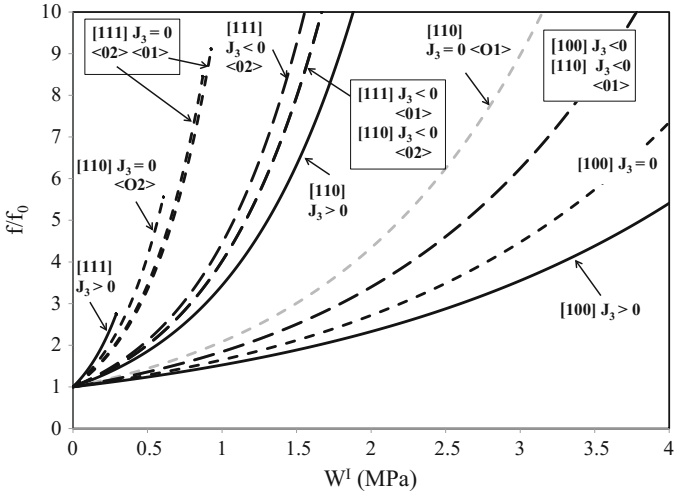

Fig. 8.38 Effect of crystal orientation on porosity evolution for creep loadings corresponding to either $J_3 < 0$, $J_3 = 0$ (shear), or $J_3 > 0$ and the same triaxiality $T = 1$ for a single crystal characterized by $k = 0.3$, $L_{11} = 1$, $L_{12} = 1.60$ and $L_{44} = 0.25$

characterized by $k = -0.3$, among all creep loadings considered the fastest growth rate occurs for shear loadings in the $[111]J_3 = 0\langle O2\rangle$ and the slowest growth rate occurs for axisymmetric loadings with minimum principal stress along the [001] cubic axis (denoted $[100]J_3 < 0$ loading) (see Fig. 8.33).

In summary, neglecting the tension–compression asymmetry of the fully dense single crystal leads to nearly isotropic predictions of the creep response for loadings with principal axes of stresses aligned with the $\langle 100\rangle$ crystallographic directions, and a lack of sensitivity to the loading path (for the same triaxiality and mean stress, no effect of the Lode parameter). If the tension–compression asymmetry of the matrix is taken into consideration, the model predicts a difference in mechanical response between secondary orientations. Most importantly, consideration of the tension–compression asymmetry of the matrix revealed that the manner in which the void growth rate accumulates under multiaxial creep is strongly dependent on both the anisotropy and the tension–compression asymmetry of the material.

References

1. Abramoff MD, Magalhaes PJ, Ram SJ (2004) Image processing with ImageJ. Biophotonics Int 11:36–42
2. Argon AS, Im J, Safoglu R (1975) Cavity formation from inclusions in ductile fracture. Metall Trans A 6:825. https://doi.org/10.1007/BF02672306
3. Asaro RJ, Needleman A (1985) Overview no. 42. Texture development and strain hardening in rate dependent polycrystals. Acta Metall 33:923–953

4. Benzerga AA, Besson J (2001) Plastic potentials for anisotropic porous solids. Eur J Mech ASolids 20:397–434. https://doi.org/10.1016/S0997-7538(01)01147-0
5. Cazacu O, Plunkett B, Barlat F (2006) Orthotropic yield criterion for hexagonal closed packed metals. Int J Plast 22:1171–1194
6. Cazacu O, Stewart JB (2009) Analytic plastic potential for porous aggregates with matrix exhibiting tension–compression asymmetry. J Mech Phys Solids 57:325–341
7. Chu CC, Needleman A (1980) Void nucleation effects in biaxially stretched sheets. J Eng Mater Technol ASME 102:249–256
8. Cristescu N (1967) Dynamic plasticity. North Holland Publishing Company, Amsterdam
9. Cristescu N (1989) Rock rheology. Kluwer Academic Publishers, USA
10. Gurland J (1972) Observations on the fracture of cementite particles in a spheroidized 1.05% c steel deformed at room temperature. Acta Metall 20:735–741. https://doi.org/10.1016/0001-6160(72)90102-2
11. Gurson AL (1975) Plastic flow and fracture behavior of ductile materials incorporating void nucleation, growth and coalescence. Ph.D. dissertation, Brown University
12. Gurson AL (1977) Continuum theory of ductile rupture by void nucleation and growth: part I—yield criteria and flow rules for porous ductile media. J Eng Mater Technol 99:2–15
13. Hill R (1948) A theory of the yielding and plastic flow of anisotropic metals. Proc R Soc Lond A Math Phys Eng Sci 193(1033):281–297
14. Huez J, Helbert A, Feaugas X, Guillot I, Clavel M (1998) Damage process in commercially pure α-titanium alloy without (Ti40) and with (Ti40-H) hydrides. Metall Mater Trans A 29:1615–1628
15. Jia Y, Bai Y (2016) Experimental study on the mechanical properties of AZ31B-H24 magnesium alloy sheets under various loading conditions. Int J Fract 197:25–48
16. Lebensohn R, Idiart M, Castañeda PP, Vincent P-G (2011) Dilatational viscoplasticity of polycrystalline solids with intergranular cavities. Philos Mag 91:3038–3067
17. Lebensohn RA, Cazacu O (2012) Effect of single-crystal plastic deformation mechanisms on the dilatational plastic response of porous polycrystals. Int J Solids Struct 49:3838–3852
18. Liu D, Zhang D, Liang J, Wen Z, Yue Z (2014) Prediction of creep rupture life of a V-notched bar in DD6 Ni-based single crystal superalloy. Mater Sci Eng A 615:14–21
19. Monchiet V, Cazacu O, Charkaluk E, Kondo D (2008) Macroscopic yield criteria for plastic anisotropic materials containing spheroidal voids. Int J Plast 24:1158–1189
20. Pan J, Saje M, Needleman A (1983) Localization of deformation in rate sensitive porous plastic solids. Int J Fract 21:261–278
21. Perzyna P (1966) Fundamental problems in viscoplasticity. In: Advances in applied mechanics. Elsevier, New York, pp 243–377
22. Pushkareva M, Adrien J, Maire E, Segurado J, Llorca J, Weck A (2016) Three-dimensional investigation of grain orientation effects on void growth in commercially pure titanium. Mater Sci Eng A 671:221–232
23. Rasband WS (1997) ImageJ. U. S. National Institutes of Health, Bethesda, Maryland, USA. https://imagej.nih.gov/ij/
24. Revil-Baudard B (2010) Simulation du comportement mécanique des alliages de titane pour les procédés de mise en forme à froid. Ph.D. thesis, École Nationale Supérieure des Mines de Paris
25. Revil-Baudard B, Cazacu O (2013) On the effect of the matrix tension–compression asymmetry on damage evolution in porous plastic solids. Eur J Mech ASolids 37:35–44
26. Revil-Baudard B, Cazacu O, Flater P, Chandola N, Alves JL (2016) Unusual plastic deformation and damage features in titanium: experimental tests and constitutive modeling. J Mech Phys Solids 88:100–122
27. Rice JR, Tracey DM (1969) On the ductile enlargement of voids in triaxial stress fields. J Mech Phys Solids 17:201–217
28. Schneider CA, Rasband WS, Eliceiri KW (2012) NIH image to ImageJ: 25 years of image analysis. Nat Methods 9:671

29. Srivastava A, Needleman A (2012) Porosity evolution in a creeping single crystal. Model Simul Mater Sci Eng 20:035010
30. Srivastava A, Needleman A (2015) Effect of crystal orientation on porosity evolution in a creeping single crystal. Mech Mater 90:10–29
31. Srivastava A, Revil-Baudard B, Cazacu O, Needleman A (2017) A model for creep of porous crystals with cubic symmetry. Int J Solids Struct 110:67–79
32. Stewart JB, Cazacu O (2011) Analytical yield criterion for an anisotropic material containing spherical voids and exhibiting tension–compression asymmetry. Int J Solids Struct 48: 357–373